REACTION KINETICS AND STRUCTURAL EVOLUTION FOR THE FORMATION OF NANOCRYSTALLINE SILICON CARBIDE VIA CARBOTHERMAL REDUCTION

A Thesis
Presented to
The Academic Faculty

by

Zhe Cheng

In Partial Fulfillment
Of the Requirements for the Degree
Master of Science in Materials Science and Engineering

Georgia Institute of Technology
November 2004

REACTION KENETICS AND STRUCTURAL EVOLUTION FOR THE FORMATION OF NANOCRYSTALLINE SILICON CARBIDE VIA CARBOTHERMAL REDUCTION

Approved by:

Michael D. Sacks, Advisor
School of Materials Science and Engineering

Joe K. Cochran
School of Materials Science and Engineering

Thomas H. Sanders
School of Materials Science and Engineering

Date Approved: November 2004

ACKNOWLEDGEMENT

I would like to thank my advisor, Dr. Michael D. Sacks, for his guidance, support, and help in the past years. I greatly appreciate the enormous efforts that Dr. Sacks made to help me finish the thesis. As the thesis gradually takes its shape, I realize how much I have obtained from writing it and how precious such an experience is to me. Thanks to Dr. Joe. Cochran and Dr. Thomas H. Sanders for serving on my thesis reading committee and their kindly advice in the past year. I would also like to thank Dr. Chang-an Wang, Dr. Zhaohui Yang, and Mr. Greg A. Staab for assistance with experimental methods and for helpful discussions. I would like to express my gratitude to my wife, Shujia Mei, for her love, understanding, encouragement, and support in the process of writing this thesis. Funding of this research was provided by AFOSR grant No. F49620-01-1-0112.

TABLE OF CONTENTS

LIST OF TABLES

LIST OF FIGURES

SUMMARY

Nanocrystalline beta silicon carbide (β-SiC) was synthesized at relatively low temperature (<1300°C) by carbothermal reduction (CTR) reactions in carbon/silica reactant mixtures. Fine-scale mixing of the reactants was achieved by using solution-based processing and a subsequent pyrolysis heat treatment. A reactant mixture with C/Si molar ratio of 2.4 was transformed almost completely to β-SiC with average crystallite size <25 nm by heat treatment at 1300°C for 16 h.

The CTR reaction mechanism was investigated using several experimental methods. First, the condensates of the volatile species generated during the CTR reaction were collected and analyzed. The results supported previous investigations which suggested that the CTR reaction was a multi-step process that involved silicon monoxide (SiO) vapor as a reaction intermediate. Second, the isothermal kinetics of the CTR reaction were investigated for reactant mixtures with C/Si molar ratios of 2.4 and 4.6. The reaction rates were determined by weight loss measurements and quantitative X-ray diffraction (QXRD) analysis of the amounts of SiC formed. The reaction kinetics showed the best fit to a "shrinking-core" model in which an interfacial reaction was the rate-controlling step. Higher reaction rates were observed for the samples prepared with the higher C/Si ratio. Third, structural evolution of the CTR reaction product was investigated using the following characterization techniques: Scherrer analysis of XRD data to determine SiC crystallite sizes; gas adsorption analysis to determine specific surface area, specific pore volume, and pore size distribution; light scattering to determine particle size distributions; and scanning and transmission electron microscopies (SEM, TEM, HRTEM) to observe powder

microstructural features. The characterization results were consistent with the interface-controlled "shrinking-core" reaction model. In combination with the kinetic data, the available evidence suggested that the reaction between SiO vapor and carbon (at the carbon surfaces) was the rate-controlling step for the overall CTR reaction. The structural characterization study also showed that the starting materials used for the CTR reaction (i.e., the pyrolyzed carbon/silica reactant mixtures) had a hierarchical structure. The relatively large pyrolyzed particles (mostly in the size range of ~10-200 μm) were composed of densely-packed small "clusters" (mostly in the size range of ~50 - 500 nm). The clusters were apparently composed of nearly-dense, nano-scale, interpenetrating networks of carbon and silica. The CTR reaction occurred initially at cluster-cluster interfaces and each cluster was a unit for the "shrinking-core" reaction.

CHAPTER I

INTRODUCTION

Silicon carbide (SiC) exists in two basic forms: α-SiC and β-SiC. α-SiC has a hexagonal structure, while β-SiC belongs to the cubic family with a ZnS structure. SiC has desirable mechanical and thermal properties which make it widely used as a structural material. SiC is also a semiconductor with wide band gap and high saturation electron drift velocity. It may be fabricated into electronic device for applications in harsh environment, or in the high power, high frequency territory (Parill, 1991).

The primary industrial method for producing SiC is by the Acheson process, which involves the carbothermal reduction (CTR) of silica and carbon using coarse powder mixtures. This process requires high temperature and the resulting SiC product must undergo grinding and purification steps to produce powders that are suitable for technical ceramics (Guichelaar, 1997). In the last twenty years, several methods have been developed to prepare SiC by using starting materials that allow for a finer scale of mixing of the silica and carbon reactants. Among them, solution-based processing routes are of particular interest because they are capable of producing fine-grained SiC powders, fibers, and films at much lower temperature. However, there are relatively few studies that were focused on understanding the mechanism of the carbothermal reduction using powders prepared by solution-based processing. Furthermore, there have been no detailed studies in which such materials were used to simultaneously determine the reaction kinetics, identify the volatile species produced, and characterize the microstructure evolution during the carbothermal reduction reaction process.

The objective of this research was to understand the reaction mechanism of nanocrystalline SiC formation via carbothermal reduction in the fine-scale carbon/silica mixtures. To achieve the objective, a solution-based synthesis method was employed in the current study to obtain a fine-scale mixing of the reactants (i.e., carbon and silica). The CTR reaction mechanism was investigated through analyzing the volatile condensates generated during the reaction, determining the reaction kinetics, and characterizing the structural evolution that occurred in the reaction product. The reaction kinetics was investigated by measuring the weight change of the sample before and after the reaction and by measuring the amount of SiC formed in the product (via quantitative X-ray diffraction (QXRD) analysis). Various techniques such as XRD, gas adsorption analysis, light diffraction particle size analysis, SEM and TEM, etc. were adopted to characterize the structure development during the reaction.

In this thesis, Chapter II reviews previous investigations of the synthesis of SiC and the mechanisms of SiC formation via carbothermal reduction reactions. In Chapter III, the experimental procedures and some of the data handling protocols are described. Chapter IV presents the experimental results for the characterization of volatile condensates, reaction kinetics, and characterization of the CTR reaction product. A comprehensive reaction model is proposed and the relationships between the reaction kinetics and the structural development are discussed. In Chapter V, conclusions are drawn concerning the mechanism of SiC formation via carbothermal reduction for the material system used in this study. Some recommendations for future research in this area are also made.

CHAPTER II

BACKGROUND

2.1 Synthesis of Nanocrystalline SiC through Carbothermal Reduction

The primary method to synthesize SiC is by carbothermal reduction reaction, i.e., carbon reacts with silica (SiO_2) to produce SiC and carbon monoxide (CO) gas. The chemical equation for this reaction is commonly written as:

$$SiO_{2\,(s)} + 3C_{\,(s)} \rightarrow SiC_{\,(s)} + 2CO_{\,(g)} \qquad (2\text{-}1\text{-}1)$$

There are various processing methods to obtain carbon/silica mixtures (which are used for the carbothermal reduction reaction) with different scales of mixing. Depending on the nature of the reactants, those processing methods can usually be grouped into four categories which will be briefly reviewed below.

1. The reactants are physical mixtures of distinct powders of silica (or silica-bearing material) and carbon (or carbon-bearing material).

Carbon (or carbon-bearing material) and silica (or silica-bearing material) powders are physically mixed together and heat treated to produce SiC. Depending on the size of the particles, the mixing scale ranges from submicron to several tens or hundreds of micron.

The Acheson process is a typical synthesis method within this category and is also the prevailing method in industrial production of SiC. The raw materials used in the Acheson process are usually very coarse: graphite or petroleum coke is used as the carbon source and silica sand or quartz is used as the silica source. The carbon-bearing and silica-bearing powders are mixed. A graphite core is placed in the center of the

carbon/silica powder mixture. The graphite core serves as an electrode and heating element. High temperatures (> 2000^{o}C) are generated when an electric current is passed through the graphite core. This causes the carbon to react with silica, thereby resulting in the formation of a hollow cylinder of SiC and the volatilization of CO.

Although the Acheson process has disadvantages, such as high reaction temperature, coarse product grain size, low product purity and high energy input, it has been the dominant mass production method for more than a hundred years due to the relatively low cost and simplicity of operation. Specifically, the advantages of the Acheson process include: (1) The process utilizes raw materials which are cheap and available in large quantities. (2) The process has inherent thermal efficiency from the internal joule heating. (3) Complex equipment is not needed to obtain the high temperature used in the process. (4) An inert atmosphere is not required during the reaction. The process involves using a large excess amount of carbon. Some of the carbon near the outside region of the carbon/silica mixture will be oxidized. However, a low P_{O2} is maintained throughout much of the interior of the mixture due to the large concentrations of CO/CO_2 that are generated during the reaction. (5) The composition gradient that develops from the graphite core to the outside of the powder batch (which is a result of the radial temperature gradient) also makes it easy to collect the product (Guichelaar, 1997).

In addition to coarse powder mixtures, such as in the Acheson process, mixtures of finer carbon and/or silica powders are also used to synthesize SiC. In this case, one or both of the reactants have high specific surface area and small (e.g., submicron) particle sizes. For example, carbon black or activated carbon may be used as carbon sources,

while colloidal silica or fumed silica may be used as silica sources. By this means, the reaction temperature is usually reduced and SiC with finer particle size may be obtained because the scale of mixing is reduced as compared to mixtures prepared with the coarse powders. For example, Krstic (1992) mixed carbon black (mean particle size < 0.2 μm) and silica (mean particle size < 40 μm) and obtained submicron SiC by using heat treatments at 1400-1800°C in vacuum. Čerovič et al. (1995) prepared a mixture from colloidal SiO_2 suspension (mean crystallite size of 18 nm) and activated carbon (specific surface area 960 m^2/g). The mixture was heat treated at 1550°C for 3 h and SiC with submicrometer particle size was produced. Seo et al. (1998) obtained SiC with crystallite size of ~100 nm by heat treating a mixture of silica (mean particle size of 0.8 μm) and carbon black (mean crystallite size of 40-100 nm) at 1420°C for less than 30 min.

However, there may be problems when mixtures are prepared from raw materials with fine particle sizes. First, the scale of mixing may still be large (e.g., ≥ 1 μm) even though fine particles (≤ 1 μm) are used. This is because the fine powders usually form some aggregates which are composed of primary particles. As a result, the actual mixing scale is determined by the size of those aggregates. Second, the SiC product may have a mixed morphology of equiaxed particles and acicular "whiskers" (Čerovič et al. (1995) and Seo et al. (1998)). Third, the product may contain a significant amount of unreacted carbon and/or silica due to the large scale of mixing and local compositional inhomogeneity in the mixture.

2. The reactants are liquid mixtures in which both silicon-bearing and carbon-bearing materials are in liquid form or are solubilized in a liquid.

Carbon-bearing materials (e.g., sugar, phenolic resin, etc.) and silica-bearing materials (e.g., tetraethoxysilane (TEOS), methyltrimethoxysilane (MTMS), etc.) are both dissolved in a solvent (usually ethanol) and form a homogeneous solution. (Precipitation into distinct particles may occur at some later stage in processing.) The mixed solution is processed to obtain a gel via methods such as solvent removal, freeze drying, chemical gelation, thermal gelation, etc. The gel is then heat treated at ~800-1100^{o}C in inert atmosphere to remove the volatile species and produce a fine-scale carbon/silica mixture. (This type of heat treatment is referred to as "pyrolysis" in this thesis.) The fine scale carbon/silica mixture is then heat treated again to produce SiC by carbothermal reduction reactions.

Tanaka and Kurachi (1988) used tetraethoxysilane (TEOS) and phenolic resin to produce SiC. Toluenesulfonic acid and water were added to promote hydrolysis/condensation and polymerization reactions. A gel product was pyrolyzed at 1000^{o}C for 2 h in nitrogen to produce an amorphous carbon/silica mixture. The pyrolyzed material was heat treated at temperatures in the range of 1500 to 1800^{o}C for 30 min to produce SiC by carbothermal reduction reactions. The SiC product had submicron grain size (the crystallite size depends on the heat treatment temperature) and high purity (without much excess carbon or silica). Similar starting materials (i.e., TEOS/phenolic resin) were used by Hasegawa et al. (1995), Raman et al. (1995), Ono and Kurachi (1991), Huang et al. (1998), Narisawa et al. (1998), Li et al. (2000). The main differences were concentrations of the reactants (water, TEOS, phenolic resin) and the type and amount of acid used in the process. Raman et al. (1995) also prepared SiC using mixed solutions of TEOS and ethycellulose, or monomethyl-triethoxysilane

(MTES) and ethycellulose. Meng et al. (2000) prepared SiC using a mixed solution of TEOS and saccharose.

The major advantage of solution-based methods is that carbon-bearing and silica-bearing precursors are mixed on the molecular scale. Subsequent processing (solvent removal, pyrolysis, etc.) may result in some segregation of the components such that the scale of mixing is no longer molecular. However, the silica/carbon mixtures produced by solution methods are generally more intimately mixed compared to batches prepared by mixing of distinct powders. Finer-scale mixing of the reactants means that chemical inter-diffusion distances will be shorter and the interfacial contact area between the reactants will be higher. As a result, the reaction rates will be higher if other factors (i.e., temperature, atmosphere, etc.) are kept the same. The resulting SiC product usually has smaller crystallite sizes and the powders may also be less aggregated. Hence, the powders usually require less milling (grinding). Another advantage of solution-based methods is that high-purity SiC can be produced if the starting materials are high purity. The major disadvantage of solution-based methods is that processing costs tend to be high. Although many soluble carbon precursors are inexpensive (e.g., phenolic resin, sugar, etc.), solution-based silica sources are invariably much more expensive than powders such as sand. Furthermore, the use of inert atmosphere furnaces also drives the cost higher.

3. Hybrid mixtures are used in which one reactant is in particulate form while the other reactant is either a liquid or is solubilized to form a liquid precursor solution.

As an example, the particulate component may be colloidal silica, while the soluble component may be sugar or a carbon-bearing polymer (or oligmer). Wei et al.

(1984) prepared SiC by mixing a colloidal SiO_2 suspension (mean crystallite size of 14 nm) and either a sucrose or a phenolic resin solution. The mixture was freeze dried and then heat treated to convert the sugar or resin to carbon. The silica/carbon mixture was then heat treated in argon at a temperature of 1600°C for 4-16 h. The SiC product had crystallite sizes of ~10-20 nm and aggregate sizes of ~1 μm. Čerovič et al. (1995) and Martin et al. (1998) obtained similar results using similar starting materials.

The method based on using particulate/liquid hybrid mixtures has some of the advantages of the mixed solution method, such as better mixing of the carbon and silica as compared with the mixing of distinct powders. In addition, SiC with fine crystallite sizes can be produced. However, since one component has a particulate form, the mixing is not expected to be as good as the method of mixed solutions.

4. The reactants are a fine-scale silica/carbon mixture formed as a decomposition product from Si-C-containing synthetic polymers or from naturally-occurring Si-C-containing precursors.

This method is distinct from other methods in that both carbon and silica come from a single source. Examples include synthetic polymers such as polycarbosilane (PCS) or naturally-occurring precursors such as rice hulls. The precursors are usually pyrolyzed during which decomposition products (e.g., CH_4, H_2, etc.) are volatilized and fine-scale carbon/silica mixtures are formed. Higher temperature heat treatment results in the formation of SiC via carbothermal reduction.

Yajima (1976) first studied the preparation of SiC fiber from carbosilane polymers. These polymers (and other Si-C-containing polymers) were also used to produce SiC powders with crystallite size as small as several nanometers (Soraru et al.

(1990), Bouillon et al. (1991)). Laine and Babonneau (1993) reviewed the synthesis of SiC from synthetic polymers. The synthesis of SiC from rice hulls was investigated by Lee and Cutler (1975). They pyrolyzed rice hulls (containing 18 wt% of silica) in a non-oxidizing atmosphere at 900^{o}C for 2 h to obtain an intimate mixture of amorphous carbon and silica. The pyrolyzed material had a C/Si molar ratio of around 5.6:1 (47 wt% of silica, 53 wt% of carbon), i.e., carbon rich compared to the 3:1 molar ratio in Equation (2-1-1). The pyrolyzed material was then heat treated at temperatures in the range of 1350-1560^{o}C in argon. The SiC product had fine size (<0.1 μm) and some of it had an acicular (whisker-like) shape. Krishnarao and Godkhindi (1992) and Panigraphi et al. (2001) also obtained SiC from rice hulls. The rice hulls were first heat treated in air at 700^{o}C. The product was then heat treated in vacuum (~1-7 Pa) at temperatures in the range of 1150-1650^{o}C for 30-180 min. Krishnarao and Godkhindi (1992)'s study indicated that the silica distribution in the rice hulls was not uniform and this would lead to a non-uniform SiC product.

The advantage of using Si-C-containing synthetic polymers or rice hulls is that the fine-scale mixing of silicon and carbon is already present in the raw material. However, each type of precursor has some disadvantages. The synthetic polymers are very expensive. The synthesis methods are complicated and require highly-controlled processing conditions. In contrast, rice hulls are inexpensive and naturally occurring. However, the naturally-occurring material contains large concentrations of undesirable impurity elements (including alkali metals). In addition, the silica distribution in the rice hulls is not uniform and the C/Si ratio also deviates far from the stoichiometric ratio (i.e., a C/Si molar ratio of 3 as in Equation (2-1-1)). As a result, there is a significant amount

of excess carbon and/or unreacted silica left after the heat treatment which is difficult to separate from the SiC (Krishnarao and Godkhindi, 1992).

2.2 Mechanism Study on Carbothermal Reduction Synthesis of SiC

2.2.1 Single-Step or Multiple-Step Reaction?

Different mechanisms have been proposed for the formation of SiC via carbothermal reduction. Some investigators suggested that the reaction is a single-step solid-state reaction. van Dijen and Metselaar (1991) studied the reaction between carbon black (crystallite size of 35 nm) and fumed silica (crystallite size of 125 nm). (The authors declared that the scale of mixing was ~3 μm. This suggests that powders consisted of aggregates of the primary particles.) From microstructural observations (i.e., SEM), they claimed that only the carbon particles which were in contact with the SiO_2 particles reacted to form SiC. Based solely on this observation, they concluded that the carbothermal reduction reaction was purely a solid-state reaction.

Krstic (1992) suggested (without experimental evidence) that direct solid-state reaction could take place to a limited extent at temperatures below 1400^{o}C. He believed that such reaction would cease quickly once a SiC layer was formed due to low chemical interdiffusion coefficients of carbon and silicon within SiC.

There are many more investigations which indicate that the formation of SiC by carbothermal reduction involves two (or more) elementary steps. In addition, most investigators believe that vapor-phase species play an important role in the formation of SiC. In particular, results from several investigations suggest that SiO vapor are formed

during the carbothermal reduction reaction (Klinger et al. (1966), Khalafalla and Haas (1972), Viscomi and Himmel (1978), Weimer et al.(1993), et. al.)

Khalafalla and Haas (1972) studied the reaction between coarse quartz (-70/+100 mesh) and coarse graphite (-70/+100 mesh). The powder mixture (C/Si molar ratio of = 1.0) was heated up to high temperatures (i.e., 1400-1515^{o}C) in vacuum (i.e., 0.25 to 10^{-6} torr) and the weight change during the reaction was monitored. They found a considerable amount of brownish condensate on the "colder exit section of the furnace." The brownish condensate was described as "amorphous," although they also observed "incomplete" XRD patterns for cristobalite (a polytype of SiO_2) and silicon metal. They believed the brownish deposits (containing cristobalite and Si) came from the disproportionation of SiO according to:

$$2SiO_{(g)} \rightarrow Si_{(s)} + SiO_{2(s)} \qquad (2\text{-}2\text{-}1)$$

Pure Si was also observed in the reaction product between carbon and silica in the studies of Vodop'yanov et al. (1983)(detecting method not specified), Weimer et al. (1993) (by XRD), and Meng et al. (2000) (by TEM). These investigators all attributed the presence of Si in the reaction product to the disproportionation of SiO. In addition, Weimer et al. (1993) and Seo et al. (1998) carried out thermodynamic calculations for the disproportionation of SiO. Seo et al. determined that the free energy change for reaction (2-2-1) was given by:

$$\Delta G^{0} = -664.4 + 0.3171\ T \ \text{(kJ/mol)} \qquad (2\text{-}2\text{-}2)$$

Although Weimer et al. did not give a specific relationship between temperature and free energy, they stated that the formation of Si metal from reaction (2-2-1) was favorable at

temperatures below 1860°C. This temperature is quite close to the value (T=1823°C) that gives $\Delta G^0 = 0$ in Equation (2-2-2).

Tanaka and Kurachi (1988) proposed the following chemical equation in order to account for the generation of SiO vapor in the process of carbothermal reduction:

$$SiO_{2\,(s)} + (1+\alpha)\,C_{(s)} \rightarrow \alpha\,SiC + (1-\alpha)\,SiO_{(g)} + (1+\alpha)\,CO_{(g)} \qquad (2\text{-}2\text{-}3)$$

where α is the yield of SiC from silica. Based on Equation (2-2-3), they calculated the expected SiC yields by weight, α_T , and compared them to the experimental values, α_E. The results are listed in Table 2-2-1. Good agreement between the theoretical and experimental SiC yields was observed for samples which had initial C/Si molar ratios smaller than 2.63. Those samples gave near-stoichiometric products. For samples with higher C/Si molar ratios, the products were carbon-rich. There was a discrepancy between the theoretical and experimental yields for the two samples with C/Si molar ratio $\geq$ 2.63. The reason for this discrepancy was that the calculations were made with the assumption that all the carbon was consumed in the reaction. This assumption was obviously not valid for those cases, as Table 2-2-1 shows that the products after complete CTR reaction contained residual carbon. These results indicate that excess silica is required to achieve complete CTR. Hence, it is clear that some silica is "lost" during the heat treatment and the implication is that the loss occurs due to SiO volatiles that move away from the reaction mixture. Chen et al. (2000) also found that the number of moles of SiC formed via CTR was always less than the number of moles of SiO_2 consumed. (Their study was carried out using quartz and carbon particles with particle sizes of ~41-43 μm.) Again, this is indirect evidence that SiO forms during the CTR reaction and that

Table 2-2-1 Comparison of calculated and experimental yields of CTR for samples with different starting compositions, from Tanaka and Kurachi (1988).

C/Si molar ratio in pyrolyzed sample	α_T	α_E	w_{C-free}^{CTR} (wt%)	w_O^{CTR} (wt%)	C/Si molar ratio after complete CTR
3.10	1.00	0.80	14	Negligible	1.5
2.63	0.81	0.74	9	Negligible	1.3
2.52	0.77	0.78	Negligible	Negligible	1.0
2.26	0.61	0.65	Negligible	Negligible	1.0
1.70	NA	NA	Negligible	Negligible	1.0

Note: α_T is theoretical yield of SiC; α_E is experimental yield of SiC; w_{C-free}^{CTR} is weight percentage of excess carbon in the product after complete reaction; w_O^{CTR} is weight percentage of oxygen in the product after complete reaction.

some of the SiO is "lost" because it moves away from the reaction zone and does not participate in the SiC-forming reaction.

2.2.2 Generation of SiO Vapor in the Multi-step Reaction

Three reaction routes have been proposed to account for the generation of SiO vapor. One route is the solid-state reaction between silica and carbon to form SiO vapor and CO vapor:

$$SiO_{2\,(s)} + C_{\,(s)} \rightarrow SiO_{\,(g)} + CO_{\,(g)} \qquad (2\text{-}2\text{-}4)$$

This reaction was proposed by Blumenthal et al. (1966), Khalafalla and Haas (1972), and Weimer et al. (1993).

The second route, as shown by Equations (2-2-5) and (2-2-6), includes the solid-gas reaction between silica and CO that generates SiO and CO_2, and the solid-gas reaction between CO_2 and carbon to regenerate CO:

$$SiO_{2\,(s)} + CO_{\,(g)} \rightarrow SiO_{\,(g)} + CO_{2\,(g)} \tag{2-2-5}$$

$$CO_{2\,(g)} + C_{\,(s)} \rightarrow 2CO_{\,(g)} \tag{2-2-6}$$

This route was proposed by Schwerdtfeger (1966), Lee and Miller (1977), Krstic (1992), and Chen and Lin (1997).

The third route, as shown by Equations (2-2-7) and (2-2-8), includes the dissociation of silica into SiO and O_2, and the solid-gas reaction between carbon and O_2 to form CO. This route was proposed by Klinger et al. (1966) and Lee and Cutler (1975).

$$SiO_{2\,(s)} \rightarrow SiO_{\,(g)} + \frac{1}{2} O_{2\,(g)} \tag{2-2-7}$$

$$\frac{1}{2} O_{2\,(g)} + C_{\,(s)} \rightarrow CO_{\,(g)} \tag{2-2-8}$$

To determine which of the three reaction routes is most probable, Weimer et al. (1993) carried out some thermodynamic calculations. The results are shown in Figure 2-2-1. Based on that figure, Weimer declared that the first route, i.e., Equation (2-2-4), is the most energetically favorable reaction. Direct contact between silica and carbon is diminished as the CTR reaction proceeds. Therefore, Weimer et al. also believed that the dominating mechanism of SiO formation might change to one of the other two routes at a later stage in the reaction. They stated that the solid-gas reaction (Equations (2-2-5) and (2-2-6)) was more favorable based on "both free energy and enthalpy changes."

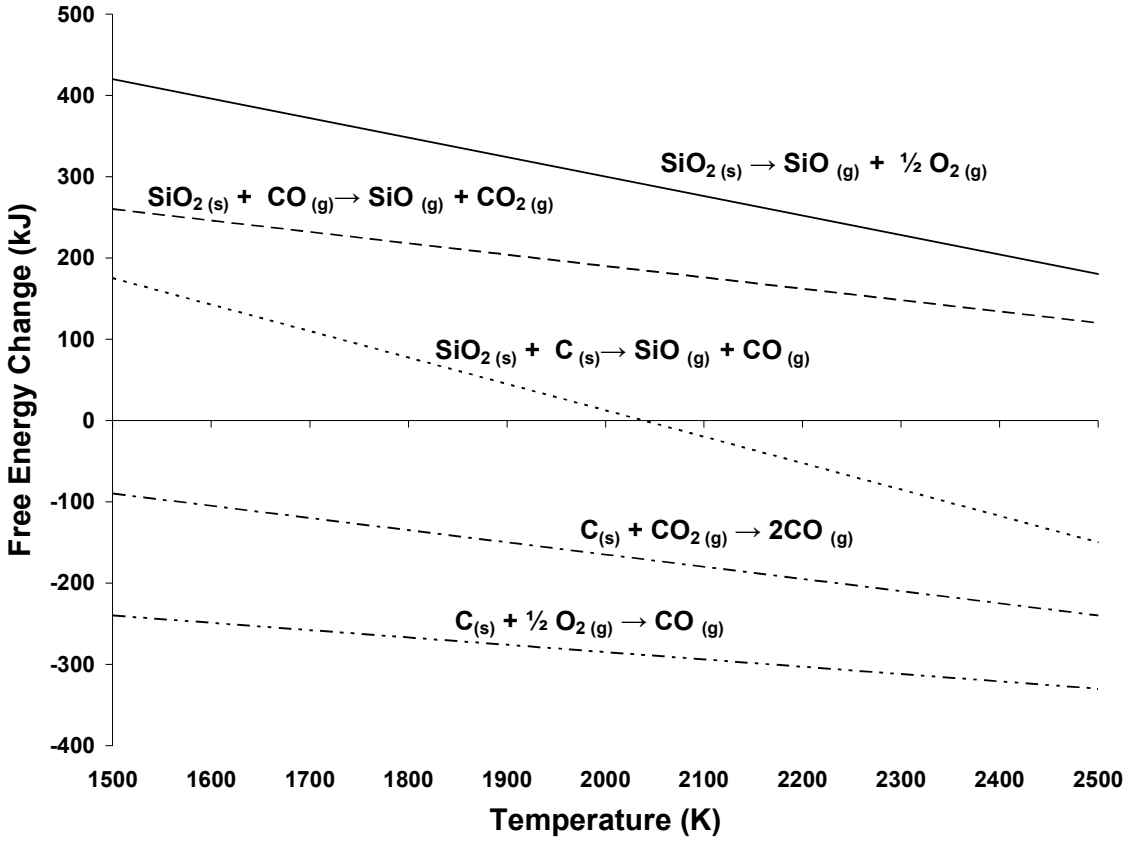

Figure 2-2-1 Free energy change for a variety of reactions which might involve the generation of SiO vapor, from Weimer et al. (1993).

Blumenthal et al. (1966) studied the reaction between silica and carbon (C/Si molar ratio from 1/3 to 1, i.e., extremely carbon-deficient compared to the stoichiometric ratio of 3 in Equation (2-1-1)) at 1300-1500^{o}C in vacuum. Using the initial and final weights of the sample, they determined the percentage weight losses for samples given heat treatments at various temperatures/times. They compared these values with the calculated percentage weight losses obtained by using measured amounts of CO evolved from the samples and applying these CO weight losses to three different CO-generating reactions. These reactions include two shown previously in Equations (2-1-1) and (2-2-4) and a third reaction below which generates Si vapor:

$$SiO_{2\,(s)} + 2C_{\,(s)} \rightarrow Si_{\,(g)} + 2CO_{\,(g)} \qquad (2\text{-}2\text{-}9)$$

Their results showed that, at temperatures above ~1400°C, the measured weight loss was closest to the weight loss calculated from Equation (2-2-4), i.e., the reaction in which SiO is generated via solid-state reaction. In addition, Blumenthal et al. carried out room temperature infrared spectroscopy on the gaseous product collected from the high temperature reaction between silica and carbon. They identified CO as the only carbon-containing gaseous species. This observation is consistent with the reaction in Equation (2-2-4), but inconsistent with the reaction in Equation (2-2-5) since CO_2 is generated in the later reaction.

Lee and Miller (1977) suggested that SiO was generated via Equations (2-2-5) and (2-2-6) based on kinetic considerations. They believed that the solid-state reaction in Equation (2-2-4) would be slower than the gas-phase reaction in Equation (2-2-5). However, they still proposed that the initial CO required in Equation (2-2-5) was provided by the direct solid-state reaction in Equation (2-2-4). Lee and Miller did not provide any experimental proof to support their argument.

Schwerdtfeger (1966) found that silica spheres lost weight after heat treatment in $CO+CO_2$ atmosphere at 1500°C for 10-50 hours. He believed that the weight loss of silica was due to SiO formation via reaction (2-2-5). However, it should be noted that the weight loss of SiO_2 in a strong reducing atmosphere can also be explained by the dissociation of silica as shown in Equation (2-2-7).

Lee and Cutler (1975) studied the reaction between coarse silica particles (i.e., sand, particle size of ~800 μm) and carbon particles (i.e., charcoal, particle size of ~70 μm) at 1500°C in argon. The particles (i.e., sand and charcoal) were separated and

analyzed using XRD after partial reaction. It was stated that "the SiC formed on the surface of carbon and there was a reduction in the size of the sand." Hence, the authors concluded that SiC formation occurred via the vapor phase in which SiO was first formed and then the SiO reacted with carbon. The whole reaction process was believed to include the following steps:

$$SiO_{2\,(s)} \rightarrow SiO_{\,(g)} + \frac{1}{2} O_{2\,(g)} \qquad (2\text{-}2\text{-}10)$$

$$\frac{1}{2} O_{2\,(g)} + C_{\,(s)} \rightarrow CO_{\,(g)} \qquad (2\text{-}2\text{-}11)$$

$$SiO_{\,(g)} + C_{\,(s)} \rightarrow Si_{\,(g)} + CO_{\,(g)} \qquad (2\text{-}2\text{-}12)$$

$$Si_{\,(g)} + C_{\,(s)} \rightarrow SiC_{\,(S)} \qquad (2\text{-}2\text{-}13)$$

Lee and Cutler (1975) also carried out some experiments that showed the reaction rate between coarse particle mixtures of carbon and silica depended on the size of the silica particles. (The carbon/silica mixtures were heat treated at 1470^{o}C in Ar for 30 min to carry out the CTR reaction.) A higher reaction rate was observed with a smaller silica particle size (see Table 2-2-2). Based on this observation, they concluded that the dissociation of silica according to Equation (2-2-10) was the rate limiting step among the four reaction steps listed above (Equations (2-2-10) - (2-2-13)). They reached this conclusion because they believed that the dissociation of SiO_2 is "the only reaction dependent on the surface area of silica." However, it should be noted both of their experimental observations cited above (i.e., the reduction in silica particle size during CTR and the dependence of the reaction rate on the silica particle size) can not preclude the possibility that SiO forms by Equations (2-2-4) or (2-2-5).

Table 2-2-2 Effect of silica particle size on the yield of SiC formed from the reaction between silica and carbon, from Lee and Cutler (1975).

Carbon Particle Size (μm)	Silica Particle Size (μm)	SiC Yield
70	40	29.0%
70	800	1.8%

Note: The carbon/silica mixtures were heat treated at 1470^{o}C for 30 min in Ar to carry out the CTR reaction.

In summary, the available (but somewhat limited) evidence tends to support the reaction in Equation (2-2-4) as the mechanism by which SiO is generated in carbothermal reduction reaction between carbon and silica.

2.2.3 Generation of SiC from SiO Vapor in the Multi-step Reaction

Several routes have been proposed to account for the formation of SiC with SiO as a reactant. The first possible route, as proposed by Viscomi and Himmel (1978), Weimer et al. (1993), and Benaissa et al. (1994), is that the SiC is formed by solid-gas reaction between carbon and SiO vapor as shown below:

$$SiO_{(g)} + 2\,C_{(s)} \rightarrow SiC_{(s)} + CO_{(g)} \qquad (2\text{-}2\text{-}14)$$

The second possible route is through the gas-phase reaction between SiO and CO to form SiC and CO_2. CO is regenerated by the reaction between CO_2 and carbon:

$$SiO_{(g)} + 3CO_{(g)} \rightarrow SiC_{(s)} + 2CO_{2\,(g)} \qquad (2\text{-}2\text{-}15)$$

$$CO_{2\,(g)} + C_{(s)} \rightarrow 2CO_{(g)} \qquad (2\text{-}2\text{-}16)$$

The route of gas phase reaction was suggested by Viscomi and Himmel (1978) and by Weimer et al. (1993).

A third route for SiC formation is by the reaction between silicon and carbon:

$$Si_{(g,\,l,\,s)} + C_{(s)} \rightarrow SiC_{(g)} \qquad (2\text{-}2\text{-}17)$$

In this case, the silicon comes from the reaction between SiO vapor and carbon:

$$SiO_{(g)} + C_{(s)} \rightarrow Si_{(g,\,l,\,s)} + CO_{(g)} \qquad (2\text{-}2\text{-}18)$$

or the dissociation of SiO:

$$SiO_{(g)} \rightarrow Si_{(g,\,l,\,s)} + \frac{1}{2} O_{2\,(g)} \qquad (2\text{-}2\text{-}19)$$

This route was proposed by Lee and Cutler (1975).

Weimer et al. (1993) carried out thermodynamic calculations to determine which of the three routes of SiC formation is most probable. The results are shown in Figure 2-2-2. Weimer et al. declared that the reaction route shown in Equation (2-2-14)) is the most energetically favorable reaction in the temperature range from 1500 to 2500K. However, they also stated that the route shown in Equation (2-2-15) would be thermodynamically favorable below ~1200K. (The latter statement is not evident in Figure 2-2-2 because the lowest temperature shown is 1500K.)

Viscomi and Himmel (1978) did an experiment to separate the reaction to generate SiO vapor (via the reaction shown in Equation (2-2-4)) from the formation of SiC (via the reaction shown in Equation (2-2-10)). They heat treated a pellet consisting of a coarse powder mixture of silica and carbon (particle size < 45 μm, C/Si molar ratio of 3) at 1500°C in flowing N_2. On the downstream side of the pellet ($T \approx 1475\,^{o}C$), they placed some lampblack (99.5% carbon, particle size of 1 μm) to serve as a sink for SiO vapor. They found that the exposed surface of the lampblack was covered with a reaction

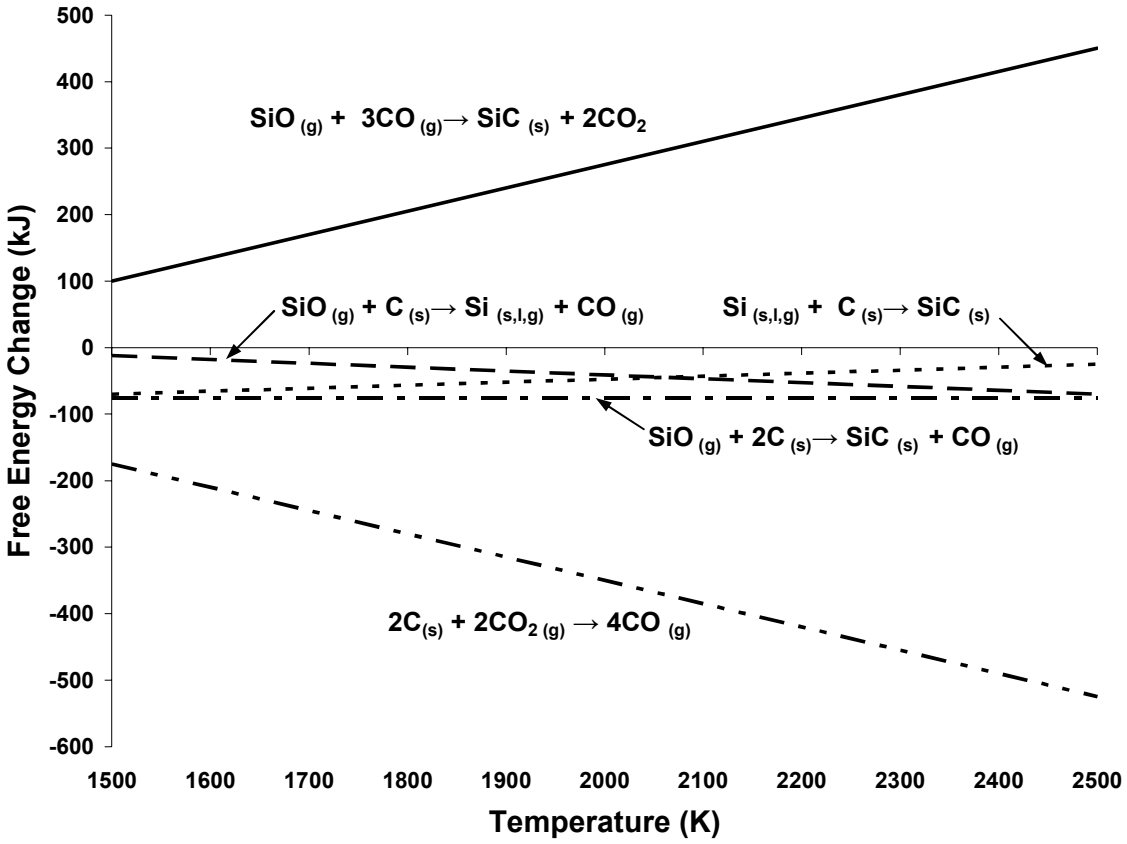

Figure 2-2-2 Free energy change for a variety of reactions which involve SiO vapor to account for the formation of SiC, from Weimer et al. (1993).

product and XRD analysis showed that product was mostly β-SiC. (The rest of the product was Si_3N_4 due to the use of a nitrogen atmosphere in the experiment.) Benaissa et al. (1994) heated an equimolar mixture of Si and SiO_2 powders to 1240^{o}C under reduced pressure to produce SiO, as shown by:

$$Si_{(s)} + SiO_{2\,(s)} \rightarrow 2SiO_{(g)} \qquad (2\text{-}2\text{-}20)$$

The SiO vapor was then pumped to a region where activated carbon was placed (also at 1240^{o}C). β-SiC was formed on the surface of activated carbon. Therefore, the results in the studies by Viscomi and Himmel and Banaissa et al. provide direct support for the

mechanism of SiC formation through a gas-solid reaction between SiO vapor and carbon (Equation (2-2-14)).

Viscomi and Himmel (1978) also suggested that SiC formed by the reaction in Equation (2-2-11) based on another observation using experiment setup described above. They found a blue condensate which consisted of α-SiC in the cold zone of the furnace. Since there was neither silicon nor carbon in that region of the furnace, they attributed the formation of the α-SiC to the gaseous phase reaction shown in Equation (2-2-15).

There is no experimental evidence to support Equation (2-2-17) as the operative CTR mechanism in silica/carbon mixtures. Lee and Cutler (1975) proposed this route without providing any experimental support. Klinger et al. (1966) calculated the equilibrium vapor pressure of Si metal based on Equation (2-2-13) and found that the value was only 3.2×10^{-5} torr at 1450^{o}C. Such a low vapor pressure makes it unlikely that the reaction proceeds through this route.

2.3 Reaction Kinetics and Structure Evolution for SiC formation by Carbothermal Reduction

The kinetics of the carbothermal reduction reaction has been investigated extensively in the past years. A wide range of reaction rate constants and activation energies values have been obtained in various studies. In addition, different reaction models (e.g., nucleation and growth, shrinking core, etc.) and reaction rate-limiting steps (e.g., interface reaction or diffusion) have been proposed by various researchers to describe the formation of SiC and/or the consumption of silica and carbon. The difference observed in the kinetic behavior may be due to the difference in the material systems, the reaction condition, and/or the method of investigation. In addition to

reaction rate studies, the structural evolution (i.e., changes in crystallite size, surface area, etc.) of the product formed by the reaction has also been studied by some researchers. A brief review of the reaction kinetics and structural evolution studies for SiC formation by carbothermal reduction reaction is given below. Some background information concerning methods used to study the reaction kinetics and existing kinetic models will also be provided in this section.

2.3.1 Methods of Kinetic Study on SiC Formation via Carbothermal Reduction

Generally, the kinetic studies of SiC formation are conducted via three different methods. The first is to monitor the weight change during carbothermal reduction. Because volatile materials are produced in the reaction, the weight loss can be a good indication of the progress of reaction. Most researchers, including Khallafalla and Haas (1972), Lee and Cutler (1975), Shimoo (1990), Ono and Kurachi (1991), van Dijen and Metselaar (1991), and Narisawa and Okabe (1998), employed this method to study the reaction kinetics.

The second method to study reaction kinetics is to monitor the amount of CO generated or the concentration of CO in a closed system. According to Equation (2-1-1), the amount of CO generated is related to the amount of SiC formed at a fixed ratio. Blumenthal et al. (1966) and Klinger et al. (1966) adopted this method.

The third method to study reaction kinetics is to determine the actual amount of SiC generated during the CTR. The amount of SiC in the product can be determined by chemical analysis, such as reported by Weimer et al. (1993). The amounts of carbon and oxygen in the product were measured and the rest of the material was assumed to be silicon. Quantitative X-ray diffraction (QXRD) analysis on the product also provides

information about the concentration of SiC in product from which the reaction kinetics can be determined.

2.3.2 Forms of Kinetic Curves

For isothermal kinetics study, the results are usually represented by plots of extent of reaction versus reaction time. The extent of reaction can be defined as the fractional weight loss or the fraction of SiC formed, depending on the method of study. The kinetic data usually follow one of two different graphical forms: sigmoidal or deccelatory.

For sigmoidal kinetic behavior, the reaction rate is low initially; the rate increases and reaches a maximum in the middle of the reaction; after that, the rate slows down when the reaction is close to completion. Sigmoidal kinetic behavior is usually associated with the nucleation and growth process (which will be explained in detail later). Such behavior was observed in the following investigations of SiC formation by carbothermal reduction: Klinger and Strauss (1966), Khallafalla and Haas (1972), Ono and Kurachi (1991) (for the samples heat treated at 1522-1548^{o}C), van Dijen and Metselaar (1991), Narisawa et al. (1998) (for the samples heat treated at 1500^{o}C), and Panigraphi et al. (2001).

For deccelatory kinetic behavior, the rate is highest at the beginning of the reaction and decreases as the reaction proceeds. Such behavior was found in the investigations by Blumenthal et al. (1966), Lee and Cutler (1975), Ono and Kurachi (1991) (for the samples heat treated at 1608 and 1689^{o}C), Weimer et al. (1993), and Narisawa et al. (1998) (for the samples heat treated at 1600 and 1700^{o}C) .

2.3.3 Common Kinetic Models for Reaction Between Solids

Before reviewing the different kinetic studies for SiC formation via CTR, a brief review of the most common kinetic models is given first. This review includes the nucleation and growth model, interface-controlled "shrinking core" model, diffusion-controlled model, etc.

2.3.3.1 Nucleation and Growth Model

Nucleation and growth is one of the most common reaction models. According to Hulbert (1969), this model "considers the nucleation of product at active sites and the rate at which the nucleated particles grow." Such a reaction mechanism is possible when the product is partially miscible in one of the reactants. The generalized mathematical expression of the nucleation and growth model is given by:

$$-\ln(1-\alpha) = (kt)^m \tag{2-3-1}$$

or

$$\ln[-\ln(1-\alpha)] = m\ln t + m\ln k \tag{2-3-2}$$

in which α is the extent of reaction, k is the reaction rate constant, t is the reaction time, and m is the exponent parameter which is determined by the specific reaction mechanism.

Depending on the nucleation rate, the geometry of the nuclei, and the rate-limiting mechanism for the growth of nuclei, the nucleation and growth process can be divided into different categories. For example, if the rate of nucleation (number of new nuclei formed per unit volume per unit time) remains constant throughout the reaction, the process is said to have "constant nucleation rate." If the nucleation is so fast that the all nucleation sites are exhausted at a very early stage of the reaction, the process is said to have "zero nucleation rate" ("saturation of active sites"). If the nucleation rate is decreasing during the reaction, the process is said to have "decreasing nucleation rate."

In regard to the shape of the nuclei, growth of the nuclei is referred to as "3-D growth" if growth is uniform in all directions, i.e., nuclei grow into three-dimensional spheres. In "2-D growth," the nuclei grow into flat, thin sheets. In "1-D growth," the nuclei grow into straight, long rods. In regard to the rate-limiting growth mechanism, the process is referred to as "diffusion controlled" if the transport rate of one reactant through the product layer to the reaction sites is slower compared to the rate of consumption of that reactant at the reaction site (i.e., at the phase boundary between the reactant and the product). In contrast, the growth rate is referred to as "phase-boundary controlled" or "interface-controlled" if the consumption rate of the reactant at the reaction site is slower compared to the transport rate of reactants through the product layer to the reaction sites.

The nucleation and growth process can be defined by considering combinations in the nucleation rate (constant nucleation, zero nucleation, or decreasing nucleation), the nuclei growth geometry (3-D, 2-D or 1-D), and the rate-limiting step in the growth (diffusion or reaction). Each of the combination has its corresponding value (or range of values) for the exponent parameter m. Table 2-3-1 from Hulbert (1969) provides a summary of the m values (or range of values) for the various nucleation and growth processes.

To test whether or not the nucleation and growth model is applicable to a certain reaction, $\ln[1 - \ln(1 - \alpha)]$ is plotted as a function of $\ln t$. If a straight line is obtained, the model MAY be applicable. It should be noted that a good fit to the kinetic equation does not necessarily mean that the reaction is the nucleation and growth type. The microstructure evolution of the reaction product also has to be examined. The structural evolution must be consistent with the mechanism determined by the exponent m in order

Table 2-3-1 Summary of nucleation and growth models with different nuclei geometry and growth mechanism, and their corresponding ranges for the exponent parameter *m* value, from Hulbert (1969).

Growth geometry	Nucleation rate	Phase-boundary controlled	Diffusion controlled
3-D growth (i.e., spheres)	Constant nucleation rate	4	2.5
	Zero nucleation rate (saturation of active sites)	3	1.5
	Decreasing nucleation rate	3-4	1.5-2.5
2-D growth (i.e., plates)	Constant nucleation rate	3	2.0
	Zero nucleation rate (saturation of active sites)	2	1.0
	Decreasing nucleation rate	2-3	1-2
1-D growth (i.e., rods)	Constant nucleation rate	2	1.5
	Zero nucleation rate (saturation of active sites)	1	0.5
	Decreasing nucleation rate	1-2	0.5-1.5

to validate the applicability of the model. The same principle applies when considering the validity of other kinetic models that will be described below.

2.3.3.2 Interface-Controlled "Shrinking-Core" Model and Other Related Models

The interface-controlled "shrinking-core" model is also commonly used to describe reactions in solids. According to Hulbert (1969), when the transport (diffusion) of a reactant through the product layer is "so rapid that the reactants could not combine fast enough at the reaction interface to establish equilibrium," the reaction is said to be "interface-controlled" and the rate-determining step is the chemical process occurring at

the interface. This usually happens when a porous, discontinuous product phase is generated on the outside of the reactants in the reaction, i.e. a porous product layer has formed over a relatively dense reactant core. In such a case, the rate of the reaction is determined by the total interfacial area available. If the product phase undergoes three-dimensional growth, the reactant core is consumed and its volume contracts, while the product layer grows towards the center of the spherical reactant core. Therefore, the model is referred to as a "shrinking-core" model. The kinetic equation for such a reaction model is given by:

$$1-(1-\alpha)^{1/3} = k_{PB}t = \frac{k}{r_0}t \qquad (2\text{-}3\text{-}3)$$

where α is the extent of reaction, t is the reaction time, r_0 is the initial size of the reactant particle, k_{PB} or k is the reaction rate constant (depending on whether the particle size has been included or not).

The assumptions to obtain Equation (2-3-3) include: (1) the reaction is phase boundary controlled, (2) the reaction rate is proportional to the surface area of the unreacted phase, and (3) the nucleation step occurs instantaneously so that the surface of each reactant particle is covered with a product layer.

Some expectations from the interface-controlled "shrinking-core" model include the following: (1) The reaction rate usually slows down as the reaction proceeds. As the reactants are consumed, the available reaction interfacial area usually decreases. Since the reaction rate is dependent on the total interfacial area of reactant, the overall rate would decrease accordingly. (2) The reaction product is expected to have uniform microstructural features, such as crystallite size. This is because the reaction mechanism remains the same as the reaction interface sweeps through the reactant particle.

The interface-controlled "contracting-area" model describes reactions which are interfaced controlled but have two-dimensional growth of the product phase. The reaction kinetics for this model are described by the following equation:

$$1-(1-\alpha)^{1/2} = k_{PB}t = \frac{k}{r_0}t \qquad (2\text{-}3\text{-}4)$$

where α is the extent of reaction, t is the reaction time, r_0 is the initial particle size of the reactant, and k_{PB} or k is the reaction rate constant.

2.3.3.3 Diffusion Models

There are several kinetic models which are grouped together because the rate is controlled by diffusion, but they do not follow the kinetics of nucleation and growth models. Jander's equation (Hulbert (1969)) is shown in Equation (2-3-5):

$$[1-(1-\alpha)^{1/3}]^2 = \frac{2kDt}{r_0^2} \qquad (2\text{-}3\text{-}5)$$

where k is the reaction rate constant, α is the extent of reaction, D is the diffusion coefficient, and r_0 is the initial particle size of the reactant. According to Hulbert (1969), the basic assumptions for Jander's equation include: (1) the chemical reaction at the interface is faster than the transport (diffusion) of reactant to the interface; (2) the surface of the component (reactant) at which the reaction take places is completely and continuously covered with particles of the other component (reactant); (3) the increase in thickness of the product layer follows the parabolic rate law of diffusion; (4) the diffusion coefficients of the species being transported are constant during the reaction; (5) the molar volume ratio of product formed to the reactant consumed is unity.

The Ginstling - Brounshtein equation (Hulbert (1969)) is a modification of Jander's equation. The basic assumptions are the same as in Jander's model except for the parabolic diffusion rate. The parabolic law is based on the assumption that the reaction interfacial area remains constant. However, the reaction interfacial area usually decreases for spherical particles as the reaction proceeds. As a result, the change in size (and, therefore, the total interfacial area) of the unreacted material is considered in the Ginstling - Broushtein equation shown below (Equation (2-3-6)). Note that the parameters in Equation (2-3-6) have the same meaning as in Jander's equation (Equation (2-3-5)).

$$1-\frac{2}{3}\alpha-(1-\alpha)^{2/3}=\frac{2kDt}{r_0^2} \qquad (2\text{-}3\text{-}6)$$

Carter's equation (Hulbert (1969)) is a further modification of the Ginstling - Brounshtein equation. It accounts for the difference in the volume of the product layer with respect to the volume of reactant consumed. As stated earlier, an assumption for both Jander's equation and the Ginstling - Brounshtein equation is that the molar volume ratio of product formed to the reactant consumed is unity. This is an over simplification. A "*Z*" term is introduced to represent the volume of the reaction product formed per unit volume of reactant consumed, and the following equation was obtained:

$$\frac{Z-(Z-1)(1-\alpha)^{2/3}-[1+(Z-1)\alpha]^{2/3}}{Z-1}=\frac{2kDt}{r_0^2} \qquad (2\text{-}3\text{-}7)$$

2.3.3.4 Other Kinetic Equations

In addition to the reaction models discussed above, there are also several other kinetic equations (Weimer (1997)) to describe reactions with solid reactants, such as:

First order equation:

$$\ln \frac{1}{1-\alpha} = kt \tag{2-3-8}$$

Power law equation:

$$\alpha = (kt)^n \tag{2-3-9}$$

or

$$\ln \alpha = n \ln k + n \ln t \tag{2-3-10}$$

Austin and Rickett equation:

$$\frac{\alpha}{1-\alpha} = (kt)^n \tag{2-3-11}$$

or

$$\ln \frac{\alpha}{1-\alpha} = n \ln k + n \ln t \tag{2-3-12}$$

2.3.4 Previous Studies on Reaction Kinetics and Structure Evolution of SiC in Carbothermal Reduction

Studies of the reaction kinetics of SiC formation via carbothermal reduction reaction are reviewed in this section. The processing method, the characteristics of the starting materials, the reaction kinetics data (e.g., reaction model, rate constants, and activation energy), and the effects of processing variables (composition, atmosphere, particle size, etc.) on the reaction kinetics will be presented and discussed. In addition, the results of structural characterization on the reaction product, if available, will also be presented.

- Blumenthal et al. (1966)

Blumenthal et al. (1966) studied the reaction between amorphous carbon black (mean crystallite size of 17 nm) and α-cristobalite (~2.8 μm particle size) or colloidal silica (~15 nm particle size). The powder mixtures (C/Si molar ratios of 1.0 and 0.33)

were pressed into pellets and heat treated at 1300-1600^{o}C in vacuum (i.e. 10^{-3} to 3 torr). The pressure rise in the system during the reaction due to gas emissions was recorded and related to the reaction kinetics. The following observations were made:

1. The rate of CO generation was linear in the early stage of the reaction and decreased as the reaction approached completion. The calculated reaction activation energy was in the range from 230 ± 42 kJ/mol to 293 ± 42 kJ/mol.
2. The reaction rate increased as the contact area between carbon and silica increased. (The contact area was increased by increasing the Si/C ratio while keeping the silica particle size the same, or by decreasing the silica particle size while keeping the same C/Si ratio.)
3. Samples with C/Si molar ratio of 0.33 had a higher reaction rate than samples with C/Si molar ratio of 1.0. The increased reaction rate with increased Si/C molar ratio was attributed to an increased contact area between the silica and carbon particles. However, this result does not necessarily provide much guidance about the effect of composition on reaction kinetics because the silica particle size (2.8 μm) was much larger than the carbon particle size (17 nm). Due to size difference, the number of carbon particles was much greater than the number of silica particles and the carbon particles probably covered the silica particles completely for both samples.

- Klinger et al. (1966)

Klinger et al. (1966) studied the reaction between coarse crystalline powders of quartz (particle size of 105-149 μm) and graphite (particle size < 44 μm). The mixed powder (with C/Si molar ratio = 4.2) was heated treated in a vacuum furnace. The total

amount of CO generated in the reaction was determined by monitoring the pressure increase in the furnace during the reaction. The following observations were made concerning the reaction kinetics and the product structure:

1. When the reaction temperature was lower (i.e., between 1445 and 1610^{o}C) and the reaction time was shorter (i.e., within 120 min at 1545^{o}C, 20 min at 1586^{o}C, 7 min at 1610^{o}C, etc.), a linear rate law was observed, i.e.,

$$n_{CO} = k_l t \tag{2-3-13}$$

where n_{CO} is the amount of CO evolved, t is the reaction time, and k_l is the linear reaction rate constant. A reaction activation energy of 490 ± 75 kJ/mol was obtained for these reaction temperature/time conditions.

2. When the reaction temperature was higher (i.e., above 1610^{o}C) or the reaction time was longer (i.e., more than 120 min at 1545^{o}C, 20 min at 1586^{o}C, 7 min at 1610^{o}C, etc.), the reaction appeared to be accelerating and a power rate law with exponent of 1.5 was observed, i.e.,

$$n_{CO} = (k_a t)^{3/2} \tag{2-3-14}$$

where k_a is the reaction rate constant. A reaction activation energy of 510 ± 84 kJ/mol was obtained for these temperature/time conditions. Klinger et al. attributed the acceleration of the reaction rate at higher temperature or longer time to the nucleation of cristobalite from the quartz phase. They believed that the reaction between graphite and cristobalite was more rapid than reaction between graphite and quartz. However, they presented no evidence to support this claim.

4. The SiC product had roughly the same size and morphology as the starting graphite particles.

- Khalafalla and Haas (1972)

The SiC synthesis procedure used by Khalafalla and Haas was described before in section 2.2.1. The weight loss during the reaction was recorded and used to obtain the reaction kinetics. They made the following observations:

1. Under isothermal condition, a sigmoidal kinetic curve of fractional weight loss vs. reaction time was observed. The incubation period was shorter with increasing temperature.
2. When the fractional weight loss, y, was less than 0.15, the data fit best to a cubic kinetic equation:

$$y = (kt)^3 + \varepsilon \tag{2-3-15}$$

where ε was a dimensionless constant of 8.7×10^{-3}. A reaction activation energy of 322 kJ/mol was obtained.

3. When the fractional weight loss y was greater than 0.15, the data fit the Austin and Rickett equation with an exponent of 2.2:

$$\frac{y}{1-y} = (kt)^{2.2} \tag{2-3-16}$$

4. The authors suggested that the CTR reaction might be controlled by the transformation of quartz to a non-crystalline "transitional phase" of silica. This conclusion was based on the activation energy value (i.e., 322 kJ/mol) that they obtained from studying the early stage (<15% weight loss) of the CTR reaction. The value was similar to the activation energy (i.e., 301 kJ/mol) reported by Roberts (1959) for the transformation of quartz to the "transitional phase."
5. The reaction rate decreased with increased CO pressure in the reaction atmosphere (Figure 2-3-1).

- Lee and Cutler (1975)

Lee and Cutler (1975) studied the kinetics of SiC formation from rice hulls. Some details of the study were given in sections 2.1 and 2.2.2. The weight loss change was monitored for the reaction. The authors made the following observations:

1. A plot of weight loss versus reaction time was overall deccelatory, but there was a region with linear reaction rate up to ~60% conversion. The reaction rate constant was obtained from the region with the linear rate and the reaction activation energy was 544 kJ/mol.

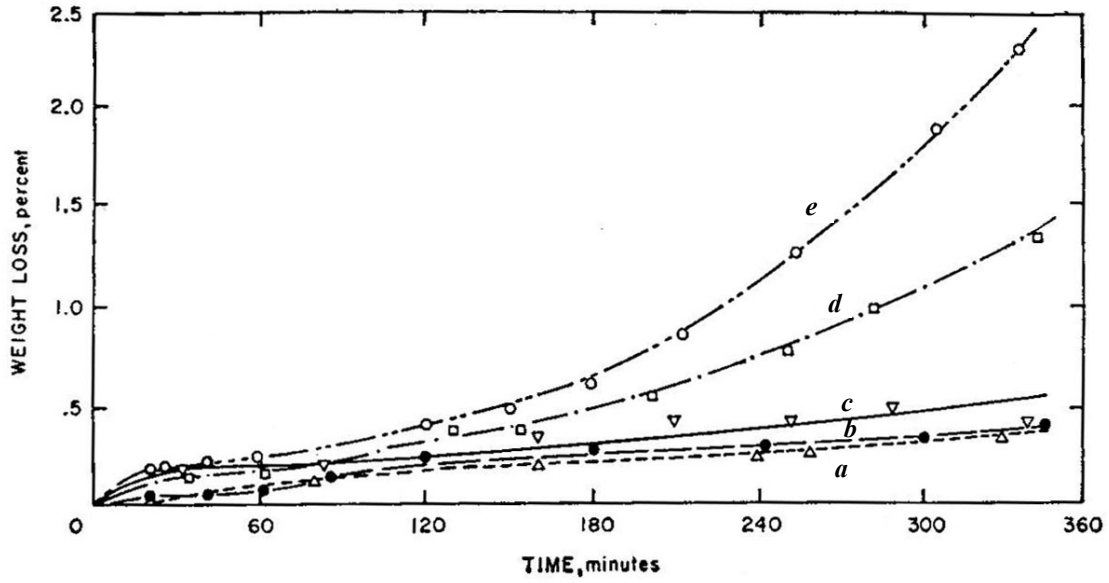

Figure 2-3-1 Effect of CO pressure on the reaction rate between graphite and quartz: (a) "blank", (b) 0.25 torr, (c) 0.02 torr, (d) 10^{-3} torr, (e) 10^{-6} torr, from Khalafalla and Haas (1972). (The "blank" refers to the combined weight loss from separate heat treatments of quartz and graphite in 10^{-6} torr vacuum. Hence, the results indicate that there was essentially no CTR reaction between the quartz and graphite until the CO pressure was less than 0.25 torr.)

2. The reaction rate decreased as the CO partial pressure increased. The reaction rate constants are shown in Figure 2-3-2. An empirical equation, as shown below, was obtained to relate the CO partial pressure to the reaction rate constant:

$$k = AP_{CO}^{-1/3} \exp(-\frac{E}{RT}) \qquad (2\text{-}3\text{-}17)$$

where k is the reaction rate constant, P_{CO} is the partial pressure of CO, A is a pre-exponential constant, and E is the activation energy.

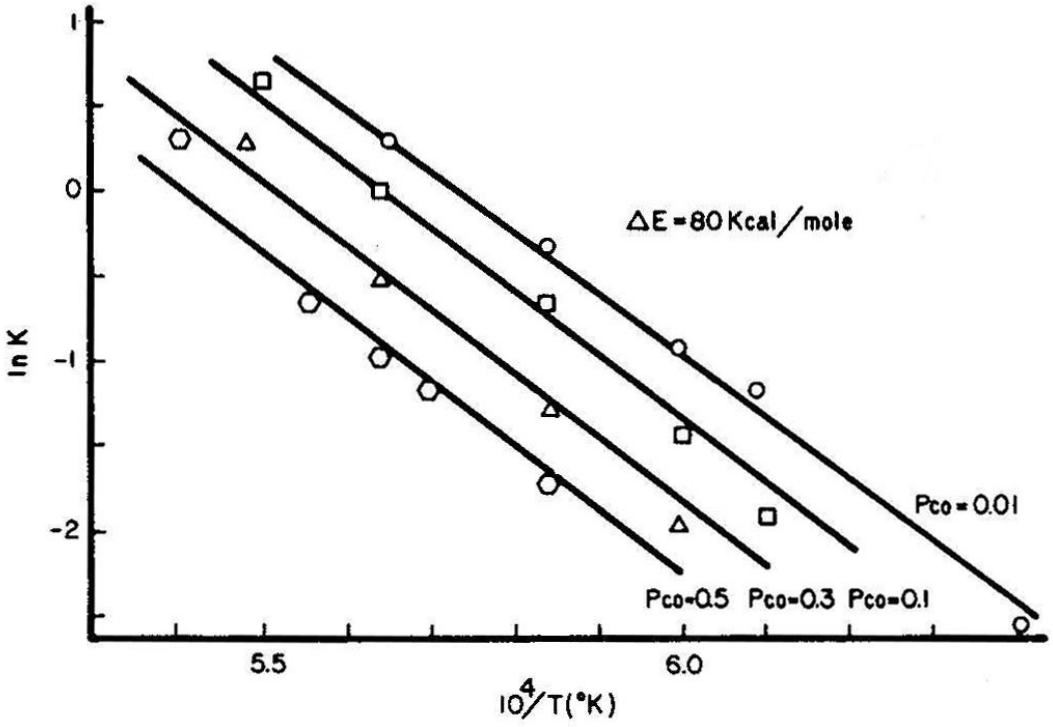

Figure 2-3-2 Arrhenius plot for the formation of SiC from rice hulls, from Lee and Cutler (1975). The reaction slowed down when CO partial pressure was increased.

- Viscomi and Himmel (1978)

The experimental procedure of Viscomi and Himmel has been described earlier in section 2.2.3. They made the following observations about the reaction kinetics:

1. Plots of the amount of reaction product formed versus time had an overall deccelatory shape in some cases. However, a region with linear reaction rate was observed from the start of the reaction and this linear rate continued for a substantial portion of the overall kinetic curve. The reaction rate constant was obtained from the linear portion of the conversion curve. The calculated activation energy was 552 kJ/mol.
2. The authors believed that the reaction of SiO at carbon surfaces to form SiC was the rate limiting step (Equation (2-2-10)). This is because some SiO was lost during the reaction, which suggested that the reaction of SiO at the carbon interface was relatively slow compared to the rate at which SiO was generated.

- Shimoo (1990), and Shimoo et al. (1996)

Shimoo (1990) studied the reaction between silica (mean particle size ≈ 143 μm) and carbon black (mean particle size ≈ 4.5 μm) or an activated carbon (mean particle size ≈ 51 μm). The powder mixtures (C/Si molar ratio = 3.0) were pressed and heat treated at 1600-1800^{o}C in flowing argon atmosphere. The weight of the sample was monitored before and after the reaction. The following observations were made about the reaction:

1. The weight loss kinetics data for the reaction between carbon black and silica was fit to Jander's equation (Equation (2-3-5)). The reaction activation energy was 544 kJ/mol. In the early stage of the reaction, it was observed that dense particles

of carbon black were surrounded by a continuous SiC layer. The author concluded that the rate-determining step was the diffusion of carbon in SiC.

2. The weight loss kinetic data for the reaction between activated carbon and silica was fit to the Ginstling - Brounshtein equation (Equation (2-3-6)). The reaction rate was higher compared to the rate observed for the reaction between the carbon black and the silica. The reaction activation energy was 244 kJ/mol. The higher reaction rate was attributed to the higher porosity/higher specific surface area of the activated carbon as compared with the carbon black. The authors claimed that gas (SiO) diffusion through the porous layer of the carbon particles was the rate-controlling step in the early stage of the reaction.

Shimoo et al. (1996) studied the weight loss kinetics for the heat treatment of Nicalon® fibers in argon. (Nicalon® fibers have a complex structure consisting of amorphous regions of carbon, silica, and Si-C-O, as well as weakly crystalline regions of SiC.) During heat treatments at temperature above 1500^{o}C, carbothermal reduction reaction occurred and the fibers transformed into a highly porous β-SiC product. They made the following observations:

1. The kinetic curve of the percentage of weight loss (i.e., ratio of actual weight loss to the initial weight) versus reaction time had an overall deccelatory shape. However, a region with linear reaction rate was observed from the start of the reaction and this linear rate continued for a substantial portion of the overall kinetic curve.

2. The weight loss data fit the nucleation and growth model with an exponent *m* value of 3/2. (Similar results were reported by Ono and Kurachi (1991) and Narisawa et al. (1998), as discussed below.)

- Ono and Kurachi (1991), and Narisawa et al. (1998)

Both Ono and Kurachi (1991) and Narisawa et al. (1998) studied the carbothermal reduction reaction for fine-scale carbon/silica mixtures prepared by pyrolysis of precursors obtained from solution-processed TEOS/phenolic resin mixtures. The synthesis method was essentially the same as that used by Tanaka and Kurachi (1991), as described in section 2.1. In brief, raw materials (TEOS and phenolic) were mixed at room temperature in the presence of toluenesulphonic acid. The gel products were pyrolyzed at 1000^{o}C for 1 h (in Narisawa's study) or 2 h (in Ono and Kurachi's study) to produce an amorphous "black glassy solid." The pyrolyzed material was heat treated at high temperature (i.e., 1500-1700^{o}C) in flowing Ar. The sample weight change was monitored during the experiment. The following observations were made concerning the reaction kinetics:

1. In both studies, the kinetic curves of fractional weight loss vs. reaction time had a sigmoidal shape when the reaction temperature was low (i.e., 1522-1540^{o}C in the study by Ono and Kurachi and 1500^{o}C in the study by Narisawa). Figure 2-3-3 shows results for the Ono and Kurachi study. The curves took a deccelatory shape when the reaction temperature was high (i.e., 1608-1689^{o}C in the Ono and Kurachi study (Figure 2-3-3) and 1600-1700^{o}C in Narisawa et al. study). The reaction kinetics could be described by the nucleation and growth model with the exponent parameter m = 3/2, i.e.,

$$-\ln(1-\alpha) = (kt)^{3/2} \tag{2-3-18}$$

Figure 2-3-4 shows the fit to the nucleation and growth model for the study by Ono and Kurachi.

2. Based on the *m* values (i.e., *m* = 1.5), Ono and Kurachi (1991) proposed that (1) the reaction had zero nucleation rate (i.e., all SiC nuclei formed immediately after the reaction started), (2) the SiC nuclei growth was three-dimensional, and (3) the growth of SiC nuclei was diffusion-controlled.

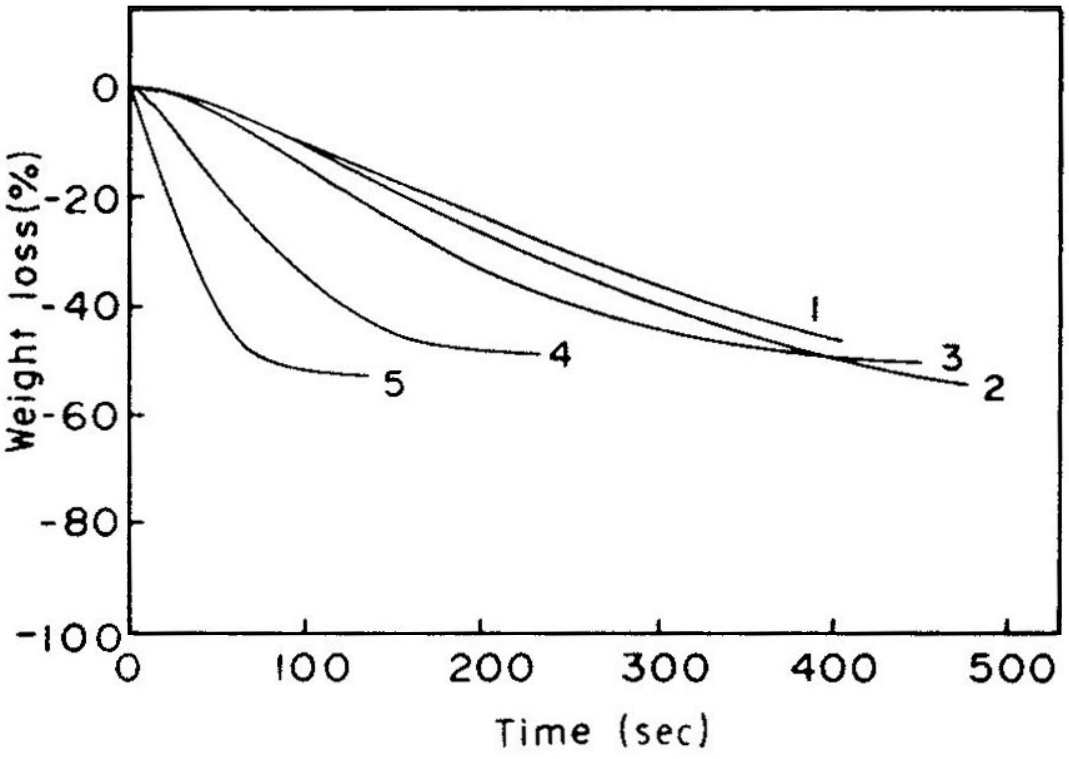

Figure 2-3-3 Plots of weight loss against CTR reaction time at various temperatures for a precursor with C/SiO_2 molar ratio of 2.65. The temperatures were (1) 1522°C, (2) 1540°C, (3) 1548°C, (4) 1608°C, (5) 1689°C, from Ono and Kurachi (1991).

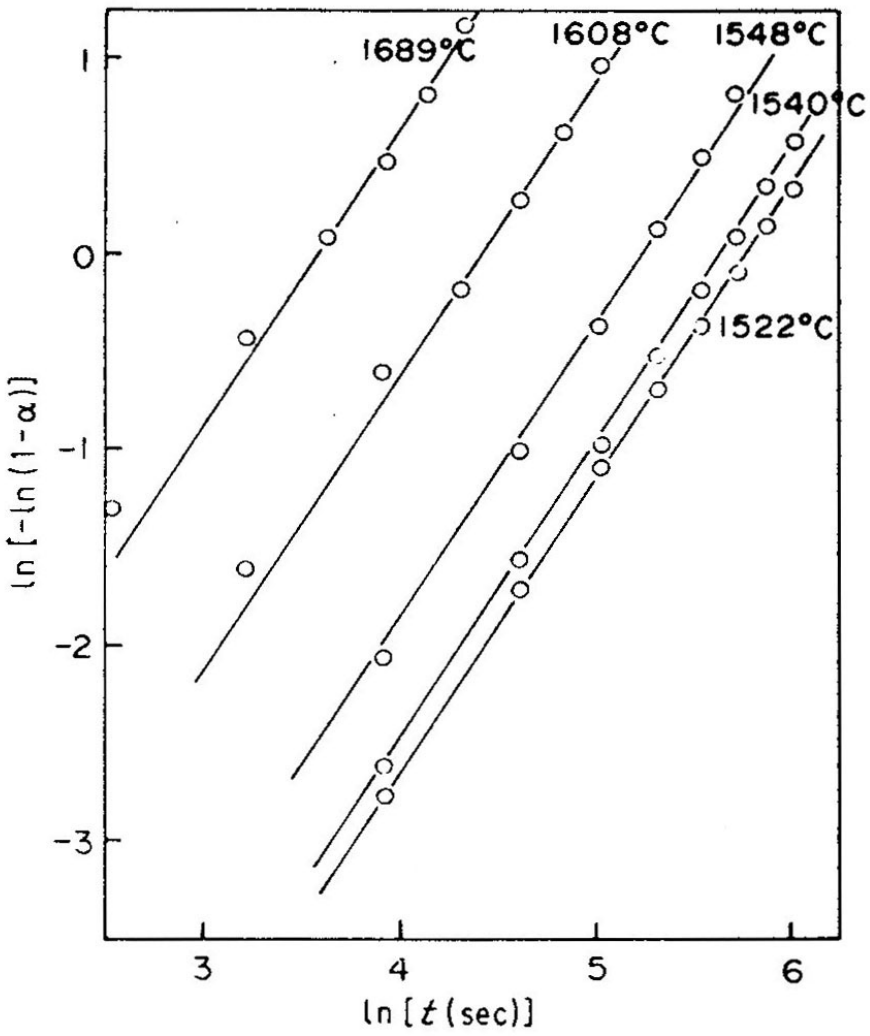

Figure 2-3-4 Plots of weight loss kinetic data showing the fit to the Avrami-Erofe'ev equation (i.e., $\ln[-\ln(1-\alpha)] = m\ln t + m\ln k$), from Ono and Kurachi (1991).

3. Ono and Kurachi reported an activation energy of 391 kJ/mol. This value is similar to the activation energy for diffusion of carbon at the phase boundaries of SiC (i.e., 305kJ/mol, Francis and Colbe (1968)). Therefore, Ono and Kurachi concluded that the "carbothermal reduction reaction of SiO_2 by carbon in an amorphous SiO_2-C mixture is controlled by the diffusion of carbon to the growing surface of the β-SiC crystal."
4. Narisawa et al. studied the effect of starting composition on reaction kinetics. Some of their results are shown in the Table 2-3-2. They concluded that the reaction rate was independent of the composition (i.e., C/Si molar ratio) of the pyrolyzed material. However, it should be noted that the reaction was completed very quickly ($\leq$ 100 sec) at 1600-1700^{o}C so the rate constants measured at 1500^{o}C may have been more reliable. The latter rate constants showed that the reaction rate actually increased with increasing C/Si molar ratio. (This topic will be discussed further in section 4.5.2.)
5. Narisawa et al. also studied the effect of C/Si molar ratio (in the pyrolyzed material) on the size of SiC crystallites formed in the reaction. The results are summarized in Table 2-3-3. The growth of SiC crystallites was significantly inhibited by the presence of excess carbon after the reaction was complete. (The samples with C/Si molar ratio of 3.84 had a significant amount of "free" (residual) carbon after the reaction was complete.)

Table 2-3-2 Rate constants (k) for the SiC carbothermal reduction reaction using pyrolyzed materials with different starting composition (i.e., C/Si molar ratio), from Narisawa et al. (1998).

C/Si molar ratio	k ($\times 10^{-5}$ $sec^{-3/2}$)		
	1500°C	1600°C	1700°C
2.07	0.46	9.10	32.2
2.97	0.54	9.10	46.4
3.84	0.66	6.32	43.9

Table 2-3-3 SiC crystallite size along the <111> direction (d_{111}) and fractional weight loss (X_{WL}) after carbothermal reduction reaction at indicated temperatures for 60 min for three different compositions, from Narisawa et al (1998).

C/Si molar ratio before CTR	1500°C		1600°C		1700°C	
	d_{111} (nm)	X_{WL}	d_{111} (nm)	X_{WL}	d_{111} (nm)	X_{WL}
2.07	9.6	0.63	18.6	1.0	33.7	1.0
2.97	9.1	0.67	21.5	1.0	27.2	1.0
3.84	10.8	0.75	13.4	1.0	16.1	1.0

- van Dijen and Metselaar (1991)

van Dijen and Metselaar (1991) studied the reaction between carbon and silica (C/Si molar ratio = 3.2) at temperatures in the range of ~1300-1800^{o}C. (Details about raw materials have been given in section 2.2.1.) The reaction kinetics was obtained from weight loss measurements. They made the following observations:

1. The weight loss data was fit to three kinetic equations: the linear rate equation (Equation (2-3-9) with n = 1), Jander's equation (Equation (2-3-5)), and Carter's equation (Equation (2-3-7)). Activation energies of 310 kJ/mol, 440 kJ/mol and 375 kJ/mol were obtained, respectively, from those three equations. The authors believed that Jander's equation was the most appropriate for their data, but they did not provide a clear explanation for this conclusion. They also suggested that the activation energy was associated with the diffusion of carbon atoms in carbon, but they did not provide any supporting experimental evidence.
2. The reaction rate increased when the gas flow rate of (i.e., helium) was increased from 0.05 L/min to 0.1 L/min, while a further increase of flow rate to 0.2 L/min did not influence the reaction rate significantly.
3. The grain growth of SiC at temperatures in the range of 1700-1800^{o}C followed the "normal grain growth" equation:

$$d^2 - d_0^2 = kt \tag{2-3-19}$$

where d is the maximum grain diameter for a given time t, d_0 is the maximum grain diameter at t=0, and k is the grain growth rate constant. The calculated activation energy for grain growth was 450 kJ/mol.

- Kevorkijan et al. (1992)

Kevorkijan et al. studied the reaction between colloidal silica (specific surface area of 200 m^2/g) and two grades of carbon black (specific surface areas of 70 m^2/g and 560 m^2/g). Powder mixtures were heat treated in the range of 1150 to 1500^oC in vacuum (~ 1 Pa) for less than 2 h. The carbon black with specific surface area of 560 m^2/g yielded primary SiC particles with average diameter of 10-20 nm, while the carbon black with specific surface area of 70 m^2/g yielded primary SiC particles with 50-100 nm in diameter. Hence, the authors concluded that the SiC particle size was dependent upon the particle size of the carbon reactant.

- Weimer et al. (1993)

Weimer et al. synthesized SiC using two kinds of carbon black powder (mean crystallite sizes of 30 nm and 218 nm) and colloidal silica (mean crystallite size of 22 nm) or quartz (mean particle size 1.1 μm). Reactions were carried out at temperatures in the range of 1575-2300^oC with very short holding times (several seconds) in a flowing Argon atmosphere. Sample weights were monitored during the reaction. The following observations were made:

1. The weight loss data fit the interface controlled "shrinking-core" model as shown in Equation (2-3-20).

$$1-(1-\alpha)^{1/3} = kt = \frac{k_0 \exp(-\frac{E}{RT})}{d} t \qquad (2\text{-}3\text{-}20)$$

where α is the extent of reaction, t is the reaction time, k is the reaction rate constant, k_0 is the pre-exponential constant, E is the activation energy, R is the gas

constant, and d is the initial carbon particle size. Table 2-3-4 shows the rate constants (k) obtained at different temperatures in the Weimer et al. study. Weimer et al. plotted $\ln(k \cdot d)$ against inverse temperature ($1/T$) (Figure 2-3-5), and the slope of the line gave $-E/R$. The calculated reaction activation energy was 382 ± 34 kJ/mol.

2. Silicon was detected by XRD in the CTR product for the early and intermediate stages of the reaction. Weimer believed (without providing experimental proof) that the silicon came from the dissociation of SiO.
3. The reaction rate increased with decreasing size of the carbon particles, while the size of silica particles did not have much effect on the reaction rate. (It should be noted that the latter conclusion was based on very limited data.)
4. The morphology of the SiC crystallites was similar to that of the starting carbon particles.
5. SiC crystallite sizes were less than 100 nm. As expected, higher temperature heat treatment resulted in larger crystallite size. Weimer et al. believed that the starting carbon particle size also influenced the SiC crystallite size greatly because they observed a similarity between the SiC crystallite and the original carbon particle.

Based on observations 2-4, the authors concluded that the reactions to form SiO (Equations (2-2-4) and (2-2-5)) were fast and that the reaction of SiO at carbon surfaces (Equation (2-2-10)) was the overall rate-limiting step for the CTR reaction.

Table 2-3-4 Rate constants (k) and activation energy (E) for the SiC carbothermal reduction reaction, from Weimer et al. (1993).

C particle size d (nm)	k ($\times 10^{-2}$ sec^{-1})					E (kJ/mol)
30	1575°C	1625°C	1675°C	1700°C	1725°C	382
	1.2	2.0	6.2	8.9	13	
218	1900°C	2000°C				
	9.2	15				

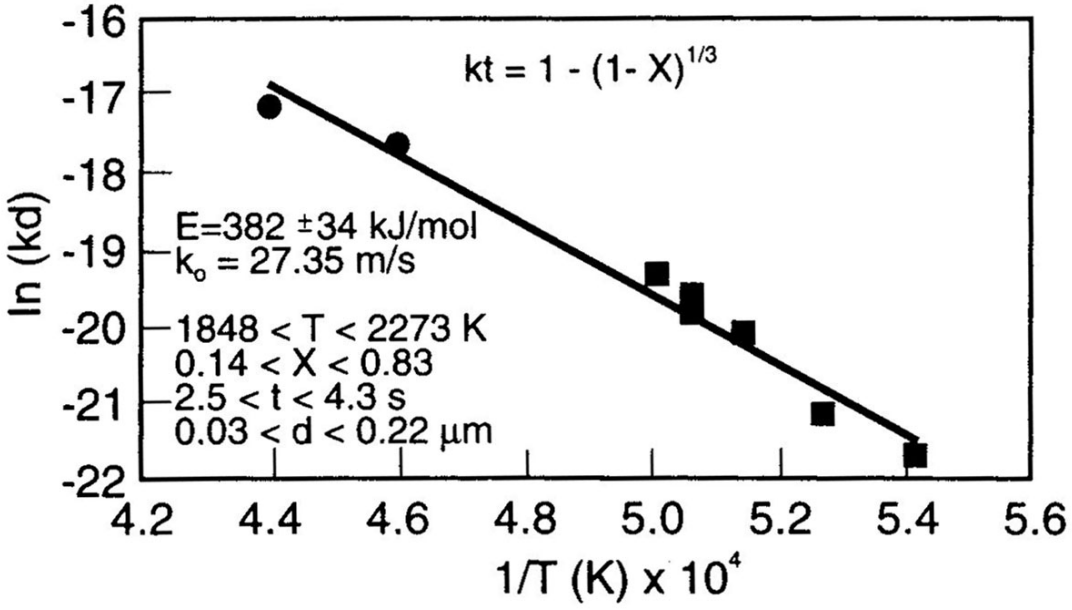

Figure 2-3-5 Reaction kinetics data obtained based on the interface-controlled "shrinking-core" model (Equation (2-3-20)): ■ the initial carbon particle size (d) was 30 nm; ● the initial carbon particle size (d) was 218 nm, from Weimer et al. (1993).

It should be noted that the activation energy reported above (382 ± 34 kJ/mol) was questionable. According to Equation (2-3-20), the activation energy value should be independent of the carbon particle size. However, an activation energy of 511 kJ/mol was calculated for reactions carried out at $\leq 1725^{o}$C with ~30 nm carbon particles, while an activation energy of 201 kJ/mol was calculated for reactions carried out at 1900-2000^{o}C with ~218 nm carbon particles. These results suggest that the data handling protocol in this study may not have been sound.

- Benaissa et al. (1994) and Keller et al. (1999)

Benaissa et al. studied the reaction between SiO (obtained by heating a mixture of Si and SiO_2) and activated carbon at 1240^{o}C. A bimodal pore size distribution was observed in reaction products which contained SiC and unreacted carbon (Figure 2-3-6). The first mode, with mostly 2-5 nm pores, was believed to be associated with the activated carbon reactant because similar pores similar pores were observed in the pure reactant. In addition, these pores could be eliminated from the reaction product by heating the sample in air at 800^{o}C. The second mode, with mostly 10-30 nm pores, was presumably associated with the SiC crystallites.

Keller et al. also studied the formation of SiC by the reaction of SiO (obtained by heating a mixture of Si and SiO_2) and activated carbon at temperatures in the range of 1200 to 1350^{o}C. After the reaction, excess carbon in the product was removed by heating the product in air at 600^{o}C for 2 h. The following observations were made:

1. Table 2-3-5 shows that the surface area of the SiC decreased with increasing extent of reaction.
2. The reaction product showed a bimodal pore size distribution when the extent of

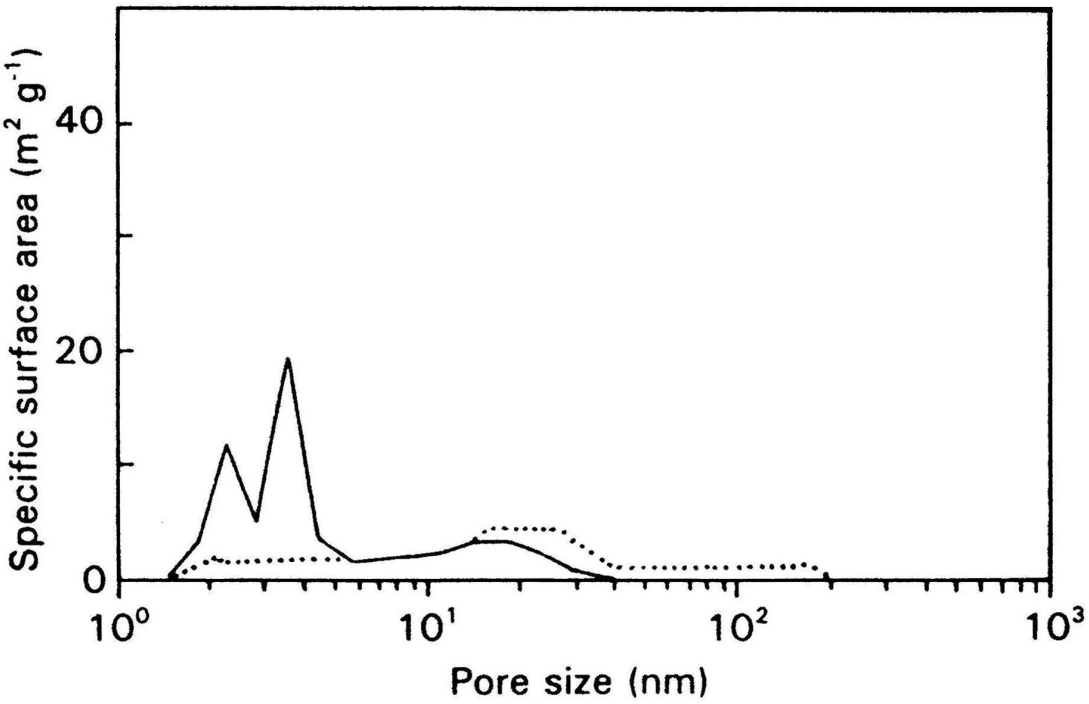

Figure 2-3-6 Pore size distributions for the reaction product between SiO and activated carbon after 7 h heat treatment at 1240°C. The solid line and the dotted line are the pore size distributions before and after heat treatment of the product in air at 800°C, from Benaissa et al. (1994).

reaction was limited (i.e., 1200°C data in Figure 2-3-7). The mode sizes were centered at ~ 5 nm and ~ 30 nm, respectively. With further reaction, the small pores (~5 nm) disappeared and only the larger pores remained in the product. (It should be noted that the y axis unit for Figure 2-3-7 from Keller's study was incorrect. The "adsorbed volume" should have the unit of $m^3 \cdot g^{-1} \cdot nm^{-1}$ instead of $m^2 \cdot g^{-1} \cdot nm^{-1}$ in the figure.) The authors did not explain why the small mesopores (mostly < 10 nm) disappeared as the reaction proceeded. These pores might have been the small associated with residual carbon. It is possible that the heat treatment at 600°C/2h in air was not sufficient to remove all the carbon.

Table 2-3-5 Specific surface area of SiC product with different extent of conversion, from Keller et al. (1999).

Reaction time (h)	1250°C		1300°C	
	SA_{BET} (m2/g)	C → SiC (%)	SA_{BET} (m2/g)	C → SiC (%)
1	112	16	65	32
2	77	26		
3	60	39	31	63
4	49	46		
5	46	59	26	77
7	41	62	14	79
10	26	70	10	85

Note: SA_{BET} is BET specific surface area; C → SiC is the percentage of conversion from carbon to SiC; the SiC had been heat treated in air at 600°C for 2 h to remove excess carbon.

- Martin et al. (1998)

Martin et al. studied the structural evolution of SiC using a starting mixture prepared from a colloidal silica sol (mean particle size of 10 nm) and a sugar solution. After pyrolysis, the fine-scale carbon/silica mixture was heat treated at 1500-1800°C for 15-30 min in vacuum (~20 Pa).

Table 2-3-6 shows specific surface area and XRD crystallite size data for samples heat treated under different conditions. Specific values for the extent of reaction (e.g., percent conversion values) were not provided for these samples, but the authors indicated that the CTR reaction was mostly complete in all samples. It is not clear why there was

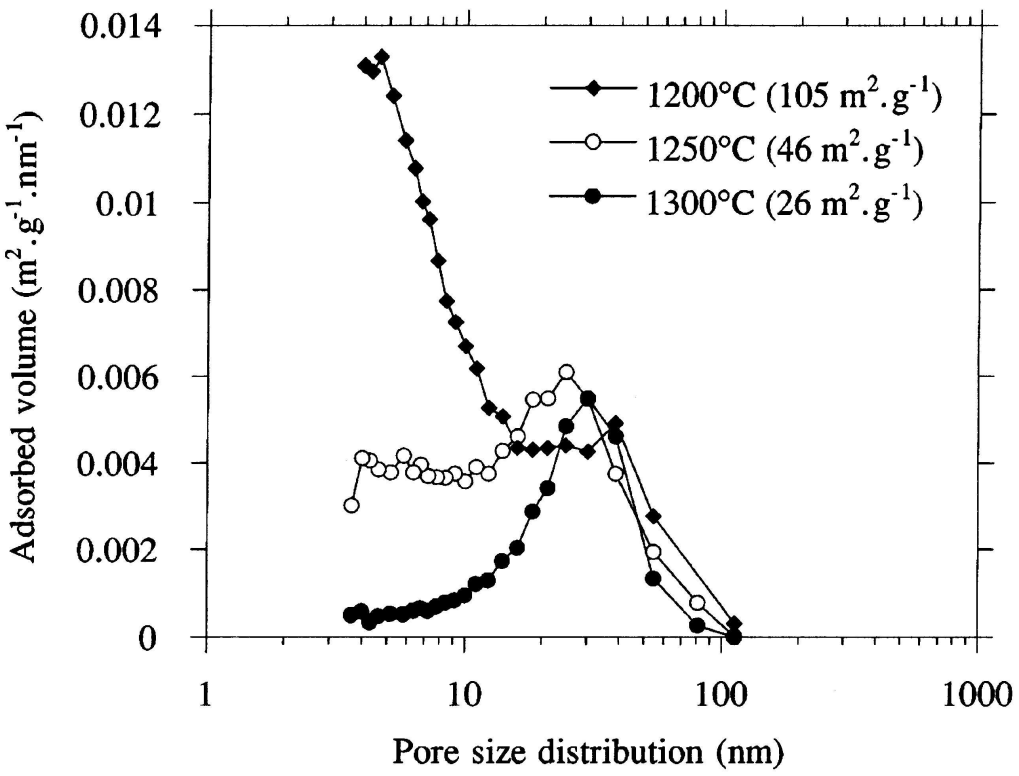

Figure 2-3-7 Pore size distribution of SiC synthesized from reaction between SiO and activated carbon at different temperatures for 5 h, from Keller et al. (1999).

relatively little change in the specific surface areas and the crystallite sizes with increasing temperature (i.e., except for the 1800°C/30 min sample). If the reaction was mostly completed, it would normally be expected that the SiC crystallites would coarsen with increasing temperature. (Some minor increases in crystallite size with increasing temperature were observed in the study, but the specific surface area does not show a clear decreasing trend.) One possible explanation for the limited increase in the crystallite size with increased temperature is that diffusion was inhibited by the presence of free carbon. The authors reported that the samples all had carbon contents in the range of 36 ± 2 wt%. This constant value for the carbon content seems to confirm that the reaction was

Table 2-3-6 Specific surface area and mean crystallite size for the SiC product heat treated at different conditions, from Martin et al. (1998).

Heat treatment condition	Specific surface area (m^2/g)	Mean crystallite size (from XRD) (nm)
1500°C/15min	26.6	18
1550°C/15min	26.7	20
1550°C/20min	31.1	20
1600°C/15min	23.7	20
1600°C/30min	19.0	
1700°C/15min	29.6	21
1700°C/30min	27.0	
1800°C/15min	28.0	22
1800°C/20min	27.2	22
1800°C/30min	6.8	

Note: The SiC crystallite size was calculated from the broadening of the SiC(220) diffraction line.

essentially complete in all samples and the mean value of 36 wt% indicates that the samples contained substantial free carbon. (A pure SiC would have 30 wt% carbon.)

- Chen et al. (2000)

Chen et al. synthesized SiC by heat treating mixtures of quartz and carbon particles (both particle sizes were ~41-43 μm) at 1300-1550°C in a flowing (0.6-3 L/min) He atmosphere. After the reaction, the product was heat treated at 700°C for 4 h in air.

The amounts of SiC and unreacted silica were determined from XRD and weight loss data. They made the following observations:

1. The reaction rate was slower when the He flow rate was higher. They attributed this to larger losses of SiO at higher flow rate. Recall that van Dijen and Metselaar (1991) observed an increased reaction rate with increasing gas flow rate. However, they used much lower flow rate (0.05-0.2 L/min). It is possible that CO removal was suppressed at very low gas flow rates. The CTR reaction would be inhibited by a high local partial pressure of CO.
2. Increased reaction rates were observed in powder mixtures as the carbon particle size decreased. (The mean carbon particle sizes varied from 134 to 90 to 51 μm, while the silica particle size was fixed at 68μm.)

- Panigraphi et al. (2001)

Panigraphi studied the kinetics of SiC production from rice husks. The rice husks were dried and pyrolyzed to produce a mixture of carbon and silica with a C/Si molar ratio of 5:1. Then, the pyrolyzed powder was pressed into pellets and heat treated at 1150-1650^{o}C in vacuum. The reaction rate was not affected by the compact pressure. In fact, the reaction rate was approximately the same for loose powder compacts and pressed pellets. They attributed this to a trade-off between two factors: (1) Compaction is expected to increase the reaction rate due to more extensive particle-particle contacts between the silica and carbon. (2) Compaction is expected to decrease the reaction rate because of greater difficulty in removing CO from the compact. The reaction will be suppressed if there is a high local CO concentration.

CHAPTER III

EXPERIMENTAL PROCEDURES

This chapter gives the experimental procedures for: (i) synthesis of the powders used to investigate SiC formation by carbothermal reduction (CTR) reactions (section 3.1), (ii) determination of the sample compositions before and after CTR (section 3.2), (iii) examination of vapor-phase deposited material that was formed from volatile species generated during the CTR reaction (section 3.3), (iv) investigation of the CTR reaction kinetics (section 3.4), and (v) structural characterization of the materials before and after the CTR reaction (section 3.5).

3.1 Synthesis of Nanocrystalline SiC

As stated in the introduction, the aim of this study is to reveal the reaction mechanism of carbothermal reduction synthesis of SiC, which is represented by the following equation:

$$SiO_{2\,(s)} + 3C_{\,(s)} \rightarrow SiC_{\,(s)} + 2CO_{\,(g)} \qquad (3\text{-}1\text{-}1)$$

An intimate mixing of carbon and silica is desirable in order to achieve lower CTR reaction temperature and finer SiC (product) particle size. In this study, soluble carbon-bearing and silica-bearing raw materials were used to produce solutions with molecular-scale mixing of the components. The solutions were processed to produce powder precursors. These powders were heat treated (i.e., pyrolyzed) in order to decompose the precursors and form fine-scale carbon/silica mixtures. After the pyrolysis, carbothermal reduction reaction was carried out at higher temperature to transform the fine-scale carbon/silica mixture

into SiC. As discussed in Chapter II, this method has the advantage of producing nano-sized SiC with narrow particle size distribution at relatively low temperature.

The overall process used in this study for the preparation of nanocrystalline SiC is summarized by the flow chart in Figure 3-1-1. The specific processing steps shown in the figure are discussed in detail below. The steps of solution-based processing, drying, and pyrolysis were mostly carried out by Mr. Greg A. Staab and Dr. Chang-an Wang at Georgia Institute of Technology. The carbothermal reduction reaction, as represented by Equation (3-1-1), was investigated by the author.

In the synthesis, a low-molecular-weight (Mn<2000) phenolic resin ("novolac" type, GP775D69, Georgia Pacific, Atlanta, GA) was used as a soluble carbon source. It has a high carbon yield of 0.3973. (The carbon yield of phenolic resin was determined by heat treating the resin at 1150^{o}C for 1 h in flowing argon atmosphere. The yields for two separate heat treatments were 0.3989 and 0.3957, respectively, and the average value, i.e., 0.3973, was used as the carbon yield for that phenolic resin). Figure 3-1-2 is an illustration of an idealized phenolic resin oligomer with 4 units. (The actual structure will be more complicated). Tetraethoxysilane (TEOS, [$Si(OC_2H_5)_4$], Alfa Aesar, Ward Hill, MA) was the soluble source for silica. The chemical structure for TEOS is shown in Figure 3-1-3. TEOS was used as a precursor because procedures for producing fine-scale (<10 nm) polysilicate species by hydrolysis and condensation reactions are well-described in the scientific literatures (Brinker and Scherer, 1990). Ethanol (absolute, Chemical Stock Room, Georgia Institute of Technology) was distilled and used as solvent. Nitric acid (69.0-70.0 wt%, J. T. Baker, Philipsburg, NJ) was used to adjust the pH of the solution. Deionized water (conductivity ~0.3 μS/cm) was the reactant for hydrolysis.

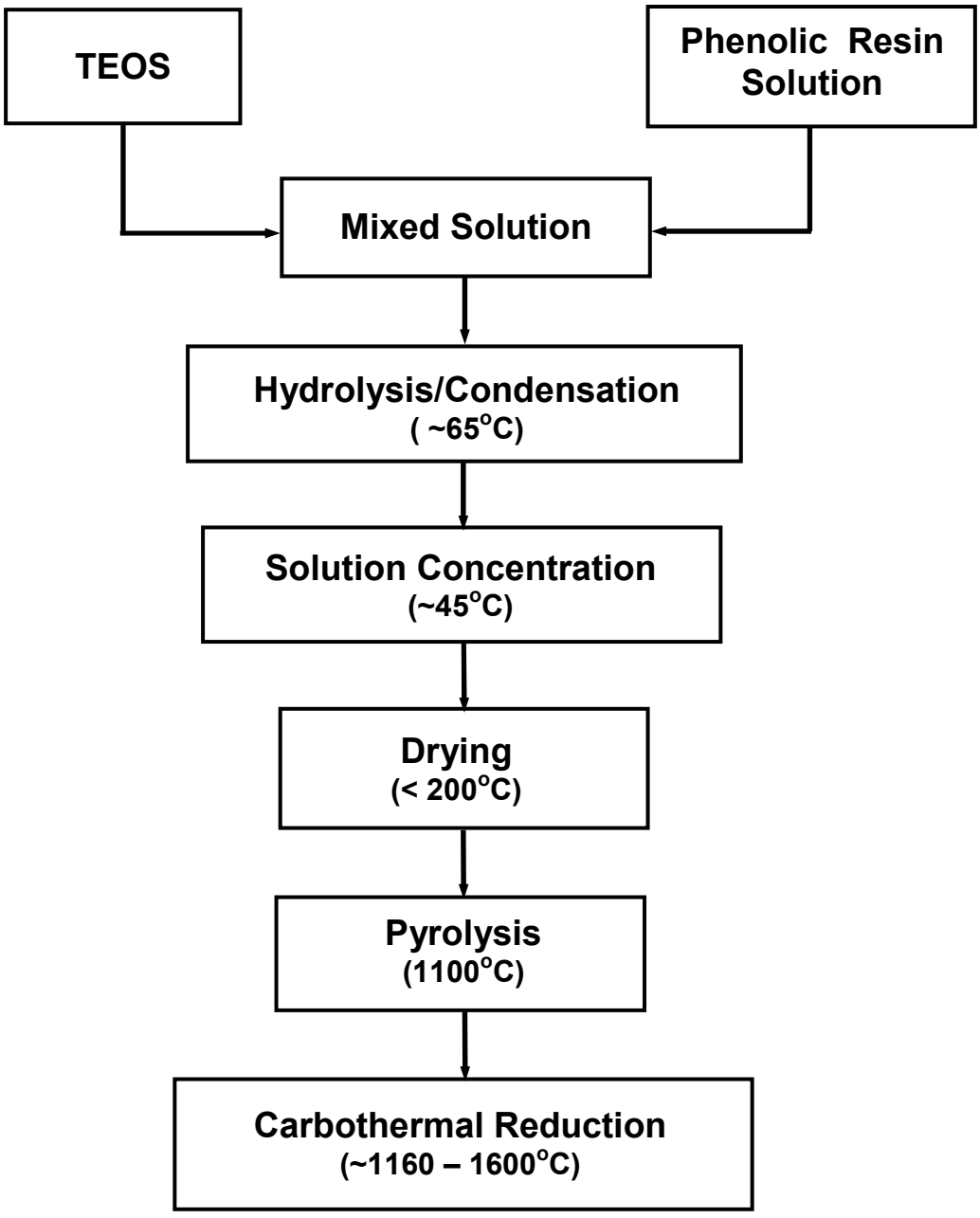

Figure 3-1-1 Flow chart for the synthesis of nanocrystalline SiC.

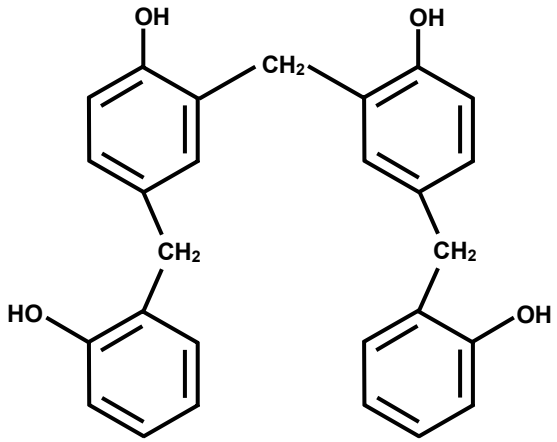

Figure 3-1-2 Illustration for oligomer of four phenolic units.

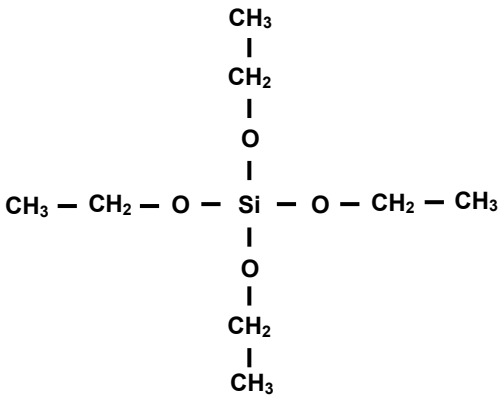

Figure 3-1-3 Illustration of the TEOS molecule structure.

According to the ideal Equation (3-1-1), the molar ratio of C/Si to produce phase-pure stoichiometric SiC should be 3:1. In the present study, samples with different C/Si molar ratios were prepared. "Silica-rich" samples (i.e., C/Si molar ratio smaller than 3) were made because some silica was lost during carbothermal reduction reaction due to the formation of SiO vapor. (This will be shown later in Chapter IV.) Therefore, excess silica was needed to produce powders that were nearly single phase SiC. "Carbon-rich" samples (i.e., C/Si molar ratio greater than 3) were made to investigate the effect of composition (C/Si molar ratio) on reaction kinetics and structural evolution of reaction product during the CTR reaction.

There were four powder samples studied in detail in this work: SC8, SC35, SC42 and SC46. SC8 series was "carbon-rich", while SC35 was "silica-rich". SC8 and SC35 were used to study the kinetics of carbothermal reduction reaction and the structural characteristics of the reaction product (e.g., crystallite size, porosity, specific surface area, etc.). The SC42 and SC46 samples had very similar composition to the SC35 sample and were used as supplementary materials for characterization of the reaction products. Table 3-1-1 summarizes the amounts of starting materials used and the expected C/Si molar ratios of the pyrolyzed materials for the four different series of samples. Step-by-step procedures for the preparation of the SC8 and SC35 powders are given below.

- Preparation of SC8

1. TEOS and ethanol were distilled before the synthesis. Schematics for the distillation setup are given in Figure 3-1-4. TEOS or ethanol were placed into a 1L round-bottom flask and some boileezers (Fisher Chemicals, Fair Lawn, NJ) were added into it. The round-bottom flask was placed in a heating mantle. The flask was connected to a

Table 3-1-1 Amount of raw materials used, the molar ratio for raw materials, and the expected C/Si molar ratio in the pyrolyzed materials for the SC8, SC35, SC42 and SC46 series of samples.

Series	Phenolic Resin (g)	TEOS (g)	Ethanol (g)	Water (g)		HNO_3 [1] (g)	TEOS : EtOH : H_2O : HNO_3 (molar ratio)	Expected C/Si Molar Ratio before CTR [2]
				directly added	from the 20 wt% HNO_3			
SC8	151.15	298.88	223.95	51.00	3.62	0.90	1 : 3.39 : 2.11 : 0.01	3.5
SC35	60.73	280.20	209.95	45.10	3.40	0.85	1 : 3.39 : 2.00 : 0.01	1.5
SC42	60.72	273.76	205.12	44.06	3.31	0.82	1 : 3.39 : 2.00 : 0.01	1.5
SC46	60.77	280.21	210.07	45.09	3.42	0.86	1 : 3.39 : 2.00 : 0.01	1.5

Notes:

1. This represents the actual weight of HNO_3 in the 20 wt% HNO_3 solution that was added to the mixed TEOS/phenolic resin/ethanol solution.
2. The "expected C/Si molar ratio before CTR" is an estimate based on the following assumptions: (i) There was no loss of Si during solution processing or the subsequent pyrolysis heat treatment. (ii) The amount of carbon was determined based on the yield (39.73 wt%) obtained when phenolic resin samples were heat treated under the pyrolysis conditions specified earlier in this section. It was assumed that the carbon yield was not affected by the solution processing during which the phenolic resin and the TEOS were mixed together. Consider an example using the SC8 sample. The amount of SiO_2 before CTR is given by 298.88/208.37 = 1.434 mol, where 298.88 is the weight (in gram) of TEOS in the batch and 208.37 is the molecular weight of TEOS. The amount of C before CTR is given by $(151.15 \times 0.3973)/12 = 5.004$ mol, where 151.15 is the amount of phenolic resin in the batch and 12 is the atomic weight for C.

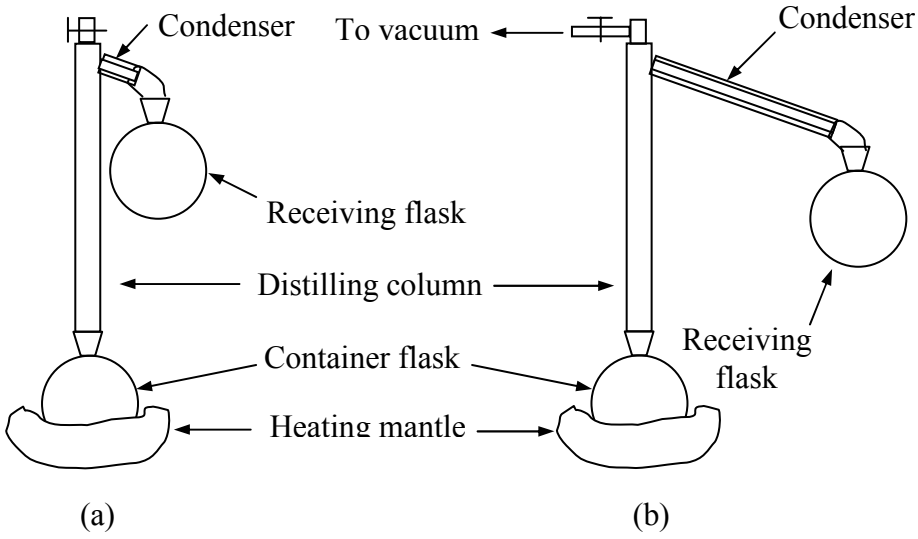

Figure 3-1-4 Schematics for setup used to distill (a) ethanol and (b) TEOS.

distilling column which was held upright. The top of the distilling column was connected to the receiving flask (which was another 1 L round-bottom flask) via a condenser. For TEOS, vacuum was applied during distillation. The speed of distillation was controlled to be ~2 drops/second (~8 ml/min). The distillation of TEOS was carried out to remove polysilicate species and particulate impurities that may have been present in the as-received material. The distillation of ethanol was carried out mostly to remove water that may have been absorbed from the atmosphere. After the distillation, the flask containing distilled TEOS or ethanol was plugged with a glass stopper and sealed with thermoplastic tape (Parafilm®, Pechiney Plastic Packaging, Chicago, IL) until usage.

2. 151.15 g of phenolic resin was measured and put into a 1 L round-bottom flask. 158.00 g of ethanol was added to the flask with phenolic resin. A magnetic stir bar was put into the flask. The phenolic resin and ethanol were mixed at room temperature for

~2 h. The phenolic resin dissolved completely in the ethanol. A transparent orange-colored solution was obtained.

3. 298.88 g of TEOS was added to the phenolic resin/ethanol solution and the solution was mixed for 1 min.
4. 51.00 g of deionized water (DI water) and 4.52 g of 20 wt% nitric acid solution (made by diluting the original 69.0-70.0 wt% nitric acid with DI water) were added to a 100 ml Erlenmeyer flask (E. flask). The solution was stirred for 30 seconds. Then, 65.95 g of ethanol was added to the E. flask and the solution was stirred for another 1 min. (The amount of water in the 20 wt% nitric acid was included in calculating the molar ratio of H_2O to TEOS given in Table 3-1-1.)
5. The ethanol/acid/water mixture from step 4 was added drop-wise (at a rate of approximately 20 ml/min) to the 1 L flask containing phenolic resin/TEOS/ethanol solution via a 10 ml pipette. The solution was stirred for 10 min. When exposed to water, TEOS tends to undergo hydrolysis such that silanol bonds (Si-OH) are formed, as illustrated in Figure 3-1-5 and Equation (3-1-2). Siloxane bonds (Si-O-Si) tend to form by condensation reactions between two silanol groups or between a silanol group and an ethoxy group (see Equations (3-1-3) and (3-1-4)).

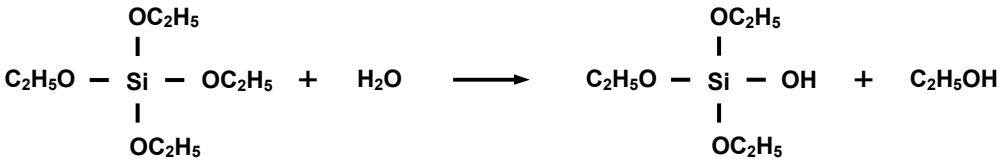

Figure 3-1-5 Illustration of hydrolysis of TEOS showing the replacement of one ethoxy group by one hydroxyl group.

Hydrolysis

$$\equiv Si - OCH_2CH_3 + H_2O \longrightarrow \equiv Si - OH + HOCH_2CH_3 \quad (3\text{-}1\text{-}2)$$

Water Condensation

$$\equiv Si - OH + HO - Si \equiv \longrightarrow \equiv Si - O - Si \equiv + H_2O \quad (3\text{-}1\text{-}3)$$

Alcohol Condensation

$$\equiv Si - OCH_2CH_3 + HO - Si \equiv \longrightarrow \equiv Si - O - Si \equiv + HOCH_2CH_3 \quad (3\text{-}1\text{-}4)$$

6. The flask containing mixed solutions from step 5 was placed in an oil bath at 65°C for 5 h with a nitrogen (N_2) purge. (The heat treatment of the sol was to accelerate the hydrolysis/condensation reactions prior to the subsequent concentration step.) No obvious viscosity change was observed during this heat treatment.
7. After the heat treatment in the oil bath, the stir bar was removed from the solution and the transparent sols were concentrated at 40-60°C on a rotary evaporator (Model R-114, Büchi Laborator-Technik, Switzerland). The viscosity of the sol increased as solvent was removed. The sol began to boil and some foam was formed as the evaporation occurred. The sol remained transparent until most of the solvent was removed. In the late stages of the concentration process, the color of the sol changed from amber to light pink; the light pink sol was opaque. Further heat treatment at this stage resulted in relatively little solvent loss, but the viscosity of the sol increased very substantially. The foam lost its flexibility and would not expand despite full vacuum applied by the rotary evaporator.

8. The flask was removed from the rotary evaporator. It was placed in the vacuum oven and dried at 50°C in vacuum for 72 h to remove volatile species. After that, a porous, brittle material was obtained.
9. The porous and brittle material was collected from the flask by a spatula. The collected material was crushed and ground with alumina mortar and pestle. The ground material was sieved through a 150 mesh sieve manually to produce a free-flowing powder with relatively coarse agglomerate size.
10. The sieved powder was then dried again in a vacuum oven. The temperature of the oven was set at 50°C initially and then it was raised gradually to approximately 110°C over several hours. The drying was continued at ~110°C for ~12 h. After that, the sample was cooled down under vacuum.
11. The dried powder was put into alumina boats. The boats were placed in the center of the three-zone tube furnace (Model 54259, Lindberg, Watertown, WI) for pyrolysis. The furnace was heated up to 300°C at a rate of 5°C/min, to 600°C at 3°C/min, to 1100°C at 5°C/min, and then held at 1100°C for 4 h. The gas atmosphere for the heat treatment was flowing argon (Ar, >99.999%, Airgas, Randor, PA). The flow rate was ~0.1 L/min. This pyrolysis condition was selected based on two experimental observations: (i) Thermal gravimetric analysis, TGA (Model STA 409, Netzsch, Exton, PA) of the SC8 dried gel indicated that the weight loss due to pyrolytic decomposition was essentially complete after heat treatment at 1100°C (see Figure 4-1-9 in section 4.1.3). (ii) X-ray diffraction (XRD) showed that essentially no SiC was present in an 1100°C-pyrolyzed SC8 sample (see section 4.1.1 and Appendix E).

12. The pyrolyzed sample was then heat treated at temperatures in the range of 1160-1600^{o}C in a high temperature tube furnace (Model M11, Centorr Furnace, Nashua, NH) for different times in flowing argon with a flow rate of ~0.7 L/min. The furnace was heated by a graphite element. The temperature was measured by a type B thermocouple (Flow Autoclave Systems Inc., Columbus, OH). Trace amounts of water and/or oxygen in the argon were removed by passing the argon (Ar, >99.999%, Airgas, Randor, PA) through a getter furnace (Model 2B200 120V, Centorr Associates Inc., Nashua, NH) before into the M11 furnace. The details of the sample setup in the M11 furnace will be described later in section 3.4.1.

- Preparation of SC35

1. TEOS and ethanol were distilled before the experiment.
2. 60.75 g of phenolic resin was measured and put into a 1 L glass flask. 159.46 g of ethanol was added to the glass flask with phenolic resin. A magnetic stir bar was put into the flask. The phenolic resin and ethanol was mixed at room temperature for 1 h. The phenolic resin dissolved completely in the ethanol. A transparent orange-colored solution was obtained.
3. 280.22 g of TEOS was added to the phenolic resin/ethanol solution and the solution was mixed for 5 min.
4. 45.10 g of DI water and 4.25 g of 20 wt% nitric acid solution were added to a 100 ml E. flask. The solution was stirred for 30 seconds. 51.46 g of ethanol was added to the E. flask and the solution was stirred for another 1 min.

5. The ethanol/acid/water mixture from step 4 was added drop-wise (at a rate of approximately 20 ml/min) via a 10 ml pipette to the 1 L flask containing phenolic resin/ TEOS/ethanol solution. The solution was stirred for 5 min.
6. The flask containing mixed solutions was placed in the oil bath at 65^{o}C for 1 h with a N_2 purge. No viscosity change was observed during this heat treatment.
7. After the heat treatment in the oil bath, the stir bar was removed from the solution and the transparent sols were concentrated at 35-40^{o}C on the rotary evaporator for ~2.5 h. The viscosity of the sol increased as solvent was removed. The sol began to boil and some foam was formed as the evaporation occurred. At the end of the concentration, the color changed from amber to orange and part of the sol became opaque. The foam lost flexibility and would not expand despite full vacuum applied by the rotary evaporator.
8. The flask was removed from the rotary evaporator. It was placed in the vacuum oven and dried at ~42^{o}C in vacuum for ~15 h to remove volatile species. The temperature was then increased gradually to 70^{o}C and dried for ~20 h. After that, a porous, brittle material was obtained.
9. The porous and brittle material was collected from the flask by a spatula. The collected material was crushed and ground with agate mortar and pestle. The ground material was sieved through a 150 mesh sieve manually to produce a free-flowing powder with relatively coarse particle size.
10. The sieved powder was then dried again in vacuum. The temperature of the oven was set at 50^{o}C initially and then it was raised gradually to approximately 110^{o}C over

several hours. The drying was continued at ~110°C for ~24 h. Then, the sample was cooled down under vacuum.

11. The dried powder was put into alumina boats. The boats were placed in the center of the Lindberg three-zone furnace for pyrolysis. The furnace was heated up to 300°C at a rate of 5°C/min, to 600°C at 3°C/min, to 1100°C for 5°C/min, and then held at 1100°C for 2 h. The gas atmosphere for the heat treatment was flowing Ar atmosphere with a flow rate of ~0.1 L/min.
12. The pyrolyzed sample was then heat treated at temperatures in the range of 1160-1600°C in the M11 furnace for different times in flowing argon with a flow rate of ~0.7 L/min.

- Preparation of SC42 and SC46

As mentioned earlier, the SC42 and SC46 samples were prepared with the similar composition as the SC35 samples (refer to Table 3-1-1) in order to have additional material for characterizing the pyrolyzed and carbothermally-reduced powders. The procedures were essentially the same as described for the SC35 batch preparation.

- Preparation of dried material from TEOS

Some dried material was prepared from TEOS (i.e., without phenolic resin) sol by Dr. Chang-an Wang. The sol contained TEOS, ethanol, water and nitric acid with molar ratio of TEOS : EtOH : H_2O : HNO_3 = 1 : 3.4 : 2 : 0.01. The sol was dried at 145°C to obtain a powder. (No further details on the sample preparation procedure were available.)

- Preparation of dried material from phenolic resin

Some dried material was prepared from phenolic resin by Dr. Chang-an Wang. A solution was dried at 50°C to obtain dried resin. (No further details on the sample preparation procedures were available.)

- Sample identification

In the current study, samples given pyrolysis heat treatment were labeled according to the series number and the temperature and time of pyrolysis. For example, "SC35-1100(2h)" denotes a sample from the SC35 series which was pyrolyzed at 1100°C for 2h. Samples given carbothermal reduction heat treatment were labeled according to the series number and the temperature and time of the carbothermal reduction reaction. For example, "SC8-1160(20h)" denotes a sample from the SC8 series which was heat treated at 1160°C for 20 h after the pyrolysis heat treatment at 1100°C.

3.2 Determination of Sample Compositions Before and After CTR

The "LECO combustion method" (Sherry Laboratories, Muncie, IN) was the primary method used in this study to determine the carbon content of the heat-treated materials. (In the LECO method, the sample is combusted in oxygen at high temperature and the CO_2 generated during the combustion process is analyzed and used to calculate the total carbon content of the sample.) Suppose the carbon content (i.e., weight fraction) of a pyrolyzed material is w_C^{pyro}. Assume that the pyrolyzed material was composed of carbon and silica only. Therefore, the silica content in the pyrolyzed material, w_{SiO2}^{pyro}, should be:

$$w_{SiO2}^{pyro} = 1 - w_C^{pyro} \tag{3-2-1}$$

Therefore, the C/Si molar ratio in the pyrolyzed material, $x_{C/Si}^{pyro}$, should be

$$x_{C/Si}^{pyro} = \frac{w_C^{pyro}/12}{w_{SiO2}^{pyro}/60} = 5 \times \frac{w_C^{pyro}}{1 - w_C^{pyro}} \qquad (3\text{-}2\text{-}2)$$

where 12 is the atomic weight of carbon and 60 is the formula weight of SiO_2. Take the example of SC35-1100(2h) pyrolyzed material in which w_C^{pyro} = 0.3260 from the LECO analysis. Therefore, the silica content, w_{SiO2}^{pyro}, should be:

$$w_{SiO2}^{pyro} = 1 - w_C^{pyro} = 1 - 0.3260 = 0.6740$$

The C/Si molar ratio in the SC35 pyrolyzed material, $x_{C/Si}^{pyro}$, should be:

$$x_{C/Si}^{pyro} = 5 \times \frac{w_C^{pyro}}{1 - w_C^{pyro}} = 5 \times \frac{0.3260}{1 - 0.3260} = 2.4$$

The carbon contents of the pyrolyzed materials were also determined from the weight loss that occurred by heat treating the pyrolyzed materials in the tube furnace (Model 55031, Lindberg, Watertown, WI) or in the TGA furnace (Model STA 409, Netzsch, Exton, PA) in air at 1050-1150^{o}C for 1-2 h. Prior to the oxidation heat treatment, the samples were dried overnight at ~80^{o}C in a vacuum oven. (These studies were carried out by Dr. Chang-an Wang of Georgia Institute of Technology.) The entire weight loss was attributed to the oxidization of carbon in the pyrolyzed sample. Therefore, the material that remained after the heat treatment was assumed to be only SiO_2. For example, the average weight yield of the SC35 pyrolyzed material after oxidation at 1050^{o}C (2h) was 0.6777. Therefore, the carbon content should be 1- 0.6777 = 0.3223, which is very close to the result obtained by the LECO method (i.e., 0.3260).

Pyrolyzed materials which were given sufficient heat treatment to complete the CTR reaction will be referred to as "fully-converted materials." The total carbon content of

these samples, w_{C-Tot}^{CTR}, was determined by the LECO method. Assume that a fully-converted material is composed of SiC and excess (or "free") carbon only. Therefore, the silicon content, w_{Si}^{CTR}, in the material should be:

$$w_{Si}^{CTR} = 1 - w_{C-Tot}^{CTR} \tag{3-2-3}$$

Therefore, the C/Si molar ratio in the fully-converted material, $x_{C/Si}^{CTR}$, should be:

$$x_{C/Si}^{CTR} = \frac{w_C^{CTR}/12}{w_{Si}^{CTR}/28} = 2.34 \times \frac{w_C^{CTR}}{w_{Si}^{CTR}} \tag{3-2-4}$$

where 28 is the atomic weight for silicon. The content of SiC in the fully-converted sample, w_{SiC}^{CTR}, should be:

$$w_{SiC}^{CTR} = \frac{w_{Si}^{CTR} \times 40}{28} = 1.43 \times (1 - w_C^{CTR}) \tag{3-2-5}$$

where 40 is the formula weight of SiC. Therefore, the content of free carbon in the fully-converted sample, w_{C-free}^{CTR}, should be:

$$w_{C-free}^{CTR} = 1 - w_{SiC}^{CTR} = 1 - 1.43 \times (1 - w_C^{CTR}) \tag{3-2-5}$$

LECO analysis for the SC35 fully-converted material gave a total carbon content, w_{C-Tot}^{CTR}, of 0.3148. Therefore, silicon content in the sample, w_{Si}^{CTR}, should be:

$$w_{Si}^{CTR} = 1 - w_{C-Tot}^{CTR} = 1 - 0.3148 = 0.6852$$

The C/Si molar ratio in the fully-converted sample should be:

$$x_{C/Si}^{CTR} = 2.34 \times \frac{0.3148}{0.6852} = 1.08$$

The content of SiC in the fully-converted material, w_{SiC}^{CTR}, should be:

$$w_{SiC}^{CTR} = 1.43 \times (1 - w_{C-Tot}^{CTR}) = 1.43 \times (1 - 0.3148) = 0.98$$

The content of free carbon in the fully-converted material, w_{C-free}^{CTR}, should be:

$$w_{C-free}^{CTR} = 1 - w_{SiC}^{CTR} = 1 - 0.98 = 0.02$$

3.3 Collection and Identification of Volatile Intermediate Condensates

As discussed in section 2.2.1, several studies indicated that the SiC formation by carbothermal reduction involves the formation of SiO vapor as an intermediate reaction product. The formation of SiO volatiles during the CTR reaction was confirmed indirectly in this study. This was done by collecting and analyzing condensed product that had formed in a colder zone of the furnace (i.e., downstream from the reaction hot zone). An illustration of the experiment setup is given in Figure 3-3-1.

SC46-1100(2h) pyrolyzed sample was placed in the hot zone of M11 furnace for heat treatment, as illustrated in Figure 3-3-1. High-purity Ar was passed through the furnace tube at a flow rate of ~0.7 L/min. On the downstream side of the powder in the cold zone of the furnace, a clean piece of alumina, serving as the substrate for vapor deposition, was supported upright using a high purity graphite block. The surface of the alumina substrate was kept perpendicular to the direction of gas flow. If the reaction involved SiO formation, it was expected that some of the SiO would be carried downstream by the flowing Ar and would condense on the alumina substrate.

After reaction at 1160^{o}C for 8 h, the alumina substrate was taken out. It was then coated with gold for 1 min with a sputter coater (Model PS-2, International Scientific Instruments, England). Energy dispersive X-ray spectroscopy, EDX (Model 3600-0398, Kevex X-ray, Foster, CA) was used to obtain elemental analysis of the deposits. The analysis was carried out by Dr. Zhaohui Yang of the Georgia Institute of Technology.

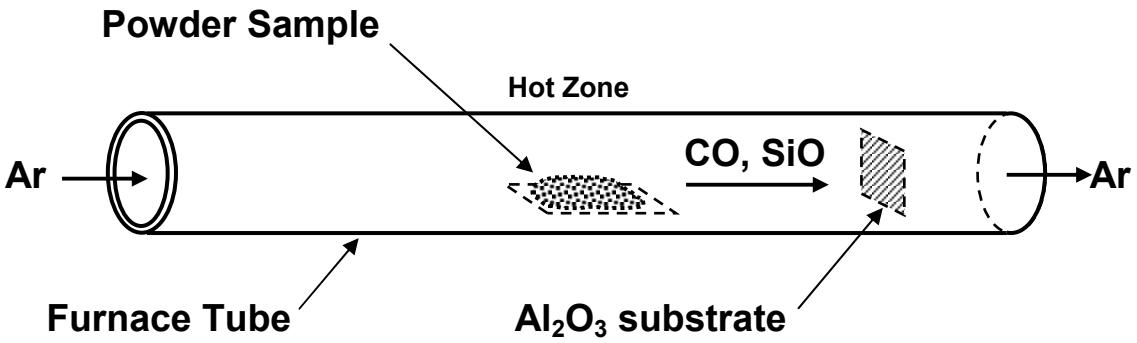

Figure 3-3-1 Illustration for vapor deposition experiment during carbothermal reduction.

The material deposited on the surface of the graphite tube in the colder zone of the M11 furnace was also collected after high temperature (> ~1600^{o}C) heat treatment of the M11 furnace under vacuum. X-ray diffraction, XRD (Model PW1800, Philips Analytical, Netherlands) was performed on the material. The radiation was the Cu K_α line, which was comprised of $K_{\alpha1}$ and $K_{\alpha2}$ double lines. The average wavelength was 0.154184 nm ($\lambda_{\alpha1}$ = 0.154056 nm and $\lambda_{\alpha2}$ = 0.154439 nm). No filter was used because the radiation was passed through a monochromator. The XRD data was collected using a continuous scan mode with a scanning speed of 3º/min. (In the continuous scan mode, the sample and the detector both move continuously). The scanning range was between 10º and 80º for the 2θ angle.

3.4 Isothermal Reaction Kinetics Study of SiC formation by CTR

In this study, the reaction kinetics of carbothermal reduction reaction was investigated by monitoring the reaction weight loss and the actual amount of SiC formed under isothermal condition. For the second method, the actual amount of SiC formed

was determined by quantitative XRD (QXRD) analysis. The details of these two methods are given below.

3.4.1 Weight Loss Measurement

Sample weights were measured before and after the carbothermal reduction heat treatments at different temperatures and times. Some corrections were applied to the raw weight loss data. The pyrolyzed and carbothermally-reduced samples have a tendency to absorb moisture when exposed to the ambient atmosphere (especially in a high humidity environment). It is important to eliminate the effect of moisture adsorption on the weight loss measurement. However, moisture adsorption could not be avoided in this study because the powders had to be exposed to the atmosphere for the measurement. (It was not practical to place the furnace and balance in a zero-humidity environment.) Therefore, a comparison method was used to correct the carbothermal reduction weight loss data. The procedure is described below.

Before the heat treatment, ~0.8 g of pyrolyzed powder was placed in glass bottle A. The powder was dried in air at ~170^{o}C for ~2-4 h in an oven to remove the moisture already absorbed in the sample. A similar bottle B, with roughly the same amount of powder, was also dried at the same time as bottle A. After drying, the bottles were removed from the oven and placed in a desiccator during cooling to room temperature. Powder in bottle A was used for the carbothermal reduction heat treatment, while powder from bottle B was used to monitor the percentage of weight gain from moisture adsorption during sample preparation.

For carbothermal reduction heat treatment, the powders were mounted on two SiC substrates. The substrates were placed in a boat made of graphite foil (Grafoil®, UCAR

Carbon Company Inc., Cleveland, OH). Each of the SiC substrates was 25 mm long, 20 mm wide and ~1 mm thick. The Grafoil® boat was 75 mm long and the foil thickness was 0.38 mm. Figure 3-4-1 is an illustration of the mounting of powder on the SiC substrates in the Grafoil® boat. The weights of the two SiC substrates, the Grafoil® boat, and the total weight of the SiC substrates plus the graphite boat were each measured before and after the heat treatment using an analytical balance (Model AG285, Mettler Toledo, Switzerland).

When preparing the sample for carbothermal reduction, the dried powder from bottle B was poured onto a clean piece of weighing paper with known weight and the total weight was recorded. Then the powder from bottle A was loaded onto the two SiC substrates. (The height of the pile of powder was ~1 mm.) Each substrate with powder was weighed and put in the Grafoil® boat. The total weight of boat with powder and substrates was also recorded. After that, the weight of the weighing paper with powder

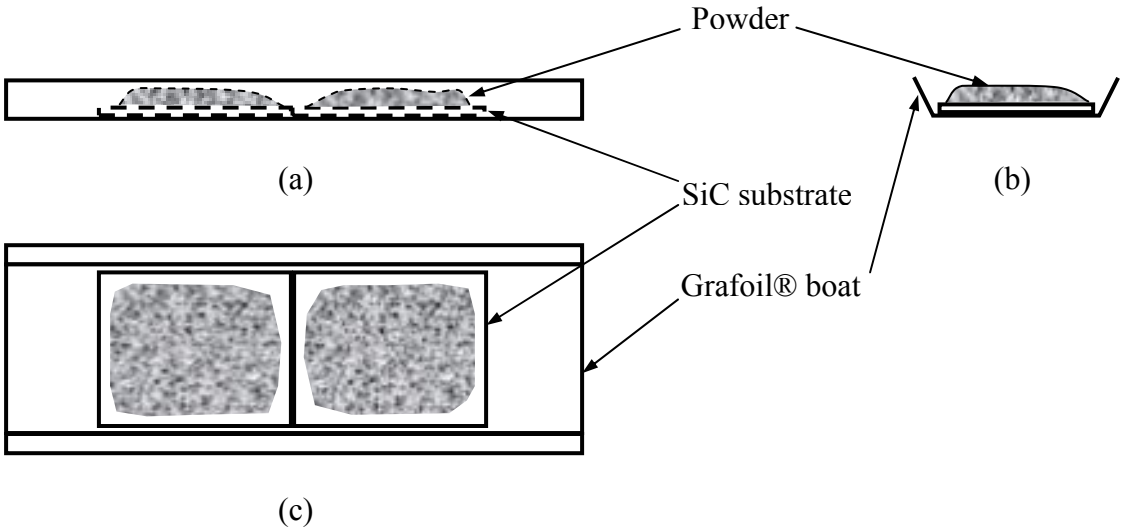

Figure 3-4-1 Illustration of the mounting of powder on the SiC substrates in the Grafoil® boat: (a) front view, (b) side view, (c) top view.

from bottle B was measured again. The weight gain of powder from bottle B during sample preparation was attributed to moisture adsorption. It is reasonable to assume that sample A and sample B have similar percentage of weight gain due to moisture adsorption during the period of sample preparation. Therefore, a good estimation was obtained for the amount of moisture in the powder just prior to the start of the carbothermal reduction heat treatment.

The Grafoil® boat (with SiC substrates and powder) was then placed in the center of the M11 furnace tube to carry out the carbothermal reduction heat treatment. The temperatures used for the kinetic study were in the range of 1160 to 1300^{o}C. All heat treatments were carried out with Ar flowing at a constant flow rate of 0.7 L/min. The heating rate used in the kinetic study was 80^{o}C/min until 90^{o}C below the isothermal (hold) temperature. Then, the temperature was raised sequentially at 60^{o}C/min for 1 min, 20^{o}C/min for 1 min, 5^{o}C/min for 1 min, 2^{o}C/min for 2 min and 1^{o}C/min for 1 min. (The purpose of this heating schedule was to avoid substantial overshoot of the desired hold temperature. With this method, the temperature overshoot was normally limited to ~1^{o}C.) After that, the furnace was held at constant temperature for times in the range of 0.5 h to 48 h. In addition to heat treatments for the kinetics study, some additional heat treatments were carried out at higher temperatures (in the range of 1475-1600^{o}C) to determine the maximum weight loss of the carbothermal reduction reaction and to obtain fully-converted materials for the quantitative XRD (QXRD) analysis.

After the carbothermal reduction heat treatment, the Grafoil® boat with powder and SiC substrates was taken out of the furnace and weighed. The weight of the boat with only the SiC substrates was also measured after the heat treatment in order to

monitor the weight change. No significant weight change was observed for the SiC substrates and the Grafoil® boat in all the heat treatments. The powder product was placed into a glass bottle and dried in air at ~170^{o}C to remove the moisture that was absorbed after removing the sample from the furnace. Then, the dried powder in the bottle was exposed to the ambient environment for 5 min. The weight gain during this period provided an estimate of the moisture absorbed from the time the powder sample was removed from the furnace to the time when it was weighed.

Another correction to the raw weight loss data is referred to as the "blow-off correction." This correction was needed because some powder was blown off from the Grafoil® boat in the M11 furnace before the heat treatment. The furnace was initially evacuated (using a mechanical pump) and heated up to ~300^{o}C. After checking that there was no leak of air, Ar was filled into the furnace. The problem with powder being blown from the Grafoil® boat occurred at the moment when the gas inlet value was opened. Since the furnace was under vacuum, opening of the valve caused a burst of gas (i.e., Ar) into the furnace which resulted in the "blow-off" of a small amount of powder.

The experiment to determine the amount of powder lost due to "blow-off" was the same as a standard kinetic heat treatment experiment, except for that the pyrolyzed sample was only heated up to ~300^{o}C instead of the higher temperature used for CTR experiments. It was assumed that the total weight loss after the blow-off experiment consisted of two parts: the removal of adsorbed moisture and the powder loss due to the blow-off effect. If the weight loss due to moisture removal is $w_{m\text{-}pyro}$ and the total weight loss is w_T, then the weight loss due to blow-off, w_b, should be:

$$w_b = w_T - w_{m-pyro} \tag{3-4-1}$$

The amount of powder blown off the boat was believed to remain relatively constant for a given type of powder (e.g. SC35 or SC8) over the course of the kinetics study. Repeated experiments were carried out for the SC35 and SC8 powders to determine an average w_b value for each. (The results are described in section 4.3.1.)

3.4.2 Quantitative XRD Study

Quantitative X-ray Diffraction (QXRD) analysis was used to determine the fractional amount of SiC that was formed in each sample after the carbothermal reduction heat treatment. The procedure is described in detail in this section.

The first step in the QXRD analysis was to establish a calibration curve for each batch (i.e., for both SC35 and SC8 samples). The calibration curves were prepared using powder mixtures of the starting materials (i.e., the reactants) and the final product obtained after the maximum extent of the carbothermal reduction reaction. In addition, an internal standard was added to the powder mixtures. The starting materials in this study were the amorphous carbon/silica mixtures formed by the pyrolysis heat treatments at 1100^{o}C (i.e., SC8-1100(4h) and SC35-1100(2h)). The final products were obtained by carrying out carbothermal reduction heat treatments on the pyrolyzed materials at a temperature/time condition (i.e., 1495^{o}C for 2 h) that would give "complete reaction." ("Complete reaction" means that the reaction was carried out to the maximum extent possible. The final products contained SiC plus some residual carbon.) The internal standard used in this study was a high-purity silicon powder (KemaNord IV, KemaNord Industrial Chemicals, Sweden).

The mixtures used for the calibration curves contained varying proportions of the "1100°C" (reactant) and "1495°C" (product) powders. For both SC8 and SC35 calibration curves, the percentages of "1495°C" materials in "1100°C/1495°C" mixtures were 1, 3, 5, 10, 20, 30, 40, 60, 70, 80, 90, and 100. Each powder sample used for the calibration curve also contained 15% of the Si internal standard based on the total weight of powder (i.e., the "1100°C/1495°C" powder mixture plus the added Si). The amount of the powder sample used in the experiments was determined by considering both the size of the XRD sample holder and the need to have good accuracy in weighing the components for each sample. Therefore, the amount of the "1100°C/1495°C" powder mixture was 0.3 g and the amount of the Si standard was 0.053 g.

Before making the mixtures, all the powders were dried in vacuum at 120°C for 5 h to remove moisture adsorbed. After drying, the powders were put in a desiccator and cooled to room temperature. This procedure helped to eliminate the errors in the weight percentages for each component in the powder mixtures. (The amount of adsorbed moisture was expected to be different for the various components.)

The powder was mixed using a 5 ml cylindrical glass vial. When making the mixtures, 0.053 g of Si was first added into the vial directly. Then, the "1100°C" and "1495°C" powders were added. For example, when making a mixture with 30% of "1495°C" powder for the SC35 series, the amount of SC35-1100(2h) pyrolyzed powder was $0.3\ \text{g} \times (1.0 - 0.3) = 0.21\ \text{g}$, while the amount of SC35-1495(2h) fully-converted sample is $0.3\ \text{g} \times 0.3 = 0.09\ \text{g}$. Since it is difficult to add exactly 0.05300 g of Si, or 0.09000 g of SC35-1495(2h), the actual weight of each sample added was noted in order to calculate the actual composition of the mixture. For example, suppose 0.20982 g of

SC35-1100(2h), 0.09025 g of SC35-1495(2h), and 0.05340 g of Si were mixed. Therefore, the actual concentration of "1495°C" powder in the "1100°C/1495°C" powder mixture would be [0.09025/(0.09025+0.20982)] × 100% = 30.08%, and the actual percentage of Si in the entire mixture would be [0.05340/(0.09025+0.20982+0.05340)] × 100% = 15.1%. The actual percentages of the "1495°C" powder in the "1100°C/1495°C" powder mixture were used as the x-coordinates in the calibration curves.

After all the materials ("1100°C", "1495°C" and Si) were added, the vials were sealed with screw-on caps. Then, the vials were wrapped with a flexible thermoplastic film (Parafilm®, Pechiney Plastic Packaging, Chicago, IL) in order to prevent the screw-on caps from becoming loose during subsequent mixing operations. Six or fewer vials were put into a 0.5 L plastic bottle. The inner diameter of the plastic bottle was slightly bigger than the height of the vial with cap. The plastic bottle with vials was placed on a roller mill for 5 h or longer. Because the vials were wrapped with Parafilm®, the friction between the end of the vials and the inside surface of the plastic bottle was significant. The six vials lined-up automatically when the plastic bottle was rolled on the roller mill. The vials rolled around the longitudinal axis of the plastic bottle with a same angular speed as the bottle. Figure 3-4-2 is an illustration of the movement of the vials on the roller mill during the mixing. The powders were tossed into air and a good mixing was achieved.

After the mixing on the roller mill, the vials were removed from the plastic bottle. A single vial, well sealed with Parafilm®, was transferred to a 1 L plastic bottle. The plastic bottle was then shaken for 15 min using a paint shaker (Model 5400, Red Devil Inc., Union, NJ). The shaking action helped to remove small amounts of Si that tended to

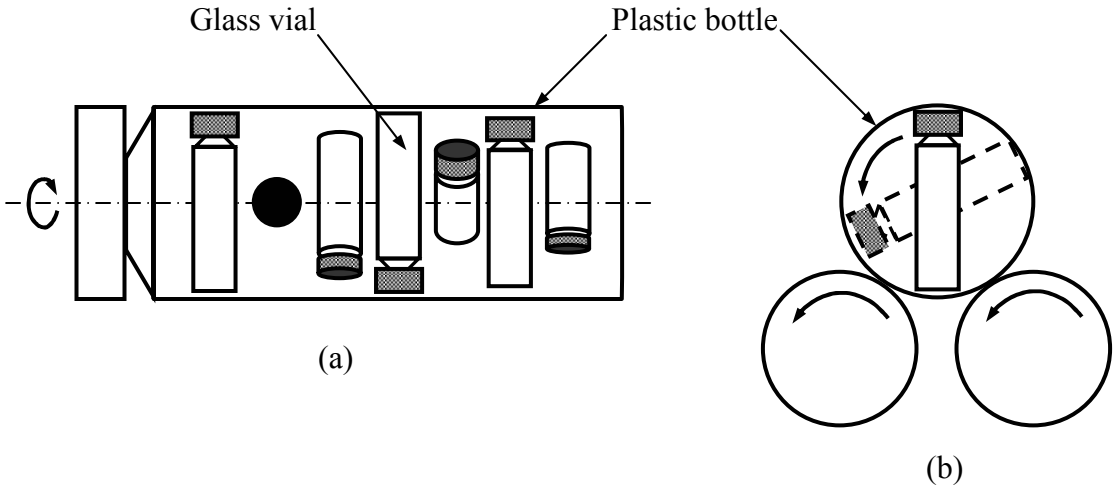

Figure 3-4-2 Illustration of the mixing of the powder on the roller mill: (a) front view, (b) view from the left.

cling to the inside of the glass vials. Only one vial was processed each time because breakage tended to occur with multiple vials. (Vials collided with each other under the high-speed, high-amplitude motion induced by the paint shaker.)

Essentially the same method was used to prepare powder mixtures with the samples of unknown composition that were produced in the study of the carbothermal reduction reaction kinetics. In this case, however, the amount of the heat-treated powder was 0.2 g. The amount of Si was maintained at 17.67 wt% of the heat-treated sample, i.e., 0.2 g × 0.1767 = 0.0353 g. This also maintained the Si concentration in the overall mixture as 15 wt% since [0.0353 / (0.2 + 0.0353)] ×100% = 15%.

The sample holders used for XRD analysis on powders were fabricated using glass slides. The holders were made in order to minimize the amount of material required for analysis. (The amount of material available was limited in many cases.) The holders were fabricated from two glass slides. A 1 cm-diameter hole was drilled through one

slide and the slide was then ground to a thickness of ~500-600 μm. This slide was glued to a second slide that served as the base. The cylindrical cavity formed by the two glass slides had a volume of ~0.04-0.05 cm^3. The amount of powder required to fill the cavity was ~50-100 mg. There was a significant variation in the amount of powder required to fill the cavity. The main reason for this variation was because the solid density of the powders varied significantly. (As will be shown later in Chapter IV, the SC35 pyrolyzed material had a measured apparent solid density of 1.93 g/cm^3 and the fully-converted SC35 samples had a calculated theoretical solid density of 3.16 g/cm^3.) The amount of powder required to fill the cavity in the glass sample holder may also have varied because of differences in the packing densities for the different powders.

To prepare a sample for XRD measurement, the cavity of the sample holder was initially overfilled with powder to a slight extent. The top (open) surface of the powder was then lightly compacted and leveled with the top glass surface of the holder. This was done by using a smooth glass slide to apply a light pressure. The glass slide was also used to lightly scrape away any excess powder that was present (i.e., powder that remained on the top glass surface of the holder.) The sample holder was then placed on a metal support with the help of plasticene. The glass surface (of sample holder) was leveled with that of the metal support. Figure 3-4-3 is a schematic of the sample holder setup for XRD measurement.

XRD measurements were carried out on the Philips PW1800 diffractometer described in section 3.3. The same radiation source was used for the QXRD study, but the scanning condition was different. The data was collected using a "step scan" mode with a step size of 0.01° and scan speed of 0.5 second/step. (In the "step scan" mode, the

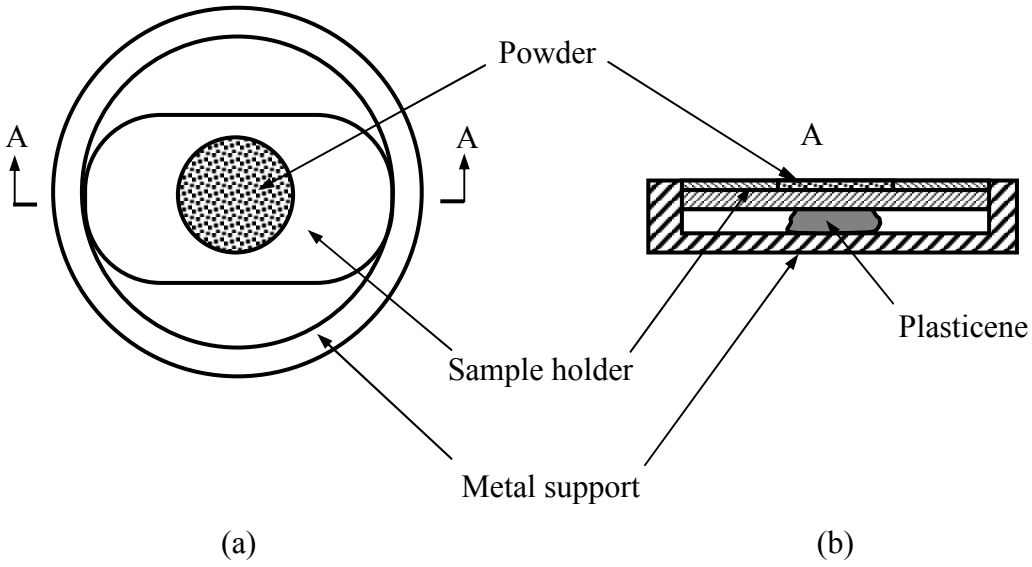

Figure 3-4-3 Illustration of the sample holder setup for XRD measurement: (a) top view and (b) view from cross-section A.

sample and the detector move step-wise. They move one step (0.01° in this case) and stay at that position for fixed time period (0.5 seconds in this case) to detect the X-ray intensity. This process is repeated continuously for the selected scanning range.) The scanning range was for 2θ angles between 31° and 65°, where θ is defined by the Bragg equation:

$$\lambda = 2d \sin\theta \tag{3-4-2}$$

where λ is the wavelength, d is the inter-planar distance, and θ is the Bragg angle. The selected scanning range includes the Si(220) line at 2θ = 47.30°, Si(311) line at 2θ = 56.10°, β-SiC(111) line at 2θ = 35.60°, and β-SiC(220) line at 2θ = 59.98°.

As described earlier, each XRD sample was prepared with ~0.05 g of powder while each mixture contained either ~0.35 g (calibration curve samples) or ~0.24 g (unknown heat-treated samples) of powders. Therefore, it was possible to carry out XRD measurements on 5 to 7 distinct samples from each powder mixture. This was done by

withdrawing the appropriate sample amount (i.e. ~0.05 g) from the vials on a one-by-one basis. The use of multiple XRD measurement was very important for obtaining accurate SiC/Si peak intensity ratios because complete compositional homogeneity could not be assured in the 0.05 g samples, despite the extensive mixing procedure that was used in preparing the sample mixtures. There were always parts of the mixtures that were either Si-rich or SiC-rich, as compared with the overall composition. If only one XRD measurement was made, the composition in that sample may have deviated significantly from the overall SiC/Si composition in the whole mixture. By carrying out XRD measurements on ~5-7 samples that comprised the overall powder mixture, it was possible to obtain average SiC/Si intensity ratios that were representative of the overall composition of the powder mixture.

The XRD patterns of the calibration curve samples were processed to get the relative intensity ratio of the SiC line to the Si line in each of the samples. First, the XRD patterns were treated by α_2 stripping, which was done by the Philips PC-APD software (version 3.6, Philips Analytical, Netherlands). Then, the background intensity was determined and the range for integration was chosen. The choice of the background intensity value may influence the relative intensity ratio significantly. In this study, a single background intensity value was chosen for the entire range of the XRD pattern. This value was obtained from the 2θ range of 49-55^o. The range was chosen because: (1) the background in this range always had the lowest intensity and showed the least variation and (2) there were no SiC or Si diffraction lines in this range. The exact value of the background intensity was determined by a "zero-area method". To be more specific, if the measured intensity was above the selected background level, the area was

considered to be positive; if the measured intensity was below the background level, the area was considered to be negative. Then, the background level was chosen so that the total area between the measured pattern and the background level in this range equaled zero. Figure 3-4-4 is an illustration for the "zero-area method" for choosing the background value. This overall method is justified by the following points:

- The average effect is taken over a relatively large 2θ range (49-55^{o}).
- The choice of the background intensity value is objective, i.e. it is not dependent upon subjective decisions by the person analyzing the data.
- Integrated intensities for diffraction lines would be nearly independent of the range of integration because the net area gained by expanding or narrowing the range of integration would be zero due to this "zero-area" background selection method. (In reality, the integrated intensity values would depend slightly on the range of integration due to small variations of the background at different 2θ angles.)

The main disadvantage of this method for selecting the background is that the background intensity value at 49-55^{o} may not be the same as the values determined at the 2θ angles for the Si and SiC lines. Despite this, the advantages of the method would seem to outweigh the disadvantages.

The following 2θ ranges were selected to obtain the integrated intensities for the SiC and Si diffraction lines: 33-38^{o} for the β-SiC(111) line, 59-61^{o} for the β-SiC(220) line; 46.8-47.8^{o} for the Si(220) line, 55.6-56.6^{o} for the Si(311) line. For each selected diffraction line in the XRD pattern, the background intensity value and the starting and ending 2θ values for integration were input into the PC-APD software and the integrated

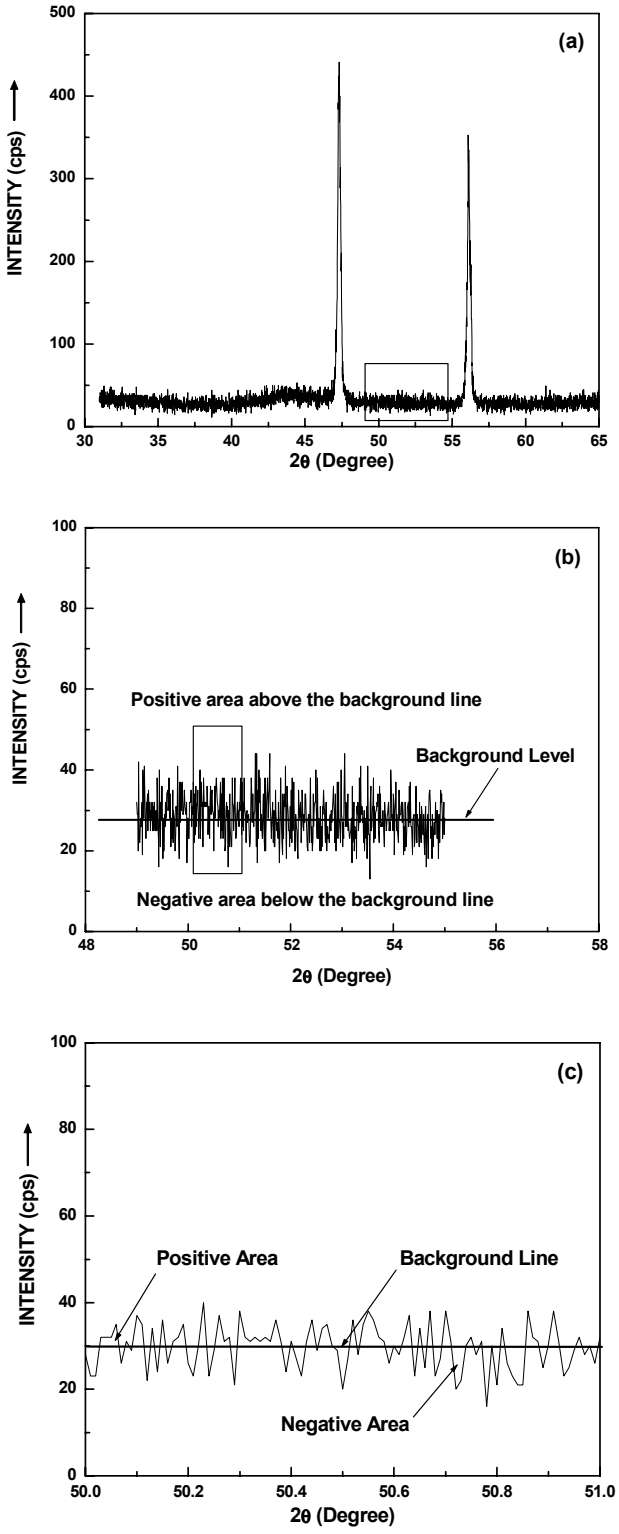

Figure 3-4-4 XRD patterns for SC5-1100(2h)+15%Si mixtures to illustrate the "zero area method": (a) complete pattern from 31-65^{o}, (b) zoom-in pattern for the range of 49-55^{o}, and (c) zoom-in pattern for the range of 50-51^{o}.

intensity values were calculated. The software obtained the integrated intensities by adding together the area below the diffraction line and above the chosen background intensity line in the 2θ range provided.

The calibration curves for the QXRD study were obtained using the integrated peak intensity values. First, the background-corrected integrated line intensity ratios were calculated for SiC(111)/Si(220) and for SiC(220)/Si(311). Second, the SiC/Si line intensity ratios were adjusted to account for the difference between the actual concentration of Si in the powder mixture and the targeted value of 15 wt%. Suppose the SiC/Si line intensity ratio, I_R' , in the measured sample is given by:

$$I_R' = \frac{I_{SiC(hkl)}}{I_{Si(h'k'l')}} \tag{3-4-3}$$

The adjusted intensity ratio is given by:

$$I_R = \frac{I_R' \cdot w_{Si\_QXRD}}{15} \tag{3-4-4}$$

where w_{Si_QXRD} is the actual weight percentage of Si in the powder mixture.

The I_R values are the y-coordinates for the points on the calibration curve. The calibration curves are obtained by plotting the I_R values as a function of the concentration of fully-converted ("1495^{o}C") material in the "1100^{o}C/1495^{o}C" mixtures. A linear curve fitting procedure (following the least-squares method) was applied to the data, with the fitted line forced through the origin.

The same method was applied to obtain the SiC/Si integrated line intensity ratios for the heat-treated samples with unknown amounts of SiC. The intensity ratios were compared to those on the calibration curve in order to determine the amounts of fully-converted material in the samples. The detailed results are presented in Chapter IV.

3.5 Structural Characterization of the Materials Before and After CTR

Methods used to characterize the structure of the heat-treated powders are described in this section. The characterization methods used include XRD line broadening measurements to determine crystallite size, gas adsorption measurements to determine surface area and porosity, light diffraction measurements to determine particle size distribution, pycnometer measurements to determine powder densities, scanning electron microscopy (SEM) and transmission electron microscopy (TEM).

3.5.1 Crystallite Size Measurement by XRD Line Broadening

The SiC crystallite size was determined from the broadening of the XRD diffraction lines using the Scherrer equation, as shown in Equation (3-5-1):

$$D_{hkl} = \frac{0.9\lambda}{\beta_{hkl} \cos\theta} \tag{3-5-1}$$

where D_{hkl} is the size of the crystal measured in a direction perpendicular to the (hkl) reflecting planes, λ is the radiation wavelength, θ is the Bragg angle, and β_{hkl} is the true width of the diffraction line at a height where the intensity is one-half of the maximum intensity. Because Cu K_α double line was the radiation source, α_2 stripping must be performed first to obtain the true line shape contributed by the Cu $K\alpha_1$ line. The wavelength of the Cu $K\alpha_1$ line is 0.15406 nm.

If the XRD diffraction lines have Cauchy shape, the value of β_{hkl} can be obtained from the following equation:

$$\beta_{hkl} = B - b \tag{3-5-2}$$

where B is the measured width of the diffraction line and b is the portion of the measured width that is due to instrumental broadening. Therefore, the crystallite size D_{hkl} (in nm) is given by:

$$D_{hkl} = \frac{0.9 \times 0.15406}{(B-b) \times \cos\theta} nm \qquad (3\text{-}5\text{-}3)$$

in which B, b and θ are all in radians.

The sample preparation procedure for the crystallite size measurement was the same as that used for the QXRD study. Samples were scanned using the "step scan" mode with step size of 0.02^o and scanning speed of 1.0 second/step. The range of scanning was $30\text{-}80^o$ for 2θ. Coarse-grained (>~20 μm) pure Si (i.e., the same as used in the QXRD study) was scanned using the same procedure in order to obtain the instrumental broadening b at different 2θ angles. The results are shown in Table 3-5-1.

With the results in Table 3-5-1, linear interpolation was used to obtain b values for any angles within the different 2θ ranges. The equations are listed below:

$28.667^o < 2\theta < 47.524^o$ $\quad b = [0.000583 \times (2\theta - 28.667)] + 0.058$

$47.524^o < 2\theta < 56.331^o$ $\quad b = [0.002270 \times (2\theta - 47.524)] + 0.069$

$56.331^o < 2\theta < 69.346^o$ $\quad b = [0.000307 \times (2\theta - 56.331)] + 0.089$

$69.346^o < 2\theta < 76.570^o$ $\quad b = [0.004150 \times (2\theta - 69.346)] + 0.093$

For example, the line broadening b at $2\theta = 35.600^o$ would be

$$b = [0.000583 \times (35.600 - 28.667)] + 0.058 = 0.062^o$$

To obtain the line width B, the line profile was fitted using a Lorentzian function. The details of the method will be given in Appendix A.

Table 3-5-1 Measured widths of XRD diffraction lines for Si with large grain size.

2θ (degree)	28.667	47.524	56.331	69.346	76.570
Width (degree)	0.058	0.069	0.089	0.093	0.123

The scanning range of 30-80^{o} covered the three major diffraction lines for β-SiC, i.e., the (111) line at 35.60^{o}, (220) line at 59.98^{o}, and (311) line at 71.78^{o}. Crystallite sizes from all of the three lines were calculated. By assuming that the crystallites are equiaxed, the average of the three values was used to estimate the SiC crystallite size.

3.5.2 Surface Area and Porosity Measurement by Gas Adsorption

3.5.2.1 Background Information about Adsorption Analysis

- Classification of pores

Pores in solids are generally classified into three categories: Pores with diameter below ~2 nm are defined as micropores; pores with diameter in the range of ~2-50 nm are defined as mesopores; pores with diameter above ~50 nm are defined as macropores. It should be noted that these limits are arbitrary because the pore size distributions are usually continuous and there is no sharp boundary between different kinds of pores (Sing, 1989).

- Physical adsorption and adsorption isotherm

When a gas is brought into contact with an outgassed solid, gas molecules may attach to the solid surface by non-specific dispersion forces which provide the source of the attraction. This process is called *physical adsorption*. If the physical adsorption occurs in a closed system, the gas equilibrium pressure will decrease as the gas (adsorbate) adsorbs to the surface of the solid (adsorbent). The relationship between the gas equilibrium pressure, P, and the amount of gas adsorbed (on a unit weight of solid), n, at a constant temperature in a closed system is called an *adsorption isotherm*. Therefore, the general mathematical expression of the adsorption isotherm is:

$$n = f(P)_{T,\ gas,\ solid} \qquad (3\text{-}5\text{-}4)$$

In practice, the volume of gas adsorbed per unit weight of solid , V_{ad}, is used as a measure of the amount of gas adsorbed (the volume is transformed to the equivalent volume at standard temperature and pressure, or STP), while the relative pressure, P/P_0 (P_0 is the saturation gas pressure at that temperature), is used more often than P as a measure of pressure (Gregg and Sing, 1982).

The adsorption isotherms usually include six basic types (I - VI), as shown in Figure 3-5-1. According to Gregg and Sing (1982), the Type I isotherm is "characterized by a plateau which is nearly or quite horizontal, and which may cut the $P/P_0 = 1$ axis sharply or may show a 'tail' as saturation pressure is approached." The Type I isotherm is characteristic of the gas adsorption on a microporous solid having a relatively small external surface. The Type II isotherm represents unrestricted monolayer-multilayer adsorption on a non-porous or macroporous adsorbent. The knee of the isotherm (i.e., point B in Figure 3-5-1(b) and (d)) indicates the approximate volume of adsorbed gas that is required to achieve the equivalent of monolayer coverage of the solid surface by gas molecules. The Type IV isotherm is like the Type II isotherm at lower relative pressures, but it has a hysteresis loop at higher relative pressures. The Type IV isotherm is usually associated with capillary condensation of adsorbate in the mesopores of the adsorbent. The adsorbate starts to condense in the smallest pores at the lowest relative pressures. As the relative pressure increases, pores with increasing size are filled with condensed adsorbate. This process continues until all the pores are filled. After that, there would not be much change in the volume of gas adsorbed. The Type III and Type V isotherms

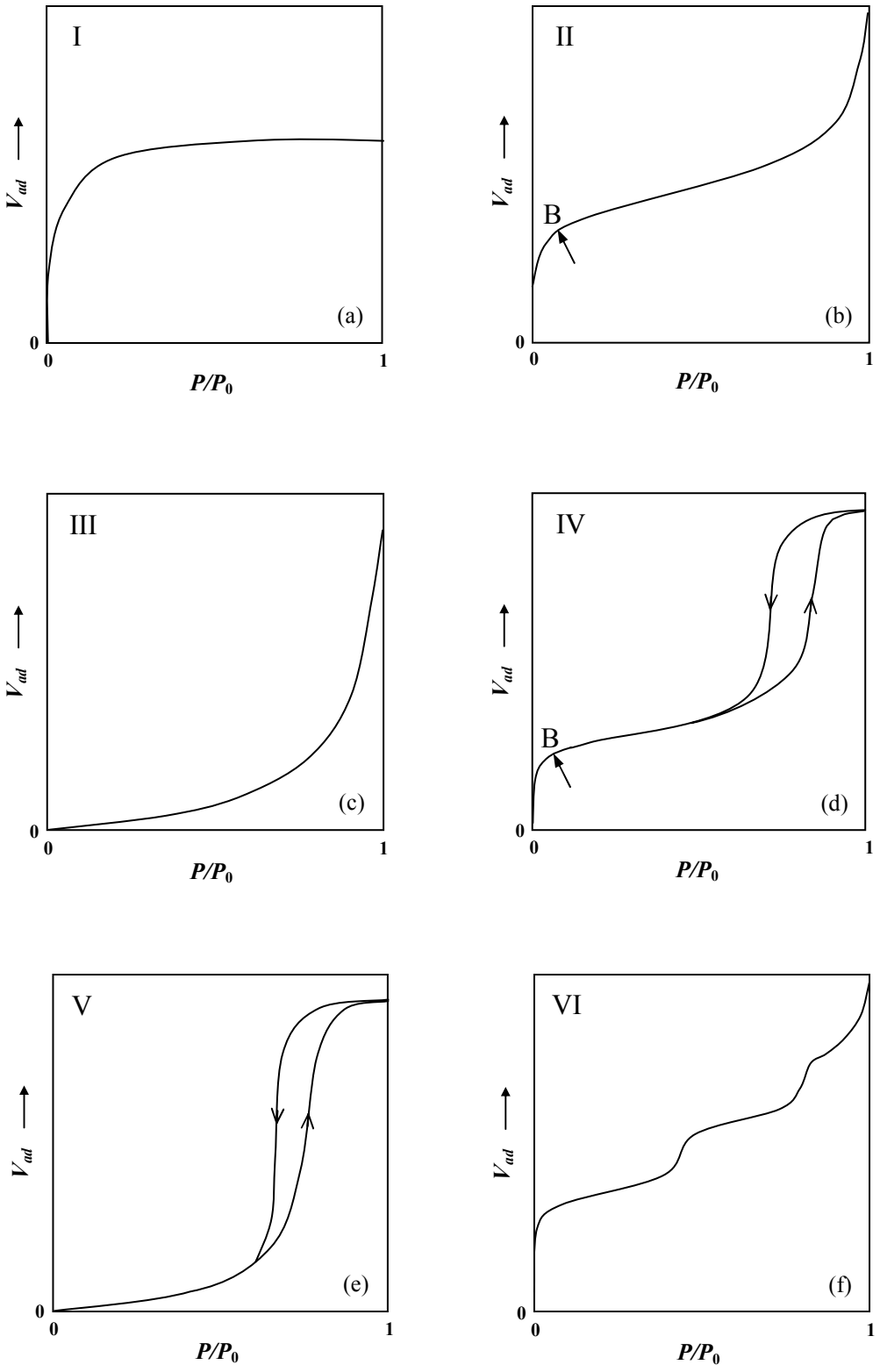

Figure 3-5-1 Types of gas adsorption isotherms, from Gregg and Sing (1982).

are characteristic of weak adsorbent-adsorbate interactions. High adsorbate concentrations (i.e., high pressures P) are required before significant adsorption occurs. Type VI adsorption isotherms are relatively rare and are characteristic of adsorption of nonpolar gas molecules (e.g., He, Ar, and CH_4) on homogeneous surface (e.g., graphitized carbon black) (Gregg and Sing, 1982, p.3 and p.84).

- Classification of adsorption hysteresis

The adsorption isotherms for mesoporous materials usually show hysteresis. This means that the adsorption curves (in which the volume adsorbed is measured with increasing relative pressure) are not retraced by the desorption curves (in which the volume desorbed is measured with decreasing relative pressure). Figure 3-5-2 show four types of hysteresis loops that are commonly encountered in the literature. The Type H1 loops are sometimes characteristic of porous materials with narrow distributions of mesopore size, such as the materials containing tubular or ink-bottle shaped mesopores. The Type H2 loops are sometimes associated with a broad distribution of mesopores. The Type H3 and Type H4 loops do not exhibiting limited adsorption at high P/P_0. Type H3 loops have been observed with aggregates of platy particles. Type H4 loops have been associated with narrow slit-shaped pores (Sing, 1989). However, it should be noted that there is not a very clear understanding of the relationships between pore characteristics and the shapes of the hysteresis loops observed in adsorption isotherms. There are limited studies in which direct observations of pore characteristics (e.g., via microscopy) have been correlated with the hysteresis behavior. There may be other explanations for the various hysteresis types shown in Figure 3-5-2. For example, compaction of powders

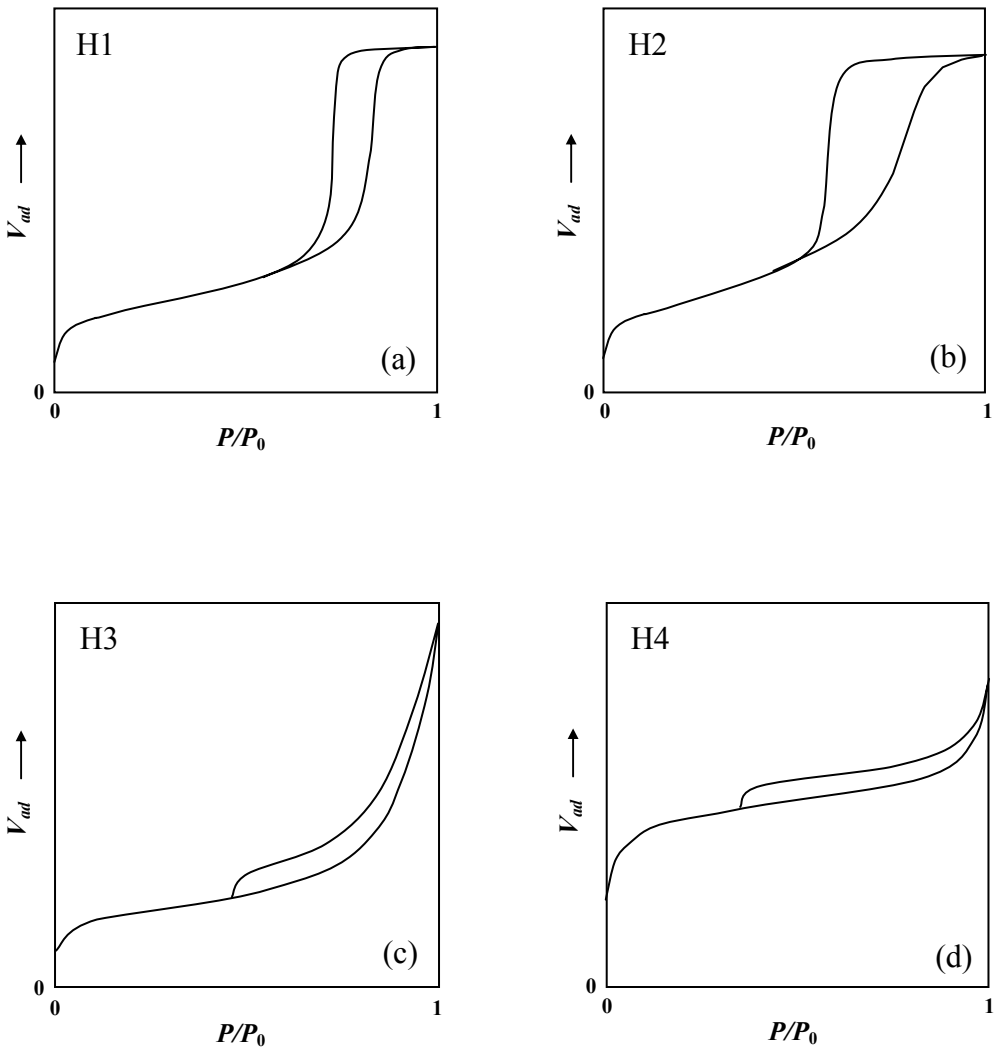

Figure 3-5-2 Types of hysteresis loops in adsorption isotherms, from Gregg and Sing (1982).

at varying pressures can lead to different types of hysteresis loops in the measured adsorption isotherms, as shown in Figures 3-5-3 and 3-5-4 (Avery and Ramsay, 1973). It is evident that some of the hysteresis loops shown in these figures are similar to the types shown in Figure 3-5-2.

- Surface area determination based on BET and Langmuir equations

From the adsorption isotherm, the specific surface area could be obtained based on either the BET or Langmuir equation as shown below:

BET equation

$$\frac{P/P_0}{V_{ad}(1-P/P_0)} = \frac{1}{V_m C} + \frac{C-1}{V_m C}\frac{P}{P_0} \tag{3-5-5}$$

Langmuir equation

$$\frac{P/P_0}{V_{ad}} = \frac{b}{V_m} + \frac{P/P_0}{V_m} \tag{3-5-6}$$

in which P/P_0 is the relative pressure, V_{ad} is the volume of gas adsorbed (in cm^3/g STP) at relative pressure P/P_0, V_m is the monolayer capacity (in cm^3/g STP) which is the gas volume (reduced to STP) that is sufficient to form a complete adsorbed monolayer on the sample surface, and C and b are constants in the two equations (Gregg and Sing, 1982).

For both BET and Langmuir equations, the specific surface area, SA (in m^2/g), is calculated by the following equation:

$$SA = \frac{V_m}{22414} A_m N_A \tag{3-5-7}$$

in which V_m is the monolayer capacity (in cm^3/g STP) from the BET or Langmuir equation; N_A is the Avogadro constant, $N_A = 6.023\times10^{23}$; A_m is the cross-sectional area of the analysis gas. $A_m = 0.162$ nm^2 for N_2.

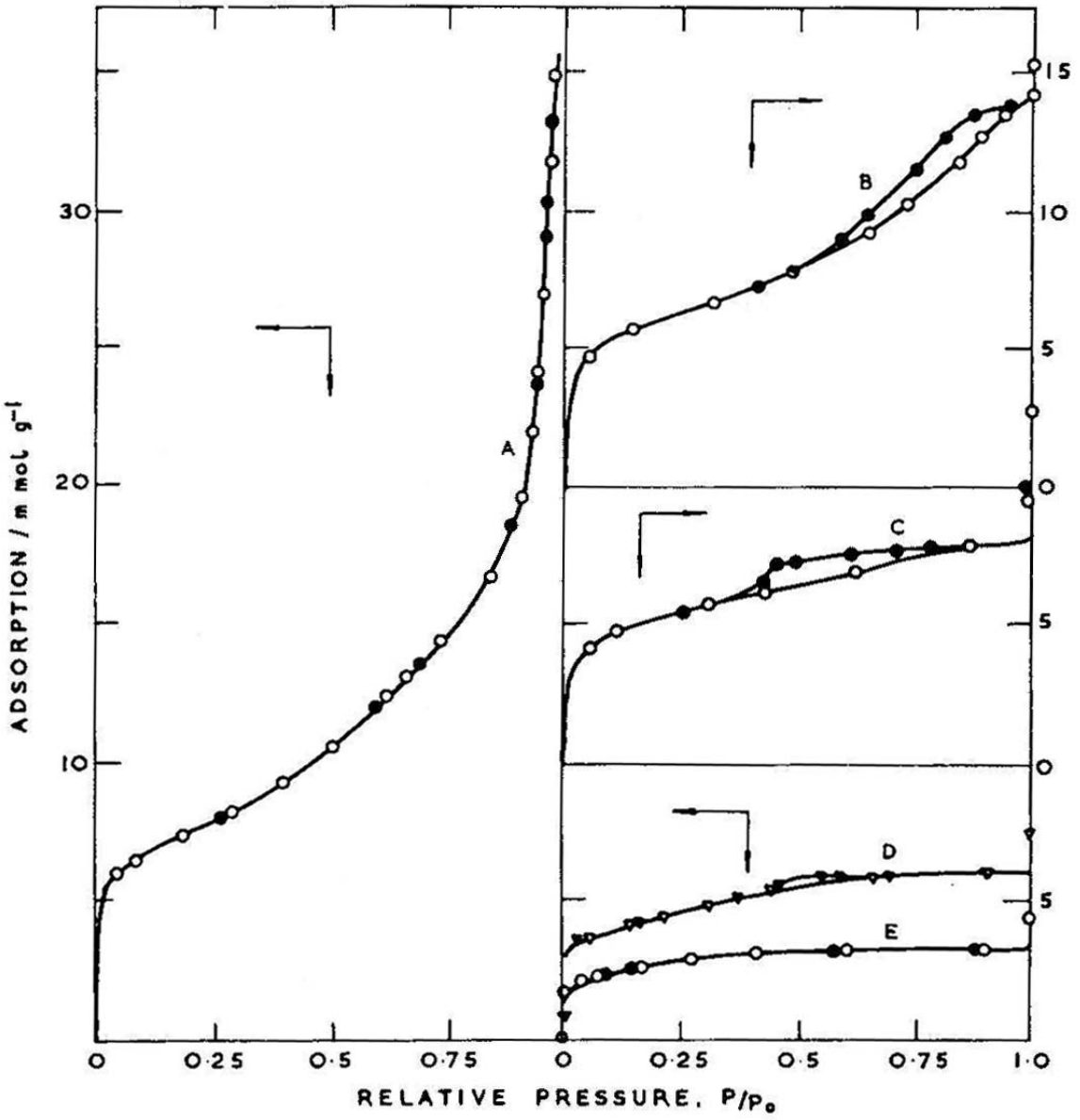

Figure 3-5-3 Adsorption/desorption isotherms of nitrogen at 77K on uncompressed silica powder (A) and pressed powder compacts (B-E). The pressures used to form the compacts were: 2×10^4 psi (B), 8×10^4 psi (C), 10^5 psi (D), and 2×10^5 psi (E). Solid symbols denote desorption, from Avery and Ramsay (1973).

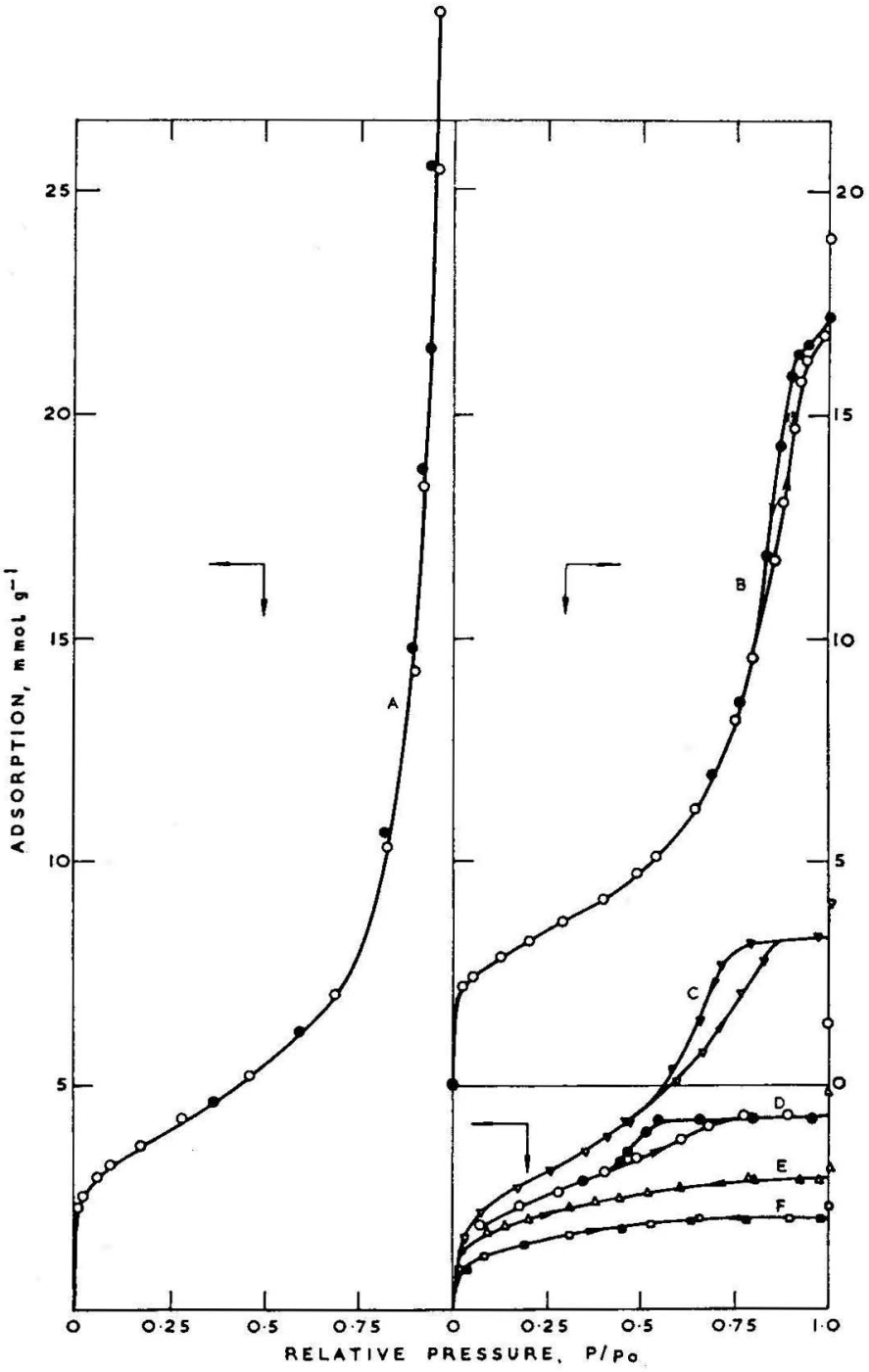

Figure 3-5-4 Adsorption/desorption isotherms of nitrogen at 77K on uncompressed zirconia powder (A) and pressed powder compacts (B-F). The pressures used to form the compacts were 6×10^3 psi (B), 2×10^4 psi (C), 6×10^4 psi (D), 1.4×10^5 psi (E), and 2×10^5 psi (F). Solid symbols denote desorption, from Avery and Ramsay (1973).

To obtain V_m, C, and b in the BET and Langmuir equations, the data from the adsorption isotherm (i.e., (P/P_0, V_{ad}) pairs) in the relative pressure range from ~0.05 to ~0.30 are fitted to those equations. (The BET and Langmuir models are generally applicable only at pressures within this range.) Linear regression is carried out on the $(\frac{P/P_0}{V_{ad}(1-P/P_0)}, P/P_0)$ data pairs for the BET model (based on Equation (3-5-5)) and on the $(\frac{P/P_0}{V_{ad}}, P/P_0)$ data pairs for the Langmuir model (based on Equation (3-5-6)). From the results of the linear regressions, the values of V_m (from BET and/or Langmuir) are calculated and then the specific surface areas are determined from Equation (3-5-7). In addition, the values of C in the BET model, b in the Langmuir model, and the correlation coefficient of the linear regression, r_L, are obtained.

The BET model is usually applicable to samples showing Type II or Type IV adsorption isotherms. The C value in the BET equation should be positive to have physical meaning. Actually, it is desirable that the C value be roughly on the order of 100 to obtain reliable surface area data (Sing, 1989). Figure 3-5-5 shows the relationship between the shapes of the adsorption isotherm and the corresponding C values (from Figure 2.1 of Gregg and Sing (1982)). For the Langmuir model, the b value should also be a positive value to have physical meaning and it is desirable that the b value be less than 0.02. The Langmuir model is generally applicable to microporous samples showing Type I isotherms.

- Total specific pore volume

The Type IV isotherm in Figure 3-5-1 shows a case in which the adsorption isotherm reaches a plateau value for the adsorbed volume, V_{ad}, as the saturation vapor

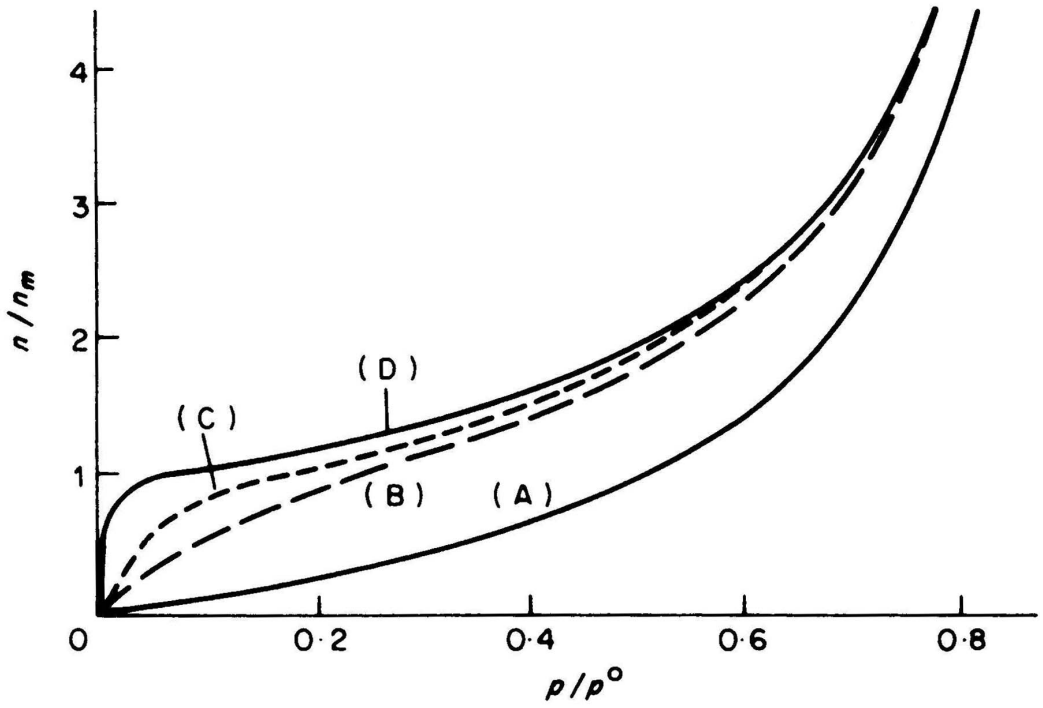

Figure 3-5-5 Relationship between the shapes of the adsorption isotherm and the *C* values in the BET model: (A) $C = 1$, (B) $C = 11$, (C) $C = 100$, and (D) $C = 10000$, from Figure 2.1 of Gregg and Sing (1982). n/n_m is the ratio of adsorbed volume to the monolayer capacity and P/P^o is the relative pressure.

pressure, P_0, is approached (i.e., as $P/P_0 \rightarrow 1$). This indicates that the accessible mesopores in the material have been filled with nitrogen (i.e., by capillary condensation). Hence, the total "specific pore volume," V_{Pore}, in a mesoporous material is determined from the total adsorbed volume as P/P_0 approaches 1. It should be emphasized that this determination of the "total specific pore volume" is limited in at least two respects. First, only open, accessible pores are filled with nitrogen, so any closed, isolated pores in the material would not be included in V_{Pore}. Second, it becomes very difficult to measure pores by the capillary condensation method when the pore radii become larger than ~50-100 nm. Hence, the V_{Pore} value will not include most or all of the macropores that may be present in the

sample. The presence of larger pores is sometimes indicated by the lack of a distinct plateau in the adsorption isotherm at high P/P_0 values. In this case, the adsorbed volume will continue to increase with increasing P/P_0 values.

- Mesopore size distribution

The mesopore size distribution can be obtained from a Type IV isotherm. The mesopore size distribution is calculated using the Kelvin equation:

$$r_K = -\frac{2\gamma V_L}{RT\ln(P/P_0)} \tag{3-5-8}$$

in which P/P_0 is the relative pressure at which condensation occurs in pores with Kelvin radius of r_K, γ is the surface tension of the liquid (usually nitrogen), V_L is the molar volume of the liquid (usually nitrogen), and R is the gas constant (R = 8.314J/(mol · K)). If nitrogen is used as the analysis gas, the values used in Equation (3-5-8) for liquid nitrogen are: $\gamma = 8.88\times10^{-3}$ N/m, V_L = 34.68 cm^3/mol, and T = 77.35 K (p. 164, Gregg and Sing (1982)). Substituting to these values in Equation (3-5-8) gives:

$$r_K = -\frac{0.953}{\ln(P/P_0)} \text{ nm} \tag{3-5-9}$$

In the actual calculation of pore size distribution, a correction is often made to the Kelvin radius, r_K, to account for the thickness of the adsorbed layer on the wall of the pores, r_T. This will be explained later in section 3.5.2.3.

3.5.2.2 Measurement Method and Data Collected

In the current study, the specific surface area (in m^2/g) and porosity (including the specific pore volume (in cm^3/g) and BJH pore size distribution) of the heat-treated powders were characterized by a gas adsorption analyzer (Model ASAP 2000,

Micromeritics, Norcross, GA). Before the measurement, the powder was degassed at 300°C for ~2-3 h to remove the adsorbed water. Nitrogen was used as the analysis gas for all the samples. The following parameters were defined:

P_i absolute vapor pressure of the adsorbate (nitrogen) under equilibrium, in mm Hg

Pr_i relative pressure, $Pr_i = P_i / P_0$, in which P_0 is the saturation vapor pressure of the nitrogen at liquid nitrogen temperature

V_{ad_i} Specific volume of gas (nitrogen) absorbed, in cm^3/g STP, at pressure P_i in the adsorption process. (The measured volume in cm^3 was reduced to the volume of an equivalent amount of gas at Standard Temperature and Pressure (STP). The specific volume is the STP volume divided by the weight of the sample.)

V_{de_i} Specific volume of gas (nitrogen) absorbed, in cm^3/g STP, at pressure P_i in the desorption process.

The instrument recorded the amounts of gas (i.e., nitrogen) adsorbed, V_{ad_i} (or V_{de_i}), on the sample at liquid nitrogen temperature (i.e., 77 K) over a range of nitrogen gas pressures, P_i. It is noted that during the measurement the nitrogen pressure was controlled by using helium as the dilution gas.

Table 3-5-2 lists the values of relative pressure, Pr_i, used in the measurements and the types of analyses (surface area, BJH adsorption/desorption, and micropore) which were carried out with the data. After the adsorption measurements and the initial analysis using the ASAP software, the information (isotherm data, specific surface area, total pore volume, and pore size distribution) was exported from the ASAP software and some

Table 3-5-2 List of relative pressure values used for various gas adsorption analyses carried out on heat-treated powder samples.

No.	Pr_i	r_K (nm)	SA	μP	Ad	De	No.	Pr_i	r_K (nm)	SA	μP	Ad	De
1	0.005			X			31	0.990	95.3				X
2	0.020			X			32	0.980	47.4				X
3	0.050		X	X			33	0.970	31.4				X
4	0.080		X	X			34	0.960	23.5				X
5	0.100	0.4	X	X	X		35	0.940	15.5				X
6	0.120	0.5	X	X	X		36	0.920	11.5				X
7	0.150	0.5	X	X	X		37	0.890	8.2				X
8	0.180	0.6	X	X	X		38	0.860	6.4				X
9	0.200	0.6	X	X	X		39	0.830	5.1				X
10	0.250	0.7	X	X	X		40	0.800	4.3				X
11	0.300	0.8		X	X		41	0.750	3.3				X
12	0.350	0.9		X	X		42	0.700	2.7				X
13	0.400	1.0		X	X		43	0.650	2.2				X
14	0.450	1.2		X	X		44	0.600	1.9				X
15	0.500	1.4		X	X		45	0.550	1.6				X
16	0.550	1.6		X	X		46	0.500	1.4				X
17	0.600	1.9		X	X		47	0.450	1.2				X
18	0.650	2.2			X		48	0.400	1.0				X
19	0.700	2.7			X		49	0.350	0.9				X
20	0.750	3.3			X		50	0.300	0.8				X
21	0.800	4.3			X		51	0.250	0.7				X
22	0.830	5.1			X		52	0.200	0.6				X
23	0.860	6.4			X		53	0.150	0.5				X
24	0.890	8.2			X		54	0.100	0.4				X
25	0.920	11.5			X								
26	0.940	15.5			X								
27	0.960	28.2			X								
28	0.980	47.4			X								
29	0.990	95.3			X								
30	0.995	191.1			X	X							

Note:

The abbreviations used in the table are defined as follows:

SA specific surface area analysis
μP specific micropore analysis
Ad BJH adsorption analysis
De BJH desorption analysis
r_K equivalent Kelvin radius at Pr_i calculated from Equation (3-5-9)

If "X" is given to a certain field, then the adsorption data from that point was used for the type of analysis in that field (SA, μP, Ad or De).

further analyses (described below) were carried out.

3.5.2.3 Data Processing in Adsorption Analysis

- Specific surface area

The BET and Langmuir specific surface area values, as well as the fitted parameters V_m, C, b, and r_L, were obtained from the ASAP software directly. The C, b, and r_L values were analyzed to determine which equation (BET or Langmuir) was more appropriate for the data. The judgment was based on the following criteria:

1. If the BET model gave a positive C value and the Langmuir model gave a positive b value, then the specific surface area value from the model which gave a better linear correlation coefficient was chosen.
2. If the Langmuir model gave a positive b value, while the BET model gave a negative C value, then the specific surface area from the Langmuir model was used. Similarly, if the BET model gave a positive C value and the Langmuir model gave a negative b value, then specific surface area from the BET model was used.

In any case, if the correlation coefficient was low (e.g., below 0.99), the equation (BET or Langmuir) might not be very applicable.

- Total specific pore volume

The total specific pore volume, V_{Pore}, of the material was given by the ASAP software directly. The total specific pore volume value was calculated by converting the volume of nitrogen adsorbed at a designated maximum pressure, Pr_{max}, to the volume of equivalent liquid nitrogen. In this study, Pr_{max} was chosen to be 0.995. (Using a nitrogen

adsorbate, the equivalent Kelvin radius, r_K, at this relative pressure is ~191 nm.) Suppose V_{ad_max} was the volume (in cm^3/g STP) of adsorbed nitrogen at relative pressure Pr_{max}. V_{Pore} was given by:

$$V_{Pore} = V_{ad\_max} \cdot D_{N2} \tag{3-5-10}$$

where D_{N2} is a factor to convert the gas volume to a liquid volume. D_{N2} is 0.0015468 for the conversion from nitrogen gas to liquid nitrogen at 77K.

- Adsorption isotherm and pore size distribution

The adsorption and desorption isotherm data exported from the ASAP software included a series of values for P_i, Pr_i, V_{ad_i}, and V_{de_i}. Isotherm plots of V_{ad_i} vs. Pr_i (for adsorption isotherm) and V_{de_i} vs. Pr_i (for desorption isotherm) were made. For example, Figure 3-5-6 show the adsorption and desorption isotherms for the SC35-1300(8h) and SC8-1250(8h) samples. From the adsorption and desorption isotherm data, the mesopore size distribution can be obtained. In the ASAP software, the mesopore size distribution was calculated based on the "BJH method", in which the mesopores are considered to be cylindrical-shaped with two open ends. The volume filled with condensed liquid nitrogen in a pore is considered to consist of two parts: the core part and the adsorbed layer. An illustration of the pore structure is given in Figure 3-5-7. The BJH pore diameter, D, equals twice the core radius, r_C, plus twice the adsorbed layer thickness, r_T , i.e.:

$$D = 2r_C + 2r_T \tag{3-5-11}$$

It should be noted that Figure 3-5-7 is an over-simplified schematic whose purpose is just to illustrate the idea of a "core" and an adsorbed layer in a pore. In the actual BJH method, as will be shown later in this section, the BJH pore diameter is NOT calculated directly from Equation (3-5-11).

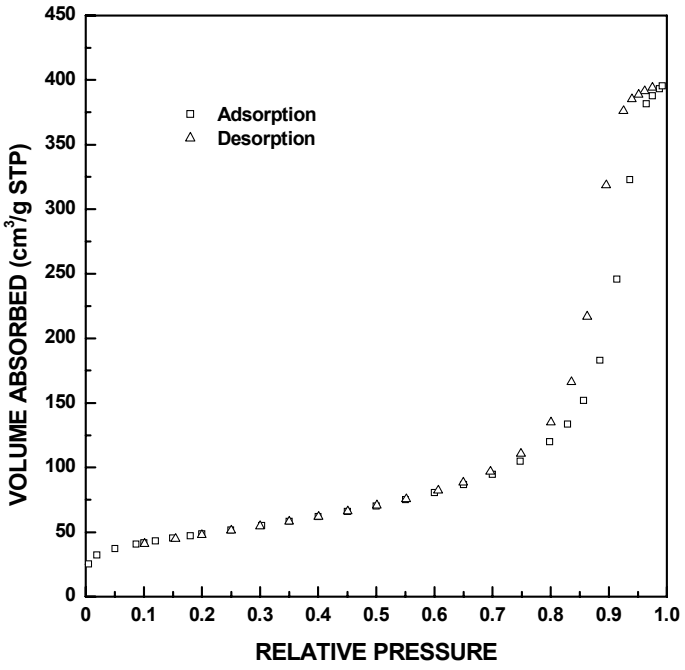

(a)

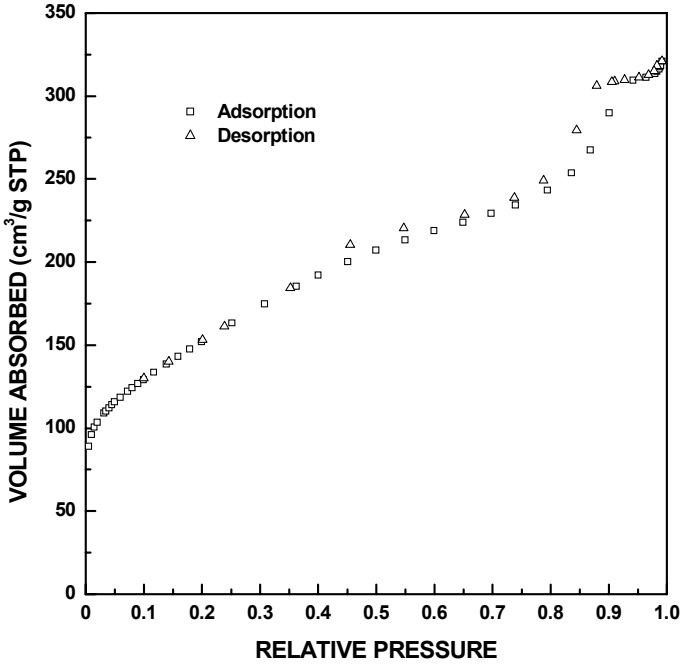

(b)

Figure 3-5-6 Adsorption/desorption isotherms for (a) SC35-1300(8h) and (b) SC8-1250(8h) heat-treated samples.

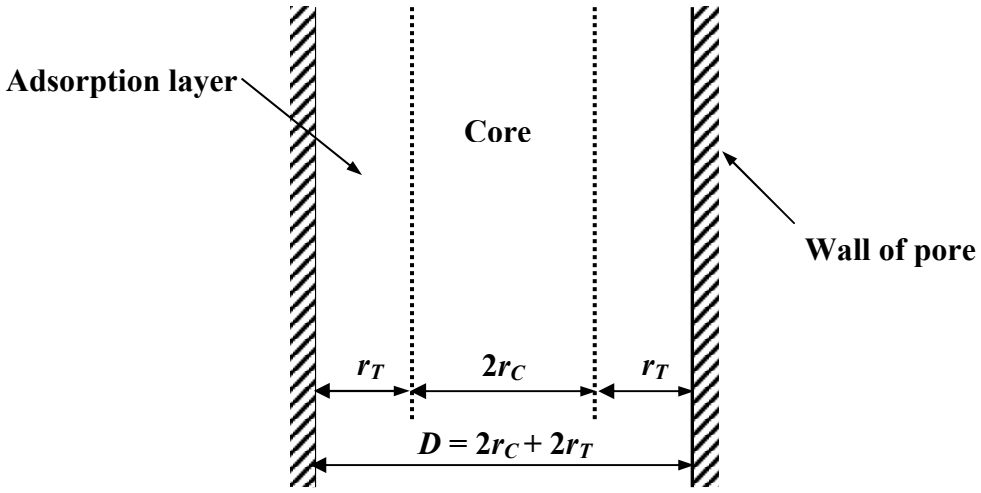

Figure 3-5-7 Illustration of the structure of pores with adsorbed layers.

As indicated by Equation (3-5-8), the relationship between the radius of the core part, r_C, and the relative pressure P/P_0 can be determined using the Kelvin equation:

$$r_C = r_K = -\frac{2\gamma V_L}{RT\ln(P/P_0)} \tag{3-5-12}$$

in which P/P_0 is the relative pressure at which condensation occurs in pores with Kelvin radius of r_K, γ is the surface tension of the liquid (nitrogen), V_L is the molar volume of the liquid (nitrogen), and R is the gas constant (R = 8.314J/(mol · K)).

During the desorption process, the liquid N_2 which had previously condensed in the core of the pore is evaporated first and a layer of adsorbate remains on the wall of the pore. This adsorbed layer becomes thinner with subsequent decreases in pressure. Ideally, in a specific step of desorption (i.e., a specific relative pressure interval), one of the following two scenarios might be present:

(i) There are pores, which had been previously filled by liquid nitrogen, that become open and exposed to the outside gas environment in this desorption step (i.e., the liquid nitrogen in the cores of these "previously-filled pores" are evaporated completely and the adsorbed nitrogen layer on the wall of these pores are exposed.) These pores are referred to as "newly-opened pores" in the BJH method, while the rest of the pores whose cores had been emptied in previous desorption steps are referred to as "previously-opened pores." The amount of nitrogen desorbed in such a step (i.e., in a relative pressure interval) consists of the amount of liquid nitrogen emptied by evaporation from the filled core in this step plus the amount of nitrogen desorbed from the walls of both the "newly-opened pores" and all of the "previously-opened pores." Accordingly, this relative pressure interval (i.e., desorption step) is referred to as "an interval with newly-exposed pores."

(ii) There are no pores whose filled cores are emptied in this desorption step. In this case, the amount of nitrogen desorbed in this step (i.e., in this relative pressure range) only contains the amount of nitrogen desorbed from the walls of all "previously-opened pores." Such a relative pressure interval is referred to as "an interval without newly-exposed pores."

In both cases, the amount of nitrogen desorbed in the desorption step (i.e., in the relative pressure interval) is converted to the volume of condensed liquid and a relationship between the incremental pore volume and the pore size (i.e., a pore size distribution) can be established.

The detailed procedure for treatment of the raw gas adsorption/desorption data is described below. A description of the BJH analysis based on the desorption process is

given below. However, data from both the desorption and the adsorption isotherms were analyzed in this study.

1. The relative pressure Pr_i and volume adsorbed V_{ad_i} data pairs from the adsorption isotherm were arranged in strictly decreasing order from (Pr_1, V_{ad_1}) (the point with highest pressure/volume) to (Pr_N, V_{ad_N}) (the point with lowest pressure/volume), such that $Pr_{i+1} < Pr_i$ and $V_{ad\_i+1} < V_{ad\_i}$. For the adsorption isotherm, the point for $i = 1$ is the No. 30 in Table 3-5-2, the point for $i = 2$ is No. 29, the point for $i = 3$ is No. 28, etc. The same procedure was followed for the desorption isotherm. The point for $i = 1$ is No. 30 in Table 3-5-2, the point for $i = 2$ is No. 31, the point for $i = 3$ is No. 32, etc.
2. Starting from the first data pair with the highest relative pressure (Pr_1, V_{ad_1}), the total volumes of N_2 gas absorbed (V_{ad_i}) at different relative pressures (Pr_i) were converted into liquid equivalent volumes, V_{L_i}, by the following equation:

$$V_{L\_i} = V_{ad\_i} \cdot D_{N2} \tag{3-5-13}$$

   where D_{N2} is the density conversion factor as defined before when describing Equation (3-5-10).
3. Let R_{C_1} be the Kelvin radius for the core of the pore corresponding to the highest relative pressure (Pr_1). R_{C_1} is given by:

$$R_{C\_1} = -\frac{A_K}{\ln \mathrm{Pr}_1} \tag{3-5-14}$$

   where A_K = 0.953 nm for N_2 at 77K, as shown in Equation (3-5-9). It should be kept in the mind that the core radius, R_{C_1}, is not equivalent to the actual pore radius. As explained before, the pore radius includes the thickness of the adsorbed layer. The R_{C_1} value is adjusted later for the thickness of the adsorbed layer during subsequent calculation steps.

The thickness of the adsorbed layer at the start of the first interval (i.e., at the highest pressure Pr_1) was calculated using the Harkins and Jura equation (Jura and Harkins, 1943). The "default values" for nitrogen of A = 13.9900, B = 0.0340, and C = 0.500 were used for the constants in the Harkins and Jura equation:

$$r_{Tw\_1} = [\frac{13.990}{0.0340 - \log(\mathrm{Pr}_1)}]^{0.500} \times 0.1 \text{ nm} \qquad (3\text{-}5\text{-}15)$$

(These default values for A, B, and C were determined by de Boer et al. (1966) based on the adsorption of nitrogen on alumina.)

4. The calculations in steps 4-8 were made for each relative pressure interval. Variable *i* refers to the interval number. For example, $i = 1$ is for the first interval from Pr_1 to Pr_2. *k* refers to the total number of relative pressure intervals (i.e., desorption steps) in which there are new pores being exposed (i.e., case (1) as described before). The initial value of *k* is set as zero. *j* is a counting variable. *j* refers to each previous interval during which new pores were opened. Therefore, $j = 1, 2, 3, \ldots, k$ (p. C-8, ASAP2000 operator's manual, Norcross, GA).

   For the relative pressure interval from Pr_i to Pr_{i+1}, (in which $Pr_i > Pr_{i+1}$), the thickness of the adsorbed layer at the lower end (i.e., relative pressure of Pr_{i+1}) of the interval was calculated by the Harkins and Jura equation:

$$r_{Tw\_i+1} = [\frac{13.990}{0.0340 - \log(\mathrm{Pr}_{i+1})}]^{0.500} \times 0.1 \text{ nm} \qquad (3\text{-}5\text{-}16)$$

   Therefore, the reduction in thickness of the wall layer due to desorption from all previously-opened pores in this relative pressure interval is given by:

$$\Delta r_{Tw} = r_{Tw\_i} - r_{Tw\_i+1} \qquad (3\text{-}5\text{-}17)$$

5. The annular cross-sectional area of the wall layer desorbed for pores in the j th (j = 1, 2, 3, … k) relative pressure interval in which there were "newly-opened pores" during the current relative pressure interval (i.e., from Pr_i to Pr_{i+1}), CSA_{A_j}, is given by:

$$CSA_{A\_j} = 3.1416 \cdot [(R_{C\_j} + \Delta r_{Tw})^2 - R_{C\_j}{}^2] \tag{3-5-18}$$

Consider a case in which the current interval is from Pr_4 to Pr_5 (i.e., i = 4) and the number of "intervals with new pores being exposed" is 3, i.e., k = 3. For example, suppose that the first interval when there were newly-opened pores (i.e., j = 1) was from Pr_1 to Pr_2 (i.e., i = 1), the second interval when there were newly-opened pores (i.e. j = 2) was from Pr_2 to Pr_3 (i.e., i = 2), and the third interval when there were newly-opened pores (i.e., $j = 3 = k$) was from Pr_4 to Pr_5 (i.e., i = 4). Note that, in this example, it is assumed that there were no new pores exposed in the relative pressure interval from Pr_3 to Pr_4 (i.e., $i = 3$). Therefore,

$$CSA_{A\_1} = 3.1416 \cdot [(R_{C\_1} + \Delta r_{Tw})^2 - R_{C\_1}{}^2]$$

$$CSA_{A\_2} = 3.1416 \cdot [(R_{C\_2} + \Delta r_{Tw})^2 - R_{C\_2}{}^2]$$

$$CSA_{A\_3} = 3.1416 \cdot [(R_{C\_3} + \Delta r_{Tw})^2 - R_{C\_3}{}^2]$$

Note that if the current interval is the first interval from Pr_1 to Pr_2 (i.e., i = 1), k = 0 and this step is omitted because there were no pores that had been "previously opened."

6. The total volume of the layer (in condensed state) which was occupied by the nitrogen that desorbed from the walls of all previously-opened pores, V_{d_i}, in the current interval from Pr_i to Pr_{i+1} is given by:

$$V_{d\_i} = \sum_{j=1}^{k} Lp_j \cdot CSA_{A\_j} \tag{3-5-19}$$

where Lp_j is the length of pores previously opened. Using the example in step 5, Lp_1 (j = 1) is length of the pores that were opened in the first interval from Pr_1 to Pr_2 (i.e., i = 1), Lp_2 (j = 2) is length of the pores that were opened in the second interval from Pr_2 to Pr_3 (i.e., i = 2), Lp_3 (j = 3 = k) is length of the pores that were opened in the third interval from Pr_4 to Pr_5 (i.e., i = 4). If i > 1, all Lp_j values come from step 7 below. If i = 1, i.e., the current interval is the first interval from Pr_1 to Pr_2 and there were no pores that were "previously opened." Therefore, V_{d_1} is set to zero.

7. Two desorption processes, case (i) and case (ii), were described previously. The data is treated differently for these two cases, as described below.

   (1) If V_{d_i} is less than the total volume of nitrogen (in liquid state) desorbed in the current interval (V_{L_i} - V_{L_i+1}), i.e. $V_{d\_i} < V_{L\_i}$ - V_{L_i+1}, then desorption due to core evaporation is occurring in addition to desorption from the walls of previously-opened pores in the interval from Pr_i to Pr_{i+1}. Therefore, the desorption step in this interval belongs to case (i). Note that, for the first interval from Pr_1 to Pr_2, $V_{d\_1} = 0$ and $V_{L\_1} > V_{L\_2}$ (see steps 2 and 6). Therefore, the first interval must be an "interval with newly-opened pores."

   Let k (i.e., the number of intervals with new pores exposed, as defined in step 4) be increased by 1, i.e.,

$$k = k + 1 \tag{3-5-20}$$

   For the first interval from Pr_1 to Pr_2, $k = k + 1 = 0 + 1 = 1$ because the initial value of k is zero.

   The volume of nitrogen (in the condensed state) desorbed from newly-opened pores in the current interval (from Pr_i to Pr_{i+1}) is given by:

$$V_{C\_i} = (V_{L\_i} - V_{L\_i+1}) - V_{d\_i} \tag{3-5-21}$$

The Kelvin radius for the lower pressure end of the interval, R_{C_k+1}, is given by:

$$R_{C\_k+1} = -\frac{A_K}{\ln \mathrm{Pr}_{i+1}} \tag{3-5-22}$$

If the current interval is the first interval from Pr_1 to Pr_2 (i.e., $i = 1$), the end point of the first interval, $R_{C\_2} = -\frac{A_K}{\ln \mathrm{Pr}_2}$.

All new pores opened in this interval (i.e., from Pr_i to Pr_{i+1}) are represented by one pore having a "length-weighted average pore diameter" and a corresponding length sufficient to account for the required volume of adsorbate. The weighted average pore diameter, D_{avg_k}, is defined by:

$$D_{avg\_k} = \frac{2(R_{C\_k} + R_{C\_k+1}) \cdot R_{C\_k} \cdot R_{C\_k+1}}{R_{C\_k}^2 + R_{C\_k+1}^2} \tag{3-5-23}$$

The relative pressure corresponding to D_{avg_k}, Pr_{avg_k}, is given by:

$$Pr_{avg\_k} = \exp(-\frac{2A_K}{D_{avg\_k}}) \tag{3-5-24}$$

where $A_K = 0.953$ nm for N_2 at 77K, as shown in Equation (3-5-9). Using Equation (3-5-16), the thickness of the adsorbed layer at pressure Pr_{avg_k}, r_{Twavg_k}, is given by

$$r_{Twavg\_k} = [\frac{13.990}{0.0340 - \log(\mathrm{Pr}_{avg\_k})}]^{0.500} \tag{3-5-25}$$

The decrease in thickness of the wall layer by desorption from the walls of newly-opened pores during the lower portion of the pressure interval (i.e., from Pr_{avg_k} to Pr_{i+1}), Δr_{Td_k}, is given by:

$$\Delta r_{Td} = r_{Twavg} - r_{Tw\_i+1} \tag{3-5-26}$$

(Note that, in the calculation of pore length, it is assumed that the pores exposed in this interval were represented by one pore with diameter of D_{avg_k} which equals the Kelvin radius for relative pressure Pr_{avg_k}. Therefore, only when the relative pressure was lower than Pr_{avg_k}, could there be reduction in the adsorbed layer thickness. This is the reason why the calculation in Equation (3-5-26) was applied to the lower portion of the interval. This is also the reason for an adjustment to D_{avg_k} that is shown later in Equation (3-5-31).)

The cross-sectional area of the core of the newly-opened pores is given by:

$$CSA_{C\_k} = 3.1416 \cdot [(D_{avg\_k} / 2) + \Delta r_{Td})]^2 \qquad (3\text{-}5\text{-}27)$$

The length of the newly-opened pores in this interval from Pr_i to Pr_{i+1} is given by:

$$Lp_k = V_{C\_i} / CSA_{C\_k} \qquad (3\text{-}5\text{-}28)$$

(2) If V_{d_i} is greater than the current incremental of volume desorbed (V_{L_i} - V_{L_i+1}), i.e. $V_{d\_i} > V_{L\_i}$ - V_{L_i+1}, only desorption from walls of all previously-opened pores has occurred and no new pores were opened in this interval. (V_{d_i} is a calculated volume based on Equation (3-5-19). There may be considerable errors in determining the Lp_j and CSA_{A_j} values. Therefore, there could be cases in which $V_{d\_i} > V_{L\_i}$ - V_{L_i+1}, even though this is physically unrealistic.) The current desorption step belongs to case (ii). The total surface area of walls of all previously-exposed pores, SA_{w_i}, is given by:

$$SA_{w\_i} = \sum_{j=1}^{k} (3.1416 \cdot Lp_j \cdot D_{avg\_j}) \qquad (3\text{-}5\text{-}29)$$

where D_{avg_j} is the length-weighted average pore diameter in the jth interval in which there were newly-opened pores. The change in adsorbed layer thickness, Δr_{Tw}, that accounts for the actual volume desorbed in this interval, was calculated again as:

$$\Delta r_{Tw} = \frac{V_{L\_i} - V_{L\_i+1}}{SA_{w\_i}} \tag{3-5-30}$$

(In this case, the calculated Δr_{Tw} replaced the value calculated from Equation (3-5-17).) Since no cores were evaporated in this pressure interval, no new pores were revealed. Thus, no ending radius and average pore diameter are calculated for this interval. (This indicates the report may have fewer tabulated intervals for the BJH pore size distribution analysis compared to the number of experimental pressure intervals.)

8. Diameters for pores opened previously were then adjusted for the change in thickness of the adsorbed wall layer during the interval from Pr_i to Pr_{i+1}.

   (1) If new pores are opened in the current interval (from Pr_i to Pr_{i+1}), the average diameter in this interval, D_{avg_k}, is adjusted by the change in adsorbed layer thickness during the lower portion (i.e., Pr_{avg_k} to Pr_{i+1}) of the current desorption interval, Δr_{Td}, i.e.,

$$D_{avg\_k} = D_{avg\_k} + 2\Delta r_{Td} \tag{3-5-31}$$

   For all other previously-opened pores, the adjustment due to the change in adsorbed layer thickness during the current interval, Δr_{Tw}, was made to the average diameters of previously-opened pores, D_{avg_j}, for all j from 1 to k-1, i.e.,

$$D_{avg\_j} = D_{avg\_j} + 2\Delta r_{Tw},\ j = 1, 2, \ldots, k\text{-}1 \tag{3-5-32}$$

   where Δr_{Tw} comes from Equation (3-5-17). (Note that j is from 1 to k-1 because the average diameter in the current interval (also the latest interval in which there are newly-opened pores) is adjusted according to Equation (3-5-31).) The change in adsorbed layer thickness during the current interval is also added to the radii corresponding to the ends of the pressure intervals, R_{C_j}, for all j from 1 to k:

$$R_{C\_j} = R_{C\_j} + \Delta r_{Tw}, j = 1, 2, \ldots, k \quad (3\text{-}5\text{-}33)$$

(Note that j is from 1 to k because the lower-end diameter of the latest interval, (i.e., R_{C_k+1}) corresponds to the lowest relative pressure of Pr_{i+1} to this point. Therefore, no adjustment to R_{C_k+1} is needed now until the pressure is reduced further in future steps.)

(2) If no new pores are opened in the current interval, for all previously-opened pores, the adjustment due to the change in adsorbed layer thickness during the current interval, Δr_{Tw}, was made to the average diameters of previously-opened pores, D_{avg_j}, for all j from 1 to k, i.e.,

$$D_{avg\_j} = D_{avg\_j} + 2\Delta r_{Tw}, \; j = 1, 2, \ldots, k \quad (3\text{-}5\text{-}34)$$

where Δr_{Tw} comes from Equation (3-5-30). (Note that j is from 1 to k, as compared to 1 to k-1 in Equation (3-5-33). This is because no new pores are exposed in the current interval and the change in adsorbed layer thickness was the same for all previous intervals in which there are newly-opened pores including the latest one (i.e., $j = k$).) The change in adsorbed layer thickness during the current interval is also added to the radii corresponding to the ends of the pressure intervals, R_{C_j}, for all j from 1 to k+1:

$$R_{C\_j} = R_{C\_j} + \Delta r_{Tw}, j = 1, 2, \ldots, k+1 \quad (3\text{-}5\text{-}35)$$

(Note that j is from 1 to k+1, as compared with 1 to k in Equation (3-5-35) because there are no new pores opened in the current interval (from Pr_i to Pr_{i+1}) and the lower-end pressure of the current interval, Pr_{i+1}, must be smaller than the relative pressure corresponding to R_{C_k+1}, which is the lower-end diameter for the latest interval in which there are newly-opened pores.)

9. Steps 4 to 8 are repeated for each pressure interval from the high pressure range to the low pressure range. After all calculations described above have been performed, the BJH pore diameter corresponding to the ends of the intervals are calculated:

$$D_j = 2 \cdot R_{C\_j} \tag{3-5-36}$$

for all j from 1 to k+1. (k + 1 corresponds to the lower limit of the last interval that has newly-opened pores.)

10. The incremental pore volume, ΔV_j, in the interval between D_j and D_{j+1} ($D_j > D_{j+1}$) for all j from 1 to k is calculated from (D_{avg_j}, Lp_j) by using the following equation:

$$\Delta V_j = 3.1416 \cdot Lp_j \cdot (D_{avg\_j}/2)^2,\ j = 1, 2 \ldots k \tag{3-5-37}$$

The above procedure from step 1 to step 10 is illustrated in the flow chart shown in Figure 3-5-8.

After processing of the isotherm data by the method described above, the ASAP2000 software exported the BJH pore size data which includes:

D_j BJH pore diameter - higher end (j = 1, 2, 3, … k)

D_{j+1} BJH pore diameter - lower end (j = 1, 2, 3, … k)

D_{avg_j} length-weighted average diameter for pores with BJH diameter in the range from D_j to D_{j+1}

ΔV_j incremental pore volume (in cm^3/g) for pores with BJH diameter in the range from D_j to D_{j+1}.

The pore size distribution data was analyzed using the method described below.

1. For both the adsorption and desorption isotherm, data sets (D_j, D_{j+1}, D_{avg_j}, ΔV_j, j = 1, 2, 3,…k) were rearranged in order of increasing pore size. In this case, n was used as the counting variable. The ends of the interval in terms of pore size were represented

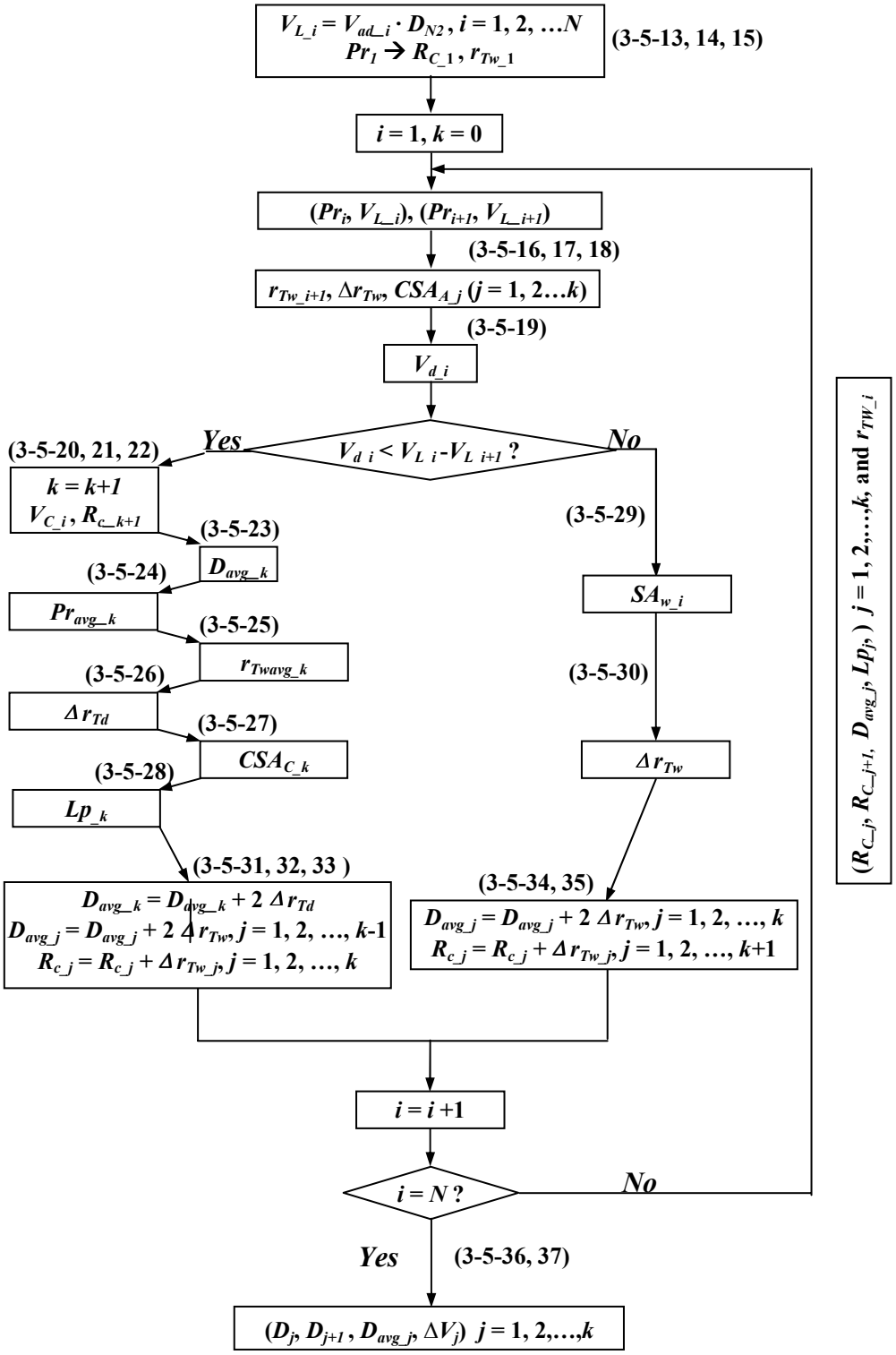

Figure 3-5-8 Flow chart for the data handling in the ASAP2000 software to obtain the BJH adsorption/desorption pore size distribution. Note that when k = 0, calculation of CSA_{A_j} was omitted.

by D_{n-1} and D_n with $D_{n-1} < D_n$ (n = 1, 2, …, k) and the incremental pore volume was represented by ΔV_n. The cumulative pore volume, V_n, is given by:

$$V_n = V_{n-1} + \Delta V_n, \quad n = 1, 2, 3, \ldots, k \tag{3-5-38}$$

where V_0 is set to be zero. This is carried out for all the data from the BJH pore size analysis. The cumulative pore volume, V_n, reaches the maximum value, $V_{BJH\text{-}Total}$, after all the incremental pore volume is added according to Equation (3-5-38) for either the adsorption isotherm or the desorption isotherm. Cumulative pore size distribution plots are made with V_n as the y coordinate and D_n as the x coordinate. Figure 3-5-9 shows an example of cumulative pore size distribution plots for the SC35-1300(8h) and SC8-1250(8h) samples.

For some of the "early-stages" samples (i.e., samples with low extent of reaction), a correction was applied to the cumulative pore size distribution. Figure 3-5-10 shows the adsorption/desorption isotherm plots for two samples, SC35-1200(1h) and SC8-1250(40min), for which the correction was applied. (These samples have fractional weight losses of 0.03 and 0.11, respectively. The term "fractional weight loss" will be defined explicitly in section 4.3.) The isotherms show a rapid increase in adsorbed volume at high relative pressure, with an asymptotic approach to the P/P_0=1 line (parallel to the y-axis). It is believed that this upward bending is not due to the filling of pores. Instead, it represents the condensation of liquid nitrogen on the bulk surface of the sample. Therefore, a correction to the cumulative pore size distribution data was made for these samples. The pore size distribution data (D_n, V_n) was cut off at a BJH diameter of 50 nm. The relative pressure (P/P_0), corresponding to 50 nm diameter is ~0.96. Data above this relative pressure were not used in calculations of

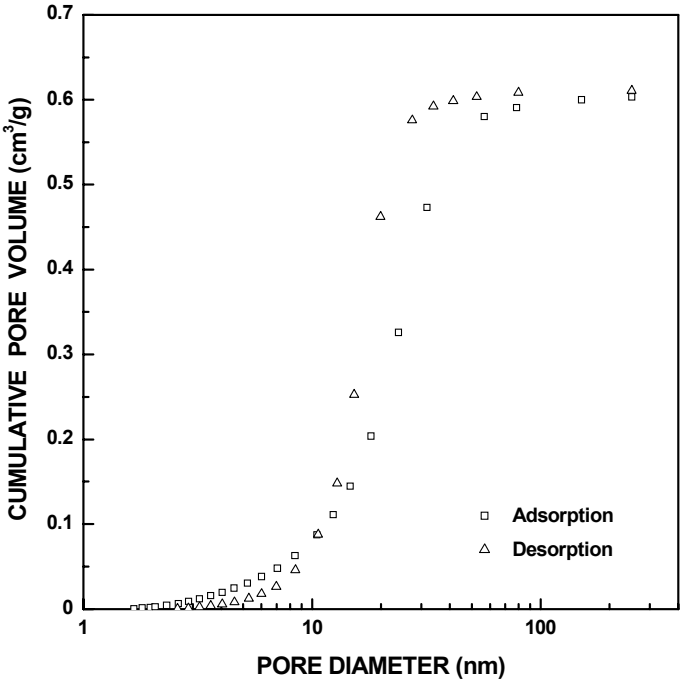

(a)

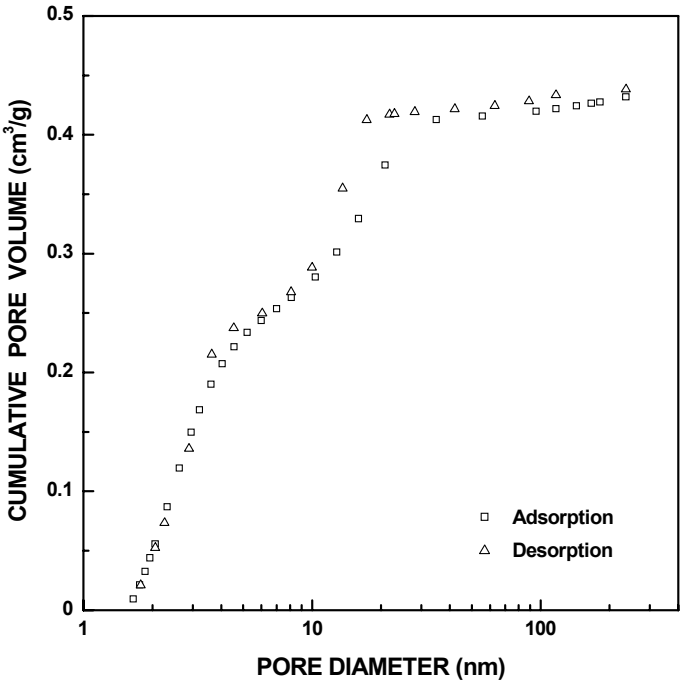

(b)

Figure 3-5-9 Plots of cumulative specific pore volume distribution vs. pore diameter for (a) SC35-1300(8h) and (b) SC8-1250(8h) samples.

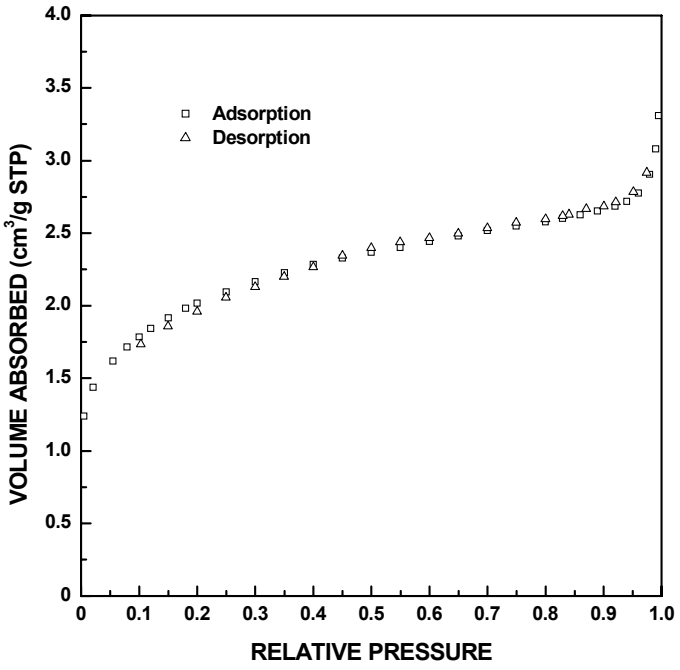

(a)

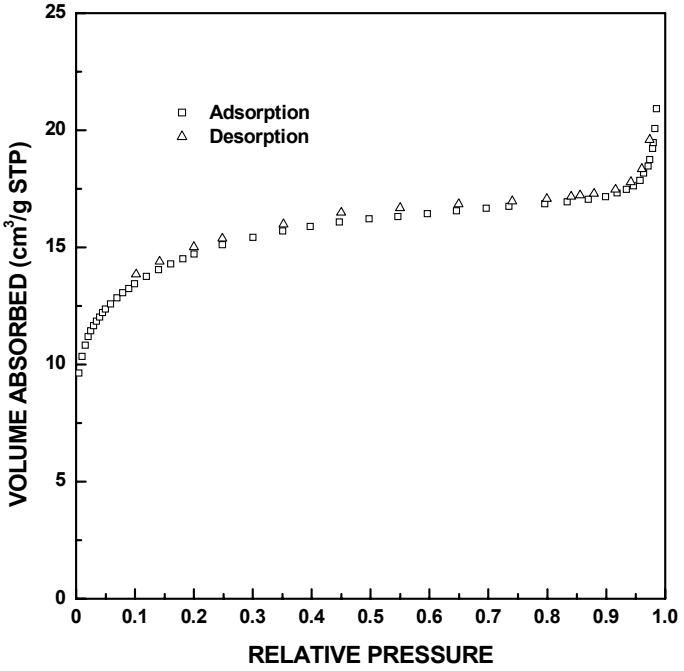

(b)

Figure 3-5-10 Adsorption/desorption isotherm plots for (a) SC35-1200(1h) and (b) SC8-1250(40min) samples which show the upward bending as P/P_0 approaches 1.0.

the BJH pore volume. The maximum cumulative pore volume corresponding to the cut-off point (i.e., 50 nm) was obtained by linear interpolation. Consider an example using the data for SC35-1200(1h). For the desorption isotherm, data points 21 and 22 give D_{21} = 41.67 nm, V_{21}= 0.00276 cm^3/g, and D_{22} = 77.2 nm, V_{22} = 0.00299 cm^3/g. Therefore, the corrected maximum BJH cumulative pore volume, $V_{BJH\text{-}Total}$ (i.e., the BJH cumulative pore volume at 50 nm) for this sample is given by:

$$V_{BJH-Total} = V_{21} + (50 - D_{21}) \times \frac{V_{22} - V_{21}}{D_{22} - D_{21}}$$

$$= 0.00282 \ (cm^3/g)$$

Figure 3-5-11 shows the cumulative pore size distribution for the SC35-1200(1h) sample before and after the cut-off correction.

2. For both the adsorption and desorption isotherms, the normalized cumulative pore volume, V_{N_n} (in percent), was obtained by the following equation:

$$V_{N\_n} = \frac{V_n}{V_{BJH-Total}} \times 100\,\% \qquad (3\text{-}5\text{-}39)$$

where V_n is the BJH cumulative pore volume and $V_{BJH\text{-}Total}$ is the maximum BJH cumulative pore volume for the adsorption or desorption isotherm. Figure 3-5-12 shows the normalized pore size distribution plots (V_{N_n} vs. D_n) for the SC35-1300(8h) and SC8-1250(8h) samples. Plots are shown for both the adsorption and desorption data. Figure 3-5-13 shows the normalized pore size distribution plots for the SC35-1200(1h) and the SC8-1250(40min) samples, both of which have been treated with the 50 nm cut-off correction.

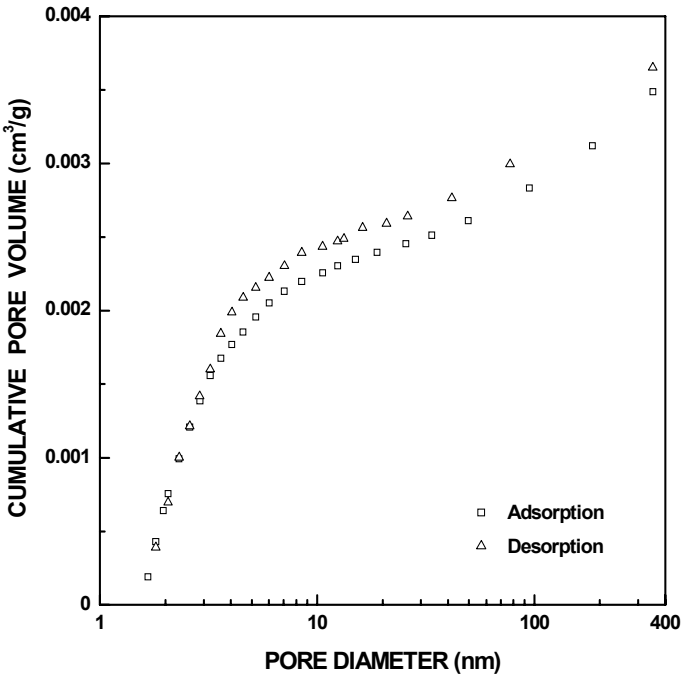

(a)

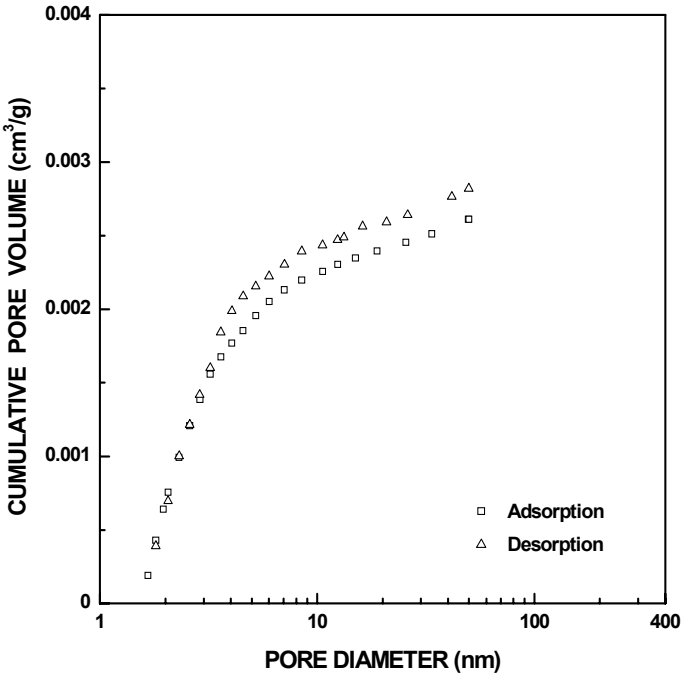

(b)

Figure 3-5-11 Plots of cumulative specific pore volume vs. pore diameter for SC35-1200(1h) before (a) and after (b) the cut-off correction.

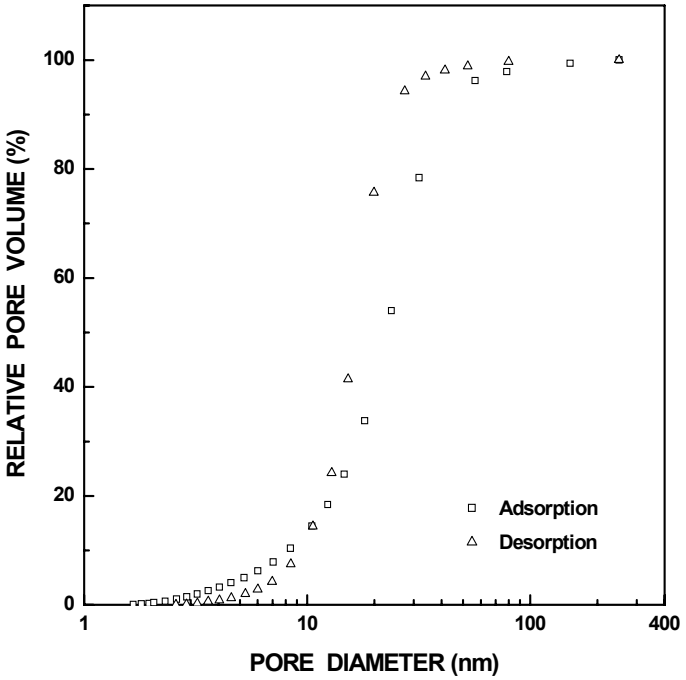

(a)

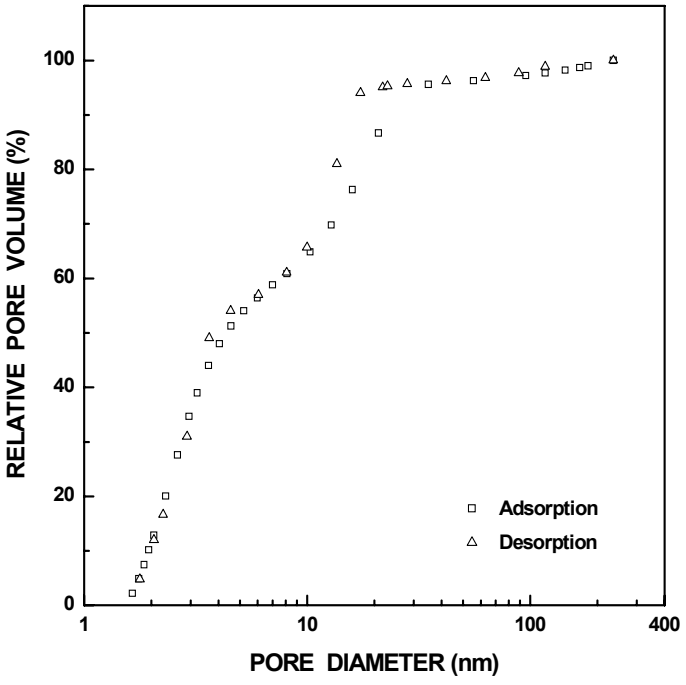

(b)

Figure 3-5-12 Plots of relative ("normalized") pore volume vs. pore diameter for (a) SC35-1300(8h) and (b) SC8-1250(8h) samples.

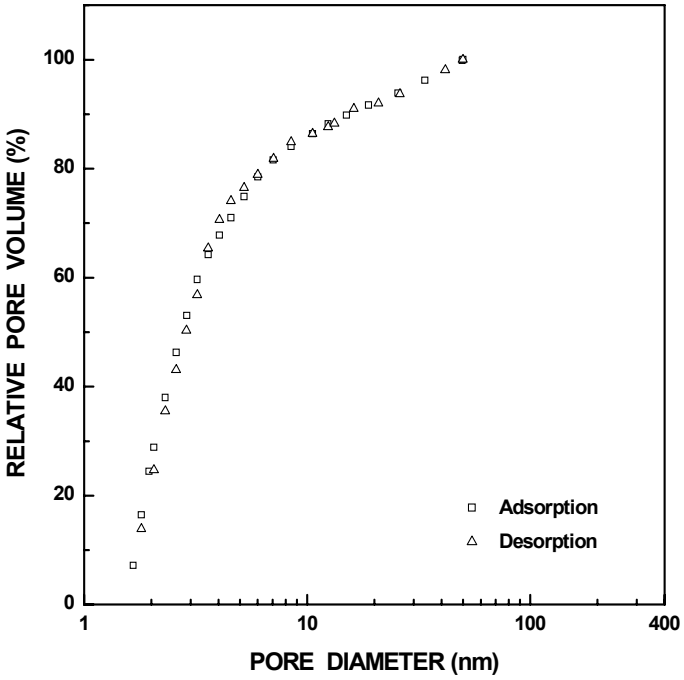

(a)

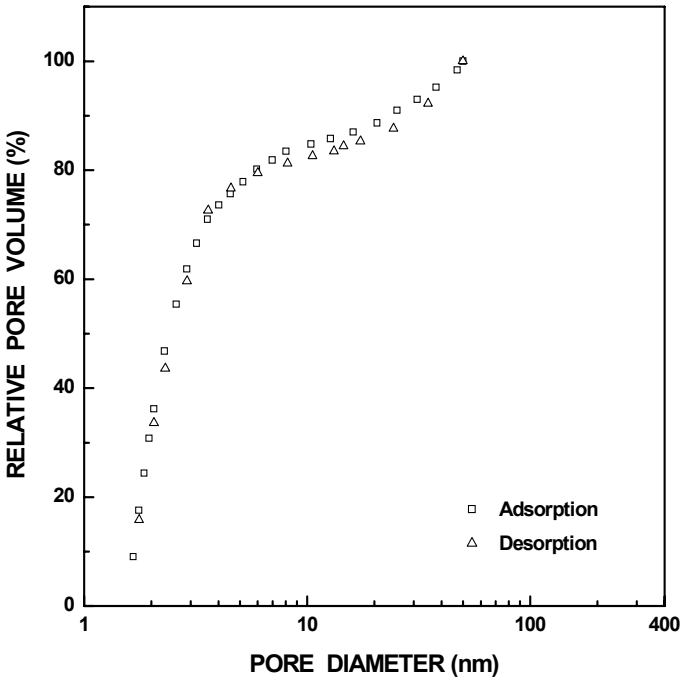

(b)

Figure 3-5-13 Plots of relative ("normalized") pore volume vs. pore diameter for (a) SC35-1200(1h) and (b) SC8-1250(40min) samples. The pore diameter was cut off at 50 nm.

3. Let D_{10}, D_{50}, and D_{90} represents the BJH pore diameters below which the cumulative pore volume accounts for 10%, 50% and 90%, respectively, of the maximum cumulative pore volume, $V_{BJH\text{-}Total}$. The D_{10}, D_{50}, and D_{90} values are calculated by linear interpolation between the nearest data points in the normalized cumulative pore size distribution. Consider an example using the adsorption isotherm for the SC35-1300(8h) sample. Data point 19 and 20 are the nearest data points for determining D_{50}. D_{19} = 18.10 nm and V_{N_19} = 33.8%. D_{20} = 23.88 nm and V_{N_20} = 54.0%. Therefore, D_{50} is given by:

$$D_{50} = D_{19} + (50\% - V_{N\_19}) \times \frac{D_{20} - D_{19}}{V_{N\_20} - V_{N\_19}}$$

$$= 18.10 + (50\% - 33.8\%) \times \frac{23.88 - 18.10}{54.0 - 33.8} = 22.73 \text{ nm}$$

4. The specific pore volume frequency, $(\frac{dV}{dD})_n$, was calculated using the following equation:

$$(\frac{dV}{dD})_n = \frac{\Delta V_n}{\Delta D_n} = \frac{V_n - V_{n-1}}{D_n - D_{n-1}} \qquad (3\text{-}5\text{-}40)$$

Plots of $(\frac{dV}{dD})_n$ vs. D_n were made using both the adsorption and desorption data. Figure 3-5-14 shows example plots for the SC35-1300(8h) and SC8-1250(8h) samples.

5. The relative ("normalized") specific pore volume frequency, $(\frac{dV}{dD})_{N\_n}$, was calculated using the following equation:

$$(\frac{dV}{dD})_{N\_n} = \frac{\Delta V_{N\_n}}{\Delta D_n} = \frac{V_{N\_n} - V_{N\_n-1}}{D_n - D_{n-1}} \qquad (3\text{-}5\text{-}41)$$

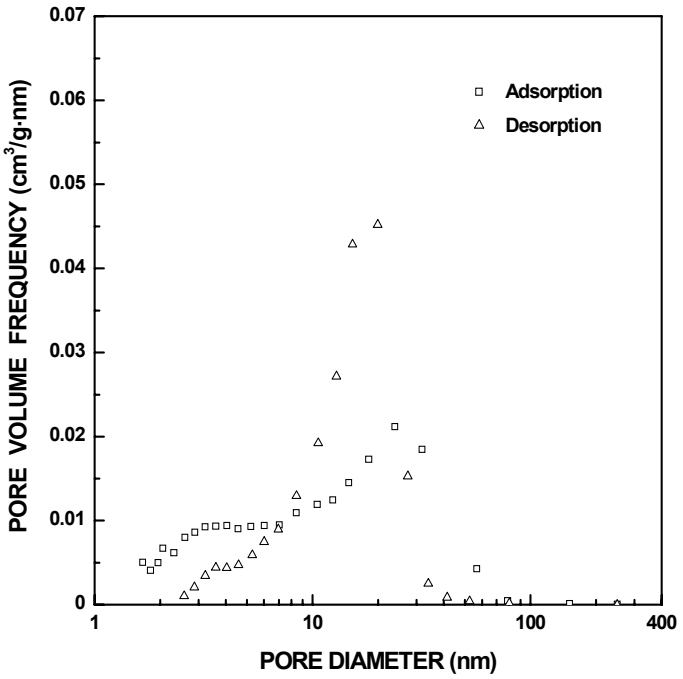

(a)

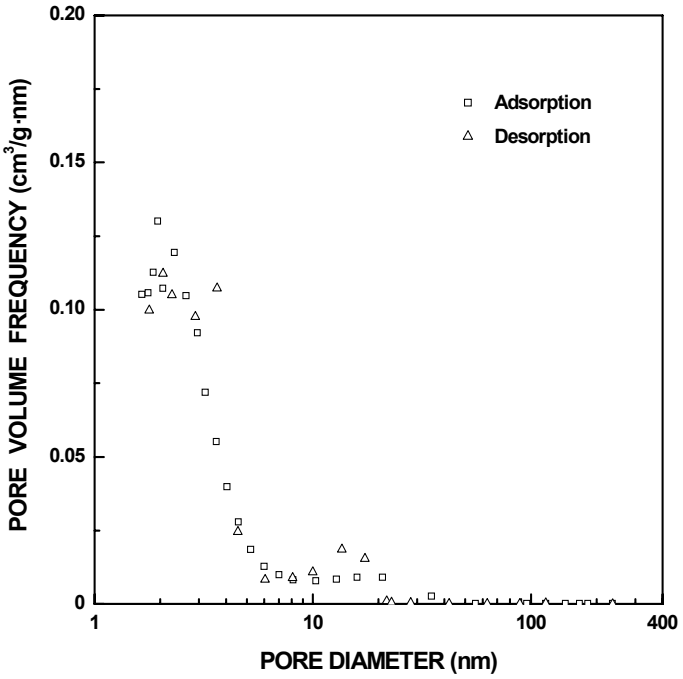

(b)

Figure 3-5-14 Plots of the specific pore volume frequency vs. pore diameter for (a) SC35-1300(8h) and (b) SC8-1250(8h) samples.

Plot of $(\frac{dV}{dD})_{N\_n}$ vs. D_n were made using both the adsorption and desorption data. Figure 3-5-15 shows example plots for the SC35-1300(8h) and SC8-1250(8h) samples.

6. The pore size distribution was separated into two parts: one was for pores with diameter smaller than 5 nm and the other was for pores with diameter 5 nm and above. For each part, the total specific pore volume, the relative pore volume, the total specific surface area, and the relative surface area were calculated. Linear interpolation was used to determine the volume and surface area values at 5 nm. Consider an example using the desorption data for the sample SC35-1300(8h). Data points 6 and 7 are the closest points to the 5 nm diameter dividing point. D_6 = 4.58 nm and V_6 = 0.00820 cm^3/g. D_7 = 5.30 nm and V_7 = 0.01245 cm^3/g. The maximum cumulative pore volume, $V_{BJH\text{-}Total}$, was 0.61042 cm^3/g. Therefore the specific pore volume for pores with diameter smaller than 5 nm, $V_{BJH\ (Dia.\ <\ 5nm)}$, is given by:

$$V_{BJH(Dia.<5nm)} = V_7 + (5 - D_6) \times \frac{V_7 - V_6}{D_7 - D_6}$$

$$= 0.00820 + (5 - 4.58) \times \frac{0.01245 - 0.00820}{5.30 - 4.58}$$

$$= 0.01068 \ cm^3/g$$

The percentage of pores with diameter smaller than 5 nm, $V^N_{BJH(Dia.<5nm)}$, is given by:

$$V^N_{BJH(Dia.<5nm)} = \frac{V_{BJH(Dia.<5nm)}}{V_{BJH-Total}} \times 100\% = \frac{0.01068}{0.61042} \times 100\% = 1.7\%$$

The specific pore volume for pores with diameter ≥5 nm, $V_{BJH(Dia.\geq 5nm)}$, is given by:

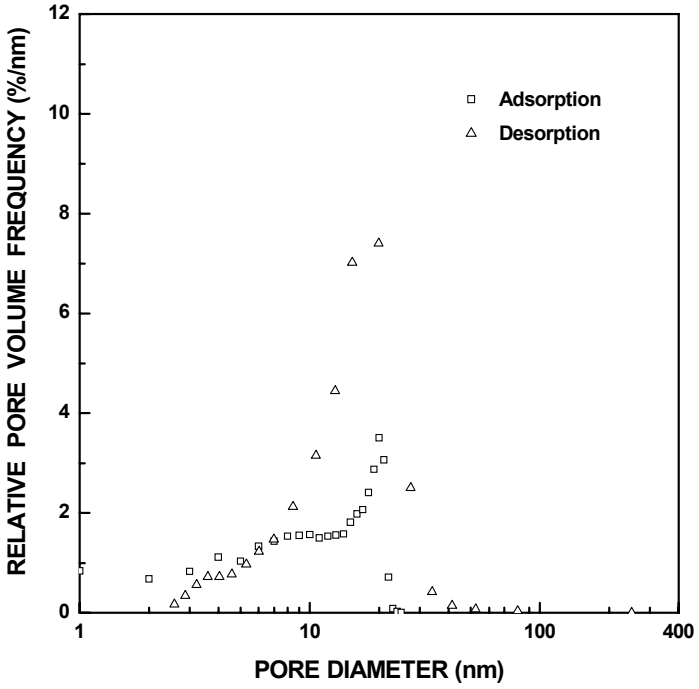

(a)

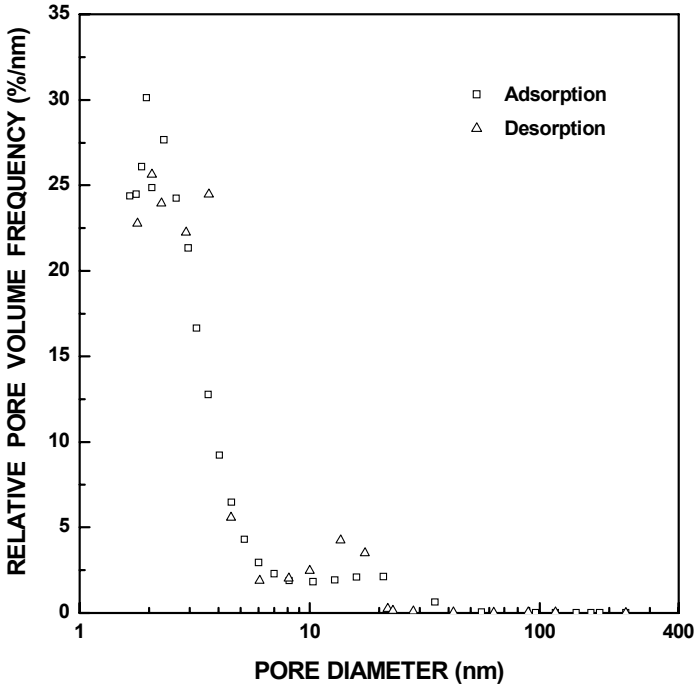

(b)

Figure 3-5-15 Plots of relative ("normalized") specific pore volume frequency vs. pore diameter for (a) SC35-1300(8h) and (b) SC8-1250(8h) samples.

$$V_{BJH(Dia.\geq 5nm)} = V_{BJH-Total} - V_{BJH(Dia.<5nm)} \quad (3\text{-}5\text{-}42)$$

The percentage of pores with diameter ≥5 nm, $V^{N}_{BJH(Dia.\geq 5nm)}$, is given by:

$$V^{N}_{BJH(Dia.\geq 5nm)} = 100\% - V^{N}_{BJH(Dia.<5nm)} \quad (3\text{-}5\text{-}43)$$

Using the desorption data, the values for the SC35-1300(8h) sample are:

$$V_{BJH(Dia.\geq 5nm)} = V_{BJH-Total} - V_{BJH(Dia.<5nm)} = 0.61042 - 0.01068 = 0.59975 \ (\text{cm}^3/\text{g})$$

$$V^{N}_{BJH(Dia.\geq 5nm)} = 100\% - V^{N}_{BJH(Dia.<5nm)} = 100\% - 1.7\% = 98.3\%$$

In addition, the median diameter, D_{50}, for the pores ≥5 nm and <5 nm were calculated in a similar manner as described above in step 3 except that the relative specific pore volume (percentage) was calculated based on either $V_{BJH(Dia.\geq 5nm)}$ or $V_{BJH(Dia.<5nm)}$ (i.e., instead of using $V_{BJH\text{-}Total}$).

- Micropore analysis

In addition to the mesopore size distribution, the ASAP software also provides the surface area and volume for micropores smaller than ~2 nm. The adsorbed layer thickness values, r_{Ti}, are calculated by the ASAP software at different relative pressure, Pr_i, values (from 0.005 to 0.6) using the Harkins and Jura equation (Equation (3-5-15)). Then, the adsorbed volume, V_{ad_i}, was plotted against the adsorbed layer thickness r_{Ti}. This type of plot is known as a *t*-plot. Figure 3-5-16 is an illustration of a *t*-plot for the SC8-1250(8h) sample.

Linear fitting based on the least-squares method was performed for points on the *t*-plot with layer thickness between 0.35 nm and 0.50 nm. (Note that 0.35 nm is the average thickness of a single layer of adsorbed nitrogen (p.95, Gregg and Sing, 1982). Therefore, the pore diameter for the lower limit for the fitting is at least twice the

thickness of a single nitrogen layer, while the pore diameter for the upper limit is approximately three (or more) times the thickness of a single nitrogen layer. The choice of these limits is somewhat arbitrary.) The linear fitting provides a y-intercept, V_{int}, and a slope, k_{micro}. The micropore volume, V_{micro}, is given by:

$$V_{micro} = V_{\text{int}} \cdot D_{N2} \tag{3-5-44}$$

where D_{N2} is the gas to liquid density conversion factor for liquid nitrogen at 77K, as described previously. The micropore specific surface area, SA_{micro}, is given by:

$$SA_{micro} = SA - (k_{micro} \cdot D_{N2}) \tag{3-5-45}$$

where SA is the total specific surface area of the sample determined by the BET (or Langmuir) method.

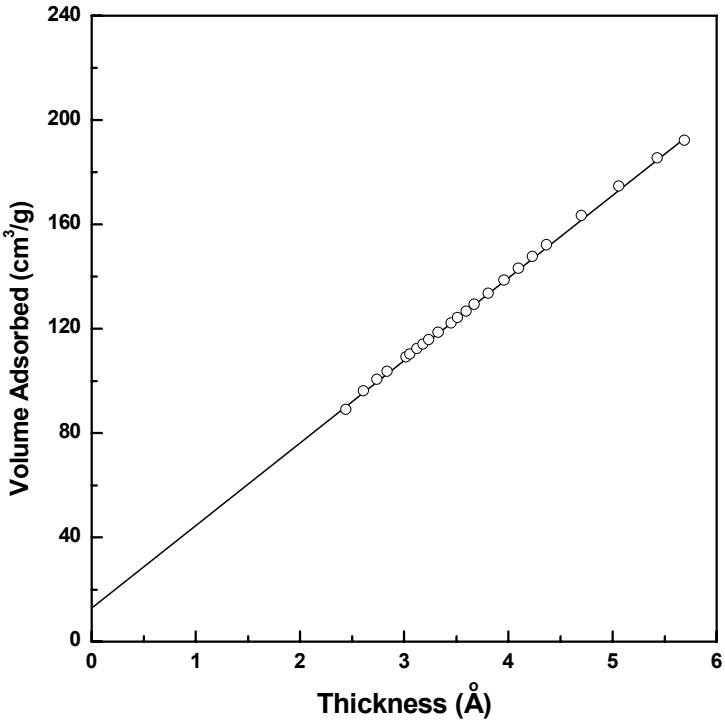

Figure 3-5-16 Plot of volume adsorbed vs. adsorbed layer thickness (from the Harkins and Jura equation) (*t*-plot) for the SC8-1250(8h) sample.

3.5.3 Particle Size Distribution Measurement by Light Diffraction

3.5.3.1 Method for Particle Size Distribution Measurement

Particle size distributions were determined using a light scattering method (Model LS 13320, Beckman Coulter, Miami, FL). The basic components of the systems are a monochromatic source of illumination, a spatial filter to focus the light beam, a sample chamber which holds the sample and allows the particles to interact with the light beam, and an array of photo-detectors that record the intensity patterns for the light scattered by the particles.

In the general case, the intensity pattern for the scattered light is rather complex and depends on the properties of the light source (wavelength and polarization), properties of the particles (sizes, shapes, concentration, and complex refractive index), and the angle of scattering. Experimentally, scattered light intensities are measured at known scattering angles using light sources with known properties and using suspensions with fixed particle concentration. The scattering pattern is deconvoluted using theoretical equations which relate the scattering intensity to the scattering angle, particle size, and particle shape. Mie theory is usually applied when particles are smaller than the wavelength of the incident light. The theory requires knowledge of the particle complex refractive index. In addition, the theory is based on the assumption that particles have a spherical shape. Fraunhofer diffraction theory can be used when particles are much larger than the wavelength of the incident light. Fraunhofer theory is easier to apply because the particle refractive index is not needed. (For large particles (or highly absorptive particles), most of the scattered intensity is concentrated at very small angles in the forward direction (i.e., "forward diffraction"), so it is not necessary to know the refractive index.) Both theories were

applicable to this investigation because the powders that were characterized had a wide range of particles sizes. For example, fully-converted CTR samples which had been milled (ground) had particles that were mostly submicrometer, with the smallest particles extending to the lower limit of detection of the instrument (~40 nm). In contrast, pyrolyzed powders and as-heat-treated CTR powders (unground) had particles that were mostly greater than 5 μm, with the largest sizes extending to ~200 μm.

Measurements of particle size distributions via light scattering are carried out using dilute particle/liquid suspensions. The concentration is sufficient to provide enough scattered light to reach the detectors with adequate signal-to-noise ratio, but low enough to minimize particle-particle interactions and multiple light scattering. In the LS 13320 instrument, the suspensions are loaded into a "liquid module" which consists of a sample cell and a circulation system. The sample cell allows the particles in the suspension to be exposed to illuminating source. The circulation system has a pump which allows the cell to be filled and rinsed automatically. It also serves the function of keeping particles suspended in the liquid. This becomes increasingly important as the size of the particles increases because the rate of particle sedimentation is proportional to the diameter squared.

3.5.3.2 Sample Preparation before Particle Size Distribution Measurement

Some samples (particle/liquid suspensions) were prepared using ultrasonication (Model VC600, Sonics & Materials Inc., Danbury, CT). The sonication frequency was 20,000 Hz and the power was 600 watts. The sonication force was applied to the suspension indirectly; a plastic container containing the suspension was placed on top of an ultrasonically vibrating metal platen. Other suspensions were prepared without

sonication. Instead, the particle/liquid suspensions were placed in a plastic bottle and rotated on a roller mill.

SC8 and SC35 pyrolyzed powders were prepared using 0.1 wt% solids in deionized water. In addition, 0.1 wt% of Photo-flo® (Kodak, Rochester, NY) was used as a wetting and/or dispersing agent. (Photo-flo® is aqueous solution consisting of propylene glycol and polyethoxy/polyphenoxy alcohols.) Suspensions were sonicated for 14 minutes prior to the particle size measurements. It should be noted that all suspensions described in this section were diluted with distilled water when placed in the LS 13320 sample chamber for the particle size analysis measurements (see section 3.5.3.3).

A suspension of SC8-1250(16h) particles was prepared using 0.05 wt% solids in ethanol. Two types of wetting and/or dispersing agents were added at a concentration of 0.1 wt%: Hypermer® KD-2 (ICI Specialty Chemicals, Wilmington, DE) and K-30 PVP (polyvinyl pyrrolidone, ISP Technologies Inc., Wayne, NJ). Suspensions were sonicated for 14 minutes prior to the particle size measurements.

A suspension with SC35-1300(16h) particles was prepared using 0.0125 wt% solids in deionized water. The suspension was adjusted to pH = 9.5 using ammonium hydroxide (Fisher Scientific, Fair Lawn, NJ) in order to obtain good particle dispersion. The suspension was sonicated for 14 min. The pH of the suspension lowered after the sonication, so additional base was added to bring the pH back to 9.5. The suspension was sonicated again and the pH remained at ~9.5.

Additional samples were prepared and tested by Dr. Zhaohui Yang of Georgia Institute of Technology. These samples included SC42 pyrolyzed material and SC42 CTR samples which had been heat treated at 1300^{o}C for 1 h, 2 h, 3 h, 4 h, 6 h, 8 h, 12 h,

and 24 h. Suspension was prepared using ~0.3-0.4 wt% powder in deionized water with the pH adjusted to 9.5. Suspensions were either tumbled on a roller mill or sonicated for 14 minutes before the particle size measurement.

The particle size distribution was also determined after milling the SC42-1300(24h) powder. The milling was done in a Spex mill (Model 8000, Spex Certiprep, Metuchen, NJ). 2 g of the SC42-1300(24h) powder was put in a polyethylene vial (cylinder shaped with diameter of 1 cm and length of 5 cm). Two SiC media (8 mm diameter) were added. The sample was milled for a total of 10 min. To ensure proper milling, the vial was opened and the powder was scratched off the walls of the vial after every 2 min of milling. A suspension of the milled SC42-1300(24h) powder was prepared at pH = 9.5 in the same way as described for the SC35-1300(16h) sample.

3.5.3.3 Measurement Condition and Data Analysis for Particle Size Distribution

The LS 13320 instrument was operated using two light sources. The main light source has a wavelength of 750 nm and is produced from a laser diode, while a secondary tungsten-halogen source is projected through a set of filters to produce three wavelengths (450, 600, and 900 nm). The latter light source is part of a so-called "PIDS assembly." (PIDS = polarized intensity differential scattering.) The PIDS assembly is used as the primary source for detecting fine particles and improves the resolution of the measured size distributions for powders which contain submicrometer particles. The PIDS data was included for the measurements made in this study because some of the powders contained submicrometer particles.

Measurements were carried out using a pump speed which was 40% of the maximum speed. The suspensions prepared were added to the sample chamber. The sample chamber initially contained distilled water (approximately 100 cm^3) prior to the addition of the sample suspension. Therefore, the actual concentrations of particles in the suspensions inside the chamber were much lower than that of the suspensions that had been prepared initially. (The particle concentrations in the sample chamber were on the order of a few hundred ppm by weight.)

The optical model (Fraunhofer or Mie) that was used in analyzing the light scattering data depended upon the range of measured particle sizes for each sample. The choice of the model that was used for each sample is described in detail later in sections 4.1.6 and 4.4.6. As noted earlier, application of the Mie theory requires knowledge of the complex refractive index. For this reason, the Mie theory was applied in this study only for samples which contained a significant fraction of submicrometer particles. Hence, the Fraunhofer model was used for all the pyrolyzed samples (section 4.1.6) and some of the CTR samples (section 4.4.6), while the Mie model was used for other CTR samples (section 4.4.6). Many of the latter samples consisted mostly of β-SiC or they contained a substantial fraction of β-SiC. The values of refractive index n and adsorption coefficient k for β-SiC, used to calculate the particle size distributions, are shown in Table 3-5-3. The refractive index n values came from work of Alterolvitz and Woolman (1991). Their sample was a thick film (on the order of 10 μm) single crystal of β-SiC. The extinction coefficient k value came from the work of Patrick and Choyke (1969). The sample was a single crystal of β-SiC grown by a vapor-phase method. In addition, Alterolvitz and Woolman (1991) verified that the extinction coefficient was below 0.02, although they

Table 3-5-3 Refractive index n and extinction coefficient k for β-SiC.

Wavelength (nm)	n	k
450	2.69	0.001
600	2.62	0.0002
750	2.62	0.0002
900	2.55	0.0003

could not obtain the specific values because it was below the measurement limit of their equipment.

The complete particle size distribution and various statistical parameters were obtained from the LS13320 software. This includes the d_{10}, d_{25}, d_{50}, d_{75}, and d_{90} diameter values which represent the particle diameter at which the cumulative particle volume accounts for 10%, 25%, 50%, 75% and 90%, respectively, of the maximum cumulative particle volume. Measurements were made multiple times for each sample. Average values from these measurements will be reported. Consider an example using the SC35-1100(2h) pyrolyzed sample. The d_{10} values for six consecutive runs were 28.45, 29.21, 28.07, 27.60, 23.33, and 27.97 μm. Therefore, the average d_{10} from these six runs is given by:

$$d_{10} = \frac{28.45 + 29.221 + 28.07 + 27.60 + 23.33 + 27.97}{6} = 27\ \mu\text{m}$$

The standard deviation for d_{10} for this sample is 2 μm. Therefore, the average d_{10} value is reported as 27 ± 2 μm. Similarly, the modes from individual runs for the same sample were 87.9, 87.9, 96.5, 96.5, 87.9, and 96.5. The average mode, d_{mode}, is given by:

$$d_{mode} = \frac{87.9 \times 3 + 96.5 \times 3}{6} = 92 \ \mu m$$

The standard deviation for d_{mode} for this sample is 5 μm. Therefore, the average mode d_{mode} value is reported as 92 ± 5 μm.

The particle size distribution data from multiple runs were also combined to obtain one average distribution. The arithmetic mean diameter, based on volume percentage, was used as the mean diameter of the distribution. To be more specific, suppose d_i is the particle diameter in a narrow size range, n_i is the percentage of particles with diameter in that narrow range around d_i, then the mean particle diameter of d_{mean} is given by:

$$d_{mean} = \exp\left(\frac{\sum n_i d_i^4 \ln d_i}{\sum n_i d_i^3}\right) \tag{3-5-46}$$

The standard deviation of the average distribution, SD_a, is given by:

$$SD_a = \sqrt{\frac{\sum n_i (d_i - d_{mean})^2}{\sum n_i}} \tag{3-5-47}$$

3.5.4 SEM

SEM was used to observe the structure of the heat-treated powders. Samples were prepared by two methods. In one method, the powders were first dispersed in ethanol at solid concentration of ~0.1 wt%. The powder suspension was then sonicated for 14 min to break up large agglomerates. Approximately 0.1 ml of the suspension was deposited on a piece of conductive carbon tape that had been previously placed on an aluminum SEM mount. The mount was placed in a PTFE (Teflon®) stand and the stand was put in an oven to remove the ethanol. Some samples were sputter coated in a sputter

coater (Model PS-2, International Scientific Instruments, England) with a thin gold coating (~10 nm) prior to SEM observations.

In the second method, a liquid solution of methylmethacrylate monomer (MMA, Fisher Chemicals, Fair Lawn, NJ) and 2,2'-azobisisobutyronitrile (AIBN, Aldrich Chemicals Company Inc., Milwaukee, WI) was infiltrated into the powder samples. AIBN serves as the initiator for the polymerization of MMA. The concept for this method is to use a low-viscosity liquid to infiltrate the porosity of the powder samples and subsequently carry out an in-situ polymerization reaction to form a hard solid polymer (PMMA). The presence of PMMA in the pores enabled the powder particles to be polished. The polished sections allow the porous structure of the powder to be viewed more readily. The specific sample preparation steps are described below.

Solid AIBN was first ground in the alumina mortar. Approximately 5 g of liquid MMA was poured into a 20 ml glass vial. The ground AIBN was added to the MMA. The concentration of AIBN in MMA was ~0.2-0.4 wt%. A magnetic stir bar was placed into the vial and the mixture was stirred for ~10 min to aid the dissolution of the AIBN in the MMA. 0.2 g of sample powder was put into a 4 ml cylindrical glass vial with inner diameter of ~10 mm. 0.6 g of the MMA solution (with AIBN) was added to the latter vial. The suspension was stirred with a thin wooden stick to help the liquid to wet the powder and to penetrate into the pore channels. The bottle with powder suspension was then covered with a PTFE lid. Several small holes were punched into the lid to prevent excessive buildup of pressure during polymerization. The vial was put into a water bath with the temperature at ~70-75^{o}C. The MMA would usually polymerize and harden in ~2-4 hours. After the PMMA hardened completely, the vial was removed from the water

bath. The PTFE lid was removed and the vial was broken in order to recover a solid block of PMMA with embedded sample powders. Then, the bottom side of the PMMA/powder block which had been at the bottom of the vial was ground slightly to determine if there were any cracks and holes. If not, the block was placed on a clean piece of glass with the ground side facing down. An aluminum ring with diameter of 2.5 cm and height of 1.5 cm was placed around the PMMA block. Quickmount® resin (Buehler Ltd., Lake Bluff, IL) was poured into the ring and allowed to cure. The mounted sample was then ready for grinding and polishing.

Grinding was carried using a grinding machine (Ecomet®, Buehler, Lake Bluff, IL) equipped with a diamond particle-embedded metal disk (TBW Industries Inc., Furlong, PA). Successive grinding steps were carried out using disks with diamond particles sizes of 68 μm, 30 μm, and 12 μm. Samples were held manually against the rotating diamond-embedded disks. After the grinding steps, samples were polished using the same type of grinding machine described above, except that the rotating platen was now equipped with a polishing cloth (LECLOTH^{TM}, LECO Corporation, St. Joseph, MI) that was soaked with an alumina suspension. Samples were polished manually in two successive steps using aqueous suspensions with ~20 wt% alpha alumina particles (LECO Corporation, St. Joseph, MI) with nominal sizes of 1.0 μm and 0.3 μm.

Some polished samples were directly sputter coated with gold for 1 min prior to SEM observations. In other cases, the PMMA was first removed from the polished samples. The polished samples were cut from the sample mounts using a precision diamond saw (Model Isomet® 4000, Buhler, Lake Bluff, IL). The cut sample was placed on a 3 cm diameter alumina stub with the polished surface facing upward. The sample

was then heated in a tube furnace in a flowing Ar atmosphere. The heating schedule was 2°C/min to 550°C with hold of 2 h at 550°C. This produced a porous powder "compact" with polished particles at the top surface. The corner of a clean glass slide was used to transfer some of the polished particles to carbon tape which was attached to an alumina SEM mount, such that the polished surface facing upward. Samples were either viewed directly in the SEM or were sputter coated with a gold coating.

A field emission SEM (Model 1530, LEO, Thornwood, NY) was used for the microscopy observations. The operating voltage was in the range of 2-6 kV. The observations were carried out by Dr. Raj Pulugurtha and Dr. Zhaohui Yang of Georgia Institute of Technology.

3.5.5 TEM and High Resolution TEM (HRTEM)

The TEM samples were prepared in two methods; they will be referred to as the "dispersion method" and the "(epoxy) embedding method."

For the dispersion method, the powder was first dispersed in ethanol at solid concentration of 0.1 wt%. The suspension was sonicated for 14 min to break up large agglomerates. Several drops of the suspension were added to a copper grid with lacey carbon film (SPI #3840C, Structural Probe Inc., West Chester, PA). The grid was then covered with a glass beaker and dried at room temperature. After drying, the grid was ready for TEM observation.

For the embedding method, a two-part epoxy resin (353ND, Epoxy Technology, Billerica, MA) was used as the embedding material and a copper tube with 0.125 inch (3.18mm) outside diameter and 0.014 inch (0.36mm) wall thickness was used as support

for the epoxy-embedded sample. A piece of the copper tube was first cut to a length of 1.5 cm. The cut piece was cleaned in xylene (W. M. Barr & Co. Inc., Memphis, TN) to remove oil inside the tube. Approximately 0.5 g of the two parts of the epoxy were mixed in a small polyethylene container. The ratio of the hardener to the epoxy was 1:10 by weight. The mixture was stirred with a wooden stick until the color appeared to be uniform. The mixture was allowed to sit in air until any bubbles formed by mixing had disappeared. Approximately 0.2 g of powder was added to the container with mixed epoxy. Then, the powder-epoxy mixture was stirred with a wooden stick for ~2 min until it appeared uniform. A small syringe with a tip diameter of ~1.5 mm was used to collect the mixture and subsequently inject it into the copper tube until the tube was full. The filled copper tube was then held vertically by a piece of PTFE block with holes drilled in it. The block with the tube was placed in oven at 110^{o}C for 1-2 h to allow the epoxy to harden.

After removing the tube from the oven, the epoxy stuck on the outside wall of the tube was removed with a small knife. The tube was cut into ~1 mm thick slices using a diamond saw (Model Isomet® 4000, Buhler, Lake Bluff, IL). If a slice was free of cracks and pores, it was glued to the mount of tripod polisher (Model 590W, South Bay Technology, San Clemente, CA) using a thermoplastic bonding material (MWH135, South Bay Technology, San Clemente, CA). The slice was ground using a grinding machine (Ecomet®, Buehler, Lake Bluff, IL) on a series of SiC grinding paper (Carbimet®, Buehler, Lake Bluff, IL). The mount was then heated on a hot plate to soften the bounding material. The cut slice was flipped over with the unground side facing upward. The mount was allowed to cool down so that the bonding material hardened

again. The other side of the slice was then ground with the tripod polisher using the same series of grinding papers. The final thickness of the sample was in the range of ~100-150 μm.

The sample slice was then removed from the mount by heating. It was soaked in acetone to clean off the thermoplastic bonding material. The slice was then glued with the thermoplastic bonding material to the center of a sapphire disk. The sapphire disk was put on dimpler (Model D500i, VCR Group Incorporated, South San Francisco, CA) and dimpled for ~2-10 h The dimpling load was 20 g and the speed of the rotation was 30 rpm. A 6 μm diamond suspension was used in the early stage of dimpling in order to remove ~60 μm of the sample thickness. The sample was cleaned with water and a 1 μm diamond suspension was used in the final stage of dimpling. A dimple in the center of the sample was obtained and the thickness at the center was ~20-25 μm. The dimpled slice was removed carefully from the sapphire disk using mild heating conditions. (Excessive temperature would cause the epoxy to curl and separate from the supporting copper ring.)

The dimpled slice was cleaned in acetone and glued with a thermoplastic bonding material to the sample support for ion milling (Model 691, Gatan, Pleasanton, CA). The turning speed of the sample was 3 rpm. For the SC35-1100(2h) sample, the acceleration voltage was 5 kV and the working angle of the ion guns are ~5-6^{o}. The ion currents for both guns were ~15-20 μA during the ion milling. Such milling condition caused significant heating effect as indicated by the observation of a red glow at the edge of the hole being milled. For all other samples prepared, the acceleration voltage was chosen to be 4 kV. The ion currents for both guns were ~15-20 μA during the ion milling. The

working angles of the two ion guns were set at $+3^{o}$ and -1^{o}. After milling, there was a hole in the center of the sample and SiC particles were located along the edge of the hole. When observed under optical microscope, the edge of the hole had a colorful interference fringe which indicated that the thickness was below or around one micron. The support with the sample glued on it was soaked in acetone in a beaker in order to remove the sample. The sample was cleaned with acetone and allowed to dry in air.

The samples were observed using two transmission electron microscopes (TEM). One was a low-resolution TEM (Model 100C, JEOL, Tokyo, Japan) which was operated at 100kV. The magnification factor used with the JEOL 100C TEM was in the range of 10^{4} - 1.9×10^{5}. The other microscope was a high-resolution TEM, HRTEM (Model 4000EX, JEOL, Tokyo, Japan). The point resolution was 1.8Å. The 4000EX TEM was operated at 400 kV and the magnification factor used was in the range of 2×10^{5} - 10^{6}.

3.5.6 Powder Solid Density Measurement by Pycnometer

The solid densities of SC42-1100(2h) pyrolyzed material and phenolic resin heat treated at 1100^{o}C and 1300^{o}C were measured using a glass pycnometer (capacity of ~3 ml) by Dr. Zhaohui Yang of Georgia Institute of Technology. The procedure is given below:

1. The dry weight of the pycnometer, W_{pyc}, is measured using an analytical balance (AX205, Mettler Toledo, Switzerland).
2. The pycnometer is filled with deionized water and the total weight is measured. The procedure is repeated several times in order to determine an average weight, $W_{pyc\text{-}wat}$.

3. The temperature of the water was measured in order to obtain the corresponding density of water at that temperature, ρ_{wat}.

4. The volume of the pycnometer, V_{pyc}, is given by:

$$V_{pyc} = \frac{W_{pyc-wat} - W_{pyc}}{\rho_{wat}} \tag{3-5-48}$$

5. The pycnometer was dried in an oven. (No details about the drying conditions are available.) The weight of the dried pycnometer was determined using the analytical balance. Approximately 1.5 g of powder sample was put in the dry pycnometer. The pycnometer was weighed again using the analytical balance and the weight of the powder, W_{pow}, was determined by difference. The pycnometer was then filled with deionized water and the weight, $W_{pyc\text{-}wat\text{-}pow}$, was determined using the analytical balance.

6. The weight of water in the pycnometer from step 5, W_{wat}, is given by:

$$W_{wat} = W_{pyc\text{-}wat\text{-}pow} - W_{pyc} - W_{pow} \tag{3-5-49}$$

7. The volume of the water in the pycnometer from step 5, V_{wat}, is given by:

$$V_{wat} = \frac{W_{wat}}{\rho_{wat}} \tag{3-5-50}$$

8. The volume of the powder, V_{pow}, is given by:

$$V_{pow} = V_{pyc} - V_{wat} \tag{3-5-51}$$

9. The apparent density of the powder, ρ_{pow}, is given by:

$$\rho_{pow} = \frac{W_{pow}}{V_{pow}} \tag{3-5-52}$$

Several measurements were usually carried out for each sample. The average density and standard deviation were reported.

3.5.7 Powder Packing Density Measurement

The packing densities of the SC8 and SC35 pyrolyzed materials were measured by the procedure given below.

1. The water content of the powder, w_{wat}, was determined by drying it in an oven at 170^{o}C (2h) and monitoring the weight before and after the drying.
2. The weight of an empty, closed-end glass tip, W_{tip}, was determined.
3. The tip was filled with deionized water to a marked line and the weight of the tip plus water, $W_{tip\text{-}wat}$, was measured.
4. The volume of the tip, V_{tip}, is given by:

$$V_{tip} = \frac{W_{tip-wat} - W_{tip}}{\rho_{wat}} \tag{3-5-53}$$

5. Water was removed from the tip and the tip was dried. Powder was gradually loaded into the tip until the marked line was reached. The tip was tapped during filling in some cases, while in other cases there was no tapping during the filling. The weight of the tip plus powder was measured. (The weights are designated as $W_{tip\text{-}pow\text{-}tap}$ and $W_{tip\text{-}pow}$ for the cases with tapping and without tapping, respectively.)
6. The weights of powder filled in the tip without tapping, W_{pow} , and with tapping, $W_{pow\text{-}tap}$, are given by:

$$W_{pow} = (W_{tip-pow} - W_{tip})(1 - w_{wat}) \tag{3-5-54}$$

$$W_{pow-tap} = (W_{tip-pow-tap} - W_{tip})(1 - w_{wat}) \tag{3-5-55}$$

7. If no tapping was applied when the tip was filled with powder, the packing density without tapping, ρ_p, is given by:

$$\rho_p = \frac{W_{pow}}{V_{tip}} \tag{3-5-56}$$

If tapping was applied when the tip was filled with powder, the packing density, $\rho_{p\text{-}tap}$, was calculated in the same way:

$$\rho_{p-tap} = \frac{W_{pow-tap}}{V_{tip}} \tag{3-5-57}$$

CHAPTER IV

RESULTS AND DISCUSSION

As stated in Chapter I, the main purpose of this study was to reveal the mechanism of SiC formation through the carbothermal reduction reaction (CTR). To achieve this, experiments in three major areas have been conducted: (i) analysis of deposits (collected downstream from reaction zone) which developed due to volatile formation during the reaction, (ii) kinetics of the reaction, and (iii) structural evolution of the solid reaction product.

In this chapter, the characterization results on the starting materials (the dried and pyrolyzed materials) before carbothermal reduction reaction are presented first. The result of volatile deposit analysis is presented next. Then, the results of the kinetic study (i.e. data of isothermal weight loss and fractional amount of SiC formed determined by quantitative X-ray diffraction (QXRD) study) will be given. The appropriate kinetic model for the CTR reaction is identified and the reaction mechanism is proposed. After that, results from characterization of the product structure such as crystallite size, surface area and porosity, particle size distribution, and particle morphology from SEM and TEM observation will be presented. The results are discussed and compared with those from other researchers to provide a complete picture of the reaction mechanism for the formation of SiC through the carbothermal reduction reaction.

4.1 Characterization of the Materials before CTR

In this section, results of characterization on the materials before carbothermal reduction reaction (i.e., the dried and pyrolyzed materials) will be presented for both the SC35 and the SC8 samples.

4.1.1 XRD Patterns of the Dried and Pyrolyzed Materials

As described in section 3.1, the so-called "dried materials" were obtained by drying the concentrated TEOS/phenolic resin mixed solutions in vacuum at 110^{o}C. The XRD patterns for the SC35 and SC8 dried materials are shown in Figures 4-1-1 and 4-1-2. Both the SC8 and SC35 dried materials were XRD amorphous. The very broad peak at two-theta (2θ) angles in the approximate range of 15-30^{o} in the SC35 sample is associated mostly with amorphous silica. This is indicated by the observation of a very similar broad peak in the XRD pattern (Figure 4-1-3) for a dried sample that was prepared from a TEOS-derived sol (i.e., a sol prepared with no phenolic resin). A very broad XRD peak in a similar 2θ range is also observed in a dried sample prepared from a phenolic resin solution (see Figure 4-1-4). However, this peak is shifted to slightly lower 2θ angles compared to the peaks in Figures 4-1-1 and 4-1-3. The peak in Figure 4-1-4 shows better overlap at the lower 2θ angles with the peak in Figure 4-1-2 for the SC8 dried sample. This observation apparently reflects the fact that the SC8 sample has a considerably higher phenolic resin concentration compared to the SC35 sample (i.e., based on the starting compositions that were given in section 3.1).

The XRD patterns of the SC35-1100(2h) and SC8-1100(4h) pyrolyzed materials are shown in Figure 4-1-5 and Figure 4-1-6, respectively. The pyrolyzed materials were still amorphous according to XRD. There are two very broad peaks at 2θ ranges of ~15-

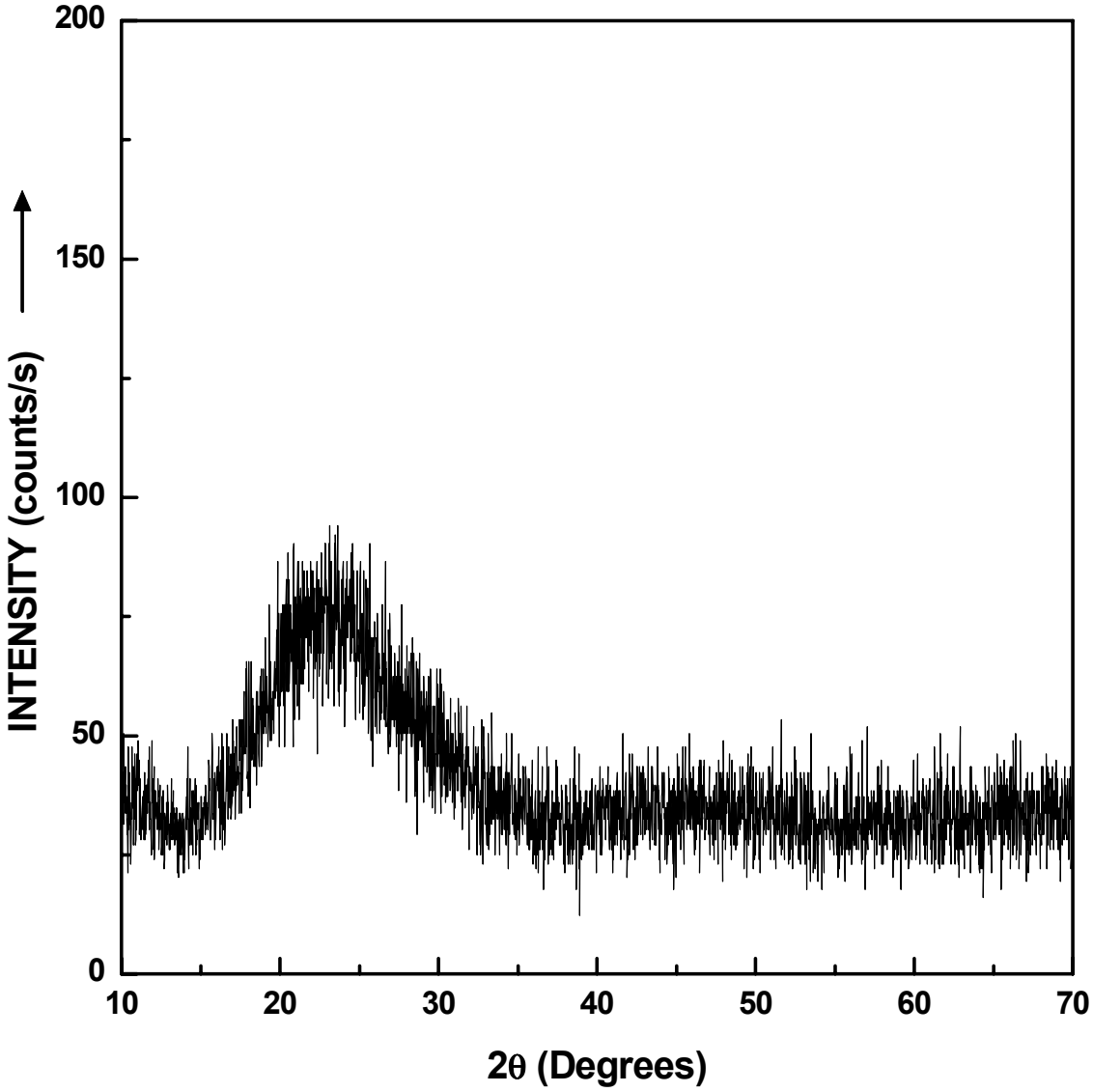

Figure 4-1-1 XRD pattern of the SC35 dried material.

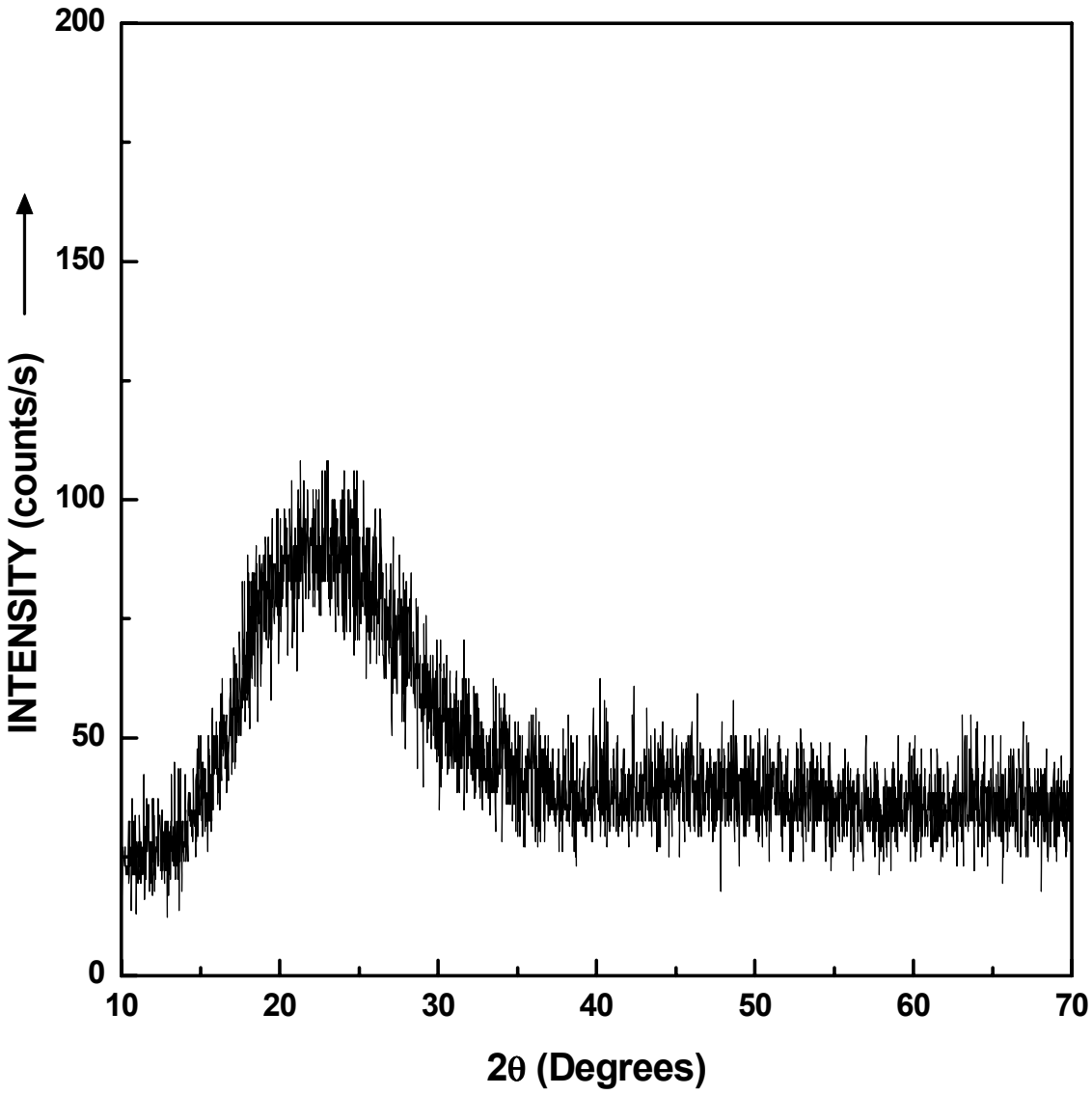

Figure 4-1-2 XRD pattern of the SC8 dried material.

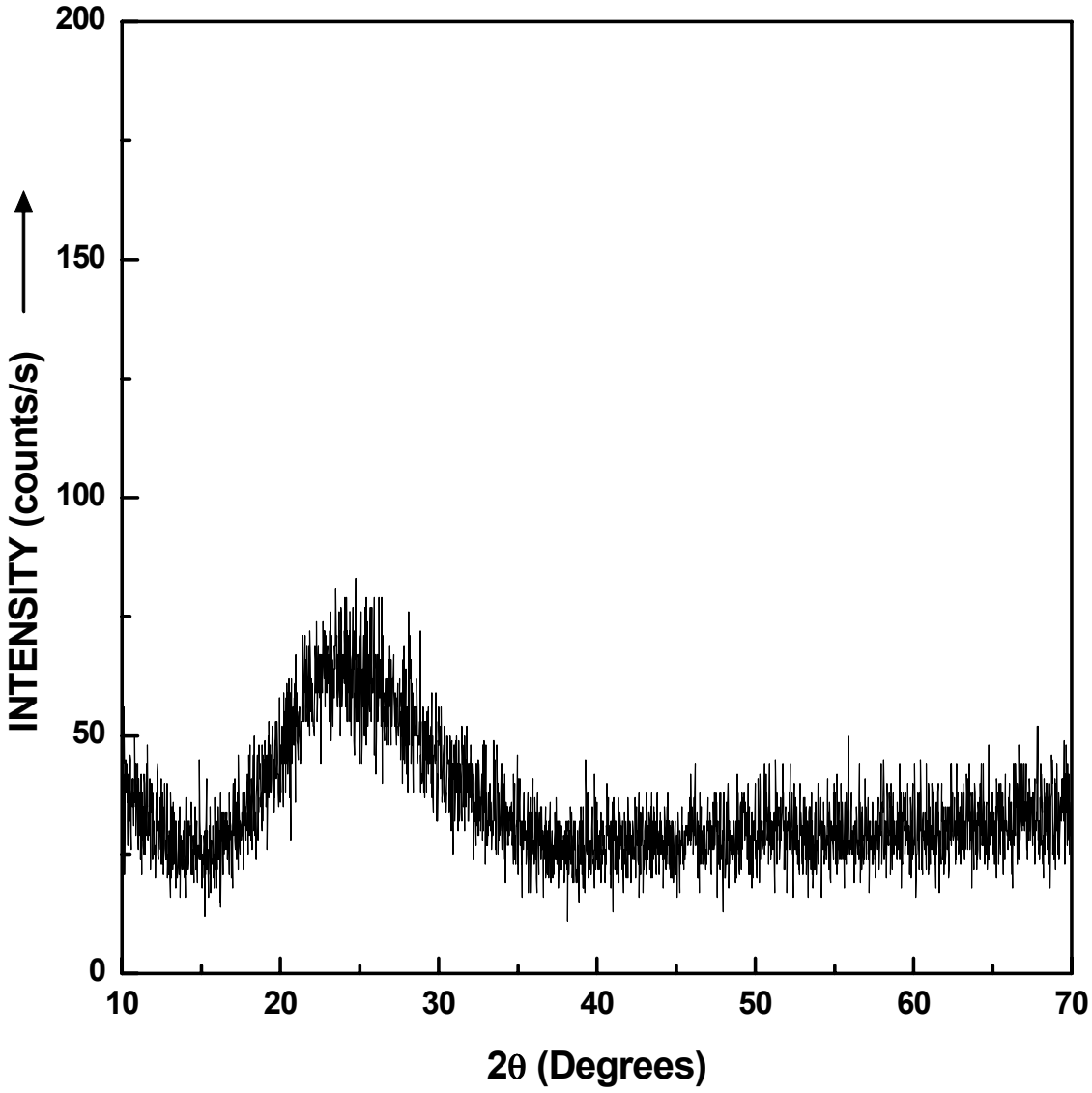

Figure 4-1-3 XRD pattern of the dried material obtained from a TEOS sol.

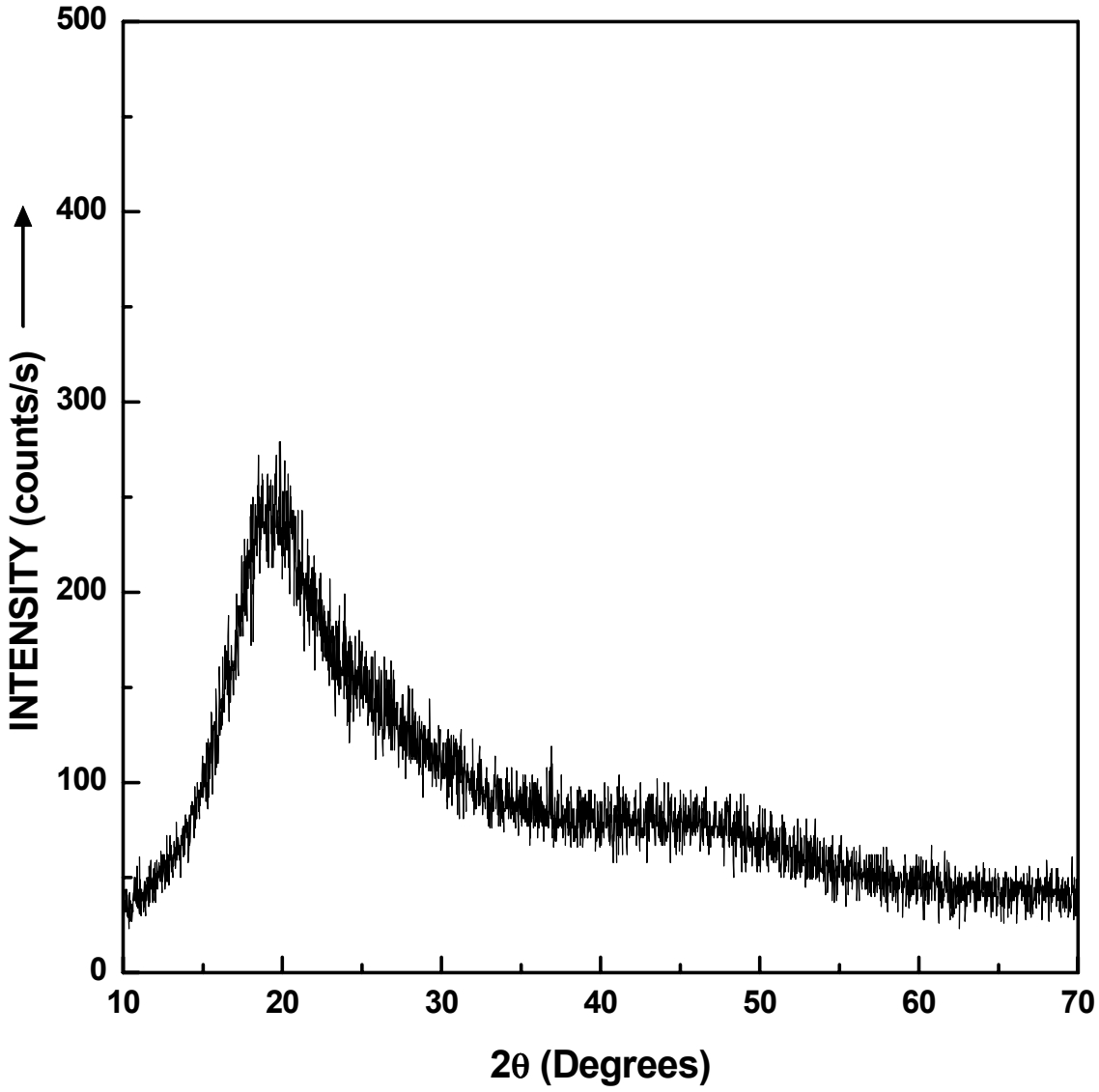

Figure 4-1-4 XRD pattern of the dried material obtained from a phenolic resin solution.

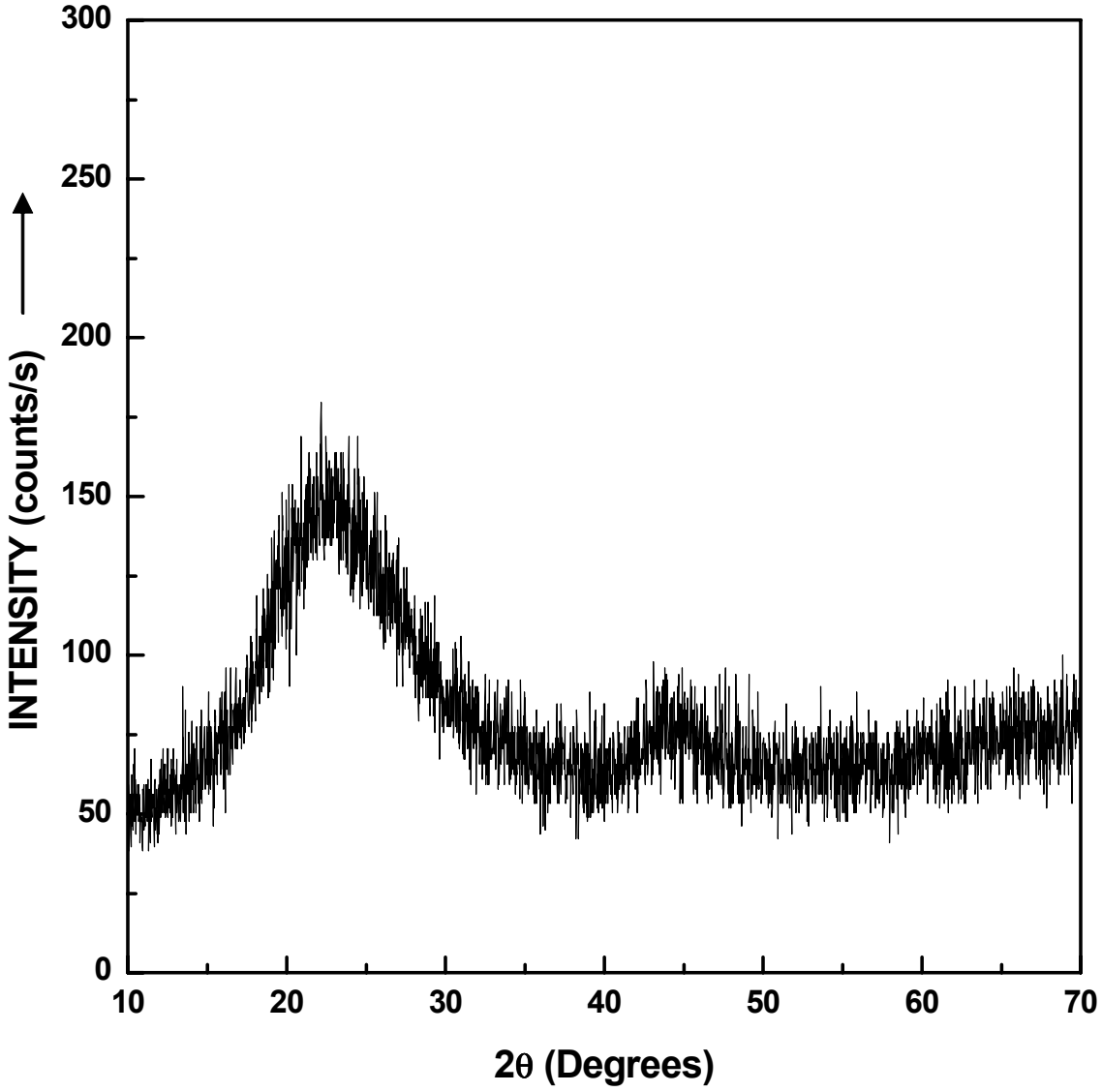

Figure 4-1-5 XRD pattern for the SC35-1100(2h) pyrolyzed material.

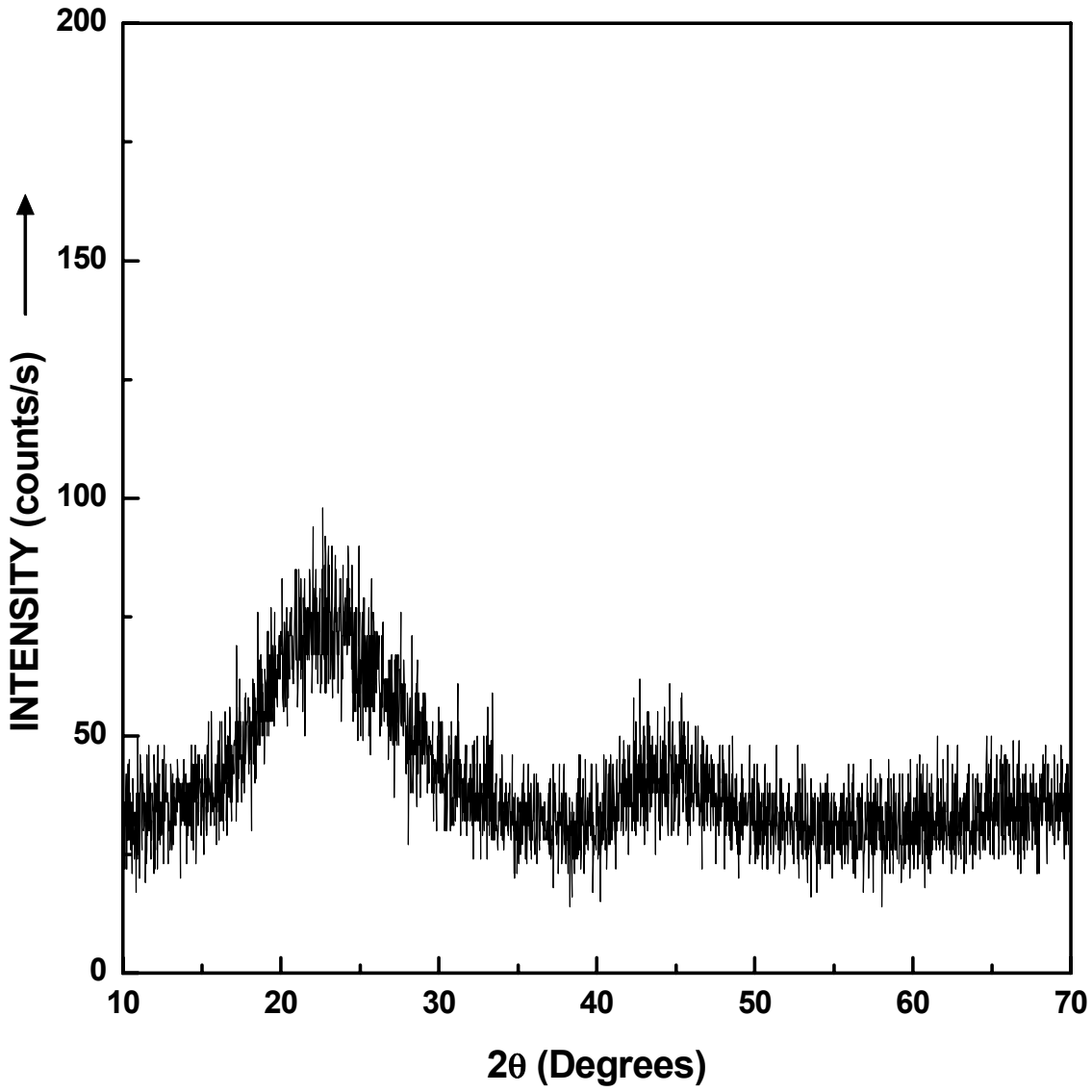

Figure 4-1-6 XRD pattern for the SC8-1100(4h) pyrolyzed material.

30° and ~40-50°. Figures 4-1-7 and 4-1-8 show the XRD patterns for pyrolyzed materials from the dried TEOS gel and phenolic resin, respectively. By comparing Figures 4-1-5 and 4-1-6 with Figures 4-1-7 and 4-1-8, it is concluded that the very broad peak at the 2θ range of ~15-30° is due to both amorphous silica and carbon, and the very broad peak at the 2θ range of ~40-50° is due to amorphous carbon. (XRD patterns similar to the ones described in this study were reported by Takahashi et al. (2000) and Huang et al. (2002) for amorphous silica and by Ma et al. (2002) for amorphous carbon.)

4.1.2 Yield for Pyrolysis Heat Treatment of the Dried Materials

As stated in section 3.1, the SC35 dried material was pyrolyzed at 1100°C for 2 h in Ar and the SC8 dried material was pyrolyzed at 1100°C for 4 h in Ar. The pyrolysis heat treatment was used to obtain a fine scale mixture of carbon and silica by "decomposition" of the dried material and removal of the volatile species. The yield for pyrolysis heat treatment, Y_{pyro}, is defined by:

$$Y_{pyro} = \frac{W_{pyro}}{W_{dry}} \tag{4-1-1}$$

in which W_{dry} is the weight of the dried material before pyrolysis heat treatment and W_{pyro} is the weight of the product after the pyrolysis heat treatment. The pyrolysis yield, Y_{pyro}, is a decimal fraction. Table 4-1-1 summarizes the yields for the pyrolysis heat treatments of the SC35 and SC8 dried materials. The average yield values for the pyrolysis heat treatments were 0.6947 and 0.5905 for the SC35 and SC8 dried materials, respectively.

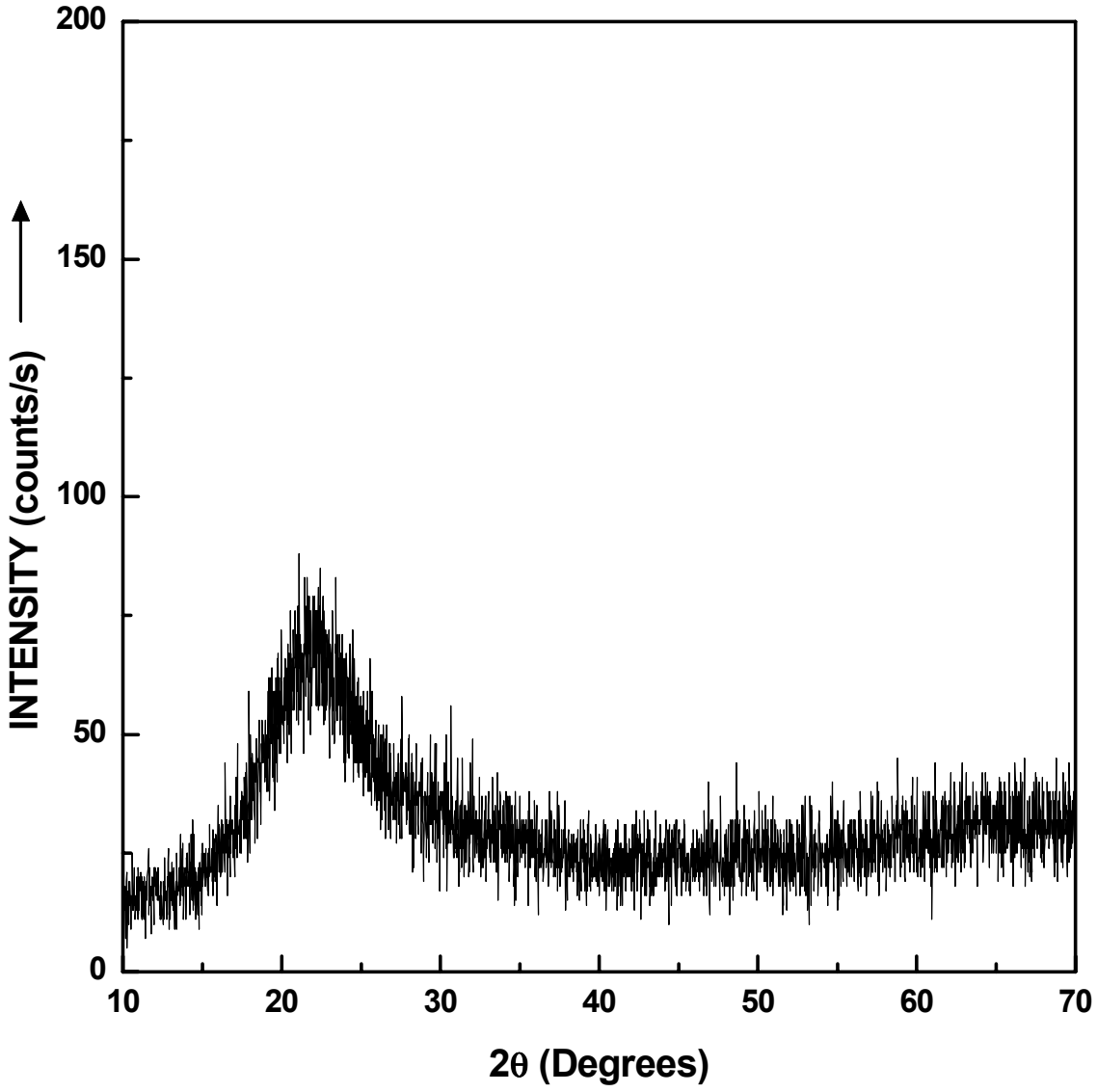

Figure 4-1-7 XRD pattern of amorphous silica obtained from the pyrolysis of TEOS dried material at 1100^{o}C for 4 h.

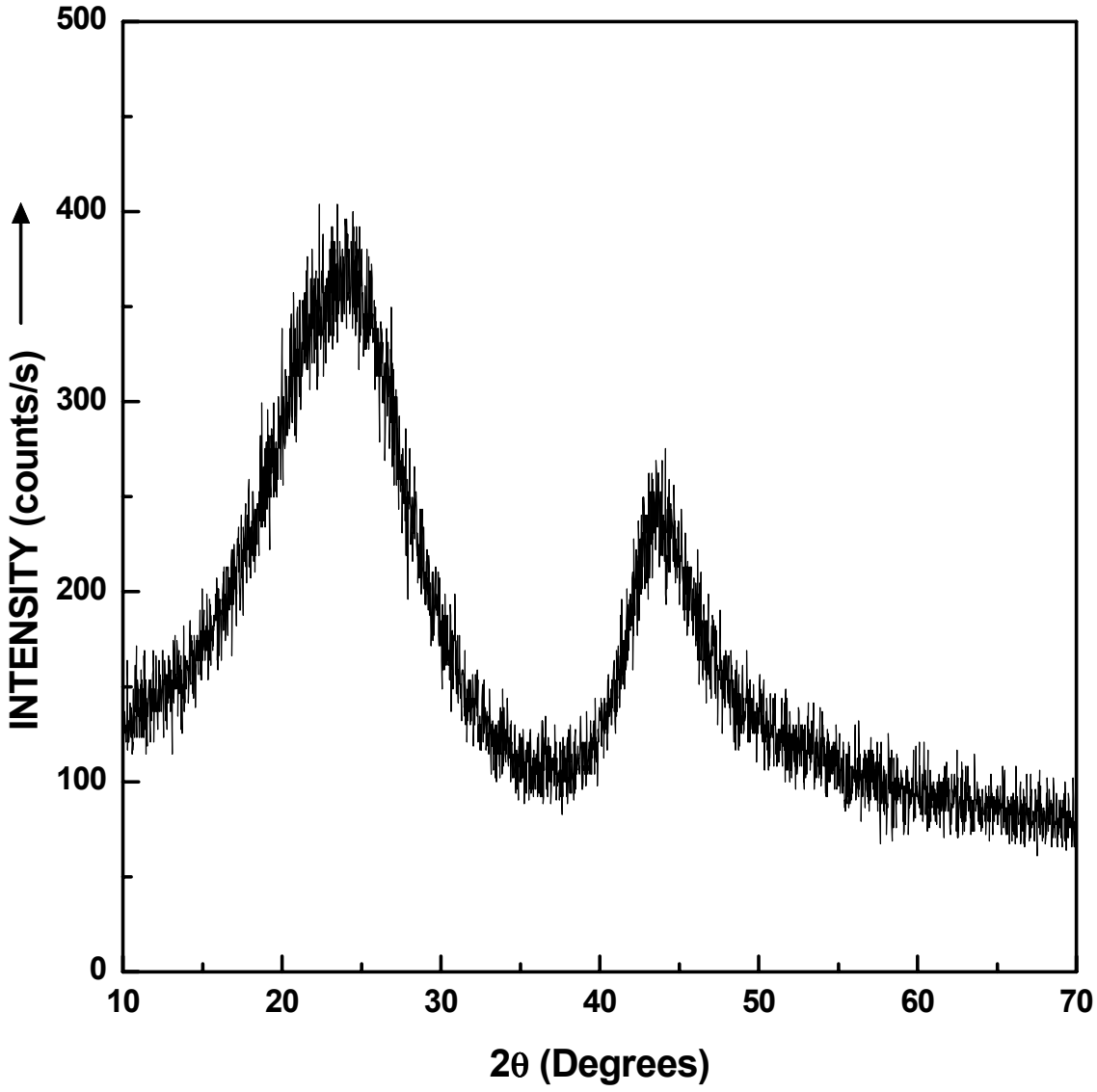

Figure 4-1-8 XRD pattern of amorphous carbon obtained from the pyrolysis of phenolic resin at 1100°C for 2 h.

Table 4-1-1 The yield (in decimal fraction) for pyrolysis heat treatment of the SC35 and SC8 dried materials.

	SC35	SC8
Yield for batch #1	0.6947	0.5914
Yield for batch #2	0.6938	0.5901
Yield for batch #3	0.7122	0.5901
Average yield	0.6947	0.5905
Standard deviation	0.0104	0.0013

4.1.3 Thermal Gravimetric Analysis of Dried SC8 Material

Figure 4-1-9 shows a thermal gravimetric analysis (TGA) plot of residual weight percentage vs. temperature for a dried SC8 powder which had been heat treated in vacuum at 100^{o}C for 2.5 h sample prior to the TGA analysis. The sample was heated in the TGA furnace at 3^{o}C/min to 900^{o}C, then at 1^{o}C/min to 1530^{o}C, and then held at 1530^{o}C for 2 h. The atmosphere was flowing argon (~50 cm^{3}/min). Figure 4-1-9 shows that most of the pyrolytic decomposition (~27 wt% loss) of the precursors was completed between ~200-700^{o}C. There was a gradual, relatively small, weight loss (~6 wt% loss) from ~700-1200^{o}C, followed by a rapid, relatively large, weight loss (~26 wt% loss) between ~1200-1400^{o}C. The latter weight loss is attributed to the carbothermal reduction reaction. The former weight loss is attributed to a combination of weight losses due to (i) the completion of pyrolytic decomposition of the precursors (at the lower temperatures in the specified range) and (ii) the onset of the carbothermal reduction reaction (at the higher temperatures in the specified range).

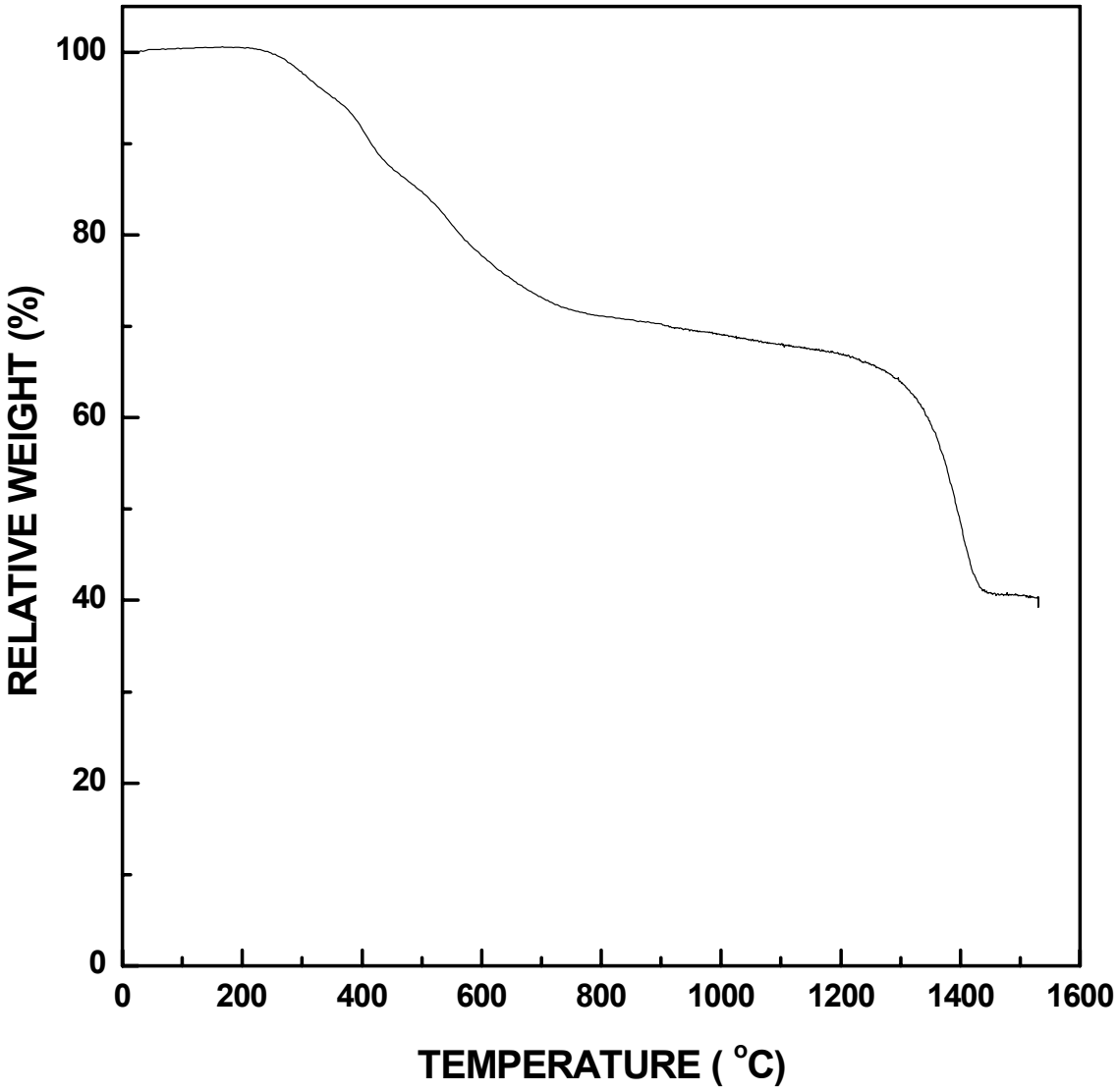

Figure 4-1-9 TGA result of SC8 dried gel. The heating schedule is 3°C/min to 900°C, 1°C/min to 1530°C, hold 2 h. The atmosphere is argon.

It should be noted that the absolute weight percentages shown in Figure 4-1-9 are apparently inaccurate. This is indicated by two observations. First, the residual weight percentage after heat treatment to 1200°C (~67 wt%) was considerably higher than the pyrolysis yields (after heat treatment at 1100°C/4 h) that were reported in Table 4-1-1 for SC8 samples (average value of 59.1 wt%). It is presumed that the TGA experiment was inaccurate because three independent pyrolysis experiments gave yields that were in very close agreement (see Table 4-1-1). Second, the overall weight percentage yield for the sample in the TGA experiment was determined independently by weighing the sample on an analytical balance before and after the heat treatment. The overall weight percentage yield was significantly lower for the measurement made on the analytical balance (i.e., 33.4 wt% vs. 39.5 wt% for the TGA measurement). This result suggests that powder was probably blown out of the TGA crucible either when the furnace was first evacuated or when it was back-filled with argon gas. This would account for both the higher yield at 1200°C in the TGA and the higher overall yield observed in the TGA at the end of the heat treatment.

4.1.4 Composition of the Pyrolyzed Materials

The carbon content (by weight) of the pyrolyzed materials, w_C^{pyro}, was determined by the LECO combustion method. The carbon content, w_C^{pyro}, is a decimal fraction. For the SC35 pyrolyzed material, w_C^{pyro} = 0.3260; for the SC8 pyrolyzed material, w_C^{pyro} = 0.4809. Assume that the pyrolyzed materials were composed of carbon and silica only ($w_C^{pyro} + w_{SiO2}^{pyro} = 1$), the silica content ($w_{SiO2}^{pyro}$) and the C/Si molar ratio in the pyrolyzed

material ($x_{C/Si}^{pyro}$) were calculated for the SC35 and SC8 pyrolyzed materials. For SC35, the silica weight content was:

$$w_{SiO2}^{pyro} = 1 - w_C^{pyro} = 1 - 0.3260 = 0.6740$$

The C/Si molar ratio was:

$$x_{C/Si}^{pyro} = \frac{w_C^{pyro}/12}{w_{SiO2}^{pyro}/60} = \frac{0.3260/12}{0.6740/60} = 2.4$$

For SC8, the silica weight content was:

$$w_{SiO2}^{pyro} = 1 - w_C^{pyro} = 1 - 0.4809 = 0.5191$$

The C/Si molar ratio was:

$$x_{C/Si}^{pyro} = \frac{w_C^{pyro}/12}{w_{SiO2}^{pyro}/60} = \frac{0.4809/12}{0.5191/60} = 4.6$$

Later in this thesis, the SC35 series will be referred to as a series with "initial C/Si molar ratio of 2.4" and the SC8 series will be referred to as a series with "initial C/Si molar ratio of 4.6."

As stated in section 3.2, heat treatments of pyrolyzed material in a tube furnace in air were also carried out to determine the carbon content. For the SC35 pyrolyzed material, oxidation in the tube furnace resulted in carbon contents of 0.3235 and 0.3211 for two independent heat treatments, both of which were very close to the result obtained from the LECO carbon content analysis.

It is noted that, for both the SC35 and SC8 pyrolyzed samples, the C/Si molar ratio calculated from the measured carbon content was much higher compared to the "Expected C/Si molar ratio before CTR" listed in Table 3-1-1. The reason for this is not completely clear. One possible explanation is that the TEOS in the sols was only partially

hydrolyzed because of the relatively low water concentration used in the synthesis. Hence, additional carbon would develop in the samples during pyrolysis because of residual ethoxide groups that were present in the dried materials. Table 3-1-1 shows that the H_2O/TEOS molar ratio for the SC8 and SC35 samples was ~2. A molar ratio of 4 would be required for complete replacement of the ethoxy groups if the only reaction that removed the ethoxy groups from the TEOS was the hydrolysis reaction shown in Equation (3-1-2). However, some ethoxide groups could also be eliminated by condensation reactions, such as the one shown in Equation (3-1-4). Nevertheless, it seems likely that reaction conditions used in this study resulted in incomplete removal of the ethoxy groups from the TEOS.

4.1.5 Surface Area and Porosity of the Pyrolyzed Materials

Gas adsorption measurements on pyrolyzed materials provided information about the surface area and porosity of the reactants before the carbothermal reduction reaction. Figures 4-1-10 and 4-1-11 show the adsorption isotherm plots of the SC35-1100(2h) pyrolyzed material and SC8-1120(1h) sample respectively. The SC8-1120(1h) sample is believed to have similar adsorption characteristics to that of the SC8-1100(4h) pyrolyzed material because the heat treatment temperature was very low and the holding time was short. The isotherm for the SC35 pyrolyzed material looks like a combination of Type II and Type III isotherms, while the isotherm for the SC8-1120(1h) sample looks like a combination of Type I and Type III isotherms. For both samples, the isotherms indicate that there is very limited porosity because the total amount of gas adsorbed is extremely low. The isotherm for the SC42 material pyrolyzed at 600^{o}C for 2 h is shown in Figure

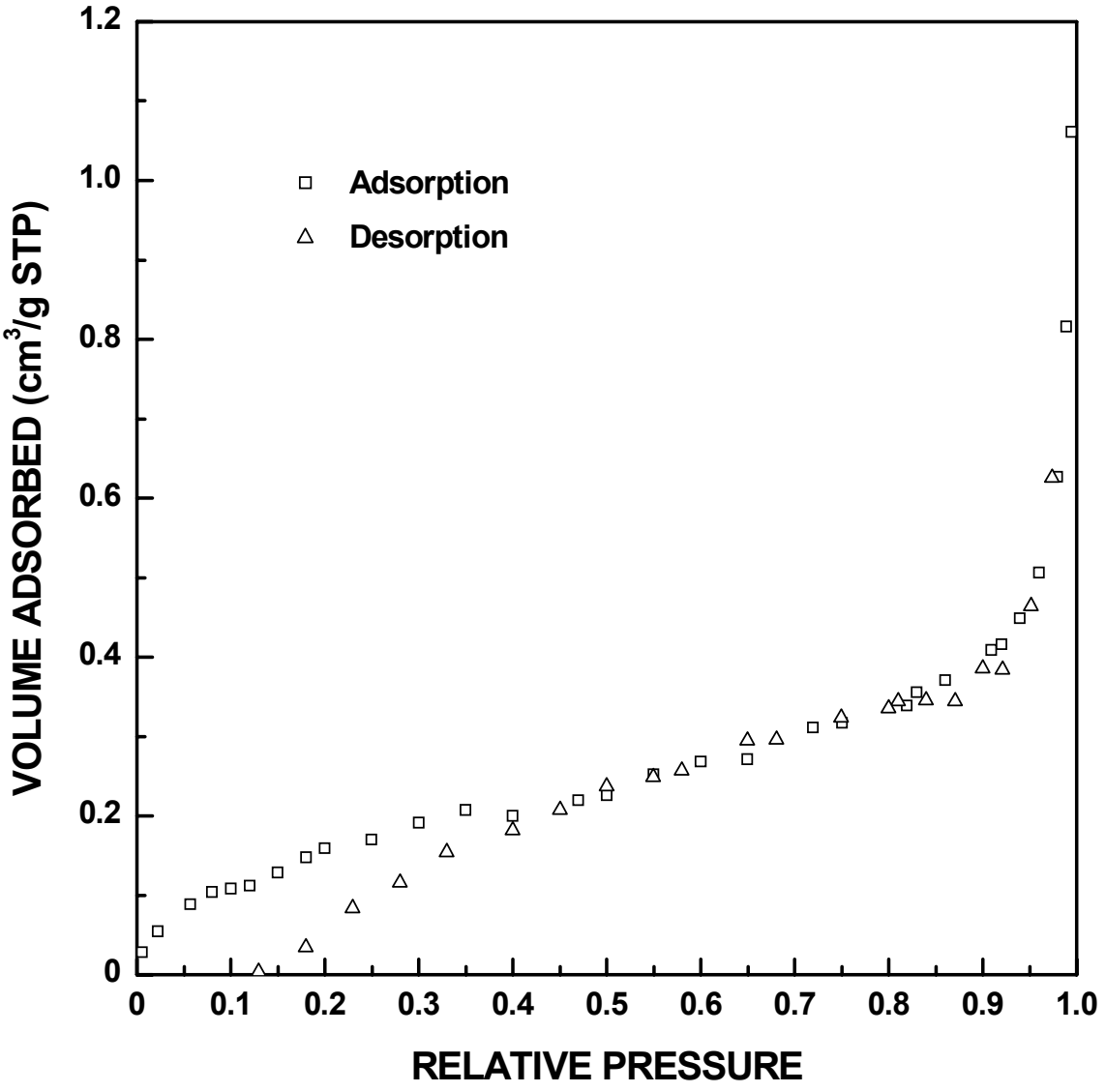

Figure 4-1-10 Adsorption/desorption isotherm plots for the SC35-1100(2h) pyrolyzed material.

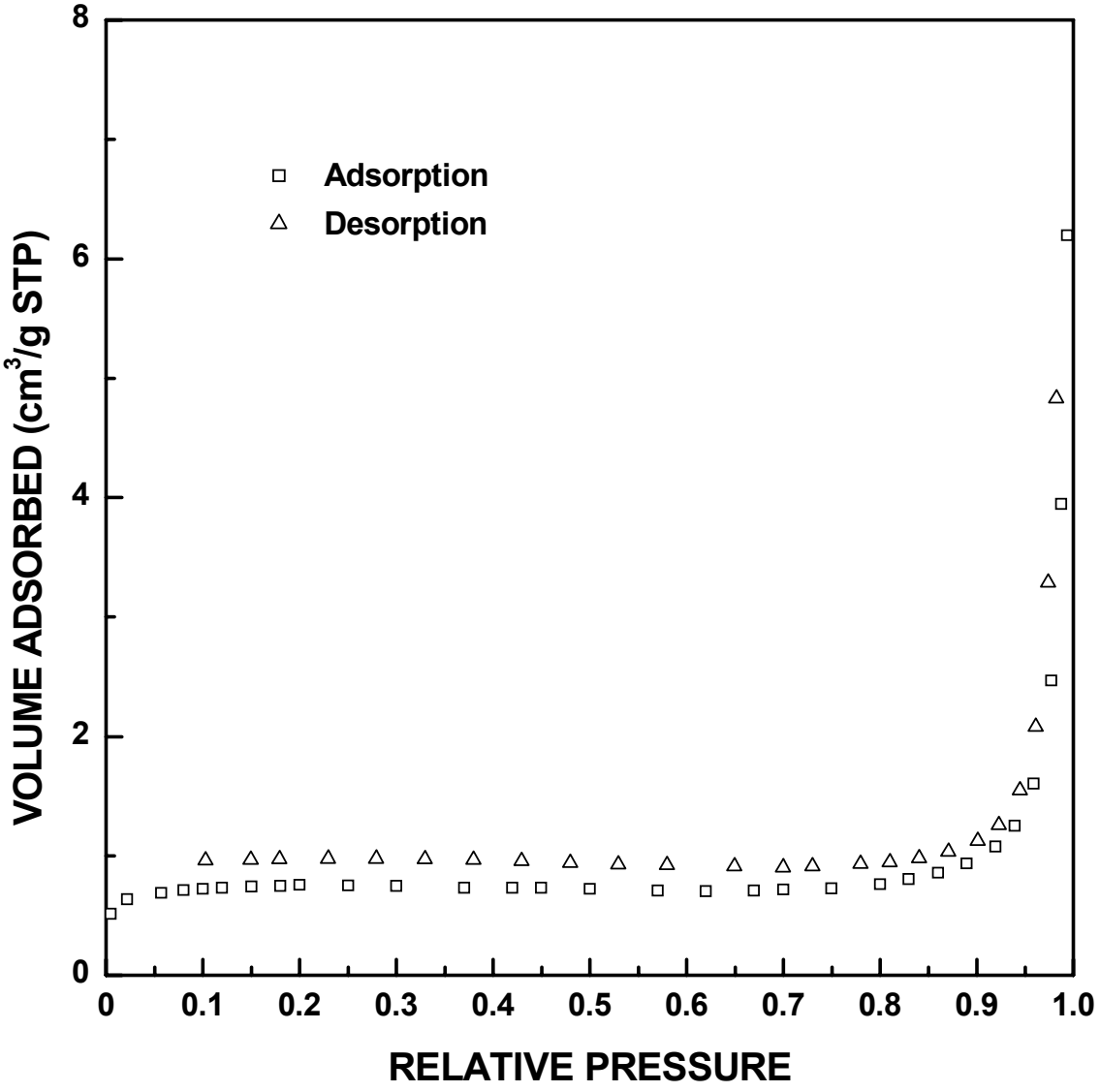

Figure 4-1-11 Adsorption/desorption isotherm plots for the SC8-1120(1h) sample.

4-1-12. (The SC42 series has a very similar composition to the SC35 series.) The isotherm is Type I (Singh, 1989). There is a significant amount of micropores as indicated by the much larger amount of adsorbed gas volume in comparison to the 1100°C/1120°C-pyrolyzed materials.

The differences in gas adsorption behavior for the samples heat treated at different temperatures (i.e., 1100 and 600°C) can be seen more clearly from the specific surface area and total pore volume data, as listed in Table 4-1-2. For 1100°C/1120°C-pyrolyzed materials, both the specific surface area and the total pore volume are very small. The carbon-rich SC8 sample (1120°C) has slightly higher surface area and pore volume as compared with the silica-rich SC35 sample (1100°C). For the 600°C-pyrolyzed sample (i.e. SC42-600(2h)), the specific surface area is 357 m^2/g. This difference is because the emission of the gaseous product at ~600°C generated numerous micropores and resulted in a large product surface area after the pyrolysis. (No yield information for the SC42-600(2h) sample was available. However, based on the TGA result in Figure 4-1-9 for the SC8 dried sample, it is expected that most of the pyrolytic decomposition was completed in the SC42-600(2h) sample.) When the pyrolysis temperature was increased to 1100-1120°C, micropores were still presumably generated during the heat treatment. However,

Table 4-1-2 Specific surface area and total pore volume for the SC35-1100(2h), SC8-1100(4h), SC8-1120(1h) and SC42-600(2h) heat-treated materials.

	SC35-1100(2h)	SC8 - 1100(4h)	SC8 - 1120(1h)	SC42-600(2h)
Average specific surface area (m^2/g)	0.7	3.1	3.4	357.1
Total pore volume (cm^3/g)	0.0016	NA	0.0096	0.1349

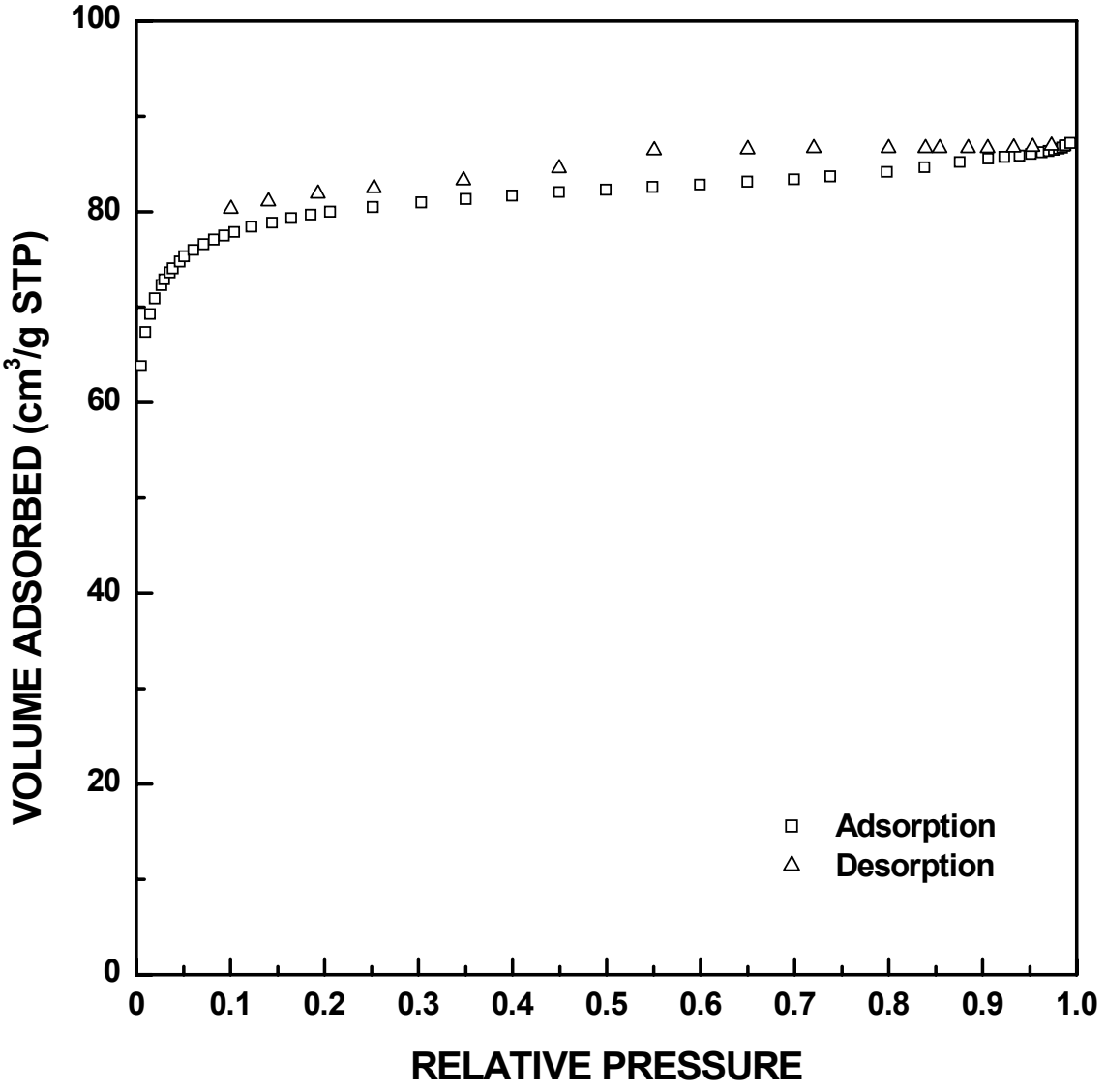

Figure 4-1-12 Adsorption/desorption isotherm plots for the SC42 material pyrolyzed at 600°C for 2 h.

it is hypothesized that some sintering, via viscous flow of silica in the carbon/silica mixture, occurred at the higher temperature and that this caused the micropores to close or to be eliminated. Therefore, the surface area and specific pore volume for the 1100/1120^{o}C-pyrolyzed samples are very small. The SC8 pyrolyzed sample may have higher specific surface area because the higher carbon content (and lower silica content) would inhibit the viscous sintering of silica and the sample would retain some of the pores formed during pyrolysis. Additional evidence to support the hypothesis that some sintering occurs during 1100^{o}C pyrolysis due to viscous flow of silica is presented in section 4.4.6.

Figures 4-1-13 to 4-1-15 show the cumulative pore size distributions for the SC35-1100(2h), SC8-1120(1h) and SC42-600(2h) pyrolyzed samples. Corresponding plots of the relative cumulative pore volume distributions, pore volume frequency distributions, and relative pore volume frequency distributions are shown in Figures 4-1-16 - 4-1-18, Figures 4-1-19 - 4-1-21, and Figures 4-1-22 - 4-1-24, respectively. It should be noted that pore size distribution data for the first two samples may not be reliable because the isotherms are not Type IV (Sing, 1989, p.9). In addition, the specific pore volumes are extremely low. Detailed discussion of the gas adsorption isotherms and the pore size distribution data will be given later in section 4.4.7.

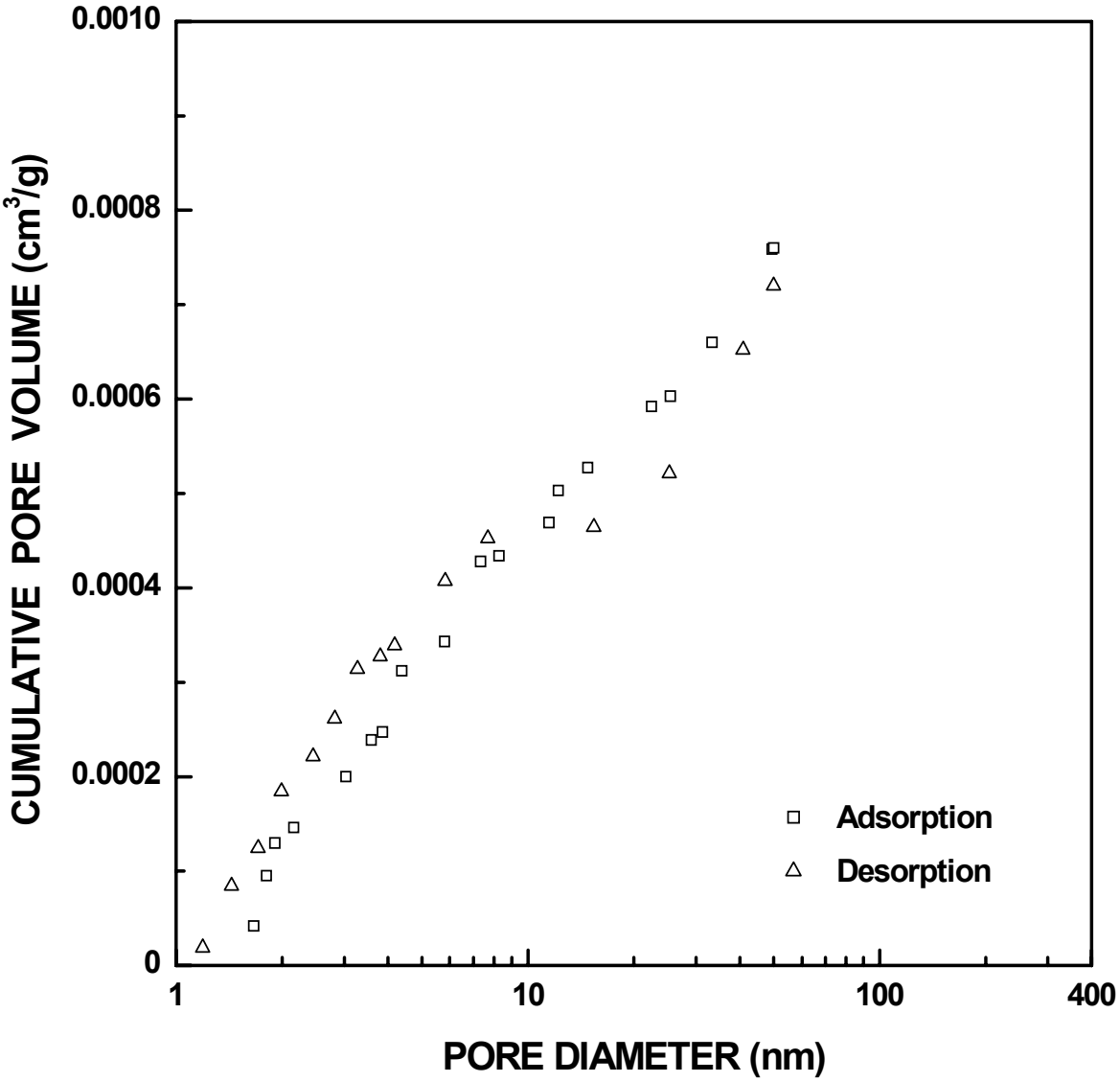

Figure 4-1-13 Plots of cumulative specific pore volume vs. pore diameter for the SC35-1100(2h) pyrolyzed material. The pore diameter was cut off at 50 nm.

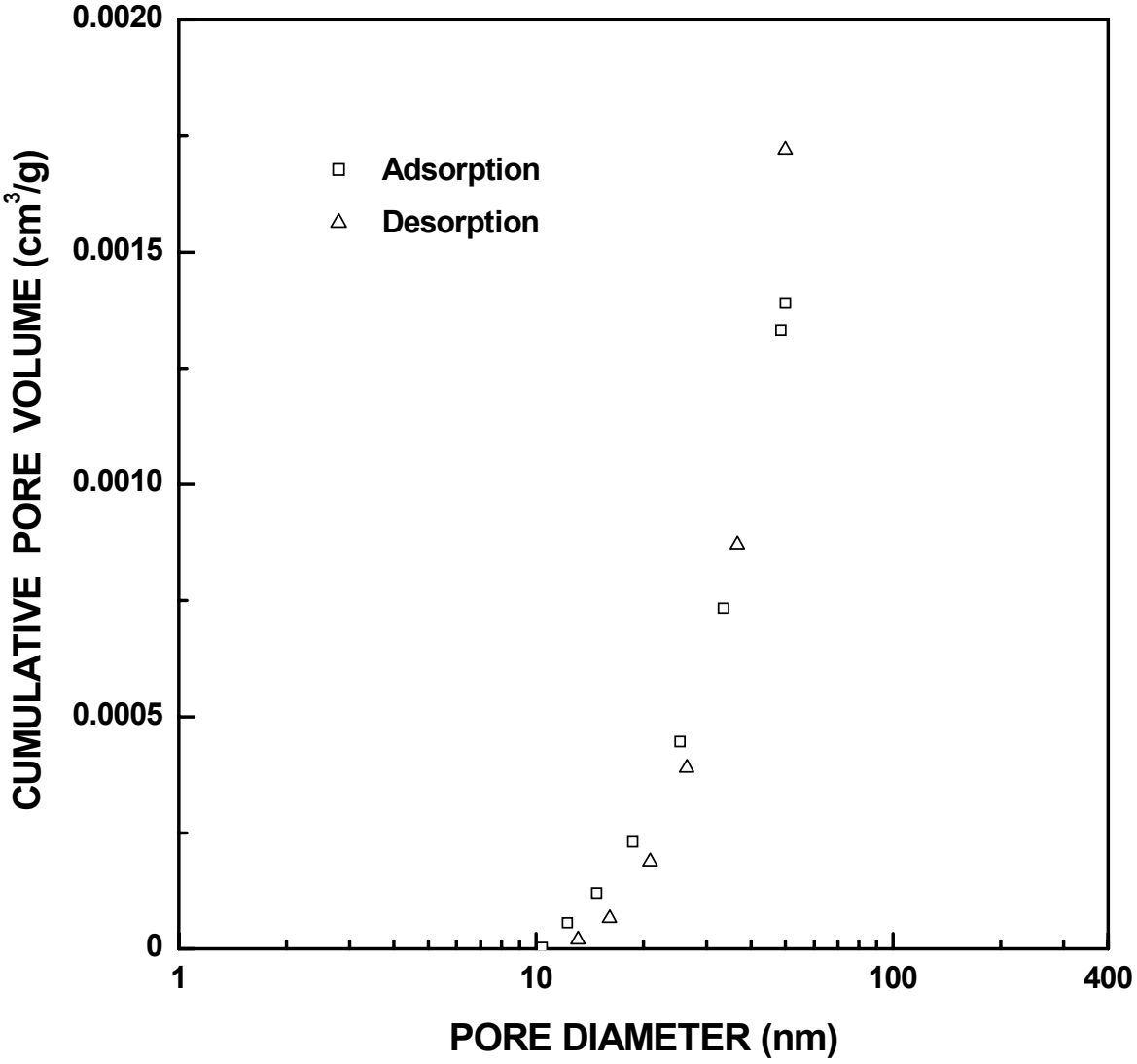

Figure 4-1-14 Plots of cumulative specific pore volume vs. pore diameter for the SC8-1120(1h) sample. The pore diameter was cut off at 50 nm.

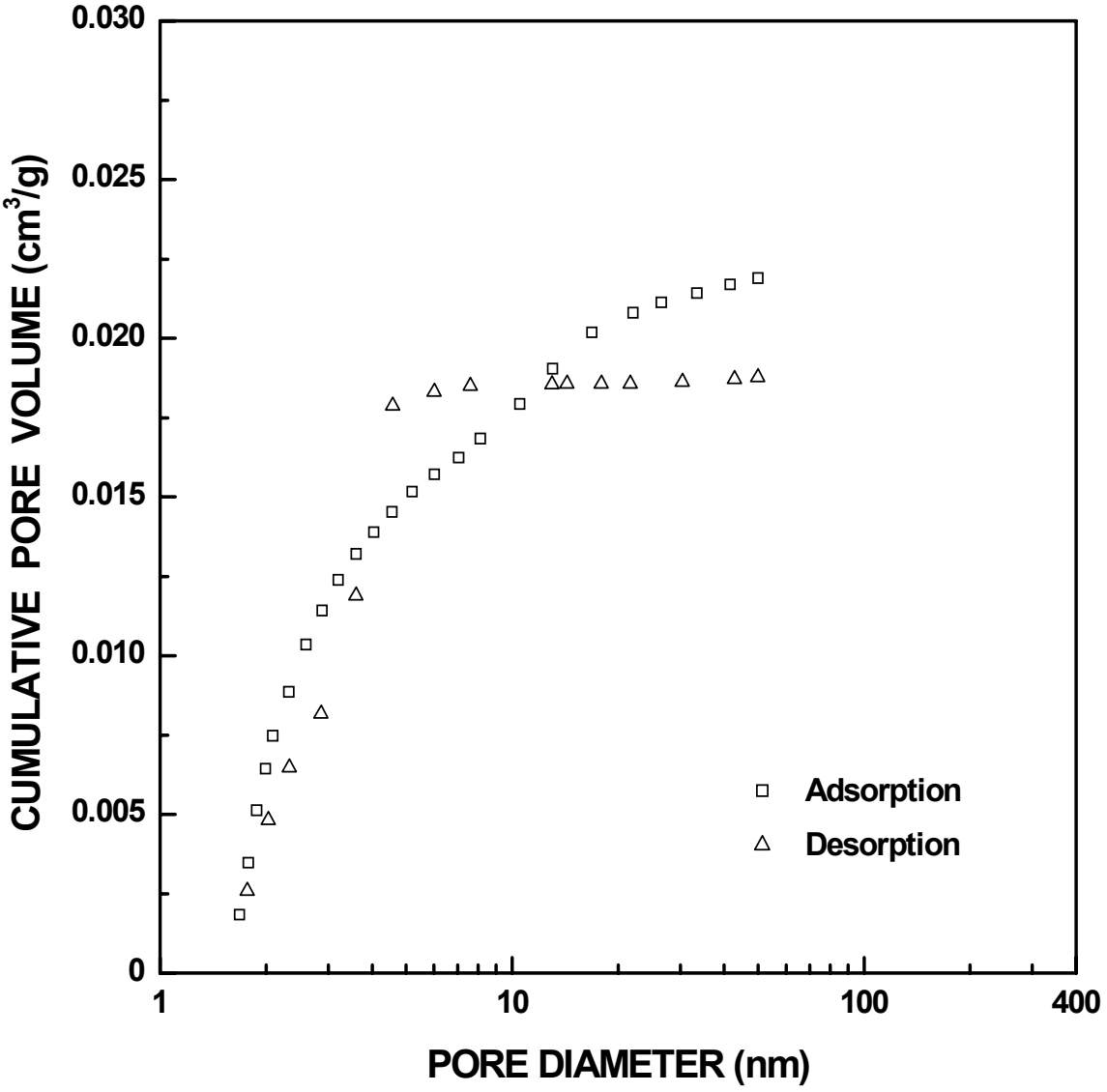

Figure 4-1-15 Plots of cumulative specific pore volume vs. pore diameter for the SC42-600(2h) pyrolyzed material. The pore diameter was cut off at 50 nm.

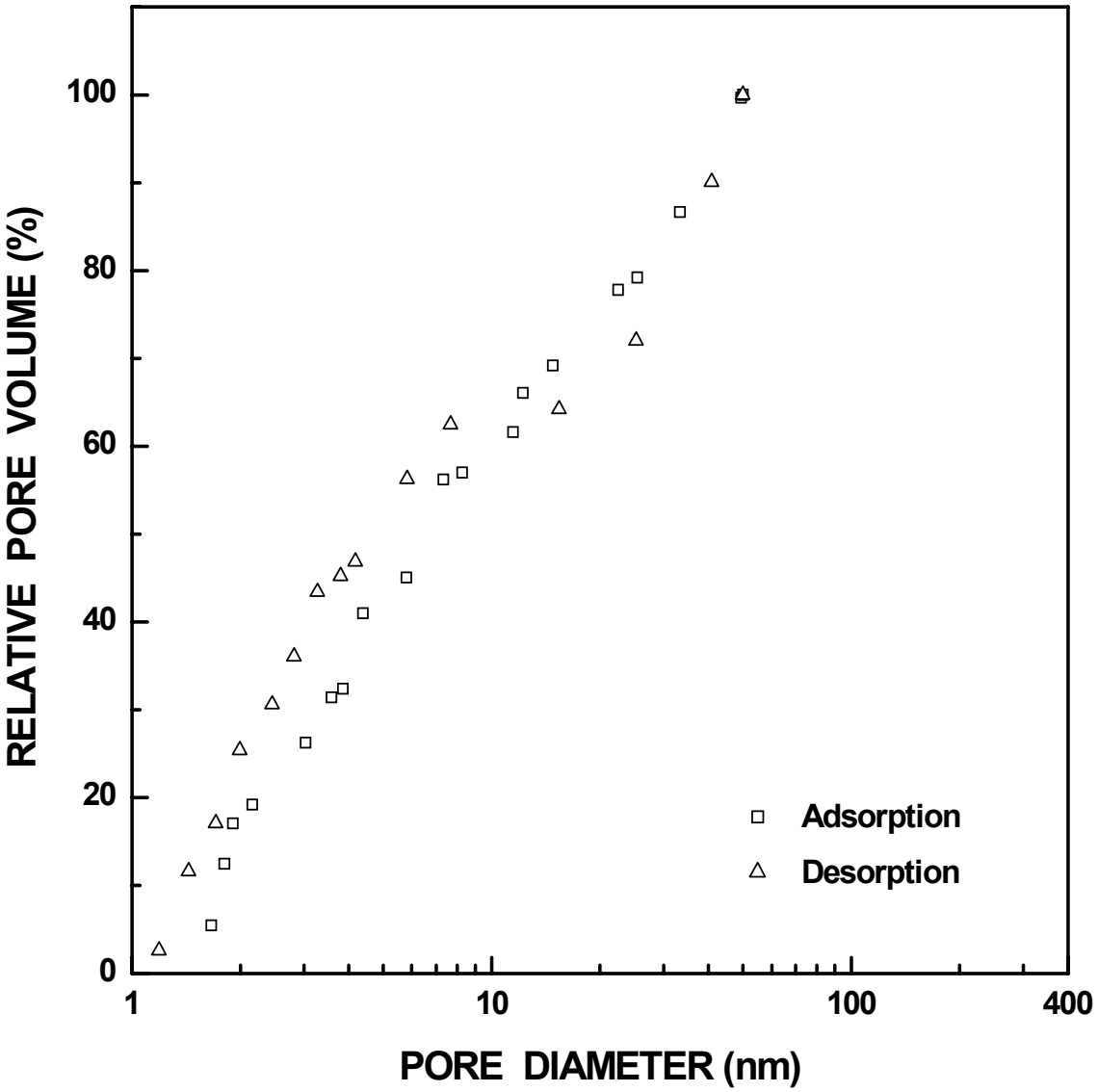

Figure 4-1-16 Plots of relative ("normalized") pore volume vs. pore diameter for the SC35-1100(2h) sample. The pore diameter was cut off at 50 nm.

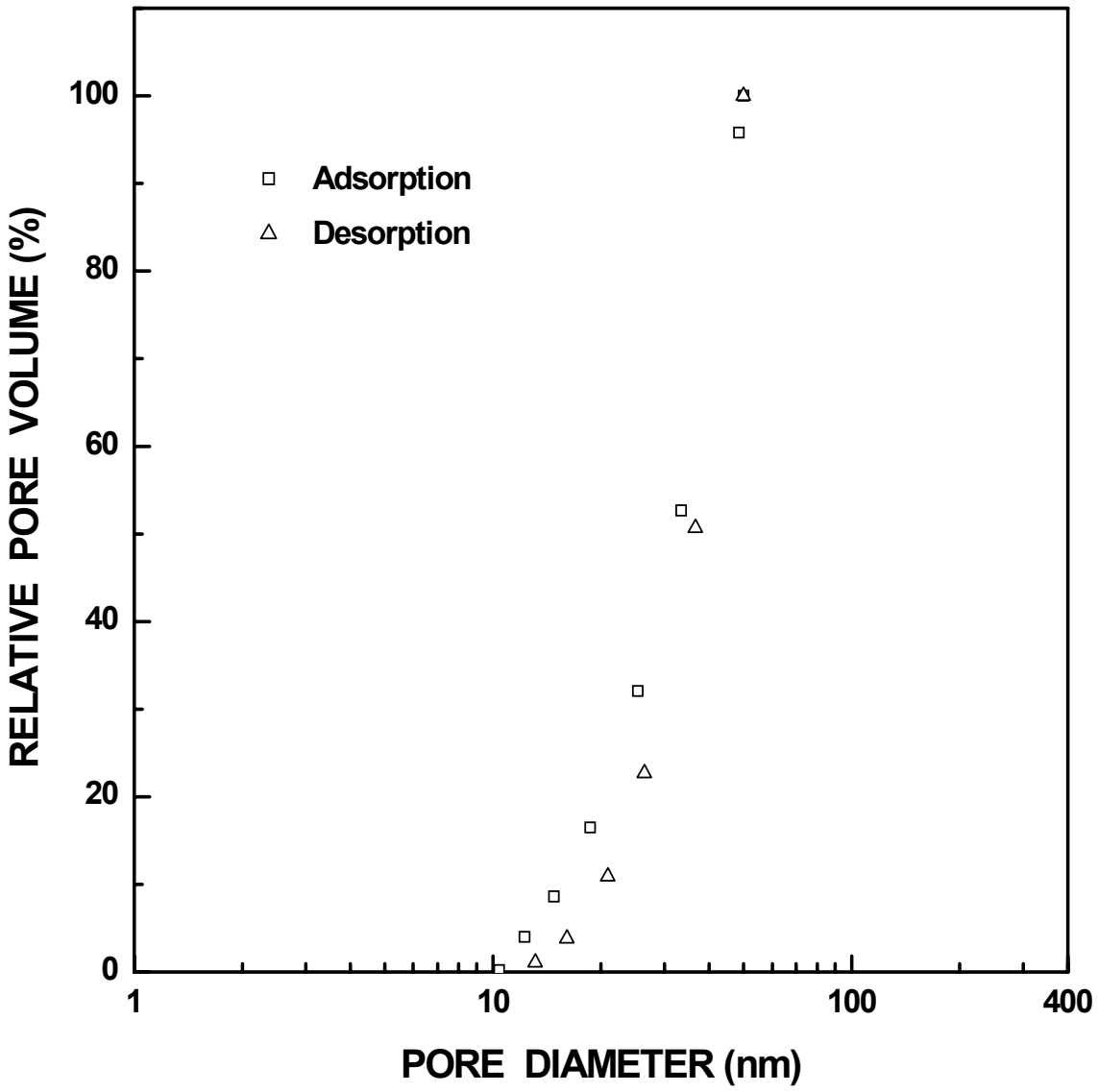

Figure 4-1-17 Plots of relative ("normalized") pore volume vs. pore diameter for the SC8-1120(1h) sample. The pore diameter was cut off at 50 nm.

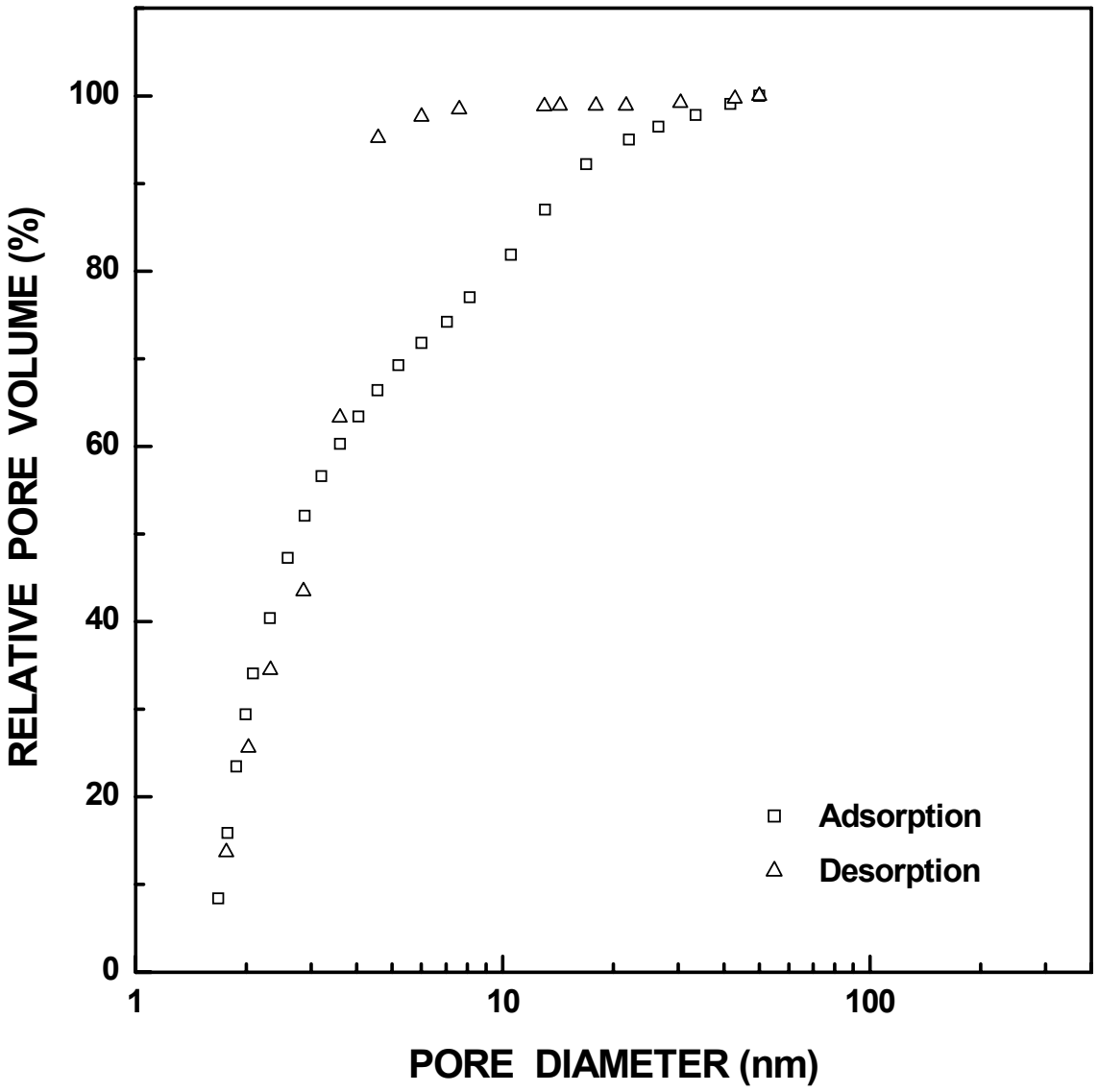

Figure 4-1-18 Plots of relative ("normalized") pore volume vs. pore diameter for the SC42-600(2h) sample. The pore diameter was cut off at 50 nm.

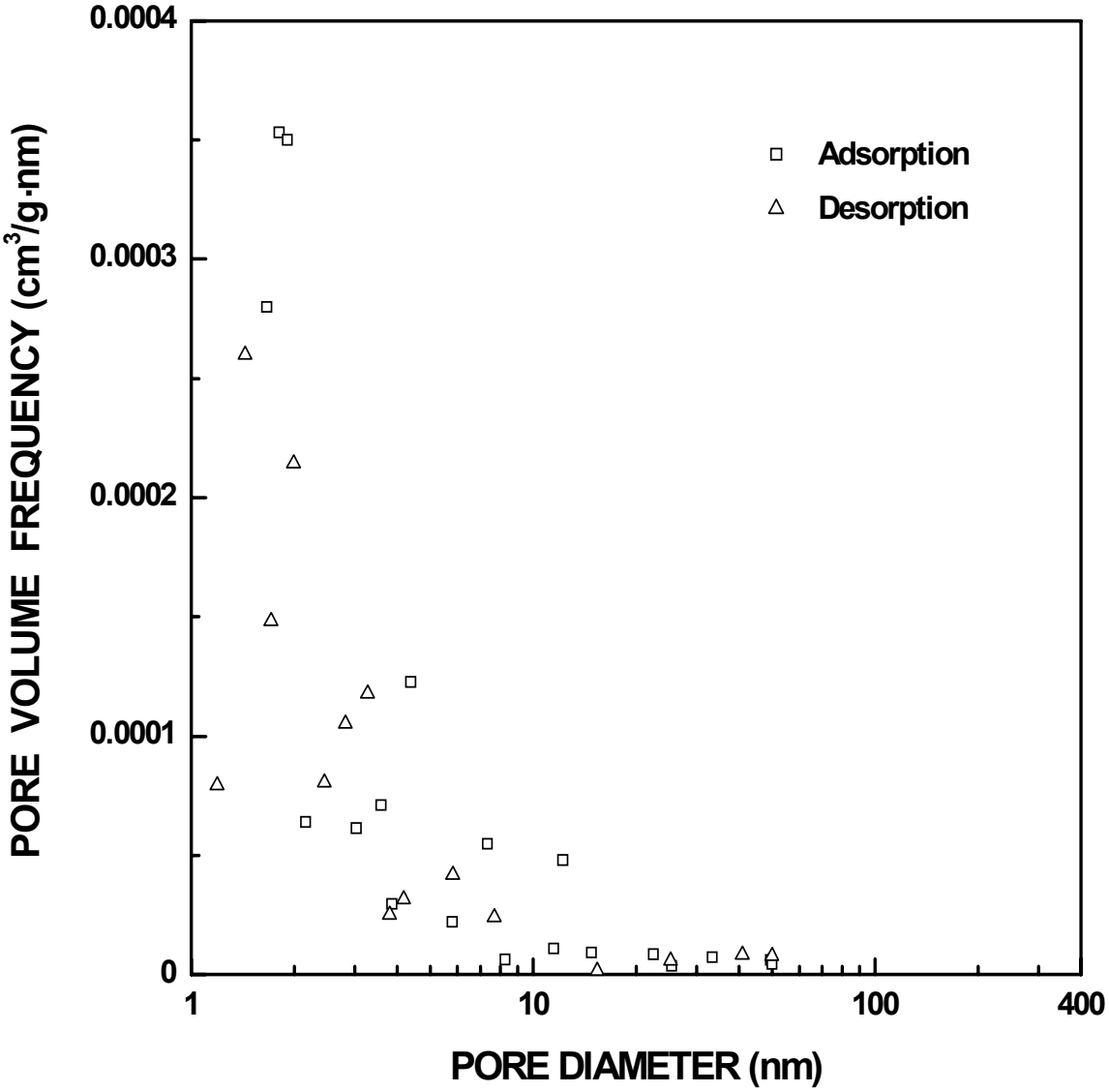

Figure 4-1-19 Plots of specific pore volume frequency vs. pore diameter for the SC35-1100(2h) sample. The pore diameter was cut off at 50 nm.

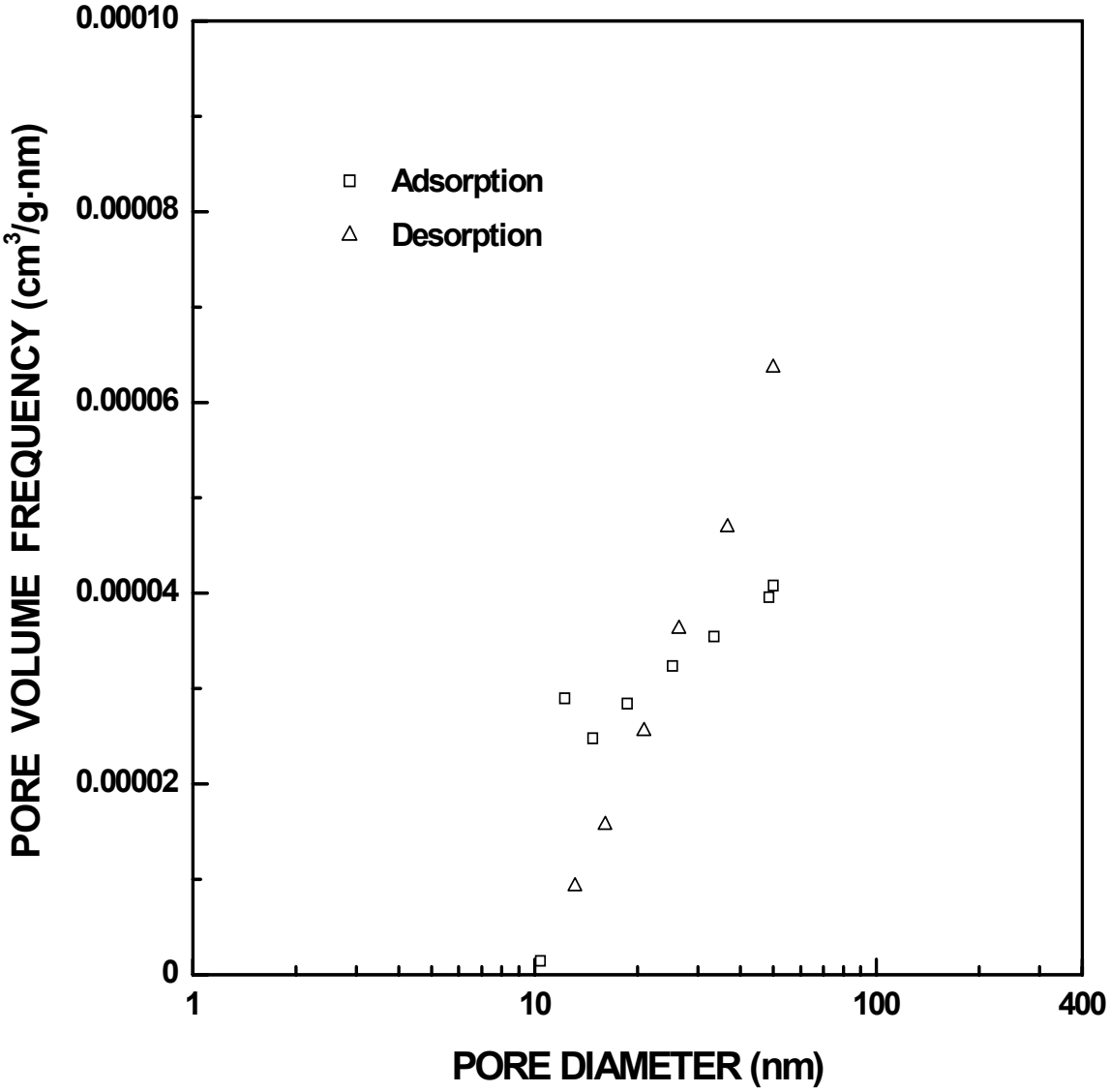

Figure 4-1-20 Plots of specific pore volume frequency vs. pore diameter for the SC8-1120(1h) sample. The pore diameter was cut off at 50 nm.

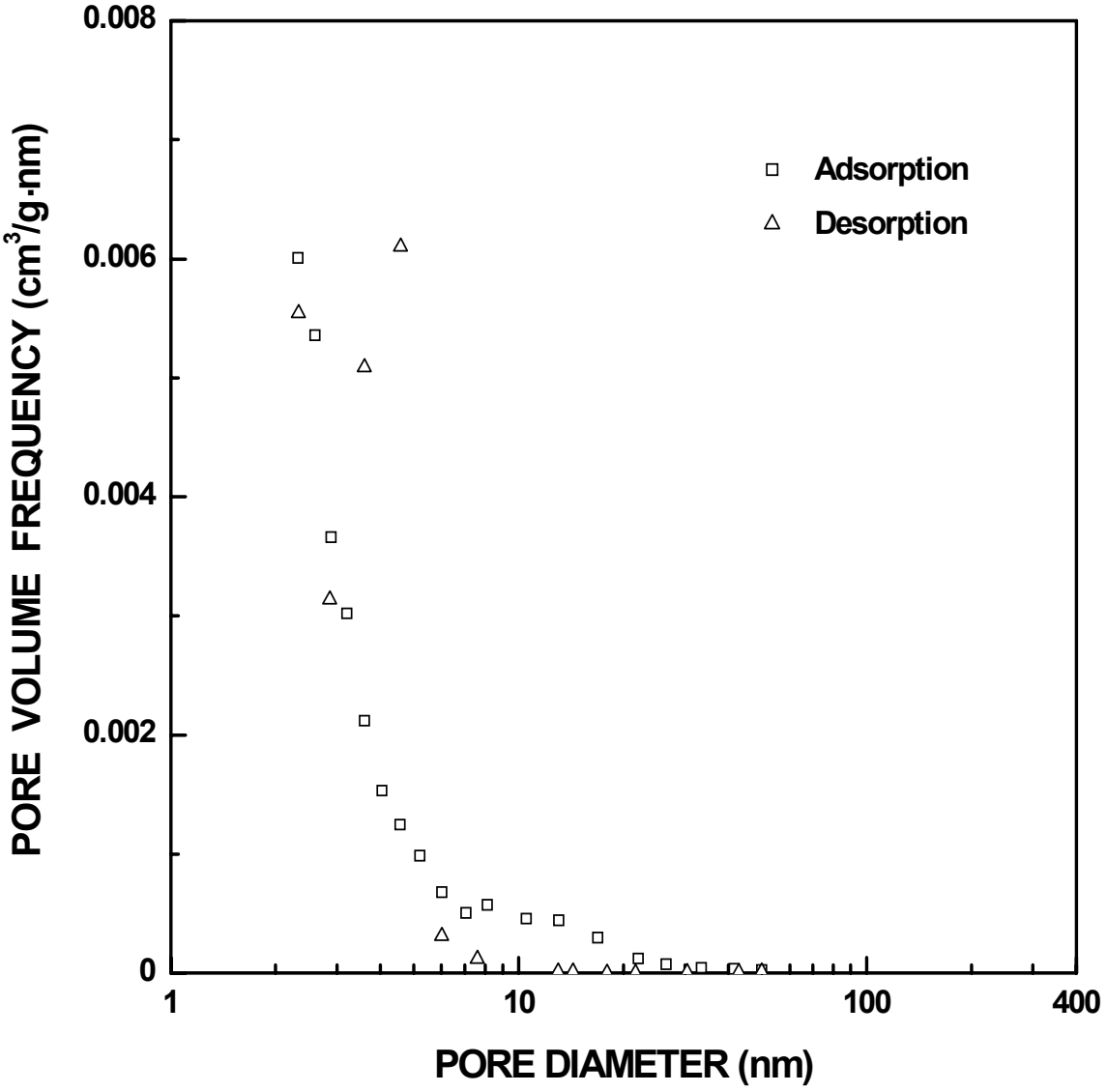

Figure 4-1-21 Plots of specific pore volume frequency vs. pore diameter for the SC42-600(2h) sample. The pore diameter was cut off at 50 nm.

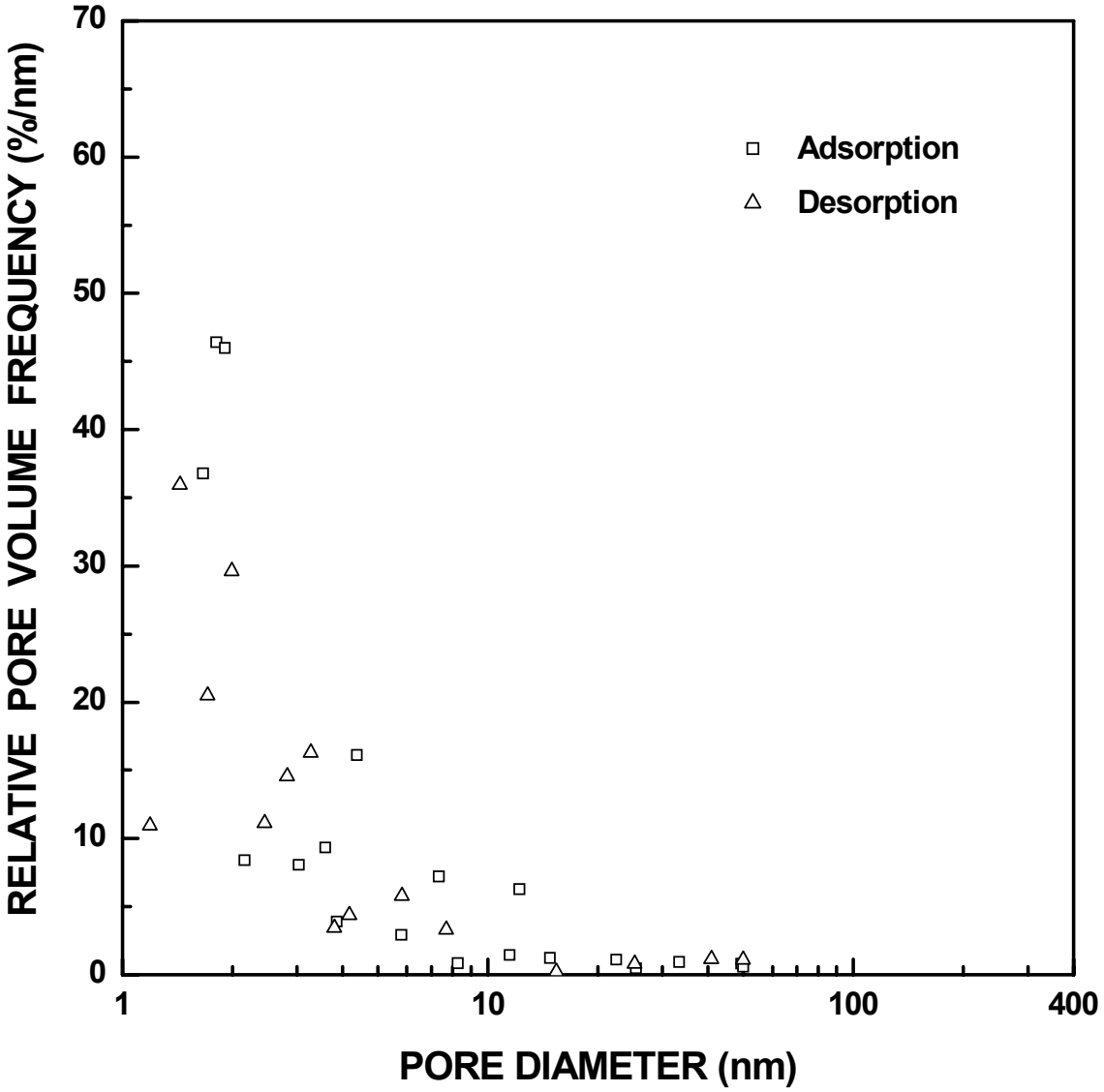

Figure 4-1-22 Plots of relative ("normalized") pore volume frequency vs. pore diameter for the SC35-1100(2h) sample. The pore diameter was cut off at 50 nm.

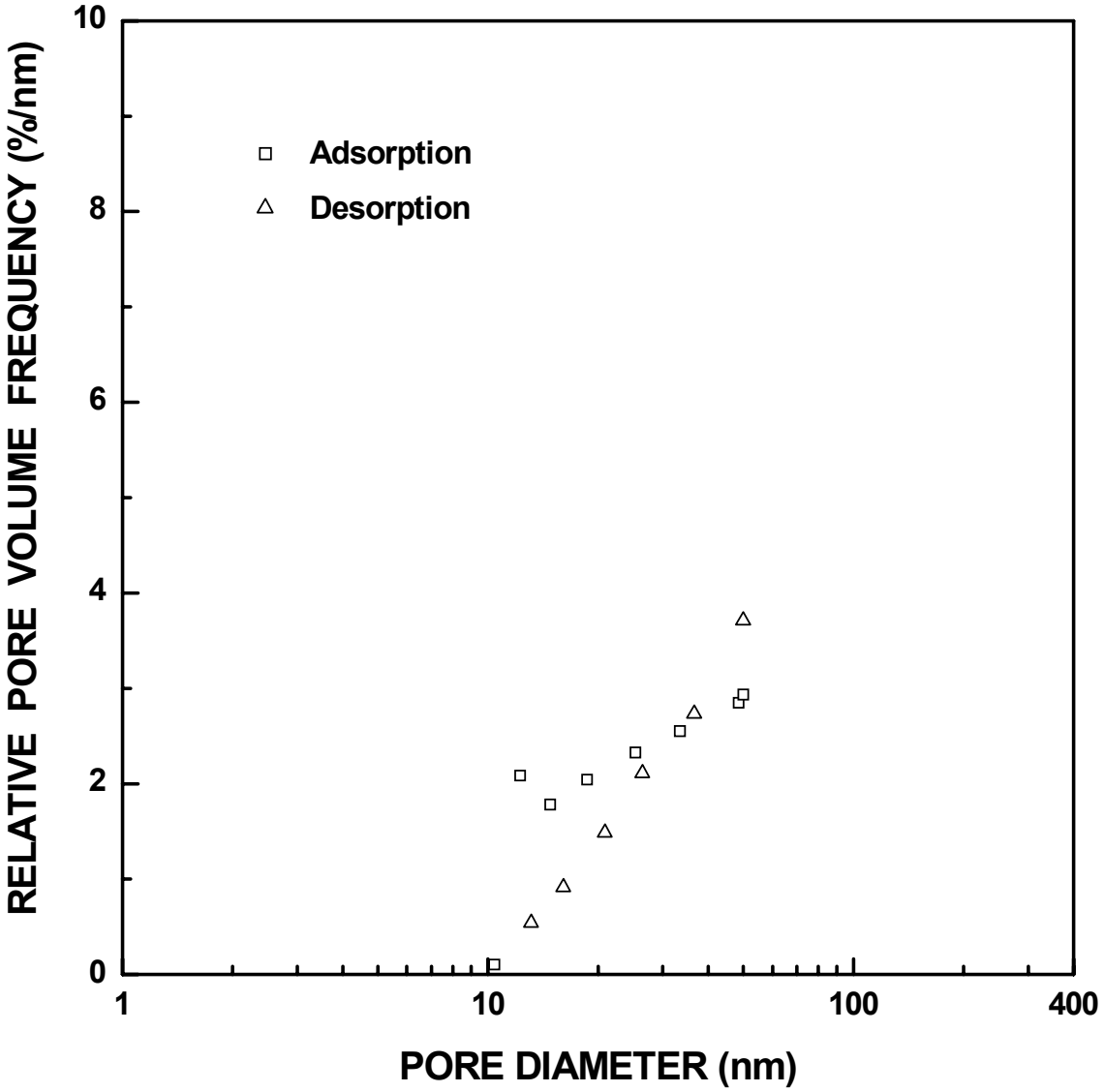

Figure 4-1-23 Plots of relative ("normalized") pore volume frequency vs. pore diameter for the SC8-1120(1h) sample. The pore diameter was cut off at 50 nm.

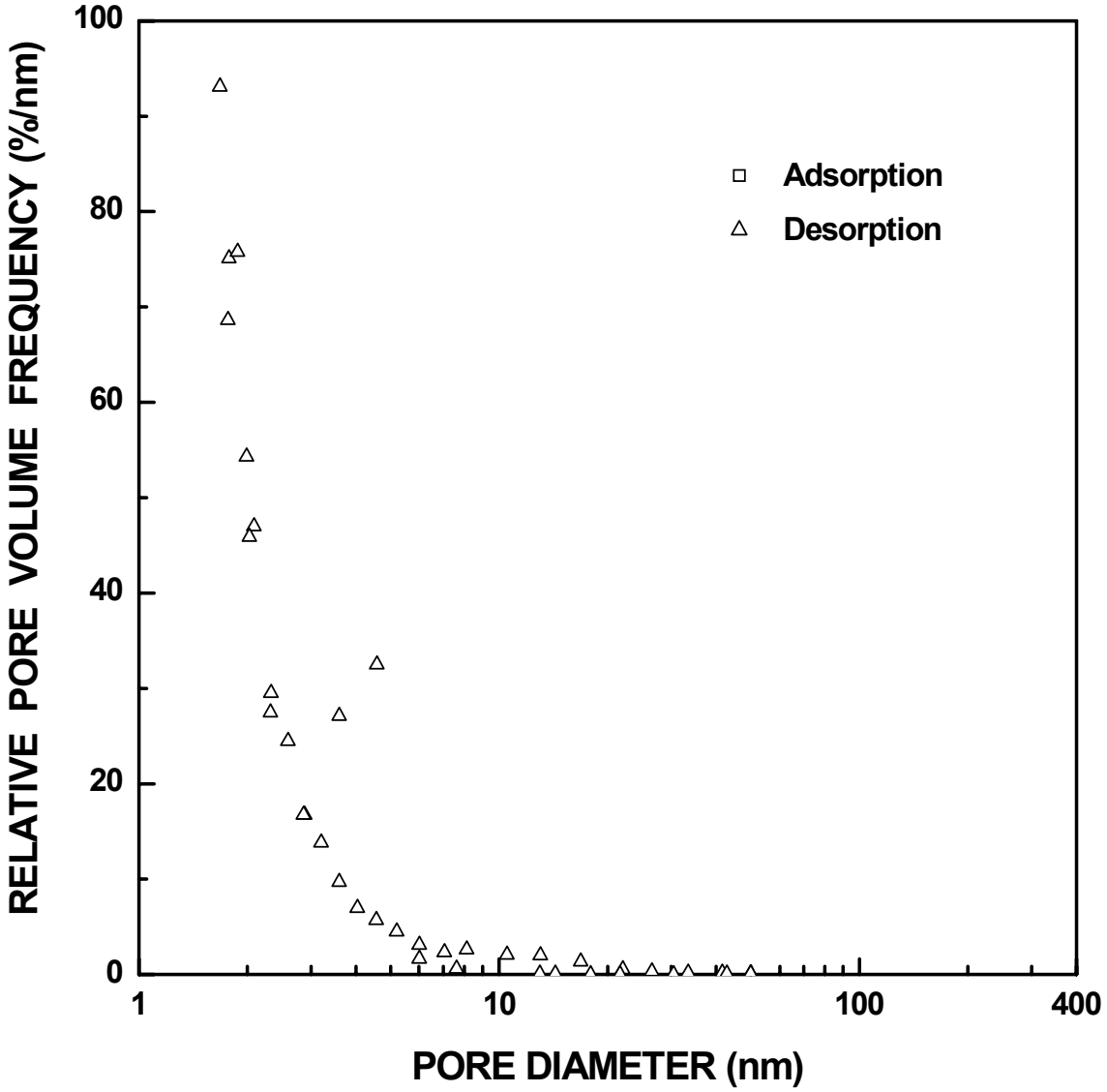

Figure 4-1-24 Plots of relative ("normalized") pore volume frequency vs. pore diameter for the SC8-600(2h) sample. The pore diameter was cut off at 50 nm.

4.1.6 Particle Size Distribution of the Pyrolyzed Materials

The particle size distribution results for the SC35, SC42 and SC8 pyrolyzed materials are shown in Figures 4-1-25 - 4-1-29. Samples for particle size measurement were prepared using either the sonication or tumbling methods described in section 3.5.3. The shape of the distribution was similar for all the samples. There is single mode centered at particle diameters in the range of ~73-96 μm.

The particle size distributions shown in Figures 4-1-25 - 4-1-29 were obtained using the Fraunhofer light scattering model because of the relatively large size of the particles. In order to determine if this approach was reasonable, the distributions were compared with those determined by using the Mie light scattering model under two extreme conditions. In one case, optical property values (i.e., the real components of the refractive index and the extinction coefficients at wavelengths of 450, 600, 750, and 900 nm) for silica were used in the calculations of the particle size distributions (Philipp, 1985). (The optical property values used for silica are listed in Table 4-1-3.) In the other case, the optical property values for graphite were used (Borghesi and Guizzetti, 1991). (The property values are also listed in Table 4-1-3.) The d_{10}, d_{50}, and d_{90} diameters for each calculation condition are shown in Table 4-1-4. Overall, the differences in the calculated diameters are small, especially for the d_{50} and d_{90} values. (As expected, the differences become more significant as the particle size decreases.) Hence, the use of the Fraunhofer model is justified.

Table 4-1-5 presents some other statistical data of the particle size distributions (based on the Fraunhofer model) for the SC35, SC42 and SC8 pyrolyzed materials. The characteristic sizes (i.e., mean, mode, median (d_{50}), d_{10}, and d_{90}) for the SC35 pyrolyzed

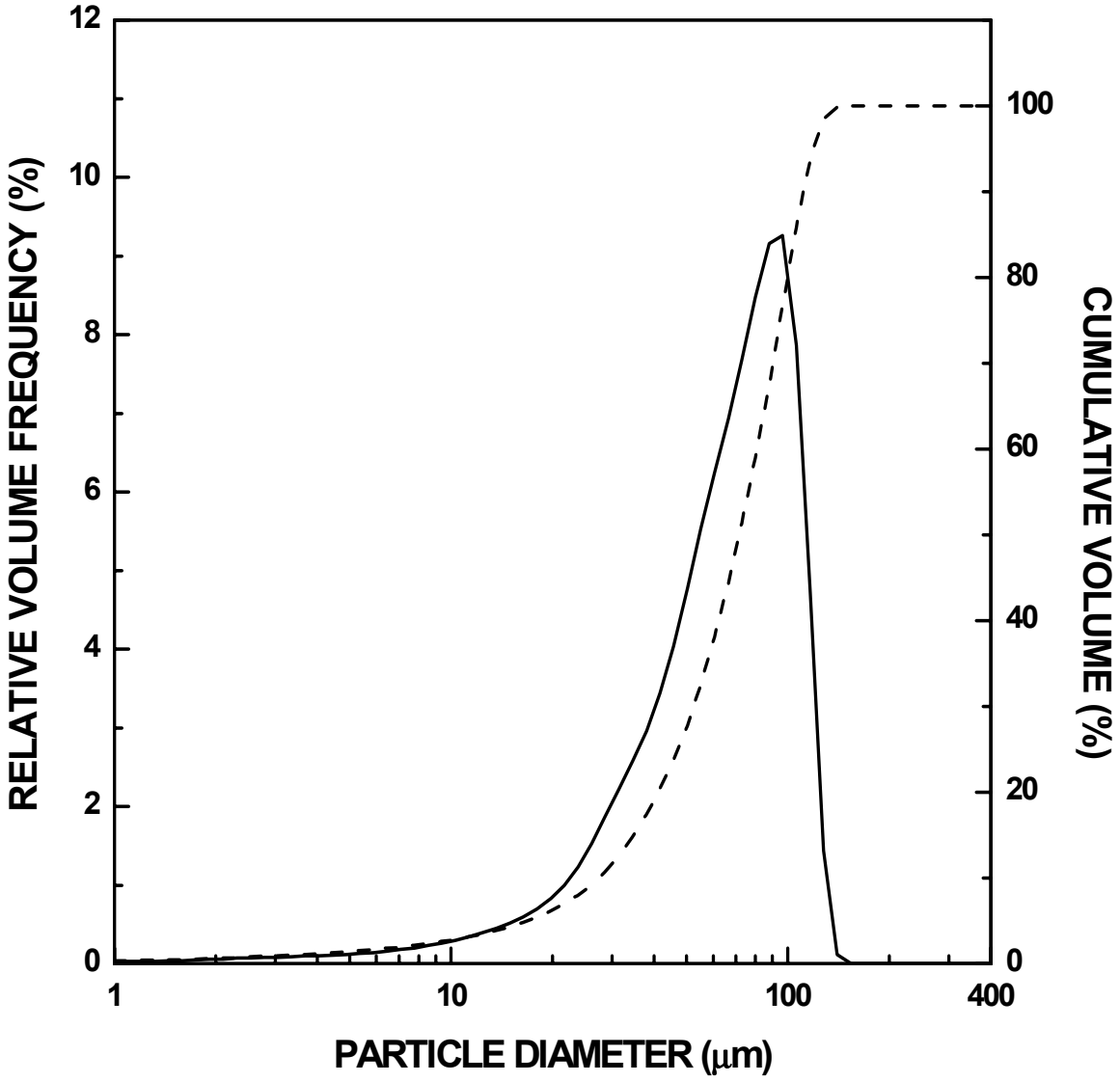

Figure 4-1-25 Particle size distribution plot for the SC35 pyrolyzed sample (initial C/Si molar ratio = 2.4). The sample was prepared with sonication. The solid line is for the differential distribution and the dashed line is for the cumulative distribution.

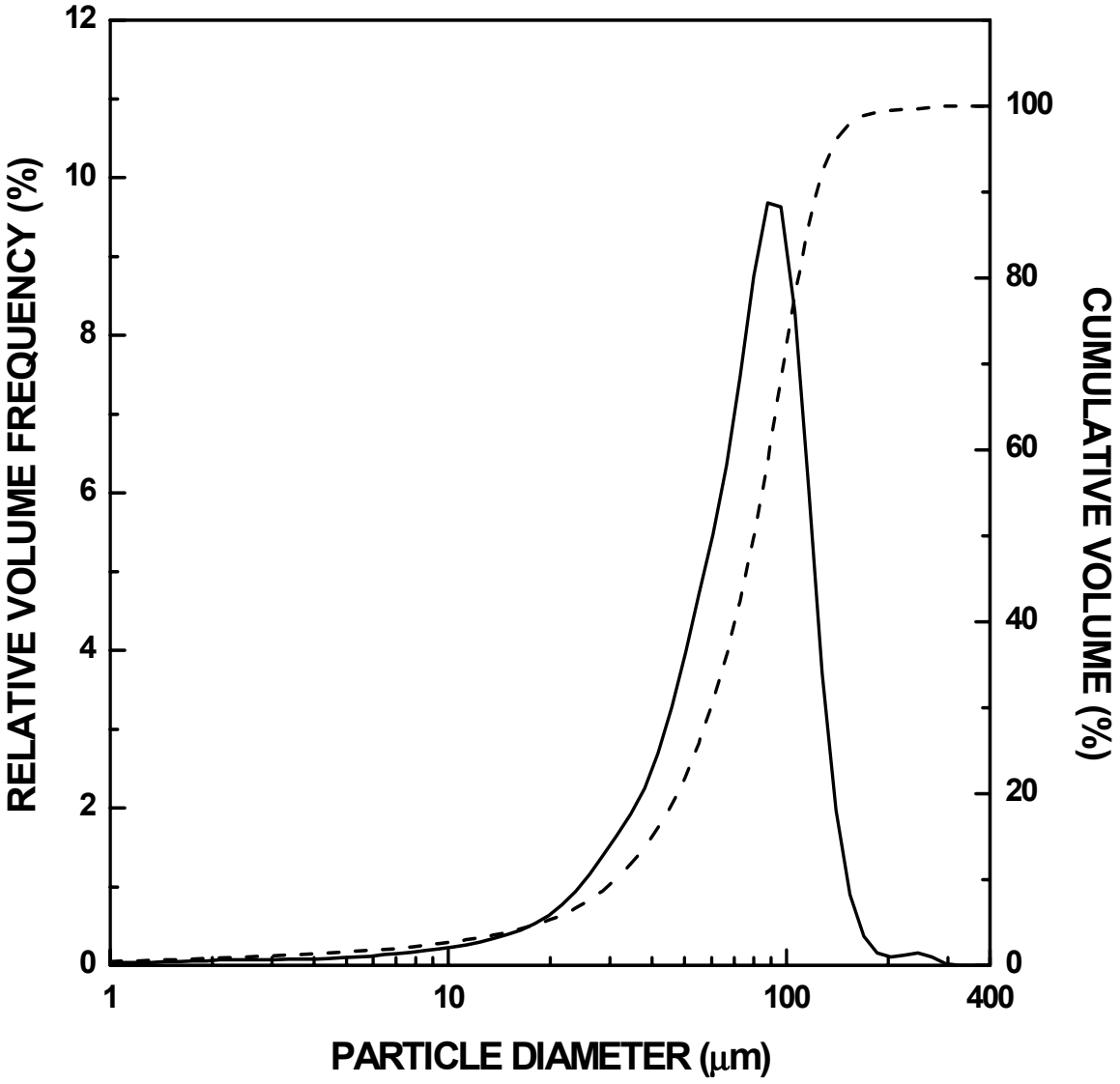

Figure 4-1-26 Particle size distribution plot for the SC42 pyrolyzed sample (initial C/Si molar ratio = 2.4). The sample was prepared with sonication. The solid line is for the differential distribution and the dashed line is for the cumulative distribution.

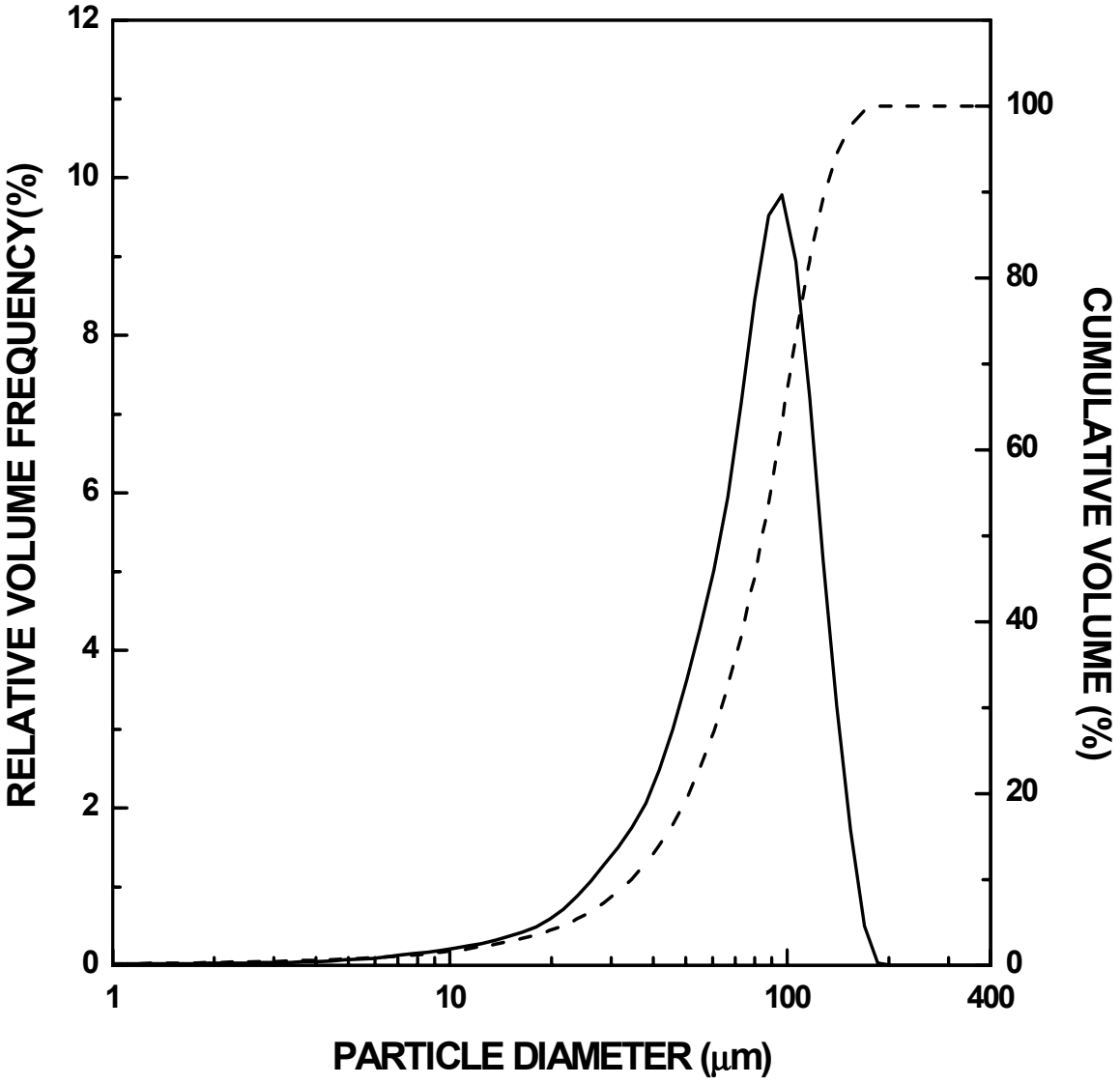

Figure 4-1-27 Particle size distribution plot for the SC42 pyrolyzed sample (initial C/Si molar ratio = 2.4). The sample was prepared with tumbling. The solid line is for the differential distribution and the dashed line is for the cumulative distribution.

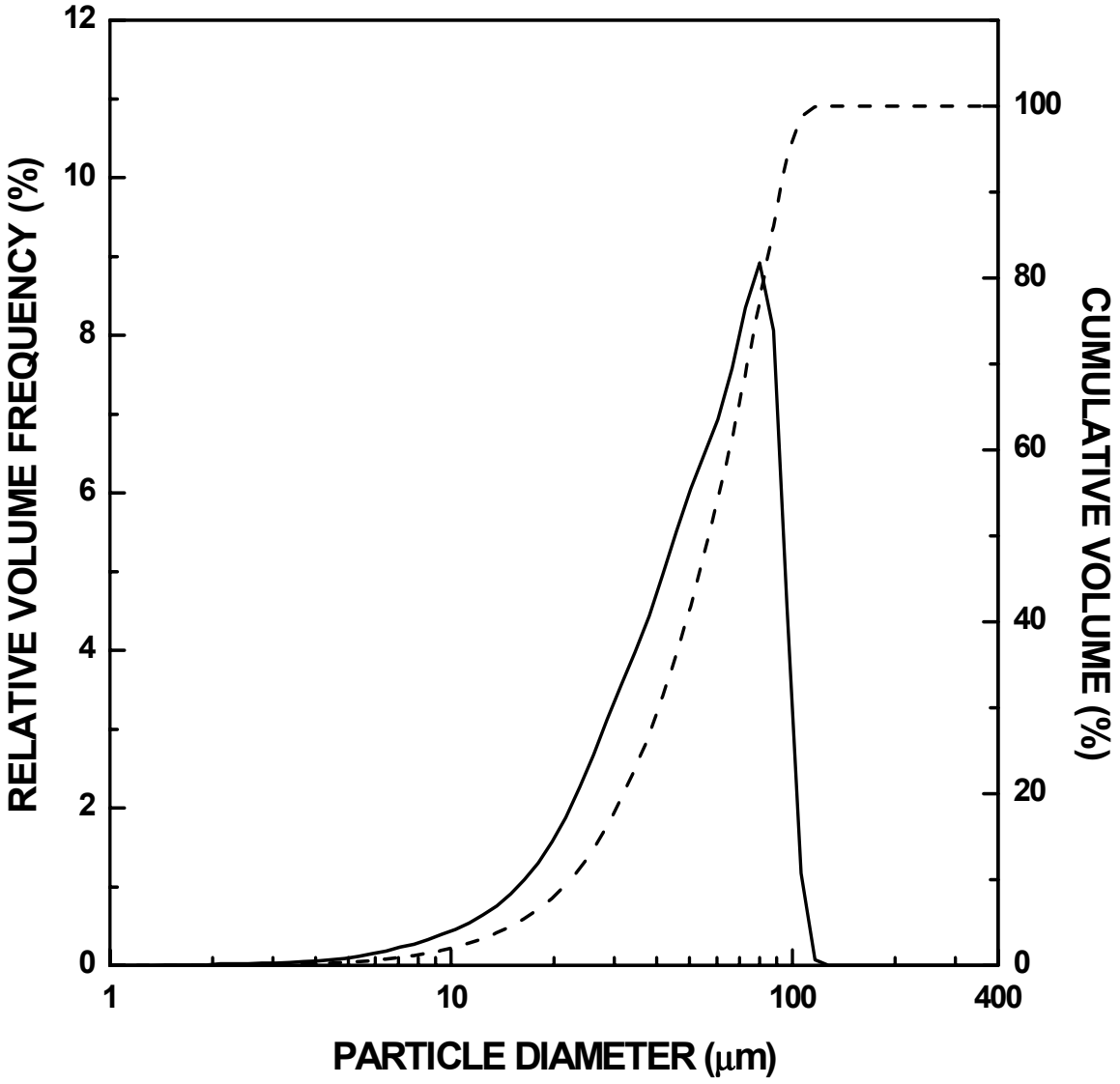

Figure 4-1-28 Particle size distribution plot for the SC8 pyrolyzed sample (initial C/Si molar ratio = 4.6). The sample was prepared with sonication. The solid line is for the differential distribution and the dashed line is for the cumulative distribution.

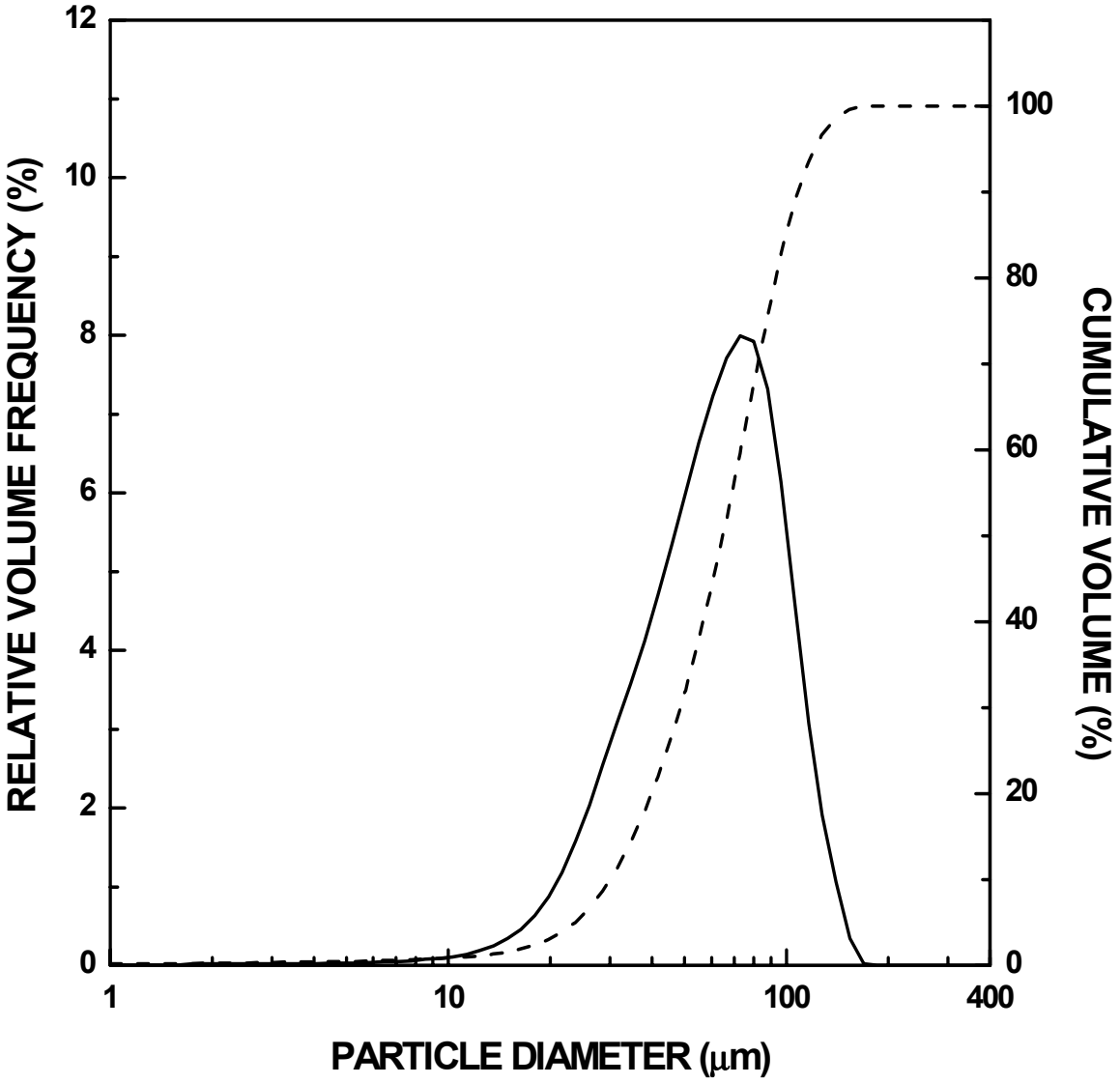

Figure 4-1-29 Particle size distribution plot for the SC8 pyrolyzed sample (initial C/Si molar ratio = 4.6). The sample was prepared with tumbling. The solid line is for the differential distribution and the dashed line is for the cumulative distribution.

Table 4-1-3 Optical properties for silica and graphite.

Wavelength (nm)	Silica		Graphite	
	n	*k*	*n*	*k*
450	1.47	0	2.63	1.28
600	1.46	0	2.75	1.50
750	1.45	0	3.03	1.85
900	1.45	0	3.15	1.96

Note: *n* is the refractive index and *k* is the extinction coefficient. The optical constants for silica come from Philipp (1985) and the optical constants for graphite come from Borghesi and Guizzetti (1991).

sample were slightly larger than that for the SC8 pyrolyzed sample. As expected, the particle sizes measured for samples prepared with sonication were smaller than those prepared with tumbling. This is because the higher energy input caused more breakage of the pyrolyzed particles compared with the lower energy input of tumbling.

4.1.7 SEM Micrographs of the Pyrolyzed Materials

Figures 4-1-30 to 4-1-35 show the SEM micrographs of the SC42 pyrolyzed material (which has a very similar composition to the SC35 pyrolyzed material). These micrographs seem to indicate that the samples are nearly completely dense (i.e., pore-free). However, since these micrographs have magnifications in the range of 10,000X to 40,000X, the presence of very small pores (e.g., micropores) cannot be ruled out definitively. Nevertheless, the microscopy results are consistent with the low specific surface area and low specific pore volume for the SC35-1100(2h) sample, as shown in Table 4-1-2.

Table 4-1-4 d_{10}, d_{50}, and d_{90} values of the particle size distributions for the SC35, SC42 and SC8 pyrolyzed materials. The particle size distributions were calculated using the Fraunhofer and Mie models. Optical properties for silica and graphite were used with the Mie model.

Sample		SC35-1100(2h) pyrolyzed	SC42-1100(2h) pyrolyzed		SC8-1100(4h) pyrolyzed	
Sample processing before measurement		After sonication	After sonication	After tumbling	After sonication	After tumbling
Number of Runs		6	2	7	3	10
Fraunhofer	d_{10} (μm)	26 ± 2	30 ± 1	33 ± 2	21 ± 0	29 ± 1
	d_{50} (μm)	68 ± 3	76 ± 1	80 ± 1	54 ± 1	62 ± 1
	d_{90} (μm)	106 ± 4	117 ± 3	123 ± 3	88 ± 3	103 ± 2
Mie (Silica optical properties)	d_{10} (μm)	30 ± 2	33 ± 0	35 ± 1	23 ± 0	29 ± 1
	d_{50} (μm)	70 ± 4	78 ± 1	81 ± 1	55 ± 1	63 ± 1
	d_{90} (μm)	106 ± 4	117 ± 3	123 ± 3	88 ± 3	102 ± 1
Mie (Graphite optical properties)	d_{10} (μm)	28 ± 2	31 ± 0	34 ± 2	22 ± 0	29 ± 1
	d_{50} (μm)	69 ± 3	77 ± 1	81 ± 1	54 ± 1	62 ± 1
	d_{90} (μm)	106 ± 4	117 ± 2	123 ± 3	88 ± 3	103 ± 2

Note: d_{10}, d_{50}, and d_{90} represent that 10%, 50%, and 90% of the total volume were contributed by particles smaller than the corresponding sizes.

Table 4-1-5 Statistics of the particle size distributions for the SC35, SC42 and SC8 pyrolyzed materials. The particle size distributions were calculated based on the Fraunhofer model.

	SC35-1100(2h) pyrolyzed	SC42-1100(2h) pyrolyzed		SC8-1100(4h) pyrolyzed	
Sample processing before measurement	After sonication	After sonication	After tumbling	After sonication	After tumbling
Number of Runs	6	2	7	3	10
Average d_{10} (μm)	26 ± 2	30 ± 1	33 ± 2	21 ± 0	29 ± 1
Average d_{50} (μm)	68 ± 3	76 ± 1	80 ± 1	54 ± 1	62 ± 1
Average d_{90} (μm)	106 ± 4	117 ± 3	123 ± 3	88 ± 3	103 ± 2
Average Mode (μm)	92 ± 5	88 ± 0	96 ± 0	80 ± 0	73 ± 0
Mean for the distribution (μm)	68	76	79	55	64
Standard deviation for the distribution	30	35	34	25	29

Note: d_{10}, d_{50}, and d_{90} represent that 10%, 50%, and 90% of the total volume were contributed by particles smaller than the corresponding sizes.

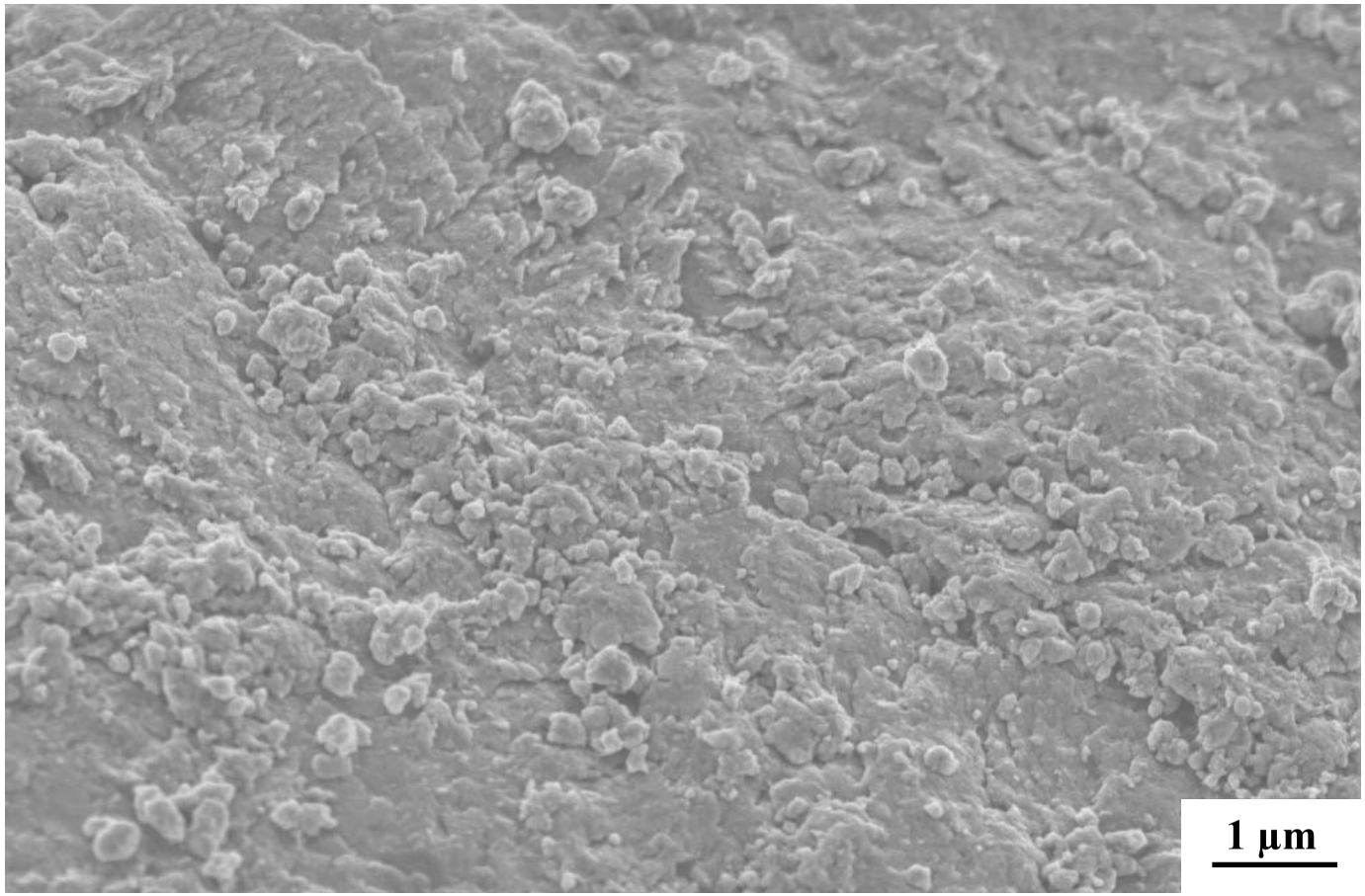

Figure 4-1-30 SEM micrograph of SC42-1100(2h) pyrolyzed sample. The powder was viewed directly without gold sputtering.

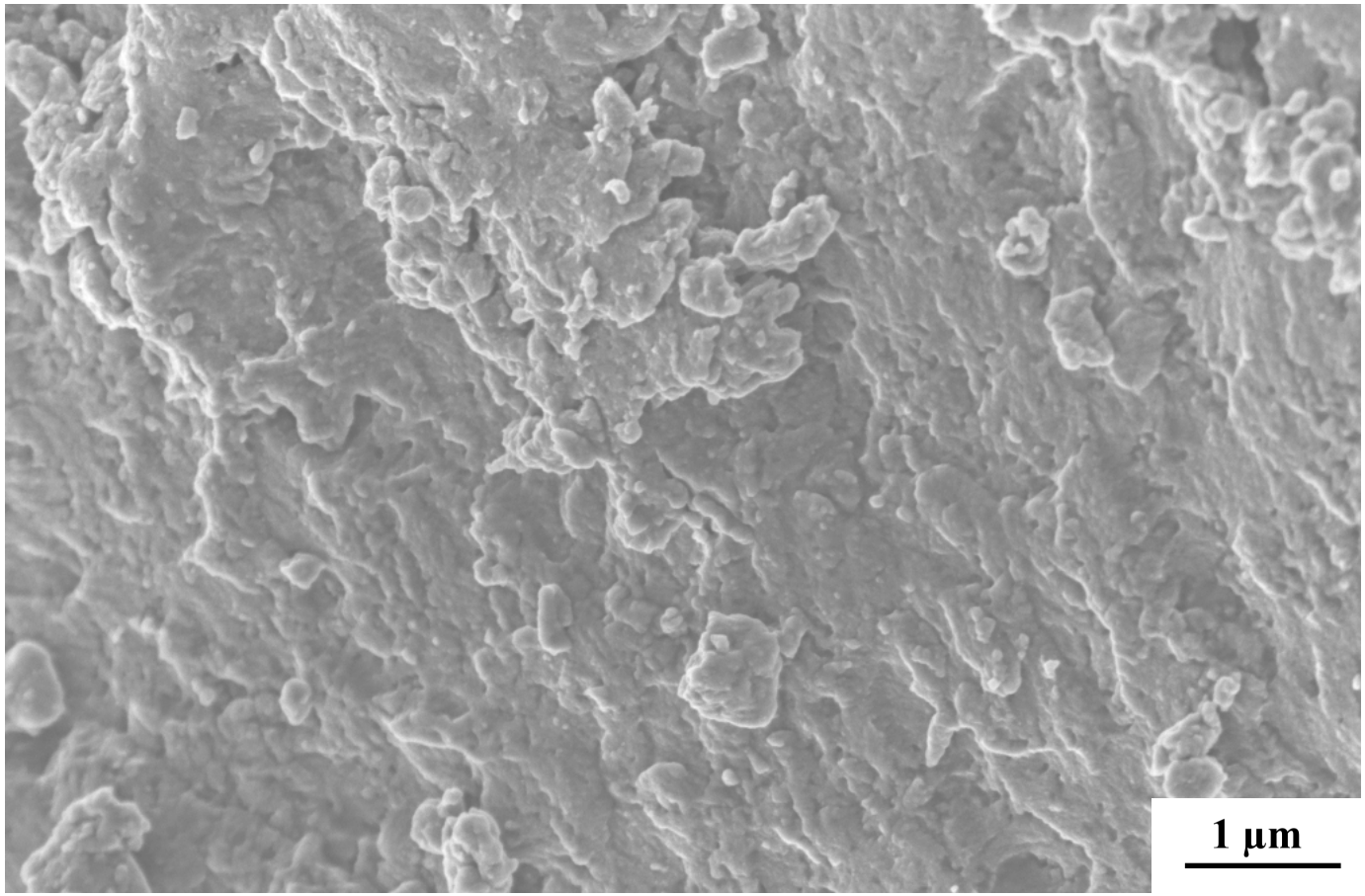

Figure 4-1-31 SEM micrograph of SC42-1100(2h) pyrolyzed sample. The powder was viewed directly without gold sputtering.

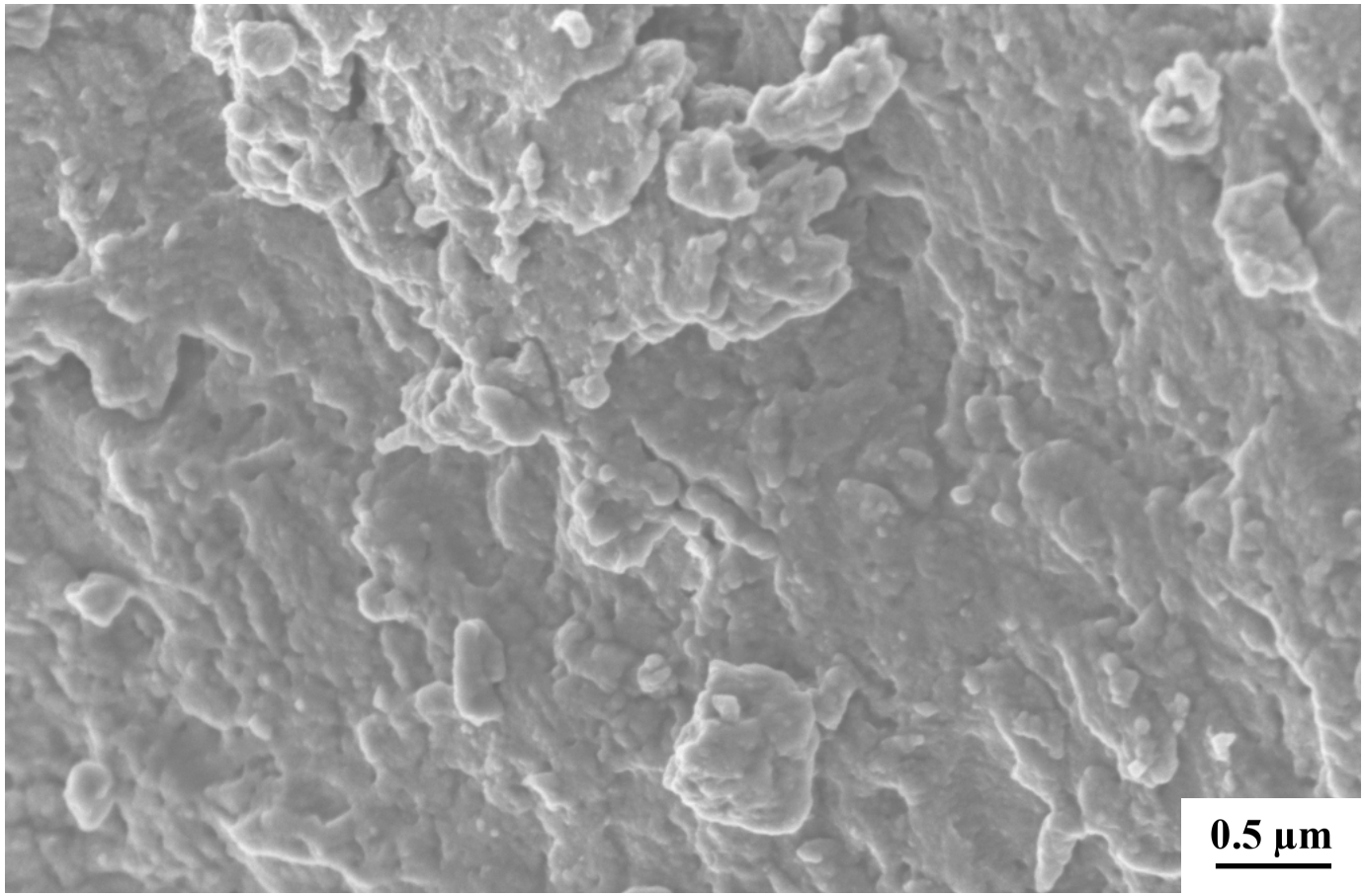

Figure 4-1-32 SEM micrograph of SC42-1100(2h) pyrolyzed sample. The powder was viewed directly without gold sputtering.

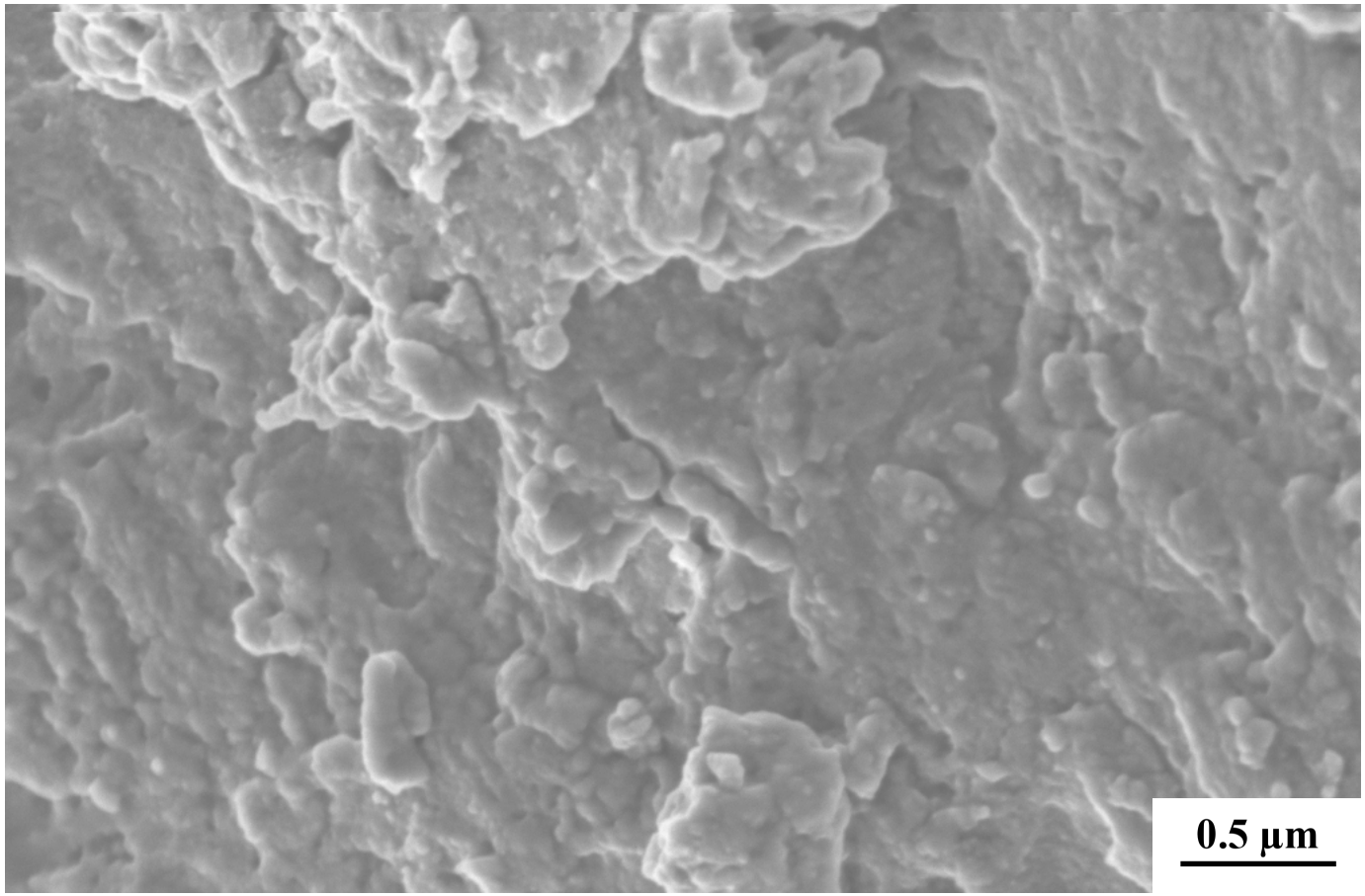

Figure 4-1-33 SEM micrograph of SC42-1100(2h) pyrolyzed sample. The powder was viewed directly without gold sputtering.

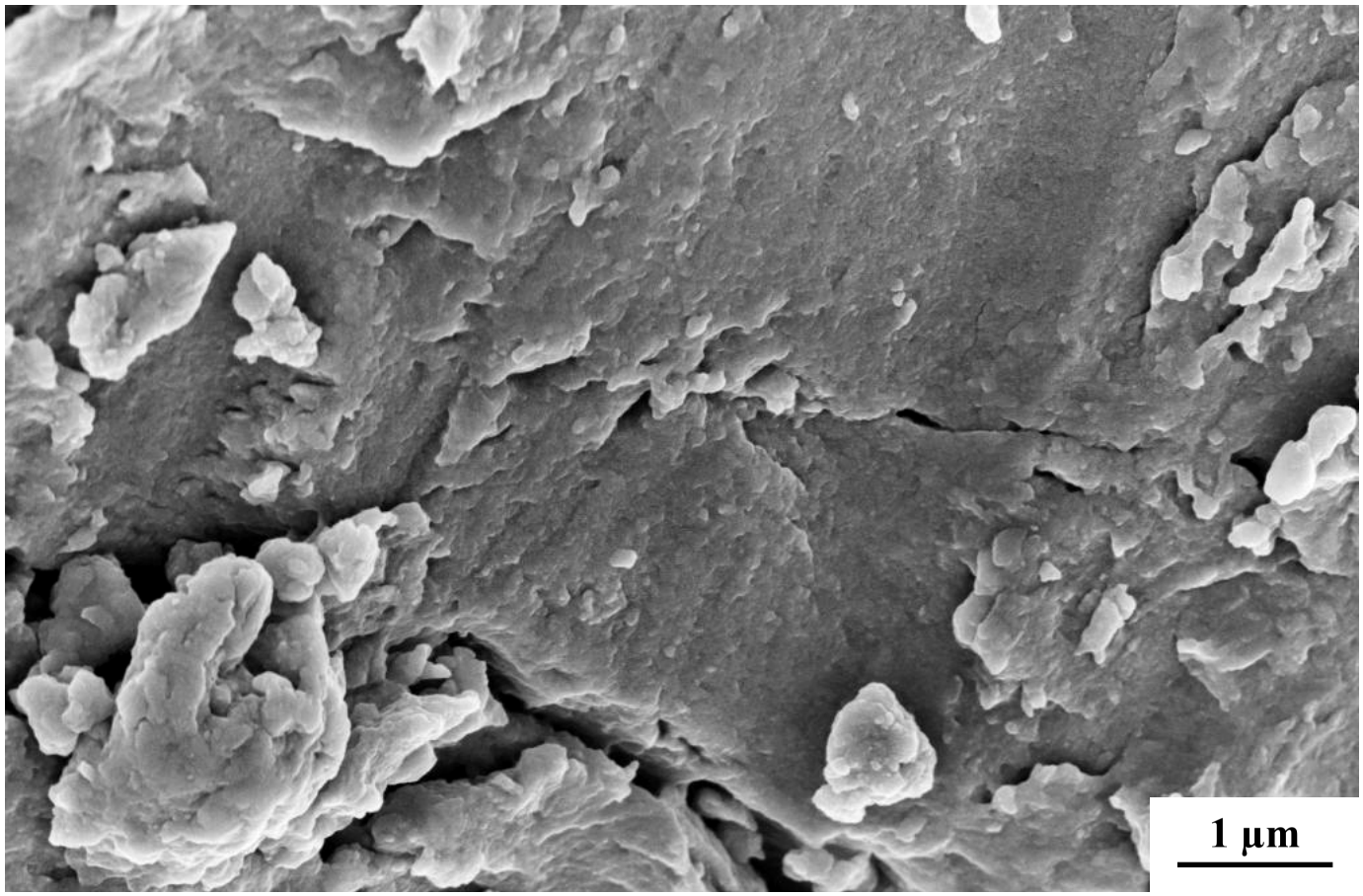

Figure 4-1-34 SEM micrograph of SC42-1100(2h) pyrolyzed sample. The powder was sputtered with gold for 30 sec.

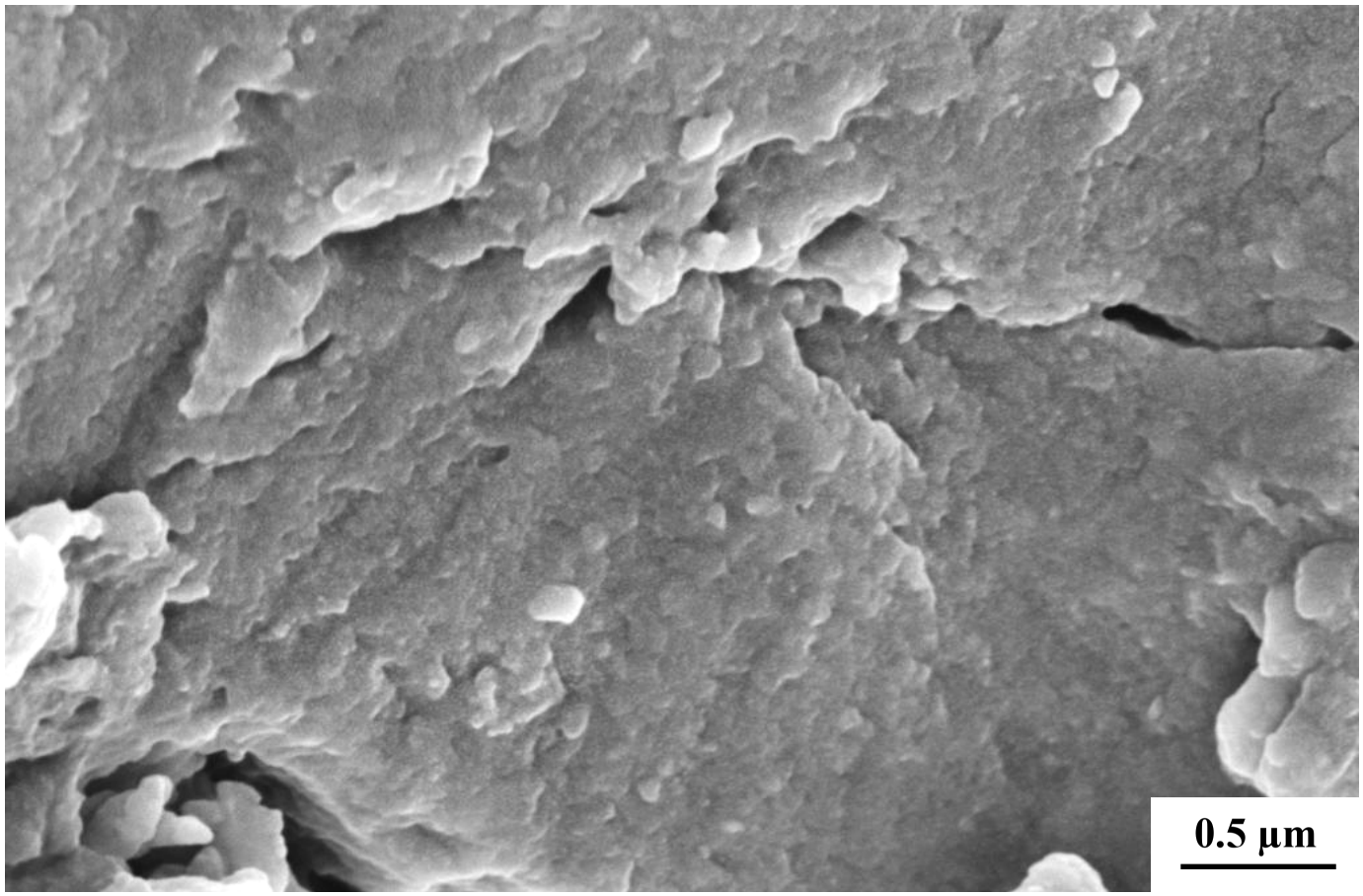

Figure 4-1-35 SEM micrograph of SC42-1100(2h) pyrolyzed sample. The powder was sputtered with gold for 30 sec.

The lowest magnification micrograph (Figure 4-1-30) shows many particulate-like entities on the surface of the particle with sizes that are mostly within the ~50-300 nm range. It is proposed that the relatively large pyrolyzed particles (~80 μm median diameter) are actually comprised of much smaller (mostly submicron) silica/carbon clusters that are arranged in a nearly space-filling manner. (This will be discussed later in detail in section 4.4.5.)

Although large regions of the samples appear to be highly dense, the pyrolyzed particles contain numerous defects in the form of relatively large crack-like voids as shown in Figures 4-1-34 and 4-1-35. Most of these large defects (greater than ~0.2 μm) would not be detected from the pore size analysis obtained by gas adsorption/capillary condensation measurements because of their sizes.

4.1.8 TEM Micrographs of the pyrolyzed materials

Figures 4-1-36 and 4-1-37 show a TEM micrograph and the corresponding electron diffraction pattern of the SC35-1100(2h) pyrolyzed sample. The micrograph shows a dispersed spheroidal phase in a matrix. The typical diameters of the dispersoids are in the range of ~5-8 nm. Several rings could be identified from the diffraction pattern. (It is not certain if there are diffraction rings within the bright center region.) Table 4-1-6 lists the measured diffraction ring diameters, Φ, the observed diffraction ring intensities, Int_O, and the calculated d-spacings, d_C, based on the diffraction pattern.

Figures 4-1-38 and 4-1-39 are high-resolution TEM (HRTEM) micrographs of the SC35 pyrolyzed sample. These micrographs show that the spheroidal phase is crystalline while the matrix is amorphous. The lattice parameter measured from the high resolution

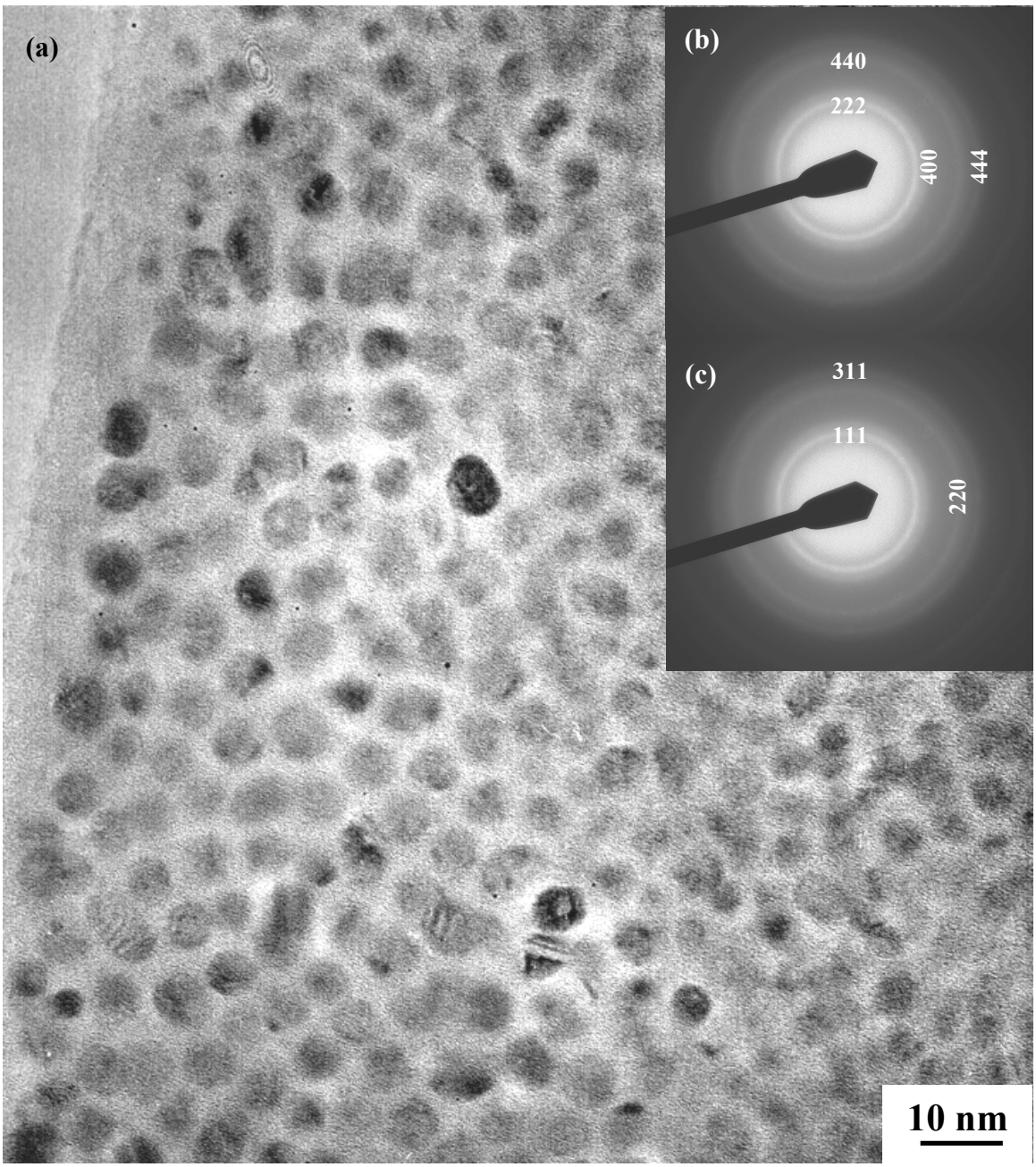

Figure 4-1-36 TEM image (a) and the corresponding electron diffraction pattern indexed according to β-cristobalite (b) and diamond (c) for the SC35-1100(2h) pyrolyzed material.

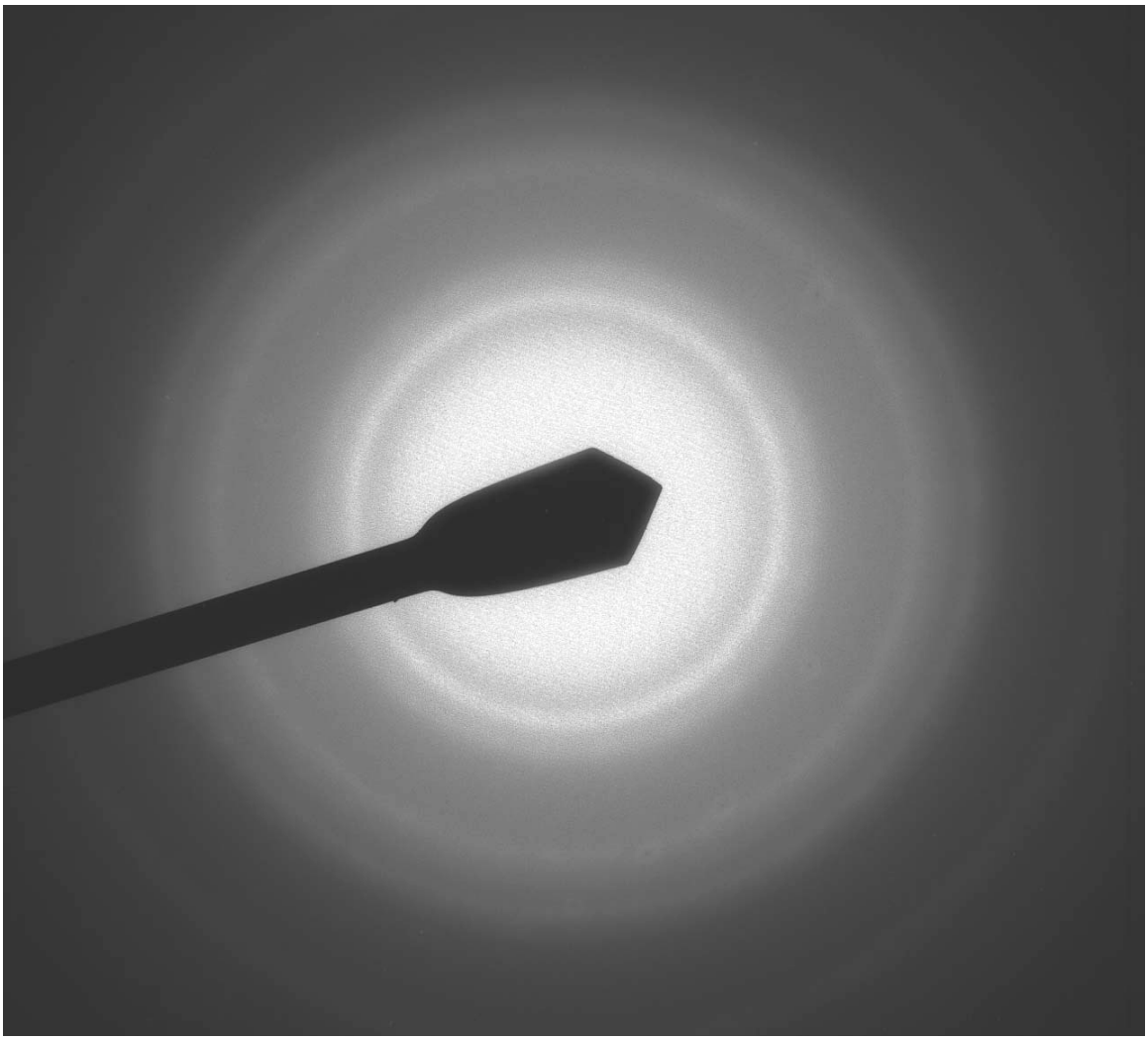

Figure 4-1-37 A zoom-in electron diffraction pattern for the SC35-1100(2h) pyrolyzed material.

Table 4-1-6 Comparison of the measured diffraction pattern information for the SC35-1100(2h) sample and the JCPDS information for β-cristobalite and cubic diamond.

SC35-1100(2h)			β-cristobalite (JCPDS No. 27-0605)			Diamond (JCPDS No.06-0675)		
Φ [1] (mm)	d_C [2] (nm)	Int_O [3]	d_{hkl} (nm)	*h k l*	*Int*	d_{hkl} (nm)	*h k l*	*Int*
			0.411	1 1 1	100			
			0.252	2 2 0	12			
			0.215	3 1 1	1			
20.1	0.199	1	0.206	2 2 2	4	0.206	1 1 1	100
23.0 [4]	0.174	2	0.178	4 0 0	1			
			0.164	3 3 1	7			
			0.146	4 2 2	5			
			0.137	5 1 1	2			
33.2	0.120	3	0.126	4 4 0	2	0.126	2 2 0	25
			0.121	5 3 1	3			
			0.119	4 4 2	<1			
			0.113	6 2 0	<2			
			0.109	5 3 3	<1			
			0.107	6 2 2	<1			
38.6	0.104	4	0.103	4 4 4	<1	0.108	3 1 1	16

Note:

1. Φ is the measured diffraction ring diameter on the negative.
2. d_C is the calculated lattice spacing based on Φ. The camera constant is $L \cdot \lambda$ = 2 nm · mm where L is the camera length (i.e., the distance from the focal plane to the image plane) and λ is the wavelength of the electron wave. d_C is given by:
$$d_C = \frac{2L \cdot \lambda}{\Phi} \text{ nm}$$
3. Int_O represents the intensity of the observed diffraction rings on a qualitative rating scale, i.e., 1, 2, 3, and 4 are for diffraction rings from the most intense to the least intense, respectively.
4. This ring was quite vague and broad. It may come from broadening of another ring or from the amorphous matrix (i.e., instead of from crystalline regions).

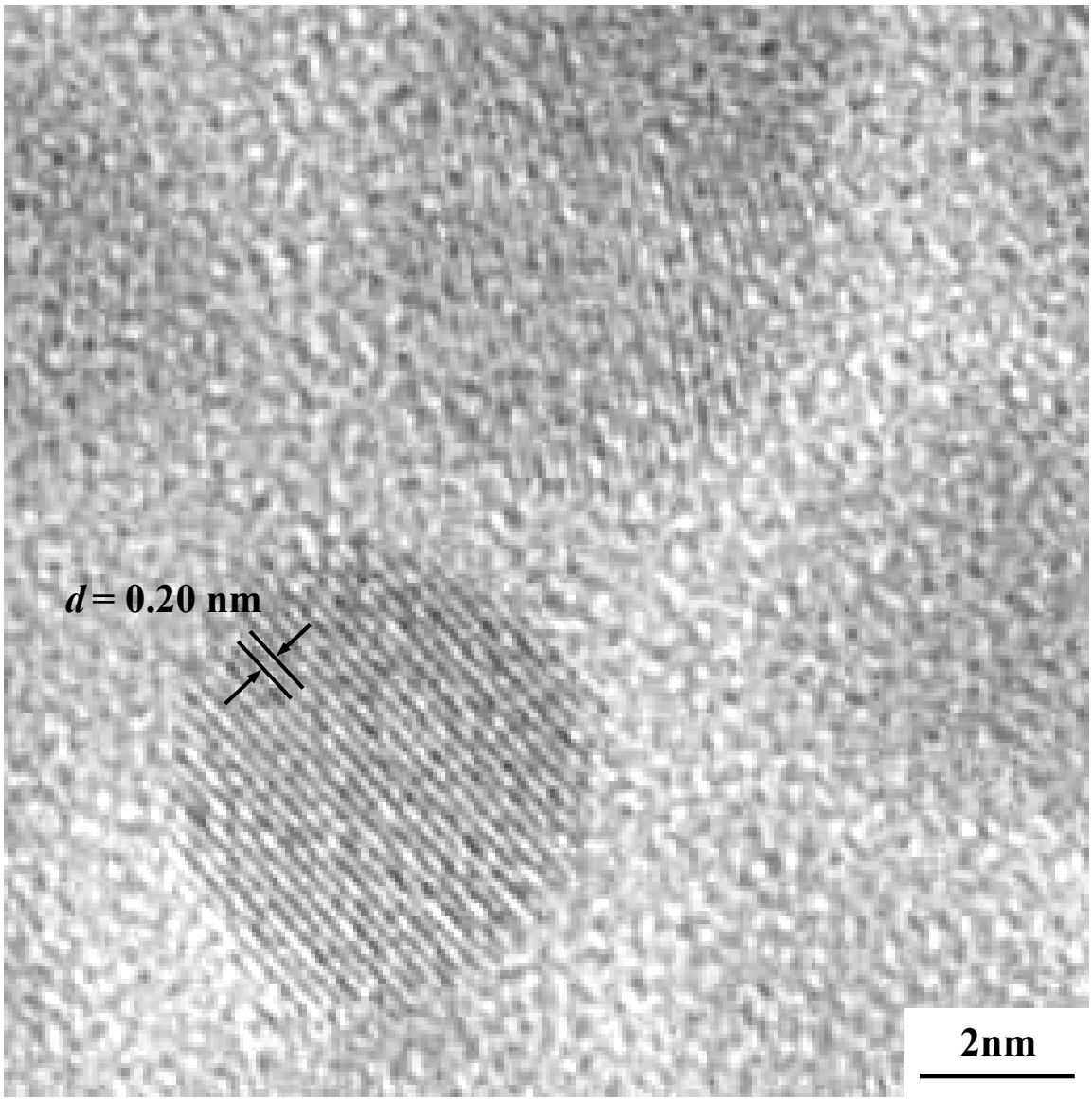

Figure 4-1-38 High resolution TEM image for the SC35-1100(2h) pyrolyzed material. The measured lattice spacing in the spheres matched that for both diamond (111) planes and β-cristobalite (222) planes reasonably well.

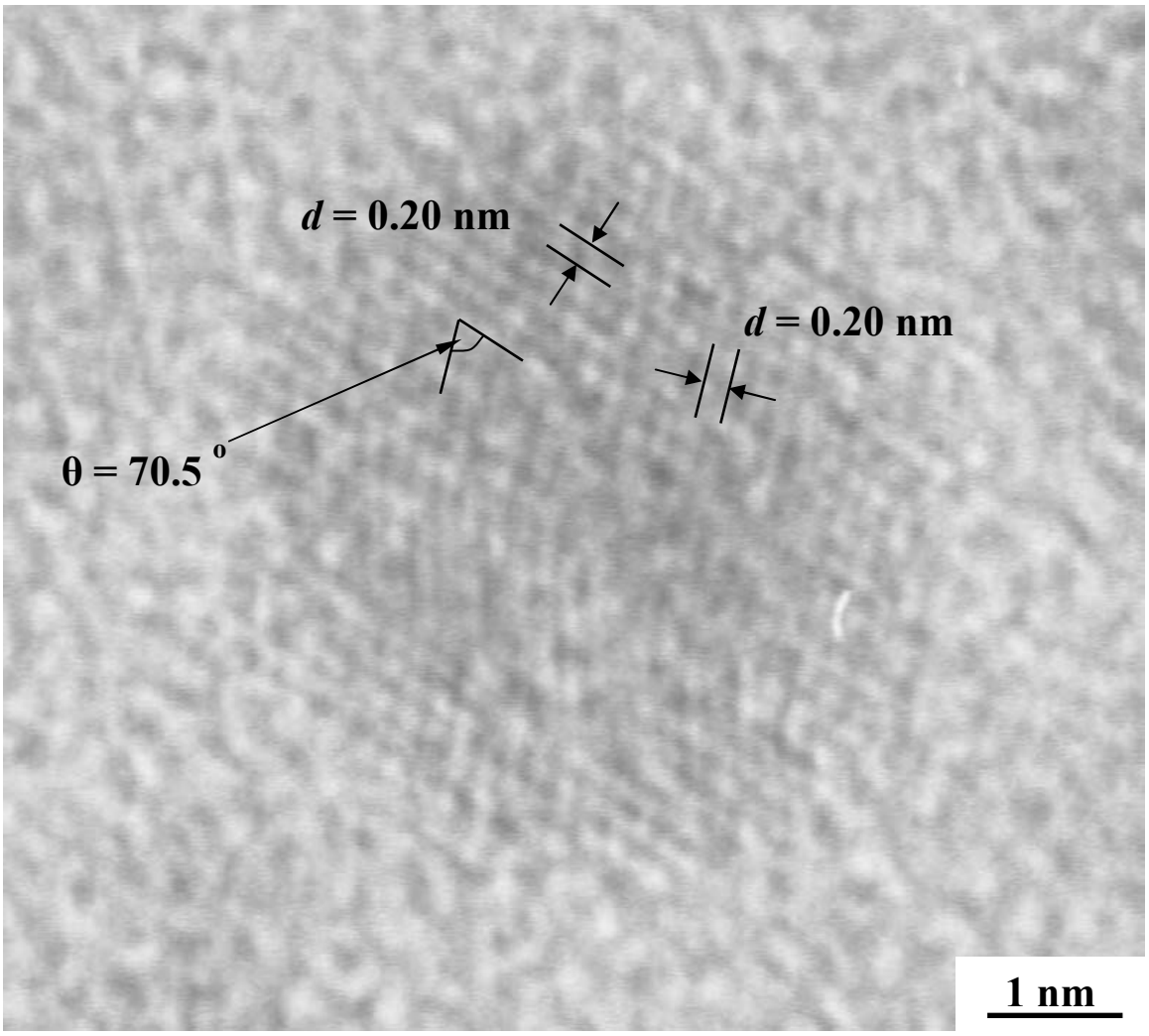

Figure 4-1-39 High resolution TEM image for the SC35-1100(2h) pyrolyzed material showing a crystalline sphere in the amorphous matrix. The *d*-spacing and the angle between the two planes match those of both diamond (111) plane and *β*-cristobalite (222) plane reasonably well.

images were in the range of 0.202 - 0.210 nm.

The observation in Figure 4-1-36 of a significant amount of a well-crystallized phase in the SC35-1100(2h) pyrolyzed sample is not consistent with the XRD pattern shown in Figure 4-1-5. This suggests that crystallization occurred during sample preparation or during observation in the TEM. In fact, the most likely explanation is that crystallization occurred during the ion milling procedure used to prepare the sample for TEM observations. This is believed based on the following:

(1) Crystallization in pyrolyzed samples was only observed in one sample. This sample was prepared using more aggressive ion milling conditions compared to the conditions used in other samples. The beam energy was ~5 keV and the milling angle was as high as ~5-6^{o} for the SC35-1100(2h) sample, while ≤4 keV and milling angle ≤3^{o} were used for other samples. There was significant local heating during ion milling of the SC35-1100(2h) sample as indicated by the observation of a red glow at the edge of the hole being milled.

(2) Crystallization of amorphous carbon films due to low energy ion beam irradiation has been reported previously (Patsalas et al. (1999) and Patsalas and Logothetidis (2001)). For example, Patsalas and Logothetidis (2001) prepared amorphous carbon films with thicknesses in the range of 30-200 nm which were deposited on Si substrates by magnetron sputtering of a graphite source under varying bias voltages. Samples were given a post-growth argon ion beam bombardment (IBB) using ion energies and ion fluences in the ranges of 0.5-1.5 keV and 2.65-13.25 $\times$ 10^{16} ions/cm^{2}, respectively. Depending on the sputtering and IBB conditions, they observed the formation of cubic diamond, hexagonal diamond, graphite, and silicon carbide. (Graphite and silicon carbide were observed for samples with larger IBB fluences. This was attributed to heating of the samples with the

longer IBB times.) Patsalas et al. (1999) reported similar results in an earlier study which also included some experiments carried out using 6 keV ion milling for HREM samples. They presented an image showing a cubic diamond crystallite (~6 nm) and a SiC crystallite (~3 nm).

Crystallization of amorphous silica films has also been observed under conditions of low-energy neutral beam irradiation. Mizutani (1995) prepared 30-100 nm thick SiO_2 films by thermal oxidation of Si substrates. Alpha cristobalite and alpha quartz crystallites (with estimated sizes of "a few nanometers") were formed in films that were irradiated using neutral beams of Kr and Ne, respectively. (The beam energy was 350 eV and the dose was $10^{17}/cm^2$.) Crystallization was not observed when the substrates were bombarded with Kr^+ and Ne^+ ion beams with the same kinetic energy and dose as used with the neutral beams.

The IBB conditions used to prepare the SC35-1100(2h) sample in the current study were similar to or more aggressive than those used in the study by Patsalas et al. As noted earlier, the ion energy was ~5 keV. According to the equipment manual, the peak ion current density was 10 mA/cm^2. Therefore, the peak ion flux was: $10\times10^{-3}C/(sec\cdot cm^2) \times 6.25 \times 10^{18}$ ions/C = 6.25×10^{16} ions/$(sec\cdot cm^2)$. For the SC35-1100(2h) sample, the milling time at 5 keV was on the order of 1 min. Therefore, the ion fluence would be approximately 6.25×10^{16} ions/$(sec\cdot cm^2) \times 60$ sec = 3.75×10^{18} ions/cm^2. This dosage is higher than that used in the studies by Patsalas and Logothetidis (2001). Therefore, it is reasonable to conclude that the IBB conditions used in this study were sufficient to induce crystallization in the SC35 pyrolyzed sample.

Table 4-1-6 shows the lattice spacings that were obtained from the electron diffraction pattern for the SC35-1100(2h) sample and the lattice spacings (and

corresponding planes) for cubic diamond and β-cristobalite, as given in JCPDS Nos. 06-0675 and 27-0605, respectively. The *d*-spacings observed in the SC35-1100(2h) sample were close to the d-spacings listed for the cubic diamond structure. However, the sample had an additional ring corresponding to a *d*-spacing of ~0.178 nm. This ring was vague and broad, so it is possible that it was associated with the amorphous matrix instead of the spheroidal crystallites. The *d*-spacing and the angle (70.5^o) between planes obtained from the HRTEM image also matched well those of the diamond (111) plane (d_{111} = 0.206 nm and $\theta = 70.5^o$). The relative intensities of the rings in the diffraction pattern were also consistent with the relative intensities expected from the JCPDS card.

The *d*-spacings observed in the SC35-1100(2h) sample were also close to the d-spacings for *some* of the *d*-spacings listed in Table 4-1-6 for β-cristobalite. The *d*-spacing and the angle (70.5^o) between planes obtained from the HRTEM image also matched well those of the β-cristobalite (222) plane (d_{222} = 0.206 nm and $\theta = 70.5^o$). Nevertheless, the spheroidal crystallites are probably not β-cristobalite for the following reasons: (1) Diffraction rings for the lower-index (111) and (220) planes were not observed in the electron diffraction pattern for the SC35-1100(2h) sample, even though higher intensities are expected for these planes. Their absence indicates that either the spheroidal crystallites are not β-cristobalite or that the rings could not be distinguished due to the high brightness in that region of diffraction pattern. (2) Diffraction rings were not observed for higher-index planes in β-cristobalite, such as the (331) and (442) planes, which normally would give similar or larger intensities than the (222) plane. (3) β-cristobalite is a high-temperature phase of silica which converts to α-cristobalite upon cooling. Stabilization of β-cristobalite at room temperature requires incorporation of other metallic ions into the

structure (Perrota et al. (1989) and Thomas et al. (1994)). The materials used in this study were of sufficiently high purity that the stabilization of β-cristobalite at room temperature would not be expected. (4) The volume fractions of the two phases in Figure 4-1-36 were estimated using a stereological point-counting method (Underwood, 1981, p29). In this method, a grid is placed over a section of the micrograph and the number of points, *Pi*, intersecting each phase is counted. The volume fraction of a phase, *Vp*, is given by the ratio of the number of points intersecting the phase divided by the total number of points, *Pn*:

$$Vp = Pi/Pn \qquad (4\text{-}1\text{-}2)$$

In this case, 187 total points were counted using the TEM image in Figure 4-1-36. The calculated volume fractions for the dispersed spheroidal phase and the matrix phase were 37% and 63%, respectively. These volume fractions are reasonably close to the estimated volume fractions of carbon and silica, respectively, in the SC35 pyrolyzed material (see Table 4-1-9 in section 4.1.9). Therefore, this stereological analysis provides further evidence that the dispersed spheroidal phase is diamond.

Unfortunately, no chemical analysis on the spheroidal crystallites was obtained. Nevertheless, based on the above considerations, it is tentatively concluded that the crystallites are cubic diamond.

4.1.9 Apparent Solid Density of the Pyrolyzed Materials

The apparent solid densities of the SC42-1100(2h) pyrolyzed material (which is very similar in composition to the SC35 pyrolyzed material) and a glassy carbon sample obtained by pyrolysis (1100^{o}C/2h) of the phenolic resin were measured using a

pycnometer by Dr. Zhaohui Yang of Georgia Institute of Technology. The results are summarized in Table 4-1-7.

The measured apparent density of the SC42-1100(2h) pyrolyzed material can be compared with values calculated from the measured carbon content, the measured carbon density, and estimated silica densities. Suppose the density of carbon in the SC42-1100(2h) pyrolyzed material, ρ_C, is equivalent to the density of carbon obtained by pyrolyzing phenolic resin (i.e., ρ_C = 1.49 g/cm^3); suppose the density of silica, ρ_{SiO2}, is in the range of 2.2-2.3 g/cm^3 (Sacks and Tseng, (1984, Part I)). The rule of mixture gives:

$$\frac{1}{\rho_{SC42}^{pyro}} = \frac{w_{SiO2}^{pyro}}{\rho_{SiO2}} + \frac{w_C^{pyro}}{\rho_C} \tag{4-1-3}$$

in which ρ_{SC42}^{pyro} is the SC42 pyrolyzed material density, w_{SiO2}^{pyro} is the weight fraction of silica in the pyrolyzed material, and w_C^{pyro} is the weight fraction of carbon in the pyrolyzed

Table 4-1-7 The apparent solid densities measured by pycnometer for the SC42-1100(2h) sample and a glassy carbon sample (obtained by pyrolysis of the phenolic resin at 1100^{o}C for 2h).

	SC42 pyrolyzed material	Pyrolyzed material from phenolic resin
Density from run #1 (g/cm^3)	1.920	1.484
Density from run #2 (g/cm^3)	1.959	1.499
Density from run #3 (g/cm^3)	1.943	
Density from run #4 (g/cm^3)	1.956	
Average density (g/cm^3)	1.944	1.492
Standard deviation (g/cm^3)	0.018	0.011

material. For the SC42 pyrolyzed material, LECO carbon content analysis yielded $w_C^{pyro} = 0.3155$. Therefore, $w_{SiO2}^{pyro} = 1 - w_C^{pyro} = 0.6845$. If ρ_{SiO2} = 2.20 g/cm^3, ρ_{SC42}^{pyro} = 1.91 g/cm^3; if ρ_{SiO2} = 2.25 g/cm^3, ρ_{SC42}^{pyro} = 1.94 g/cm^3; and if ρ_{SiO2} = 2.30 g/cm^3, ρ_{SC42}^{pyro} = 1.96 g/cm^3. Therefore, there is very good agreement between the measured density and the calculated apparent density for the SC42 pyrolyzed materials.

Such agreement enables us to estimate the apparent density of the SC35-1100(2h) and SC8-1100(4h) pyrolyzed material. For the SC35 pyrolyzed material (which has a very similar composition to the SC42 pyrolyzed material), w_C^{pyro} = 0.3160, and w_{SiO2}^{pyro} = $1 - w_C^{pyro}$ = 0.6840. If ρ_{SiO2} = 2.20 g/cm^3, ρ_{SC35}^{pyro} = 1.90 g/cm^3; if ρ_{SiO2} = 2.25 g/cm^3, ρ_{SC35}^{pyro} = 1.93 g/cm^3; ρ_{SiO2} = 2.30 g/cm^3, ρ_{SC35}^{pyro} = 1.95 g/cm^3. For the SC8 pyrolyzed material, $w_C^{pyro} = 0.4809$, and $w_{SiO2}^{pyro} = 1 - w_C^{pyro}$ = 0.5191. If ρ_{SiO2} = 2.20 g/cm^3, ρ_{SC8}^{pyro} = 1.79 g/cm^3; if ρ_{SiO2} = 2.25 g/cm^3, ρ_{SC8}^{pyro} = 1.81g/cm^3; ρ_{SiO2} = 2.30 g/cm^3, ρ_{SC8}^{pyro} = 1.82 g/cm^3.

The volume contents of the carbon phase and silica phase in the pyrolyzed materials were also estimated based on carbon and silica density information. A silica density of 2.25 g/cm^3 and a carbon density of 1.49 g/cm^3 were used in the calculations. If v_C^{pyro} and v_{SiO2}^{pyro} are the volume contents of carbon and silica, respectively, in the pyrolyzed materials, we have:

$$v_C^{pyro} = \frac{w_C^{pyro} / \rho_C}{w_C^{pyro} / \rho_C + w_{SiO2}^{pyro} / \rho_{SiO2}} \tag{4-1-4}$$

$$v_{SiO2}^{pyro} = 1 - v_C^{pyro} \tag{4-1-5}$$

Table 4-1-8 summarizes the composition information and the densities of the SC35, SC42, and SC8 pyrolyzed materials.

A problem with the above calculations for the volume fractions of silica and carbon in the SC8 and SC35 pyrolyzed materials is that they were based on using a measured carbon density that was an apparent solid density (and was not a true solid density). The carbon density measured in this study was consistent with the typical range of values reported for relatively coarse "glassy carbon" samples prepared by heat treatment of

Table 4-1-8 Composition and density information for the SC35, SC42, and SC8 pyrolyzed materials.

Sample	SC35 pyrolyzed	SC42 pyrolyzed	SC8 pyrolyzed
Carbon weight fraction by LECO (w_C^{pyro})	0.3260	0.3155	0.4809
Silica weight fraction (w_{SiO2}^{pyro})	0.6740	0.6845	0.5191
C/Si molar ratio ($x_{C/Si}^{pyro}$)	2.4	2.4	4.6
Carbon volume fraction (v_C^{pyro}) **	0.42	0.41	0.58
Silica volume fraction (v_{SiO2}^{pyro}) **	0.58	0.59	0.42
Measured density (g/cm^3)	1.94*	1.94	
Calculated density ** (g/cm^3)	1.93	1.94	1.81

Note:

* The measured density for the SC42-1100(2h) pyrolyzed material is used for the density of the SC35-1100(2h) pyrolyzed material because the composition is almost identical.

** The volume fraction values and the density were calculated based on a silica density of 2.25 g/cm^3 and a carbon density of 1.49 g/cm^3.

phenolic resins at various temperatures (Fischbach and Rorabaugh (1977), Ko et al. (2001), and Kawamura et al. (2003)). However, available evidence indicated that those samples contained substantial amounts of closed porosity. Furuta et al. (1969) reported true (solid) densities for carbons derived from phenolic resins by using measured *d*-spacings obtained from X-ray diffraction analysis. The density values gradually increased in the range of 2.12-2.26 g/cm^3 as the heat treatment temperature increased from 1000^{o}C to 3000^{o}C. This was due to increasing crystallinity of the carbon with increasing heat treatment temperature. The highest density value reported by Furuta et al. (i.e., 2.26 g/cm^3) equals the true density of well-crystallized graphite. Density values of 1.9-2.1 g/cm^3 have been reported for submicrometer vapor-grown carbon fibers (Tibbetts et al. (1993) and Endo et al. (2001)). XRD patterns indicated that the samples which were not well-crystallized (Tibbetts et al. (1993)). The higher density values in these studies were associated with fibers which had a higher degree of graphitization (Endo et al. (2001)).

Based on the above information, it is presumed that the pyrolyzed phenolic resin sample used for the density measurement in Table 4-1-7 contained closed porosity. (Alternatively, it is possible that open pores could not be penetrated by water during the pycnometric measurement). Furthermore, this type of porosity was apparently in the carbon phase of the SC35 pyrolyzed material because the measured apparent density was very close to values calculated by using the measured apparent density of the pyrolyzed phenolic resin. (The silica densities used in the calculations (2.25 g/cm^3 ± 0.05 g/cm^3) are assumed to be accurate.) It is concluded that the calculated volume fractions for silica and carbon in the SC8 and SC35 pyrolyzed samples (Table 4-1-8) are not reliable.

Based on the XRD results shown in section 4.1.1 and Appendix G, the free carbon in the pyrolyzed and CTR samples in this study can be described as a "glassy carbon" and it is clearly not well-crystallized graphite. Very rough estimates of the true volume fractions of carbon and silica (i.e., v_{C-T}^{pyro} and v_{SiO2-T}^{pyro}, respectively) in the SC8, SC35, and SC42 pyrolyzed materials were made by assuming that the true solid density of the carbon was 2 g/cm^3 and that the silica true solid density was 2.25 g/cm^3. The calculated volume fraction values are given in Table 4-1-9.

Table 4-1-9 Composition and density information for the SC35, SC42, and SC8 pyrolyzed materials.

Sample	SC35 pyrolyzed	SC42 pyrolyzed	SC8 pyrolyzed
Carbon weight fraction by LECO (w_C^{pyro})	0.3260	0.3155	0.4809
Silica weight fraction (w_{SiO2}^{pyro})	0.6740	0.6845	0.5191
Calculated density * (g/cm^3)	2.16	2.16	2.12
True carbon volume fraction (v_{C-T}^{pyro}) *	0.35	0.34	0.51
True silica volume fraction (v_{SiO2-T}^{pyro}) *	0.65	0.66	0.49

Note:

* The density and volume fraction values were calculated based on a silica density of 2.25 g/cm^3 and a carbon density of 2 g/cm^3.

4.1.10 Composition of Dried Materials from TEOS/Phenolic Resin Mixed Solutions

Given that the dried material is a mixture of phenolic resin and polysilicates, the weight fractions of phenolic resin and polysilicates are w_{PR}^{dry} and w_{PS}^{dry}, respectively ($w_{PR}^{dry} + w_{PS}^{dry} = 1$). W_{PR}^{dry} is the weight of phenolic resin in the dried material, and W_C^{pyro} is the weight of carbon in the pyrolyzed material. We will have:

$$W_C^{pyro} = W_{PR}^{dry} \cdot Y_C^{pyro} \tag{4-1-6}$$

where Y_C^{pyro} is the carbon yield for pyrolysis of the phenolic resin in the dried material. As stated in section 3.1.1, the carbon yield for the pyrolysis of phenolic resin dried material was 0.3973. The same value was used for Y_C^{pyro}, i.e., it was assumed that the carbon yield of phenolic resin was the same for the pyrolysis of the phenolic resin and the dried material from the phenolic resin/TEOS mixed solution. For the dried material, we have the following relationship:

$$W_{PR}^{dry} = W_{dry} \cdot w_{PR}^{dry} \tag{4-1-7}$$

As explained previously, the pyrolyzed material is assumed to be a mixture of carbon and silica only. The weight fractions of carbon and silica in the pyrolyzed materials are w_C^{pyro} and w_{SiO2}^{pyro} respectively ($w_C^{pyro} + w_{SiO2}^{pyro} = 1$). Hence, for the pyrolyzed material, we have:

$$W_C^{pyro} = W_{pyro} \cdot w_C^{pyro} \tag{4-1-8}$$

where W_{pyro} is the weight of the pyrolyzed material. From Equations (4-1-6), (4-1-7) and (4-1-8), we have:

$$W_{pyro} \cdot w_C^{pyro} = W_C^{pyro} = W_{PR}^{dry} \cdot Y_C^{pyro} = W_{dry} \cdot w_{PR}^{dry} \cdot Y_C^{pyro} \tag{4-1-9}$$

Therefore, from Equations (4-1-7) and (4-4-9), we have:

$$w_{PR}^{dry} = \frac{W_{PR}^{dry}}{W_{dry}} = \frac{W_{pyro} \cdot w_C^{pyro}}{W_{dry} \cdot Y_C^{pyro}} \tag{4-1-10}$$

Combining Equation (4-1-10) with Equation (4-1-1), we get:

$$w_{PR}^{dry} = \frac{w_C^{pyro} \cdot Y_{pyro}}{Y_C^{pyro}} \tag{4-1-11}$$

In Equation (4-1-11), the weight fraction of carbon in the pyrolyzed material, w_C^{pyro}, was determined by the LECO carbon content analysis described earlier in section 4.1.4; Y_{pyro} and Y_C^{pyro} were determined during the pyrolysis heat treatment of the dried TEOS/phenolic resin mixture and the dried phenolic resin sol, respectively.

For the SC35 series, from the previous discussion, w_C^{pyro} = 0.3235, Y_{pyro}=0.6947, and Y_C^{pyro}=0.3973. Therefore,

$$w_{PR}^{SC35-dry} = \frac{w_C^{pyro} \cdot Y_{pyro}}{Y_C^{pyro}} = \frac{0.3235 \times 0.6947}{0.3973} = 0.5656$$

$$w_{PS}^{SC35-dry} = 1 - w_{PS}^{SC35-dry} = 1 - 0.5656 = 0.4344$$

Similarly, for the SC8 series, w_C^{pyro} = 0.4809, Y_{pyro}=0.5905, and Y_C^{pyro}=0.3973. Therefore,

$$w_{PR}^{SC8-dry} = \frac{w_C^{pyro} \cdot Y_{pyro}}{Y_C^{pyro}} = \frac{0.4809 \times 0.5905}{0.3973} = 0.7148$$

$$w_{PS}^{SC8-dry} = 1 - w_{PS}^{SC8-dry} = 1 - 0.7148 = 0.2852$$

If the density of the dried phenolic resin, ρ_{PR}, is 1.27g/cm^3 and the density of the dried polysilicate species, ρ_{PS}, is 1.85g/cm^3 (Haraguchi et al., 1998, *Journal of Materials Science*), the volume fraction of the phenolic resin in the dried material, v_{PR}^{dry}, would be

$$v_{PR}^{dry} = \frac{w_{PR}^{dry} / \rho_{PR}}{w_{PR}^{dry} / \rho_{PR} + w_{PS}^{dry} / \rho_{PS}} \tag{4-1-12}$$

while the volume fraction of polysilicates in the dried material, v_{PR}^{dry}, would be

$$v_{PS}^{dry} = 1 - v_{PR}^{dry} \tag{4-1-13}$$

For the SC35 dried material,

$$v_{PR}^{SC35-dry} = \frac{0.5656/1.27}{0.5656/1.27 + 0.4344/1.85} = 0.6548$$

$$v_{PS}^{SC35-dry} = 1 - v_{PR}^{SC35-dry} = 0.3452$$

For the SC8 dried material,

$$v_{PR}^{SC8-dry} = \frac{0.7148/1.27}{0.7148/1.27 + 0.2852/1.85} = 0.7850$$

$$v_{PS}^{SC8-dry} = 1 - v_{PR}^{SC8-dry} = 0.2150$$

4.1.11 Packing Density of the Pyrolyzed Materials

The results of packing density measurements for the SC35 and SC8 pyrolyzed samples are shown in Table 4-1-10. The SC35 pyrolyzed material has a slightly higher value for packing density both with tapping and without tapping. The packing density values are somewhat low considering the individual particles are quite dense. One reason for this might be that the particles are irregular in shape. Another reason must be the tendency for the finer particles to adhere to surfaces due to "surface forces" (e.g., van der Waals force, capillary forces, etc.). Powder flow and rearrangement into a denser packing would be hindered if particles adhere either to each other or to the walls of the glass tip in which the powder was filled.

Table 4-1-10 Packing density for the SC35-1100(2h) and SC8-1100(4h) pyrolyzed materials.

	SC35	SC8
Packing density without tapping (g/cm^3)	0.886	0.771
Relative density without tapping *	46%	43%
Packing density with tapping (g/cm^3)	1.085	0.982
Relative density with tapping *	56%	54%

Note:

* The relative density was calculated using apparent solid densities of 1.93 g/cm^3 and 1.81 g/cm^3 for the SC35 and SC8 pyrolyzed materials, respectively. However, it was noted in section 4.1.9 that the carbon in these samples is probably microporous. Hence, the true relative densities are probably lower than the values reported above.

4.2 The Two-step Reaction Mechanism and the Identification of Volatile Deposits

4.2.1 The Two-step Reaction Mechanism

As stated in Chapter II, most researchers believe the carbothermal reduction reaction (CTR) is a multi-step process. The first step is the reaction between silica and carbon to form SiO and CO as shown by the following equation:

$$SiO_{2\,(s)} + C_{\,(s)} \rightarrow SiO_{\,(g)} + CO_{\,(g)} \qquad (4\text{-}2\text{-}1)$$

The second step is believed to be the reaction between SiO vapor and solid carbon to produce SiC and CO as shown by the following equation:

$$SiO_{\,(g)} + 2C_{\,(s)} \rightarrow SiC_{\,(s)} + CO_{\,(g)} \qquad (4\text{-}2\text{-}2)$$

As stated previously, the pyrolyzed material from TEOS/phenolic resin mixed solution is a fine scale carbon/silica mixture. A simple illustration of the two-step reaction for the CTR reaction from the pyrolyzed material is given in Figure 4-2-1. Before the reaction, the pyrolyzed material is composed of randomly mixed nanoscale silica and carbon regions (top left drawing). Upon heating of the pyrolyzed material, the tiny silica and carbon regions react with each other, generate SiO and CO, and leave a network of porous carbon on the outside of the original pyrolyzed particle, as depicted in the top right drawing in Figure 4-2-1. The SiO from the first reaction migrates to neighboring carbon regions and reacts at the carbon surface (bottom left drawing) to form SiC and CO. As a result, the porous carbon layer at the outside of the particle is replaced by a porous SiC layer (bottom right drawing). It should be noted that this illustration of the two-step processes is just a simplification of the reaction process. In reality, the two steps, instead of happening one after another, might actually happen simultaneously and

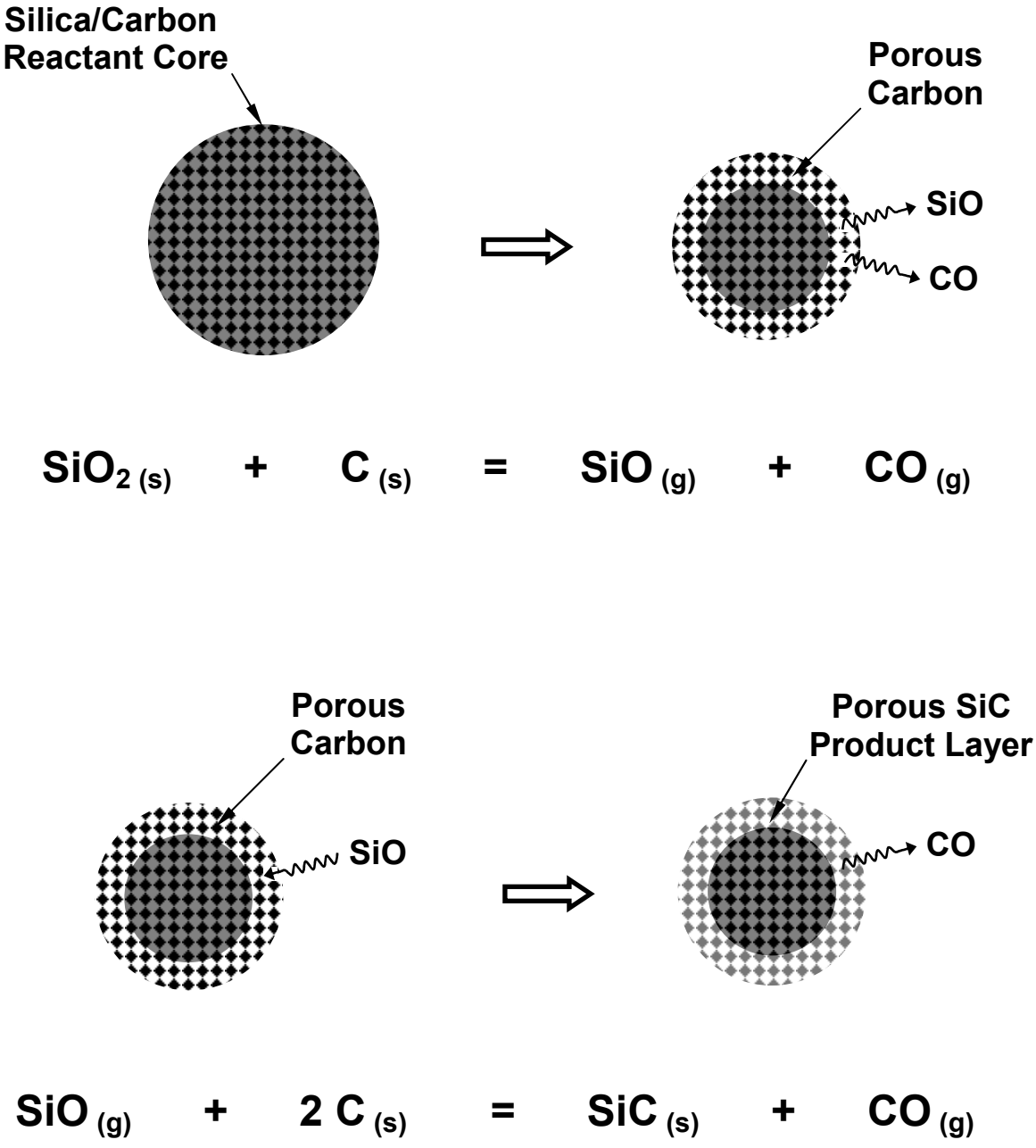

Figure 4-2-1 Illustration of a two-step reaction for the formation of SiC through carbothermal reduction in the current pyrolyzed material made from TEOS/phenolic resin mixed solution.

not be distinctly separated.

4.2.2 Identification of Volatile Deposits

Experiments were carried out to collect and analyze the volatile condensate during the reaction. The collection and analysis of the volatile deposits were important to the clarification of the reaction mechanism because the overall reaction has been proposed to be a multi-step process that involves SiO as an intermediate product of the reaction. The procedure for collecting the volatile condensate during carbothermal reduction was described in section 3.3.

After heat treatment at 1160^{o}C for 8 h, the alumina substrate surface (placed on the downstream side of the pyrolyzed material in a colder part of the furnace) was covered with a thin layer of brown material. Figure 4-2-2 is the energy dispersive X-ray spectroscopy (EDX) pattern of the alumina substrate surface before and after the vapor deposition. Before the deposition, the Al peak is seen; after the deposition, the Al peak disappears while a strong Si peak appears. (The peak of gold is from sputter coating of gold on the sample during sample preparation. Oxygen peaks were not observed because their intensities were only several hundred counts/second, which is very low compared to the Al or Si peaks intensities shown in Figure 4-2-2.) It is evident from the EDX pattern that Si-containing volatile(s) were produced during carbothermal reduction reaction.

The volatile is most likely SiO vapor because the SiO_2 and Si vapor pressure at 1160^{o}C should be quite low. In the following, the vapor pressures of SiO, as well as SiO_2 and Si, were estimated based on the thermodynamic data in the literature. According to Klinger et al.(1966), the standard free energy change for the reaction

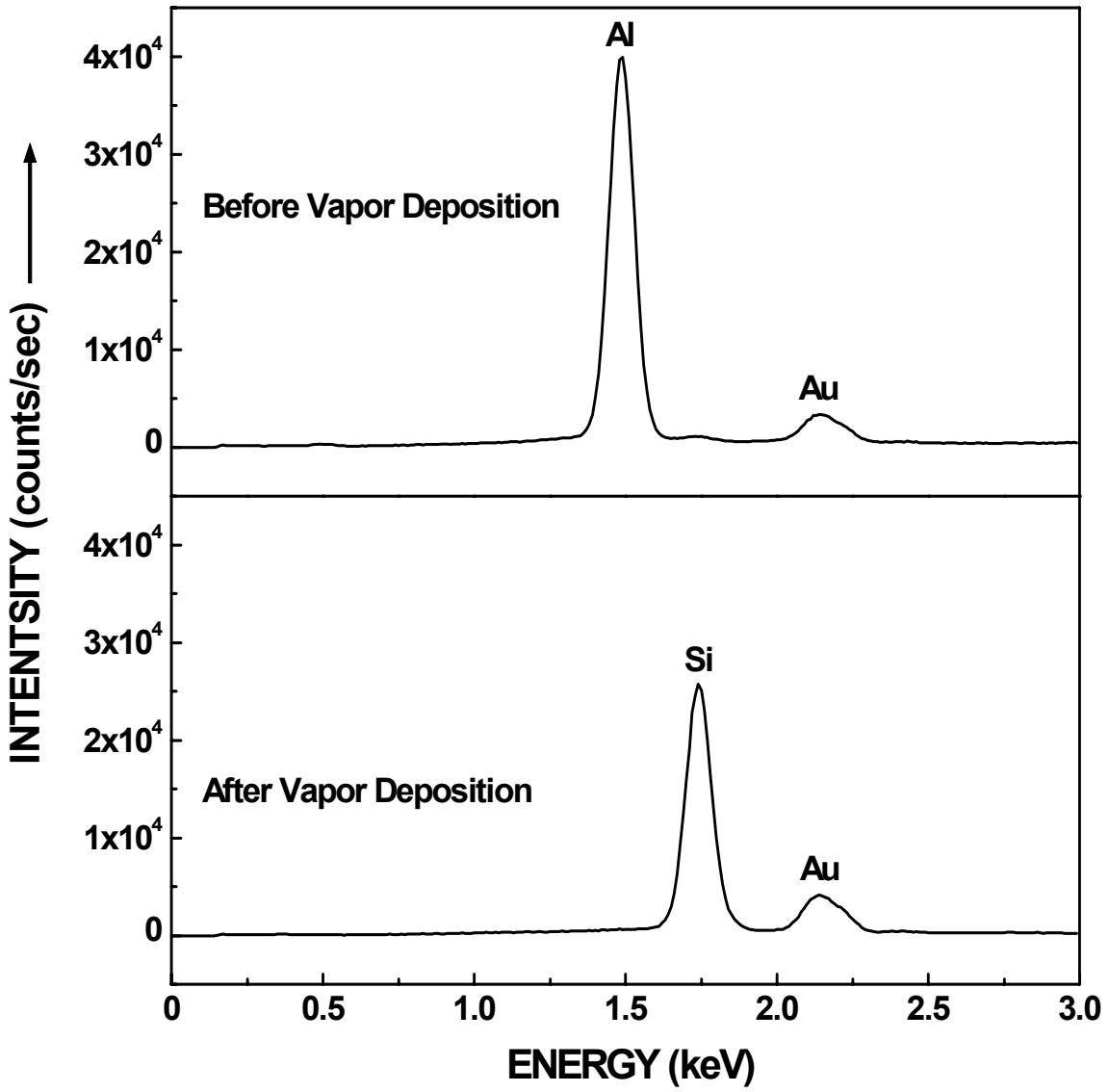

Figure 4-2-2 EDX spectra from the surface of an alumina substrate before and after a vapor deposition experiment carried out at 1160^{o}C for 8h.

$$SiC_{(s)} = C_{(s)} + Si_{(g)} \quad (4\text{-}2\text{-}3)$$

is given by:

$$\Delta G_T^0 = 499820 - 149T \text{ J/mol} \quad (4\text{-}2\text{-}4)$$

where T is in K. Therefore, the equilibrium pressure of Si vapor, P_{Si}, should be:

$$P_{Si} = P^0 \exp(-\frac{\Delta G_T^0}{RT}) \quad (4\text{-}2\text{-}5)$$

where P^0 is the standard pressure (i.e., atmosphere pressure, 101325 Pa), R is the gas constant (8.314 J/mol·K). Hence, the equilibrium Si vapor pressure at 1160°C should be:

$$P_{Si} = 101325 \times \exp[-\frac{499820 - 149 \times (1160 + 273)}{8.314 \times (1160 + 273)}] = 3.8 \times 10^{-6} \text{ Pa}$$

Similarly, the free energy change for the reaction

$$SiO_2 (\alpha\text{-quartz}) = SiO_{2\,(g)} \quad (4\text{-}2\text{-}6)$$

is given by:

$$\Delta G_T^0 = 541535 - 156T \text{ J/mol} \quad (4\text{-}2\text{-}7)$$

Therefore, the equilibrium pressure of SiO_2 vapor, P_{SiO2}, should be:

$$P_{SiO2} = P^0 \exp(-\frac{\Delta G_T^0}{RT}) \quad (4\text{-}2\text{-}8)$$

At 1160°C, the equilibrium vapor pressure of SiO_2 should be:

$$P_{SiO2} = 101325 \times \exp[-\frac{541535 - 156 \times (1160 + 273)}{8.314 \times (1160 + 273)}] = 2.5 \times 10^{-7} \text{ Pa}$$

The free energy change for the reaction

$$SiO_2(\alpha\text{-quartz}) + C_{(s)} = SiO_{(g)} + CO_{(g)} \quad (4\text{-}2\text{-}9)$$

is given by:

$$\Delta G_T^0 = 670402 - 327T \text{ J/mol} \quad (4\text{-}2\text{-}10)$$

The free energy change for

$$SiO_{(g)} + 2C_{(s)} = SiC_{(s)} + CO_{(g)} \quad (4\text{-}2\text{-}11)$$

is given by:

$$\Delta G_T^0 = -70082.0 - 5.4T \text{ J/mol} \quad (4\text{-}2\text{-}12)$$

From Equations (4-2-9), we have

$$P_{SiO} \cdot P_{CO} = (P^0)^2 \exp(-\frac{\Delta G_T^0}{RT}) \quad (4\text{-}2\text{-}13)$$

At 1160°C,

$$\frac{P_{SiO} \cdot P_{CO}}{(P^0)^2} = \exp[-\frac{670402 - 327 \times (1160 + 273)}{8.314 \times (1160 + 273)}] = 4.66 \times 10^{-8} \quad (4\text{-}2\text{-}14)$$

From Equation (4-2-11), we have

$$\frac{P_{CO}}{P_{SiO}} = \exp(-\frac{\Delta G_T^0}{RT}) \quad (4\text{-}2\text{-}15)$$

At 1160°C,

$$\frac{P_{CO}}{P_{SiO}} = \exp[-\frac{-70082.0 - 5.4 \times (1160 + 273)}{8.314 \times (1160 + 273)}] = 686 \quad (4\text{-}2\text{-}16)$$

Therefore, from Equations (4-2-14) and (4-2-16), the equilibrium vapor pressure of SiO would be:

$$P_{SiO} = 101325 \times (\frac{4.66 \times 10^{-8}}{686})^{0.5} = 0.8 \text{ Pa}$$

From the above calculation, it is clear that the equilibrium vapor pressure of SiO at 1160°C is orders of magnitude greater than that of Si and SiO_2 vapor. Therefore, SiO vapor should be the volatile species that condensed onto the alumina substrate during the experiment.

As described in section 3.3, the deposits on the tube surface in the cold zone of M11 furnace after high temperature heat treatment under vacuum were also examined by XRD analysis. The results are shown in Figure 4-2-3. Silicon (JCPDS No. 27-1402) and silica were identified in the deposits formed by condensation of the volatile formed during the reaction. The silica phase was found to be in the form of quartz (JCPDS No. 46-1405) and/or amorphous silica. (The very broad peak at 2θ of ~15-30^{o} in the two XRD patterns in Figure 4-2-3 is very similar to the peak observed in Figure 4-1-7. As noted previously, the peak location is consistent with that usually reported for amorphous silica.) Unfortunately, it was not clear why sometimes quartz was present while sometimes only amorphous silica was present.

The coexistence of Si and SiO_2 in the volatile condensate is consistent with the observations by Khalafalla and Haas (1972). As stated in section 2.2.1, they proposed hat the Si and SiO_2 in the condensates come from the dissociation of SiO at low temperature, as represented by:

$$2SiO_{(g)} \rightarrow Si_{(s)} + SiO_{2\,(s)} \qquad (4\text{-}2\text{-}17)$$

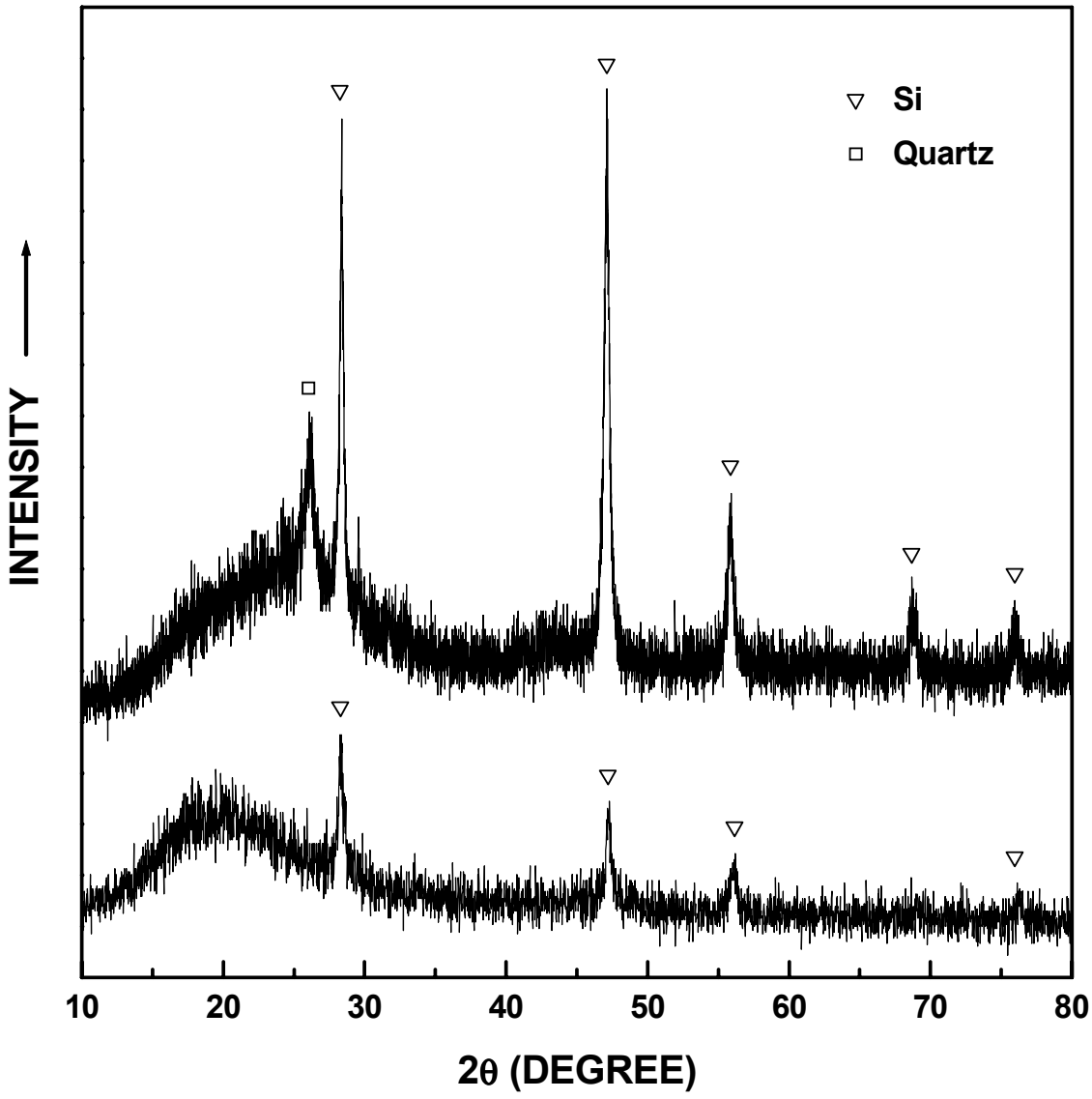

Figure 4-2-3 XRD patterns of the deposits inside the furnace tube after high temperature heat treatment under vacuum.

4.3 Reaction Kinetics of Carbothermal Reduction (CTR) Synthesis of SiC

4.3.1 Some Information about the Materials after Complete CTR

- Full Conversion Yield of CTR

Before discussing the actual kinetic data, some information about the yield and final composition after the complete carbothermal reduction reaction is presented first. Table 4-3-1 shows the full conversion yield, *Y*, or the yield when the carbothermal reduction reaction was completed for the SC8 and SC35 samples. The full conversion yield is a decimal fraction. As described in section 3.4.1, the values of full conversion yield were obtained by monitoring the yield of heat treating the pyrolyzed powders (SC8 and SC35) at 1495^{o}C for 2 h in the M11 furnace with argon flow rate of 0.7 L/min. Experiments have shown that the pyrolyzed sample went through maximum weight loss under such conditions. Further heat treatment led to grain growth while the product weight remained unchanged.

- Composition and density of the material after complete CTR

As stated in section 3.2, the total carbon contents, w_{C-Tot}^{CTR} (a decimal fraction), of the fully-converted samples (e.g., SC35-1475(2h) and SC8-1475(2h)), were obtained by the LECO combustion method. The total carbon content of sample SC8-1475(2h) is 0.6006 and the carbon content of SC35-1475(2h) is 0.3148. The SC8 sample contained a great amount of excess carbon (compared to pure SiC), while the SC35 sample had a carbon content that was almost that of stoichiometric SiC.

The fully-converted materials are assumed to be a mixture of amorphous carbon and crystalline β-SiC. (This assumption is reasonable because the samples always turn out to be carbon rich as will be shown later in section 4.5.) The weight contents of SiC

Table 4-3-1 The full conversion yield (a decimal fraction), *Y*, for the carbothermal reduction reaction of SC35 and SC8 materials.

Heat treatment condition	SC8	SC35
1495°C (2h) Run #1	0.4903	0.3296
1495°C (2h) Run #2	0.4904	0.3296
1495°C (2h) Run #3	0.4826	0.3282
1495°C (2h) Run #4	0.4851	0.3305
1495°C (2h) Run #5	NA	0.3291
1495°C (2h) Run #6	NA	0.3301
Average yield	0.4879	0.3295
Standard deviation	0.0042	0.0009

(w_{SiC}^{CTR}) and excess carbon (w_{C-free}^{CTR}) in the fully-converted material could also be calculated. After full CTR reaction, the total silicon content, w_{Si}^{CTR}, in the materials is:

$$w_{Si}^{CTR} = 1 - w_{C-Tot}^{CTR} \tag{4-3-1}$$

Therefore,

$$w_{SiC}^{CTR} = \frac{1 - w_{C-Tot}^{CTR}}{28} \times 40 \tag{4-3-2}$$

$$w_{C-free}^{CTR} = 1 - w_{SiC}^{CTR} \tag{4-3-3}$$

In addition to the weight fraction, the volume fraction of SiC and free carbon were estimated for the SC35 and SC8 fully-converted materials. Based on the considerations in section 4.1.9, the true density of the free carbon (ρ_C) was crudely

estimated to be 2 g/cm^3. Sacks (1999) determined the density of nanocrystalline SiC to be $\rho_{SiC} \approx 3.2$ g/cm^3. The volume fractions of SiC, v_{SiC}^{CTR}, and free carbon, v_{C-free}^{CTR} (where $v_{SiC}^{CTR} + v_{C-free}^{CTR} = 1$) were obtained by:

$$v_{SiC}^{CTR} = \frac{w_{SiC}^{CTR} / \rho_{SiC}}{w_{SiC}^{CTR} / \rho_{SiC} + w_{C-free}^{CTR} / \rho_C} \tag{4-3-4}$$

$$v_{C-free}^{CTR} = 1 - v_{SiC}^{CTR} \tag{4-3-5}$$

The solid density of the SC35 and SC8 fully-converted materials could also be estimated. Suppose that the density after complete CTR reaction is ρ_{CTR}. The rule of mixtures is:

$$\frac{1}{\rho_{CTR}} = \frac{w_{SiC}^{CTR}}{\rho_{SiC}} + \frac{w_{C-free}^{CTR}}{\rho_C} \tag{4-3-6}$$

Table 4-3-2 summarizes the information about the composition (by weight and by volume) and the density for SC35 and SC8 materials after the complete carbothermal reduction reaction. The information for the SC42 fully-converted material is also listed in the table. (The SC42 samples have very similar C/Si molar ratio to the SC35 samples).

4.3.2 Weight Loss Kinetics

4.3.2.1 Correction for Moisture Adsorption and Powder Blown-off

After the carbothermal reduction heat treatment, the sample weight change and the moisture content were obtained. The amount of powder that was used for correction of the powder blown off the substrate when gas was backfilled into the furnace was also determined. The following parameters were introduced to analyze the weight loss data:

W_0 weight of pyrolyzed sample before carbothermal reduction reaction

Table 4-3-2 Information about composition and density of SC8-1475(2h), SC35-1475(2h) and SC42-1495(2h) fully-converted materials.

Sample	SC8-1475(2h)	SC35-1475(2h)	SC42-1495(2h)
Carbon weight fraction w_{C-Tot}^{CTR}	0.6006	0.3148	0.3107
Si weight fraction w_{Si}^{CTR}	0.3994	0.6852	0.6893
C/Si molar ratio $x_{C/Si}^{CTR}$	3.51	1.07	1.05
SiC weight fraction w_{SiC}^{CTR}	0.5706	0.9789	0.9847
Free carbon weight fraction w_{C-free}^{CTR}	0.4294	0.0211	0.0153
SiC volume fraction v_{SiC}^{CTR}	0.45	0.97	0.98
Free carbon volume fraction v_{C-free}^{CTR}	0.55	0.03	0.02
Calculated density * (g/cm^3)	2.54	3.16	3.17

Note:

* The densities and volume fractions were calculated using a SiC true density of 3.2 g/cm^3 and a carbon true density of 2 g/cm^3.

W weight of powder after carbothermal reduction reaction (W_0 and W contain the weight of moisture absorbed by the powder)

y_n nominal fractional yield for the carbothermal reduction reaction without moisture correction and blown-off correction; y_n is defined as:

$$y_n = \frac{W}{W_0} \tag{4-3-7}$$

The values of y_n for each heat-treated sample in the kinetic study are given in Appendix B.

To correct the effect of moisture adsorption, the following parameters are introduced:

$w_{m\text{-}pyro}$ weight fraction of moisture in the pyrolyzed sample before carbothermal reduction reaction; $w_{m\text{-}pyro}$ is a decimal fraction; the values of $w_{m\text{-}pyro}$ for each sample are given in Appendix B

$w_{m\text{-}CTR}$ weight fraction of moisture in the sample after carbothermal reduction reaction; $w_{m\text{-}pyro}$ is a decimal fraction; the values of $w_{m\text{-}CTR}$ for each sample are listed in Appendix B

y_m the yield for carbothermal reduction reaction after correction of moisture adsorption; y_m is obtained by:

$$y_m = \frac{W(1-w_{m-CTR})}{W_0(1-w_{m-pyro})} = \frac{y_n(1-w_{m-CTR})}{(1-w_{m-pyro})} \tag{4-3-8}$$

$X_{WL\text{-}m}$ fractional weight loss for the carbothermal reduction after correction of moisture adsorption. $X_{WL\text{-}m}$ is obtained from:

$$X_{WL-m} = \frac{1-y_m}{1-Y} \tag{4-3-9}$$

Y full conversion yield for carbothermal reduction as defined in section 4.3.1; considering experiment error, for the SC35 pyrolyzed sample (initial C/Si molar ratio = 2.4), the average Y value was taken as 0.33; for the SC8 pyrolyzed sample (initial C/Si molar ratio = 4.6), the average Y value was taken as 0.49.

Of all these parameters listed, W_0, W, y_n, $w_{m\text{-}pyro}$, $w_{m\text{-}CTR}$ came from the individual carbothermal reduction experiments (refer to Chapter III for procedure of determining W_0, W, $w_{m\text{-}pyro}$ and $w_{m\text{-}CTR}$). Substituting y_m from Equation (4-3-8) into Equation (4-3-9), we have:

$$X_{WL-m} = \frac{1}{1-Y} \cdot [1 - \frac{y_n (1 - w_{m-CTR})}{(1 - w_{m-pyro})}] = \frac{(1 - w_{m-pyro}) - y_n (1 - w_{m-CTR})}{(1-Y)(1 - w_{m-pyro})}$$

Therefore,

$$X_{WL-m} = \frac{1 + (y_n \cdot w_{m-CTR}) - y_n - w_{m-pyro}}{(1-Y)(1 - w_{m-pyro})} \qquad (4\text{-}3\text{-}10)$$

If the effect of powder being swept away by flowing gas (Ar) is also considered, more parameters are introduced as follows:

w_b the amount of powder blown off the substrate when gas was introduced into the furnace; w_b is a decimal fraction

y_{mb} yield for carbothermal reduction after the effects of moisture adsorption and powder blow-off are corrected

$X_{WL\text{-}mb}$ fractional weight loss for carbothermal reduction after the effects of moisture adsorption and powder blow-off are corrected

The values of w_b were determined in a series of blown-off tests, whose results are shown in Table 4-3-3. The average fraction of powder blown off the substrate for the SC8 pyrolyzed sample is much larger than that for the SC35 pyrolyzed sample. Two possible reasons for the difference are suggested: (1) The M11 furnace was back-filled with argon gas in a more controlled manner for the SC35 samples. The heat treatments for the kinetics studies were carried out first with the SC8 samples and then with the SC35 samples. At the time of the SC8 heat treatments, the author was not fully cognizant of the problem of powder blow-off. The gas inlet valve was opened relatively quickly when the SC8 samples were heat treated, i.e., compared to the experiments carried out later with the SC35 samples. Hence, it is likely that significantly more powder was blown-off in the SC8 experiments for this reason. (2) Differences in particle size distribution might be another contributing

factor for the difference in the amount of blown-off powder for the SC8 and SC35 samples. The results in Table 4-1-5, Figure 4-1-25, and Figure 4-1-28 indicated that the SC35 pyrolyzed particles apparently had larger sizes compared to the SC8 pyrolyzed particles. Hence, powder blow-off may have been less likely with the larger (and heavier) SC35 particles. (It should be noted that the aforementioned table and figures provide a comparison of samples which were prepared for particle size analysis using the sonication method. A direct comparison was not available for samples prepared by the tumbling method. Therefore, it cannot be concluded with complete certainty that the *starting* particle sizes were larger for the SC35 pyrolyzed sample.)

Table 4-3-3 Weight fractions of powder blown off from substrate (w_b) for the SC35 and SC8 pyrolyzed materials in the blow-off tests.

Test #	SC35	SC8
1	0.0106	0.0352
2	0.0088	0.0302
3	0.0131	0.0199
4	0.0157	0.0247
5	0.0027	0.0200
6	NA	0.0225
7	NA	0.0203
Average	0.0102	0.0247
Standard deviation	0.0049	0.0059

Similar to Equation (4-3-10), the following equation was obtained to calculate the fractional weight loss with the effects of both moisture adsorption and powder blown-off taken into account:

$$X_{WL-mb} = \frac{1 - y_{mb}}{1 - Y} = \frac{1 + (y_n \cdot w_{m-CTR}) - y_n - w_{m-pyro} - w_b}{(1 - Y)(1 - w_{m-pyro} - w_b)} \qquad (4\text{-}3\text{-}11)$$

In the following part of this thesis, unless otherwise specified, the term "fractional weight loss" (X_{WL}) always represents the fractional weight loss value after correction for both moisture adsorption and powder blown-off (i.e., $X_{WL} \equiv X_{WL\text{-}mb}$). The values of $X_{WL\text{-}mb}$ are given in Appendix B for all the samples heat treated for the kinetics studies.

4.3.2.2 Fractional Weight Loss Data

Figures 4-3-1 and 4-3-2 show the fractional weight loss after moisture correction ($X_{WL\text{-}m}$) versus reaction time for SC35 and SC8 samples, respectively, that were heat treated at various temperatures. Plots of fractional weight loss after both moisture correction and correction for blown-off powder ($X_{WL\text{-}mb}$) versus reaction time for the same samples are shown by Figures 4-3-3 and 4-3-4, respectively. The curves of fractional weight loss vs. time (sometimes referred to as "conversion curves") shift down slightly after the blown-off correction.

The fractional weight loss vs. reaction time curves for both SC35 and SC8 series show deccelatory shape, i.e., the reaction rate was fastest at the beginning of the reaction and slowed down as the reaction proceeded As expected, the reaction rate increased as reaction temperature was increased. (No incubation stage is observed in the conversion curves.) For the SC8 series (initial C/Si molar ratio = 4.6), the reaction was ~94% complete after heat treatment at 1250^{o}C for 16 h (Figure 4-3-4). For the SC35 series

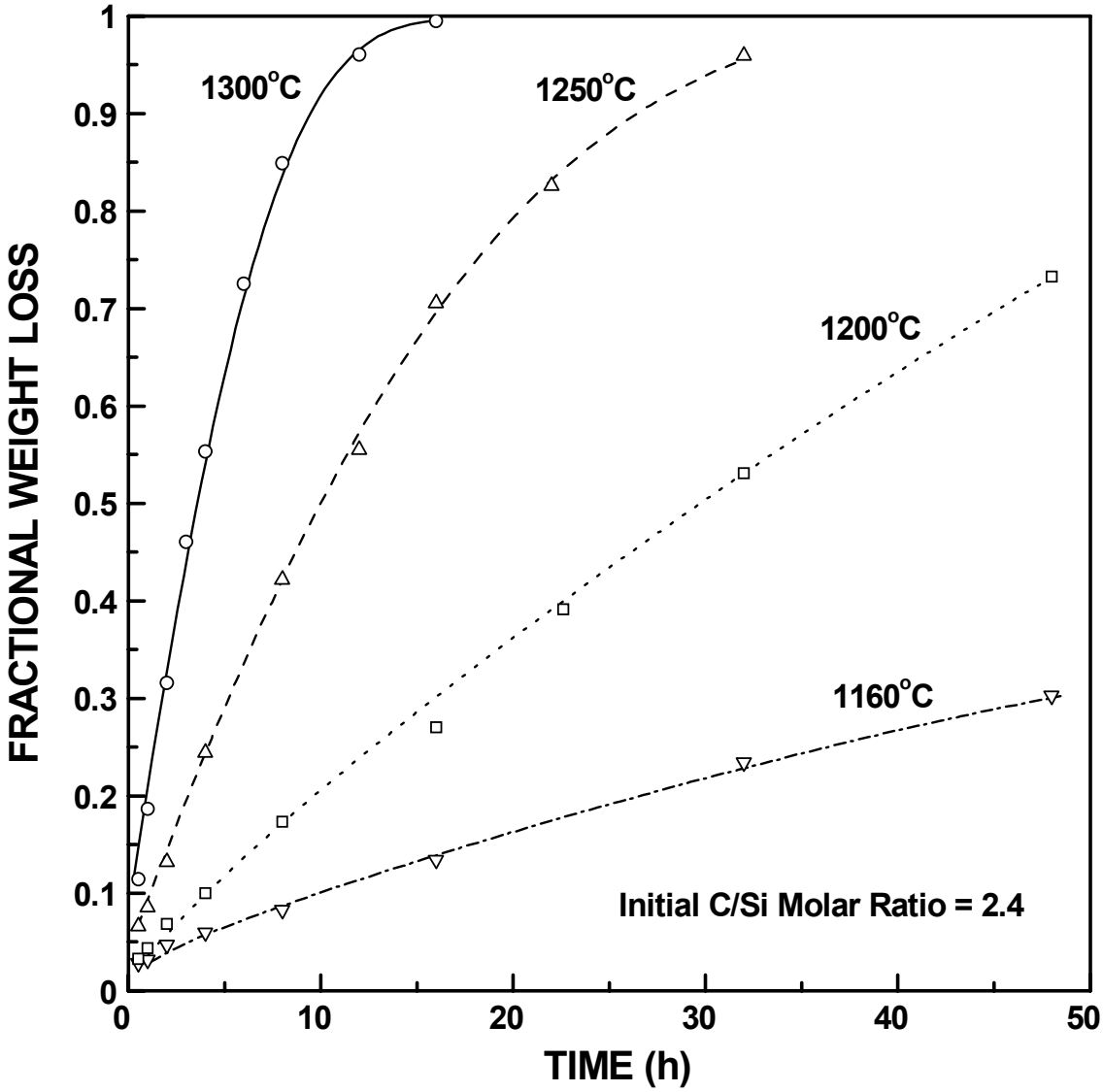

Figure 4-3-1 Plots of fractional weight loss after correction of the moisture adsorption effect ($X_{WL\text{-}m}$) vs. reaction time for the SC35 samples (initial C/Si molar ratio = 2.4) which were heat treated at the indicated temperatures.

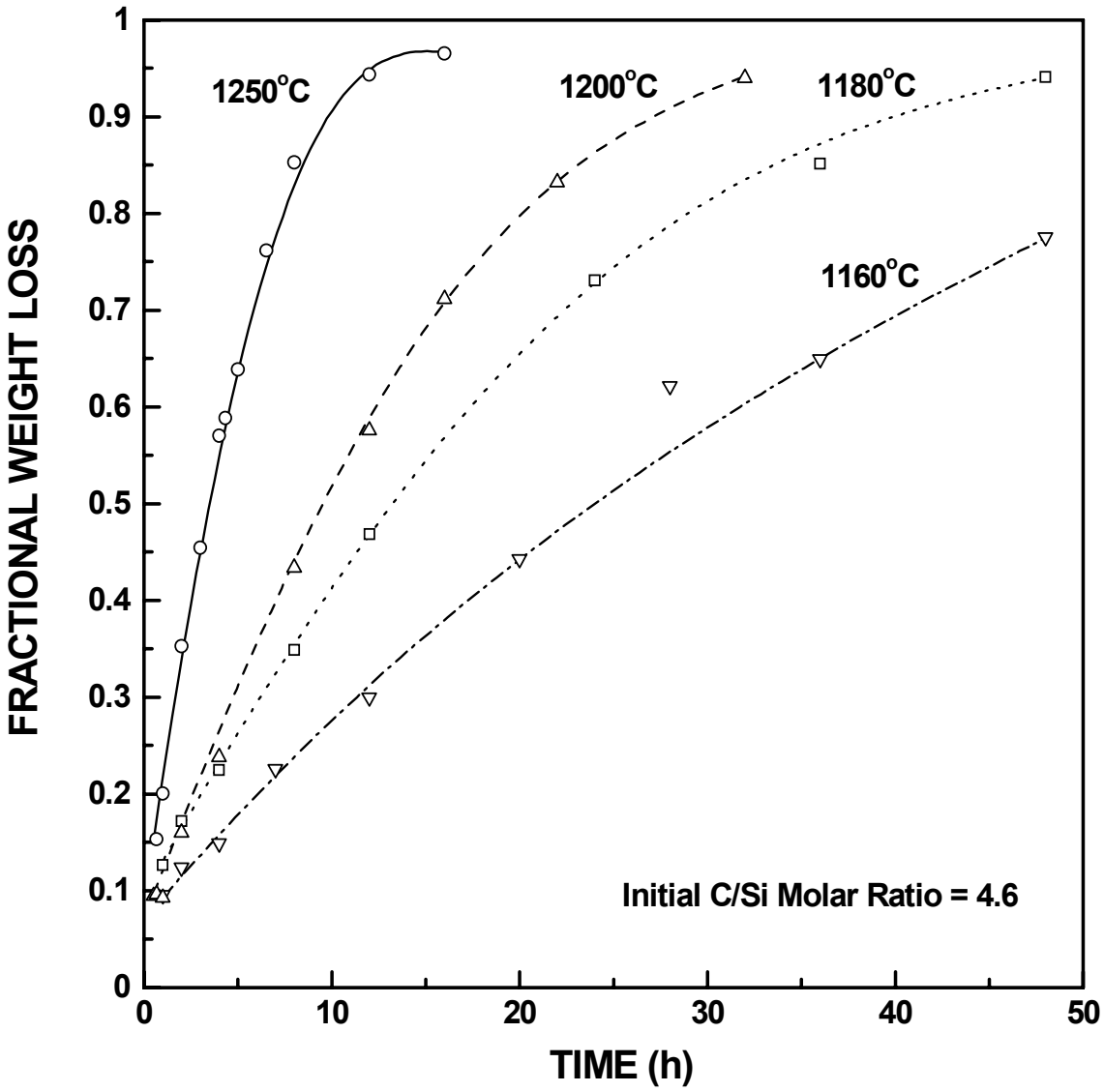

Figure 4-3-2 Plots of fractional weight loss after correction of the moisture adsorption effect ($X_{WL\text{-}m}$) vs. reaction time for the SC8 samples (initial C/Si molar ratio = 4.6) which were heat treated at the indicated temperatures.

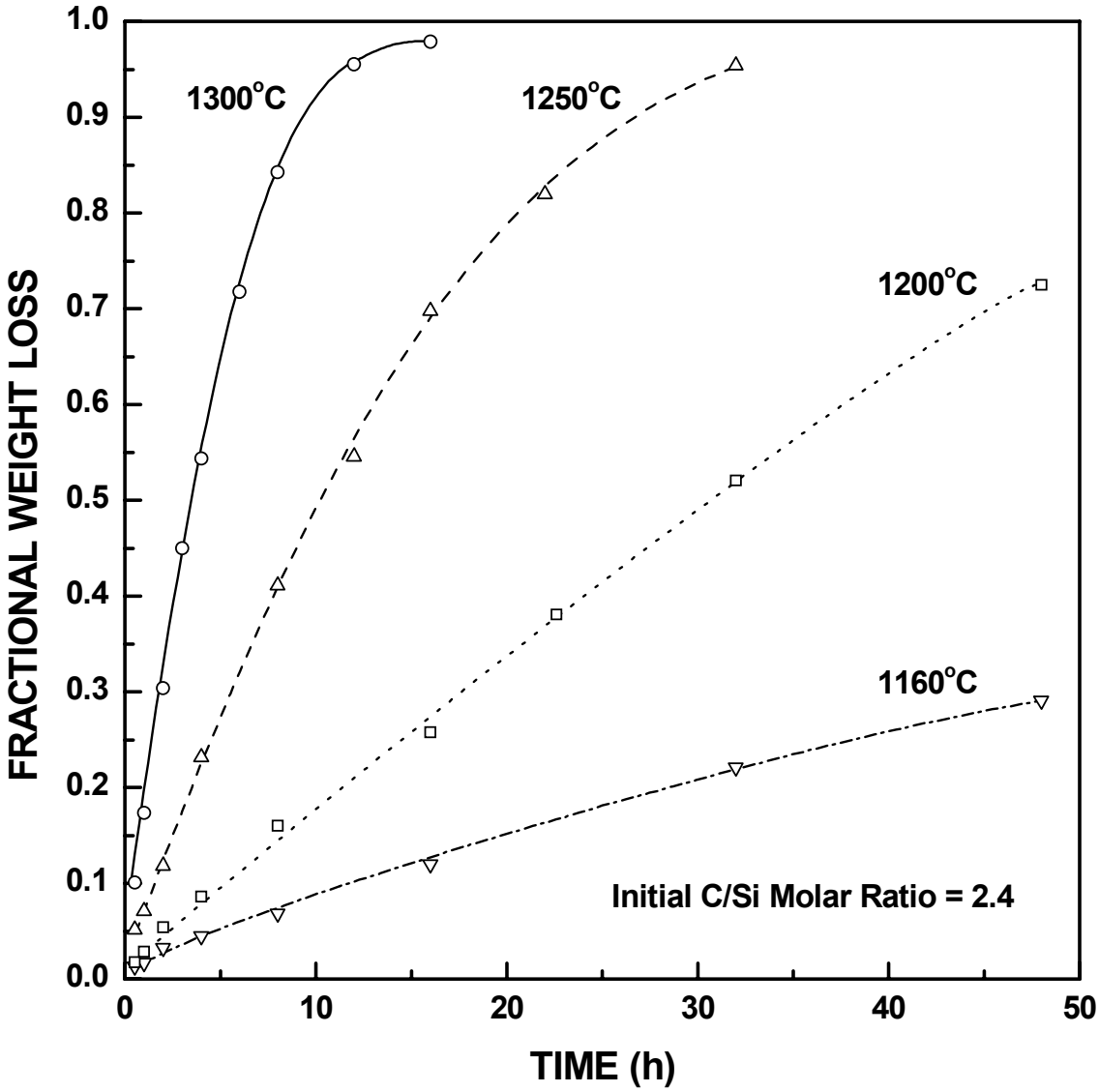

Figure 4-3-3 Plots of fractional weight loss after correction of moisture adsorption and blown-off powder ($X_{WL\text{-}mb}$) vs. reaction time for the SC35 samples (initial C/Si molar ratio = 2.4) which were heat treated at the indicated temperatures.

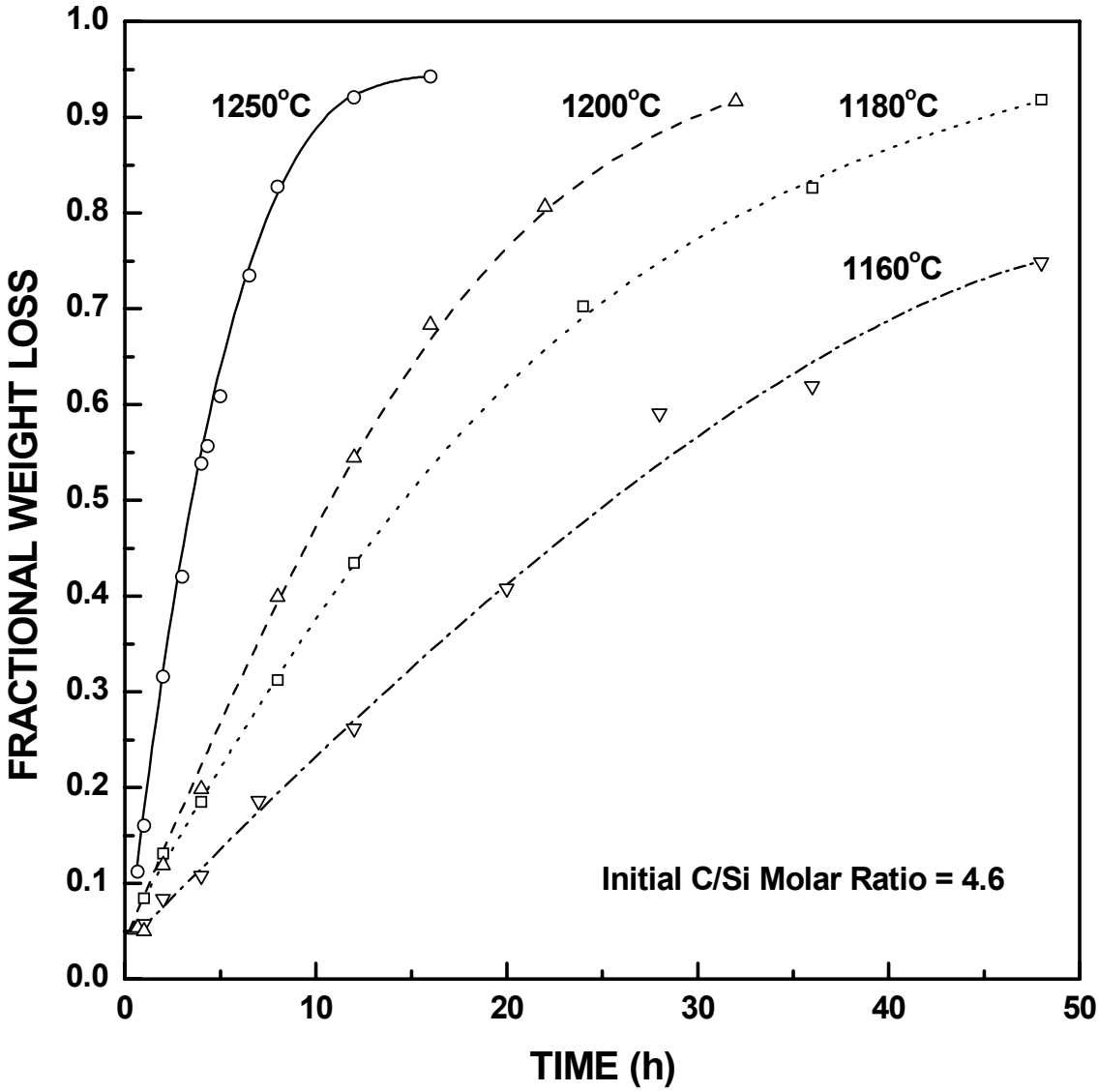

Figure 4-3-4 Plots of fractional weight loss after correction of moisture adsorption and blown-off powder ($X_{WL\text{-}mb}$) vs. reaction time for the SC8 samples (initial C/Si molar ratio = 4.6) which were heat treated at the indicated temperatures.

(initial C/Si molar ratio = 2.4), the reaction was ~98% complete after heat treatment at 1300°C for 16 h (Figure 4-3-3).

4.3.2.3 Fitting of Weight Loss Data to Different Kinetic Models

To study the reaction kinetics, the fractional weight loss data was fitted to different kinetic models for solid-state reaction. In the current study, unless specified otherwise, the fractional weight loss, X_{WL} (in most cases, $X_{WL} \equiv X_{WL\text{-}mb}$), was used as the extent of reaction for analyzing weight loss data.

- Interface-controlled "shrinking-core" model

Among all the models, the experimental data was found to exhibit the best fitting to the interface-controlled "shrinking-core" model. As stated in Chapter II, the mathematical expression of this model is:

$$1-(1-X_{WL})^{1/3} = k_{PB}t \qquad (4\text{-}3\text{-}12)$$

in which X_{WL} is fractional weight loss and k_{PB} is the reaction rate constant. Figure 4-3-5 and Figure 4-3-6 are plots of the value for the left side of Equation (4-3-12) vs. reaction time t for the SC35 and SC8 samples, respectively. The data was corrected for moisture adsorption only (i.e., $X_{WL} \equiv X_{WL\text{-}m}$). Figures 4-3-7 and 4-3-8 show the corresponding plots using the data that was corrected for both moisture adsorption and powder blown-off effects (i.e., $X_{WL} \equiv X_{WL\text{-}mb}$). There is not much difference between those two types of plots for the SC35 series. However, for the SC8 series, the fitted lines move to significantly lower values after correction for blown-off powder. This indicates a better quality of the fitting because Equation (4-3-12) requires that the data intercept the origin (i.e., the fractional weight loss X_{WL} should equal zero when the time is zero).

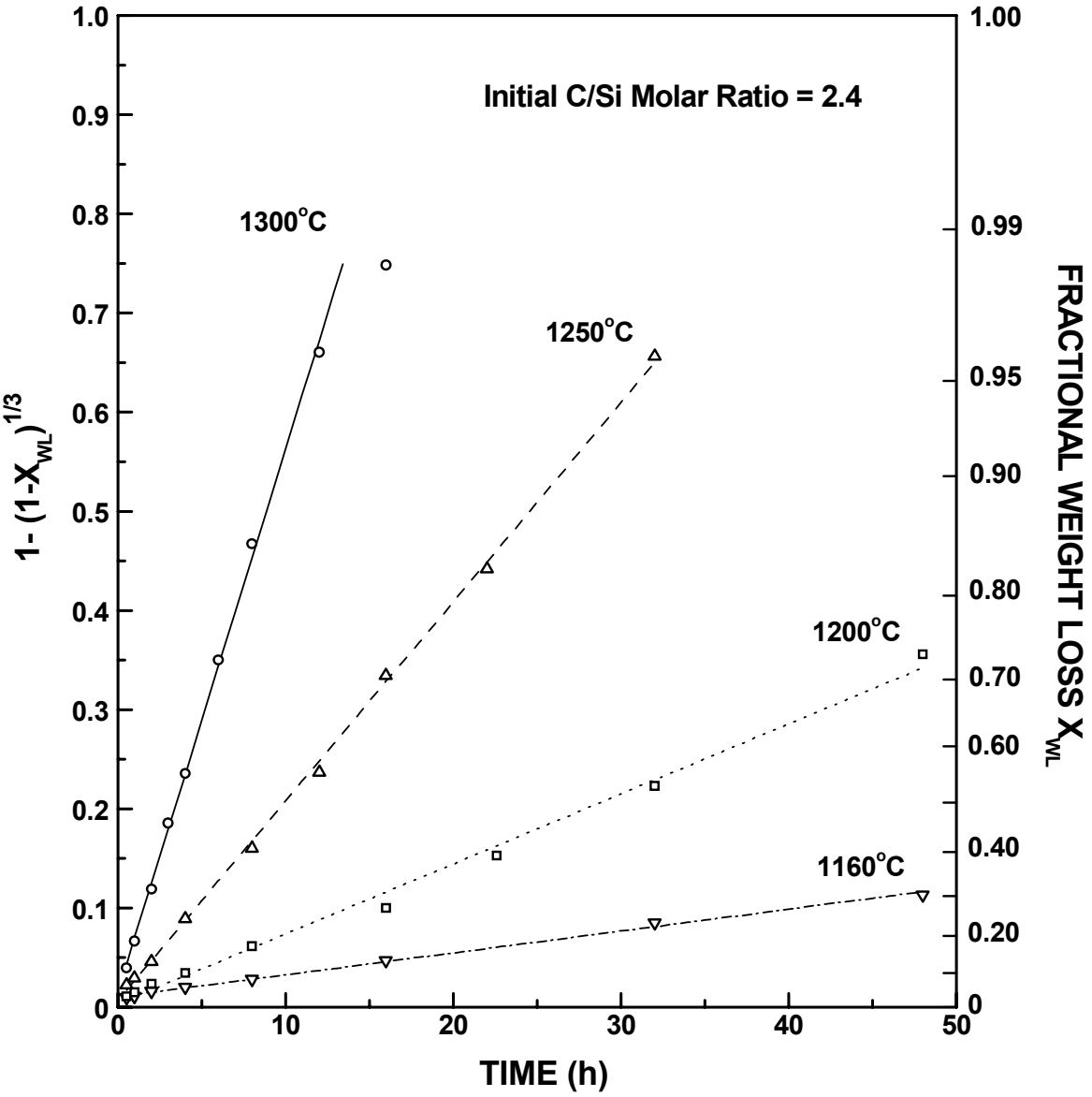

Figure 4-3-5 Plots in which the weight loss kinetic data after correction of the moisture adsorption is fit to the equation of the interface-controlled "shrinking-core" model for the SC35 series (initial C/Si molar ratio = 2.4).

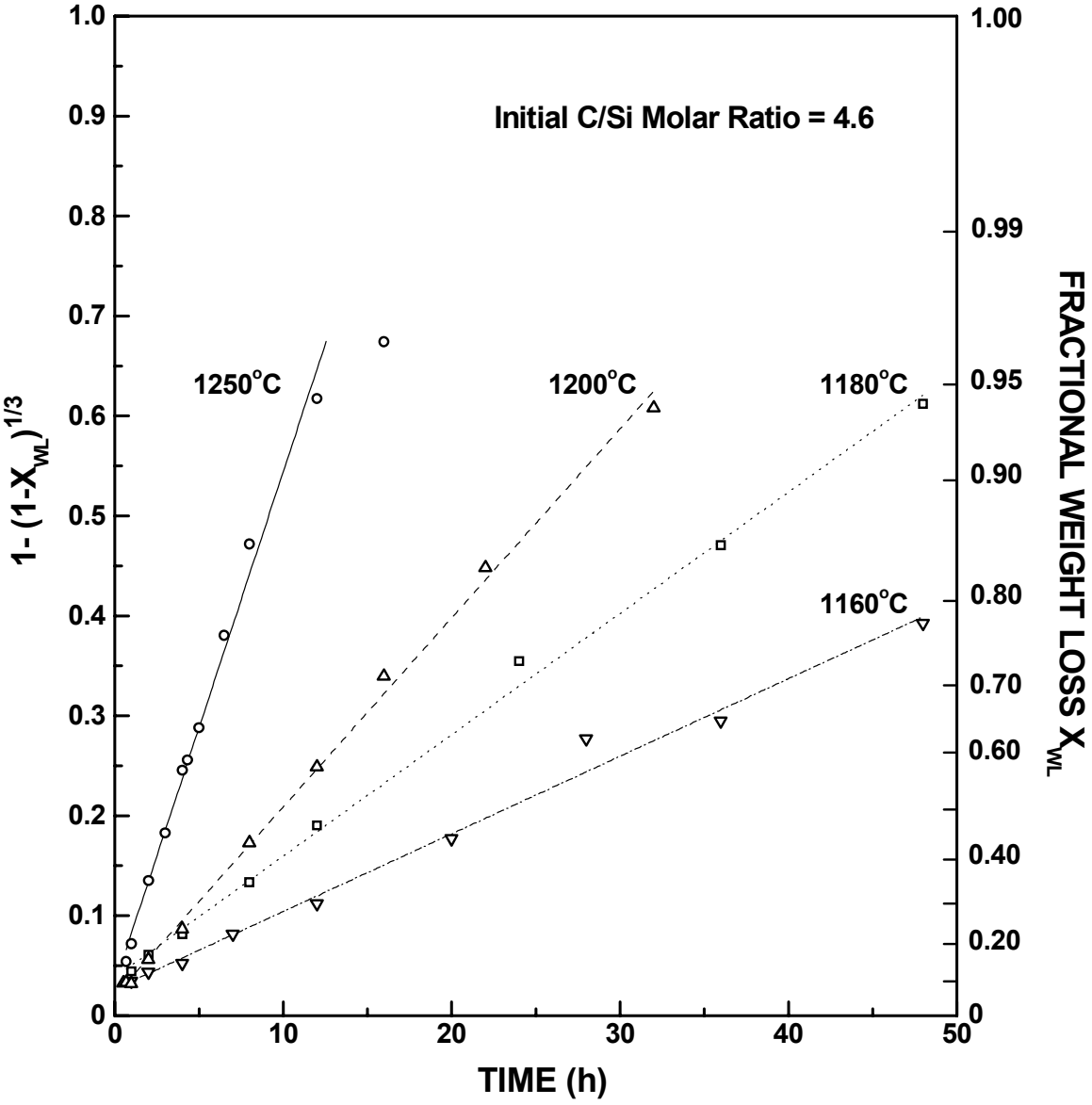

Figure 4-3-6 Plots in which the weight loss kinetic data after correction of the moisture adsorption is fit to the equation of the interface-controlled "shrinking-core" model for the SC8 series (initial C/Si molar ratio = 4.6).

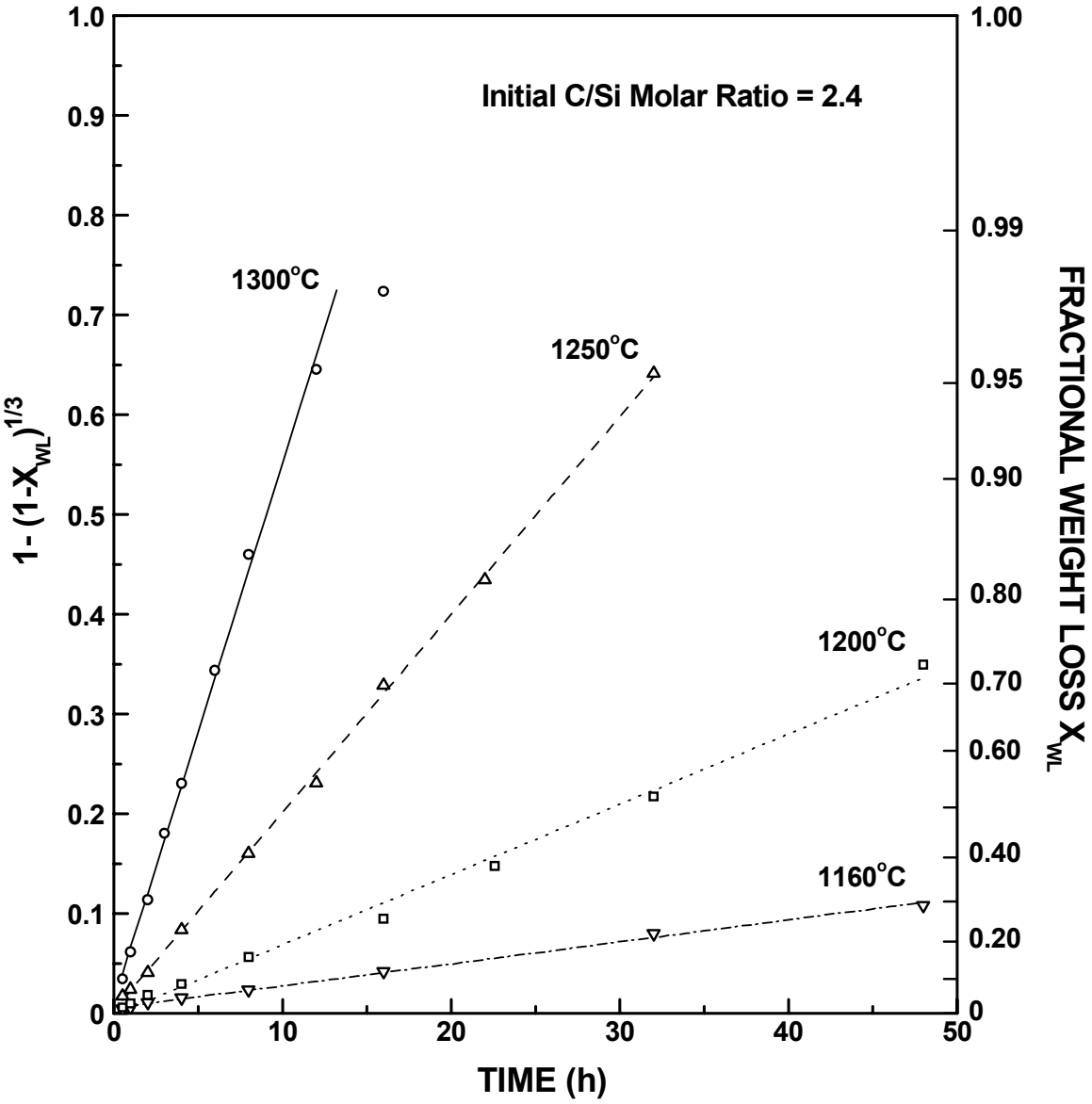

Figure 4-3-7 Plots in which the weight loss kinetic data after correction of the moisture adsorption and blown-off powder is fit to the equation of the interface-controlled "shrinking-core" model for the SC35 series (initial C/Si molar ratio = 2.4).

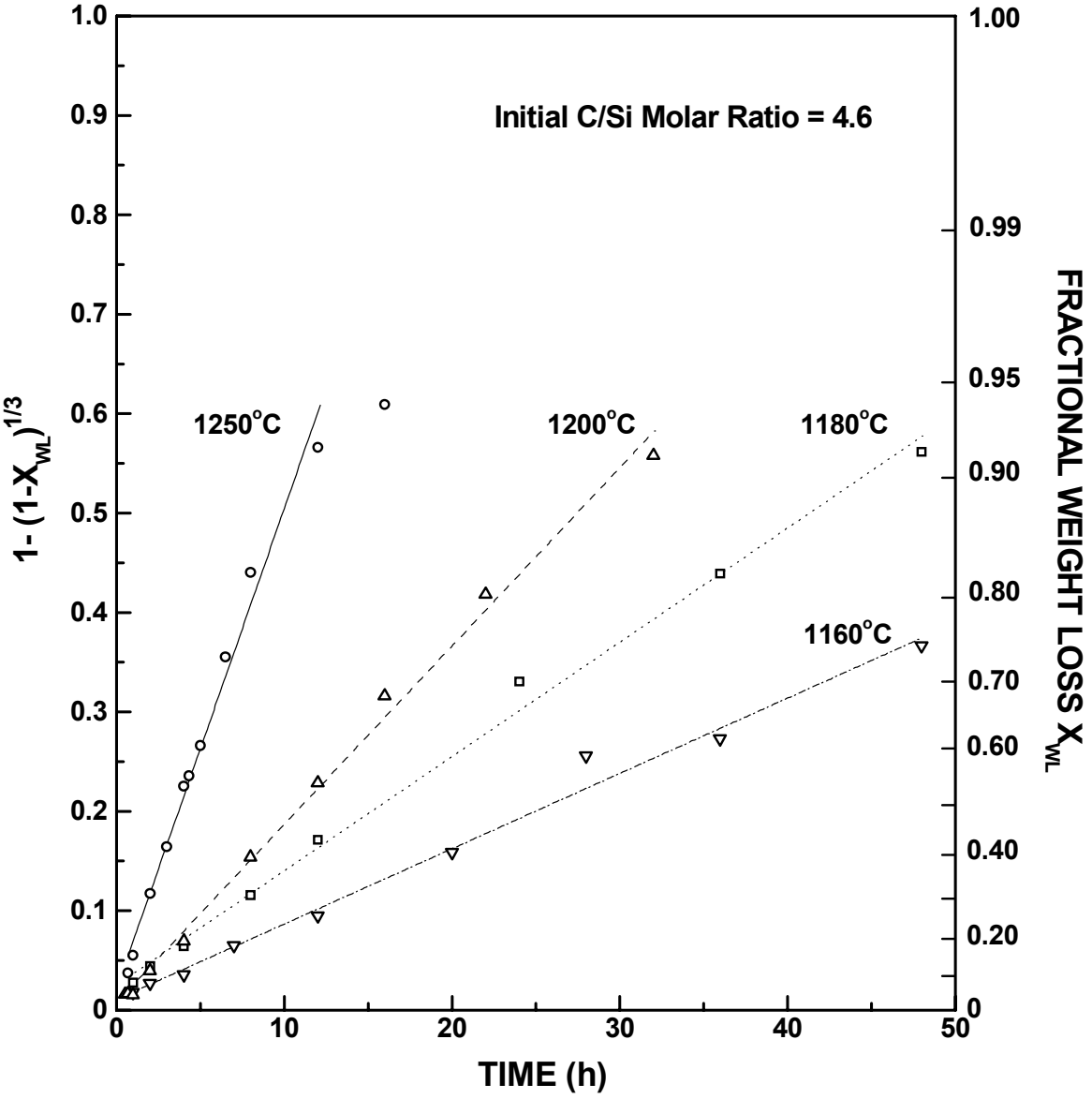

Figure 4-3-8 Plots in which the weight loss kinetic data after correction of the moisture adsorption and blown-off powder is fit to the equation of the interface-controlled "shrinking-core" model for the SC8 series (initial C/Si molar ratio = 4.6).

For both SC8 and SC35 sample series, as seen in the fitted plots, a good linear relationship is observed between $1 - (1 - X_{WL})^{1/3}$ and the reaction time t for most of the reaction. Linear fits based on the least-squares method were performed for each sample series (SC35 and SC8) at each temperature (e.g., 1160°C) on the data pairs of (y_i, x_i) in which y_i is $1 - (1 - X_{WL})^{1/3}$ and x_i is reaction time t. The fitted slope is the reaction rate constant, k_{PB}, at different temperatures. The values of k_{PB}, as well as the linear correlation coefficient r_L values, were obtained from the LINEST function of Microsoft® Excel 2002. They are listed in Tables 4-3-4 and 4-3-5 for the SC35 and SC8 data, respectively. The reaction activation energy was also obtained by fitting the rate constant data (k_{PB}) at different temperatures to the Arrhenius equation. The results are also shown in Table 4-3-4 and 4-3-5. A detailed discussion of the activation energy will be given later in this chapter.

- Nucleation-and-growth model

In addition to the interface-controlled "shrinking-core" model, the weight loss data also fits the nucleation-and-growth model reasonably well. As described in section 2.3.3.1, the mathematical expression for the nucleation-and-growth model is:

$$-\ln(1 - X_{WL}) = (k_{NG}t)^m \tag{4-3-13}$$

or

$$\ln[-\ln(1 - X_{WL})] = m \ln k_{NG} + m \ln t \tag{4-3-14}$$

in which X_{WL} is fractional weight loss, k_{NG} is the reaction rate constant, and m is the exponent parameter.

Figures 4-3-9 and 4-3-10 are plots showing the fit of the weight loss data (X_{WL} = $X_{WL\text{-}mb}$) to Equation (4-3-14) for the SC35 and SC8 data, respectively. Except for the early

Table 4-3-4 The reaction rate constants k_{PB} and the activation energy for the carbothermal reduction reaction for SC35 samples.

Temperature (^oC)	k_{PB} (h^{-1})	r_L	Fitting range for time t	Fitting range for X_{WL}
1160	$(2.21 \pm 0.05) \times 10^{-3}$	0.9982	0.5 - 48 h	0.0132-0.2909
1200	$(7.04 \pm 0.21) \times 10^{-3}$	0.9969	0.5 - 48 h	0.0178-0.7249
1250	$(19.83 \pm 0.20) \times 10^{-3}$	0.9996	0.5 - 32 h	0.0516-0.9539
1300	$(53.94 \pm 1.00) \times 10^{-3}$	0.9990	0.5 - 12 h	0.1005-0.9554
Reaction activation energy E (kJ/mol)		423 ± 19		

Table 4-3-5 The reaction rate constants k_{PB} and the activation energy for the carbothermal reduction reaction for SC8 samples.

Temperature (^oC)	k_{PB} (h^{-1})	r_L	Fitting range for time t	Fitting range for X_{WL}
1160	$(7.57 \pm 0.29) \times 10^{-3}$	0.9947	1 - 48 h	0.0513-0.7458
1180	$(11.50 \pm 0.33) \times 10^{-3}$	0.9972	1 - 48 h	0.0800-0.9157
1200	$(17.94 \pm 0.56) \times 10^{-3}$	0.9971	1 - 32 h	0.0455-0.9138
1250	$(48.34 \pm 1.96) \times 10^{-3}$	0.9935	0.67 - 12 h	0.1078-0.9181
Reaction activation energy E (kJ/mol)		375 ± 3		

Note: The results in Tables 4-3-4 and 4-3-5 were obtained by fitting the kinetic data (after correction for moisture adsorption and blown-off powder, i.e., $X_{WL} = X_{WL\text{-}mb}$) to the interface-controlled "shrinking-core" model. The linear correlation coefficients r_L and the ranges of fitting (time and X_{WL} values) for the carbothermal are also given in the tables.

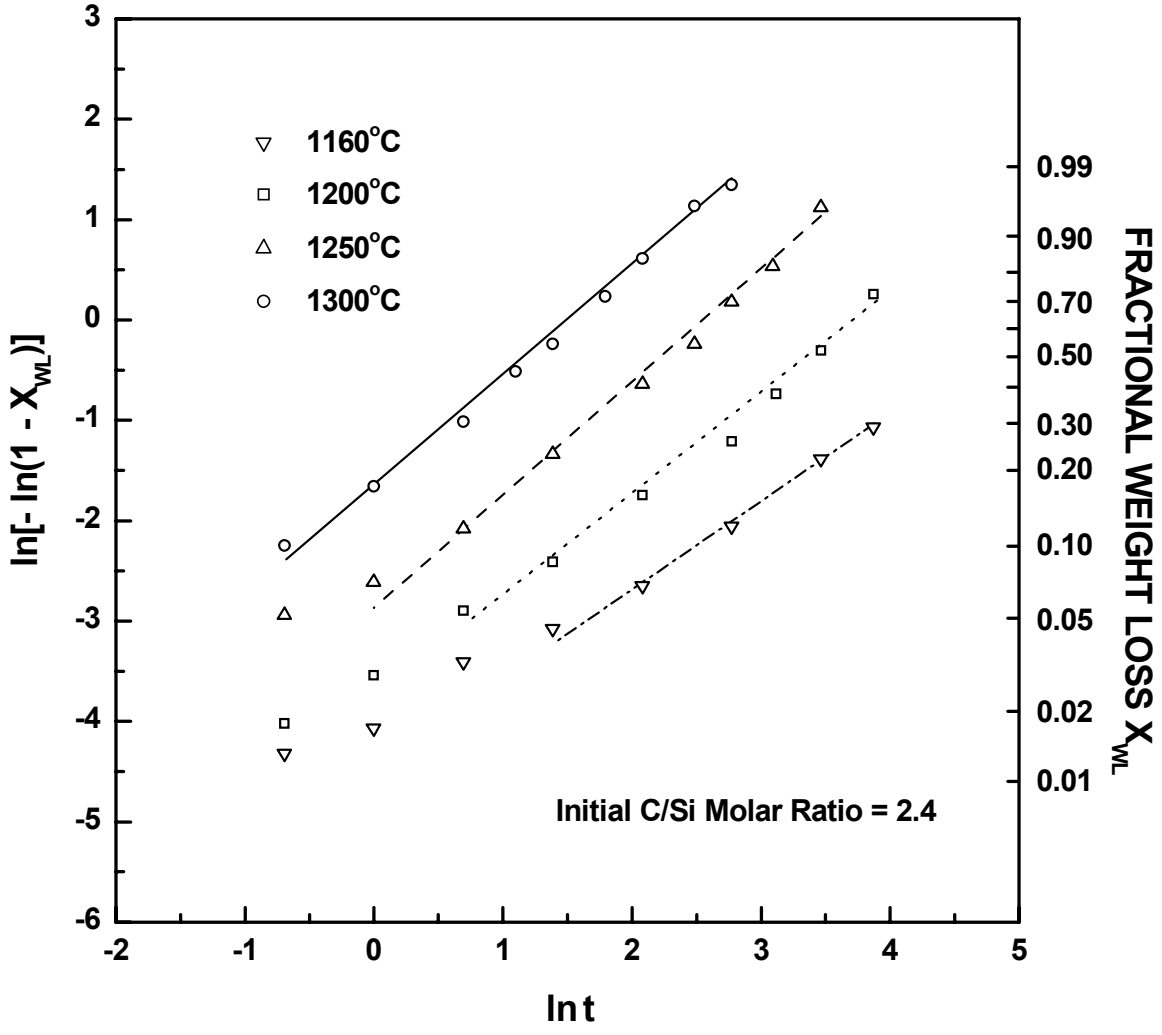

Figure 4-3-9 Plots in which the weight loss kinetic data after correction of the moisture adsorption and blown-off powder is fit to the equation of the nucleation-and-growth model for the SC35 series (initial C/Si molar ratio = 2.4); reaction time *t* is in hour.

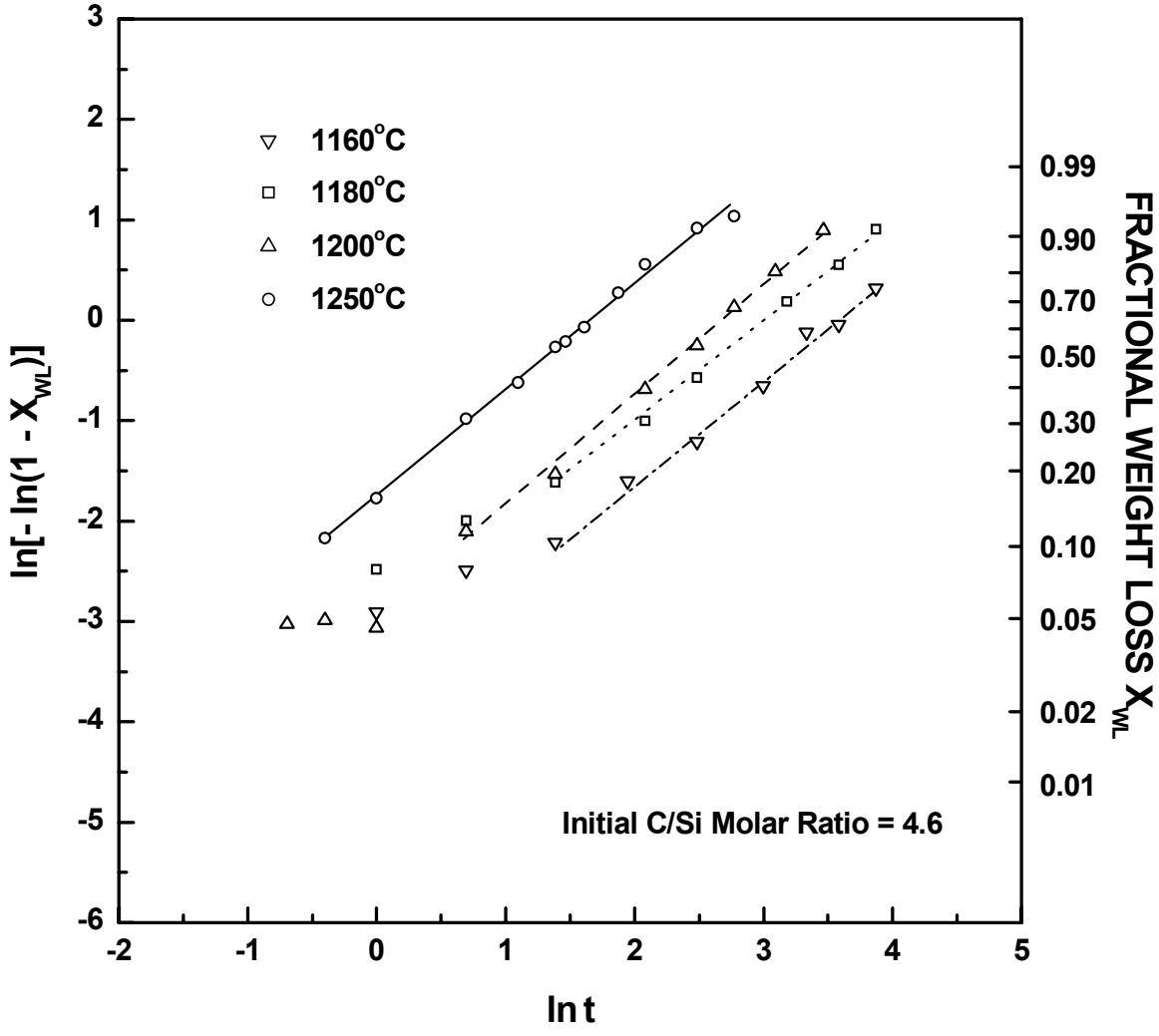

Figure 4-3-10 Plots in which the weight loss kinetic data after correction of the moisture adsorption and blown-off powder is fit to the equation of the nucleation-and-growth model for the SC8 series (initial C/Si molar ratio = 4.6); reaction time *t* is in hour.

stage (i.e., X_{WL} < ~0.10), a linear relationship is exhibited between ln[– ln(1–X_{WL})] and ln t. To obtain the exponent parameter m and the rate constant k_{NG}, linear fitting based on the least-squares method was performed for each sample series (SC35 and SC8) at each temperature on the data pairs (y_i, x_i), in which y_i is $\ln[-\ln(1-X_{WL})]$ and x_i is $\ln t$. The slope of the fitted line is the exponent parameter m and the y intercept is $m \ln k_{NG}$. Tables 4-3-6 and 4-3-7 list the m and k_{NG} values calculated from the fitted results for the SC35 and SC8 data, respectively. The reaction activation energy, obtained by fitting the rate constant data to the Arrhenius equation, is also shown in those tables. It should be noted that the k_{NG}, m, and activation energy values in Tables 4-3-6 and 4-3-7 were obtained using somewhat different fitting ranges for the t and X_{WL} values compared to the ranges used for the interface-controlled "shrinking-core" model. In contrast, Tables 4-3-8 and 4-3-9 show the k_{NG}, m, and activation energy values for the case in which the fitting ranges were the same as used in the interface-controlled "shrinking-core" model. The correlation coefficients were somewhat lower for the nucleation-and-growth model in most cases. Figures 4-3-9 and 4-3-10 show that the nucleation-and-growth model did not show a good fit to the data at low X_{WL} values.

- Diffusion-based models

The weight loss data was also fit to kinetic equations based on diffusion models, such as Jander's equation, Ginstling-Brounshtein's equation, and Carter's equation. As stated in section 2.3.3.3, the equations are:

Jander's equation

$$[1-(1-X_{WL})^{1/3}]^2 = k_{Diff}\, t \qquad (4\text{-}3\text{-}15)$$

Table 4-3-6 The reaction rate constants k_{NG}, the exponent parameters m, and the activation energy for the carbothermal reduction reaction for SC35 samples.

T (^oC)	k_{NG} (h^{-1})	m	r_L	Fitting range for time t	Fitting range for X_{WL}
1160	$(6.41 \pm 0.86) \times 10^{-3}$	0.89 ± 0.02	0.9995	8 - 48 h	0.0683-0.2909
1200	$(22.2 \pm 5.6) \times 10^{-3}$	0.98 ± 0.05	0.9929	2 - 48 h	0.0538-0.7249
1250	$(73 \pm 11) \times 10^{-3}$	0.98 ± 0.05	0.9915	0.5 - 32 h	0.0516-0.9539
1300	$(216 \pm 13) \times 10^{-3}$	1.07 ± 0.03	0.9975	0.5 - 16 h	0.1005-0.9788
Reaction activation energy E (kJ/mol)			467 ± 18		

Table 4-3-7 The reaction rate constants k_{NG}, the exponent parameters m, and the activation energy for the carbothermal reduction reaction for SC8 samples.

T (^oC)	k_{NG} (h^{-1})	M	r_L	Fitting range for time t	Fitting range for X_{WL}
1160	$(27.9 \pm 4.9) \times 10^{-3}$	1.02 ± 0.04	0.9964	4 - 48 h	0.1034-0.7458
1180	$(48.7 \pm 9.9) \times 10^{-3}$	0.94 ± 0.05	0.9923	2 - 48 h	0.1259-0.9157
1200	$(68.8 \pm 6.3) \times 10^{-3}$	1.11 ± 0.03	0.9984	2 - 32 h	0.1144-0.9138
1250	$(191 \pm 9) \times 10^{-3}$	1.05 ± 0.02	0.9981	0.67 - 16 h	0.1078-0.9402
Reaction activation energy E (kJ/mol)			380 ± 16		

Note: The rate constants were obtained by fitting the kinetic data (after correction for moisture adsorption and blown-off powder, i.e., $X_{WL} = X_{ML\text{-}mb}$) to the nucleation-and-growth model. The linear correlation coefficients r_L and the ranges of fitting (time and X_{WL} values) and are also listed in the tables.

Table 4-3-8 The reaction rate constants k_{NG}, the exponent parameters m, and the activation energy for the carbothermal reduction reaction for SC35 samples.

T (^oC)	k_{NG} (h^{-1})	m	r_L	Fitting range for time t	Fitting range for X_{WL}
1160	$(4.04 \pm 1.01) \times 10^{-3}$	0.72 ± 0.07	0.9947	0.5 - 48 h	0.0132-0.2909
1200	$(20.8 \pm 3.5) \times 10^{-3}$	0.91 ± 0.08	0.9952	0.5 - 48 h	0.0178-0.7249
1250	$(73 \pm 11) \times 10^{-3}$	0.98 ± 0.05	0.9915	0.5 - 32 h	0.0516-0.9539
1300	$(215 \pm 13) \times 10^{-3}$	1.06 ± 0.03	0.9968	0.5 - 12 h	0.1005-0.9554
Reaction activation energy E (kJ/mol)			523 ± 45		

Table 4-3-9 The reaction rate constants k_{NG}, the exponent parameters m, and the activation energy for the carbothermal reduction reaction for SC8 samples.

T (^oC)	k_{NG} (h^{-1})	m	r_L	Fitting range for time t	Fitting range for X_{WL}
1160	$(25.4 \pm 6.4) \times 10^{-3}$	0.86 ± 0.05	0.8564	1 - 48 h	0.0513-0.7458
1180	$(48.2 \pm 9.5) \times 10^{-3}$	0.89 ± 0.04	0.8854	1 - 48 h	0.0800-0.9157
1200	$(68.9 \pm 4.5) \times 10^{-3}$	1.13 ± 0.02	0.9990	1 - 32 h	0.0455-0.9138
1250	$(195 \pm 6) \times 10^{-3}$	1.02 ± 0.01	0.9993	0.67 - 12 h	0.1078-0.9181
Reaction activation energy E (kJ/mol)			400 ± 25		

Note: The rate constants were obtained by fitting the kinetic data (after correction for moisture adsorption and blown-off powder, i.e., $X_{WL} = X_{ML\text{-}mb}$) to the nucleation-and-growth model. The linear correlation coefficients r_L and the ranges of fitting (time and X_{WL} values) are also listed in the tables.

Ginstling-Brounshtein's equation

$$1-\frac{2}{3}\alpha-(1-X_{WL})^{2/3}=k_{Diff}t \qquad (4\text{-}3\text{-}16)$$

Carter's equation

$$\frac{Z-(Z-1)(1-X_{WL})^{2/3}-[1+(Z-1)X_{WL}]^{2/3}}{Z-1}=k_{Diff}t \qquad (4\text{-}3\text{-}17)$$

In the three equations above, k_{Diff} is the reaction rate constant and X_{WL} is fractional weight loss. For Carter's equation, Z represents the volume of the reaction product formed per unit volume of reactant consumed (Hulbert, 1969). As will be shown in Appendix C, $Z = 0.23$ for SC35 series and $Z = 0.41$ for SC8 series.

However, it turns out that the weight loss data fits none of the diffusion equations satisfactorily. For example, Figures 4-3-11 and 4-3-12 shows the fitting of the weight loss data to the Carter's equation for SC35 and SC8 series respectively. The experimental data points deviate significantly from the expected straight line, indicating that Carter's equation does not describe the reaction kinetics in the current system. The fitted plots to Jander's equation and Ginstling-Brounshtein's equation are shown in Appendix D.

- Other models

The weight loss data in this study was also fit to other kinetic models, such as the interface-controlled "contracting-area" reaction model (Hulbert, 1969), and some other kinetic equations, such as the first-order reaction equation, power law equation, and the Austin and Rickett's equation (Weimer, 1997), etc. The plots in which the weight loss data are fit to those reaction equations are presented in Appendix D. The other reaction equations were not used because (i) the data fits were poor and/or (ii) the kinetic equations do not have a clear physical meaning as compared with the first two models discussed in

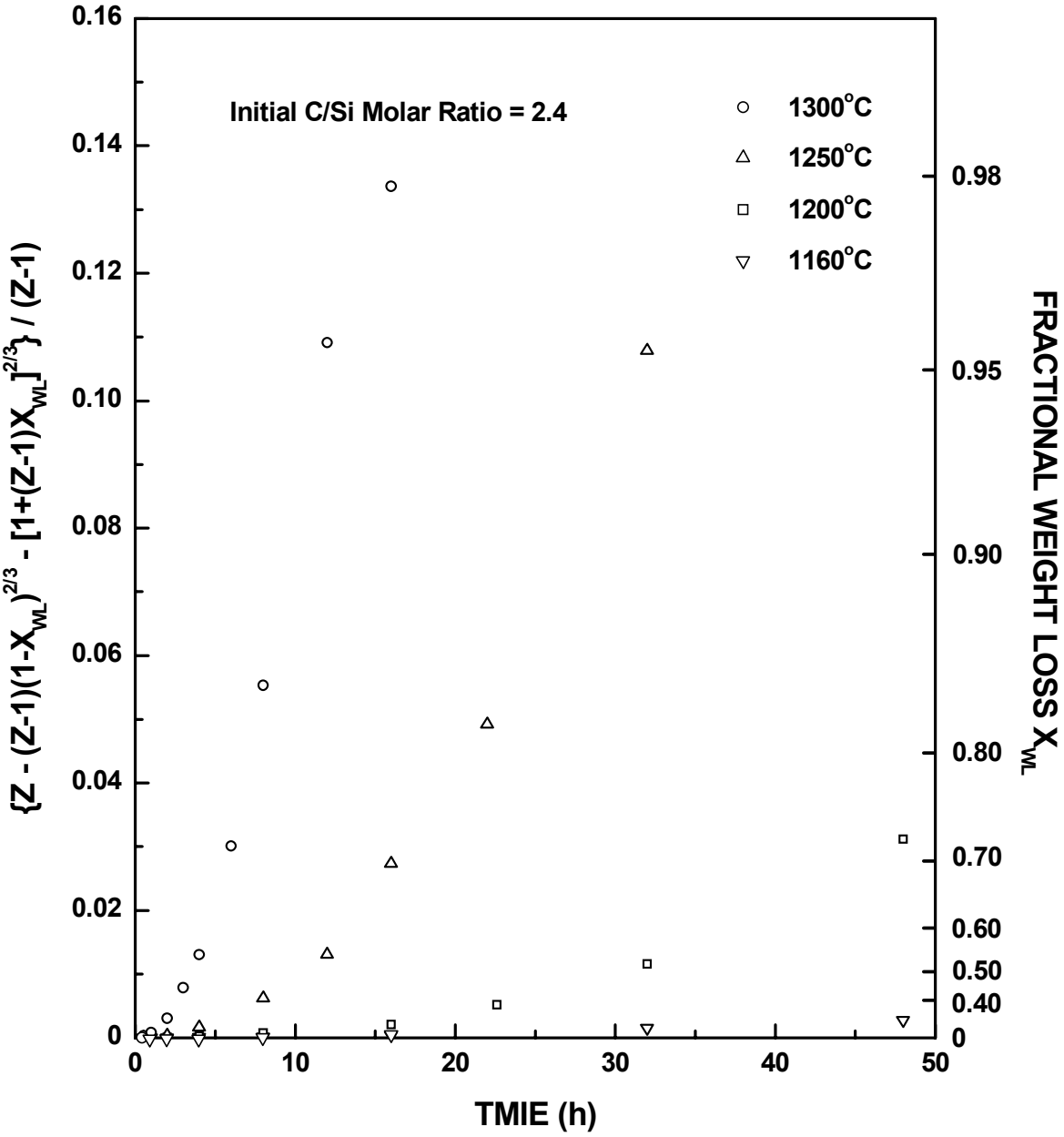

Figure 4-3-11 Plots in which the weight loss kinetic data is fit to the equation of the Carter's equation for the SC35 series (initial C/Si molar ratio = 2.4), Z=0.23.

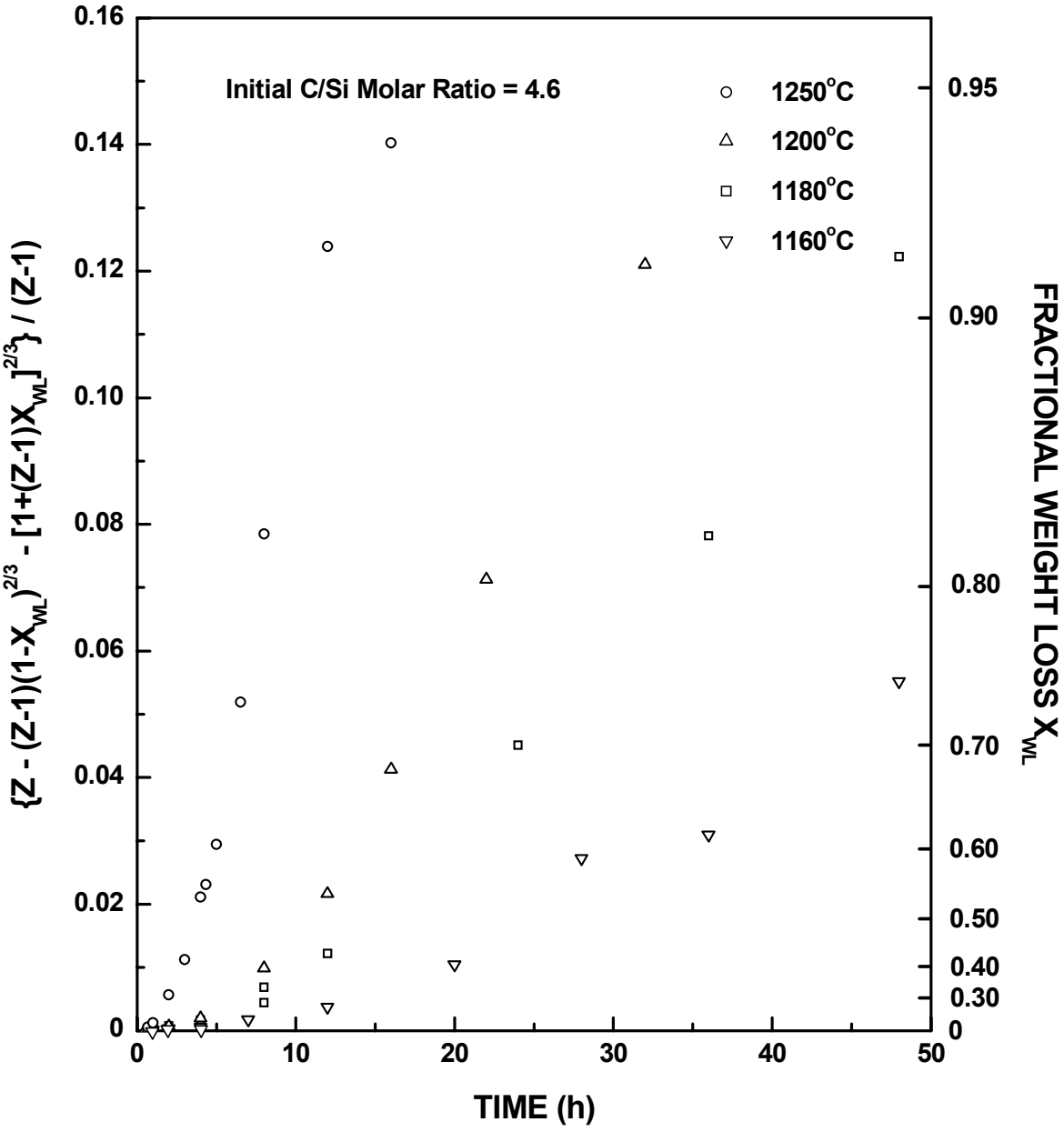

Figure 4-3-12 Plots in which the weight loss kinetic data is fit to the equation of the Carter's equation for the SC8 series (initial C/Si molar ratio = 4.6), Z=0.41.

this section (i.e., the interface-controlled "shrinking-core" model and the nucleation-and-growth model). The only equation for which there was a relatively good fit of the experimental was the first-order reaction equation. (Tables D-1 and D-2 show the results of fitting the data shown in Figures D-5 and D-6, respectively.) However, this equation was not used in any further analysis of the data because of the second reason stated.

4.3.2.4 Identification of the Best Model that Describe the Kinetics of CTR

The mathematical fitting of the weight loss data to the various kinetic equations eliminated most of the kinetic models and left only two: the interface-controlled "shrinking-core" model and the nucleation-and-growth model. Both models showed reasonably good fits to the data: (i) the correlation coefficients were high, and (ii) the equations fit the data over a significant portion of the reaction. However, the applicable range for the interface-controlled "shrinking-core" model is $0 < X_{WL} < \sim 0.95$; the applicable range for the nucleation-growth model is $\sim 0.1 < X_{WL} < \sim 0.95$. Additional information was considered in order to determine which of the two models was more appropriate for the kinetic data observed in this study.

As stated in section 2.3.3.2, the interface-controlled "shrinking-core" model is based on the following assumptions: (1) the reaction is interface-controlled; (2) the reaction rate is proportional to surface area of unreacted phase; (3) the nucleation step occurs instantaneously so that the surface of each reactant particle is covered with a (porous) product layer. Structural characterization is required to address the first and third assumptions and this will be discussed later in detail (sections 4.4 and 4.5). In short, however, both of the assumptions are met from observations on the structural

development of the reaction product. For the second assumption, a direct implication is that the reaction would be deccelatory, i.e., the reaction rate would decrease as the reaction proceeds because the surface area of the unreacted material would usually be the largest at the start of the reaction and decrease during the reaction. This is consistent with the shape of the conversion curves for both SC35 and SC8 series, as shown in Figures 4-3-1 to 4-3-4.

For the nucleation-and-growth model, it is important to consider the values of the exponent parameter *m*. For the current system, the exponent *m* values are between 0.9 and 1.1 (refer to Tables 4-3-6 and 4-3-7). Such exponent parameter, *m*, values are usually representative of one of the following five situations:

- diffusion-controlled two-dimensional growth with zero nucleation rate
- diffusion-controlled two-dimensional growth with decreasing nucleation rate
- diffusion-controlled one-dimensional growth with decreasing nucleation rate
- interface-controlled one-dimensional growth with zero nucleation rate
- interface-controlled one-dimensional growth with decreasing nucleation rate

The test of these situations also requires information about product microstructure, such as the crystallite size. However, as will be shown later in detail (section 4.4.1, 4.4.2, and Appendix H), the results of structural studies are in conflict with all of the scenarios that would fit the nucleation-and-growth model. As a result, the interface-controlled "shrinking-core" model is the most appropriate model to describe the kinetic process for the formation of SiC via carbothermal reduction.

4.3.2.5 Reaction Activation Energy from Weight Loss Data

The interface-controlled "shrinking-core" model was used to determine the apparent activation energy of the reaction, E, by fitting the rate constant k at different temperatures to the Arrhenius equation:

$$k = Ae^{-\frac{E}{RT}} \tag{4-3-18}$$

or

$$\ln k = \ln A - \frac{E}{R}(\frac{1}{T}) \tag{4-3-19}$$

where A is the geometric factor, R is the gas constant, and T is absolute temperature. A linear fit based on the least-squares method was carried out on the data pair (y_i, x_i) in which y_i is $\ln k$ while x_i is 1/T. The slope of the fitted line gives $-E/R$ and the y intercept gives $\ln A$.

Figures 4-3-13 and 4-3-14 are plots of the reaction rate constants (data from Tables 4-3-4 and 4-3-5, respectively) versus inverse reaction temperature for the SC35 and SC8 series, respectively. The rate constants are plotted on a logarithmic scale and the unit of the rate constant is inverse hours. As shown in Table 4-3-4 and Table 4-3-5, E = 423±19 kJ/mol for the SC35 series and E = 375±3 kJ/mol for the SC8 series. This suggests that the reaction mechanism is the same for the two different sample series. However, it is noted from Tables 4-3-4 and 4-3-5 and from Figures 4-3-13 and Figures 4-3-14 that the reaction rate constants for the carbon-rich SC8 series (initial C/Si molar ratio = 4.6) are significantly higher than those for the silica-rich SC35 series (initial C/Si molar ratio = 2.4) at the same temperature. (The values are ~3.4 times higher at 1160^{o}C and ~2.4 times higher at 1250^{o}C.) The interpretation of this result will be discussed after presenting results on the structural evolution of the samples in section 4.5.

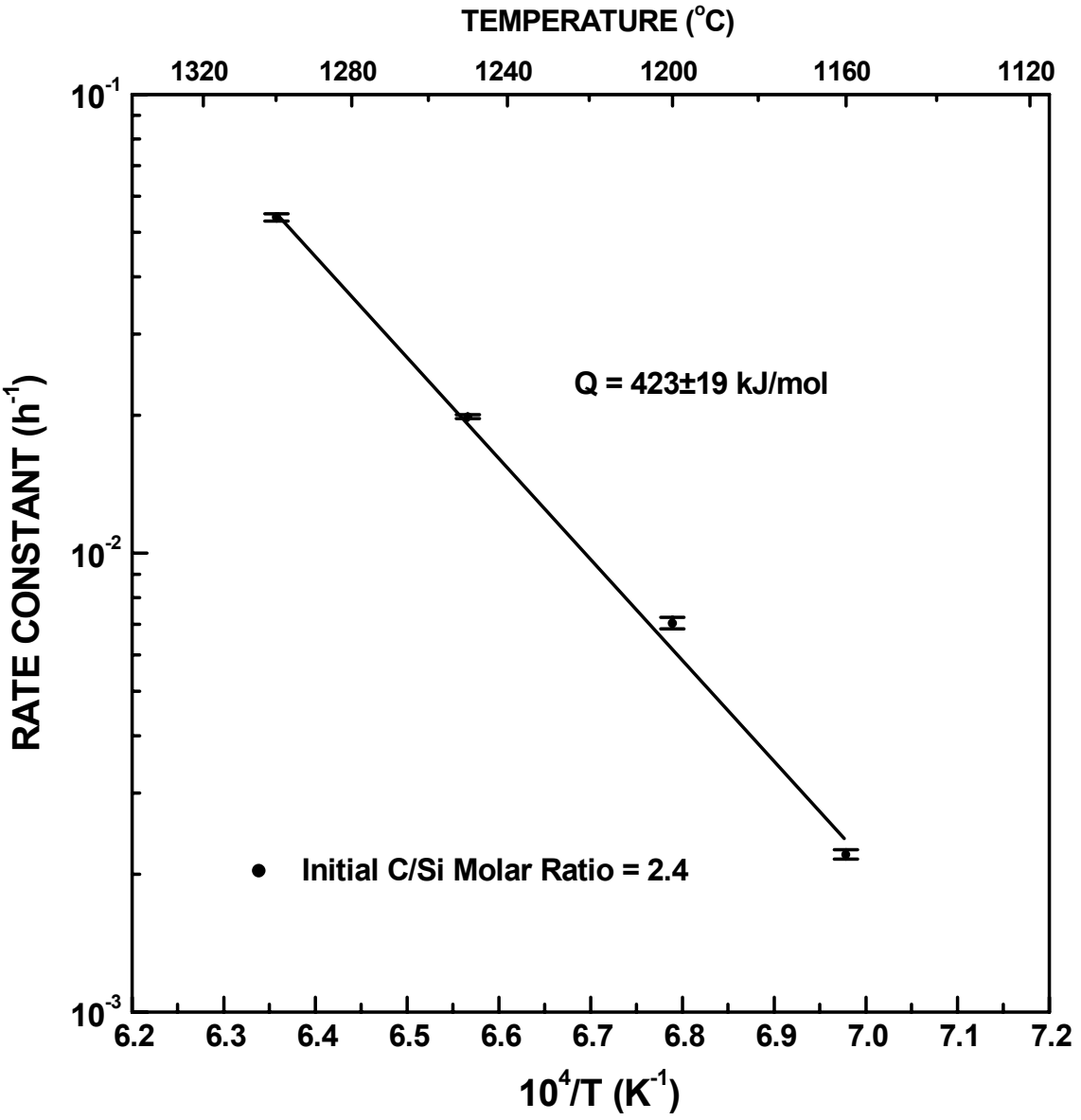

Figure 4-3-13 Plot of reaction rate constant (from Table 4-3-4) vs. inverse temperature for the SC35 (initial C/Si molar ratio = 2.4) samples.

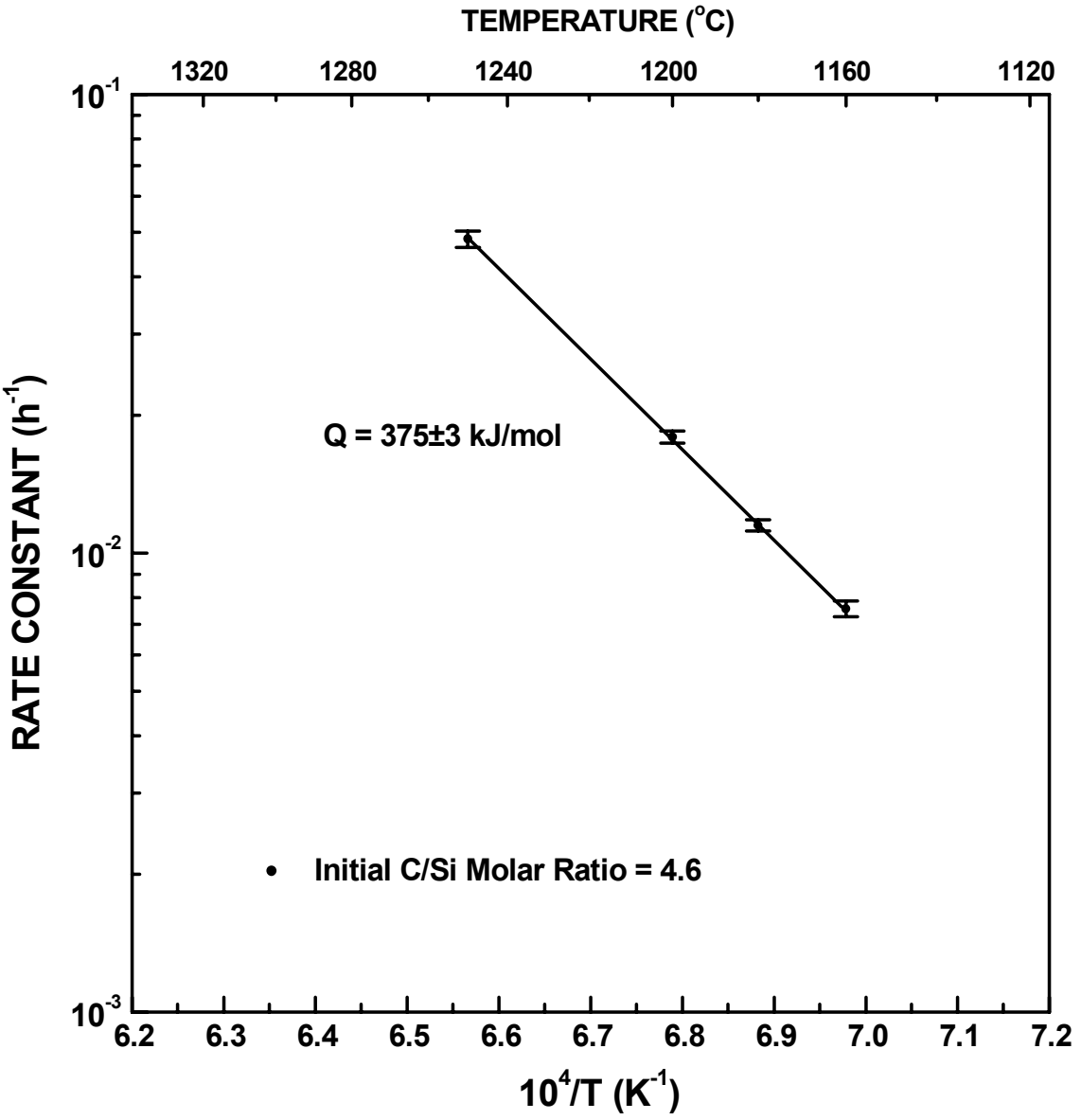

Figure 4-3-14 Plot of reaction rate constant (from Table 4-3-5) vs. inverse temperature for the SC8 (initial C/Si molar ratio = 4.6) samples.

4.3.3 Quantitative XRD (QXRD) Study

4.3.3.1 Calibration Curve for QXRD Study

Figures 4-3-15 and 4-3-16 are the QXRD calibration curves obtained for the SC8 and SC35 samples. The calibration curves were obtained by linear fitting the calibration data pair (y_i, x_i) (y_i is relative intensity, x_i is the weight percent of the fully-converted material) based on a least-squares method. The fitted slope, s_{QXRD}, as well as the linear correlation coefficient r_L are listed in Table 4-3-10. Note that when performing the linear fitting, the fitted lines were forced through the origin. This is based on the assumption that there was no SiC in both the SC35 and SC8 pyrolyzed materials. This assumption was supported by the experimental observations described below.

1. XRD diffraction patterns of the SC8 and SC35 pyrolyzed samples show no obvious SiC diffraction lines (see Figures 4-1-5 and 4-1-6)
2. The electron diffraction pattern of the SC35 pyrolyzed sample (Figures 4-1-36 and 4-1-37) did not match that of SiC.
3. The diffraction intensities in the pyrolyzed samples were integrated over the 2θ range for the two most intensive SiC diffraction lines, i.e. ~33-38^o for the SiC(111) line and ~58-62^o for the SiC(220) line. The obtained integral intensity values were compared with the integral intensities measured for some samples used in the calibration curve (i.e., the "1100^{o}C/1495^{o}C" powder mixture described in section 3.4.2) with small but known amount (i.e. ~1-5 wt%) of fully-converted material (i.e., the "1495^{o}C" material described in section 3.4.2). The results showed that the amounts of SiC in the pyrolyzed samples, if there were any, were negligible. Details of these results are given in Appendix E.

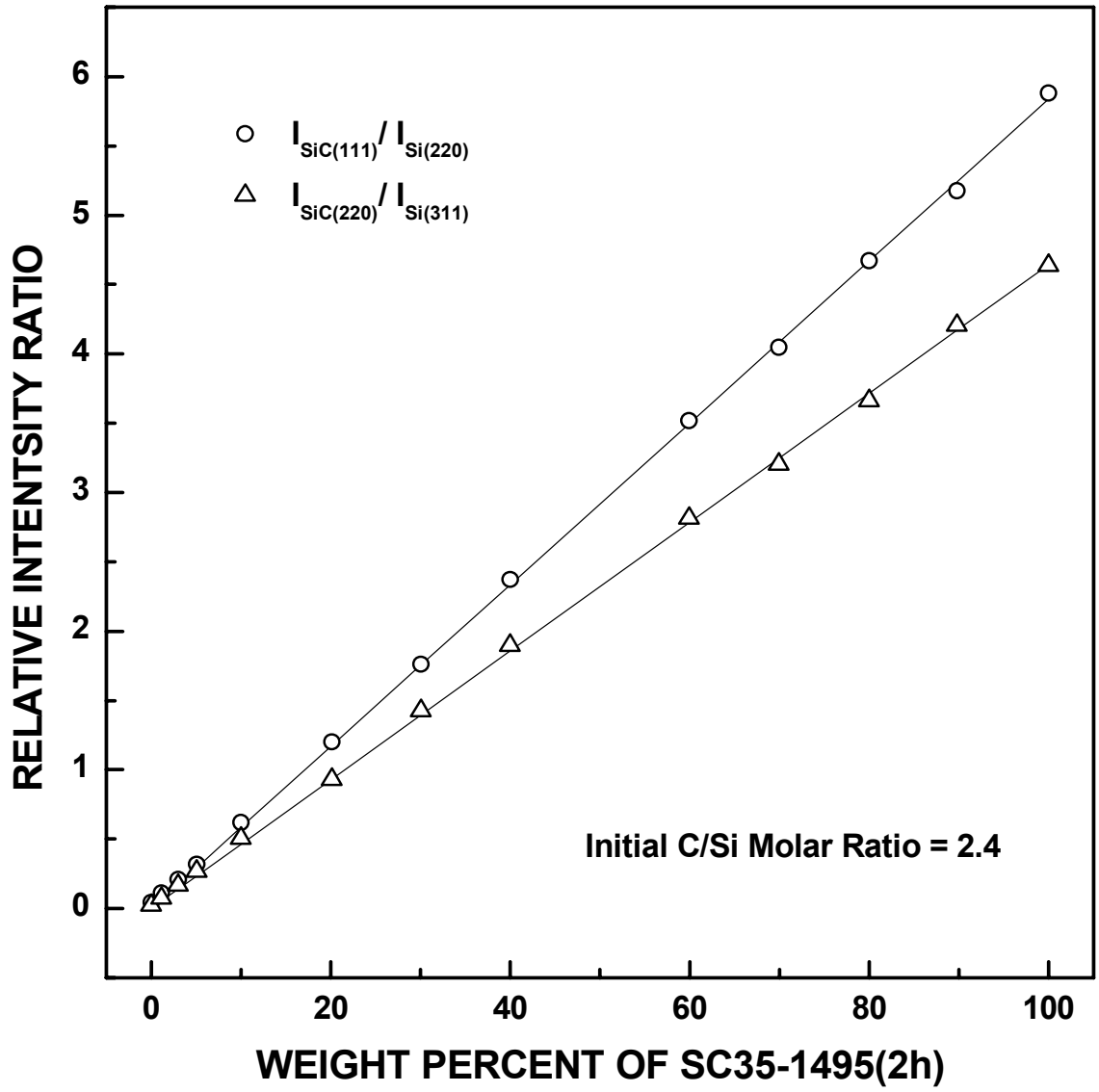

Figure 4-3-15 Calibration curves for quantitative XRD study for the SC35 series with initial C/Si molar ratio = 2.4. The *x* – axis gives the weight percent of "1495°C" fully-converted powder (SC35-1495(2h)) in the "1100°C/1495°C" powder mixture. Plots are shown for intensity ratios using the two main β-SiC diffraction lines, i.e., (111) and (220).

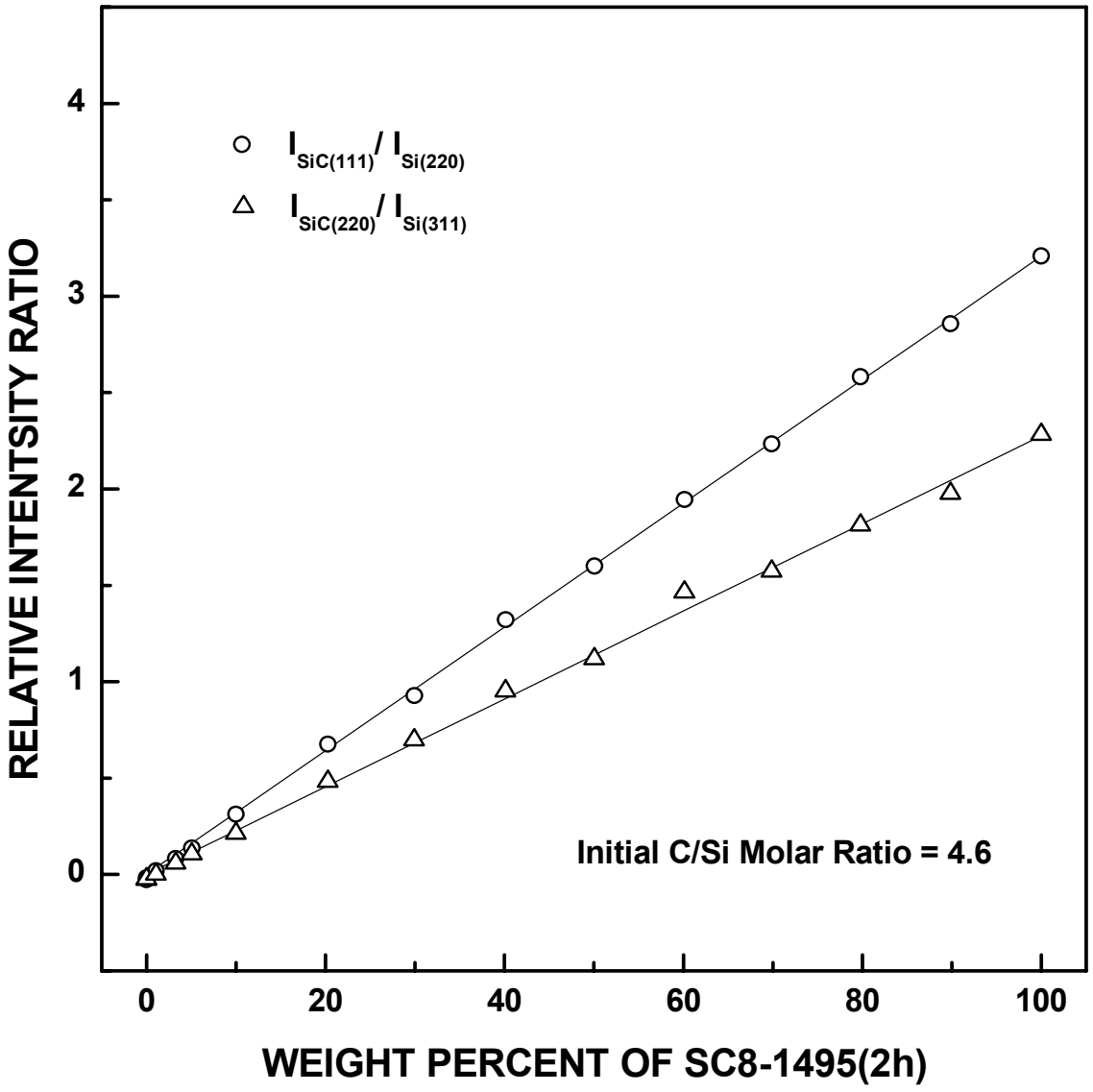

Figure 4-3-16 Calibration curves for quantitative XRD study for the SC8 series with initial C/Si molar ratio = 4.6. The x – axis gives the weight percent of "1495°C" fully-converted powder (SC8-1495(2h)) in the "1100°C/1495°C" powder mixture. Plots are shown for intensity ratios using the two main β-SiC diffraction lines, i.e., (111) and (220).

Table 4-3-10 Fitted slopes s_{QXRD} and the linear correlation coefficients r_L of the calibration curves for the SC35 and SC8 sample series.

Sample series	Calibration curve	s_{QXRD}	r_L
SC35	SiC(111) line / Si (220) line	0.05838	0.9998
	SiC (220) line / Si (311) line	0.04644	0.9998
SC8	SiC (111) line / Si (220) line	0.03208	0.9998
	SiC (220) line / Si (311) line	0.02275	0.9989

4.3.3.2 Weight Fraction of Fully-Converted Material in the CTR Product

In order to obtain the weight fraction of fully-converted material ("1495^{o}C") in the unknown heat-treated samples, w_{CTR}, the following parameters are introduced:

W the weight of product after CTR

W_{CTR} the weight of fully-converted material in the product

$$W_{CTR} = W \cdot w_{CTR} \tag{4-3-20}$$

I_R intensity ratio of the SiC line to the corresponding Si line (i.e., the SiC(111) line to the Si(220) line, and the SiC(220) line to the Si(311) line) for a given sample

X_{QXRD} fractional conversion to SiC calculated from QXRD data; X_{QXRD} is the ratio of the actual amount of SiC formed to the maximum amount of SiC that can be formed for a given sample.

Suppose that the sample after a carbothermal reduction heat treatment contains unreacted (i.e., pyrolyzed) and fully-converted materials, i.e., just like the "1100^{o}C/1495^{o}C" powder mixtures used in the QXRD calibration curves. The intensity ratio, I_R, for that

sample and the slope of the corresponding calibration curve, s_{QXRD}, will give the weight fraction of fully-converted sample in the product w_{CTR}:

$$w_{CTR} = \frac{I_R}{s_{QXRD} \times 100} \tag{4-3-21}$$

Suppose the initial sample weight is W_0, the full conversion yield for the reaction is Y (as defined before in section 4.3.1), the maximum amount of fully-converted material, $W_{CTR}^{\max}$, that can be produced is given by:

$$W_{CTR}^{\max} = W_0 \cdot Y \tag{4-3-22}$$

Therefore, the fractional conversion (by weight) to SiC, X_{QXRD}, is given by:

$$X_{QXRD} = \frac{W_{CTR}}{W_{CTR}^{\max}} = \frac{W \cdot w_{CTR}}{W_0 \cdot Y} \tag{4-3-23}$$

Let the yield of carbothermal reduction, y, for the sample be defined by:

$$y = \frac{W}{W_0} \tag{4-3-24}$$

Therefore, X_{QXRD} can be represented as .

$$X_{QXRD} = \frac{w_{CTR} \cdot y}{Y} \tag{4-3-25}$$

Apparently, except for the two cases of $y = 0$ and $y = Y$, $X_{QXRD} > w_{CTR}$ because the sample yield (y) is always larger than the full conversion yield (i.e., $y > Y$). X_{WL} is the fractional weight loss of the sample:

$$X_{WL} = \frac{1 - y}{1 - Y} \tag{4-3-26}$$

or

$$y = 1 - X_{WL}(1 - Y) \tag{4-3-27}$$

Combining Equations (4-3-25) and (4-3-27):

$$X_{QXRD} = \frac{w_{CTR}[1 - X_{WL}(1 - Y)]}{Y} \qquad (4\text{-}3\text{-}28)$$

Equation (4-3-28) was used to calculate the fractional conversion to SiC from QXRD data. Take the example of the mixture from SC35-1300(6h) and Si. The SiC(111) to Si(220) line intensity ratio is I_R=2.236. The slope of the calibration curve for the SiC(111) line to the Si(220) line in SC35 series is s_{QXRD} = 0.05838. Therefore, by assuming that sample SC35-1300(6h) is also chemically composed of unreacted pyrolyzed material (i.e., SC35-1100(2h)) and fully-converted material (i.e., SC35-1495(2h)), the proportion of the fully-converted material in that sample can be obtained as follows:

$$w_{CTR} = \frac{I_R}{s_{QXRD} \times 100} = \frac{2.236}{0.05838 \times 100} = 0.3829$$

The full conversion yield for SC35 pyrolyzed material is Y = 0.33, while the fractional weight loss for the sample is X_{WL} = 0.7173. (The weight loss value after correction for moisture adsorption and blown-off power was used.) Therefore, the fractional conversion to SiC is:

$$X_{QXRD} = \frac{0.3829 \times [1 - 0.7173 \times (1 - 0.33)]}{0.33} = 0.6027$$

Figures 4-3-17 to 4-3-20 show plots of fractional conversion to SiC vs. reaction time for the SC35 and SC8 samples. Results are shown using both the intensity ratios of the SiC(111) line to the Si(220) line and the SiC(220) line to the Si(311) line. The values of fractional conversion to SiC obtained from the intensity ratios of the SiC(111) line to the Si(220) line are very close to those from the intensity ratios of the SiC(220) line to the Si(311) line. These results are also similar to those obtained from weight loss data (Figures 4-3-3 and 4-

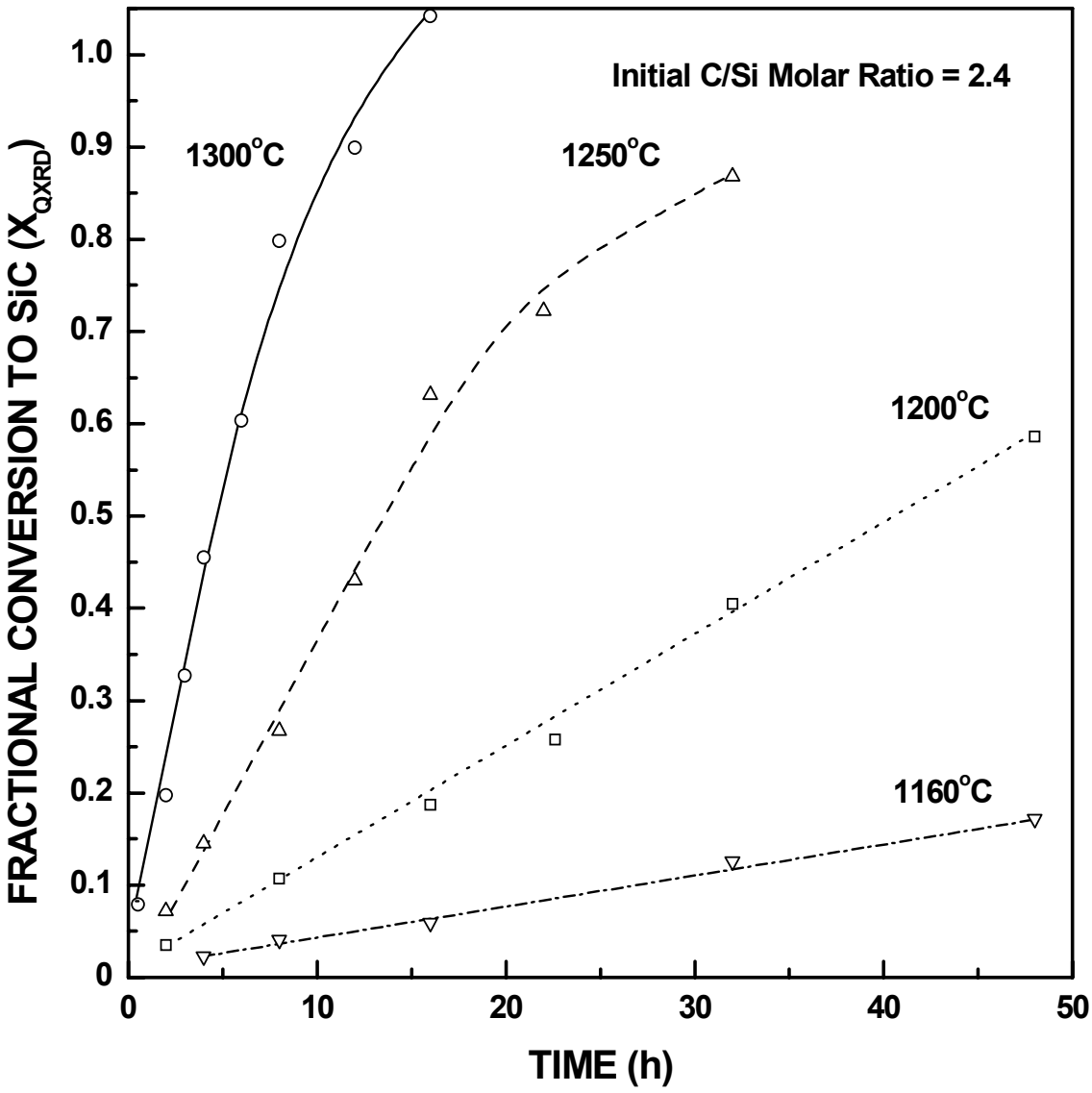

Figure 4-3-17 Plots of fractional conversion to SiC (determined by the QXRD study based on the intensity ratios of the SiC(111) line to the Si(220) line) vs. time for SC35 samples (initial C/Si molar ratio = 2.4) which were heat treated at the indicated temperatures. Note the SC35-1300(16h) is greater than 1 due to experimental error.

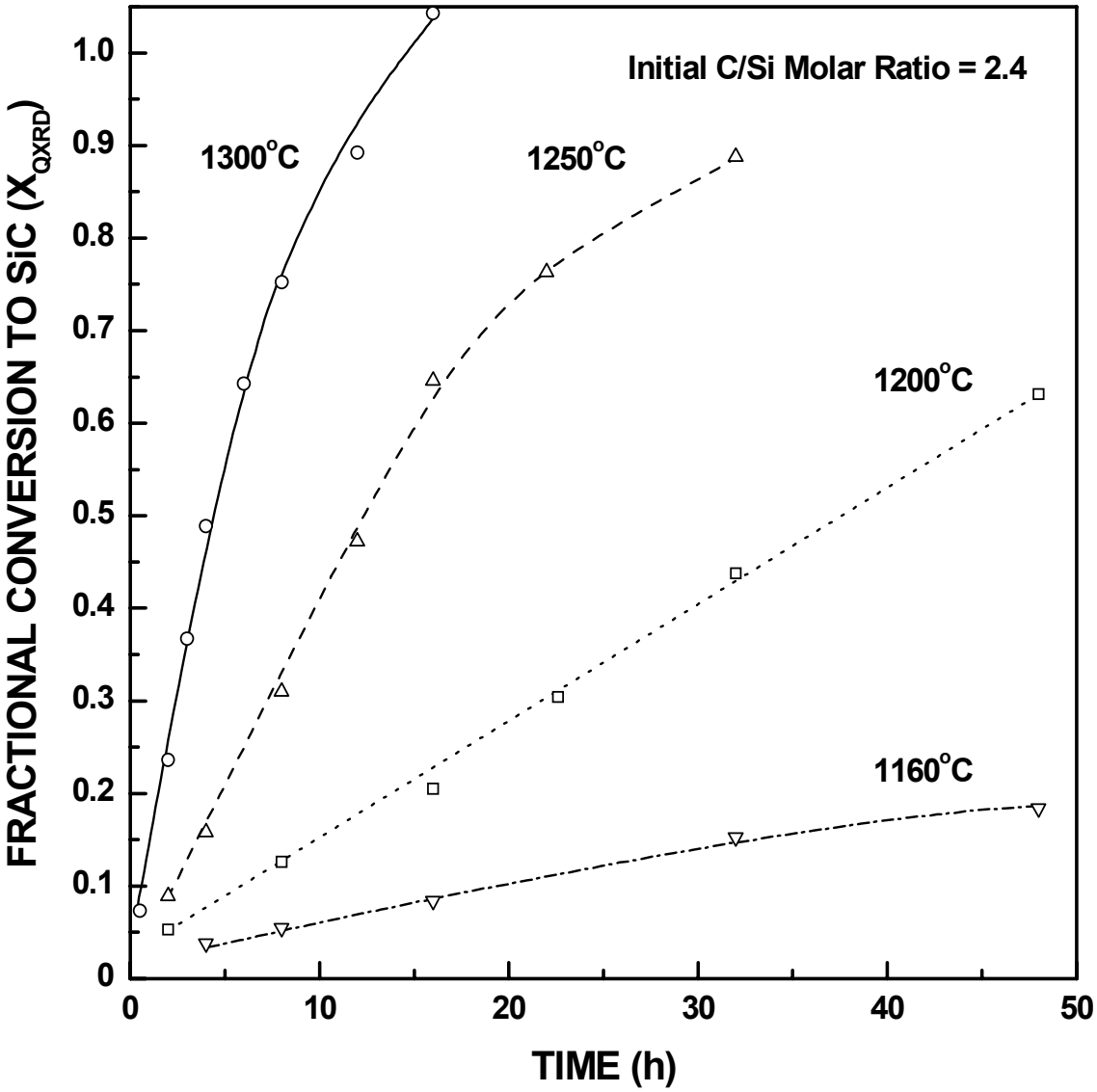

Figure 4-3-18 Plots of fractional conversion to SiC (determined by the QXRD study based on the intensity ratios of the SiC(220) line to the Si(311) line) vs. time for SC35 samples (initial C/Si molar ratio = 2.4) which were heat treated at the indicated temperatures. Note the SC35-1300(16h) is greater than 1 due to experimental error.

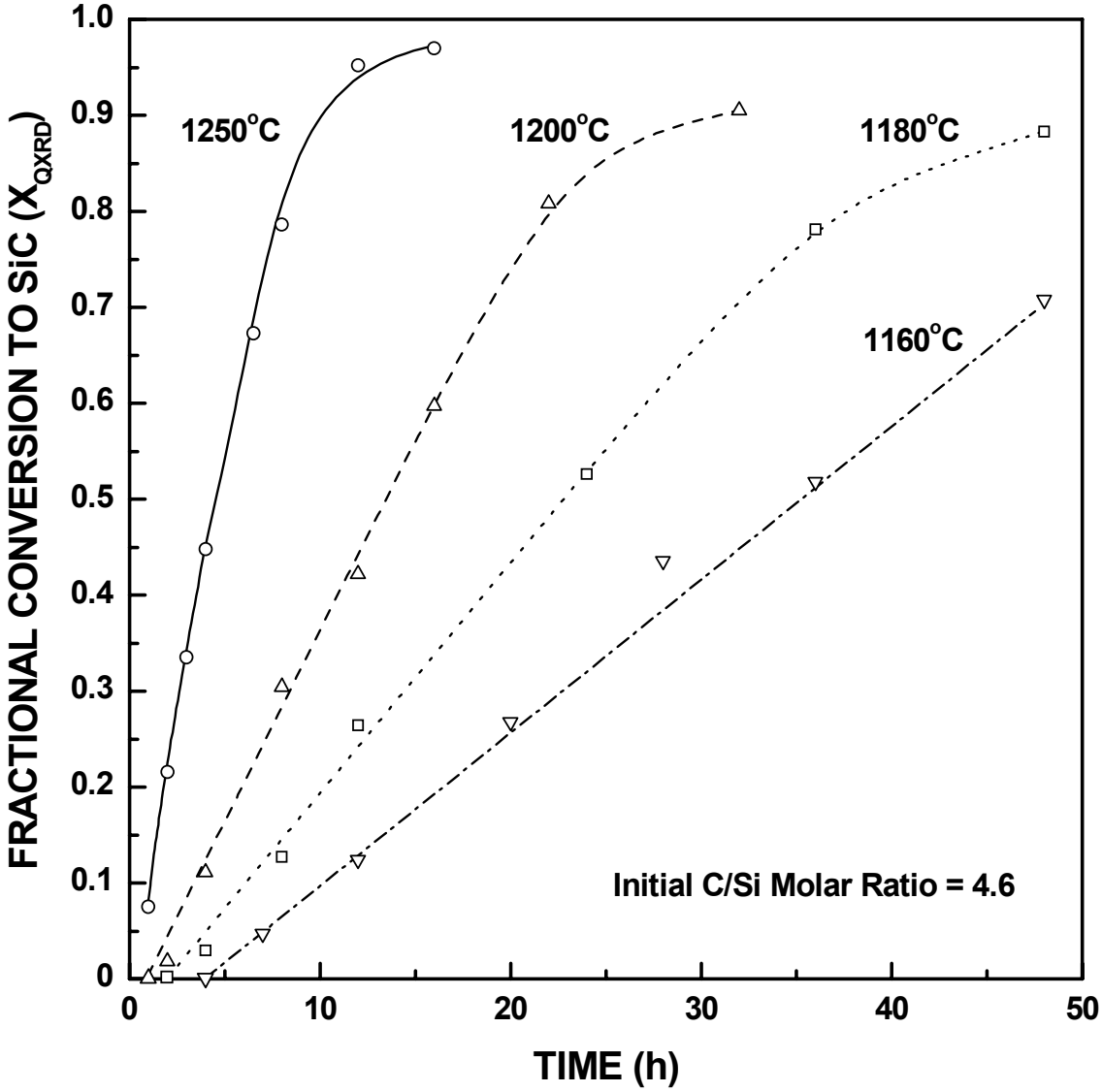

Figure 4-3-19 Plots of fractional conversion to SiC (determined by the QXRD study based on the intensity ratios of the SiC(111) line to the Si(220) line) vs. time for SC8 samples (initial C/Si molar ratio = 4.6) which were heat treated at the indicated temperatures.

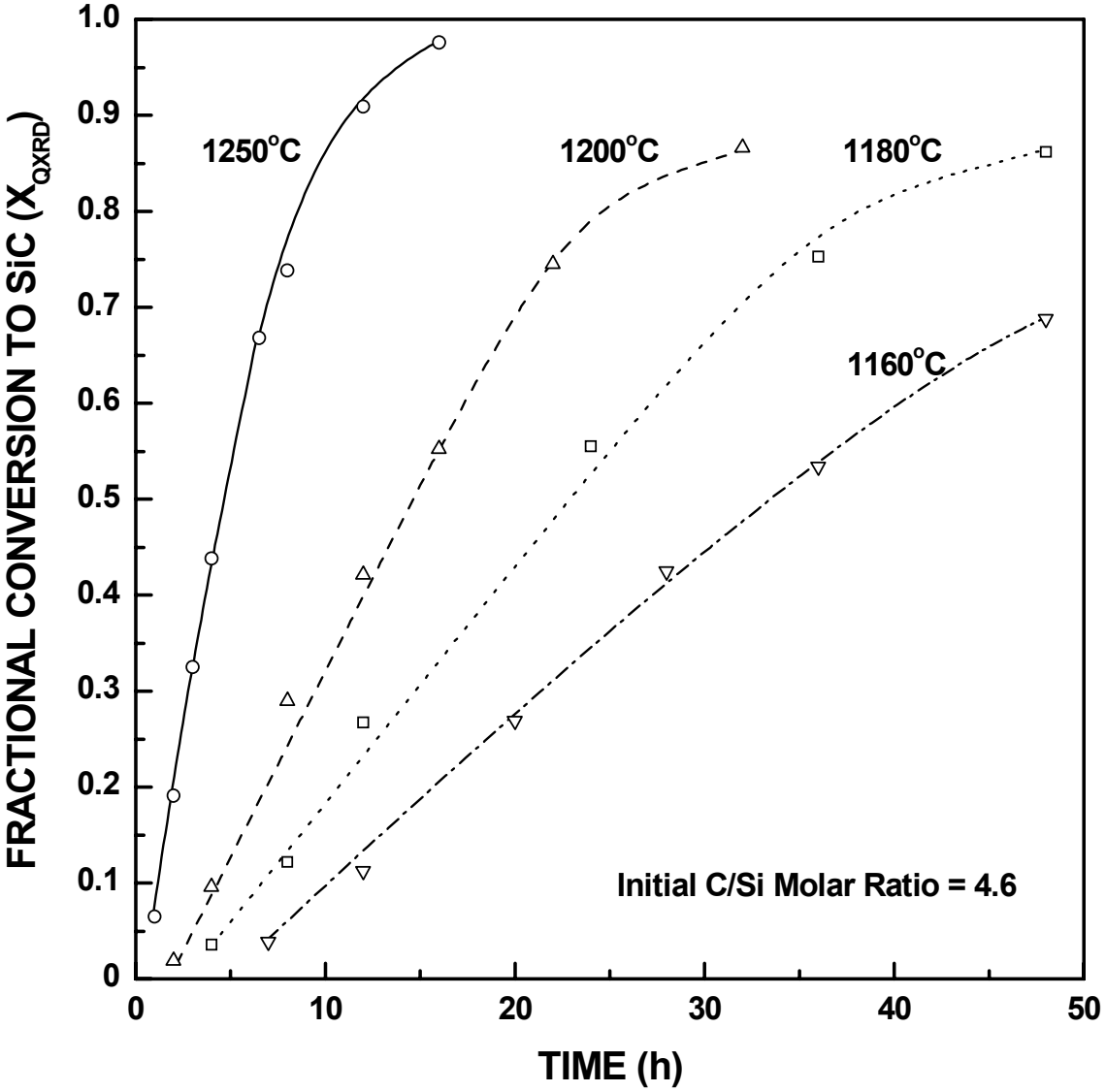

Figure 4-3-20 Plots of fractional conversion to SiC (determined by the QXRD study based on the intensity ratios of the SiC(220) line to the Si(311) line) vs. time for SC8 samples (initial C/Si molar ratio = 4.6) which were heat treated at the indicated temperatures.

3-4) in that the conversion curves are basically deccelatory. No incubation stage was observed for the SC35 samples. However, for the SC8 samples, there seemed to be an incubation period at low temperatures. The reason for this behavior is not understood. As shown in the figures, the carbothermal reduction reactions are almost complete at 1300°C for 16 h for the SC35 samples and at 1250°C for 16 h for the SC8 samples.

As will be shown later in section 4.5.1, the complete CTR reaction (i.e., from the pyrolyzed material to the fully-converted material) takes the form of:

$$SiO_2 + z\,C \rightarrow (1 - y)\,SiC + x\,C + y\,SiO + (z - 1 - x + y)\,CO \qquad (4\text{-}3\text{-}29)$$

where z is the initial C/Si molar ratio in the pyrolyzed material, x is the molar ratio of free carbon (in the product) to initial silica, and y is the molar ratio of SiO lost to initial carbon. Consider an example using the SC35 pyrolyzed material in which z = 2.39, x = 0.05, and y = 0.33 (see Table 4-5-1). Suppose the reaction proceeds linearly according to Equation (4-3-29) throughout the entire reaction process. Also suppose that u moles of SiO_2 are consumed after time t. According to Equation (4-3-29), 2.39u moles of the initial carbon will also be consumed and the following products will be formed: 0.67u moles of SiC (i.e., the ratio of SiO_2 consumed to SiC produced is a constant), 0.33u moles of SiO, 0.05u moles of "free carbon," and 1.67u moles of CO. The above information can be shown as follows:

	SiO_2	+ 2.39 C	→ 0.67 SiC	+ 0.33 SiO	+ 0.05 C	+ 1.67 CO
Before CTR	1	2.39	0	0	0	0
After time t	1- u	2.39- 2.39u	0.67u	0.33u	0.05u	1.67u
After complete CTR	0	0	0.67	0.33	0.05	1.67

The fractional weight loss, X_{WL}, at time *t* when 0.67*u* moles of SiC have formed is given by:

$$X_{WL} = \frac{(0.33u \cdot 44) + (1.67u \cdot 28)}{(0.33 \cdot 44) + (1.67 \cdot 28)} = u$$

where 44 and 28 are the formula weight of SiO and CO, respectively. The fractional conversion to SiC, X_{QXRD}, at time *t* is given by:

$$X_{QXRD} = \frac{0.67u}{0.67} = u$$

Therefore, X_{QXRD} will equal X_{WL} if the assumption is correct that Equation (4-3-29) is applicable throughout the CTR reaction. Hence, a plot of X_{QXRD} vs. X_{WL} would give a straight line which extends from coordinates of (0,0) to coordinates of (1,1).

Figures 4-3-21 and 4-3-22 show plots of fractional conversion to SiC (X_{QXRD}) vs. fractional weight loss (X_{WL}) for the SC35 and SC8 samples, respectively. (The fractional weight losses were corrected for adsorbed moisture and blown-off powder.) The data follow a single trend line independent of the reaction temperature. However, the trend lines were below the expected diagonal line from (0,0) to (1,1) for both the SC35 and SC8 samples. In addition, the X_{WL} intercept value on the x-axis was ~0.05-0.10 for the SC8 samples. Figure 4-3-23 shows a plot of X_{QXRD} vs. X_{WL} for the case in which the fractional weight loss for the SC8 samples was corrected only for moisture adsorption (and not for blown-off powder). In this case, the X_{WL} intercept value was larger. The reasons for the deviation of the data in Figures 4-3-21 - 4-3-23 from the predicted behavior are discussed below.

First, the assumption that the CTR reaction proceeds linearly according to Equation (4-3-29) may not be accurate. For example, suppose the "conversion efficiency" is lower in

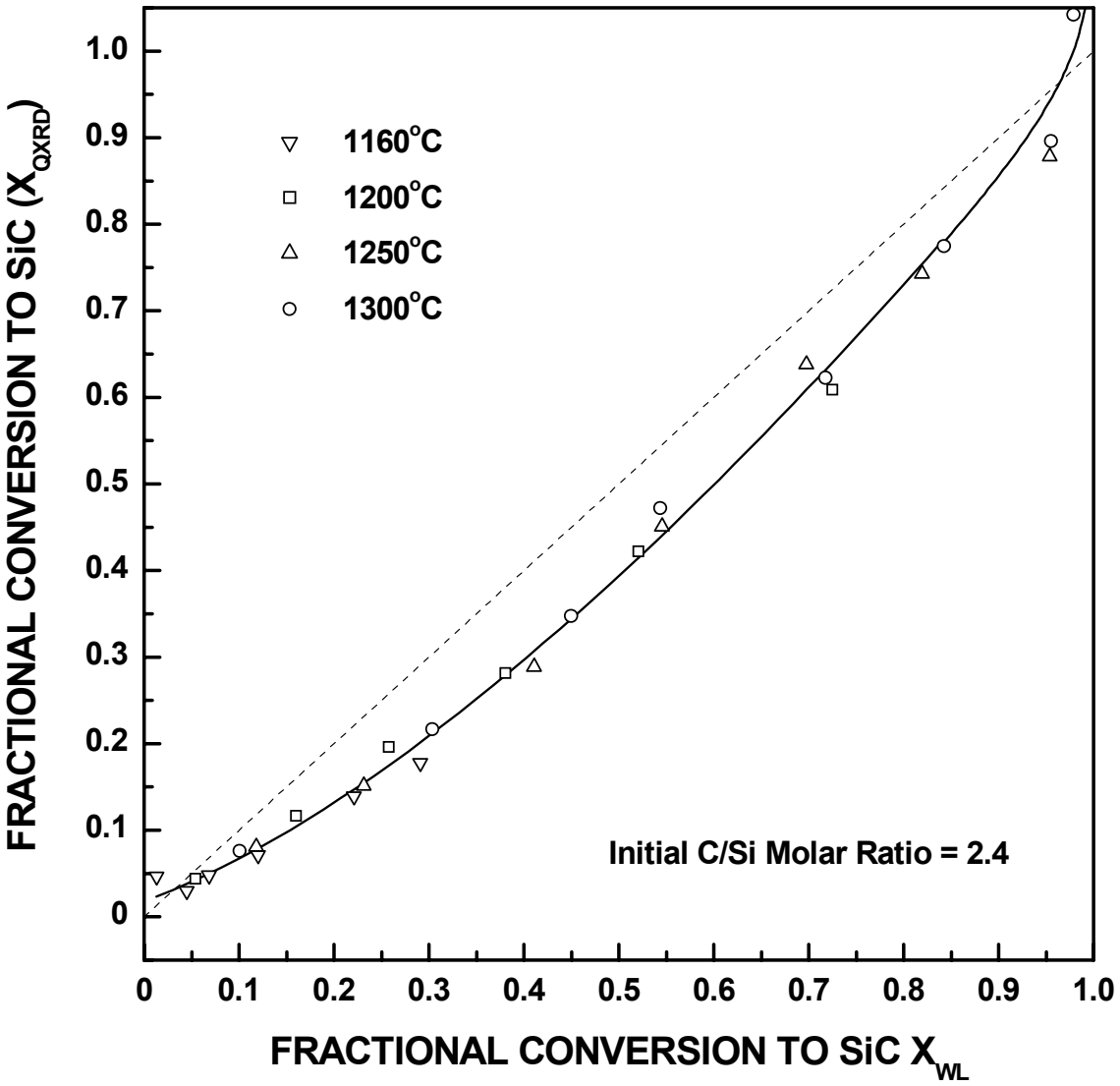

Figure 4-3-21 Fractional conversion to SiC (X_{QXRD}) versus fractional weight loss (X_{WL}) plot for the SC35 samples. The fractional conversion is the average of the values obtained from the SiC(111)/Si(220) and SiC(220)/Si(311) intensity ratios. The fractional weight loss was obtained after correction for moisture adsorption and powder blown-off (i.e., $X_{WL} = X_{WL\text{-}mb}$).

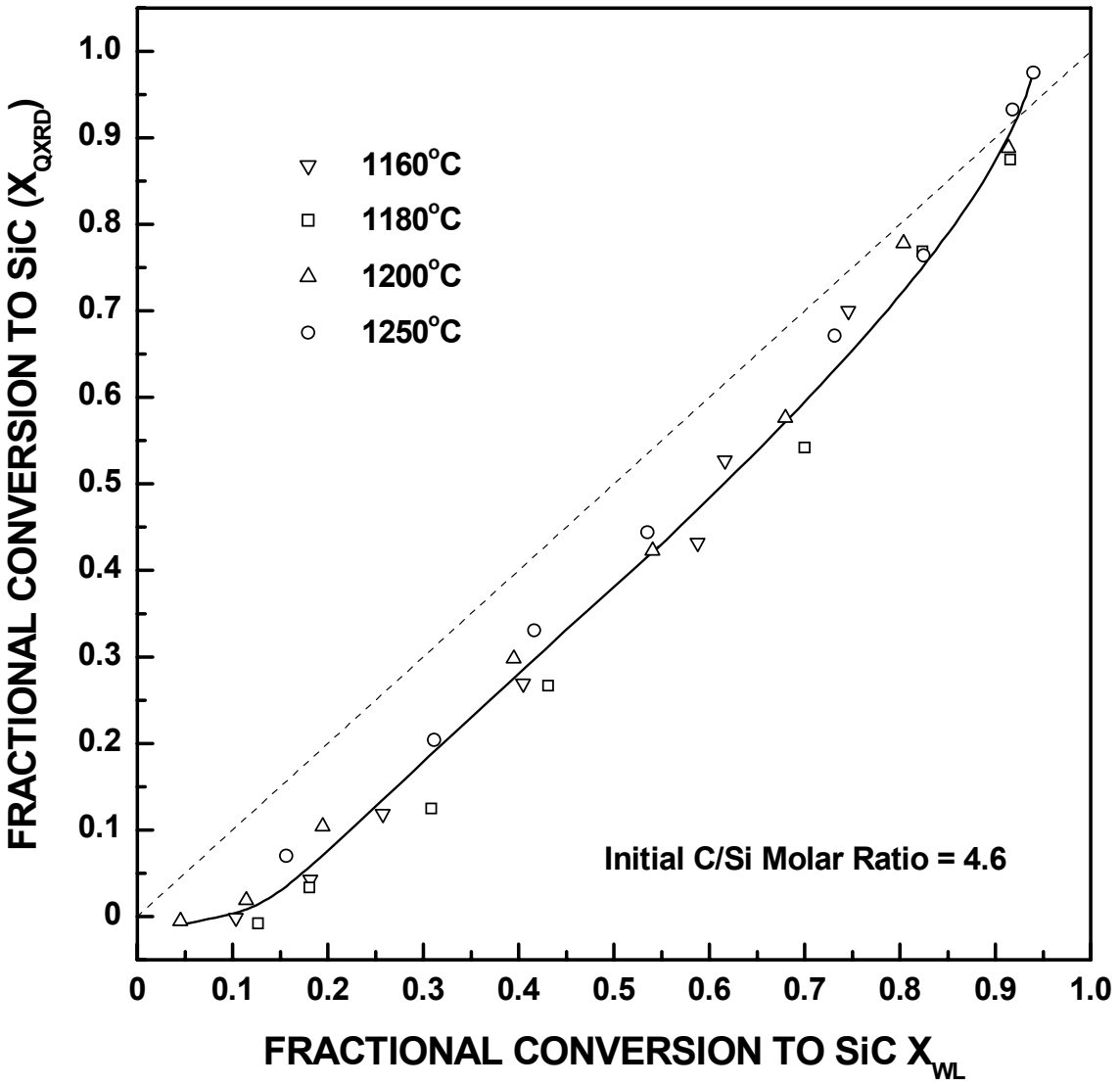

Figure 4-3-22 Fractional conversion to SiC (X_{QXRD}) versus fractional weight loss (X_{WL}) plot for the SC8 samples. The fractional conversion is the average of the values obtained from the SiC(111)/Si(220) and SiC(220)/Si(311) intensity ratios. The fractional weight loss was obtained after correction for moisture adsorption and powder blown-off (i.e., $X_{WL} = X_{WL\text{-}mb}$).

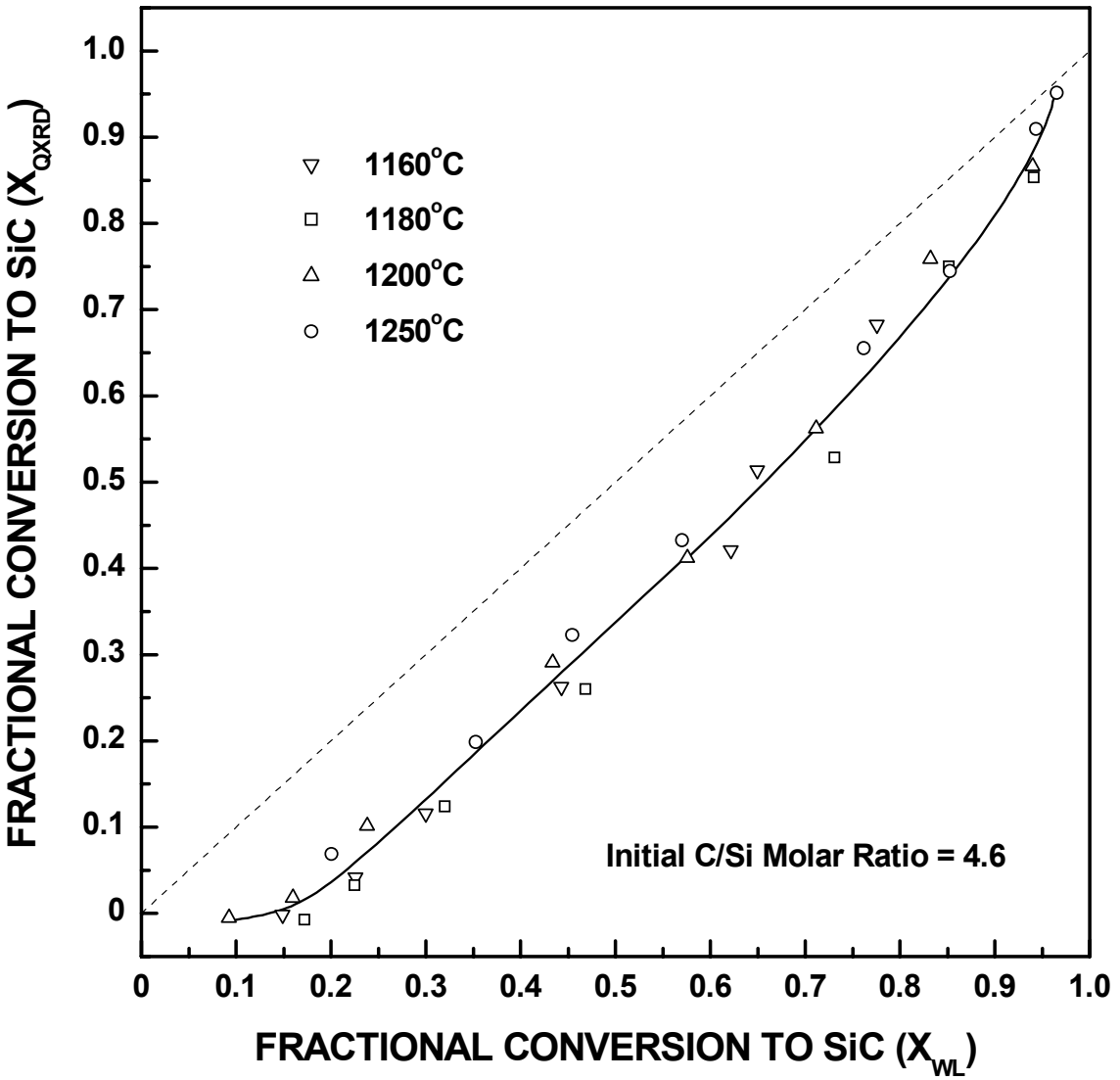

Figure 4-3-23 Fractional conversion to SiC (X_{QXRD}) versus fractional weight loss (X_{WL}) plot for the SC8 samples. The fractional conversion is the average of the values obtained from the SiC(111)/Si(220) and SiC(220)/Si(311). The fractional weight loss was obtained after correction for moisture adsorption only (i.e., $X_{WL} = X_{WL\text{-}m}$).

the early stage of the reaction. In this case, for u moles of SiO_2 consumed, the amount of SiC formed would be less than $0.67u$ moles and the amount of SiO loss would be greater than $0.33u$ moles. Hence, the amount of SiC formed would be less per unit amount of weight loss. As a result, the fractional weight loss would be greater than the fractional conversion to SiC (i.e., $X_{WL} > X_{QXRD}$). Consider an arbitrary specific example in which the early stage conversion efficiency was lower such that $0.60u$ moles of SiC and $0.40u$ moles of SiO formed for u moles of SiO_2 consumed. This would result in the following:

	SiO_2	+ 2.39 C	→ 0.67 SiC	+ 0.33 SiO	+ 0.05 C	+ 1.67 CO
Before CTR	1	2.39	0	0	0	0
Time t	$1-u$	$2.39-2.39u$	$0.60u$	$0.40u$	$0.19u$	$1.60u$
After complete CTR	0	0	0.67	0.33	0.05	1.67

The fractional weight loss, X_{WL}, at time t when u moles of SiO_2 have been consumed is given by:

$$X_{WL} = \frac{(0.40u \cdot 44) + (1.60u \cdot 28)}{(0.33 \cdot 44) + (1.67 \cdot 28)} = 1.02u$$

The fractional conversion to SiC, X_{QXRD}, at time t is given by:

$$X_{QXRD} = \frac{0.60u}{0.67} = 0.90u$$

Therefore, $X_{QXRD} < X_{WL}$ in this case. If the conversion efficiency was lower during the early stage of the reaction, then the conversion efficiency would have to be higher at a later stage in the reaction in order to reach the experimentally observed values of $y = 0.33$ and $x = 0.05$ (Table 4-5-1).

Another factor that may contribute to the difference between the fractional conversion to SiC and the fractional weight loss is related to experiment error. For example, it has been discussed previously that moisture adsorption and blown-off powder affect the accuracy of the weight loss measurement. Although corrections were made to account for these effects, it is possible that the corrections were not as precise as expected. The blown-off powder correction was carried out after all the experiments were finished. If the real weight loss due to blown-off powder was greater than the amount of the correction, then the measured yield (y) would be lower than the real reaction yield. This error would be further magnified when the fractional weight loss (X_{WL}) was calculated because fractional weight loss is given by:

$$X_{WL} = \frac{1-y}{1-Y}$$

and 1-Y is always smaller than unity. As a result, the obtained fractional weight loss would be greater than the real value for the reaction.

X_{QXRD} values were calculated by using the fractional weight loss (X_{WL}) values (Equation (4-3-28)). Hence, X_{QXRD} values may contain more error than the X_{WL} values alone. Therefore, the X_{WL} values were used as the measure of the extent of reaction when presenting the structure characterization results later in this thesis. Nevertheless, the X_{QXRD} values still can be used to examine the kinetics of the reaction, as will be shown in the next section.

4.3.3.3 Fitting of QXRD Data to Kinetic Models

The calculated values for the fractional conversion to SiC (X_{QXRD}) were fit to the same kinetic models that were evaluated with the weight loss (X_{WL}) data. The best fit of the

data was still obtained using the interface-controlled "shrinking-core" model, as illustrated in Figures 4-3-24 - 4-3-27. Once again, a good linear relationship is shown between $1 - (1 - X_{QXRD})^{1/3}$ and reaction time t over almost the entire reaction. The slopes of the fitted straight lines give the reaction rate constants at the various reaction temperatures. Tables 4-3-11 and 4-3-12 show the values of the reaction rate constants (k_{PB}), the linear correlation coefficients (r_L), and the reaction activation energies calculated from the Arrhenius equation for the SC35 and SC8 samples, respectively, using the data from the SiC(111)/Si(220) line intensity ratios. Tables 4-3-13 and 4-3-14 show the corresponding values calculated using the data from the SiC(220)/Si(311) line intensity ratios.

The XRD data for the fractional conversion to SiC was also fit to the nucleation-and-growth model. The results were similar to those observed with the weight loss data (Figures 4-3-9 and 4-3-10). The exponent m values were again ~1.0. As discussed previously, this m value is associated with either reaction-controlled or diffusion-controlled one-dimensional growth, or diffusion-controlled two-dimensional growth. However, as will be discussed later in detail in section 4.4, the structural characterization of the reaction product is not consistent with these reaction mechanisms.

4.3.3.4 Reaction Activation Energy from QXRD Study

Figures 4-3-28 and 4-3-29 show Arrhenius plots of the rate constant vs. inverse temperature for the SC35 and SC8 data, respectively, that were obtained from the QXRD study using the interface-controlled "shrinking-core" equation. For SC8 samples, the calculated apparent activation energy, E, is 400±7 kJ/mol using data from the QXRD study based on the intensity ratio of the SiC(111) line to the Si(220) line. This is similar

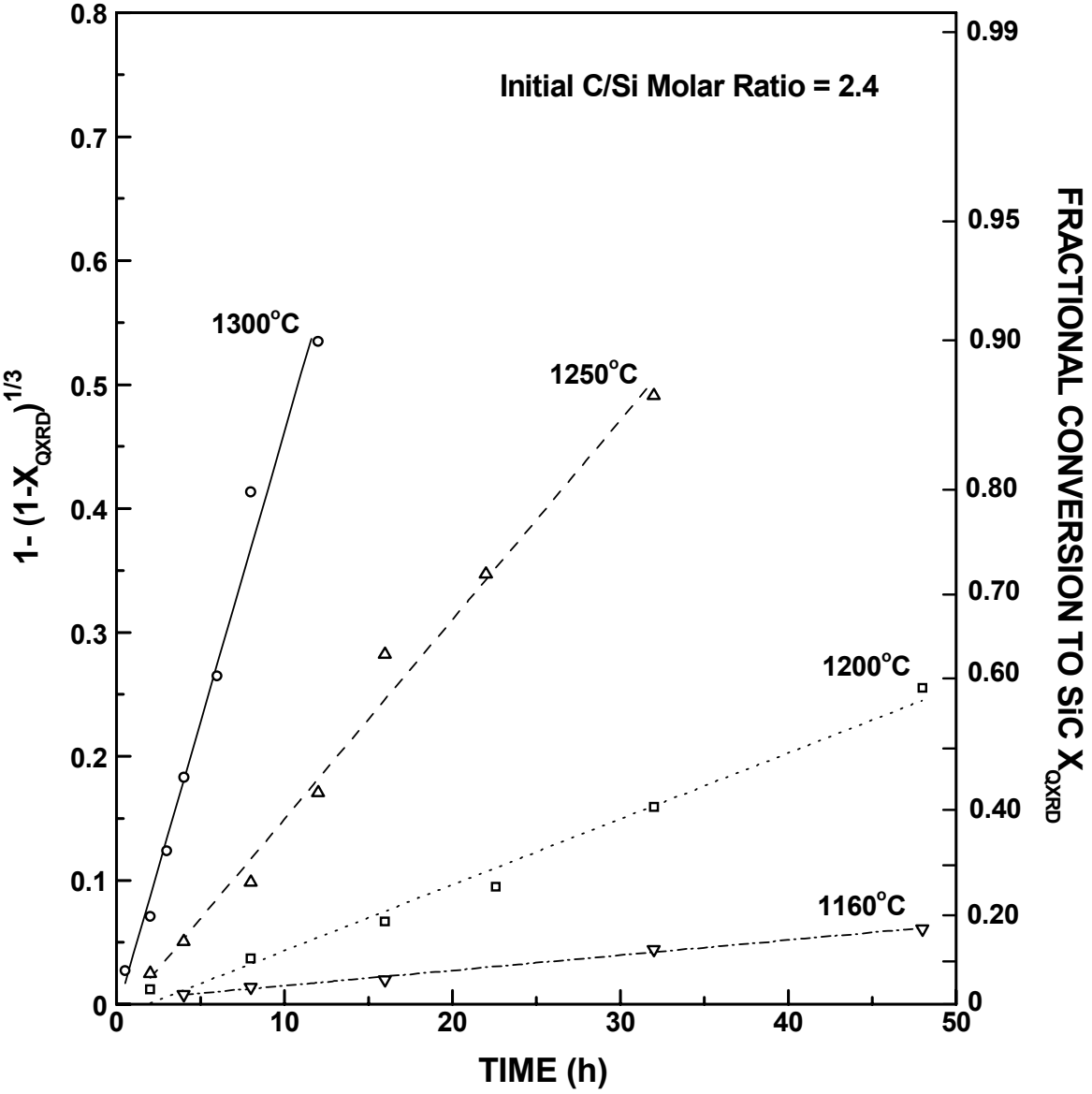

Figure 4-3-24 Plots in which the kinetic data for the fractional conversion to SiC (determined by the QXRD study based on the intensity ratios of the SiC(111) line to the Si(220) line) for SC35 samples (initial C/Si molar ratio = 2.4) are fit to the reaction equation for the interface-controlled "shrinking-core" model.

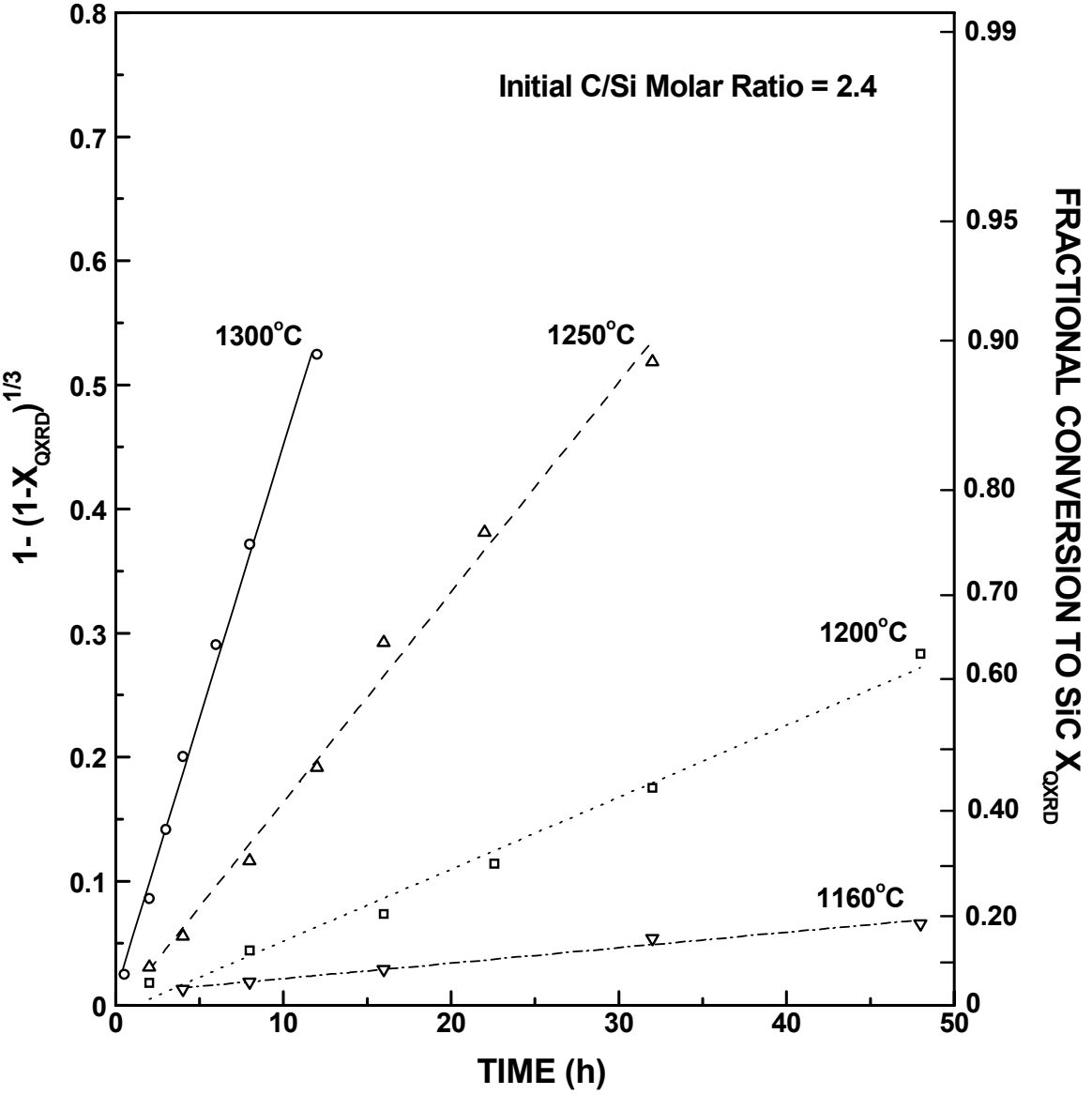

Figure 4-3-25 Plots in which the kinetic data for the fractional conversion to SiC (determined by the QXRD study based on the intensity ratios of the SiC(220) line to the Si(311) line) for SC35 samples (initial C/Si molar ratio = 2.4) are fit to the reaction equation for the interface-controlled "shrinking-core" model.

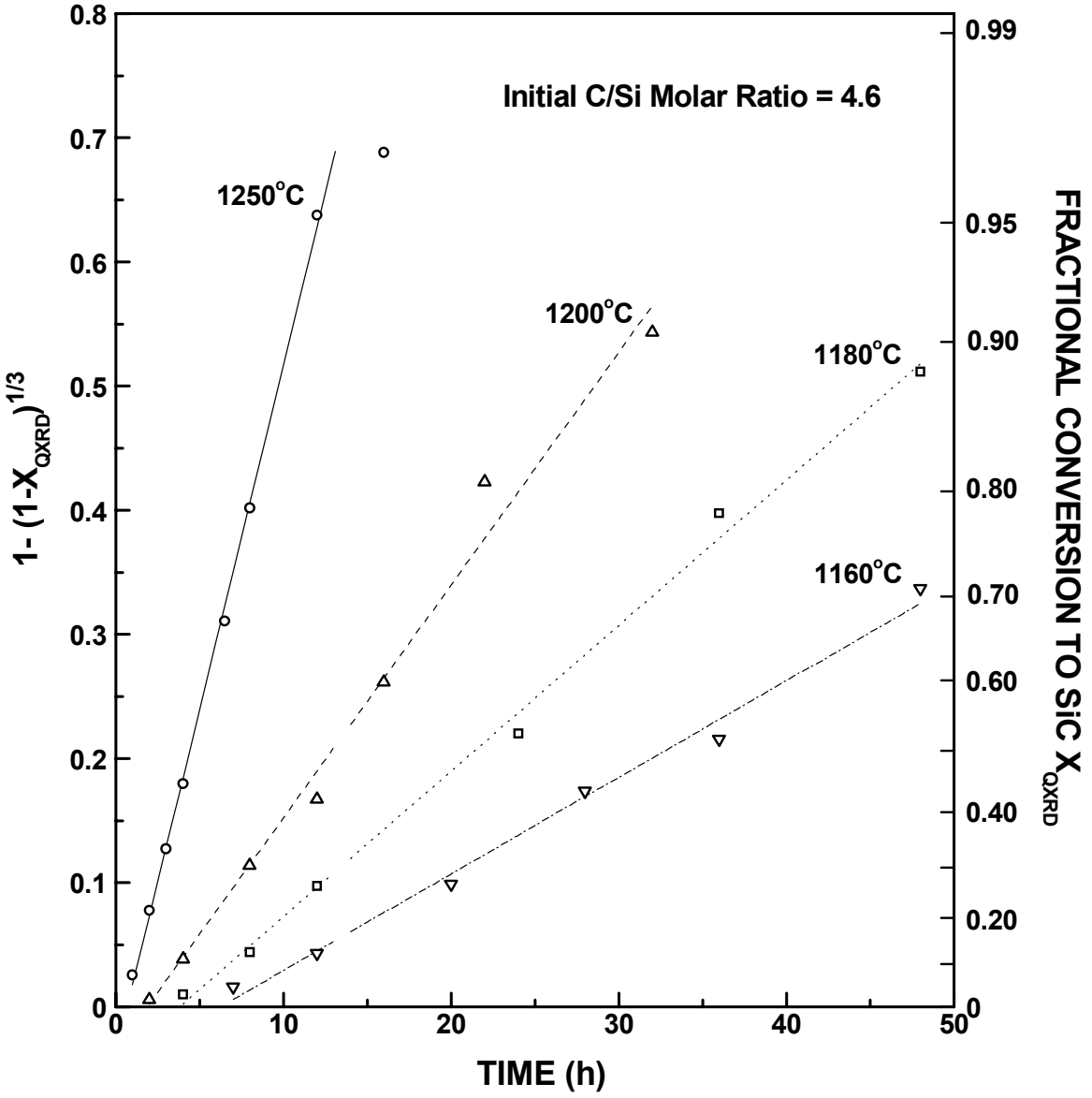

Figure 4-3-26 Plots in which the kinetic data for the fractional conversion to SiC (determined by the QXRD study based on the intensity ratios of the SiC(111) line to the Si(220) line) for SC8 samples (initial C/Si molar ratio = 4.6) are fit to the reaction equation for the interface-controlled "shrinking-core" model.

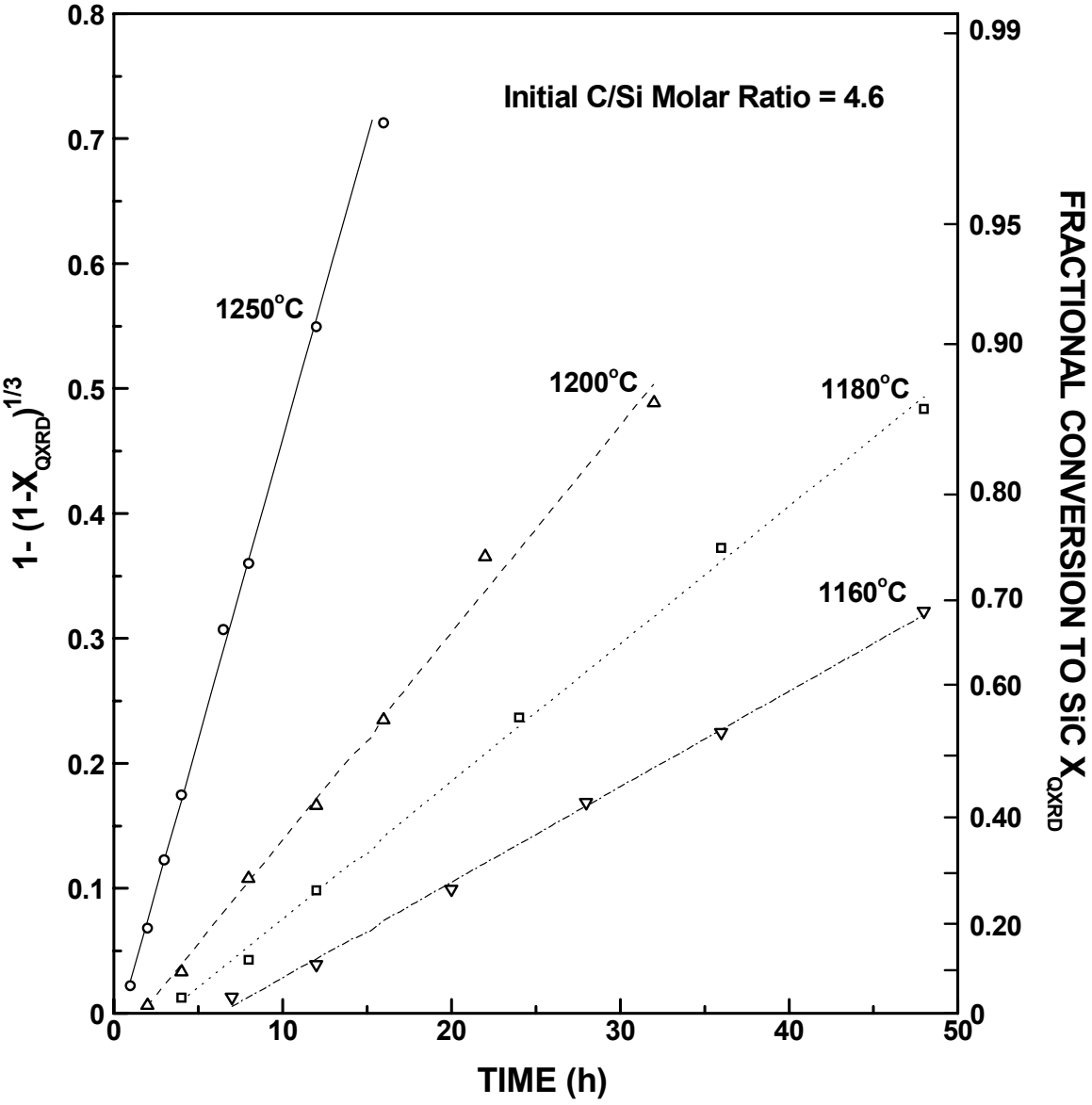

Figure 4-3-27 Plots in which the kinetic data for the fractional conversion to SiC (determined by the QXRD study based on the intensity ratios of the SiC(220) line to the Si(311) line) for SC8 samples (initial C/Si molar ratio = 4.6) are fit to the reaction equation for the interface-controlled "shrinking-core" model.

Table 4-3-11 The reaction rate constants k_{PB} and the activation energy for the carbothermal reduction reaction for SC35 samples based on QXRD data

T (^{o}C)	k_{PB} (h^{-1})	r_L	Fitting range		
			t	X_{WL}	X_{QXRD}
1160	$(1.22 \pm 0.06) \times 10^{-3}$	0.9970	4 - 48 h	0.0451-0.2909	0.0228-0.1716
1200	$(5.32 \pm 0.31) \times 10^{-3}$	0.9931	2 - 48 h	0.0538-0.7249	0.0353-0.5865
1250	$(16.08 \pm 0.77) \times 10^{-3}$	0.9942	2 - 32 h	0.1179-0.9539	0.0724-0.8680
1300	$(46.89 \pm 2.56) \times 10^{-3}$	0.9924	0.5 - 12 h	0.1005-0.9554	0.0787-0.8993
Reaction activation energy E (kJ/mol)		478 ± 36			

Table 4-3-12 The reaction rate constants k_{PB} and the activation energy for the carbothermal reduction reaction for SC8 samples based on QXRD data.

T (^{o}C)	k_{PB} (h^{-1})	r_L	Fitting range		
			t	X_{WL}	X_{QXRD}
1160	$(7.81 \pm 0.35) \times 10^{-3}$	0.9940	7 - 48 h	0.1819-0.7458	0.0472-0.7101
1180	$(11.78 \pm 0.37) \times 10^{-3}$	0.9980	4 - 48 h	0.1808-0.9157	0.0302-0.8855
1200	$(18.85 \pm 0.96) \times 10^{-3}$	0.9936	2 - 32 h	0.1144-0.9138	0.0181-0.9070
1250	$(55.94 \pm 0.98) \times 10^{-3}$	0.9992	1 - 12 h	0.1561-0.9181	0.0753-0.9547
Reaction activation energy E (kJ/mol)		400 ± 7			

Note: The results in Tables 4-3-11 and 4-3-12 were obtained by fitting the kinetic data (after correction for moisture adsorption and powder blown-off powder, i.e., $X_{WL} = X_{WL\text{-}mb}$) to the interface-controlled "shrinking-core" model. The linear correlation coefficients, r_L, and the ranges of fitting (time, X_{WL}, and X_{QXRD} values) are also given in the tables. The data based on SiC(111)/Si (220) line intensity ratios were used.

Table 4-3-13 The reaction rate constants k_{PB} and the activation energy for the carbothermal reduction reaction for SC35 samples based on QXRD data.

T (^{o}C)	k_{PB} (h^{-1})	r_L	Fitting range		
			t	X_{WL}	X_{QXRD}
1160	$(1.24 \pm 0.09) \times 10^{-3}$	0.9915	4 - 48 h	0.0451-0.2909	0.0379-0.1845
1200	$(5.80 \pm 0.33) \times 10^{-3}$	0.9938	2 - 48 h	0.0538-0.7249	0.0531-0.6314
1250	$(16.90 \pm 0.67) \times 10^{-3}$	0.9961	2 - 32 h	0.0259-0.9539	0.0893-0.8883
1300	$(44.04 \pm 1.43) \times 10^{-3}$	0.9974	0.5 - 12 h	0.1005-0.9554	0.0733-0.8925
Reaction activation energy E (kJ/mol)		467 ± 47			

Table 4-3-14 The reaction rate constants k_{PB} and the activation energy for the carbothermal reduction reaction for SC8 samples based on QXRD data.

T (^{o}C)	k_{PB} (h^{-1})	r_L	Fitting range		
			t	X_{WL}	X_{QXRD}
1160	$(7.67 \pm 0.17) \times 10^{-3}$	0.9990	7 - 48 h	0.1819-0.7458	0.0387-0.6897
1180	$(11.06 \pm 0.25) \times 10^{-3}$	0.9990	4 - 48 h	0.1808-0.9157	0.0363-0.8645
1200	$(16.67 \pm 0.56) \times 10^{-3}$	0.9972	2 - 32 h	0.1144-0.9138	0.0188-0.8684
1250	$(48.45 \pm 0.90) \times 10^{-3}$	0.9991	1 - 12 h	0.1561-0.9181	0.0649-0.9106
Reaction activation energy E (kJ/mol)		375 ± 13			

Note: The results in Tables 4-3-13 and 4-3-14 were obtained by fitting the kinetic data (after correction for moisture adsorption and blown-off powder, i.e., $X_{WL} = X_{WL\text{-}mb}$) to the interface-controlled "shrinking-core" model. The linear correlation coefficients, r_L, and the ranges of fitting (time, X_{WL}, and X_{QXRD} values) are also given in the tables. The data based on SiC(220)/Si (311) line intensity ratios were used.

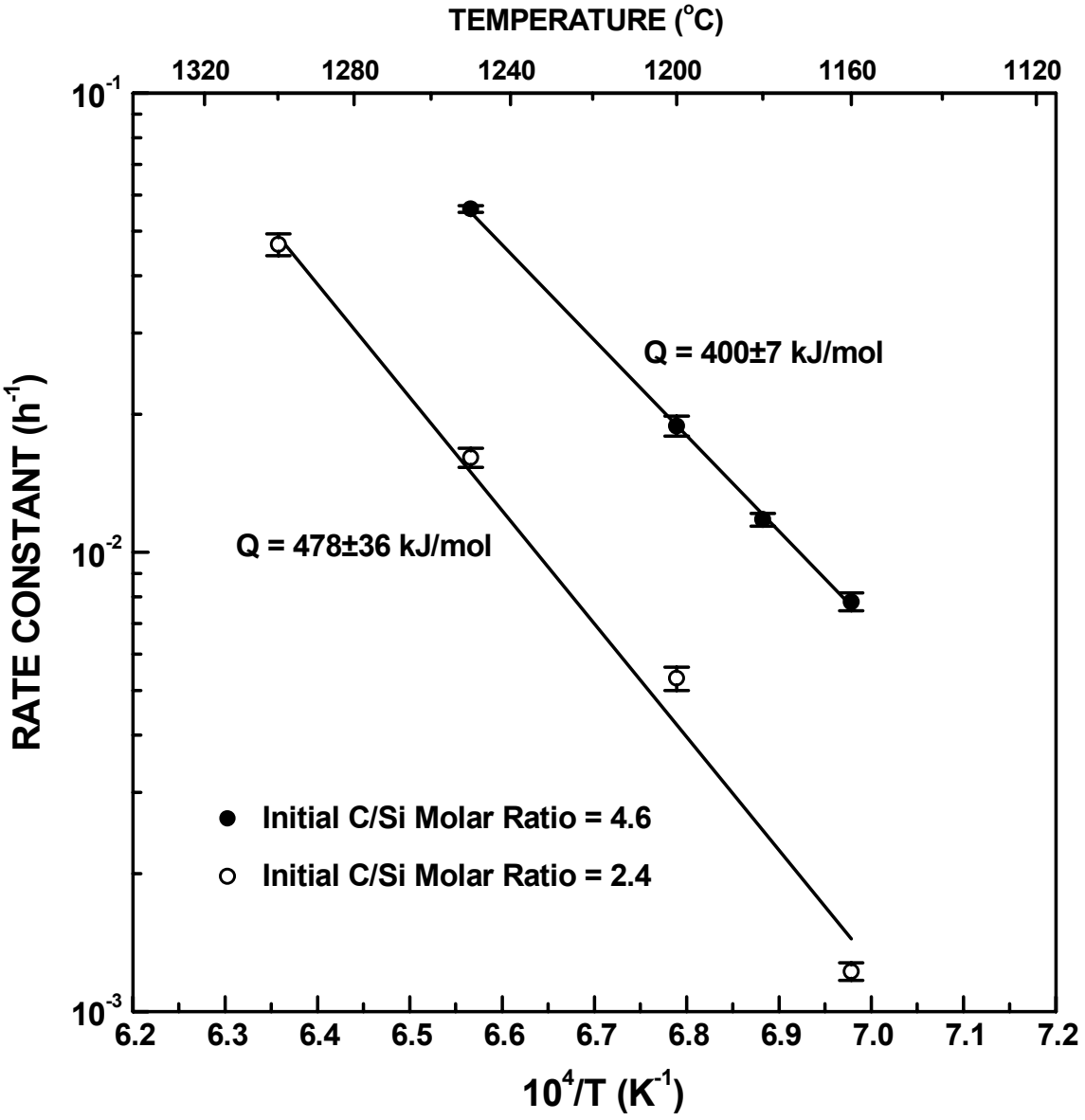

Figure 4-3-28 Plots of reaction rate constant (determined by the QXRD study based on the intensity ratios of the SiC(111) line to the Si(220) line) as a function of inverse temperature for the SC35 (initial C/Si molar ratio = 2.4) and SC8 (initial C/Si molar ratio = 4.6) samples.

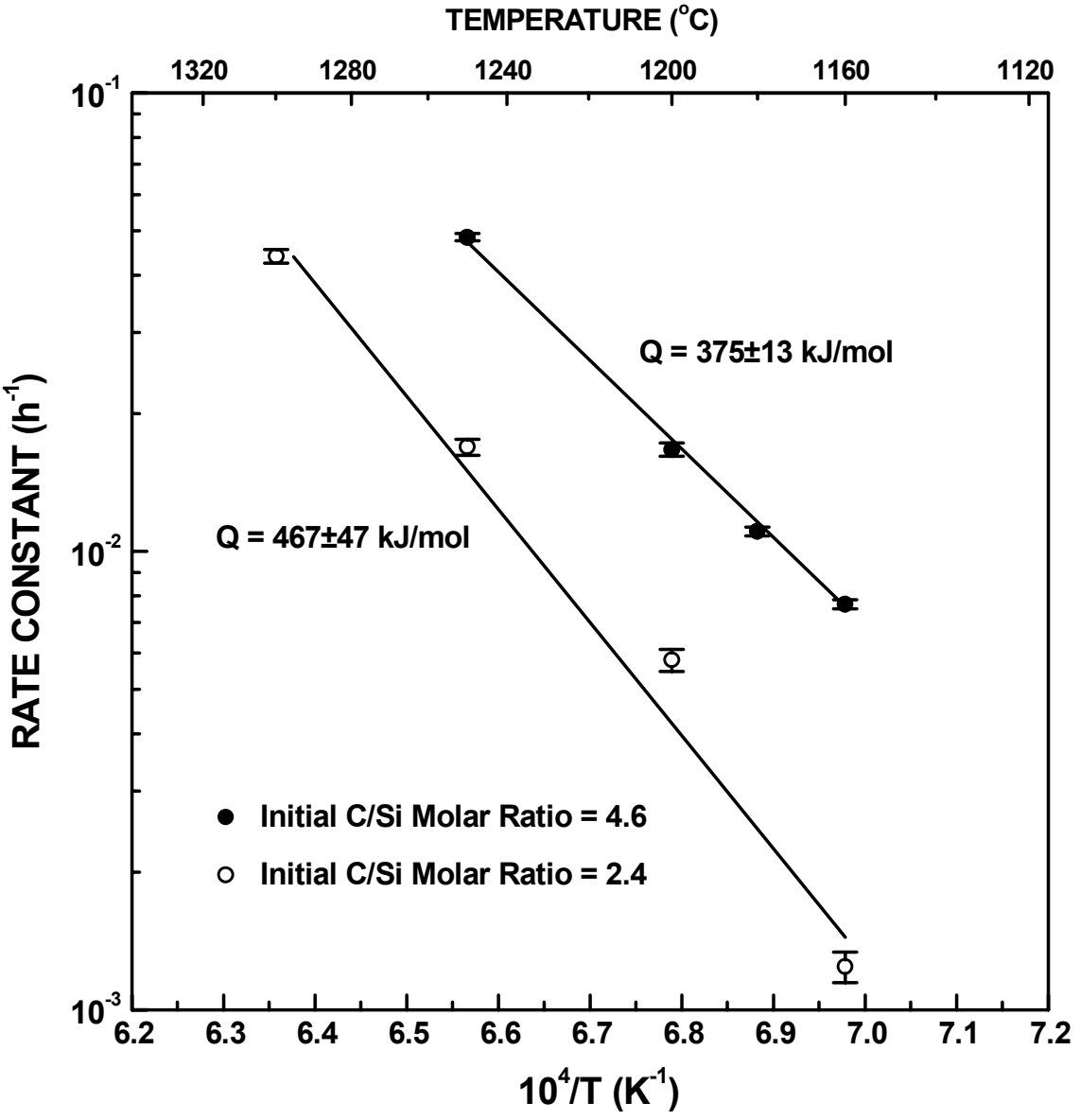

Figure 4-3-29 Plots of reaction rate constant (determined by the QXRD study based on the intensity ratios of the SiC(220) line to the Si(311) line) as a function of inverse temperature for the SC35 (initial C/Si molar ratio = 2.4) and SC8 (initial C/Si molar ratio = 4.6) samples.

to the value determined from the weight loss (X_{WL}) data (i.e., 375±3 kJ/mol). For the SC35 series, E = 478±36 kJ/mol, which is higher than the value from the weight loss (X_{WL}) data (i.e. 423±19 kJ/mol). This difference in values is mostly attributed to the 1160°C data showing a deviation from the trend followed at the higher temperatures. The reaction rate was very slow at 1160°C for the SC35 samples and there was a relatively small amount of SiC formed (e.g., $X_{QXRD} < 20\%$ after 48 h at 1160°C). Therefore, the error associated with the amount of SiC measured by QXRD study was more significant for the SC35 samples heat treated at lower temperature. Actually, if the rate constants from the three points at higher temperatures (1200, 1250, and 1300°C) are used, the calculated activation energy would be 419 ± 4 kJ/mol, much closer to the value obtained from the weight loss data (i.e., 423±19 kJ/mol).

The activation energy values from the QXRD study based on the intensity ratio of the SiC(220) line to the Si(311) line are close to those obtained from weight loss data: $E = 375 \pm 13$ kJ/mol for the SC8 series and $E = 467 \pm 47$ kJ/mol for the SC35 series. If the 1160°C point is excluded from the calculation for the SC35 activation energy, then a value of 391 ± 5 kJ/mol is obtained.

4.3.4 Structural Expectation from the Kinetic Model Identified

As discussed earlier in this section, the CTR reaction kinetics showed the best mathematical fit to the equation for the interface-controlled "shrinking-core" model. Figure 4-3-30 is a schematic illustration of the evolution from reactants to product in the "shrinking-core" reaction model for the formation of SiC via carbothermal reduction. The starting material (top left illustration) is a fine-scale carbon/silica mixture. As the reaction proceeds, a porous SiC layer develops on the outside of the pyrolyzed material (top right illustration). With continued reaction, the volume fraction of porous SiC grows, the volume fraction of the reactant core contracts, and the reaction interface moves inside towards the center of the original reactant (pyrolyzed) particle. This process continues until the reactant core is completely consumed (bottom right illustration).

There are several expectations regarding the structural characteristics of the reaction product if the reaction follows (i) the interface-controlled "shrinking-core" model and (ii) the two-step reaction sequence illustrated in Figure 4-2-1. The first expectation is that pores develop as the SiC reaction product is formed. (This also leads to the expectation that the amount of porosity increases with increasing extent of reaction.) As discussed in section 4.2, the carbon and silica in the pyrolyzed material initially react to form SiO and CO gas according to Equation (4-2-1). Hence, pore formation will occur initially as the reactants are consumed. It is also expected that this porosity will be substantially retained when the SiC product forms because the next step of the reaction involves a relatively small change in the solid volume. This is illustrated by a simple calculation. Based on information in section 4.1.9, assume that the true solid density of carbon is 2 g/cm^3 and the true solid density of SiC is 3.2 g/cm^3. The second step of the

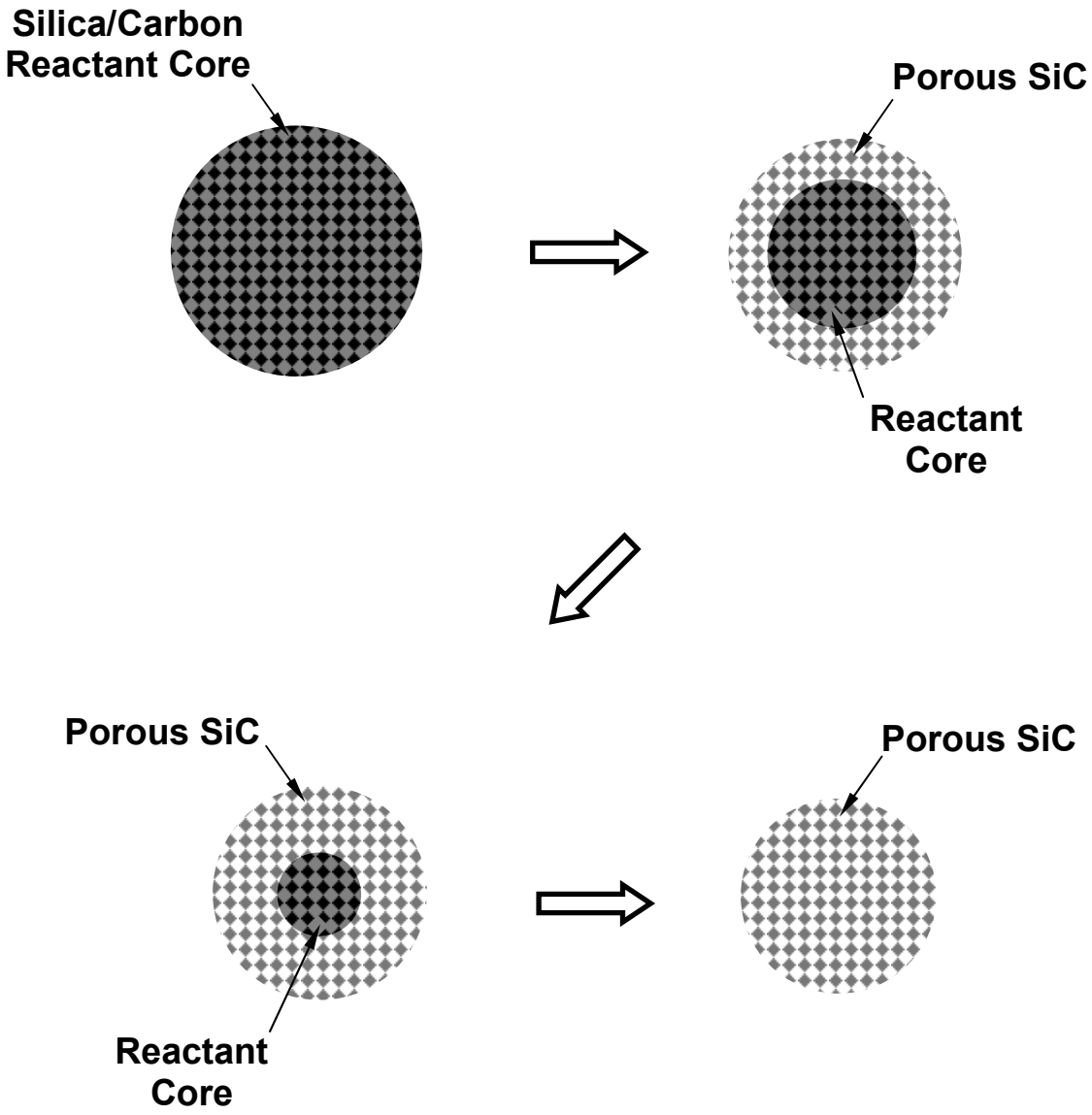

Figure 4-3-30 Illustration of the "shrinking-core" effect during SiC formation through carbothermal reduction.

reaction is:

$$SiO_{(g)} + 2C_{(s)} \rightarrow SiC_{(s)} + CO_{(g)} \qquad (4\text{-}3\text{-}30)$$

The volumes of the carbon reactant and the SiC product are given by:

$$V_C = \frac{2 \times 12}{\rho_C}$$

$$V_{SiC} = \frac{40}{\rho_{SiC}}$$

Therefore, the volume ratio of SiC produced to carbon consumed would be

$$\frac{V_{SiC}}{V_C} = \frac{5\rho_C}{3\rho_{SiC}} = \frac{5 \times 2}{3 \times 3.2} = 1.04$$

This means that there would be almost no change in the solid volume according to the reaction in Equation (4-3-30). Hence, this reaction does not provide any mechanism to eliminate pores that would be formed by the first step in the reaction. Therefore, the pore volume should increase as the reaction proceeds unless the as-formed SiC product starts to densify via sintering.

As a side note, it is pointed out that the formation of a porous reaction product is consistent with some kinetic considerations associated with the interface-controlled "shrinking-core" model. The model requires that (1) the diffusion of the reactants be much faster compared to the reaction at the interface and (2) the nucleation is instantaneous so that the reactant is covered by a product layer. The proposed reaction involves SiO and CO gases as a reaction intermediate and reaction product, respectively. A porous SiC layer would enable the fast transport of both of these gases (Hulbert, 1969).

Another structural expectation of the proposed reaction model is that a uniform microstructure (e.g., crystallite size and pore size) will develop as the reaction interface

sweeps through the pyrolyzed particle. This is because the microstructure of the pyrolyzed material is expected to be uniform and the reaction mechanism remains the same as the reaction interface moves towards the center of the reactant. Hence, the SiC product microstructure should remain unchanged unless there are diffusional mechanisms that operate in the porous SiC regions to promote processes such as densification, grain growth, and/or coarsening.

It will be shown later in section 4.4 that the structural expectations described above are fulfilled for most of the reaction.

4.4 Structural Evolution During Carbothermal Reduction

In this section, characterization of structural changes in the solid product formed during the carbothermal reduction will be discussed. Specifically, the SiC crystallite size, the specific surface area, and the pore characteristics (specific volume) were determined. SEM and TEM micrographs of the powders with different extents of conversion will also be presented.

4.4.1 Crystallite Size Development

4.4.1.1 Crystallite Size of SC35 Samples after CTR

Figure 4-4-1 shows plots of average SiC crystallite size (obtained by XRD line broadening method) vs. reaction time at temperatures in the range of 1160-1300^{o}C for the SC35 series (initial C/Si molar ratio of 2.4). Figure 4-4-2 shows the same data re-plotted as the average crystallite size vs. the fractional weight loss for the carbothermal reduction reaction. The following observations are made from these figures: (1) The average crystallite size in Figure 4-4-2 follows a single trend that is independent of the reaction temperature. This suggests that the reaction mechanism does not change over the range of the temperature investigated (i.e., 1160-1300^{o}C). (2) The first data point shown in these figures was measured for a sample with fractional weight loss of ~0.26. It was not possible to measure crystallite sizes at earlier stages in the reaction (i.e., smaller fractional weight losses) because the β-SiC peak intensities were too low to obtain reliable results. (3) The average crystallite size measured at the earliest point in the carbothermal reduction reaction (i.e., at fractional weight loss of ~0.26) was only ~9 nm. This small crystallite size indicates that a fine scale of mixing (of the silica-rich and carbon-rich components) was achieved in the pyrolyzed materials used for the

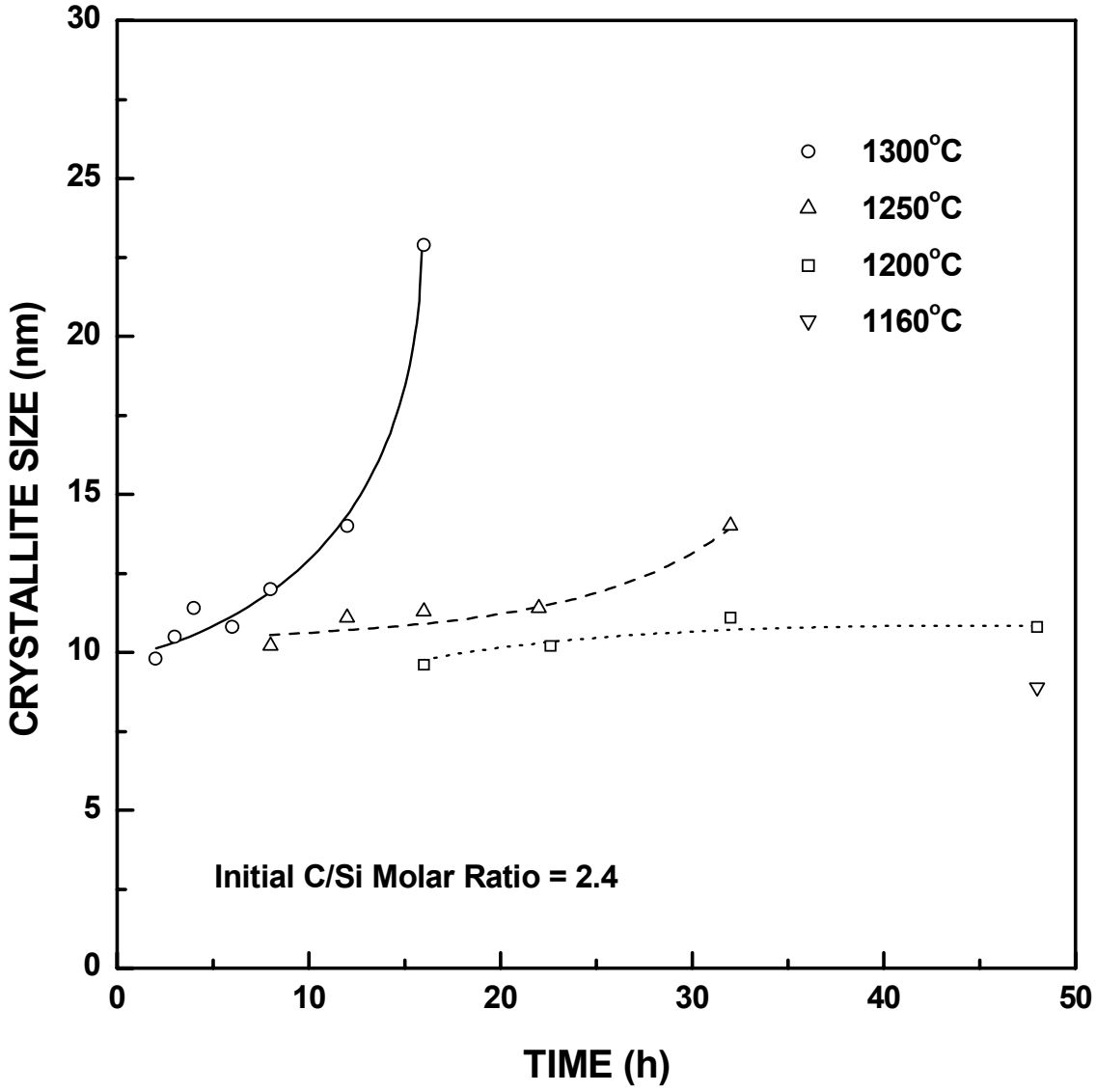

Figure 4-4-1 Plots of SiC average crystallite size vs. reaction time for SC35 samples (initial C/Si molar ratio = 2.4) heat treated at different temperatures.

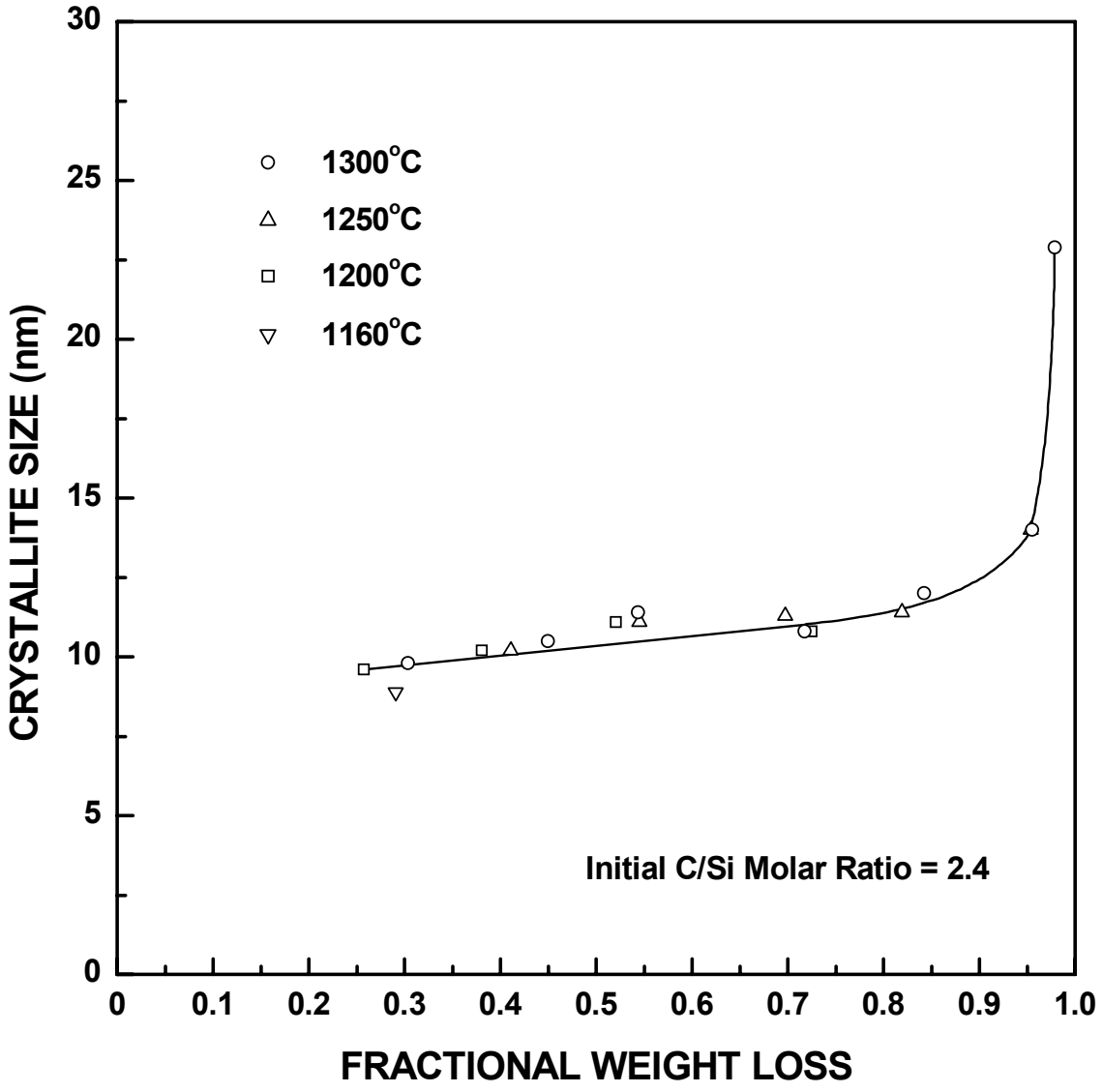

Figure 4-4-2 Plot of SiC average crystallite size vs. fractional weight loss (after both corrections for moisture adsorption and blown-off powder) for SC35 samples prepared with initial C/Si molar ratio = 2.4 at different temperatures.

carbothermal reduction reaction. (4) It is evident from both figures that the crystallites show only minor increases in average size for most of the reaction. For example, the crystallite size only increased from ~9 nm to ~12 nm as the extent of reaction increased from $X_{WL} \approx 0.26$ to $X_{WL} \approx 0.80$. It is only after longer times at the highest temperature (i.e., when the fractional weight loss is > 0.95) that a significant increase in average crystallite size is observed.

The very limited increase in SiC crystallite size over most of the reaction is consistent with the interface-controlled "shrinking-core" model. As explained in section 4.3.4, it is expected from the proposed reaction model that a relatively uniform crystallite size of SiC would be obtained as the reaction proceeded (i.e., unless there were diffusional mechanisms that operated in the porous SiC regions which promoted grain growth or coarsening). During the reaction, porous reacted SiC regions and dense unreacted regions co-exist as the overall reaction proceeded. If the microstructure of the porous SiC regions continued to evolve, (i.e., there was adequate diffusion operative to promote grain growth or coarsening), then the average SiC grain size would have increased significantly with time. However, this was not observed in the current system. The crystallite size did not show a significant increase until the late stage of the reaction.

In contrast, the limited increase in SiC crystallite size over much of the reaction does not appear to be consistent with the nucleation-and-growth model. Recall from section 4.3 (Tables 4-3-6 and 4-3-7) that data fitting to this model gave exponent m values of ~1. As described in Chapter II, this exponent value could be associated with the following scenarios:

1. diffusion-controlled 2-D growth with zero nucleation rate (single nucleation event)

2. diffusion-controlled 2-D growth with decreasing nucleation rate (multiple nucleation events)
3. diffusion-controlled 1-D growth with decreasing nucleation rate (multiple nucleation events)
4. interface-controlled 1-D growth with zero nucleation rate (single nucleation event)
5. interface-controlled 1-D growth with decreasing nucleation rate (multiple nucleation events)

The crystallite size measurements are not consistent with any of above scenarios for two reasons. First, suppose the reaction occurs via a single nucleation event (i.e., zero nucleation rate) which is followed by growth. In this case, the mean crystallite size should increase steadily with time as the reaction proceeds. However, this is contrary to the observation made in this study. Second, suppose the reaction occurs via multiple nucleation events. In this case, it is possible that the mean crystallite size of the product could remain constant with time. (Although the older (first nucleated) crystallites would grow as the reaction proceeded, the newer crystallites would be smaller. Hence, it is possible that the mean size could remain nearly constant after an initial period of growth.) However, the problem with the assumption of multiple nucleation events is that it requires the crystallites to grow in only one or two dimensions. There is no evidence to support such growth mechanisms. In fact, the available evidence strongly indicates that the SiC crystallites undergo three-dimensional growth. This is indicated by the observation that the XRD line broadening measurements (used to determine the SiC crystallite sizes) show that crystallite sizes are similar along different crystallographic directions. (Detailed results are provided in Appendix H.) In addition, TEM observations (discussed in detail in section

4.4.2) show that the SiC crystallites have an equiaxed morphology. In summary, the crystallite size measurements shown in Figures 4-4-1 and 4-4-2 and Table H-1 not only provide support for the interface-controlled "shrinking-core" model, but also provide support for the argument that the nucleation-and-growth model is not applicable in this case.

The mean SiC crystallite size showed a rapid increase during the late stage of the reaction (i.e., when the fractional weight loss is greater than ~0.95). This is expected because it has been shown that SiC coarsens when excess (free) carbon is removed and when dopants that prevent coarsening (e.g, boron, aluminum) are absent (Sacks et al., 1999). The same effect of free carbon on the coarsening of SiC after CTR was also observed by Narisawa et al. (1998) in their study of SiC formation from a similar TEOS/phenolic resin system (Table 2-3-4). Rapid crystallite growth occurred during the late stage of the reaction because many regions of the particle will have little or no free carbon remaining. Hence, nearly all regions of the sample were simultaneously undergoing coarsening.

Localized removal of carbon might possibly explain the small, but obvious, increase in average crystallite size over much of the range of the reaction. As the reaction proceeds, there may be some localized regions in which enough of the carbon has been removed that some coarsening can begin and then continue to occur while the reaction is proceeding in other areas of the sample. Such regions, if present, apparently remain relatively limited (in total volume) until the overall reaction reaches greater than ~0.95 fractional weight loss.

The SiC crystallite size data for the SC35 series was fit to a conventional equation that describes the grain growth of solids, as shown by:

$$G^m - G_0^m = k_G t \qquad (4\text{-}4\text{-}1)$$

in which G is the average grain size at time t, G_0 is the average grain size when $t = 0$, k_G is the grain growth rate constant, and m is the exponent parameter. However, none of the common values of m (i.e., 1-4) fit the experimental data satisfactorily.

4.4.1.2 Crystallite Size of SC8 Samples after CTR

Figure 4-4-3 shows plots of average SiC crystallite size vs. reaction time at temperatures in the range of 1160-1250^{o}C for the SC8 series (initial C/Si molar ratio of 4.6). Figure 4-4-4 shows the same data re-plotted as the average crystallite size vs. the fractional weight loss for the carbothermal reduction reaction. Similar to the SC35 series, the average crystallite size in Figure 4-4-3 follows a single trend that is independent of the reaction temperature. The first data point shown in these figures was measured for a sample with fractional weight loss of ~0.26. The average crystallite size was ~12 nm. As in the SC35 series, there is only a small increase in the SiC crystallite size for most of the reaction and then the crystallite size increases rapidly in the late stage of the reaction.

4.4.1.3 Comparison of SiC Crystallite Size for SC35 and SC8 Samples

Figure 4-4-5 shows a comparison of SiC crystallite size vs. fractional weight loss for the SC35 and SC8 series. One interesting observation is that the average crystallite size for the carbon-rich SC8 samples is slightly larger than the silica-rich SC35 samples until the very end of the reaction. A possible reason for this difference is discussed below.

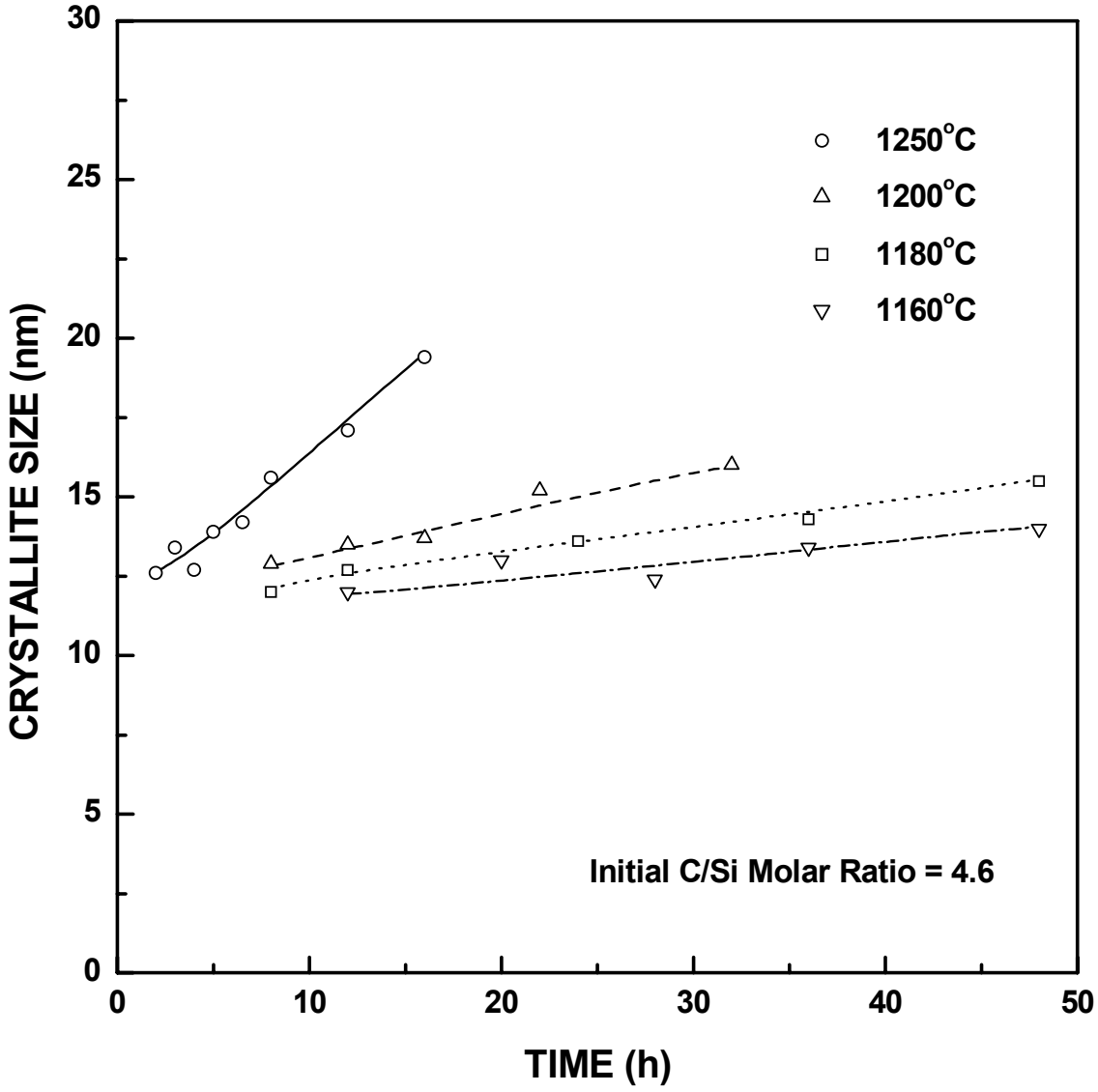

Figure 4-4-3 Plots of SiC average crystallite size vs. reaction time for SC8 samples (initial C/Si molar ratio = 4.6) heat treated at different temperatures.

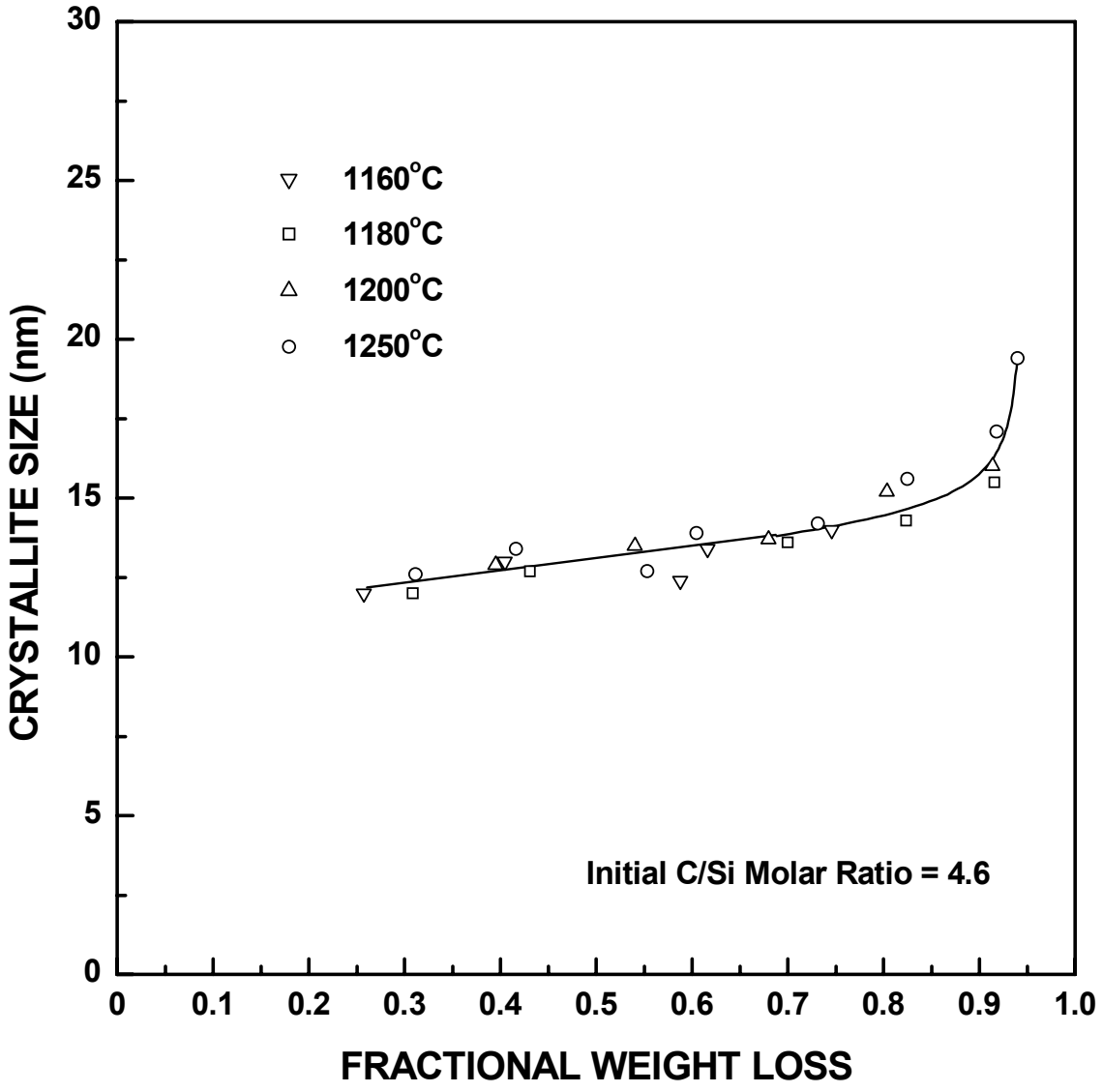

Figure 4-4-4 Plot of SiC average crystallite size vs. fractional weight loss (after both corrections for moisture adsorption and blown-off powder) for SC8 samples prepared with initial C/Si molar ratio = 4.6 at different temperatures.

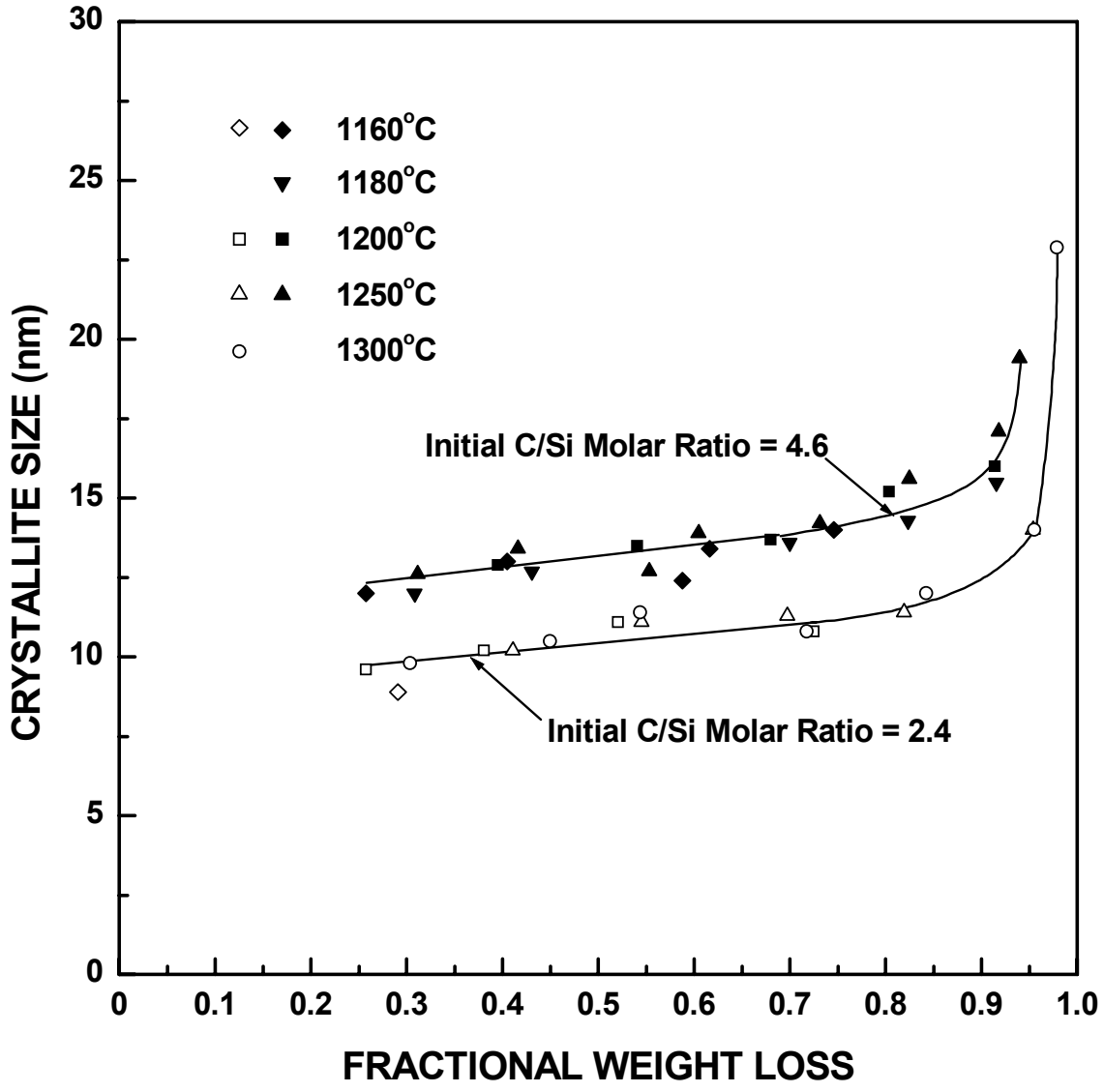

Figure 4-4-5 Plots of SiC average crystallite size vs. the fractional weight loss (after correction for moisture adsorption and blow-off powder) for heat-treated samples prepared with initial C/Si molar ratios of 2.4 (SC35 samples) and 4.6 (SC8 samples).

As discussed previously, the pyrolyzed particles consist of a nearly-dense, fine-scale mixture of carbon and silica. The scale of mixing is presumably dependent on two major factors. The first is the size of the polysilicate species that form in the sol. (These species are considerably larger than the size of the phenolic resin oligomers. Based on previous research with similar sols (Brinker and Scherer (1990) p.187), the polysilicate species in the sol are probably on the order of ~3-7 nm.) The second factor is the extent of segregation that occurs during subsequent processing of the sol (i.e., concentration, drying, and pyrolysis). Although the detailed structure of the pyrolyzed samples is not known, it is presumed that the carbon and silica phases form an interpenetrating network. This is suggested because of the relatively high-volume fraction of each phase. Although the structural features of the mixture are presumably complex, it is still useful to try to define some type of "average feature size" for each phase. For example, suppose random straight lines were drawn through cross-sections of high magnification images of the silica/carbon sample. These lines would intersect silica and carbon phases. The distribution of lengths of each line that intercepts each phase could be measured and an average intercept size could be defined.

For convenience in the discussion, assume that the SC35 and SC8 pyrolyzed samples consist of silica regions which are uniform-sized spherical particles and that these silica regions are distributed in a continuous carbon matrix. (As suggested above, this simple model is unlikely for the SC8 and SC35 samples.) For the SC35 pyrolyzed sample, the estimated amounts of each phase were ~65 vol% silica and ~35 vol% carbon (Table 4-1-9). For the SC8 pyrolyzed sample, the estimated amounts of each phase were ~49 vol% silica and ~51 vol% carbon (Table 4-1-9). Figure 4-4-6(a) schematically illustrates a

highly idealized structure of the SC35 sample. To produce a sample with higher carbon content (e.g., such as SC8), the structure shown in Figure 4-4-6(a) could be changed by: (i) decreasing the number of silica particles (as shown in Figure 4-4-6(b)), (ii) decreasing the diameter of the silica particles but keeping the same number of particles (as shown in Figure 4-4-6(c)), or (iii) some combination of (i) and (ii). The result of this exercise is that the "average feature size" for the carbon regions (e.g., such as defined by some linear intercept) increases when the carbon volume fraction is increased, such as the case when SC8 samples are considered. Therefore, it is believed that the SC8 samples have carbon regions with a larger "average feature size" compared to the SC35 samples. As discussed previously (section 4.2), it is believed that SiC forms by reaction of SiO gas on the carbon particle surfaces. Hence, it might be surmised that the size of the SiC particles that develop is proportional to the "average feature size" of the carbon regions. This could explain the slightly larger SiC crystallite sizes for the SC8 samples that were observed for most of the reaction.

A similar geometrical argument can be made by reversing the geometry for the carbon and silica phases shown in Figure 4-4-6. Figure 4-4-7 shows the case where carbon particles are the particulate phase and silica is the continuous phase. Figure 4-4-7(a) depicts the case for SC35 (i.e., the silica-rich sample). The carbon content of the sample can be increased (as in SC8) by either increasing the size of the carbon particles (as in Figure 4-4-7(b)) or increasing the number of carbon particles (as in Figure 4-4-7(c)). In both cases, the "average feature size" of the silica regions decreases. However, only the case depicted in Figure 4-4-7(b), in which the carbon particle size is increased, would

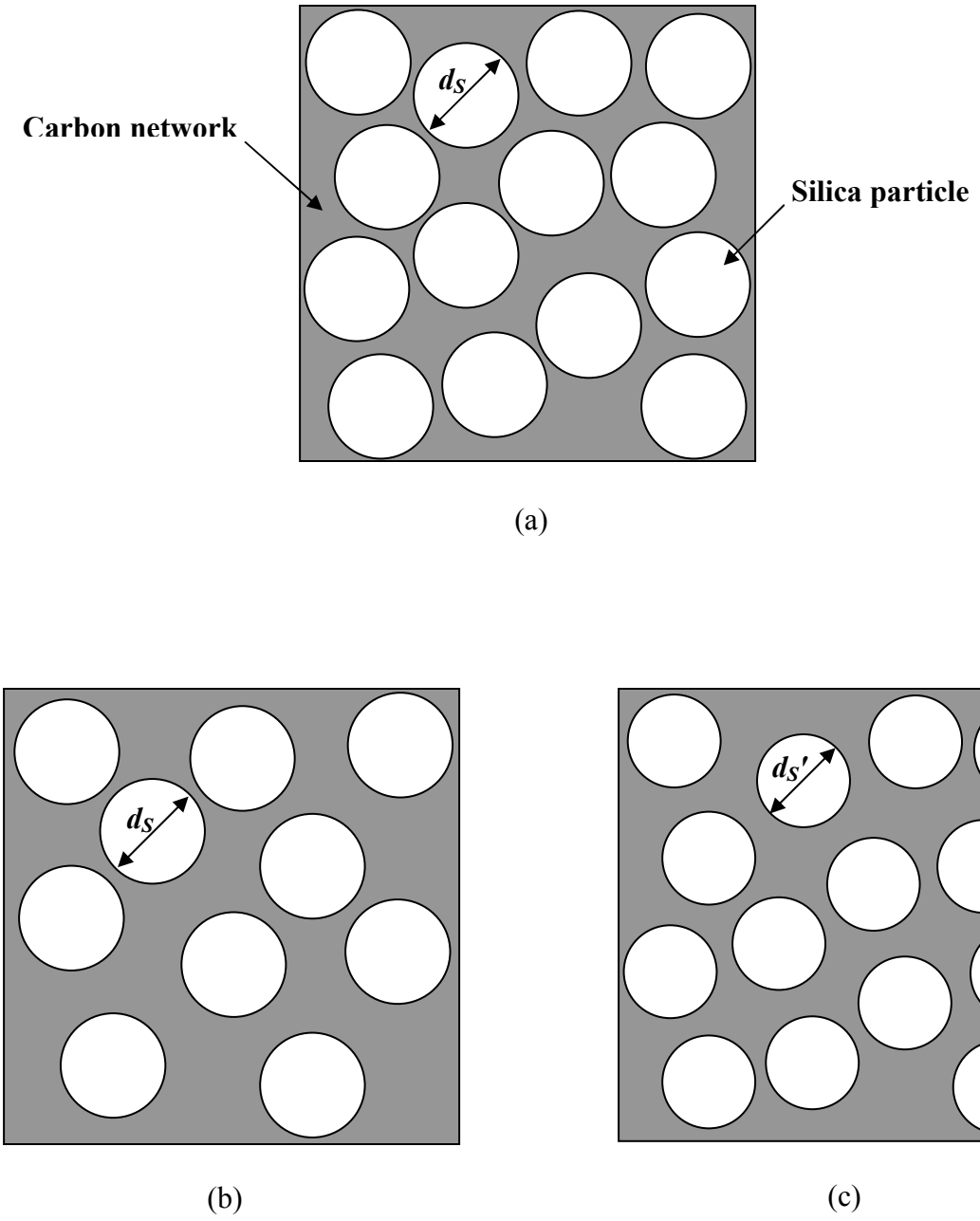

Figure 4-4-6 Illustration of the idealized structure of pyrolyzed material comprising a carbon matrix and spherical silica particles: (a) carbon volume content is ~35%, silica particle diameter is d_S; (b) carbon volume content is ~51% and silica particle diameter is also d_S; (c) carbon volume content is ~51%, and silica particle diameter is $d_S' = 0.91\ d$. Note that the silica particles are depicted as uniform-sized spheres, while the actual silica regions have irregular shapes and a distribution of sizes.

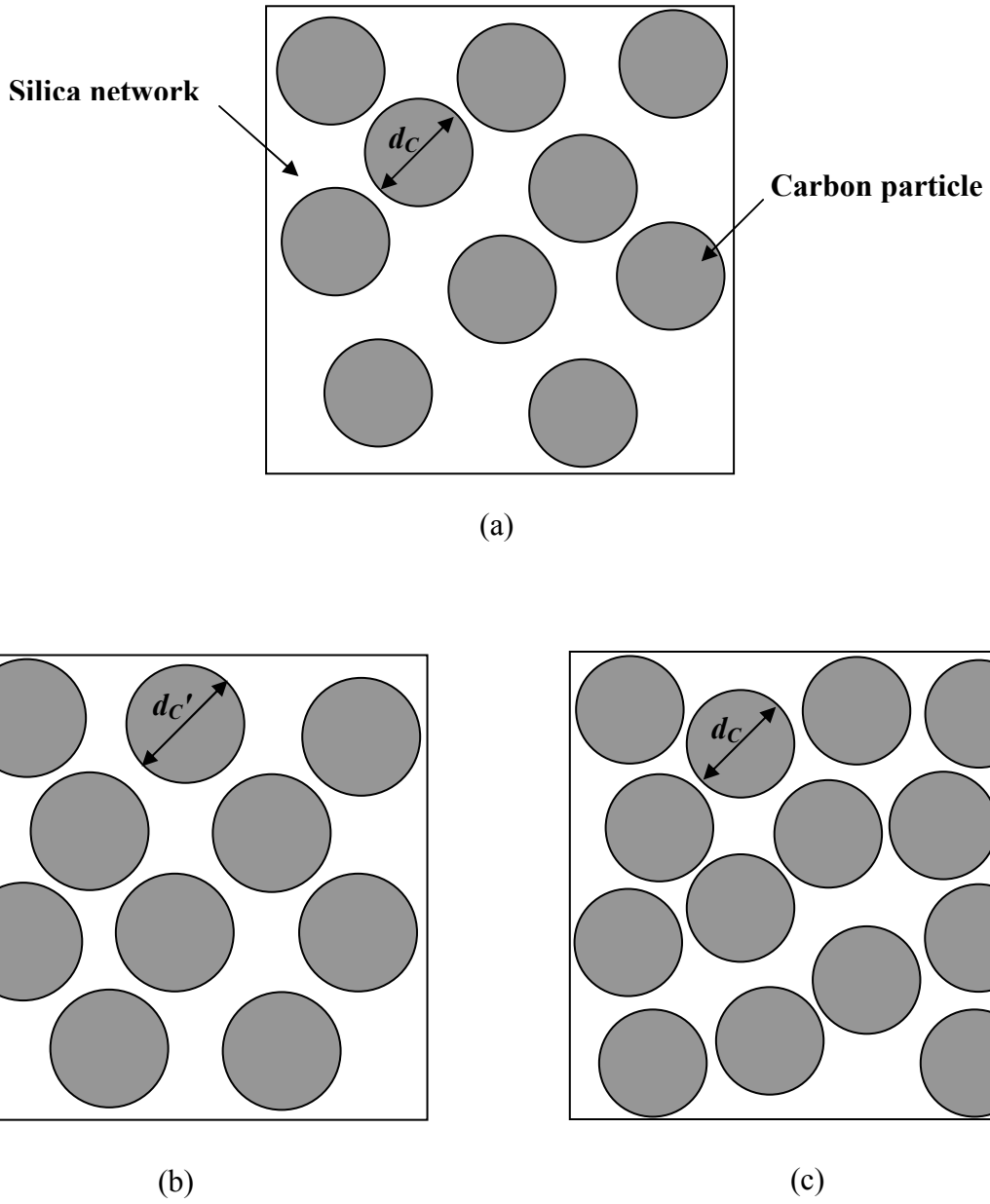

Figure 4-4-7 Illustration of the idealized structure of pyrolyzed material comprising a silica matrix and spherical carbon particles: (a) carbon volume content is ~35% and carbon particle diameter is $\boldsymbol{d_C}$; (b) carbon volume content is ~51% and carbon particle diameter is $\boldsymbol{d_C'} = 1.11\boldsymbol{d_C}$; (c) carbon volume content is ~51% and carbon particle diameter is also $\boldsymbol{d_C}$. Note that the carbon particles are depicted as uniform-sized spheres, while the actual carbon regions have irregular shapes and a distribution of sizes.

account for the increased SiC crystallite size for the SC8 samples compared to the SC35 samples.

When the carbothermal reduction reaction is fully completed and grain coarsening becomes more significant, SC35 samples show much more rapid growth of the SiC crystallites compared to the SC8 samples. Table 4-4-1 shows results for the samples heat treated for 2 h at 1495^{o}C and 1600^{o}C. As expected, the large amount of free carbon in the SC8 samples inhibits the SiC crystallite growth, resulting in much smaller sizes compared to the SC35 samples. This is consistent with the results that were reported by Narisawa et al. (1998), as shown in Table 2-3-4.

Table 4-4-1 Crystallite size of SC35 and SC8 high temperature heat-treated samples.

Heat treatment condition	Samples	$D_{(111)}$ (nm)	$D_{(220)}$ (nm)	$D_{(311)}$ (nm)	D_{avg} (nm)	Standard deviation (nm)
1495(2h)	SC35	40.7	40.4	36.7	39.2	2.2
	SC8	31.7	32.2	26.2	30.0	3.3
1600(2h)	SC35	61.1	63.7	64.2	63.0	1.6
	SC8	35.8	39.5	36.0	37.1	2.1

4.4.2 TEM Observation on the Carbothermal Reduction Product

Figures 4-4-8 and 4-4-9 show the HRTEM micrographs of the SC42-1300(30min) sample which has a fractional weight loss of 0.12. The micrographs show SiC crystallites in an amorphous matrix. The measured *d* spacing for the SiC is ~0.25 nm. This matches

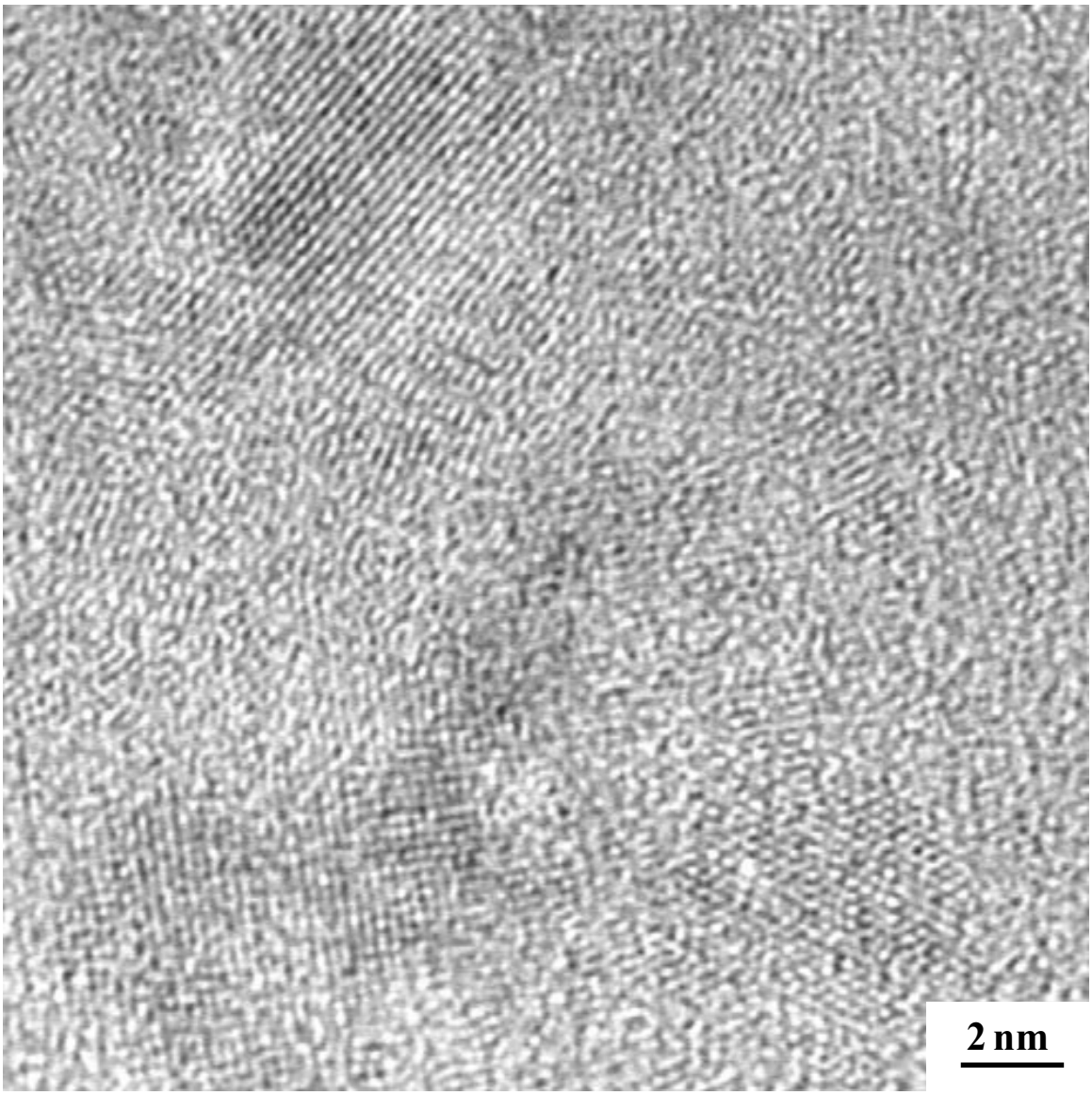

Figure 4-4-8 HRTEM image of the SC42-1300(30min) sample (X_{WL} = 0.12) showing multiple β-SiC crystallites in an amorphous matrix. The sample was prepared by the "embedding-method."

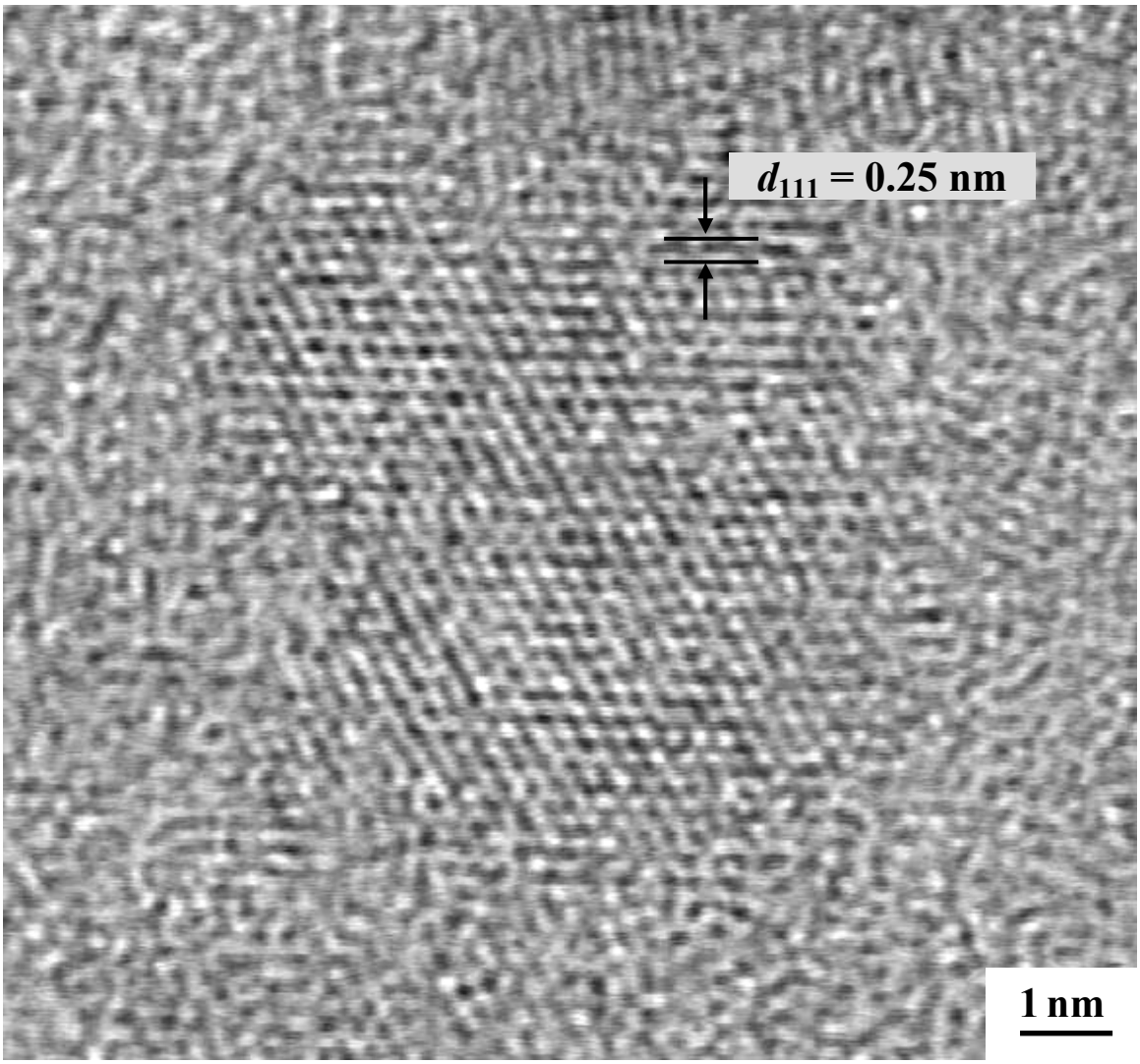

Figure 4-4-9 HRTEM image of the SC42-1300(30min) sample (X_{WL} = 0.12) showing the lattice fringes of a β-SiC crystallite. The electron beam was along the <011> zone axis. The sample was prepared by the "embedding method."

closely the inter-planar distance for the β-SiC (111) planes (d_{111} = 0.252 nm, JCPDS No. 29-1129). The SiC crystallites in Figures 4-4-8 and 4-4-9 have sizes that are smaller than the values of ~8-9 nm that were obtained by XRD line broadening measurements on the SC35-1160(48h) and SC35-1200(16h) samples (see Figures 4-4-1 and 4-4-2 and Table H-1). However, the latter two samples had fractional weight losses of 0.29 and 0.26, respectively, which indicates that the extent of reaction was greater than in the SC42-1300(30min) sample. Hence, it would not be surprising if the mean SiC crystallite size was somewhat smaller for the SC42-1300(30min) sample.

Figures 4-4-10 and 4-4-11 show HRTEM images of the SC42-1300(2h) sample which had a fractional weight loss of 0.35. The β-SiC crystallites appear to be slightly larger for this sample, although it is difficult to be certain because of the poor image quality. As expected, the measured *d*-spacing remained the same (0.25 nm), again matching the inter-planar distance for the β-SiC (111) planes.

Figures 4-4-12 to 4-4-15 show TEM micrographs of an ~3 μm particle of the SC42-1300(3h) sample with a fractional weight loss of 0.63. The following observations can be made from these micrographs: (1) The particle is a highly porous aggregate (Figures 4-4-13 to 4-4-15). (As will be shown in section 4.4.3, this sample is expected to have a relative porosity of ~40%.) The observation of substantial porosity is consistent with the proposed reaction mechanism based on the interface-controlled shrinking-core model, as illustrated in Figure 4-3-29. (2) The overall particle is composed of smaller porous clusters. These clusters vary greatly in size, but many appear to be in the range of ~50-250 nm (Figures 4-4-12 and 4-4-14). (3) The β-SiC crystallites have fairly uniform sizes with diameters

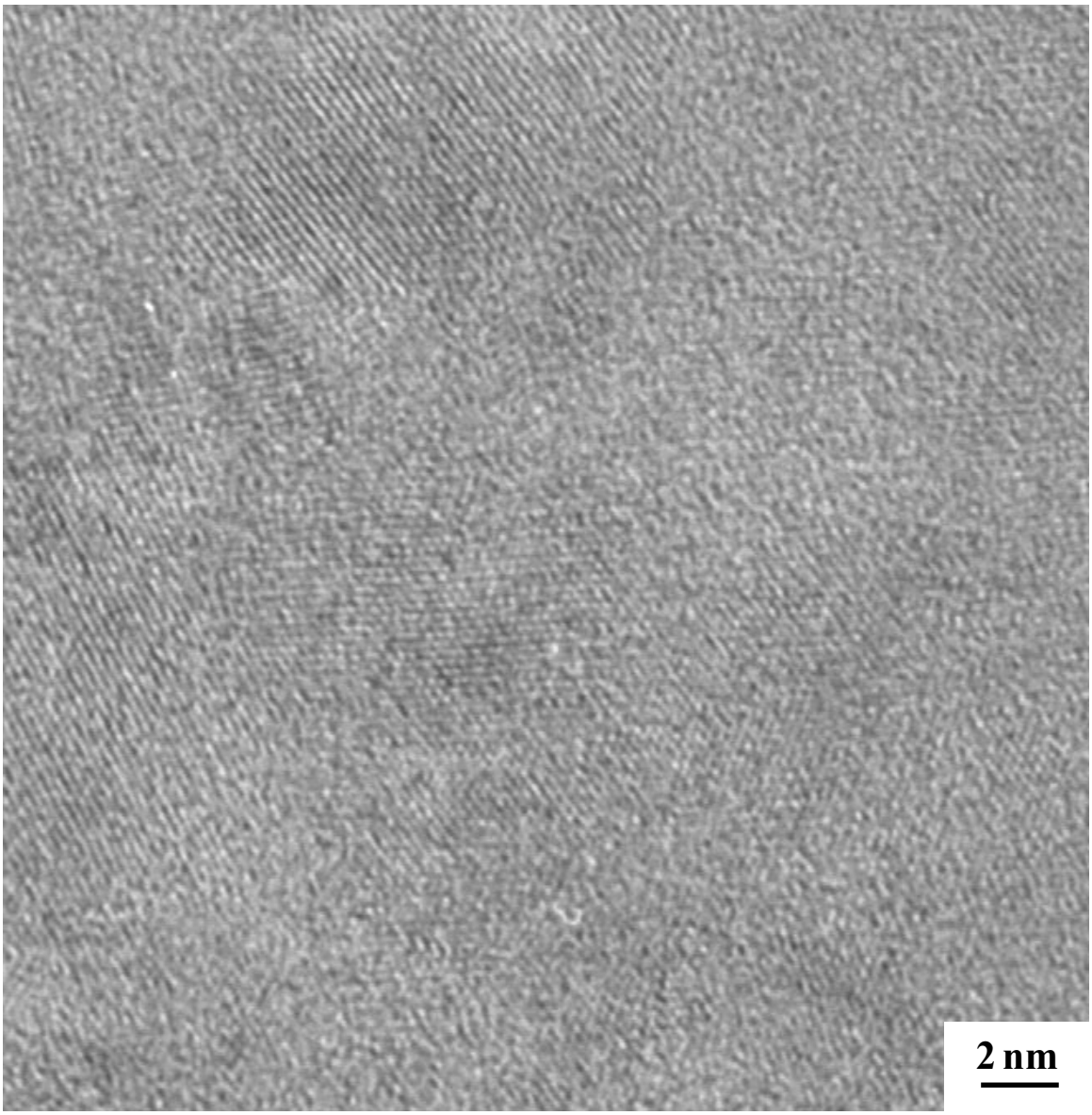

Figure 4-4-10 HRTEM image of the SC42-1300(2h) sample (X_{WL} = 0.35) showing multiple β-SiC crystallites in an amorphous matrix. The sample was prepared by the "embedding method".

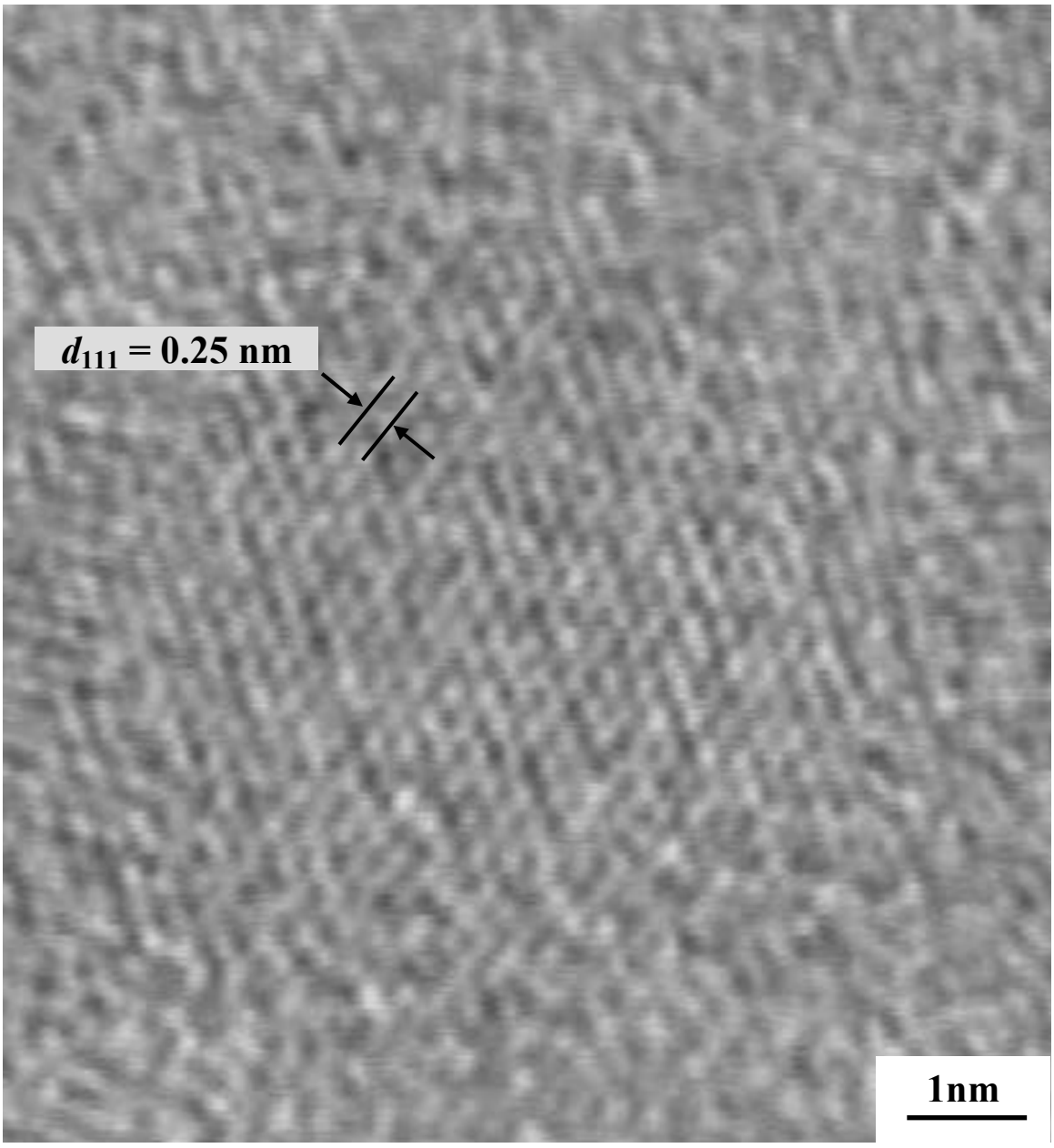

Figure 4-4-11 HRTEM image of the SC42-1300(2h) sample (X_{WL} = 0.35) showing a β-SiC crystallite in an amorphous matrix. The electron beam was along the <011> zone axis. The sample was prepared by the "embedding method."

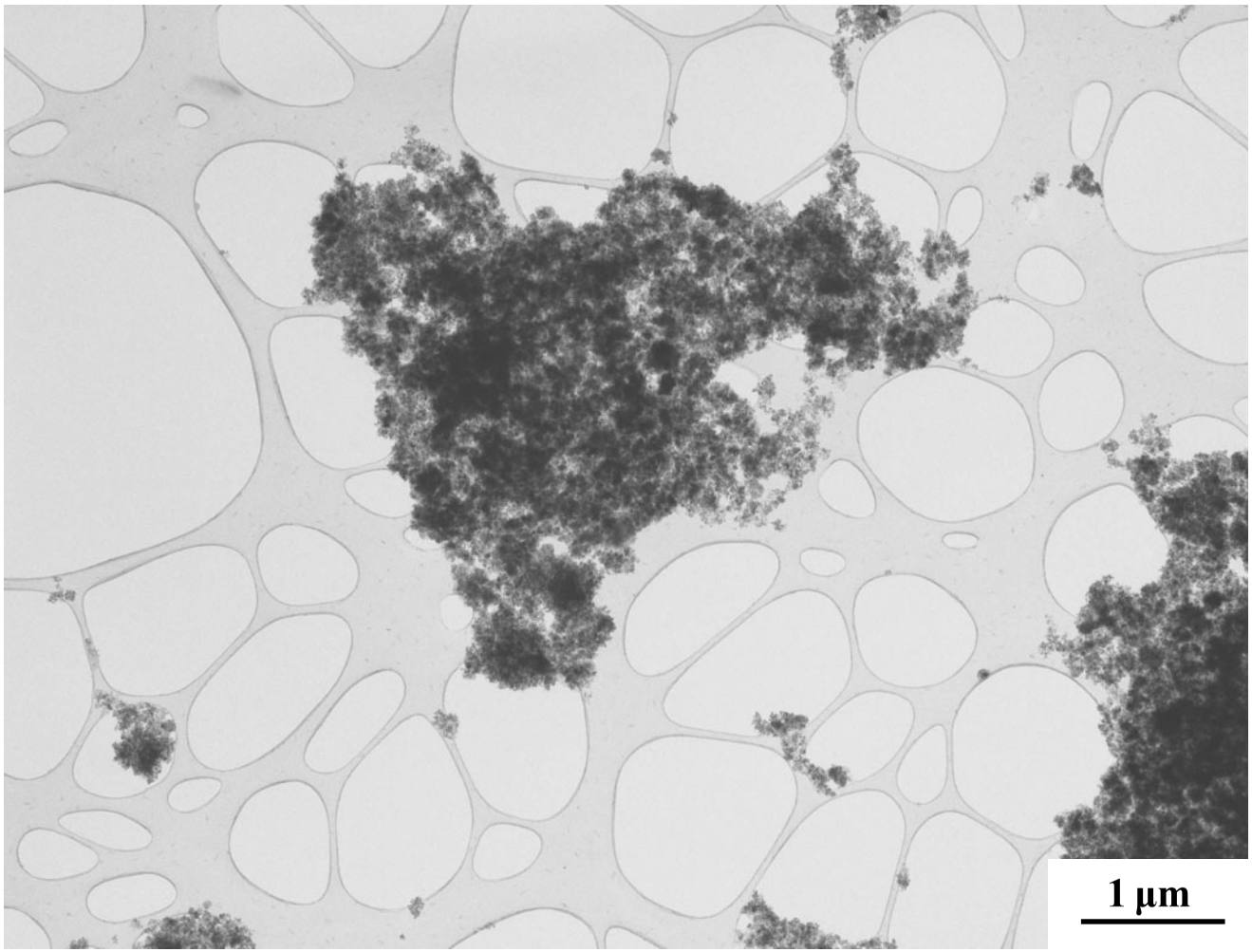

Figure 4-4-12 TEM image of the SC42-1300(3h) sample (X_{WL} = 0.63) showing an ~3 µm particle. The sample was prepared by the "dispersing method."

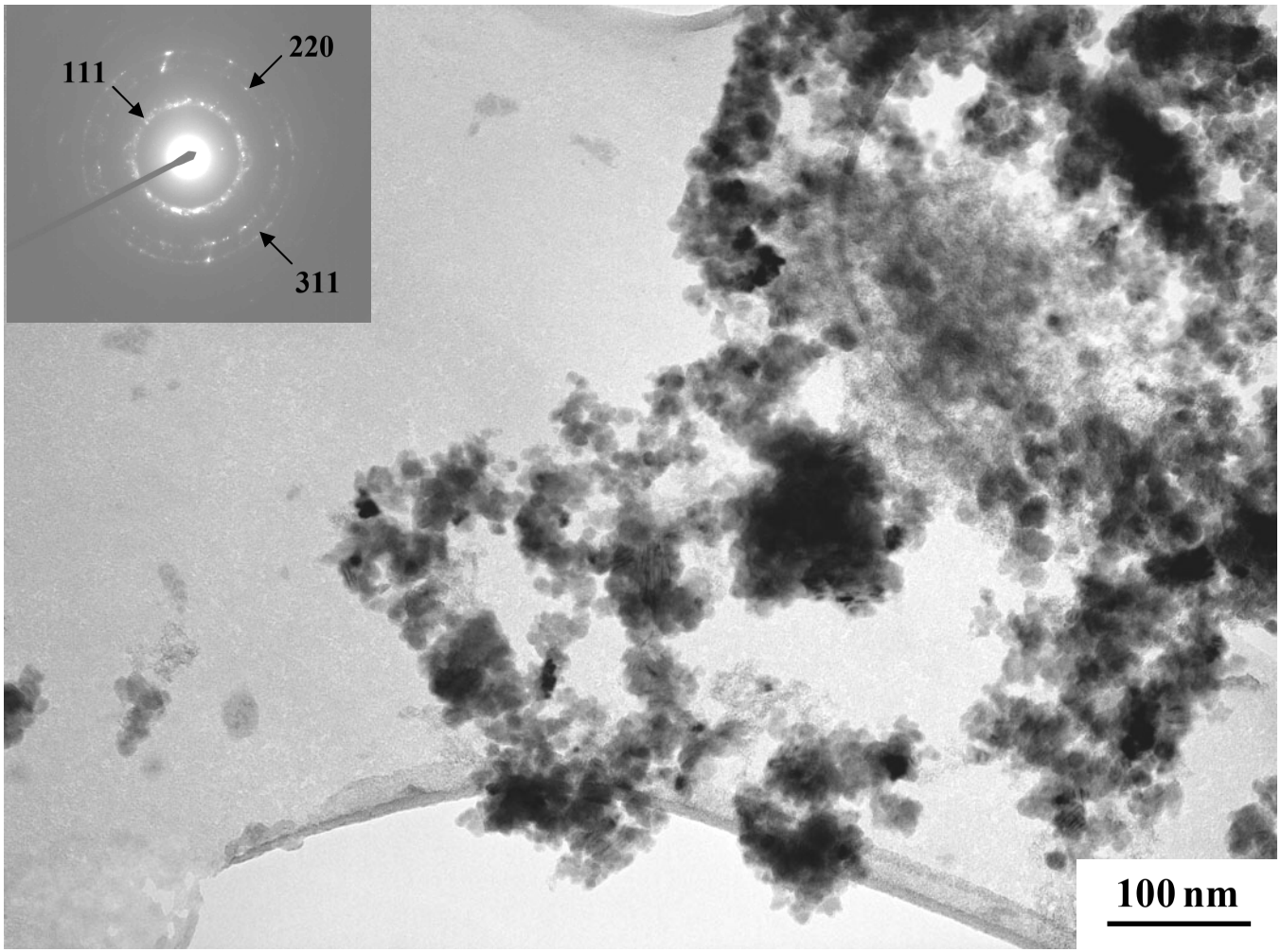

Figure 4-4-13 TEM image and the corresponding electron diffraction pattern of the SC42-1300(3h) sample (X_{WL} = 0.63) showing clusters of primary particles. The sample was prepared by the "dispersing method."

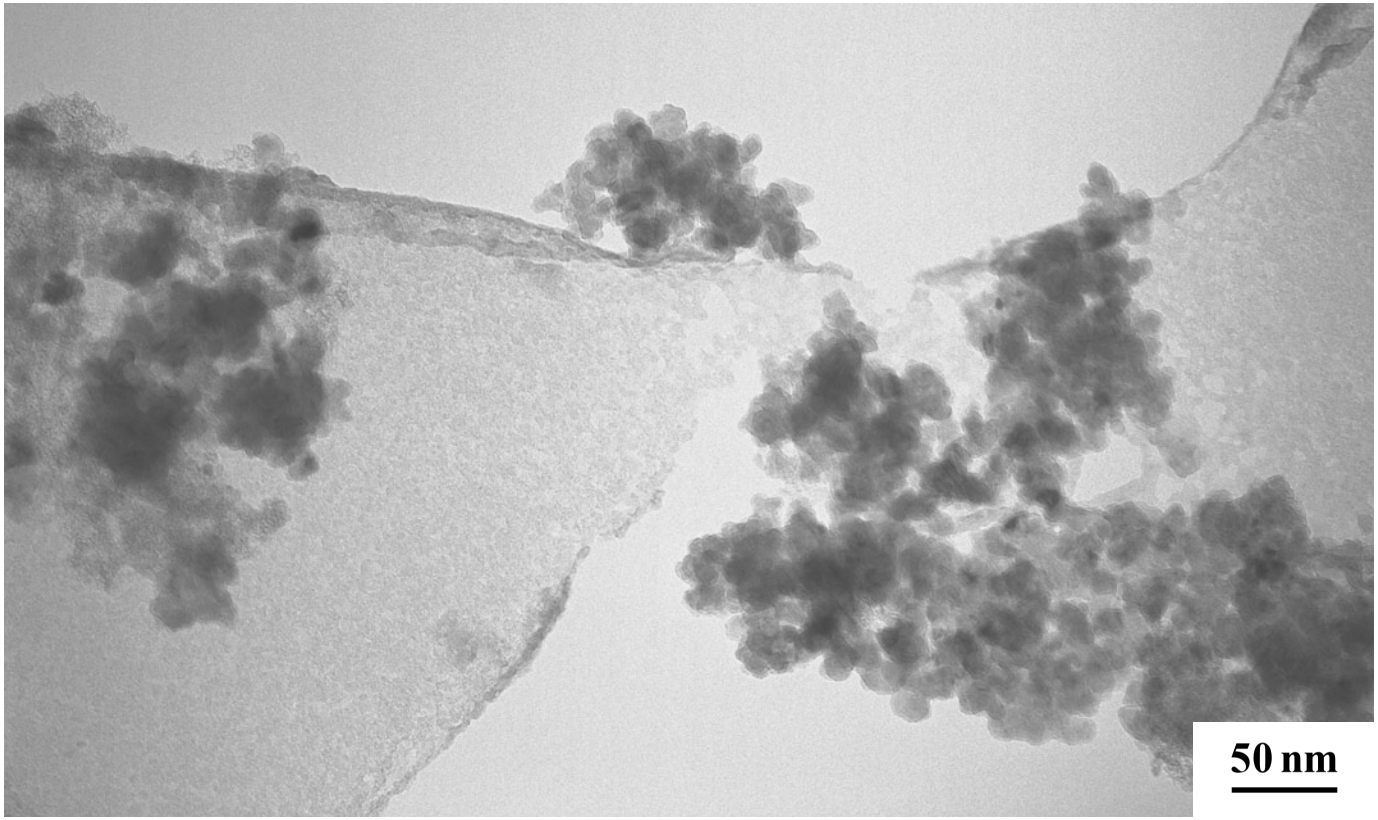

Figure 4-4-14 TEM image of the SC42-1300(3h) sample (X_{WL} = 0.63) showing clusters of primary particles (i.e., β-SiC crystallites and perhaps some residual carbon and silica). The sample was prepared by the "dispersing method."

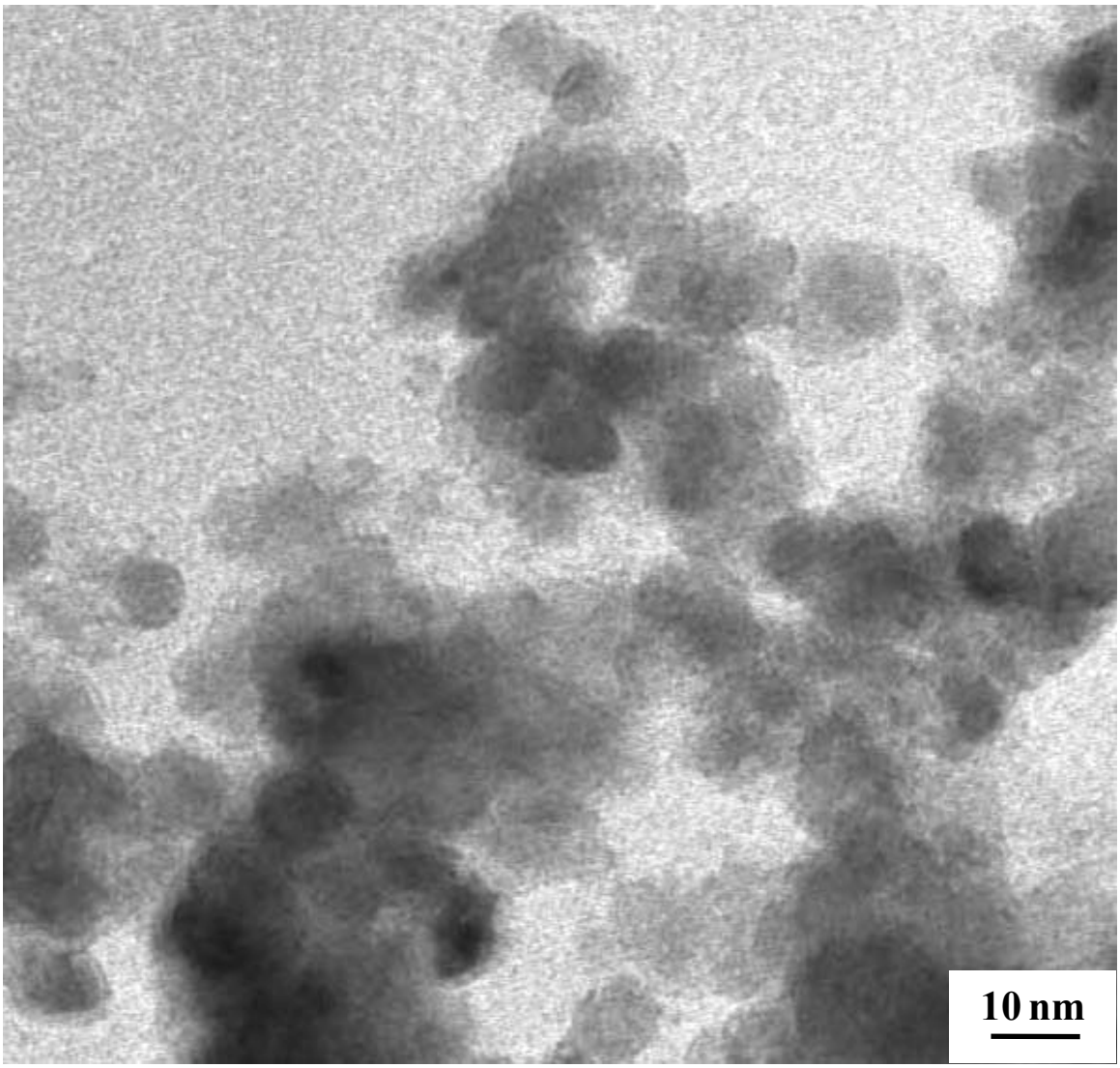

Figure 4-4-15 TEM image the SC42-1300(3h) sample (X_{WL} = 0.63) showing multiple equiaxed β-SiC crystallites. The sample was prepared by the "dispersing method."

roughly on the order of 10 nm (Figures 4-4-14 and 4-4-15). This sizes appear to be consistent with the XRD line broadening results reported in Figures 4-4-1 and 4-4-2 and Table H-1. (4) The β-SiC crystallites have an equiaxed shape. This is consistent with the crystallite size measurements obtained by XRD line broadening in which it was shown that sizes were similar when measured in different crystallographic directions. These observations indicate that the SiC crystallites develop by three-dimensional growth. As discussed in section 4.4.1, 3-D growth is consistent with the interface-controlled shrinking-core model, but it is inconsistent with nucleation-and-growth model.

Figure 4-4-16 is an HRTEM micrograph of the same sample shown in Figures 4-4-12 - 4-4-15. The upper right portion of the micrograph shows a region in which there is an amorphous layer (~2 nm thickness) adjacent to a β-SiC crystallite. It was not determined if the amorphous layer was carbon only or a carbon/silica mixture.

Figures 4-4-17 and 4-4-18 show TEM micrographs of the SC42-1300(6h) sample which had a fractional weight loss of 0.88. The microstructural features are very similar to those observed in Figures 4-4-14 and 4-4-15 for the SC42-1300(3h) sample. Once again, the size of β-SiC crystallites is consistent with values obtained by XRD line broadening measurement.

Figures 4-4-19 is a TEM micrograph of the SC35-1300(16h) sample which had a fractional weight loss of 0.98. The β-SiC crystallites in this image are significantly larger than the average crystallite size of ~23 nm that was determined from XRD line broadening measurement. A possible explanation for this discrepancy is that the area that was imaged was not representative. In late stage of the reaction, there are some regions in the sample that have almost no residual free carbon, while other regions will have a

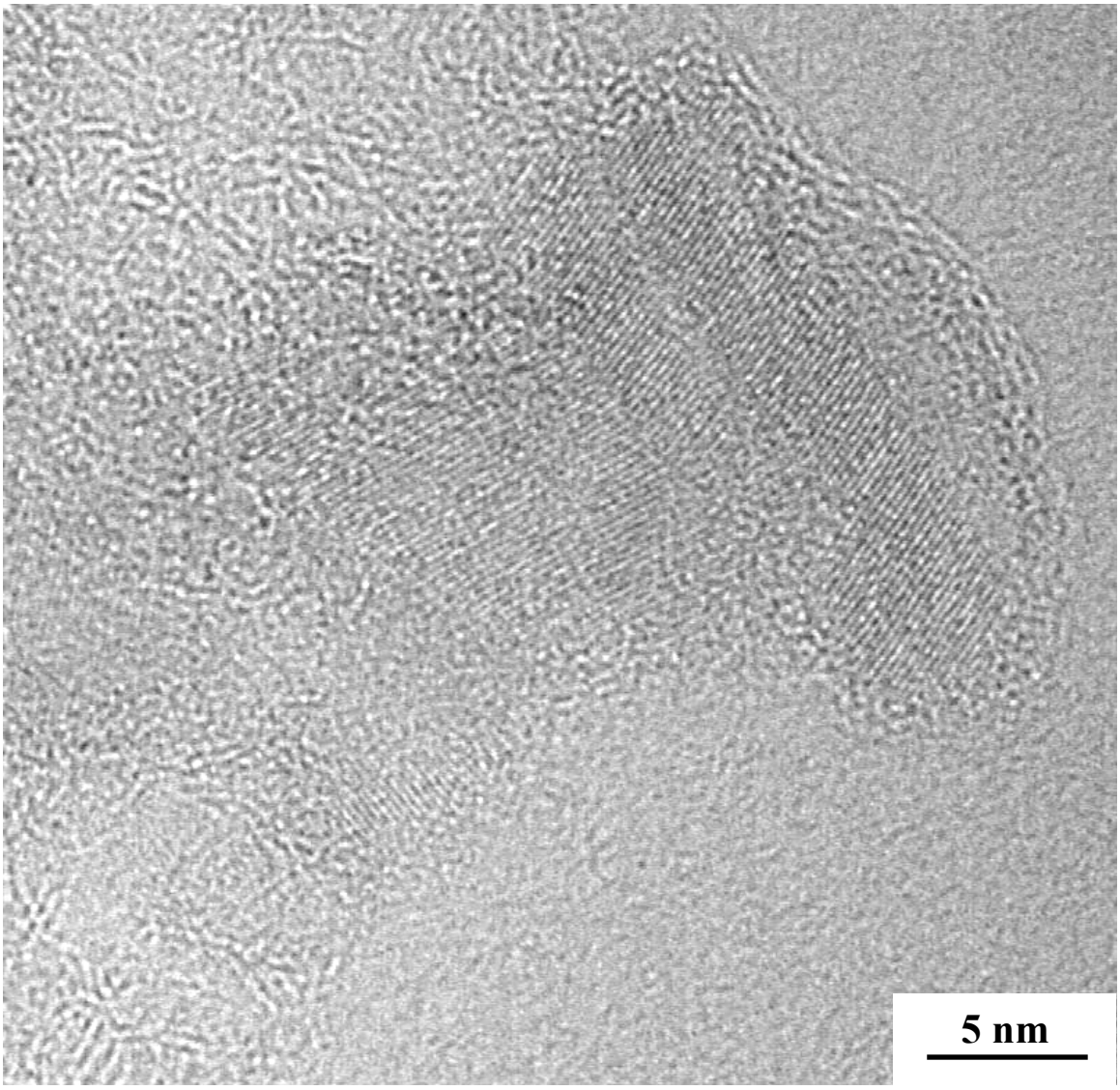

Figure 4-4-16 HRTEM image of the SC42-1300(3h) sample (X_{WL} = 0.63). The sample was prepared by the "dispersing method."

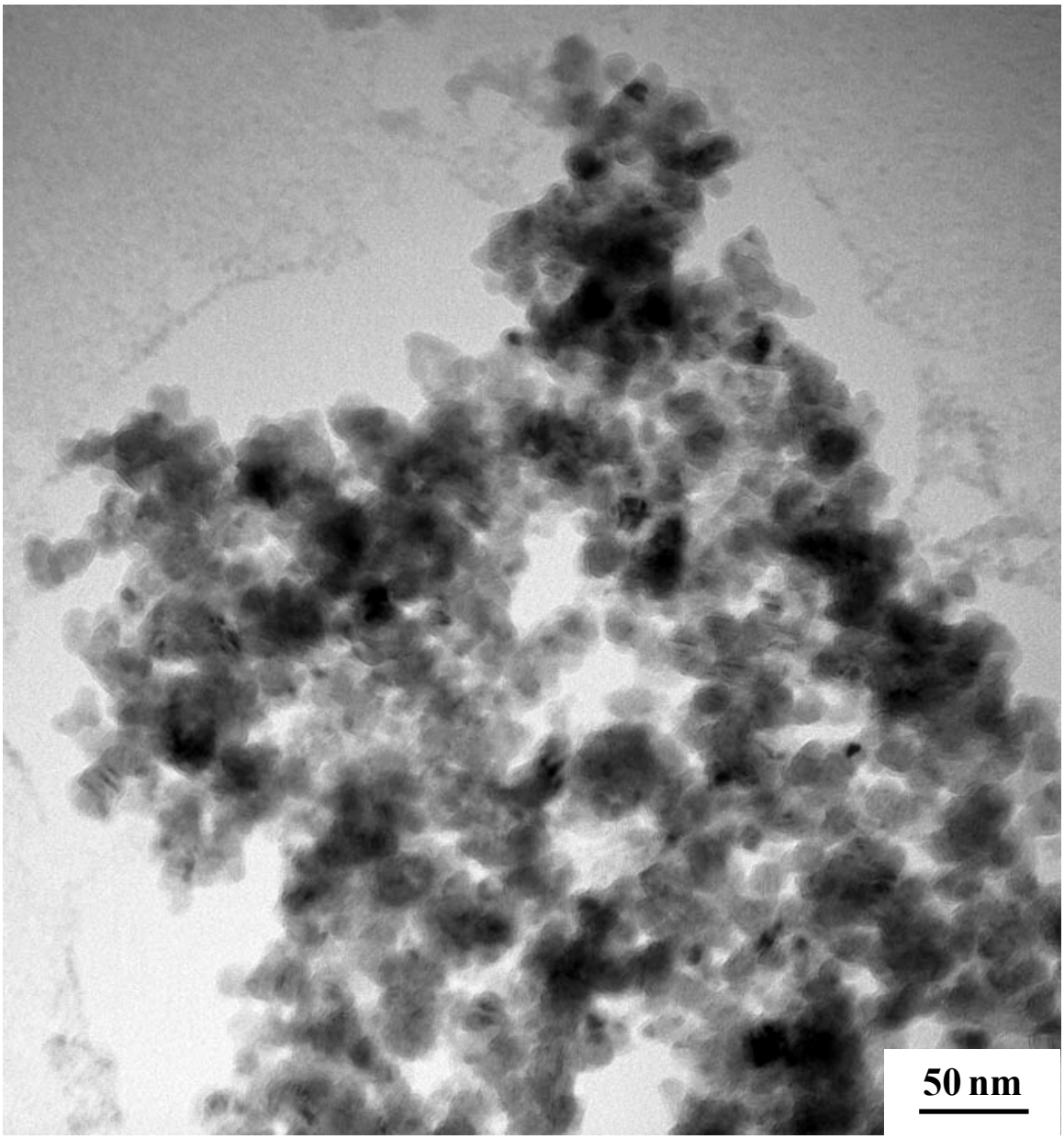

Figure 4-4-17 TEM image of the SC42-1300(6h) sample (X_{WL} = 0.88) showing clusters of equiaxed β-SiC crystallites. The sample was prepared by the "dispersing method."

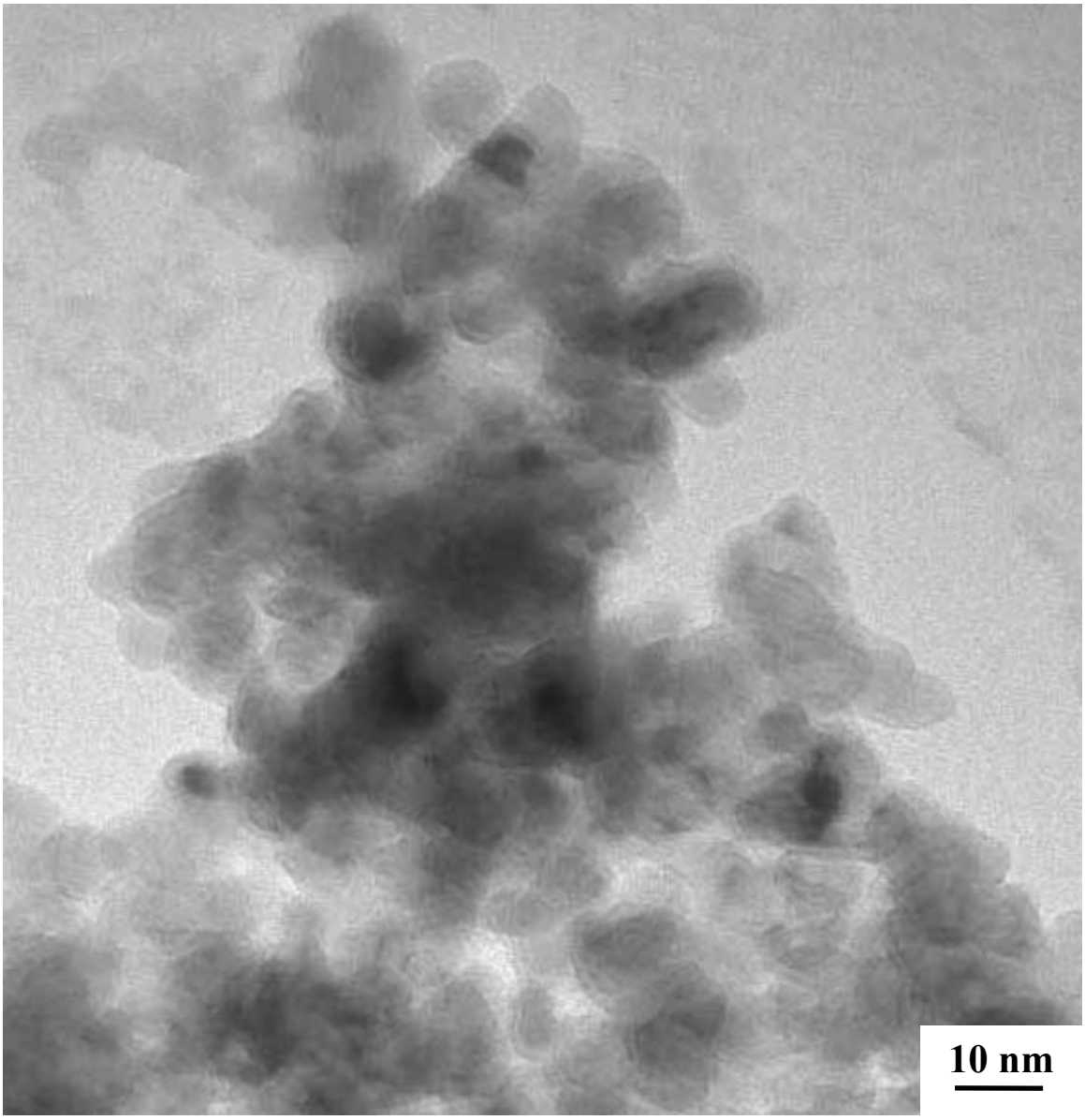

Figure 4-4-18 TEM image of the SC42-1300(6h) sample (X_{WL} = 0.88) showing a cluster of equiaxed β-SiC crystallites. The sample was prepared by the "dispersing method."

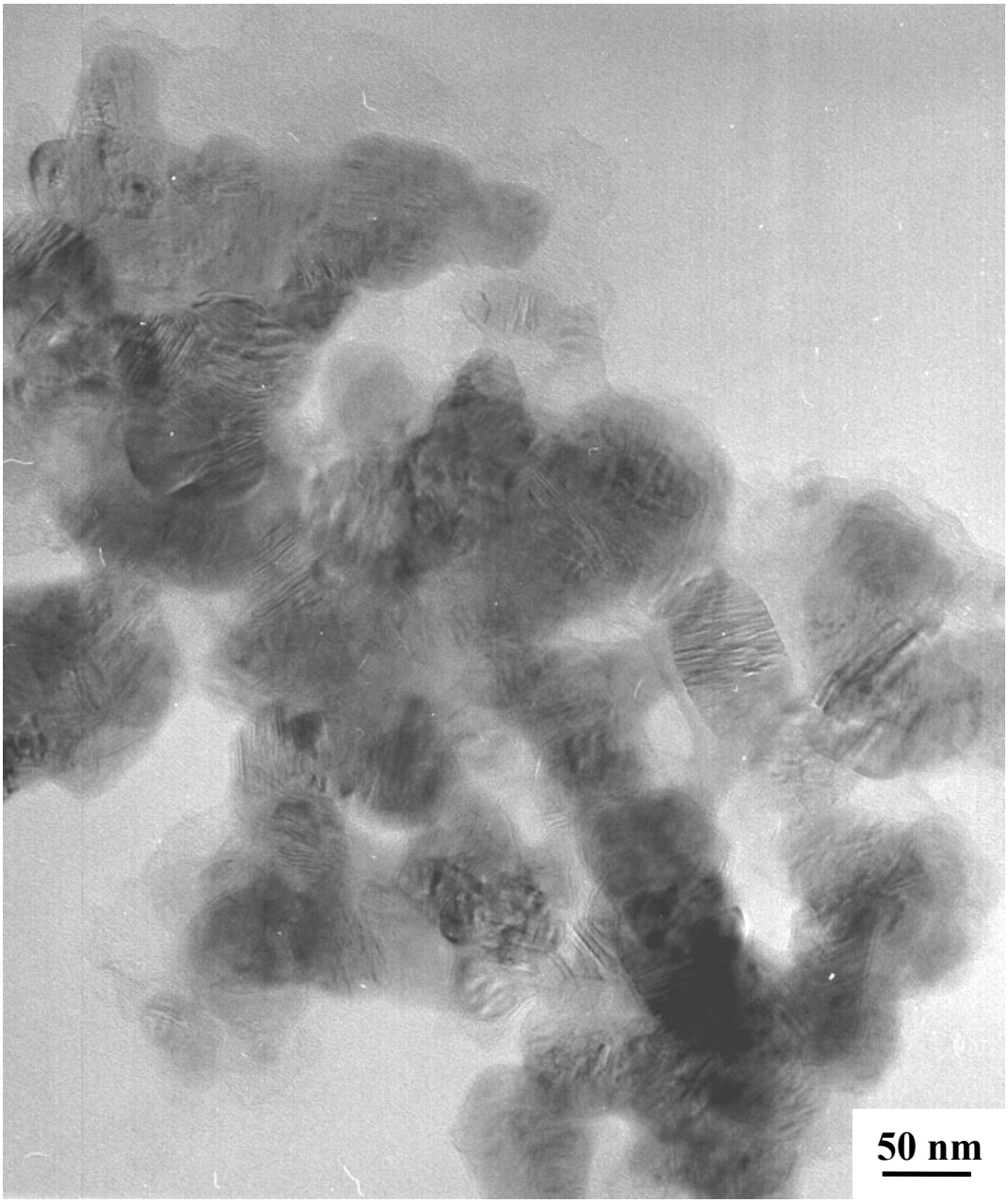

Figure 4-4-19 TEM image of the SC35-1300(16h) sample (X_{WL} = 0.98) showing some large β-SiC crystallites. The sample was prepared by the "dispersing method."

considerable amount of free carbon. Hence, the SiC crystallites would show extensive growth in some regions, but almost no growth in other regions. It is possible that the area imaged in Figure 4-4-19 was one in which the free carbon content was very low.

Figure 4-4-20 shows a HRTEM image of the two adjacent β-SiC crystallites in the SC35-1300(16h) sample. There is a thin layer of amorphous material on the surface of the SiC crystallites. This is not surprising because it is known from LECO carbon analysis that even fully converted SC35 samples have some residual free carbon. (As discussed in section 4.3.1, an SC35-1475(2h) sample has a residual free carbon content of ~2 wt%.) Therefore, it is presumed that the amorphous surface layer shown in Figure 4-4-20 is carbon. A very similar structure was reported by Huang et al. (1998) on samples which were very similar to the ones prepared in this study. Huang et al. also prepared samples from a TEOS/phenolic resin mixed solution and used a very similar C/Si ratio to the one used to prepare the SC35 samples.

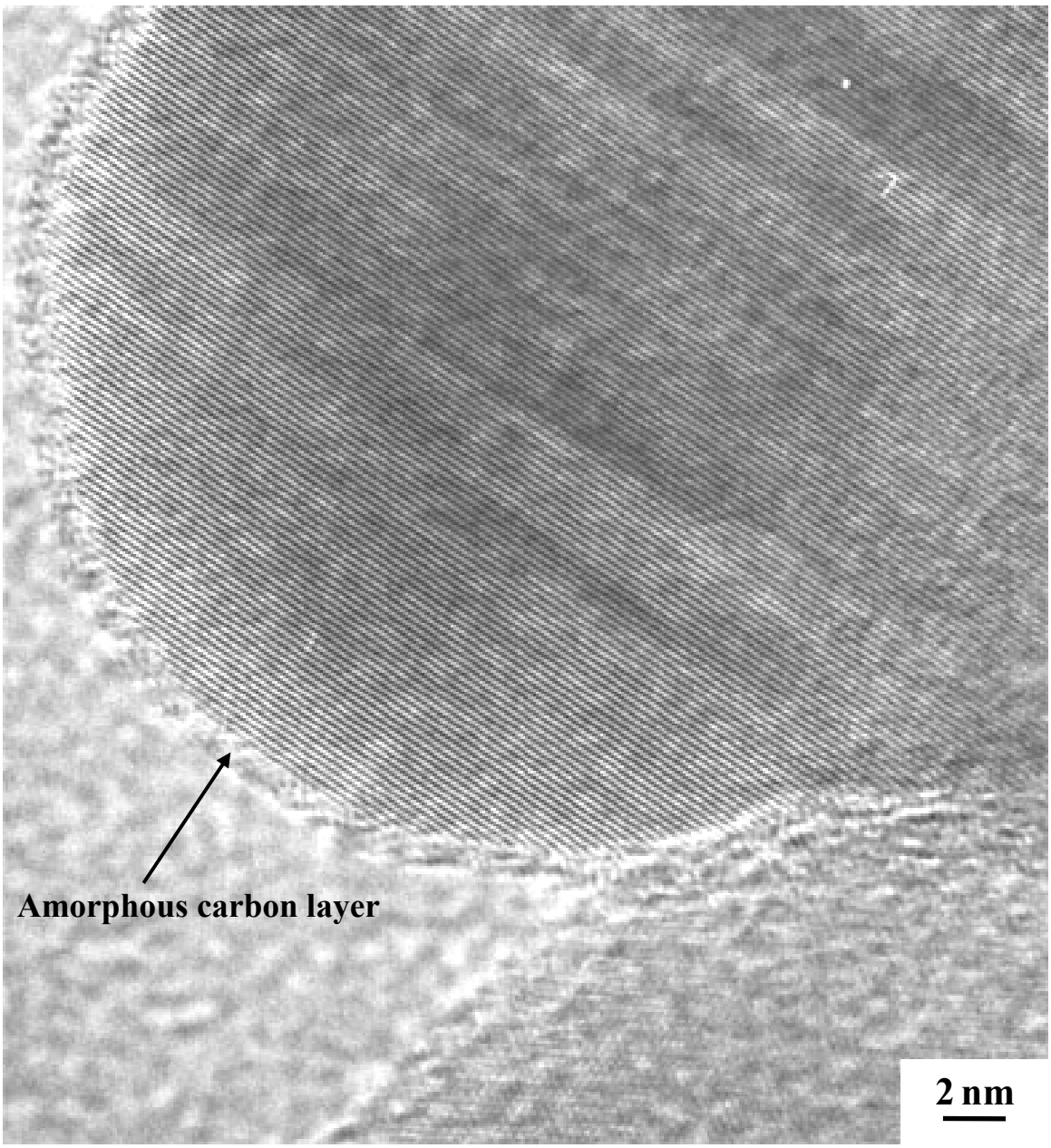

Figure 4-4-20 HRTEM image of the SC35-1300(16h) (X_{WL} = 0.98) sample showing two adjacent β-SiC crystallites. An amorphous (carbon) layer was clearly seen outside the β-SiC crystallite. The sample was prepared by the "dispersing method."

4.4.3 Total Pore Volume and Specific Surface Area

4.4.3.1 Specific Pore Volume

As described in section 3.4.2, the specific pore volumes of the samples were determined from their nitrogen gas adsorption/desorption isotherms. The specific pore volume (V_{Pore}, in cm^3/g) was obtained from the maximum cumulative pore volume in desorption isotherm at relative pressure of ~0.995. The maximum pore diameter detected by this method is ~400 nm. Hence, large pores and other defects associated with the relatively large particles that comprised the pyrolyzed powder would not be detected by this method. In addition, there might be closed pores in carbon regions of the samples that cannot be accessed by the nitrogen gas. This is suggested by the relatively low apparent densities that were measured for the pyrolyzed SC35 sample and the pyrolyzed phenolic resin sample, as described in section 4.1.9. Hence, the specific pore volumes reported given in this section might not actually be the true total specific pore volumes of the samples.

Figure 4-4-21 shows the specific pore volume vs. reaction time for SC35 samples heat treated at temperatures in the range of 1160-1300^{o}C. Figure 4-4-22 shows the same date re-plotted as the specific pore volume vs. the fractional weight loss (after correction for moisture adsorption and blown-off powder) for the carbothermal reduction reaction. The following observations were made from these figures:

1. Figure 4-4-22 shows that the specific pore volume follows a single trend as the reaction proceeds which is independent of the reaction temperature (i.e., over the range of temperatures investigated). This is the same type of observation made regarding the average SiC crystallite size (Figure 4-4-2) and again suggests that the

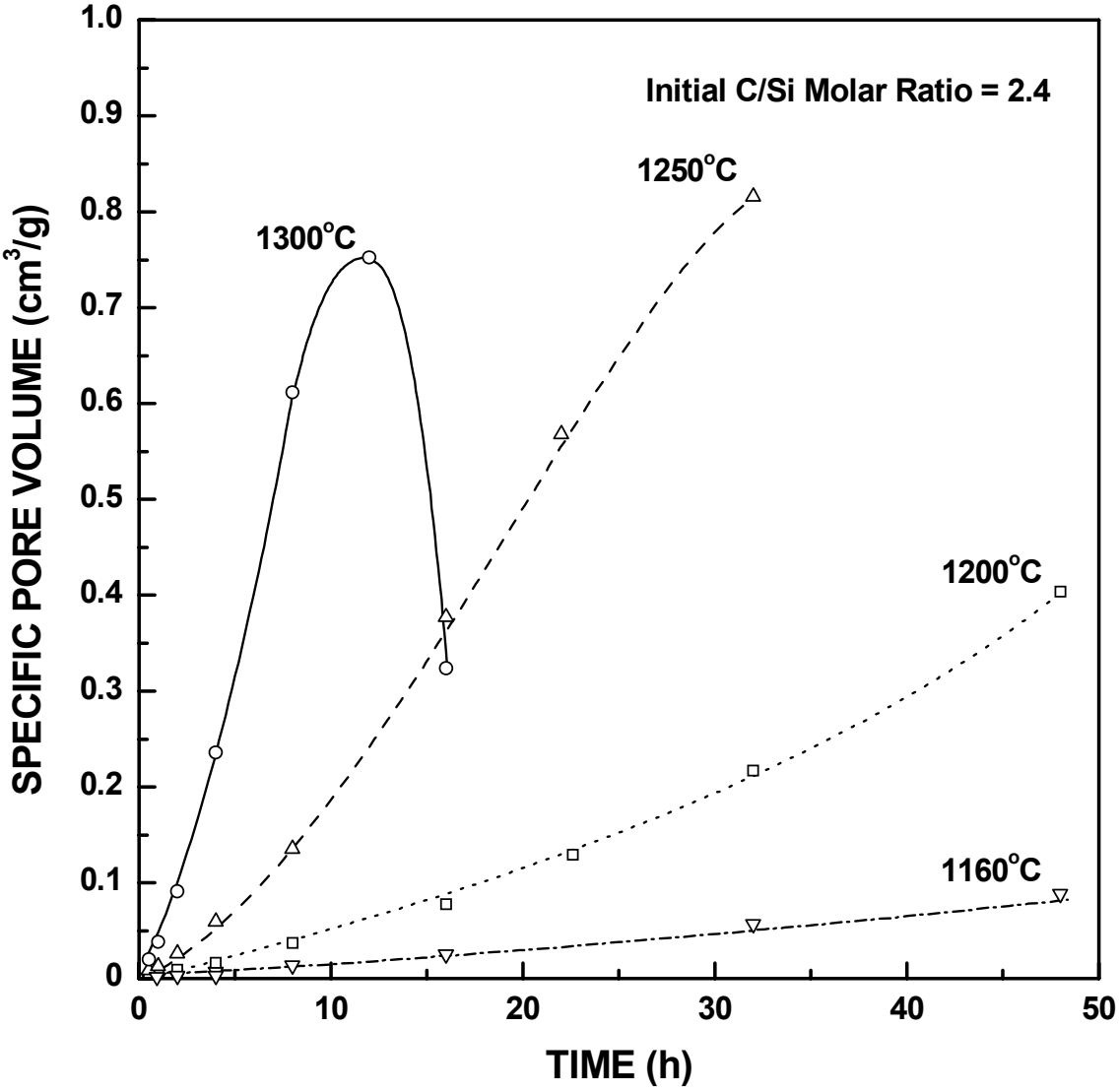

Figure 4-4-21 Plots of specific pore volume vs. reaction time for SC35 samples (initial C/Si molar ratio = 2.4) heat treated at different temperatures.

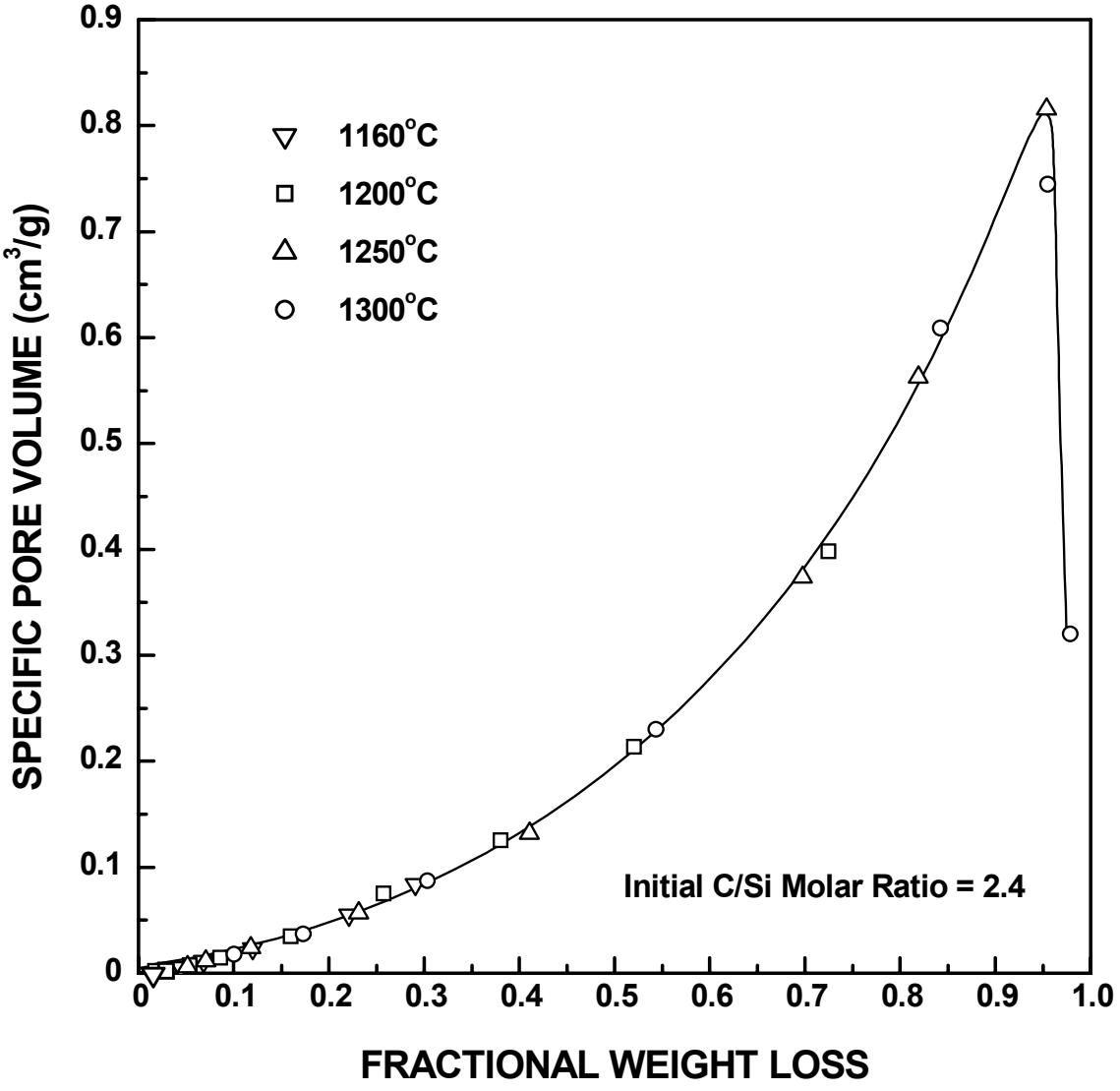

Figure 4-4-22 Plot of specific pore volume vs. fractional weight loss for SC35 samples (initial C/Si molar ratio = 2.4) heat treated at different temperatures.

reaction mechanism does not change over the range of temperatures investigated.

2. The specific pore volume increases with increasing reaction time and temperature (i.e., with increasing extent of conversion to SiC) until the late stages of the carbothermal reduction reaction. As noted in section 4.1, the starting pyrolyzed material had nearly zero porosity (i.e., ~0.002 cm^3/g). The specific pore volume increased to ~0.82 cm^3/g for a sample showing ~0.95 fractional weight loss. This increase in porosity is consistent with the structural expectations outlined earlier in section 4.3.4 for the interface-controlled "shrinking core" reaction. As indicated in the schematic in Figure 4-2-1, porous carbon regions are expected to develop initially from the first step in the reaction (Equation 4-2-1) in which silica and carbon react to produce SiO and CO volatiles. In turn, SiO reacts with these porous carbon regions in the second reaction step (Equation 4-2-2) to produce porous SiC regions (and CO volatiles).

3. The specific pore volume decreases sharply in the very late stages of the reaction. There are at least three possible reasons for a decrease in the specific pore volume in a solid sample. First, there may be a true reduction in the total pore volume within the sample. (For example, this might occur due to a densification process associated with sintering or chemical reactions.) Second, there may be a decrease in open pore volume, and a concomitant increase in closed pore volume, such that a portion of the sample's total pore volume is no longer accessible to penetration by the nitrogen gas molecules. (For example, this might occur due to diffusion processes, such as those associated with densification and chemical reactions.) Third, there may be an increase in the size of some pores such that they exceed the

maximum size that can be detected by the gas adsorption method. (For example, this might occur due to coarsening processes.)

In section 4.4.1, it was noted that the average SiC crystallite size increased sharply during the late stages of the reaction. The decrease in specific pore volume shown in Figure 4-4-22 starts to occur at the same point in the reaction (i.e., same fractional weight loss) at which the average crystallite size begins to increase. The increase in average crystallite size was attributed to coarsening similar to that reported for other SiC-based materials (Greskovich and Rosolowski (1976), Hojo (1991), and Vaßen et al. (1996)). In many cases, the coarsening of grains in porous materials is accompanied by pore coarsening (i.e., unless densification (pore volume reduction) processes are simultaneously operative) (Greskovich and Rosolowski (1976), Vaßen et al. (1996), and Clegg (2000)). Hence, the decrease in specific pore volume observed in the late stages of the reaction is consistent with the third explanation given above. This explanation is further supported by pore size distribution and particle size distribution results which are discussed later in this chapter (i.e., section 4.4.7 and 4.4.6, respectively).

The relative percentage of porosity in the CTR samples as a function of fractional weight loss during the reaction was calculated using the specific pore volume data and the estimated solid densities of the reaction products. To estimate the density of CTR reaction products, it was assumed that the products consisted of pyrolyzed material and fully converted material. The weight fraction of pyrolyzed material is w_{pyro}, the weight fraction of fully-converted material is w_{CTR}, and $w_{pyro} + w_{CTR} = 1$. These fractions were obtained

for each sample from the QXRD data, as described in section 4.3.3. The solid density, ρ_{prod}, for a given reaction product was then calculated using the following equation:

$$\frac{1}{\rho_{prod}} = \frac{w_{pyro}}{\rho_{pyro}} + \frac{w_{CTR}}{\rho_{CTR}} \tag{4-4-2}$$

where ρ_{pyro} and ρ_{CTR} are the solid densities of the pyrolyzed materials and fully-converted CTR materials, respectively. For SC35 samples, the calculated solid density of the fully-converted material is ρ_{CTR} = 3.16 g/cm^3 (see section 4.3.1). There is significant uncertainty regarding the solid density of the pyrolyzed material. The experimentally-determined apparent density of the pyrolyzed material (ρ_{pyro}) was 1.94 g/cm^3 (see section 4.1.9). However, if the true solid density of the carbon in the pyrolyzed material is taken as 2.0 g/cm^3 (also see section 4.1.9), then the calculated true solid density of the pyrolyzed material is 2.16 g/cm^3. The product density, ρ_{prod}, was calculated twice using the different ρ_{pyro} values. The relative percentage of porosity for the reaction product, V_{Pore}^{R}, was then calculated twice using the following equation:

$$V_{Pore}^{R} = \frac{V_{Pore}}{V_{Pore} + V_{\mathrm{Pr}od}} \times 100\% \tag{4-4-3}$$

where the specific solid volume for the reaction product, V_{Prod} (in cm^3/g), is equal to the inverse of the solid density of the reaction product (i.e., $V_{Prod} = 1/\rho_{prod}$) and the specific pore volume, V_{Pore}, was obtained from the gas adsorption measurement.

Figures 4-4-23a and 4-4-23b show plots of the relative percentage of porosity (V_{Pore}^{R}) in the reaction product vs. the fractional weight loss for the SC35 samples. The porosity values in these plots were calculated using ρ_{pyro} values of 1.94 g/cm^3 and 2.16 g/cm^3, respectively. As expected, the general trends in Figures 4-4-23a and 4-4-23b are very

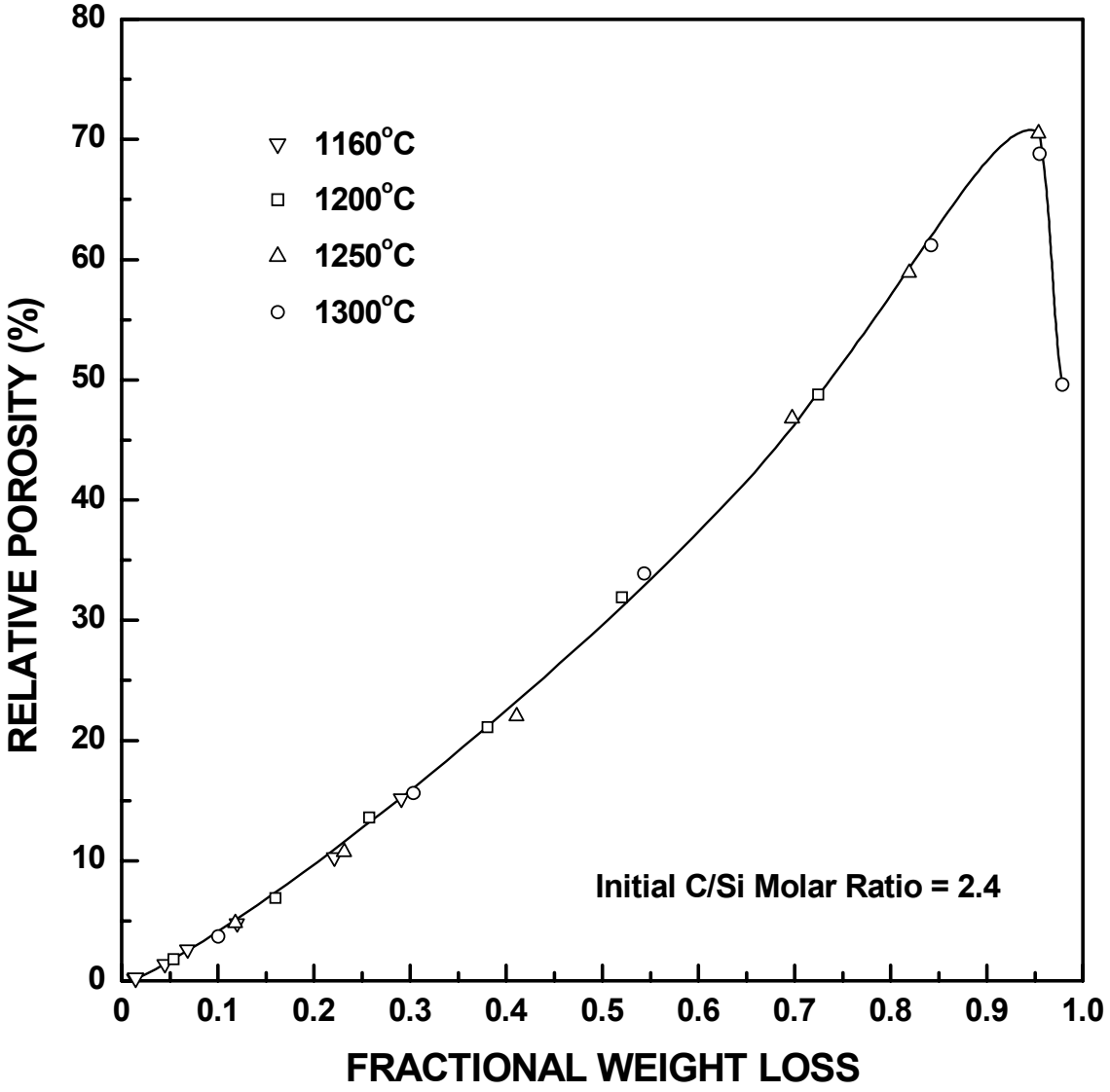

Figure 4-4-23a Plot of relative porosity vs. fractional weight loss for SC35 samples (initial C/Si molar ratio = 2.4). The porosity was calculated based on the assumption that ρ_{pyro} for the SC35 pyrolyzed material was 1.94 g/cm^3.

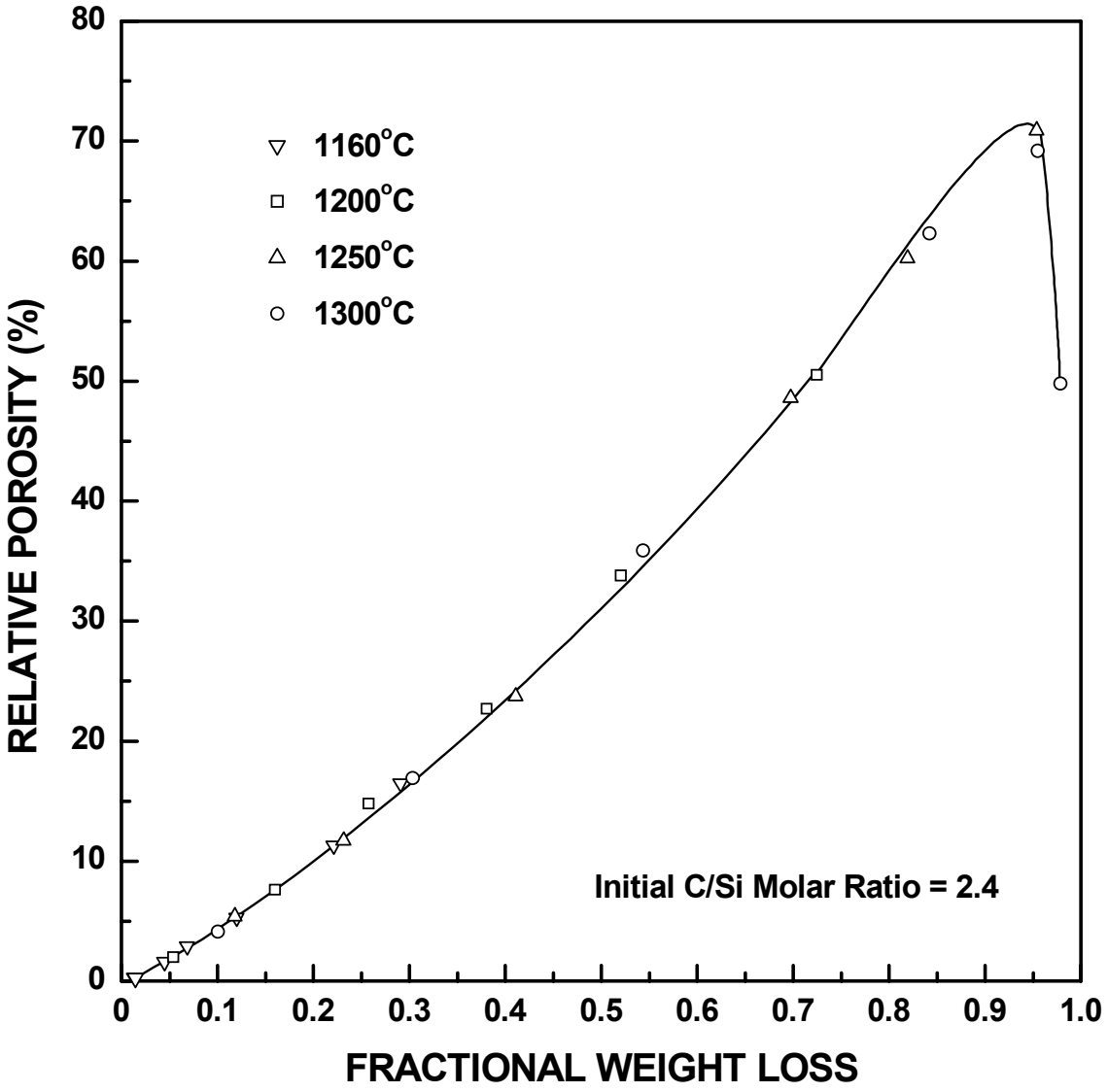

Figure 4-4-23b Plot of relative porosity vs. fractional weight loss for SC35 samples (initial C/Si molar ratio = 2.4). The porosity was calculated based on the assumption that ρ_{pyro} for the SC35 pyrolyzed material was 2.16 g/cm^3.

similar to that observed in Figure 4-4-22. V_{Pore}^{R} increases substantially as the reaction proceeds, but then starts to decrease sharply in the very late stage of the reaction. In Figures 4-4-23a and 4-4-23b, the highest relative porosity values (~71%) were reached for the sample with fractional weight loss of ~0.95 and the porosity decreased to ~50% for the sample with fractional weight loss of ~0.98. (The differences in the calculated V_{Pore}^{R} values in Figures 4-4-23a and 4-4-23b were very small.)

Figure 4-4-24 shows the specific pore volume vs. reaction time for SC8 samples heat treated at temperatures in the range of 1160-1250^{o}C. Figure 4-4-25 shows the same date re-plotted as the specific pore volume vs. the fractional weight loss (after correction for moisture adsorption and blown-off powder) for the carbothermal reduction reaction. The results show some similarities to the results in Figures 4-4-21 and 4-4-22 for the SC35 samples. The following observations are made from these figures: (1) The development of specific pore volume follows a single trend as the reaction proceeds which is independent of the reaction temperature (i.e., over the range of temperatures investigated). (2) The specific pore volume increases with increasing reaction time and temperature (i.e., with increasing extent of conversion to SiC) for most of the reaction.

Relative porosity values for the SC8 samples were calculated using Equations (4-4-2) and (4-4-3). To calculate ρ_{prod} (Equation (4-4-2)), a value of ρ_{CTR} = 2.54 g/cm^3 was used for the solid density of the fully-converted material (see section 4.3.1). In contrast, two different calculated values for the solid density of the pyrolyzed material (ρ_{pyro}) were used in the ρ_{prod} calculations. In one case, the calculated solid density of 1.81 g/cm^3 in Table 4-1-8 (section 4.1.9) was used. This value was calculated based on using the experimentally-measured apparent solid density of carbon (obtained from phenolic resin) of 1.49 g/cm^3

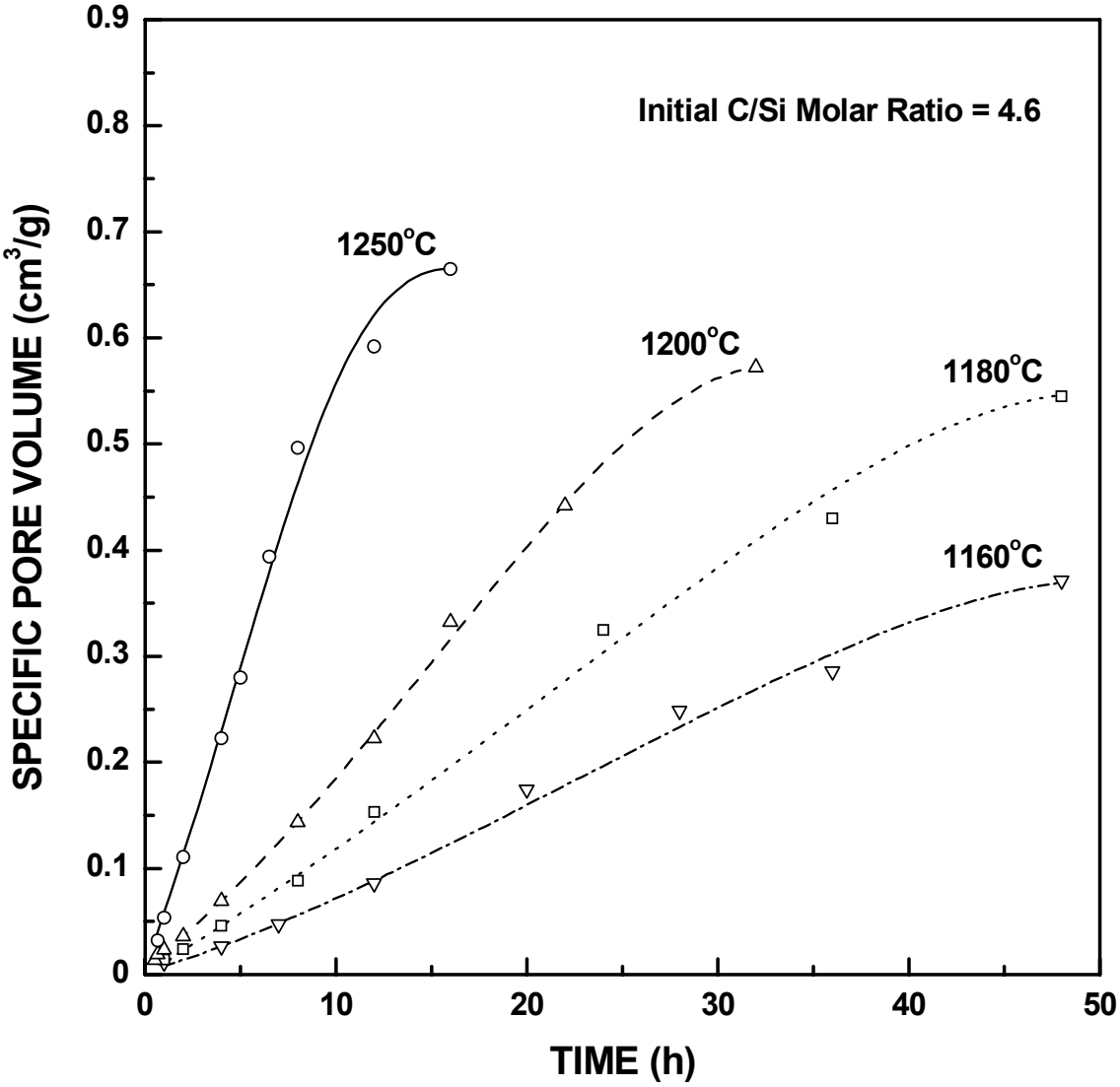

Figure 4-4-24 Plots of specific pore volume vs. reaction time for SC8 samples (initial C/Si molar ratio = 4.6) heat treated at different temperatures.

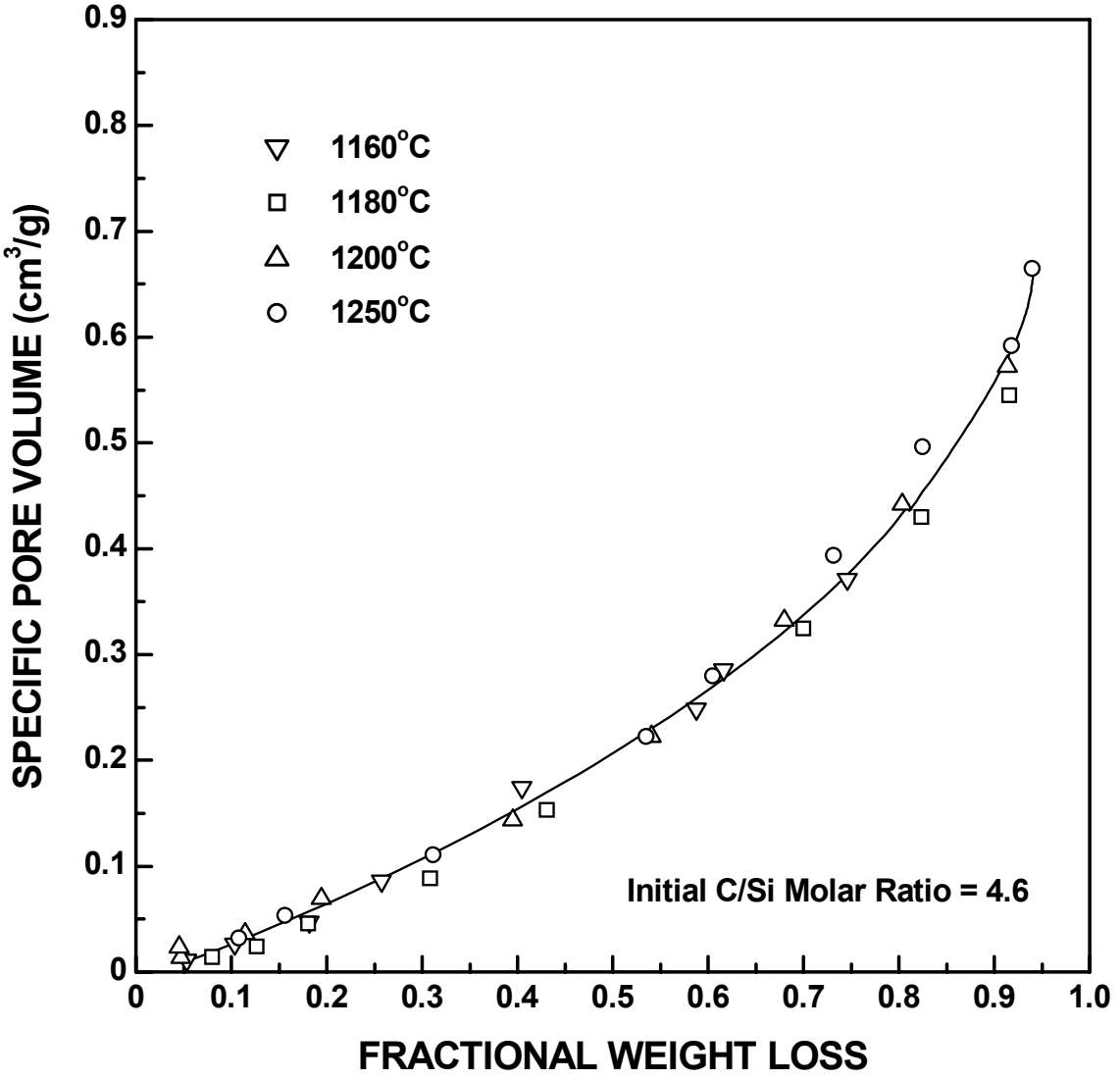

Figure 4-4-25 Plot of specific pore volume vs. fractional weight loss for SC8 samples (initial C/Si molar ratio = 4.6) heat treated at different temperatures.

(see Table 4-1-7 in section 4.1.9). In the other case, a value of ρ_{pyro} = 2.12 g/cm^3 was calculated by assuming that the solid density of carbon was 2.0 g/cm^3. Figures 4-4-26a and 4-4-26b show plots of relative percentage of porosity (V_{Pore}^{R}) in the reaction product vs. fractional weight loss for the SC8 samples. The porosity values in these plots were calculated using ρ_{pyro} values of 1.81 g/cm^3 and 2.12 g/cm^3, respectively.

There are also some differences in the pore volume development for the SC8 and SC35 samples. First, there is no decrease in specific pore volume during the late stage of the reaction for the SC8 samples. This appears to reflect a slower rate of coarsening of the SiC crystallites and the pores. Hence, most of the largest pores that are present within the samples (i.e., not counting gross defects) are still detected by the gas adsorption measurement. (This will be discussed in more detail later in section 4.4.7.) Second, the maximum pore volume (i.e., the specific pore volume and relative percentage of porosity) for the SC8 samples is smaller than that observed for the SC35 samples. The differences in the maximum specific pore volumes and maximum relative porosities for the SC35 and SC8 samples are expected based on the compositional differences. As a first approximation, it might be assumed that the maximum porosity that develops in the samples is proportional to the volume fraction of silica in the sample. In the proposed reaction mechanism, silica is removed from the samples as SiO gas during the first step of the CTR reaction (Equation (4-2-1)). This mechanism of silica removal leads to pore formation. Therefore, a greater amount of silica should result in a larger amount of pores.

A very rough estimate of the porosity that develops during the CTR reaction can be made by assuming: (i) the volume of pores equals the decrease in solid volume and (ii) the total volume of solid/pores does not change during the reaction. As will be shown later in

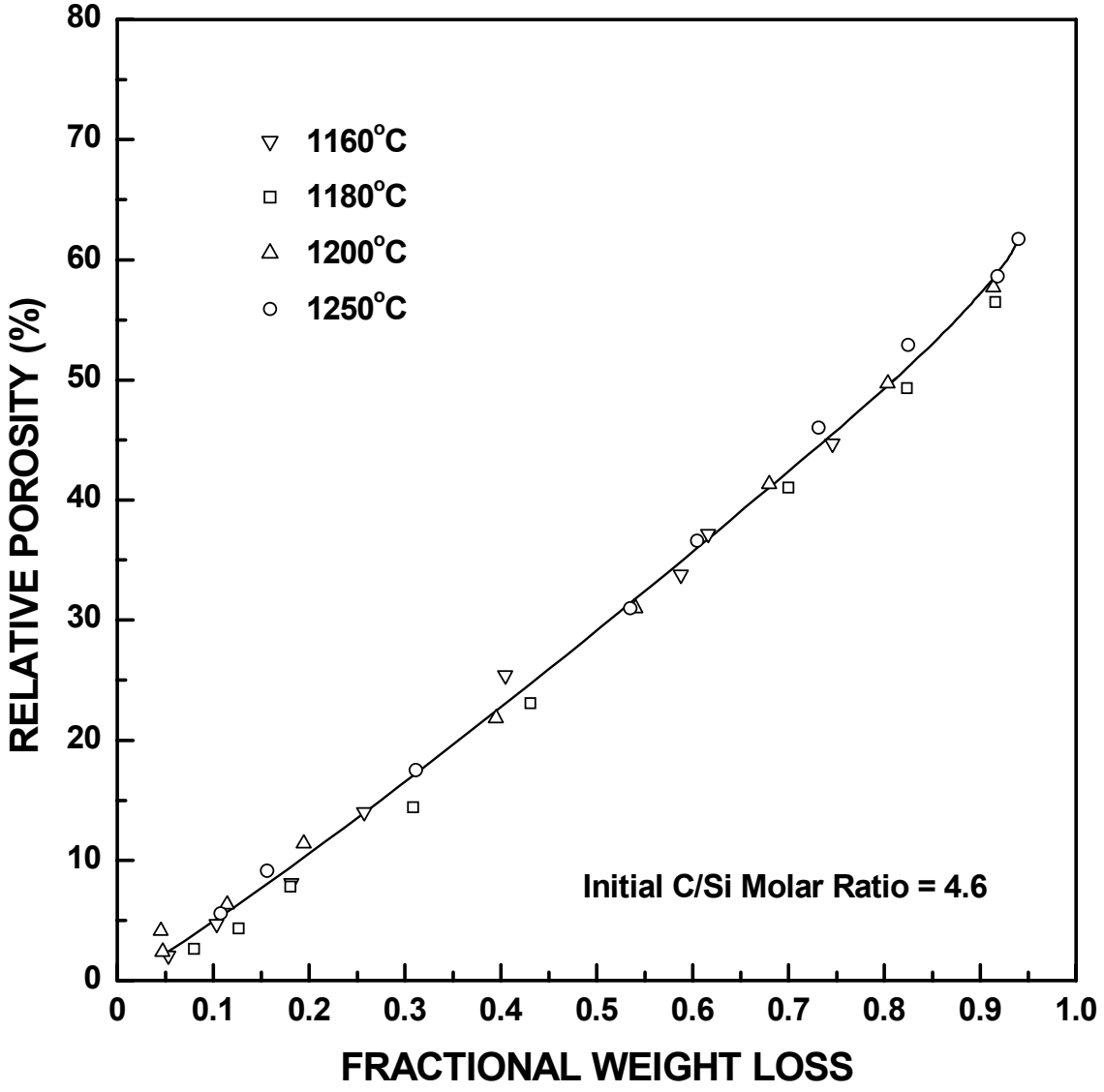

Figure 4-4-26a Plot of relative porosity vs. fractional weight loss for SC8 samples (initial C/Si molar ratio = 4.6). The porosity was calculated based on the assumption that ρ_{pyro} for the SC8 pyrolyzed material was 1.81 g/cm^3.

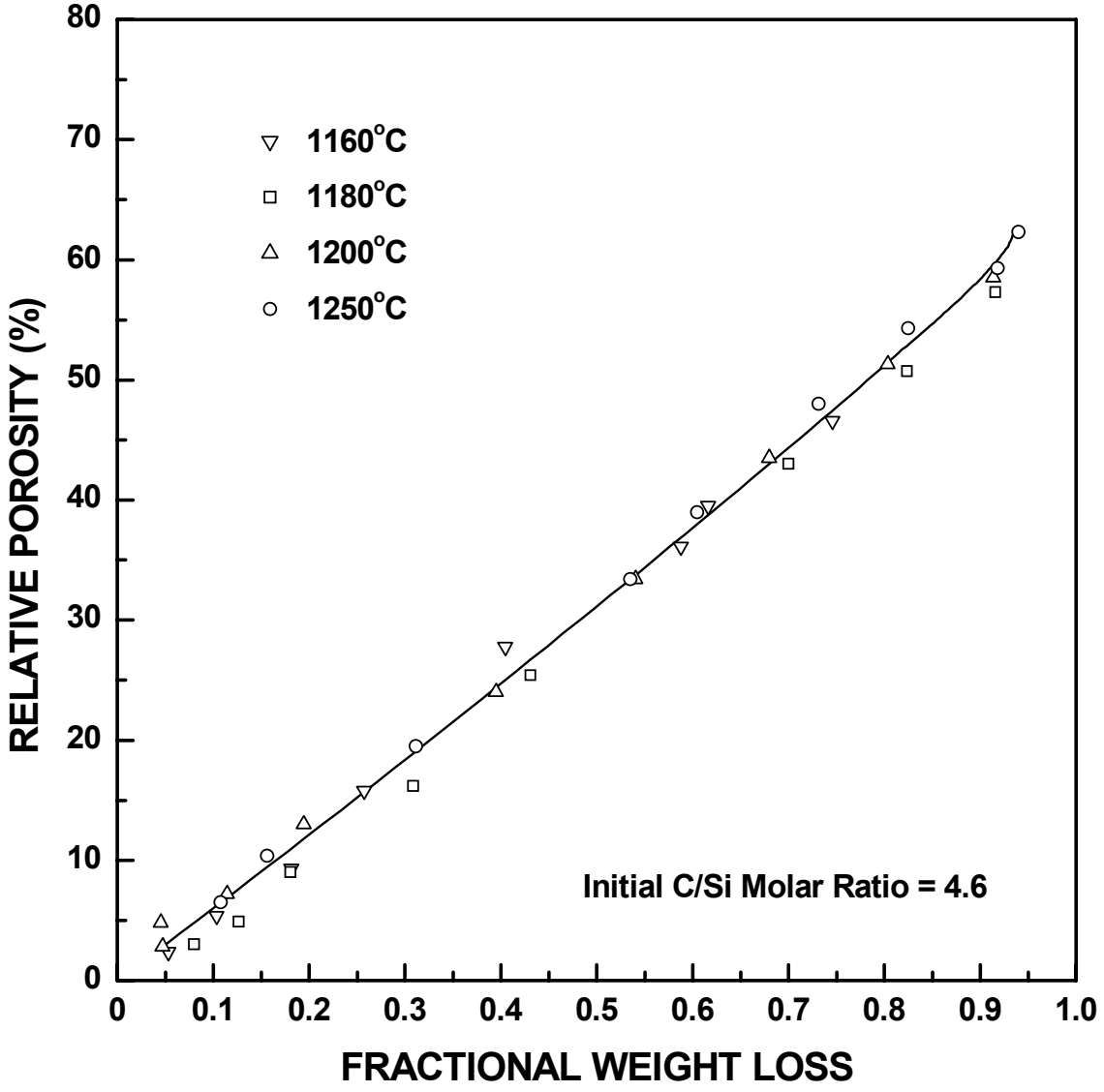

Figure 4-4-26b Plot of relative porosity vs. fractional weight loss for SC8 samples (initial C/Si molar ratio = 4.6). The porosity was calculated based on the assumption that ρ_{pyro} for the SC8 pyrolyzed material was 2.12 g/cm^3.

section 4.5.1, the CTR reaction for complete reaction in SC35 samples (i.e., from pyrolyzed material to "full conversion") is given by:

$$SiO_2 + z\,C \rightarrow (1-y)\,SiC + x\,C + y\,SiO + (z-1-x+y)\,CO \qquad (4\text{-}4\text{-}4)$$

where z is the initial C/Si molar ratio in the pyrolyzed material, x is the molar ratio of free carbon (in the product) to initial silica, and y is the molar ratio of SiO lost to initial carbon. Consider the example (discussed in section 4.3.3.2) using the SC35 pyrolyzed material in which $z = 2.39$, $x = 0.05$, $y = 0.33$ (see Table 4-5-1). Suppose that the initial amount of SiO_2 is one mole and suppose that u moles of SiO_2 are consumed after time t (where $u \leq 1$). As shown in section 4.3.3.2, the molar quantities before CTR, after time t, and after complete CTR can be represented as follows:

	SiO_2	+ 2.39 C	→ 0.67 SiC	+ 0.33 SiO	+ 0.05 C	+ 1.67 CO
Before CTR	1	2.39	0	0	0	0
After time t	1- u	2.39- 2.39u	0.67u	0.33u	0.05u	1.67u
After complete CTR	0	0	0.67	0.33	0.05	1.67

If the density of carbon in the pyrolyzed material is assumed to be 1.49 g/cm^3, the initial solid sample volume (assuming there is no porosity) before CTR reaction, V_0, is:

$$V_0 = \frac{1 \cdot 60}{2.25} + \frac{2.39 \cdot 12}{1.49} = 45.92 \text{ cm}^3$$

where 60 and 12 are the formula weights of silica and carbon (in g/mol), respectively, and 2.25 and 1.49 are the solid densities of silica and carbon (in g/cm^3), respectively. The volume of solid product at time t (extent of reaction is u), V, is given by:

$$V = \frac{(1-u) \cdot 60}{2.25} + \frac{2.39 \cdot (1-u) \cdot 12}{1.49} + \frac{0.67u \cdot 40}{3.2} + \frac{0.05u \cdot 12}{2.0} = 45.92 - 37.25\,u \text{ cm}^3$$

where 40 is the formula weight for SiC (in g/mol), 3.2 is the solid density of SiC (in g/cm^3), and 2.0 is the solid density of carbon (in g/cm^3) after the CTR reaction. The weight of sample at time t (extent of reaction u), W, is given by:

$$W = (1 \cdot 60) + (2.39 \cdot 12) - [(0.33u \cdot 44) + (1.67u \cdot 28)] = 88.68 - 61.28u \text{ g}$$

where 44 and 28 are the formula weights of SiO and CO, respectively. Therefore, based on the initial assumptions, the total pore volume is given by V_0 - V and the specific pore volume, V_{Pore}, is given by:

$$V_{Pore} = \frac{V_0 - V}{W} = \frac{37.25u}{88.68 - 61.28u} \text{ cm}^3/\text{g} \qquad (4\text{-}4\text{-}5)$$

The relative porosity, V_{Pore}^R, is given by:

$$V_{Pore}^R = \frac{V_0 - V}{V_0} \times 100\% = 0.811u \times 100\% \qquad (4\text{-}4\text{-}6)$$

If the density of carbon in the pyrolyzed material is assumed to be 2 g/cm^3, the initial solid sample volume (assuming there is no porosity) before CTR reaction, V_0, is:

$$V_0 = \frac{1 \cdot 60}{2.25} + \frac{2.39 \cdot 12}{2.0} = 41.01 \text{ cm}^3$$

The volume of solid product at time t (extent of reaction is u), V, is given by:

$$V = \frac{(1-u) \cdot 60}{2.25} + \frac{2.39 \cdot (1-u) \cdot 12}{2.0} + \frac{0.67u \cdot 40}{3.2} + \frac{0.05u \cdot 12}{2.0} = 41.01 - 32.34\,u \text{ cm}^3$$

The weight of sample at time t (extent of reaction u), W, is given by:

$$W = (1 \cdot 60) + (2.39 \cdot 12) - [(0.33u \cdot 44) + (1.67u \cdot 28)] = 88.68 - 61.28u \text{ g}$$

Therefore, based on the initial assumptions, the total pore volume is given by V_0 - V and the specific pore volume, V_{Pore}, is given by:

$$V_{Pore} = \frac{V_0 - V}{W} = \frac{32.34u}{88.68 - 61.28u} \text{ cm}^3/\text{g} \qquad (4\text{-}4\text{-}7)$$

The relative porosity, V_{Pore}^{R}, is given by:

$$V_{Pore}^{R} = \frac{V_0 - V}{V_0} \times 100\% = 0.789u \times 100\% \quad (4\text{-}4\text{-}8)$$

Figures 4-4-27a and 4-4-28a show the calculated specific pore volume and relative porosity, respectively, as a function of the fractional weight loss for the SC35 samples. The values were calculated using Equations (4-4-5) and (4-4-6), respectively. (The calculations were based on the assumption that the density of carbon in the pyrolyzed material was 1.49 g/cm^3.) For comparison, the experimental porosity values from Figures 4-4-22 and 4-4-23a are also plotted in Figures 4-4-27a and 4-4-28a, respectively. It is evident that the specific pore volumes and relative porosities calculated using Equations (4-4-5) and (4-4-6) were higher (at a given fractional weight loss) compared to the experimental values. For example, according to Equations (4-4-5) and (4-4-6), V_{Pore} = 1.16 cm^3/g and V_{Pore}^{R} = 77.0% when the fractional weight loss is 0.95 (i.e., u = 0.95). In comparison, Figures 4-4-22 and 4-4-23a show values of V_{Pore} = 0.82 cm^3/g and V_{Pore}^{R} = 70.5%, respectively, for SC35-1250(32h) with X_{WL} = 0.95. Figures 4-4-27b and 4-4-28b are the same type of plots shown in Figures 4-4-27a and 4-4-28a, respectively, except that the specific pore volume and relative porosity values were calculated using Equations (4-4-7) and (4-4-8), respectively. (The assumed density of carbon in the pyrolyzed material was 2.0 g/cm^3.) The calculated pore volumes (at a given fractional weight loss) were again higher than the experimental values, although the differences were smaller than observed in Figures 4-4-27a and 4-4-28a. For example, according to Equations (4-4-7) and (4-4-8), V_{Pore} = 1.01 cm^3/g and V_{Pore}^{R} = 75.0% when the fractional weight loss is 0.95 (i.e., u = 0.95). In comparison, Figures 4-4-22 and 4-4-23b show values of V_{Pore} = 0.82 cm^3/g and V_{Pore}^{R} = 70.9%, respectively, for

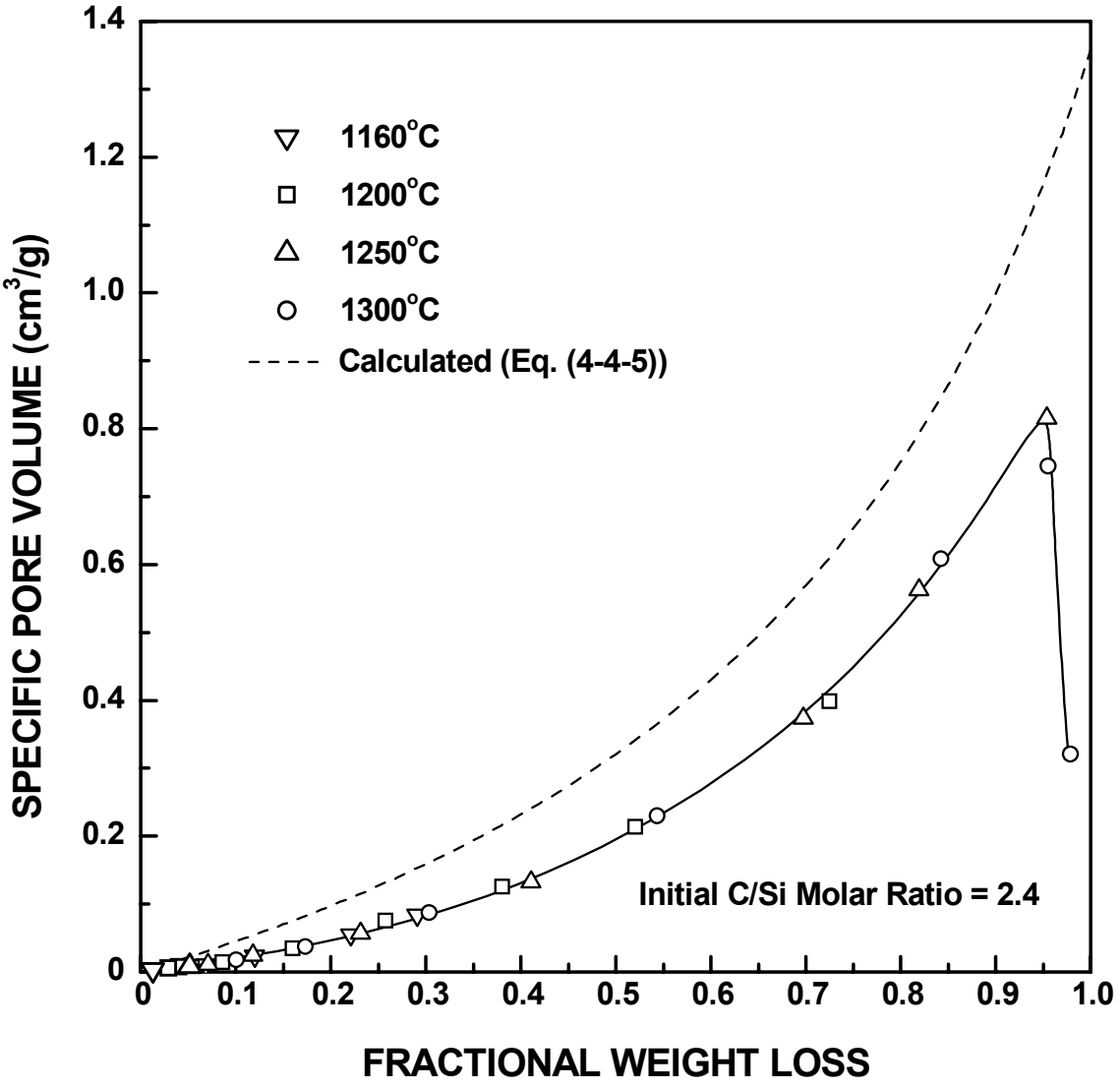

Figure 4-4-27a Plots of specific pore volume vs. fractional weight loss for SC35 samples which compare the measured values (from Figure 4-4-22) with calculated values using Equation (4-4-5).

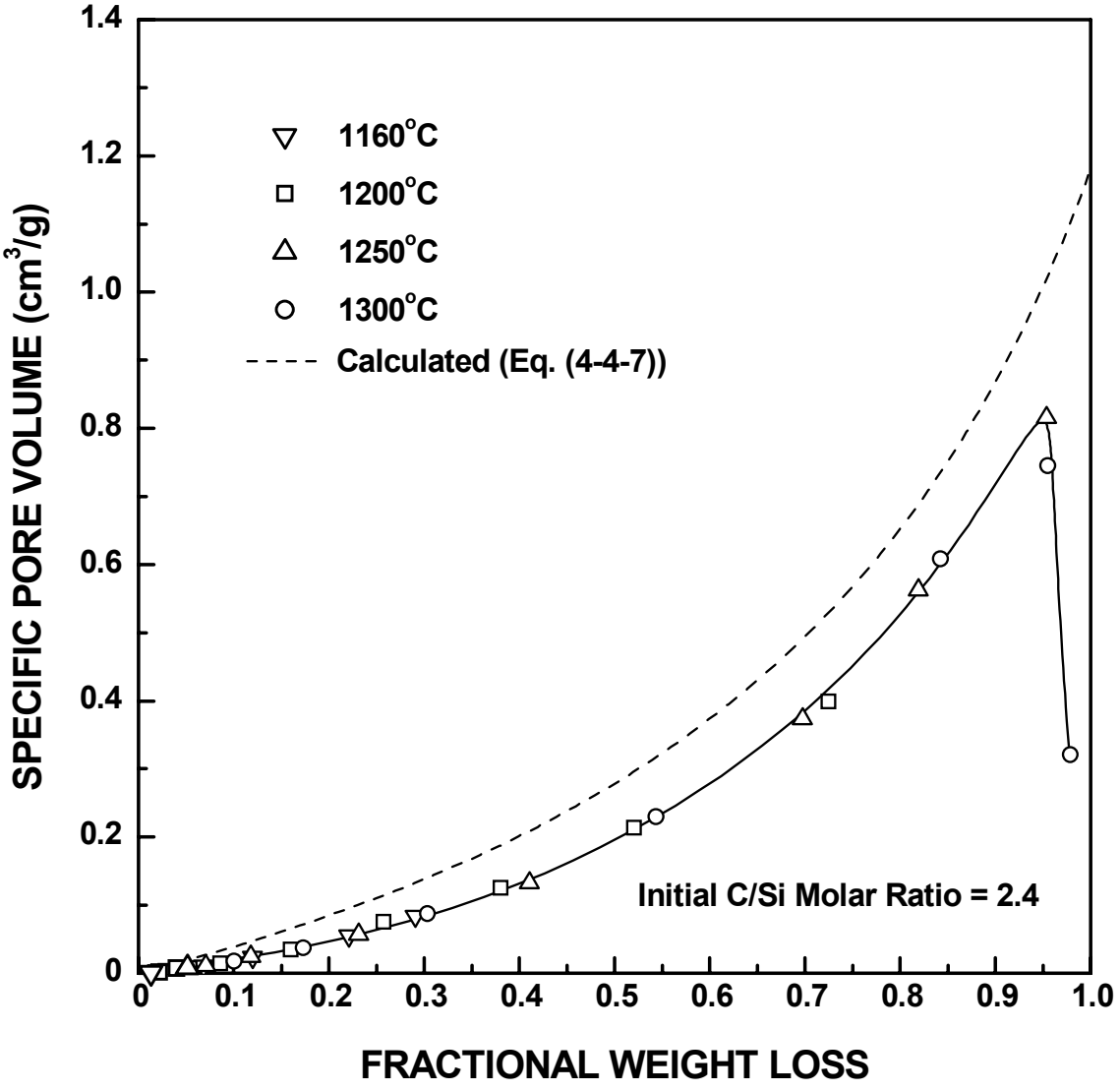

Figure 4-4-27b Plots of specific pore volume vs. fractional weight loss for SC35 samples which compare the measured values (from Figure 4-4-22) with calculated values using Equation (4-4-7).

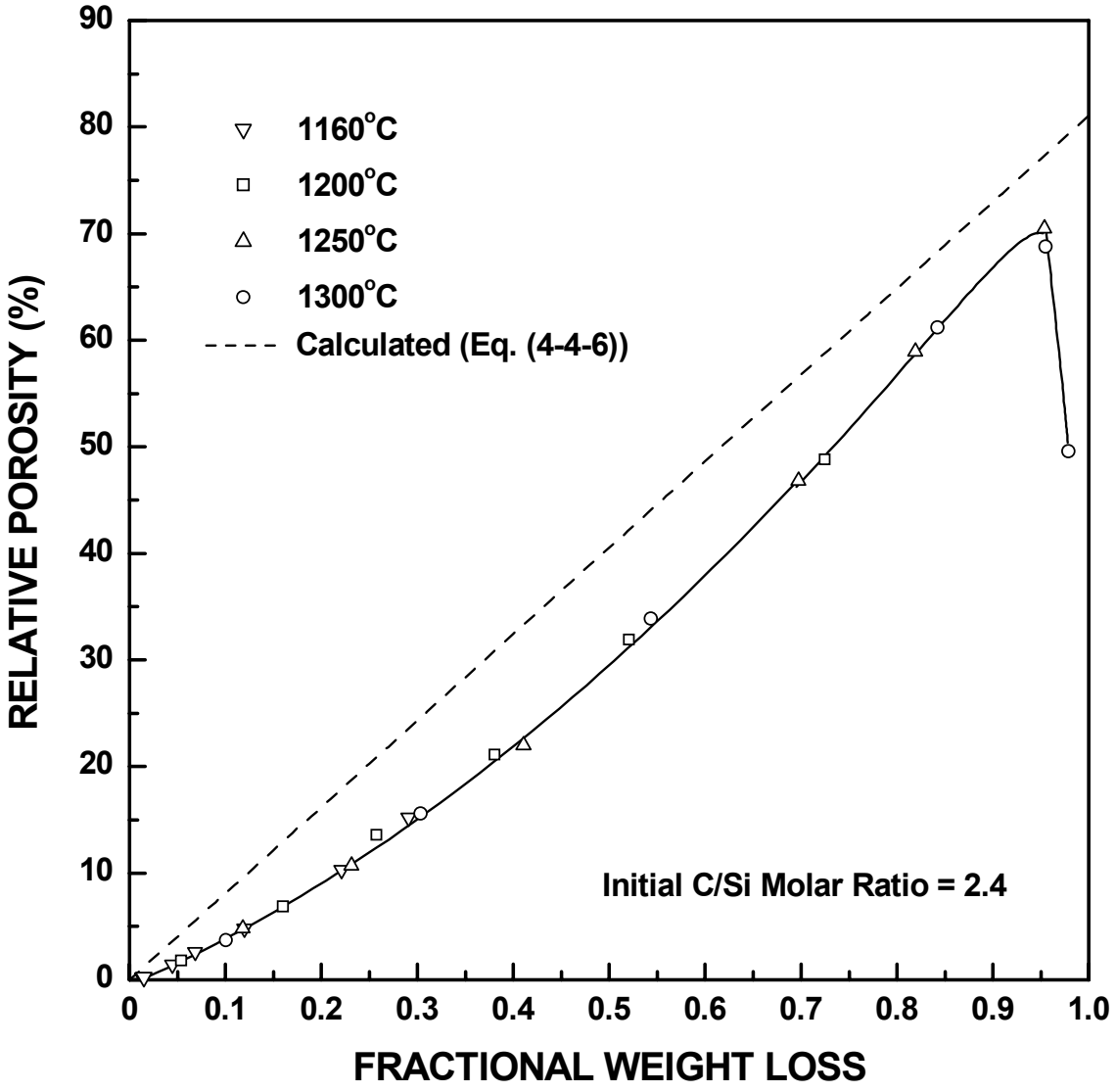

Figure 4-4-28a Plots of relative porosity vs. fractional weight loss for SC35 samples which compare the measured values (from Figure 4-4-23a) with calculated values using Equation (4-4-6).

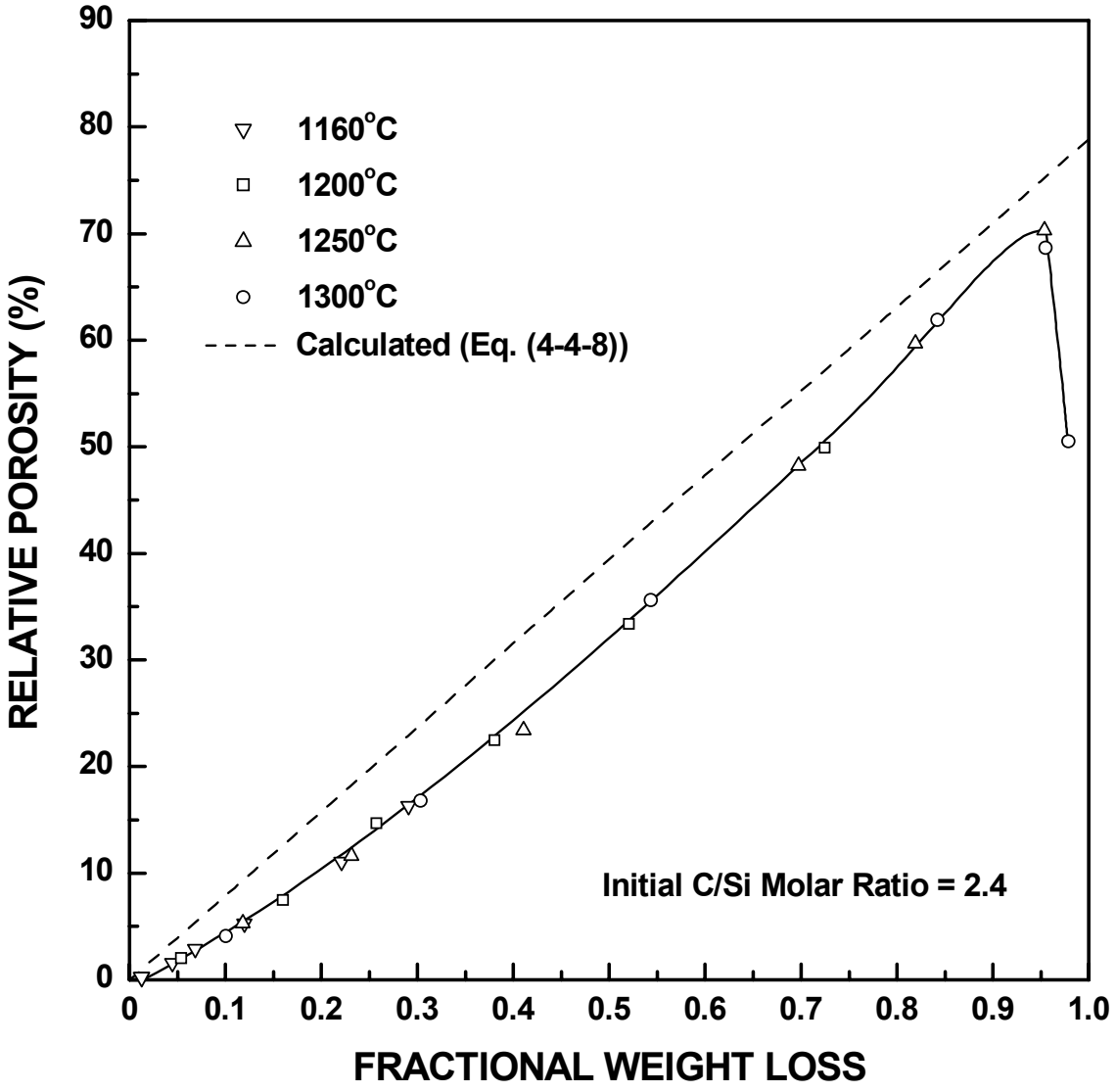

Figure 4-4-28b Plots of relative porosity vs. fractional weight loss for SC35 samples which compare the measured values (from Figure 4-4-23b) with calculated values using Equation (4-4-8).

SC35-1250(32h) with $X_{WL} = 0.95$.

Viscous sintering might be responsible for at least some of the discrepancy in the measured and calculated porosity values. As discussed in section 4.1.4, viscous sintering during the early stages of the reaction in the silica-rich SC35 samples might eliminate some pores. In addition, the viscous sintering of silica will also cause the entire particle to contract (see discussion in section 4.4.6). However, one of the assumptions for the above calculations was that the total volume of solids plus pores remained constant throughout the reaction. Both these two effects will cause the measured specific pore volume (as well as the relative porosity) to be lower than the calculated values. The effect of viscous sintering is expected to be smaller for the SC8 samples because of the much higher carbon content (and lower silica content) compared to the SC35 samples. Hence, better agreement would be expected between the experimentally measured porosity values and the corresponding values calculated using the same approaches as applied above for the SC35 samples. This is shown below.

For the SC8 pyrolyzed material, the values of z, x, and y in Equation (4-4-4) are 4.63, 2.02, and 0.19, respectively (see Table 4-5-1). As in the example for the SC35 pyrolyzed material, suppose that the initial amount of SiO_2 is also one mole and suppose that u moles of SiO_2 are consumed after time t (where $u \leq 1$). Also assume that reaction proceeds linearly according to Equation (4-4-4) throughout the entire reaction process, as discussed in section 4.3.3.2. Therefore, the molar quantities before CTR, after time t, and after complete CTR can be represented as follows:

	SiO_2 +	4.6 C →	0.81 SiC +	0.19 SiO +	2.02 C +	1.80 CO
Before CTR	1	4.63	0	0	0	0
After time *t*	1- *u*	4.63-4.63*u*	0.81*u*	0.19*u*	2.02*u*	1.80*u*
After complete CTR	0	0	0.81	0.19	2.02	1.80

If the density of carbon in the pyrolyzed material is assumed to be 1.49 g/cm^3, the initial solid sample volume (assuming there is no porosity) before CTR reaction, V_0, is:

$$V_0 = \frac{1\times 60}{2.25} + \frac{4.63\times 12}{1.49} = 63.96 \text{ cm}^3$$

The volume of solid product at time *t* (with extent of reaction of *u*), V, is given by:

$$V = \frac{(1-u)\cdot 60}{2.25} + \frac{4.63\cdot(1-u)\cdot 12}{1.49} + \frac{0.81u\cdot 40}{3.20} + \frac{2.02u\cdot 12}{2.0} = 63.96 - 41.72\,u \text{ cm}^3$$

The weight of sample at time *t* (with extent of reaction of *u*), V, is given by:

$$W = 1\times 60 + 4.63\times 12 - 0.19u\cdot 44 - 1.80u\cdot 28 = 115.56 - 58.76u \text{ g}$$

The specific pore volume, V_{Pore}, is given by:

$$V_{Pore} = \frac{V_0 - V}{W} = \frac{41.72u}{115.56 - 58.76u} \text{ cm}^3/\text{g} \qquad (4\text{-}4\text{-}9)$$

The relative porosity, V_{Pore}, is given by:

$$V_{Pore}^R = \frac{V_0 - V}{V_0}\times 100\% = 0.652u\times 100\% \qquad (4\text{-}4\text{-}10)$$

If the density of carbon in the pyrolyzed material is assumed to be 2.0 g/cm^3, the initial solid sample volume (assuming there is no porosity) before CTR reaction, V_0, is:

$$V_0 = \frac{1\times 60}{2.25} + \frac{4.63\times 12}{2.0} = 54.45 \text{ cm}^3$$

The volume of solid product at time *t* (with extent of reaction of *u*), V, is given by:

$$V = \frac{(1-u)\cdot 60}{2.25} + \frac{4.63\cdot(1-u)\cdot 12}{2.0} + \frac{0.81u\cdot 40}{3.20} + \frac{2.02u\cdot 12}{2.0} = 54.45 - 32.21\ u\ \text{cm}^3$$

The weight of sample at time t (with extent of reaction of u), V, is given by:

$$W = 1\times 60 + 4.63\times 12 - 0.19u\cdot 44 - 1.80u\cdot 28 = 115.56 - 58.76u\ \text{ g}$$

The specific pore volume, V_{Pore}, is given by:

$$V_{Pore} = \frac{V_0 - V}{W} = \frac{32.21u}{115.56 - 58.76u}\ \text{cm}^3/\text{g} \qquad (4\text{-}4\text{-}11)$$

The relative porosity, V_{Pore}, is given by:

$$V_{Pore}^R = \frac{V_0 - V}{V_0}\times 100\% = 0.592u\times 100\% \qquad (4\text{-}4\text{-}12)$$

Figures 4-4-29a and 4-4-30a show plots of the calculated specific pore volume and relative porosity, respectively, as a function of the fractional weight loss for the SC8 samples. The values were calculated using Equations (4-4-9) and (4-4-10), respectively. (The calculations were based on the assumption that the density of carbon in the pyrolyzed material was 1.49 g/cm^3.) For comparison, the experimental porosity values from Figures 4-4-25 and 4-4-26a are also plotted in Figures 4-4-29a and 4-4-30a, respectively. There is relatively good agreement between the calculated value and the measured values. For example, the calculated values from Equations (4-4-9) and (4-4-10) are V_{Pore} = 0.650 cm^3/g and V_{Pore}^R = 61.3%, respectively, when the fractional weight loss is 0.94. This agrees quite well with the experimental values for the SC8-1250(16h) sample (X_{WL} = 0.94) in which V_{Pore} = 0.665 cm^3/g and V_{Pore}^R = 61.7%, respectively. Figures 4-4-29b and 4-4-30b are the same type of plots shown in Figures 4-4-29a and 4-4-30a, respectively, except that the specific pore volume and relative porosity values were calculated using Equations (4-4-11) and (4-4-12), respectively. (The assumed density of carbon in the pyrolyzed material was

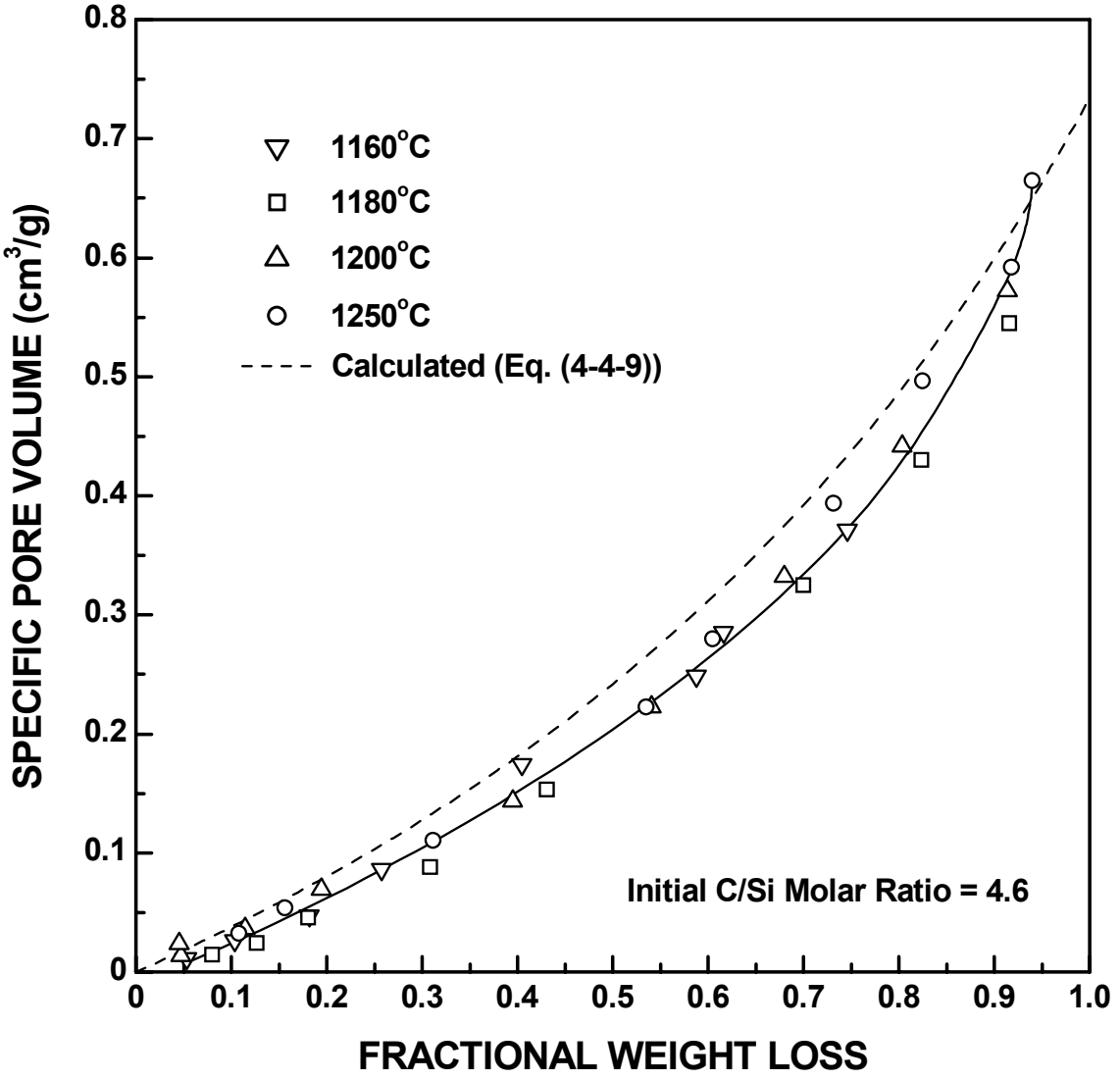

Figure 4-4-29a Plots of specific pore volume vs. fractional weight loss for SC8 samples which compare the measured values (from Figure 4-4-25) with calculated values using Equation (4-4-9).

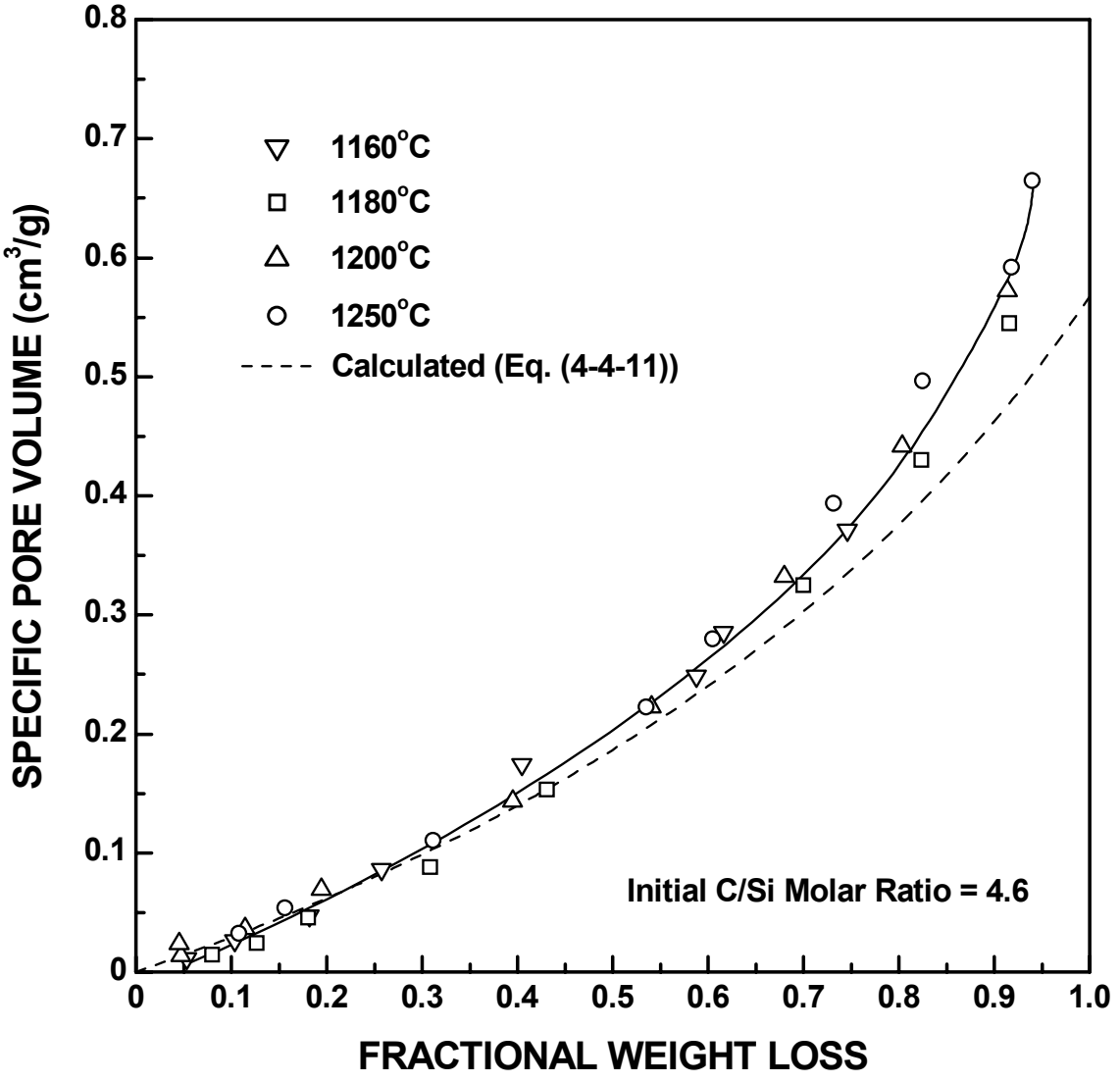

Figure 4-4-29b Plots of specific pore volume vs. fractional weight loss for SC8 samples which compare the measured values (from Figure 4-4-25) with calculated values using Equation (4-4-11).

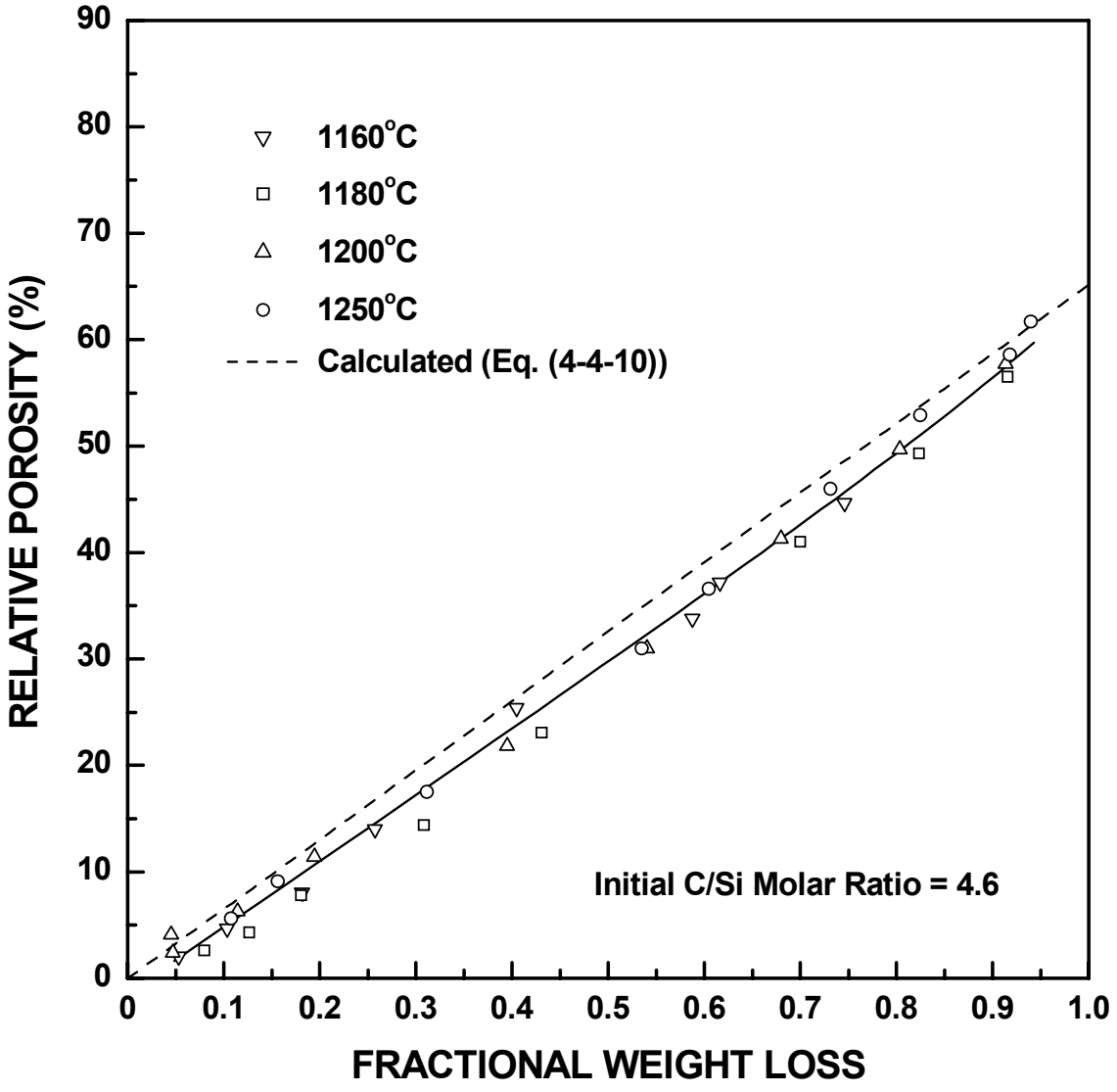

Figure 4-4-30a Plots of relative porosity vs. fractional weight loss for SC8 samples which compare the measured values (from Figure 4-4-26a) with calculated values using Equation (4-4-10).

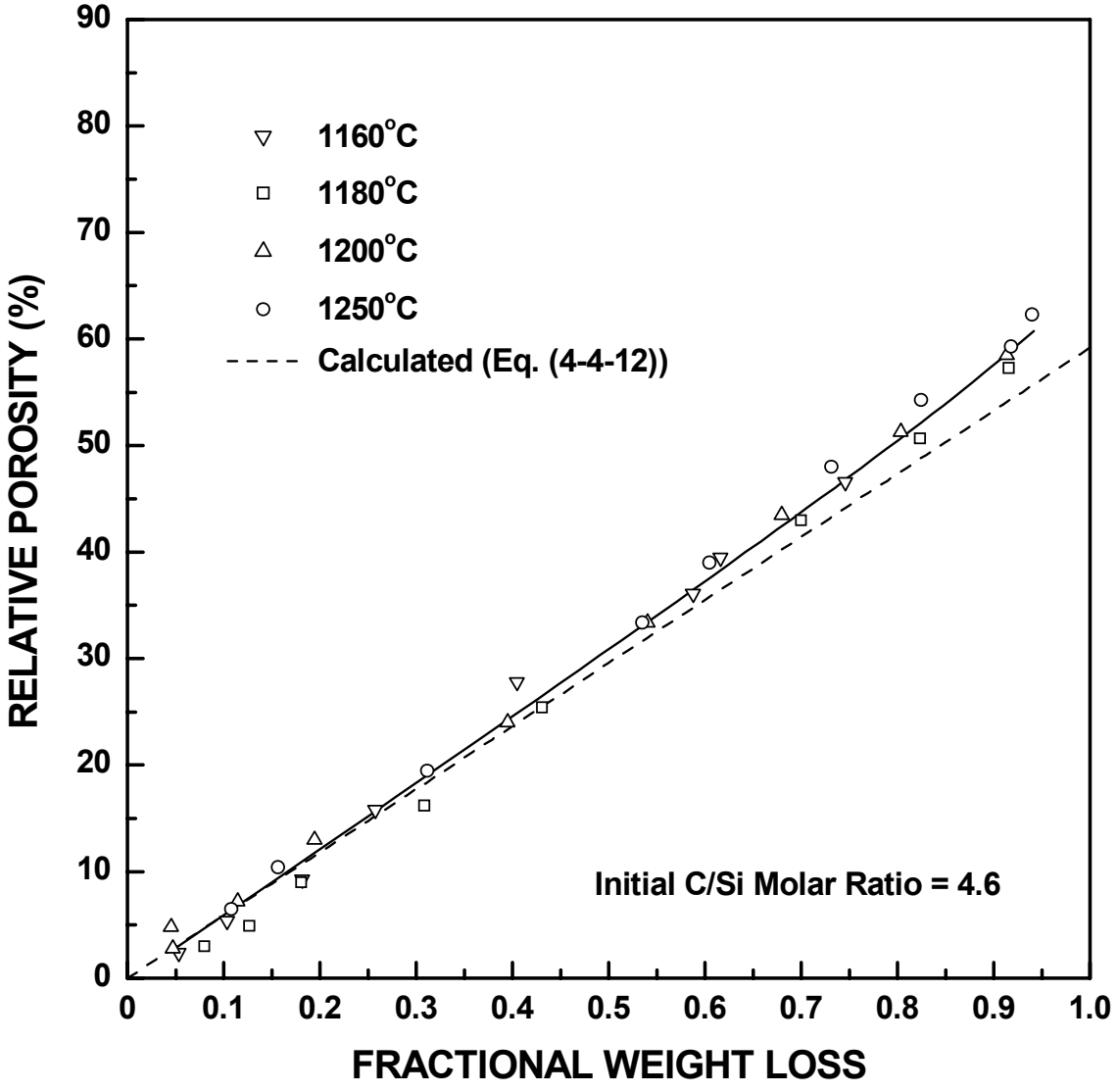

Figure 4-4-30b Plots of relative porosity vs. fractional weight loss for SC8 samples which compare the measured values (from Figure 4-4-26b) with calculated values using Equation (4-4-12).

2.0 g/cm^3.) The differences between the calculated and experimental values are larger in this case. For example, the calculated values are V_{Pore} = 0.486 cm^3/g and V_{Pore}^R = 55.6% when the fractional weight loss is 0.94. These values are lower than the experimental values of V_{Pore} = 0.665 cm^3/g and V_{Pore}^R = 62.3% for the SC8-1250(16h) sample (X_{WL} = 0.94). Overall, there was generally better agreement between the experimental and calculated porosity values for the SC8 samples (i.e., compared to that observed for the SC35 samples). This is expected because viscous sintering does not occur in the SC8 samples. (The evidence for this will be discussed in detail in section 4.4.6.)

4.4.3.2 Specific Surface Area

The specific surface areas were determined using the gas adsorption method, as described in section 3.5.2. Data was analyzed using the BET and the Langmuir models. The detailed results for all the SC35 and SC8 CTR samples are given in Appendix F. As discussed in section 3.5.2.3, the choice of whether the BET or the Langmuir value was used depended on the values of *C* and *b* in these models, as well as the linear correlation coefficients. It should be noted that during the very early stage of the reaction (e.g., X_{WL} < ~0.03 for the SC35 samples), the C values (when the BET equation was used) were very small. This indicates that the adsorbate had a relatively low affinity for the surface of these samples. The measured surface area values for these samples are less accurate compared to results obtained for samples with a greater extent of reaction.

Figure 4-4-31 shows the specific surface area vs. reaction time for the SC35 samples heat treated at temperatures in the range of 1160-1300^{o}C. Figure 4-4-32 is the same data re-plotted as the specific surface area vs. fractional weight loss (after

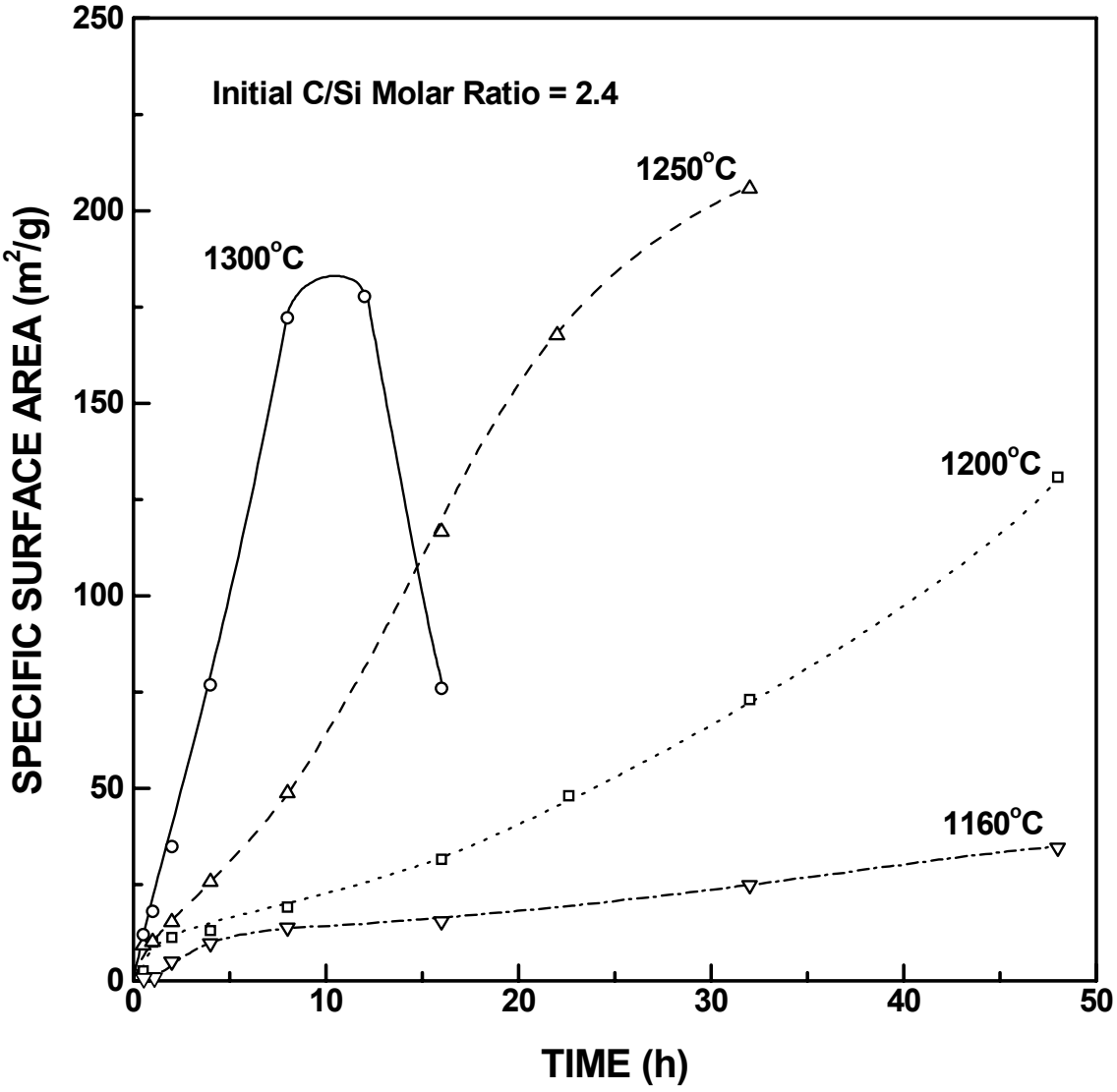

Figure 4-4-31 Plots of specific surface area vs. reaction time for SC35 samples (initial C/Si molar ratio = 2.4) heat treated at different temperatures.

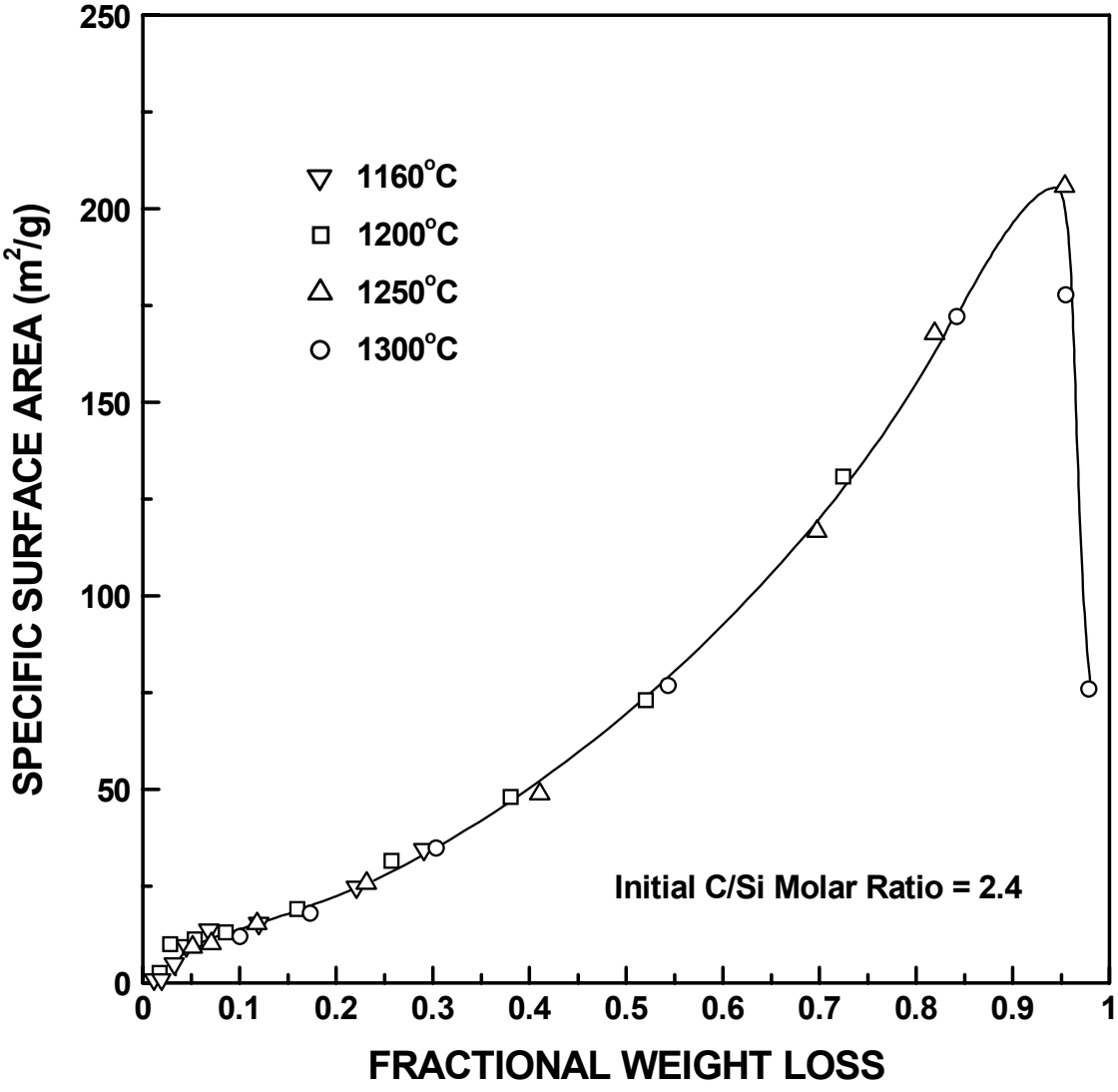

Figure 4-4-32 Plot of specific surface area vs. fractional weight loss (after correction for moisture adsorption and blow-off powder) for SC35 samples (initial C/Si molar ratio = 2.4) heat treated at different temperatures.

correction for moisture adsorption and powder blown-off) for the carbothermal reduction reaction. The following observations are made from these figures:

1. Figure 4-4-32 shows that the surface area development follows a single trend as the reaction proceeds which is independent of the reaction temperature. This is the same type of observation made regarding the SiC crystallite size and the total specific pore volume. It once again suggests that the reaction mechanism does not change over the range of temperatures investigated.
2. The surface area increases with increasing reaction time and temperature until the late stage of the carbothermal reduction reaction. This is attributed to the increase in pore-solid interfacial area that develops as a result of the increasing pore volume (as shown in Figures 4-4-21 and 4-4-22 in section 4.4.3.1).
3. The specific surface area decreases sharply at the late stage of the reaction when fractional weight loss was larger than ~0.95. This occurs at the same point in the reaction where the average SiC crystallite size starts to increase sharply and the total specific pore volume decreases sharply. As discussed in section 4.4.3.1, the latter two observations are attributed primarily to coarsening. The decrease in surface area is consistent with the coarsening of crystallites and pores.

Figure 4-4-33 shows the specific surface area vs. reaction time for the SC8 samples heat treated at temperatures in the range of 1160-1250^{o}C. Figure 4-4-34 is the same data re-plotted as the specific surface area vs. fractional weight loss for the carbothermal reduction reaction. The surface area development is similar to that of the SC35 samples in that the surface area increases with increasing extent of reaction and

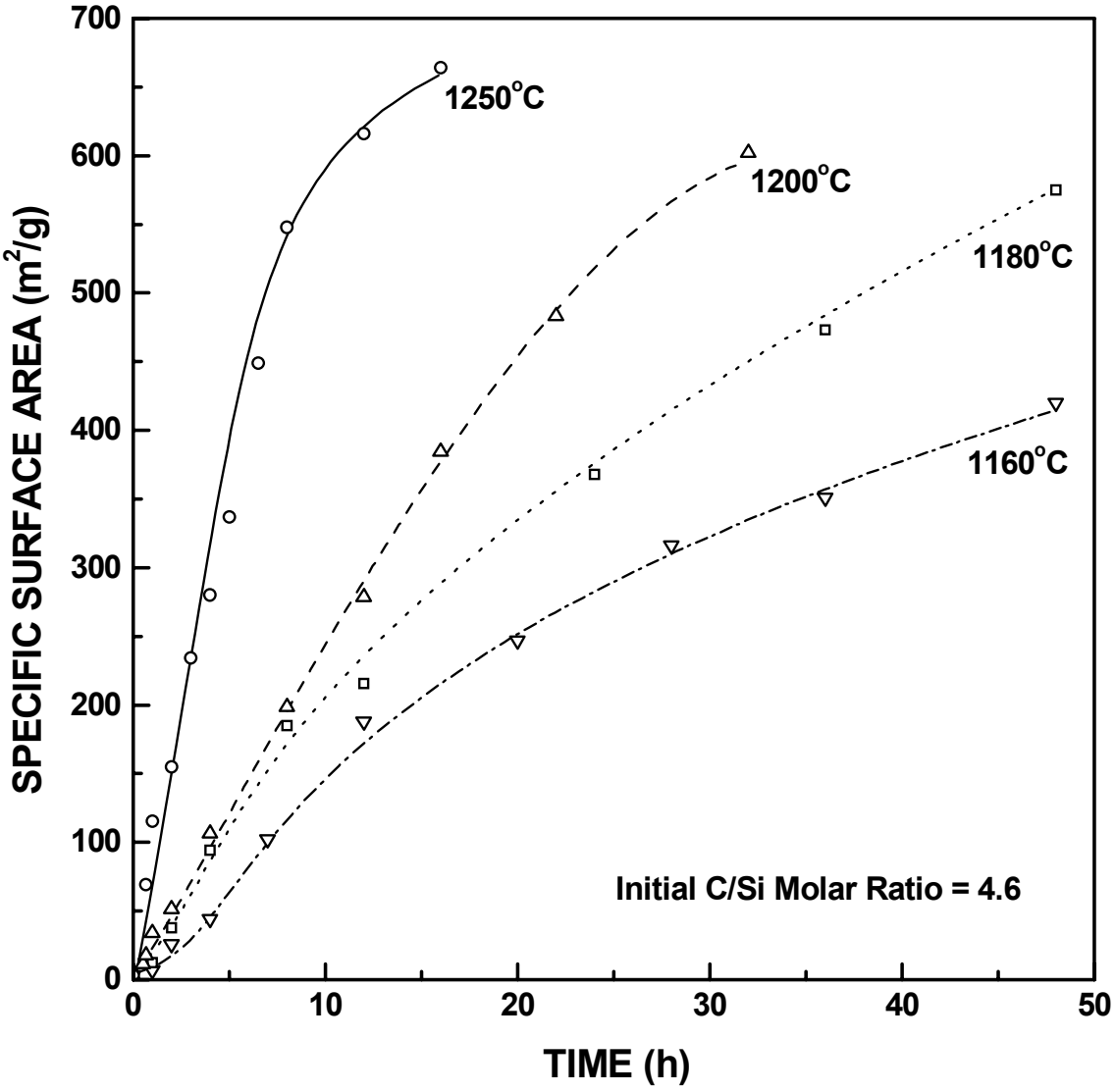

Figure 4-4-33 Plots of specific surface area vs. reaction time for SC8 samples (initial C/Si molar ratio = 4.6) heat treated at different temperatures.

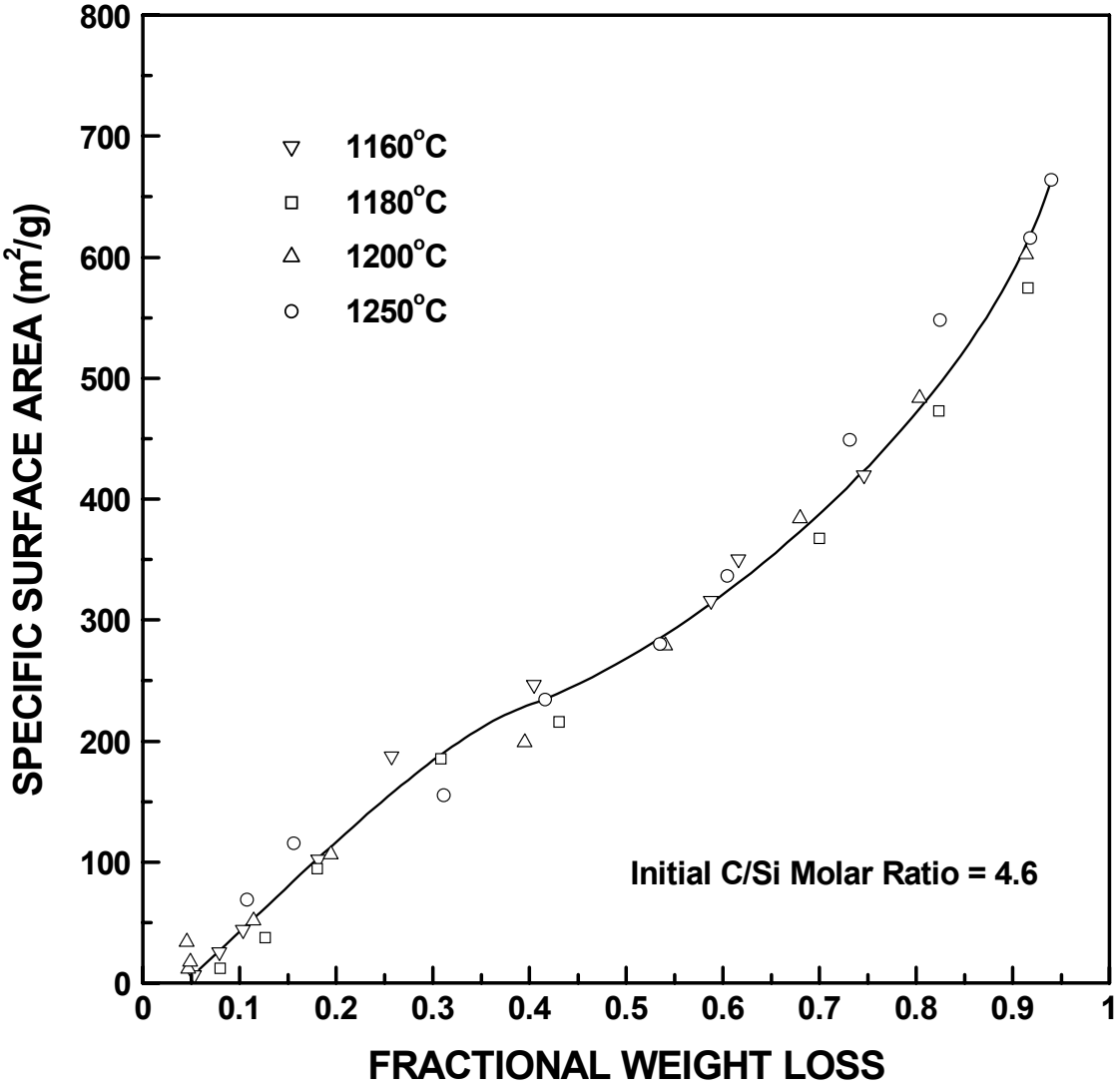

Figure 4-4-34 Plot of specific surface area vs. fractional weight loss (after correction for moisture adsorption and blow-off powder) for SC8 samples (initial C/Si molar ratio = 4.6) heat treated at different temperatures.

the increase in surface area follows a single trend that is independent of the reaction temperature.

There were also significant differences in the surface area development for the SC8 and SC35 samples.

1. There was no decrease in specific surface area during the late stage of the reaction for the SC8 samples. This is similar to the observation made regarding the pore volume (Figures 4-4-24 and 4-4-25). This appears to reflect a slower rate of coarsening of the SiC crystallites and the pores.
2. The maximum specific surface area for the SC8 samples was much larger than that for SC35 samples. The SC8 samples contain significantly more free carbon on an absolute basis compared with the SC35 samples. The higher specific surface areas for SC8 samples indicate that the carbon-rich regions in the SC8 samples develop a structure with finer pore sizes compared with the porosity that develops in the SC35 samples. This conclusion will be supported by the results of pore size analysis shown later in section 4.4.7.

4.4.4 SEM Observation on the Product of CTR

SEM observations were carried out using SC42 samples which were heat treated at 1300^{o}C for times in the range of 1-8 h. The SC42 samples had the same C/Si molar ratio as the SC35 samples.

Figures 4-4-35 and 4-4-36 show SEM micrographs for the outer surface of an SC42-1300(1h) particle with fractional weight loss of 0.27. These figures show many light-colored "featureless" regions which appear to be the same type of highly-dense

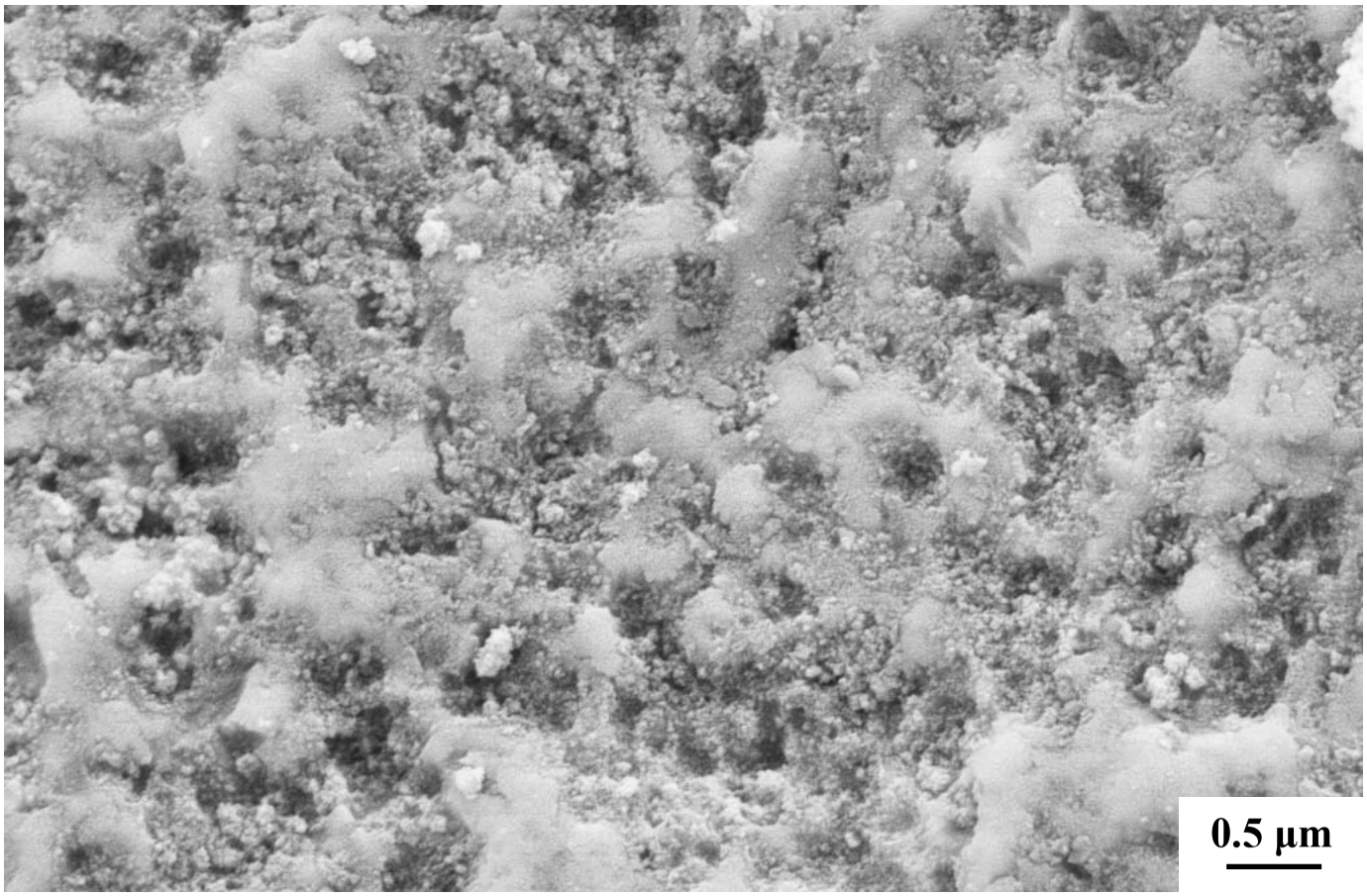

Figure 4-4-35 SEM micrograph of SC42-1300(1h) sample (X_{WL} = 0.27). The powder was dispersed in ethanol and the suspension was sonicated for 14 min. The solvent was removed by drying and the dried powder was sputter-coated for 1 min with gold.

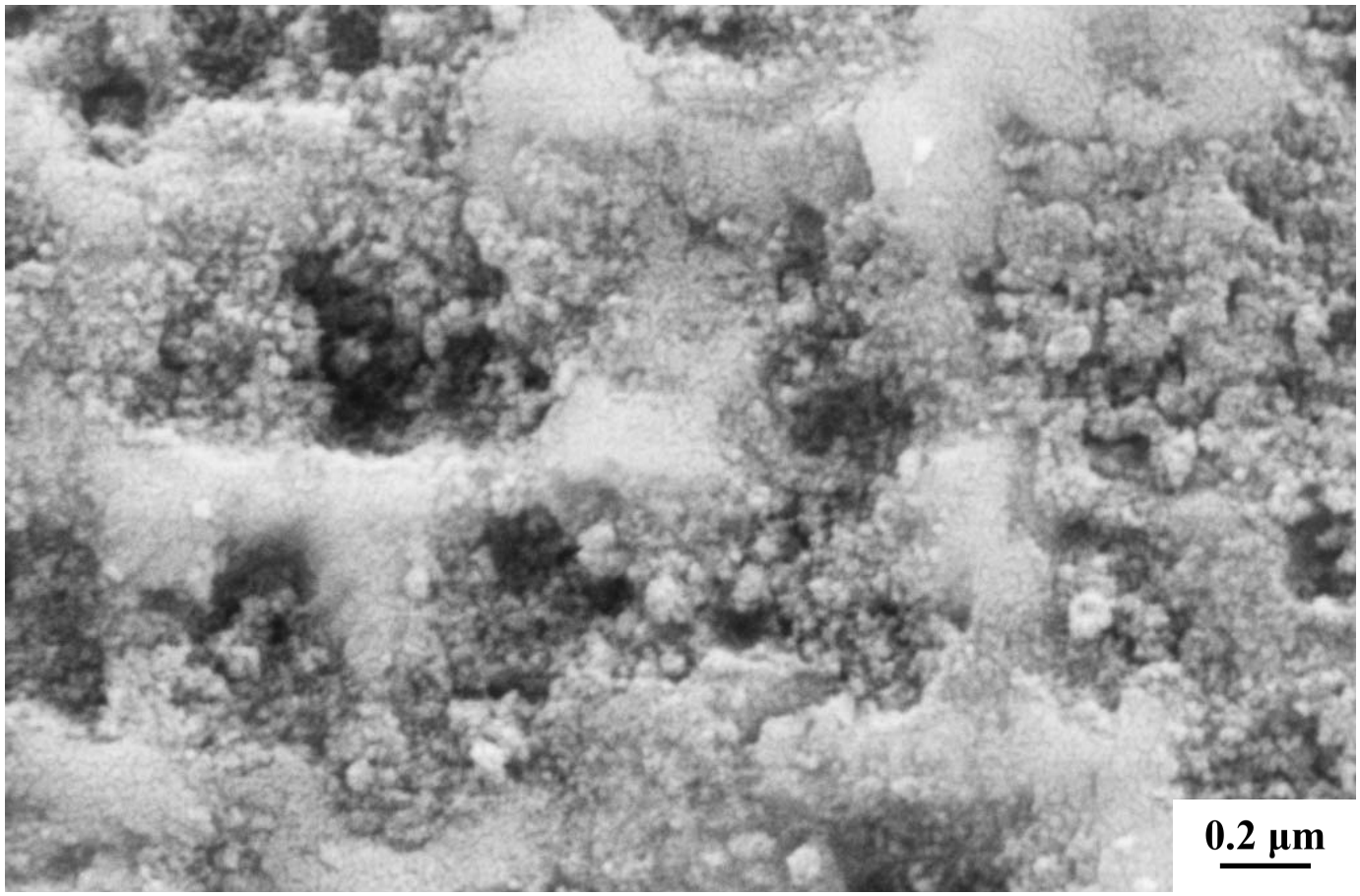

Figure 4-4-36 SEM micrograph of SC42-1300(1h) sample (X_{WL} = 0.27). The powder was dispersed in ethanol and the suspension was sonicated for 14 min. The solvent was removed by drying and the dried powder was sputter-coated for 1 min with gold.

regions that were observed throughout the original pyrolyzed particles. It appears from Figures 4-4-35 and 4-4-36 that these regions are somewhat elevated compared to the rest of the surface. In contrast, there are many pit-like regions adjacent to the dense regions. This structure is apparently an artifact of the sample preparation method used. The powder sample was dispersed in ethanol and then the suspension was sonicated for 14 min. As will be discussed in section 4.4.6, sonication results in fracture of the large porous CTR particles. Hence, the pit-like regions are apparently areas from which "chunks" of material had been removed from the surface of the large porous particles during sonication. It is interesting to note that many of the pit-like regions are on the order of a few tenths of a micrometer (e.g., see Figure 4-4-36). This tends to support the view that the original large pyrolyzed particles are comprised of much finer, nearly space-filling clusters. Figure 4-4-36 also shows that very fine particles can be observed in the pit-like regions. It is assumed that these particulates are SiC (or that they at least partially consist of SiC crystallites). The magnification of the micrograph is too low and the image lacks sufficient resolution to make a reliable estimate of the average particle size. Nevertheless, it is still evident that many of the particles are <25 nm. Such fine sizes would be expected based on the estimates of the SiC crystallite sizes that were obtained by XRD line broadening measurements (section 4.4.1) and from the TEM micrographs in section 4.4.2.

Figures 4-4-37 to 4-4-40 are SEM micrographs of the surface of the SC42-1300(3h) particle which had a fractional weight loss of 0.63. The micrographs have a different appearance from the micrographs in Figures 4-4-35 and 4-4-36 because the sample preparation method was different. The SC42-1300(3h) sample was prepared using a dry powder that was mounted in an epoxy resin and then polished. The epoxy resin was

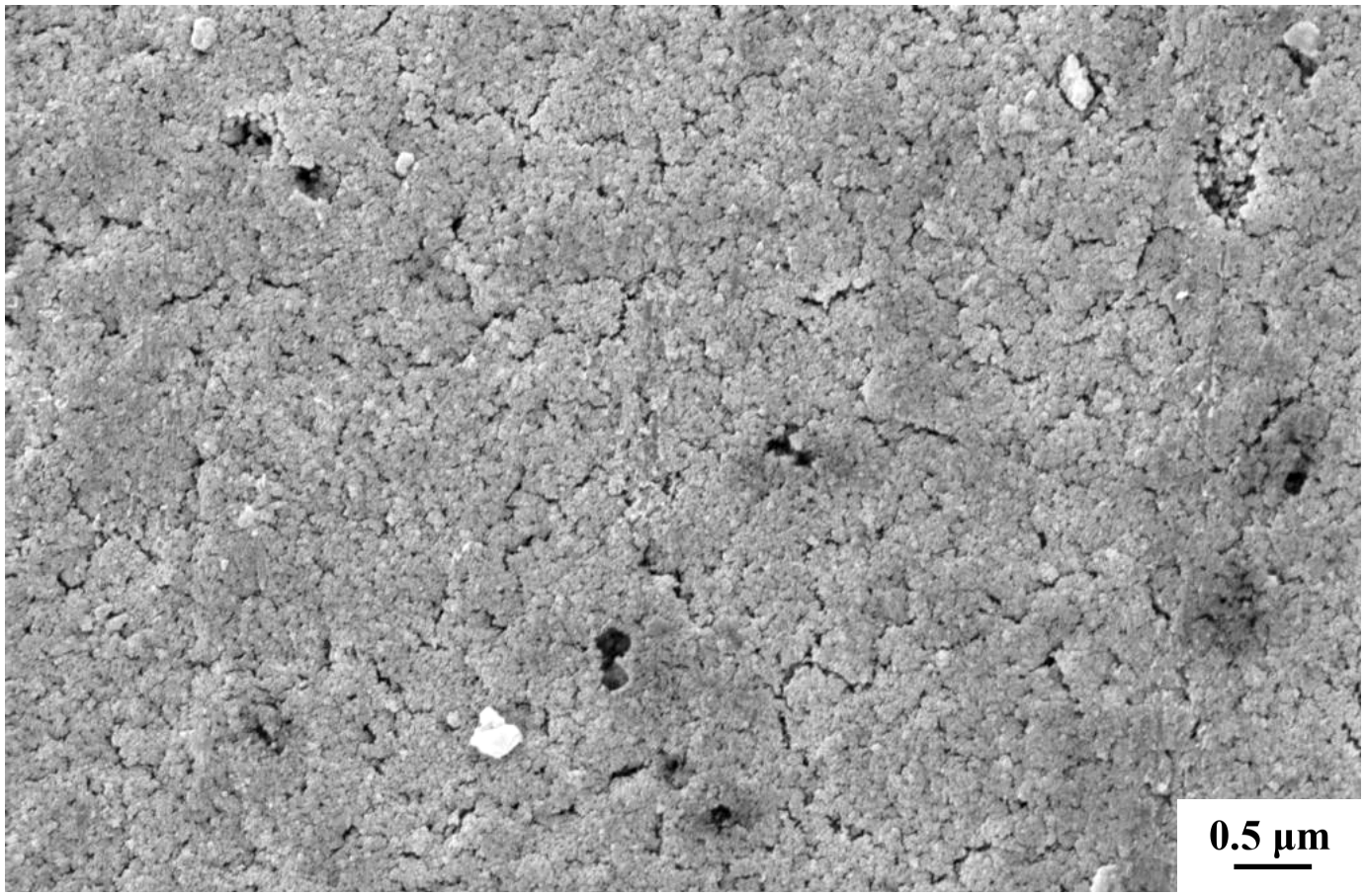

Figure 4-4-37 SEM micrograph of SC42-1300(3h) sample (X_{WL} = 0.63). The powder was embedded in epoxy resin and then polished. The resin was removed thermally (600^{o}C/2h) and then the sample was sputter-coated for 30 sec with gold.

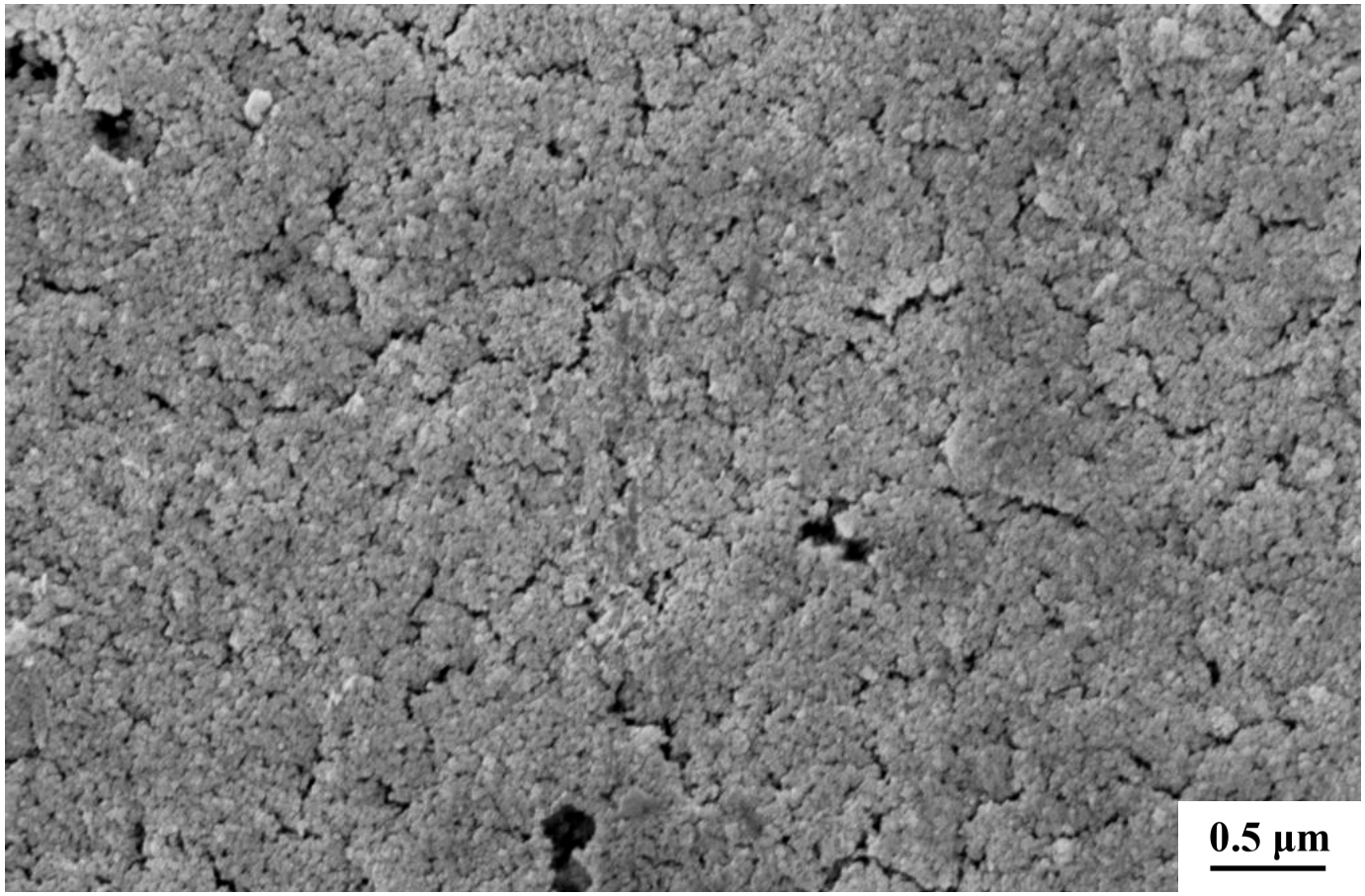

Figure 4-4-38 SEM micrograph of SC42-1300(3h) sample (X_{WL} = 0.63). The powder was embedded in epoxy resin and then polished. The resin was removed thermally (600^{o}C/2h) and then the sample was sputter-coated for 30 sec with gold.

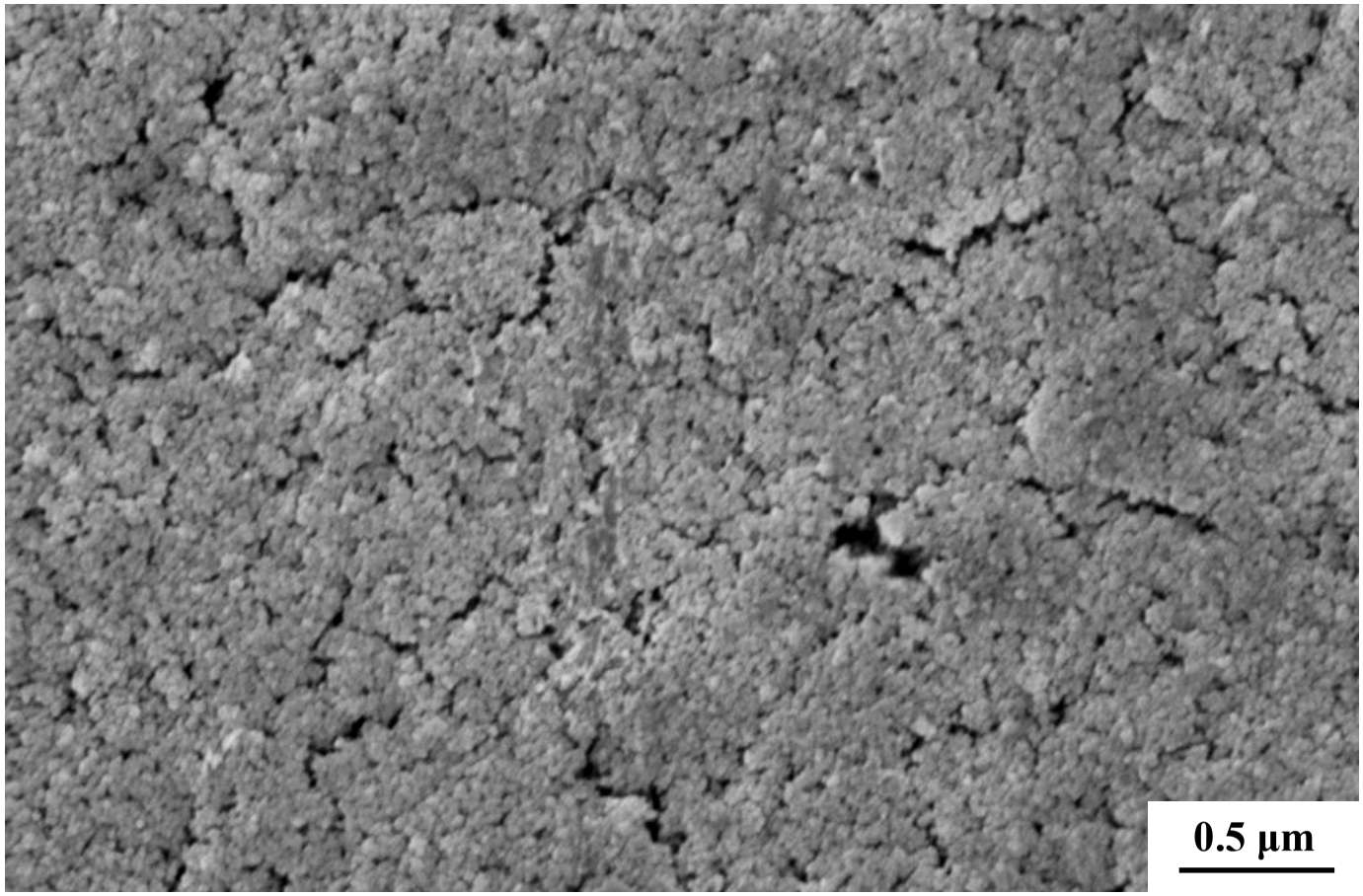

Figure 4-4-39 SEM micrograph of SC42-1300(3h) sample (X_{WL} = 0.63). The powder was embedded in epoxy resin and then polished. The resin was removed thermally (600^{o}C/2h) and then the sample was sputter-coated for 30 sec with gold.

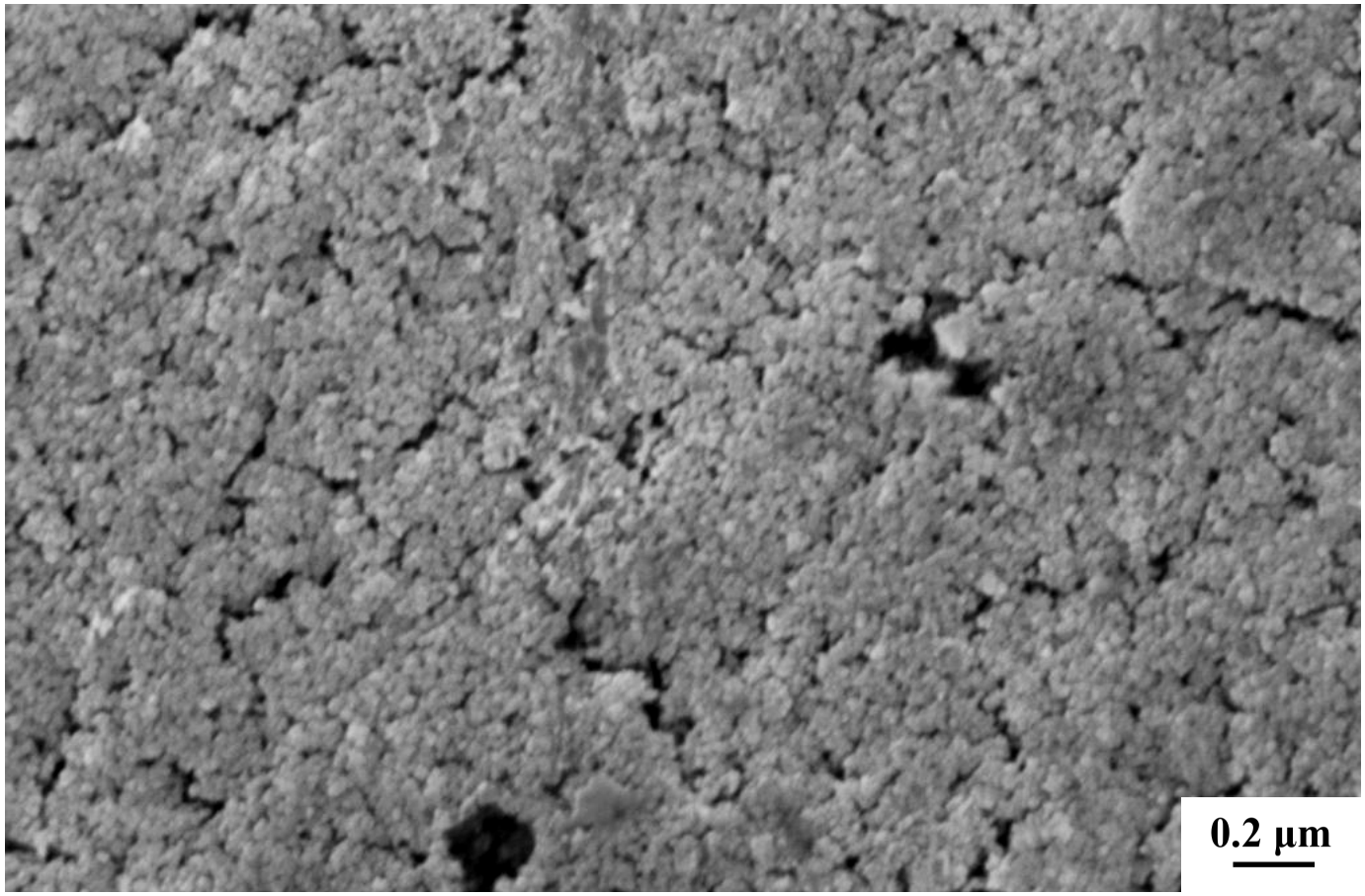

Figure 4-4-40 SEM micrograph of SC42-1300(3h) sample (X_{WL} = 0.63). The powder was embedded in epoxy resin and then polished. The resin was removed thermally (600^{o}C/2h) and then the sample was sputter-coated for 30 sec with gold.

thermally removed prior to observation in the SEM. Several features of interest are noted below.

1. The microstructure shows a hierarchical structure in which the large particles are composed of "clusters" which, in turn, are composed of very fine crystallites. (As in the case of Figure 4-4-36, the resolution is poor in these micrographs and it is difficult to estimate an average size of the fine crystallites. Nevertheless, they can be discerned in the higher magnification micrographs.) The cluster sizes vary widely, but Figures 4-4-37 to 4-4-40 indicate that most have sizes in the range of 0.1-1.0 μm. These figures also illustrate that the sample has a "mosaic-type" microstructure in that the clusters are organized in an essentially "space-filling" manner.
2. The cluster units can be discerned in Figures 4-4-37 to 4-4-40 because they are partially surrounded by "crack-like" porosity. The porosity is described as "crack-like" because it is narrow in width (i.e., compared to the cluster size), but relatively large in area. (In addition, this description seems appropriate because the appearance is somewhat analogous to a polycrystalline grain microstructure that contains extensive intergranular microcracks.)

   Crack-like porosity was also observed in the pyrolyzed particles (Figures 4-1-25 and 4-1-26), but the clusters were not readily apparent (Figures 4-1-21 to 4-1-24) and the amount of porosity was minimal in those particles. In contrast, the SC42-1300(3h) sample has a considerable amount of inter-cluster porosity, presumably as a result of the CTR reaction. Although the crack-like porosity is most visible, small intra-cluster pores (<20 nm) can also be discerned (just barely) in the highest

magnification micrographs (e.g., Figures 4-4-39 and 4-4-40). Gas adsorption/ capillary condensation measurements (shown later in section 4.4.7) indicate that fine pores (<20 nm) comprise a substantial fraction of the overall pore volume in the sample.

Figures 4-4-37 to 4-4-40 show occasional larger voids (mostly >100 nm) that are more equi-dimensional in shape. It is not known if these defects were present in the original pyrolyzed particles of if they formed during the CTR reaction.

Figures 4-4-41 and 4-4-42 show micrographs from the external surfaces of the SC42-1300(2h) and SC42-1300(4h) samples which have fractional weight loss values of 0.35 and 0.74, respectively. (These powders were observed directly in the SEM without any additional preparation, i.e., samples were not subject to sonication or to polishing.) These micrographs are additional examples which indicate that relatively large cracks were present in the original large pyrolyzed particles. The micrographs show long crack-like defects and fracture "steps" on the surface. These defects presumably developed from fractures that occurred during the crushing of the dried powders.

Figures 4-4-43 and 4-4-44 are SEM micrographs of the external surface of SC42-1300(6h) and SC42-1300(8h) samples which have fractional weight loss values of 0.87 and 0.95, respectively. (These powders were observed directly in the SEM without additional preparation, i.e., samples were not subject to sonication or to polishing.) These figures illustrate the development of SiC "agglomerates" as the reaction proceeds. These "agglomerates" have typical sizes on the order of a few tenths of a micrometer. (The term "agglomerate" is used because it is apparent that these are porous clusters that are

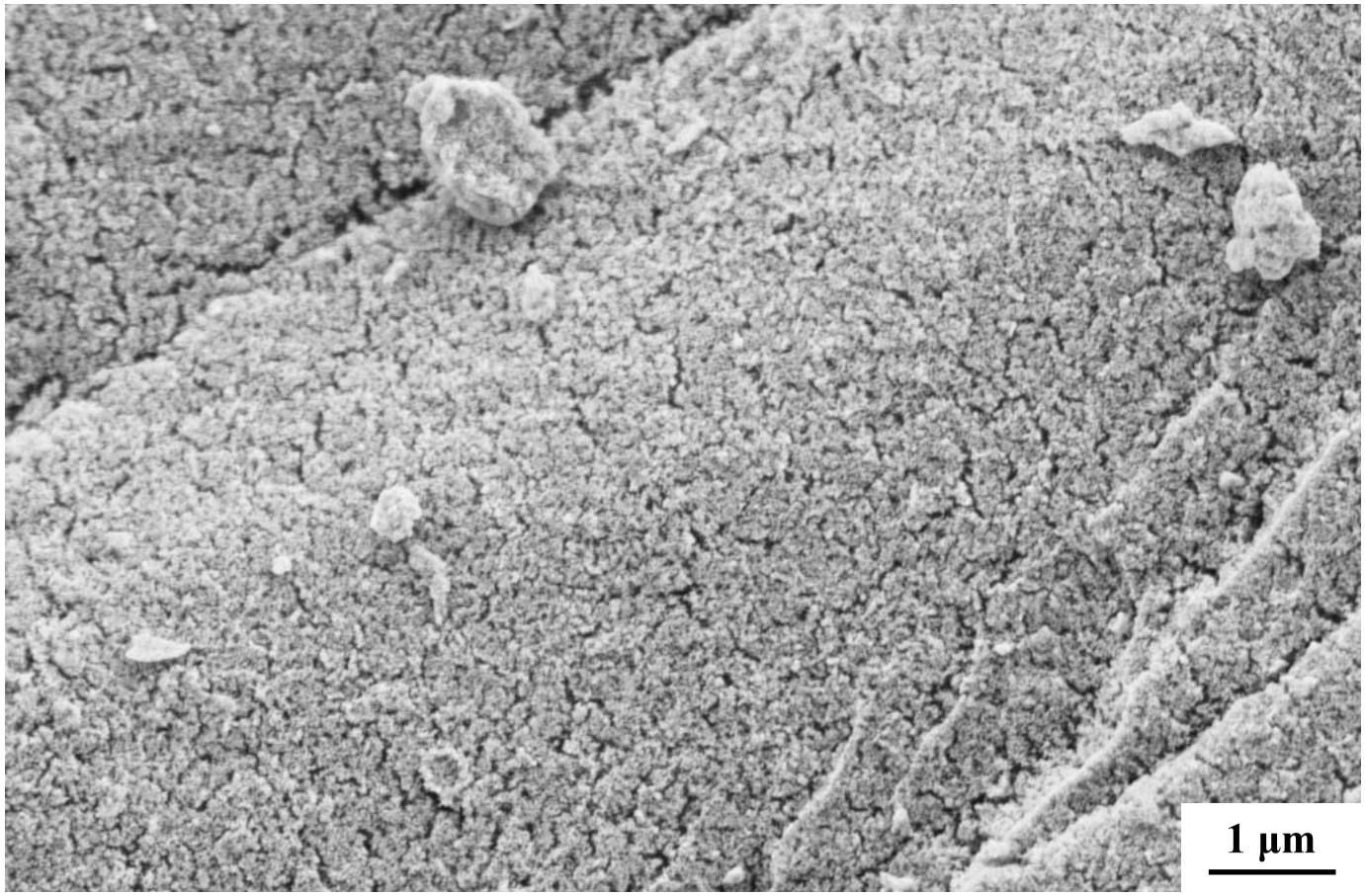

Figure 4-4-41 SEM micrograph of SC42-1300(2h) sample (X_{WL} = 0.35). The external surface of the powder was observed directly without any polishing or coating with gold.

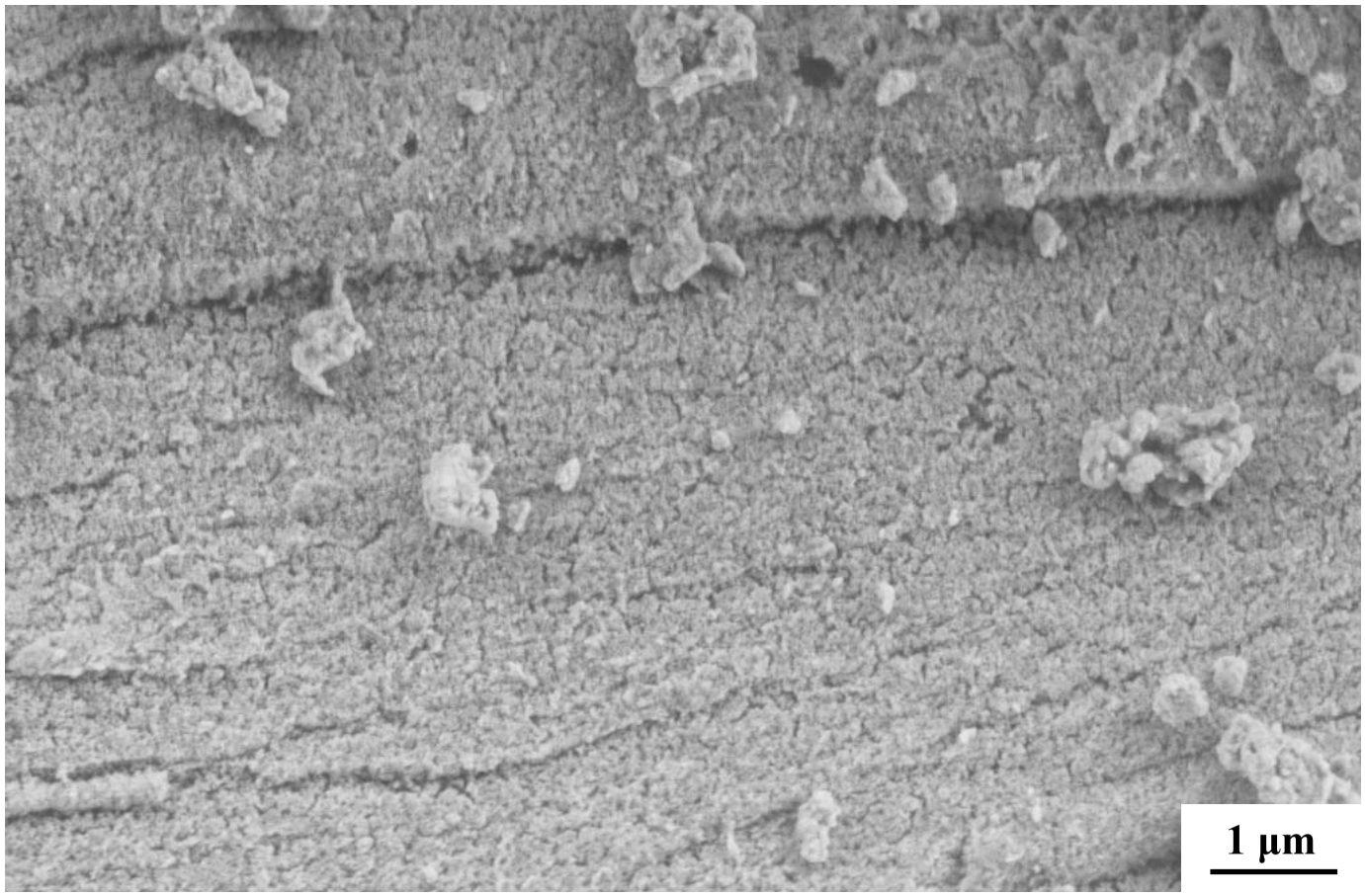

Figure 4-4-42 SEM micrograph of SC42-1300(4h) sample (X_{WL} = 0.74). The external surface of the powder was observed directly without any polishing or coating with gold.

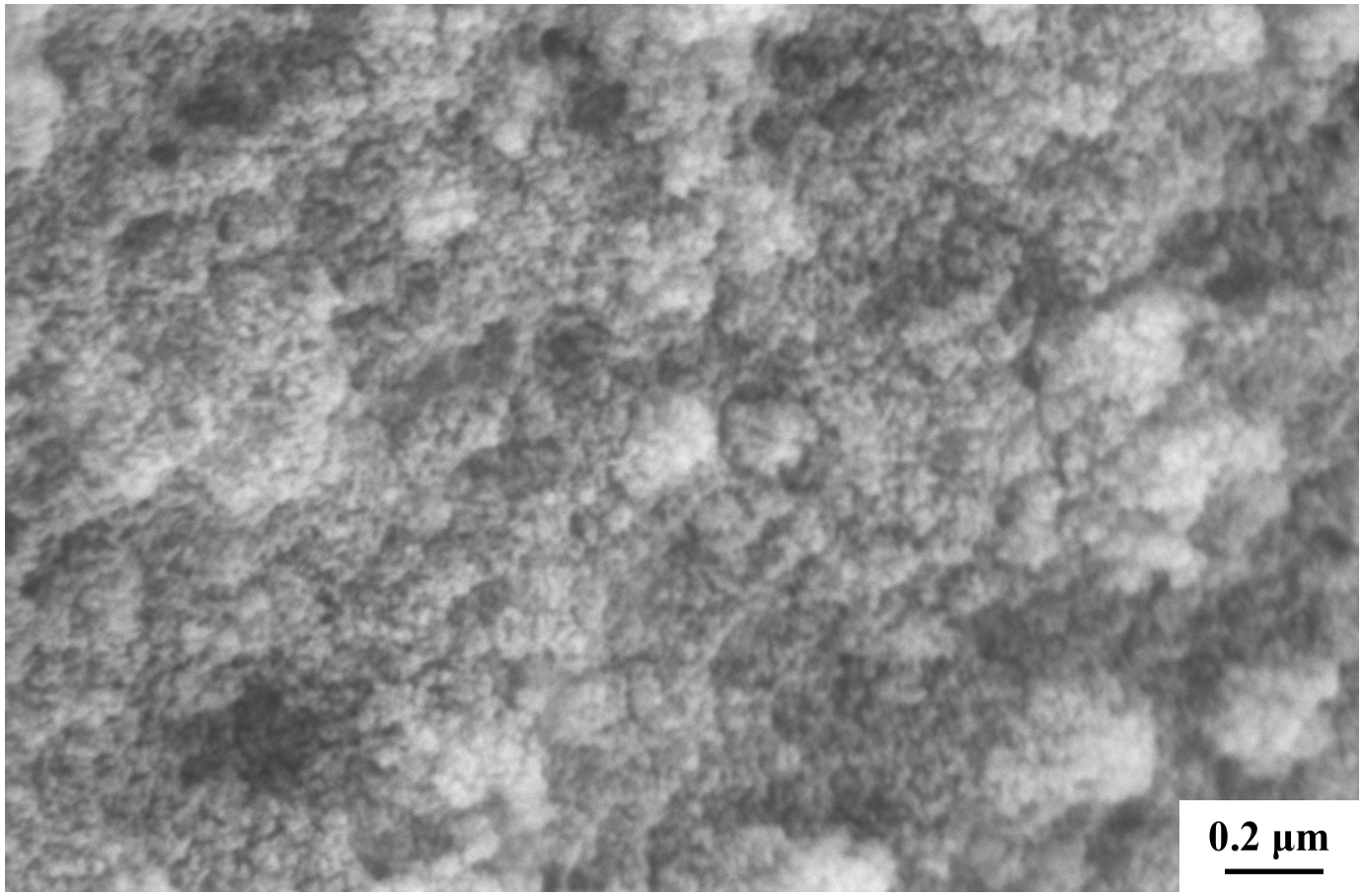

Figure 4-4-43 SEM micrograph of SC42-1300(6h) sample (X_{WL} = 0.88). The external surface of the powder was observed directly without any polishing or coating with gold.

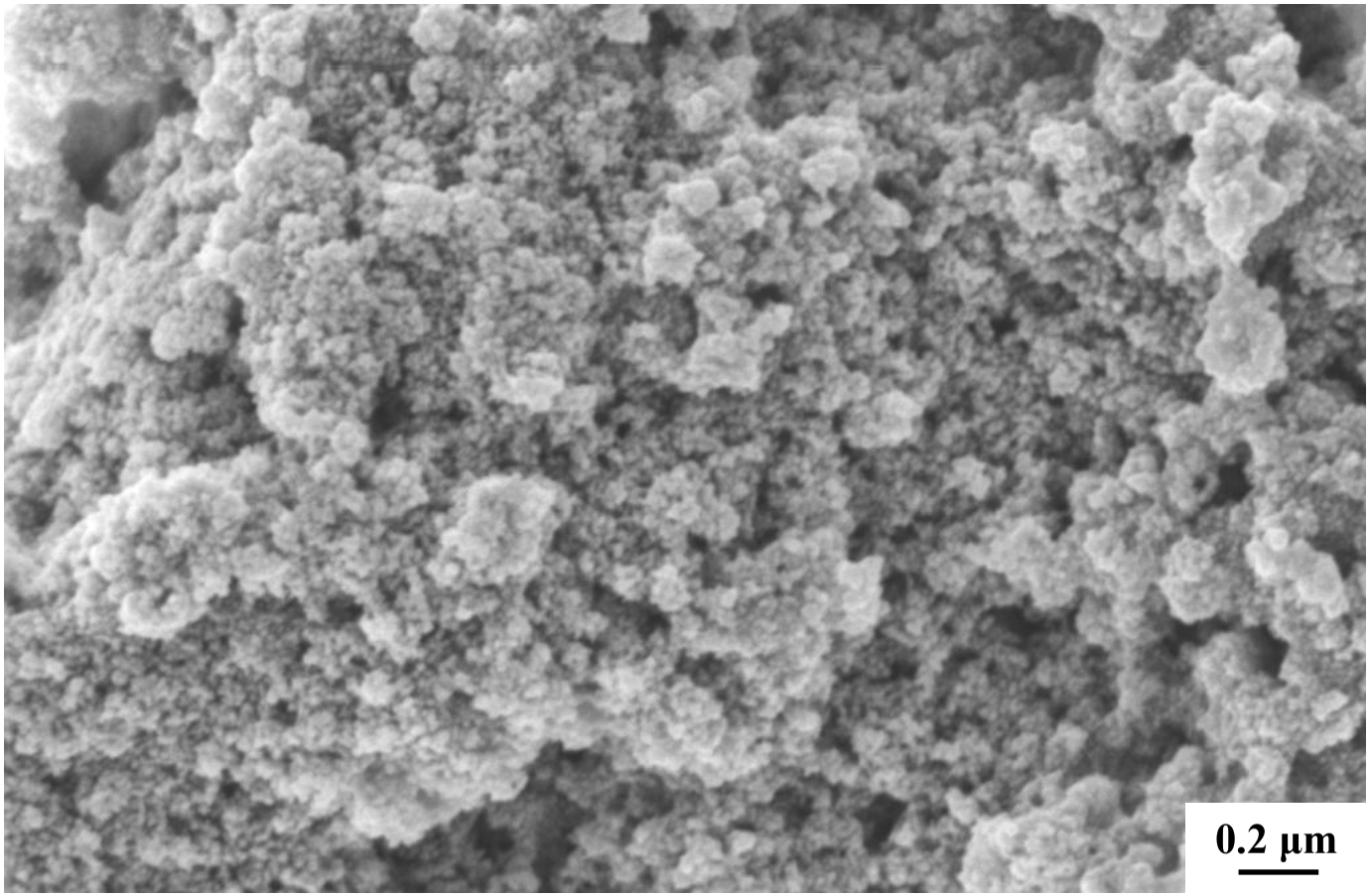

Figure 4-4-44 SEM micrograph of SC42-1300(8) sample (X_{WL} = 0.95). The external surface of the powder was observed directly without any polishing or coating with gold.

composed of finer "primary particles.") These micrographs provide further support for the hypothesis that the original pyrolyzed particles were comprised of "clusters".

4.4.5 The Hierarchical Structural Model for the Reaction

A highly-idealized schematic model for the structural development of the CTR reaction product during the shrinking-core model was shown in Figure 4-3-30. A more detailed structural model is now proposed based on the various characterization results that were described in sections 4.1.9 and 4.4.1 - 4.4.4 (i.e., measurements of pycnometric densities, crystallite sizes, specific surface areas, and pore volumes, and observations by SEM and TEM).

4.4.5.1 Hierarchical Structure of the Pyrolyzed Material

Particle size measurements described in section 4.1 showed that the pyrolyzed material consisted of relatively large particles with median diameters in the approximate range of 54-80 μm. SEM observations at various stages in the CTR reaction (section 4.4.4) indicated that these larger particles were composed of clusters with sizes mostly in the range of approximately 50-500 nm. The clusters are composed of a fine-scale mixture of silica and carbon. Indirect evidence (e.g., the reaction product crystallite size, section 4.4.1) and information from the scientific literature suggest that a characteristic size for the carbon and silica regions in the mixture is approximately on the order of ~5-10 nm. SEM observations, gas adsorption measurements (sections 4.1.7 and 4.4.4), and pycnometric measurements (section 4.1.9) indicated that the large pyrolyzed particles (and the clusters) were essentially dense, i.e., there was relatively little porosity present. However, SEM

observations and gas adsorption measurements also suggested that the large pyrolyzed particles contained some "macro defects," such as relatively large cracks and/or voids.

Schematic illustrations of the pyrolyzed materials described above are shown in Figures 4-4-45 and 4-4-46 for the SC35 and SC8 materials, respectively. The carbon and silica regions are depicted as uniform-sized, equiaxed, dense particles. However, it is presumed that the silica and carbon will actually be distributed into regions with a range of sizes and shapes. The clusters in Figures 4-4-45 and 4-4-46 are also shown as having a uniform size and shape. However, it is clear from the SEM observations at various stages in the CTR reaction (section 4.4.4) that the clusters had a range of sizes and shapes. The SC35 and SC8 pyrolyzed materials differ in composition with the former material having ~65 vol% silica/~35 vol% carbon and the latter material having ~49 vol% silica/~51 vol% carbon.

4.4.5.2 Structural Evolution During the CTR Reaction

It is hypothesized that the clusters within the pyrolyzed particles (with typical sizes on the order of a few hundred nanometers) are the basic unit for the "shrinking-core" model of the CTR reaction. The CTR reaction would be initiated at the surface of the clusters and would generate a porous SiC product layer on the surface of the clusters. The pores are formed after silica (and some carbon) are removed during the first-step of the reaction (Equation (4-2-1)). As discussed in section 4.2, the SiC would form by reaction of SiO gas with carbon (Equation (4-2-2)). As the reaction proceeds, the reaction interface would move progressively to into the interior of the cluster. This type of progression would be necessary for the reaction to proceed because the evidence (specific surface area, total pore

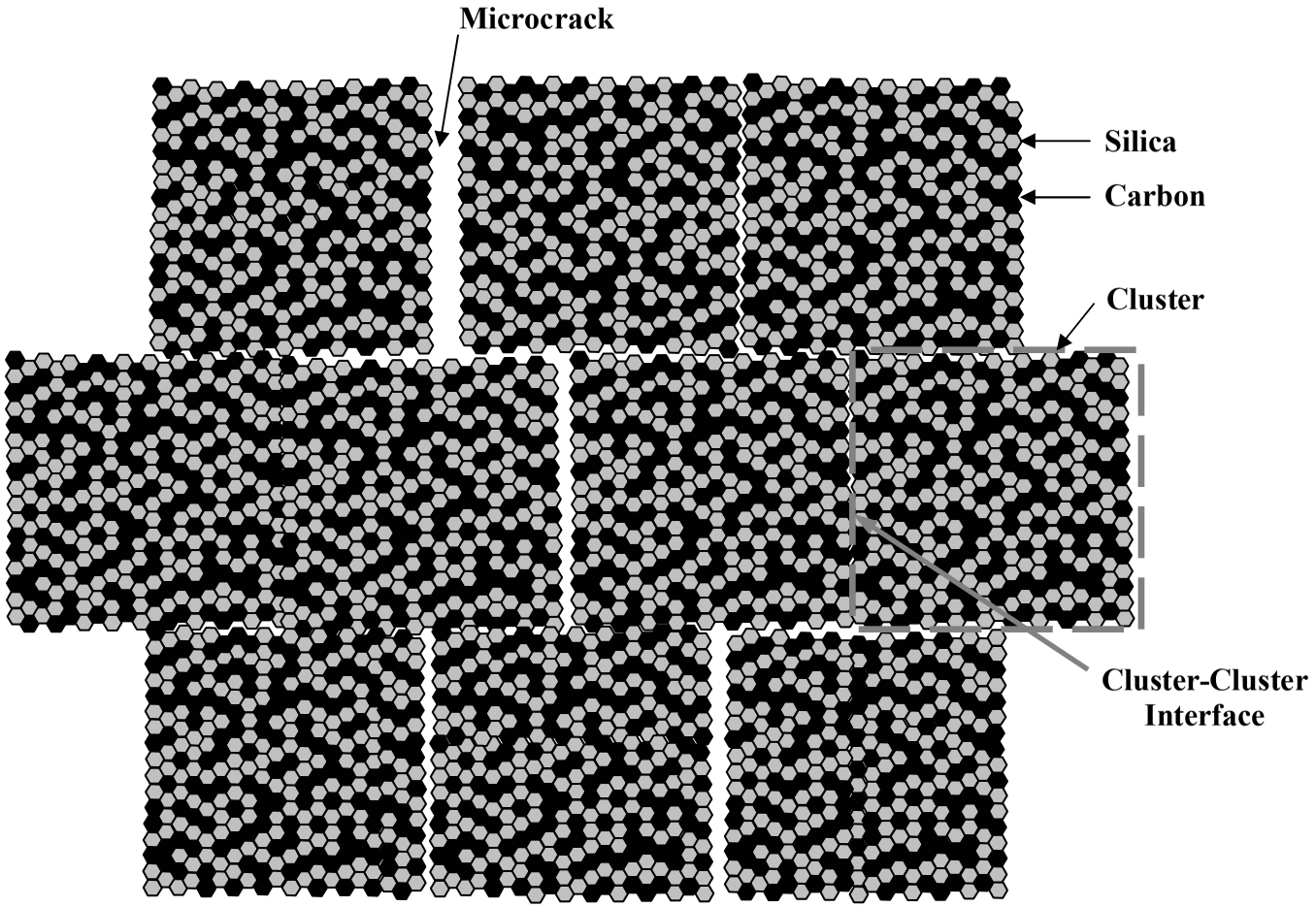

Figure 4-4-45 Illustration of the idealized structure of an SC35 pyrolyzed particle. The particle is composed of clusters. Each cluster is composed of networks of carbon and silica. There are also gross defects like microcracks in the particle. Note that, in reality, the clusters and "primary particles" should have a size distribution. The shape of the clusters and "primary particles" should also be irregular.

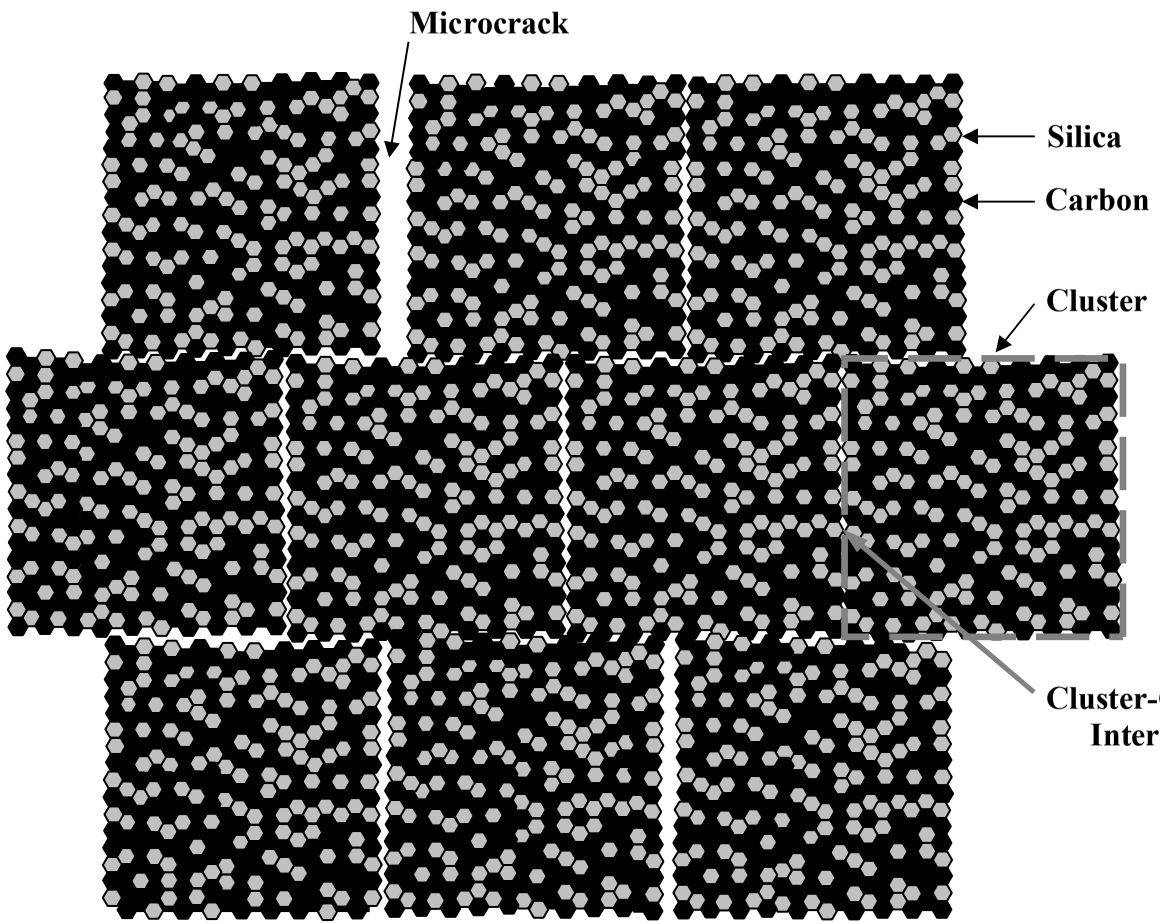

Figure 4-4-46 Illustration of the idealized structure of an SC8 pyrolyzed particle. The particle is composed of clusters. Each cluster is composed of networks of carbon and silica. There are also microcracks between the clusters. In reality, the clusters and "primary particles" should have a size distribution. Also, the shape of the clusters and "primary particles" should be irregular.

volume, SEM, apparent bulk density, etc) described in section 4.1 indicates that the clusters are essentially dense carbon/silica mixtures. Hence, the reaction could not proceed initially within the dense interiors of the clusters because gases (SiO, CO) would not be able to escape. Therefore, it is instead concluded that the CTR reaction must be initiated at the cluster surfaces.

It is also suggested that the reaction is initiated not only at clusters near the surface of the large pyrolyzed particle, but at most clusters within the pyrolyzed particle. This may seem contradictory because the pyrolyzed particles were considered to be essentially dense (i.e., pore-free). However, it was noted earlier that the pyrolyzed particles also contain some "macrodefects," such as microcracks and large pores. These defects would provide a path for the egress of the initial volatiles (i.e., SiO, CO) that are produced during the earliest stage of CTR and would enable the reaction to occur at cluster-cluster interfaces throughout the large pyrolyzed particles.

The structural evolution described above is illustrated schematically in Figures 4-4-47 - 4-4-49 for the SC35 CTR material. The trends illustrated in this figures are consistent with various observations reported in sections 4.4.3. First, the total pore volume and specific surface area would increase continuously with increasing extent of reaction. Second, a relatively uniform porous SiC structure would develop as the reaction proceeds from the cluster surfaces (and cluster-cluster interfaces) to the interior of the clusters. Therefore, the SiC crystallite size shows relatively little change during most of the reaction. It would also be predicted from this structural model that the pore size would show relatively little change for much of the reaction. However, since the clusters are essentially dense in the pyrolyzed materials, there would be a period in which the pores would first

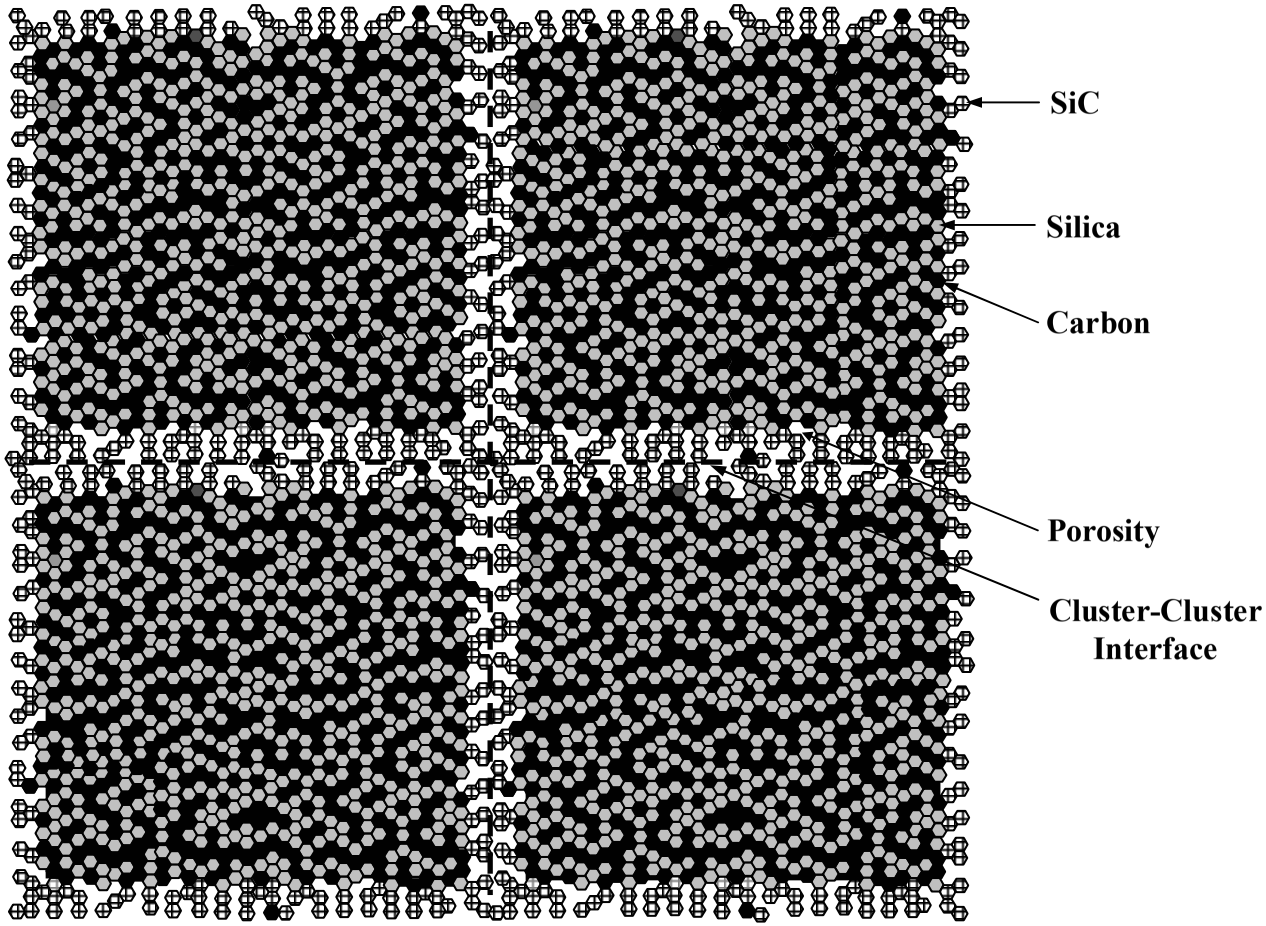

Figure 4-4-47 Illustration of the idealized structure of an SC35 particle after a small extent (~20%) of the CTR reaction. SiC crystallites have formed at the cluster surfaces and/or cluster-cluster interfaces. Mesopores begin to develop as silica is removed during the reaction. The mesopores in the inter-cluster regions form an interconnected network that percolates through the entire particle.

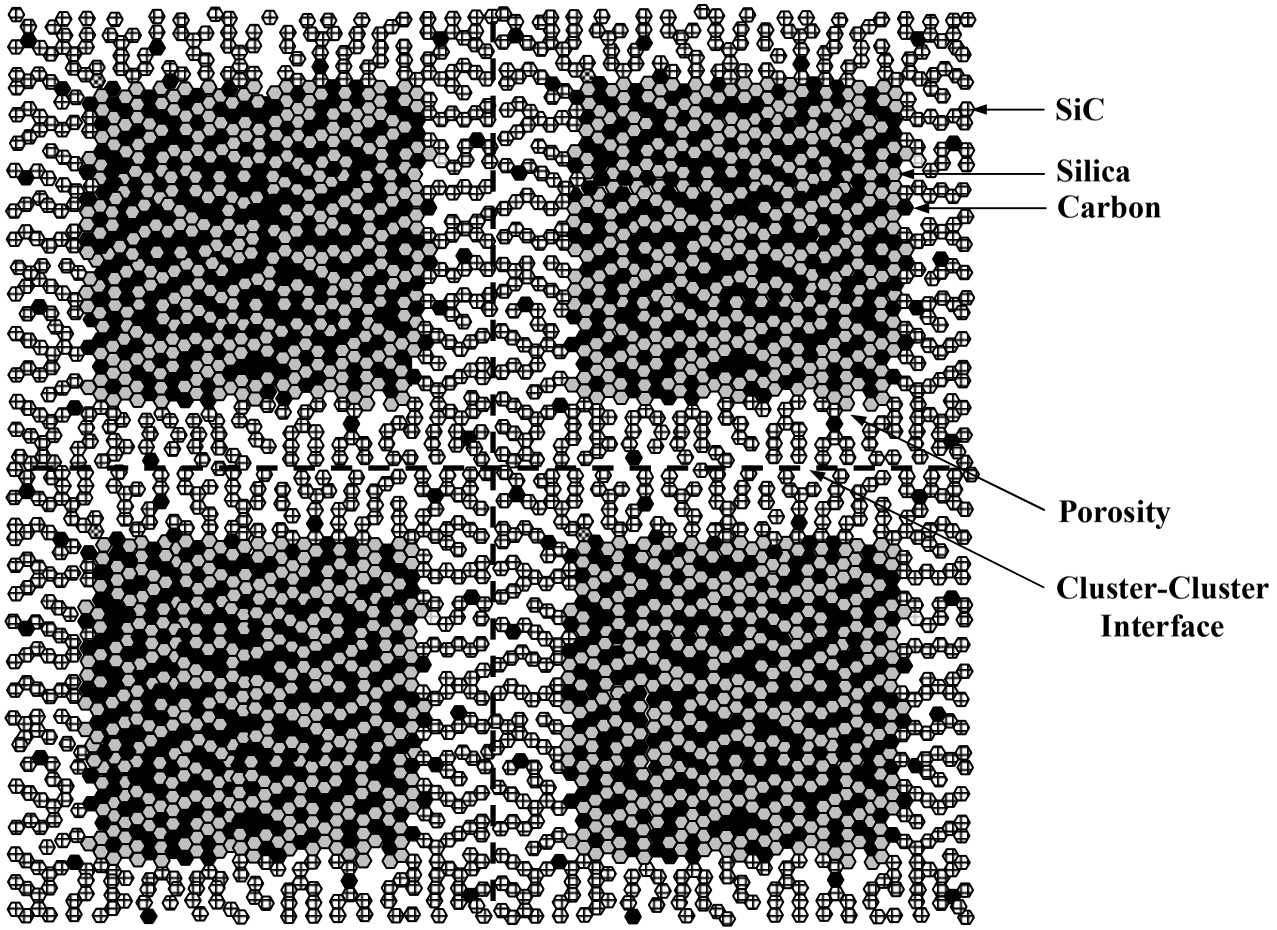

Figure 4-4-48 Illustration of the idealized structure of an SC35 particle after an intermediate extent (~50%) of the CTR reaction. The reaction interface moves inside towards the core of each cluster. The volume of porosity increases.

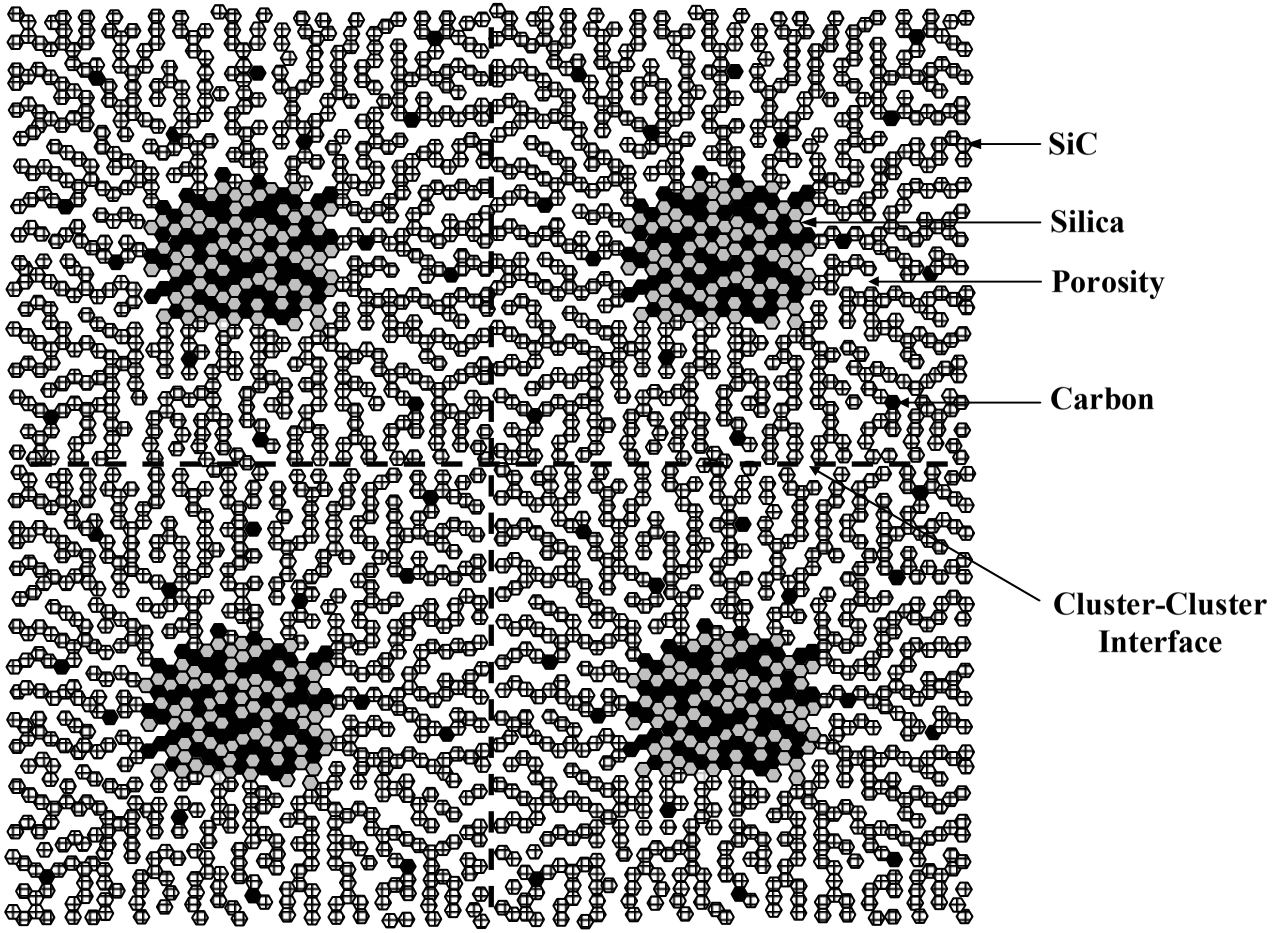

Figure 4-4-49 Illustration of the idealized structure of an SC35 particle after a high extent (~90%) of the CTR reaction. Most of the carbon and silica has been consumed and the large particle is composed mostly of a highly porous, interconnected SiC network.

have to develop and then grow. (This period is the transition depicted by the schematic illustrations in Figures 4-4-45 and 4-4-47.) After that period, the pore size should show relatively small change (i.e., as depicted in Figures 4-4-47 - 4-4-49). These trends in the evolution of the pore size as the reaction proceeds were confirmed by gas adsorption measurements, as discussed later in section 4.4.7.

The SiC crystallite size (Figure 4-4-2), specific surface area (Figure 4-4-32) and pore volume (Figure 4-4-22) measurements for the SC35 samples indicated that coarsening occurred during the very late stages of the CTR reaction (i.e., when the free carbon concentration became low). Figure 4-4-50 schematically illustrates the change in the structure.

The structural evolution for the SC8 samples should follow a similar path as in the SC35 samples. However, after the CTR reaction is completed, a fully-converted SC8 sample has approximately 45 vol% SiC and 55 vol% carbon. In contrast, a fully-converted SC35 sample has approximately 97 vol% SiC and only 3 vol% carbon. As will be discussed later in section 4.4.7.6, it is necessary to make some refinements to the structural model for the SC8 samples because of the much larger volume of free carbon.

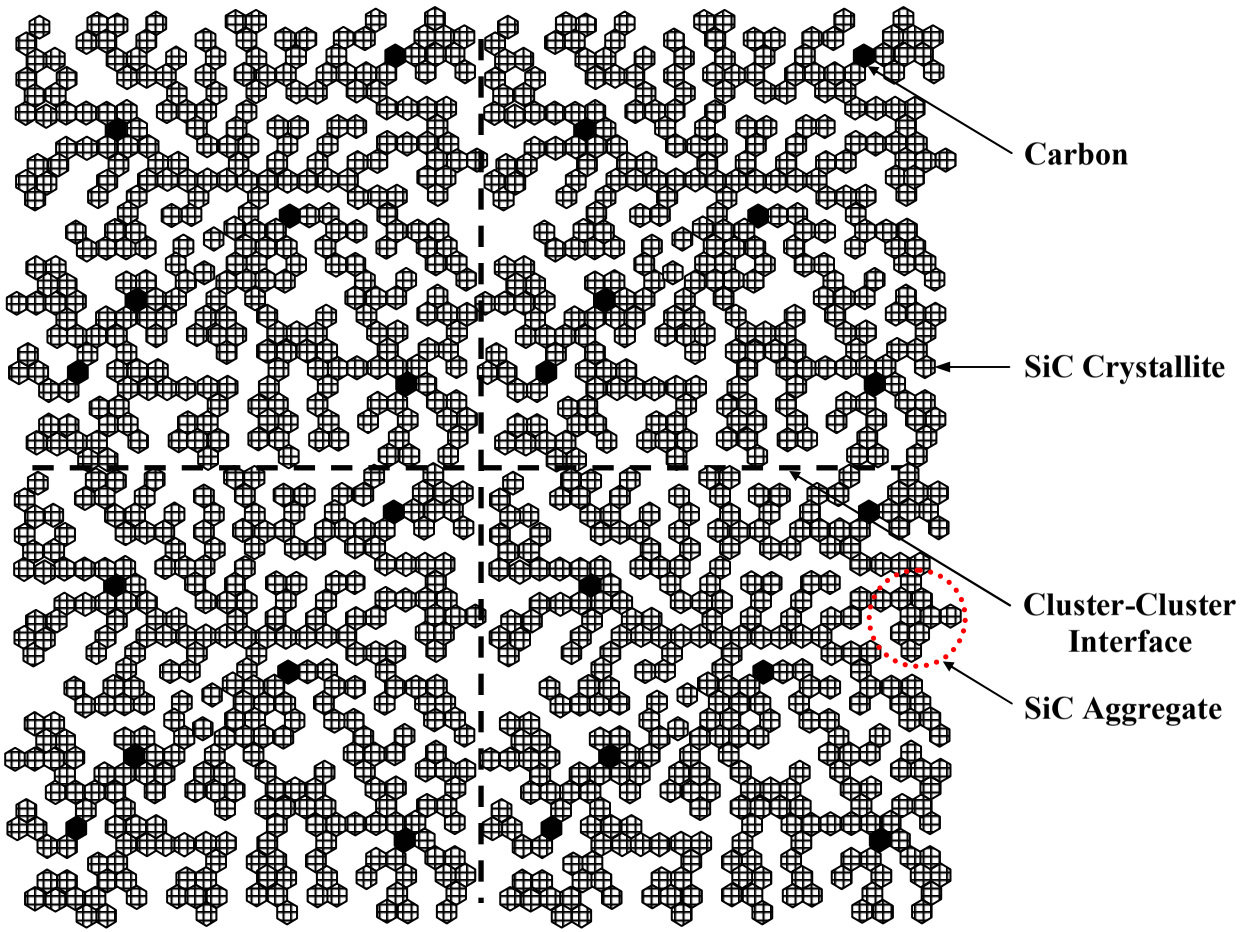

Figure 4-4-50 Illustration of the idealized structure of an SC35 particle after complete CTR reaction when coarsening becomes significant. Both the SiC crystallite size and the pore size become much larger.

4.4.6 Particle Size Distribution

The results of particle size distribution measurements for the SC8, SC35 and SC42 pyrolyzed materials were presented in section 4.1. In this section, the particle size distributions of the SC8, SC35 and SC42 CTR samples are presented. The data for the SC35-1300(16h) and SC42-1300(24h) Spex®-milled and unmilled samples were collected by the present author, while the data for rest of the samples discussed here were collected by Dr. Zhaohui Yang of Georgia Institute of Technology.

The Fraunhofer model was used to determine the particle size distributions for all of the unmilled SC42 and SC8 samples that were prepared by the tumbling method described in section 3.5.3. As shown in section 4.1.6 (Table 4-1-4), the Fraunhofer model is adequate when particles are relatively large. This point was confirmed again for the SC42-1300(8h) and SC42-1300(12) samples by using both the Fraunhofer model and the Mie model for the calculations. In the latter case, the optical property values for SiC (Alterolvitz et al. (1991) and Patrick and Choyke (1969)) were used because the CTR reaction was extensive in these samples. (The property values for SiC are shown in Table 3-5-3.) The fractional weight losses, X_{WL}, were ~0.95 and ~0.99, respectively, for the SC42-1300(8h) and SC42-1300(12) samples. Table 4-4-2 shows the d_{10}, d_{50}, and d_{90} diameters that were calculated for each condition. As expected, the differences in the calculated particle size values were small (especially for the d_{50} and d_{90} values) and the use of the Fraunhofer model was justified. (As observed previously in Table 4-1-4, the differences in particle size values for the two models became more significant as the particle size decreases.) The Fraunhofer model was also used to determine the particle size distribution for the unmilled SC42-

Table 4-4-2 Characteristic sizes of the particle size distributions for SC42-1300(8h) and SC42-1300(12h) samples.

Sample and preparation condition	Optical Model	d_{10} (μm)	d_{50} (μm)	d_{90} (μm)
SC42-1300(8h) tumbled	Fraunhofer	26 ± 1	71 ± 1	113 ± 2
	Mie (SiC optical properties)	28 ± 1	72 ± 1	114 ± 2
SC42-1300(12h) tumbled	Fraunhofer	23 ± 0	66 ± 1	108 ± 1
	Mie (SiC optical properties)	25 ± 0	67 ± 1	108 ± 1

1300(1h) sample that was prepared by sonication. This model was used because most of the particles were relatively large.

The particles sizes were considerably smaller for some of the SC35 and SC42 samples prepared by the sonication method (section 3.5.3). Therefore, it was necessary to apply the Mie model for determining the particle size distributions. For samples with high fractional weight losses, the Mie model was applied using SiC optical properties. This was the case for the following samples: unmilled SC35-1300(16h) with X_{WL} = 0.98, unmilled SC42-1300(24h) with X_{WL} = 0.99, and Spex®-milled SC42-1300(24h) with X_{WL} = 0.99.

There was not much difference in using the Fraunhofer model and the Mie model (with SiC optical property values) for the unmilled SC42-1300(8h) sample prepared by sonication (see Table 4-4-3 for the d_{10}, d_{50}, and d_{90} diameters). However, the Mie model was used in this case because some smaller particles (e.g., <3 μm) were present. Also, the fractional weight loss was relatively large (X_{WL} = 0.95), so it was reasonable to apply the Mie model with the SiC optical property values. The Mie model was more appropriate for the unmilled SC8-1250(16h) and unmilled SC42-1300(3h) samples prepared by the

Table 4-4-3 Characteristic sizes of the particle size distributions for SC42-1300(3h), SC42-1300(8h), and SC8-1250(16h) samples.

Sample and preparation condition	Optical Model	d_{10} (μm)	d_{50} (μm)	d_{90} (μm)
SC42-1300(3h) sonicated	Mie (Mixture optical properties)	1.61 ± 0.04	25 ± 2	70 ± 6
	Fraunhofer	0.75 ± 0.02	22 ± 2	69 ± 6
SC42-1300(8h) sonicated	Fraunhofer	7 ± 0	16 ± 0	28 ± 0
	Mie (SiC optical properties)	8 ± 0	16 ± 1	28 ± 0
SC8-1250(16h) sonicated	Mie (Mixture optical properties)	1.64 ± 0.04	43 ± 0	83 ± 0
	Fraunhofer	0.44 ± 0	38 ± 0	81 ± 0

sonication method because these samples contained a significant fraction of smaller particles (e.g., <3 μm). However, these samples contained significant amounts of two or more phases. The SC8-1250(16h) contained ~55 vol% carbon, ~6 vol% silica, and ~39 vol% SiC. The estimated composition for the SC42-1300(3h) sample was ~21 vol% carbon, ~37 vol% silica, and ~42 vol% SiC. (To obtain the volume percentages of carbon, silica, and SiC, the composition of the product in terms of weight was calculated first. Consider an example using SC42-1300(3h). The fractional weight loss $X_{WL} = 0.63$. Using Equations (4-4-15) and (4-4-16) (shown later in this section), the weight fractions of SC42 pyrolyzed and fully-converted materials in the sample were 0.47 and 0.53, respectively. The overall volumetric composition was then calculated using the volumetric compositions of the SC42 pyrolyzed and fully-converted materials; the pyrolyzed material contained 66 vol% silica and 34 vol% carbon and the fully-converted material contained 98 vol% SiC and 2 vol% carbon (see Table 4-1-9 and Table 4-3-2).) Due to the multiphase

composition of the samples, it is uncertain what optical property values should be used when applying the Mie model. In this case, the values used were obtained by applying the volumetric rule-of-mixtures with the individual property values (Tables 3-5-3 and 4-1-3) for silica, carbon, and silicon carbide. The property values calculated on this basis for the SC8-1250(16h) and SC42-1300(3h) sample are given in Table 4-4-4. Table 4-4-3 shows the calculated d_{10}, d_{50}, and d_{90} diameters using these property values. The corresponding diameters obtained using the Fraunhofer model are also shown for comparison.

Table 4-4-4 Refractive index (n) and extinction coefficient (k) values calculated for the SC8-1250(16h) and SC42-1300(3h) samples. The values were calculated from the individual optical property values for silica, carbon, and SiC by using a volumetric rule-of-mixtures model.

Wavelength (nm)	SC8-1250(16h)		SC42-1300(3h)	
	n	*k*	*n*	*k*
450	2.58	0.70	2.23	0.27
600	2.62	0.82	2.22	0.32
750	2.75	1.01	2.26	0.39
900	2.80	1.07	2.27	0.41

4.4.6.1 Evolution of the Particle Size Distribution during CTR

Figure 4-4-51 shows the cumulative particle size distributions for the SC42 1300^{o}C CTR samples with varying extent of reaction. These samples were prepared for the particle size analysis by using the tumbling method described in section 3.5.3.2. Figure 4-4-52 shows the same data re-plotted as frequency distributions. The distributions

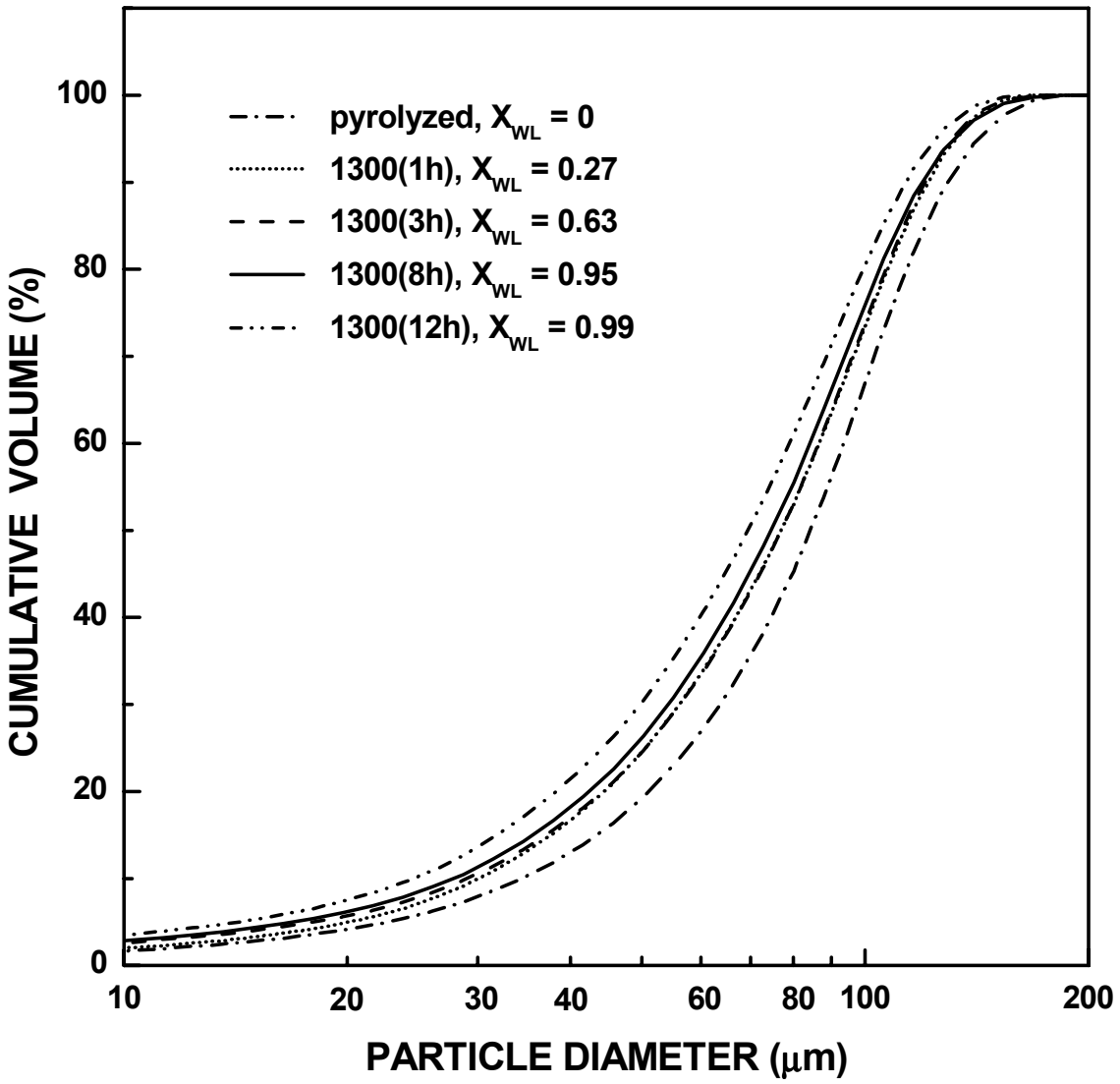

Figure 4-4-51 Cumulative particle size distribution plots for SC42-1300 CTR samples with varying extent of reaction. The samples for particle size measurement were prepared using the tumbling method.

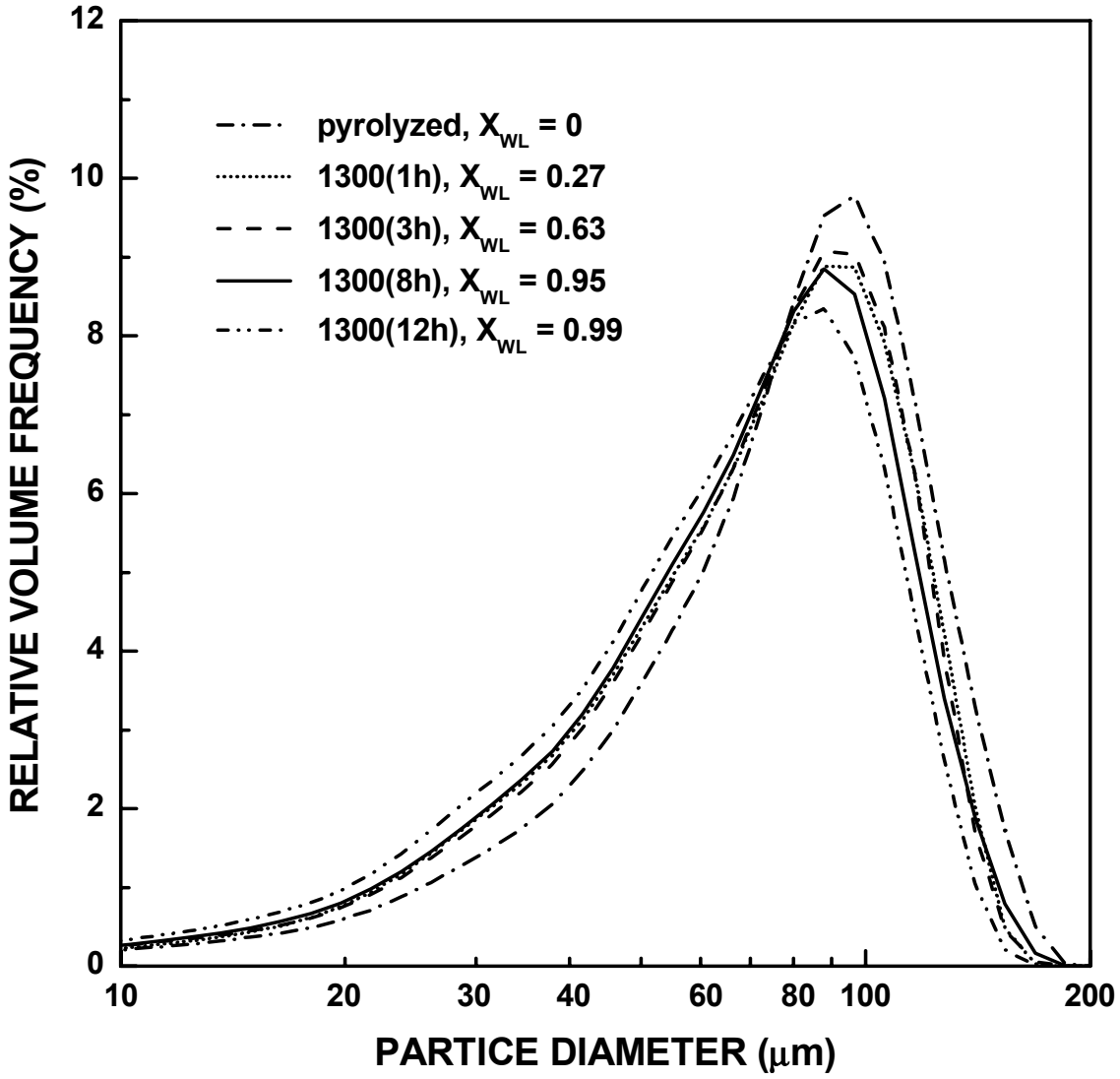

Figure 4-4-52 Relative frequency particle size distribution plots for SC42-1300 CTR samples with varying extent of reaction. The samples for particle size measurement were prepared using the tumbling method.

show a single mode centered in the range of ~88-96 μm. The data show that essentially the entire particle size distribution shifts to somewhat smaller sizes as the reaction proceeds. However, the shape of the distributions remains almost the same throughout the reaction. This indicates that the initial pyrolyzed particles have not broken into several or more fragments during the reaction. A closer look at those plots indicates that the entire distribution shifts to somewhat smaller sizes as fractional weight loss (X_{WL}) increased from 0 to 0.27. With continued reaction, there is almost no change in the particle size distribution as X_{WL} increased from 0.27 to 0.95. The distribution shifts slightly again to smaller sizes at the very late stage of the reaction, i.e., as X_{WL} increased from 0.95 to 0.99.

Figures 4-4-53 and 4-5-54 show the particle size distributions for SC42 1300^{o}C CTR samples with varying extents of reaction that were prepared using the sonication method described in section 3.5.3.2. The size distributions were very different from the samples prepared by the tumbling method. The size distributions shift to much smaller sizes as the reaction proceeds. In addition, as compared with the samples prepared by the tumbling method, there are significant amounts of particles with sizes smaller than 10 μm. The shift of the size distributions and the presence of much smaller particles are due to fracture of the original particles (after CTR) when the suspensions are prepared by sonication. The particles break to smaller sizes as the extent of reaction increases. This is attributed to the fact that the particles develop an increasing amount of porosity as the extent of reaction increases (e.g., see section 4.4.3.1). The increased porosity should result in weaker particles and, hence, increased susceptibility to fracture during sonication. The differences in the particle size distributions for the samples prepared by

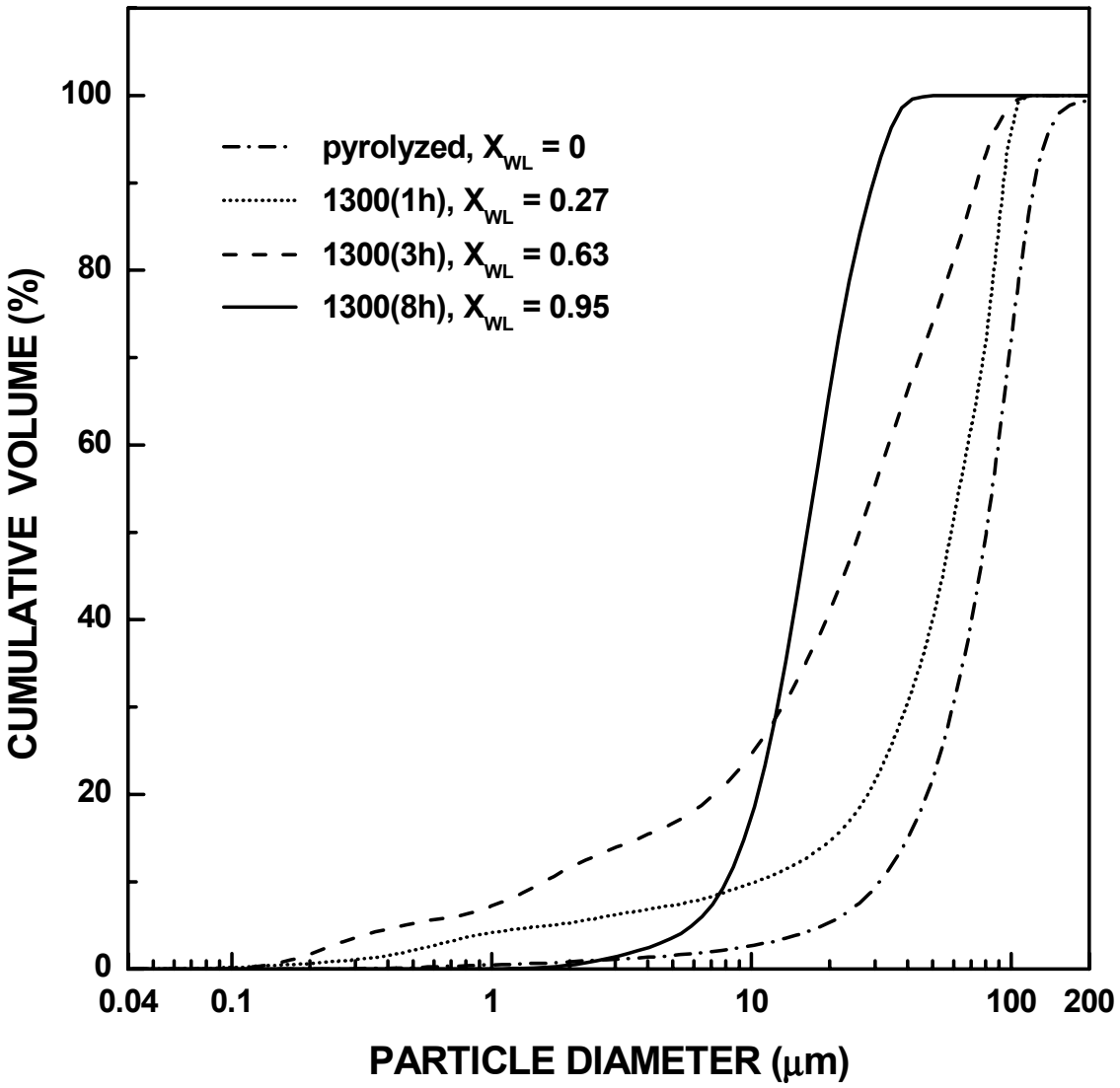

Figure 4-4-53 Cumulative particle size distribution plots for SC42-1300 CTR samples with varying extent of reaction. The samples for particle size measurement were prepared using the sonication method.

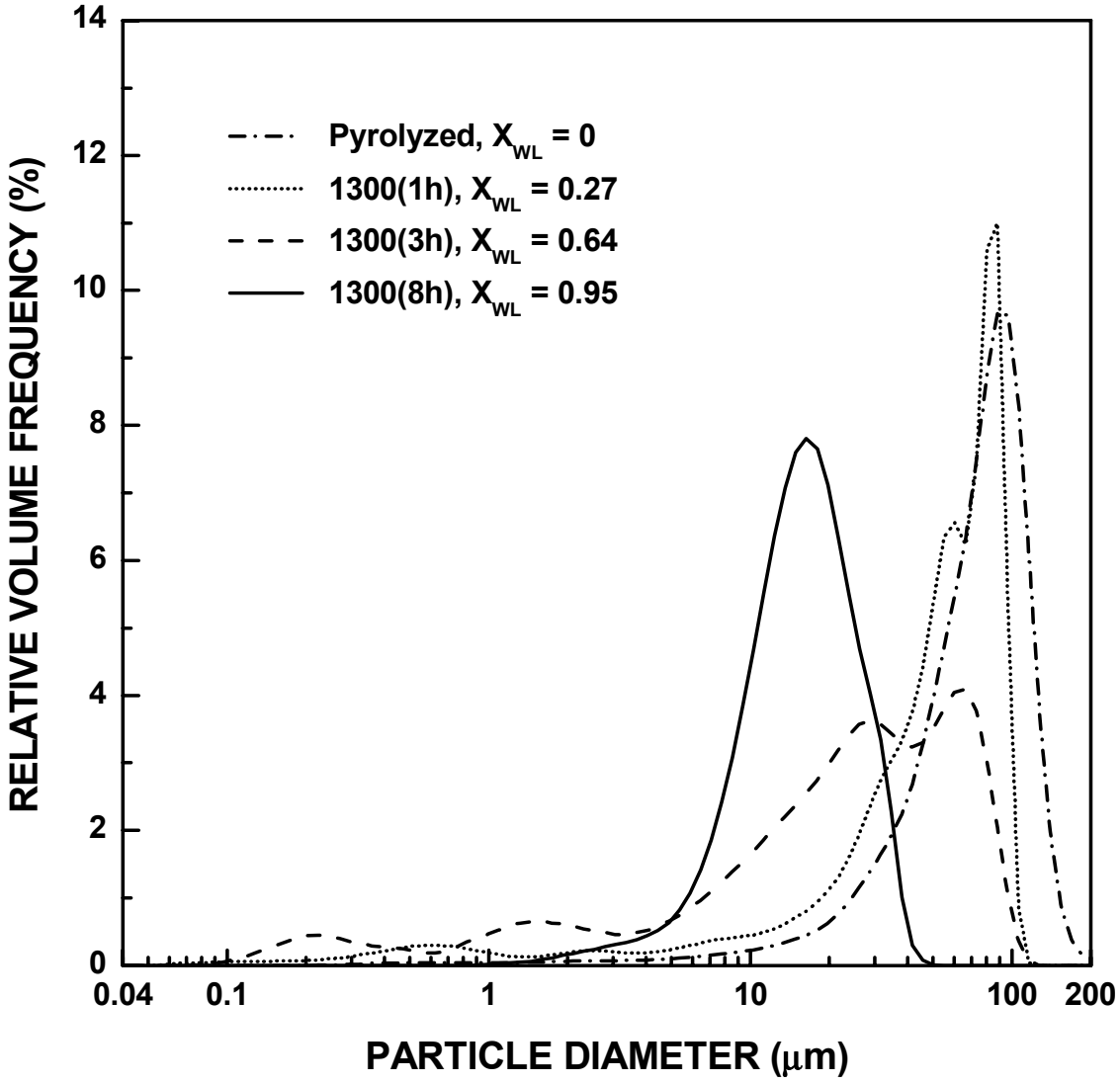

Figure 4-4-54 Relative frequency particle size distribution plots for SC42-1300 CTR samples with varying extent of reaction. The samples for particle size measurement were prepared using the sonication method.

tumbling and by sonication are illustrated directly in Figures 4-5-55 - 4-5-57 for the SC42-1300(1h) (X_{WL} = 0.27), SC42-1300(3h) (X_{WL} = 0.63), and SC42-1300(8h) (X_{WL} = 0.95) samples. The statistical data for the particle size distributions measured are listed in Table 4-4-5.

Figures 4-4-58 to 4-4-60 show the change of the d_{10}, d_{50} and d_{90} values of the particle size distributions as a function of fractional weight loss for the SC42 CTR samples heat treated at 1300°C for varying times from 0 - 24 h. (The samples were prepared for particle size analysis by the tumbling method.) Figure 4-4-61 shows all the d_{10}, d_{50} and d_{90} data on the plot. Observations made from these plots are discussed below.

1. The d_{10}, d_{50} and d_{90} values show an obvious decrease from the pyrolyzed material to the SC42-1300(1h) sample (fractional weight loss X_{WL} = 0.27). (This is expected from the previous discussion of Figures 4-4-51 and 4-4-52.) It is hypothesized that this decrease is due to sintering (densification) of the particles via the viscous flow of silica. This is suggested for the following reasons: (i) The pyrolyzed sample contains ~ 65 volume percent silica. It is well-known that silica powder compacts prepared with submicrometer particles can be sintered to nearly full density at temperatures in the range of ~1000-1100°C (using sintering times of hours to tens of hours) (Sacks and Tseng, 1984, Part II). In the present study, the silica regions ("particles") have much smaller size (i.e., roughly on the order of 10 nm) compared to the size of the particles that were used in the above referenced sintering study. This would tend to significantly reduce the temperature for densification. However, the SC35 pyrolyzed particles used in this study also have a significant volume fraction of carbon (~35 vol%). This would tend to significantly

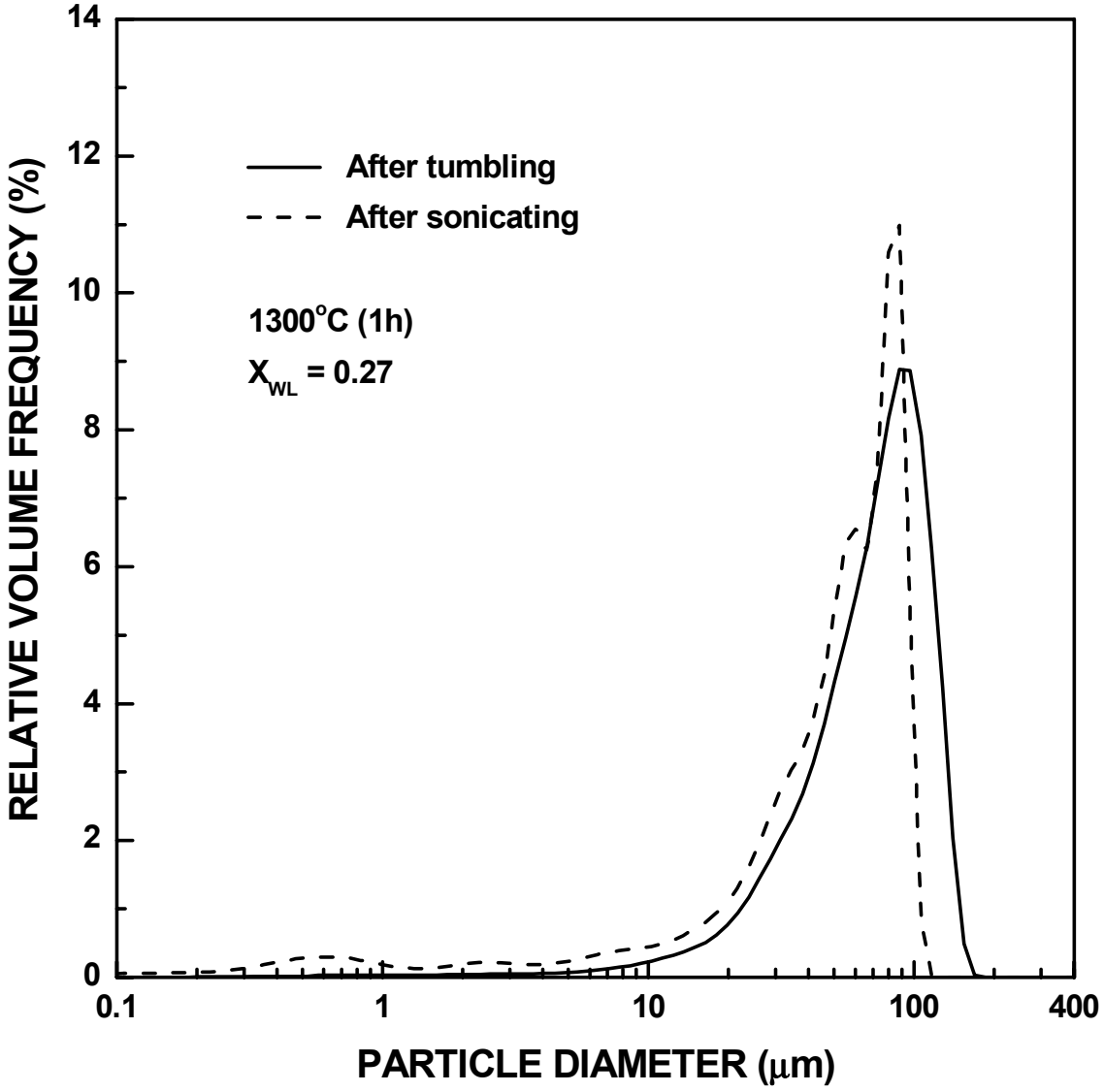

Figure 4-4-55 Comparison of relative frequency particle size distribution plots for SC42-1300(1h) samples (X_{WL} = 0.27) prepared by the tumbling method and the sonication method.

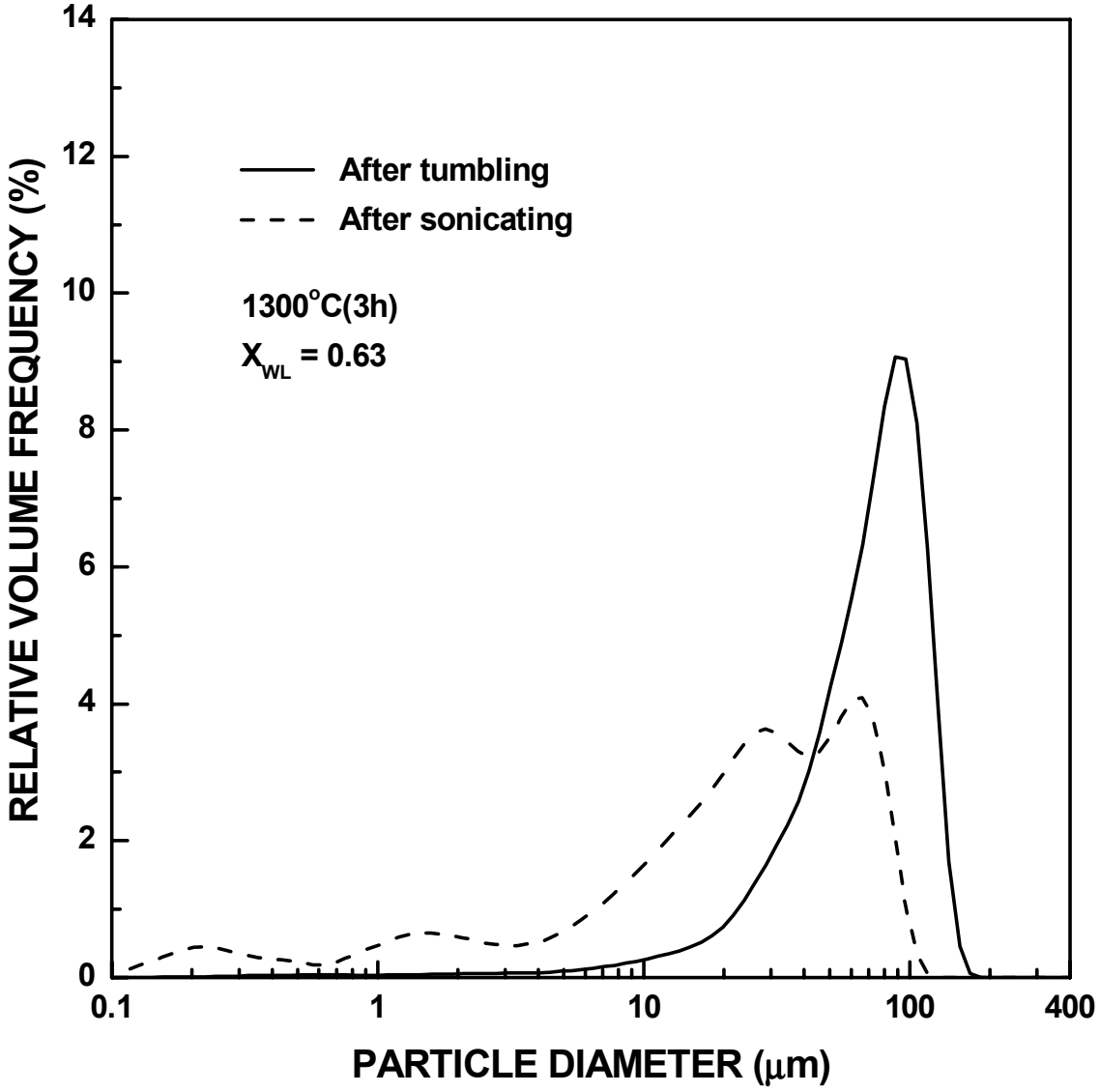

Figure 4-4-56 Comparison of relative frequency particle size distribution plots for SC42-1300(3h) samples (X_{WL} = 0.63) prepared by tumbling method and the sonication method.

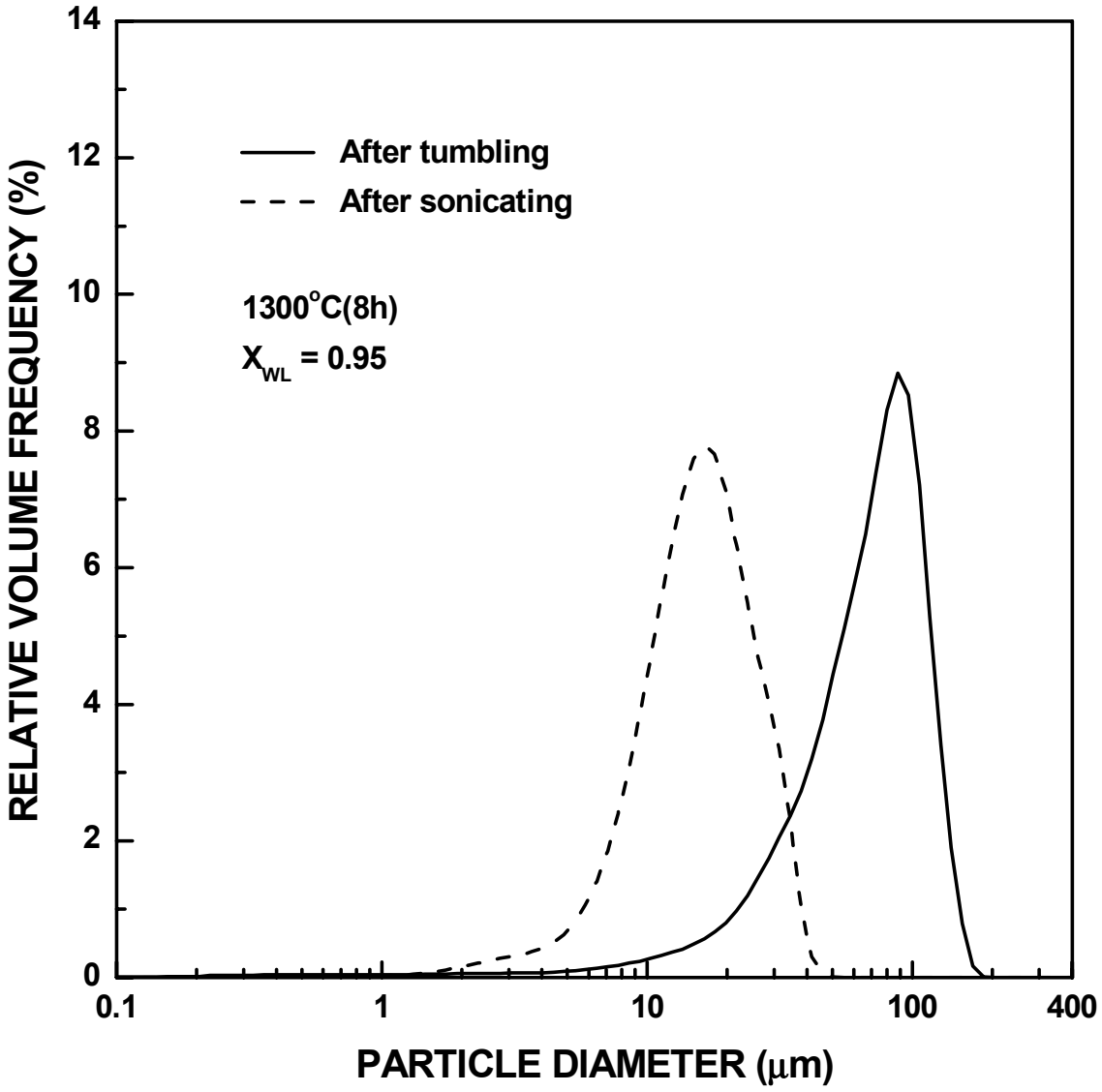

Figure 4-4-57 Comparison of relative frequency particle size distribution plots for SC42-1300(8h) samples (X_{WL} = 0.95) prepared by the tumbling method and the sonication method.

Table 4-4-5 Statistical data for particle size distributions of the SC42 pyrolyzed and 1300°C-CTR samples.

Time[1] (h)	X_{WL}	Processing[2]	# of Runs	d_{10} (μm)	d_{50} (μm)	d_{90} (μm)	Mode (μm)		Mean (μm)
							1	2	
0	0	T	7	33 ± 2	80 ± 1	123 ± 3	96 ± 0		79 ± 34
		S	2	33 ± 0	78 ± 1	117 ± 3	88 ± 0		76 ± 35
1	0.27	T	2	29 ± 0	73 ± 0	116 ± 0	88 ± 0		73 ± 33
		S	2	10 ± 0	56 ± 1	89 ± 2	84 ± 6	61 ± 0	54 ± 28
2	0.35	T	2	29 ± 0	73 ± 0	113 ± 1	96 ± 0		72 ± 31
		S	2	8 ± 1	58 ± 2	100 ± 1	84 ± 6	12 ± 2	56 ± 34
3	0.63	T	4	28 ± 1	74 ± 1	115 ± 3	90 ± 4		72 ± 33
		S	2	1.61 ± 0.04	25 ± 2	70 ± 6	63 ± 4	29 ± 0	31 ± 26
4	0.74	T	4	29 ± 1	73 ± 0	116 ± 0	88 ± 0		73 ± 33
6	0.88	T	4	28 ± 0	72 ± 0	115 ± 0	88 ± 0		72 ± 33
8	0.95	T	4	26 ± 1	71 ± 1	113 ± 2	88 ± 0		71 ± 33
		S	4	7 ± 0	16 ± 0	28 ± 0	17 ± 1		16 ± 8
12	0.99	T	4	23 ± 0	66 ± 1	108 ± 1	88 ± 0		66 ± 32
24	1.00	T	2	25 ± 0	68 ± 0	108 ± 1	88 ± 0		67 ± 31

Note:

1. Represents the time of heat treatment at 1300°C.
2. "T" indicates that the sample was prepared by the tumbling method. "S" indicates that the sample was prepared by the sonication method.

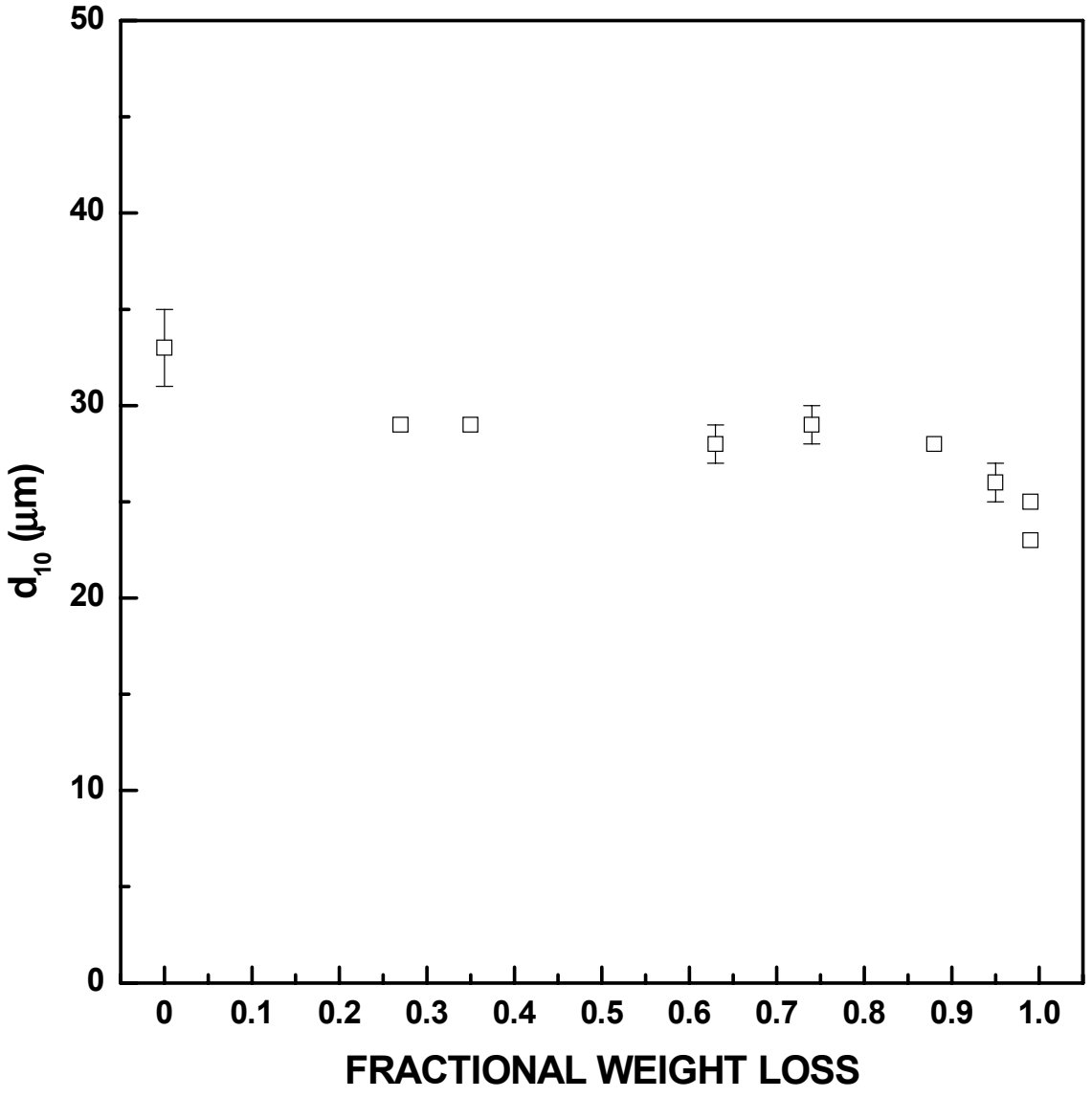

Figure 4-4-58 Plot of d_{10} of the particle size distribution vs. fractional weight loss (X_{WL}) for SC42-1300 CTR samples. The samples for particle size measurement were prepared using the tumbling method. The error bars on the data points are the standard deviation shown in Table 4-4-5.

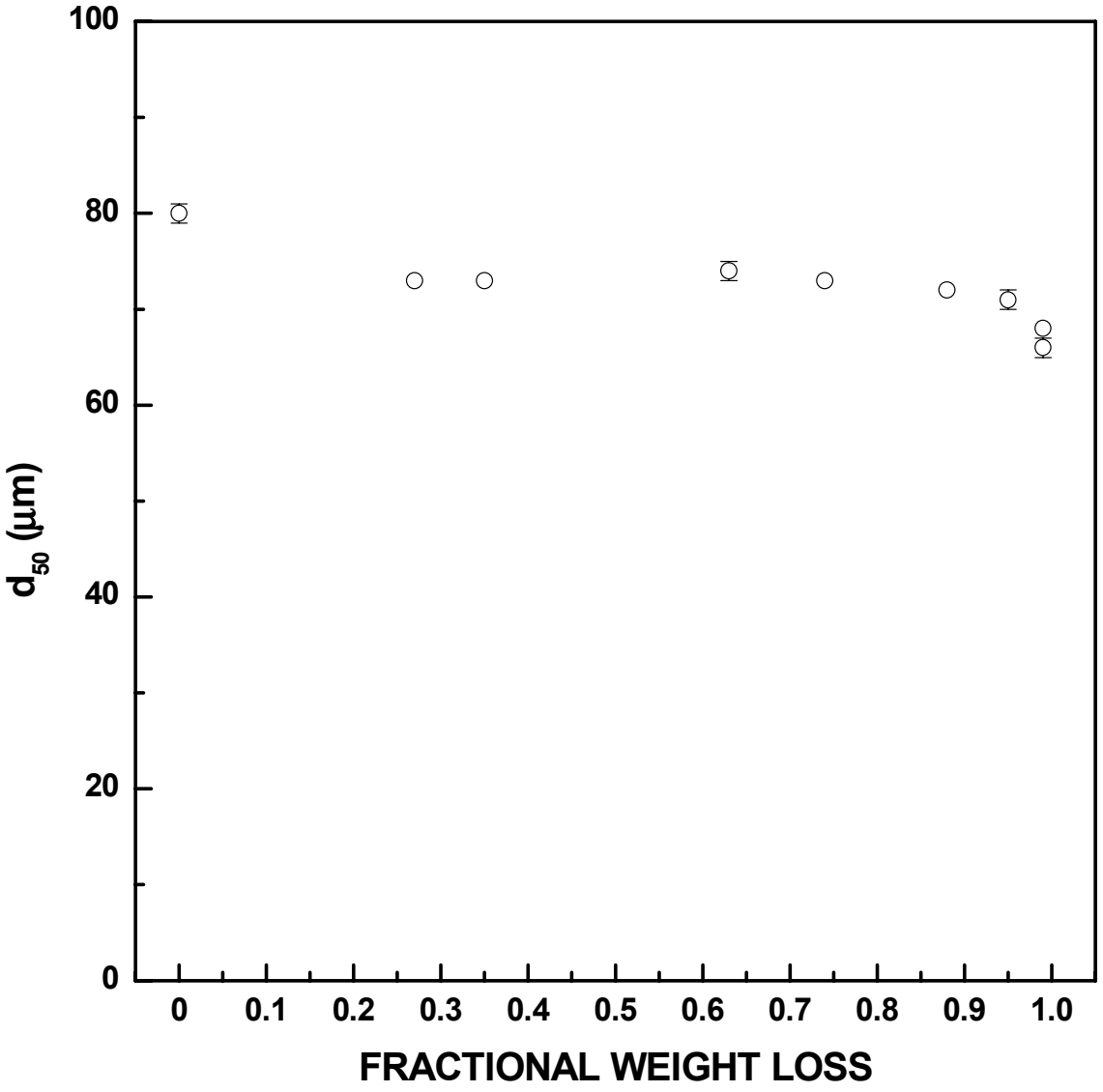

Figure 4-4-59 Plot of d_{50} of particle size distribution vs. fractional weight loss (X_{WL}) for SC42-1300 CTR samples. The samples for particle size measurement were prepared using the tumbling method. The error bars on the data points are the standard deviation shown in Table 4-4-5.

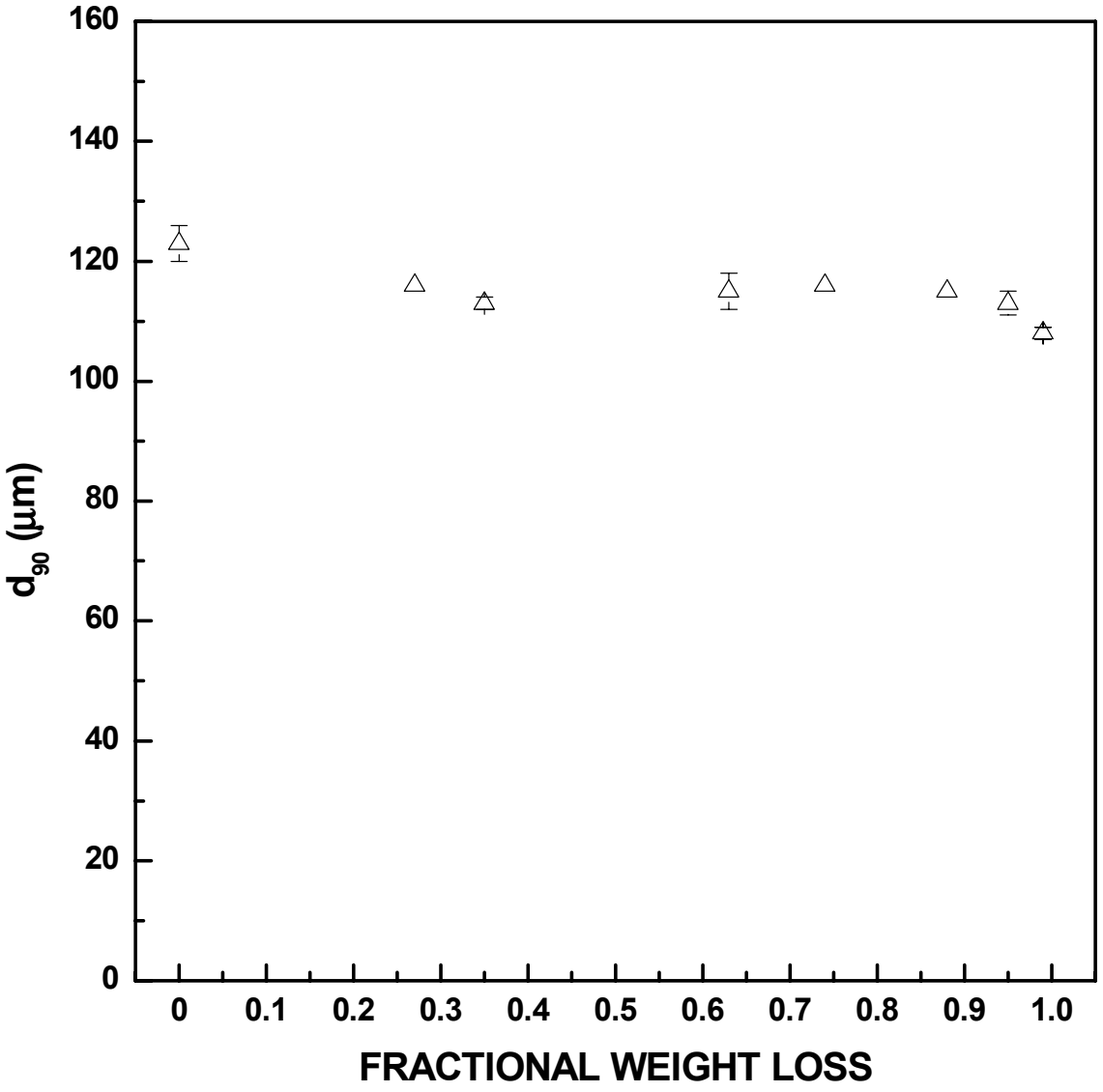

Figure 4-4-60 Plot of d_{90} of the particle size distribution vs. fractional weight loss (X_{WL}) for SC42-1300 CTR samples. The samples for particle size measurement were prepared using the tumbling method. The error bars on the data points are the standard deviation shown in Table 4-4-5.

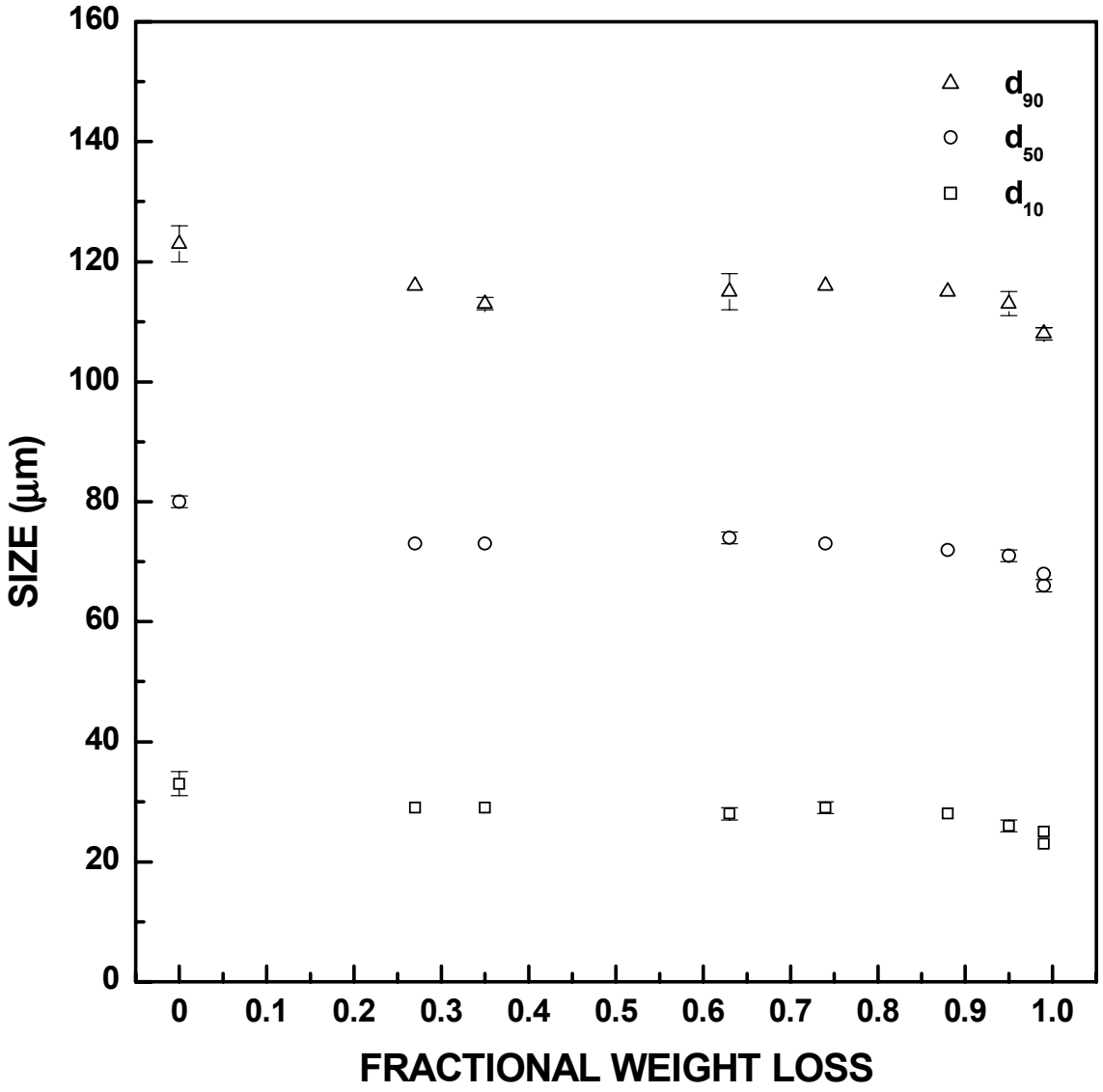

Figure 4-4-61 Plots of d_{10}, d_{50}, d_{90} of the particle size distribution vs. fractional weight loss (X_{WL}) for SC42-1300 CTR samples. The samples for particle size measurement were prepared using the tumbling method. The error bars on the data points are the standard deviation shown in Table 4-4-5.

inhibit densification. Nevertheless, the silica volume fraction is apparently high enough in the SC35 samples that some densification can occur. (ii) As discussed in section 4.1, the SC42-600(2h) sample had a specific surface area of 357 m^2/g, while the SC42-1100(2h) sample had a specific surface area of only 0.7 m^2/g. The decrease in specific surface area is attributed to closure of small pores as a result of viscous sintering. (iii) There is no evidence that viscous sintering occurs during CTR in the highly carbon-rich SC8 samples. Figures 4-4-62 and 4-4-63 show the particle size distributions for the pyrolyzed SC8-1100(4h) sample and the CTR SC8-1250(1h) sample, respectively. The latter sample had a fractional weight loss, X_{WL}, value of 0.16. The two samples were prepared for the particle size measurements using the tumbling method. Plots of both the cumulative and relative frequency distributions are shown in the figures. Statistical data for the two size distributions are shown in Table 4-4-6. Within experimental error, there are no differences in the size distributions for the two samples. This is because the sintering of silica is expected to be inhibited greatly by the large amount of carbon in the samples. As shown in Table 4-1-9, the pyrolyzed SC8 sample has ~51 vol% carbon. This high volume fraction of carbon will form a non-sinterable network in the case of the SC8 samples. Therefore, in contrast to the significant decrease in particle size observed for the SC42-1300(1h) sample (i.e., compared to the SC42 pyrolyzed sample), there is essentially no difference in the particle size distributions for the SC8 pyrolyzed and SC8-1250(1h) samples. (iv) The decrease in particle size is probably not due to an increase in the solid densities of the silica and carbon (that comprise the pyrolyzed particles) as the temperature is

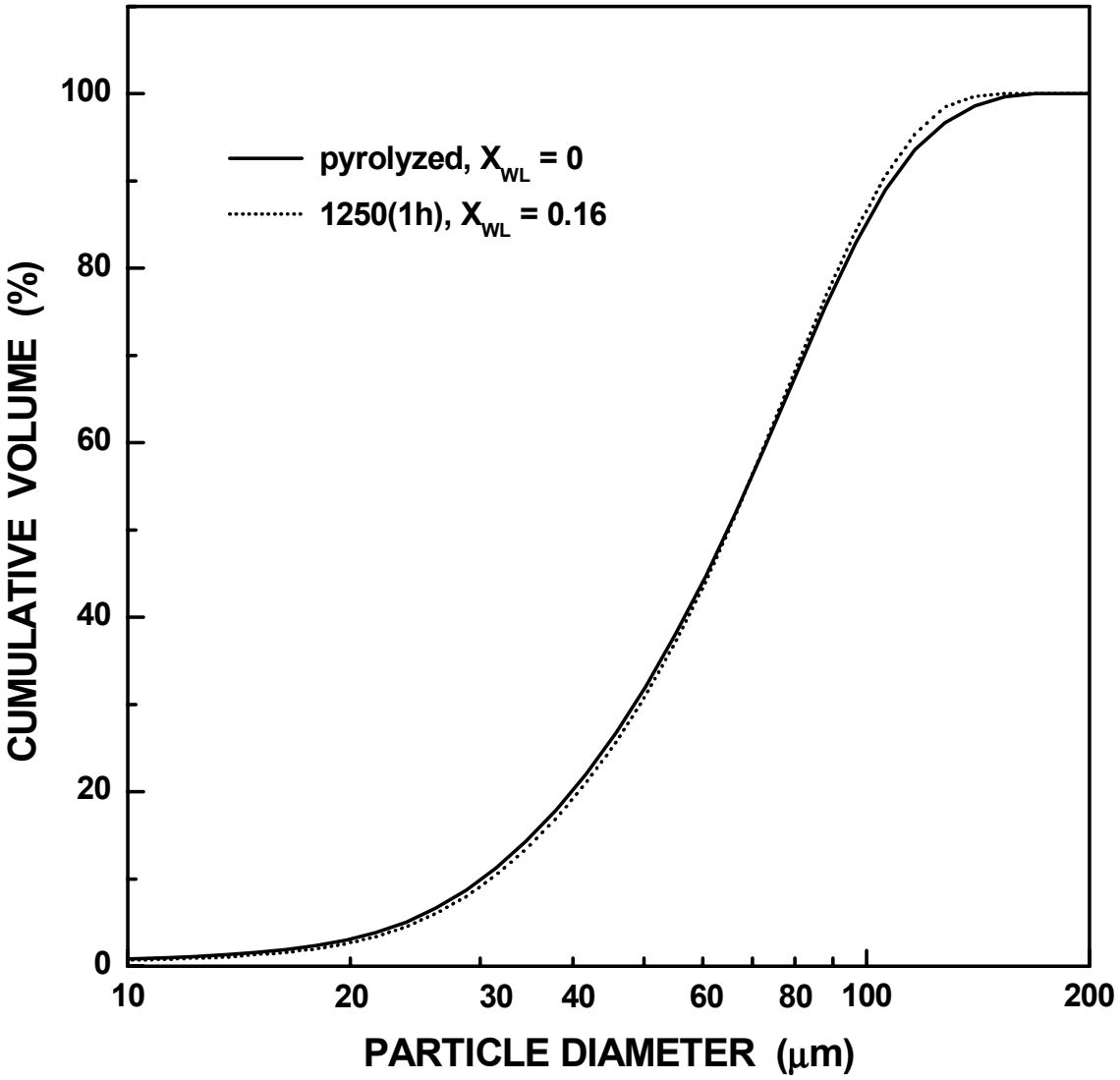

Figure 4-4-62 Comparison of cumulative particle size distribution plots for the SC8 pyrolyzed sample and SC8-1250(1h) sample (X_{WL} = 0.16). The samples for particle size measurement were prepared using the tumbling method.

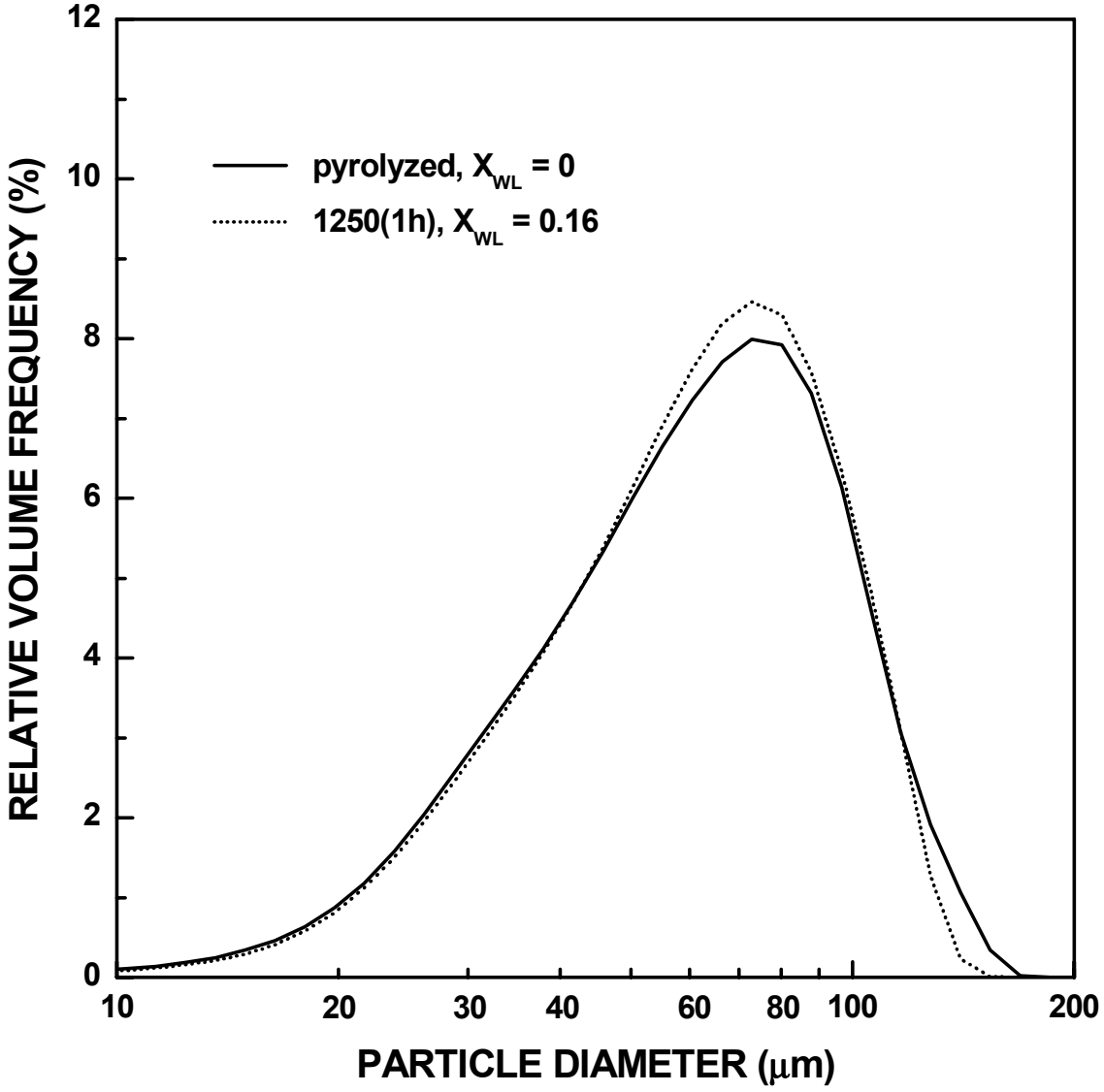

Figure 4-4-63 Comparison of relative frequency particle size distribution plots for the SC8 pyrolyzed sample and SC8-1250(1h) sample (X_{WL} = 0.16). The samples for particle size measurement were prepared using the tumbling method.

Table 4-4-6 Comparison of statistic data for particle size distributions between the SC8-1100(4h) pyrolyzed sample and the SC8-1250(1h) CTR sample (X_{WL} = 0.16). The samples were prepared with tumbling method.

Sample	d_{10} (μm)	d_{50} (μm)	d_{90} (μm)	Mode (μm)	Mean (μm)
SC8-1100(4h)	29 ± 1	62 ± 1	103 ± 2	73 ± 0	64 ± 29
SC8-1250(1h)	30 ± 0	62 ± 1	100 ± 2	73 ± 0	64 ± 27

increased from 1100°C to 1300°C. First, the silica density would not be expected to change significantly unless crystallization occurred. XRD results show that there is no detectable crystallization of silica at any stage during the CTR reaction. Second, there is no evidence that the carbon density changes significantly upon heat treatment from 1100C to 1300°C. As shown in Table 4-1-5, the apparent solid density for a carbon sample prepared by pyrolysis at 1100°C/2h was ~1.49 g/cm^3. The apparent density for a carbon sample prepared at 1300°C/2h had a slightly lower value of 1.43 g/cm^3. (This value was obtained by Dr. Zhaohui Yang of Georgia Institute of Technology.) Considering the experimental errors associated with the pycnometric measurement method, it can be concluded that there is no significant difference in the apparent solid densities for the 1100°C and 1300°C carbon samples. In addition, the study by Furuta et al. (1969) showed that the true densities of carbons derived from phenolic resins increased only slightly as the heat treatment temperature increased from 1100°C to 1300°C.

2. After the initial decrease in particle size, there was very little change with increasing extent of reaction from X_{WL} = 0.27 (SC42-1300(1h) sample) to X_{WL} = 0.95 (SC42-1300(8h) sample). This is attributed to an increasing constraint on

densification. As the reaction proceeds, there was less of the sinterable phase (silica) and more of the "non-sinterable" phase (SiC). (SiC is referred to as "non-sinterable" because it would have a much lower sintering rate, compared to silica, if samples had similar powder characteristics (e.g., particle size) and were sintered using same heat treatment conditions.)

3. The particle size decreased noticeably again in the late stages of the reaction, as discussed previously in regard to Figures 4-4-51 and 4-4-52. For example, the d_{50} particle size for the SC42-1300(8h) sample with $X_{WL} \approx 0.95$ was 71 μm, while the d_{50} particle size for a sample with $X_{WL} \approx 0.99$ (SC42-1300(12h)) was 66 μm. A similar result was obtained for the SC42-1300(24h) sample which had an X_{WL} value of ~1.0. For the latter sample, the d_{50} particle size was 68 μm. Therefore, the d_{50} particle size decreased ~7% as the extent of reaction increased from $X_{WL} \approx 0.95$ to $X_{WL} \approx 0.99$-1.00. This small decrease in particle size is attributed to a small amount of densification (i.e., shrinkage) via sintering of the porous, nanocrystalline SiC particles. It is well-known that a large amount of free carbon acts as a severe constraint upon densification and coarsening in porous SiC powder compacts (Mizrah et al. (1984) and Hojo (1991)). However, the densification and coarsening processes can proceed (to different extents) when the samples have only a limited amount of free carbon. In the present study, the sample with X_{WL} = ~0.95 had a free carbon content of ~8 vol%, while the sample with X_{WL} = ~0.99 had a free carbon content of only ~3 vol%.

The measured decrease in particle size during the late stage of the reaction for the SC42 samples can be used to provide some insight into the reason for the sharp decrease in

specific pore volume that was reported during the late stage of the reaction in the SC35 sample (e.g., see Figures 4-4-22 and 4-4-23b in section 4.4.3.1). First recall that two possible reasons were discussed in section 4.4.3.1 for the sharp decrease in specific pore volume between X_{WL} = ~0.95 and X_{WL} = ~0.98: (1) The porous SiC particles may undergo densification in which pores shrink in size and/or are eliminated completely. (2) The porous SiC particles undergo coarsening in which the pores and the SiC crystallites become larger in size. This would result in some pores becoming too large to be detected by the gas adsorption method. Since these pores had been previously detected by the method when they were smaller, a sample which underwent coarsening would have a measured pore volume that would be lower than the actual pore volume.

In section 4.4.3.1, it was concluded that the second reason was likely to be the more important reason for the sharp decrease in pore volume that was observed. This conclusion was previously based on two observations. First, measurements of the SiC crystallites showed that extensive growth began during the late stage of the reaction (i.e., precisely during the same stage when the pore volume decreased sharply). This observation is consistent with the occurrence of coarsening. Second, the SC35 samples did not have any "sintering aid," such as boron or aluminum. It is well-known (Prochazka (1975), Greskovich and Rosolowski (1976), Hojo (1991), Vaßen et al. (1996), and Clegg (2000)) that porous SiC compacts tend to undergo coarsening (in preference to densification) unless an appropriate sintering aid is present.

Using the particle size data reported in this section, a calculation is made which also supports the conclusion that the sharp decrease in specific pore volume during the late stage of the reaction is due mostly due to coarsening. Take the example of the SC42-1300(8h)

and SC42-1300(12h) samples. Assume that the partially-converted materials (SC42-1300(8h) and SC42-1300(12h)) were composed of the fully-converted material and pyrolyzed material. For the SC42-1300(8h) sample, the fractional weight loss was X_{WL} = 0.95; while for the SC42-1300(12h) sample, the fractional weight loss X_{WL} = 0.99. Suppose the initial weight of the sample was W_0, the weight of unreacted pyrolyzed material, W_{pyro}, is given by:

$$W_{pyro} = W_0(1 - X_{WL}) \tag{4-4-13}$$

The weight of fully-converted material is given by:

$$W_{CTR} = W_0 \cdot Y \cdot X_{WL} \tag{4-4-14}$$

where Y is the full conversion yield as explained in section 4.3.1 (Y = 0.33 for the SC42 series.) The weight fraction of unreacted pyrolyzed material in the product, w_{pyro}, would be

$$w_{pyro} = \frac{W_{pyro}}{W_{pyro} + W_{CTR}} = \frac{1 - X_{WL}}{(1 - X_{WL}) + (Y \cdot X_{WL})} \tag{4-4-15}$$

The weight fraction of the fully-converted material in the product, w_{CTR}, is given by:

$$w_{CTR} = 1 - w_{pyro} \tag{4-4-16}$$

Therefore, for the SC42-1300(8h) sample,

$$w_{pyro} = \frac{1 - X_{WL}}{1 - X_{WL} + Y \cdot X_{WL}} = \frac{1 - 0.95}{1 - 0.95 + 0.33 \times 0.95} = 0.1376$$

$$w_{CTR} = 1 - w_{pyro} = 1 - 0.1376 = 0.8624$$

for the SC42-1300(12h) sample,

$$w_{pyro} = \frac{1 - X_{WL}}{1 - X_{WL} + Y \cdot X_{WL}} = \frac{1 - 0.99}{1 - 0.99 + 0.33 \times 0.99} = 0.0297$$

$$w_{CTR} = 1 - w_{pyro} = 1 - 0.0297 = 0.9703$$

The bulk densities of the SC42-1300(8h) and SC42-1300(12h) samples can be obtained from the following equation:

$$\frac{1}{\rho_{prod}} = \frac{w_{pyro}}{\rho_{pyro}} + \frac{w_{CTR}}{\rho_{CTR}} \tag{4-4-17}$$

From section 4.3.1, the apparent solid density of SC42 fully-converted material, ρ_{CTR}, was estimated to be 3.17 g/cm^3. From section 4.1, the pycnometer measurement gave the apparent solid density of the pyrolyzed sample (ρ_{pyro}) as 2.16 g/cm^3. Therefore, ρ_{prod_1} = 3.0 g/cm^3 for the SC42-1300(8h) sample and ρ_{prod_2} = 3.1 g/cm^3 for the SC42-1300(12h) sample.

Now, assume that there was no breakage of the particles during the reaction and that each individual particle shrinks uniformly as the reaction time was increased from 8 h to 12 h at 1300^{o}C. (These two assumptions were supported by the observations that (i) the particle size distributions obtained by the tumbling method did not show any fine particles size fraction (Figures 4-4-51 and 4-4-52) and (ii) the shape of the size distribution did not change (Figures 4-4-51 and 4-4-52).) For simplicity, assume that the particles were spherical in shape. Suppose the weights of SC42-1300(8h) and SC42-1300(12h) particles are W_1 and W_2, respectively, and that the diameters are 71 μm and 66 μm, respectively. (The mean sizes of the distribution are used in each case.)

From Figure 4-4-23, the porosity (i.e., pore volume fraction) of the SC42-1300(8h), $V^R_{Pore\_1}$, was interpolated (based on X_{WL} = 0.95) to be 0.68. Suppose the

porosity of the SC42-1300(12h) is $V^R_{Pore\_2}$. Combining Equations (4-4-9) and (4-4-10), the average weight of the particles for the two samples is given by:

$$W_i = W_0 \cdot [1-(1-Y)\cdot X_{WL\_i}],\ i = 1, 2 \tag{4-4-18}$$

where W_1 is for the SC42-1300(8h) sample and W_2 is for the SC42-1300(12h) sample. Define V_1 as the average volume of SC42-1300(8h) particles and V_2 as the average volume of SC42-1300(12h) particles. The particle volume ratio of the SC42-1300(12h) to SC42-1300(8h) particle is given by:

$$\frac{V_2}{V_1} = \left(\frac{d_2}{d_1}\right)^3 = \left(\frac{66}{71}\right)^3 = 0.803 \tag{4-4-19}$$

The average solid volume of the particles, V_{S_i}, is given by:

$$V_{S\_i} = V_i \cdot (1-V^R_{Pore\_i}) = \frac{W_i}{\rho_{prod\_i}},\ i = 1, 2 \tag{4-4-20}$$

where V_{S_1} and V_{S_2} are for the SC42-1300(8h) and SC42-1300(12h) particles, respectively. Combining Equation (4-4-14), (4-4-15) and (4-4-16), the following relationship is obtained:

$$\frac{V_2}{V_1} = \frac{W_2 \cdot \rho_{\mathrm{Pr}od\_1} \cdot (1-V^R_{\mathrm{Pr}od\_1})}{W_1 \cdot \rho_{\mathrm{Pr}od\_2} \cdot (1-V^R_{\mathrm{Pr}od\_2})} = \frac{[1-(1-Y)\cdot X_{WL\_2})]}{[1-(1-Y)\cdot X_{WL\_1})]} \cdot \frac{\rho_{\mathrm{Pr}od\_1}}{\rho_{\mathrm{Pr}od\_2}} \cdot \frac{1-V^R_{\mathrm{Pr}od\_1}}{1-V^R_{\mathrm{Pr}od\_2}} = 0.803$$

or

$$\frac{V_2}{V_1} = \frac{1-(1-0.33)\times 0.99}{1-(1-0.33)\times 0.95} \times \frac{3.0}{3.1} \times \frac{1-0.68}{1-V^R_{Pore\_2}} = 0.803$$

Therefore, $V^R_{Pore\_2} = 0.65$.

The estimated pore volume fraction for the SC42-1300(12h) sample ($V^R_{Pore\_2}$ = 0.65) is relatively close to the value for the SC42-1300(8h) sample ($V^R_{Pore\_1}$= 0.68). This

result indicates that densification was very limited for the sample and that it removed only a small fraction of the pores. However, it should be noted that the porosity value (0.65) for the SC42-1300(12h) sample is much higher than the value extrapolated from the gas adsorption measurement results as shown in Figure 4-4-23. In that figure, the porosity had already dropped to ~0.5 at a fractional weight loss of ~0.98. This observation reinforces the previous conclusion that the decrease in pore volume observed in Figure 4-4-23 is only an apparent decrease in volume that occurs due to coarsening of the porous SiC product. As noted previously, the pores coarsened to sizes that could not be detected by the gas adsorption measurement method. Therefore, the measured porosity from gas adsorption is much less than the actual porosity for that sample.

4.4.6.2 Particle Size Distribution for Fully-Converted Samples

- As-heat treated (unmilled) samples

Figure 4-4-64 shows the particle size distribution for the SC35-1300(16h) sample with fractional weight loss X_{WL} = 0.98. Plots of both the cumulative size distribution and the frequency distribution are shown in the figure. Three modes are identified in the distribution. The first mode includes particles less than ~90 nm (~0.09 μm). (The lower limit of detection for the instrument is 0.04 μm, so some of the finest particles were apparently not detected.) This mode contained ~65 vol% of the particles. The peak value for this mode was ~53 nm (see Table 4-4-4). This size is larger than the SiC crystallite size determined by XRD line broadening (i.e., ~23 nm) which suggests that the particles in this mode consist of both individual crystallites ("primary particles") and aggregates consisting of a relatively small number of crystallites. The second mode includes particles from ~0.1-

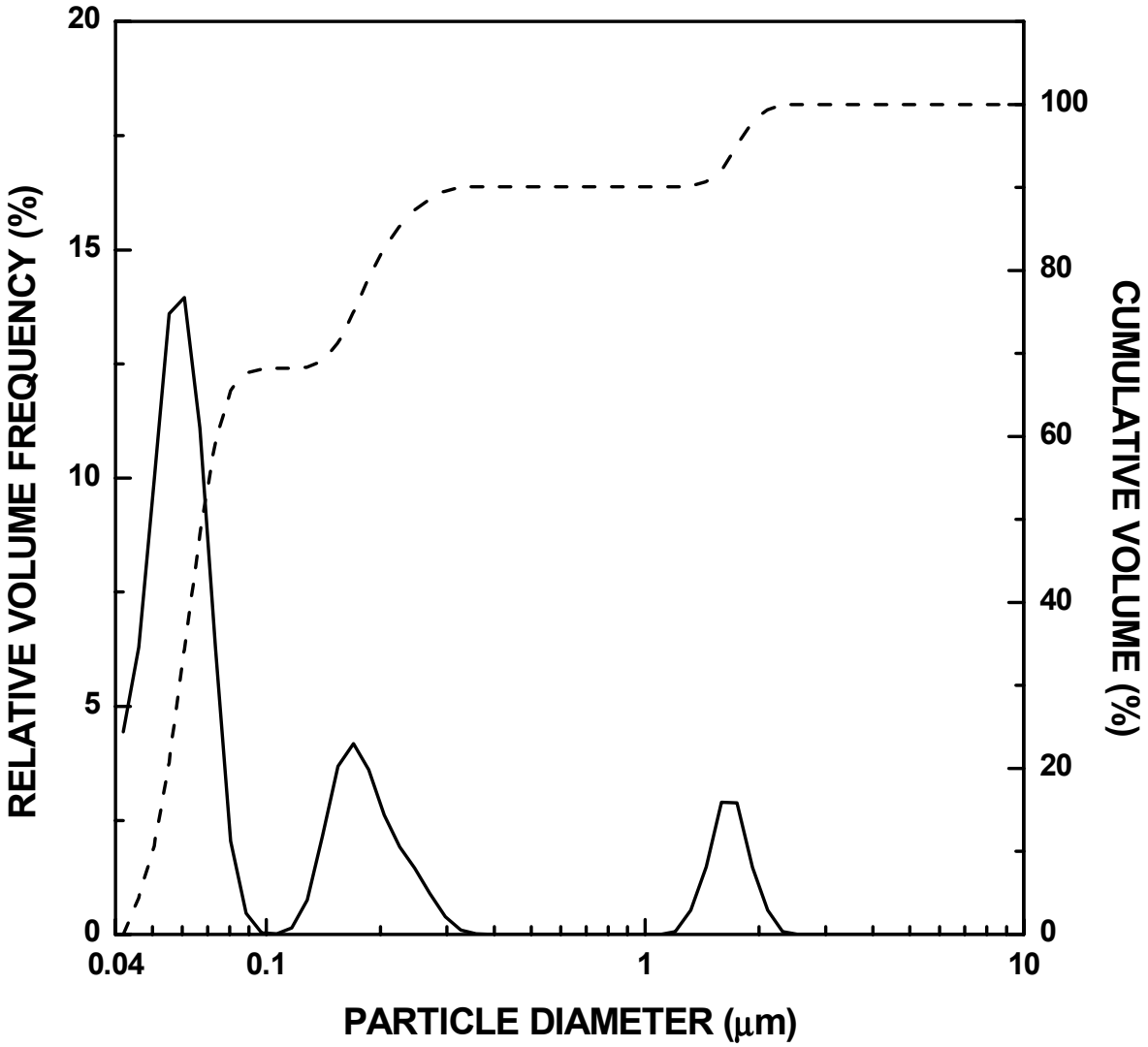

Figure 4-4-64 Relative frequency and cumulative particle size distribution plots for the SC35-1300(16h) sample (X_{WL} = 0.98). The sample for particle size measurement was prepared using the sonication method.

Table 4-4-7 Statistical data for particle size distributions of the SC8, SC35 and SC42 fully-converted materials heat treated at 1300°C.

Sample	X_{WL}	# of Runs	d_{10} (μm)	d_{50} (μm)	d_{90} (μm)	Mode (μm)			Mean (μm)
						1	2	3	
SC35-1300(16h)	0.98	4	0.048 ± 0	0.065 ± 0.001	0.80 ± 0.62	0.061 ± 0	0.170 ± 0	1.63 ± 0.08	0.25 ± 0.48
SC8-1250(16h)	0.94	2	1.64 ± 0.04	43 ± 0	83 ± 0	55 ± 0	0.910 ± 0		44 ± 29
SC42-1300(24h)	1.00	3	0.096 ± 0.001	0.31 ± 0.03	1.74 ± 0.05	1.13 ± 0.06	0.141 ± 0		0.75 ± 0.70
SC42-1300(24h) Spex®-milled	1.00	5	0.047 ± 0	0.064 ± 0.001	0.236 ± 0.008	0.055 ± 0	0.170 ± 0		0.11 ± 0.08

Note: Suspensions were prepared by the sonication method.

0.3 μm and this mode contained ~22 vol% of the particles in the distribution. This size range is representative of the cluster sizes that were illustrated in various SEM and TEM micrographs in sections 4.4.4 and 4.4.2. The third mode includes particles mostly in the size range of ~1.0-2.5 μm. This mode contained only ~10 vol% of the particles in the distribution.

It is interesting to compare the particle size distribution in Figure 4-4-64 to the size distribution for a different sample with similar fractional weight loss after CTR, i.e., SC42-1300(12h) with an X_{WL} value of ~0.99. For the latter sample, results were shown previously (Figures 4-4-51 and 4-4-52) for a case in which the tumbling method was used to prepare the sample for size analysis. Recall that there was negligible fracture of the particles when the tumbling method was used. This was indicated in Figure 4-4-51 by the observations that essentially all particles in the distribution were large and that there was uniform shift to slightly smaller sizes compared to the corresponding pyrolyzed powder sample. In contrast, the sonication method used to prepare the SC35-1300(16h) sample clearly resulted in very extensive fracture and breakdown of the original (i.e., unsonicated) large particles (Figure 4-4-64). The third mode in the distribution for this sample represents the largest fragments remaining from the original particles and these fragments are clearly much smaller than vast majority of the particles in the distribution shown in Figure 4-4-51.

It should be noted that particle breakdown during sonication of the SC35-1300(16h) sample was more extensive than observed in Figure 4-4-53 for an SC42-1300(8h) with an X_{WL} value of 0.95. This is presumably due to the fact that the SC35-1300(16) sample had a greater extent of conversion (X_{WL} = 0.98). The results in Figures 4-4-53 and 4-4-54

indicated that particles became weaker with increasing fractional weight loss during CTR. This was attributed to, at least in part, an increased amount of porosity in the sample. However, there is presumably only a small difference in total porosity for the SC42-1300(8h) and SC35-1300(16h) samples. Hence, there must be some other reason(s) for the large differences in particle breakdown behavior due to sonication. One possible reason is related to the observation that extensive coarsening of SiC crystallites and pores occurs in samples with fractional weight loss values >0.95. It is possible that the larger pores and crystallites could act as larger-scale defects that cause further weakening of the original (i.e., unsonicated) large particles. Another possible reason is that the removal of a small additional amount of free carbon from the sample results in significant weakening the original larger particles. There is no direct evidence to support the latter explanation; however, evidence is presented below which indicates that large amounts of free carbon substantially strengthen the original large particles.

Figure 4-4-65 shows the particle size distribution for the SC8-1250(16h) sample with fractional weight loss of 0.94. Plots of both the cumulative size distribution and the frequency distribution are shown. The sample used in the analysis was prepared by the sonication method. Despite the high fractional weight loss, sonication was ineffective in causing much breakdown of the particles. The size distribution shows essentially four modes (or three obvious modes plus one shoulder), but the mode with the largest particles comprises ~80 vol% of the distribution. These large particles are very similar in size to the particles for SC8 pyrolyzed and SC8-1250(1h) samples that were prepared by the tumbling method. It is not clear why the original large particles in the SC8-1250(16h) sample are so resistant to fracture during sonication. It is noted that SC8 samples have lower specific

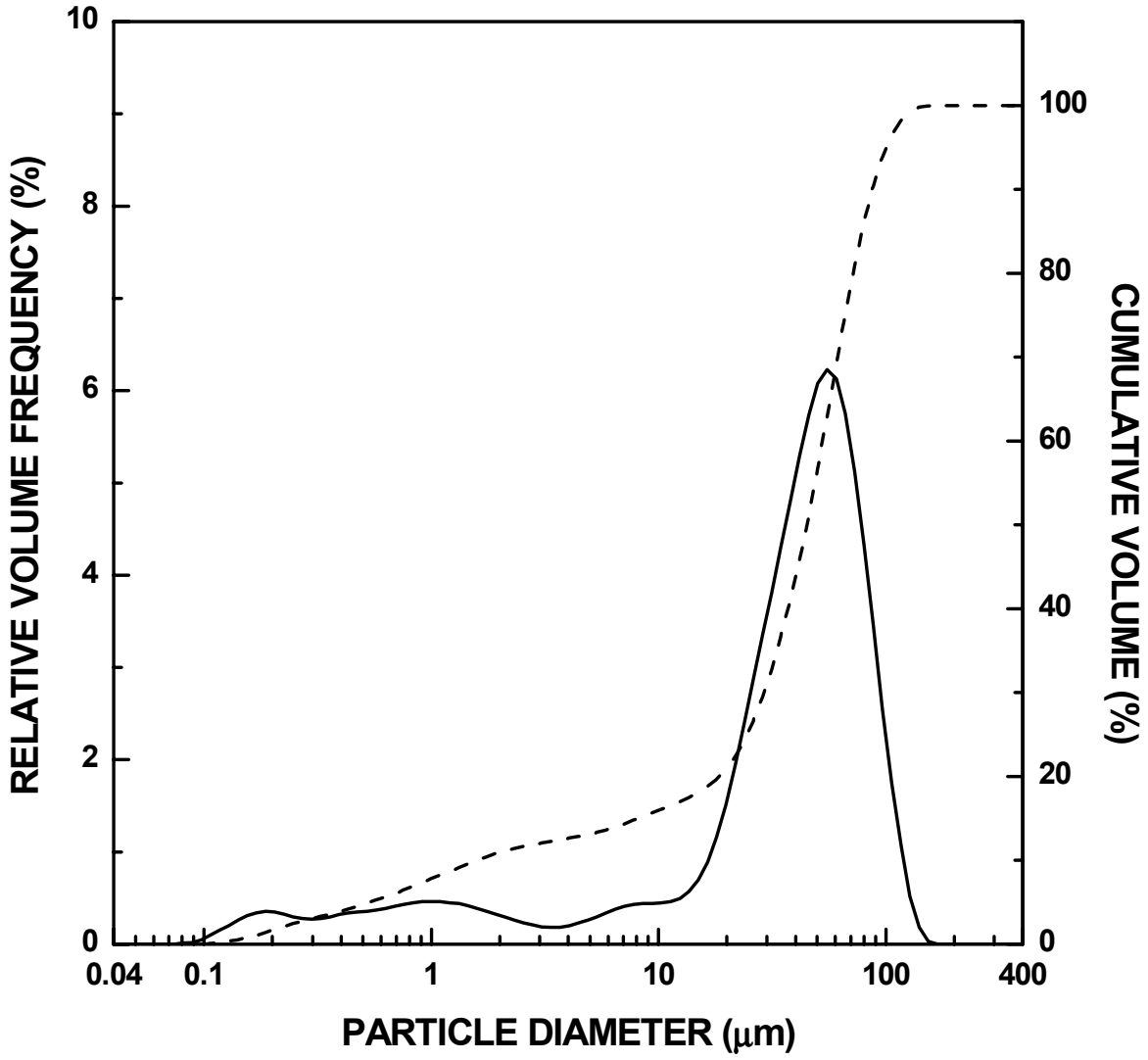

Figure 4-4-65 Relative frequency and cumulative particle size distribution plots for the SC8-1250(16h) sample (X_{WL} = 0.94). The sample for particle size measurement was prepared using the sonication method.

pore volume and lower relative porosity compared to SC35 samples for a given fractional weight loss value (see Figures 4-4-22, 4-4-23, 4-4-25, and 4-4-26). Nevertheless, the SC8-1250(16h) sample (with X_{WL} = 0.94) still has a large amount of porosity (i.e., ~0.66 cm^3/g and ~62%). One possible reason for the apparent higher strength of the SC8 particles is that a significant fraction of the pores in these particles are much finer than in the SC35 samples. (The differences in the pore size distributions for the SC8 and SC35 samples are discussed in detail in section 4.4.7.) Hence, the average defect size might be smaller in the SC8 samples. Another reason might be that the presence of a much higher volume fraction of free carbon significantly strengthens the original large particles. Even after complete CTR, an SC8 sample still would have ~55 vol% free carbon and ~45 vol% SiC. Therefore, it is evident that the glassy carbon phase in the SC8-1250(16h) sample would be in the form of a continuous network. Despite the high volume fraction of fine pores, a continuous glassy carbon network might have considerable strength.

Figure 4-4-66 shows the particle size distribution for the SC42-1300(24h) sample with fractional weight loss of 1.0. Plots of both the cumulative size distribution and the frequency distribution are shown. The sample used in the analysis was prepared by the sonication method. Based on the previous discussion in this section, the results for this sample seem somewhat surprising when compared to the particle size distribution in Figure 4-4-67 for the SC35-1300(16h) sample with X_{WL} = 0.98. This is because the SC42-1300(24h) sample has slightly higher fractional weight loss, yet the size distribution shows larger particles. For example, the mode with larger particles (~0.5-3.5 μm) comprises ~48 vol% of the distribution for the latter sample, while the mode with larger particles (~1.0-2.5 μm) for the SC35-1300(16h) sample contains only ~10 vol% of the particles. In

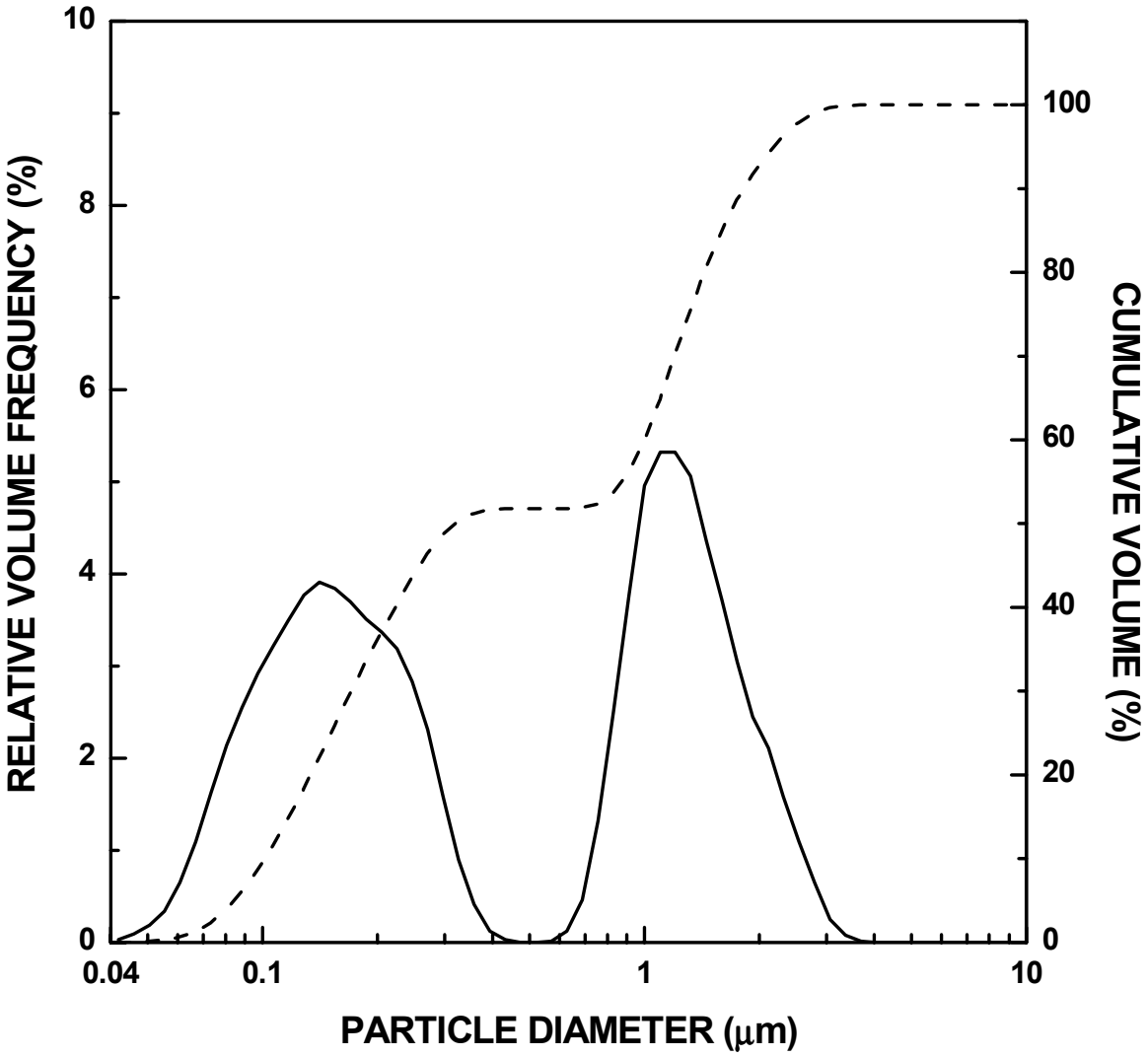

Figure 4-4-66 Relative frequency and cumulative particle size distribution plots for the SC42-1300(24h) sample (X_{WL} = 0.99). The sample for particle size measurement was prepared using the sonication method.

addition, the SC42-1300(24) sample shows only a single mode in the size range of ~0.04-0.4 μm and only ~10 vol% of the particles are < 0.1 μm. In contrast, the SC35-1300(16h) sample has two modes in this same size range and ~68 vol% of the particles are < 0.1 μm. A hypothesis to account for these differences is that more extensive sintering processes have occurred in the SC42-1300(24h) sample. Evidence has already been presented (see sections 4.4.1 and 4.4.3) that samples with very high fractional weight losses (i.e., $X_{WL} \approx$ 0.98-0.99) undergo (i) a significant amount of coarsening of grains and pores and (ii) a small amount of densification. These processes require extensive diffusion (volume, grain boundary, and/or surface) in the SiC crystallites. It is surmised that the considerably longer heat treatment time in the SC42-1300(24h) sample resulted in more extensive neck growth between crystallites. This would result in bonding between the crystallites (and between clusters of crystallites) that would be too strong to be disrupted by sonication.

- Milled Sample

Figure 4-4-67 shows the particle size distribution for an SC42-1300(24h) sample which was Spex®-milled after the CTR heat treatment. The sample used in the analysis was prepared by the sonication method. Plots of both the cumulative size distribution and the frequency distribution are shown in Figure 4-4-67. The statistical data for the particle size distribution are listed in Table 4-4-7. By comparison with Figure 4-4-66, it is clear that milling was effective in breaking down the larger fragments from the original particles. The peak mode sizes are 53 nm and 160 nm, respectively, and volume percentages associated with the modes are 67 vol% and 33 vol%, respectively. The second mode in the distribution for the milled sample is comprised of particles with sizes in the range of ~0.1-0.45 μm. This mode shows a shoulder at the larger particle sizes in the range. This

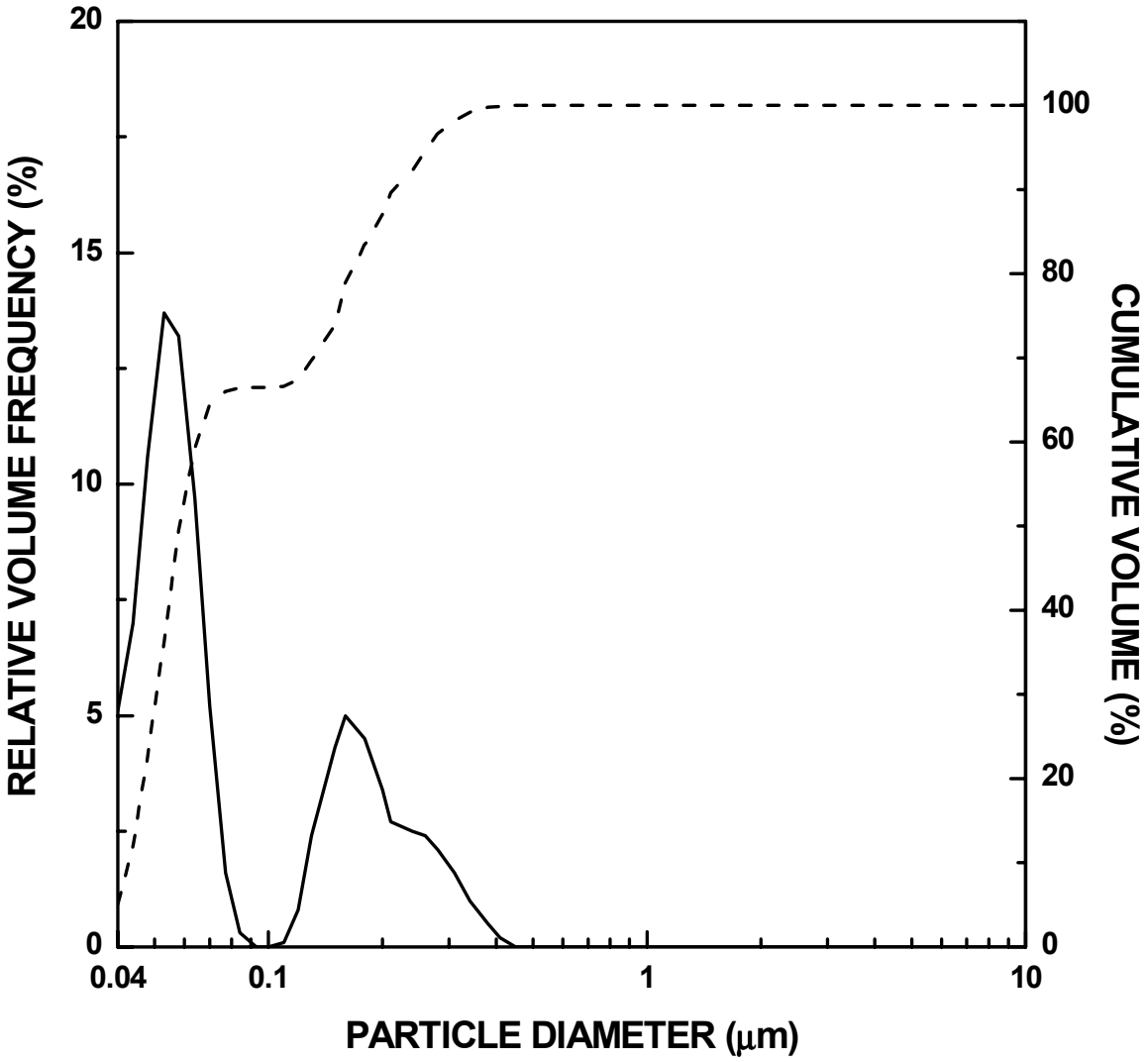

Figure 4-4-67 Relative frequency and cumulative particle size distribution plots for the SC42-1300(24h) sample (X_{WL} = 0.99). The sample was Spex®-milled and prepared using the sonication method.

observation indicates that the milling process was not completely effective in breaking down the larger fragments.

Milling was clearly not effective in breaking down the two types of smaller-sized SiC aggregates (<90 nm and ~100-300 nm). This indicates that there are strong bonds between individual SiC crystallites and it provides support for the argument that some neck growth had occurred during the late stages of the CTR reaction.

4.4.7 Adsorption Isotherm and Pore Size Distribution

In this section, the evolution of the gas adsorption isotherm data and pore size distribution data at different stages in the CTR process is described. The procedure for extracting pore size distributions from the gas adsorption/desorption isotherms was described in detail in Chapter III (section 3.4.2). The pore size distributions were obtained by applying the Kelvin equation and by using the method of Harkins - Jura to obtain the absorbed film thickness, r_T.

Before presenting the pore size distribution data, it is informative to first describe the changes that occur in the raw data (i.e., the gas adsorption/desorption isotherms) as the extent of conversion during the CTR reaction increases.

4.4.7.1 Gas adsorption/desorption Isotherms for SC35 CTR Samples

The gas adsorption/desorption isotherms for all the SC35 samples were best characterized as being either Type II or Type IV (Singh, 1989). In general, these isotherms indicate that there is a relatively strong affinity of the adsorbate (nitrogen) for the surface at the adsorption temperature. However, as noted in section 4.4.3.2, the pyrolyzed sample (SC35-1100(2h)) and samples in the very earliest stages of the reaction (e.g., SC35-1160(0.5h) with X_{WL} = 0.01 and SC35-1160(1h) with X_{WL} = 0.02) showed considerably lower "C" values (when the BET equation was applied) and higher "b" values (when the Langmuir equation was applied) compared to samples which had undergone more extensive reaction (see Appendix F). This indicates that these samples had a lower affinity of the adsorbate for the surface.

As described in section 4.1.5, the SC35 pyrolyzed material showed a Type II isotherm (Figure 4-1-10). Type II isotherms are often associated with nonporous or

macroporous materials (Sing, 1989). As in section 4.1.9, the available evidence indicates that the SC35 pyrolyzed sample is essentially dense (pore-free). However, this does not rule out the presence of macropores which are too large to be detected by the gas adsorption/capillary condensation method (Gregg and Sing, 1982, p.25 and p.164). In fact, SEM micrographs in section 4.1 showed that some large defects (e.g., cracks) were present in the large pyrolyzed particles.

The inflection point, or "knee", of the isotherm (Figure 4-1-10) was associated with reaching approximately monolayer coverage of the surface with adsorbed gas. (In this case, the monolayer capacity, V_m = 0.14947 cm^3/g, is reached at P/P_0 = 0.183) The sharp increase in the volume absorbed at high relative pressures reflects multilayer adsorption of nitrogen. The number of absorbed layer becomes "infinite" as P/P_0 approaches 1, i.e., nitrogen condenses on a flat, "bulk" surface as a liquid when P/P_0=1. The observation that the isotherm asymptotically approaches the vertical line (parallel to the y-axis) at the saturated pressure (i.e., P/P_0 = 1) apparently reflects complete wetting of the surface by the condensed liquid. The magnitude of the adsorbed volume shown in this isotherm is relatively low. This is expected, of course, because it was previously reported in section 4.1.5 that the pyrolyzed sample had a low specific surface area and a negligible amount of porosity (e.g., see Table 4-1-2).

The desorption branch of the isotherm for the pyrolyzed sample (Figure 4-1-10) does not retrace the adsorption isotherm at low relative pressures. This observation was made only for samples with low "C" values (as compared with 100) from the BET equation (or high "b" values from the Langmuir equation as compared with 0.02). This suggests that one possible reason for the effect was a relatively low affinity of the nitrogen adsorbate for

the sample surface at low nitrogen gas pressures. In other words, the behavior is somewhat characteristic of a Type III isotherm (Gregg and Sing, 1982, p. 248).

Samples which were heat treated only to the early stage of the carbothermal reduction reaction (i.e., very low fractional weight loss (X_{WL})) had gas adsorption/ desorption isotherms similar to the one shown for the pyrolyzed sample. For example, Figure 4-4-68 shows the isotherm was almost identical for sample SC35-1160(1h) (X_{WL} = 0.02). Figure 4-4-69 shows that the isotherm was also similar for sample SC35-1200(1h) (X_{WL} = 0.03). However, the isotherm for the latter sample showed a stronger affinity of the adsorbate for the surface. This was indicated by the lower values of the "*b*" constant in the Langmuir equation (Appendix F). This was also suggested by the observation that the desorption curve continued to retrace the adsorption curve to low pressures. Figures 4-4-68 and 4-4-69 also show that there are small increases in the volume of gas adsorbed with increasing fractional weight loss. This is reflected in the small increases in specific pore volumes and specific surface areas, previously shown in Figures 4-4-22 and 4-4-32, respectively. The only way to account for the small increase in the amount of gas adsorbed in these samples is through the development of a small volume fraction of pores.

The shape of the gas adsorption/desorption isotherms starts to shift as the samples are heated under conditions that gave a higher fractional weight loss. Figures 4-4-70 and 4-4-71 show the isotherms for samples SC35-1200(2h) and SC35-1250(30min), respectively. The fractional weight loss X_{WL} values for these samples are very similar (i.e., 0.0538 and 0.0516, respectively) and, therefore, the isotherms are also very similar. With greater fractional weight loss, there is, of course, an increase in the volume of gas absorbed. Again, this is why small increases in specific pore volumes and specific surface area were

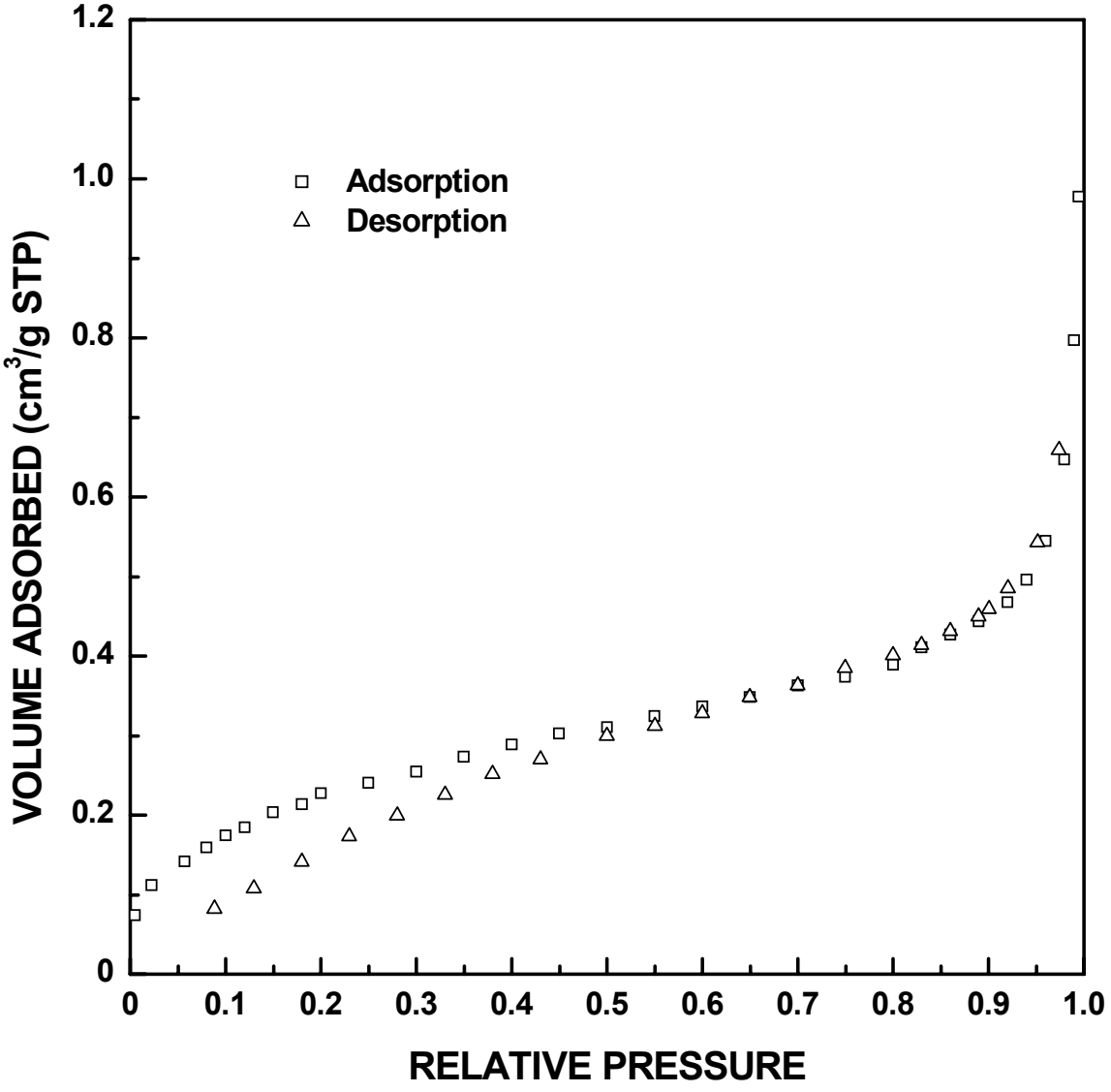

Figure 4-4-68 Adsorption/desorption isotherm plots for SC35-1160(1h) sample (X_{WL} = 0.02).

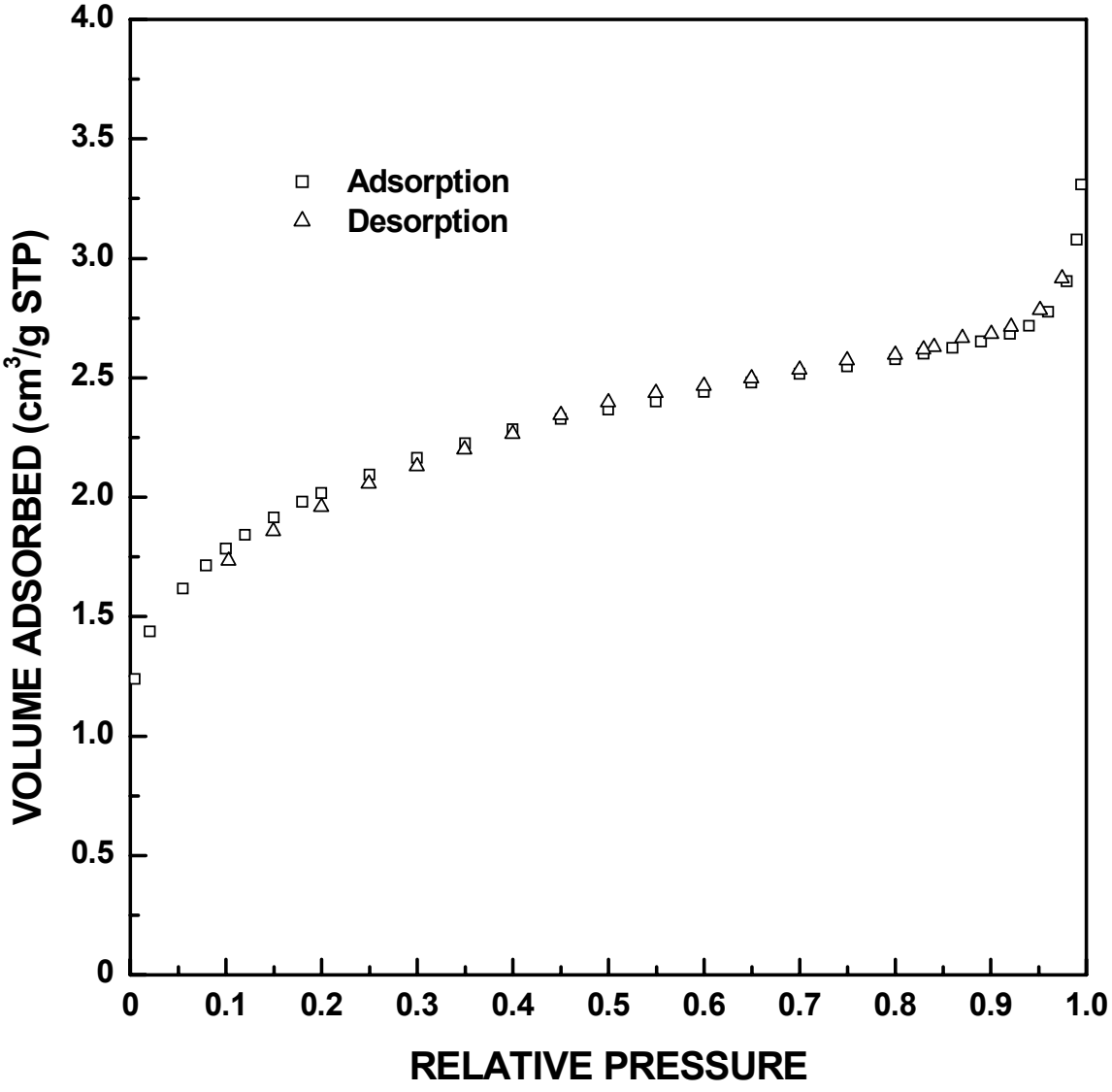

Figure 4-4-69 Adsorption/desorption isotherm plots for SC35-1200(1h) sample (X_{WL} = 0.03).

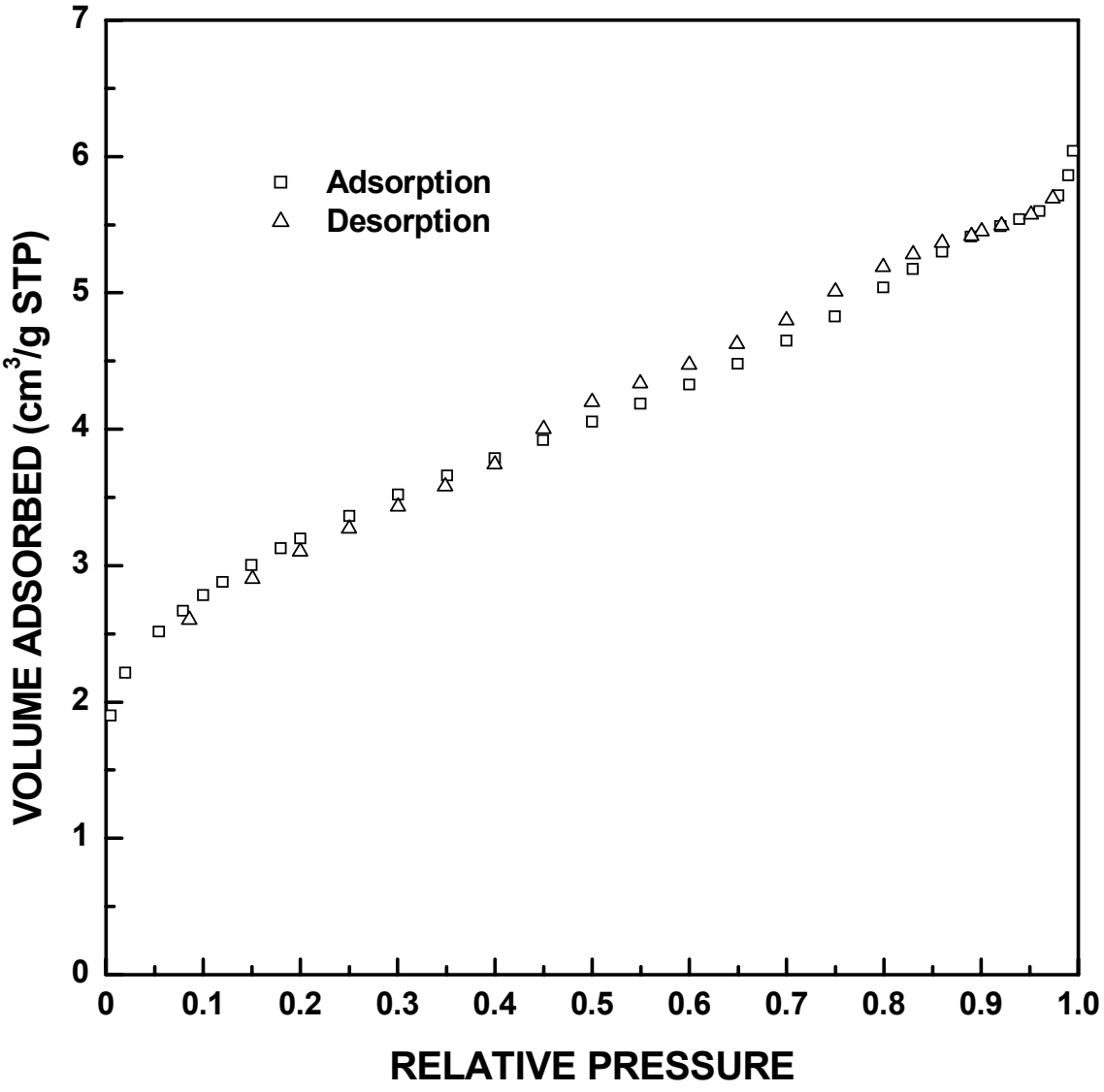

Figure 4-4-70 Adsorption/desorption isotherm plots for SC35-1200(2h) sample (X_{WL} = 0.05).

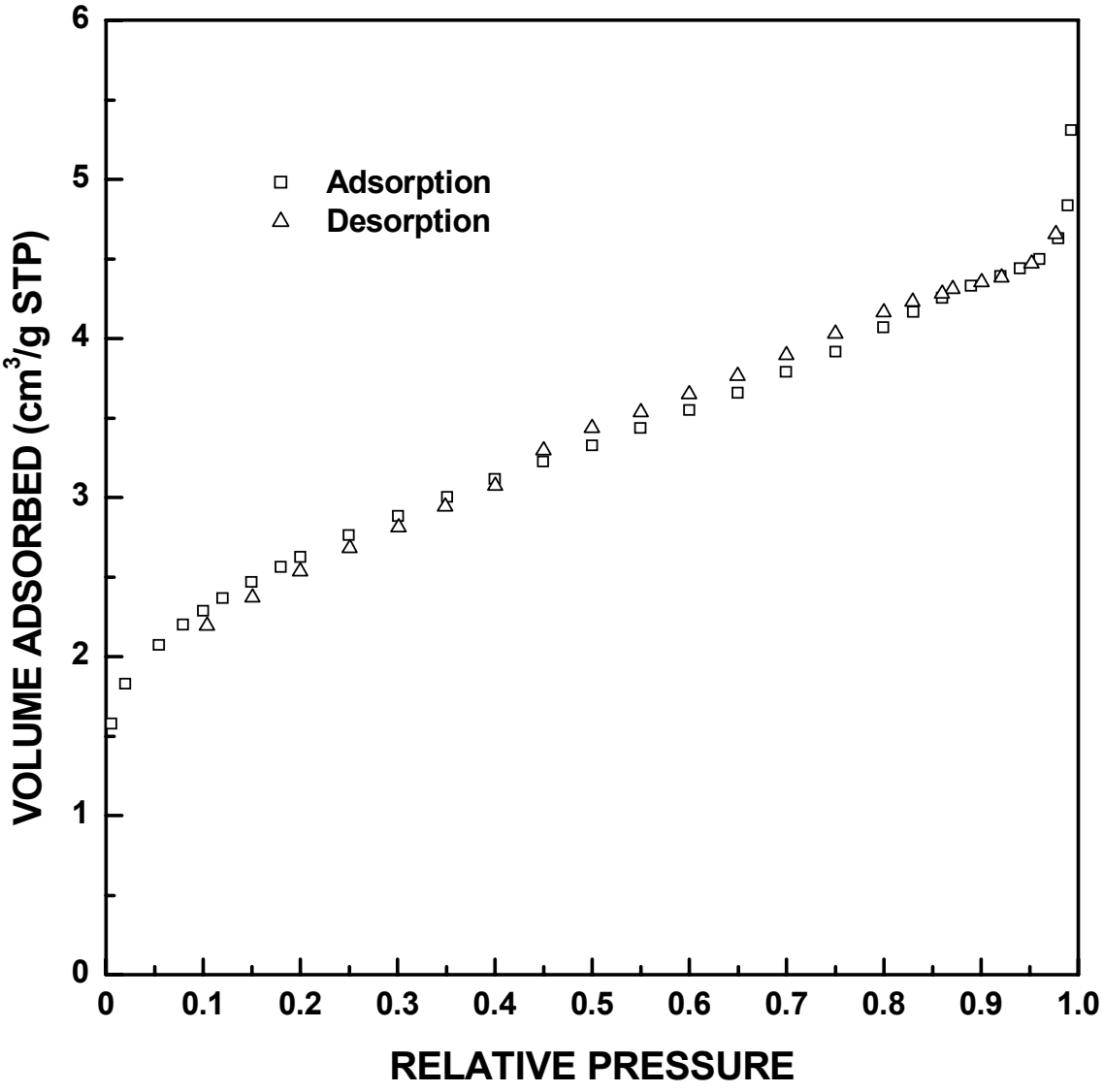

Figure 4-4-71 Adsorption/desorption isotherm plots for SC35-1250(30min) sample (X_{WL} = 0.05).

observed in Figures 4-4-21 and 4-4-32, respectively. The more significant observation is that the isotherms are just starting to shift in appearance from Type II to Type IV. Some specific changes in the isotherms are noted below.

A very small, closed hysteresis loop is observed in Figures 4-4-70 and 4-4-71 in the intermediate relative pressure range, i.e., from P/P_0 values of ~0.4 at the low end to ~0.85 at the high end. Hysteresis loops in the intermediate and upper relative pressure ranges are characteristic of samples with mesopores (i.e., samples which display Type IV isotherms (Sing, 1989, p. 4)). (The occurrence of a hysteresis in the isotherm in this pressure range indicates a difference in the processes of liquid condensation into the pores (the adsorption branch) and liquid evaporation from the pores (the desorption branch). A variety of explanations have been offered to explain this phenomenon (Gregg and Sing, 1982, p. 126).) The fact that the hysteresis loop closes at pressures below $P/P_0 = 1$ suggests that there is an upper size limit within the mesopore size range. Also, the development of the hysteresis loop in these samples is associated with the onset of some bimodality in the pore size distributions. The latter point is not apparent based on simple inspection of the isotherm, but it will be discussed in more detail later in this section.

The shape of the hysteresis loop in gas adsorption/desorption isotherms is dependent upon the morphological structure of the porosity in the sample. The hysteresis shown in Figures 4-4-70 to 4-4-71 has similarities to the so-called "Type H3" and "Type H4" (Gregg and Sing, 1982, p. 287). (The hysteresis observed in Figures 4-4-70 to 4-4-71 is essentially a hybrid of these two types.) Type H3 and Type H4 hysteresis are often associated with materials that have either slit-shaped pores or pore spaces developed from the packing of plate-like particles (Gregg and Sing, 1982, p. 287). For example, Type H3

hysteresis has been observed in isotherms for various layered aluminum silicate materials which have plate-like particles (e.g., halloysite and montmorillonite). (For example, see Figures 3.3 and 3.17 on pages 116 and 132, respectively, of Gregg and Sing, 1982.) Type H4 hysteresis has been observed in isotherms for various carbon materials. (For example, see Figures 4.2 and 4.34 on pages 196 and 243, respectively, of Gregg and Sing, 1982.) However, it has been shown that Type H3 and Type H4 hysteresis can also develop by compaction of powders. (For example, see Figures 3.22 and 4.5 on pages 155 and 205, respectively, of Gregg and Sing, 1982.)

Figures 4-4-68 to 4-4-71 also show that the volume adsorbed increases more gradually (on a relative basis) at very high relative pressure (i.e., as P/P_0 approaches 1) for samples with increasing extent of conversion. This is again representative of the beginning of a shift from the nitrogen condensation onto an essentially nonporous "bulk" surface (Type II behavior) to condensation within pores (Type IV behavior) (Sing, 1989).

The shape of the isotherms changed dramatically in samples with a greater extent of conversion. Figures 4-4-72 and 4-4-73 show the isotherms for SC35-1250(1h) and SC35-1250(2h) samples which have fractional weight loss of 0.07 and 0.12, respectively. The shapes of the hysteresis loops shift relative to the loops observed in Figures 4-4-70 and 4-4-71. The hysteresis loop for the SC35-1250(2h) sample is essentially a "Type H1" loop. (This type of hysteresis is associated with the pore structure for packing uniform-sized spherical particles, such as in agglomerates, loose packed or lightly-compacted powders, and compacts in the early stages of sintering (i.e., when pores remain open and connected). It is also observed for pores with ink-bottle shapes or pores of circular cross-section and gradually varying radius (Gregg and Sing, 1982, p.126-130).) As expected, the volume of

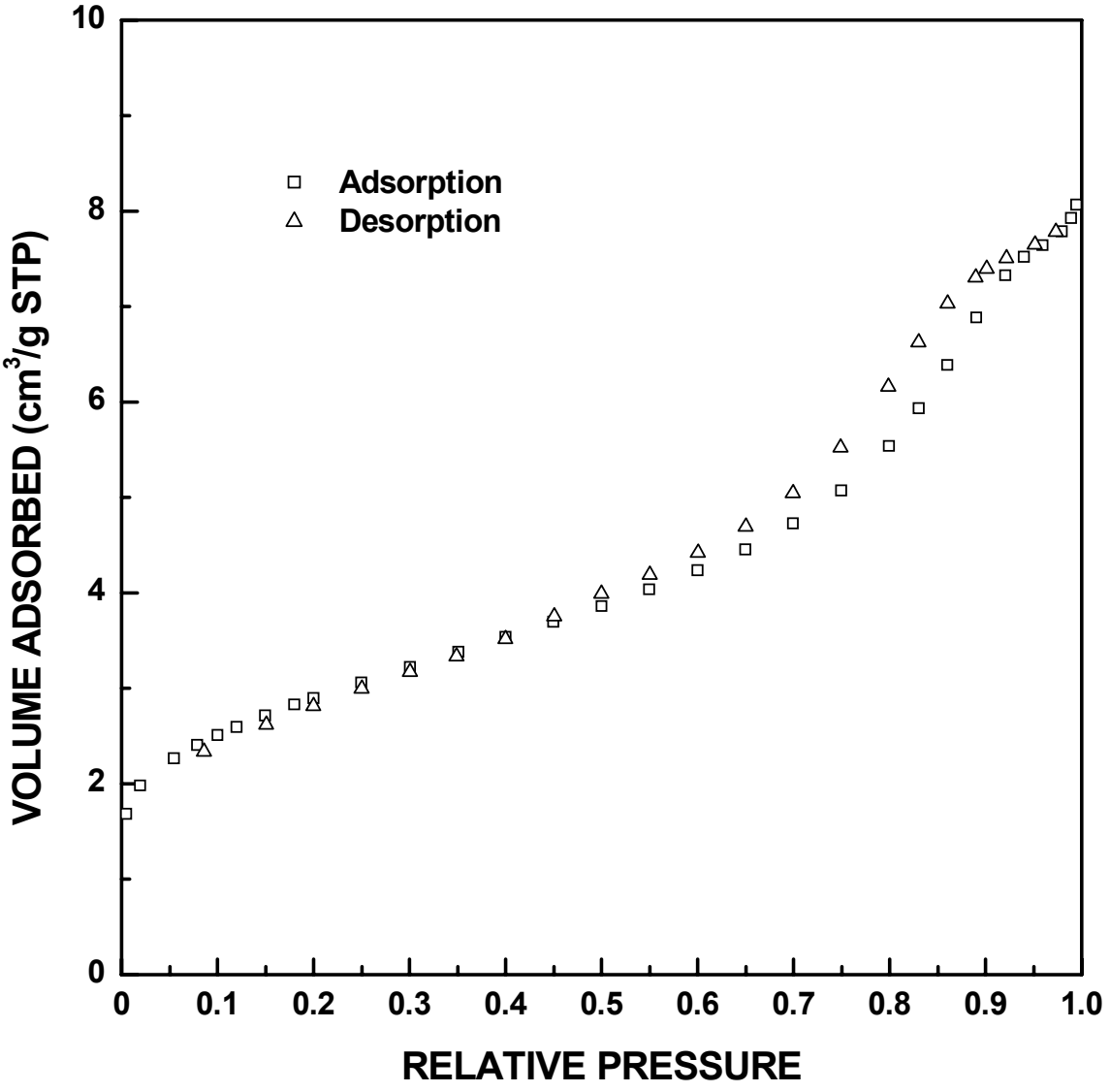

Figure 4-4-72 Adsorption/desorption isotherm plots for SC35-1250(1h) sample (X_{WL} = 0.07).

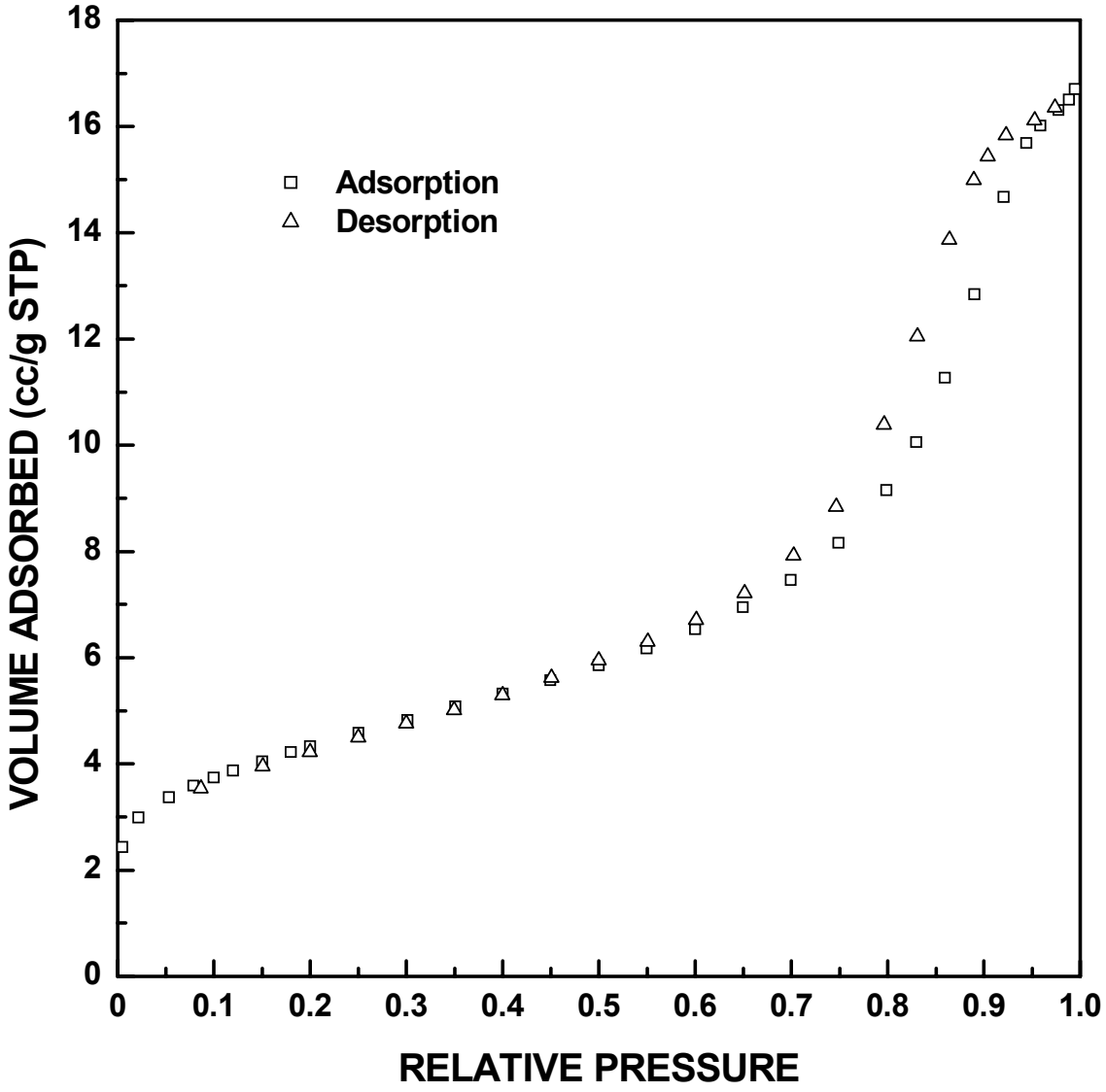

Figure 4-4-73 Adsorption/desorption isotherm plots for SC35-1250(2h) sample (X_{WL} = 0.12).

gas adsorbed continued to increase with increasing extent of conversion. (This is again why increases in specific pore volume and specific surface area are observed in Figures 4-4-22 and 4-4-32, respectively.) In addition, the shift in the majority of the hysteresis loop to higher relative pressures is indicative of a shift to larger-sized mesopores. (The pore size distributions obtained from the gas adsorption/desorption isotherms will be described in detail later in this section.)

A comparison of the gas adsorption/desorption isotherms for the SC35-1250(30min) (X_{WL} = 0.05), SC35-1250(1h) (X_{WL} = 0.07), SC35-1250(2h) (X_{WL} = 0.12), and SC35-1250(4h) (X_{WL} = 0.23) samples (Figures 4-4-71 to 4-4-74) clearly illustrates the transition in the hysteresis loops from Type H3/Type H4 mixed hysteresis to Type H1 hysteresis. The transition was largely completed in the SC35-1250(2h) (X_{WL} = 0.12) sample and was fully completed for the sample SC35-1250(4h) (X_{WL} = 0.23).

There were essentially no significant changes in the shape of the isotherms with further conversion to SiC until the late stages of the reaction. This appears to be consistent with the proposed "shrinking-core" reaction model in that continued reaction only resulted in the formation of an additional amount (i.e., volume) of porous SiC, but no significant changes in the pore characteristics (e.g., shape, size, etc.). The increasing volume of porosity as the CTR reaction proceeds is evident from the increasing adsorbed volumes in the isotherms. (Once again, this is expected from the results shown previously in Figures 4-4-22 and 4-4-32 for the changes in specific pore volume and specific surface area, respectively, as a function of the fractional weight loss.) Over a large portion of the CTR reaction, there is relatively little change in the starting and ending points (i.e., relative pressure P/P_0 values) for the hysteresis loops. (For example, compare isotherms in Figures

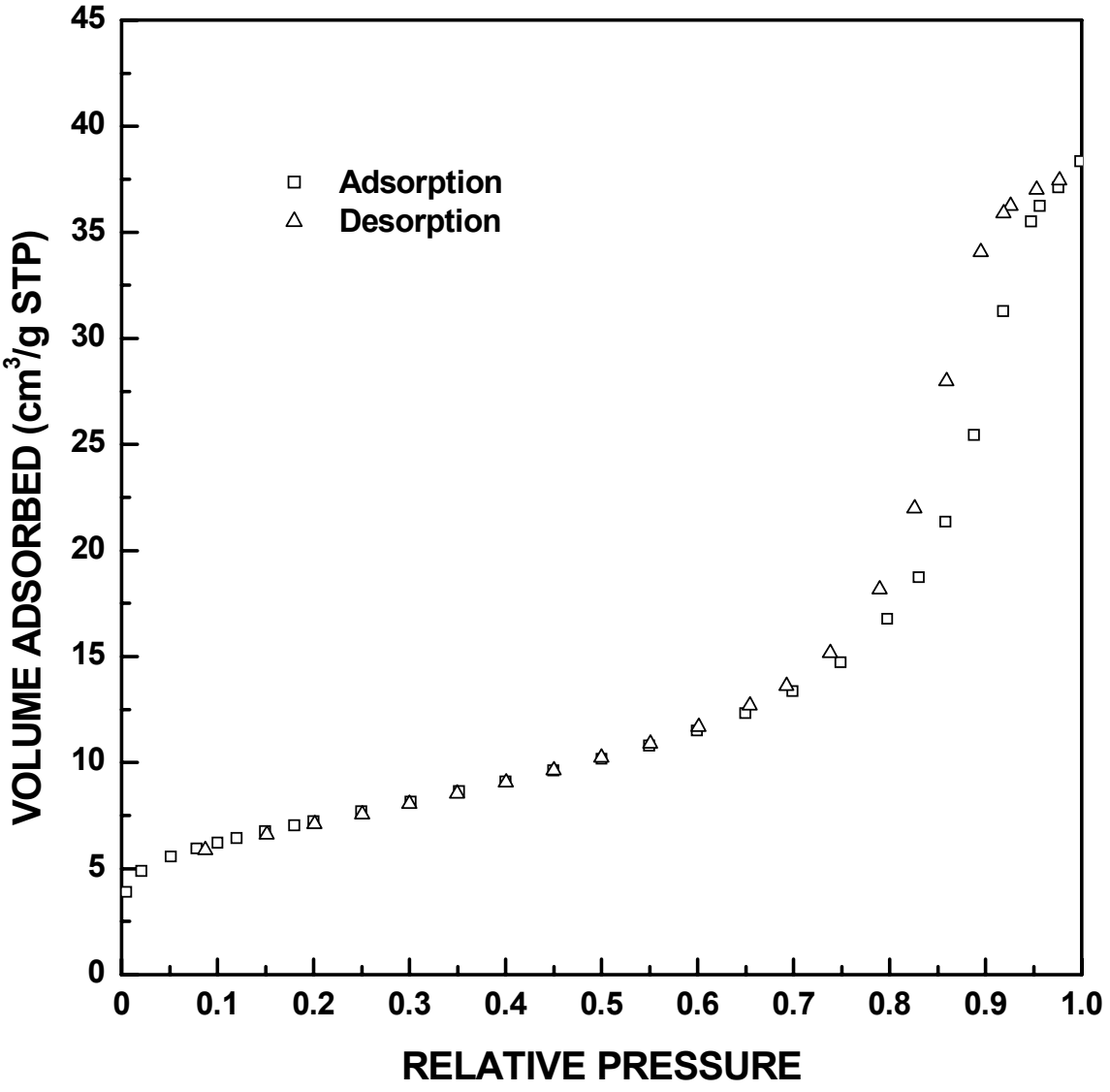

Figure 4-4-74 Adsorption/desorption isotherm plots for SC35-1250(4h) sample (X_{WL} = 0.23).

4-4-74 to 4-4-78 ranging from 0.23 to 0.82 in the fractional weight loss.) This indicates there was relatively little change in the pore size distribution, as expected from the proposed reaction model. This will be shown more directly in the next section.

There is a little shift in the hysteresis loop in the isotherms for samples in the late stages of the CTR reaction, such that the starting and ending points for the hysteresis loop are shifted to higher relative pressure values. The shift is relatively small when comparing the isotherms for the SC35-1250(22h) sample (X_{WL} = 0.82) and the SC35-1250(32h) sample (X_{WL} = 0.95), as shown in Figures 4-4-78 and 4-4-79, respectively. There is another small shift in the hysteresis loop for the SC35-1300(12h) sample which has an X_{WL} value of ~0.96 (Figure 4-4-80). However, there is much greater shift in the hysteresis loop for the SC35-1300(16h) sample which has an X_{WL} value of ~0.98 (Figure 4-4-81). These shifts indicate that the average pore size is increasing and this will be discussed in more detail later in this section.

The isotherm for the SC35-1300(16h) sample also shows a large decrease in the adsorbed volume which indicates that there is a large decrease in the measured pore volume. This decrease in porosity was illustrated previously in Figure 4-4-23 in section 4.4.3. As discussed in that section, the decrease in pore volume is attributed to two effects. The first effect is that some pores grow to sizes that cannot be detected by the gas adsorption/capillary condensation method. The fact that the hysteresis loop does not close at the high pressure range is consistent with this supposition. The second effect is that some pores are eliminated by sintering (densification). Both coarsening (pore growth) and densification (pore elimination) are simultaneously operative. However, it was

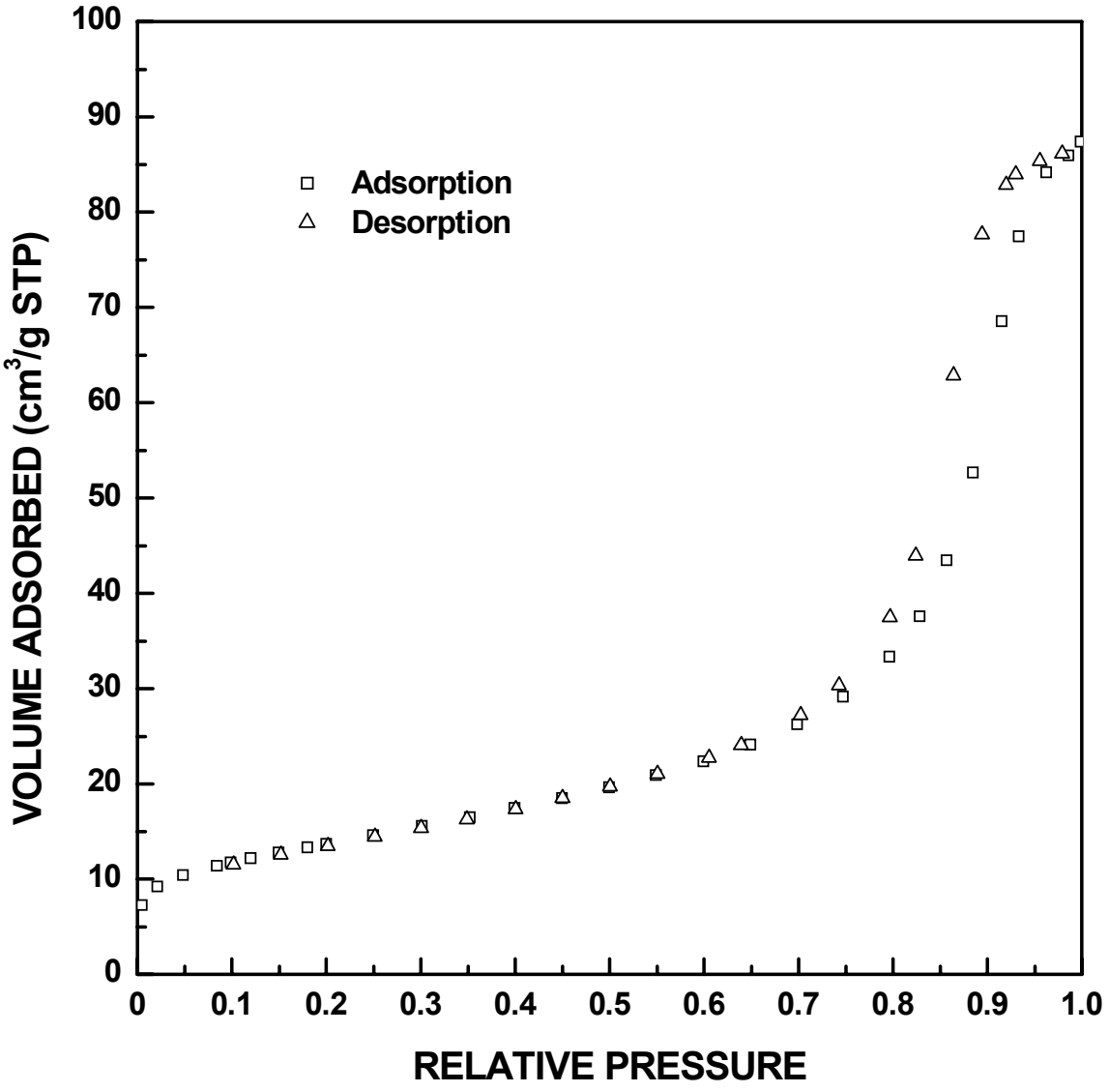

Figure 4-4-75 Adsorption/desorption isotherm plots for SC35-1250(8h) sample (X_{WL} = 0.41).

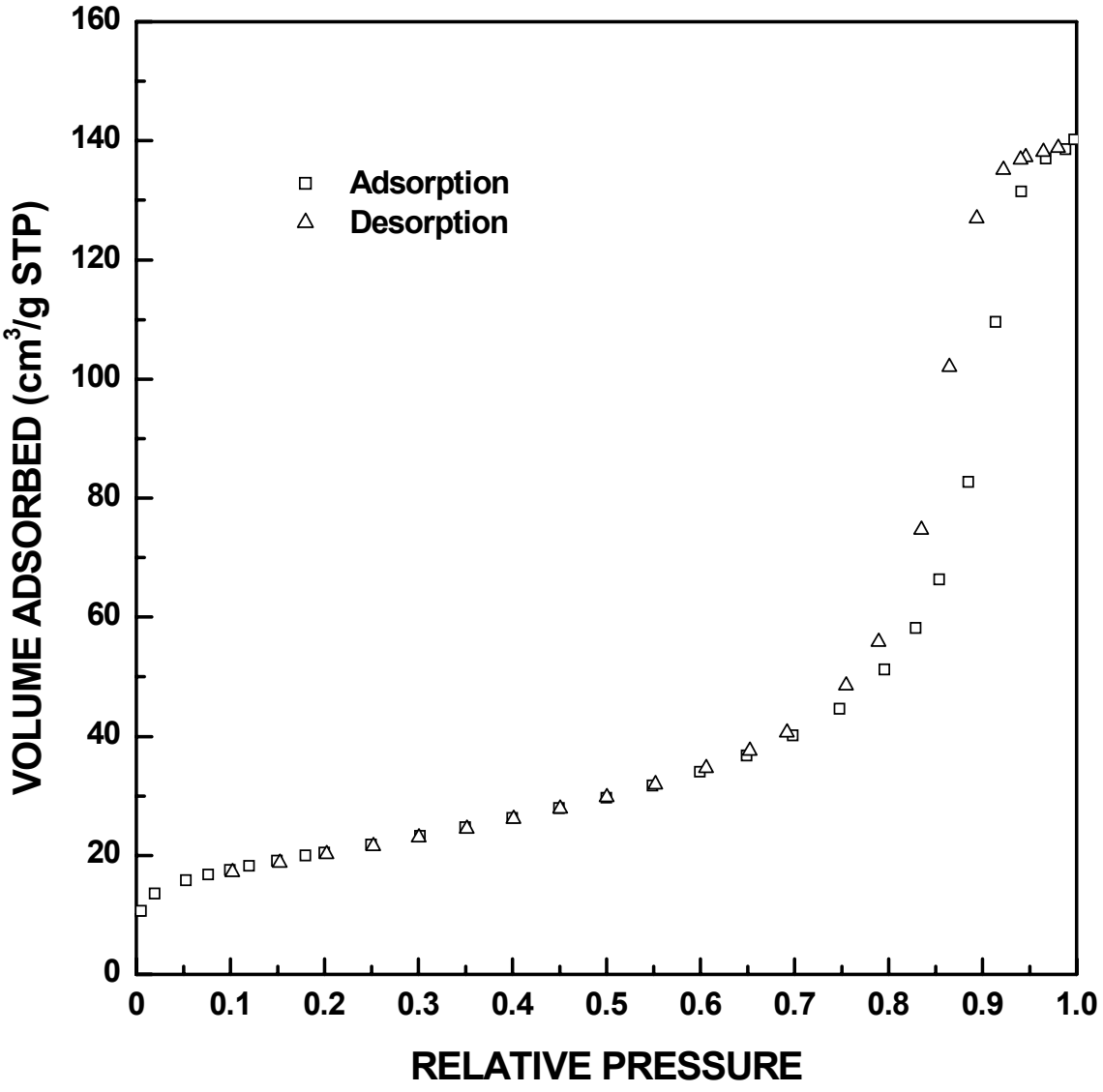

Figure 4-4-76 Adsorption/desorption isotherm plots for SC35-1200(32h) sample (X_{WL} = 0.52).

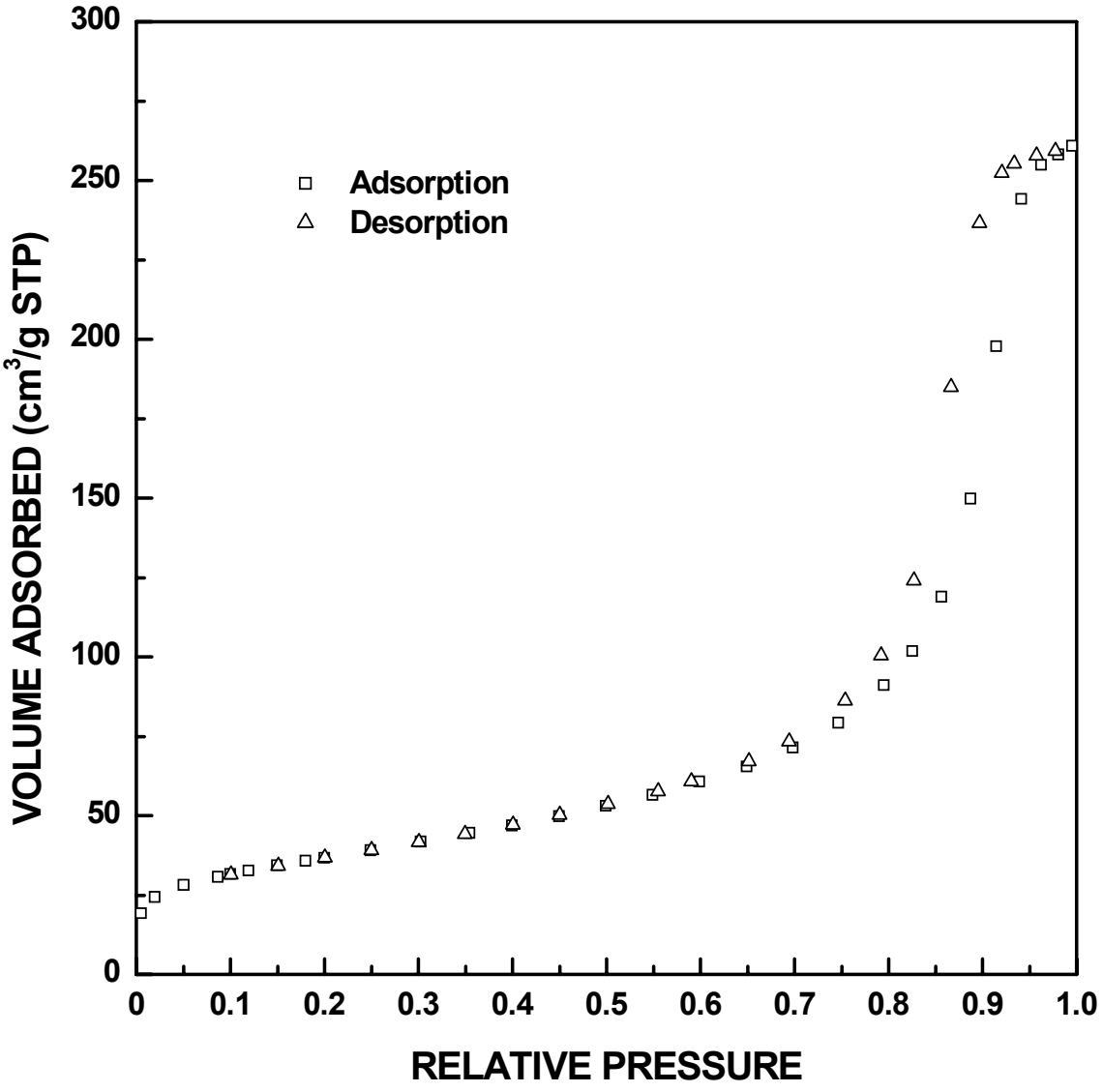

Figure 4-4-77 Adsorption/desorption isotherm plots for SC35-1200(48h) sample (X_{WL} = 0.72).

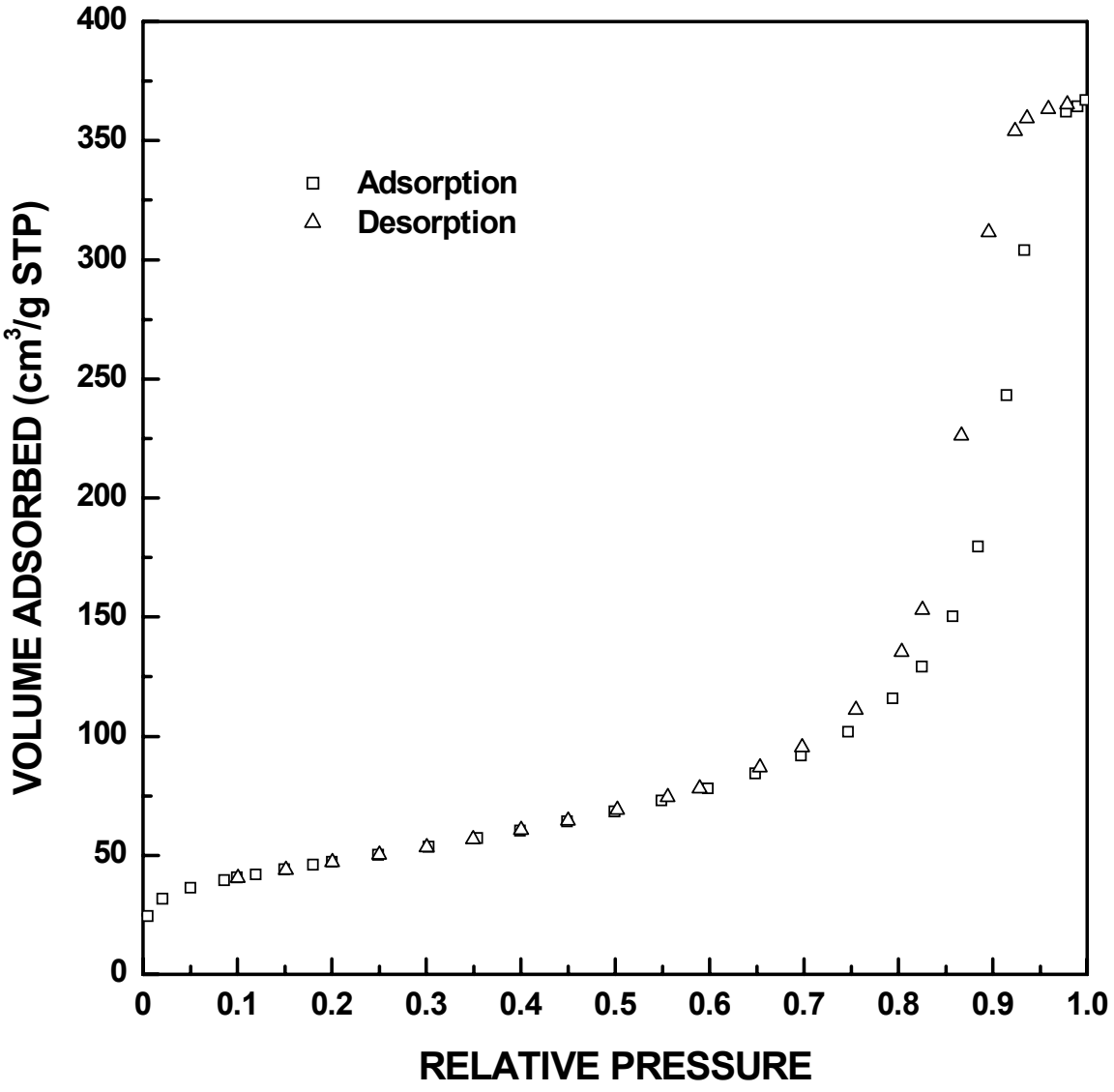

Figure 4-4-78 Adsorption/desorption isotherm plots for SC35-1250(22h) sample (X_{WL} = 0.82).

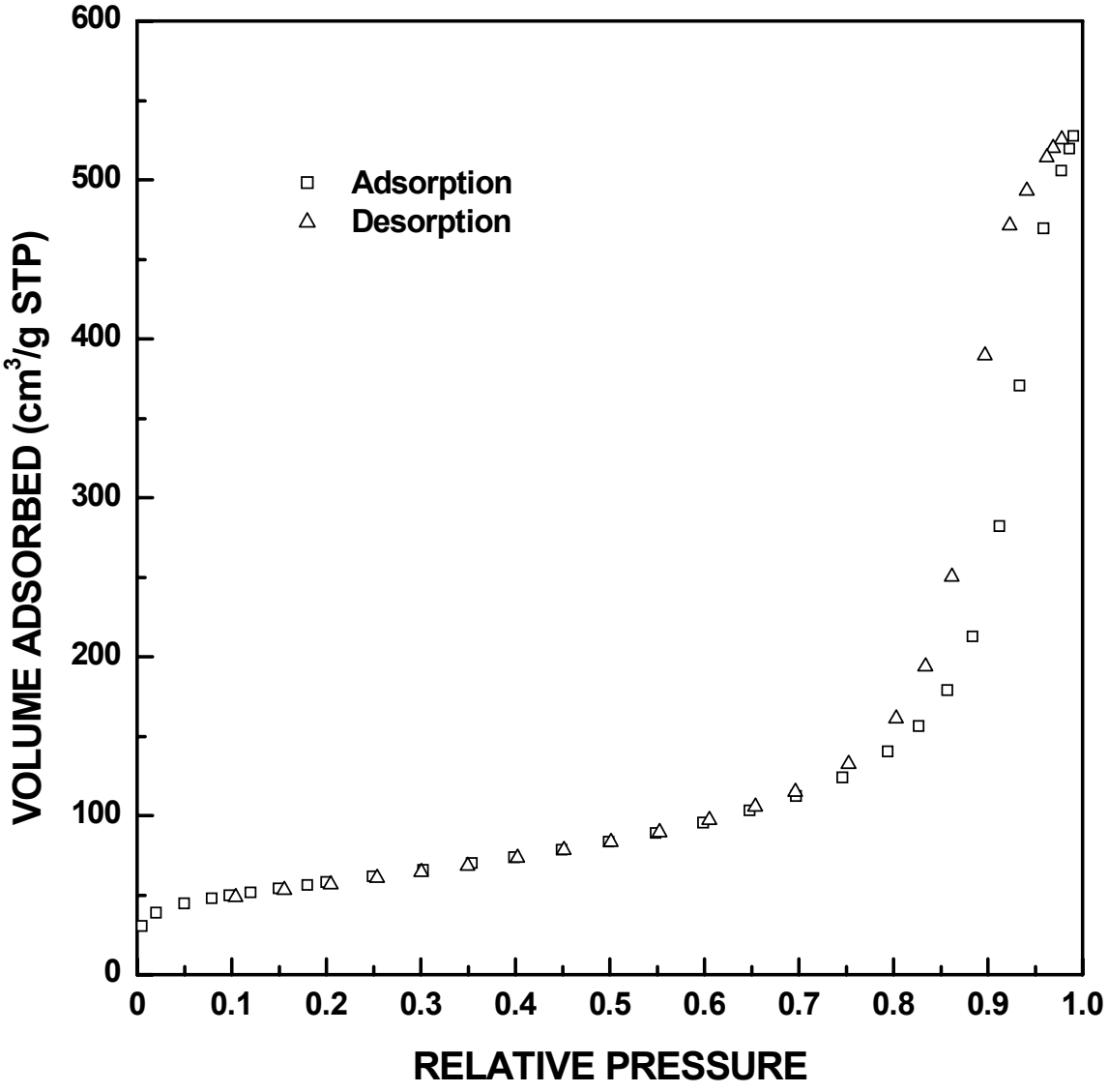

Figure 4-4-79 Adsorption/desorption isotherm plots for SC35-1250(32h) sample (X_{WL} = 0.95).

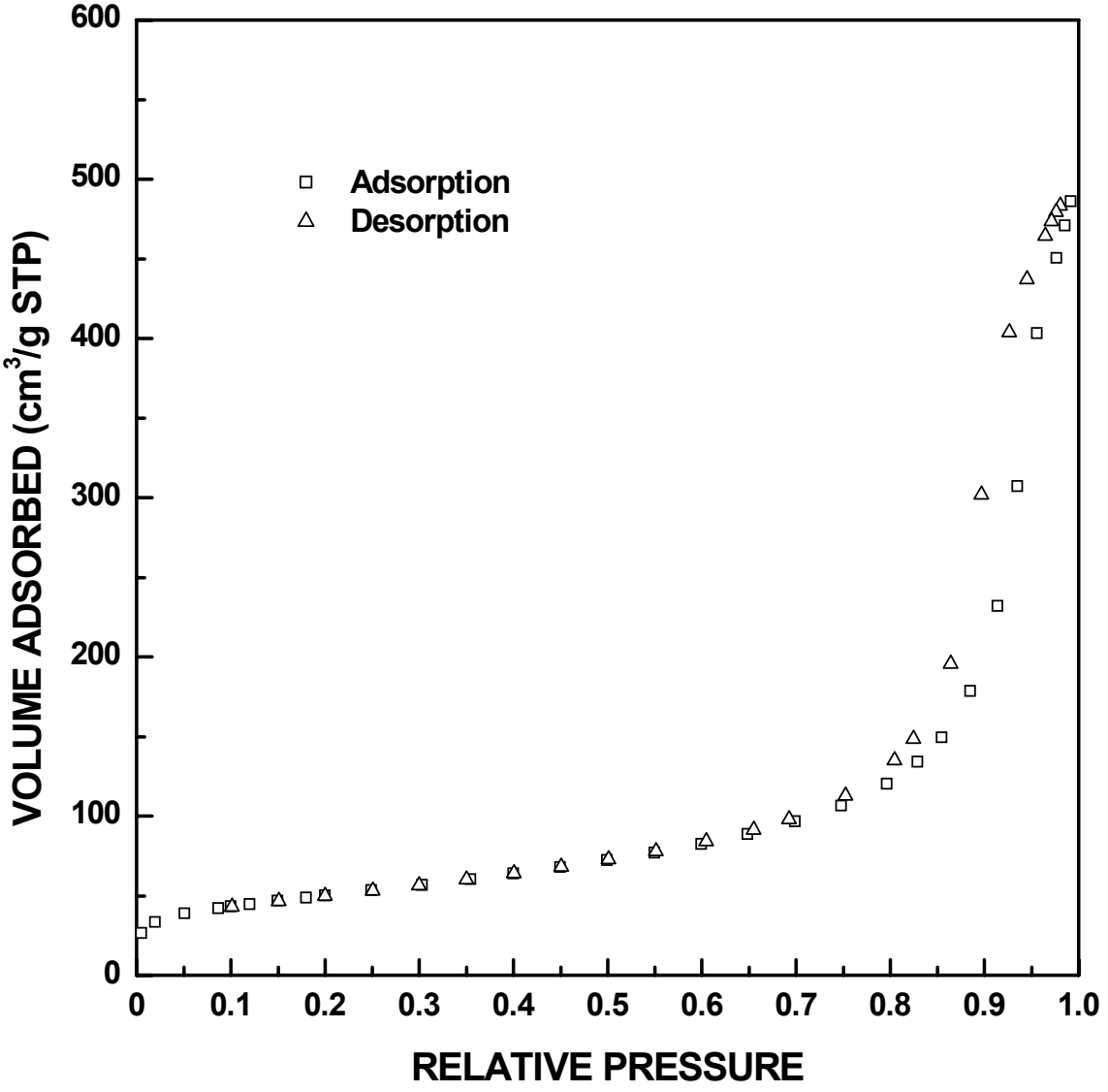

Figure 4-4-80 Adsorption/desorption isotherm plots for SC35-1300(12h) sample (X_{WL} = 0.96).

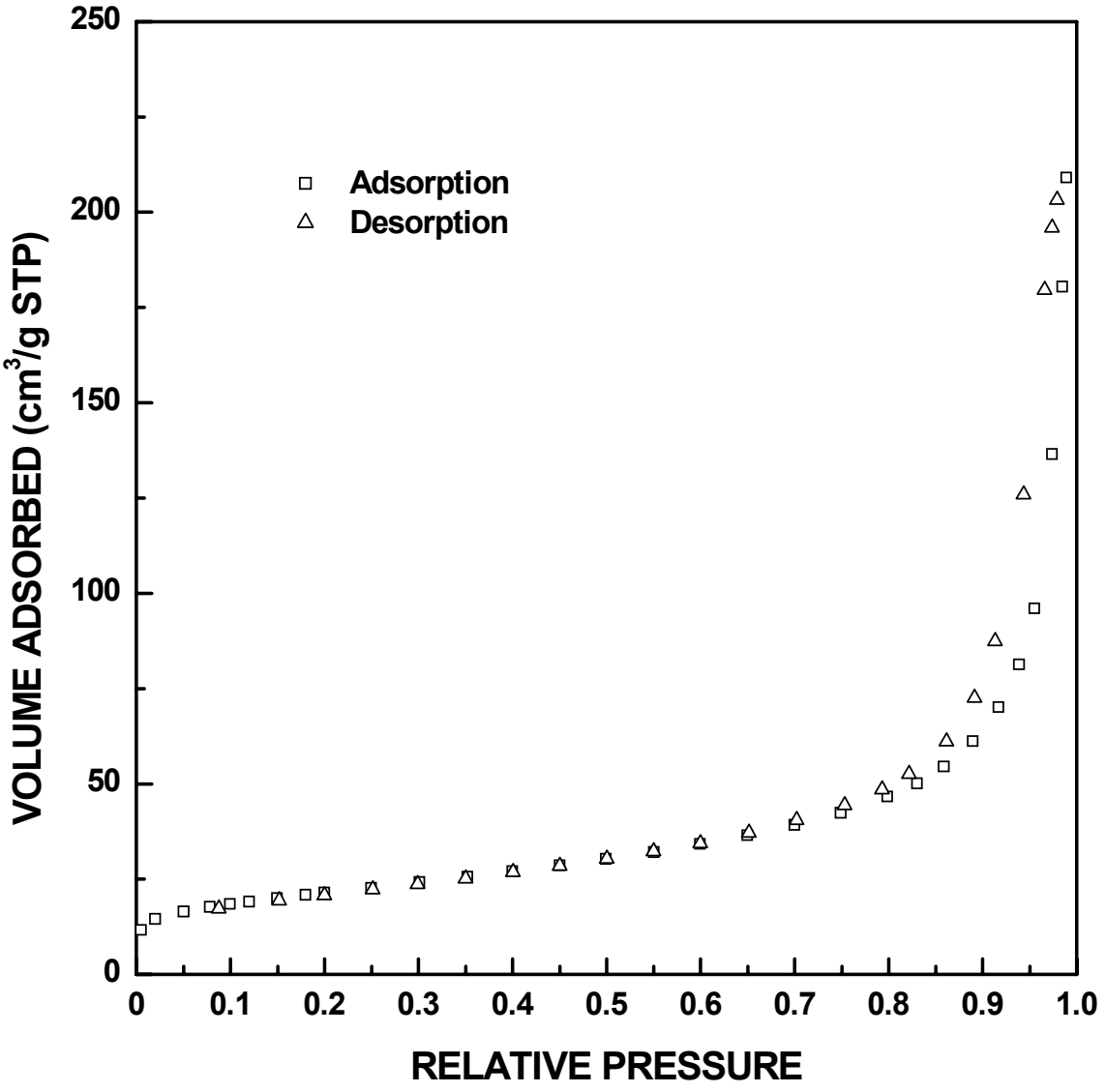

Figure 4-4-81 Adsorption/desorption isotherm plots for SC35-1300(16h) sample (X_{WL} = 0.98).

demonstrated from an analysis of changes in particle size distributions (section 4.4.6) that the first effect (coarsening) was the dominant one.

4.4.7.2 Pore Size Distribution for SC35 CTR Samples

Figures 4-4-82 to 4-4-95 show plots of the cumulative specific pore volume vs. pore diameter. These results were extracted from the gas adsorption/desorption isotherms shown in Figures 4-4-68 to 4-4-81. The figures illustrate several trends that have already been described in previous sections: (1) The total specific pore volume increases with increasing fractional weight loss, X_{WL}, throughout most of the reaction. However, as expected from Figures 4-4-21, the pore volume decreases in the late stages of the reaction (i.e. $X_{WL} \geq 0.95$). (2) The pore size distribution shifts to larger sizes in the early stages of the reaction, i.e., up to a fractional weight loss of ~0.23 (see Figures 4-4-82 - 4-4-88). This is followed by a period in which there is relatively little change in the pore size distribution (i.e., see Figures 4-4-88 - 4-4-92 for samples with X_{WL} in the range of ~0.23 to ~0.82). Finally, in the late stages of the reaction (i.e. $X_{WL} \geq 0.95$), the pore size distribution again shifts to larger sizes (see Figures 4-4-93 - 4-4-95).

The trends in the pore size distribution data were illustrated more clearly by re-plotting the data in several different ways. In each case, the correction described in section 3.5.2 was first applied to the data. (This involved subtracting the "macropore" volume from the total pore volume for several samples with low extent of conversion.) Figures 4-4-96 to 4-4-109 show "normalized" plots of the data in Figures 4-4-82 to 4-4-95. In these plots, the relative pore volume is defined as the cumulative pore volume divided by maximum pore volume. Figure 4-4-110 shows a combined plot of the "normalized"

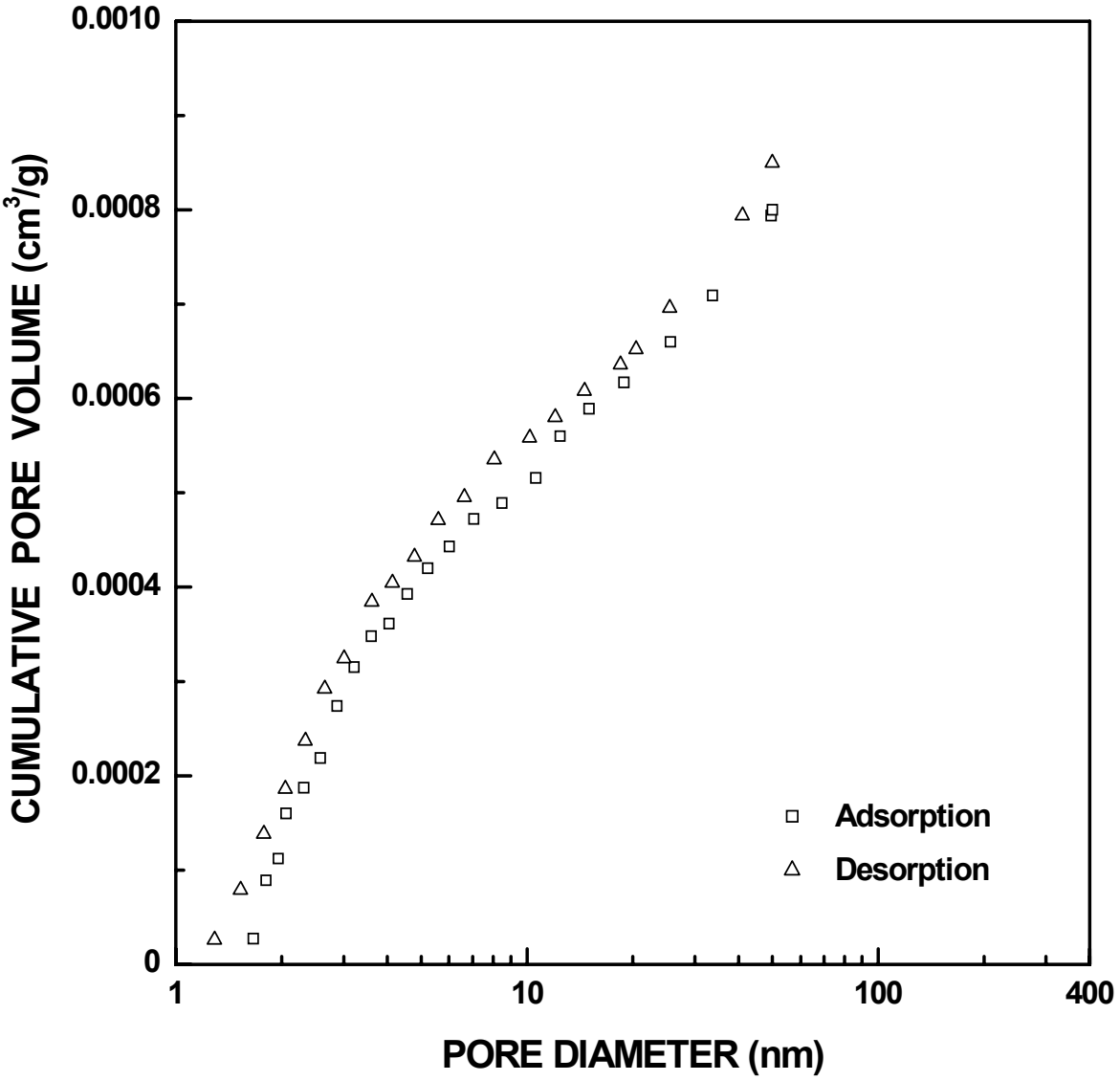

Figure 4-4-82 Plots of cumulative specific pore volume vs. pore diameter for SC35-1160(1h) sample (fractional weight loss X_{WL} = 0.02). The pore diameter was cut off at 50 nm.

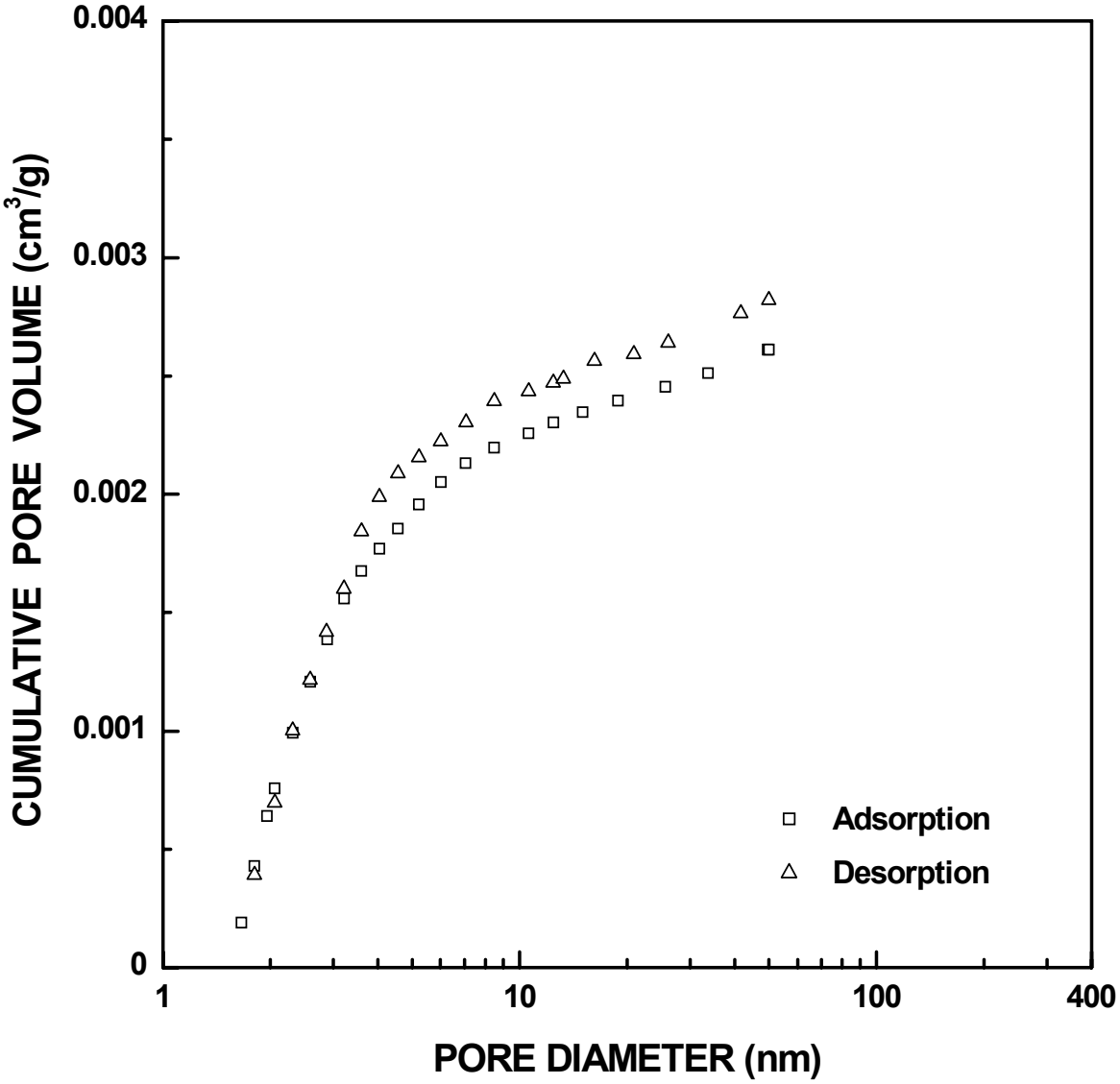

Figure 4-4-83 Plots of cumulative specific pore volume vs. pore diameter for SC35-1200(1h) sample (X_{WL} = 0.03). The pore diameter was cut off at 50 nm.

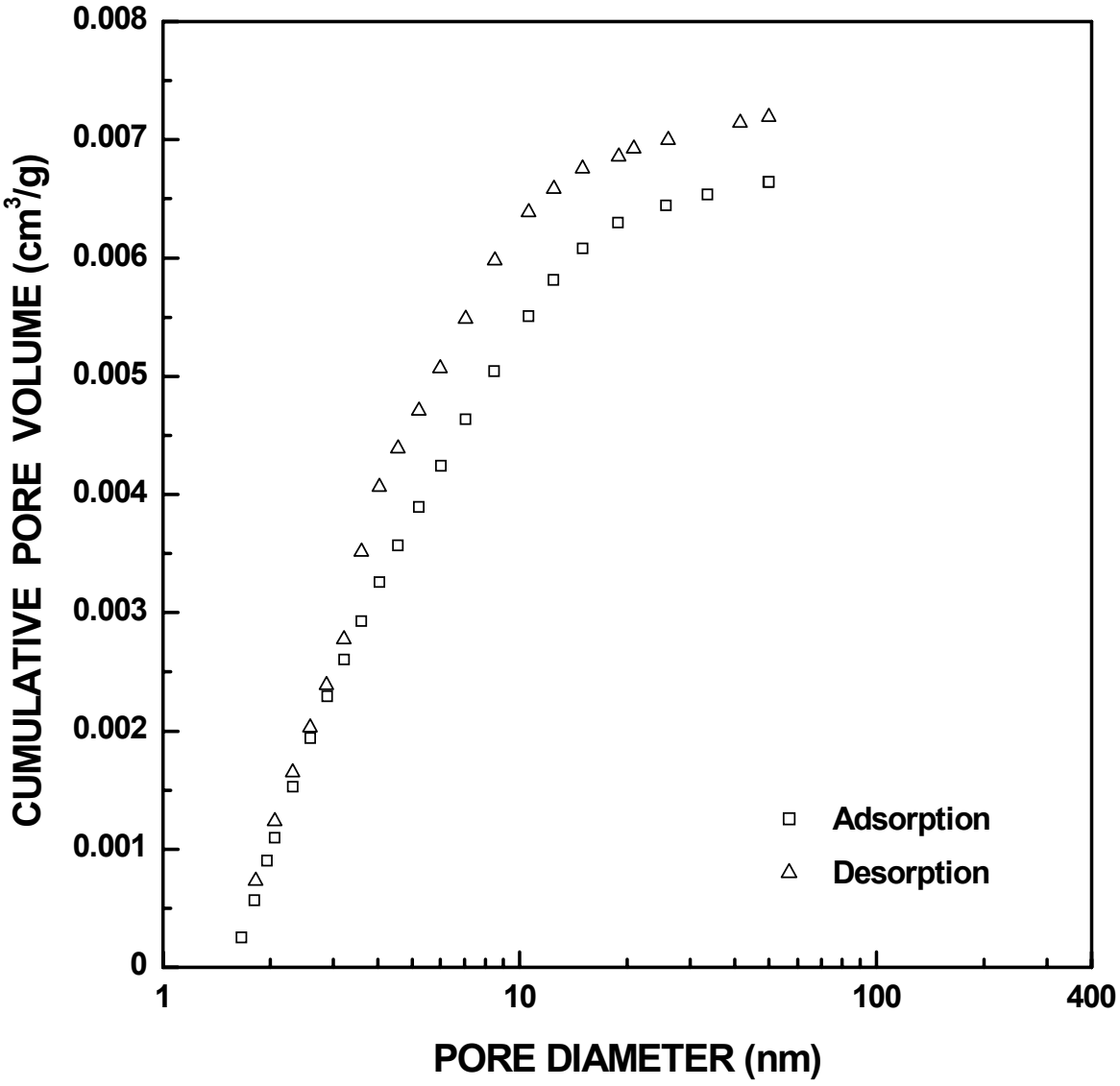

Figure 4-4-84 Plots of cumulative specific pore volume vs. pore diameter for SC35-1200(2h) sample (X_{WL} = 0.05). The pore diameter was cut off at 50 nm.

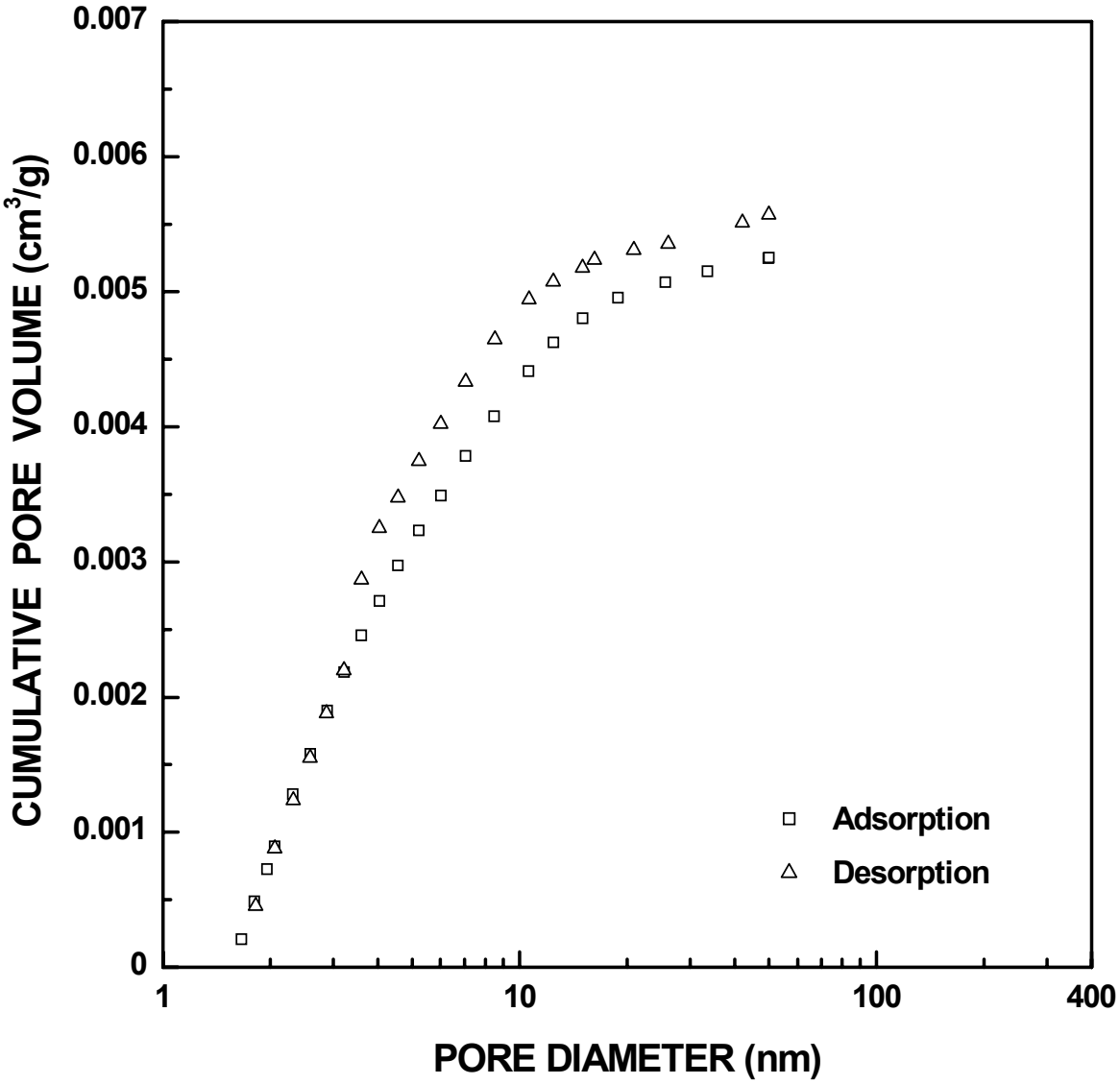

Figure 4-4-85 Plots of cumulative specific pore volume vs. pore diameter for SC35-1250(30min) sample (X_{WL} = 0.05). The pore diameter was cut off at 50 nm.

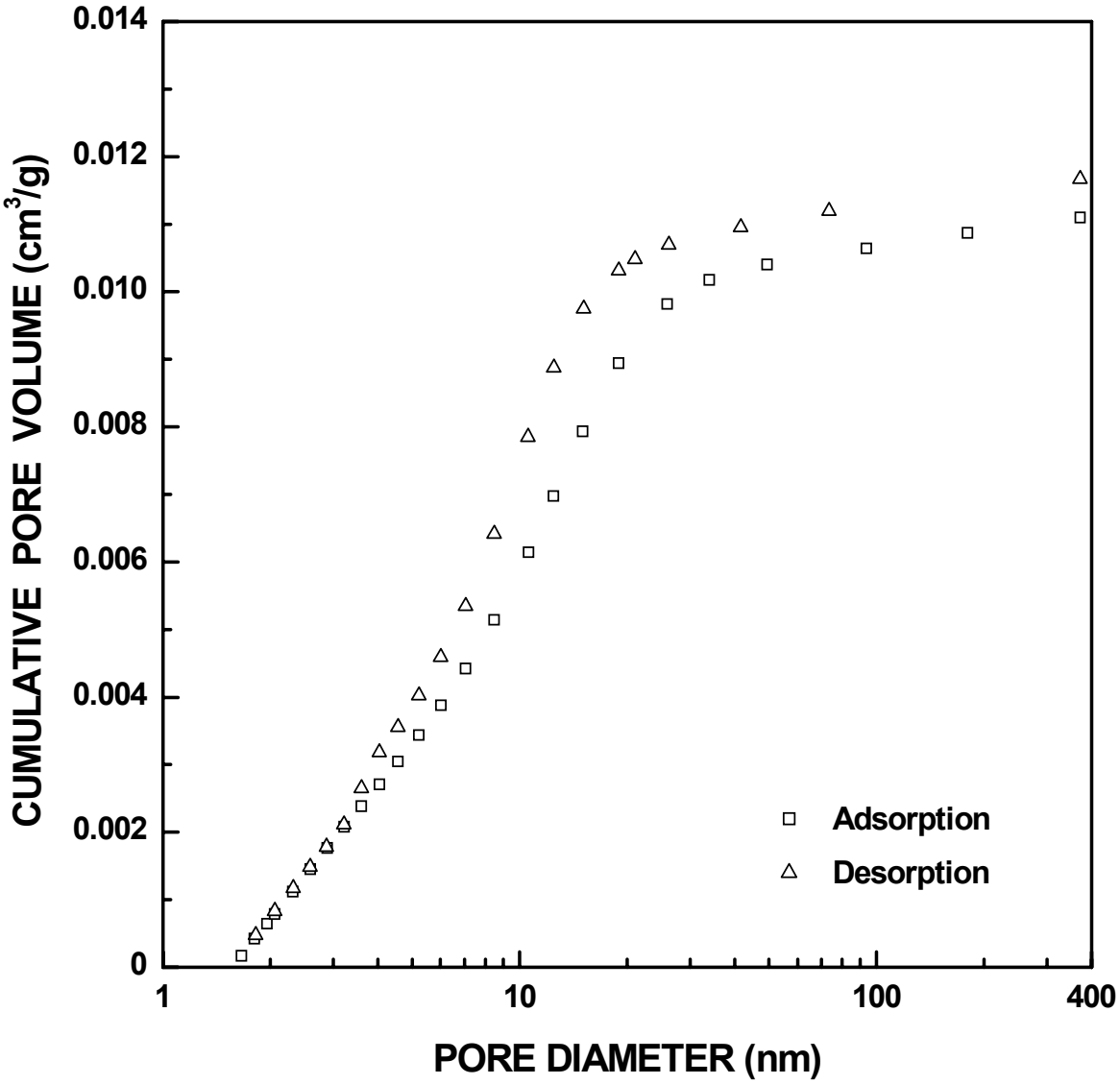

Figure 4-4-86 Plots of cumulative specific pore volume vs. pore diameter for SC35-1250(1h) sample (X_{WL} = 0.07).

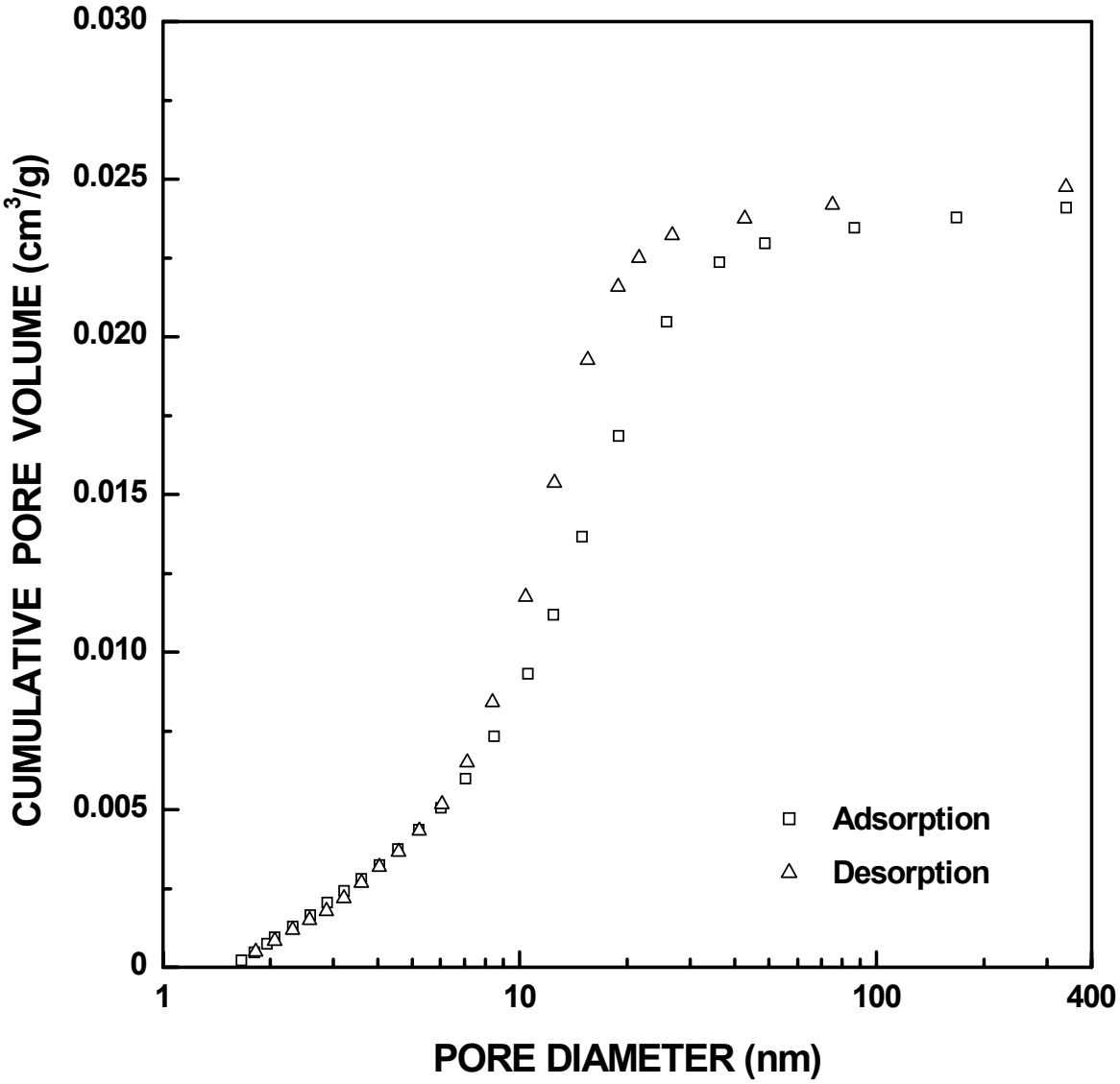

Figure 4-4-87 Plots of cumulative specific pore volume vs. pore diameter for SC35-1250(2h) sample (X_{WL} = 0.12).

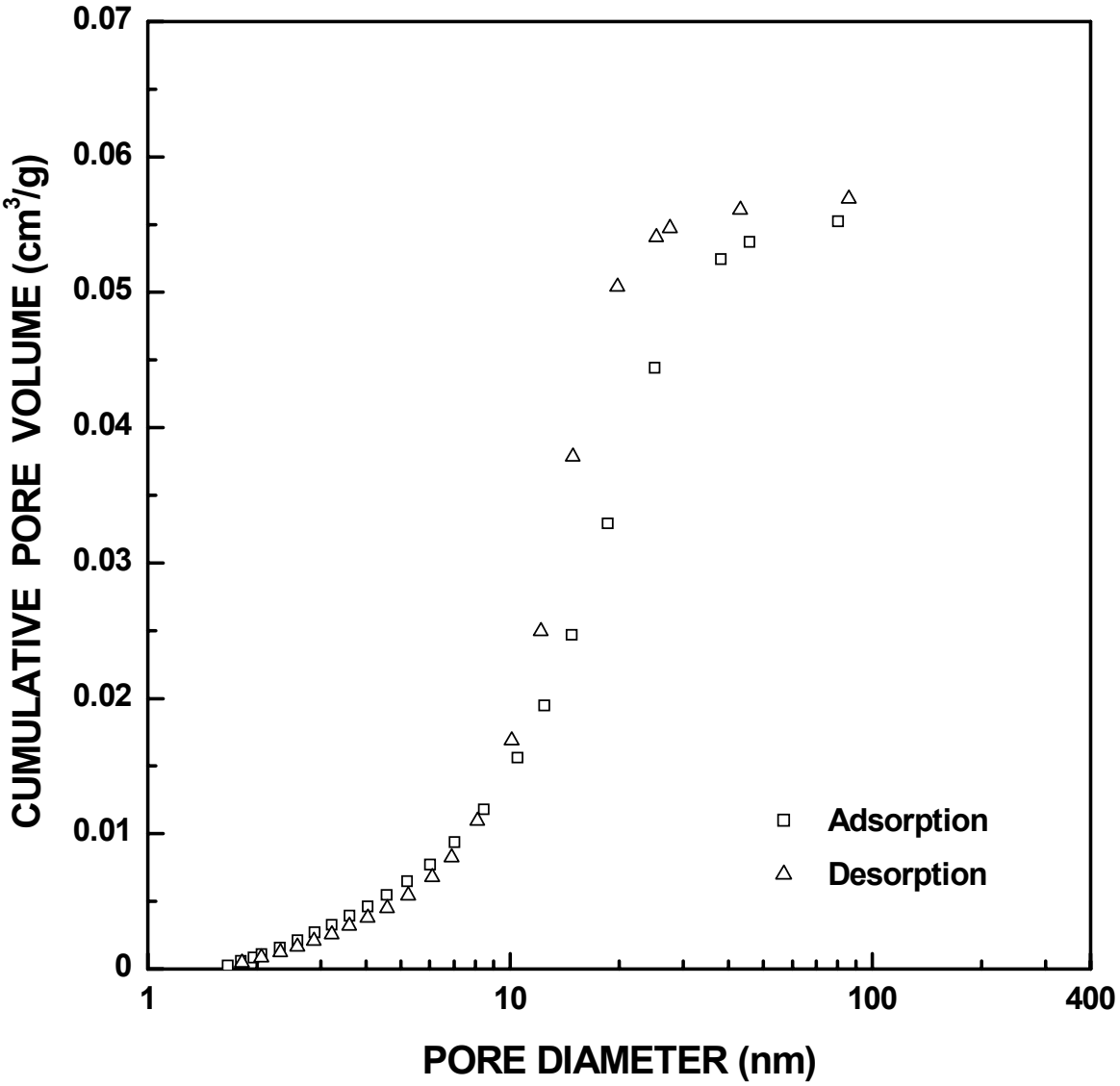

Figure 4-4-88 Plots of cumulative specific pore volume vs. pore diameter for SC35-1250(4h) sample (X_{WL} = 0.23).

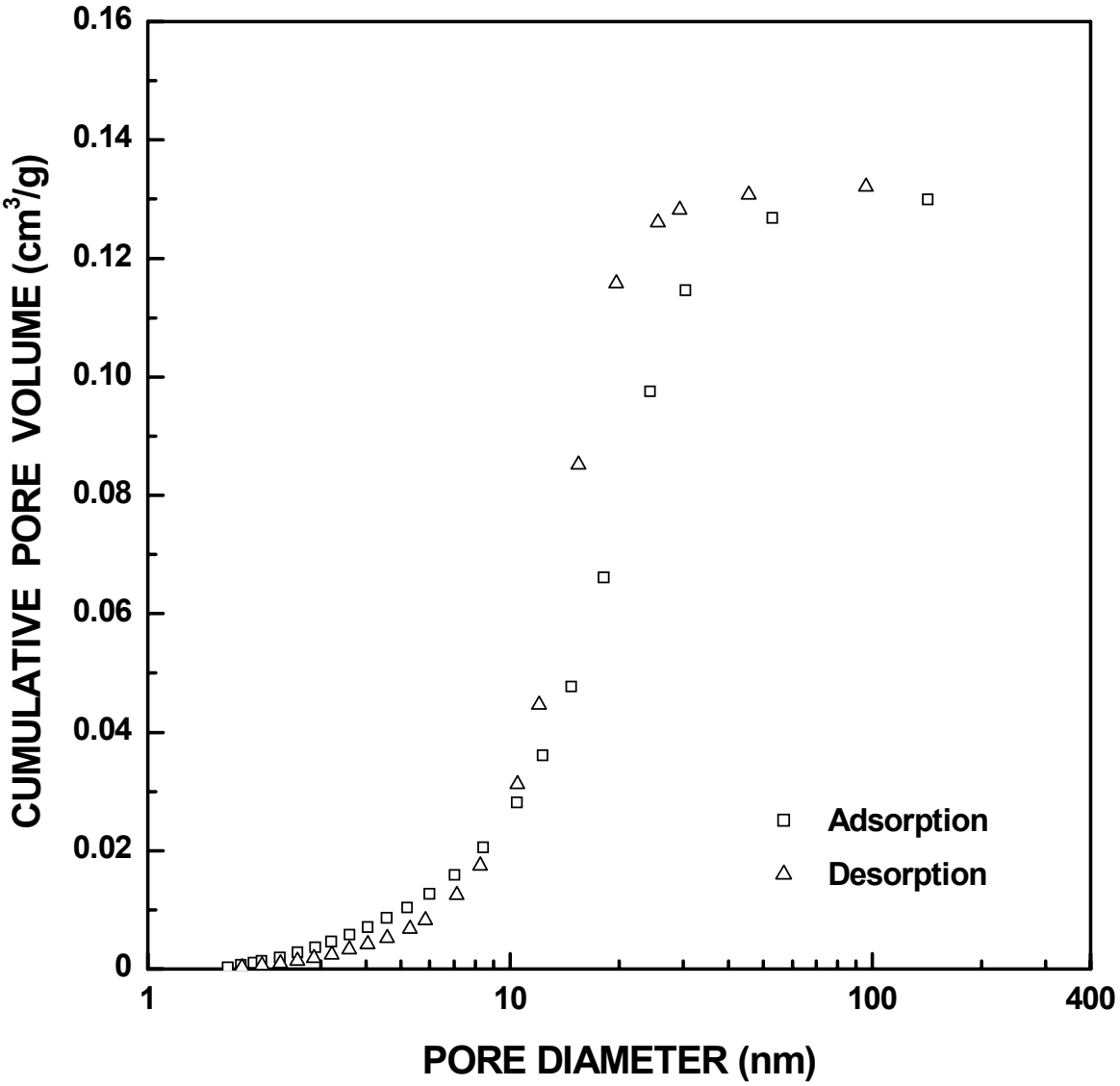

Figure 4-4-89 Plots of cumulative specific pore volume vs. pore diameter for SC35-1250(8h) sample (X_{WL} = 0.41).

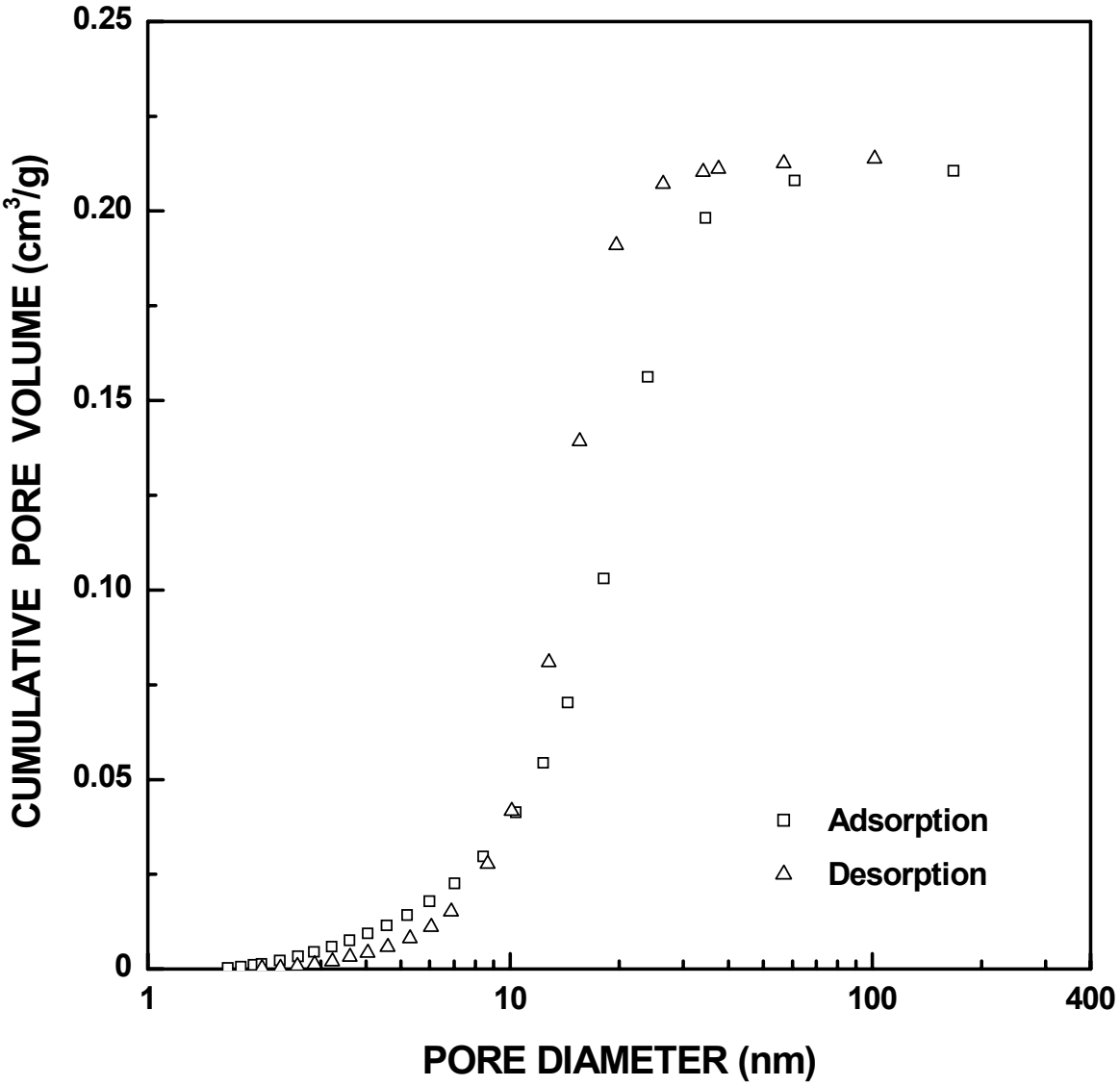

Figure 4-4-90 Plots of cumulative specific pore volume vs. pore diameter for SC35-1200(32h) sample (X_{WL} = 0.52).

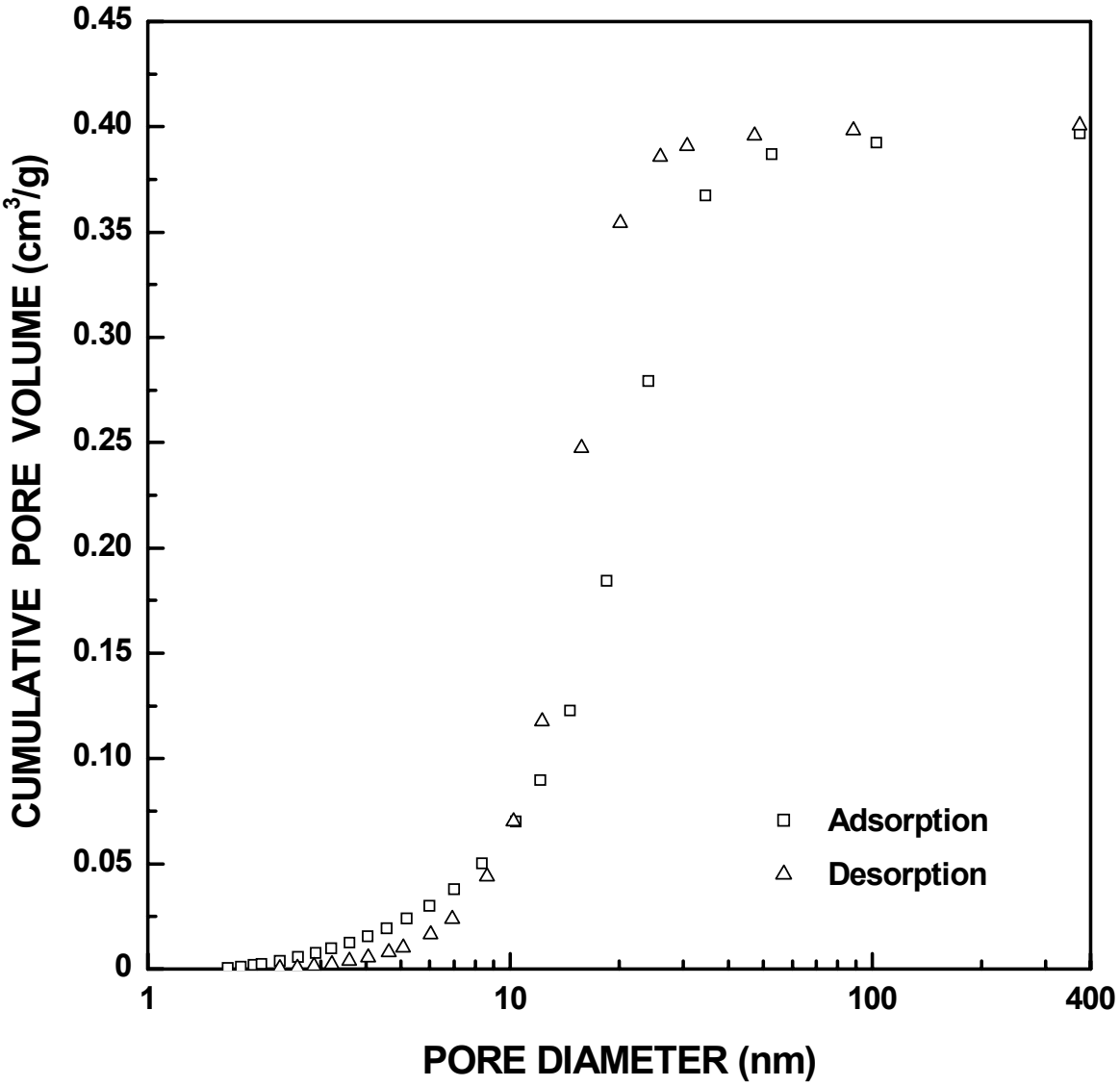

Figure 4-4-91 Plots of cumulative specific pore volume vs. pore diameter for SC35-1200(48h) sample (X_{WL} = 0.72).

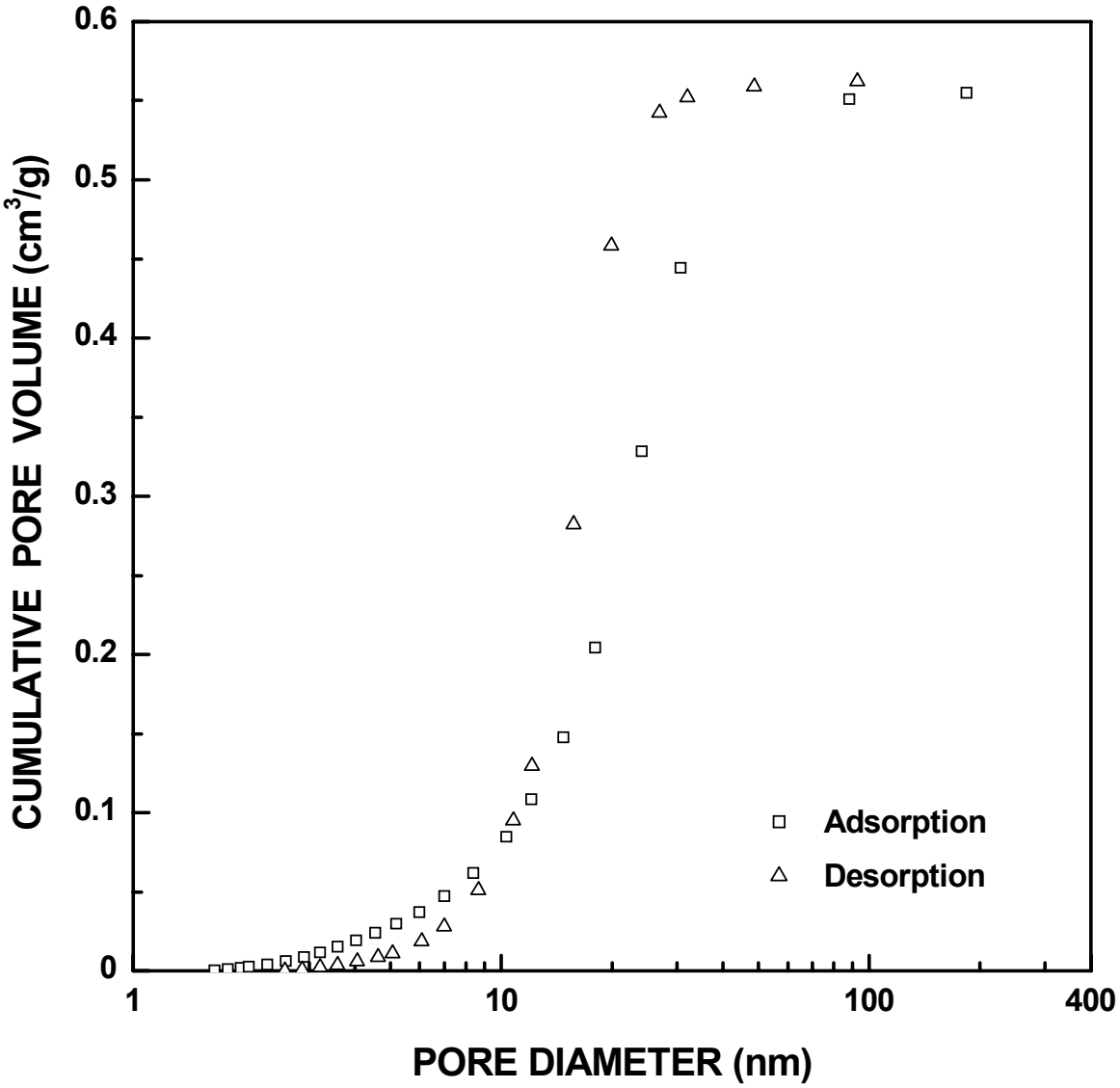

Figure 4-4-92 Plots of cumulative specific pore volume vs. pore diameter for SC35-1250(22h) sample (X_{WL} = 0.82).

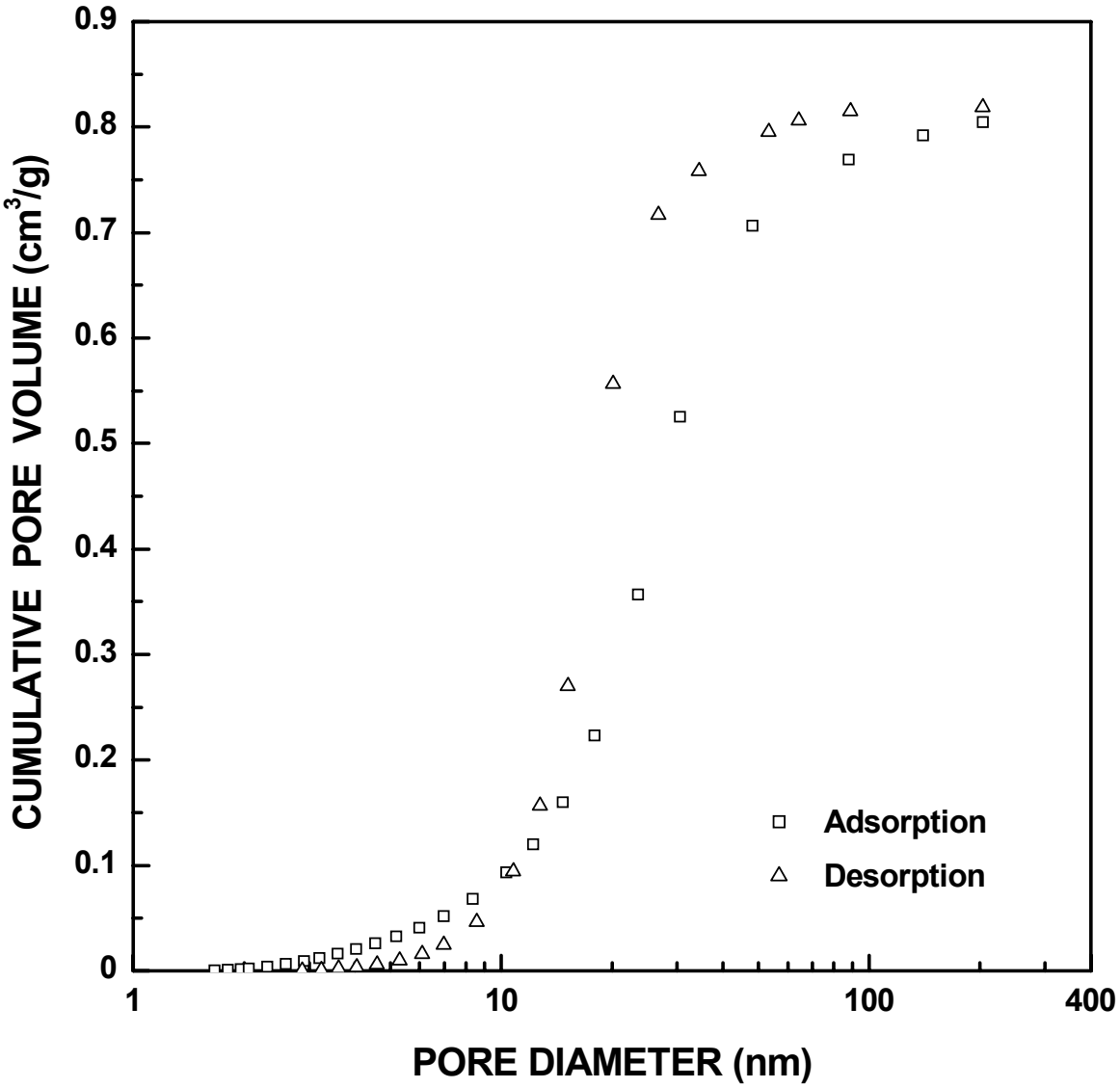

Figure 4-4-93 Plots of cumulative specific pore volume vs. pore diameter for SC35-1250(32h) sample (X_{WL} = 0.95).

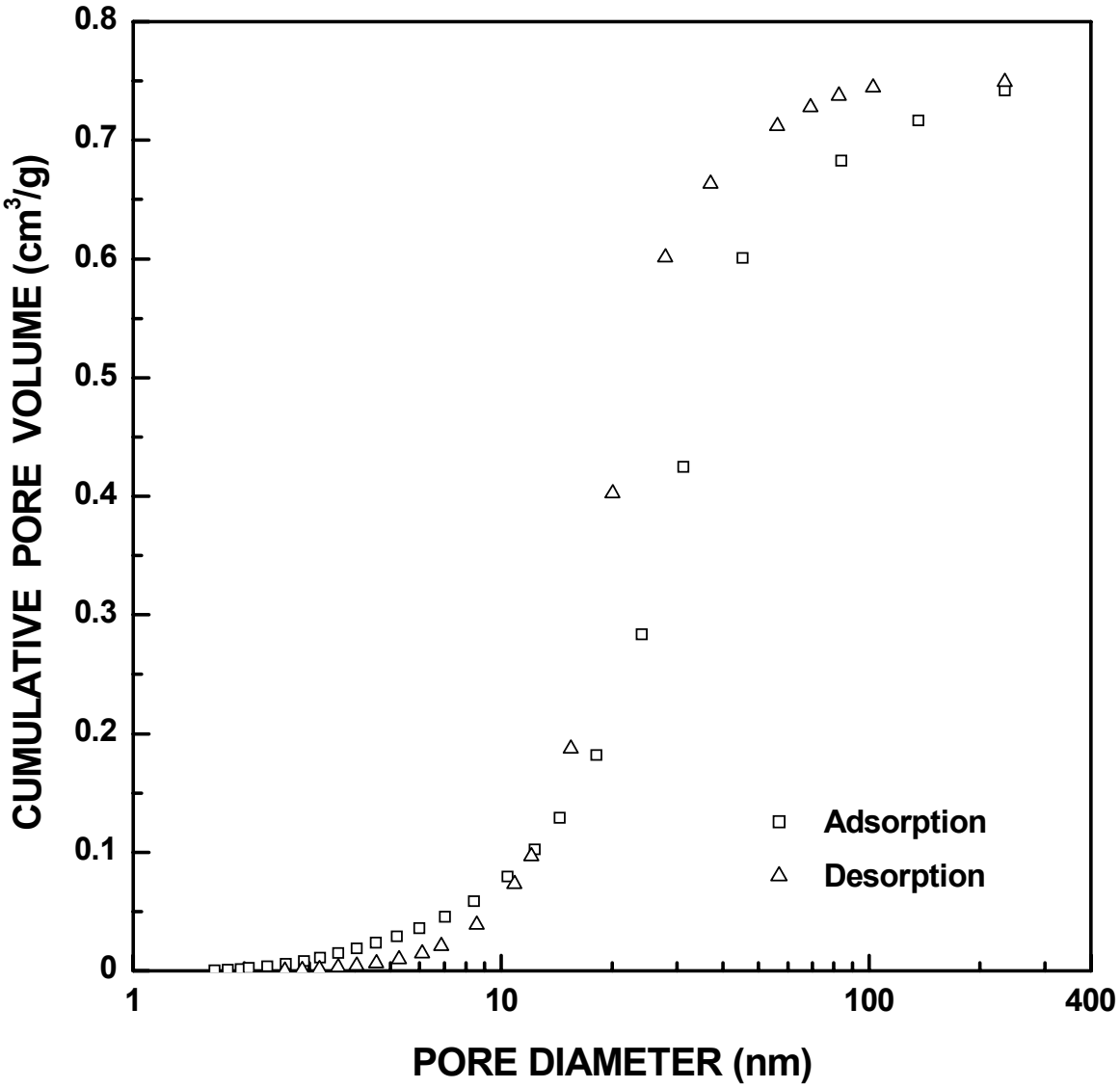

Figure 4-4-94 Plots of cumulative specific pore volume vs. pore diameter for SC35-1300(12h) sample (X_{WL} = 0.96).

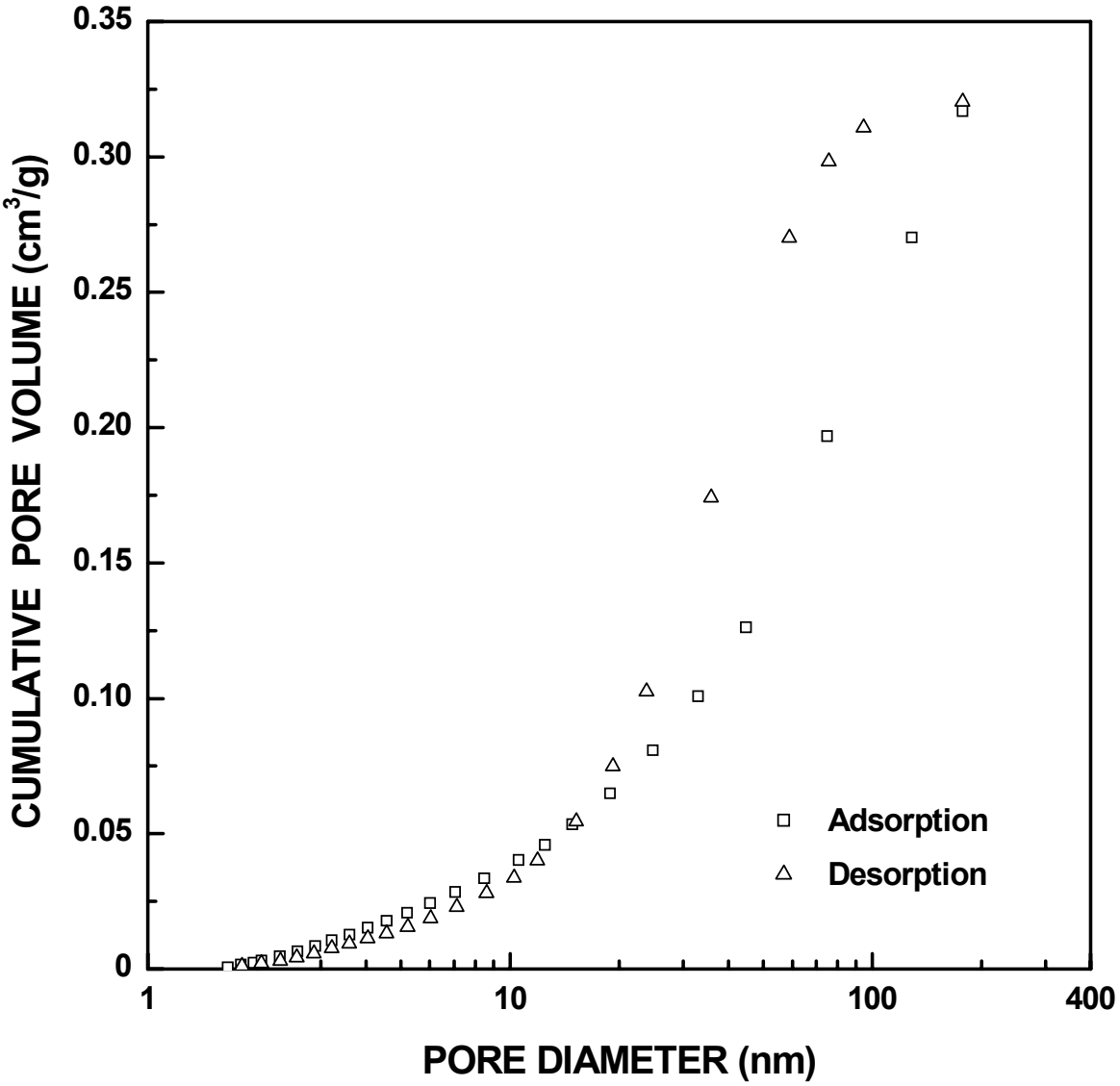

Figure 4-4-95 Plots of cumulative specific pore volume vs. pore diameter for SC35-1300(16h) sample (X_{WL} = 0.98).

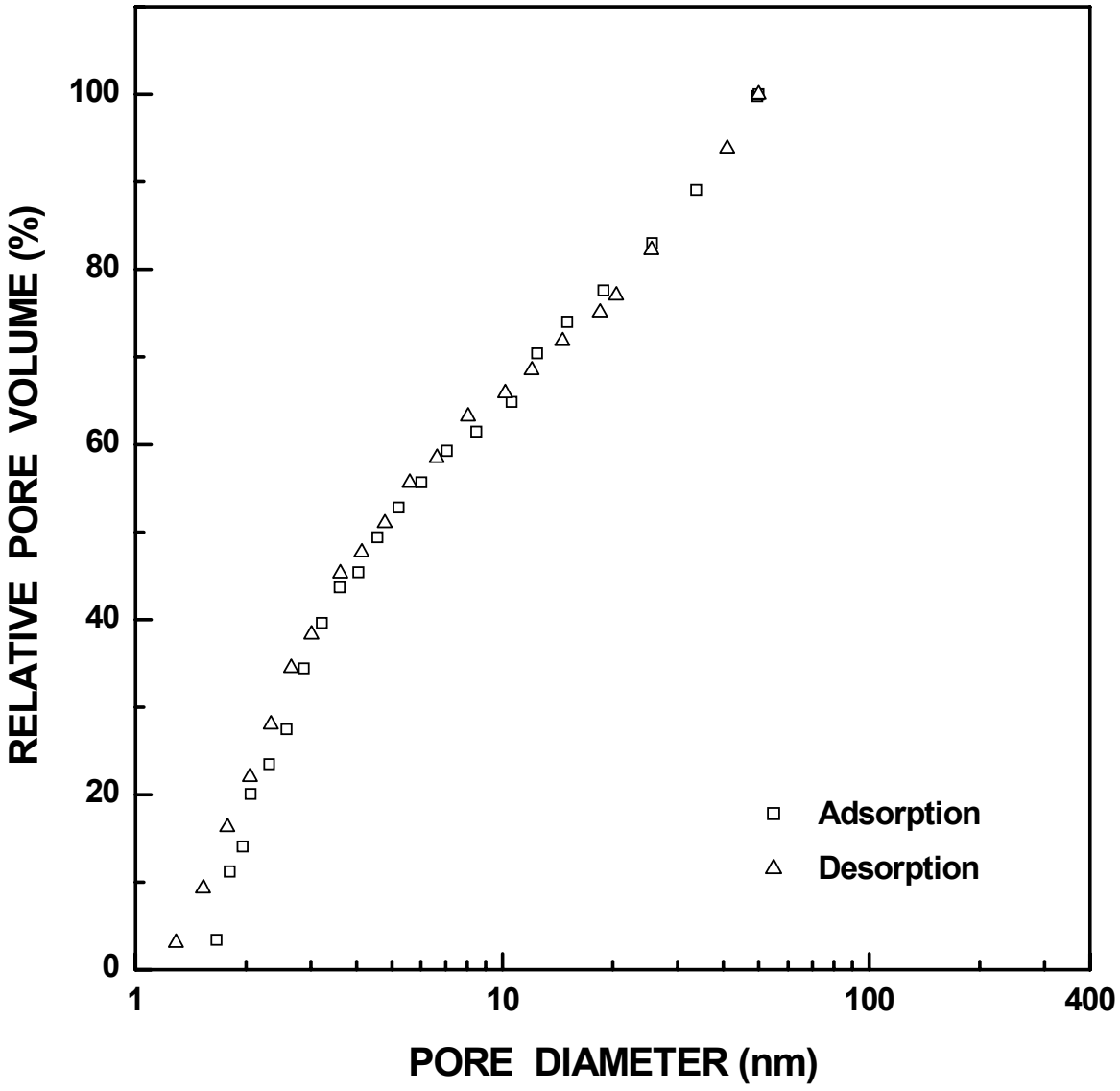

Figure 4-4-96 Plots of relative ("normalized") pore volume vs. pore diameter for SC35-1160(1h) sample (X_{WL} = 0.02). The pore diameter was cut off at 50 nm.

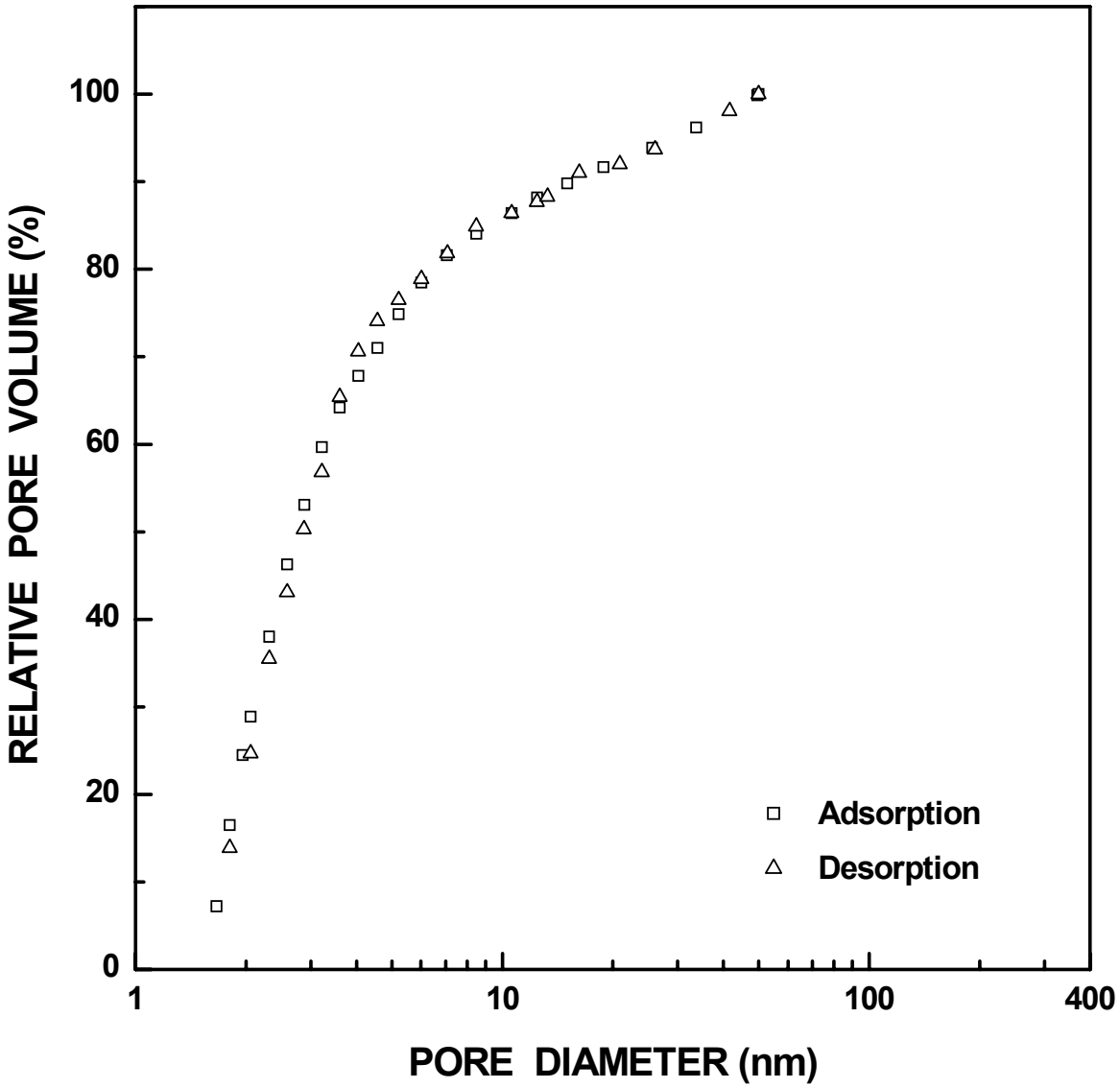

Figure 4-4-97 Plots of relative ("normalized") pore volume vs. pore diameter for (X_{WL} = 0.03). The pore diameter was cut off at 50 nm.

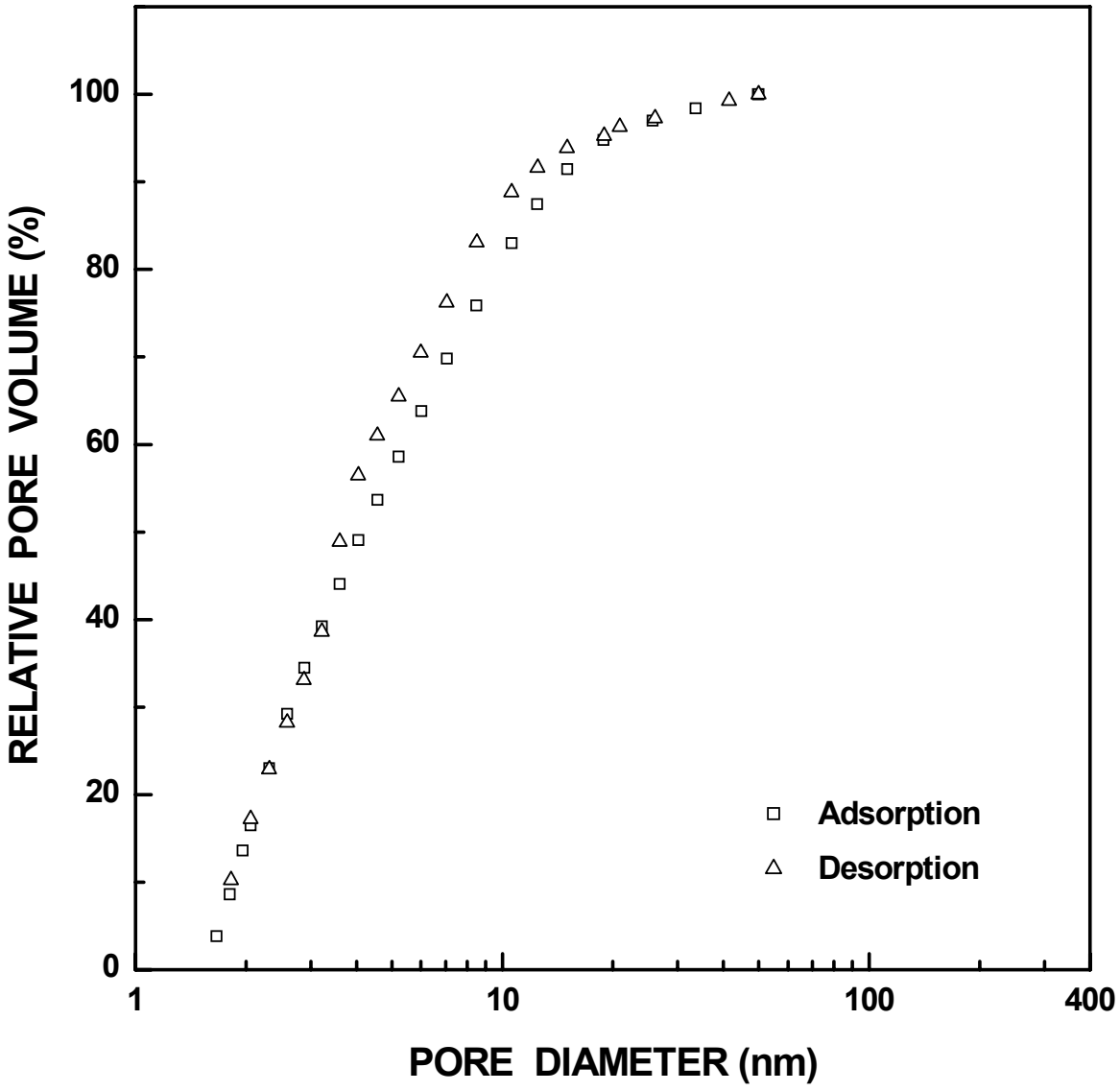

Figure 4-4-98 Plots of relative ("normalized") pore volume vs. pore diameter for SC35-1200(2h) sample (X_{WL} = 0.05). The pore diameter was cut off at 50 nm.

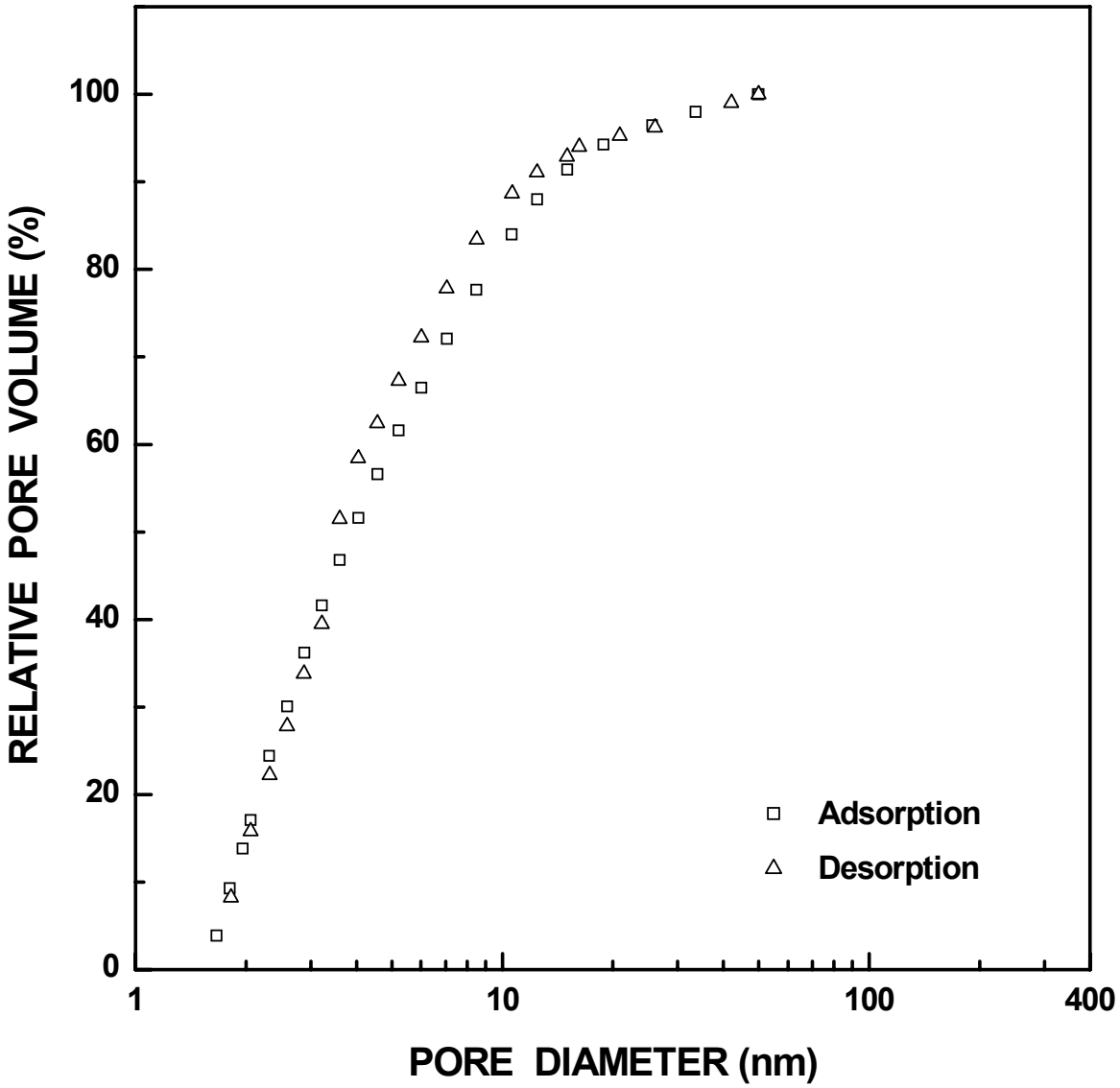

Figure 4-4-99 Plots of relative ("normalized") pore volume vs. pore diameter for SC35-1250(30min) sample (X_{WL} = 0.05). The pore diameter was cut off at 50 nm.

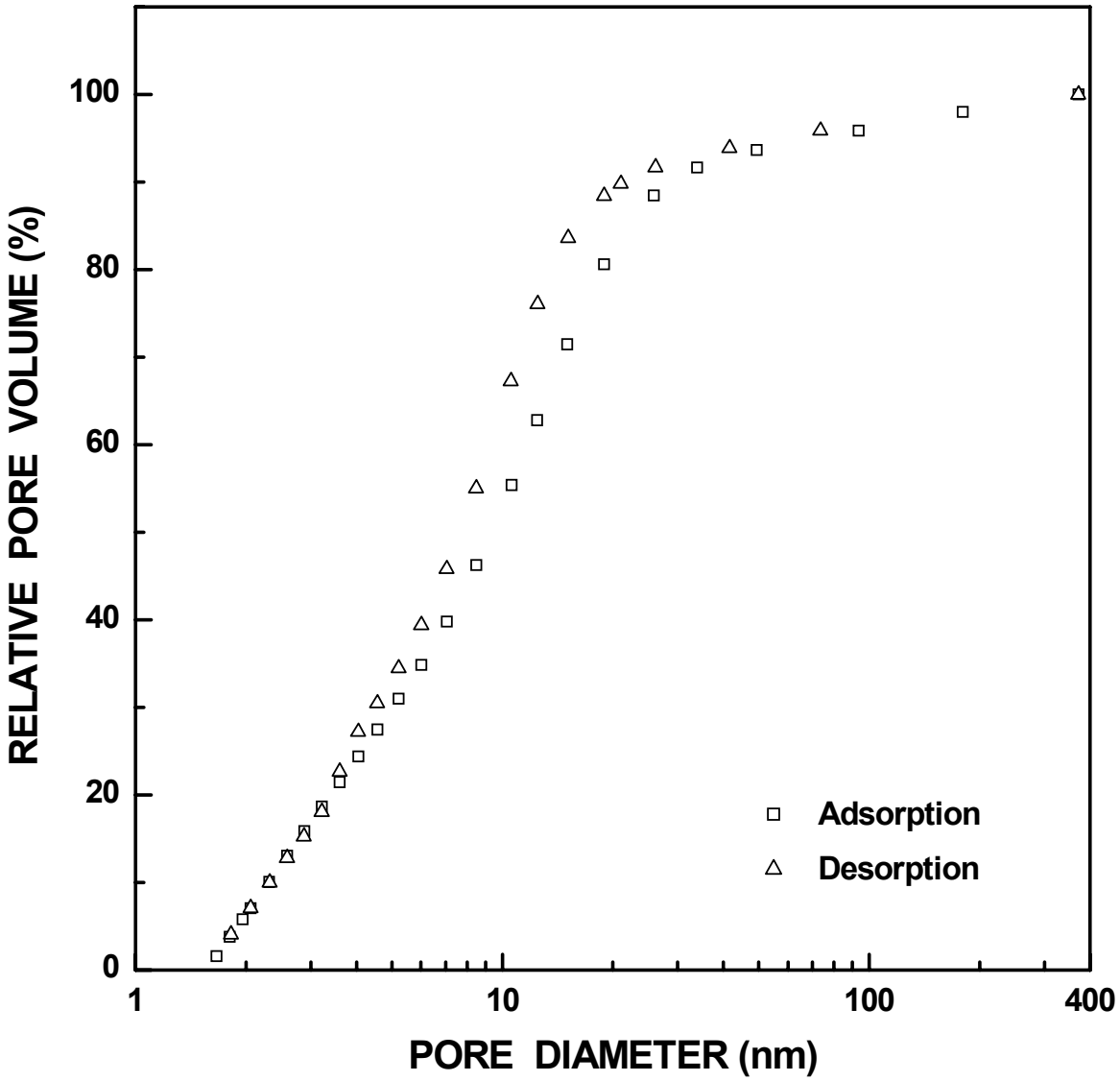

Figure 4-4-100 Plots of relative ("normalized") pore volume vs. pore diameter for SC35-1250(1h) sample (X_{WL} = 0.07).

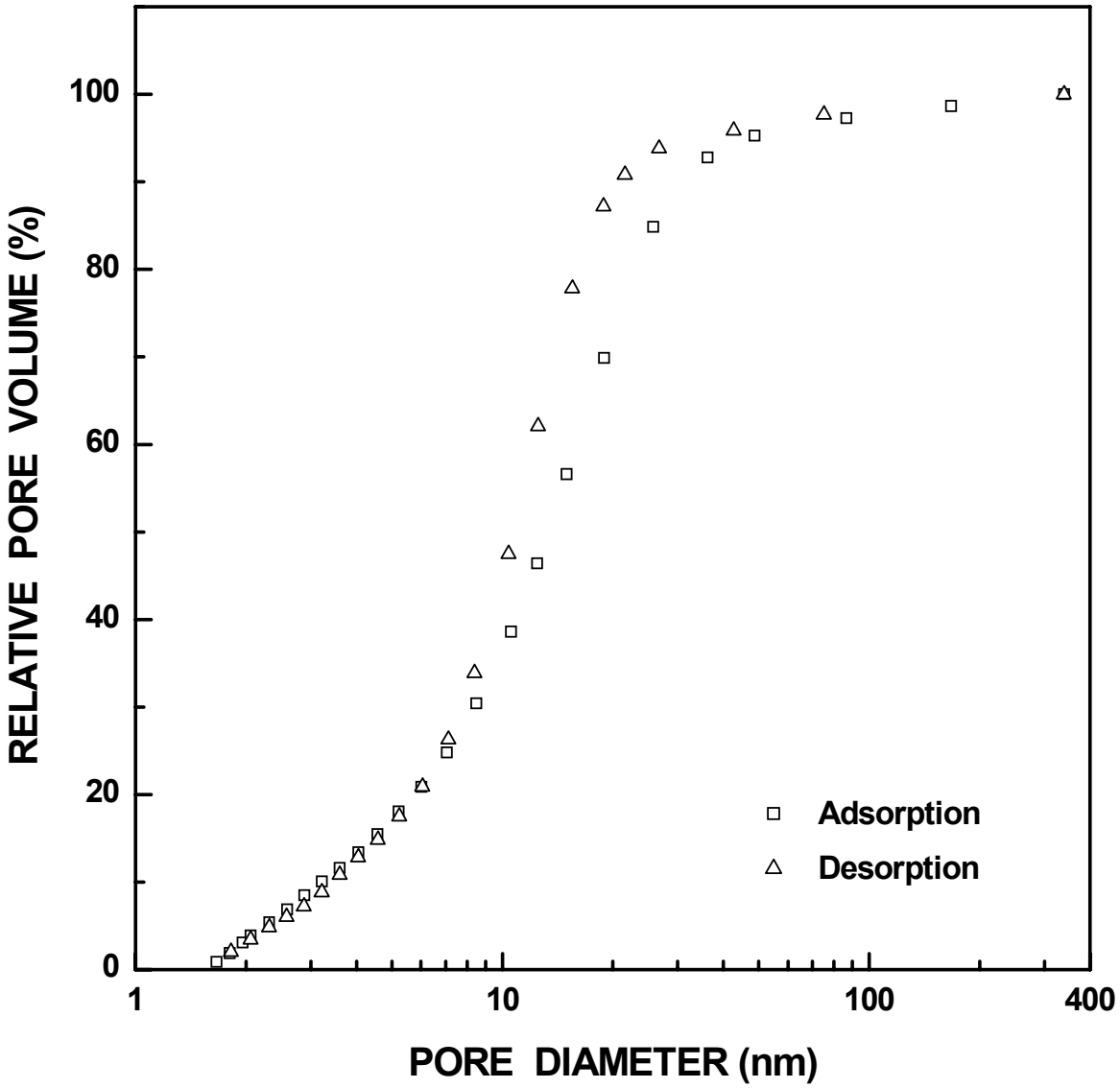

Figure 4-4-101 Plots of relative ("normalized") pore volume vs. pore diameter for SC35-1250(2h) sample (X_{WL} = 0.12).

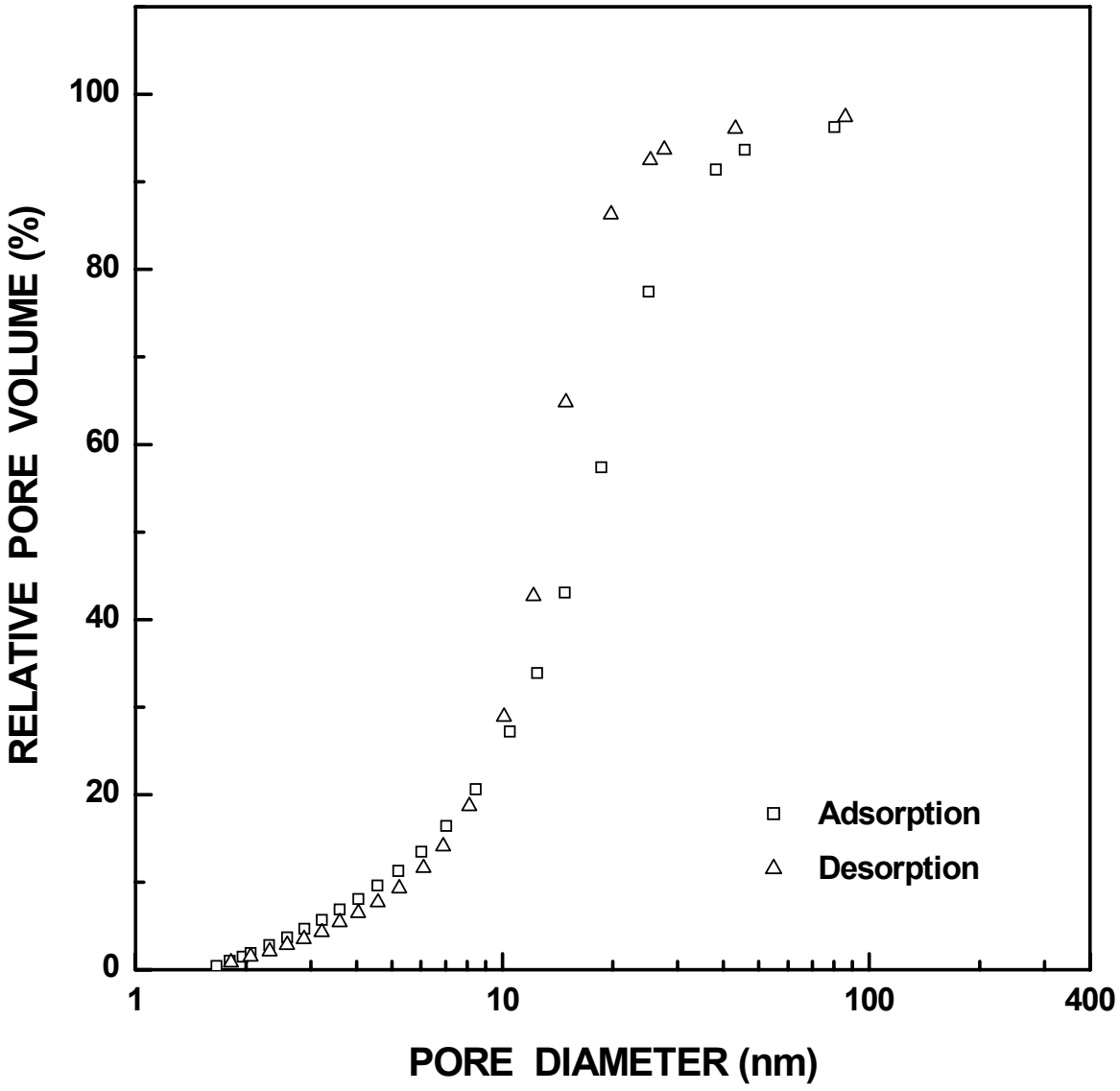

Figure 4-4-102 Plots of relative ("normalized") pore volume vs. pore diameter for SC35-1250(4h) sample (X_{WL} = 0.23).

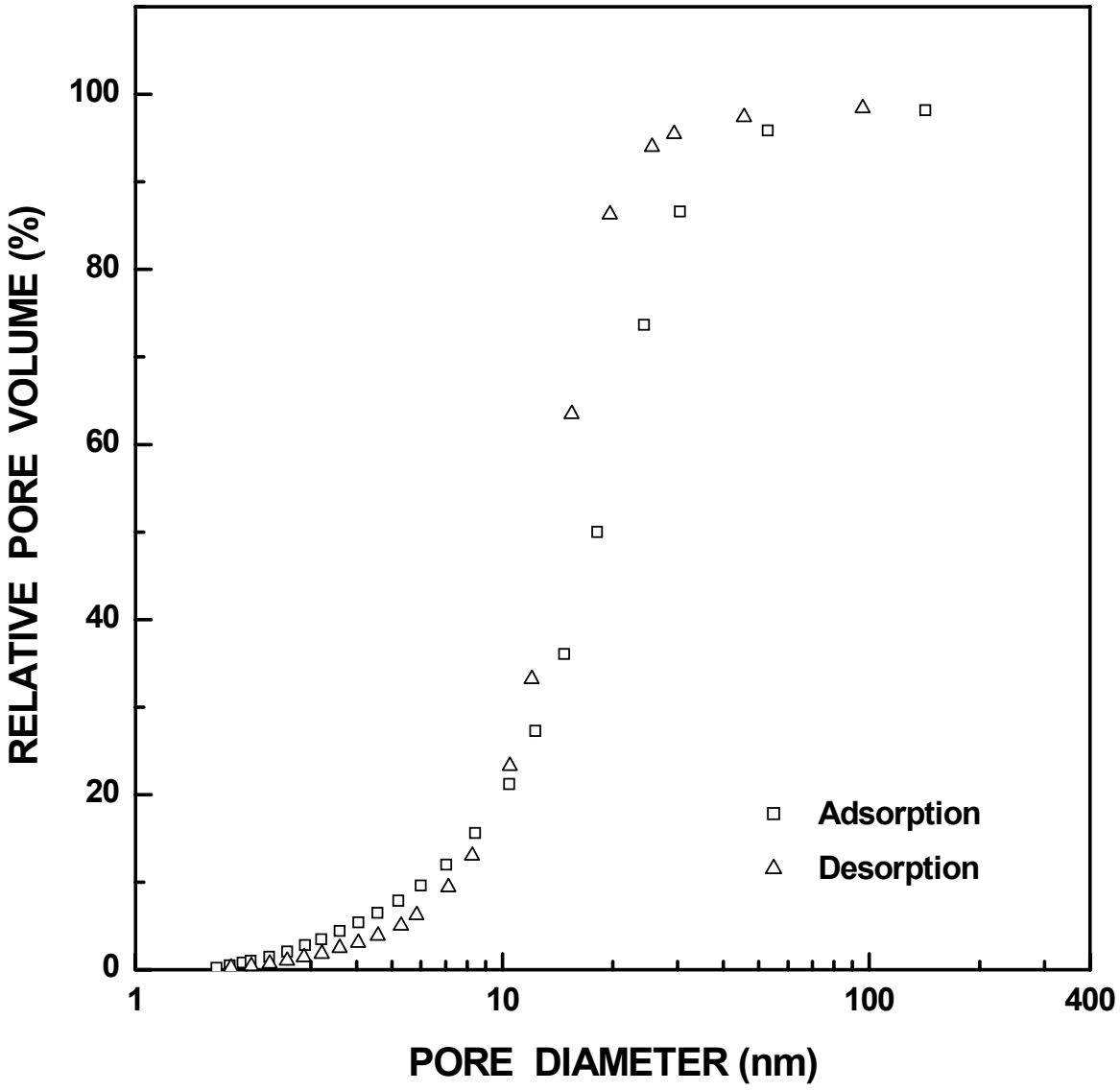

Figure 4-4-103 Plots of relative ("normalized") pore volume vs. pore diameter for SC35-1250(8h) sample (X_{WL} = 0.41).

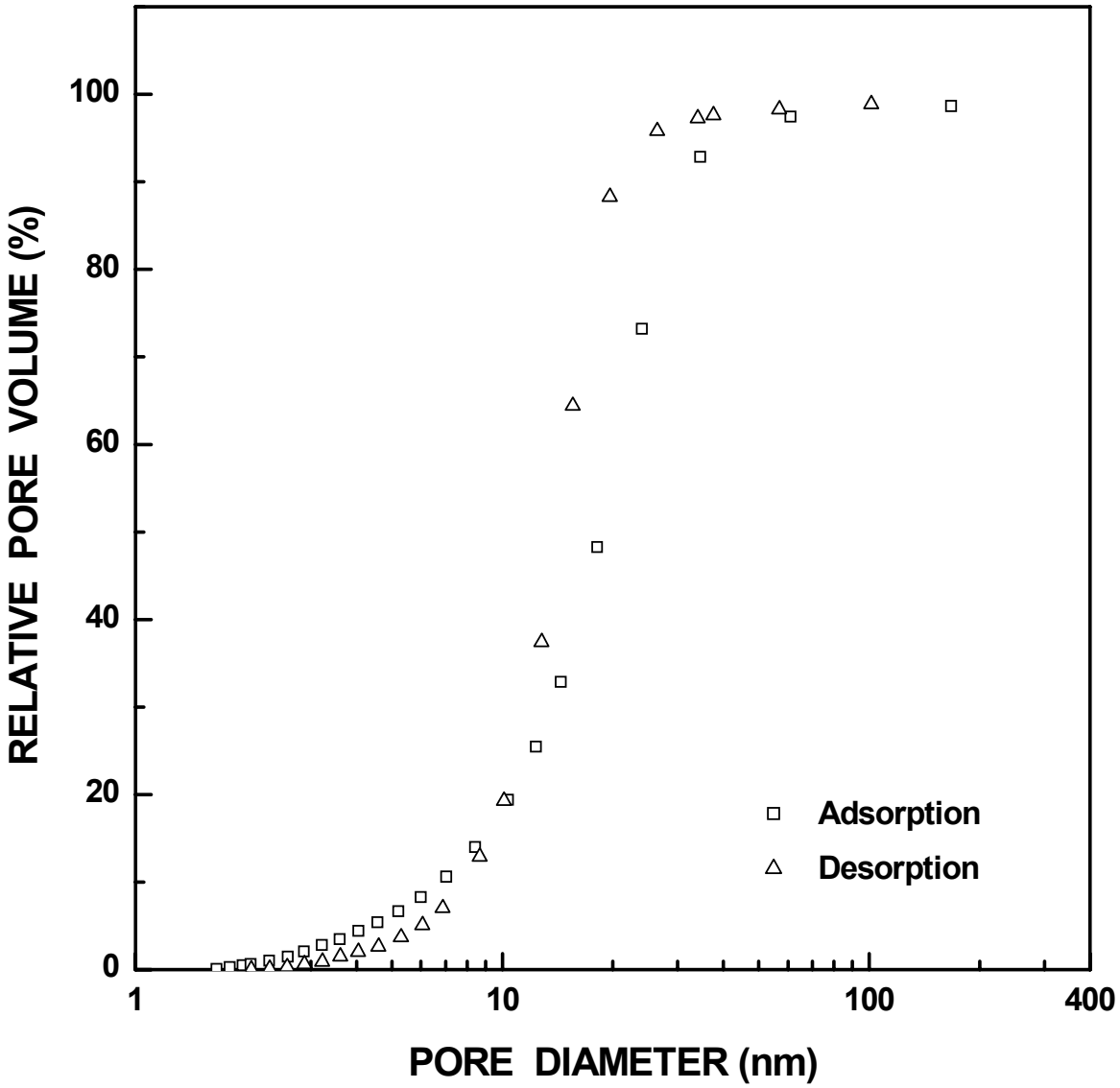

Figure 4-4-104 Plots of relative ("normalized") pore volume vs. pore diameter for SC35-1200(32h) sample (X_{WL} = 0.52).

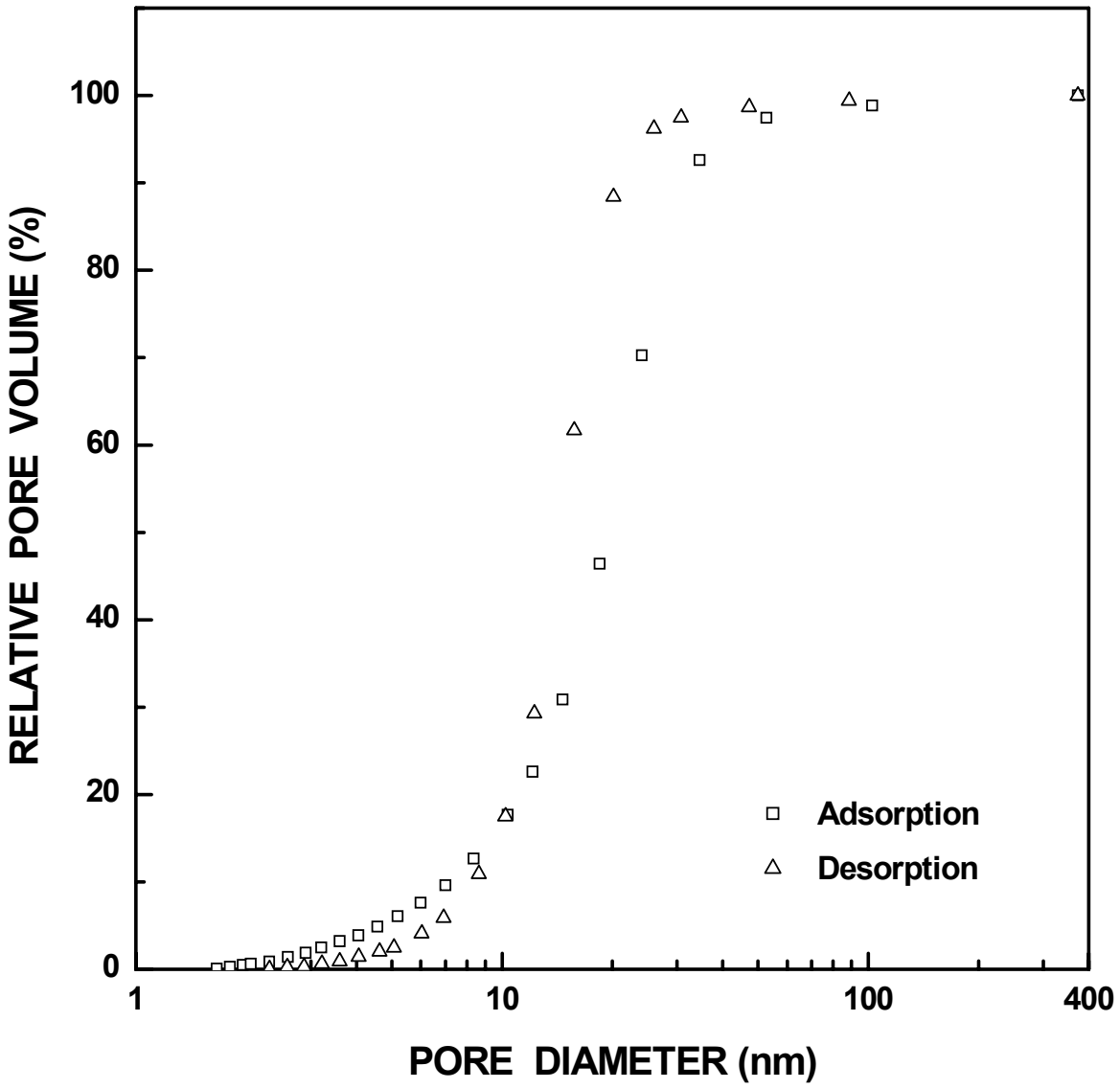

Figure 4-4-105 Plots of relative ("normalized") pore volume vs. pore diameter for SC35-1200(48h) (X_{WL} = 0.72).

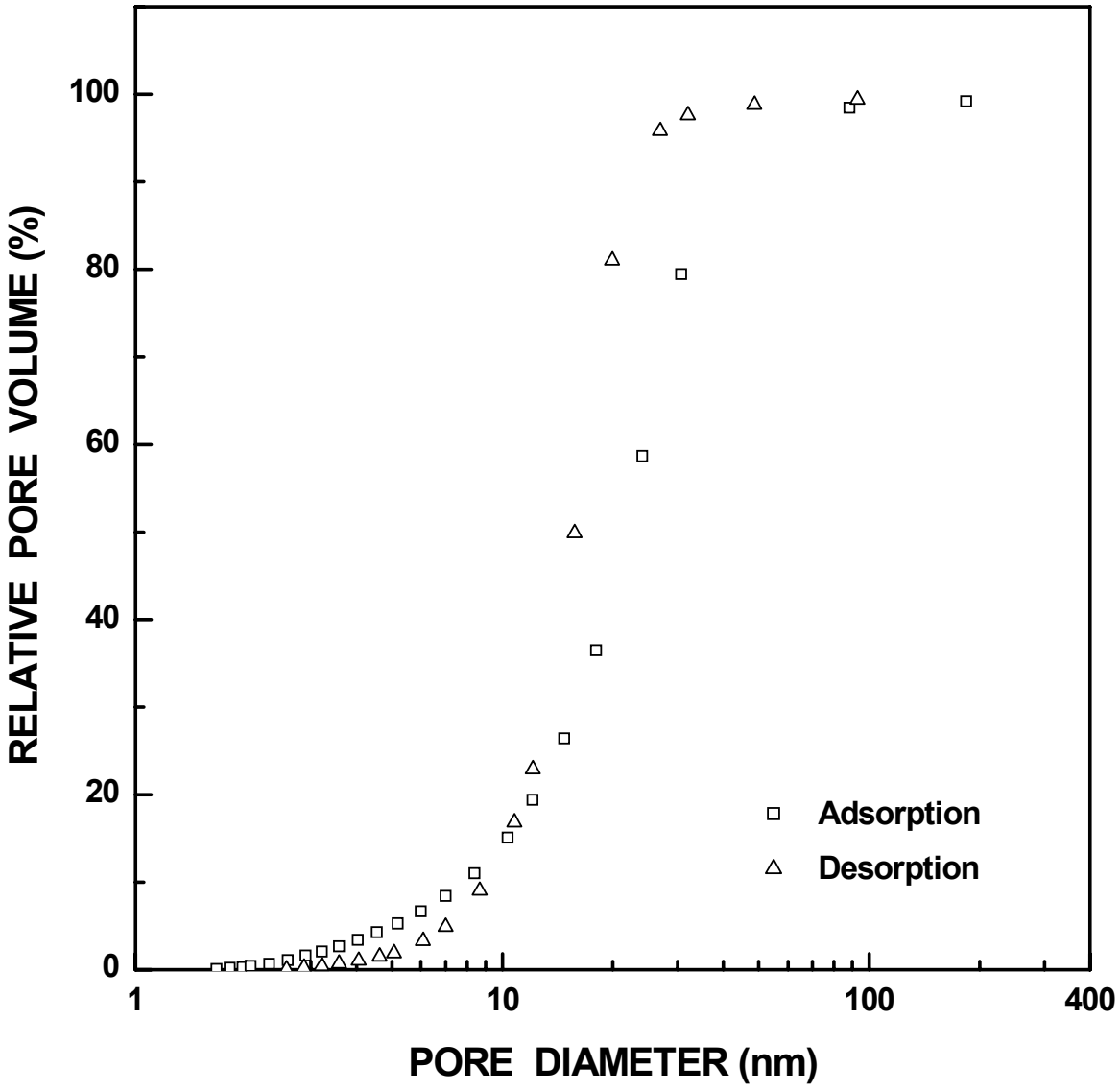

Figure 4-4-106 Plots of relative ("normalized") pore volume vs. pore diameter for SC35-1250(22h) sample (X_{WL} = 0.82).

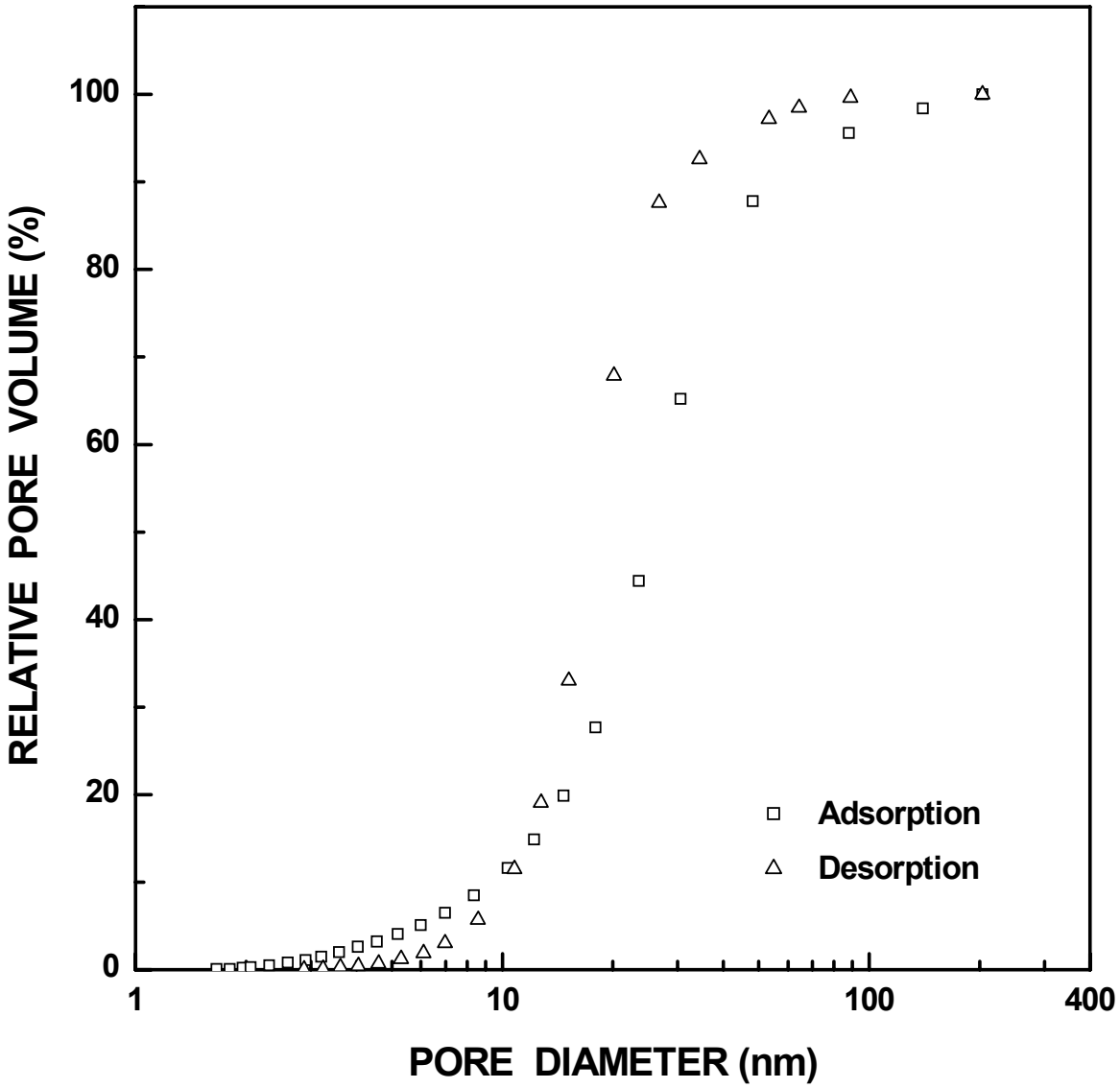

Figure 4-4-107 Plots of relative ("normalized") pore volume vs. pore diameter for SC35-1250(32h) sample (X_{WL} = 0.95).

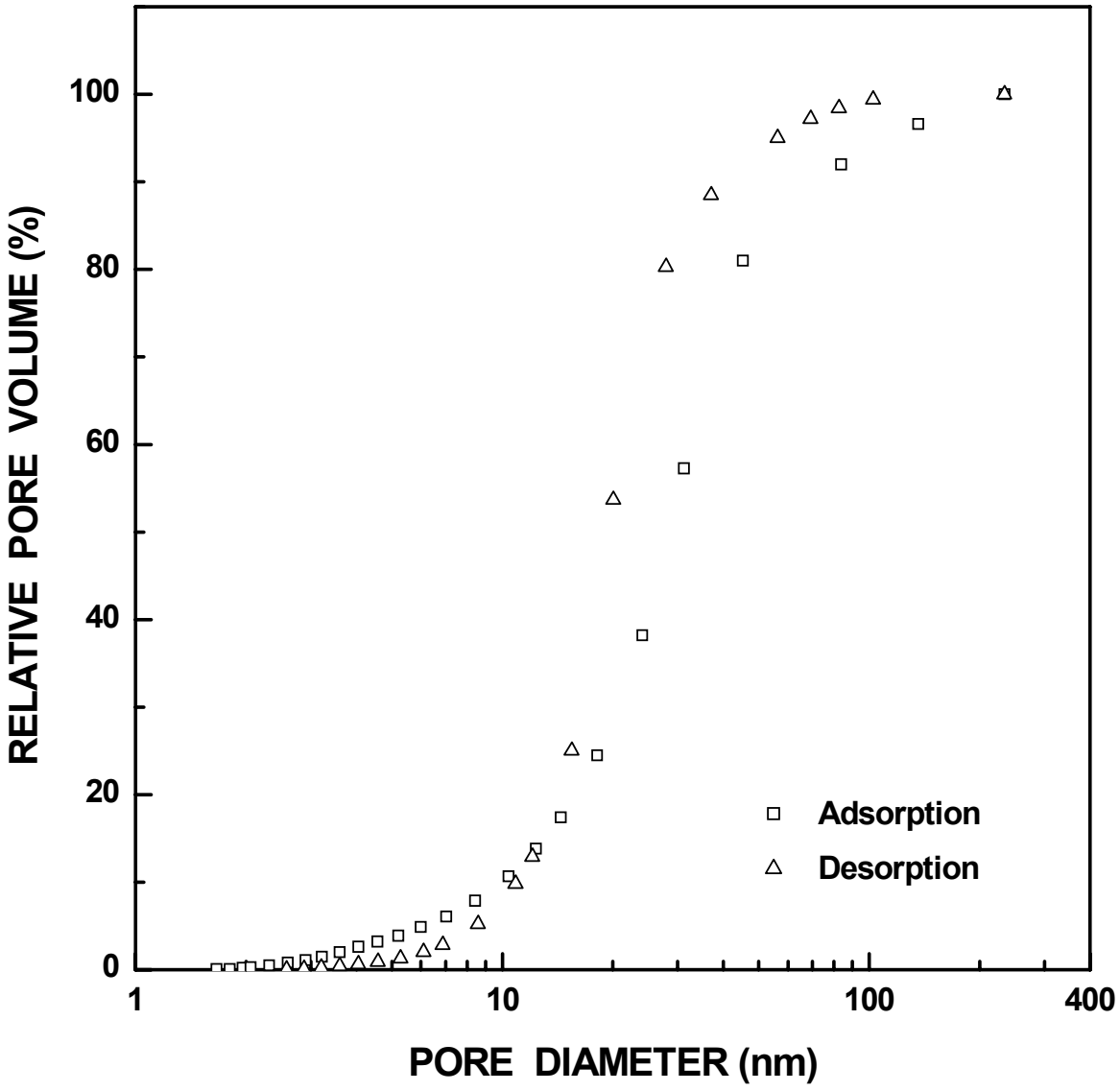

Figure 4-4-108 Plots of relative ("normalized") pore volume vs. pore diameter for SC35-1300(12h) sample (X_{WL} = 0.96).

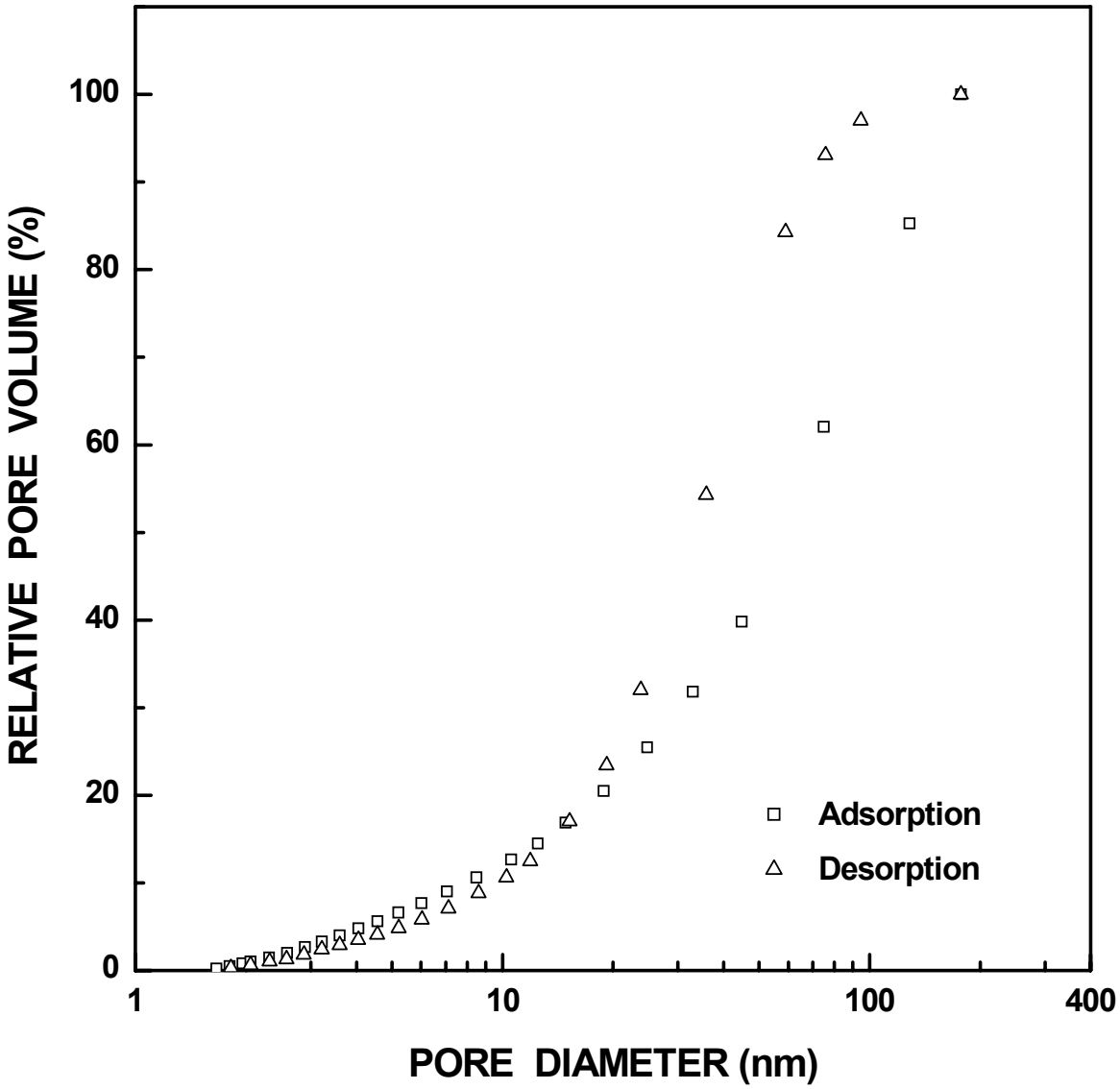

Figure 4-4-109 Plots of relative ("normalized") pore volume vs. pore diameter for SC35-1300(16h) sample (X_{WL} = 0.98).

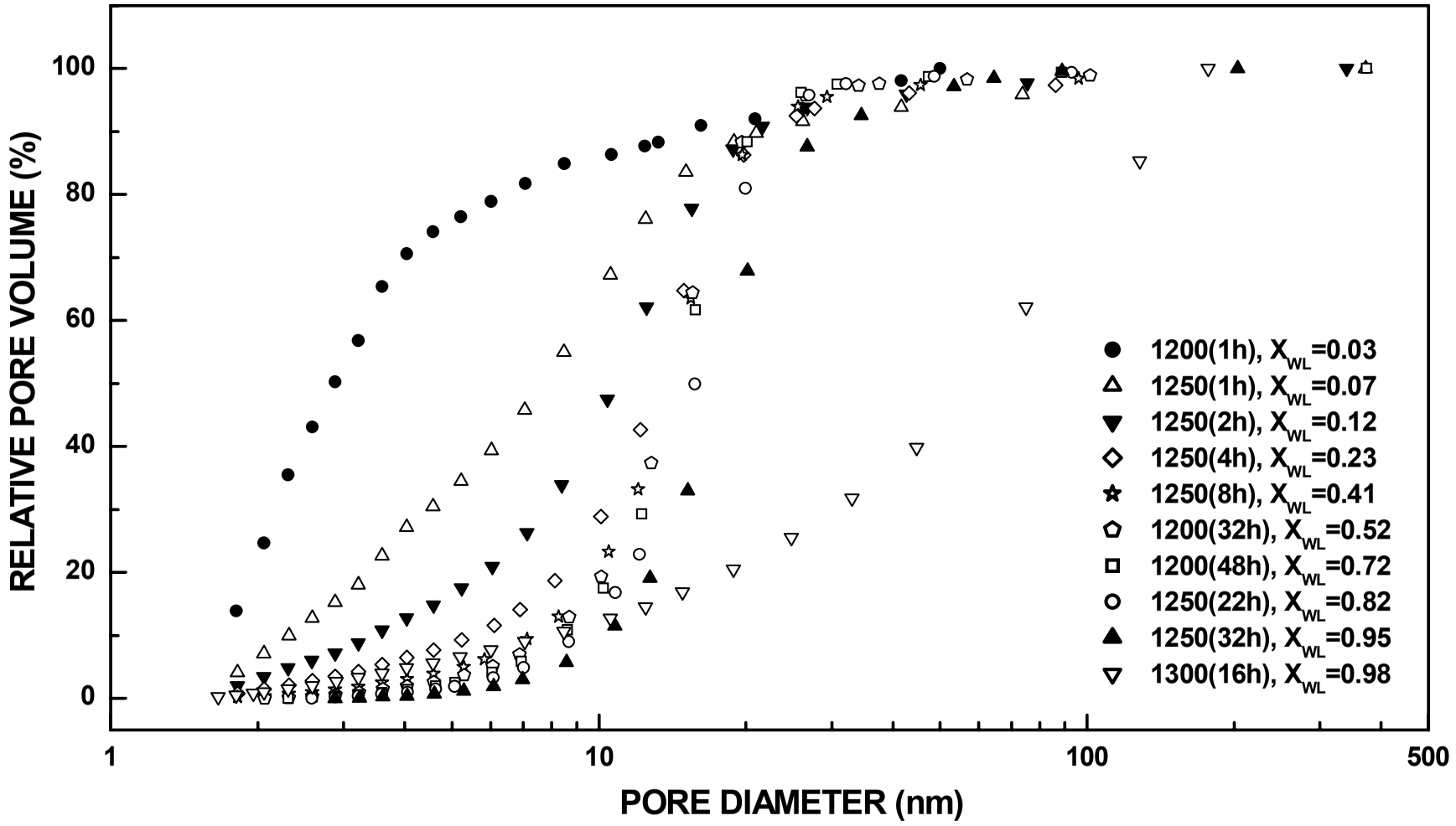

Figure 4-4-110 Normalized cumulative pore size distribution plots (from the desorption branch of the isotherm) for SC35 CTR samples with varying fractional weight loss values in the range of 0.03-0.98.

cumulative pore size distribution plots for samples with varying extents of conversion. The data from the desorption branch of the isotherm are used in these plots. The pore size distributions shift to much larger sizes as the fractional weight loss of the sample increases from X_{WL} = 0.03 (e.g., SC35-1200(1h)) to X_{WL} = 0.23 (SC35-1250(4h)). There is almost no change in the pore size distributions for samples with X_{WL} values in the range of 0.23 - 0.82. The pore size distributions begin to shift to larger sizes for the SC35-1250(32h) sample (X_{WL} = 0.95). Then there is a shift in the distribution to much larger size for the SC35-1300(16h) sample (X_{WL} = 0.98).

Figures 4-4-111 shows a plot of the median pore diameter (D_{50}) as a function of fractional weight loss. As expected from the pore size distribution plots, the median pore diameter (D_{50}) increases rapidly during the early stages of the reaction, then shows relatively little change for much of the subsequent reaction, and finally shows a sharp increase in late stages of the reaction. The 90-percentile diameter (D_{90}) of the distribution is plotted as a function of the extent of reaction in Figure 4-4-112. (The 90 percentile diameter, D_{90}, is the diameter for which 90 % of pores (by volume) are less than or equal to that size.) The D_{90} diameter remains nearly constant for most of the reaction and then a rapid increase in size is observed in the late stages of the reaction (i.e., similar to the change in D_{50} toward the end of the reaction). The 10-percentile diameter (D_{10}) of the distribution shows a continuous increase for almost the entire range of the reaction (Figure 4-4-113). The latter trend indicates that most of the pore volume that develops as the CTR reaction proceeds is associated with larger pore sizes. (This point will be illustrated more clearly in some other plots below, e.g., Figure 4-4-131.) Figure 4-4-114 shows plots of D_{10}, D_{50}, and D_{90} vs. fractional weight loss for the SC35 samples.

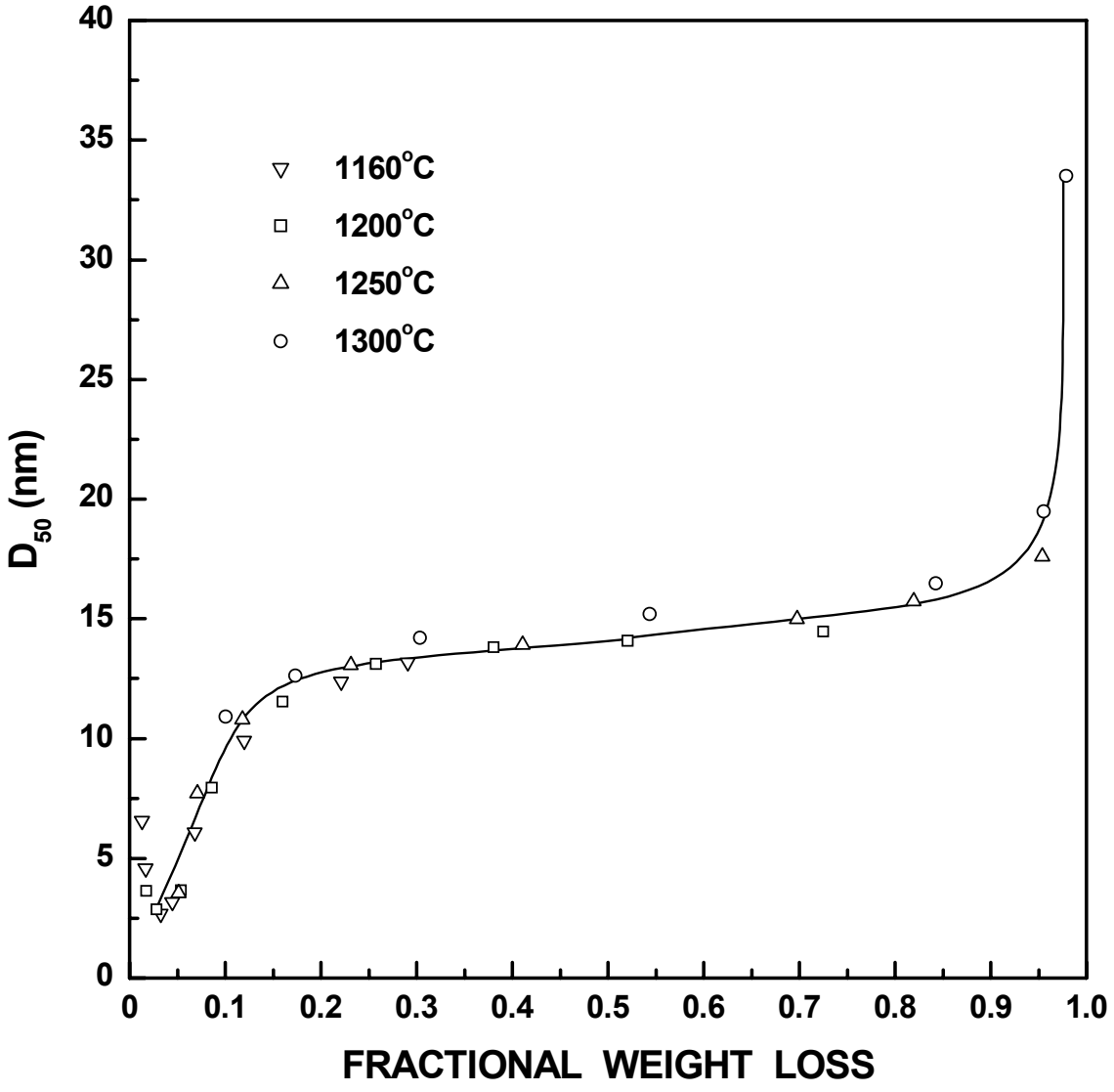

Figure 4-4-111 Plot of D_{50} (median pore diameter) vs. fractional weight loss for the SC35 CTR samples. The D_{50} data was obtained from the desorption isotherm.

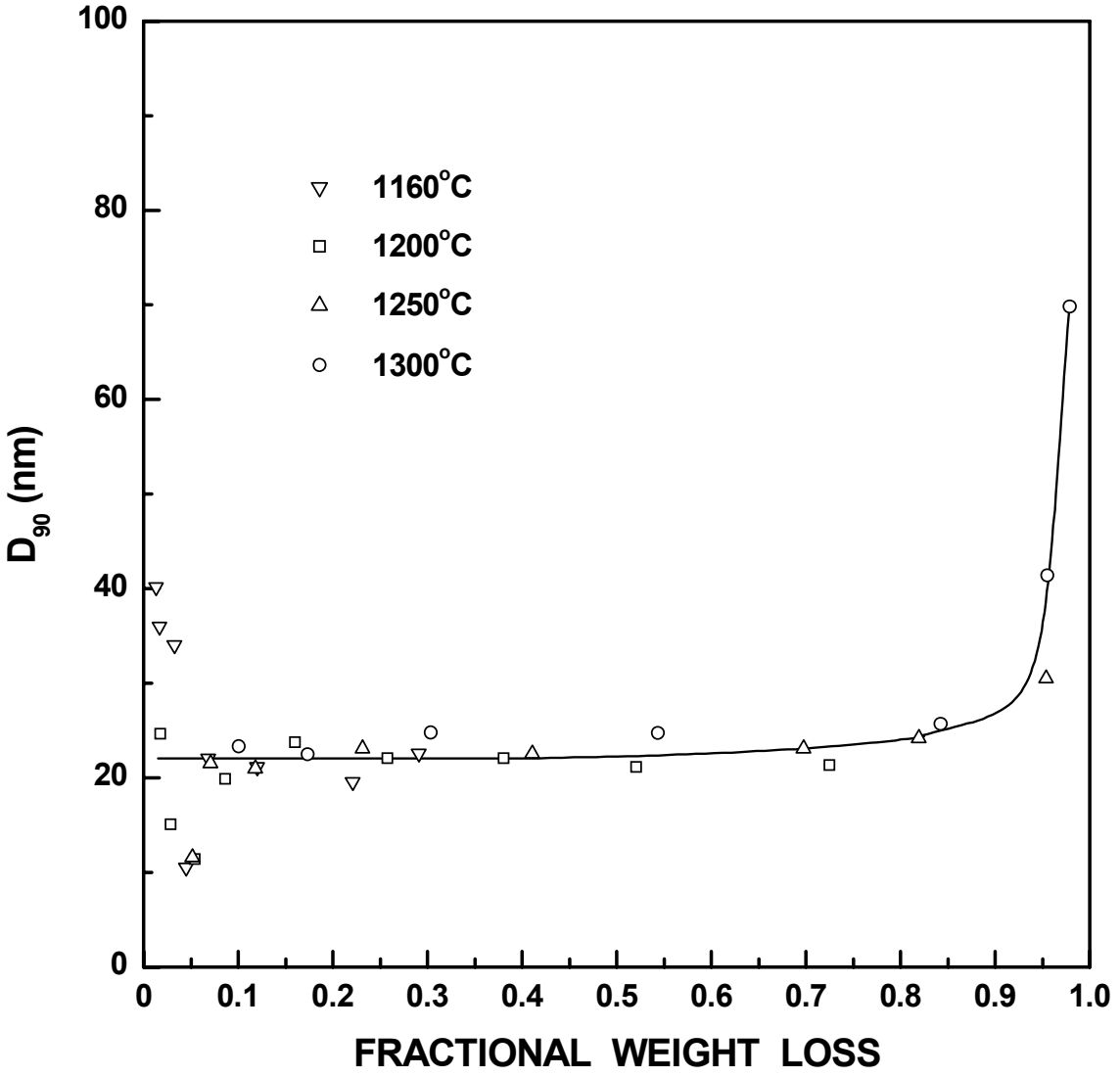

Figure 4-4-112 Plot of D_{90} (90-percentile diameter) vs. fractional weight loss for the SC35 CTR samples. The D_{90} data was obtained from the desorption isotherm.

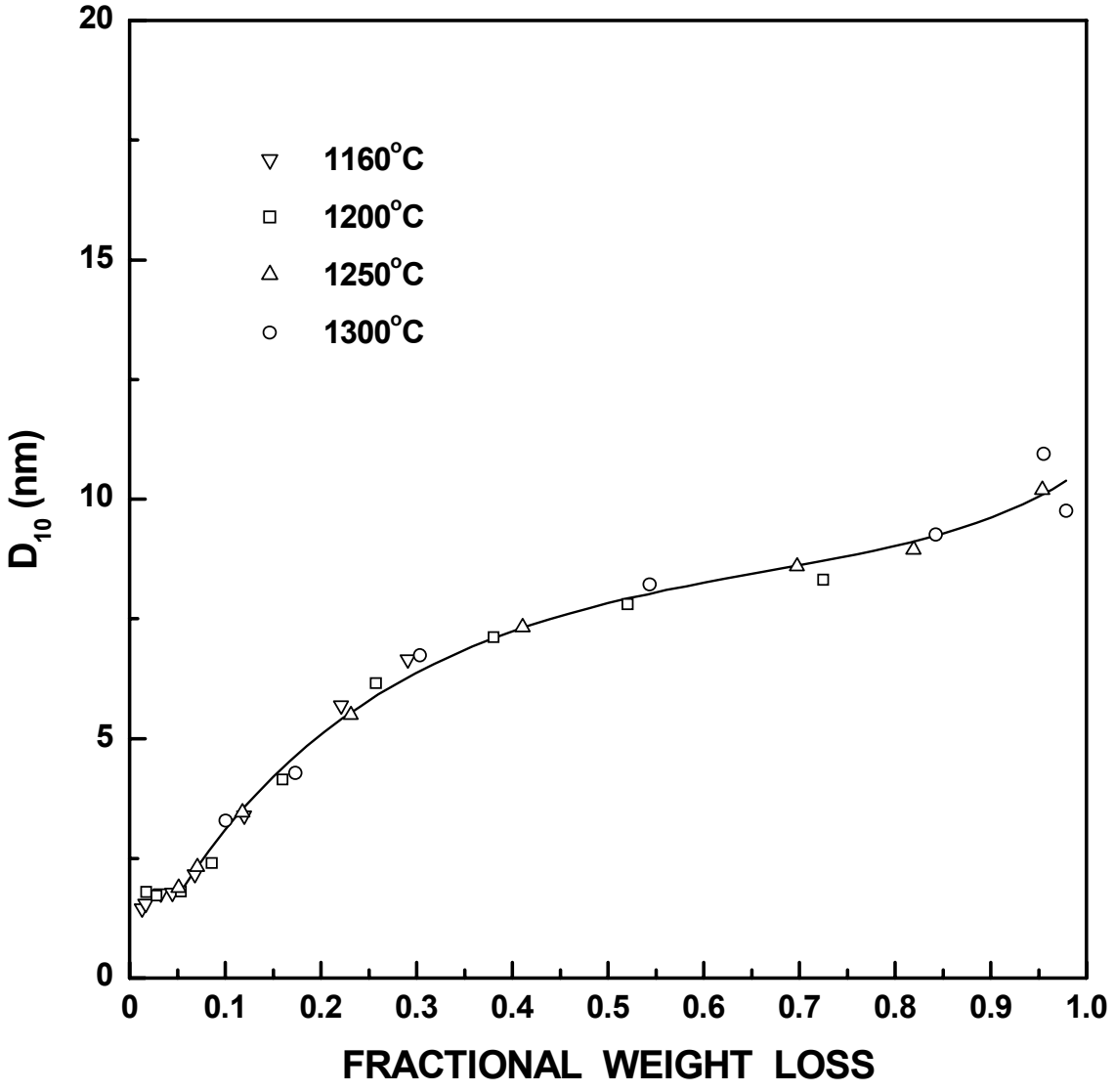

Figure 4-4-113 Plot of D_{10} (10-percentile diameter) vs. fractional weight loss for the SC35 CTR samples. The D_{10} data was obtained from the desorption isotherm.

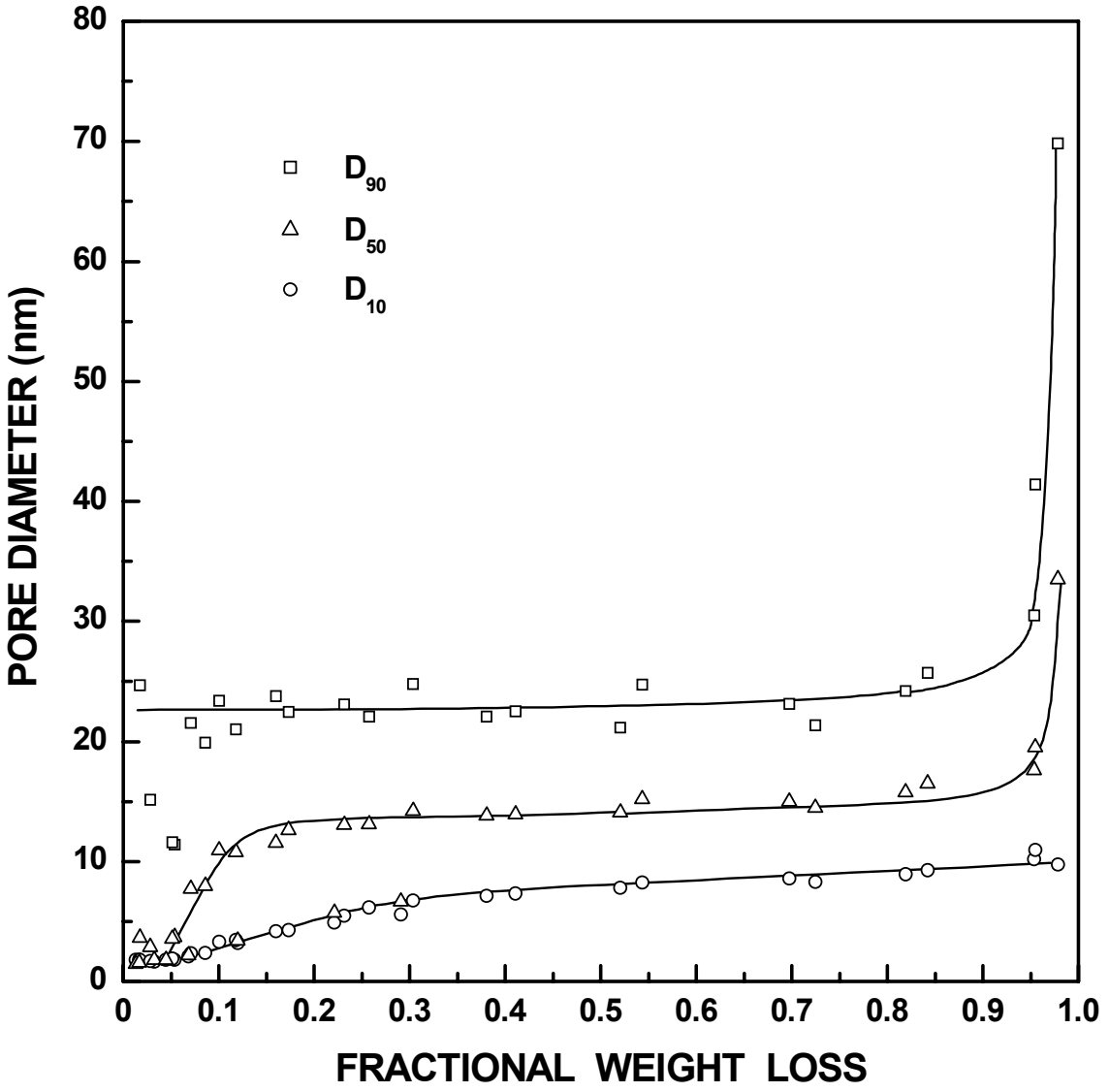

Figure 4-4-114 Plots of D_{10}, D_{50}, D_{90} (the 10-, 50-, and 90-percentile diameter) vs. fractional weight loss for the SC35 CTR samples. The data were obtained from the desorption isotherm.

Plots of the pore volume frequency vs. pore diameter are shown in Figures 4-4-115 - 4-4-128. Corresponding plots of the "normalized" relative pore volume frequency vs. pore diameter are shown in Figures 4-4-129 - 4-4-142. The latter distributions were obtained by taking the derivative of the plots of the "normalized" cumulative pore volume distribution. Changes in the breadth and the bimodality of the pore size distributions are observed more readily in these figures. The pyrolyzed sample (Figure 4-1-13) and samples in the very early stages of the reaction (e.g., SC35-1160C(1h) with X_{WL} = 0.02 and SC35-1200C(1h) with X_{WL} = 0.03 in Figures 4-4-129 and 4-4-130, respectively) have almost mostly small pores (<5 nm). Figures 4-4-131 to 4-4-133 show that the pore size distributions gradually start to broaden as a greater percentage of larger pores (e.g., ~5-20 nm) are formed, such as those observed for the SC35-1200(2h) (X_{WL} = 0.05), SC35-1250(30min) (X_{WL} = 0.05) and SC35-1250(1h) (X_{WL} = 0.07) samples. This also results in the onset of bimodality in the distributions. (This is more evident in the data derived from the desorption portion of isotherm.) As mentioned earlier, the onset of bimodality in the distribution coincides with the initial appearance of the hysteresis loop (in the mesopore range) in the isotherms (Figures 4-4-70 to 4-4-72). The bimodality in the distribution becomes more pronounced as the pore volume increases, as observed in Figures 4-4-134 for the SC35-1250(2h) sample (X_{WL} = 0.12). (Similar distributions were observed for SC35-1160(16h) with X_{WL} = 0.12, SC35-1200(4h) with X_{WL} = 0.09, and SC35-1300(0.5h) with X_{WL} = 0.10) samples, as shown in Appendix I.) The increase in pore volume is mainly due to the development of larger pores (e.g., ~5-25 nm). This same type of pore development continues for most of the reaction, as observed in Figures 4-4-135 to 4-4-140 for SC35-1250(4h) with X_{WL} = 0.23, SC35-1250(8h) with X_{WL} = 0.41, SC35-1200(32h)

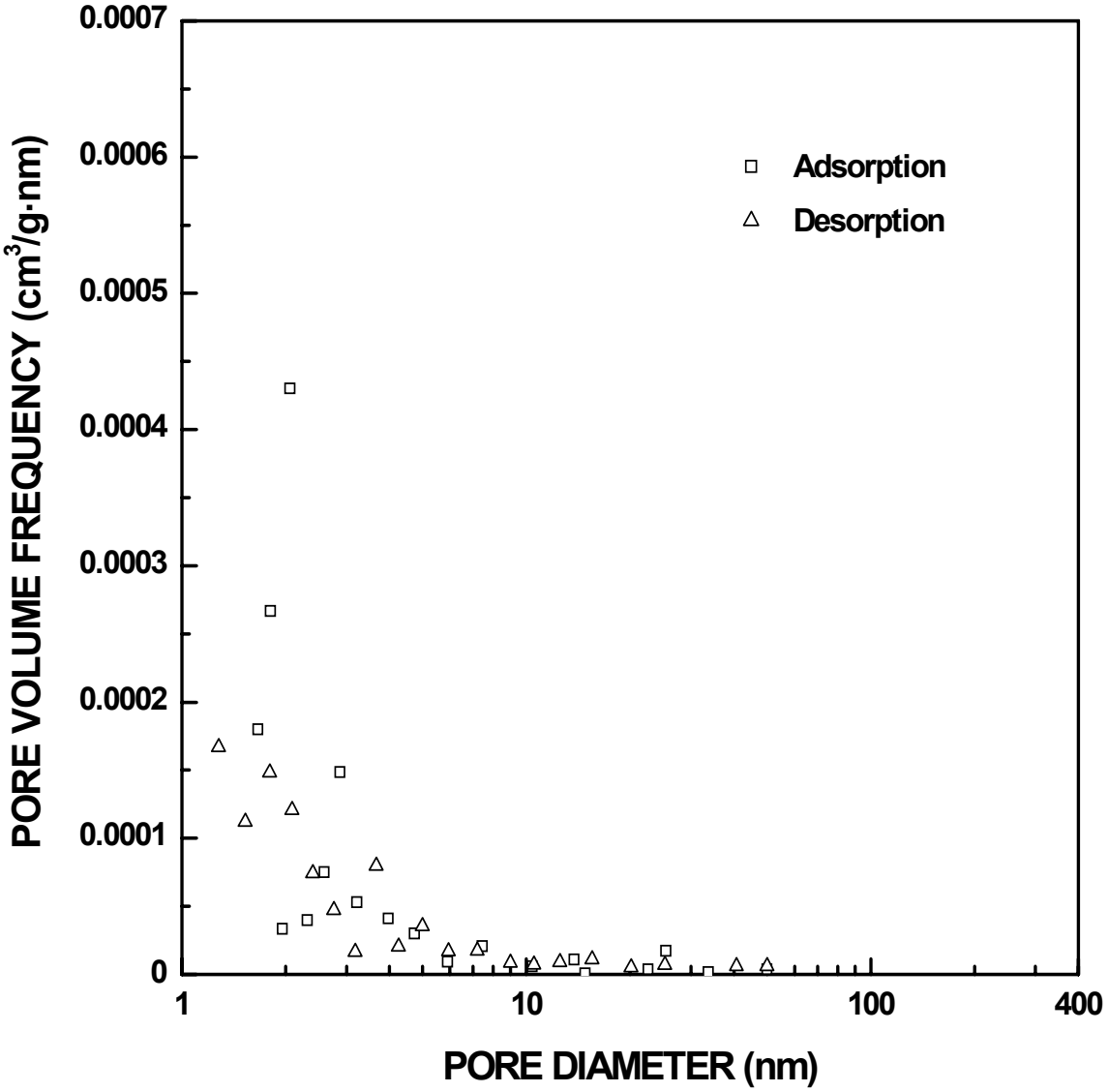

Figure 4-4-115 Plots of specific pore volume frequency vs. pore diameter for the SC35-1160(1h) sample (X_{WL} = 0.02). The pore diameter was cut off at 50 nm.

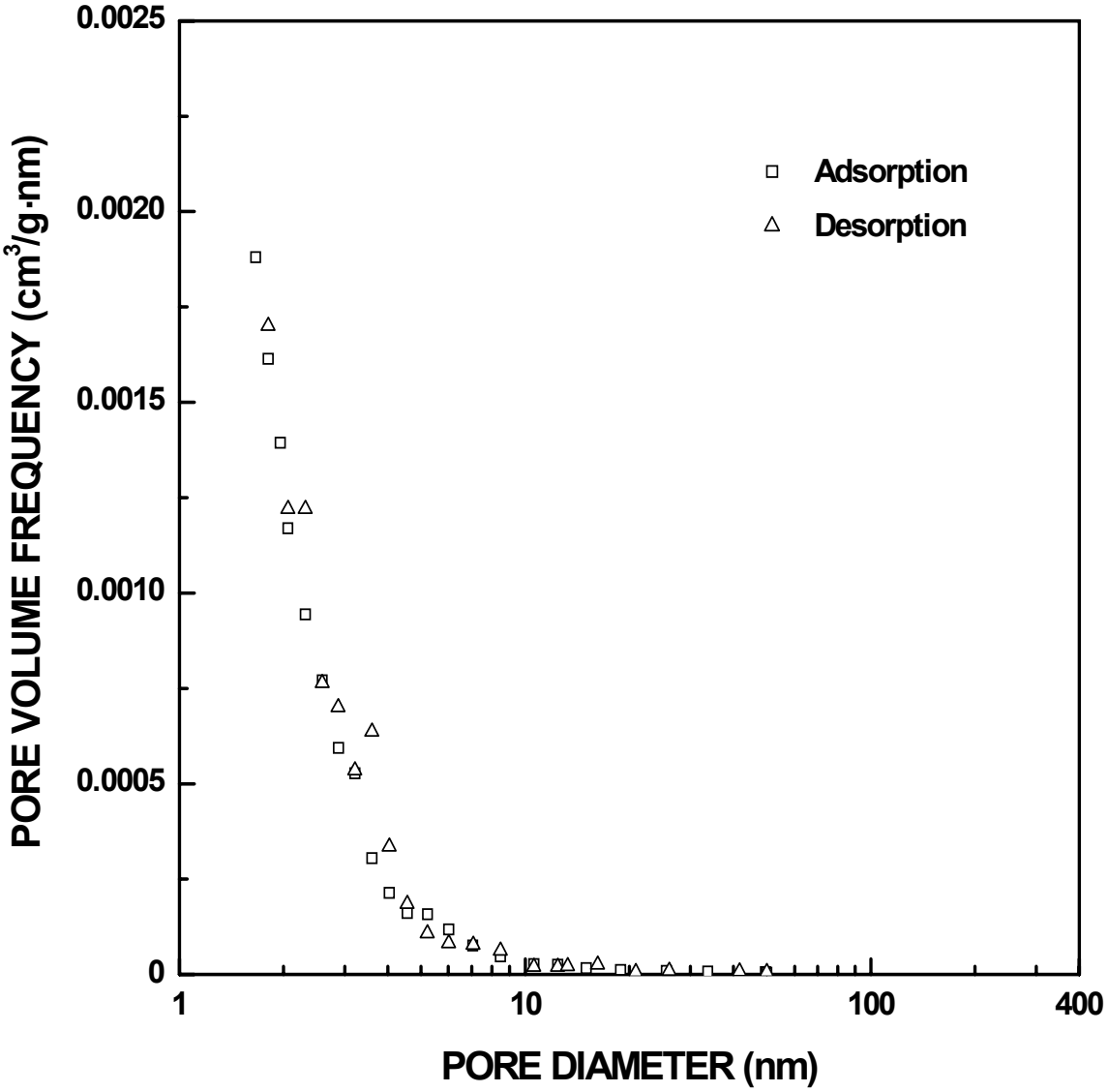

Figure 4-4-116 Plots of specific pore volume frequency vs. pore diameter for the SC35-1200(1h) sample (X_{WL} = 0.03). The pore diameter was cut off at 50 nm.

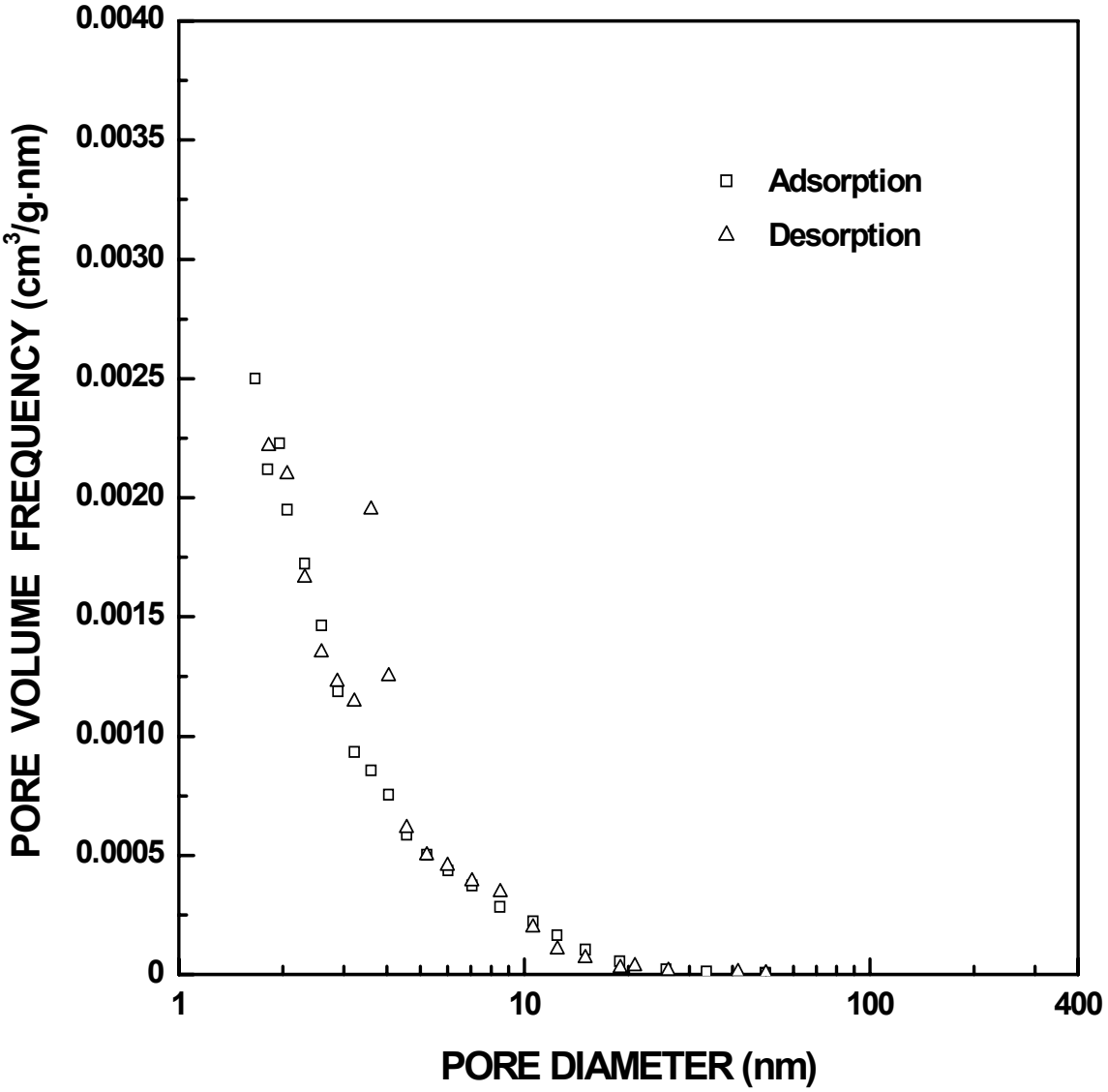

Figure 4-4-117 Plots of specific pore volume frequency vs. pore diameter for the SC35-1200(2h) sample (X_{WL} = 0.05). The pore diameter was cut off at 50 nm.

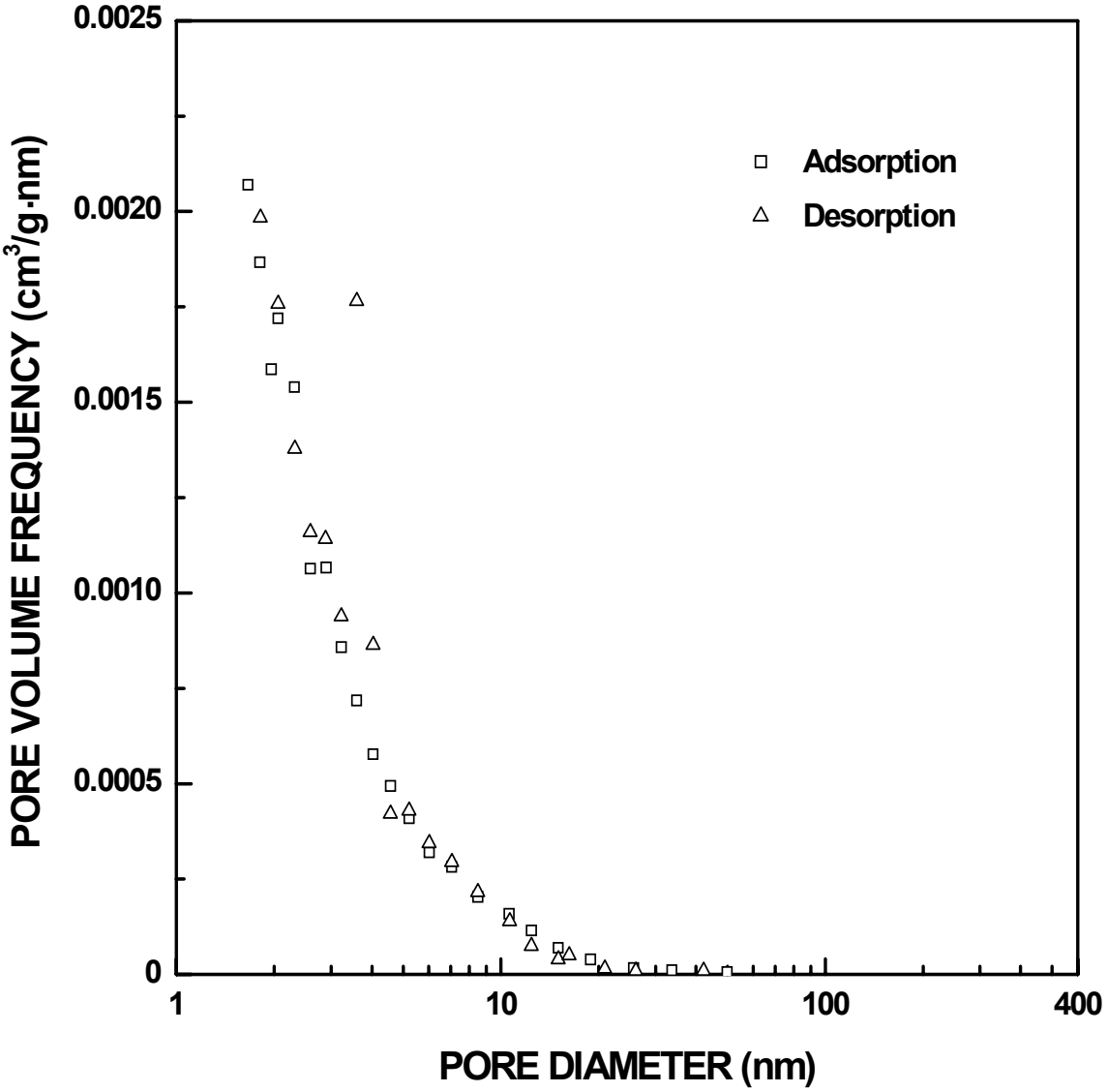

Figure 4-4-118 Plots of specific pore volume frequency vs. pore diameter for the SC35-1250(30min) sample (X_{WL} = 0.05). The pore diameter was cut off at 50 nm.

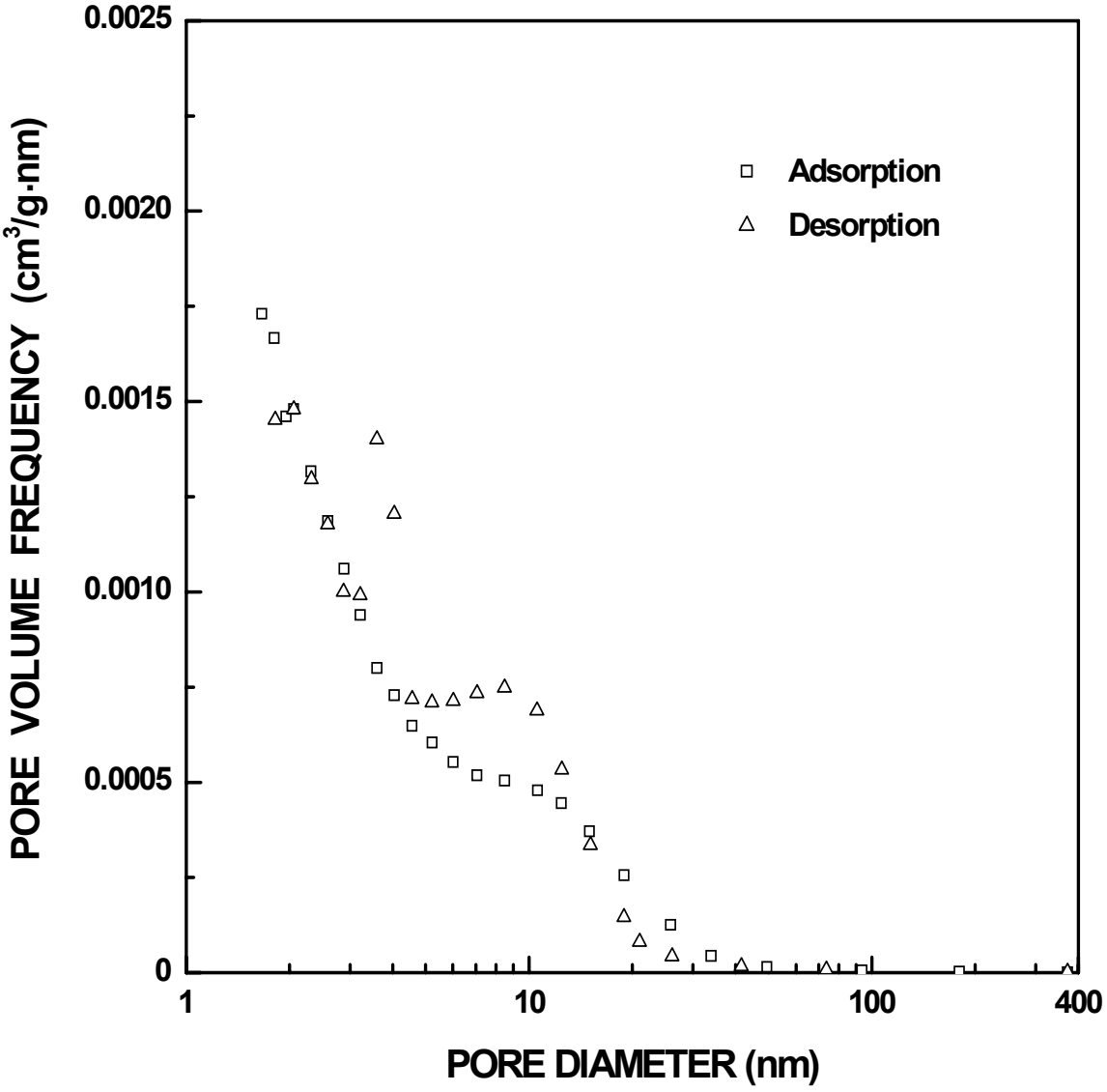

Figure 4-4-119 Plots of specific pore volume frequency vs. pore diameter for the SC35-1250(1h) sample (X_{WL} = 0.07).

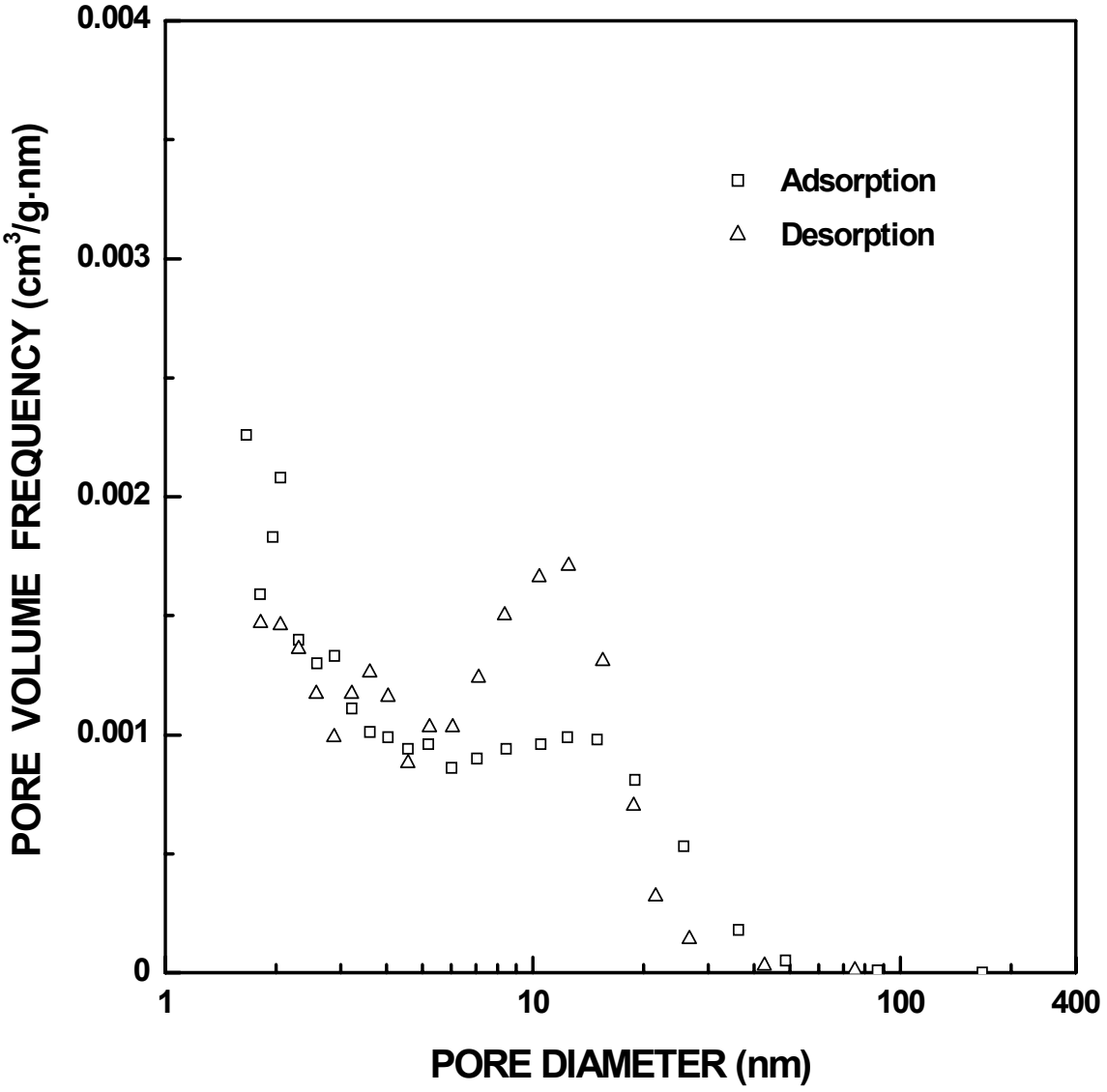

Figure 4-4-120 Plots of specific pore volume frequency vs. pore diameter for the SC35-1250(2h) sample (X_{WL} = 0.12).

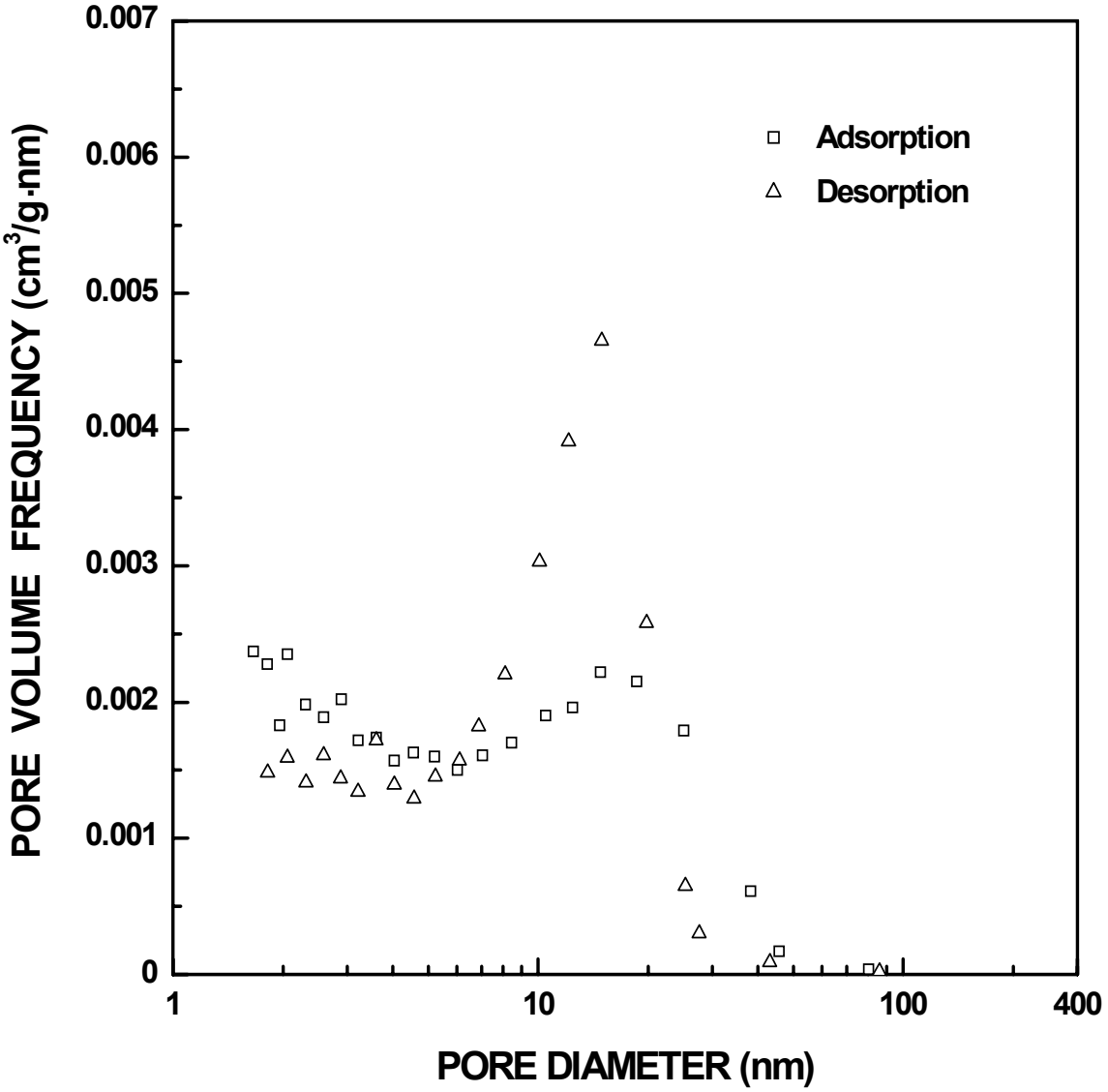

Figure 4-4-121 Plots of specific pore volume frequency vs. pore diameter for the SC35-1250(4h) sample (X_{WL} = 0.23).

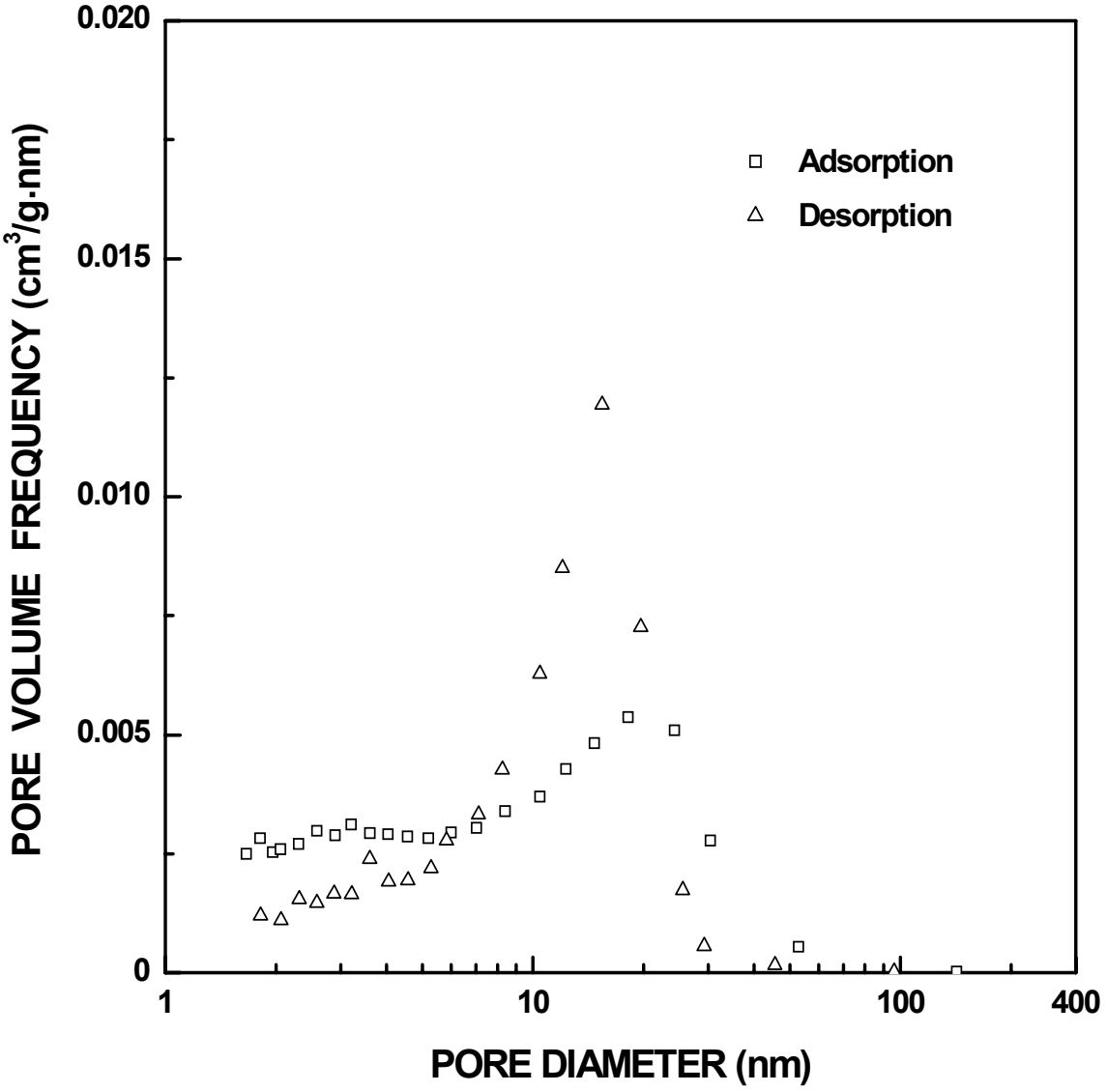

Figure 4-4-122 Plots of specific pore volume frequency vs. pore diameter for the SC35-1250(8h) sample (X_{WL} = 0.41).

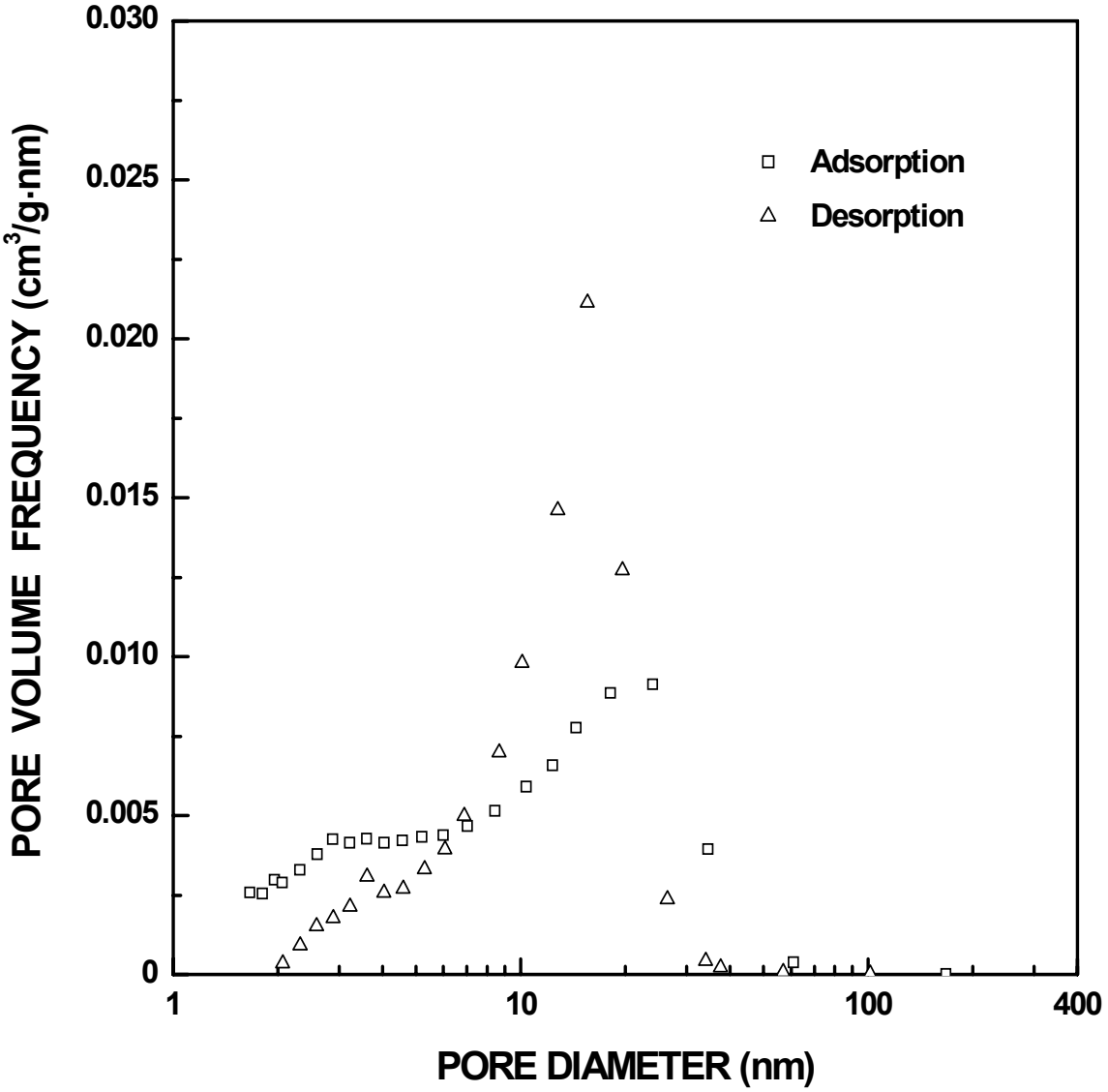

Figure 4-4-123 Plots of specific pore volume frequency vs. pore diameter for the SC35-1200(32h) sample (X_{WL} = 0.52).

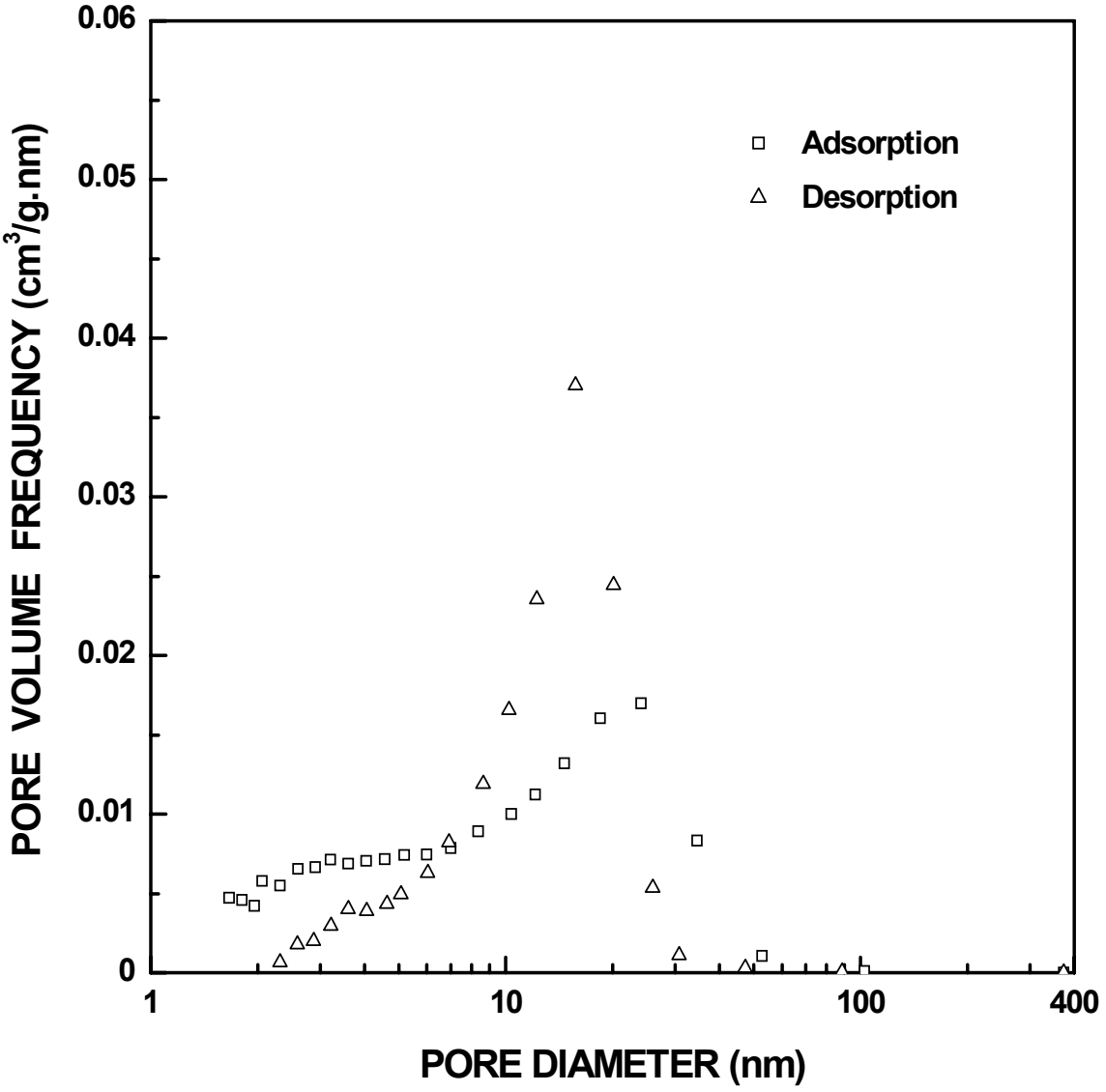

Figure 4-4-124 Plots of specific pore volume frequency vs. pore diameter for the SC35-1200(48h) sample (X_{WL} = 0.72).

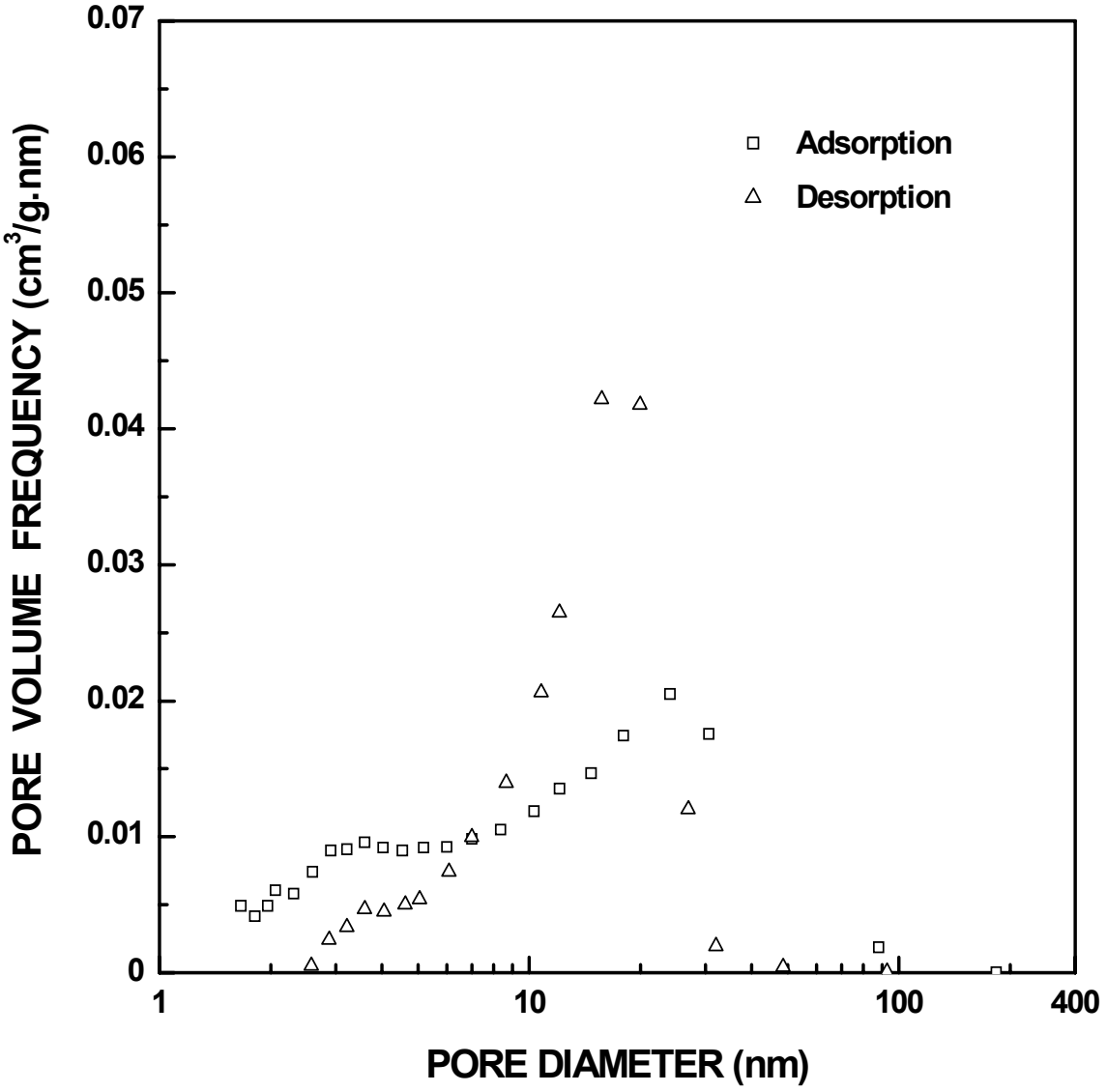

Figure 4-4-125 Plots of specific pore volume frequency vs. pore diameter for the SC35-1250(22h) sample (X_{WL} = 0.82).

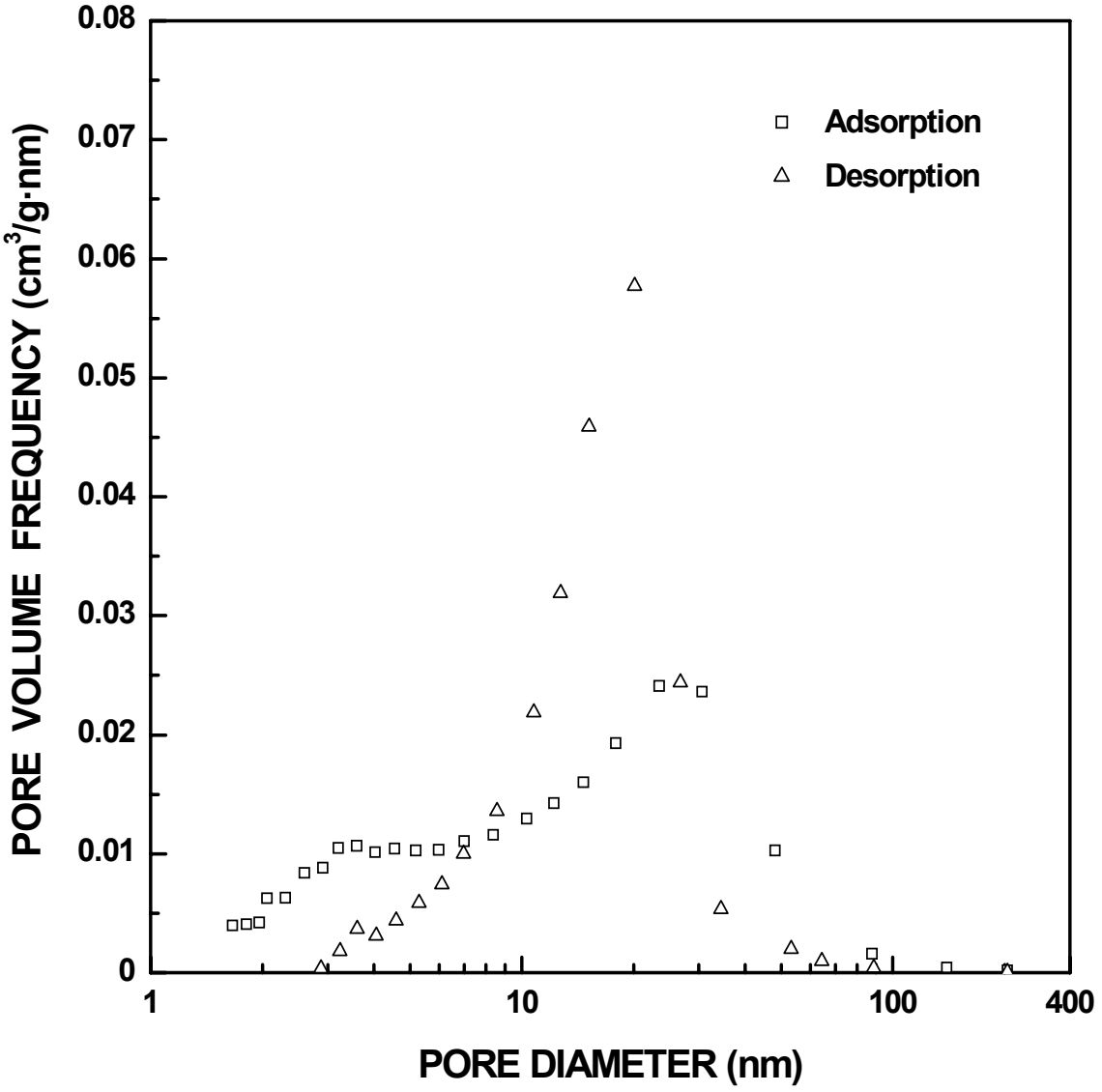

Figure 4-4-126 Plots of specific pore volume frequency vs. pore diameter for the SC35-1250(32h) sample (X_{WL} = 0.95).

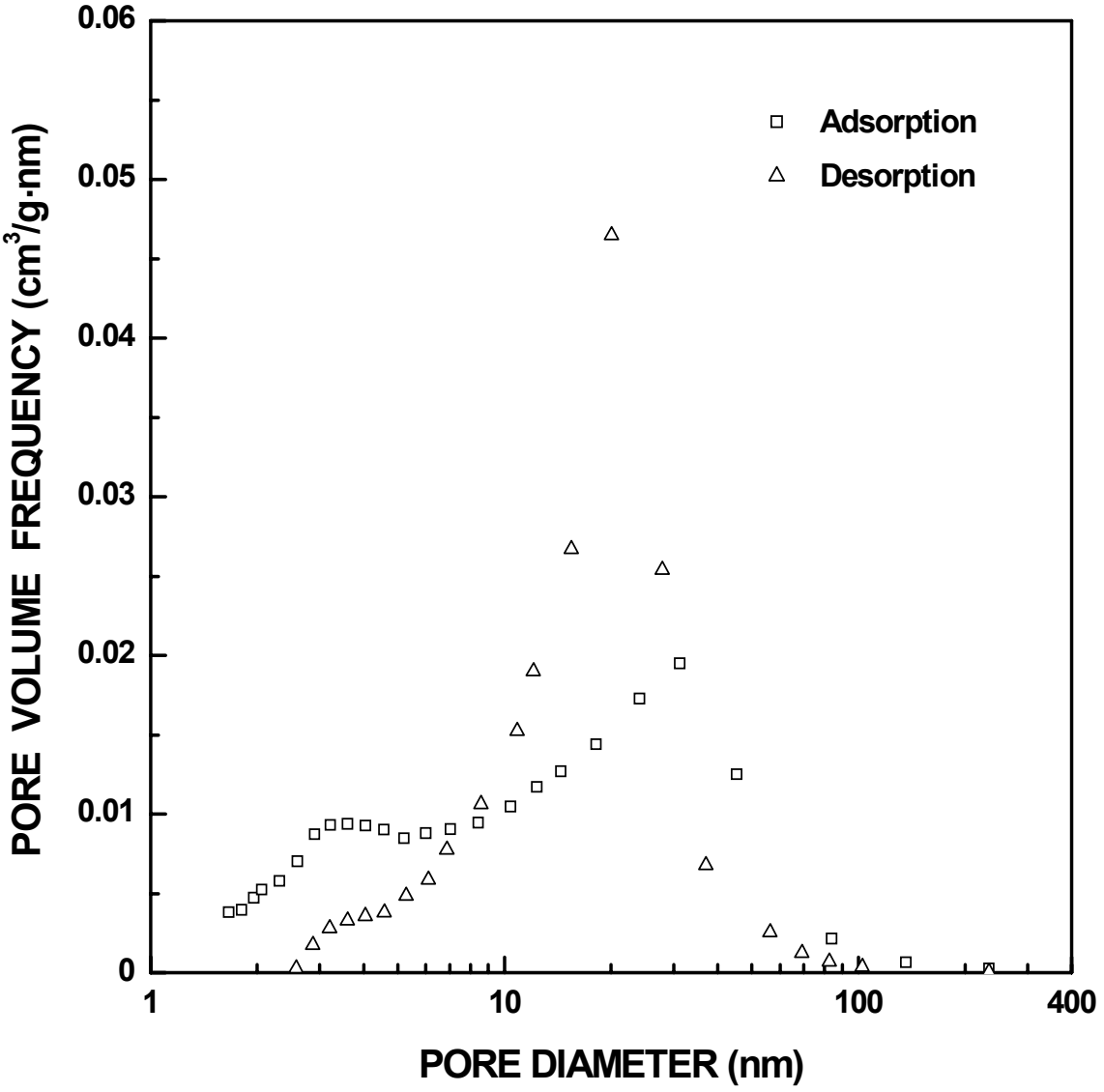

Figure 4-4-127 Plots of specific pore volume frequency vs. pore diameter for the SC35-1300(12h) sample (X_{WL} = 0.96).

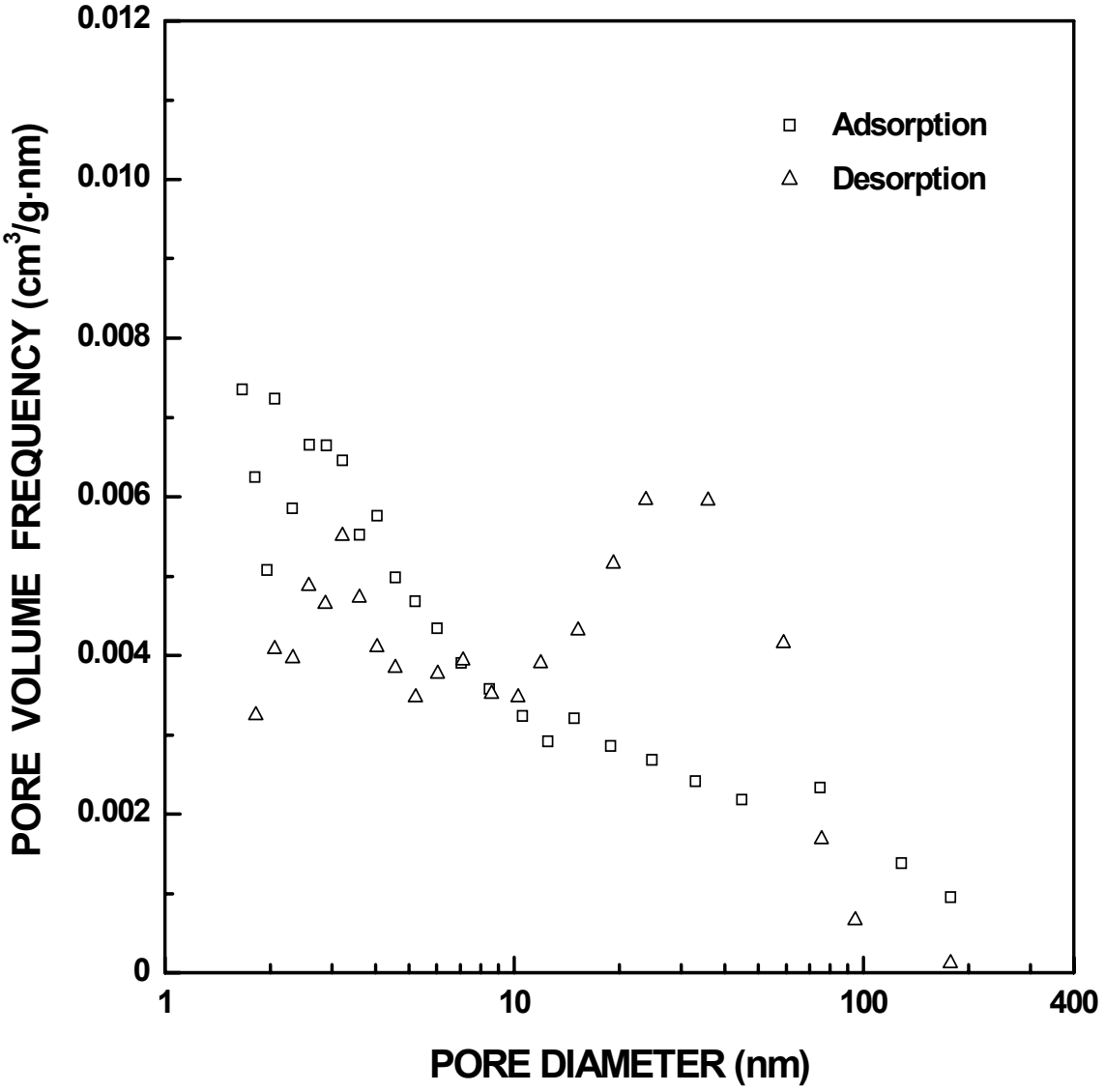

Figure 4-4-128 Plots of specific pore volume frequency vs. pore diameter for the SC35-1300(16h) sample (X_{WL} = 0.98).

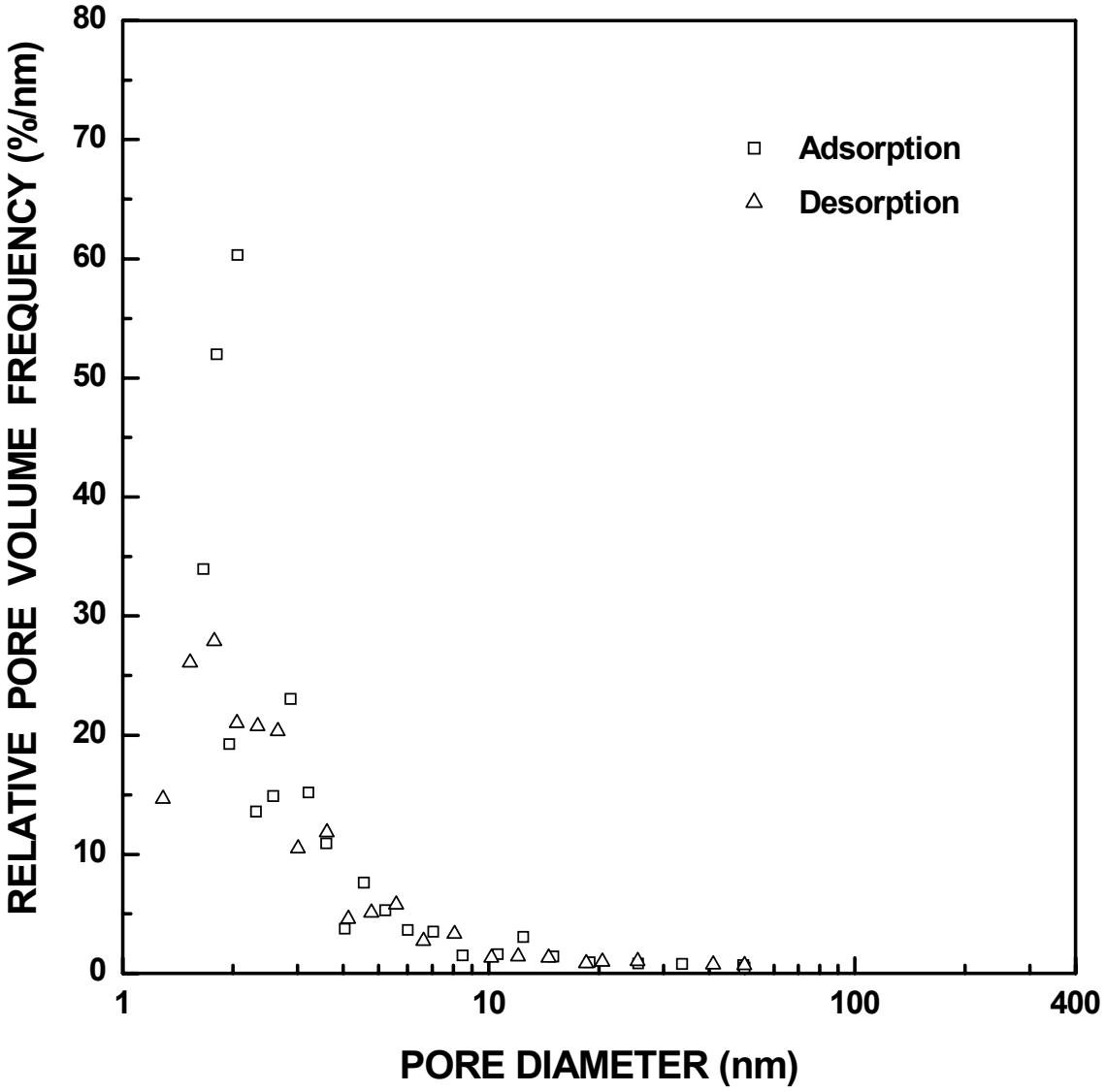

Figure 4-4-129 Plots of relative ("normalized") pore volume frequency vs. pore diameter for the SC35-1160(1h) sample (X_{WL} = 0.02). The pore diameter was cut off at 50 nm.

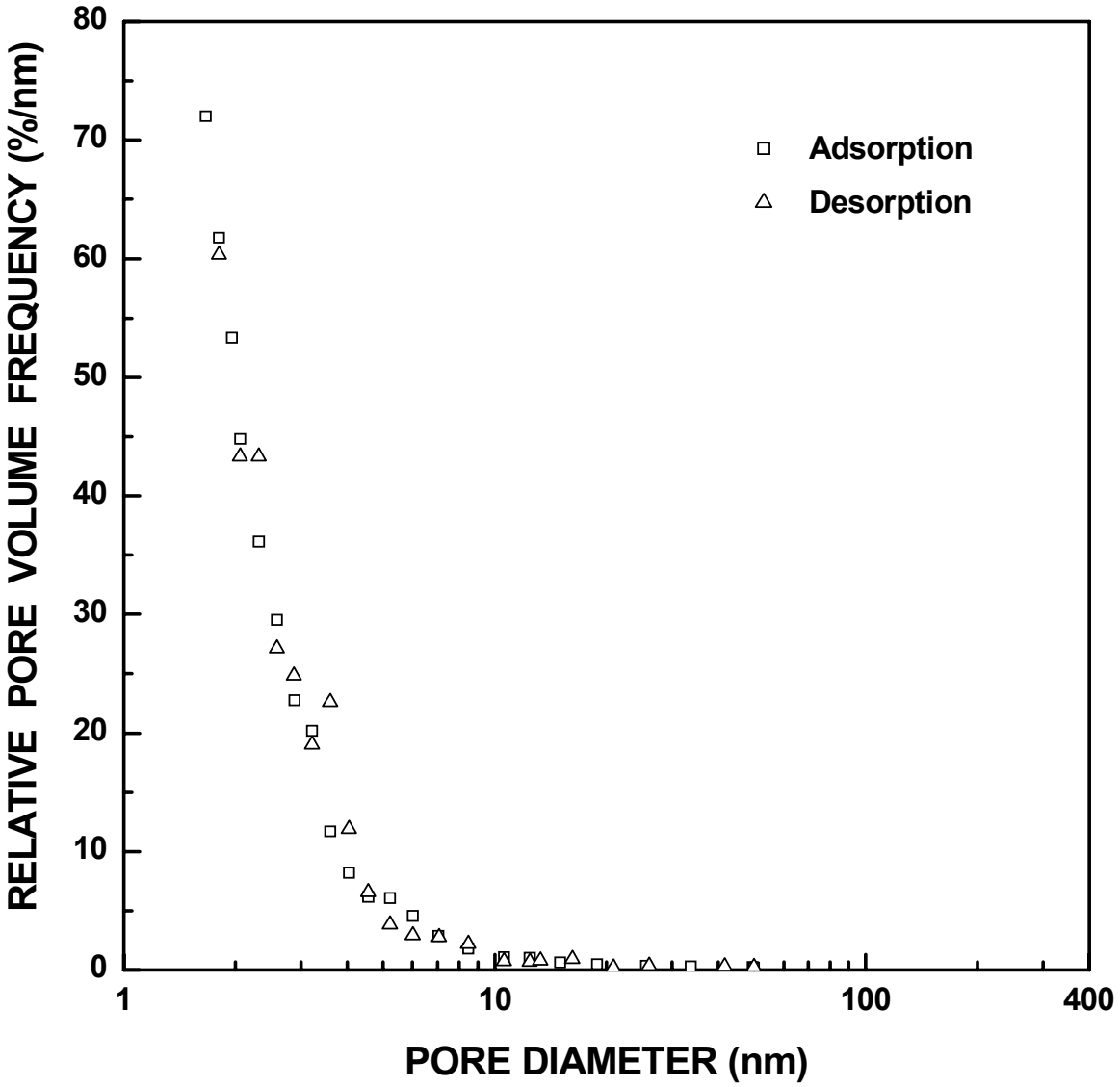

Figure 4-4-130 Plots of relative ("normalized") pore volume frequency vs. pore diameter for the SC35-1200(1h) sample (X_{WL} = 0.03). The pore diameter was cut off at 50 nm.

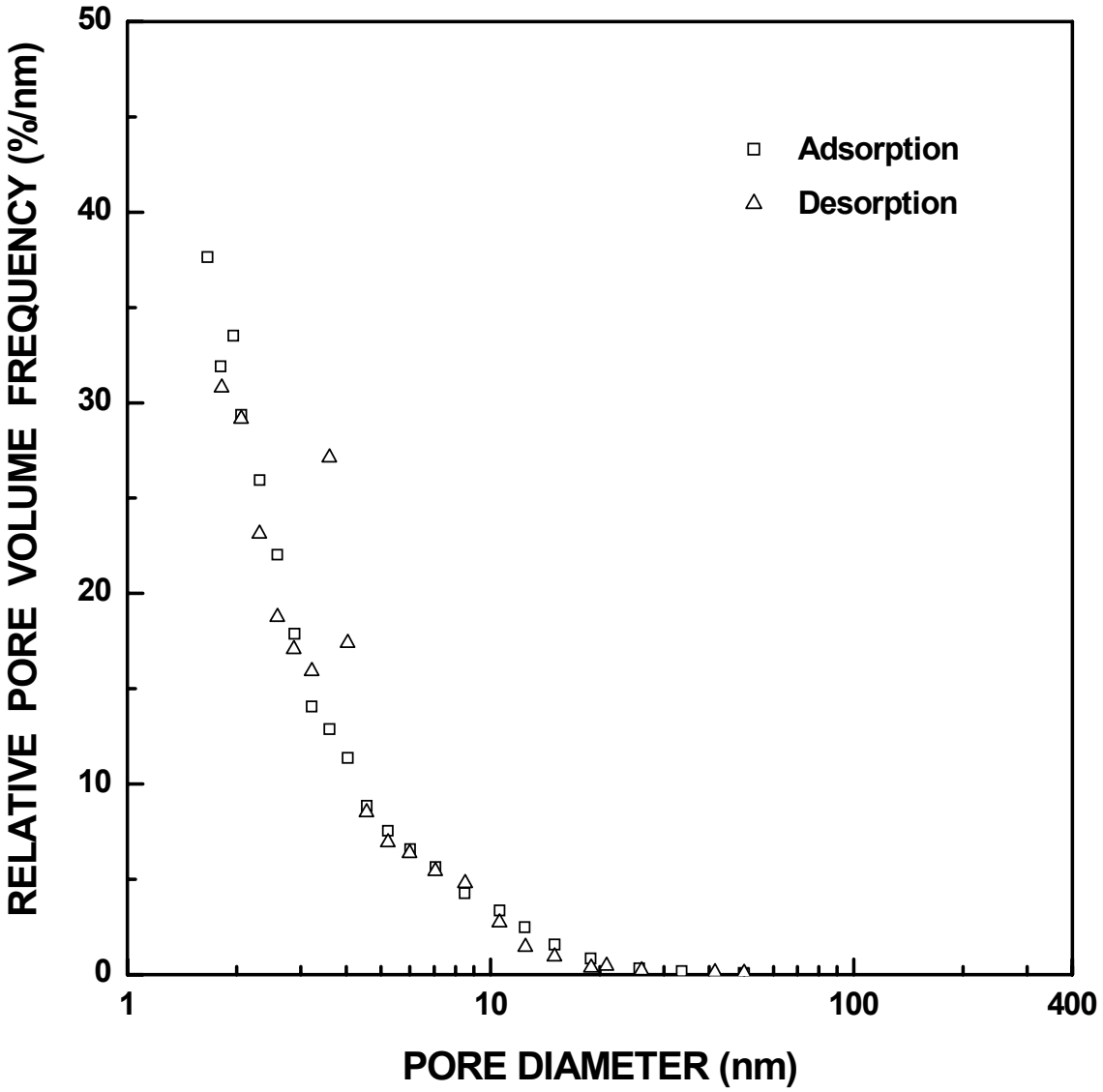

Figure 4-4-131 Plots of relative ("normalized") pore volume frequency vs. pore diameter for the SC35-1200(2h) sample (X_{WL} = 0.05). The pore diameter was cut off at 50 nm.

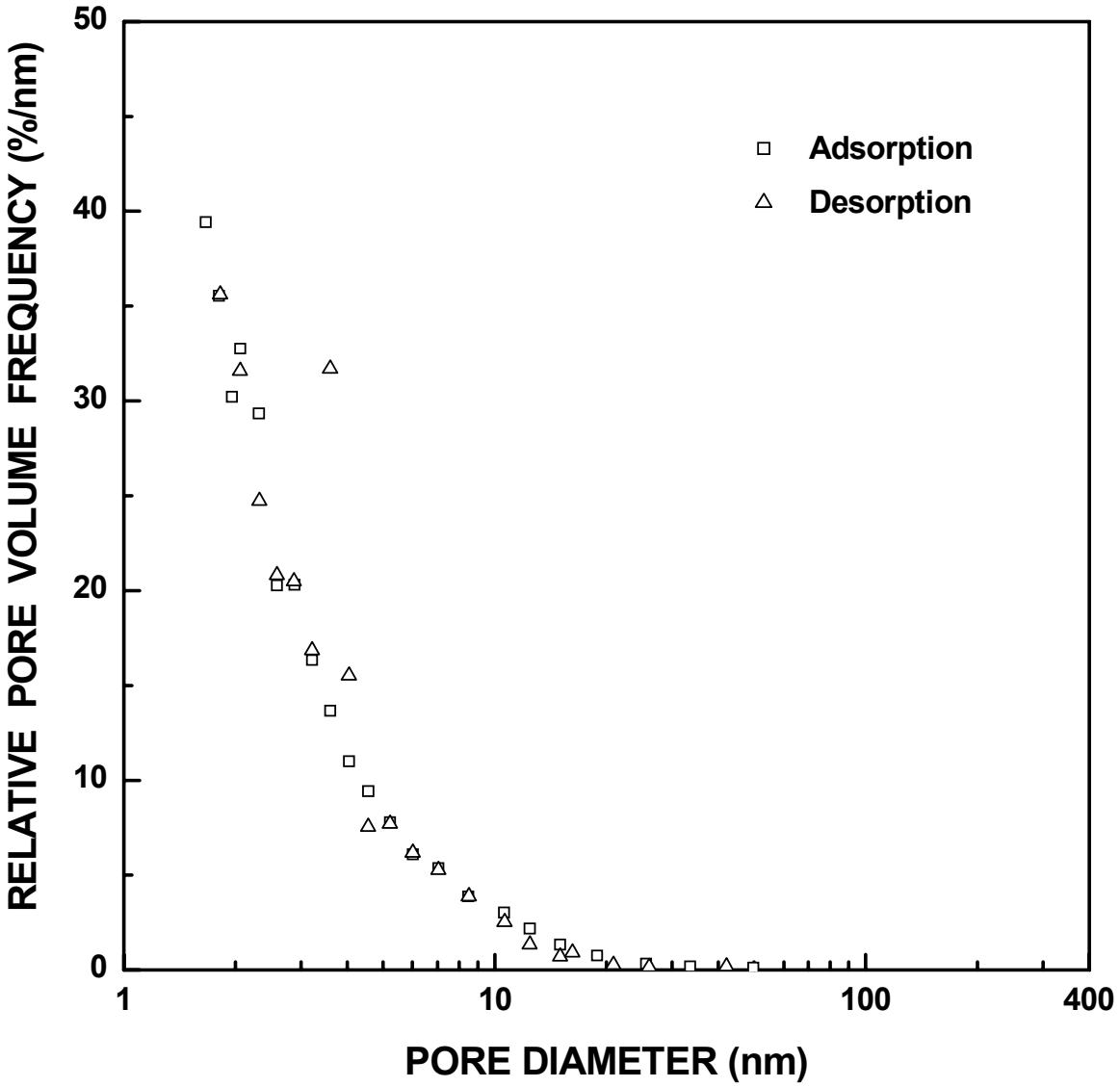

Figure 4-4-132 Plots of relative ("normalized") pore volume frequency vs. pore diameter for the SC35-1250(30min) sample (X_{WL} = 0.05). The pore diameter was cut off at 50 nm.

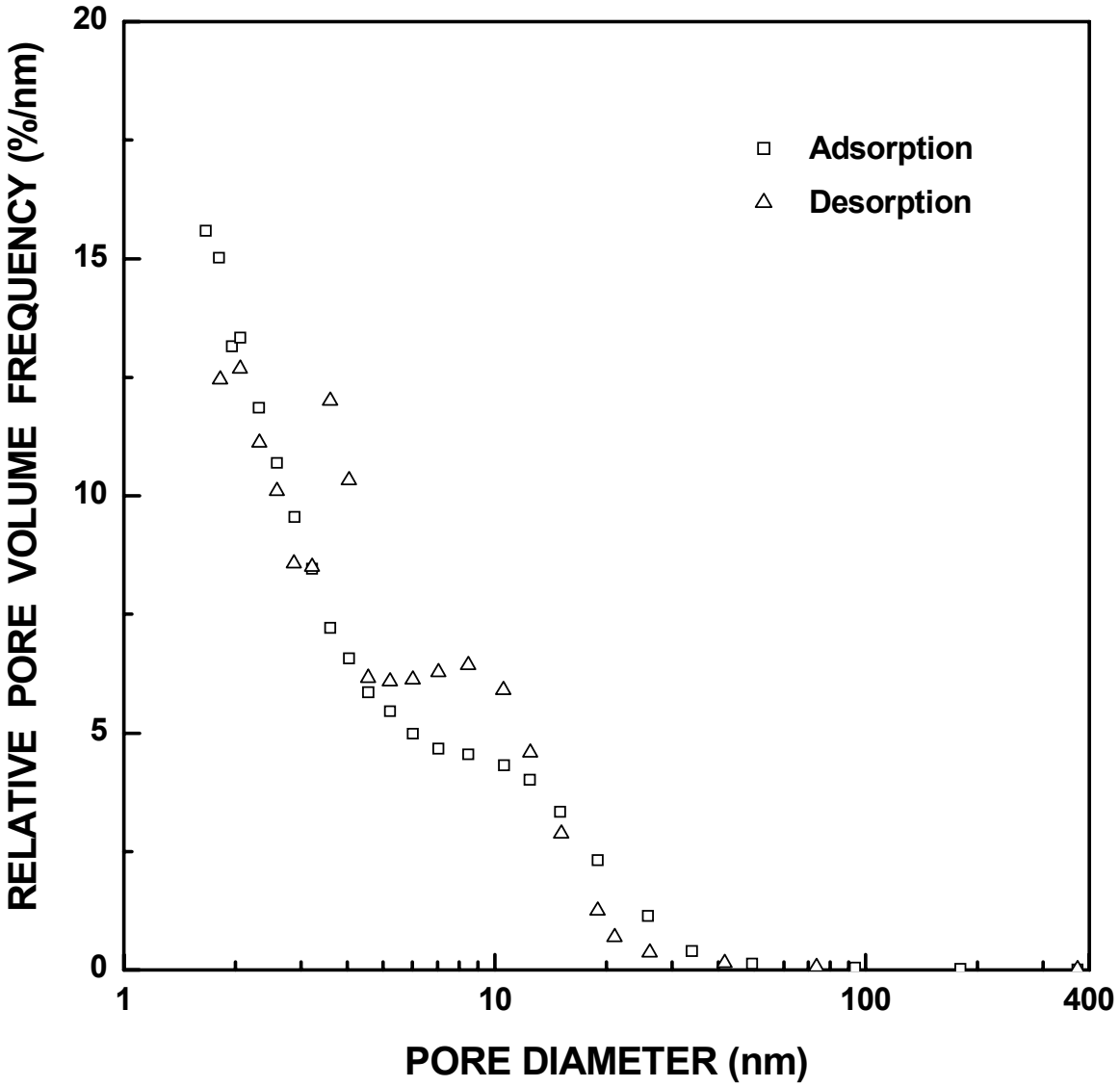

Figure 4-4-133 Plots of relative ("normalized") pore volume frequency vs. pore diameter for the SC35-1250(1h) sample (X_{WL} = 0.07).

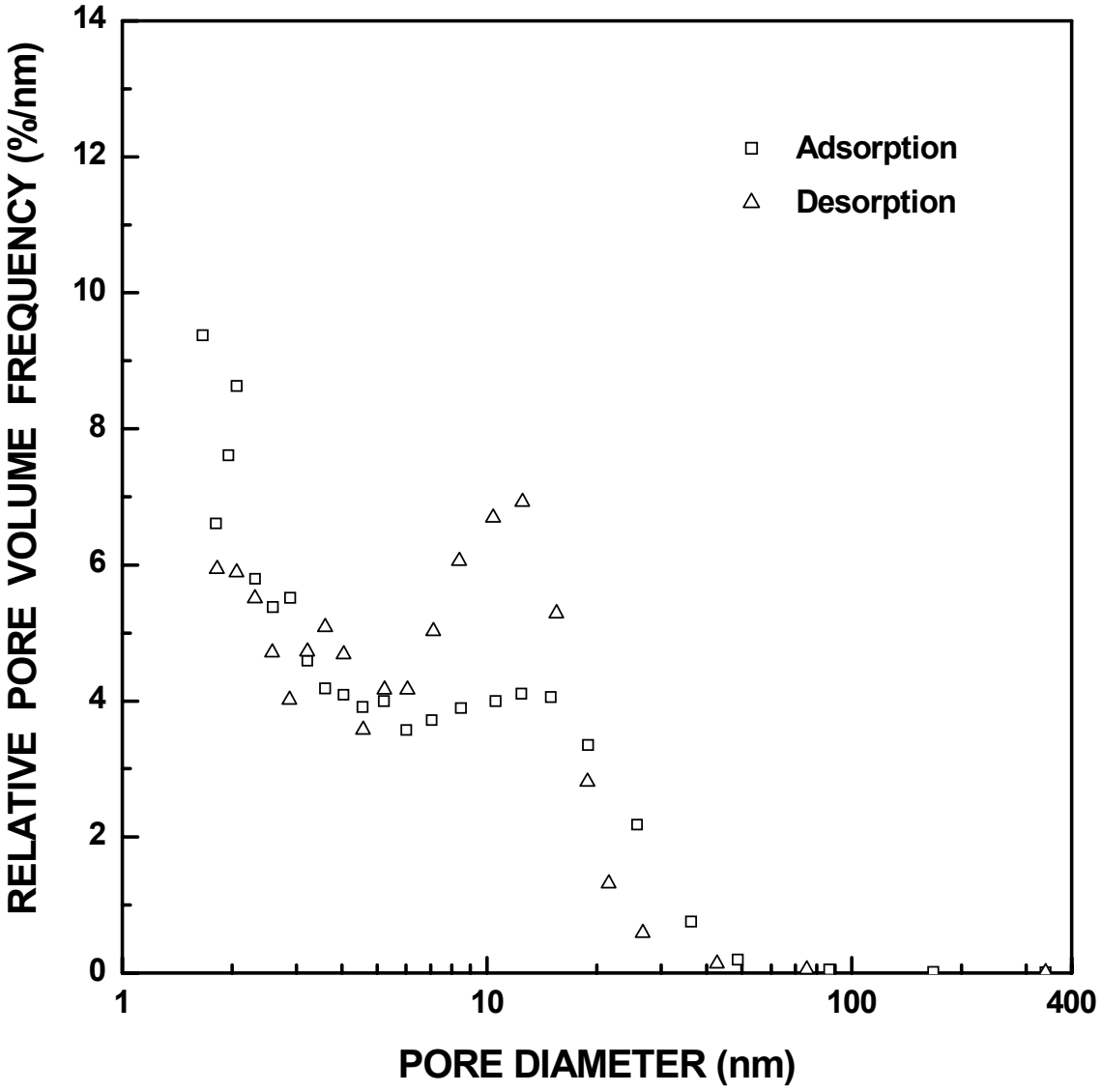

Figure 4-4-134 Plots of relative ("normalized") pore volume frequency vs. pore diameter for the SC35-1250(2h) sample (X_{WL} = 0.12).

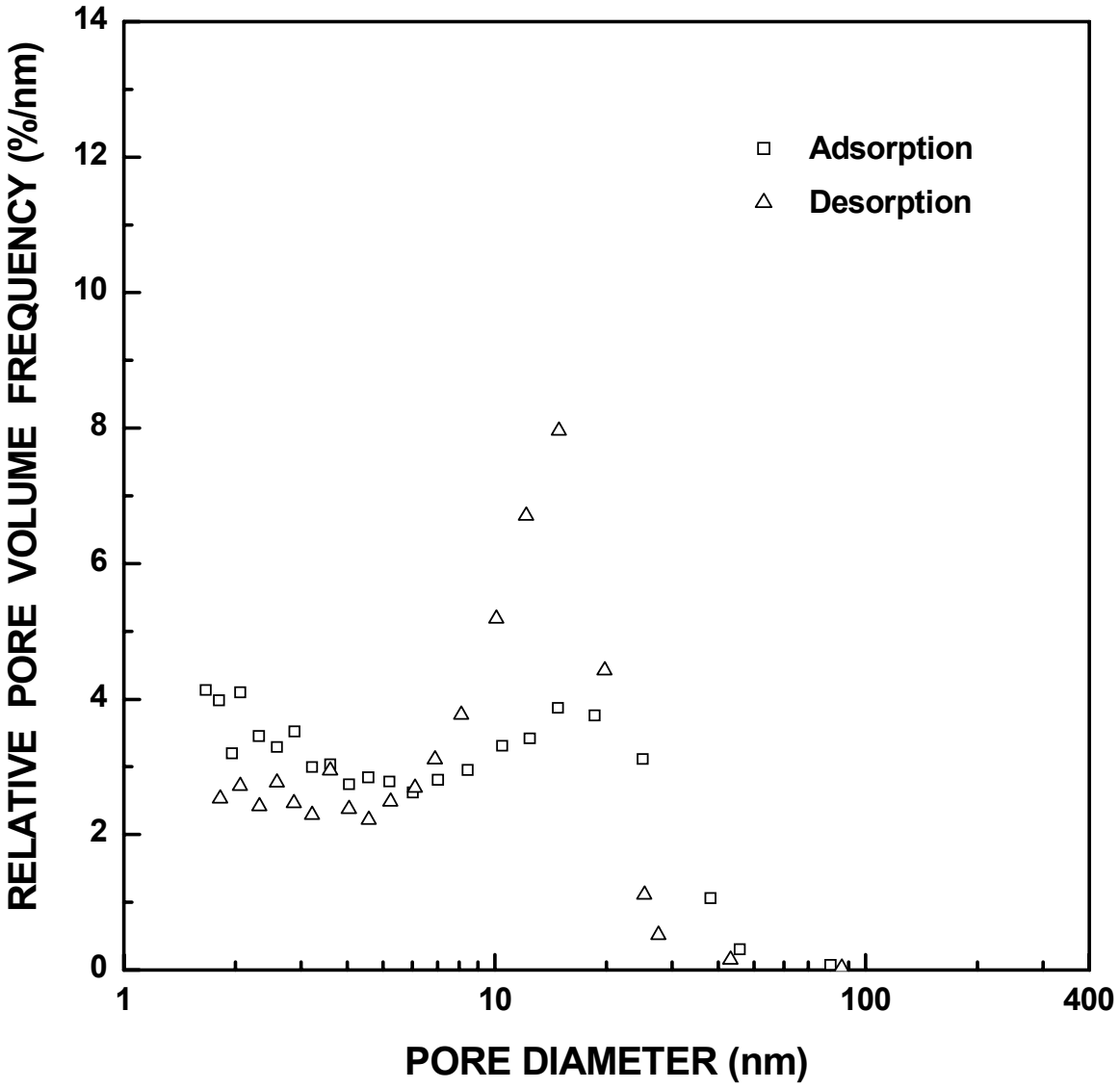

Figure 4-4-135 Plots of relative ("normalized") pore volume frequency vs. pore diameter for the SC35-1250(4h) sample (X_{WL} = 0.23).

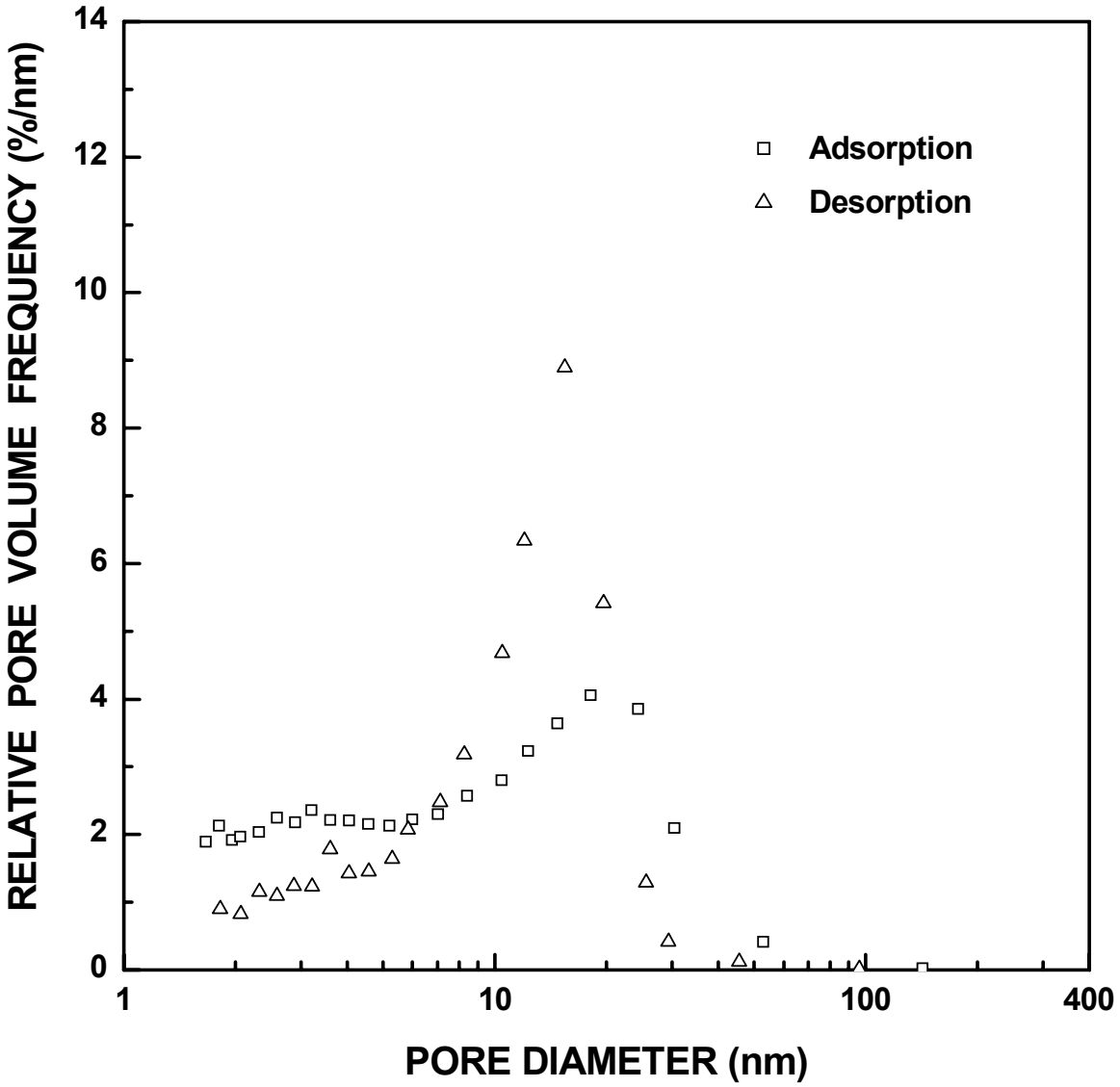

Figure 4-4-136 Plots of relative ("normalized") pore volume frequency vs. pore diameter for the SC35-1250(8h) sample (X_{WL} = 0.41).

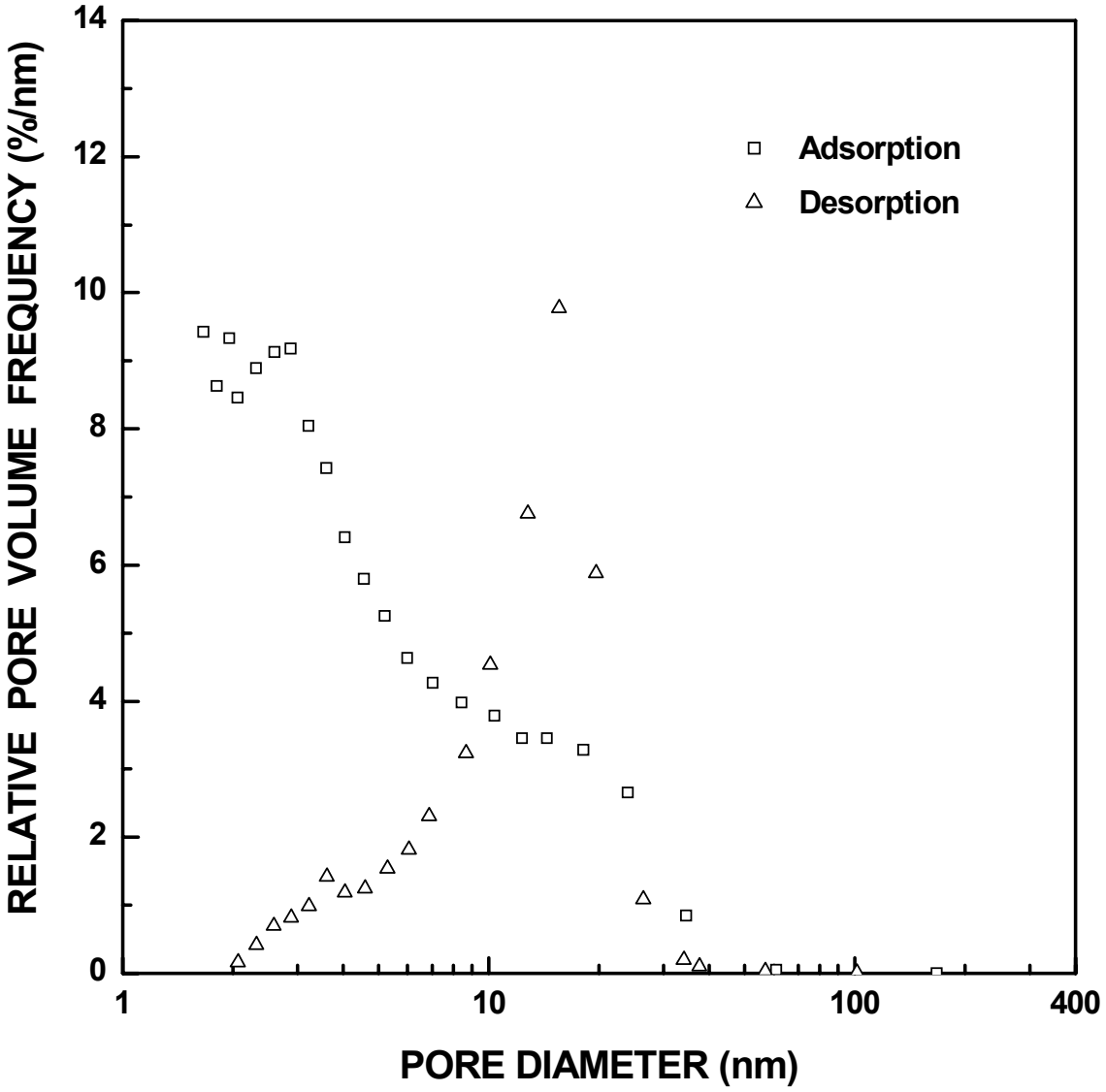

Figure 4-4-137 Plots of relative ("normalized") pore volume frequency vs. pore diameter for the SC35-1200(32h) sample (X_{WL} = 0.52).

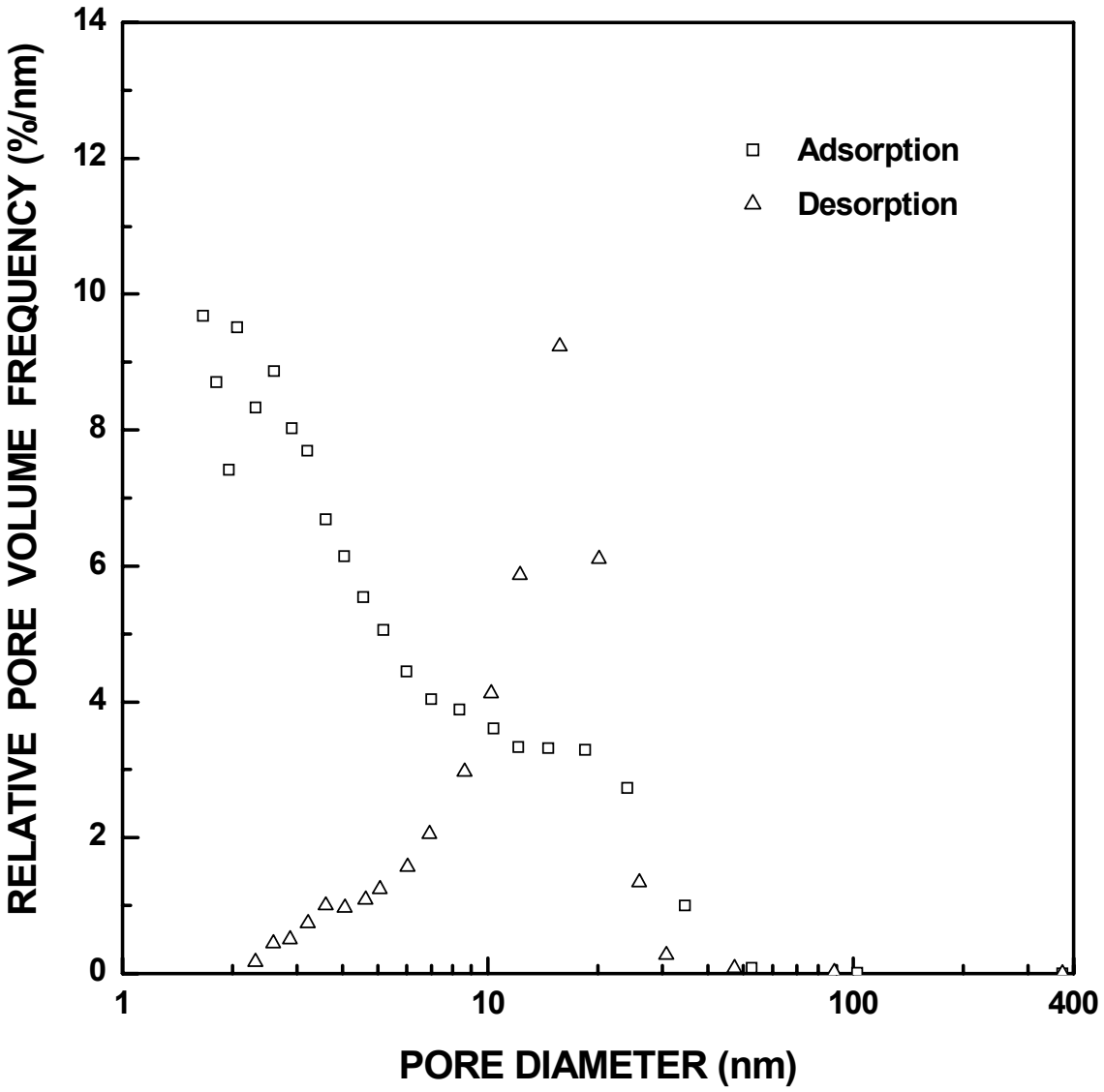

Figure 4-4-138 Plots of relative ("normalized") pore volume frequency vs. pore diameter for the SC35-1200(48h) sample (X_{WL} = 0.72).

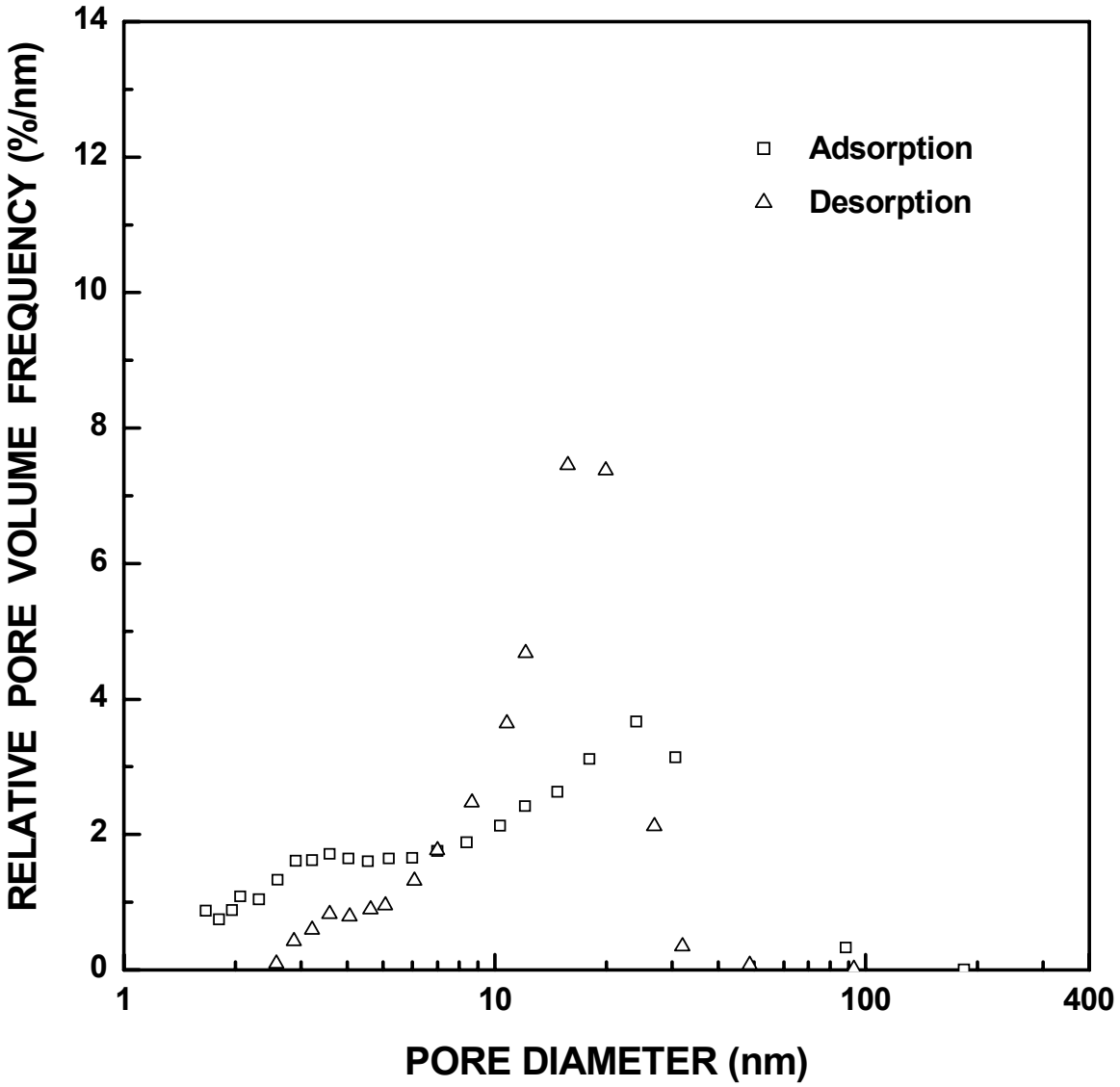

Figure 4-4-139 Plots of relative ("normalized") pore volume frequency vs. pore diameter for the SC35-1250(22h) sample (X_{WL} = 0.82).

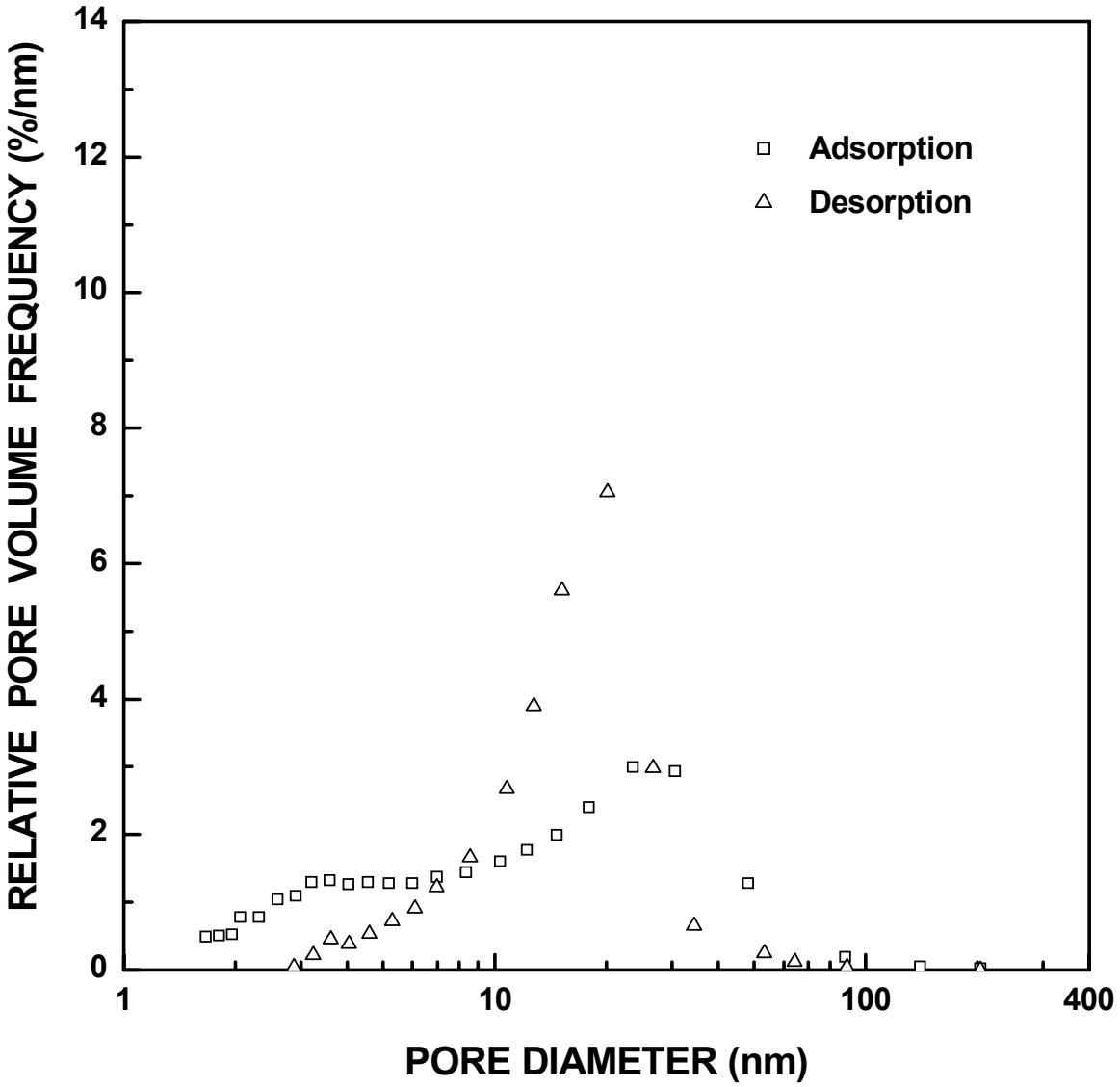

Figure 4-4-140 Plots of relative ("normalized") pore volume frequency vs. pore diameter for the SC35-1250(32h) sample (X_{WL} = 0.95).

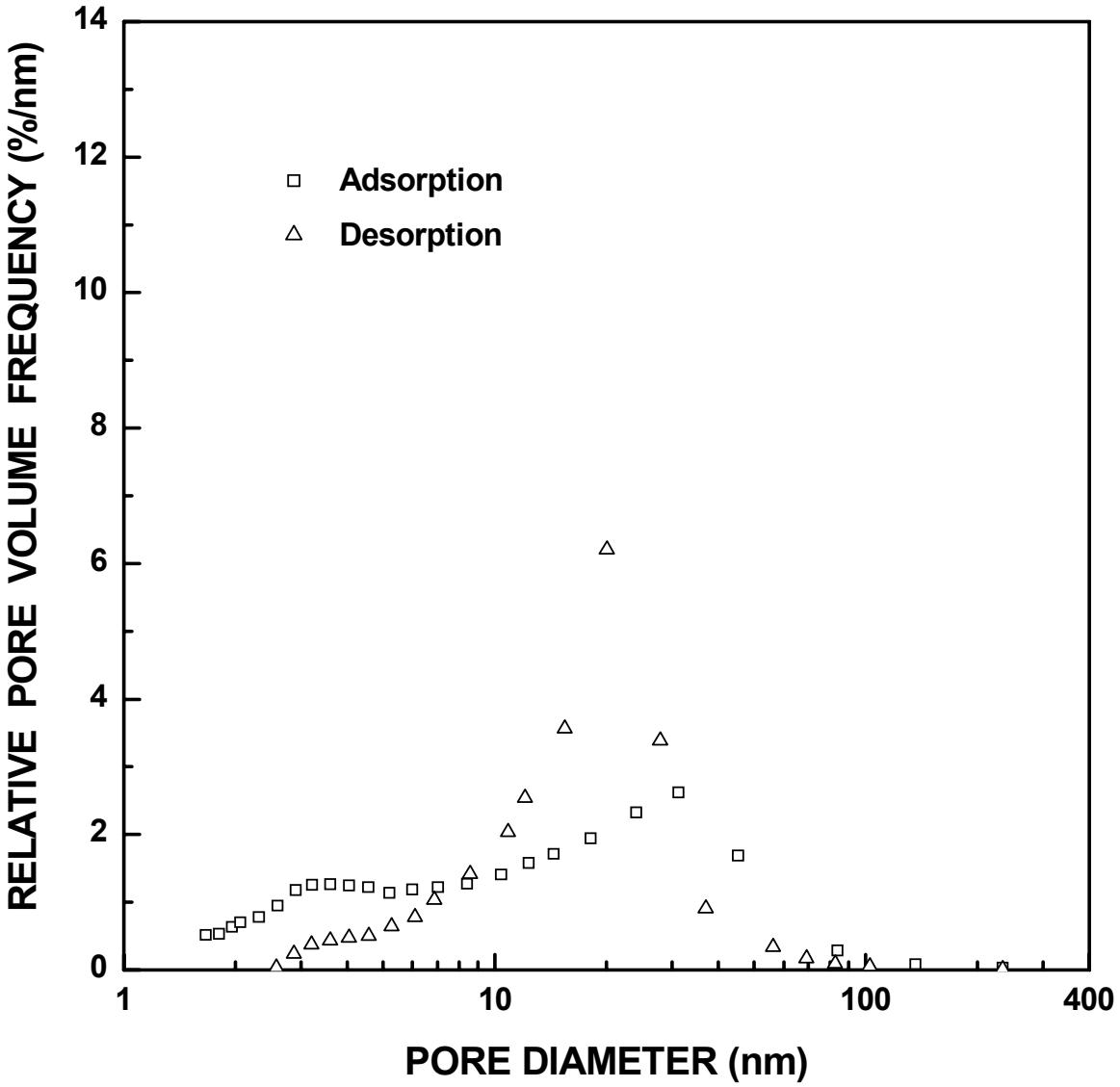

Figure 4-4-141 Plots of relative ("normalized") pore volume frequency vs. pore diameter for the SC35-1300(12h) sample (X_{WL} = 0.96).

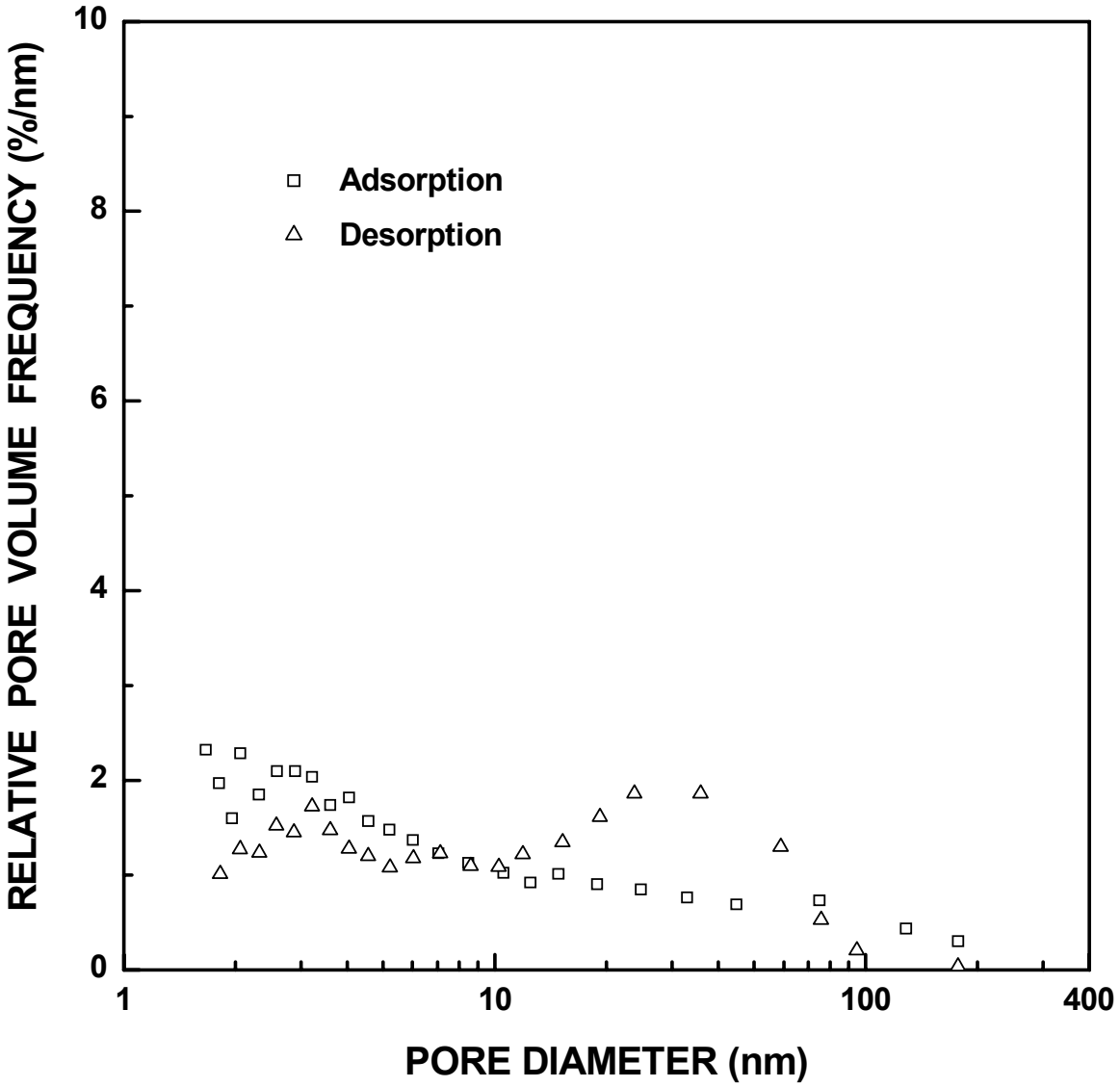

Figure 4-4-142 Plots of relative ("normalized") pore volume frequency vs. pore diameter for the SC35-1300(16h) sample (X_{WL} = 0.98).

with X_{WL} = 0.52, SC35-1200(48h) with X_{WL} = 0.72, SC35-1250(22h) with X_{WL} = 0.82, and SC35-1250(32h) with X_{WL} = 0.95. The overall pore size distributions look progressively less bimodal with increasing fractional weight loss for the samples in Figure 4-4-135 to 4-4-140 (and in comparison to Figure 4-4-134) because the small-size pores (<5 nm) become a relatively small portion of the overall pore volume.

There was very little change in the shape of the pore size distributions for the larger pores (i.e., mostly ~5-25 nm). This was illustrated by fitting the data for the larger pores to a normal distribution. The data was fit for all pores 5-60 nm. (The SC35-1300(16h) sample is an only exception. For that sample, the data was fit for all pores 5-180 nm.) Figure 4-4-143 shows a plot of the median diameter (over the range in which the data was fit) vs. fractional weight loss. (These results are very similar to the "D_{50} plot" shown in Figure 4-4-112. The values in Figure 4-4-143 are shifted to slightly higher values because only pores greater than 5 nm were used in calculating the median diameter.) Figure 4-4-144 shows that there was almost no change in the standard deviation of the distribution of the larger pores (i.e., 5-60 nm) until the very late stage of the reaction.

The pore size distributions begin to broaden again in the very late stage of the reaction, as observed by comparing the results for the SC35-1300(12h) (X_{WL} = 0.96) and SC35-1300(16h) (X_{WL} = 0.98) samples in Figures 4-4-141 and 4-4-142, respectively. As discussed previously, this reflects the onset of coarsening of pores in SiC regions which have little or no residual carbon.

The preferential development of larger pores as the CTR reaction proceeds is clearly illustrated in Figures 4-4-145 and 4-4-146. Figures 4-4-145 and 4-4-146 show plots of the specific pore volume vs. fractional weight loss (X_{WL}) for pores with diameters

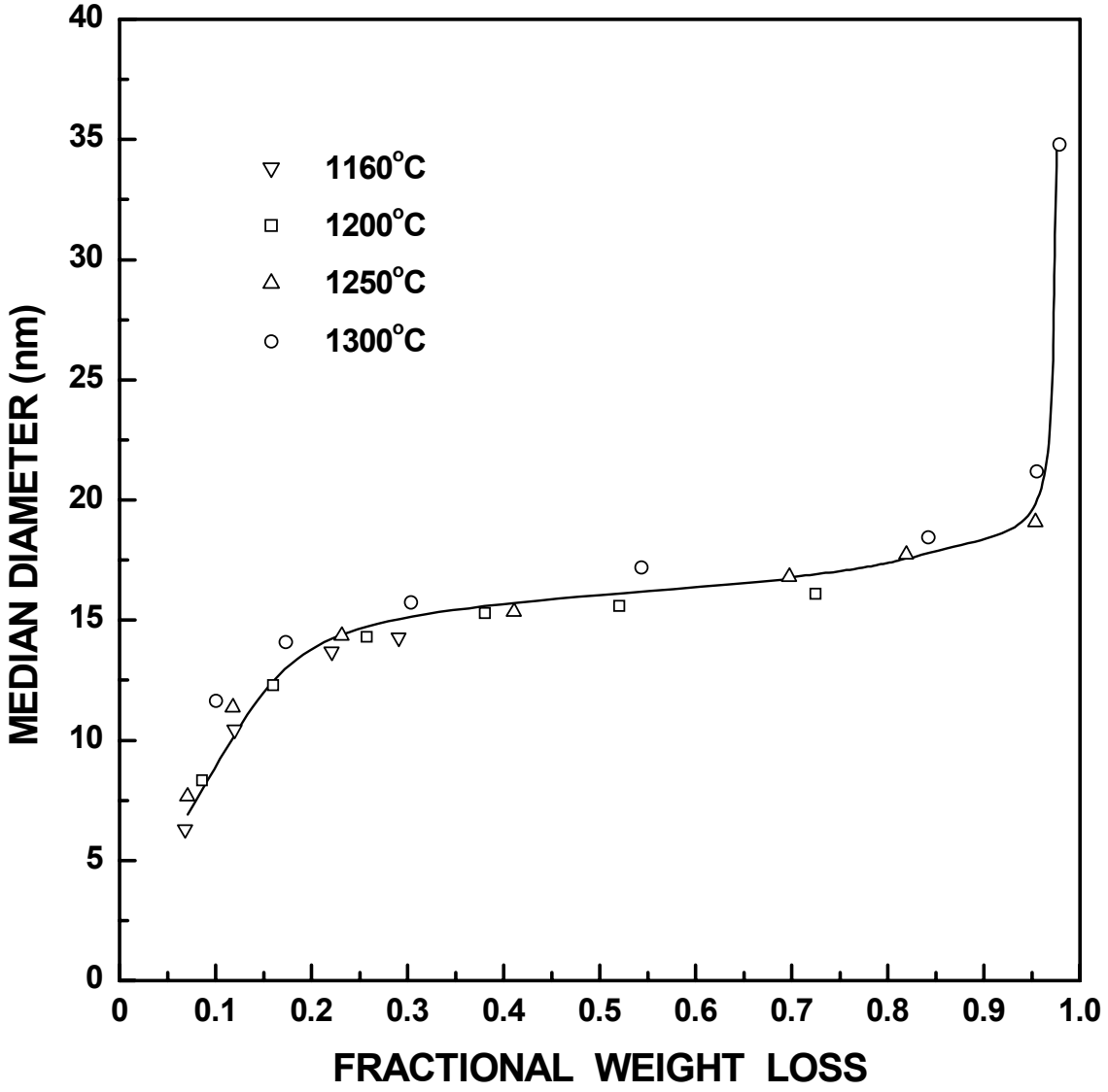

Figure 4-4-143 Plot of median diameter vs. fractional weight loss of SC35 CTR samples. The median diameter was determined using only the portion of the pore size distribution with pore sizes in the range of 5-60 nm. These pores were first fit to a normal distribution.

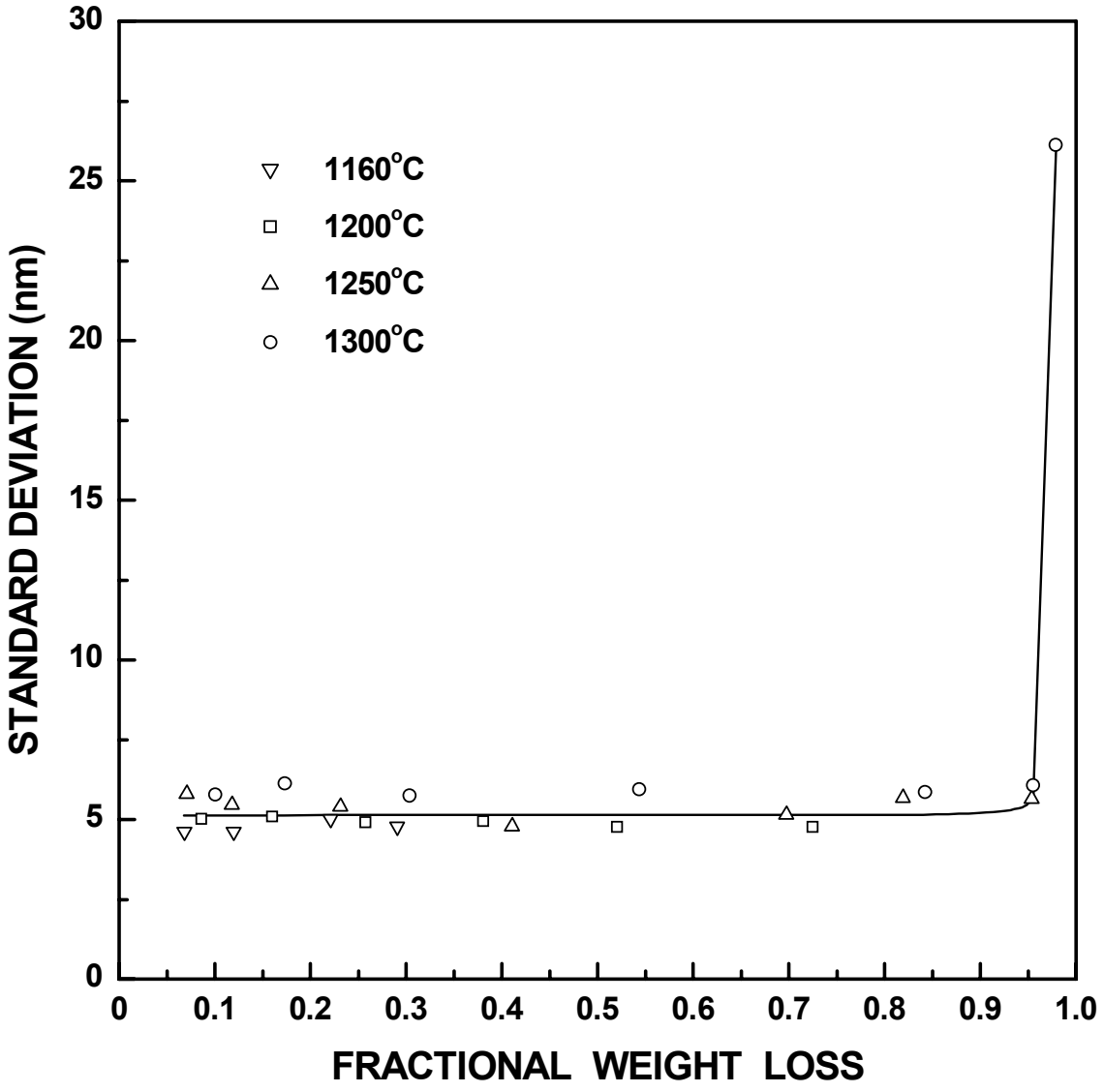

Figure 4-4-144 Plot of the standard deviation of the distribution vs. fractional weight loss of SC35 CTR samples. The standard deviation was determined using only the portion of the pore size distribution with pore sizes in the range of 5-60 nm. These pores were first fit to a normal distribution.

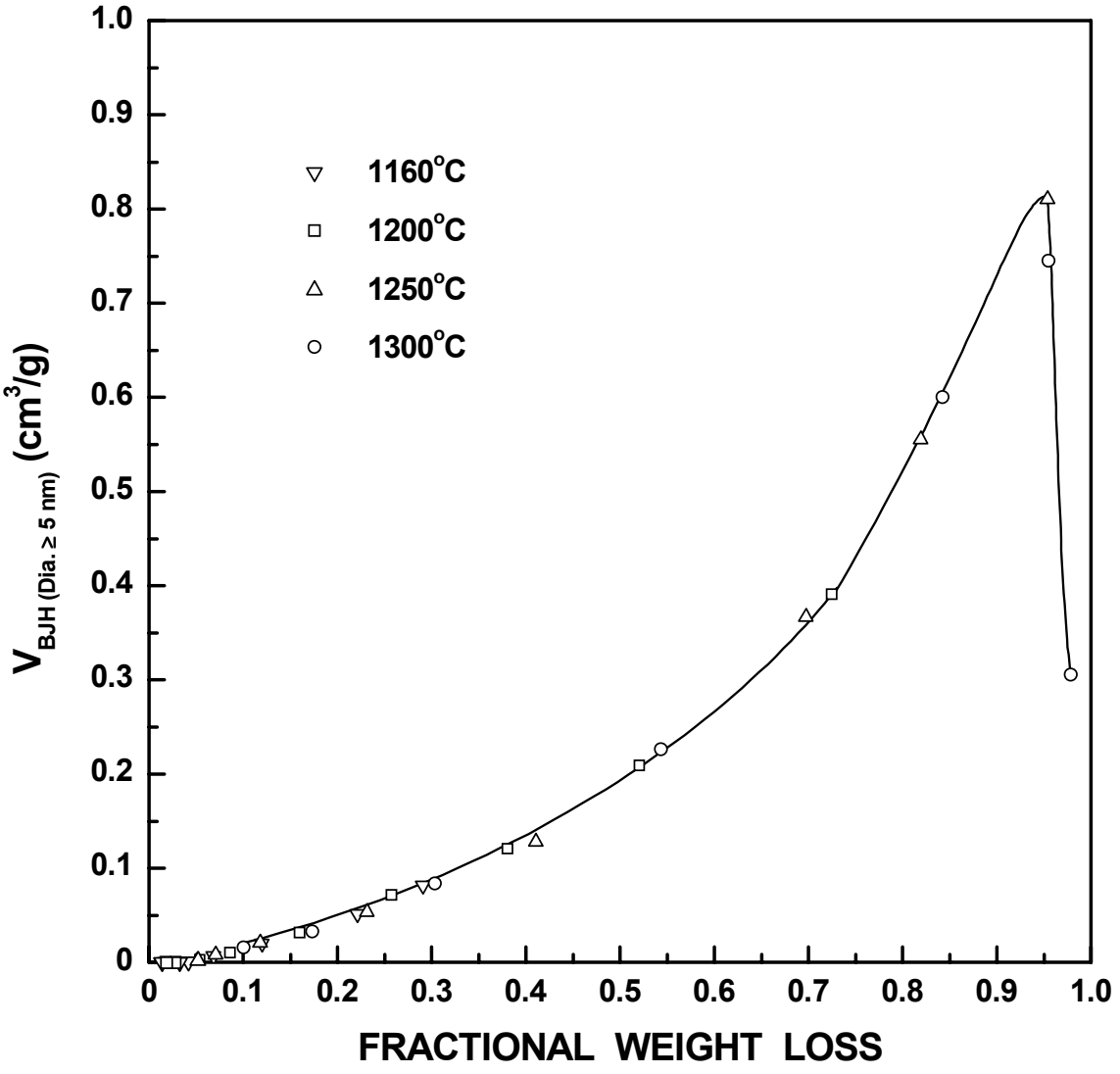

Figure 4-4-145 Plot of specific pore volume (from the desorption branch of the isotherm) for pores with diameter ≥5 nm vs. fractional weight loss for the SC35 CTR samples.

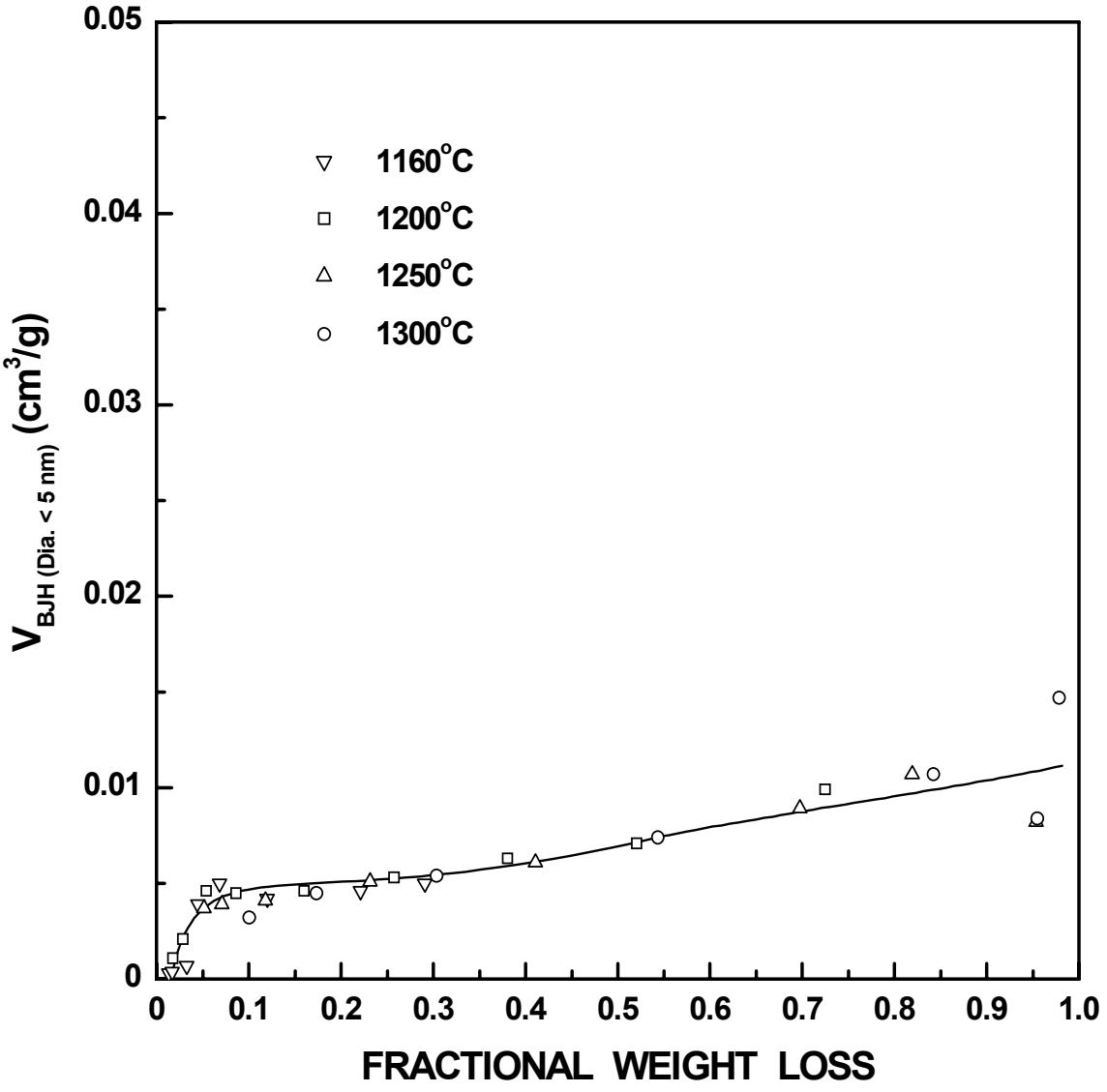

Figure 4-4-146 Plot of specific pore volume (from the desorption branch of the isotherm) for pores with diameter <5 nm vs. fractional weight loss for the SC35 CTR samples.

≥ 5 nm and diameters in the range of ~1.6 - 5 nm, respectively. In these figures, the total BJH pore volume (refer to section 3.5.2.3) for each sample was simply divided into the two size ranges specified. Figures 4-4-147 and 4-4-148 shows the same data plotted on the basis of the percentage of the total BJH pore volume in each size range. It is clear that, as the reaction proceeds, most of the increased porosity was contributed by the mesopores greater than ~5 nm. The absolute amount of pores smaller than ~5 nm increased slightly with increasing extent of reaction, but the amount of these pores as a percentage of the total pore volume decreased for most of the reaction.

Figures 4-4-149 and 4-4-150 show plots of the BJH surface area vs. fractional weight loss for pores with diameters ≥5 nm and diameters in the range of ~1.6 - 5 nm, respectively. As the reaction proceeded, most of the increased pore area was contributed by the mesopores greater than ~5 nm. Figures 4-4-151 and 4-4-152 shows the same data plotted on the basis of the percentage of the total BJH pore area in each size range.

Figures 4-4-153 and 4-4-154 show plots of the median pore diameter vs. fractional weight loss for different pore size regimes. In Figure 4-4-153, the median pore diameter was determined only for the portion of the BJH pore volume associated with pores with diameters ≥5 nm. The results are nearly identical to those shown in Figure 4-4-143 and the observed trend has been discussed in detail previously. (Note that Figures 4-4-143 and 4-4-153 show nearly identical results because the median values were determined in both cases using pore volumes that were associated with almost the same pore size ranges.) In Figure 4-4-154, the median pore diameter was determined only for the portion of the BJH pore volume associated with pores with diameters < 5 nm (i.e., ~1.6 - 5 nm). The main significance of this figure is that it indicates that the size of the smallest pores in the

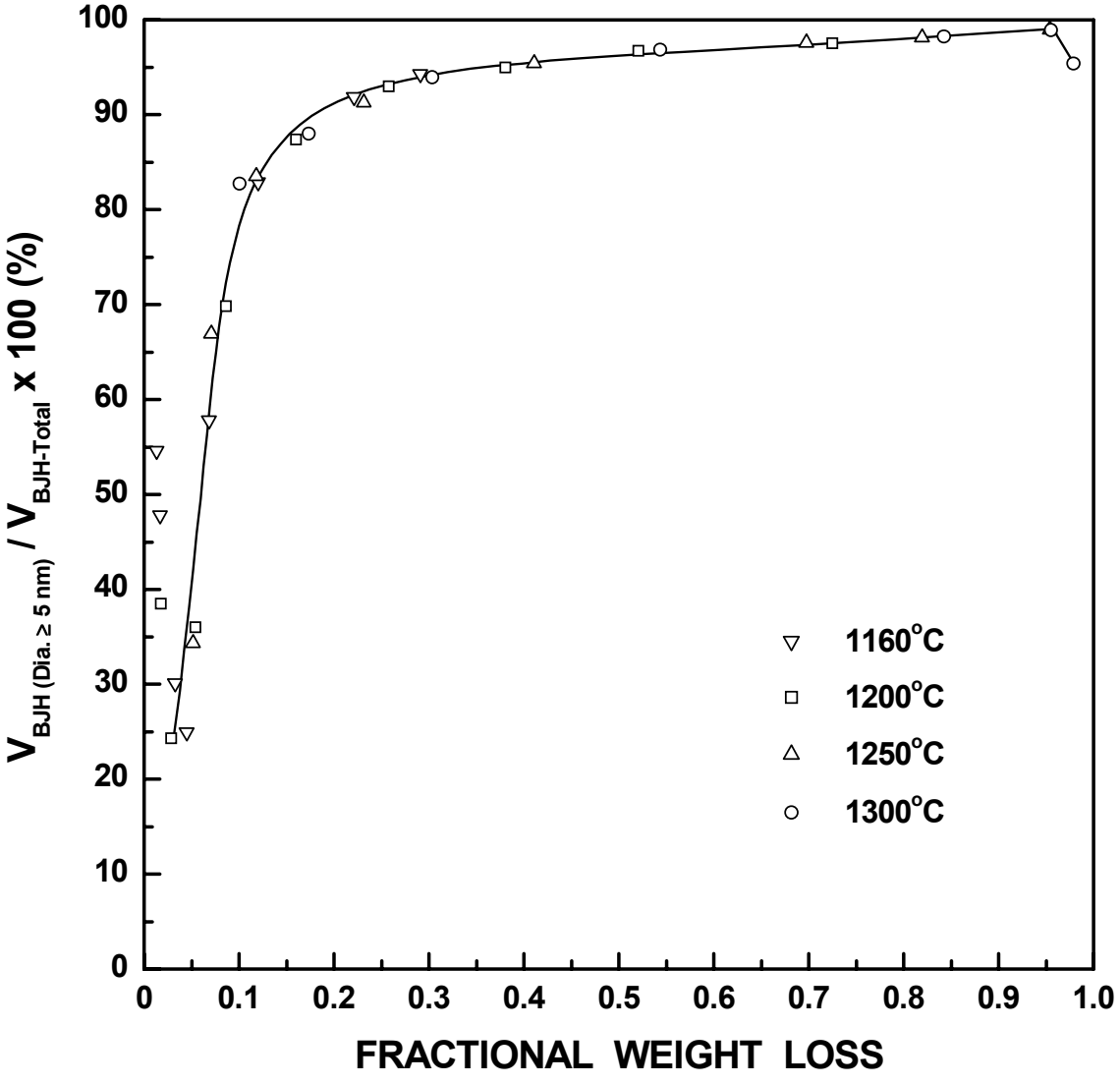

Figure 4-4-147 Plot of percentage of BJH pore volume for pores with diameter ≥5 nm (from the desorption branch of the isotherm) vs. fractional weight loss for the SC35 CTR samples.

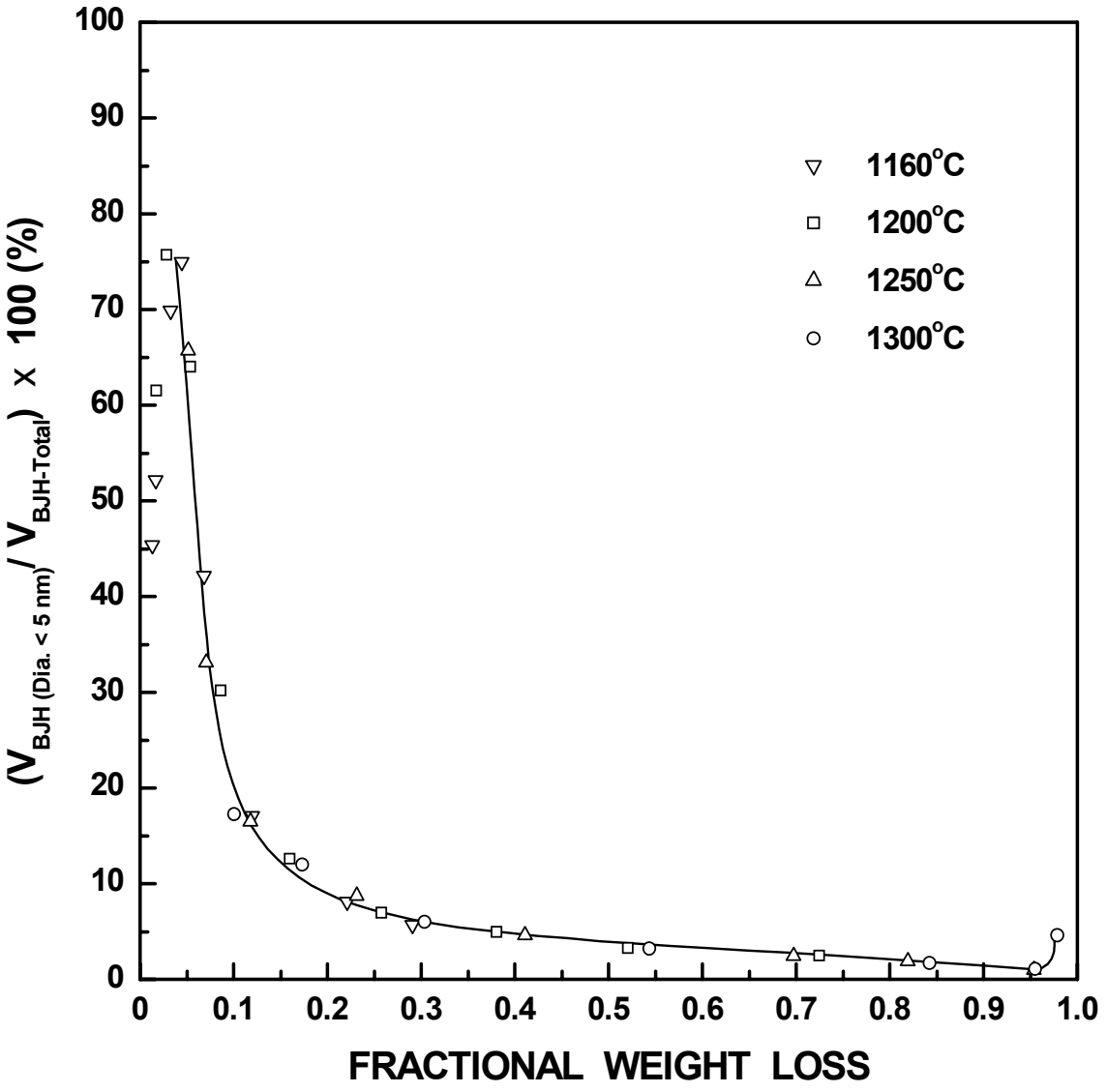

Figure 4-4-148 Plot of percentage of BJH pore volume for pores with diameter <5 nm (from the desorption branch of the isotherm) vs. fractional weight loss for the SC35 CTR samples.

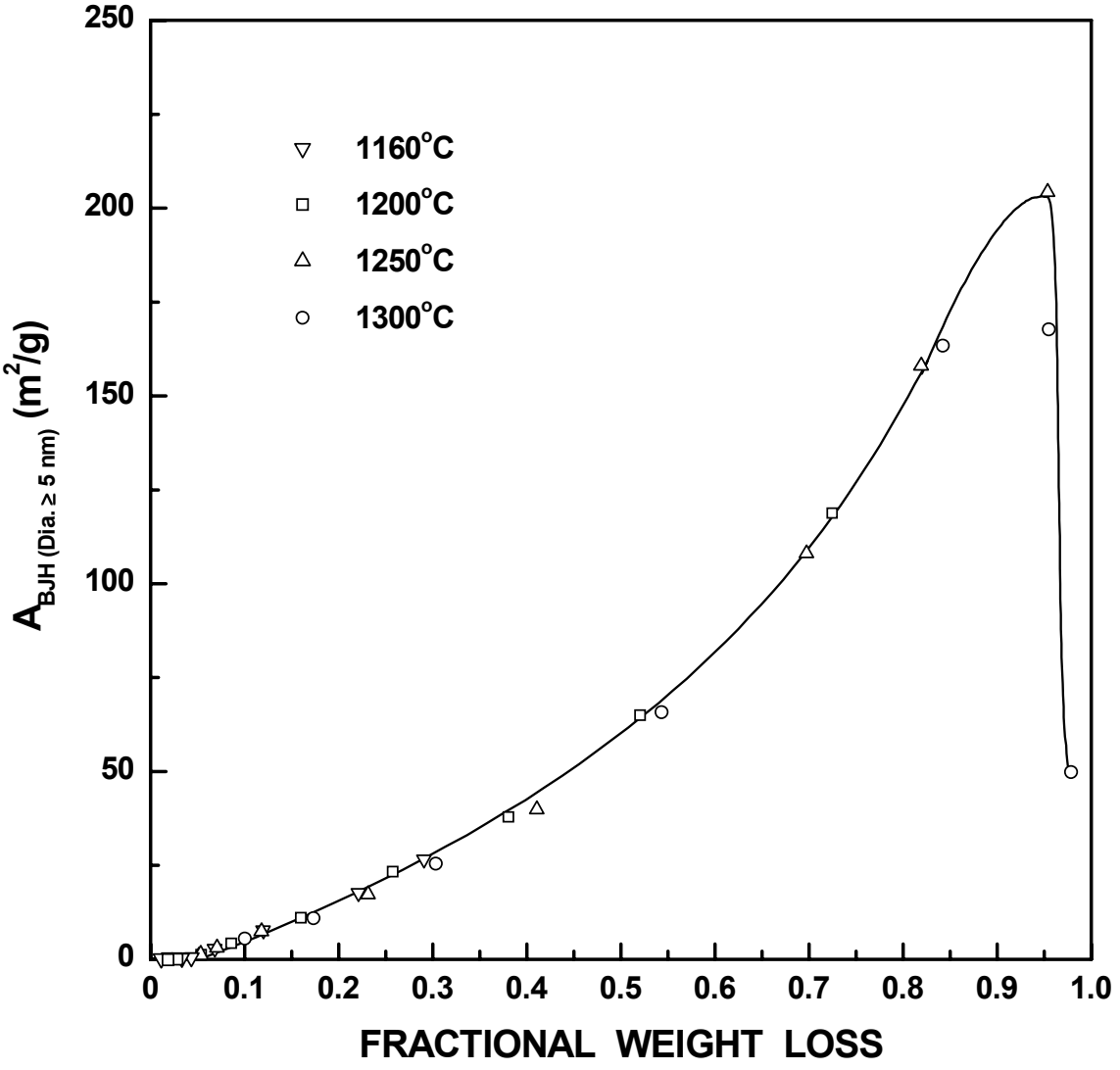

Figure 4-4-149 Plot of BJH specific surface area (from the desorption branch of the isotherm) for pores with diameter ≥5 nm vs. fractional weight loss for the SC35 CTR samples.

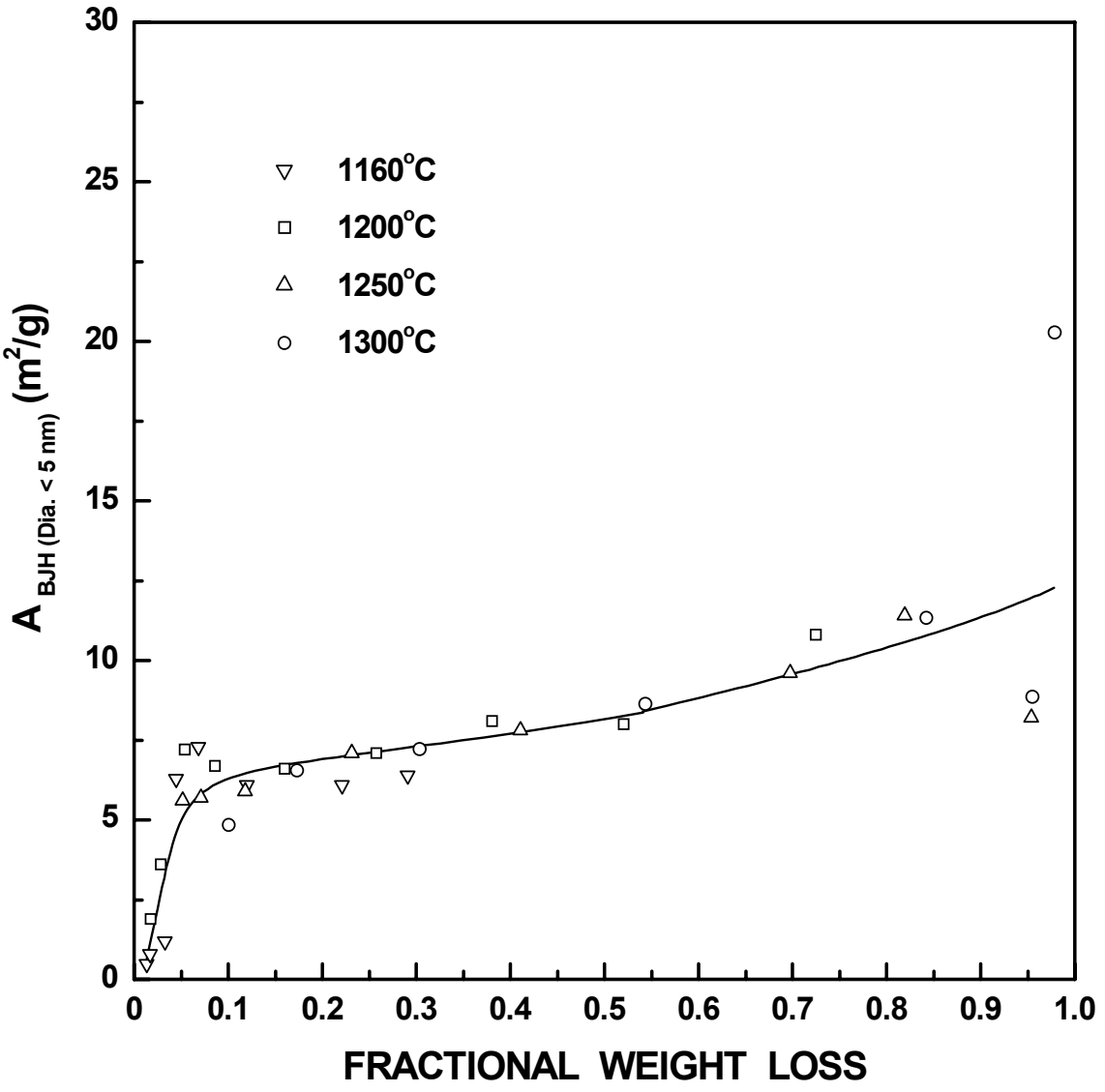

Figure 4-4-150 Plot of BJH specific surface area (from the desorption branch of the isotherm) for pores with diameter <5 nm vs. fractional weight loss for the SC35 CTR samples.

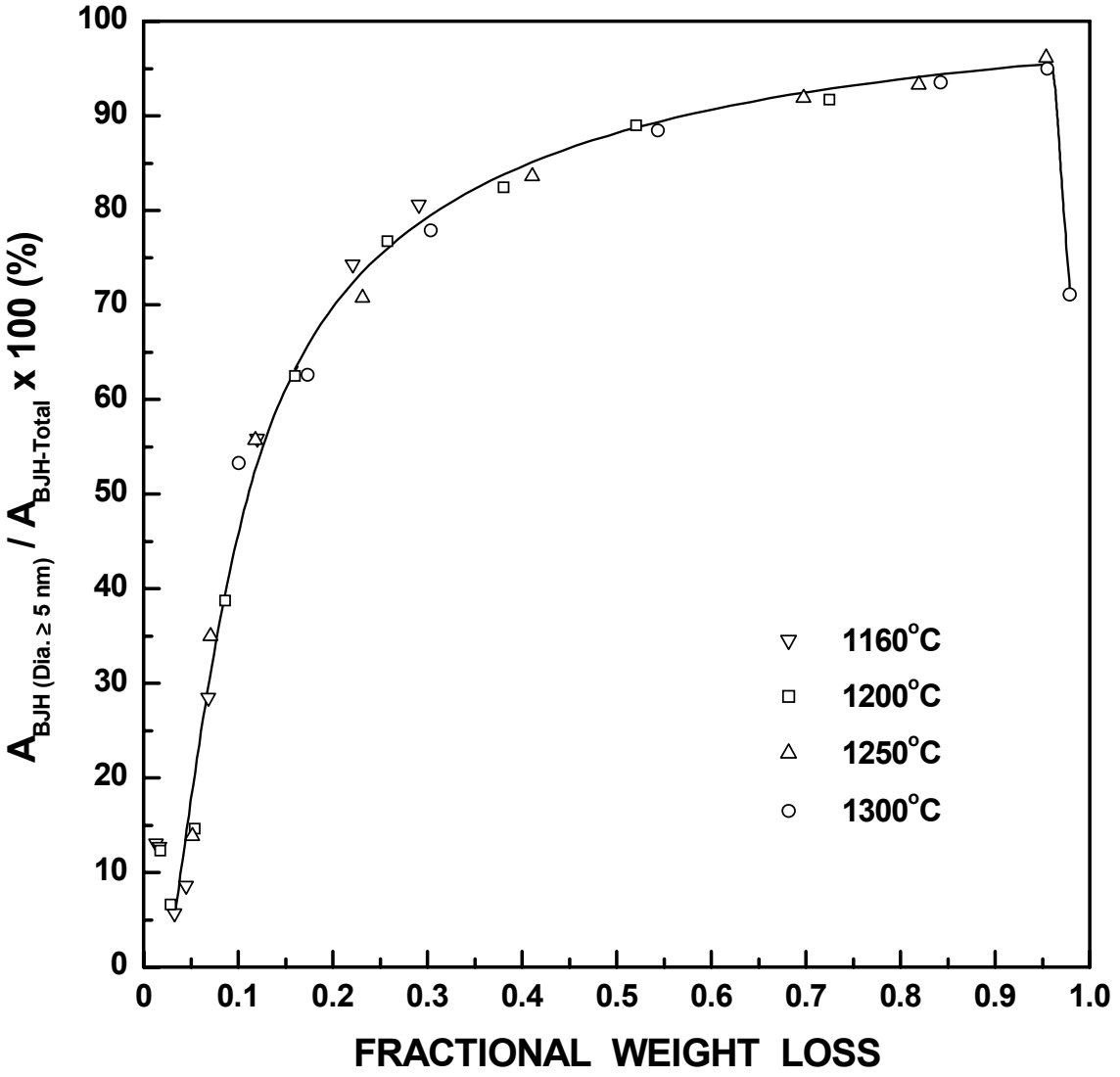

Figure 4-4-151 Plot of percentage of BJH specific surface area (from the desorption branch of the isotherm) for pores with diameter ≥5 nm vs. fractional weight loss for the SC35 CTR samples.

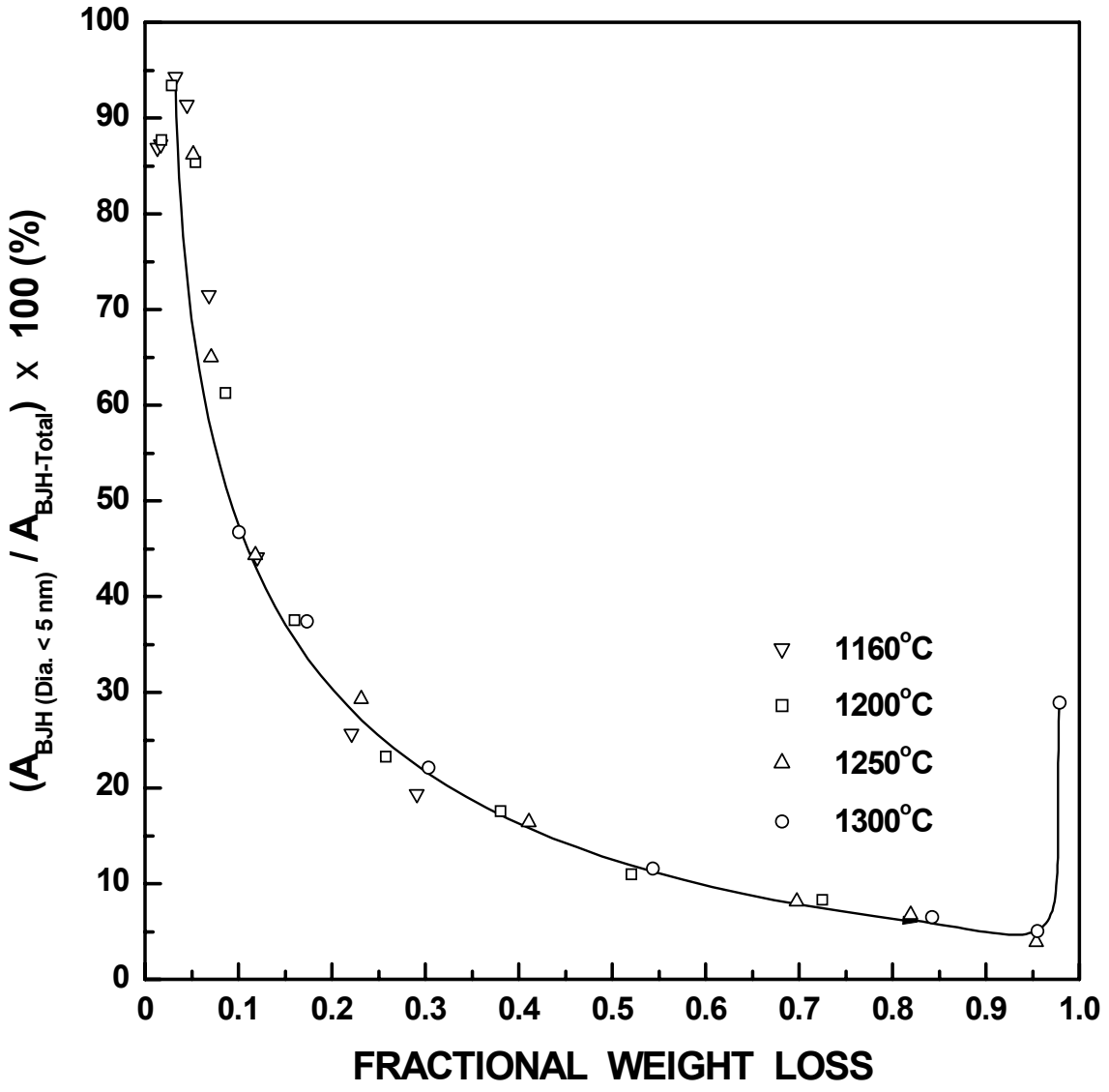

Figure 4-4-152 Plot of percentage of BJH specific surface area (from the desorption branch of the isotherm) for pores with diameter <5 nm vs. fractional weight loss for the SC35 CTR samples.

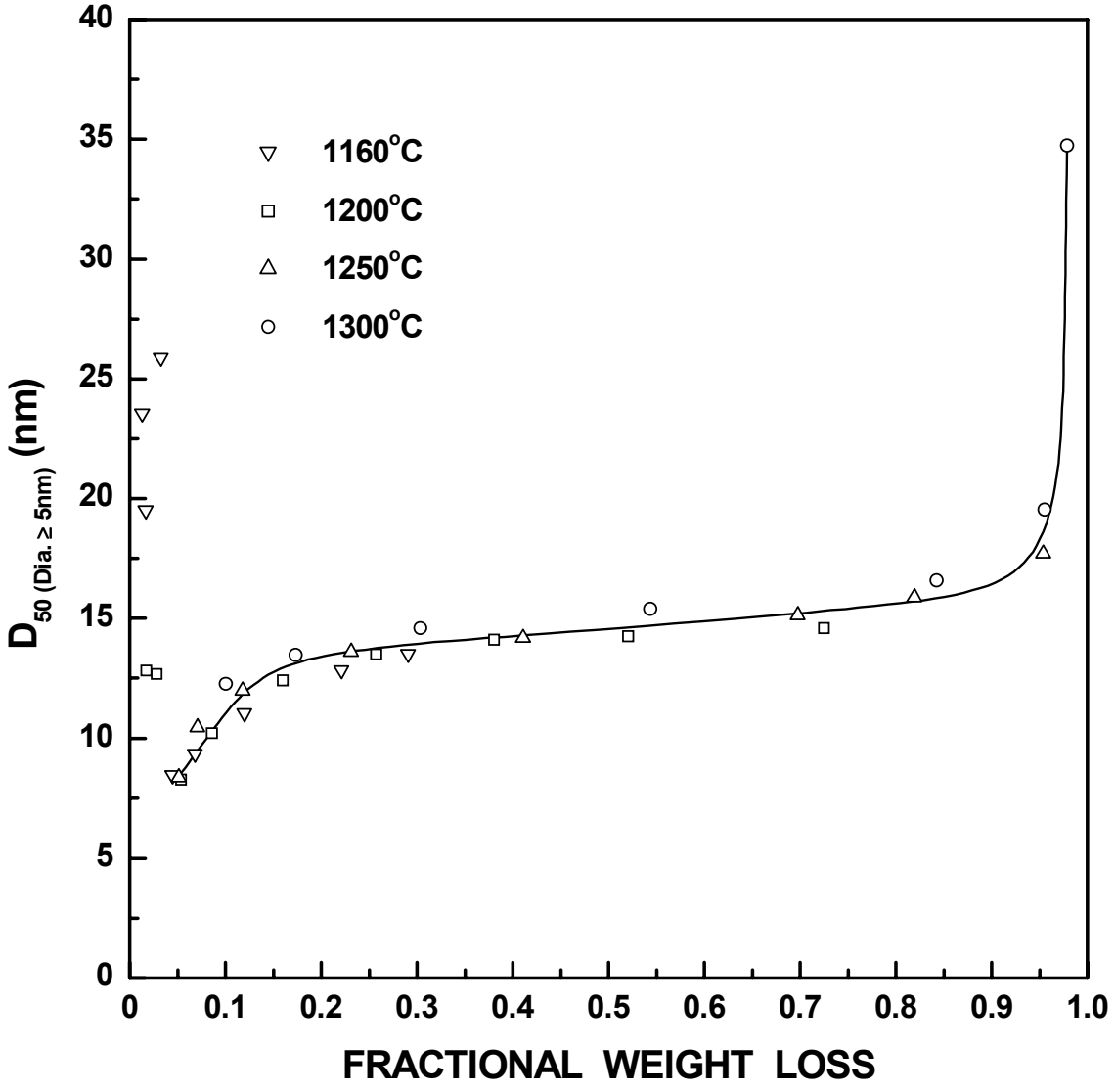

Figure 4-4-153 Plot of median pore diameter (D_{50}) vs. fractional weight loss for the SC35 CTR samples. The median diameter was determined for the portion of pore volume associated with pores ≥5 nm. The data was from the desorption branch of the isotherm.

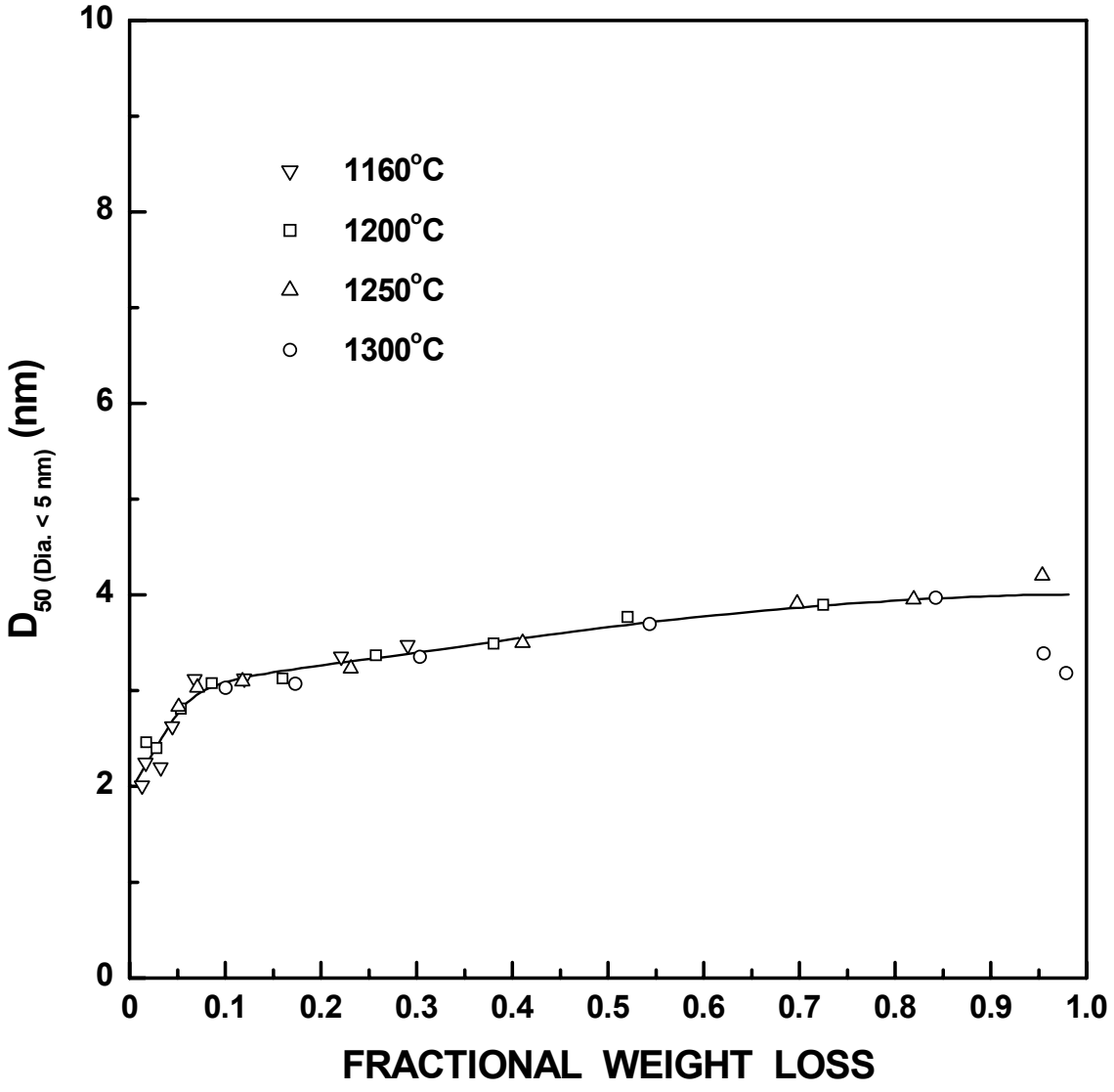

Figure 4-4-154 Plot of median pore diameter (D_{50}) vs. fractional weight loss for the SC35 CTR samples. The median diameter was determined for the portion of pore volume associated with pores <5 nm. The data was from the desorption branch of the isotherm.

distribution do not change very much during the reaction, especially after the earliest stage of the reaction (e.g., X_{WL} >0.05).

4.4.7.3 Discussion of the SC35 Pore Development in Relation to the Structural Model

From section 4.1, it is known that the starting material before CTR consists of relatively large particles (median size ~68 μm, Figure 4-1-5). As discussed in sections 4.4.5, it is believed that these relatively large particles are composed of considerably smaller clusters. These clusters are believed to be interpenetrating networks of silica and carbon. Specific surface area measurements (section 4.4.3.2), pycnometric measurements (section 4.1.9), and SEM observations (4.4.4) indicate that these clusters pack together in an essentially space-filling manner. In other words, the pyrolyzed particles contain relatively little inter-cluster porosity. The following is a detailed discussion of the porosity development in these particles during the process of CTR.

As stated in section 4.2, SiC formation via the CTR reaction is believed to have two steps. In the first step, silica is volatilized (as SiO) by reaction with carbon. Porosity forms in those locations where the silica has volatilized. As discussed in section 4.4.5, the reaction can be initiated at the outer surface of the large pyrolyzed particles and at accessible internal surfaces associated with gross defects (e.g., cracks) that are too large to be detected by gas adsorption/capillary condensation measurements. However, these surface regions represent a very small amount of specific surface area (i.e., surface area/mass of material) and the CTR conversion rate would be very low if the reaction was limited only to these areas. Instead, it was suggested previously that the reaction is initiated mostly at cluster-cluster interfaces and, therefore, the initial porosity that is developed in

the early stages of the CTR reaction formed mostly at these interfaces. As noted above, these cluster-cluster regions were presumed to have access paths (e.g., via microcracks and other defects) for CO to exit from the large pyrolyzed particles.

The porosity that formed in the earliest stage of the reaction (e.g., in samples with $X_{WL} < 0.1$ such as samples SC35-1200(2h), SC35-1250(30min), SC35-1250(1h), etc.) was small in size (i.e., mostly < 10 nm). In addition, the hysteresis loop observed in the isotherms for these samples (e.g., see Figures 4-4-70 to 4-4-72) was a hybrid of Type H3 and Type H4 hysteresis loops. One possibility is that the initial porosity that formed was associated with regions that were somewhat carbon-rich. It was noted earlier that Type H4 hysteresis has been observed in carbon samples (e.g., see Figures 4.2 and 4.34 of Gregg and Sing, 1982). In addition, it was suggested that the small size of phenolic resin oligomers might possibly allow some excess material to migrate, during drying, to the intercluster regions where the CTR reaction is likely to be initiated. Hence, it is possible that the pores that are specifically associated with the hysteresis loop (i.e., from ~0.4 to ~0.8 P/P_o values, or ~2.0 to ~ 5 nm) might be due to an inherent characteristic of the carbon structure that developed upon heat treatment. Another possibility is that this initial pore volume is simply associated with "crack-like pores" that developed when SiC formed at inter-cluster regions during the earliest stages of the reaction. More of these crack-like pores would become accessible to measurement by gas adsorption/capillary condensation as the reaction proceeded. As noted earlier, Type H3 and H4 hysteresis loops are often associated with non-cylindrical pores, such as slit-like pores or pores forming between plate-like structures.

It was shown earlier (Figures 4-4-68 to 4-4-73) that the shape of the isotherm

changed dramatically as the CTR reaction proceeded past the early stage. In particular, the hysteresis loop essentially became Type H1 by a fractional weight loss X_{WL} of ~0.1 (e.g., as in the SC35-1250(2h) sample). Even in this relatively early stage in the CTR reaction, the average pore size increased substantially, i.e., the median size exceeded ~10 nm (see Figures 4-4-111). This is because almost all the increase in pore volume as the reaction proceeds was due to the development of larger pores (e.g., ~5-20 nm). It is suggested that these pores were formed mostly from silica/carbon regions near cluster surfaces and between neighboring clusters. According to the geometric schematic based on the "shrinking-core" model presented earlier (Figures 4-4-45, 4-4-47 to 4-4-49), pores will mostly develop from the silica regions of the mixture because it is silica that volatilizes (as SiO) via reaction with carbon. Hence, the pore sizes should be somewhat related to the size of the silica regions. The observed sizes seem consistent with the above hypothesis when considering that, even in the sol state, polysilicate species are expected to be roughly on the order of ~5 nm (Figure 58 (1) of Chapter 3, Brinker and Scherer (1990)). (Of course, the size of the silica regions may be different in the current system due to some other effects. First, larger clusters of polysilicate species might develop as gelation and drying occurred. Second, the size of the silica regions that develop may have been altered by the presence of the phenolic resin. However, there is no direct information available in this study concerning either of these effects. Direct characterization by a technique such as high resolution transmission electron microscopy (HRTEM) would be useful. In fact, Haraguchi et al. (1998, *Polymer*) made TEM observations on composites prepared from phenolic resin/silica mixtures in which the silica was formed by *in-situ* hydrolysis/ condensation of silicon methoxide (TMOS). In some samples, the silica was in the form of

~10-30 nm clusters which were composed of ~5 nm primary particles. Although the processing conditions used in the current study were different from those used by Haraguchi et al., the latter study does provide some support to the above suggestion that the pore sizes that developed in the CTR samples in this study were related to the sizes of the silica regions.)

Figures 4-4-73 and 4-4-74 show that the transition in the gas adsorption/desorption hysteresis loops from Type H3/Type H4 to Type H1 hysteresis was substantially completed in the SC35-1250(2h) (X_{WL} = 0.12) sample and fully completed in the SC35-1250(4h) sample (X_{WL} = 0.23). It was pointed out previously that the Type H1 hysteresis is often associated with the filling and emptying of open, connected pores in particulate structures, such as in agglomerates, loose-packed or lightly-compacted powders, or in powder compacts in the early stages of sintering. The results in this study are consistent with the development of this type of structure. TEM observations (Figures 4-4-12, 4-4-13, 4-4-14, 4-4-16 and 4-4-17) showed the development of relatively open clusters of equiaxed SiC crystallites for the SC42-1300(3h) (X_{WL} = 0.63) and SC42-1300(6h) (X_{WL} = 0.88) samples. It was suggested earlier that the CTR reaction (and the concomitant development of the porous SiC structure) would probably occur first in the inter-cluster regions and the outer regions of the individual clusters. Therefore, it is hypothesized that the completion of the transition in the hysteresis behavior in the gas adsorption/desorption isotherms indicates that the porous SiC structure has formed a connected network (along the inter-cluster regions) throughout the large (multi-cluster) particles. This is illustrated by Figure 4-4-47. The isotherms in Figures 4-4-73 and 4-4-74 indicate that the development of this connected network is nearly completed in samples with only ~0.05-0.11 SiC volume fractions (for

SC35-1250(2h) and SC35-1250(4h) respectively). These volume fractions may seem low, but percolation theory indicates that a connected network might form at such values. For example, bond percolation occurs in model FCC and BCC structures (for monosized spheres) at only 12 and 18 volume percent, respectively (Lorenz and Ziff, 1998). (The analogy with these close-packed structures seems reasonable since it was hypothesized that the clusters are packed in a highly-dense manner.) In this view of the percolation process, the unreacted carbon/silica cores would be volumetric (three-dimensional) entities that are located on the lattice sites, while the porous SiC regions (that would form in the outer regions of the clusters) would be areal (two-dimensional) entities that comprise the lattice edges. The bond percolation threshold would be reached when the lattice edges from a continuous (connected) network throughout the body. (Zallen, 1983)

The size distributions for the larger pores (e.g., ~5-20 nm) that develop during the reaction are relatively broad, but they are mono-modal (Figures 4-4-134 to 4-4-140). Hence, there is no evidence to suggest that distinctly different sizes would be associated with pores that develop within clusters vs. pores that develop between clusters. The observation of a continuous, but fairly broad, distribution of the large pore sizes appears to be consistent with the supposition that the original clusters were packed in the pyrolyzed particles in a nearly space-filling manner.

As noted previously in section 4.4.7.1, there were essentially no changes in the shape of the gas adsorption/desorption isotherms (Figures 4-4-73 to 4-4-79) and the size distributions for the larger (~4-25 nm) pores (Figures 4-4-87 to 4-4-93) over a large portion of the CTR reaction (i.e., for X_{WL} values from ~0.12 to ~0.95). This is consistent with the proposed "shrinking-core" model in that continued reaction should only result in the

formation of an additional amount (volume) of porous SiC, but not in changes in the pore characteristics (e.g., shape, size, etc.).

The overall pore size distributions for most of the samples are bimodal (Figures 4-4-133 to 4-4-142) because they have a fraction of very fine pores (<5 nm). The mechanism for the development of these very fine pores is not very clear. One possibility is that they resulted from local silica/carbon regions in which only a small portion of the silica had been removed by the CTR reaction. (Hence, the pore size might be smaller than if all the silica had been removed from that local region.) A related possibility is that some small pores develop when the CTR reaction occurs in carbon-rich regions that contain some entrapped silica. (This implies that there were some fine (nanometer-scale) local compositional heterogeneities in the dried and pyrolyzed particles.) The reason for suggesting the latter possibility is that a much larger amount of these fine (< 5 nm) pores were developed during the CTR reaction in the highly carbon-rich SC8 samples. (This will be discussed in detail later in section 4.4.7.4) Both of the suggested possibilities are consistent with the observation that the proportion of the fine pores decreases with increasing extent of conversion (Figures 4-4-148). In the first case, the continued removal of silica as the reaction proceeded would lead to an increasing proportion of the larger pores. In the second case, the proportion of carbon-rich regions would decrease as the amount SiC increased, so the proportion of the smaller pores (primarily associated with the carbon-rich regions) would decrease.

Figures (4-4-153 and 4-4-145) show that there is a rapid increase in average pore size and rapid decrease in pore volume toward the end of the CTR reaction ($X_{WL} \geq 0.95$). The key points regarding this observation are summarized as follows:

1. The isotherm data clearly shows that some pores have grown to sizes that cannot be detected by the gas adsorption/capillary condensation method (Figures 4-4-80 and 4-4-81). As has been shown in section 4.4.6, this accounts for much of the observed decrease in pore volume toward the end of the reaction. The development of larger-sized pores is consistent with coarsening phenomena, i.e., in which the average pore size increases and the number of pores decreases. The pore coarsening is also consistent with the sharp increase in SiC crystallite size that is observed in the late stage of reaction (Figure 4-4-2). These increases in pore and crystallite sizes are also consistent with extensive prior work (Vassen, 1996, Clegg, 2000) which show that SiC undergoes coarsening when the excess carbon concentration is low and additives which inhibit coarsening (e.g., boron) are absent.
2. The broadening of the pore size distribution toward the end of the CTR reaction (Figures 4-4-140 to 4-4-142 and 4-4-144) is due to development of large pores.
3. Densification, via sintering, is also a contributing factor for the sharp decrease in pore volume observed toward the end of the CTR reaction. This has been suggested from the size distribution data (Figures 4-4-58 to 4-4-61) on the large particles that evolve from the original pyrolyzed particles. However, calculations in section 4.4.6 showed that densification would account for only a small portion of the decrease in pore volume. This is consistent with expectations based on extensive prior work reported in the literature (Vassen, 1996, Clegg, 2000). In addition, densification mechanisms alone would not produce the observed increase in the average pore size. Hence, it is evident that coarsening must be playing a major role in the observed changes in the pore size and the pore volume in these samples.

4.4.7.4 Gas adsorption/desorption Isotherms for SC8 CTR Samples

The adsorption isotherms for SC8 CTR samples with different fractional weight loss values (from 0.05 to 0.94) are shown in Figures 4-4-155 to 4-4-165. The initial isotherms (e.g., SC8-1160(1h)) are more like Langmuir-type (Type I) isotherms, as shown in Figure 4-4-155. The isotherms start to convert toward Type II behavior in the SC8-1160(4h) sample (X_{WL} = 0.10, Figure 4-4-156) and then increasingly look more like Type II isotherms for the SC8-1180(2h) (X_{WL} = 0.13, Figure 4-4-157), SC8-1160(7h) (X_{WL} = 0.18, Figure 4-4-158), and SC8-1160(12h) (X_{WL} = 0.26, Figure 4-4-159) samples. As observed for the early-stage SC35 samples (e.g., SC35-1160(1h), SC35-1200(1h), etc.), the isotherms for the SC8 early-stage samples (such as SC8-1160(1h), SC8-1160(4h), SC8-1180(2h), SC8-1160(7h), and SC8-1160(12h) in Figures 4-4-155 to 4-4-159) show large increases in the volume adsorbed at very high P/P_0 values. (The isotherms asymptotically approach the vertical line (parallel to the y-axis) at saturated vapor pressure (i.e., P/P_0 = 1) indicating that nitrogen is condensing on the "bulk" surface as a liquid.) After the initial stage, the isotherms of the SC8 samples start taking on some Type IV character. This is initially observed in samples such as SC8-1160(12h) in Figure 4-4-159. The isotherms continue to look more like Type IV isotherms with increasing extent of reaction, as observed for samples such as SC8-1160(20h) (X_{WL} = 0.40), SC8-1160(28h) (X_{WL} = 0.58), SC8-1160(48h) (X_{WL} = 0.74), SC8-1250(8h) (X_{WL} = 0.82), SC8-1250(12h) (X_{WL} = 0.92), SC8-1250(16h) (X_{WL} = 0.96) in Figures 4-4-160 to 4-4-165.

There are great differences between the isotherms of SC8 samples and those of the SC35 samples. These differences are as follows:

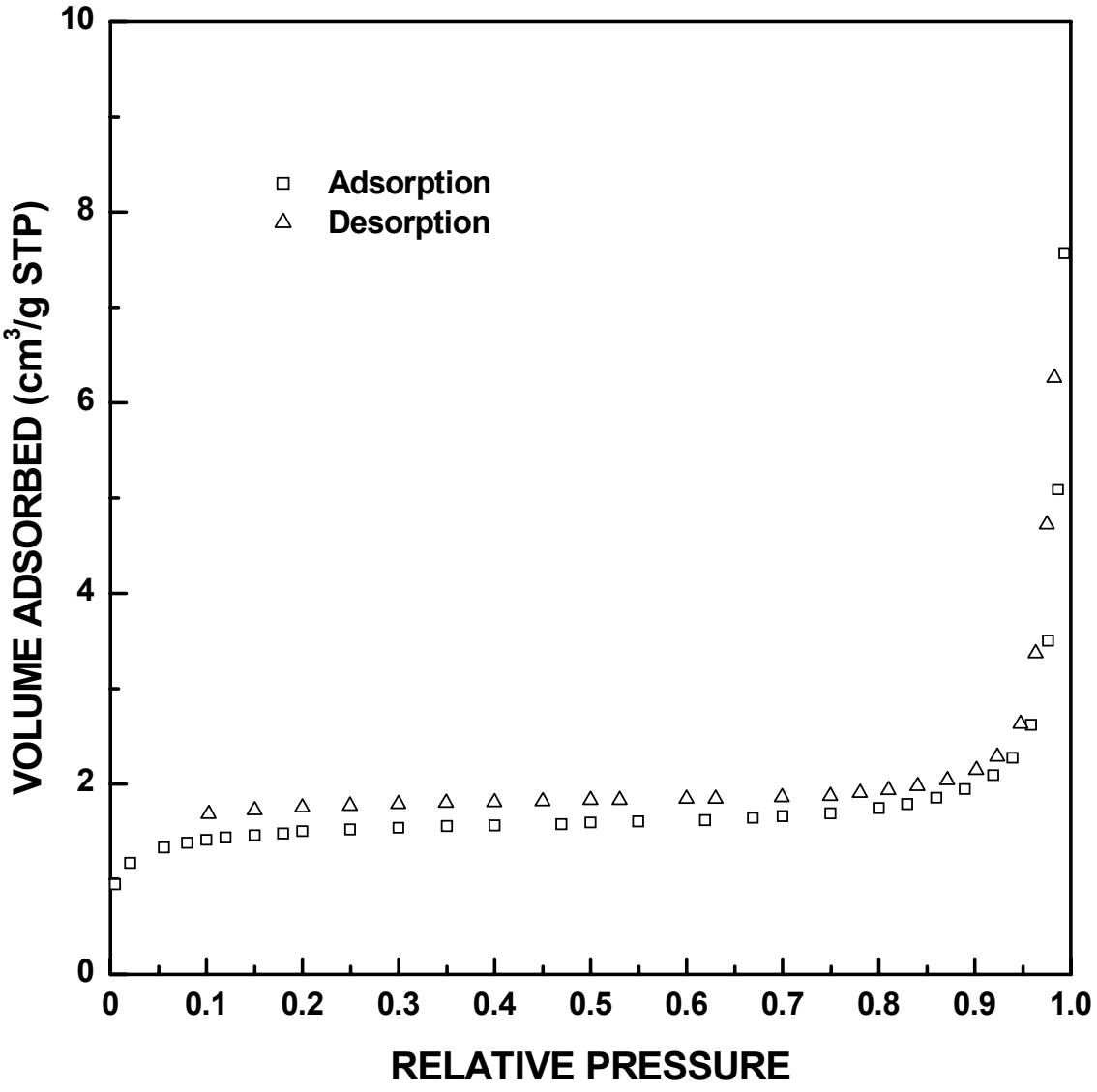

Figure 4-4-155 Adsorption/desorption isotherm plots for SC8-1160(1h) sample (X_{WL} = 0.05).

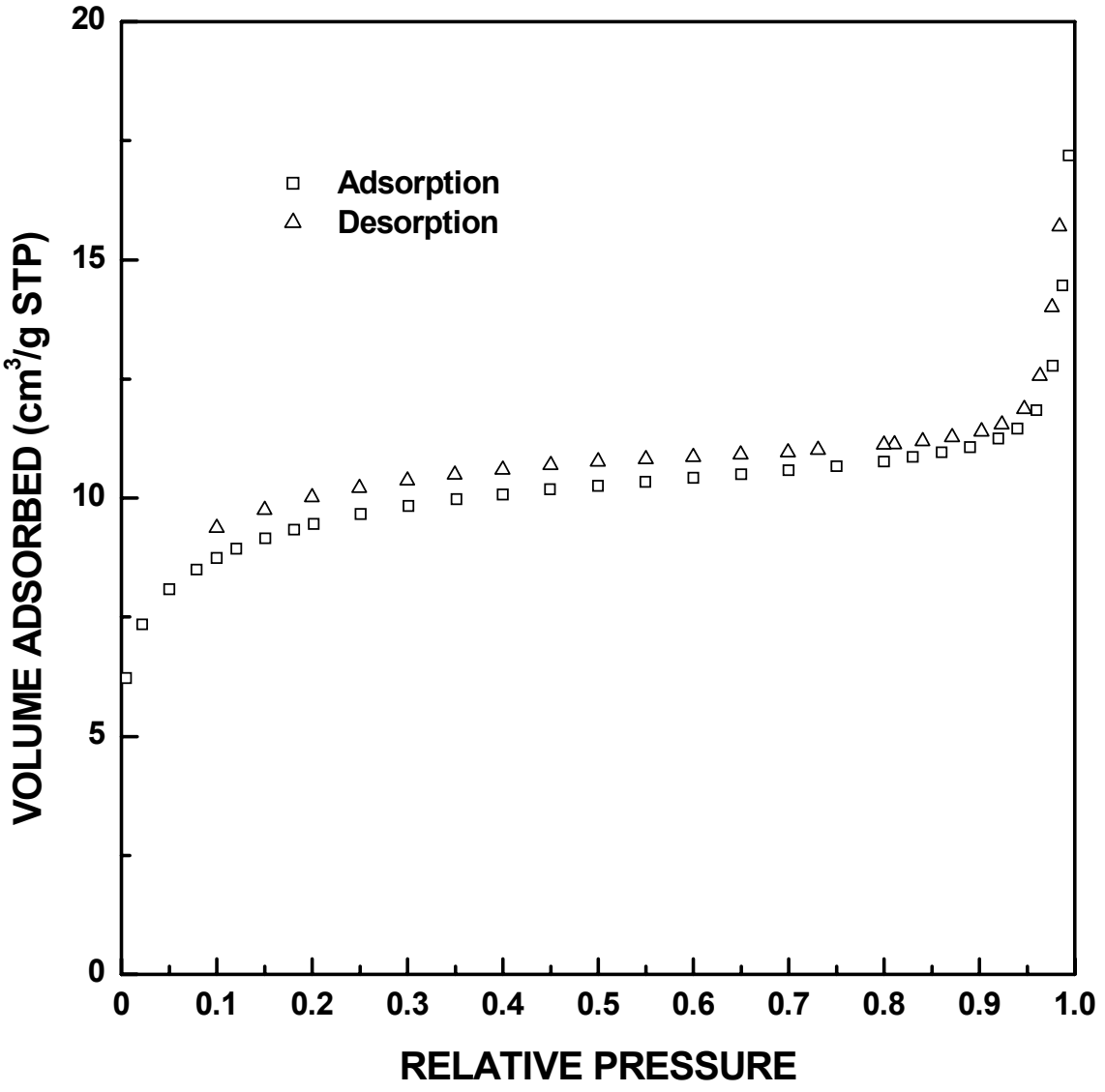

Figure 4-4-156 Adsorption/desorption isotherm plots for SC8-1160(4h) sample (X_{WL} = 0.10).

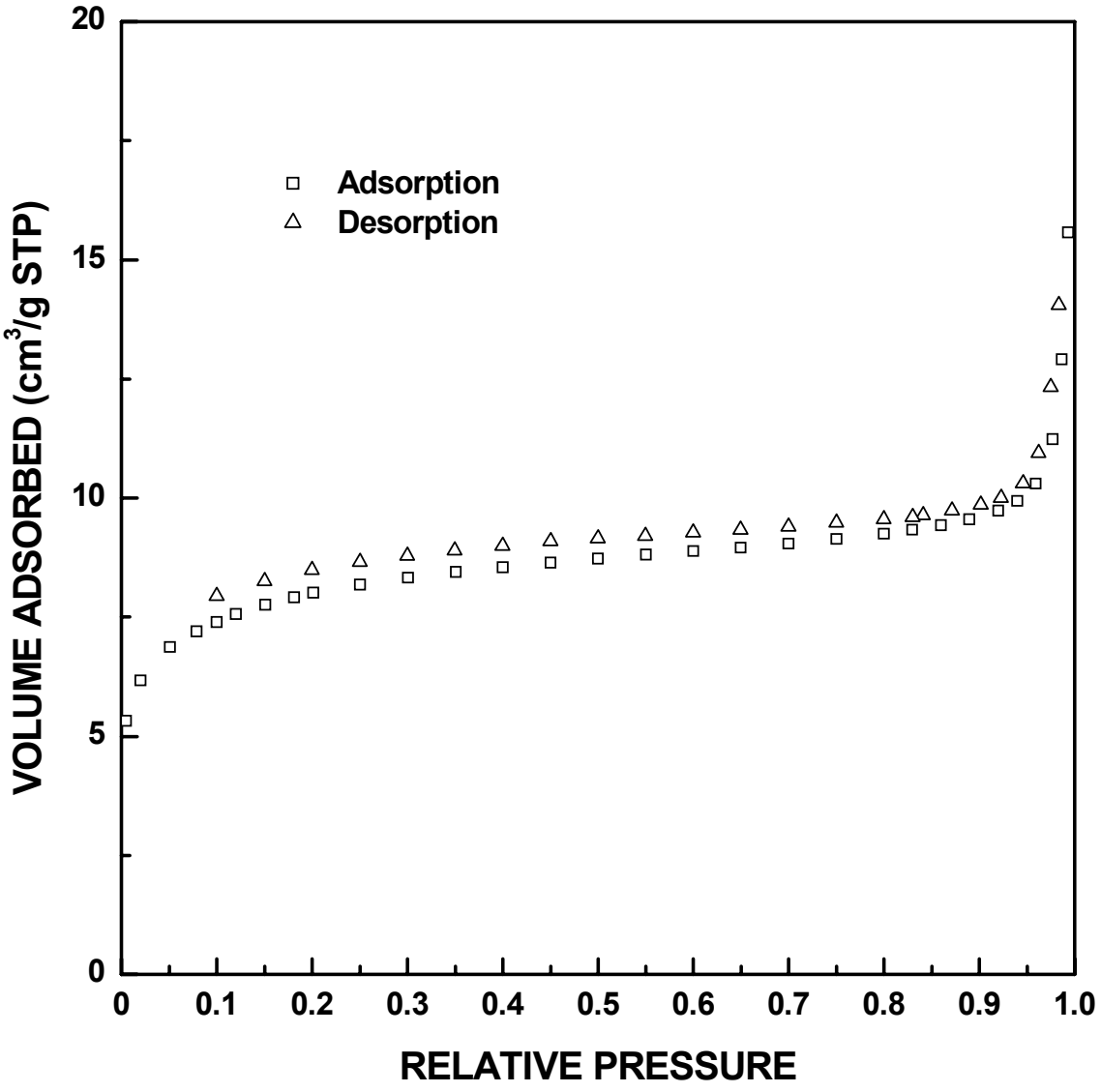

Figure 4-4-157 Adsorption/desorption isotherm plots for SC8-1180(2h) sample (X_{WL} = 0.13).

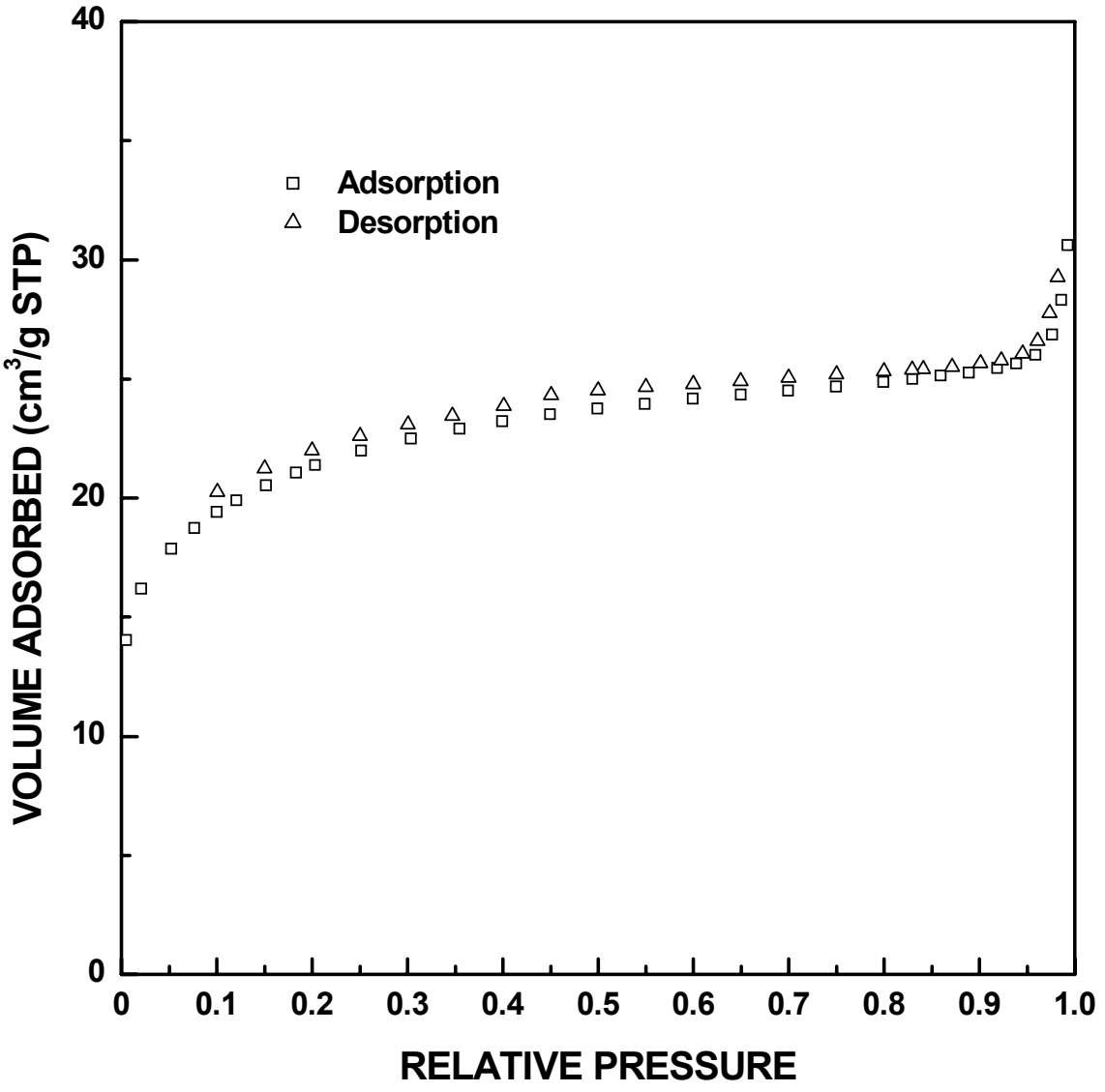

Figure 4-4-158 Adsorption/desorption isotherm plots for SC8-1160(7h) sample (X_{WL} = 0.18).

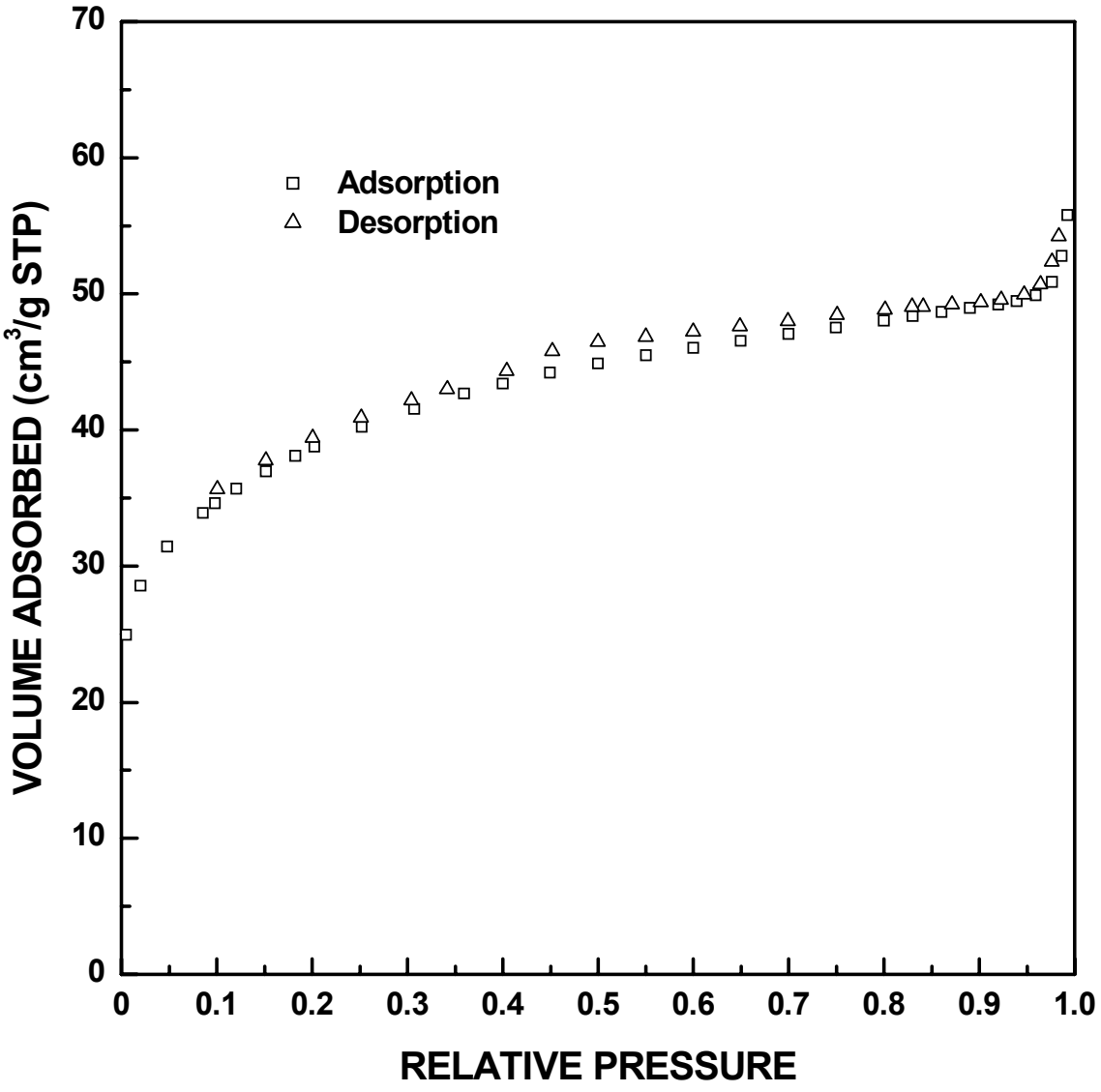

Figure 4-4-159 Adsorption/desorption isotherm plots for SC8-1160(12h) sample (X_{WL} = 0.26).

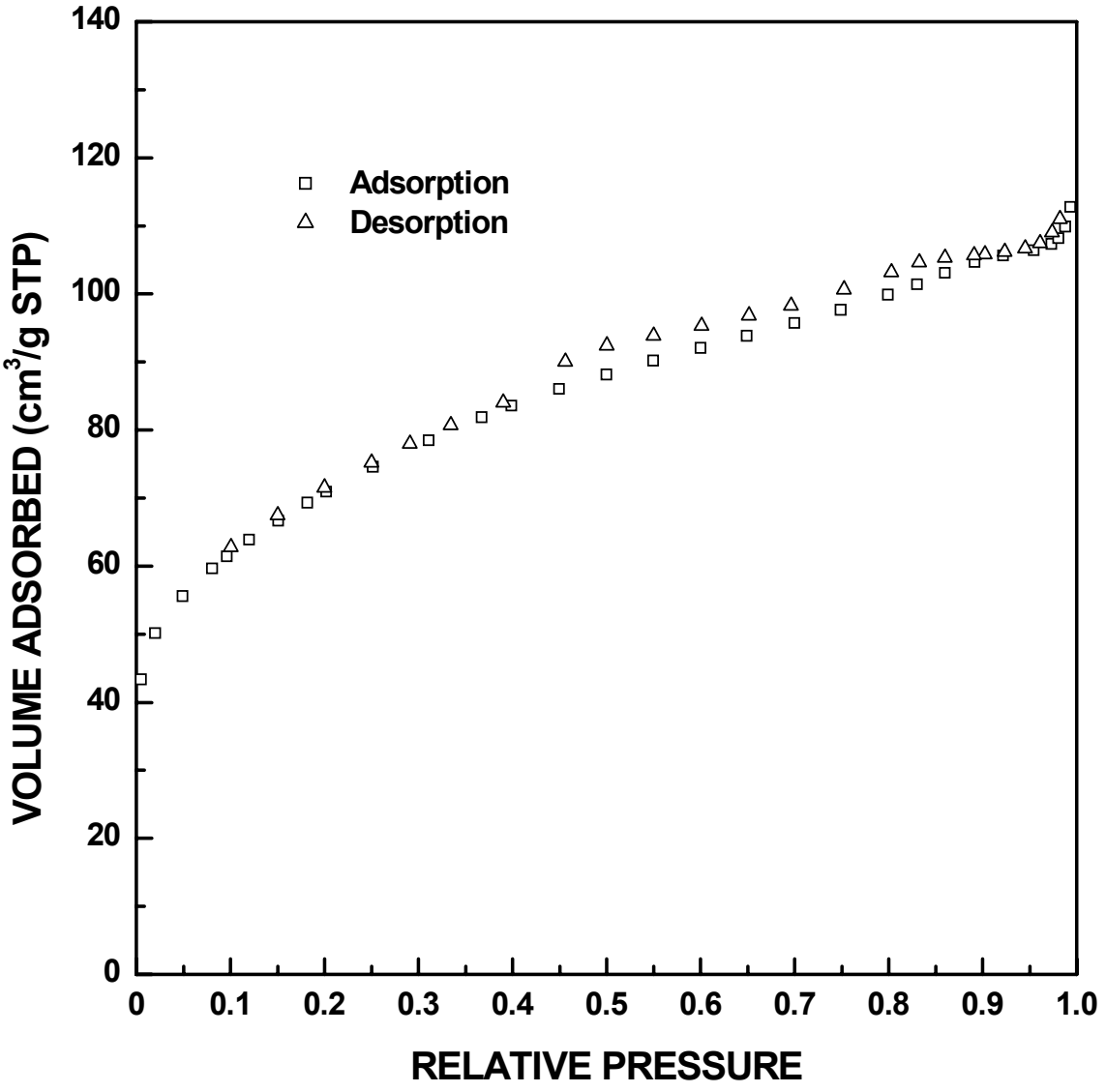

Figure 4-4-160 Adsorption/desorption isotherm plots for SC8-1160(20h) sample (X_{WL} = 0.40).

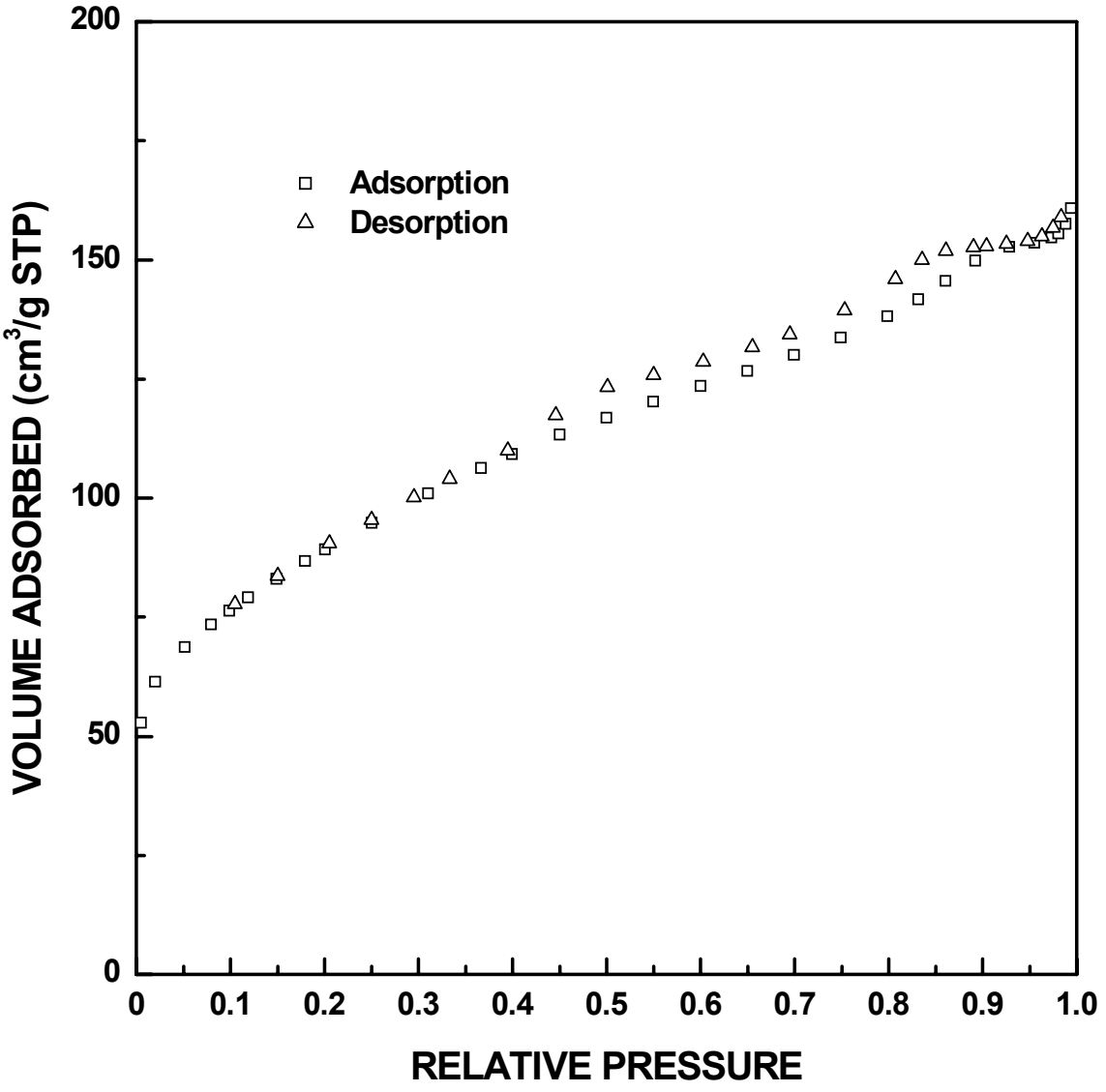

Figure 4-4-161 Adsorption/desorption isotherm plots for SC8-1160(28h) sample (X_{WL} = 0.59).

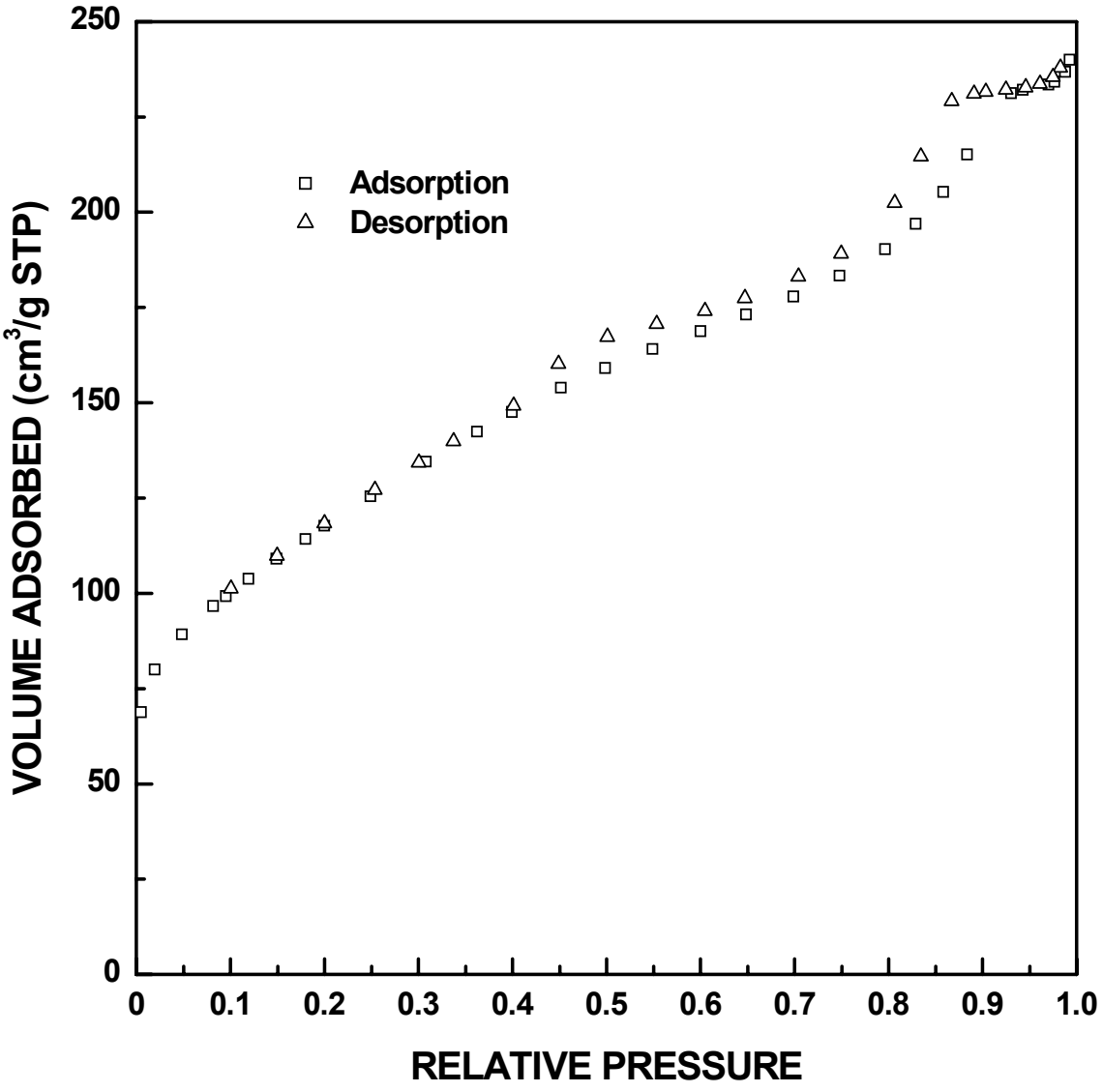

Figure 4-4-162 Adsorption/desorption isotherm plots for SC8-1160(48h) sample (X_{WL} = 0.74).

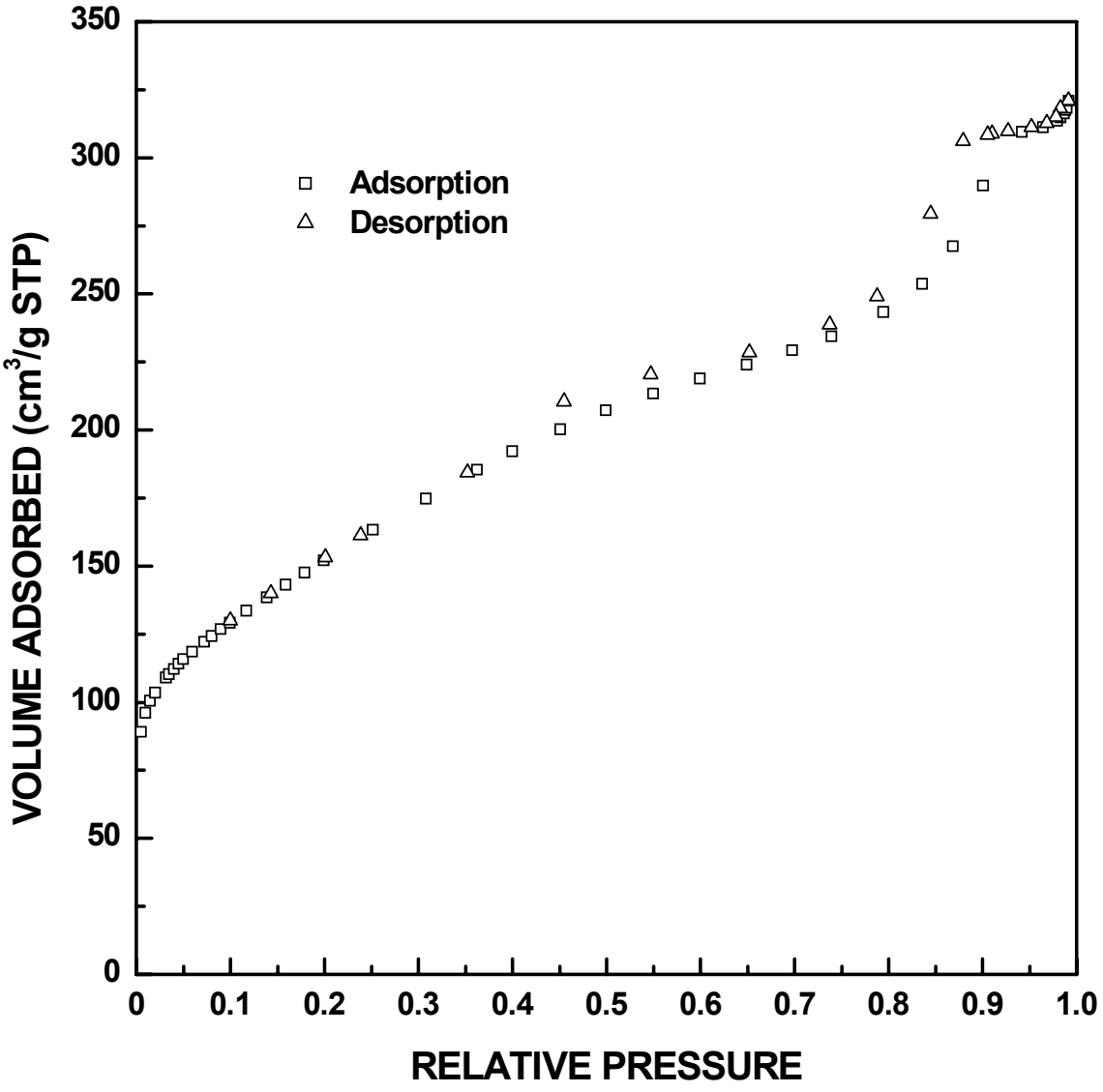

Figure 4-4-163 Adsorption/desorption isotherm plots for SC8-1250(8h) sample (X_{WL} = 0.82).

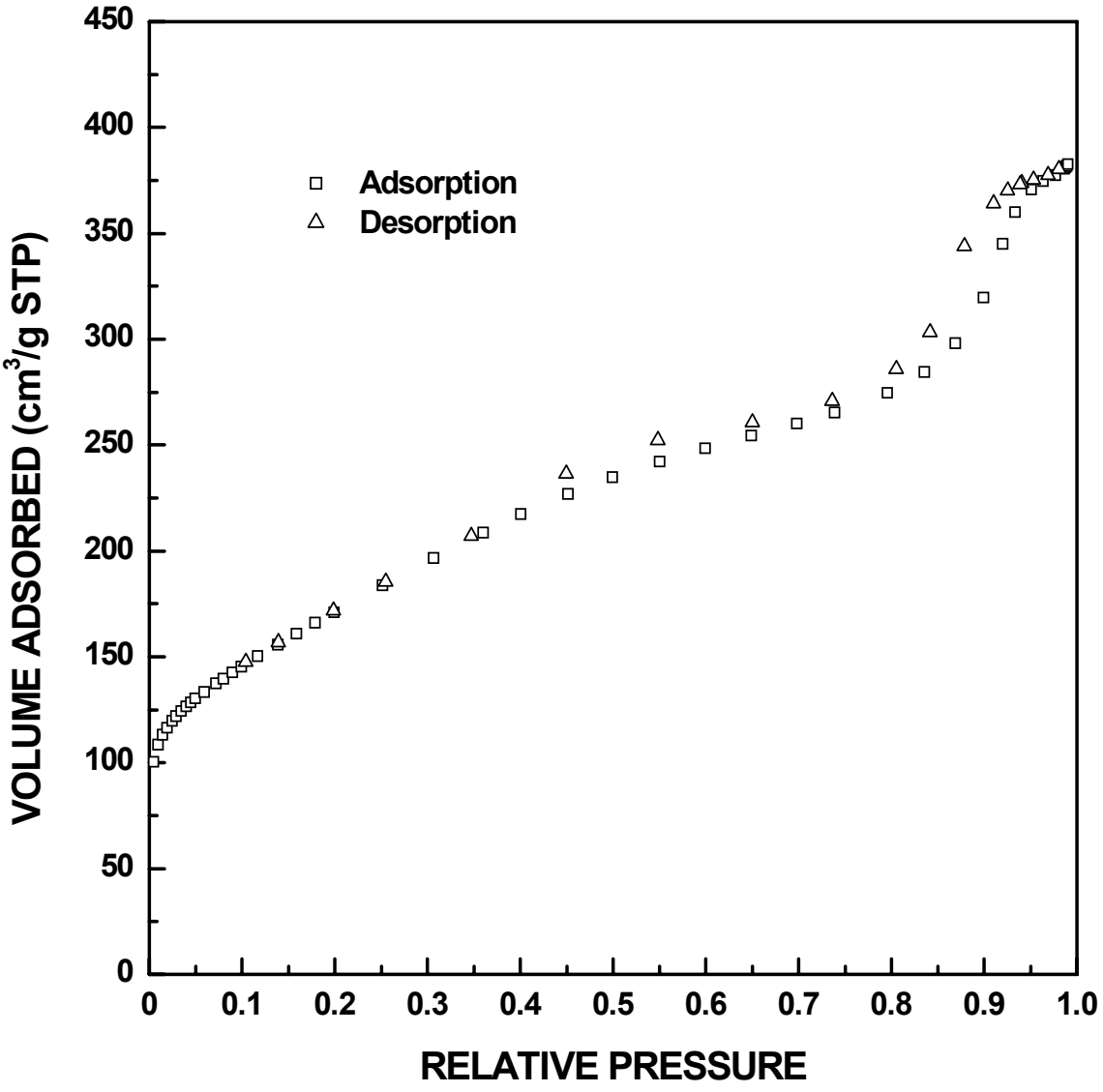

Figure 4-4-164 Adsorption/desorption isotherm plots for SC8-1250(12h) sample (X_{WL} = 0.92).

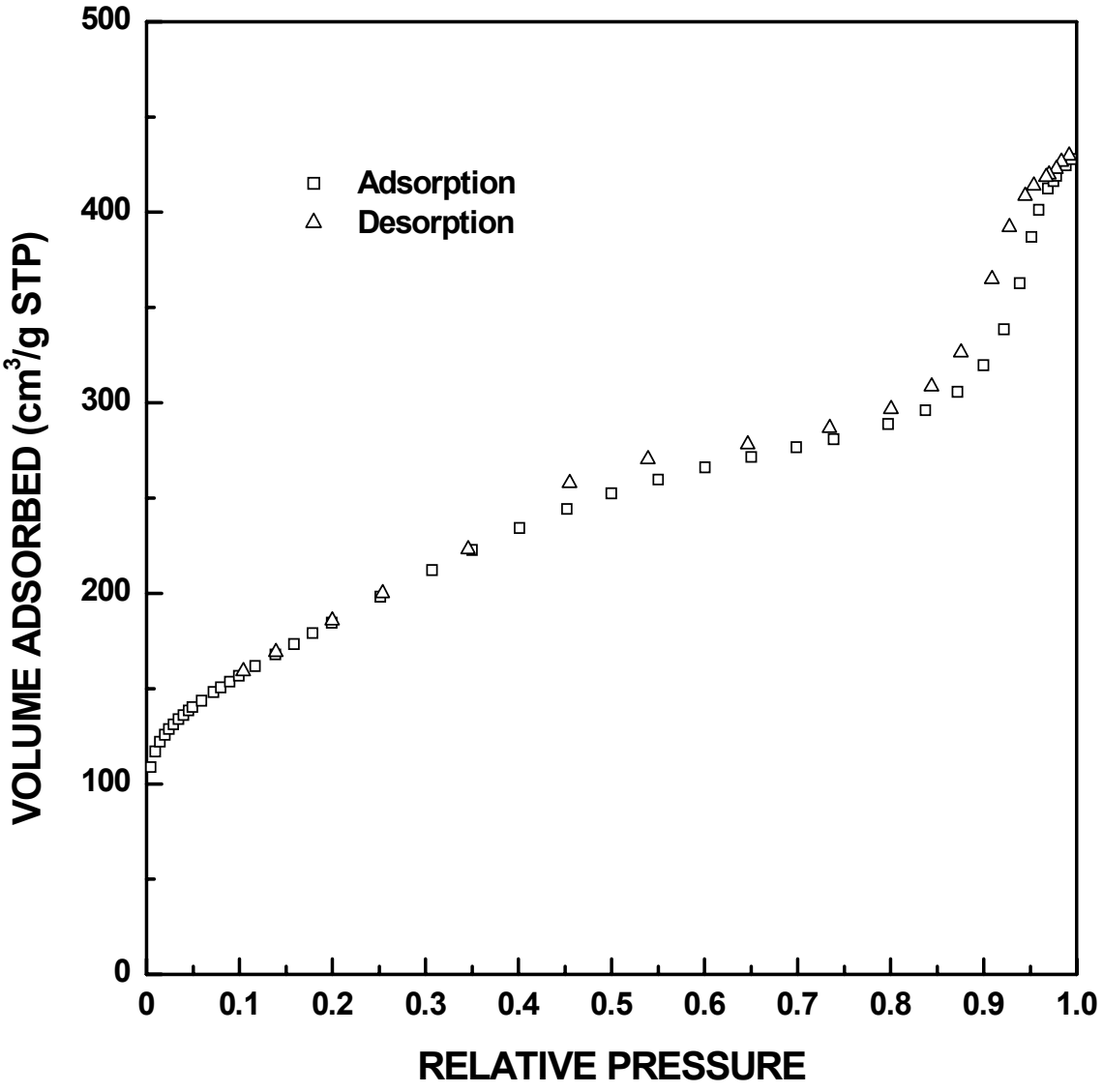

Figure 4-4-165 Adsorption/desorption isotherm plots for SC8-1250(16h) sample (X_{WL} = 0.94).

(1) The upward bending of the adsorption isotherm near the saturated vapor pressure continued to occur in samples with much greater fractional weight loss values. The upward bending was not observed for SC35 samples with fractional weight loss as low as ~0.07 (e.g., SC35-1250(1h)), while it had only started to disappear for the SC8 sample with $X_{WL} \approx 0.26$ (SC8-1160(12h)) and had mostly disappeared in a sample with $X_{WL} \approx 0.40$ (e.g., SC8-1160(20h)). The adsorbed volumes increased more gradually (on a relative basis) as P/P_0 approaches 1 with increasing increased fractional weight loss.

(2) Although the isotherms for SC8 samples start to show the Type H3/H4 hysteresis loop in the early stage of the reaction (Figures 4-4-155 - 4-4-158), samples with fractional weight less than ~0.3 actually do not have closed hysteresis loops. The desorption branch of the isotherm does not meet the adsorption branch even at the lowest pressure used for the desorption branch in these samples. There is a gradual progression toward complete "closing of the loop" as the fractional weight loss increases for the SC8-1160(7h), SC8-1160(12h), and SC8-1160(20h) samples (Figures 4-4-158 - 4-4-160). The latter sample, with an X_{WL} value of ~0.40, shows a fully closed hysteresis loop. This change is also observed for SC8-1180(4h) ($X_{WL} = 0.18$), SC8-1180(8h) ($X_{WL} = 0.31$), and SC8-1180(12h) ($X_{WL} = 0.43$) samples, as shown in Appendix I.

(3) The Type H3/H4 "hybrid" hysteresis loop was observed only in the early stages of the reaction in SC35. There was a fairly sharp transition from the Type H3/H4 "hybrid" hysteresis loop to the Type H1 hysteresis loop for samples with fractional weight losses ranging from ~0.05 to ~0.12 (Figures 4-4-70 - 4-4-73). By contrast, in SC8 samples, the Type H3/H4 "hybrid" hysteresis loop was present from the early stages to the late stages of the reaction. Type H1 behavior developed much more gradually, while at the same time

the Type H3/H4 behavior never disappeared. Therefore, for SC8 samples at intermediate and high extents of conversion, the hysteresis loop was comprised of two connected sections, the Type H3/H4 which dominated at lower pressures (smaller pore sizes) and the Type H1 which dominated at higher pressures (large pores sizes). In the SC35 samples, the lower-end pressure at which the hysteresis loop closed increased as the transformation proceeded from Type H3/H4 behavior to Type H1 behavior. In contrast, the lower-end pressure at which the loop closed remained unchanged (i.e., at $P/P_o \sim 0.4\text{-}0.45$) throughout the reaction in the SC8 samples (e.g., compare samples from lower extent of conversion, such as SC8-1160(20h) with $X_{WL} = 0.40$, to samples with higher extent of conversion, such as SC8-1200(32h) with $X_{WL} = 0.91$ or SC8-1250(12h) with $X_{WL} = 0.92$).

It is evident from comparison of the isotherms that the pore structures developed in the SC8 CTR samples are quite different from that of the SC35 CTR samples. SC8 samples clearly develop a more substantial fraction of small mesopores (< 5 nm). This is manifested by the rapid increase in adsorbed volumes in samples at relatively low P/P_0 values for the SC8 sample compared to the SC35 samples. This is illustrated in Figures 4-4-166 - 4-4-170 which show direct comparisons of the isotherms for SC8 and SC35 samples with very similar fractional weight loss values. (In the next section, figures with actual pore size information will be shown for the SC8 samples.) This rapid uptake in adsorbed volume is, of course, consistent with the higher specific surface areas measured for the SC8 samples as compared with SC35 samples at the same fractional weight loss value. It is known from section 4.4.7.2 that the pore volume that formed upon conversion in SC35 samples mostly came from the development of large pores (≥5 nm), while there

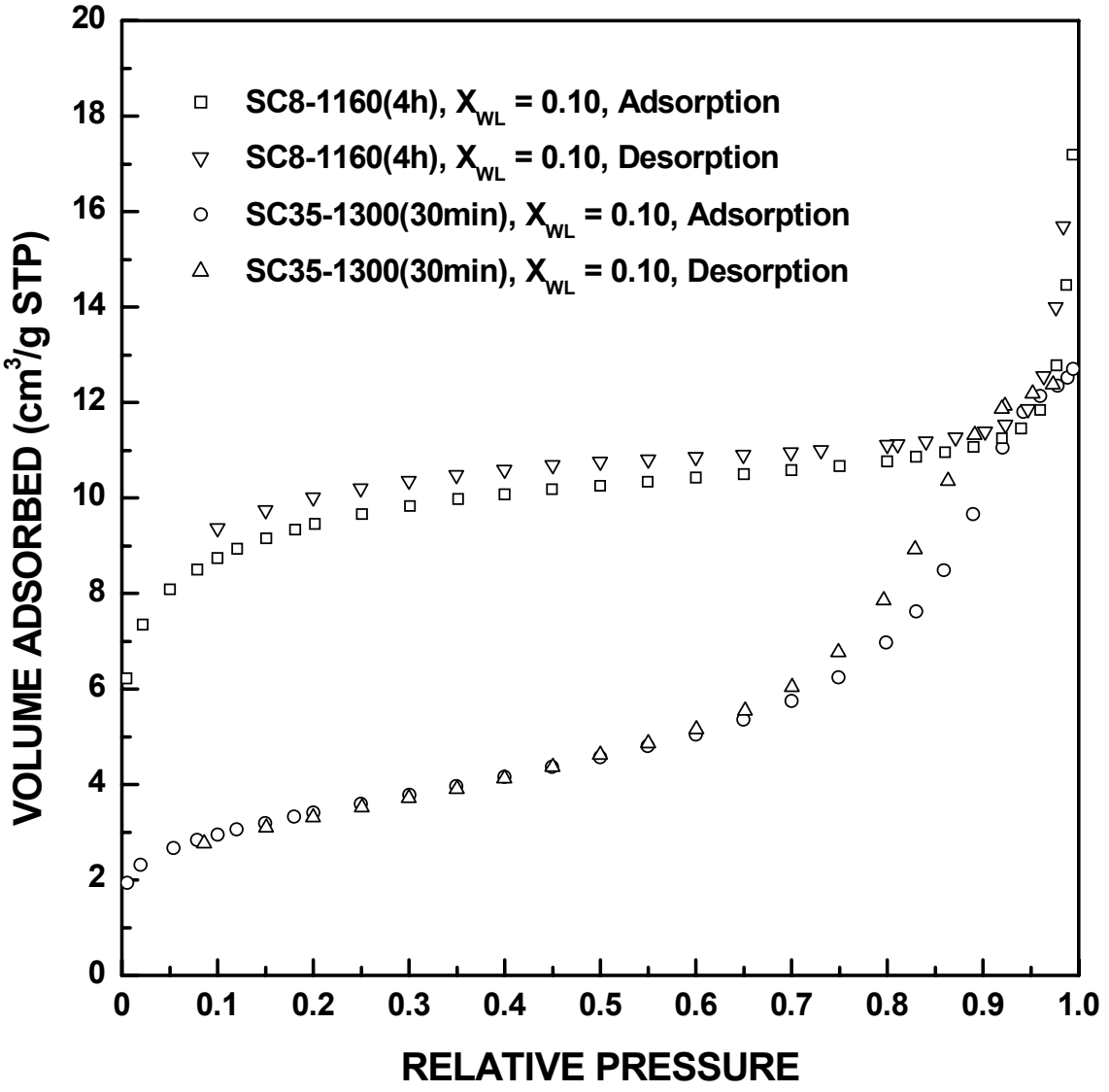

Figure 4-4-166 Comparison of adsorption/desorption isotherm plots for SC35-1300(30min) (X_{WL} = 0.10) and SC8-1160(4h) (X_{WL} = 0.10).

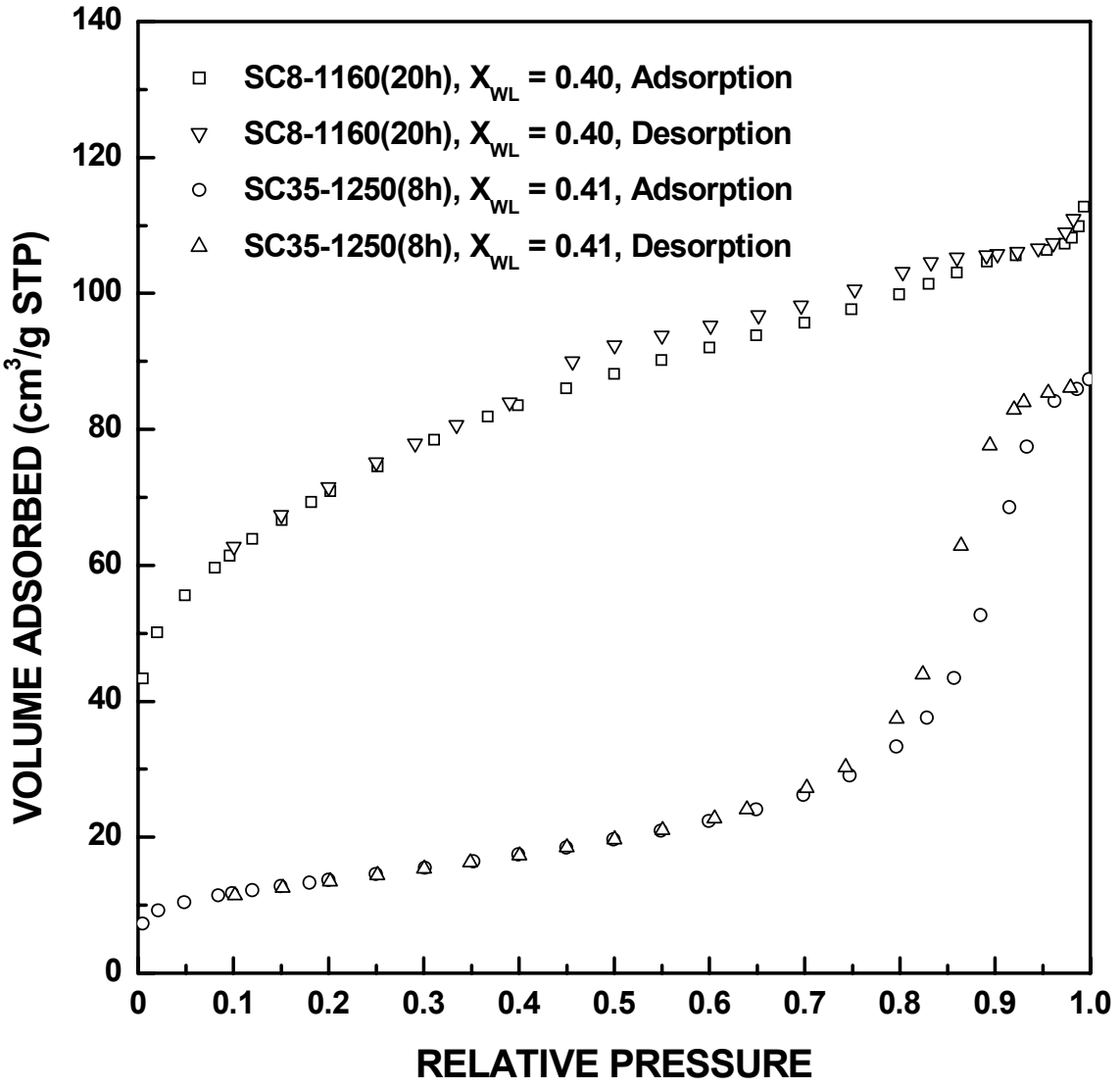

Figure 4-4-167 Comparison of adsorption/desorption isotherm plots for SC35-1250(8h) (X_{WL} = 0.41) and SC8-1160(20h) (X_{WL} = 0.40).

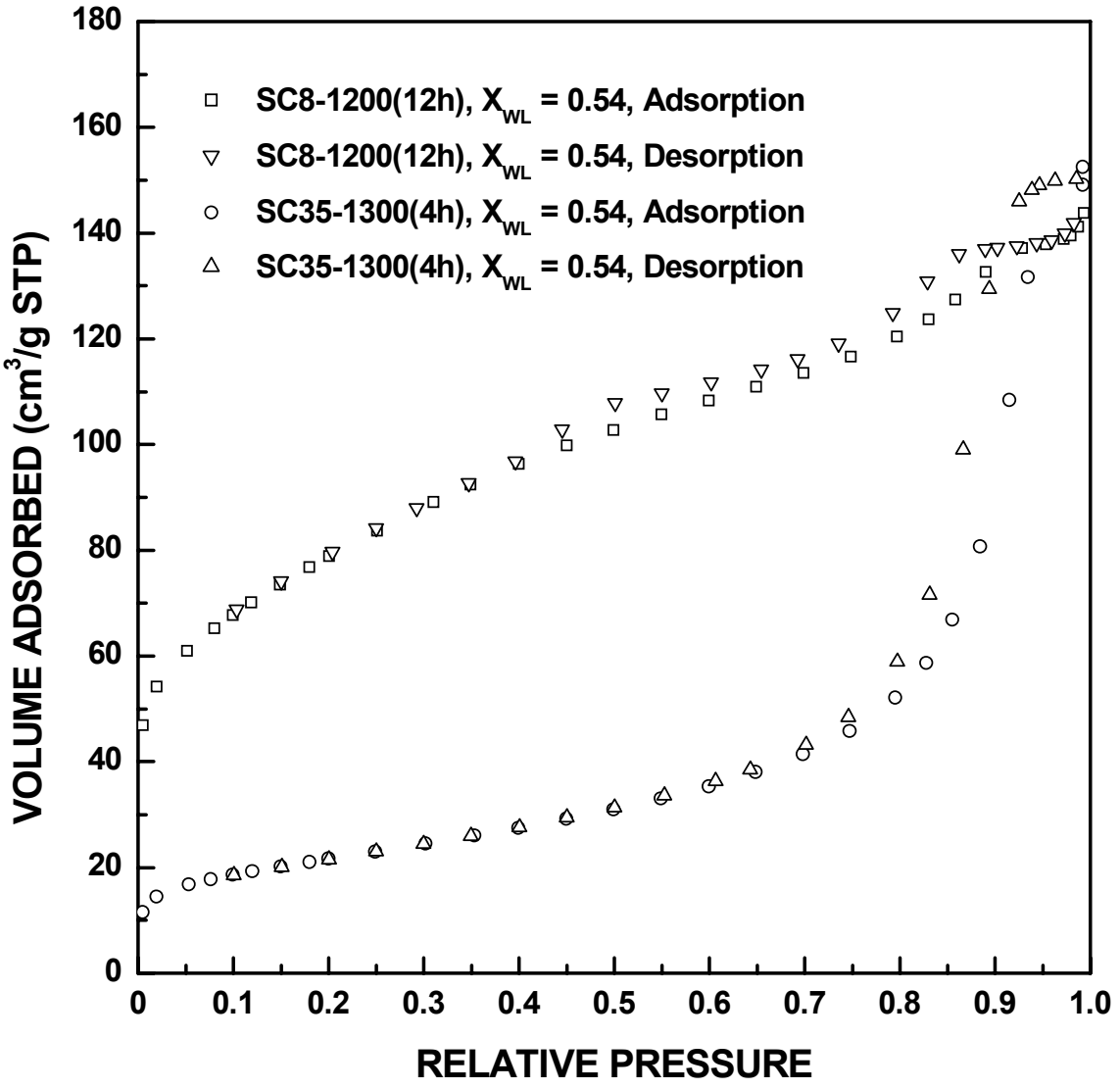

Figure 4-4-168 Comparison of adsorption/desorption isotherm plots for SC35-1300(4h) (X_{WL} = 0.54) and SC8-1200(12h) (X_{WL} = 0.54).

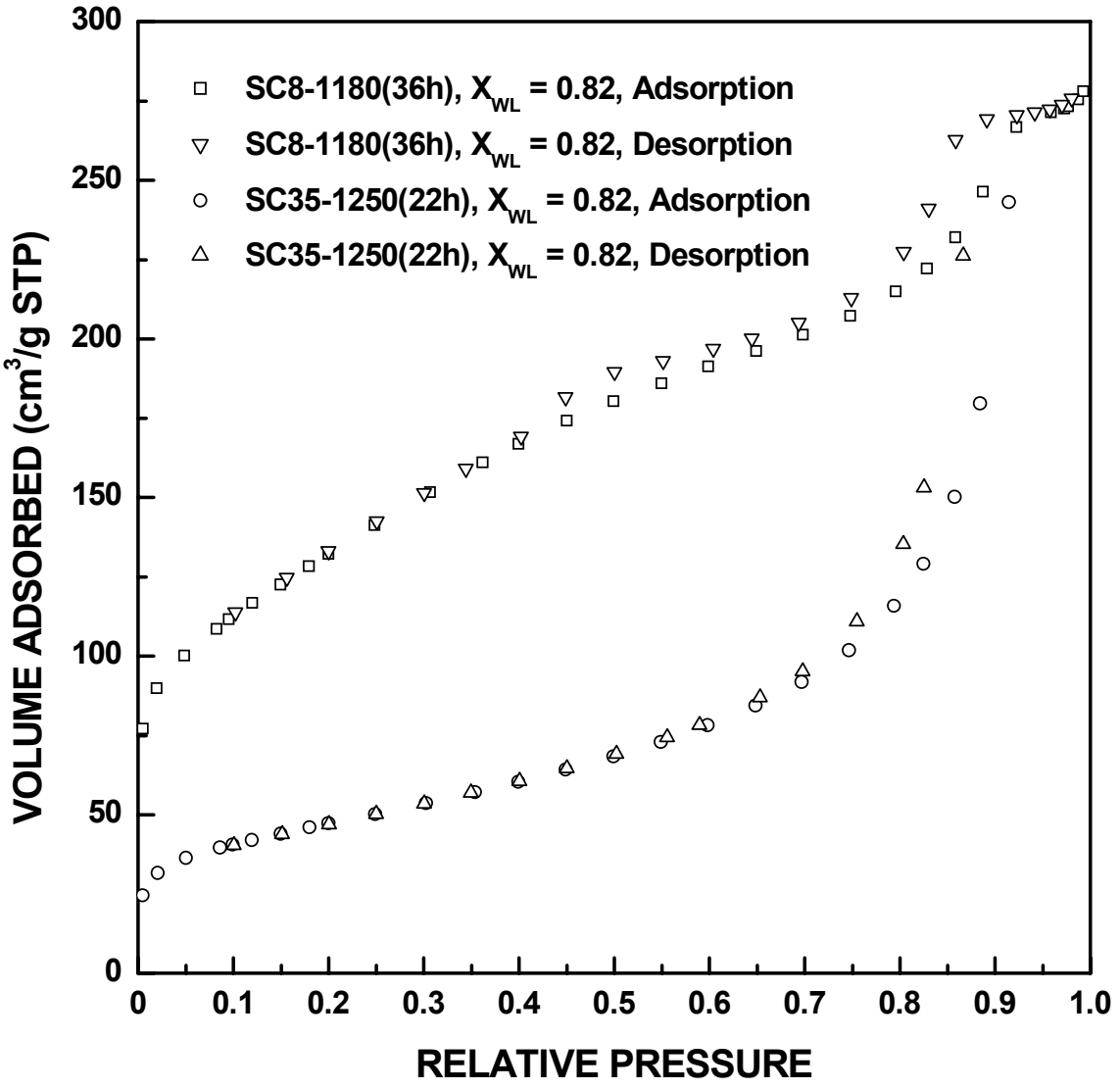

Figure 4-4-169 Comparison of adsorption/desorption isotherm plots for SC35-1250(22h) (X_{WL} = 0.82) and SC8-1180(36h) (X_{WL} = 0.82).

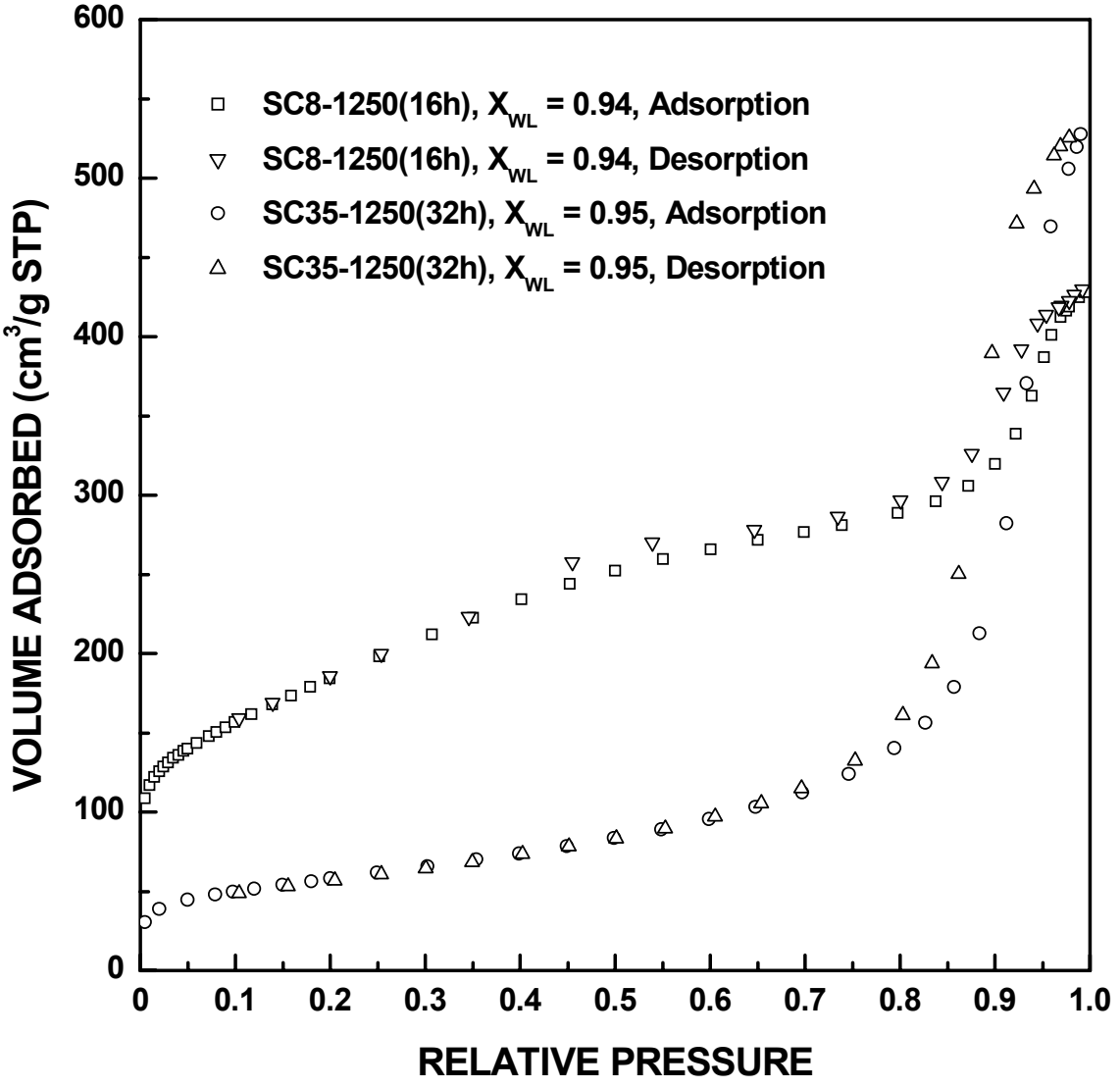

Figure 4-4-170 Comparison of adsorption/desorption isotherm plots for SC35-1250(32h) (X_{WL} = 0.95) and SC8-1250(16h) (X_{WL} = 0.94).

was relatively little volume associated with fine pores (<5 nm). This is in contrast to SC8 where both small and large pores developed upon conversion.

Larger pores (≥5 nm) did not develop significantly in SC8 samples until much larger fractional weight losses compared to the SC35 samples. In section 4.4.7.3, it was shown that the larger mesopores start to develop significantly in SC35 samples at X_{WL} values as low as ~0.07 (e.g., the SC35-1250(1h) sample). In contrast, the isotherm in Figure 4-4-160 indicates that an SC8 sample with X_{WL} = 0.40 (SC8-1160(20h)) had a small fraction of larger pores. The hysteresis loop in the latter sample is closed at a relative pressure slightly below P/P_0 = 0.9. In contrast, the hysteresis loop is closed at a relative pressure slightly above P/P_0 = 0.9 in the SC35-1250(1h) sample. (This means that larger pores were present in the SC35 sample.) Later, it will be shown more clearly in pore size distribution plots that the SC8-1160(20h) sample has a much smaller proportion of pores above 5 nm than the SC35-1250(1h) sample.

4.4.7.5 Pore Size Distribution for SC8 CTR Samples

Figures 4-4-171 to 4-4-181 show plots of the cumulative specific pore volume vs. pore diameter for the SC8 samples. These results were extracted from the gas adsorption/desorption isotherms shown in Figures 4-4-155 to 4-4-165. These figures illustrate several trends:

1. The total specific pore volume increases with increasing fractional weight loss (X_{WL}) throughout most of the reaction.
2. For samples with low fractional weight losses, such as SC8-1120(1h) (Figure 4-1-13) and SC8-1160(1h) (Figure 4-4-171), most of the pore volume is contributed by pores

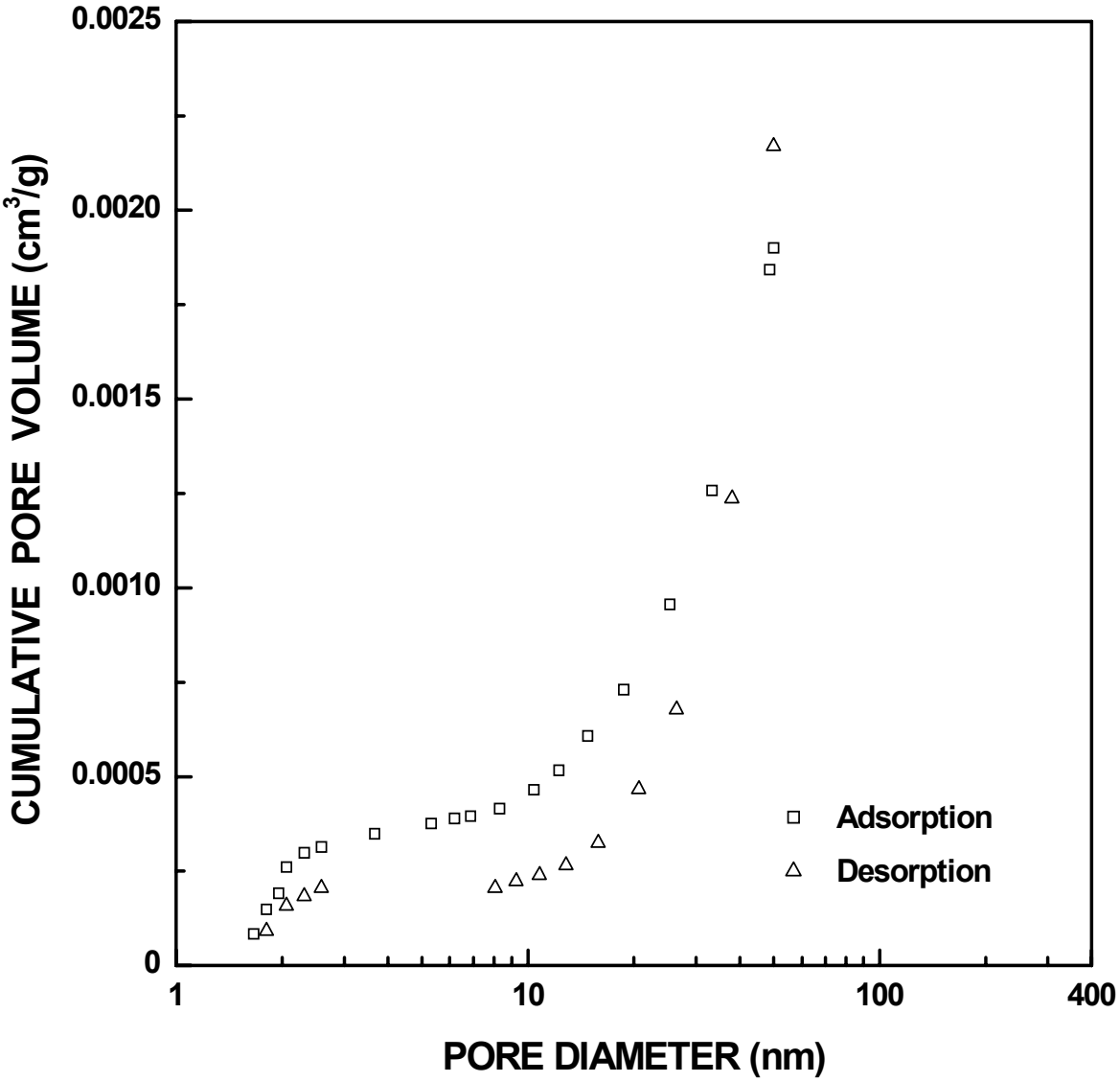

Figure 4-4-171 Plots of cumulative specific pore volume vs. pore diameter for SC8-1160(1h) sample (X_{WL} = 0.05). The pore diameter was cut off at 50 nm.

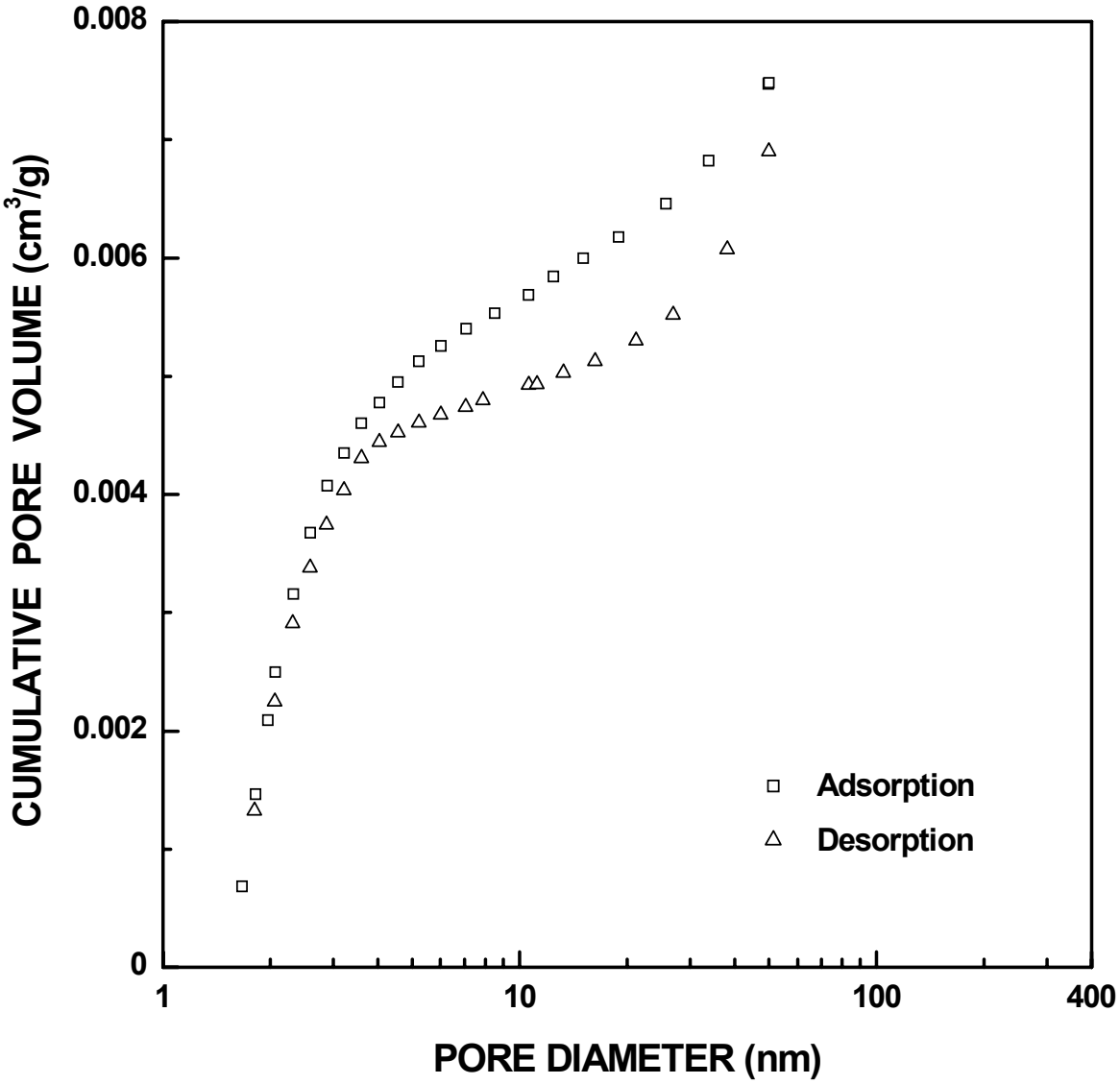

Figure 4-4-172 Plots of cumulative specific pore volume vs. pore diameter for SC8-1160(4h) sample (X_{WL} = 0.10). The pore diameter was cut off at 50 nm.

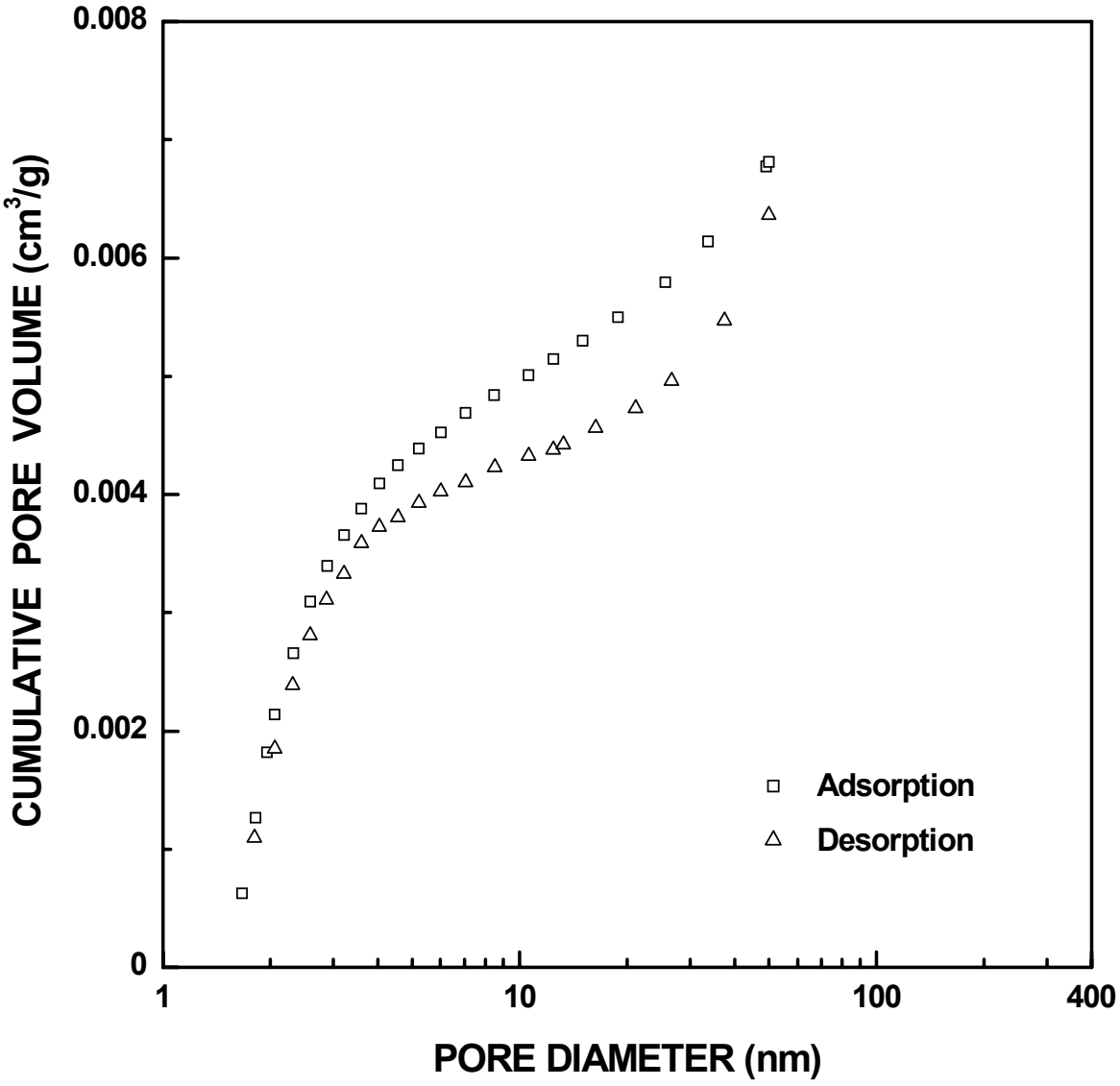

Figure 4-4-173 Plots of cumulative specific pore volume vs. pore diameter for SC8-1180(2h) sample (X_{WL} = 0.13). The pore diameter was cut off at 50 nm.

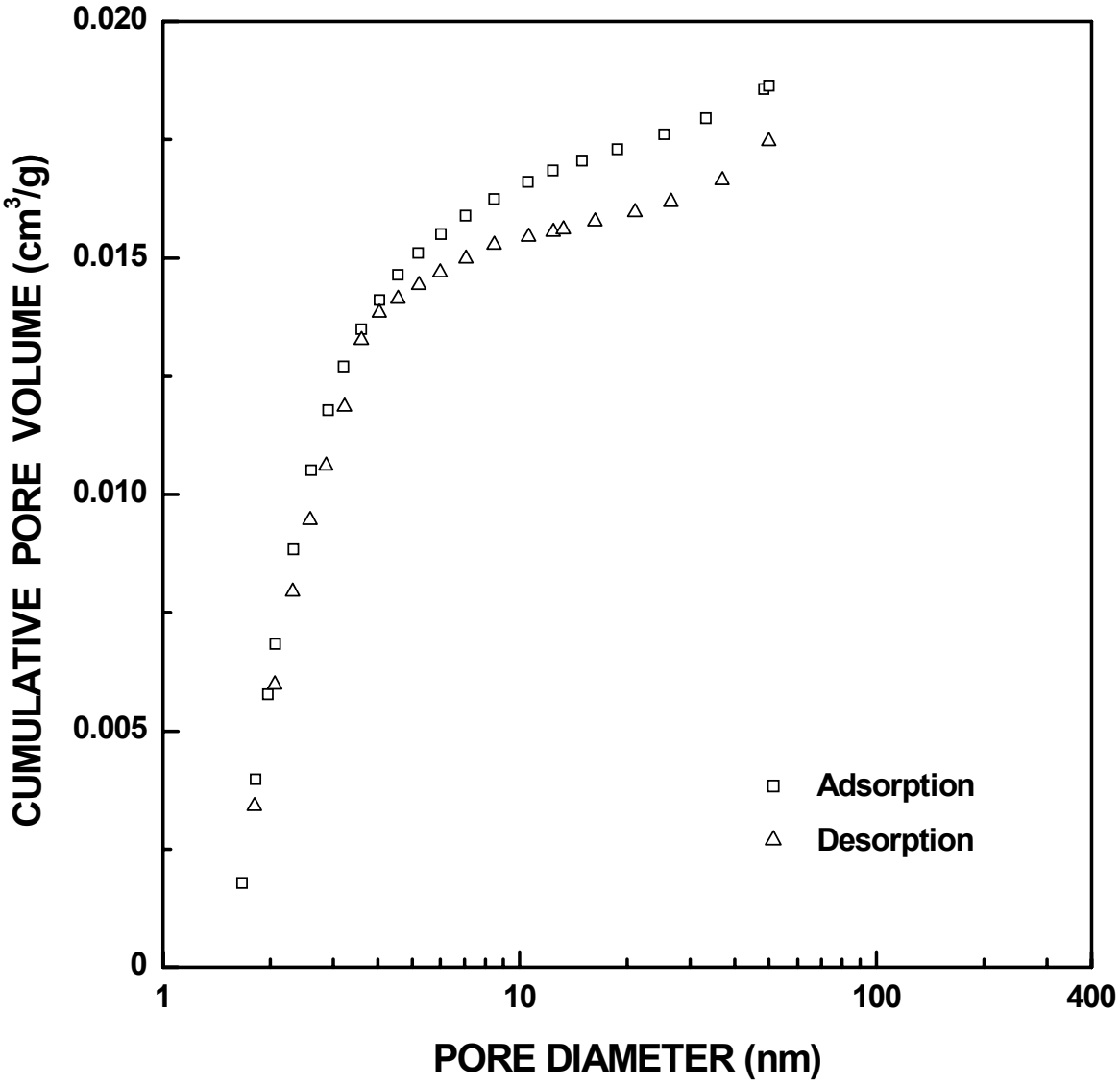

Figure 4-4-174 Plots of cumulative specific pore volume vs. pore diameter for SC8-1160(7h) sample (X_{WL} = 0.18). The pore diameter was cut off at 50 nm.

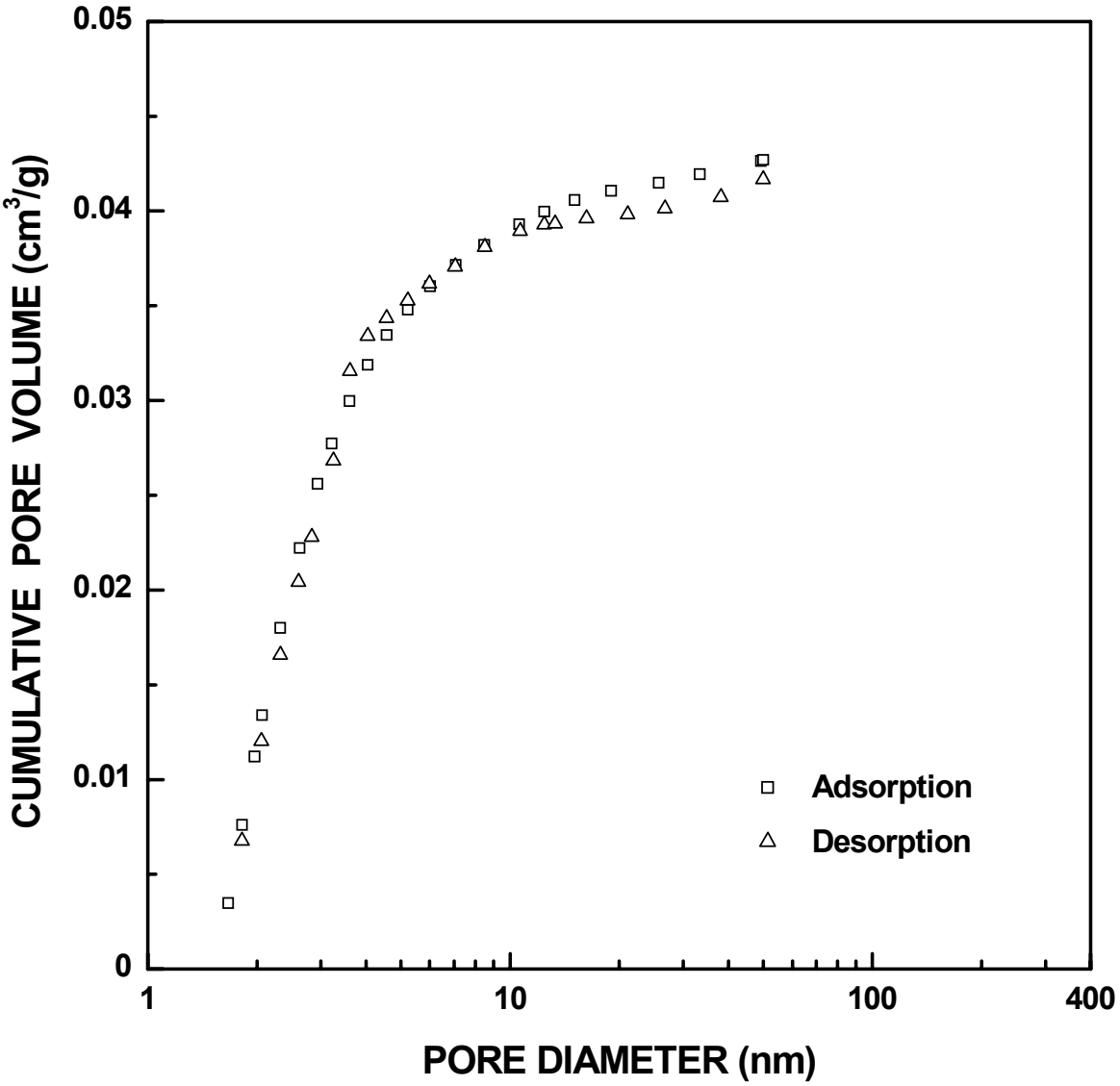

Figure 4-4-175 Plots of cumulative specific pore volume vs. pore diameter for SC8-1160(12h) sample (X_{WL} = 0.26). The pore diameter was cut off at 50 nm.

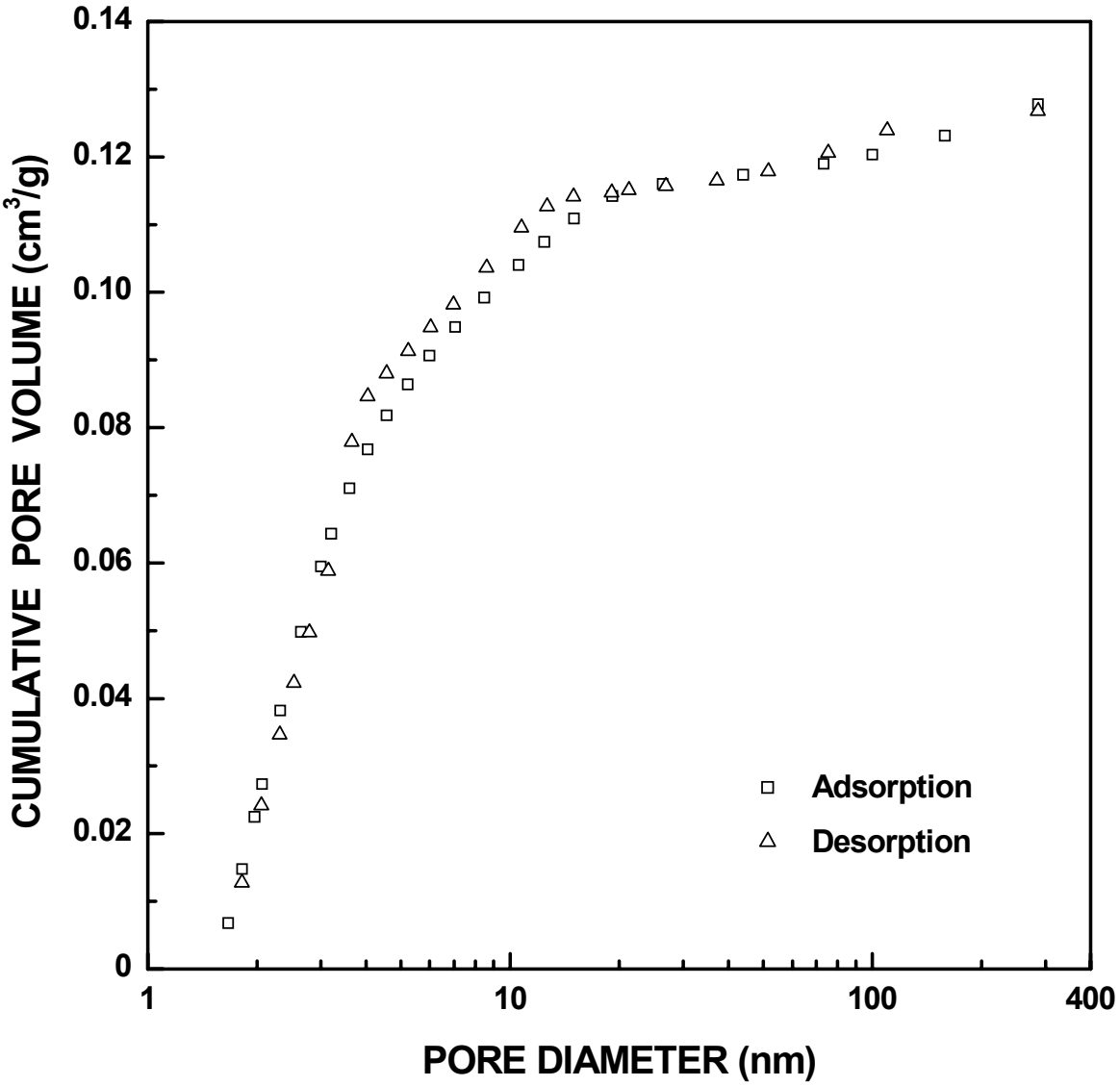

Figure 4-4-176 Plots of cumulative specific pore volume vs. pore diameter for SC8-1160(20h) sample (X_{WL} = 0.40).

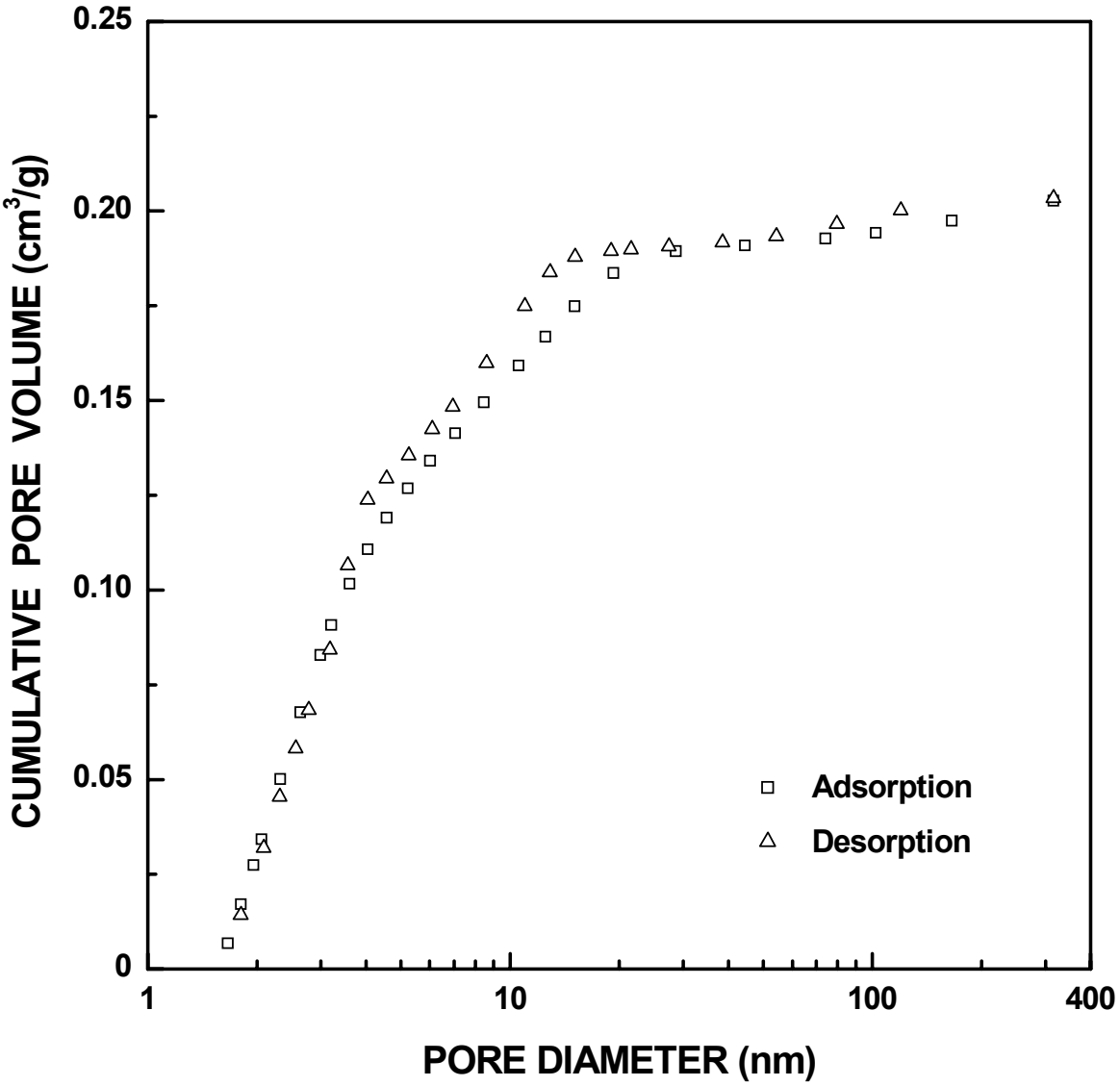

Figure 4-4-177 Plots of cumulative specific pore volume vs. pore diameter for SC8-1160(28h) sample (X_{WL} = 0.59).

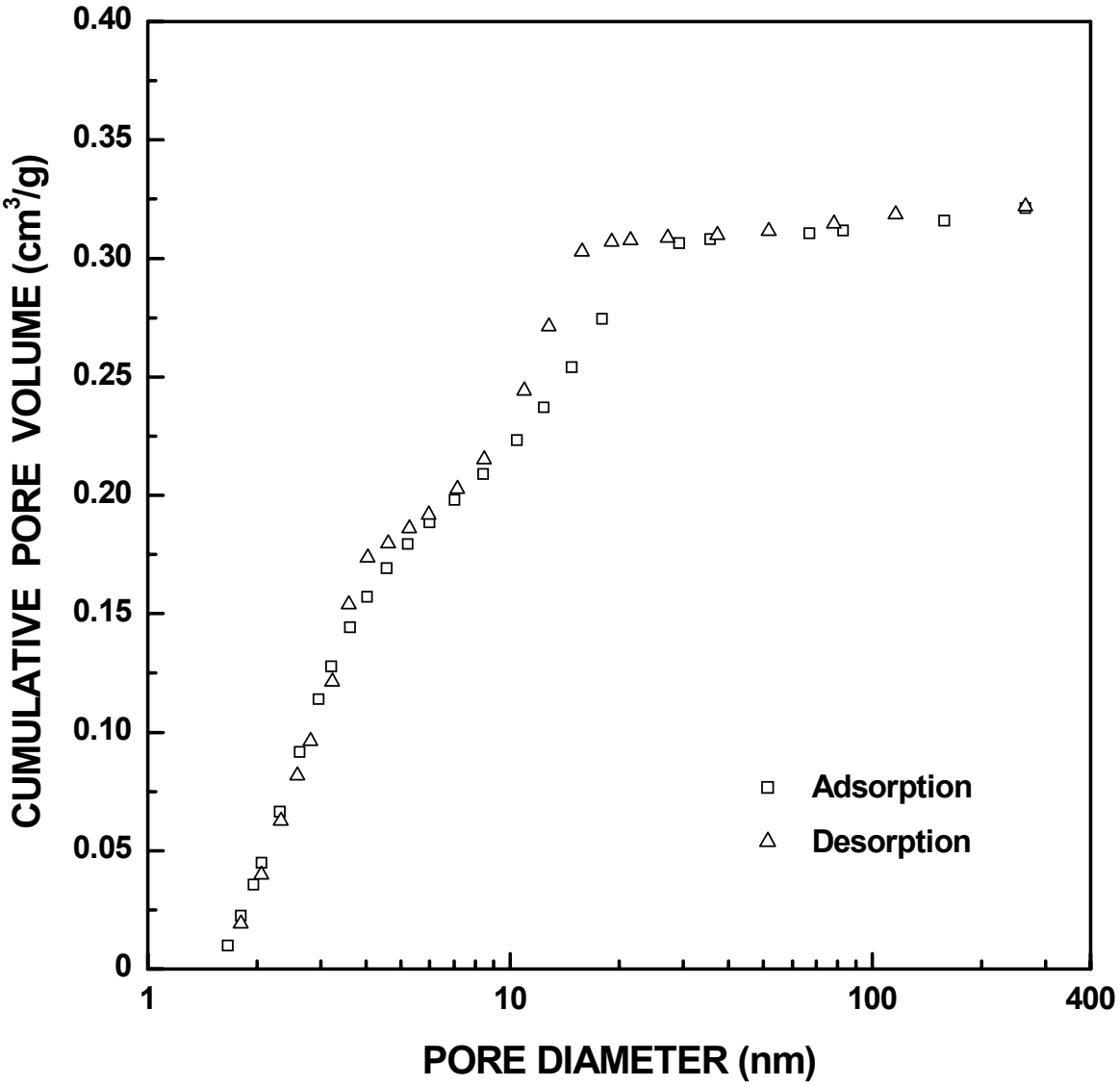

Figure 4-4-178 Plots of cumulative specific pore volume vs. pore diameter for SC8-1160(48h) sample (X_{WL} = 0.74).

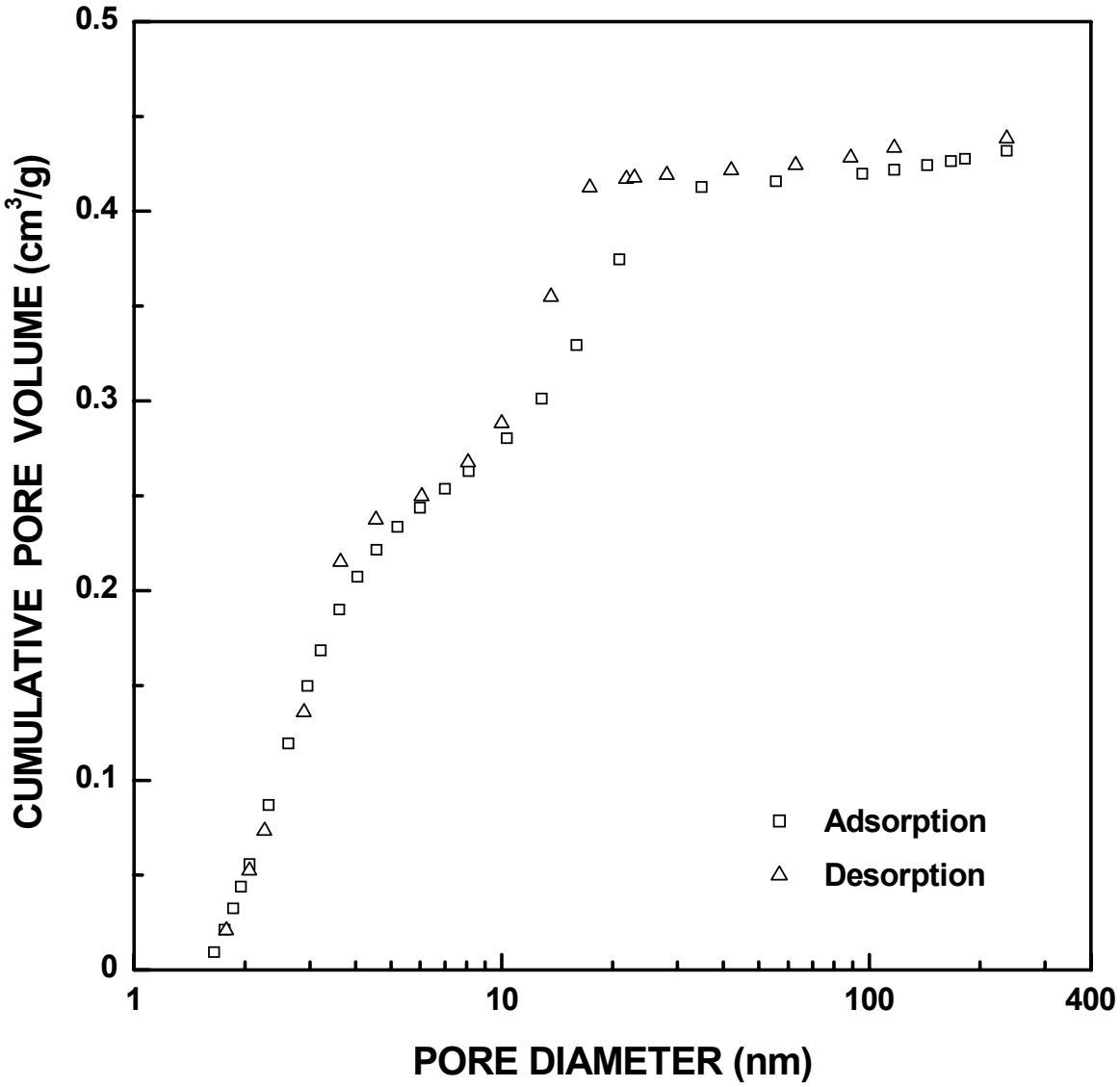

Figure 4-4-179 Plots of cumulative specific pore volume vs. pore diameter for SC8-1250(8h) sample (X_{WL} = 0.82).

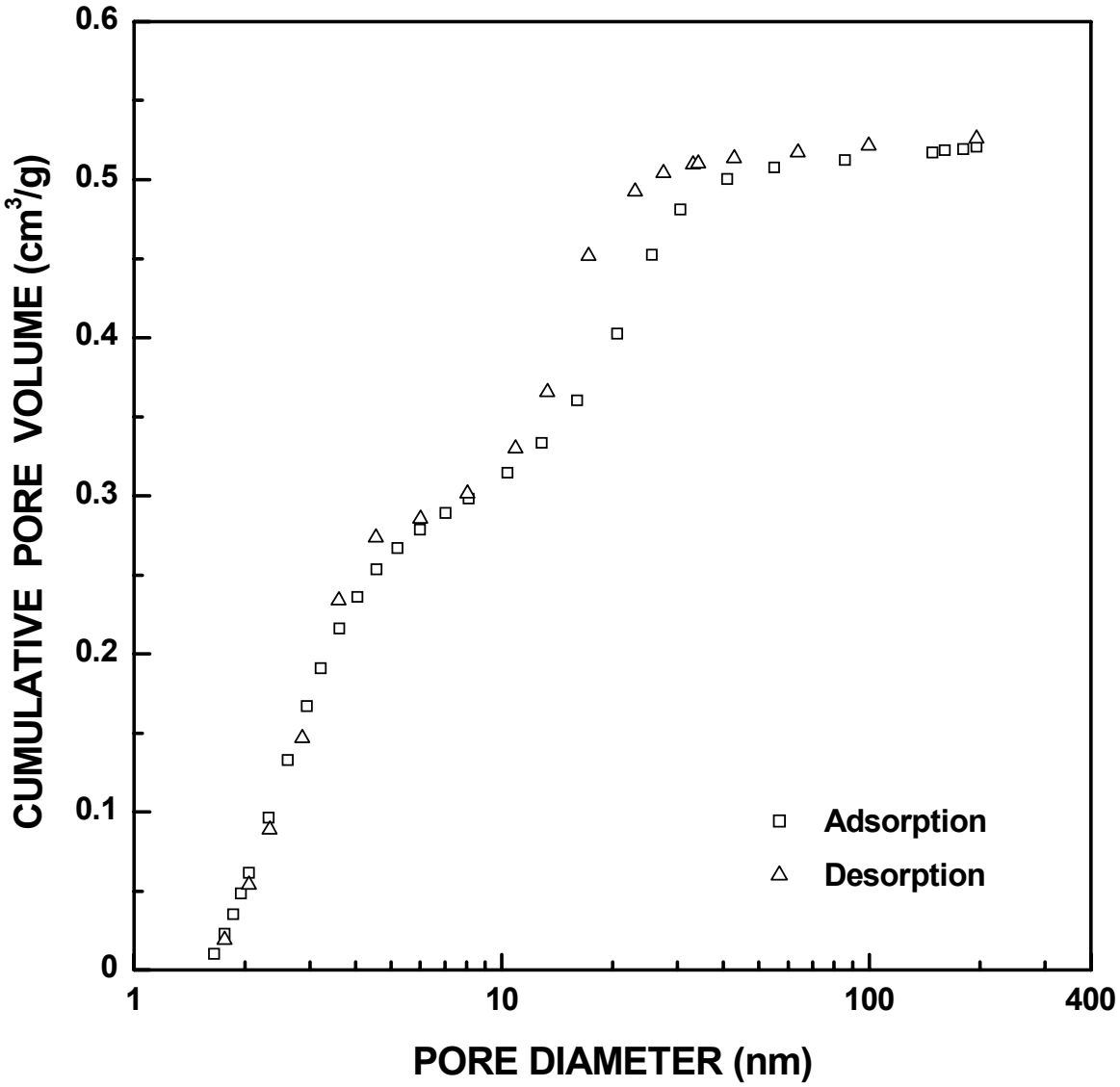

Figure 4-4-180 Plots of cumulative specific pore volume vs. pore diameter for SC8-1250(12h) sample (X_{WL} = 0.92).

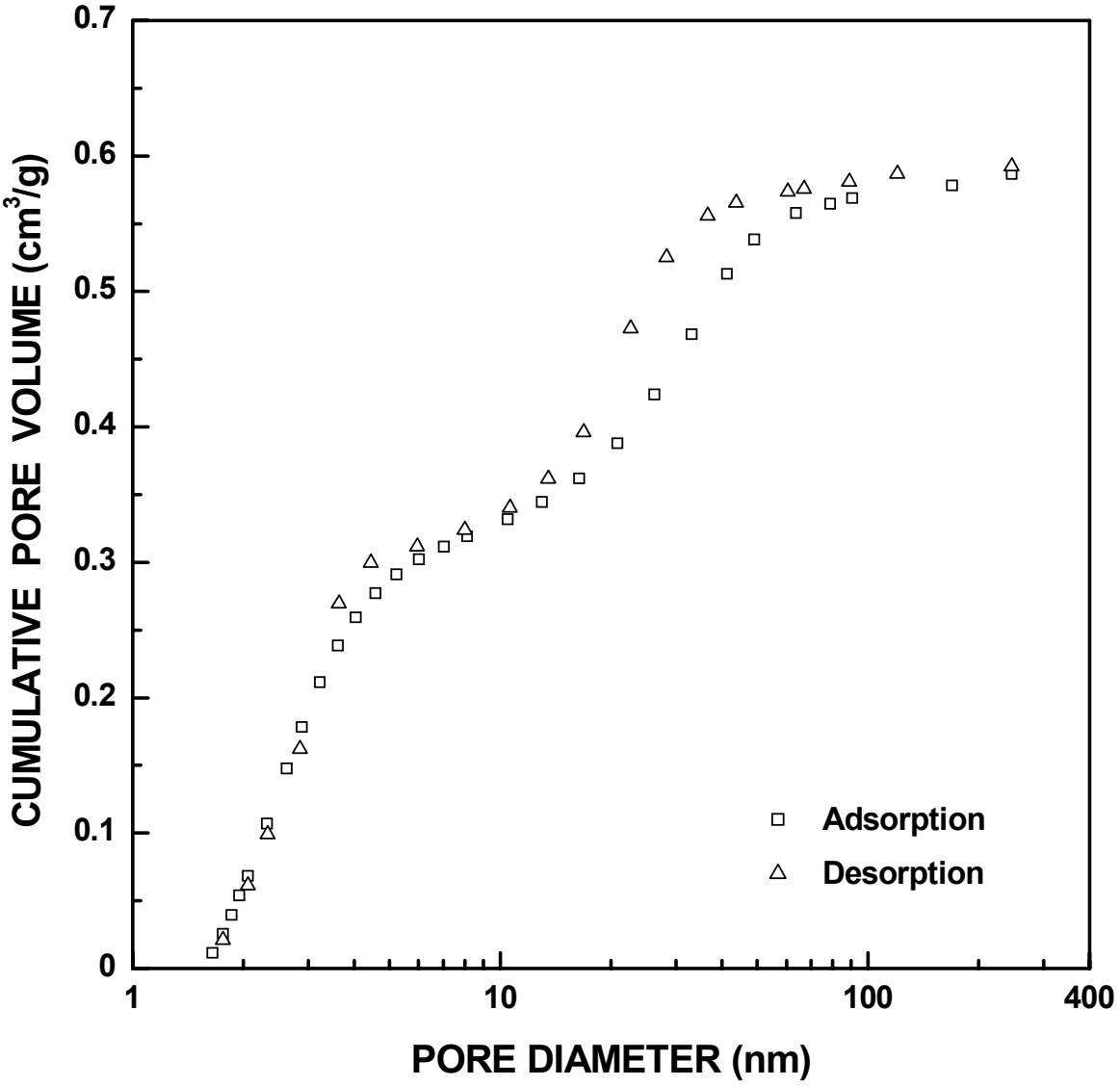

Figure 4-4-181 Plots of cumulative specific pore volume vs. pore diameter for SC8-1250(16h) sample ($X_{WL} = 0.94$).

larger than ~10 nm. However, it should be noted that the total pore volume is extremely low. These pores are most likely associated with large defects (e.g., cracks) in the original large pyrolyzed particles. Although not explicitly discussed in section 4.4.7.2, larger pores (>10 nm) also account of a significant portion of the pore volume in the SC35 pyrolyzed sample (Figure 4-1-12) and very early-stage SC35 samples (e.g., SC35-1160(1h), X_{WL} = 0.02, Figure 4-4-82). Again, the pore volumes are extremely low and these pores are most likely associated with macrodefects.

As the carbothermal reduction reaction continues in the very early stage, small pores (less than ~5 nm) develop quickly in the SC8 samples as the reaction proceeds. For example, note the changes in the distributions as the fractional weight loss increases from X_{WL} = 0.05 (SC8-1160(1h), Figure 4-4-171) to X_{WL} = 0.10 (SC8-1160(4h), Figure 4-4-172). This trend of the development of fine (<5 nm) pores continues during the early stage of the CTR reaction, as observed in Figures 4-4-173 and 4-4-174 for samples with X_{WL} = 0.13 (SC8-1180(2h)) and X_{WL} = 0.18 (SC8-1160(7h)).

The development of pores greater than ~ 5 nm becomes the more dominant process at fractional weight loss greater than ~0.20 (see Figures 4-4-174 to 4-4-181). It is also evident that pore size distribution develop bimodality at X_{WL} values greater than ~0.40. The bimodality becomes more significant as the reaction proceeds.

The trends in the pore size distribution data were illustrated more clearly by re-plotting the data in several different ways. In each case, the "cut-off" correction described in section 3.5.2 was first applied to the data. (This involved subtracting the "macropore" volume from the total pore volume for samples with relatively low extent of conversion.) Figures 4-4-182 to 4-4-192 show "normalized" plots of the data in Figures 4-4-171 to 4-4-

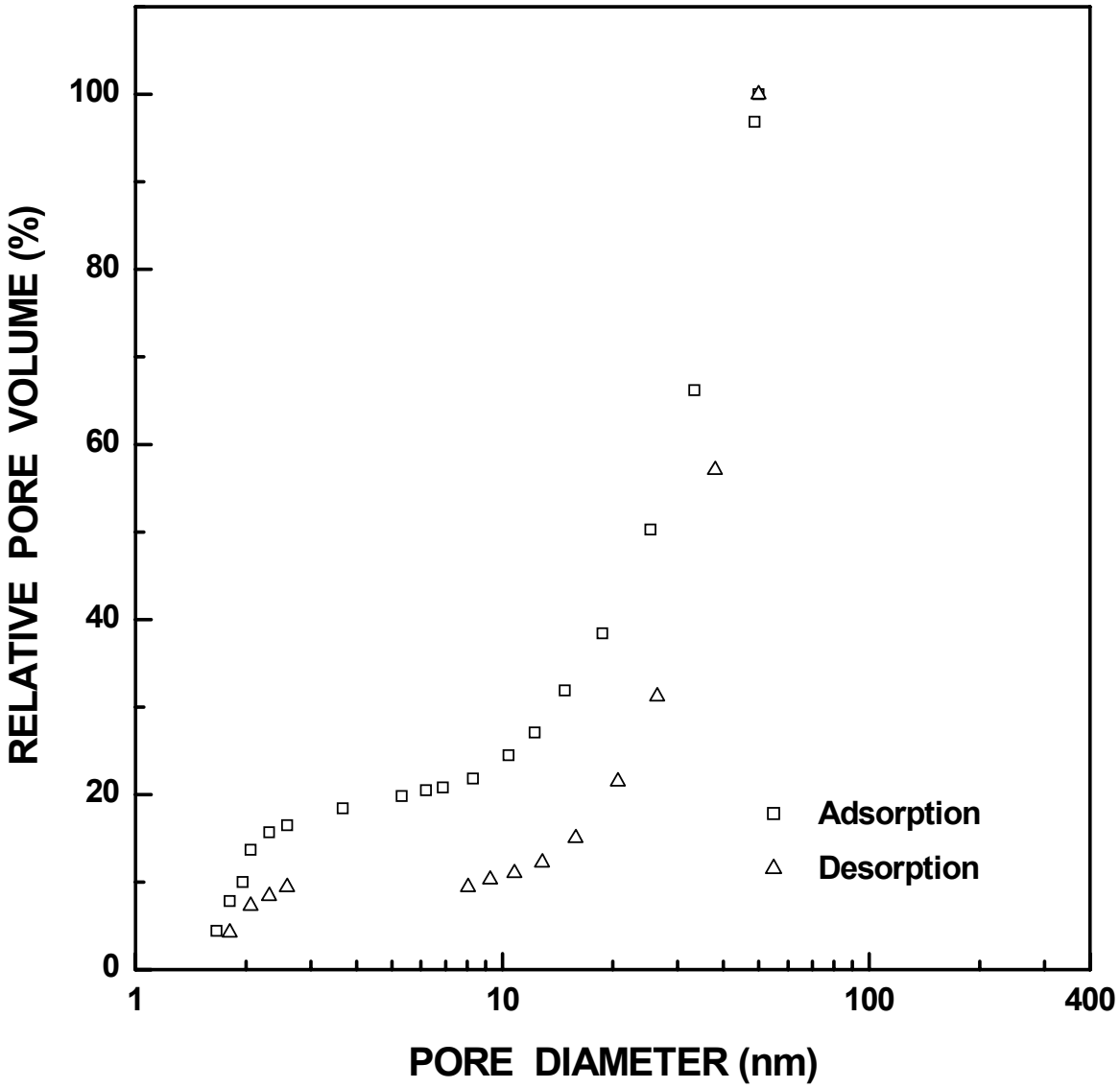

Figure 4-4-182 Plots of relative ("normalized") pore volume vs. pore diameter for SC8-1160(1h) sample (X_{WL} = 0.05). The pore diameter was cut off at 50 nm.

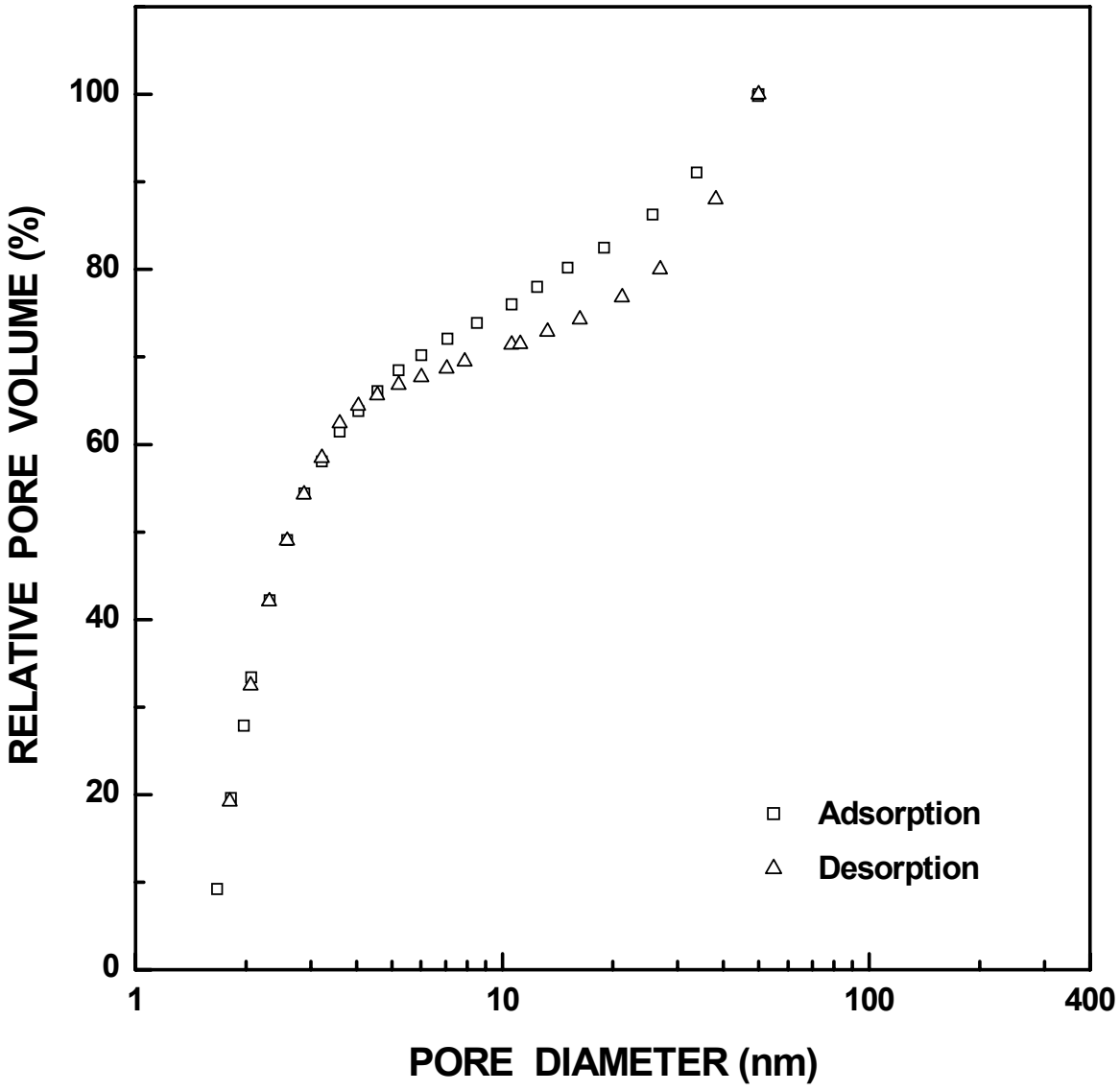

Figure 4-4-183 Plots of relative ("normalized") pore volume vs. pore diameter for SC8-1160(4h) sample (X_{WL} = 0.10). The pore diameter was cut off at 50 nm.

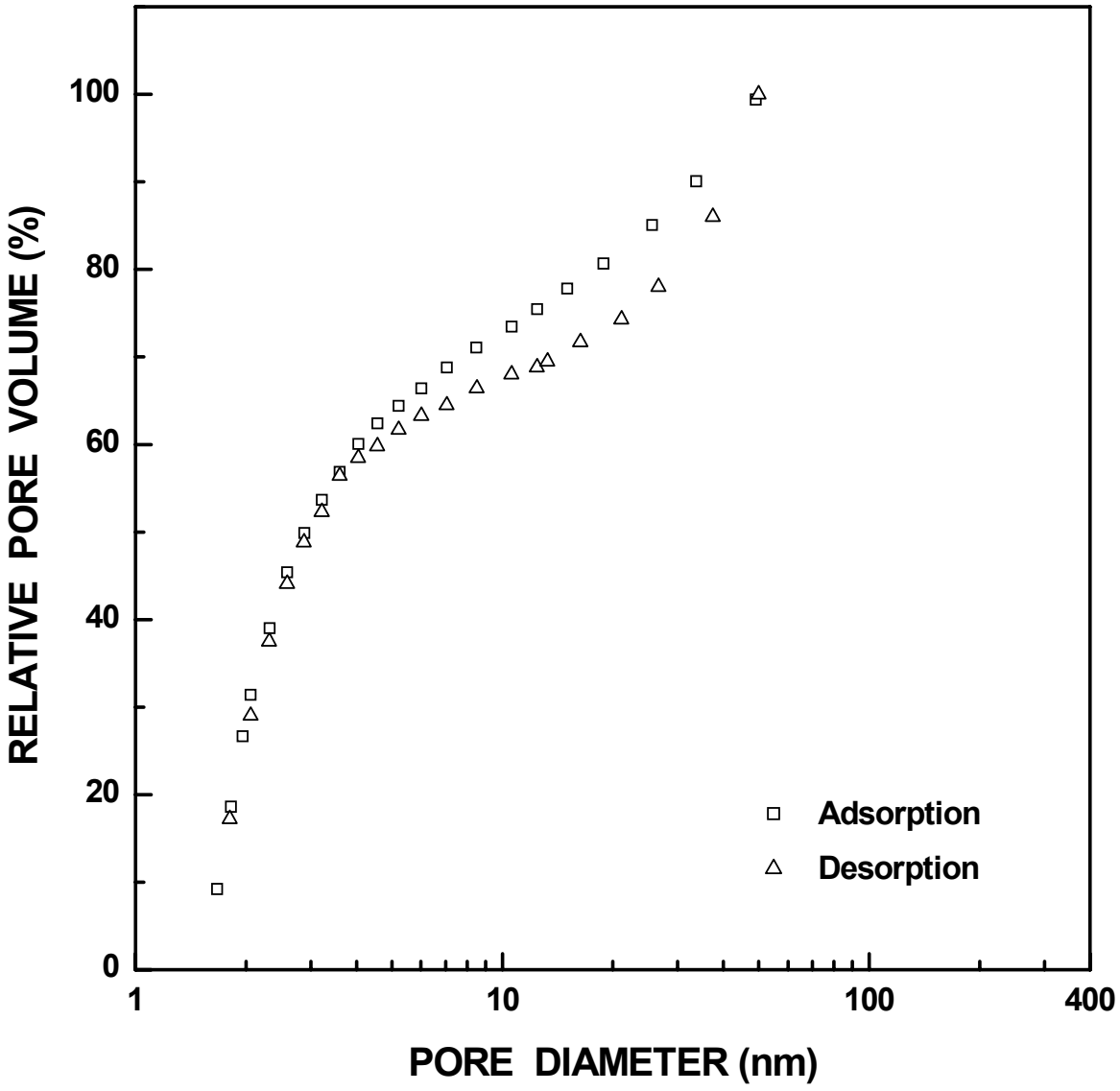

Figure 4-4-184 Plots of relative ("normalized") pore volume vs. pore diameter for SC8-1180(2h) sample (X_{WL} = 0.13). The pore diameter was cut off at 50 nm.

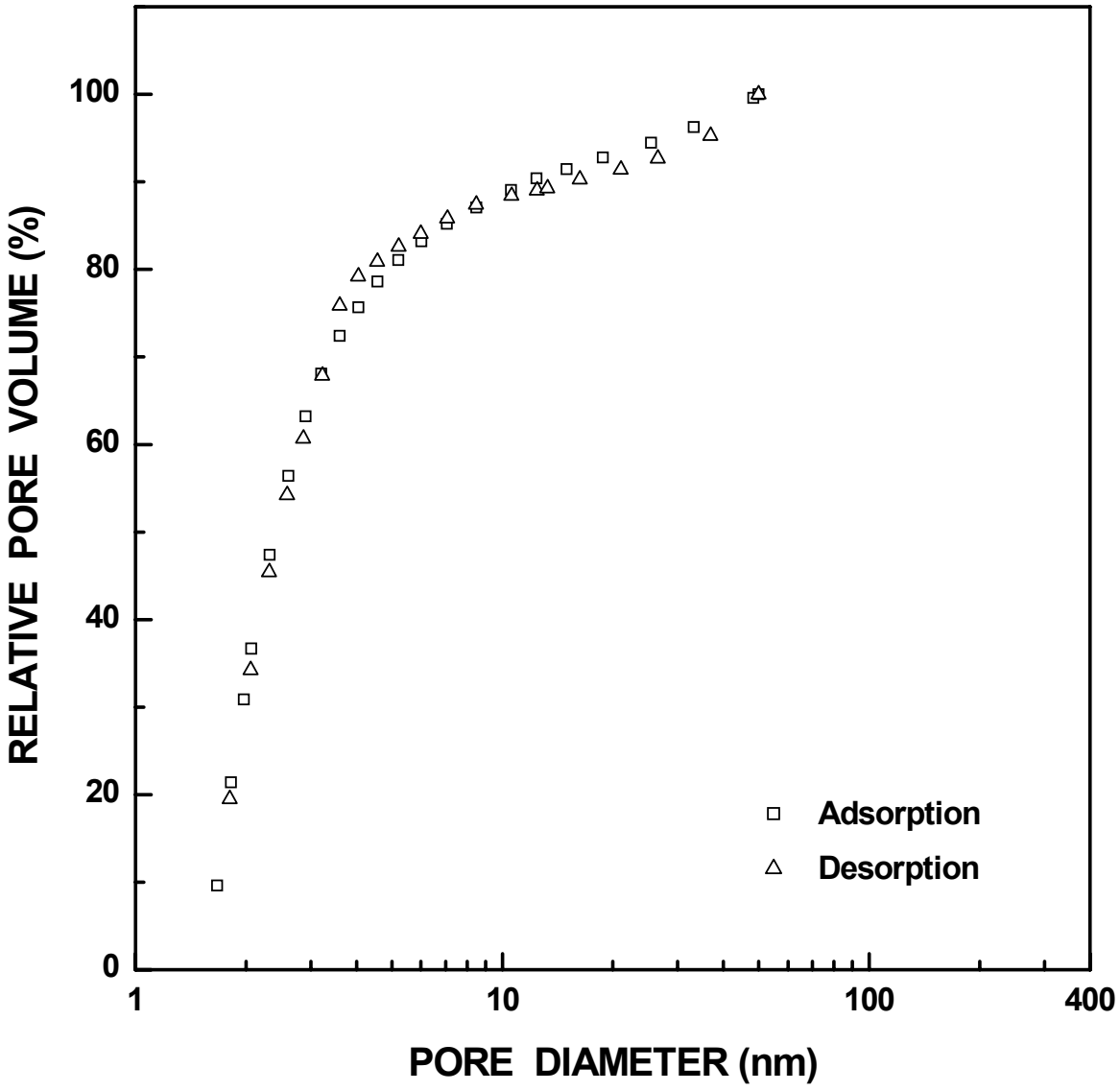

Figure 4-4-185 Plots of relative ("normalized") pore volume vs. pore diameter for SC8-1160(7h) sample (X_{WL} = 0.18). The pore diameter was cut off at 50 nm.

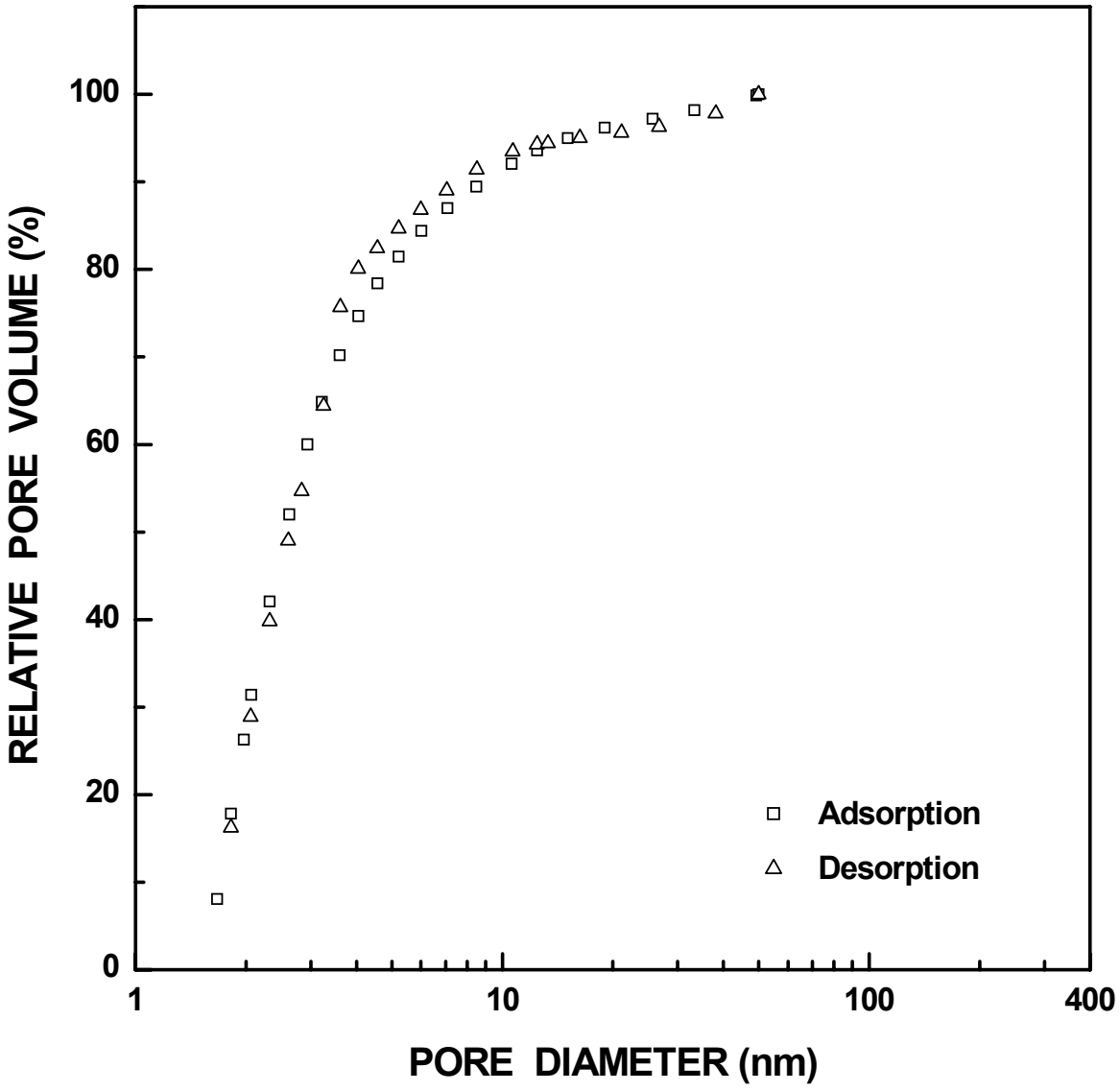

Figure 4-4-186 Plots of relative ("normalized") pore volume vs. pore diameter for SC8-1160(12h) sample (X_{WL} = 0.26). The pore diameter was cut off at 50 nm.

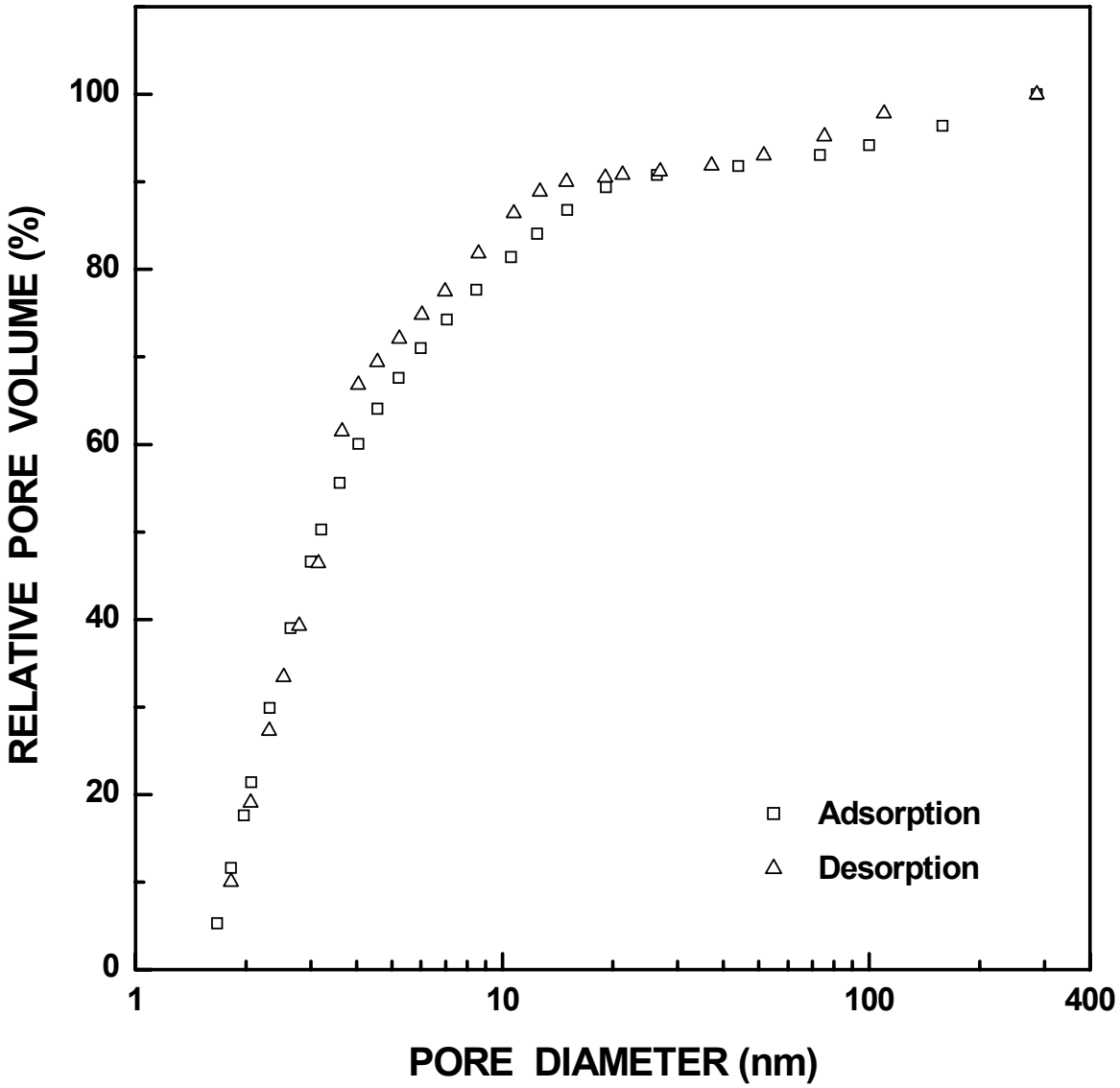

Figure 4-4-187 Plots of relative ("normalized") pore volume vs. pore diameter for SC8-1160(20h) sample ($X_{WL} = 0.40$).

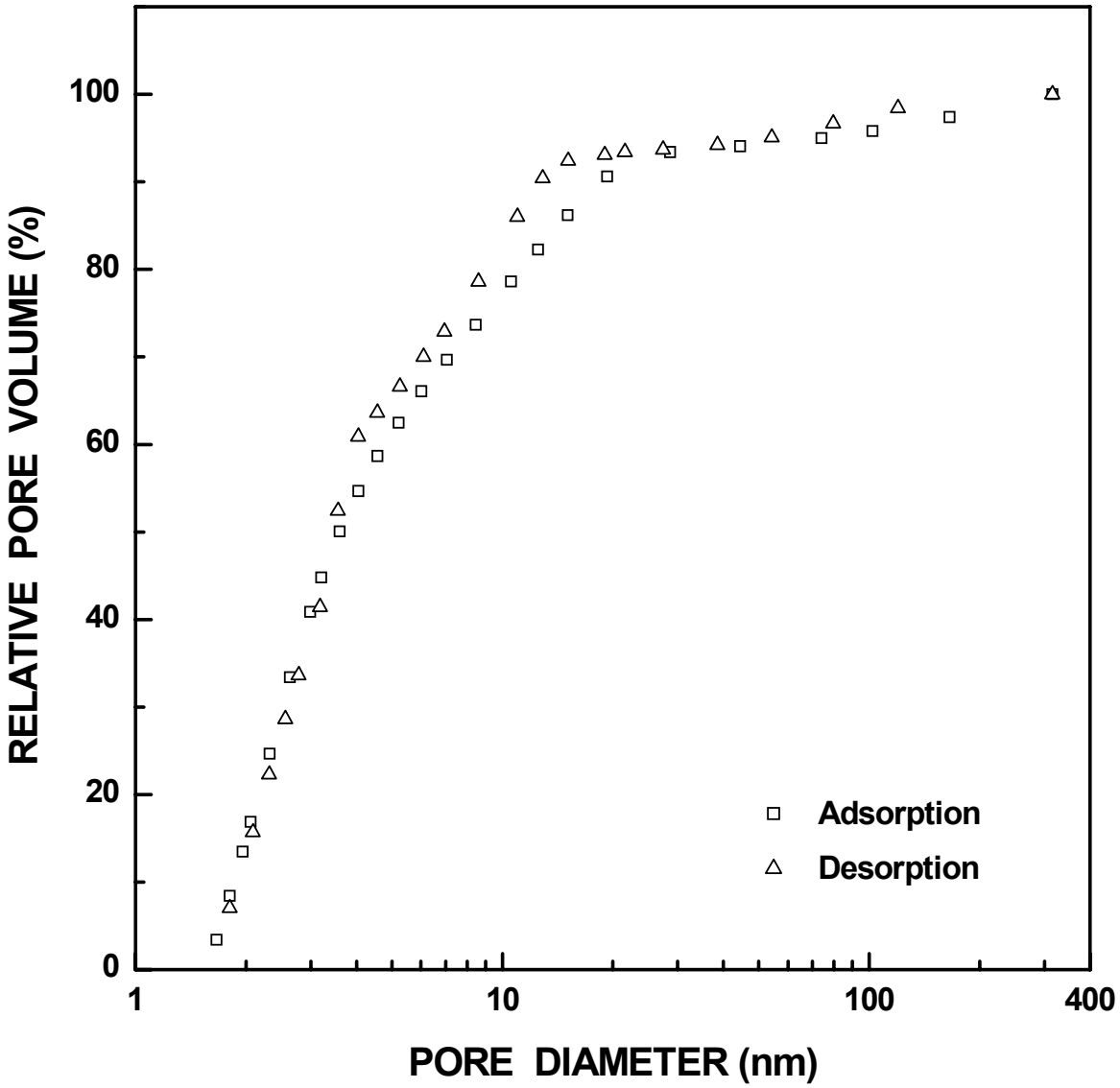

Figure 4-4-188 Plots of relative ("normalized") pore volume vs. pore diameter for SC8-1160(28h) sample ($X_{WL} = 0.59$).

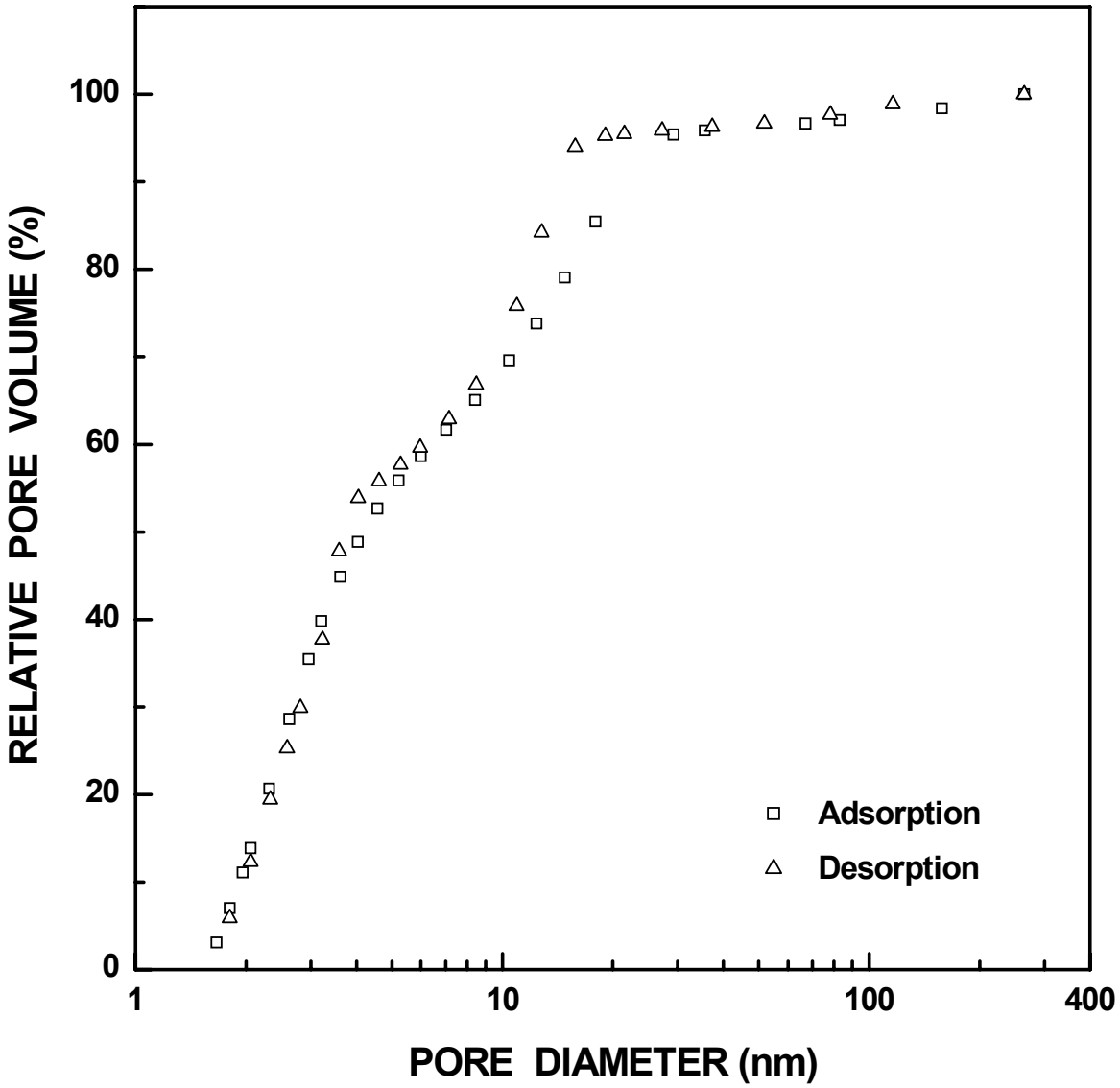

Figure 4-4-189 Plots of relative ("normalized") pore volume vs. pore diameter for SC8-1160(48h) sample ($X_{WL} = 0.74$).

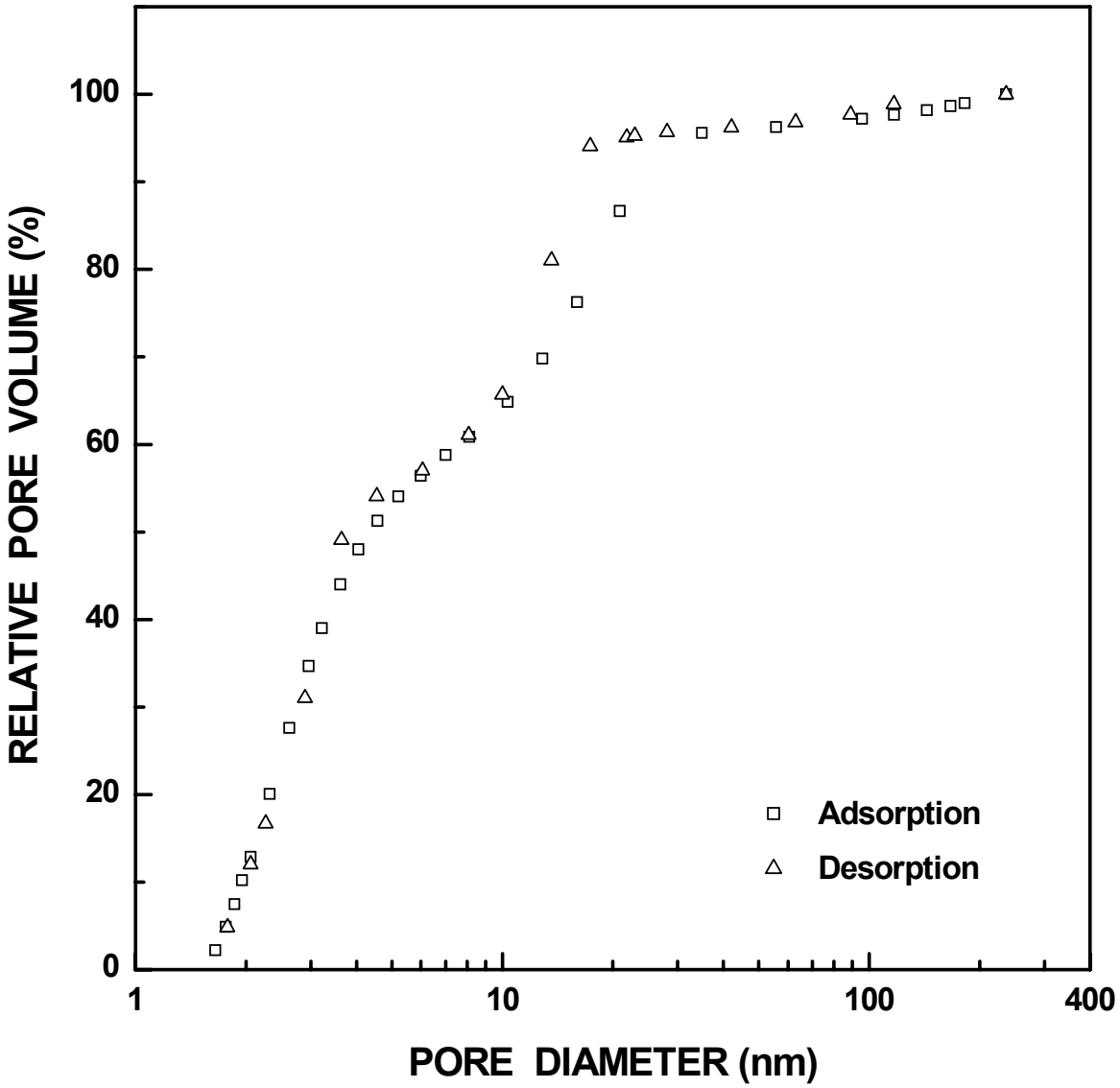

Figure 4-4-190 Plots of relative ("normalized") pore volume vs. pore diameter for SC8-1250(8h) sample ($X_{WL} = 0.82$).

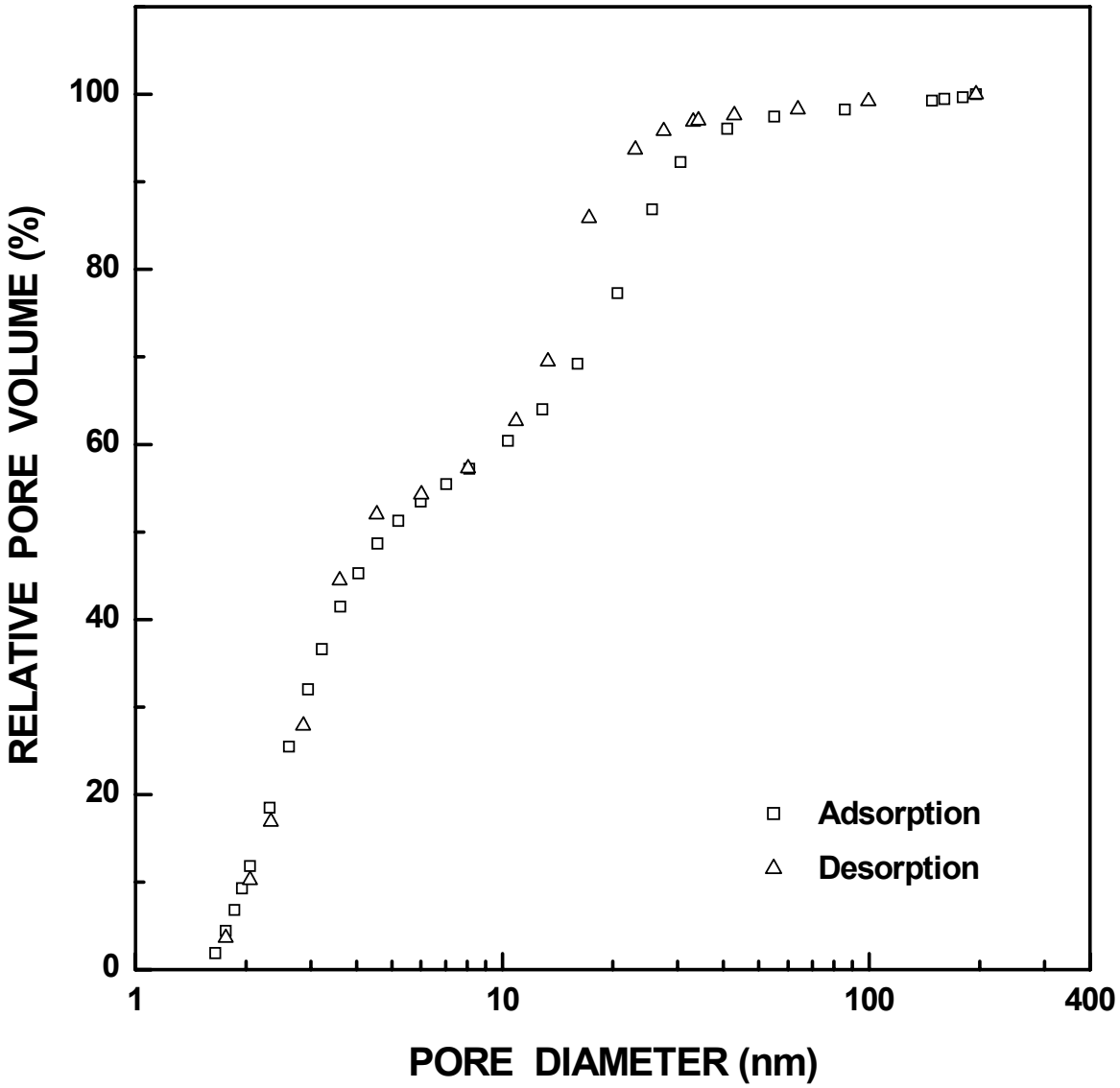

Figure 4-4-191 Plots of relative ("normalized") pore volume vs. pore diameter for SC8-1250(12h) sample ($X_{WL} = 0.92$).

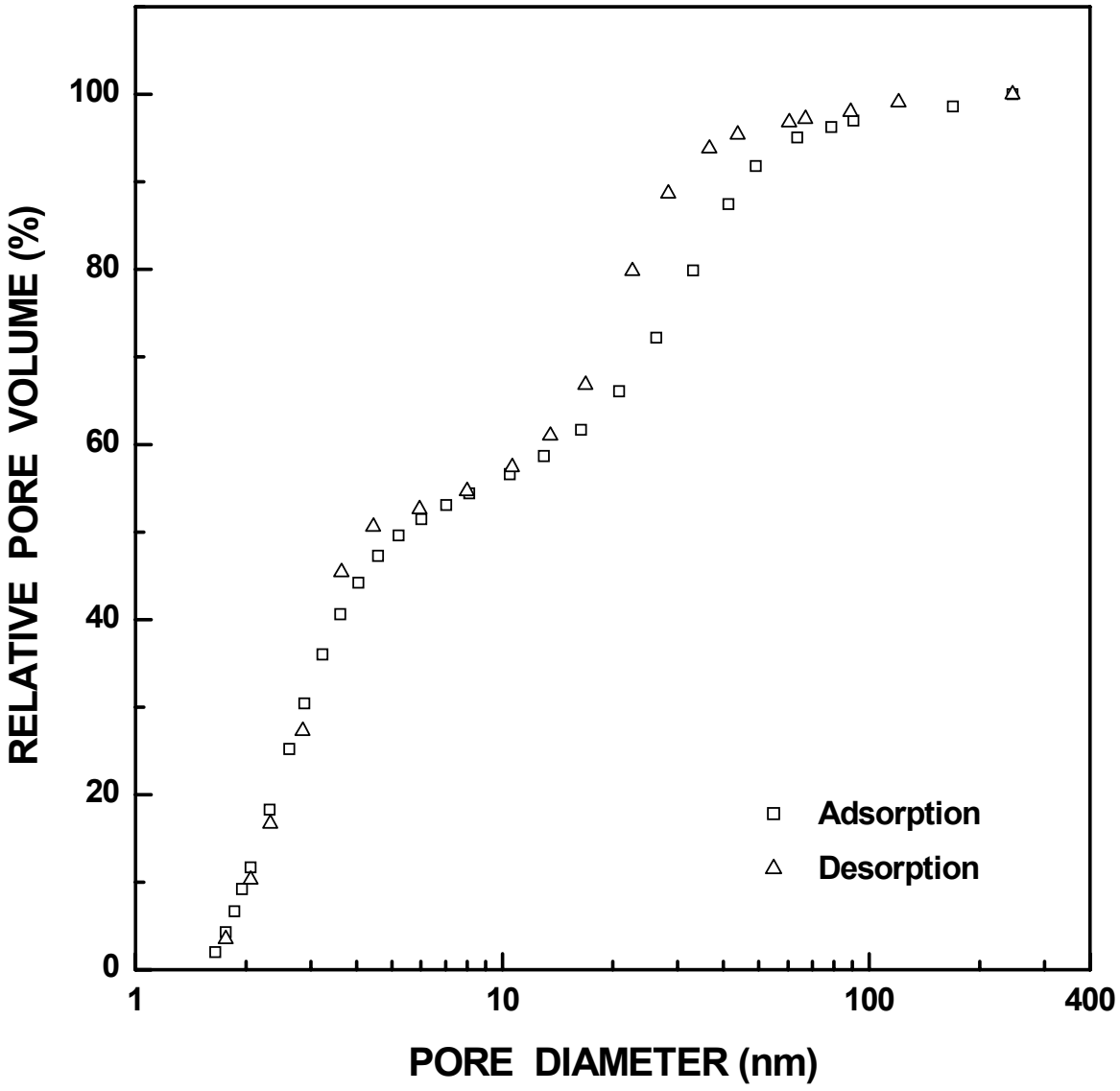

Figure 4-4-192 Plots of relative ("normalized") pore volume vs. pore diameter for SC8-1250(16h) sample ($X_{WL} = 0.94$).

181 in which the cumulative pore volume shown on the y-axis is plotted as a percentage of the maximum pore volume. Figure 4-4-193 shows a combined plot of the "normalized" cumulative pore size distributions for the pyrolyzed SC8 sample and for SC8 samples with fractional weight loss values up to 0.26. This figure clearly illustrates the development of the smaller pores (<5 nm) in the early stages of the CTR reaction. Figure 4-4-194 shows a combined plot of the "normalized" cumulative pore size distributions for SC8 samples with fractional weight loss values from 0.26 to 0.94. This figure clearly illustrates the development of the larger pores (≥5 nm) as the CTR reaction progresses. It also clearly shows the development of bimodality in the pore size distributions.

Figures 4-4-195 - 4-4-205 show plots of pore volume frequency vs. pore diameter which correspond to the cumulative pore volume plots in Figures 4-4-171 - 4-4-181. (The former plots are obtaining by taking the derivative of the latter plots.) Figures 4-4-206 to 4-4-216 show relative pore volume frequency vs. pore diameter which correspond to the relative cumulative pore volume plots in Figures 4-4-182 - 4-4-192. These plots clearly illustrate the development of larger pores (>10 nm) in samples with fractional weight losses ≥0.26. They also clearly illustrate the development of bimodality in the distributions in samples with fractional weight losses ≥ 0.40.

Figures 4-4-217, 4-4-218, and 4-4-219 show plots of the median diameter (D_{50}), 90-percentile diameter (D_{90}), and 10-percentile (D_{10}) diameter, respectively, as a function of the fractional weight loss. The steep decrease in each diameter during the early stages of the reaction reflects two things discussed previously. First, the early stage of the reaction is dominated by the development of smaller pores (<5 nm). Second, the early stage samples have an extremely small pore volume which apparently consists mostly of large pores

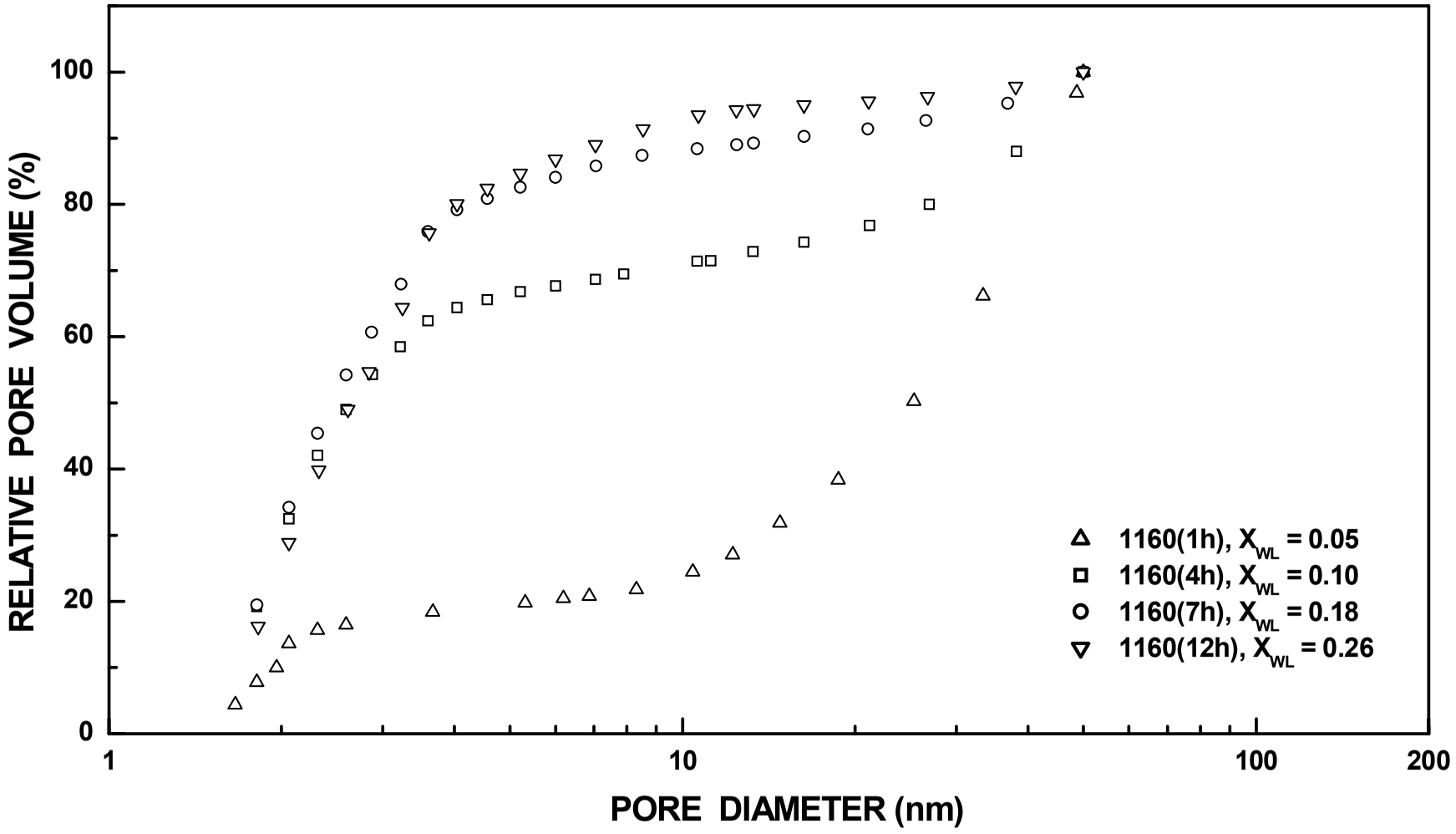

Figure 4-4-193 Normalized cumulative pore size distribution plots (from the desorption branch of the isotherm) for SC8 CTR samples with varying fractional weight loss of 0.05 - 0.26.

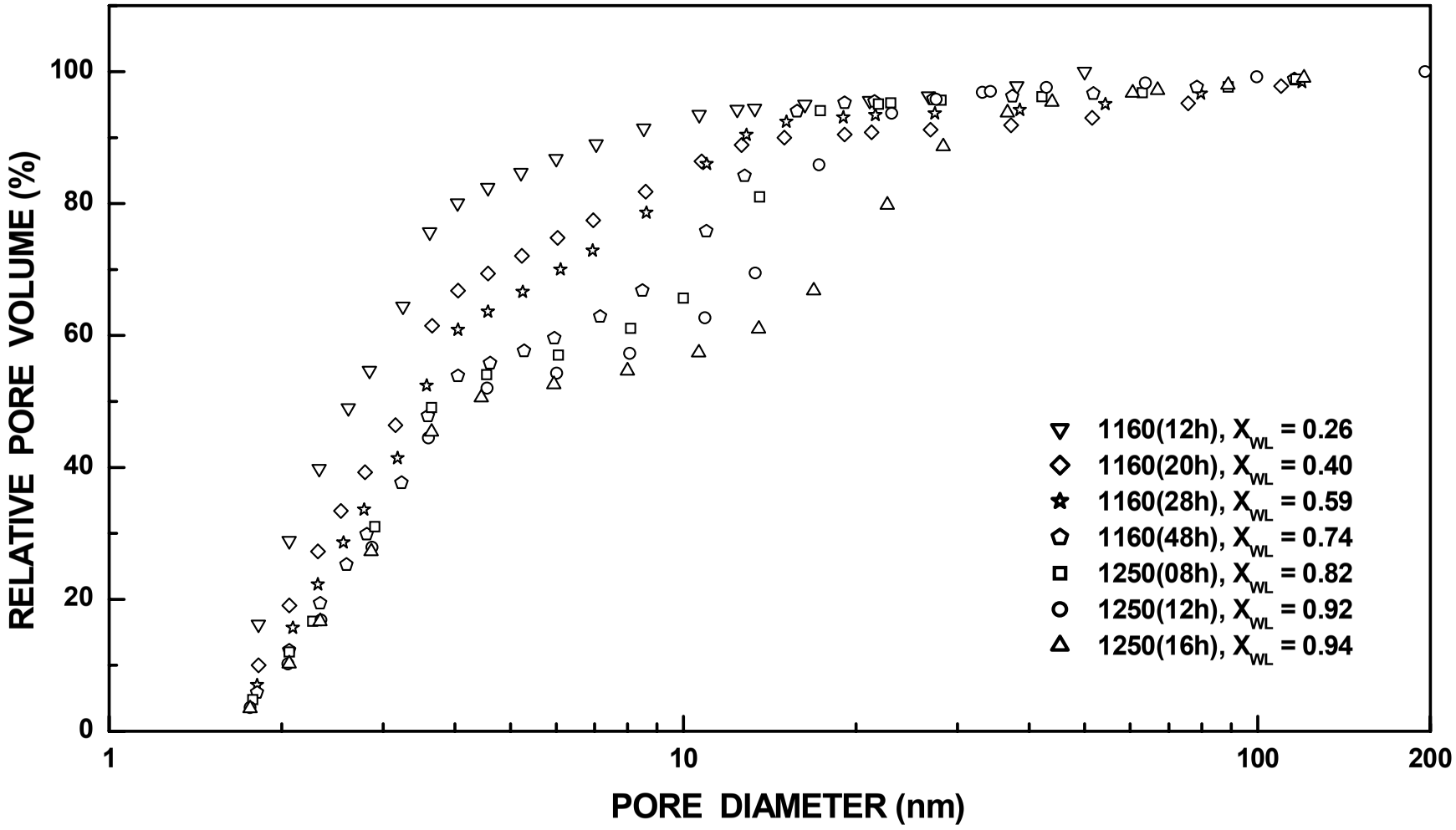

Figure 4-4-194 Normalized cumulative pore size distribution plots (from the desorption branch of the isotherm) for SC8 CTR samples with varying fractional weight loss of 0.26 - 0.94.

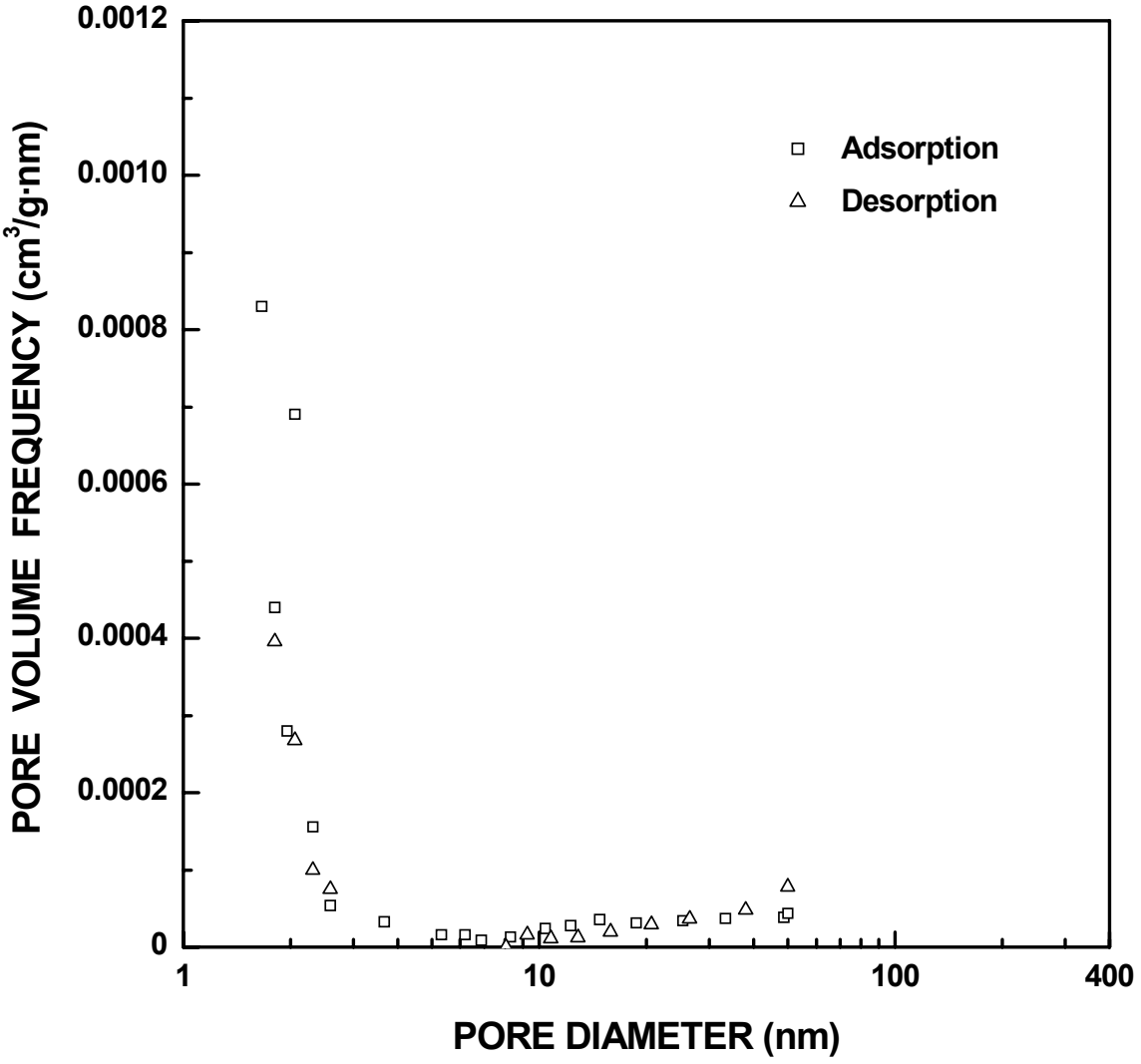

Figure 4-4-195 Plots of specific pore volume frequency vs. pore diameter for the SC8-1160(1h) sample (X_{WL} = 0.05). The pore diameter was cut off at 50 nm.

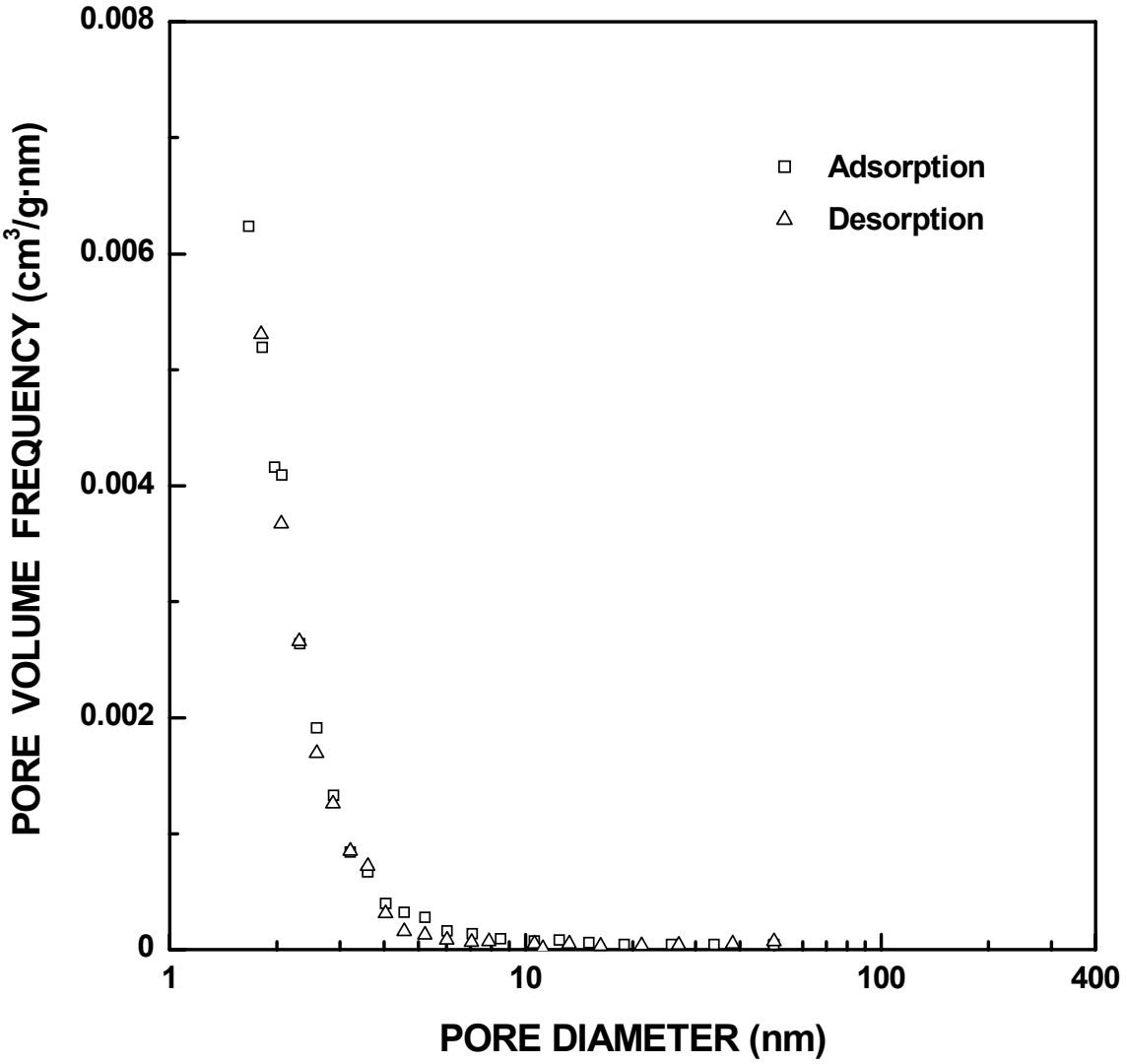

Figure 4-4-196 Plots of specific pore volume frequency vs. pore diameter for the SC8-1160(4h) sample (X_{WL} = 0.10). The pore diameter was cut off at 50 nm.

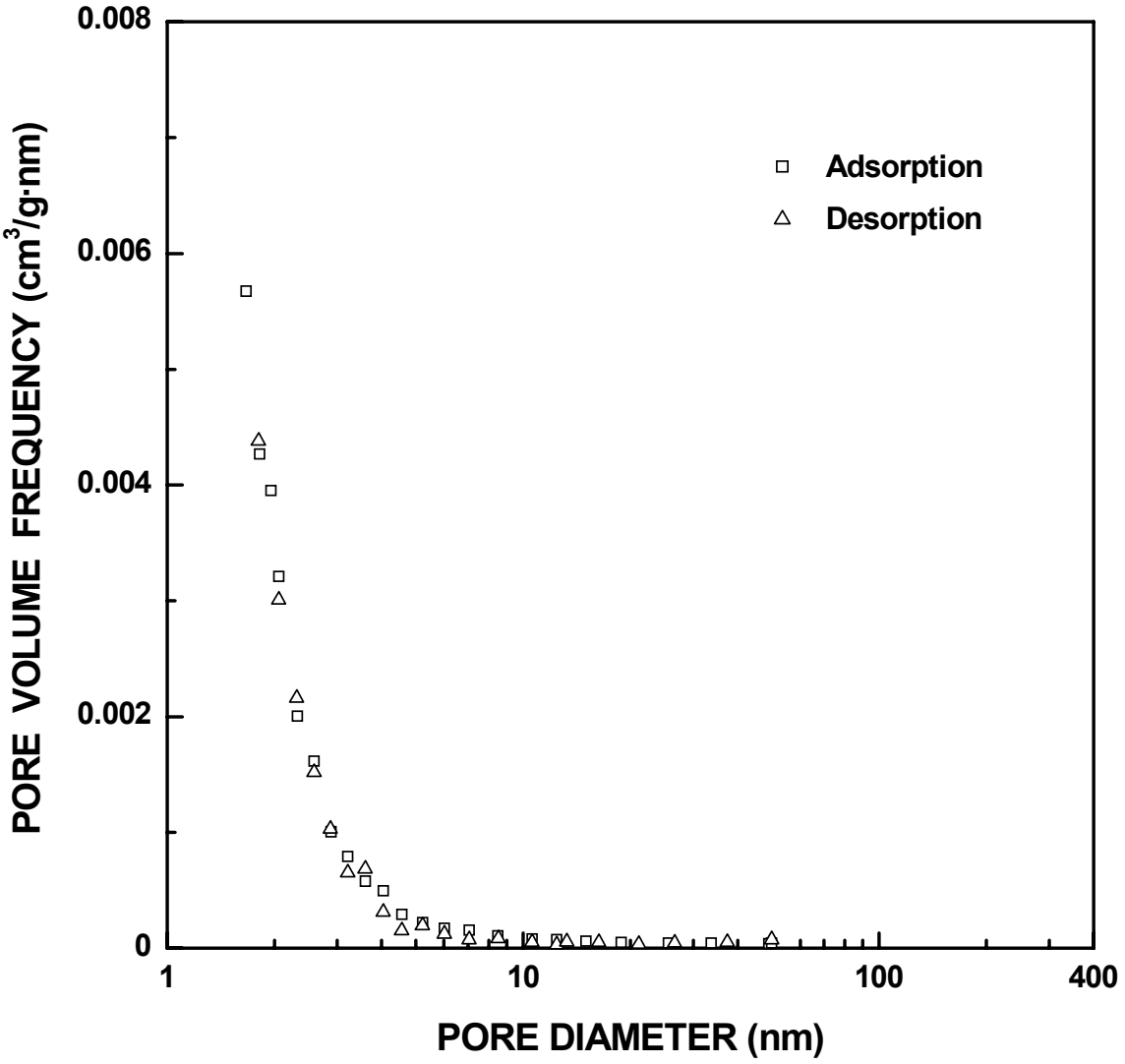

Figure 4-4-197 Plots of specific pore volume frequency vs. pore diameter for the SC8-1180(2h) sample (X_{WL} = 0.13). The pore diameter was cut off at 50 nm.

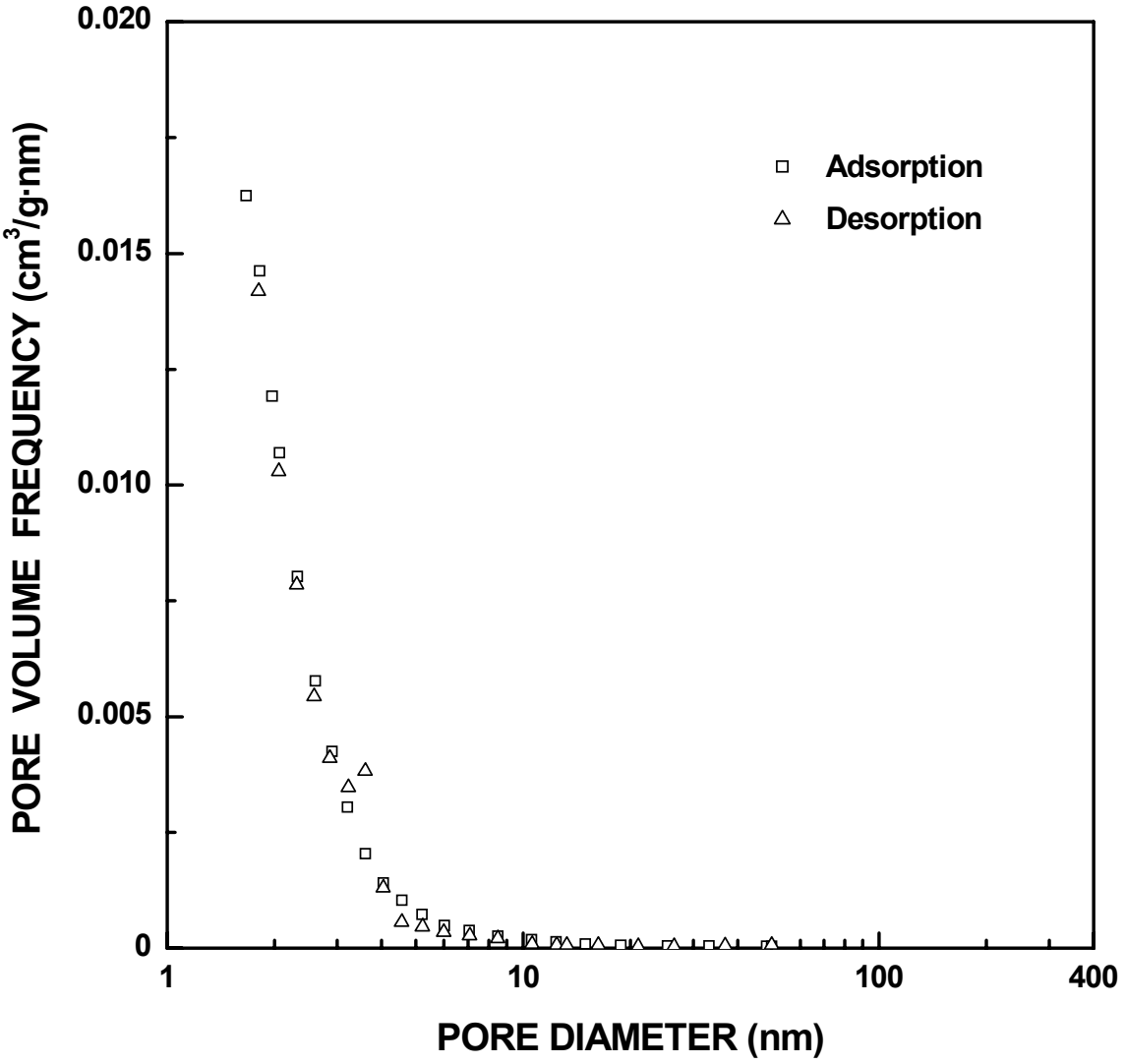

Figure 4-4-198 Plots of specific pore volume frequency vs. pore diameter for the SC8-1160(7h) sample (X_{WL} = 0.18). The pore diameter was cut off at 50 nm.

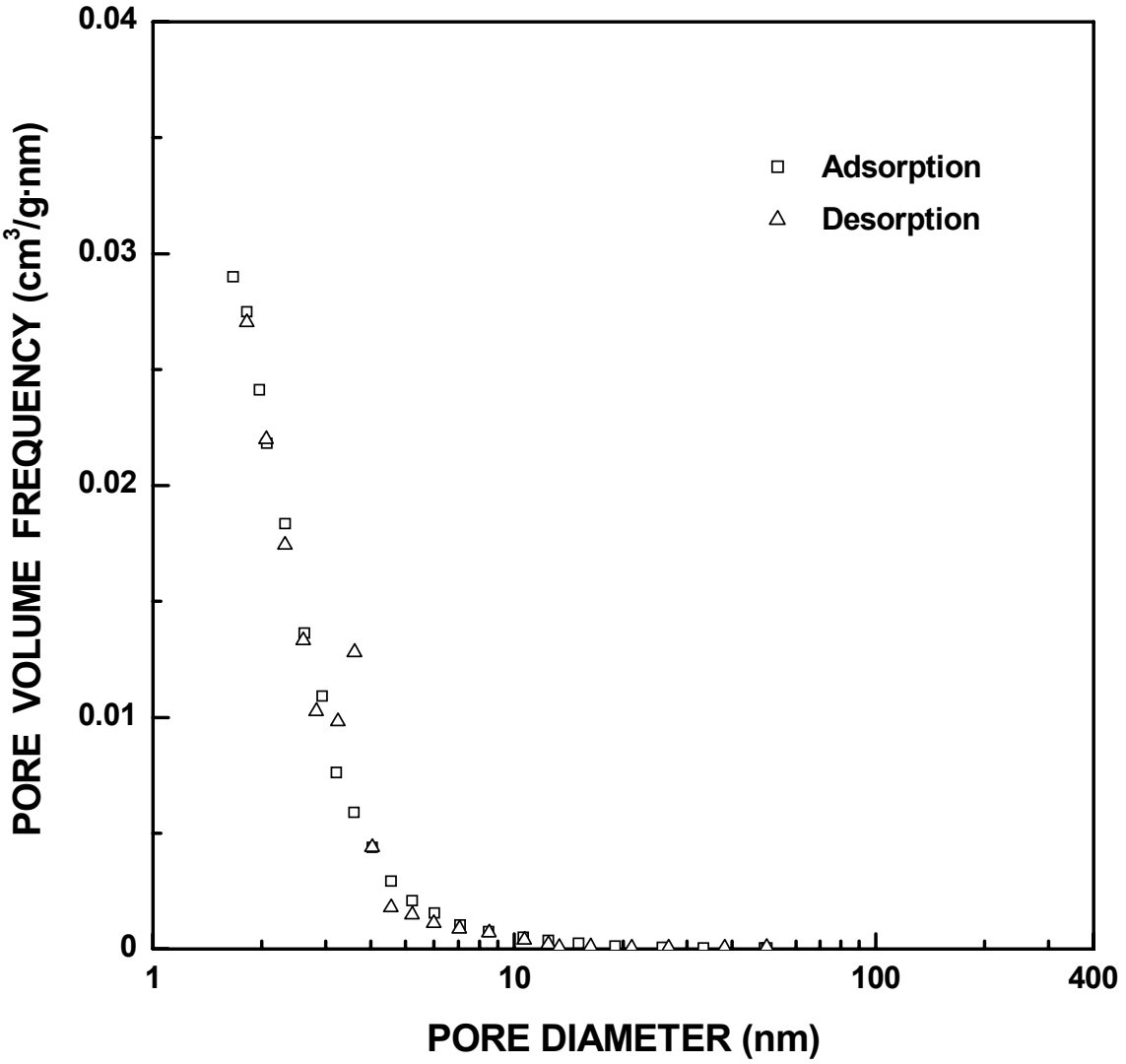

Figure 4-4-199 Plots of specific pore volume frequency vs. pore diameter for the SC8-1160(12h) sample (X_{WL} = 0.26). The pore diameter was cut off at 50 nm.

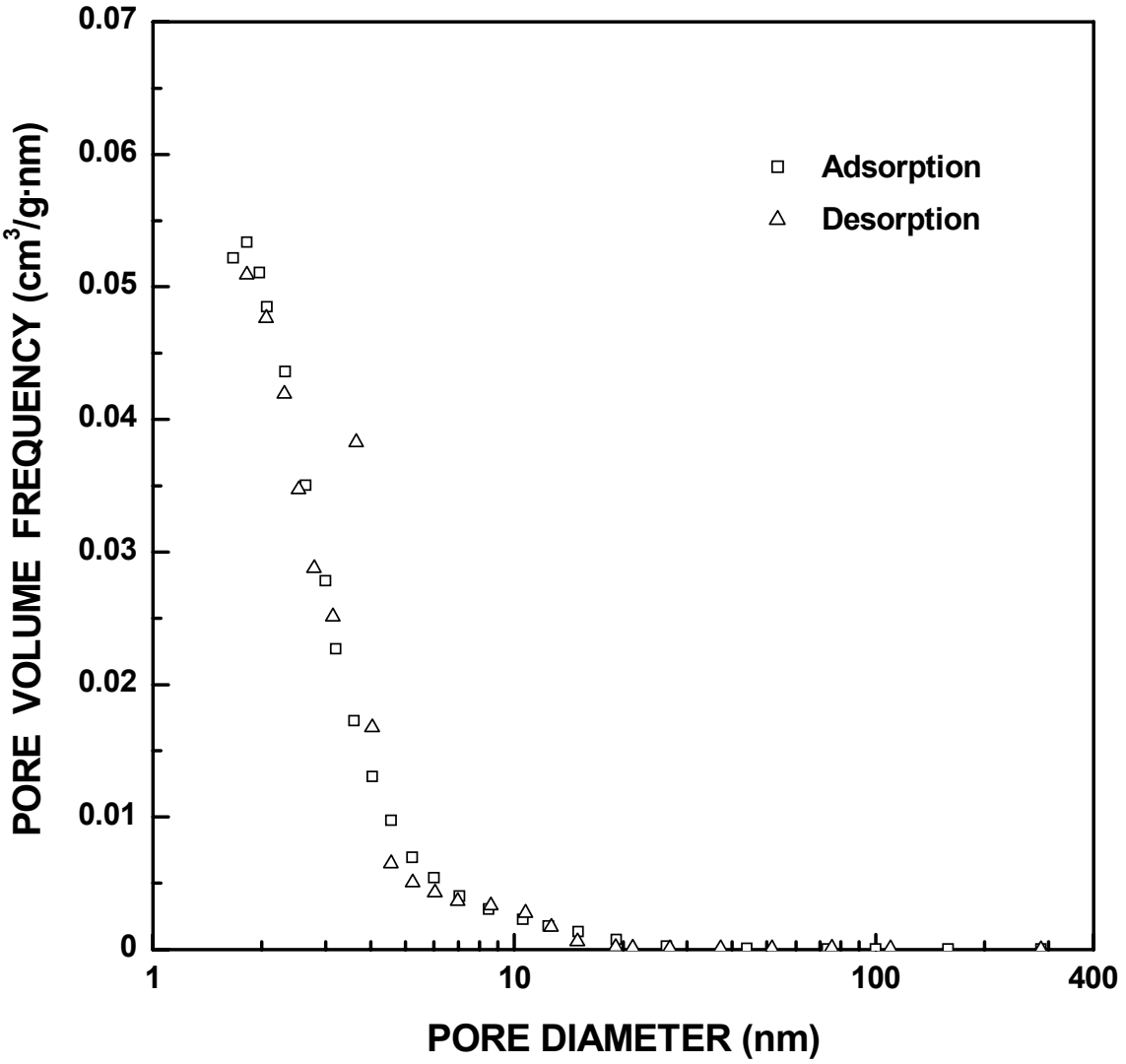

Figure 4-4-200 Plots of specific pore volume frequency vs. pore diameter for the SC8-1160(20h) sample (X_{WL} = 0.40).

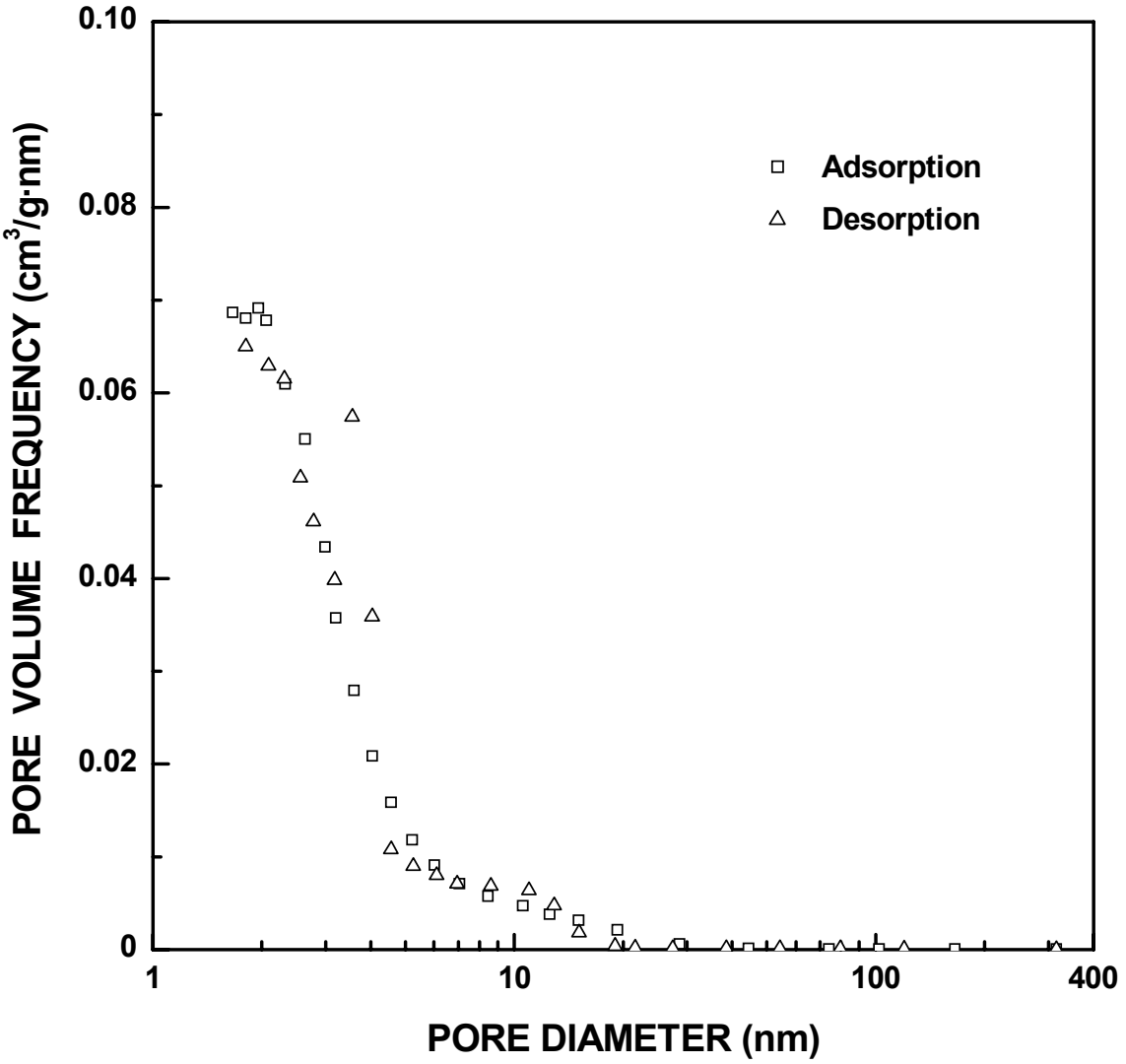

Figure 4-4-201 Plots of specific pore volume frequency vs. pore diameter for the SC8-1160(28h) sample (X_{WL} = 0.59).

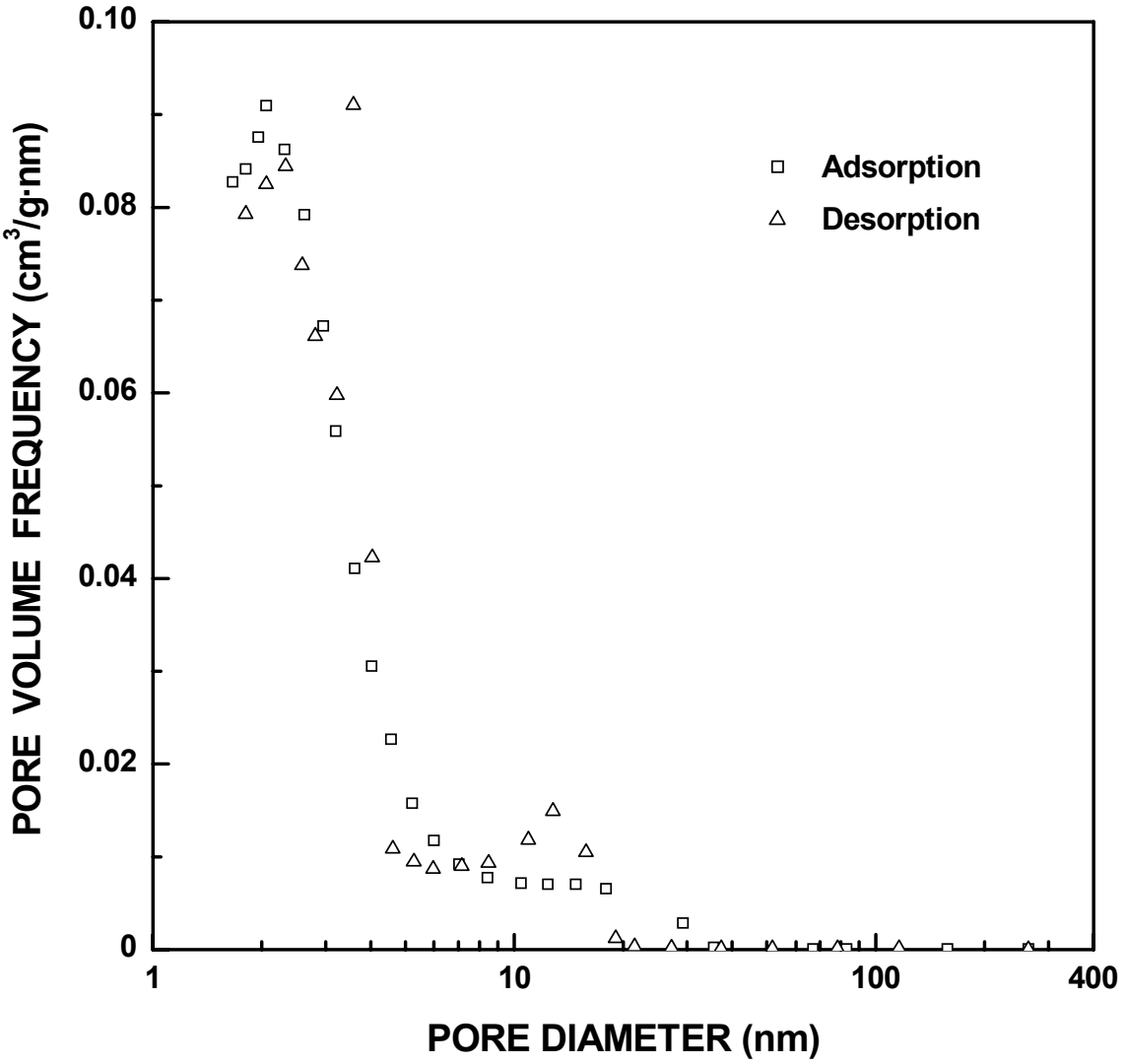

Figure 4-4-202 Plots of specific pore volume frequency vs. pore diameter for the SC8-1160(48h) sample (X_{WL} = 0.74).

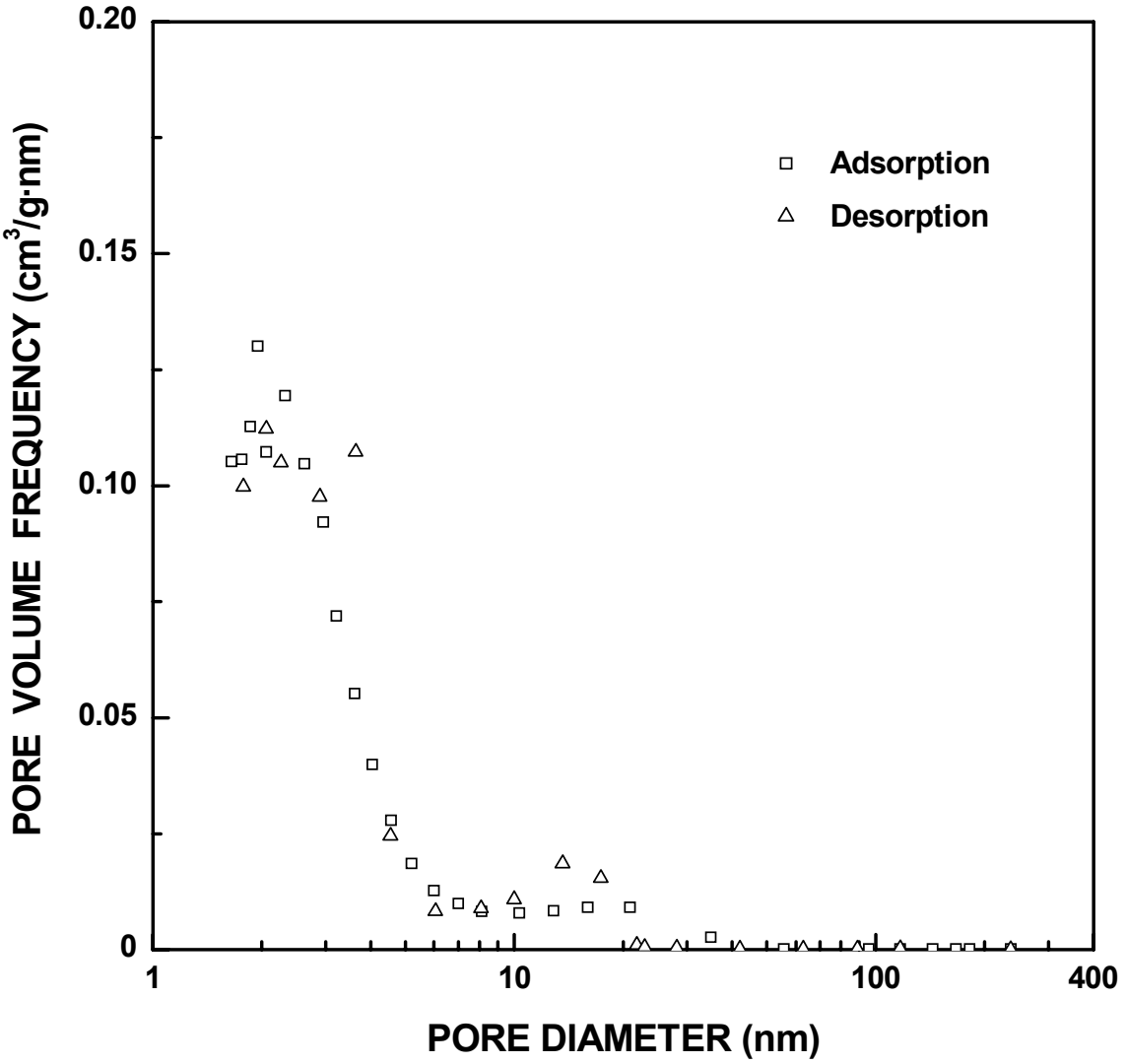

Figure 4-4-203 Plots of specific pore volume frequency vs. pore diameter for the SC8-1250(8h) sample (X_{WL} = 0.82).

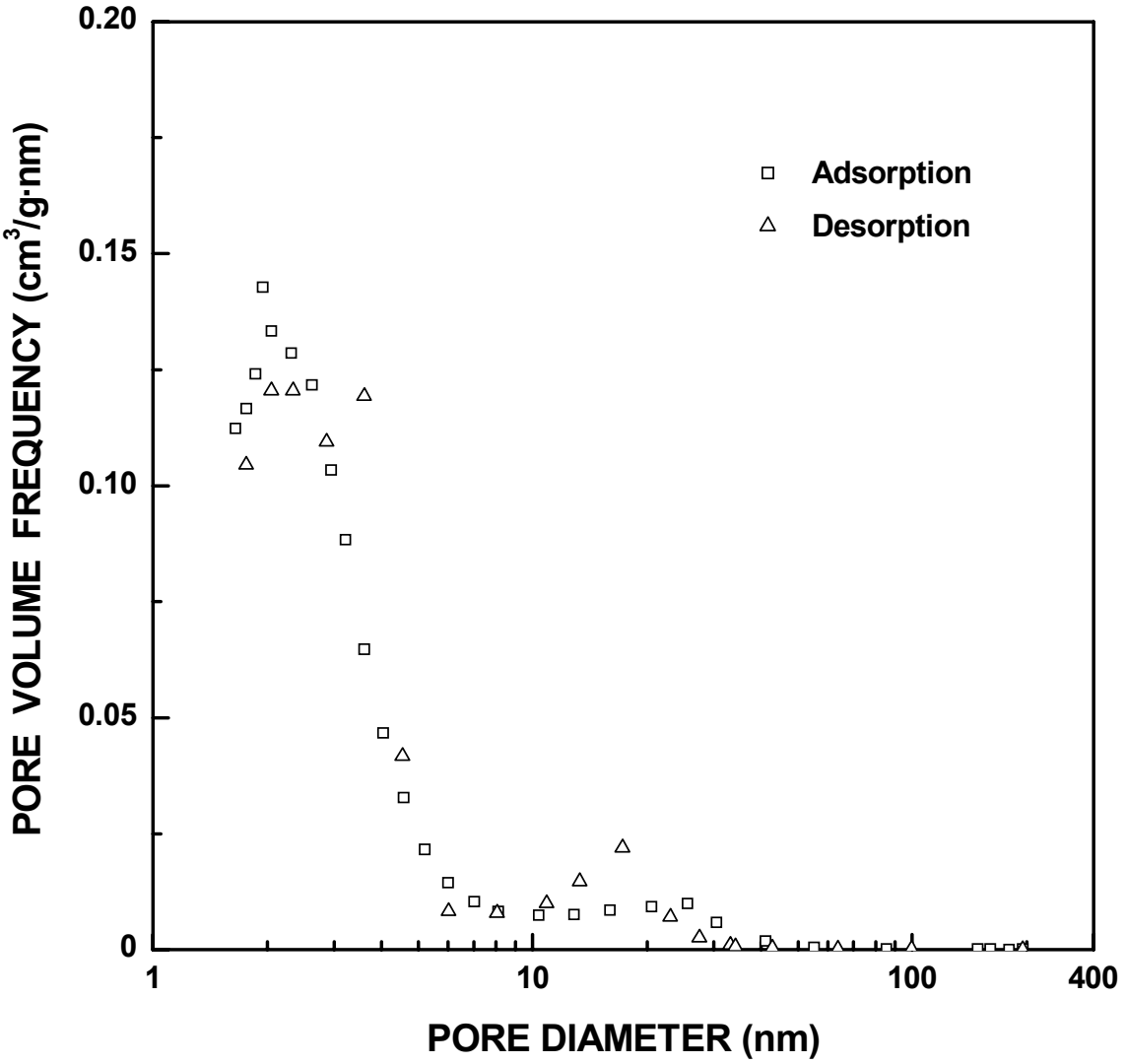

Figure 4-4-204 Plots of specific pore volume frequency vs. pore diameter for the SC8-1250(12h) sample (X_{WL} = 0.92).

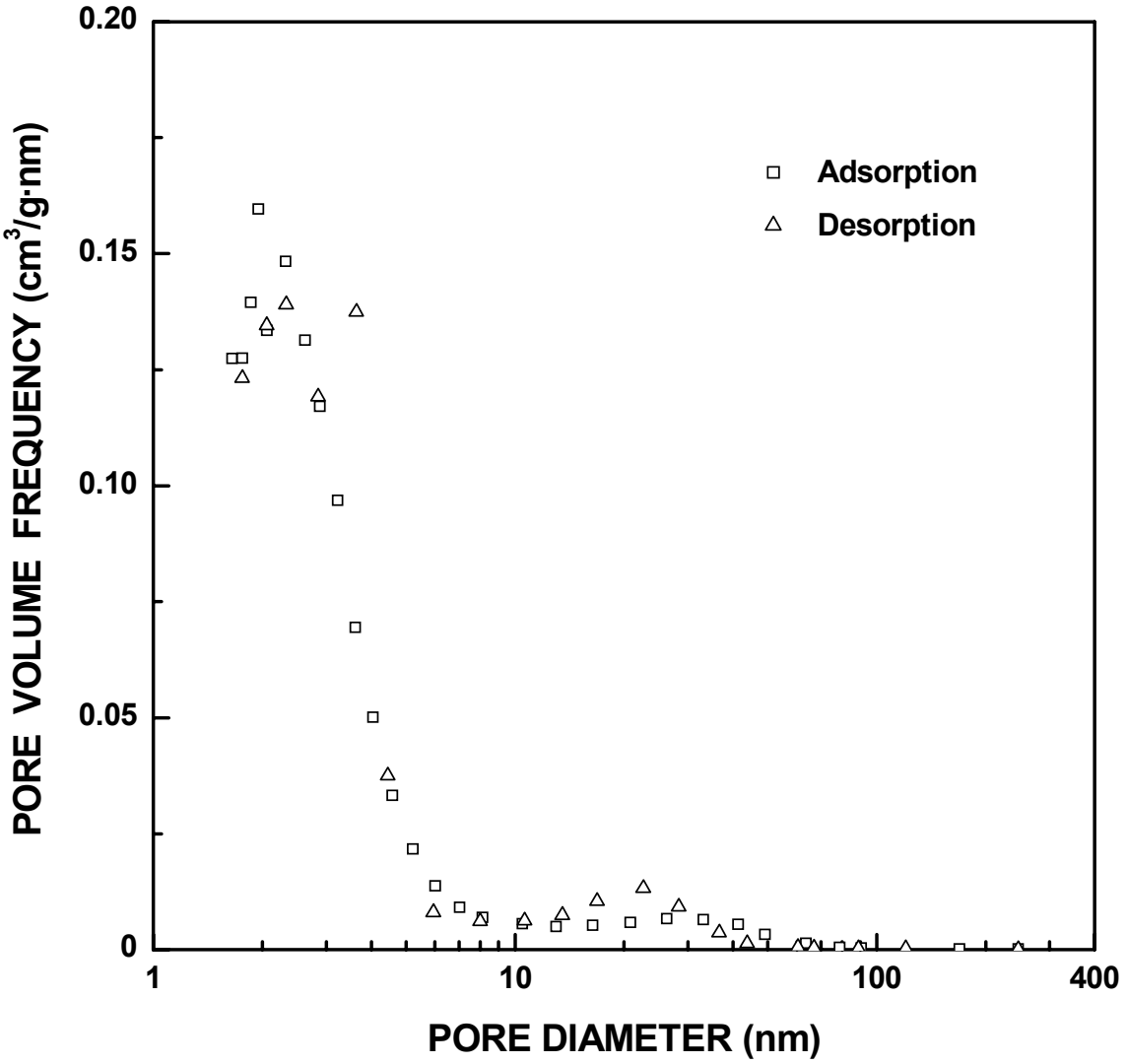

Figure 4-4-205 Plots of specific pore volume frequency vs. pore diameter for the SC8-1250(16h) sample (X_{WL} = 0.94).

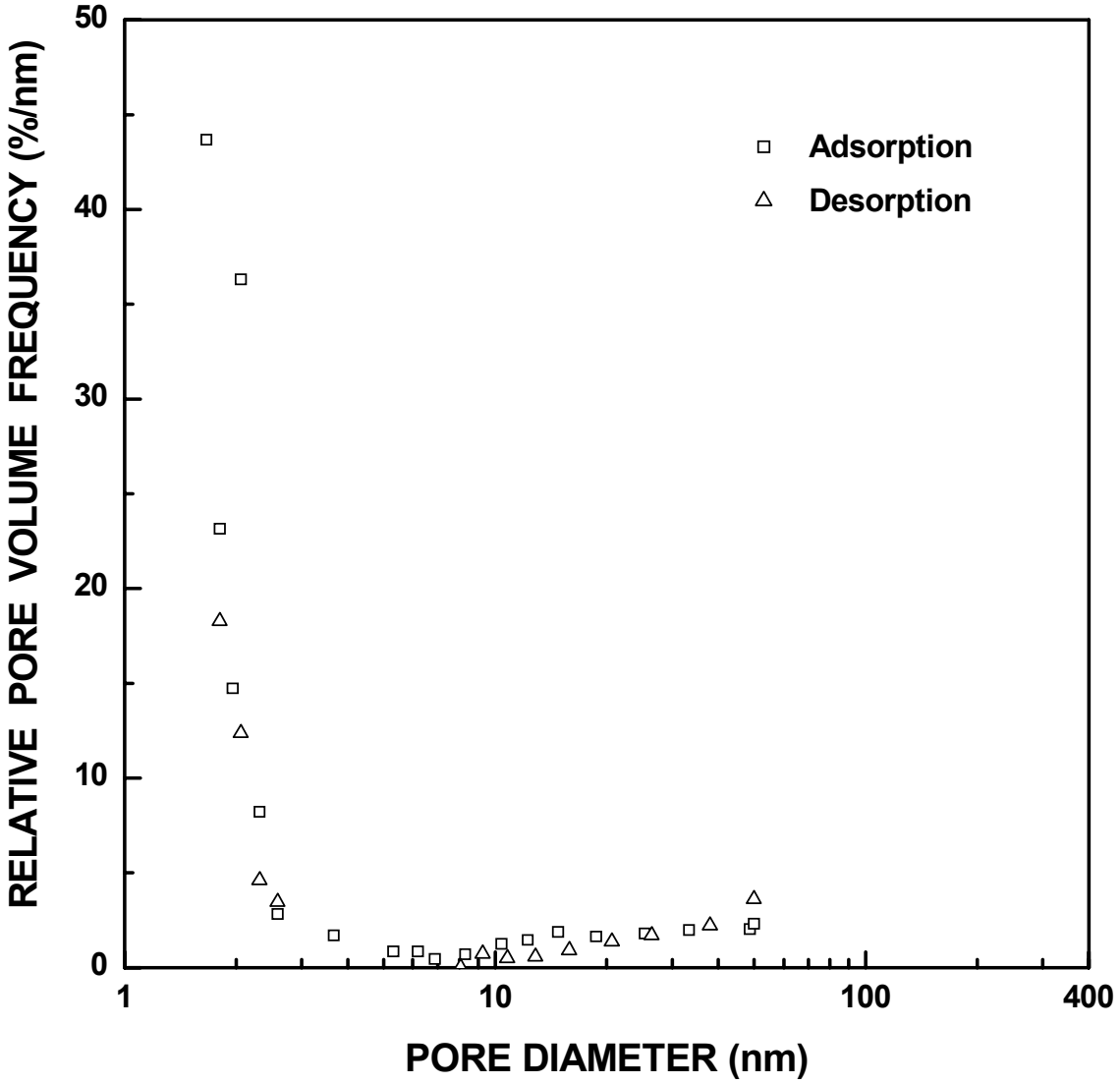

Figure 4-4-206 Plots of relative ("normalized") pore volume frequency vs. pore diameter for the SC8-1160(1h) (X_{WL} = 0.05) sample. The pore diameter was cut off at 50 nm.

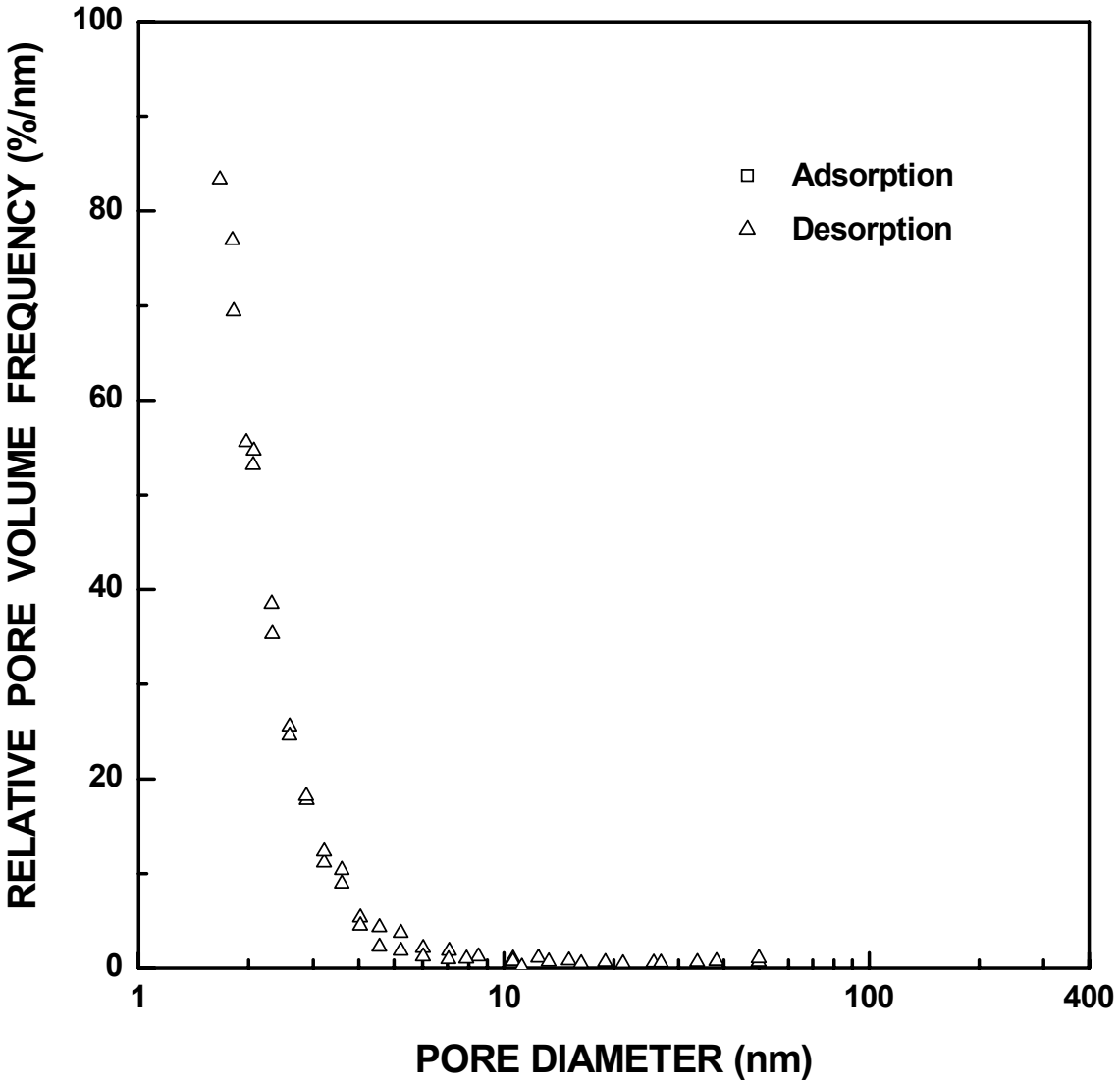

Figure 4-4-207 Plots of relative ("normalized") pore volume frequency vs. pore diameter for the SC8-1160(4h) (X_{WL} = 0.10) sample. The pore diameter was cut off at 50 nm.

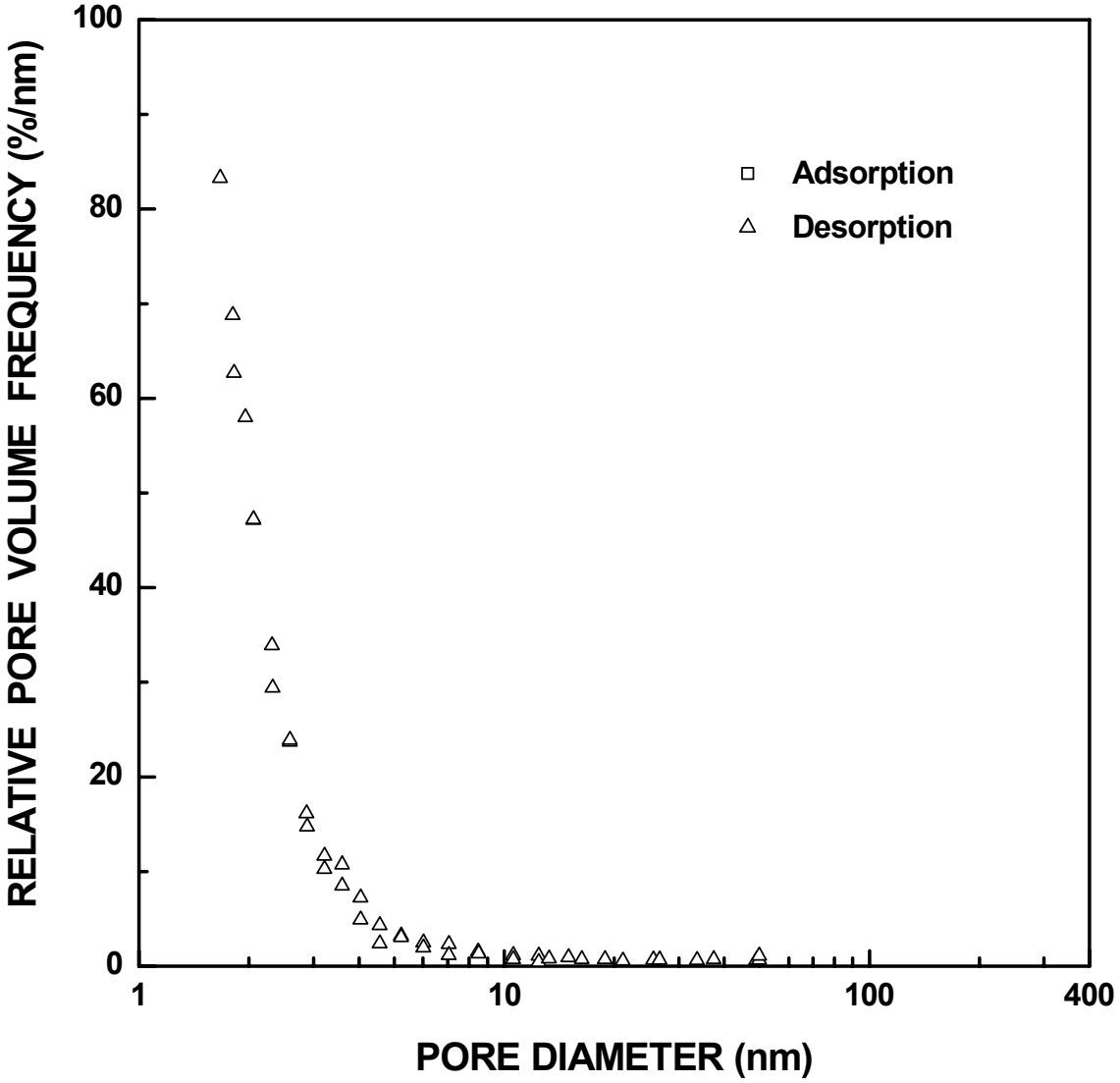

Figure 4-4-208 Plots of relative ("normalized") pore volume frequency vs. pore diameter for the SC8-1180(2h) (X_{WL} = 0.13) sample. The pore diameter was cut off at 50 nm.

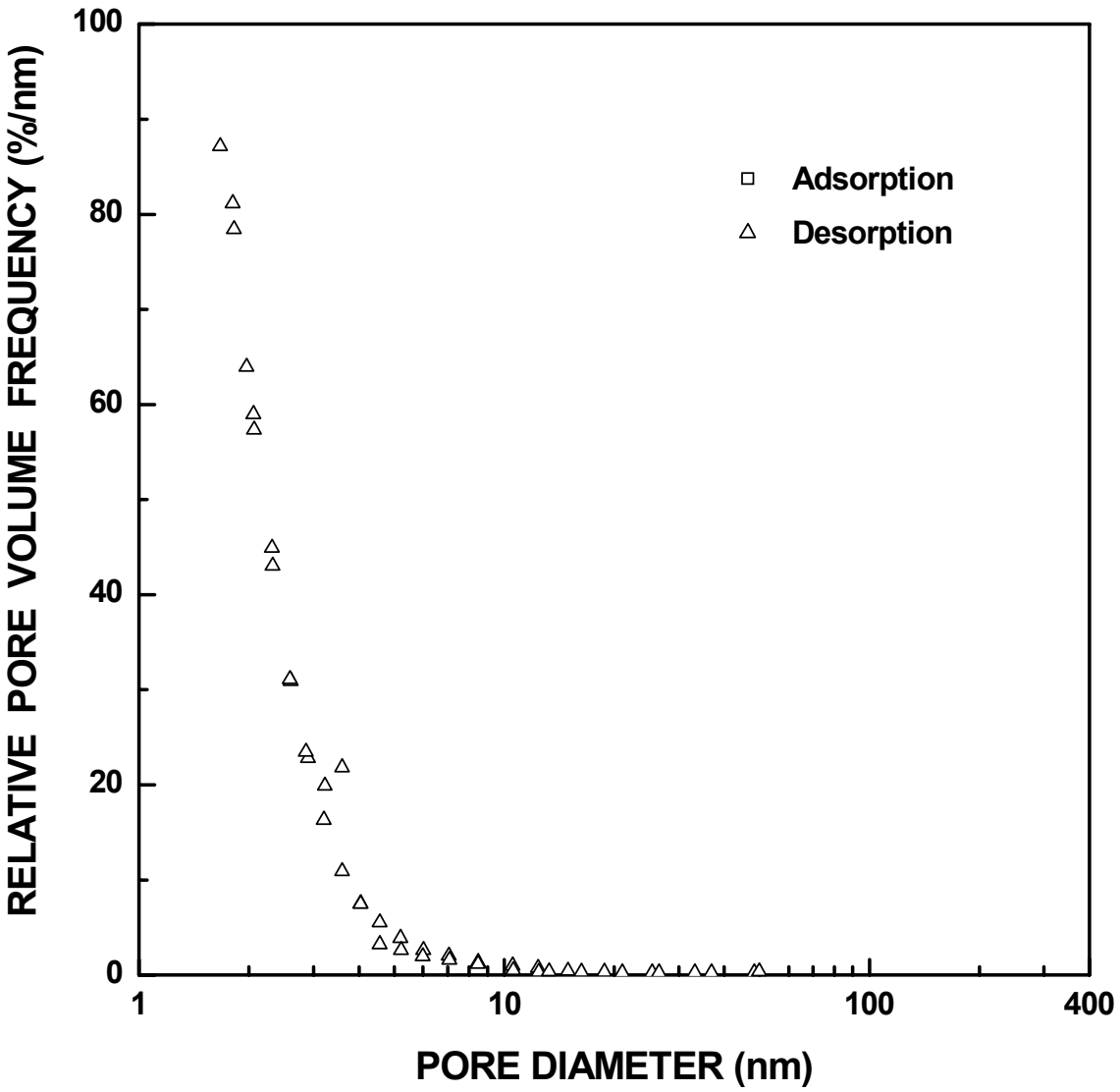

Figure 4-4-209 Plots of relative ("normalized") pore volume frequency vs. pore diameter for the SC8-1160(7h) (X_{WL} = 0.18) sample. The pore diameter was cut off at 50 nm.

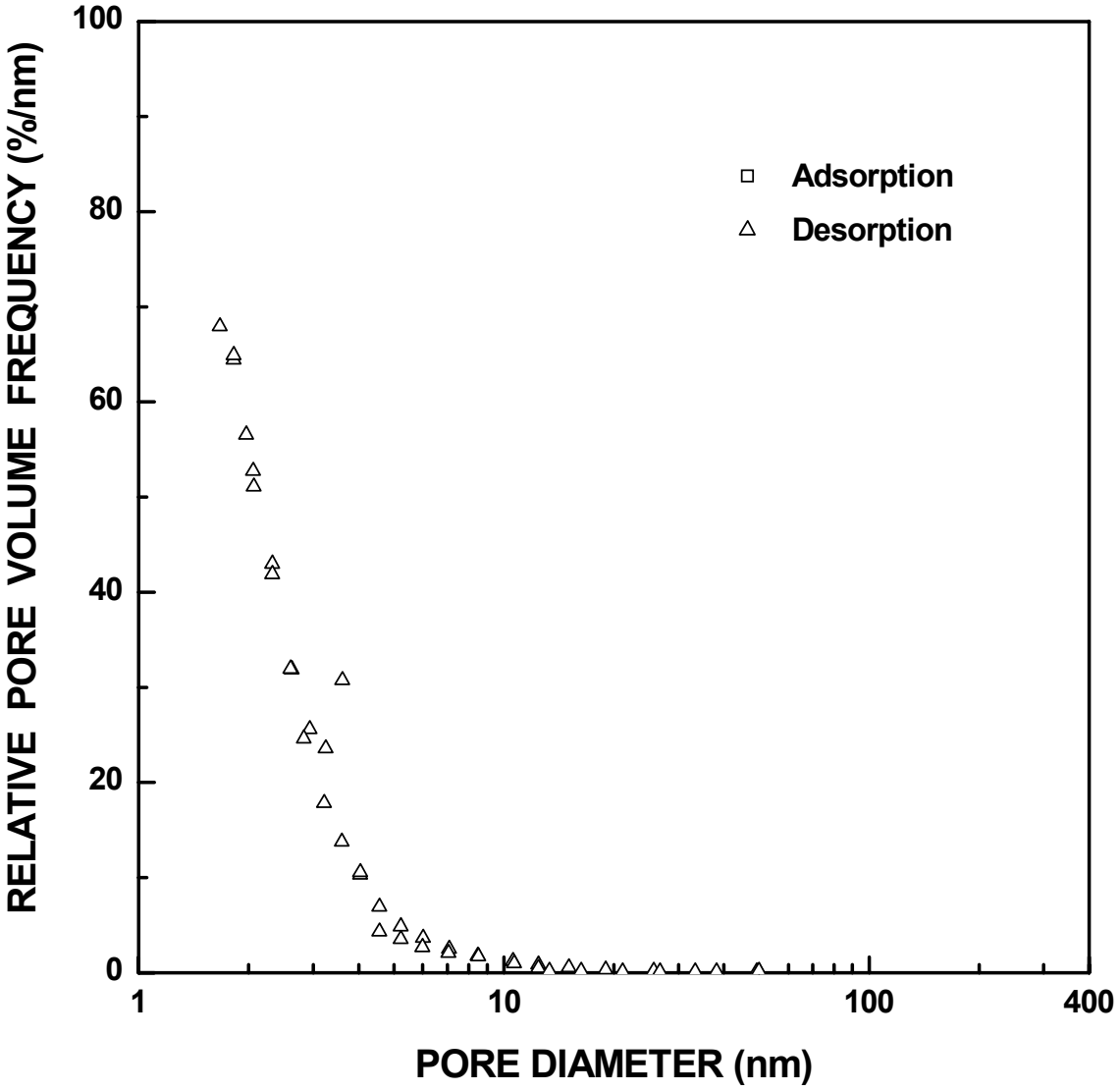

Figure 4-4-210 Plots of relative ("normalized") pore volume frequency vs. pore diameter for the SC8-1160(12h) (X_{WL} = 0.26) sample. The pore diameter was cut off at 50 nm.

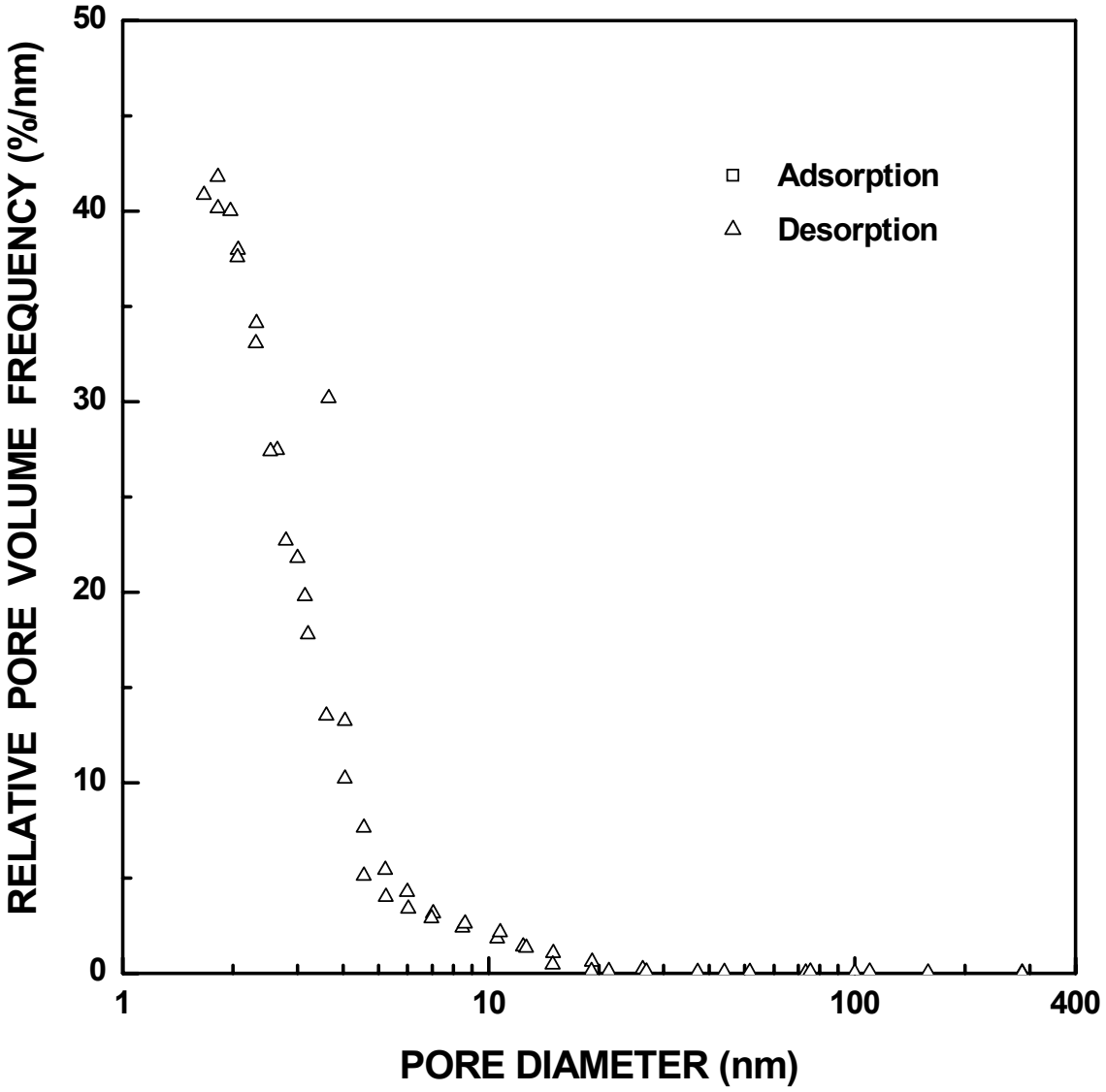

Figure 4-4-211 Plots of relative ("normalized") volume frequency vs. pore diameter for the SC8-1160(20h) (X_{WL} = 0.40) sample.

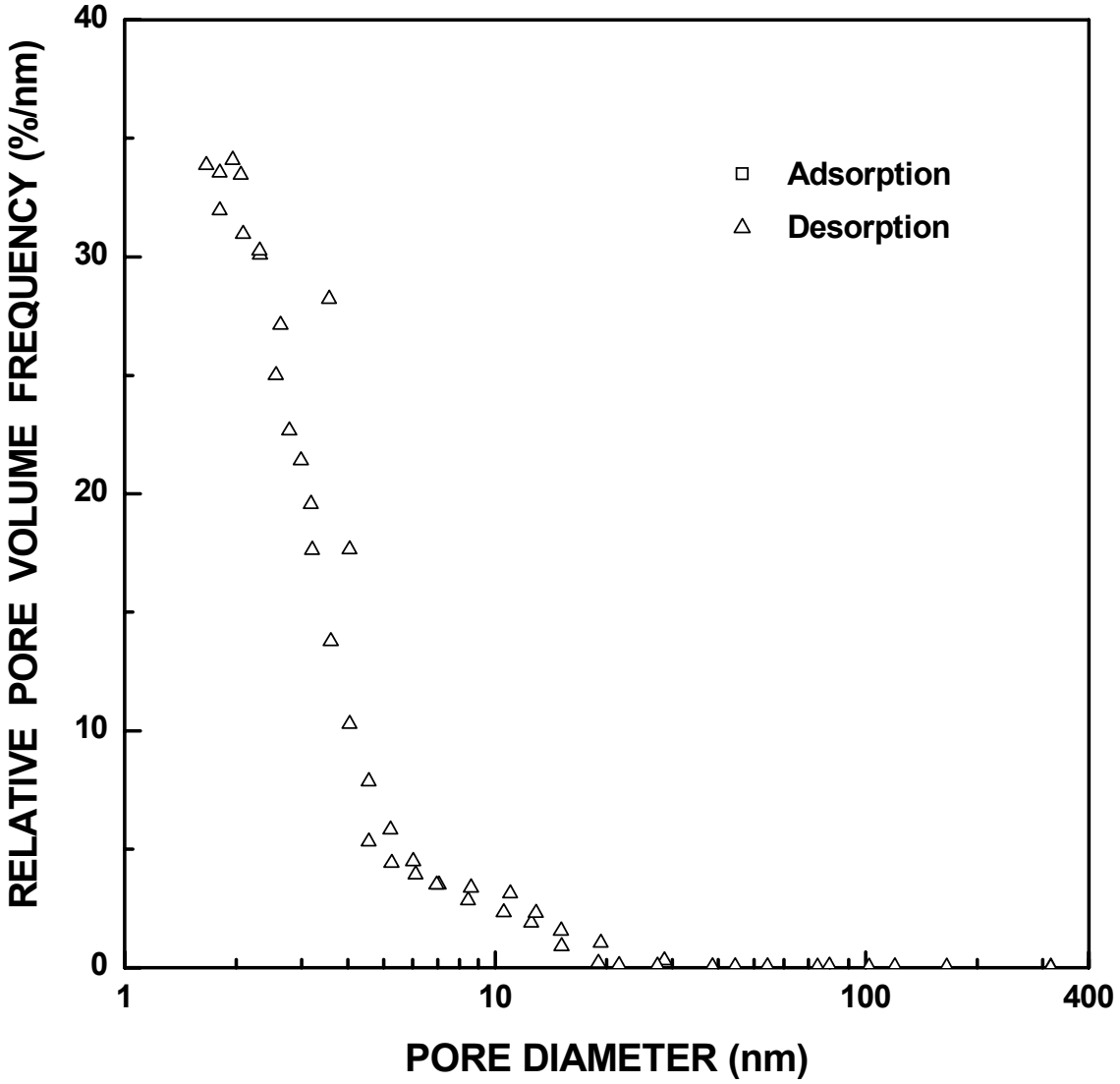

Figure 4-4-212 Plots of relative ("normalized") pore volume frequency vs. pore diameter for the SC8-1160(28h) (X_{WL} = 0.59) sample.

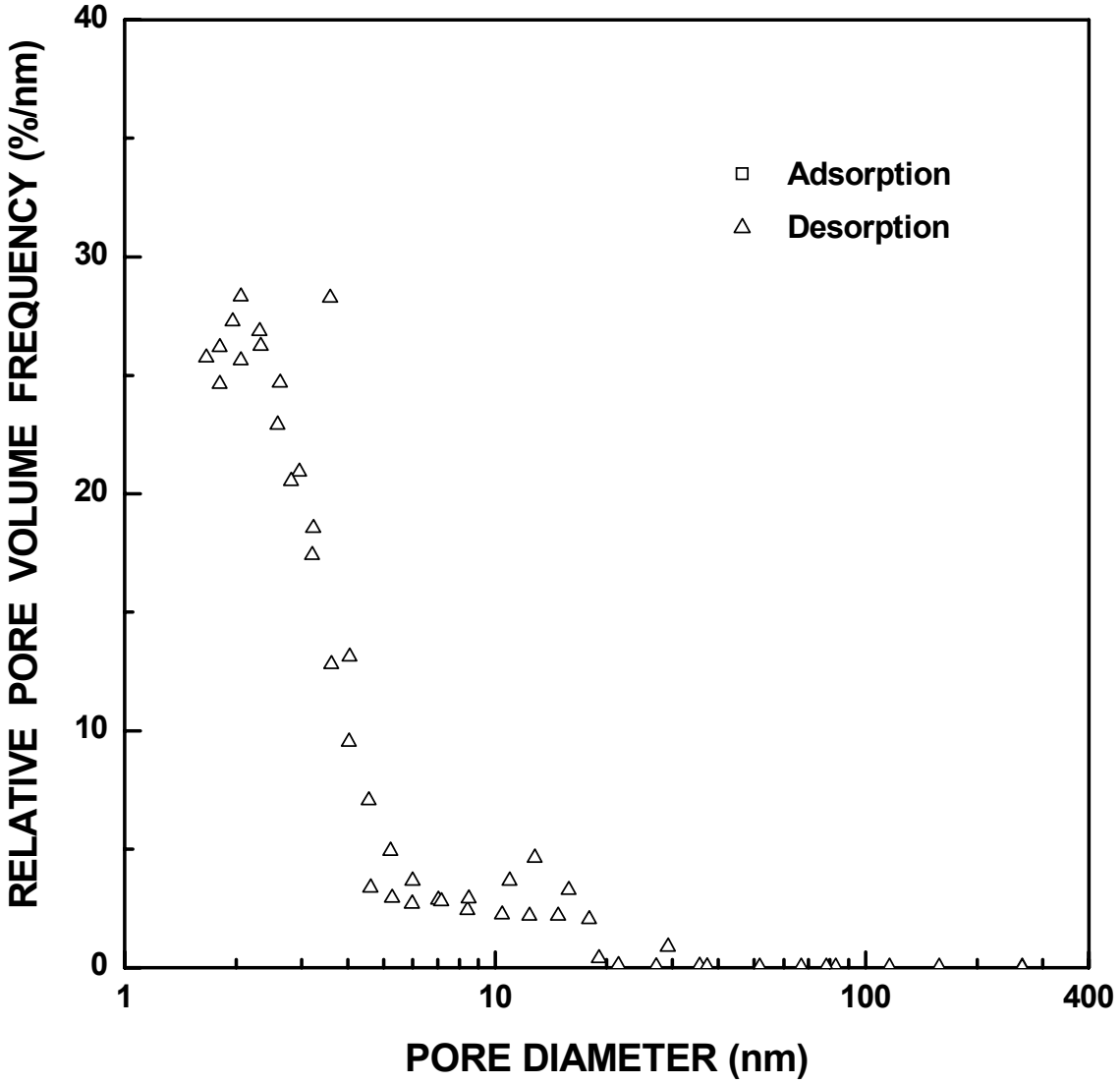

Figure 4-4-213 Plots of relative ("normalized") pore volume frequency vs. pore diameter for the SC8-1160(48h) (X_{WL} = 0.74) sample.

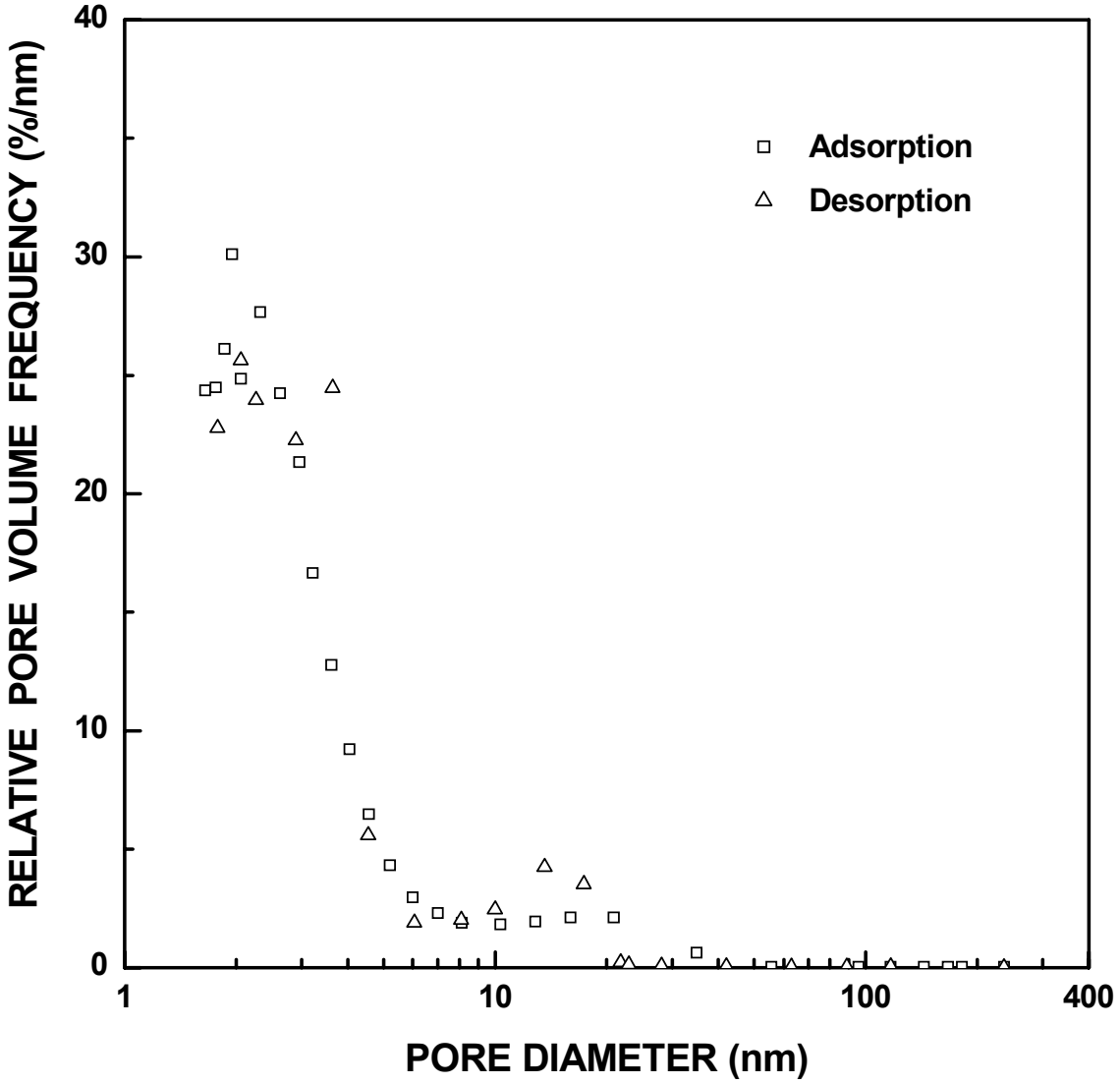

Figure 4-4-214 Plots of relative ("normalized") pore volume frequency vs. pore diameter for the SC8-1250(8h) (X_{WL} = 0.82) sample.

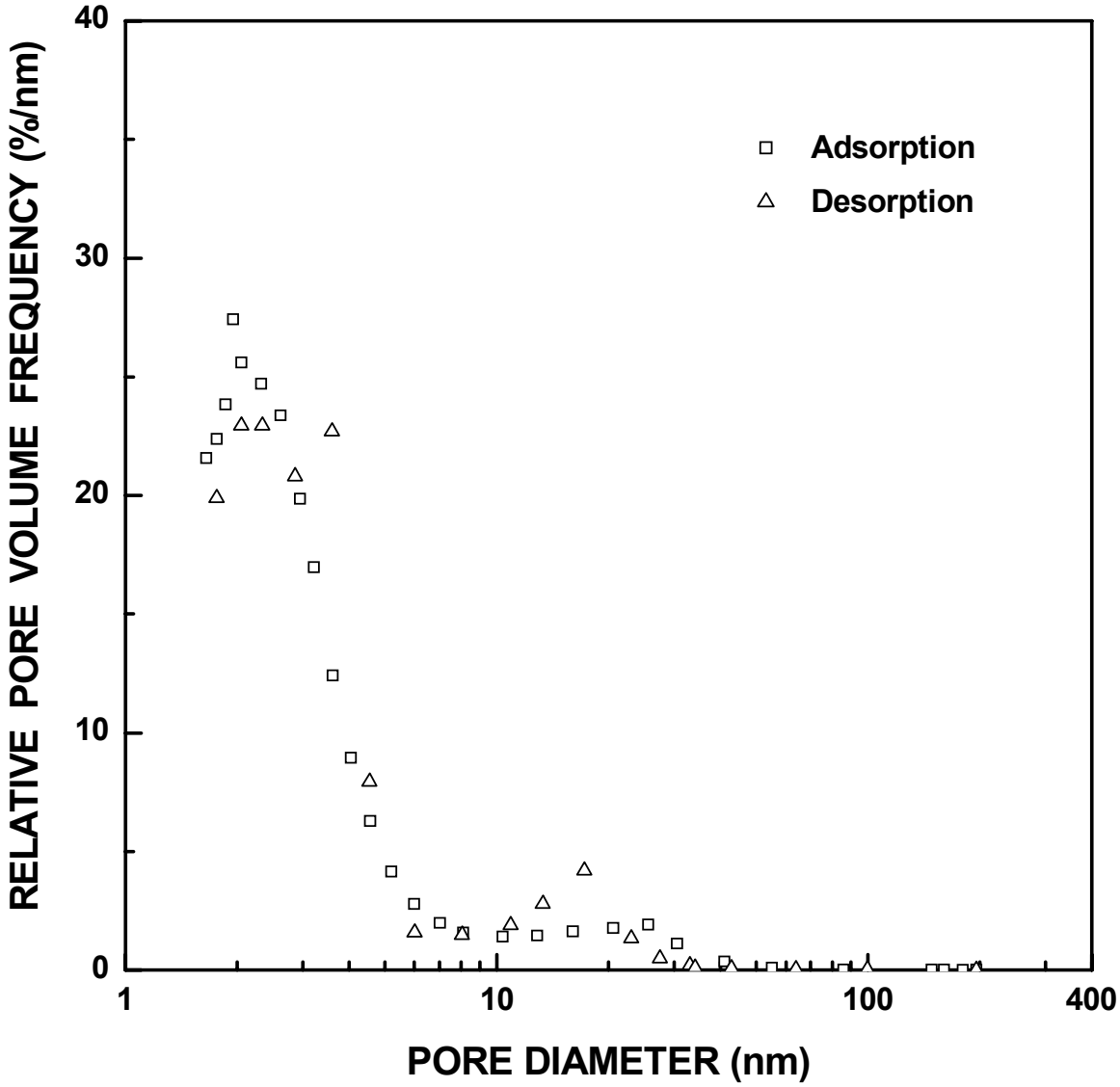

Figure 4-4-215 Plots of relative ("normalized") pore volume frequency vs. pore diameter for the SC8-1250(12h) (X_{WL} = 0.92) sample.

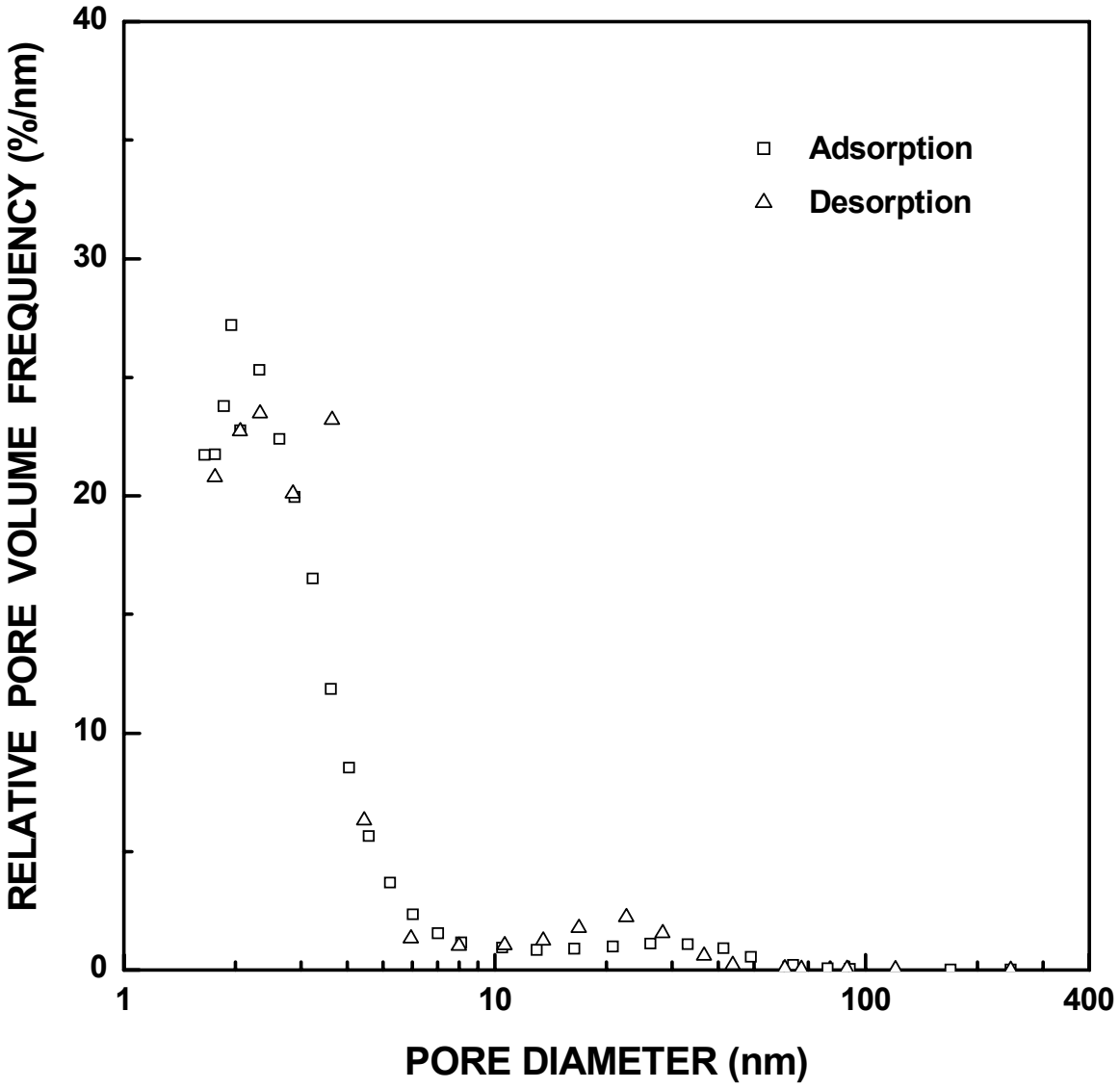

Figure 4-4-216 Plots of relative ("normalized") pore volume frequency vs. pore diameter for the SC8-1250(16h) (X_{WL} = 0.94) sample.

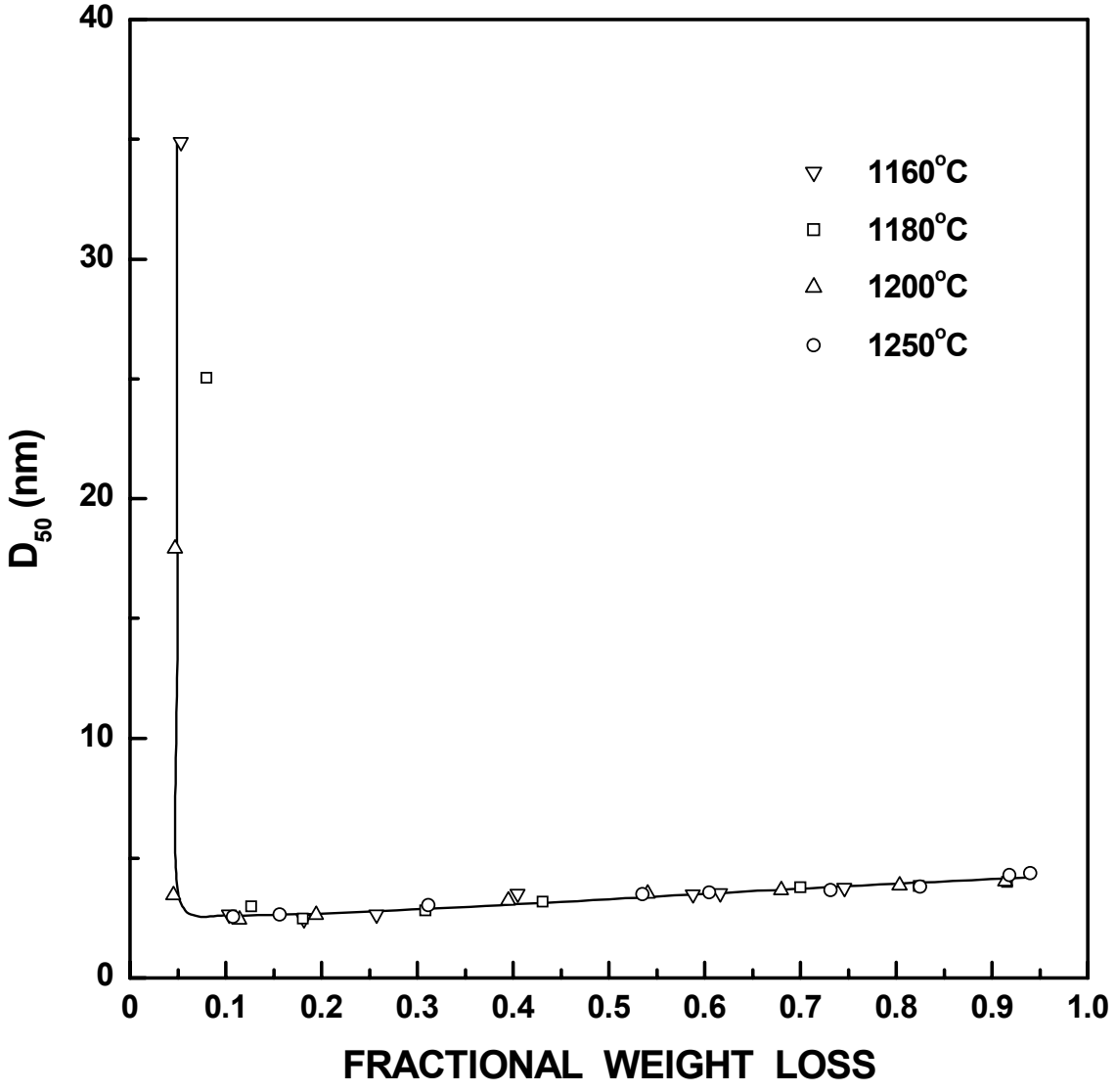

Figure 4-4-217 Plot of D_{50} (median diameter) vs. fractional weight loss for the SC8 CTR samples. The D_{50} data was obtained from the desorption branch of the isotherm.

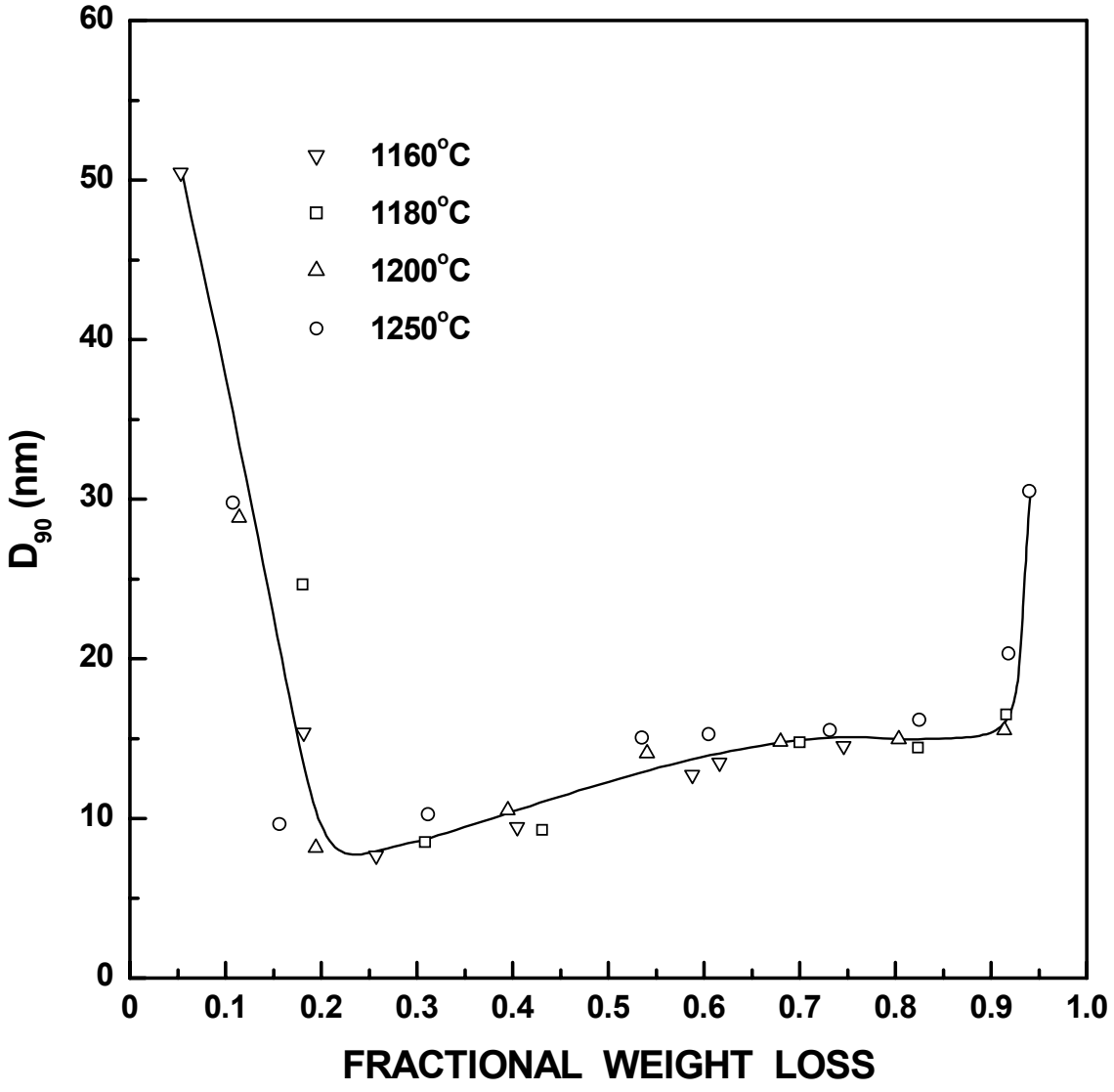

Figure 4-4-218 Plot of D_{90} (90-percentile diameter) vs. fractional weight loss for the SC8 CTR samples. The D_{90} data was obtained from the desorption branch of the isotherm.

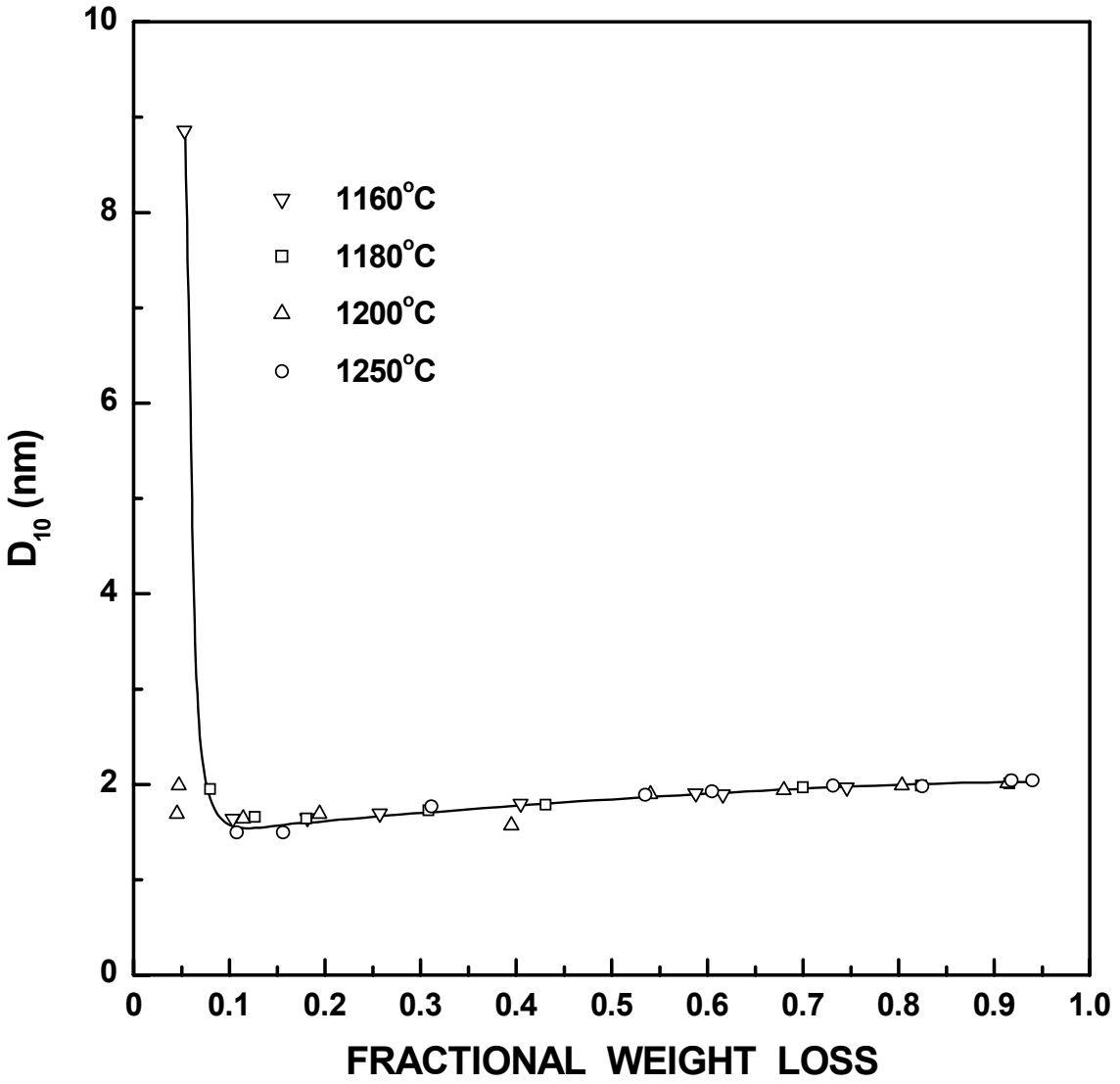

Figure 4-4-219 Plot of D_{10} (10-percentile diameter) vs. fractional weight loss for the SC8 CTR samples. The D_{10} data was obtained from the desorption branch of the isotherm.

associated with the macrodefects (e.g., cracks) that were originally present in the large pyrolyzed particles. After the early stage of the reaction, there is an increase in each diameter (D_{10}, D_{50}, and D_{90}) with increasing extent of reaction. Figure 4-4-220 shows a plot of part of the data in Figures 4-4-217 - 4-4-219 on an expanded y-axis scale. It is evident that the D_{10} diameter shows the most gradual increase as the reaction proceeds. The D_{50} diameter also increases with increasing fractional weight loss in a relatively gradual manner. The D_{90} diameter shows a more rapid increase during the reaction. This seems to reflect the fact that larger pores (greater than ~5-10 nm) develop more rapidly during the middle and later stages of the reaction. During the very late stage of reaction (X_{WL}> 0.92), there is a sharp increase in the D_{90} diameter. This presumably occurs due to coarsening, as discussing in detail previously for the SC35 samples.

Figures 4-4-221 and 4-4-222 show plots of the specific pore volume vs. fractional weight loss for pores with ≥5 nm and <5 nm, respectively. In these figures, the BJH pore volume for each sample was simply divided into the two size range specified. It is evident that significant volume fractions of both small and large pores continue to develop throughout the CTR reaction. (In contrast, similar plots for the SC35 samples (shown in Figures 4-4-145 and 4-4-146) indicated that most of the pore volume that developed throughout the CTR reaction was associated with the larger pores.)

Figures 4-4-223 and 4-4-224 show the same data as in Figures 4-4-221 and 4-4-222, respectively, but the data is plotted on the basis of the percentage of the total BJH pore volume in each of the specified size ranges. As noted previously, fine pores develop during the early stage of the reaction (X_{WL} < 0.20). For the rest of the reaction, a greater percentage of the pore volume that develops is associated with the larger pores.

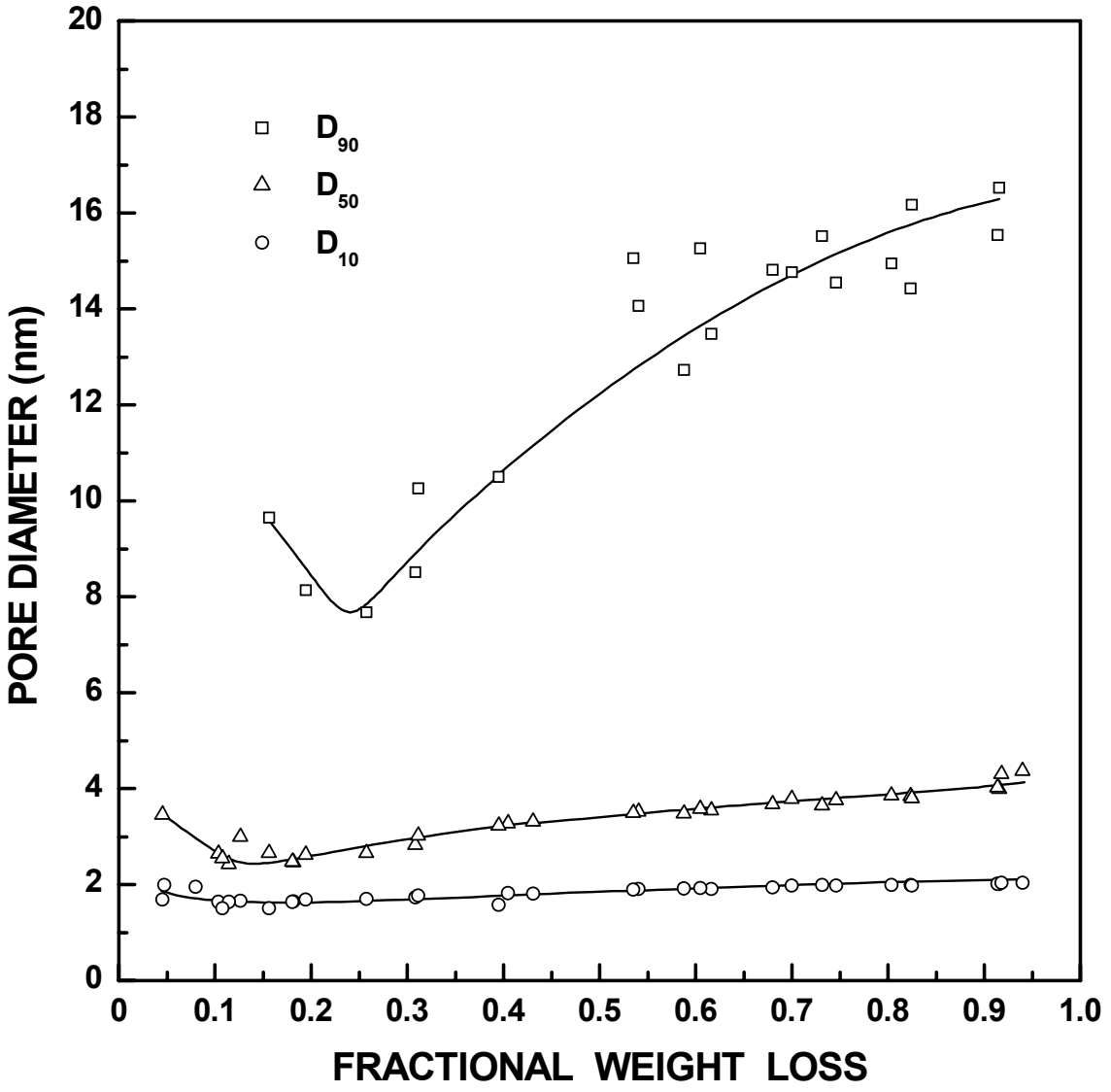

Figure 4-4-220 Plots of D_{10}, D_{50}, D_{90} (the 10-, 50-, and 90-percentile diameter) vs. fractional weight loss for the SC8 CTR samples. The D_{10}, D_{50}, and D_{90} data were obtained from the desorption branch of the isotherm.

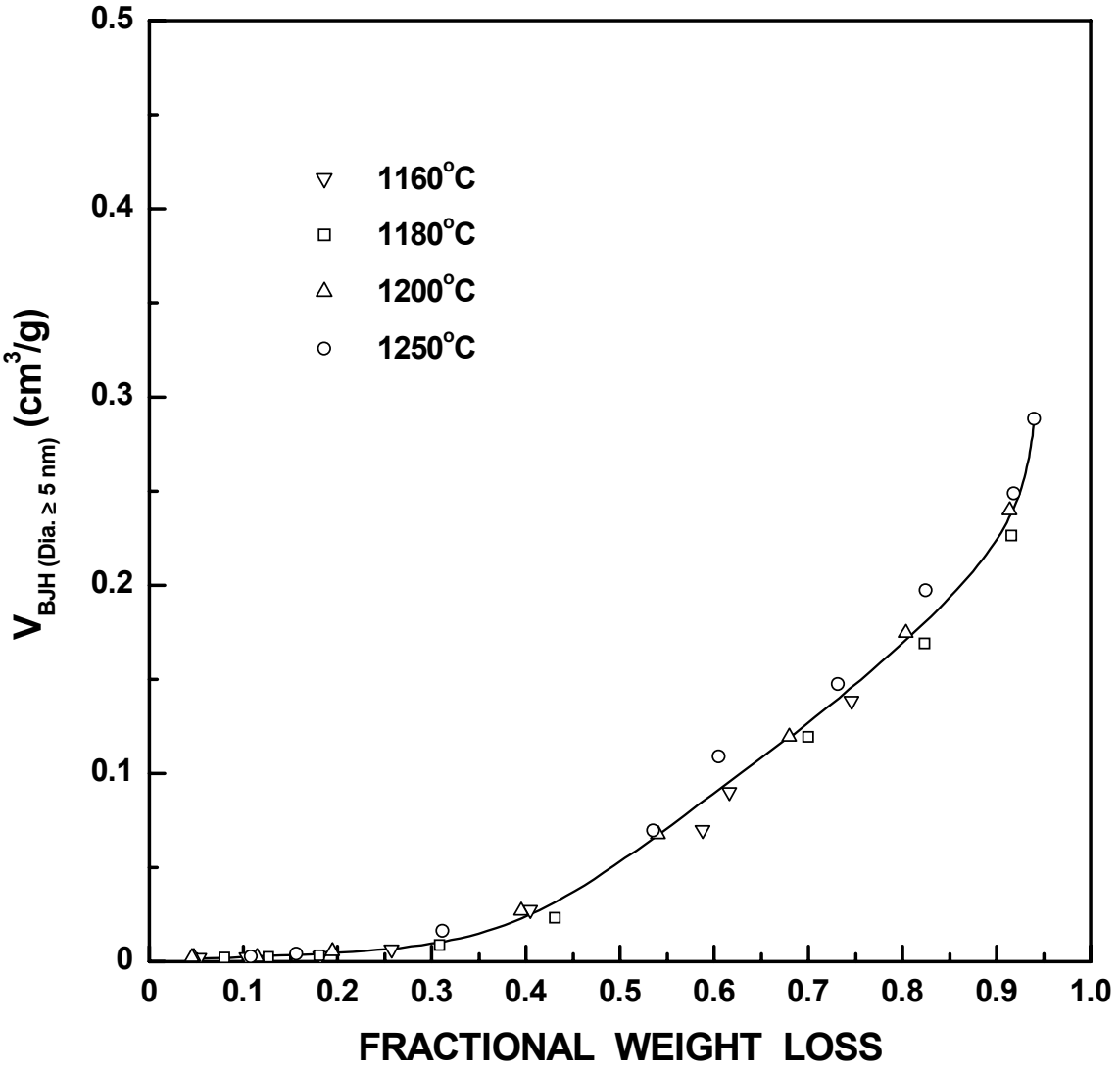

Figure 4-4-221 Plot of specific pore volume (from the desorption branch of the isotherm) for pores with diameter ≥5 nm vs. fractional weight loss for the SC8 CTR samples.

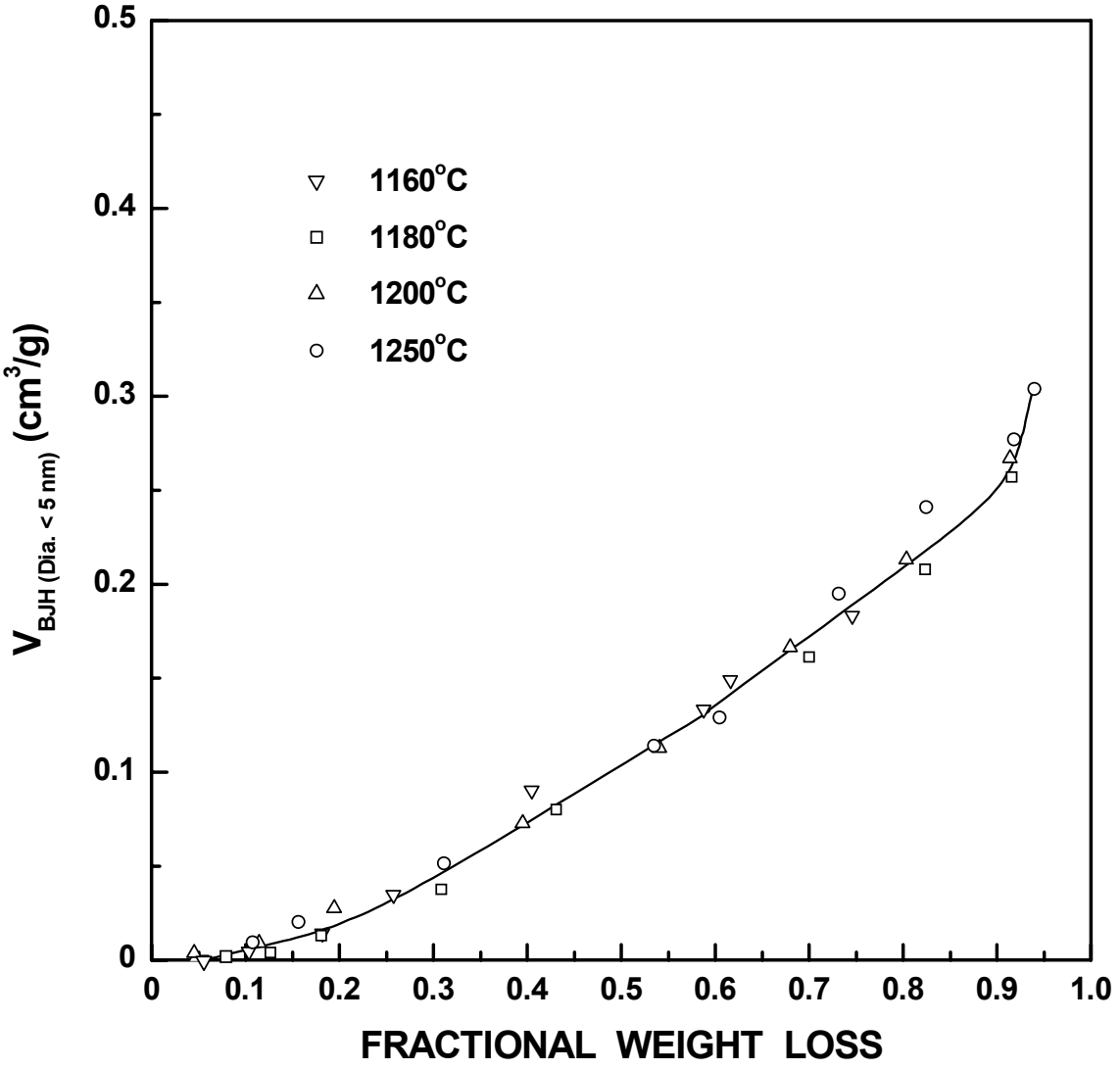

Figure 4-4-222 Plot of specific pore volume (from the desorption branch of the isotherm) for pores with diameter <5 nm vs. fractional weight loss for the SC8 CTR samples.

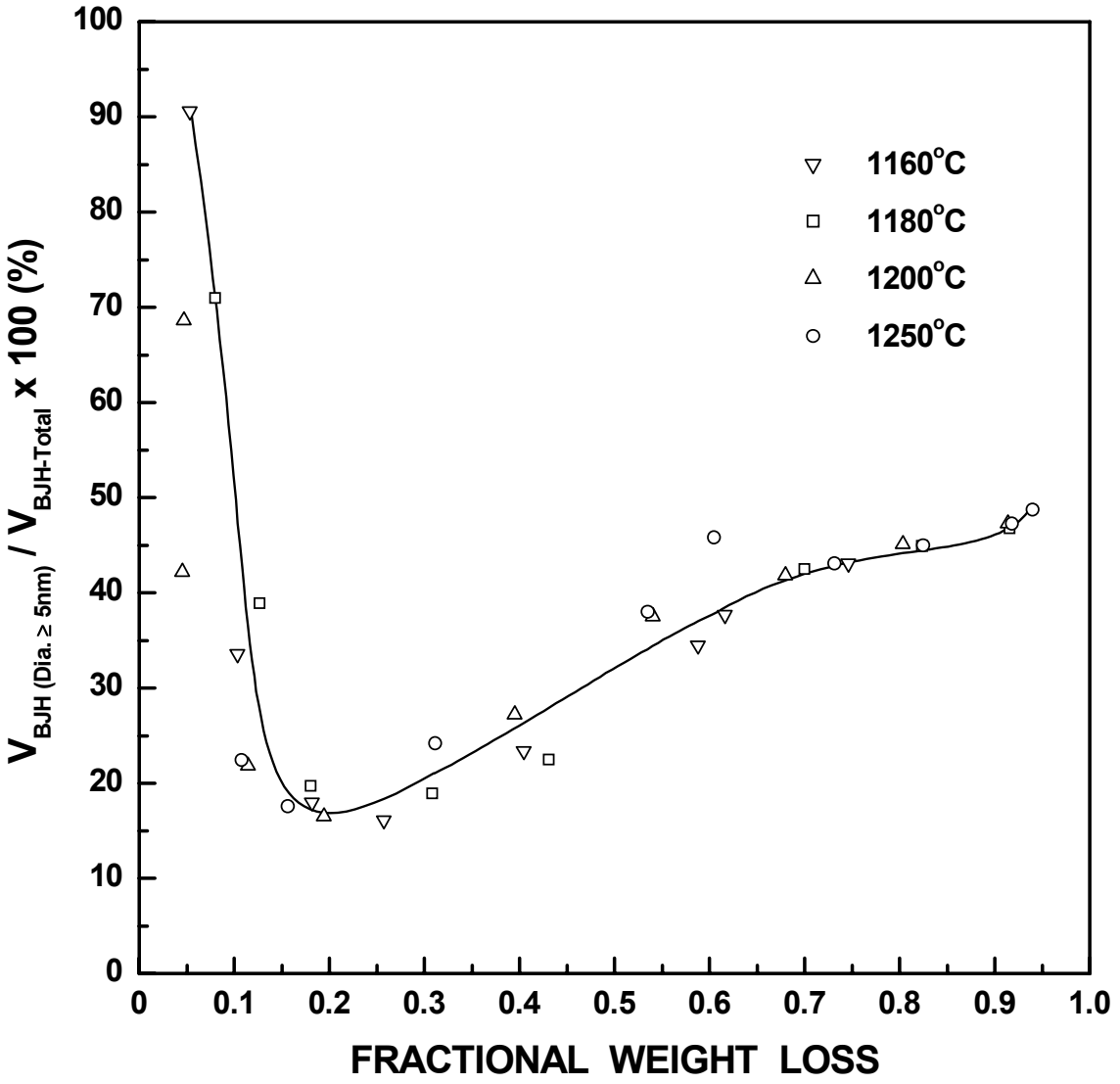

Figure 4-4-223 Plot of percentage of BJH pore volume for pores with diameter ≥5 nm (from the desorption branch of the isotherm) vs. fractional weight loss for the SC8 CTR samples.

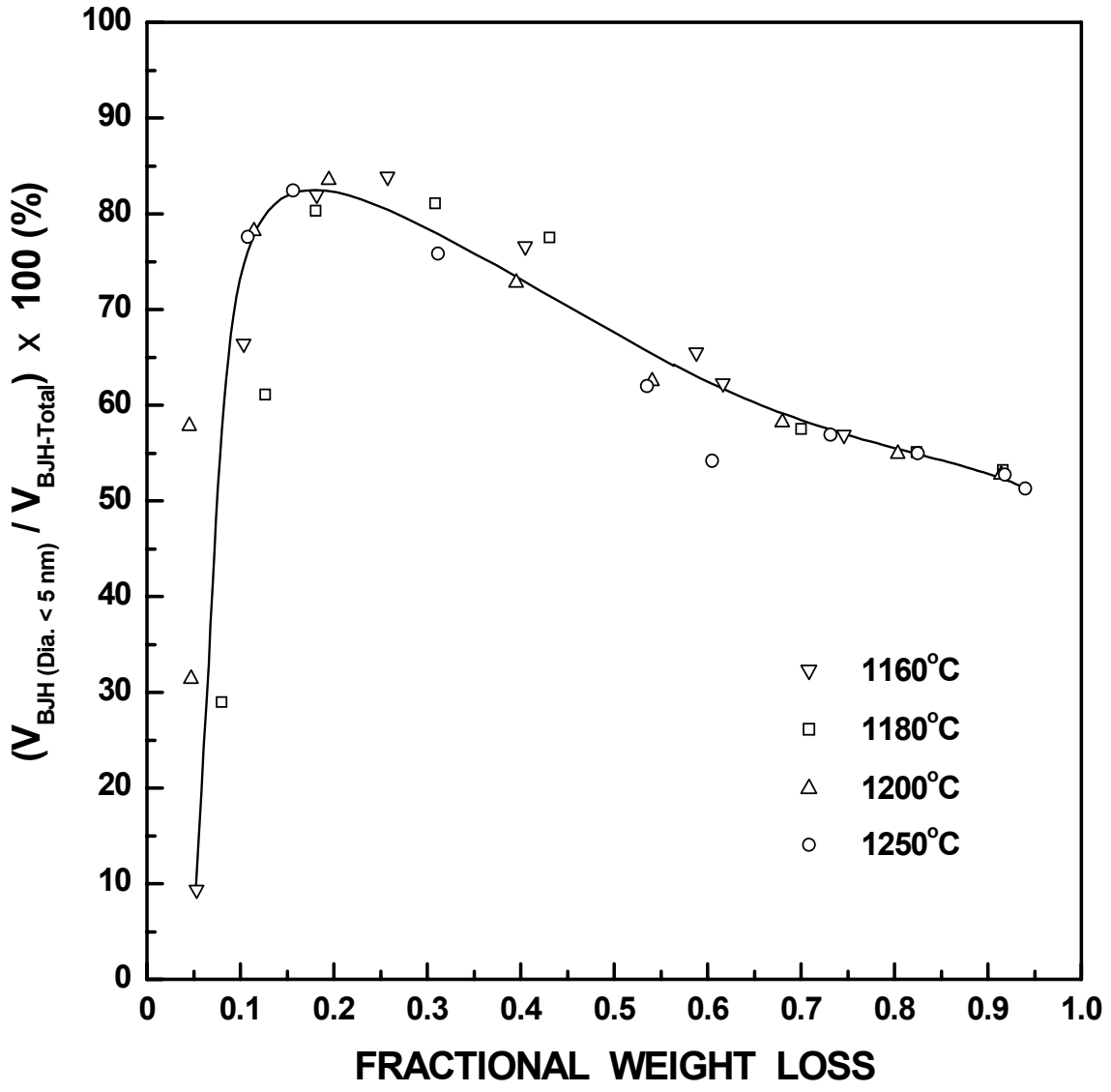

Figure 4-4-224 Plot of percentage of BJH pore volume for pores with diameter <5 nm (from the desorption branch of the isotherm) vs. fractional weight loss for the SC8 CTR samples.

Figures 4-4-225 - 4-4-228 show plots corresponding to Figures 4-4-221 - 4-4-224 except that the BJH pore specific surface areas are plotted instead of the BJH pore volumes. The plots illustrate the same trends as discussed above. The one difference is that these plots show some results which are indicative of the coarsening process that occurs during the very late stage of the reaction. Although the pore volume continues to increase during the late stage of the reaction, Figures 4-4-225 and 4-4-227 show that there is a small decrease in the specific surface area for the larger pores. The decrease in specific surface area is not observed for the smaller pores (Figures 4-4-226 and 4-4-228). These observations are consistent with coarsening because it is the larger pores which grow in size at the expense of smaller ones. (In a coarsening process, the smaller pores decrease in size and eventually disappear.)

Figures 4-4-229 and 4-4-230 show plots of the median pore diameter vs. fractional weight loss for different pore size regimes. In Figure 4-4-229, the median pore diameter was determined only for the portion of the BJH pore volume associated with pores with diameters ≥5 nm. In Figure 4-4-230, the median pore diameter was determined only for the portion of the BJH pore volume associated with pores with diameters <5 nm. The latter pores show very little change over the course of the reaction, especially after the early stage of the reaction. (The median pore size increases only from ~2.4 nm to ~2.7 nm from $X_{WL} \approx 0.2$ to $X_{WL} \approx 0.5$ and shows no further change with continued reaction.) The median diameter for the larger pores shows relatively little change from $X_{WL} \approx 0.2$ to $X_{WL} \approx 0.45$ and then shows a gradual increase from $X_{WL} \approx 0.45$ to $X_{WL} \approx 0.90$. The median diameter for the larger pores increases rapidly in the late stage of the reaction due to pore coarsening.

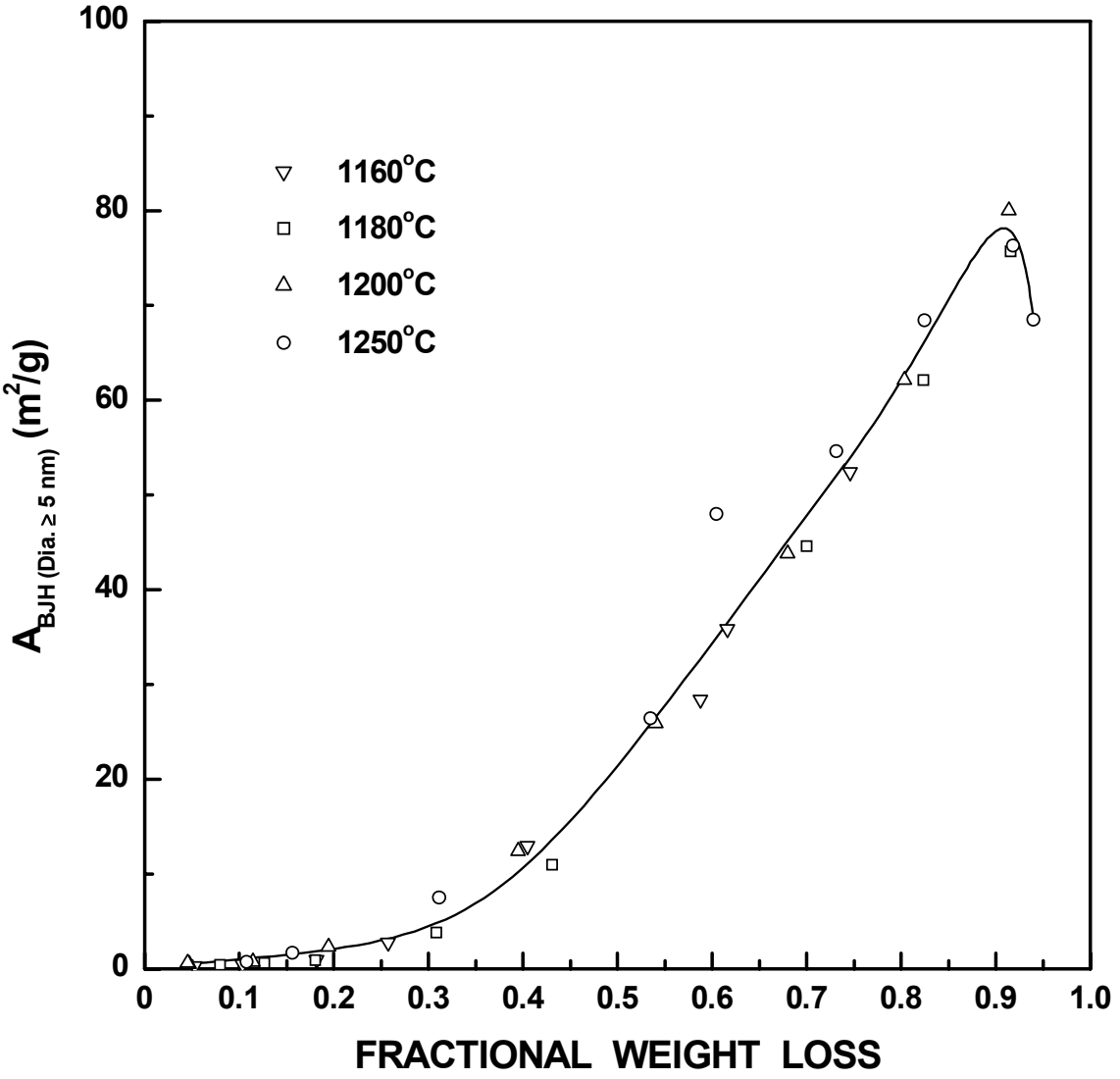

Figure 4-4-225 Plot of BJH specific surface area (from the desorption branch of the isotherm) for pores with diameter ≥5 nm vs. fractional weight loss for the SC8 CTR samples.

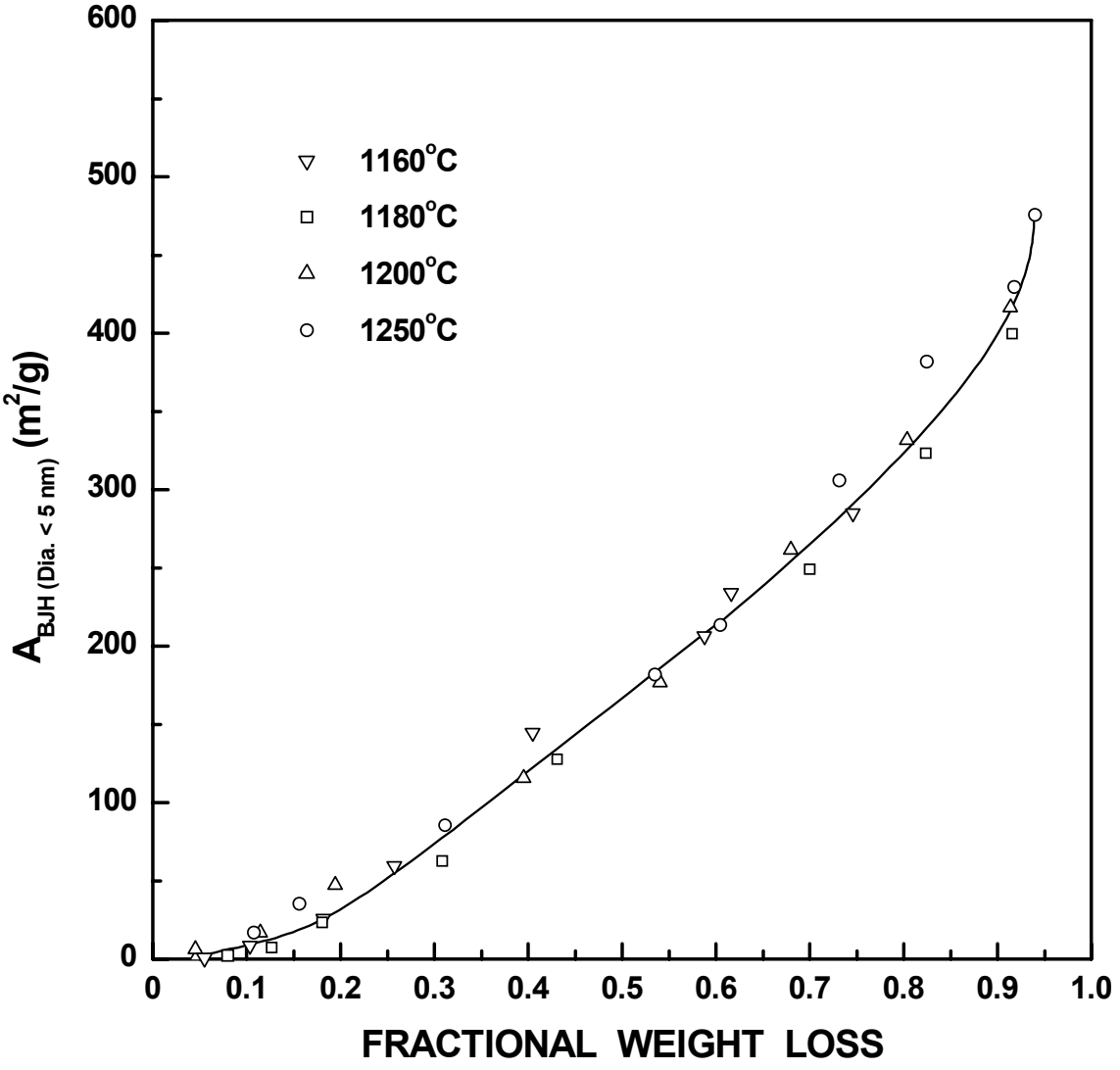

Figure 4-4-226 Plot of BJH specific surface area (from the desorption branch of the isotherm) for pores with diameter <5 nm vs. fractional weight loss for the SC8 CTR samples.

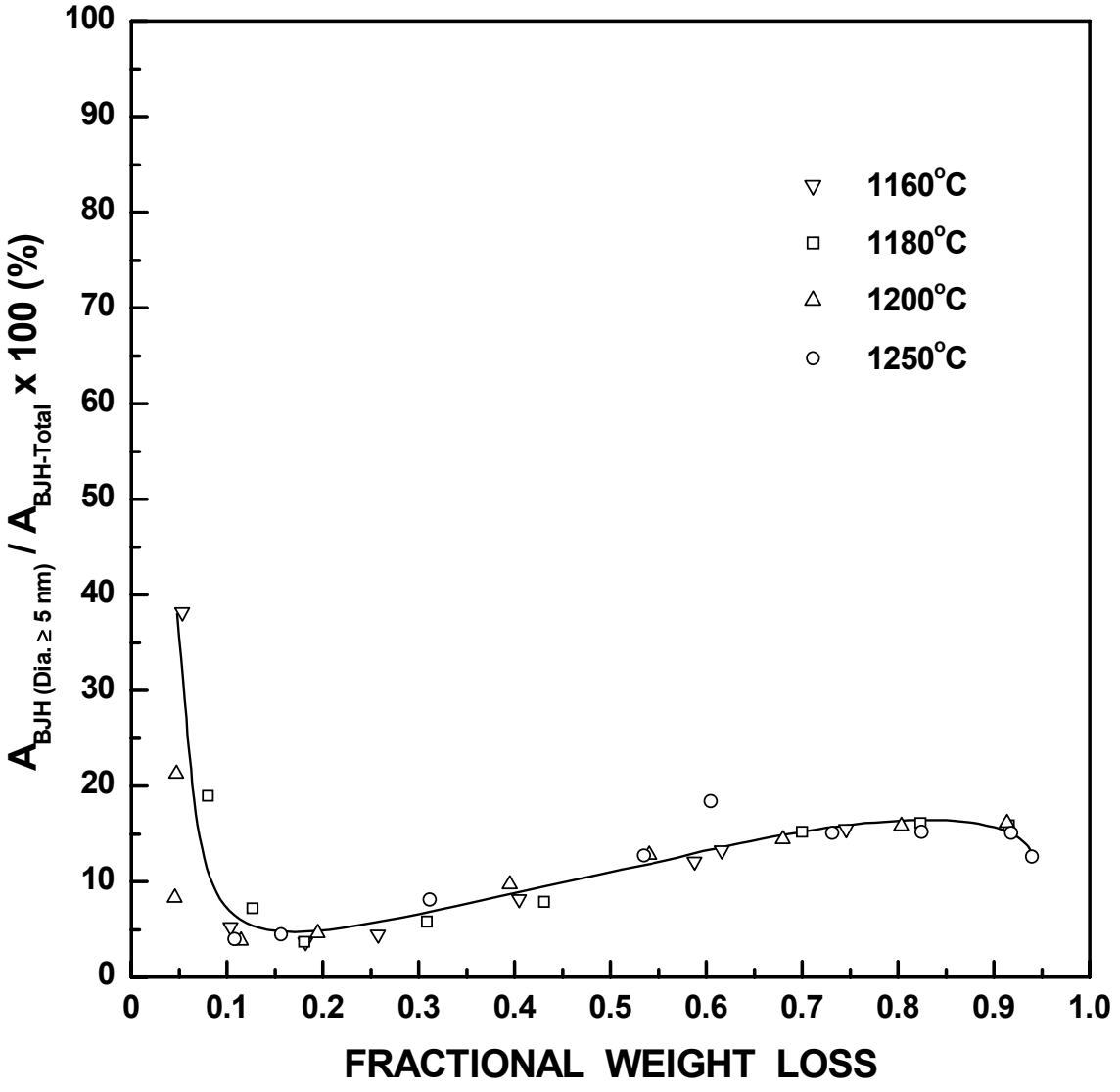

Figure 4-4-227 Plot of percentage of BJH specific surface area (from the desorption branch of the isotherm) for pores with diameter ≥5 nm vs. fractional weight loss for the SC8 CTR samples.

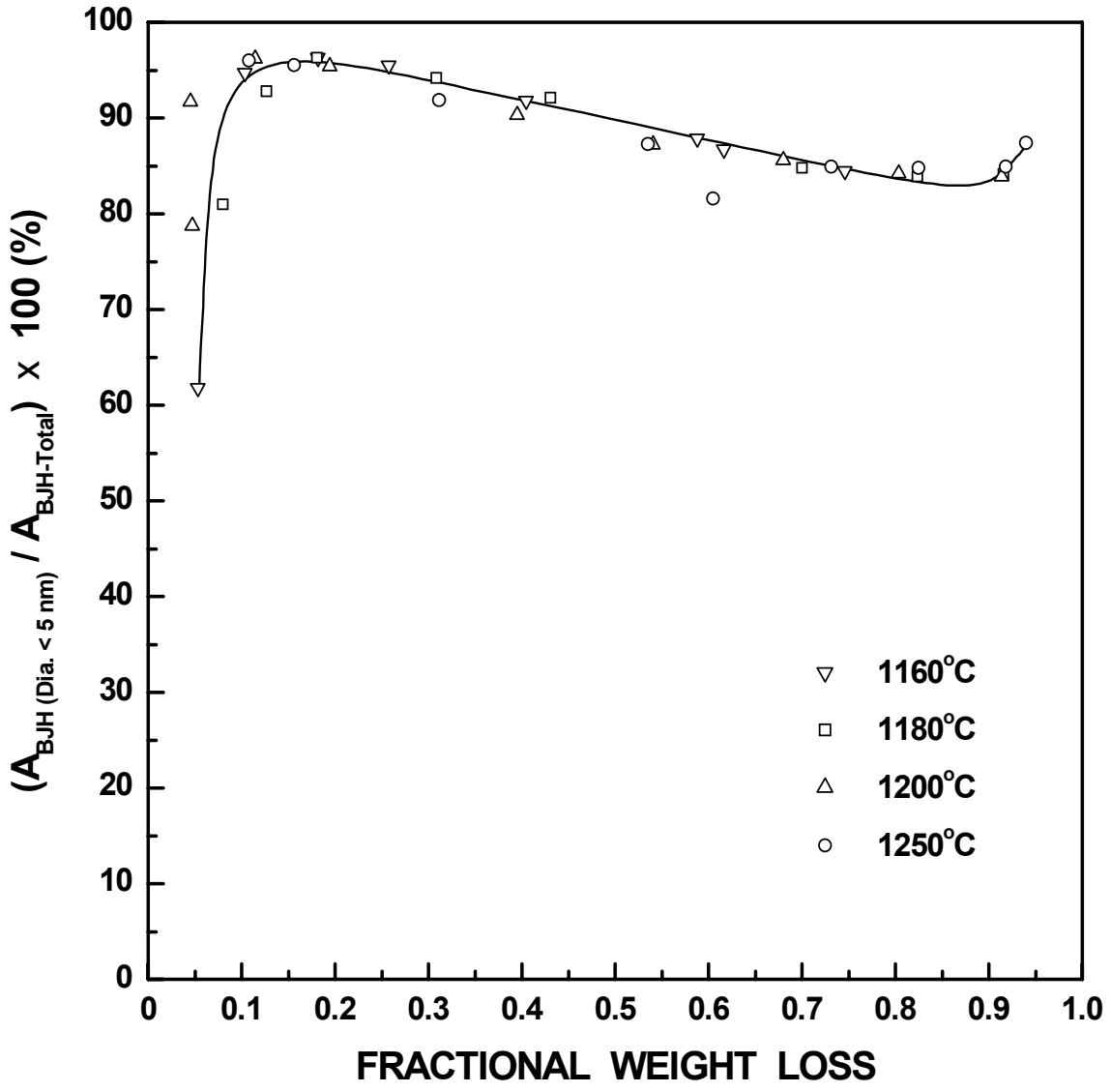

Figure 4-4-228 Plot percentage of BJH specific surface area (from the desorption branch of the isotherm) for pores with diameter <5 nm vs. fractional weight loss for the SC8 CTR samples.

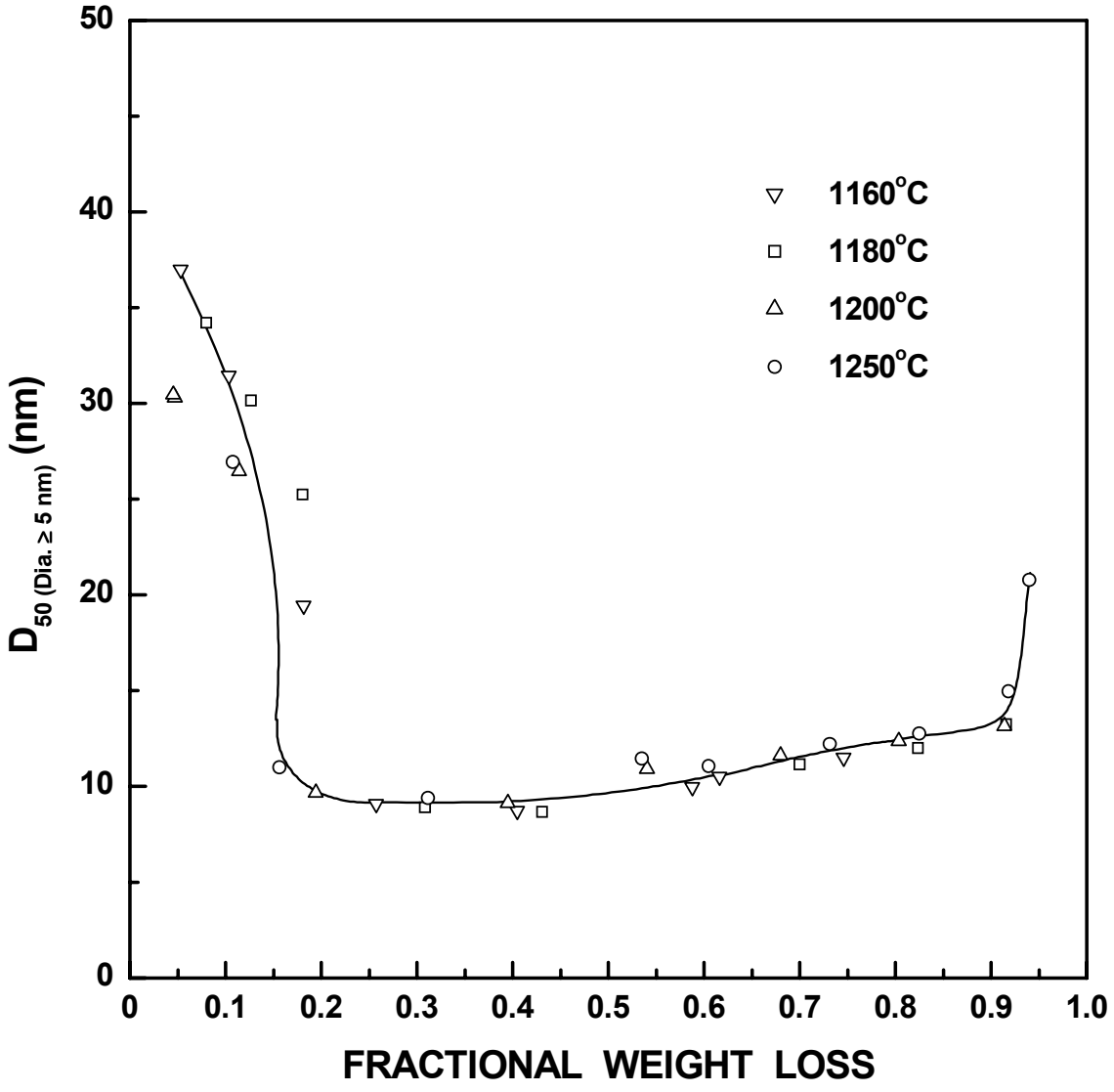

Figure 4-4-229 Plot of median pore diameter (D_{50}) vs. fractional weight loss for the SC8 CTR samples. The median diameter was determined for the portion of the pore volume associated with pores ≥5 nm. The data was obtained from the desorption isotherm.

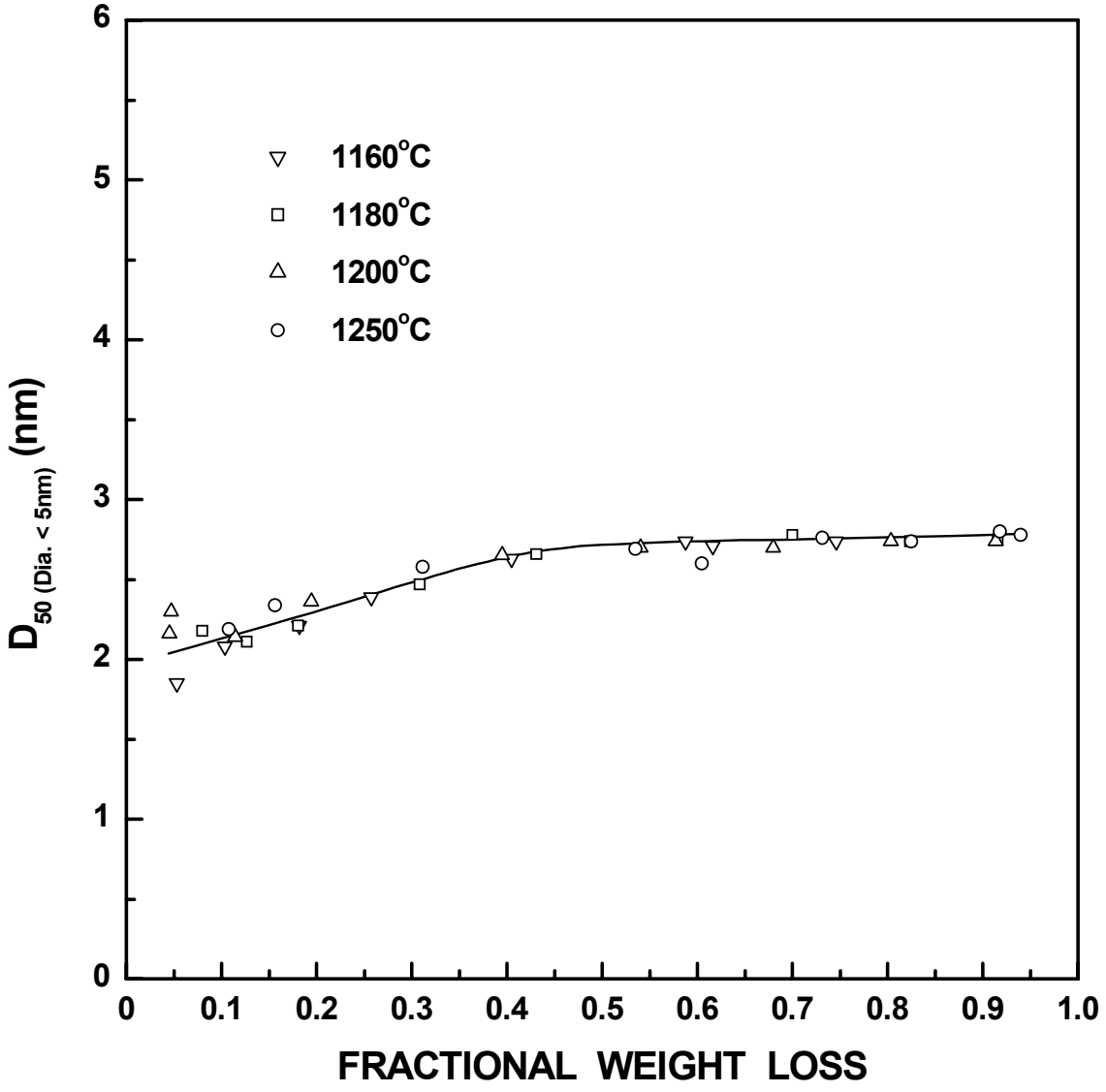

Figure 4-4-230 Plot of median pore diameter (D_{50}) vs. fractional weight loss for the SC8 CTR samples. The median diameter was determined for the portion of the pore volume associated with pores <5 nm. The data was obtained from the desorption isotherm.

4.4.7.6 Discussion on Pore Evolution in SC8 Samples in Comparison to the SC35 Samples and in Relation to the Structural Model

In section 4.4.7.3, the development of pores in the SC35 samples was discussed in relation to the structural model for the CTR reaction that was presented in section 4.4.5. The focus of this section is a similar discussion for the SC8 samples. It is evident from the results presented in sections 4.4.7.2 and 4.4.7.5 that there are some significant differences in the evolution of the pores during the CTR reaction for the SC8 and SC35 samples. Therefore, the question arises as the whether the pore evolution in the SC8 samples is consistent with the structural model proposed in section 4.4.5. If the model is appropriate, it must account for the following key differences in the SC8 and SC35 pore development: (1) The median pore size in SC35 samples increased to ~10 nm by only ~10 wt% fractional weight loss. The great majority of the pores that developed as the reaction proceeded in SC35 samples had diameters ≥ 5 nm. In contrast, SC8 samples showed substantial development of both smaller (<5 nm) and larger (≥5 nm) pores throughout the reaction. (2) The hysteresis behavior in the SC8 samples retained some part of the Type H3/Type H4 "hybrid" characteristic from its initial development in the early stages of the reaction to the end of the reaction. As the reaction proceeded, there was a gradual development of the Type H1 hysteresis in the higher relative pressure (P/P_0) regions of the isotherm, but the Type H3/Type H4 hysteresis was still observed at lower relative pressures (e.g., ~0.4-0.8). In contrast, the Type H3/Type H4 hysteresis was only observed in the early stages of the reaction in the SC35 samples, while only the Type H1 hysteresis behavior was observed after the early stages of the reaction.

Table 4-1-9 shows that the compositions for the SC8 and SC35 samples in the pyrolyzed state were approximately 49 vol% silica/51 vol% carbon and 65 vol% silica/

35 vol% carbon, respectively. Table 4-3-2 shows that the compositions for the SC8 and SC35 samples after complete CTR reaction (at 1475^{o}C, 2h) were approximately 45 vol% SiC/55 vol% carbon and 97 vol% SiC/3 vol% carbon, respectively. Hence, there was a much higher overall carbon content in the SC8 samples from the pyrolyzed sample through the final reaction product and the SC8 samples had a substantial amount of free carbon throughout the entire reaction. Therefore, it might be suggested that the differences described earlier in the gas adsorption isotherms and in the pore size distributions for the SC8 and SC35 samples can be explained by the presence of porosity that is inherently associated with the carbon regions of the samples. However, available evidence suggests that there is a problem with this interpretation. Gas adsorption measurements were carried out on phenolic resin samples which had been dried and given three different heat treatments in argon: 1100^{o}C for 2 h, 1300^{o}C for 2 h, and 1100^{o}C for 2 h followed by 1475^{o}C for 2h. The specific surface areas for the three samples were 3.7 m^2/g, 2.7 m^2/g, and 0.7 m^2/g, respectively. These relatively low values indicate that heat treatment of the phenolic resin alone does *not* produce a carbon product with a volume of fine open porosity that is consistent with the porosity that develops in the SC8 CTR samples. Despite these results, the fact that the SC8 samples develop a much larger volume fraction of smaller pores than observed in the SC35 samples indicates that, in some way, the development of the fine pores is associated with carbon-rich regions. An explanation for the seemingly contradictory results is provided below and this leads to a refinement in the structural model proposed in section 4.4.5.

The structural model proposed in section 4.4.5 was based on the starting pyrolyzed material (i.e., the large particles) consisting of nearly dense clusters. It was proposed that

these clusters were comprised of carbon and silica in the form of interpenetrating, connected networks. The pyrolyzed samples were derived from mixed sols of polysilicate species and phenolic resin oligomers. These sols were concentrated and dried prior to pyrolysis. The dried material presumably consisted of an interpenetrating network of the two phases (i.e., polysilicates and phenolic resin) because each phase was present in relatively high volume fraction. However, the formation of two interpenetrating networks does not require complete phase segregation. In other words, each network by itself is not necessarily phase-pure. In section 4.1.9, it was estimated that the SC8 dried material contained ~79 vol% phenolic resin. With such a high volume fraction, it would not be surprising if some of the polysilicate species became entrapped within phenolic-rich regions and, therefore, became completely isolated from the polysilicate network. Upon pyrolysis, this would have produced local carbon-rich regions which contained some fraction of more finely-distributed silica that was isolated (and not contiguous with) the main silica network. This might include entrapped silica regions with feature sizes that were finer than the main silica network and/or small silica regions that were completely entrapped within the carbon regions but had features with the same size as the "primary particles" comprising the main silica network. This is schematically illustrated in Figure 4-4-231. (Of course, it is also possible that the main silica network contained some finer-scale carbon regions that became completely entrapped within silica regions and, therefore, became isolated from the carbon network. However, this is not pertinent for explaining the differences in pore evolution behavior for the SC8 and SC35 samples.) The fine-scale silica entrapped within the carbon network (Figure 4-4-231) would be able to react with the surrounding carbon during the CTR reaction (e.g., at cluster surfaces and cluster-cluster

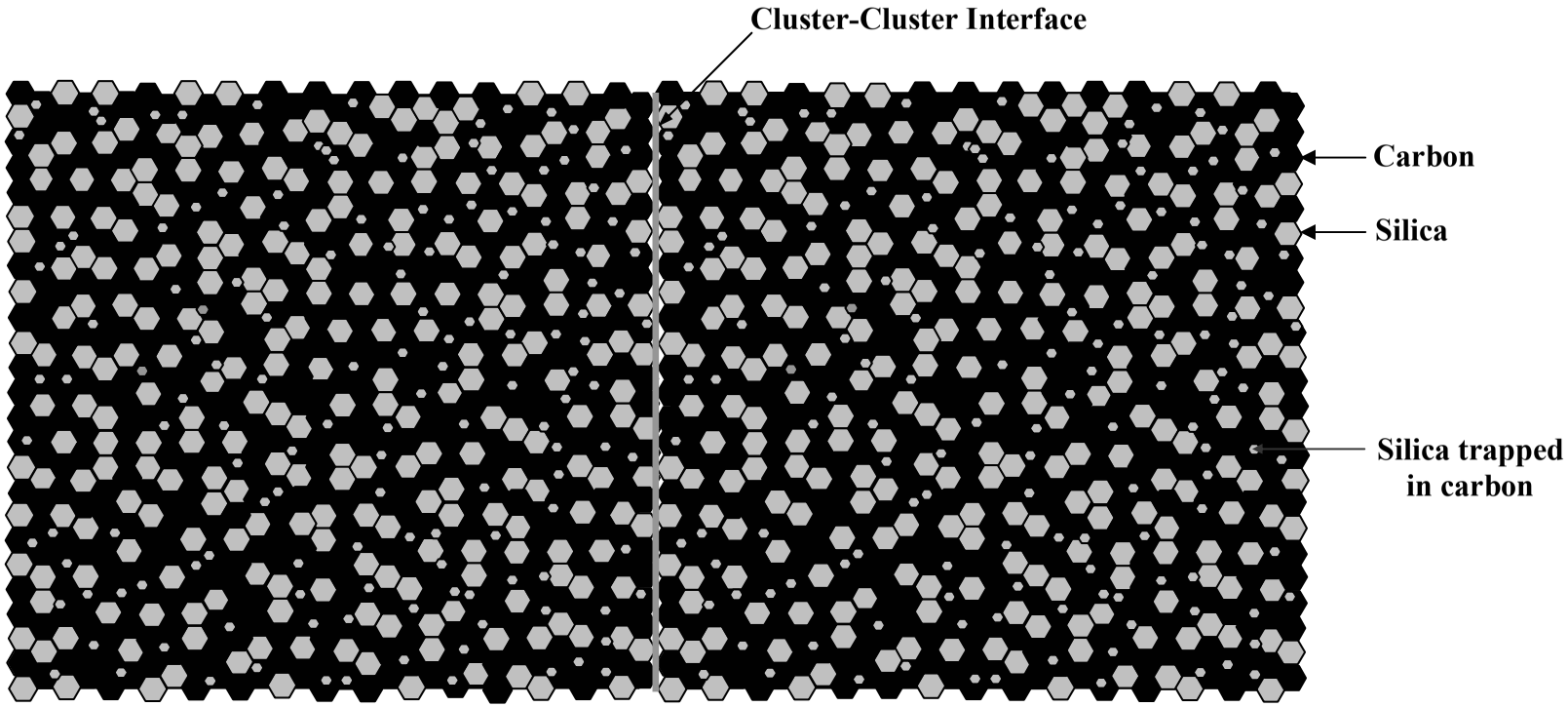

Figure 4-4-231 Illustration of the idealized structure of an SC8 particle showing two adjacent clusters. Each cluster is composed of interpenetrating networks of silica and carbon. There are also some small, isolated silica regions trapped in the carbon.

interfacial regions) in order to form both small pores and SiC. Therefore, it is suggested that the development of a relatively large volume fraction of smaller pores (<5 nm) in the SC8 samples may have resulted, at least in part, from some uniformly-distributed, fine-scale silica entrapped within highly carbon-rich regions of the pyrolyzed samples. In contrast, the coarser-scale silica network would have been the source for the larger pores that developed in the SC8 samples as the CTR reaction proceeded, i.e., just as it has been assumed to be the source of the larger pores in the SC35 samples. Therefore, the SC8 samples developed a substantial volume fraction of both smaller (<5 nm) and larger (≥5 nm) pores during the CTR reaction. For SC35 samples, the initial amount of carbon in the pyrolyzed sample (35 vol%) is much lower than in the SC8 sample (51 vol%), so it is expected that the entrapment of finer-scale silica regions would be much more limited. (This is not just due to the lower volume fraction of carbon; it would also be more unlikely for such fine-scale silica regions to remain isolated from the main silica network because of the much higher overall volume fraction of the silica in the SC35 samples. It is suggested that the fine-scale silica regions would have to be isolated within the carbon-rich regions in order for the pores that form in these regions to remain small as the reaction continues.) Schematic illustrations of the structural evolution in the SC8 samples as the reaction proceeds are shown in Figures 4-4-231 - 4-4-234.

The proposed mechanism for the continuous development of smaller pores (<5 nm) throughout the CTR reaction in the SC8 samples appears to be consistent with the observed differences in the evolution of the pore size distributions in the SC8 and SC35 samples

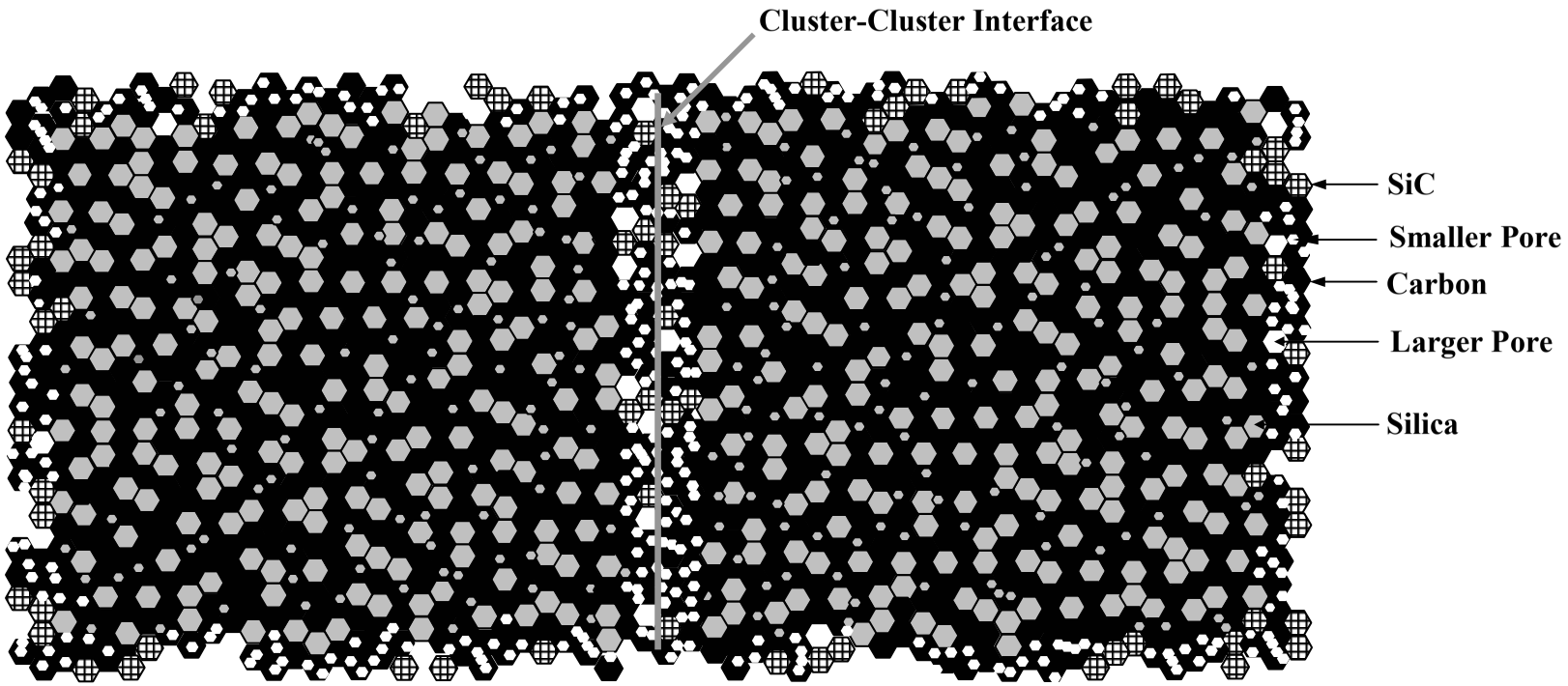

Figure 4-4-232 Illustration of the idealized structure of an SC8 particle after a small extent (~20%) of the CTR reaction. SiC crystallites have formed at the cluster surfaces and/or the cluster-cluster interfaces. Mesopores begin to develop as silica is removed during the reaction. Both larger and smaller pores develop during the reaction.

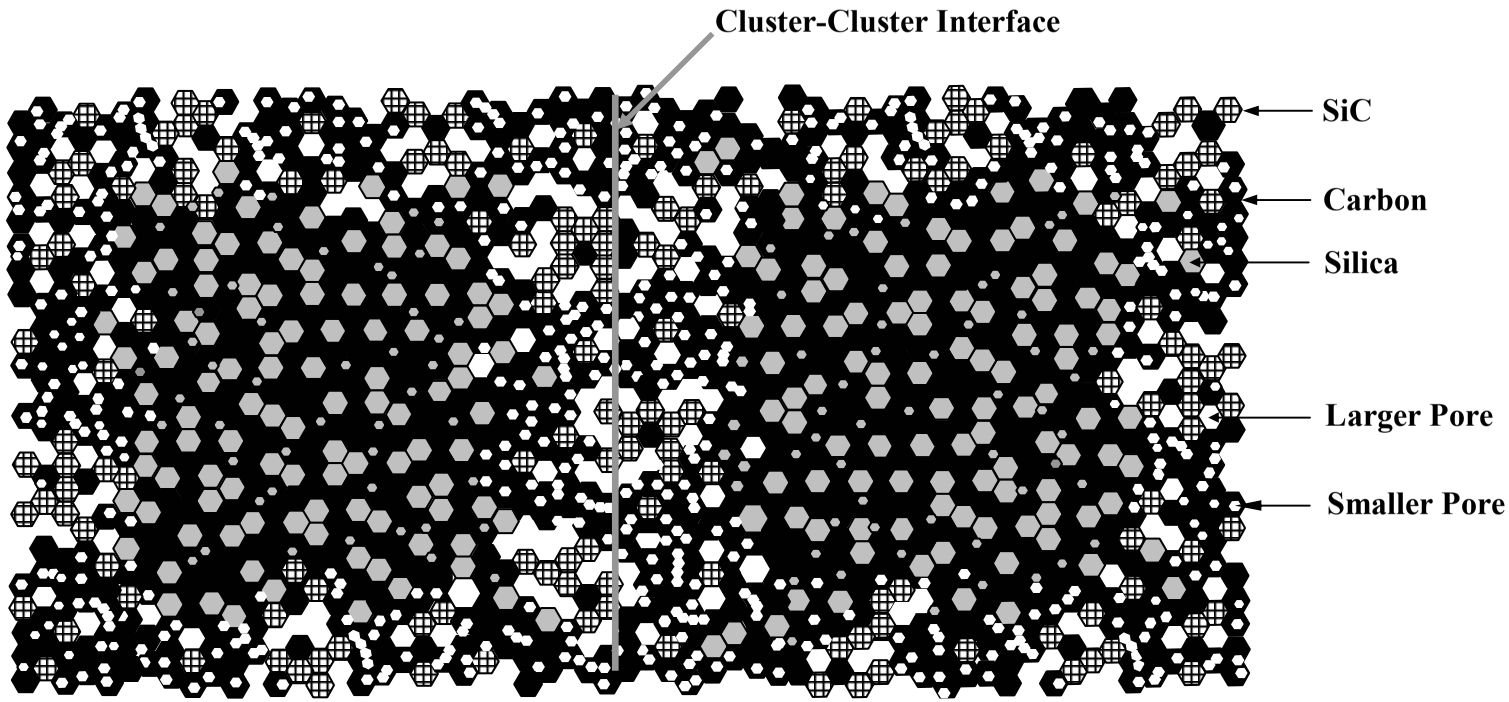

Figure 4-4-233 Illustration of the idealized structure of an SC8 particle after an intermediate extent (~50%) of the CTR reaction. The reaction interface moves inside towards the core of each cluster. Both larger and smaller pores continue to develop as the reaction proceeds. The large mesopores in the interfacial regions between clusters start to form an interconnected network.

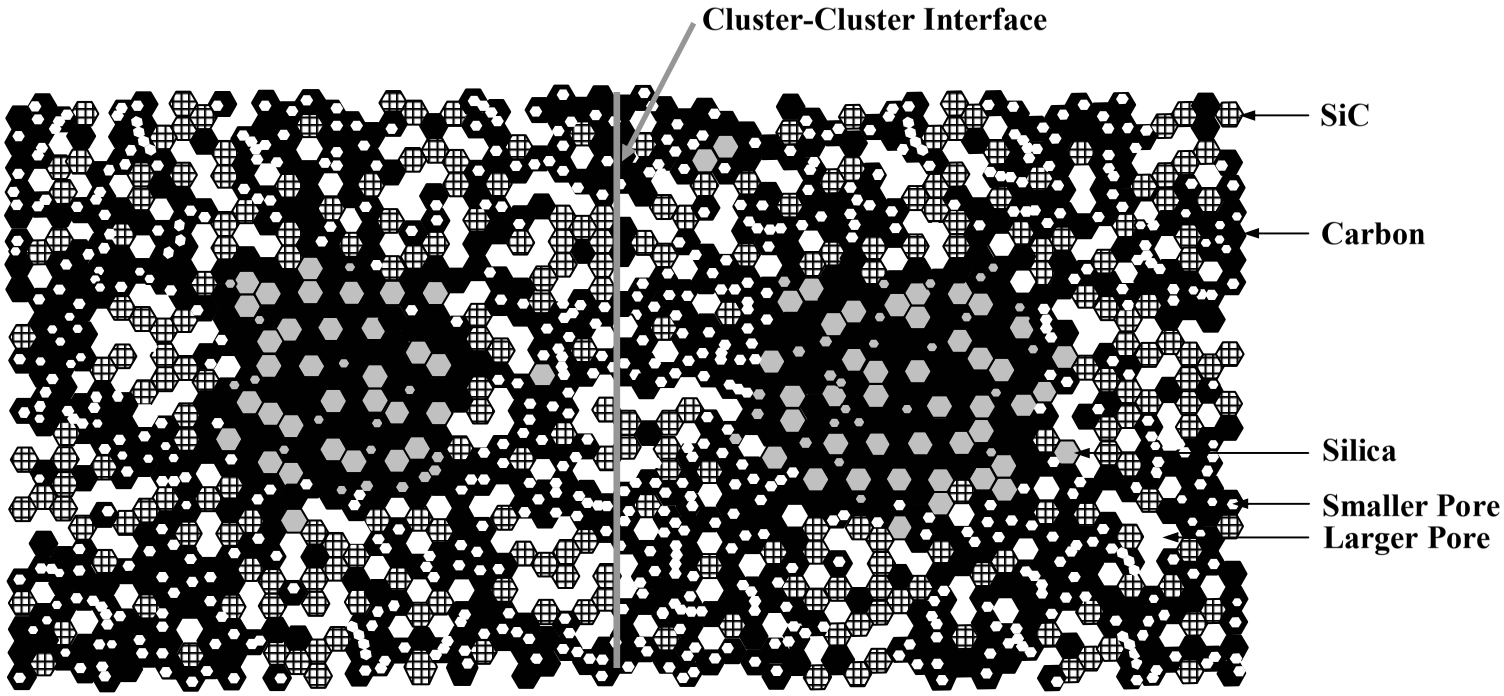

Figure 4-4-234 Illustration of the idealized structure of a SC8 particle after a high extent (~90%) of the CTR reaction. Most of the silica has been consumed, but there is still a large amount of residual carbon. Both larger and smaller pores continue to develop as the reaction proceeds.

This will be discussed below by considering different weight loss ranges during the CTR reaction.

- Fractional weight losses (X_{WL}) in the range of ~0 - 0.15

In SC8 samples, there was initially a sharp decrease in median pore size (D_{50}) from a very high value in the pyrolyzed material to ~2.5 nm in samples with $X_{WL} \approx 0.10$. It was explained previously that the large initial D_{50} diameter was due to a very small volume fraction of "macrodefects" in the pyrolyzed material. It is evident from the very small D_{50} value at $X_{WL} \approx 0.10$ that most of the new pores formed during the early stage of the reaction were relatively small (<5 nm).

Although it was not pointed out in section 4.4.7.2, the SC35 samples also showed an initial decrease in the D_{50} diameter, i.e., from the value for the pyrolyzed sample to ~2.5 nm in a sample with $X_{WL} \approx 0.03$ (see Figure 4-4-111). This initial decrease in the D_{50} value was not as large as observed for the SC8 samples. This was probably because the amount of accessible "macrodefects" was smaller in the SC35 samples. This is suggested for two reasons. First, the measured specific surface area for the SC35 pyrolyzed sample (~0.7 m^2/g) was lower than the value for the SC8 pyrolyzed sample (~3.1 m^2/g). Second, evidence was provided previously (sections 4.4.3 and 4.4.6) that viscous sintering occurred more readily in early-stage SC35 samples compared to corresponding SC8 samples. Hence, it is suggested that viscous sintering eliminated (or closed access to) more of the "macrodefects" during the initial pyrolysis process in the SC35 sample.

The SC35 samples differed from the SC8 samples in that the D_{50} diameter increased significantly for samples with fractional weight loss ≥0.03. The median pore size (D_{50}) increased from ~2.5 nm to ~11 nm from $X_{WL} = 0.03$ to $X_{WL} = 0.12$ in SC35 samples.

This increase in pore size was attributed to the removal of silica (and some carbon) from the cluster surfaces (including the cluster-cluster interfaces). The pores were initially small (in the sample with X_{WL} = 0.03) because the cluster structure was essentially dense; the pores had to first develop and then grow from the dense fine-scale silica/carbon structure. The pores were able to quickly grow (at the cluster surfaces and intercluster interfaces) to sizes comparable to the scale-feature of the continuous silica network. In addition, the cluster surfaces and intercluster regions were converted, during the early stage of the reaction, to a product that was a continuous network of mostly SiC (and porosity). (According to the shrinking-core model, continued reaction would then occur in similar manner in the adjacent regions below the surface of the cluster.) In contrast, the pore development behavior in the SC8 samples had some different features because of the high carbon content. Initially, the pore development was similar to the SC35 case in that pores had to first grow in size from an essentially dense cluster. However, growth of the pores was limited at the cluster surfaces and intercluster interfaces because of the difference in the silica distribution that was described earlier. The SC8 sample had more silica regions entrapped within carbon regions and these entrapped silica regions may also have had finer size. Furthermore, the amount of silica was far less than the amount that would be needed to consume all the carbon. Therefore, the intercluster regions and cluster surfaces developed a composite microstructure consisting of SiC and unreacted carbon, not the continuous network of mostly porous SiC that developed in SC35 samples. The SiC/carbon regions in the SC8 samples actually had a greater volume of carbon than SiC. Recall (from section 4.3.1) that the composition of a fully converted SC8 material is ~55 vol% carbon and ~45 vol% SiC. Hence, the development of larger pores (≥5 nm)

would be very limited at cluster surfaces and intercluster regions during the early stages of the reaction.

- Fractional weight losses (X_{WL}) in the range of ~0.15-0.90

In an ideal reaction that follows the shrinking-core model, the microstructural features (e.g., pore size and grain size characteristics) are expected to remain uniform as the amount of product increases during the course of the reaction. This behavior was generally observed in the SC35 samples for much of the reaction. The median pore size (D_{50}) increased gradually from ~12 nm at $X_{WL} \approx 0.16$ to ~17 nm at $X_{WL} \approx 0.84$ (Figure 4-4-217). This increase occurred because the small pores (<5 nm) that had been formed initially in the material subsequently grew into larger pores (≥5 nm) as the reaction proceeded past the early stage. After a porous SiC (percolation) path developed in the intercluster region ($X_{WL} \approx 0.15$), the pores that formed during most of the reaction in the SC35 samples were primarily uniform larger ones. This is indicated from the observation that the D_{90} diameter showed a smaller increase during the reaction than the D_{50} diameter. The D_{90} diameter increased only from ~22 nm to ~25 nm as the X_{WL} value increased from ~0.16 to ~0.84 (Figure 4-4-218). (The continued development of mostly large pores was also indicated by the observation that the D_{10} diameter showed a relatively large increase as the reaction proceeded. The D_{10} diameter increased from ~3 nm to ~9 nm as the X_{WL} value increased from ~0.16 to ~0.84.)

The pore evolution behavior in the SC8 was different in that both smaller pores and larger pores were formed throughout most of the reaction. The development of the smaller pores was more significant (i.e., based on the volume fraction formed) in the earlier stages, while the development of the larger pores was more important in the later stages. The

smaller pores that developed throughout the reaction had a fairly uniform size, while there was a continuous increase in the size of the larger pores that developed throughout the reaction. This is evident from the pore size distribution plots in Figure 4-4-193 and 4-4-194. This is also indicated from the D_{10}, D_{50}, and D_{90} diameters shown in Figures 4-4-217 - 4-4-219. The D_{10} diameter increased only from ~1.7 nm to ~2 nm as the X_{WL} value increased from ~0.18 to ~0.83. In addition, the D_{50} diameter increased only from ~2.5 nm to ~3.5 nm over the same weight loss range. In contrast, the D_{90} diameter showed a more rapid change as the reaction progressed, as the diameter increased ~8 nm to ~15 nm over the specified weight loss range. These observations reflect a significant difference in the development of the porous SiC structure in the SC8 samples, i.e., compared to the SC35 samples. For the latter samples, it was proposed that a structure analogous to agglomerates of fine SiC particles (i.e., an interconnected porous network of SiC crystallites) developed at intercluster regions in the early stages of the reaction. That structure continued to grow into the core of the clusters as the reaction proceeded. This type of structure resulted in the Type H1 hysteresis behavior that was observed in the gas adsorption/desorption isotherms. In the case of SC8 samples, it is proposed that groups of SiC crystallites remained isolated (i.e., they had limited connectivity) in the early stages of the reaction and that the intercluster region became a composite with ~55 vol% carbon/~45 vol% SiC. As the CTR reaction proceeded, the individual clusters continued to develop a SiC/carbon composite structure in accordance with the shrinking-core reaction model. However, it is suggested that eventually the increase in the volume fraction of SiC (as the reaction proceeded) produced some small regions in which isolated groupings of the fine SiC crystallites grew to sizes such that these groupings became more interconnected. In other words, there were

some regions *within* the clusters of the SC8 samples that developed into SiC "agglomerates" similar to those observed in the SC35 samples. This is consistent with the development of the more well-defined Type H1 hysteresis behavior that was observed in the later stages of the reaction in SC8 samples. Nevertheless, the connectivity of the SiC crystallites was limited because of the high overall concentration of free carbon in the samples. The SC8 samples still showed the Type H3/H4 hysteresis behavior throughout the CTR reaction which was consistent with the presence of carbon-rich regions containing crack-like or slit-like pores.

- Fractional weight losses (X_{WL}) greater than ~0.90

The SC8 samples showed similar behavior to SC35 samples in that there were sharp increases in the sizes of the SiC crystallites (Figure 4-4-5) and the large pores (Figures 4-4-112 and 4-4-218) during the late stages of the reaction. These observations were attributed to coarsening. This interpretation may seem surprising in the case of the SC8 samples because SiC coarsening is expected to be limited in samples with high carbon concentration. However, it is important to consider the effect of the spatial distribution of the carbon in the sample. Coarsening of SiC would be highly restricted if most of the SiC crystallites were surrounded by a sufficiently thick layer of carbon. In fact, the limited crystallite growth for most of the reaction (i.e., $X_{WL} < 0.90$) in both SC8 and SC35 samples can be attributed to such a structure. However, some coarsening can still occur if there are local regions comprised of groupings of SiC crystallites (e.g., agglomerates) with little or no carbon present. In the previous section, it was suggested that such local regions eventually develop in the late stages of the reaction in the SC8 samples.

4.5 Discussion on Reaction Mechanism for SiC Formation via CTR

4.5.1 Effect of Pyrolyzed Material Composition on the SiO Generation and Composition of CTR Product

The carbothermal reduction reactions in this study were carried out using a flowing gas (argon) atmosphere. Hence, some SiO formed during the first step in the reaction was swept away from the reactant mixture without having the opportunity to react with carbon. As a result, almost all samples (even those prepared with a C/Si molar ratio less than 3) had residual carbon after the reaction was carried out to the maximum extent possible.

Samples with different initial C/Si molar ratio were used to investigate the effect of composition on the amount of SiO loss during the reaction and the effect of composition on the amount of excess carbon remaining after "full conversion". (The pyrolyzed material for samples listed in Table 4-5-1 were prepared by Dr. Chang-an Wang of Georgia Institute of Technology. The heat treatments to carry out CTR were carried out by the author.) The results are shown in the Table 4-5-1. Column 1 of Table 4-5-1 shows the sample number. Column 2 of Table 4-5-1 shows the C/Si molar ratios (designated as "z" values) for the various samples prepared for this study. As described in section 3.2, such information was determined either by the LECO combustion analysis, and/or by oxidation of the pyrolyzed sample in the pyrolysis furnace. Column 3 of Table 4-5-1 shows the final carbon content, listed as a weight fraction (designed as "w_C^{CTR}" values), in samples that were heat treated at a temperature of at least 1475^{o}C for 2 h. These conditions were used to allow for "full conversion" to occur. The carbon content was also obtained by the LECO combustion method. For samples with the lowest C/Si

Table 4-5-1 x, y, Y_T values from calculation and z, w_C^{CTR}, Y values from experiment for different SC samples.

Sample series [1]	C/Si molar ratio before CTR (z)			C in sample after CTR [3] (w_C^{CTR})	C/Si molar Ratio after CTR [4]	Free C to initial SiO_2 molar ratio [5] (x)	Lost SiO to initial SiO_2 molar ratio [6] (y)	Expected yield based on composition data [7] (Y_E)	Experimental yield [8] (Y)
	LECO [2a]	F. O. [2b]	Avg.						
SC19		1.82	1.82	0.3[a]	1	0.0	0.59	0.20	0.21
SC20		2.30	2.30	0.3[a]	1	0.0	0.35	0.30	0.30
SC22		2.30	2.30	0.3[a]	1	0.0	0.35	0.30	0.33
SC35	2.42	2.39 2.36	2.39	0.3148 [b]	1.07	0.05	0.33	0.31	0.33
SC42	2.47 2.30	2.43	2.40	0.3107 [c]	1.05	0.04	0.32	0.31	0.34
SC46	2.38	2.53 2.47	2.46	0.3000 [c]	1.00	0.00	0.27	0.33	0.34
SC34		2.69	2.69	0.3643 [b]	1.34	0.24	0.28	0.34	0.35
SC32	2.74	2.74	2.74	0.3680 [b]	1.36	0.26	0.26	0.35	0.38
SC23		3.04	3.04	0.3822 [b]	1.44	0.37	0.16	0.39	0.41
SC24		3.34	3.34	0.4347 [b]	1.79	0.66	0.16	0.41	0.45
SC8	4.63		4.63	0.6006 [d]	3.51	2.02	0.19	0.49	0.49

Notes for Table 4-5-1:

1. Sample series number.

2a. Determined by LECO combustion method (LECO).

2b. Determined by direct oxidation of the pyrolyzed material in tube furnace in air (F. O.).

3. Determined by LECO combustion method.

3a. No direct composition information is available. It was assumed that the fully converted material is pure stoichiometric SiC and, therefore, that the carbon content would be 0.3.

3b. The fully converted sample was heat treated at 1475^{o}C for 2h.

3c. The fully converted sample was heat treated at 1495^{o}C for 2h.

3d. The fully converted sample was heat treated at 1600^{o}C for 2h.

4. Calculated from the data (w_C^{CTR}) in Column 3.

5. x = molar ratio of the free C (i.e., unreacted carbon after complete CTR) to the initial SiO_2 in the starting mixture.

6. y = molar ratio of the lost SiO (i.e., SiO swept away before it can react with C) to the initial SiO_2 in the starting mixture.

7. Y_E = expected weight fraction (i.e., weight remaining after CTR divided by initial weight before CTR) based on Equation (4-5-6)

8. Y = sample weight after CTR (at least at 1475^{o}C for 2h) divided by the initial sample weight before CTR.

molar ratios (i.e., SC19, SC20, and SC22), the carbon content was not determined after the CTR reaction. It was assumed that no residual free (unreacted) carbon remained and that the composition was that of stoichiometric SiC (i.e., approximately 0.70Si and 0.30C). Column 4 of Table 4-5-1 shows the calculated C/Si molar ratio (based on w_C^{CTR}) for the fully converted CTR samples in Column 3. The atomic weights were assumed to be 28 for Si and 12 for C.

Calculations were made for the amount of SiO that was lost during CTR and for the expected yield after CTR. (The amount of SiO lost refers to the SiO which does not react with carbon and which gets swept away in the flowing Ar atmosphere.) Consider a sample with an initial C/Si molar ratio of "*z*" (i.e., the Column 2 value). Suppose the amount of SiO lost from a sample after "full conversion" is designated as "*y*" where y is molar ratio of the lost SiO to the initial SiO_2 in the sample. Suppose the amount of free (unreacted) carbon remaining in the sample after "full conversion" is designated "*x*" where *x* is the molar ratio of free carbon to the initial SiO_2 in the sample. The carbothermal reduction reaction after full conversion can be represented by the following equation in which the amount of residual carbon, *x*, in the solid reaction product and the amount of SiO, *y*, that is lost during the reaction are included in the mass balance:

$$SiO_2 + z\,C \rightarrow (1-y)\,SiC + x\,C + y\,SiO + (z-1-x+y)\,CO \qquad (4\text{-}5\text{-}1)$$

In the above equation, the number of moles of Si on the left side is 1, while the number of moles of Si on the right side is also $(1-y) + y = 1$. Similarly, the number of moles of C on the left side is *z*, while the number on the right side is $(1-y) + x + (z-1-x+y) = z$. Therefore, the equation is balanced for Si and carbon. In addition, Equation (4-5-1)

should also be balanced for oxygen. The number of moles of oxygen on the left side is 2; while the number on the right side is $y + (z - 1 - x + y) = z - 1 - x + 2y$. Therefore,

$$2 = z - 1 - x + 2y$$

or

$$x - 2y = z - 3 \tag{4-5-2}$$

Based on Equation (4-5-1), the weight fraction of carbon (designated as "w_C^{CTR}" values) in the samples after "full conversion" CTR is given by

$$w_C^{CTR} = \frac{12(1 - y + x)}{40(1 - y) + 12x}$$

or
$$12(1 - w_C^{CTR})x + (40w_C^{CTR} - 12)y = 40w_C^{CTR} - 12 \tag{4-5-3}$$

From Equation (4-5-2) and (4-5-3), x and y could be obtained as follows:

$$x = \frac{3 - 10\ w_C^{CTR} - 3z + 10\ w_C^{CTR} \cdot z}{3 + 4\ w_C^{CTR}} \tag{4-5-4}$$

$$y = \frac{6 + w_C^{CTR} - 3z + 3w_C^{CTR} \cdot z}{3 + 4\ w_C^{CTR}} \tag{4-5-5}$$

Columns 5 and 6 of Table 4-5-1 show the calculated values x and y values, based on Equations (4-5-4) and (4-5-5) and the experimental compositional information (i.e., the z and w_C^{CTR} values shown in Columns 2 and 3).

Column 7 shows the expected "full conversion" yield, Y_E after CTR. Y_E is the solid sample weight remaining after "full conversion" of the CTR divided by the initial weight of the sample before CTR. It is apparent from Equation (4-5-1) that Y_E is given by:

$$Y_E = \frac{40\ (1 - y) + 12\ x}{60 + 12\ z} \tag{4-5-6}$$

The Y_E values were calculated with the x and y values in Column 5 and 6.

Column 8 of Table 4-5-1 shows the experimentally-determined "full conversion" yields, Y, after CTR. There is relatively good agreement between the "expected" yields, Y_E, and "experimentally-determined" yields, Y. This is not surprising since both yields are based on experimental measurements. The Y_E values are determined from compositional analysis data, while the Y values are determined from weight loss data. The results indicated that there is good consistency between the data collected by the two types of measurements.

The Y (and Y_E) values increase with increasing initial C/Si ratio. This would be expected simply from the fact that there is an increasing amount of excess carbon in the starting samples and this portion of the carbon provides a 100% yield after CTR. The yield also increased because more of the SiO volatile that is produced by the first step in the CTR reaction remains in the system (i.e., less is swept away in the flowing gas) and, therefore, it can react with carbon in the second step of the reaction.

Column 6 confirms that the amount of SiO volatile that is lost during CTR decreases as the C/Si ratio increases. This presumably reflects the fact that more of the SiO vapor volatiles have the opportunity to react with the C as the C/Si ratio increases. This is expected from two reasons. First, there is a greater specific volume of carbon in the sample, so each of the SiO vapor molecules that forms will, on average, have more carbon interfacial area available to impinge upon. Second, the loss of SiO requires that the SiO molecules diffuse out of the pore spaces of the sample in order to be swept away by the flowing Ar gas. At higher C/Si ratios, the diffusion path length is likely to increase. Hence, an SiO molecule would have more time, on average, to react with

carbon prior to exiting the sample. (Furthermore, it was observed in this study that samples with larger C/Si molar ratio (i.e., SC8) had smaller pore sizes. This would also increase the diffusion time for the SiO molecules to exit from the sample.) The latter argument tends to be consistent with the interpretation that the reaction between C and SiO is the slower (i.e., rate-limiting) step in the carbothermal reduction reaction.

The observed trend of increasing carbon content in the product after CTR and decreasing SiO loss with increasing C/Si ratio in the initial (pyrolyzed) material is consistent with the results of Tanaka and Kurachi (1988), as shown in Table 2-2-1. (Their starting materials were very similar to the materials used in this study. As described in section 2.2, they used TEOS/phenolic resin mixed solutions as the precursor materials.) For example, their results showed that when the C/Si molar ratio in the pyrolyzed material before CTR was 2.63, the fraction of SiO loss was 0.26 and the C/Si ratio in the product was 1.3. For the SC34 sample in this study, with initial C/Si molar ratio of 2.69, the fraction of SiO loss was 0.28 and the C/Si ratio in the product was 1.34. When Tanaka and Kurachi used an initial C/Si molar ratio of 3.10, the fraction of SiO loss was 0.20 and the C/Si ratio in the product was 1.5. For the SC23 sample in this study, with initial C/Si molar ratio of 3.04, the fraction of SiO loss was 0.16 and the C/Si ratio in the product was 1.44.

However, as discussed in section 2.2.1, there was considerable discrepancy in the calculated and measured fraction of SiO loss for some samples in the study by Tanaka and Kurachi (1988). This has been attributed to the fact that they made an assumption that all carbon was consumed in the reaction, which is, according to Table 2-2-1, invalid for samples with initial C/Si molar ratio greater than ~2.52. By contrast, in the current

study, unreacted carbon was taken into account in the calculation. As a result, very good agreement was found between the experimental and calculated yield over a wide range of initial C/Si molar ratios.

4.5.2 Effect of Pyrolyzed Material Composition on the Reaction Kinetics

Figure 4-5-1 compares the reaction rate constants calculated from the weight loss kinetics data for the SC35 and SC8 samples. Similar results were shown in Figures 4-3-28 and 4-3-29 using the data from the QXRD kinetics study. The reaction rate constants for the SC8 series (initial C/Si molar ratio = 4.6) were 2.7-3.4 times higher than the rate constants for the SC35 series (initial C/Si molar ratio = 2.4) at constant temperatures in the range of 1160-1250^{o}C (see Tables 4-3-4 and 4-3-5). The difference in the reaction rate constant is, in some way, due to the difference in the composition of the pyrolyzed materials of SC35 and SC8 series. Except for the difference in composition, the samples were prepared in the same way and the CTR reactions were carried out in the same way.

As discussed in section 4.2, the CTR reaction is believed to proceed via two elementary reaction steps:

$$SiO_{2\,(s)} + C_{\,(s)} \rightarrow SiO_{\,(g)} + CO_{\,(g)} \qquad (4\text{-}5\text{-}7)$$

$$SiO_{\,(g)} + 2C_{\,(s)} \rightarrow SiC_{\,(s)} + CO_{\,(g)} \qquad (4\text{-}5\text{-}8)$$

If the reaction that occurs at the interface in either of these steps is rate-controlling, then the overall CTR reaction rate will depend on the specific interfacial area of carbon in the system. In the present study, the SC8 samples, with much higher initial C/Si ratio compared to SC35 samples, may have developed carbon regions with higher specific interfacial area. The interfaces of interest include the carbon/silica interface in the

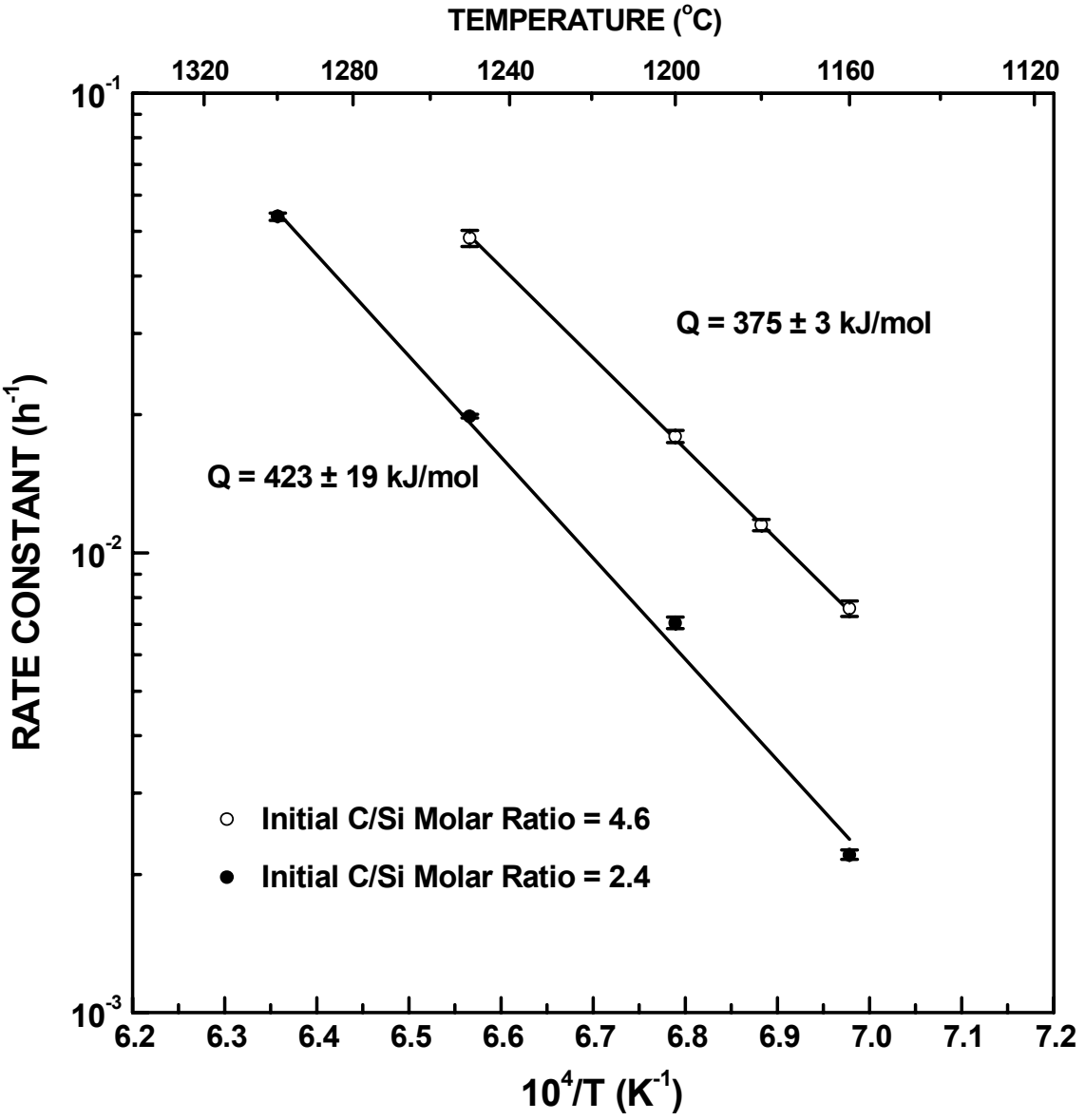

Figure 4-5-1 Plots of reaction rate constant vs. inverse temperature for the SC35 and SC8 samples. The data is the same as shown in Figures 4-3-13 and 4-3-14.

pyrolyzed and partially-reacted samples and the carbon/pore interface that develops during the first step (Equation (4-5-7)) of the CTR reaction. The initial carbon/silica interfacial area may not have been too different for the SC8 and SC35 samples because available evidence suggests that the scale of the silica and carbon networks in the pyrolyzed state was not substantially different. However, as the CTR reaction proceeded, the SC8 samples apparently developed a higher carbon/pore specific interfacial area. As shown in Figures 4-4-32 and 4-4-34 in section 4.4.3.2, the measured specific surface areas for SC8 samples were higher than those for SC35 samples at similar fractional weight losses. This observation is consistent with the higher reaction rate for the SC8 samples. It also suggests that the reaction between SiO and C was the rate-controlling step in the CTR reaction.

In contrast to this study, Narisawa et al. (1998) found a relatively small dependence of the CTR reaction rate constants on the initial C/Si molar ratio (refer to Table 2-3-2 in section 2.3.4 and Figure 4-5-3 later in this section). The contradiction might be due to the higher reaction temperatures (1500-1700^{o}C) used in the latter study. It is possible that the rate constants were so high at those temperatures that the effect of composition on the reaction rate was less significant. It is also possible that the reaction rates at the high temperatures were too high to obtain reliable rate constant data. Actually, it should be noted that rate constants were slightly higher at some temperatures for the samples with higher C/Si molar ratio in the study by Narisawa et al. For example, the rate constants at 1500^{o}C were 6.6×10^{-6} sec^{-1}, 5.4×10^{-6} sec^{-1}, and 4.6×10^{-6} sec^{-1} for the samples with C/Si molar ratios of 3.84, 2.97, and 2.07, respectively.

The effect of starting mixture composition was also investigated by Chen et al. (2000) using quartz/carbon mixtures with relatively coarse particle sizes (i.e., ~41-43 μm).

Figure 4-5-2 shows kinetic data from their study. It is observed that the reaction rate increased significantly as the C/Si molar ratio increased from 1 to 3. Higher C/Si molar ratios (4 or 5) had relatively little effect on the reaction rate. Since the carbon and silica particles in this study were relatively coarse and similar in size, the increase in the C/Si molar ratio would not be expected to significantly change the interfacial area between the carbon and silica. However, the carbon/pore interfacial area would be increased significantly with increasing C/Si ratio. If the rate-controlling step was the reaction between SiO and carbon, as suggested before, then the reaction rate should increase with increased C/Si ratio.

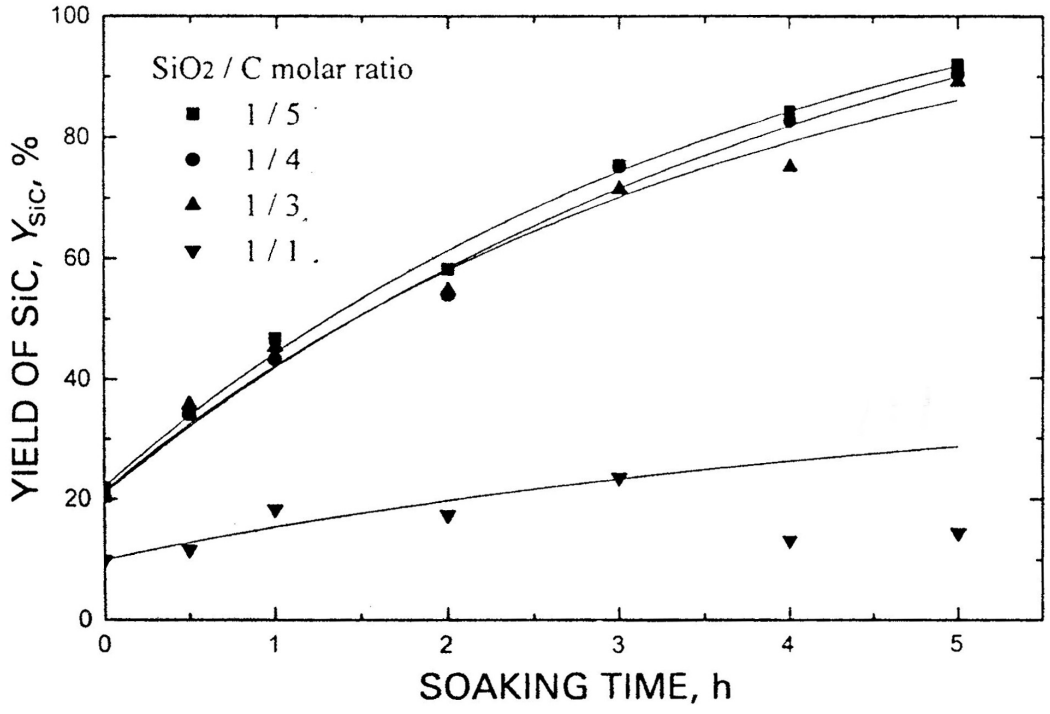

Figure 4-5-2 Yield of SiC as a function of reaction time (at 1500°C) for the reaction between carbon and silica for samples prepared with different molar ratios, from Chen et al. (2000).

4.5.3 Comparison of Reaction Rate Constant and Activation Energy with Other Studies

As stated in section 4.3, the kinetic behavior of the carbothermal reduction reaction for samples prepared from TEOS/phenolic resin solutions was consistent with the interface-controlled "shrinking-core" model in which the reaction of SiO vapor at the carbon surface to form SiC is the rate limiting step. In this section, the reaction rate constant and activation energy obtained based on that model are discussed and compared with those obtained by other researchers.

4.5.3.1 Comparison of Kinetics with Studies Which Used Similar Starting Materials

Figure 4-5-3 compares the rate constant in this study with those obtained by other researchers using similar starting materials (i.e., TEOS/phenolic resin mixed solutions). The reaction rate constants obtained in this study agree reasonably well with values reported by Ono and Kurachi (1991) and by Narisawa et al. (1998). (The rate constants in their studies were calculated according to the nucleation and growth model.) Table 4-5-2 shows the activation energies calculated from the rate constants in Figure 4-5-3. As expected, very similar activation energies were obtained in these studies.

As stated in section 2.3.4, both Ono and Kurachi (1991) and Narisawa et al. (1998) observed sigmoidal behavior in some of the fractional weight loss vs. reaction time curves. The nucleation and growth model was identified as the best model to describe the kinetics of CTR from the pyrolyzed material. According to the fitted result, they proposed that the reaction was a diffusion-controlled, 3-D growth process with zero nucleation rate.

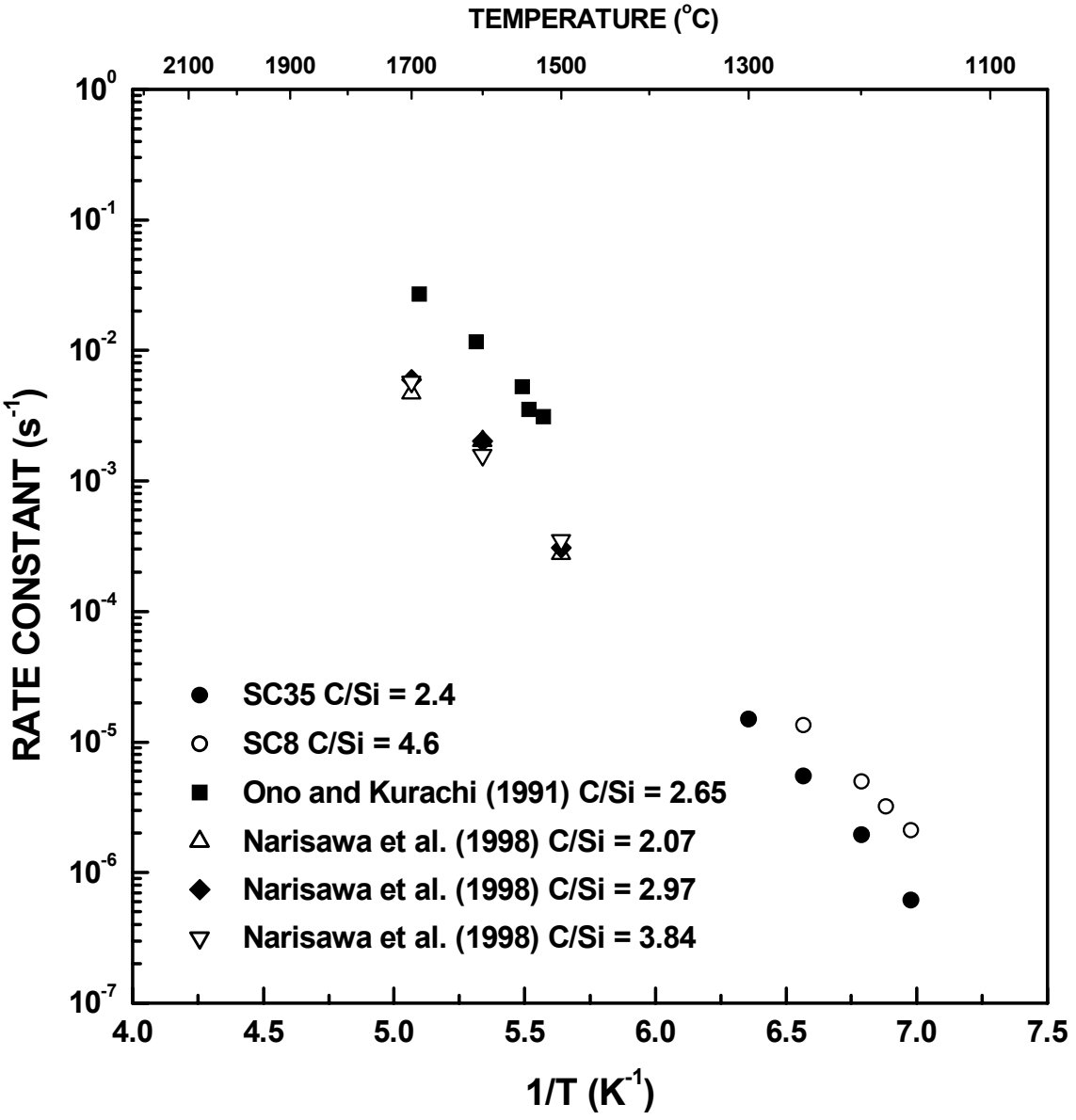

Figure 4-5-3 Plots of reaction rate constant vs. inverse temperature for the formation of SiC via carbothermal reduction (CTR) for different studies in which the reactant mixtures were prepared using TEOS/phenolic resin mixed solutions. The C/Si ratios shown in the figure were the molar ratios in the starting (pyrolyzed) materials.

Table 4-5-2 Pyrolyzed material composition, kinetic model used, and calculated activation energy for SiC CTR studies in which the reactants were prepared using TEOS/phenolic resin solutions.

Source	Starting materials	C/Si molar ratio before CTR	Kinetic model	*E* (kJ/mol)
SC35 series (this study)	TEOS/phenolic resin mixed solution	2.4	Interface-controlled "shrinking-core"	423
SC8 series (this study)		4.6		375
Ono and Kurachi (1991)	TEOS/phenolic resin mixed solution	2.6	Nucleation and growth	391
Narisawa et al. (1998)	TEOS/phenolic resin mixed solution	2.1	Nucleation and growth	414
		3.0		433
		3.8		407

It is not understood why the kinetic data fit different models for this study vs. the studies by Ono and Kurachi (1991) and Narisawa (1998). Two differences in the processing methods used in the studies are noted. First, pyrolysis of the dried materials (from the TEOS/phenolic resin mixed solution) was carried out at a lower temperature in the previous studies. (Ono and Kurachi used 1000^{o}C/2h; Narisawa used 1000^{o}C/1h; 1100^{o}C/2-4h was used in this study.) Second, higher heating rates were used in the previous CTR studies. (Ono and Kurachi heated samples in 3-5 sec using a YAG laser; Narisawa et al. inserted samples in a furnace preheated at the isothermal hold temperatures; the heating rate in this study was 80^{o}C/min except for a slower rate during the last 6 min prior to reaching the isothermal hold temperature.)

It could be argued that the SiC nuclei had already formed in the starting (pyrolyzed) material used in the present study since the pyrolysis temperature was higher. However, there was no evidence in XRD or TEM investigations to indicate that any SiC was present in the pyrolyzed materials. Another possibility is that the pyrolysis process had not been completed for the starting materials used in the previous studies. Therefore, weight losses during the initial stage of heat treatment may have been due to pyrolysis reaction instead of the CTR reaction. Incomplete pyrolysis might have resulted in a delay of the initial formation of SiC. This might have been responsible for the sigmoidal reaction kinetics that was observed at lower reaction temperatures (e.g., see Figure 2-3-3).

In regard to the effect of the CTR heating rate, it is possible that the extremely fast heating in previous systems might have caused a significant difference between the sample's actual temperature and the measured temperature. In particular, the actual sample temperature may have been lower during the early stages of the "isothermal" hold

period. Hence, the reaction was slower during that period of time and this could result in the observed sigmoidal behavior. This effect would have been less significant at higher isothermal temperatures (e.g., 1608 and 1689^{o}C in the Ono and Kurachi study) because the overall kinetics was extremely fast at these temperatures and the entire reaction was completed in just ~100 seconds. Therefore, deccelatory behavior was observed at the higher temperatures.

Finally, it is also noted that the nucleation and growth model was a relatively good fit to the data in the previous studies only at low temperatures. The fit was much poorer at the higher temperatures (e.g., 1608^{o}C and 1689^{o}C heat treatments in the study by Ono and Kurachi, see Figure 2-3-4) The clear deccelatory kinetic behavior at those high temperatures suggests that the data may have showed a better fit to the interface-controlled "shrinking-core" model. However, Ono and Kurachi only showed a fit of the low-temperature data to the "shrinking-core" model. It seems that they deliberately used the data set which had sigmoidal kinetic behavior and, not unexpectedly, a deviation from the "shrinking-core" model was observed.

4.5.3.2 Comparison of Kinetics with Studies Which Used Mixtures of Carbon and Silica Powders

Figure 4-5-4 shows the rate constants obtained by different researchers for the CTR reaction carried out using carbon/silica samples prepared by direct mixing of two separate powders. The symbols in Figure 4-5-4 are defined in Table 4-5-3, which also provides other information about the studies (i.e., carbon and silica sources, C/SiO_2 ratios, kinetic models used, and activation energies).

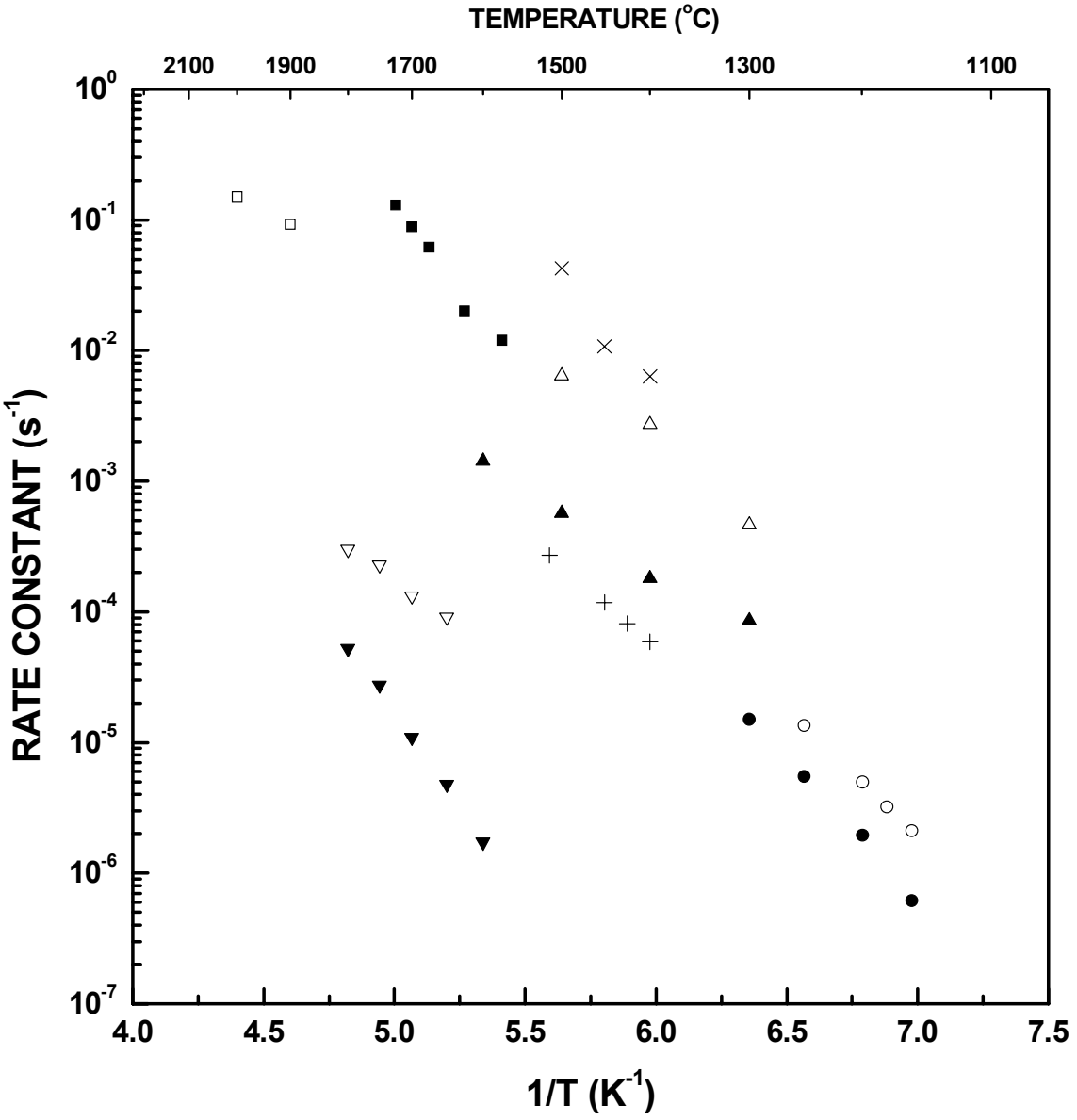

Figure 4-5-4 Plots of reaction rate constant vs. inverse temperature for the formation of SiC via carbothermal reduction (CTR). Results from the current study are compared with those obtained from mixtures of carbon and silica powders. The symbols are explained in the table on next page.

Table 4-5-3 Symbols, starting material information, kinetic model used, and calculated activation energy for the different data sets shown in Figure 4-5-4.

Symbol	Data source	Carbon source and particle size	Silica source and particle size	C/SiO_2 molar ratio	Kinetic model	E (kJ/mol)
●	SC35 series (this study)	*	*	2.4	Interface-controlled "shrinking-core"	423
○	SC8 series (this study)			4.6		375
▲	Blumental et al. (1966)	Carbon black 0.017 μm	α-Cristobalite 2.80 μm	1.0	Linear rate raw	230
△			Colloid silica 0.015 μm			288
+	Khalafalla & Haas (1972)	Graphite ~170 μm	Quartz ~170 μm	1.0	Cubic power law	322
▼	Shimoo (1990)	Carbon black 4.5 μm	Silica 143 μm	3.0	Jander's equation	544
▽		Activated carbon 51 μm	Silica 143 μm		Ginstling-Brounshtein equation	244
×	Viscomi & Himmel (1978)	Coke ~40 μm	Silica ~100 μm	3.0	Linear rate raw	552
■	Weimer et al. (1993)	Carbon black 0.030 μm	Not clear	3.1	Interface-controlled "shrinking-core"	382**
□		Carbon black 0.218 μm				

* Samples were prepared using TEOS/phenolic resin mixed solutions. After subsequent drying and pyrolysis, the starting material for the CTR reaction was an amorphous carbon/silica mixture with an estimated scale of mixing on the order of 0.01 μm .

** The activation energy was obtained from two sets of data. The carbon/silica mixtures were prepared using either 0.03 μm or 0.22 μm carbon black particles. The size of the silica particles used in the two reaction mixtures was not clearly specified.

Figure 4-5-4 and Table 4-5-3 show that there was a fairly wide range of rate constants (at a given temperature) and a fairly wide range of activation energies (230-544 kJ/mol) obtained in these studies. In general, the variation in rate constants may be attributed to at least four factors: (i) There could be differences in scale of mixing and/or the interfacial area of the carbon and silica components. This was a likely reason for at least some of the observed difference in rate constants because there was a wide range of particle sizes used in the various studies, as indicated in Table 4-5-3. (ii) The CTR reaction conditions (e.g., sample size, gas atmosphere and flow rate, heating schedule, etc.) were different. (iii) Different reaction models were used to calculate the rate constants and activation energies. For example, it was shown previously in this study (Tables 4-3-4 and 4-3-6) that rate constants differed by a factor of approximately three when applying the nucleation and growth model vs. shrinking-core model. However, this factor is not likely to account for more than one order of magnitude difference in the observed rate constants for the various studies. (iv) There could be differences in reaction mechanism.

Additional discussion is provided below concerning the differences in reaction rates observed for the present study and the studies listed in Table 4-5-3.

- Blumenthal et al. (1966)

Blumenthal et al. used very fine carbon (mean crystallite size of 17 nm) and silica as starting materials (Table 4-5-3). The powder mixtures were pressed into pellets, which brought closer contact between the carbon and silica. The reaction rate constants were similar to those in the current study. Figure 4-5-4 and Table 4-5-3 show that the reaction rate increased with smaller silica particle size. This was expected because the total

reaction interface area should have been increased greatly as the silica particle size was reduced from 2.8 μm to 0.015 μm.

- Khalafalla and Haas (1972)

Khalafalla and Haas used coarse (>100 μm) silica and carbon particles (Table 4-5-3) in their study of the CTR reaction. However, as shown in Figure 4-5-4, the rate constants were comparable to the rate constants observed in the current study. This seems to contradict the concept that using a coarser-scale mixture will result in a decreased reaction rate. One possible explanation is that the reaction rate in the study by Khalafalla and Haas was enhanced by using a high vacuum atmosphere (i.e., $P < 10^{-6}$ torr) during the reaction. As a result, the CO partial pressure in their system was extremely low. This would tend to push the CTR reaction (Equation (2-1-1)) toward more rapid formation of SiC and CO, according to LeChatelier's principle. In the current study, the reaction was carried out using a constant Ar flow rate (0.7 L/min) and, therefore, the CO partial pressure would have been significantly higher. The CO partial pressure can be roughly estimated in the following way. Suppose the sample used for the CTR reaction was SC35 pyrolyzed material. As described in section 4.5.1, the "full conversion" reaction can be represented by the empirical equation (4-5-1) with the following constants: $x = 0.05$, $y = 0.33$, $z = 2.39$. Therefore, the complete reaction for the CTR of SC35 would be:

$$SiO_2 + 2.39\ C \rightarrow 0.67\ SiC + 0.05\ C\ (excess) + 0.33\ SiO + 1.67\ CO \qquad (4\text{-}5\text{-}9)$$

In the current study, the amount of sample placed in the furnace was usually ~0.8 g. According to Equation (4-5-9), 0.8 g pyrolyzed material generates ~0.015 mol of CO. The volume of 0.015 mol CO at room temperature and one atmosphere pressure would be

approximately 0.015 mol × 22.4 L/mol = 0.34 L. The flow rate of Ar during the reaction was ~0.7 L/min at 1 atm. According to the kinetic study, the CTR reaction was almost completed after heat treatment at 1300°C for 16 h. Therefore, the total amount of Ar gas passed through the furnace tube during this period of time would roughly be 0.7 L/min × 16 × 60 min = 672 L. Therefore, a rough estimation of the CO relative pressure would be $0.34/672 = 5\times10^{-4}$. Since the Ar pressure from the cylinder outlet was ~1.7 atm (~25 psi), the CO partial pressure would be as high as:

$$1.7 \times 760 \text{ torr} \times 5\times10^{-4} = 0.6 \text{ torr}$$

Khalafalla and Haas demonstrated that that the reaction rate increased by several orders as the CO partial pressure was reduced from 0.25 torr to 10^{-6} torr (see Figure 2-3-1). Therefore, it is reasonable that the reaction rate constant obtained in their study was comparable to those in the current study, even though Khalafalla and Haas used a very coarse particle mixture.

- Shimoo (1990)

The reaction rate constants obtained by Shimoo were significantly lower compared with the rate constants obtained in the current study (and the other studies listed in Table 4-5-3). The slower kinetics in that study might have been due to the coarse raw materials used: the silica used had particle size of 143 μm and the carbon particles were either 4.5 μm (carbon black) or 51 μm (activated carbon). The gas atmosphere used during the reaction was argon.

Shimoo obtained very different activation energies for the reaction between silica and carbon black (544 kJ/mol) and the reaction between silica and activated carbon (244 kJ/mol). He believed that the first reaction was controlled by diffusion of carbon in SiC

while the second one was controlled by gas diffusion through the porous layers of the carbon particles. Such an explanation is questionable because both reactions would be expected to generate porous SiC product layers.

- Viscomi and Himmel (1977)

The reaction rate constants in the study by Viscomi and Himmel seem quite high considering the coarse powders (tens of micron in size) used for the reaction. Nitrogen atmosphere was used. It is unclear what promotes the reaction in their system. Weimer et al (1993) suggested that the high reaction rate was due to metal impurities in the carbon starting material (coke).

- Weimer et al. (1993)

Weimer et al. (1993) observed fairly high rate constants and they were reasonably consistent with the values in this study and in the study by Blumenthal et al (1966). This is probably because the particles used in the study were relatively small. Weimer et al observed an increased reaction rate when the starting particle sizes were reduced (i.e., the silica size decreased from 1.1 μm to 0.022 μm and the carbon size decreased from 0.218 μm to 0.030 μm).

As described in section 2.3.4, Weimer et al. reported an activation energy of 382±34 kJ/mol which was obtained by combining two different data sets. (Reactions were carried out using two different reactant mixtures that had been prepared with different starting carbon particle sizes. It was not clear if the same or different silica powders were used for the two different reactant mixtures.) They fit their data to the interface-controlled shrinking-core model to obtain rate constants. In calculating the activation energy, they assumed that the rate constants were inversely proportional to the starting carbon particle

size (Equation (2-3-20)). It is not clear if this assumption is reasonable. The activation energy was re-calculated by the present author using only the five data points (see Figures 2-3-5 and 4-5-4) that were obtained by Weimer et al. at the lower reaction temperatures (1575-1725^{o}C). (These data points were obtained using the reactant mixture prepared with the smaller starting carbon particle size.) The activation energy was 511 kJ/mol.

4.5.3.3 Comparison of Kinetics with Studies on Other Materials Systems

The reaction rate constants for the SC35 and SC8 samples were also compared with those obtained for samples prepared from other starting materials, i.e., rice hulls and preceramic polymer. The rate constants are shown in Figure 4-5-5 and additional information is provided in Table 4-5-4.

The reasons for the high rate constants in the studies using rice hulls may include the following: (1) Pyrolysis of rice hulls produces a very fine-scale silica/carbon mixture. (2) The C/SiO_2 ratio in the pyrolyzed rice hulls was high (i.e., ~5.0-5.6). (3) The pyrolyzed rice hulls may contain small amounts of impurities (Krishnarao and Godkhindi (1992)).

The rate constants in the study by Panigraphi et al. were higher than those reported by Lee and Cutler. This was probably because a vacuum atmosphere (i.e., ~10^{-2} torr) was used in the former study, while an atmosphere with relatively high CO pressure (i.e., ~76 torr (0.1 atm)) was used in the latter study.

The rate constants and the activation energy observed in the study by Shimoo (1996) with Nicalon® fibers were similar to values obtained in this study. This may be due to the following reasons: (i) The samples had a similar scale of mixing of the silica and carbon regions (i.e., mostly <10 nm). (ii) The silica and carbon were in intimate contact since the

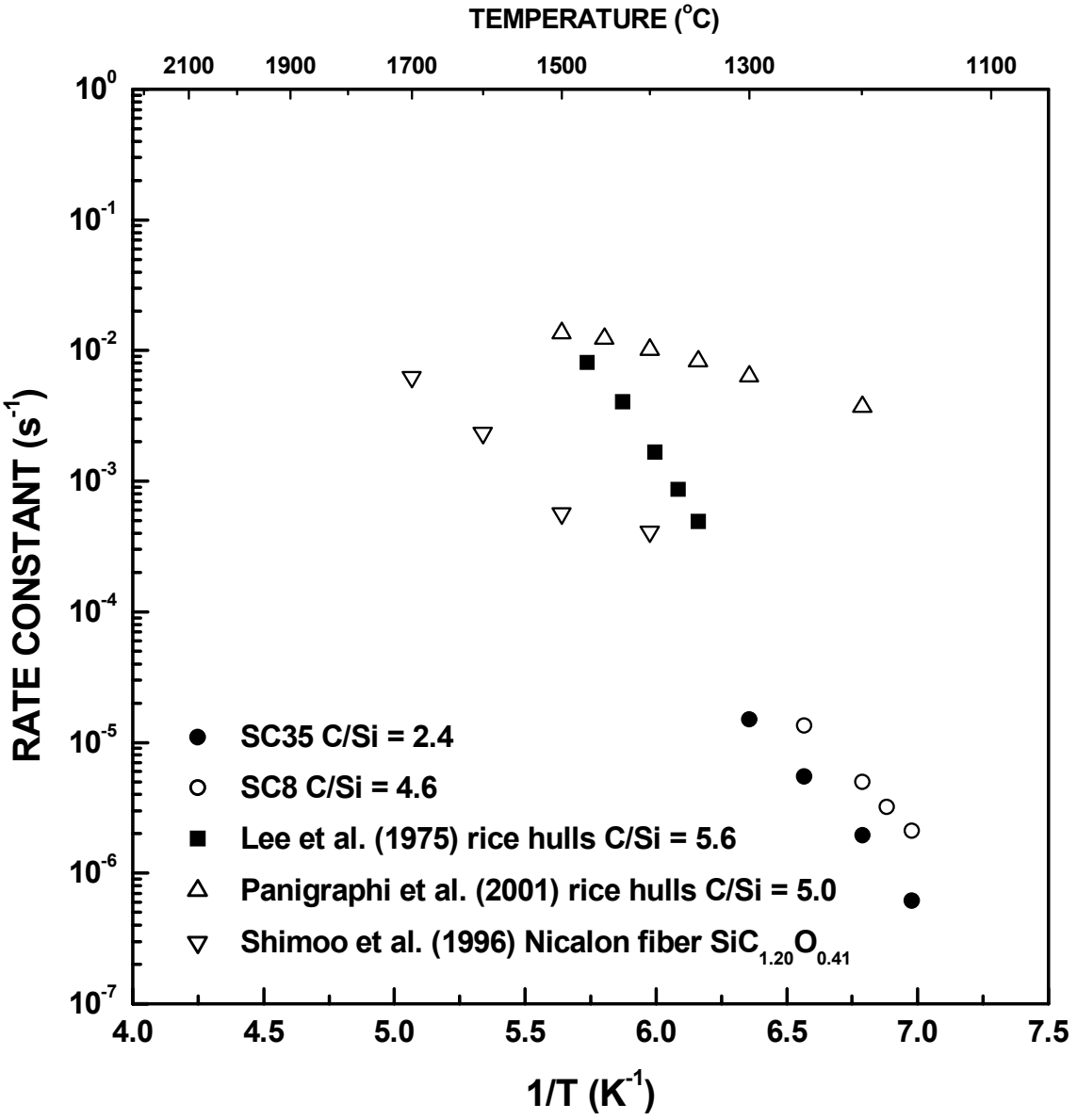

Figure 4-5-5 Plots of reaction rate constant vs. inverse temperature for the formation of SiC via carbothermal reduction (CTR). The results from the current study are compared with those obtained using preceramic polymer and rice hulls as starting materials.

Table 4-5-4 Starting material, pyrolyzed material composition, kinetic model used, and calculated activation energy for the data shown in Figure 4-5-5.

Source	Starting materials	C/Si molar ratio before CTR	Kinetic model	*E* (kJ/mol)
Lee and Cutler (1975)	Rice hulls	5.6	Linear rate law	544
Panigraphi et al. (2001)	Rice hulls	5.0	Linear rate law	92
Shimoo (1996)	Nicalon fiber ($SiC_{1.20}O_{0.41}$)		Nucleation - growth	350

starting materials used for the CTR reaction were essentially dense (i.e., mostly pore-free). (iii) The materials were fairly high in purity, i.e., significant metallic impurities were not present.

4.5.4 Overall Consideration on the Mechanism of SiC Formation via CTR

In this section, the reaction mechanism and kinetics are reviewed and discussed based on all the experimental results.

As discussed in Chapter 2 (section 2.2.1), several previous studies have indicated that the silicon carbide (SiC) carbothermal reduction reaction involves two elementary reaction steps. The first step is the reaction between silica (SiO_2) and carbon (C) to form silicon monoxide (SiO) and carbon monoxide (CO):

$$SiO_{2\,(s)} + C_{(s)} \rightarrow SiO_{(g)} + CO_{(g)} \qquad (4\text{-}5\text{-}10)$$

The second step is the reaction between SiO vapor and carbon to form SiC and CO:

$$SiO_{(g)} + 2\,C_{(s)} \rightarrow SiC_{(s)} + CO_{(g)} \qquad (4\text{-}5\text{-}11)$$

The results obtained in the current study are consistent with the formation of SiO (as indicated by Equation (4-5-10)). Specific evidence includes the following:

1. Condensates formed from the volatiles generated by the CTR reaction were collected and analyzed. EDX analysis (Figure 4-2-2) showed that the condensates were Si-rich. XRD showed that the condensates contained silica and Si metal (Figure 4-2-3). It was suggested that the Si-rich volatile formed during the reaction was actually SiO gas and that this gas subsequently dissociated into Si and SiO_2 in lower-temperature regions of the furnace. The latter conclusion was supported by calculations (section 4.2.2) in which it was shown that the estimated vapor pressure of SiO should be ~4-5 orders of

magnitude higher than the vapor pressure of Si and SiO_2 at 1160°C. This conclusion was also suggested by previous researchers, i.e., Khalafalla and Haas (1972), Weimer et al. (1993), and Meng et al. (2000).

2. Samples which had starting C/Si molar ratios close to three (e.g., SC23 in Table 4-5-1) had a substantial amount of residual carbon after the CTR reaction was carried out to the maximum extent (i.e., to "full conversion"). This means that it was necessary to use samples with starting C/Si molar ratios much smaller than three (e.g., SC35, SC42, etc. in Table 4-5-1) in order to prepare an SiC product with little or no residual carbon. These results indicate that there was a loss of Si (presumably as SiO) during the CTR reaction. After accounting for SiO loss and the presence of residual carbon, calculated reaction yields for samples with varying starting composition (i.e., varying C/SiO_2 molar ratio) closely matched the corresponding yields determined from experimental weight loss measurements (Table 4-5-1). The calculations also showed that the amount of SiO loss decreased and the reaction yield (by weight) increased with increasing carbon content (i.e., increasing starting C/Si molar ratio).

The second step in the CTR reaction (i.e., Equation (4-5-11)) is believed to be the rate-limiting step. This is supported by the following observations:

1. SiO was always lost during the CTR reaction, regardless of the starting composition (i.e., C/SiO_2 molar ratio) and Ar flow rate. This suggests the consumption of SiO (according to Equation (4-5-11)) was relatively slow compared to the generation of SiO (according to Equation (4-5-10)).
2. The reaction rate constants for carbon-rich SC8 samples were higher compared to the rate constants for silica-rich SC35 samples. The carbon/silica interfacial area was

expected to be similar in the starting (pyrolyzed) materials for the SC8 and SC35 samples. Therefore, a change in composition would not have much effect on the overall reaction rate if the first step (Equation (4-5-10)) in the reaction was rate-controlling. In contrast, if the reaction was controlled by the second step, then the reaction rate should be affected by factors that change the carbon/pore specific interfacial area. Figures 4-4-32 and 4-4-34 show that higher specific surface areas were developed in the carbon-rich SC8 samples as the reaction proceeded (and a porous product developed). This is consistent with the higher reaction rates for these SC8 samples (i.e., compared to the SC35 samples).

The reaction kinetics for the SC8 and SC35 samples were consistent with the interface-controlled "shrinking-core" model (Figure 4-3-30). Data for both the sample weight losses and the amounts of SiC formed (as determined by QXRD) during the CTR reaction showed good fits to the proposed reaction model (Figures 4-3-7, 4-3-8, 4-3-24 - 4-3-27).

The structure of the starting pyrolyzed materials used in the CTR reaction was characterized by SEM observations and measurements of gas adsorption behavior, pycnometric densities, and particle size distributions (Figures 4-1-10 to 4-1-35 /Tables 4-1-2, 4-1-3, 4-1-5, and 4-1-6). These characterization experiments showed the following: (i) The pyrolyzed materials consisted of relatively large particles (median diameters in the range of 64-79 μm) which were mostly dense (i.e., mostly pore-free), except for some defects (e.g., microcracks). (ii) The large particles were composed of finer clusters (mostly in the range of ~50-500 nm) which were also essentially dense. The clusters were believed

to be composed of fine-scale, space-filling, interpenetrating networks of silica and carbon with an average scale feature that was roughly on the order of 10 nm or less.

The fine clusters within the large pyrolyzed particles were considered to be the unit structures that evolved during the reaction according to the interface-controlled "shrinking-core" model. It was believed that the gases (i.e., SiO and CO) formed during the first reaction step were able to evolve not only from clusters at the external surfaces of the large particles, but also from cluster-cluster interfacial regions within the particles. This was possible because of the presence of microcracks within the large particles. According to the shrinking-core model, the reaction interface would move from the surface to the center of the individual clusters as the reaction proceeded.

The product that developed during CTR was believed to undergo a structural evolution as described below:

1. SiO and CO were generated when silica and carbon within the clusters reacted during the first step (Equation (4-5-10)) of the CTR reaction. This resulted in the development of porosity. Some of the SiO vapor was swept away by the Ar gas flow, but some reacted with the exposed carbon network to form SiC and CO (Equation (4-5-11)). The latter reaction was expected to have relatively little effect on the pore volume produced the first reaction step. Hence, gas adsorption measurements showed that the total specific pore volume (Figures 4-4-22 and 4-4-25) and the total specific surface area (Figures 4-4-32 and 4-4-34) of the product increased continuously for most (SC35) or all (SC8) of the CTR reaction. This behavior was consistent with the "shrinking-core" reaction model.

2. According to the proposed model, the reaction begins at cluster surfaces and cluster-cluster interfaces and then proceeds inward toward the center of the clusters. Hence, a porous SiC carbide structure was expected to develop at cluster surfaces and interfaces. Since the clusters were nearly dense (pore-free) in the starting (pyrolyzed) material, there must have been an initial stage in which pores developed at the cluster surfaces (and interfacial regions) and then grew in size as silica was consumed via Equation (4-5-10). The pores would be expected to grow to sizes comparable to the sizes of the original silica regions. In the silica-rich SC35 samples, this resulted in the development of pores that were mostly in the range of ~5-30 nm (Figures 4-4-110 and 4-4-145 - 4-4-148). The pores that developed at cluster-cluster interfacial regions linked together to form an interconnected network at a relatively early stage in the overall reaction (i.e., fractional weight losses in the range of ~0.12-0.23). (The SiC product was also expected to form an interconnected network in these regions. This is because the reaction product at "full conversion" in the SC35 samples was mostly SiC with only a small amount of residual carbon.) This development of an interconnected porous product was indicated from an analysis of the changes in the gas adsorption isotherms as the reaction proceeded (Figures 4-4-68 - 4-4-74). After the initial development of the porous network, there was relatively little change in the pore size distribution for much of the subsequent reaction (Figures 4-4-88 - 4-4-94 and Figure 4-4-110). This was consistent with expectations from the shrinking-core model; a uniform microstructure should develop as the reaction proceeds from the surface to the interior of the clusters.

In the carbon-rich SC8 samples, both smaller pores (<5 nm) and larger pores (~5-30 nm) developed throughout the reaction (Figures 4-4-193, 4-4-194, and 4-4-221 - 4-4-224). The formation of the smaller pores was more significant in the earlier stages, while the development of the larger pores was more important in the later stages (Figures 4-4-193, 4-4-194, and 4-4-221 - 4-4-224). The smaller pores that developed throughout the reaction had a fairly uniform size (Figures 4-4-220 and 4-4-230). After the initial stage of the reaction, there was a continuous increase in the size of the larger pores that developed with further reaction (Figure 4-4-229). The difference in pore development behavior (compared to the SC35 samples) was attributed to a difference in the distribution of the silica. The larger volume of smaller pores in the SC8 samples was believed to be associated with silica regions that were isolated (entrapped) within highly carbon-rich regions. Hence, it was proposed that the SiC crystallites that developed in the SC8 samples remained more isolated (and had limited connectivity), especially during the early stages of the reaction. In contrast to the SC35 samples, fully-converted intercluster regions would have a composite structure with high residual carbon content (i.e., the composition was ~55 vol% carbon/~45 vol% SiC). As the reaction proceeded, the clusters would continue to develop the same SiC/carbon composite structure in accordance with the shrinking-core reaction model. However, as the overall volume fraction of SiC increased (as the reaction proceeded), some isolated groups of fine SiC crystallites were able to grow into interconnected networks with similar character to those in the SC35 samples. This behavior was suggested by the changes observed in the gas adsorption isotherms as the reaction proceeded (Figures 4-4-155 - 4-4-165).

3. There was relatively little change in the size of the SiC crystallites for most of the CTR reaction (Figures 4-4-2 and 4-4-4). This is again consistent with the "shrinking-core" reaction model because a uniform microstructure development is expected as the reaction proceeds from the surface to the interior of the cluster. The carbon-rich SC8 samples had slightly larger crystallite sizes for most of the reaction compared to the SC35 samples (Figure 4-4-5). The SiC crystallite size should be related to the size of the carbon regions in the starting material if SiC formation proceeds according to Equation (4-5-11). It was proposed that pyrolyzed SC8 samples had slightly larger carbon regions (compared to the SC35 samples) because of the higher overall volume fraction of carbon.
4. The average SiC crystallite size and average pore diameter increased significantly toward the end of the reaction in the SC35 samples (Figures 4-4-2, 4-4-111 and 4-4-112). This was consistent with many previous studies which showed that coarsening of SiC occurs when the free carbon content is low and coarsening-inhibitors (e.g., boron) are not present (Clegg, 2000). It was also observed that the specific pore volume decreased significantly in the late stages of the reaction in the SC35 sample (Figure 4-4-22). The latter observation was attributed primarily to the growth of the pores to sizes that could not be detected by gas adsorption measurements. There was also some limited densification (shrinkage) of the sample, but particle size measurements (Figures 4-4-51, 4-4-52, and 4-4-61) showed that this could only account for a small amount of the observed decrease in pore volume.

   Despite the high residual carbon content, there was evidence that some coarsening also occurred in the SC8 samples. The average SiC crystallite size and the median size for

larger pores (≥5 nm) increased significantly during the late stage of the reaction (Figures 4-4-4, 4-4-218, 4-4-220, and 4-4-229). This behavior was attributed to coarsening in *local* regions where the carbon had been substantially depleted and the porous SiC "agglomerate" structure had formed. Coarsening would not be expected in the regions with high residual carbon content. Hence, the SC8 did not show a decrease in the specific pore volume or specific surface area in the late stages of the reaction (Figures 4-4-25 and 4-4-34). This was also consistent with the observation that the median pore diameter (based on all pores in the distribution) did *not* show a sharp increase in the late stages of the reaction (Figures 4-4-217 and 4-4-220).

CHAPTER V

CONCLUSIONS AND RECOMMENDATIONS FOR FUTURE WORK

5.1 Conclusions

The following conclusions were made from the current research:

(1) Nanocrystalline β-SiC was obtained at relatively low temperature via carbothermal reduction (CTR) reaction on a fine-scale carbon/silica mixture prepared from a solution-based processing method. Carbon/silica mixtures with a C/Si molar ratio of 2.4 were transformed almost completely to near stoichiometric β-SiC with average crystallite size smaller than 25 nm by heat treatment at 1300^{o}C for 16h.

(2) The presence of SiO as a reaction intermediate was verified by (i) chemical analysis on the volatile condensates that were collected, (ii) calculation of the SiO equilibrium vapor pressure, and (iii) estimation of the silica utilization rate from the reactant and product composition.

(3) The kinetic behavior for the CTR reaction was consistent with the interface-controlled "shrinking-core" model. The reaction of SiO vapor with solid carbon at the carbon surface was believed to be the rate-controlling step. The calculated activation energies were in the range of 375 - 423 kJ/mol.

(4) The structural evolution of the reaction product was consistent with the interface-controlled "shrinking-core" model. As the reaction proceeded, a fine crystallite size was maintained, while the product porosity and specific surface area continuously increased, i.e., until the very late stage of the reaction when coarsening became significant.

(5) The precursor with higher carbon content (i.e., SC8 sample with C/Si molar ratio of 4.6) showed higher reaction rate than the precursor with lower carbon content (i.e., SC35 sample with C/Si molar ratio of 2.4). During the CTR reaction, the SC8 sample gave a product with slightly larger crystallite size (during most of the reaction), higher specific surface area, and lower porosity compared to the SC35 sample.

(6) The fine-scale carbon/silica mixtures were believed to have a hierarchical structure. The large (several tens of micrometer) pyrolyzed particles were composed of densely-packed "clusters" which were mostly in the size range of ~50 - 500 nm. Each cluster was composed of interpenetrating networks of carbon and silica. The CTR reaction occurred initially at the interfaces between clusters, and each cluster was a unit for the "shrinking-core" reaction.

5.2 Recommendations for future work

In future, the following areas should be investigated in order to further clarify the reaction mechanism for the SiC reaction:

(1) The crystallite size development should be determined for the very early stage of the carbothermal reduction reaction. In the current study, the author was unable to obtain reliable crystallite size data for the very early stage of the reaction because of background "noise" in the XRD pattern.

(2) The interfacial structures among the three phases (carbon, silica, and SiC) should be characterized. Further investigation by HRTEM is necessary to reveal how the SiC develops from the amorphous matrix.

APPENDIX A

DETERMINATION OF FULL-WIDTH-HALF-MAXIMUM FOR CRYSTALLITE SIZE MEASUREMENT

The value of *B* in Equation (3-5-2) (i.e., the measured width of the diffraction line) was determined based on a Lorentzian fitting of the full profile of the diffraction line. Two methods were used in the processing of the data to deduct the background. In the first method (method #1), the background was treated manually. In the second method (method #2), the background was treated first by Powder 2.0 software (Version E.1999-03-03, authored by N. Dragoe, Bucharest, Romania) and then manually. The following is the step-by-step description for the two methods.

- **Method #1**

1. α_2 stripping was performed on the scanned pattern using the PC-APD software, as illustrated in Figure A-1 for the SC8-1160(48h) sample.

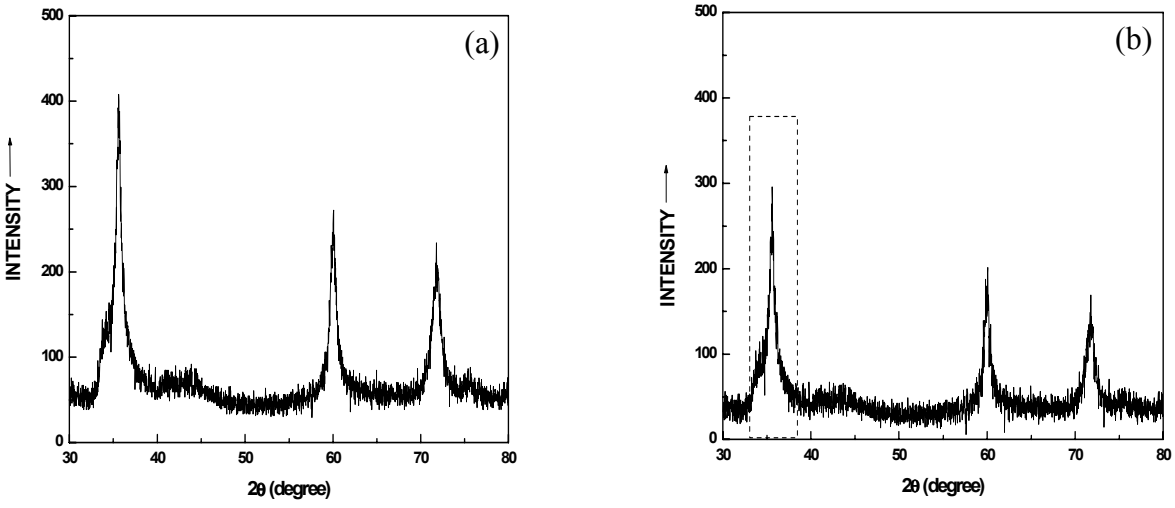

Figure A-1 XRD pattern for SC8-1160(48h) (a) before α_2 stripping, and (b) after α_2 stripping.

2. A 2θ angle range around the SiC diffraction line was picked from the α_2-stripped pattern. Lorentzian fitting of the profile of the diffraction line over the range chosen was performed with Origin® software (version 6.1, OriginLab Corporation, Northampton, MA). The range for the fitting was chosen so that the actual diffraction line was in the center of it. The limits of the range were selected at places where the diffraction line had leveled off. The ranges were usually ~33-38.2^o, ~58.5-61.5^o, ~70-73.5^o for the ***β***-SiC (111), (220), and (311) lines respectively. The choice of these specific ranges was somewhat arbitrary. However, as long as a constant range was used, the results could be compared with each other because the sizes were calculated based on the same criterion. Furthermore, a small variation in the range of 2θ (e.g., ~0.1^o) usually did not result in much change to the calculated crystallite size. However, if the range used was changed more significantly, then there might be a considerable variation in the calculated crystallite size. Consider an example using the SC8-1160(48h) sample. If the range of fitting for the (111) line is 33-38.2^o, the calculated crystallite size is 11.8 nm; if the range of fitting is expanded to 32-39^o, the calculated crystallite size is 9.9 nm; if the range of fitting is expanded to 31-40^o, the calculated crystallite size is 8.8 nm. Consider another sample using the SC8-1160(20h) sample. If the range of fitting for the (111) line is 33-38.2^o, the calculated crystallite size is 11.8 nm; if the range of fitting is expanded to 32-39^o, the calculated crystallite size is 10.6 nm; if the range of fitting is expanded to 31-40^o, the calculated crystallite size is 10.0 nm. Figure A-2 is an illustration of the (111) line and the Lorentzian fitted line for SC8-1160(48h) sample. The fitting range was chosen to be 33-38.2^o.

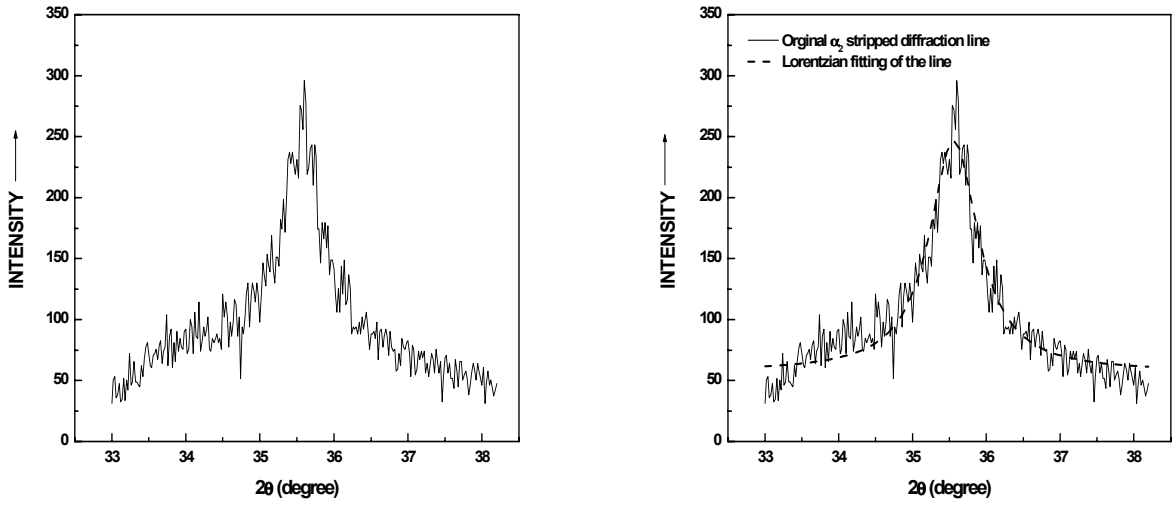

(a) (b)

Figure A-2 SC8-1160(48h) (111) line after α_2 stripping: (a) diffraction line only, (b) diffraction line and Lorentzian fitted curve of it.

3. The x- and y- coordinates of the highest point on the Lorentzian fitted curve were obtained, i.e., the maximum intensity I_{peak} (y-coordinate) and the line position 2θ (x-coordinate). For the example shown in Figure A-3, the values are $2\theta = 35.556^{o}$ and $I_{peak} = 247.3$.

4. The two intensity values at the 2θ values which were farthest from the peak center on each side of the Lorentzian fitted curve were obtained. The background intensity value was taken as the average of these two values. In Figure A-3, these intensities are 61.4 and 61.6 at the left side ($I_{bk\text{-}L}$) and the right side ($I_{bk\text{-}R}$), respectively. Hence, the background value was given by:

$$I_{bk} = (I_{bk\text{-}L} + I_{bk\text{-}R})/2 = 61.5$$

5. The half-maximum value was obtained by $I_B = (I_{peak} + I_{bk})/2$. For the example in Figure A-3, $I_B = (I_{peak} + I_{bk})/2 = 154.4$.

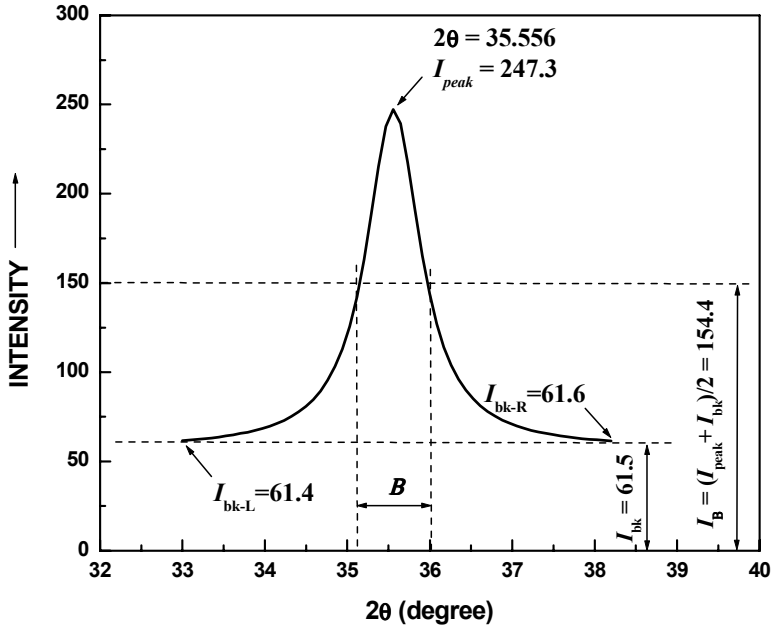

Figure A-3 Lorentzian fitted curve of β-SiC (111) line for SC8-1160(48h), showing the peak coordinates, the background height and the half maximum position.

6. The width of the fitted curve at the half height was measured. This is referred to as the full-width-half-maximum (FWHM). For the example in Figure A-3, the half-maximum height was 154.4 and the width (*B*) of the fitted curve at this height was $B_{111} = 0.798^{o}$.

7. The crystallite size was calculated using Equation (3-5-3) where *B* is the FWHM value. In this example, the value of *b* due to broadening from the instrument was 0.062^{o} , as shown in section 3.4.1. The value of $2\theta = 35.556^{o}$ and $\theta = 17.778^{o}$. Therefore, crystallite size D_{111} is given by:

$$D_{111} = \frac{0.9 \times 0.15406}{(B-b)\times\cos(\theta)} = \frac{0.9 \times 0.15406 \times 360}{2 \times 3.14 \times (0.798 - 0.062) \times \cos 17.778^{\circ}} = 11 \text{ nm}$$

where the factor $\frac{360}{2\pi}(=\frac{360}{2\times 3.14})$ was used to convert angles in degrees to angles in radians.

- **Method #2**

1. α_2 stripping was performed on the scanned pattern by the APD software in the same manner as in method #1. SC8-1160(48h) is again used here as an example.
2. The α_2-stripped pattern was imported to Powder 2.0 software (N. Dragoe, 1999) and the XRD pattern was plotted (Figure A-4 (a)).
3. The background of the α_2-stripped pattern was removed automatically by the Powder 2.0 software (Figure A-4 (b)) based on the "method of Sonneveld and Visser – TNO Delft".
4. As in method #1, a 2θ angle range around the SiC peak was picked from the α_2-stripped pattern. Lorentzian fitting was performed for the pattern in the range chosen. Figure A-5 shows an example for the Lorentzian fitted curve for SC8-1160(48h) (111) diffraction line.

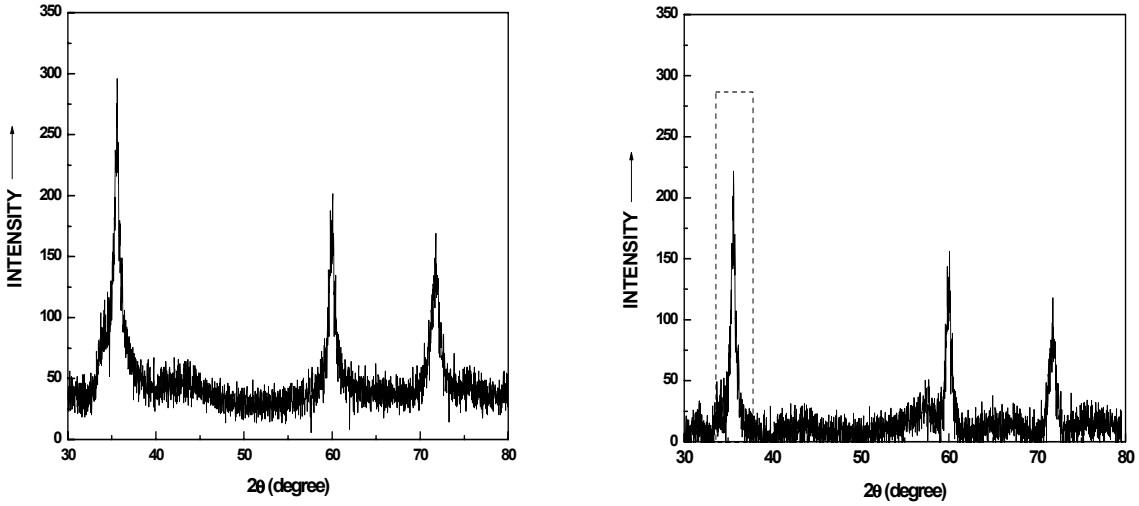

(a) (b)

Figure A-4 XRD patterns for SC8-1160(48h) after α_2 stripping: (a) before background was removed and (b) after the background was removed by Powder 2.0 software.

5. The x- and y-coordinates of the highest point on the Lorentzian fitted curve were obtained, i.e., the maximum intensity I_{peak} (y-coordinate) and the line position 2θ (x-coordinate). For the example shown in Figure A-5, the values are 2θ = 35.556^o and I_{peak} = 183.5.

6. The two intensity values at the 2θ values which were farthest from the peak center on each side of the Lorentzian fitted curve were obtained. The background intensity value was taken as the average of these two values. In Figure A-5, these intensities are 12.0 and 11.9 at the left side ($I_{bk\text{-}L}$) and the right side ($I_{bk\text{-}R}$), respectively. Hence, the background value was given by:

$$I_{bk} = (I_{bk\text{-}L} + I_{bk\text{-}R})/2 = 11.95$$

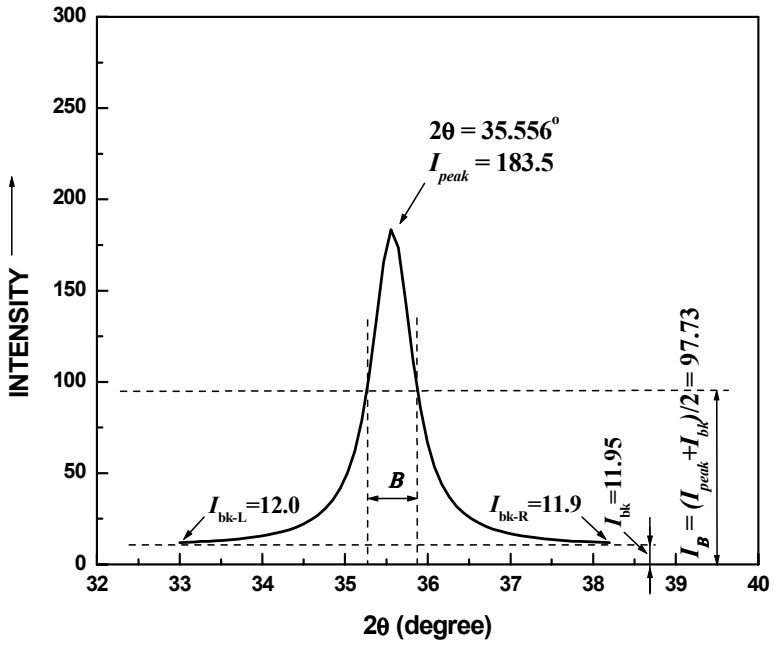

Figure A-5 Lorentzian fitted curve for the SiC (111) peak from the pattern of SC8-1160(48h) sample; the background had been removed by Powder 2.0 software.

7. The half-maximum value was obtained by $I_B = (I_{peak} + I_{bk})/2$. For the example in Figure A-5, $I_B = (I_{peak} + I_{bk})/2 = 97.73$.
8. The width of the fitted curve at the half height was measured. Again, this is referred to as the full width half maximum (FWHM). For the example in Figure A-3, the half-maximum height was 97.73 and the width (B) of the fitted curve at this height was $B_{111} = 0.604^o$.
9. The crystallite size was calculated using Equation (3-4-3) where B is the FWHM value. In this example, the value of b due to broadening from the instrument was 0.062^o. Therefore, crystallite size D_{111} was given by:

$$D_{111} = \frac{0.9 \times 0.15406}{(B-b) \times \cos(\theta)} = \frac{0.9 \times 0.15406 \times 360}{2 \times 3.14 \times (0.604 - 0.062) \times \cos 17.778^o} = 15 \text{ nm}$$

Table A-1 shows a comparison of the crystallite size calculated from the two methods for the SC8-1180(48h) sample. To mitigate the errors associated with the experiments and the data processing, the average value obtained from the two methods was used in this study. For the example in Table A-1, the average crystallite size D = (12.8+15.0)/2 = 13.9 nm.

Table A-1 Crystallite size along different crystallographic directions for SC8-1160(48h) samples calculated from method #1 and method #2.

Data treatment method	D_{111} (nm)	D_{220} (nm)	D_{311} (nm)	D_{Avg} (nm)	Standard deviation (nm)
1	11.8	15.5	11.1	12.8	2.4
2	15.5	16.8	12.8	15.0	2.0

APPENDIX B

WEIGHT LOSS INFORMATION FOR SC35 AND SC8 CTR SAMPLES

Table B-1 Summary of weight loss information for SC35 and SC8 samples.

Sample ID	y_n	$w_{m\text{-}pyro}$	$w_{m\text{-}CTR}$	$X_{WL\text{-}m}$	$X_{WL\text{-}mb}$
SC35-1160(0.5h)	0.9804	0.0026	0.0020	0.0287	0.0132
SC35-1160(1h)	0.9770	0.0015	0.0000	0.0325	0.0170
SC35-1160(2h)	0.9667	0.0024	0.0009	0.0482	0.0326
SC35-1160(4h)	0.9583	0.0017	0.0000	0.0608	0.0451
SC35-1160(8h)	0.9429	0.0021	0.0004	0.0841	0.0683
SC35-1160(16h)	0.9089	0.0020	0.0008	0.1363	0.1203
SC35-1160(32h)	0.8423	0.0023	0.0015	0.2378	0.2213
SC35-1160(48h)	0.7939	0.0037	0.0000	0.3078	0.2909
SC35-1200(0.5h)	0.9751	0.0037	0.0007	0.0333	0.0178
SC35-1200(1h)	0.9690	0.0030	0.0011	0.0442	0.0286
SC35-1200(2h)	0.9486	0.0069	0.0010	0.0695	0.0538
SC35-1200(4h)	0.9334	0.0007	0.0013	0.1018	0.0859
SC35-1200(8h)	0.8824	0.0026	0.0009	0.1760	0.1598
SC35-1200(16h)	0.8161	0.0048	0.0013	0.2744	0.2577
SC35-1200(22.6h)	0.73767	0.0024	0.0013	0.3977	0.3804
SC35-1200(32h)	0.6436	0.0028	0.0015	0.5388	0.5208
SC35-1200(48h)	0.5088	0.0034	0.0029	0.7438	0.7249
SC35-1250(0.5h)	0.9545	0.0023	0.0011	0.0673	0.0516
SC35-1250(1h)	0.9417	0.0024	0.0012	0.0865	0.0707
SC35-1250(2h)	0.9113	0.0009	0.0006	0.1339	0.1179

Note: y_n - nominal yield, $w_{m\text{-}pyro}$ - moisture content of the pyrolyzed material before CTR, $w_{m\text{-}CTR}$ - moisture content of the materials after CTR, $X_{WL\text{-}m}$ - fractional weight loss after correction for moisture adsorption, $X_{WL\text{-}mb}$ - fractional weight loss after correction for both moisture adsorption and powder blown-off.

Table B-1 (continued)

Sample ID	y_n	$w_{m\text{-}pyro}$	$w_{m\text{-}CTR}$	$X_{WL\text{-}m}$	$X_{WL\text{-}mb}$
SC35-1250(4h)	0.8351	0.0028	0.0014	0.2480	0.2314
SC35-1250(8h)	0.6985	0.0024	0.0015	0.4283	0.4108
SC35-1250(12h)	0.6284	0.0025	0.0031	0.5636	0.5455
SC35-1250(16h)	0.5269	0.0024	0.0016	0.7162	0.6974
SC35-1250(22h)	0.4455	0.0025	0.0000	0.8385	0.8191
SC35-1250(32h)	0.3580	0.0024	0.0084	0.9760	0.9560
SC35-1300(0.5h)	0.9230	0.0019	0.0017	0.1164	0.1005
SC35-1300(1h)	0.8747	0.0013	0.0011	0.1896	0.1733
SC35-1300(2h)	0.7871	0.0037	0.0019	0.3204	0.3035
SC35-1300(3h)	0.6898	0.0026	0.0000	0.4673	0.4497
SC35-1300(4h)	0.6278	0.0035	0.0013	0.5619	0.5438
SC35-1300(6h)	0.5120	0.0041	0.0000	0.7362	0.7173
SC35-1300(8h)	0.4309	0.0025	0.0017	0.8617	0.8422
SC35-1300(12h)	0.3553	0.0028	0.0000	0.9754	0.9554
SC35-1300(16h)	0.3281	0.0013	0.0026	1.0186	0.9788
SC8-1160(1h)	0.9241	0.0283	0.0023	0.1002	0.0531
SC8-1160(2h)	0.8810	0.0600	0.0014	0.1257	0.0792
SC8-1160(4h)	0.9222	0.0035	0.0017	0.1493	0.1034
SC8-1160(7h)	0.8753	0.0131	0.0024	0.2258	0.1819
SC8-1160(12h)	0.8245	0.0281	0.0015	0.2999	0.2578
SC8-1160(20h)	0.7589	0.0209	0.0013	0.4430	0.4046
SC8-1160(28h)	0.6708	0.0198	0.0022	0.6220	0.5881
SC8-1160(36h)	0.6629	0.0107	0.0019	0.6494	0.6162
SC8-1160(48h)	0.5946	0.0185	0.0025	0.7758	0.7458
SC8-1180(1h)	0.9315	0.0070	0.0028	0.1265	0.0800
SC8-1180(2h)	0.8943	0.0203	0.0004	0.1716	0.1263

Table B-1 (continued)

Sample ID	y_n	$w_{m\text{-}pyro}$	$w_{m\text{-}CTR}$	$X_{WL\text{-}m}$	$X_{WL\text{-}mb}$
SC8-1180(4h)	0.8801	0.0074	0.0015	0.2248	0.1808
SC8-1180(8h)	0.8154	0.0079	0.0004	0.3464	0.3083
SC8-1180(12h)	0.7553	0.0075	0.0018	0.4714	0.4337
SC8-1180(24h)	0.6187	0.0159	0.0023	0.7310	0.6999
SC8-1180(36h)	0.5512	0.0271	0.0018	0.8518	0.8237
SC8-1180(48h)	0.5168	0.0058	0.0029	0.9445	0.9188
SC8-1200(0.5h)	0.9414	0.0121	0.0012	0.0946	0.0473
SC8-1200(0.67h)	0.9351	0.0107	0.0000	0.1075	0.0606
SC8-1200(1h)	0.9432	0.0100	0.0000	0.0928	0.0455
SC8-1200(2h)	0.9064	0.0100	0.0000	0.1655	0.1200
SC8-1200(4h)	0.8672	0.0100	0.0000	0.2432	0.1997
SC8-1200(8h)	0.7739	0.0085	0.0017	0.4330	0.3943
SC8-1200(12h)	0.6994	0.0119	0.0021	0.5758	0.5407
SC8-1200(16h)	0.6357	0.0022	0.0002	0.7118	0.6802
SC8-1200(22h)	0.5611	0.0268	0.0015	0.8321	0.8035
SC8-1200(32h)	0.5134	0.0155	0.0015	0.9397	0.9138
SC8-1250(0.67h)	0.9169	0.0110	0.0010	0.1536	0.1078
SC8-1250(1h)	0.9014	0.0110	0.0010	0.2007	0.1561
SC8-1250(2h)	0.8120	0.0110	0.0010	0.3525	0.3118
SC8-1250(3h)	0.7789	0.0100	0.0020	0.4544	0.4163
SC8-1250(4h)	0.7035	0.0110	0.0030	0.5702	0.5350
SC8-1250(4.33h)	0.6944	0.0100	0.0030	0.5882	0.5534
SC8-1250(5h)	0.6696	0.0110	0.0040	0.6386	0.6051
SC8-1250(6.5h)	0.6071	0.0110	0.0040	0.7620	0.7316
SC8-1250(8h)	0.5611	0.0090	0.0040	0.8528	0.8247
SC8-1250(12h)	0.5144	0.0120	0.0030	0.9439	0.9181
SC8-1250(16h)	0.5046	0.0110	0.0050	0.9654	0.9402

APPENDIX C

CALCULATION OF Z VALUE OF CARTER'S EQUATION FOR SC35 AND SC8 SAMPLES

Carter's equation (Equation (4-3-11)) for the rate of a diffusion-controlled reaction contains a parameter, Z, which represents the volume of product generated per unit volume of the reactant (Hulbert, 1969). For the CTR reaction in SC35 and SC8 samples, introduce the following parameters:

W_{pyro} initial weight of the pyrolyzed sample (the reactant) before any conversion

W_{CTR} final weight of the product after complete conversion

Y full conversion yield for the carbothermal reduction reaction, as defined by

$$Y = \frac{W_{CTR}}{W_{pyro}} \tag{C-1}$$

As shown in section 4.3.1, $Y = 0.33$ for the SC35 series (initial C/Si molar ratio = 2.4) and $Y = 0.49$ for the SC8 series (initial C/Si molar ratio = 4.6)

ρ_{pyro} density of the pyrolyzed sample (the reactant)

ρ_{CTR} density of the fully converted sample

Therefore, Z can be obtained by:

$$Z = \frac{W_{CTR} / \rho_{CTR}}{W_{pyro} / \rho_{pyro}} = Y \cdot \frac{\rho_{pyro}}{\rho_{CTR}} \tag{C-2}$$

In section 4.1.9, the densities of the pyrolyzed materials were estimated. The results were ρ_{pyro} = 2.16 g/cm^3 for the SC35, and ρ_{pyro} = 2.12 g/cm^3 for the SC8. In section 4.3.1, the densities of the product materials after complete carbothermal reduction

(ρ_{CTR}) were estimated. The results were ρ_{CTR} = 3.16 g/cm^3 for SC35 and ρ_{CTR} = 2.54 g/cm^3 for SC8. Therefore, the *Z* values were obtained:

$$Z_{SC35} = Y \cdot \frac{\rho_{SC35-pyro}}{\rho_{SC35-CTR}} = 0.33 \times \frac{2.16}{3.16} = 0.2257$$

$$Z_{SC8} = Y \cdot \frac{\rho_{SC8-pyro}}{\rho_{SC8-CTR}} = 0.49 \times \frac{2.12}{2.54} = 0.4090$$

APPENDIX D

PLOTS SHOWING FITTING OF WEIGHT LOSS DATA TO OTHER KINETIC EQUATIONS

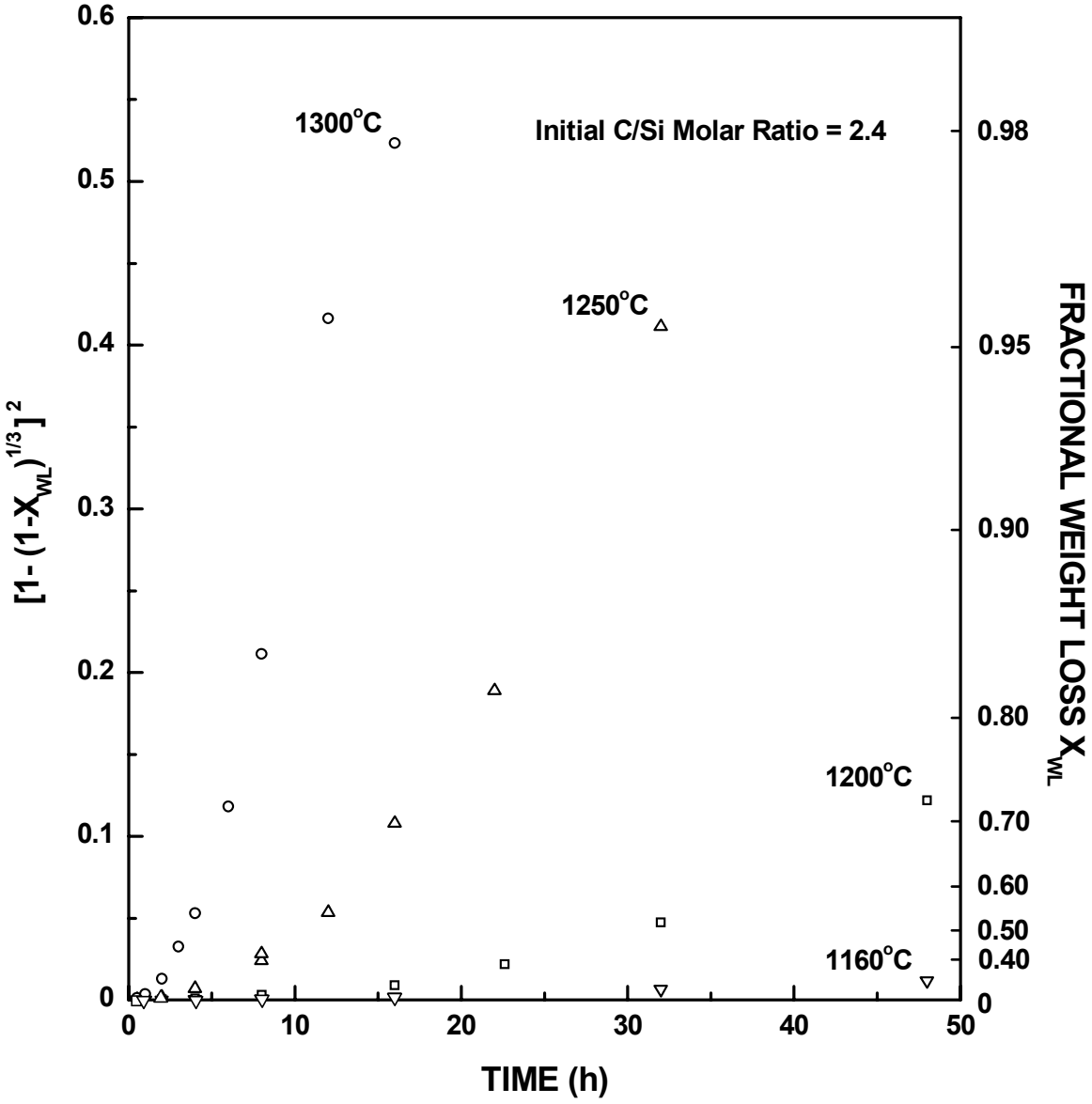

Figure D-1 Fitting of the SC35 CTR weight loss data to the Jander's equation:
$[1-(1-X)^{1/3}]^2 = kt$

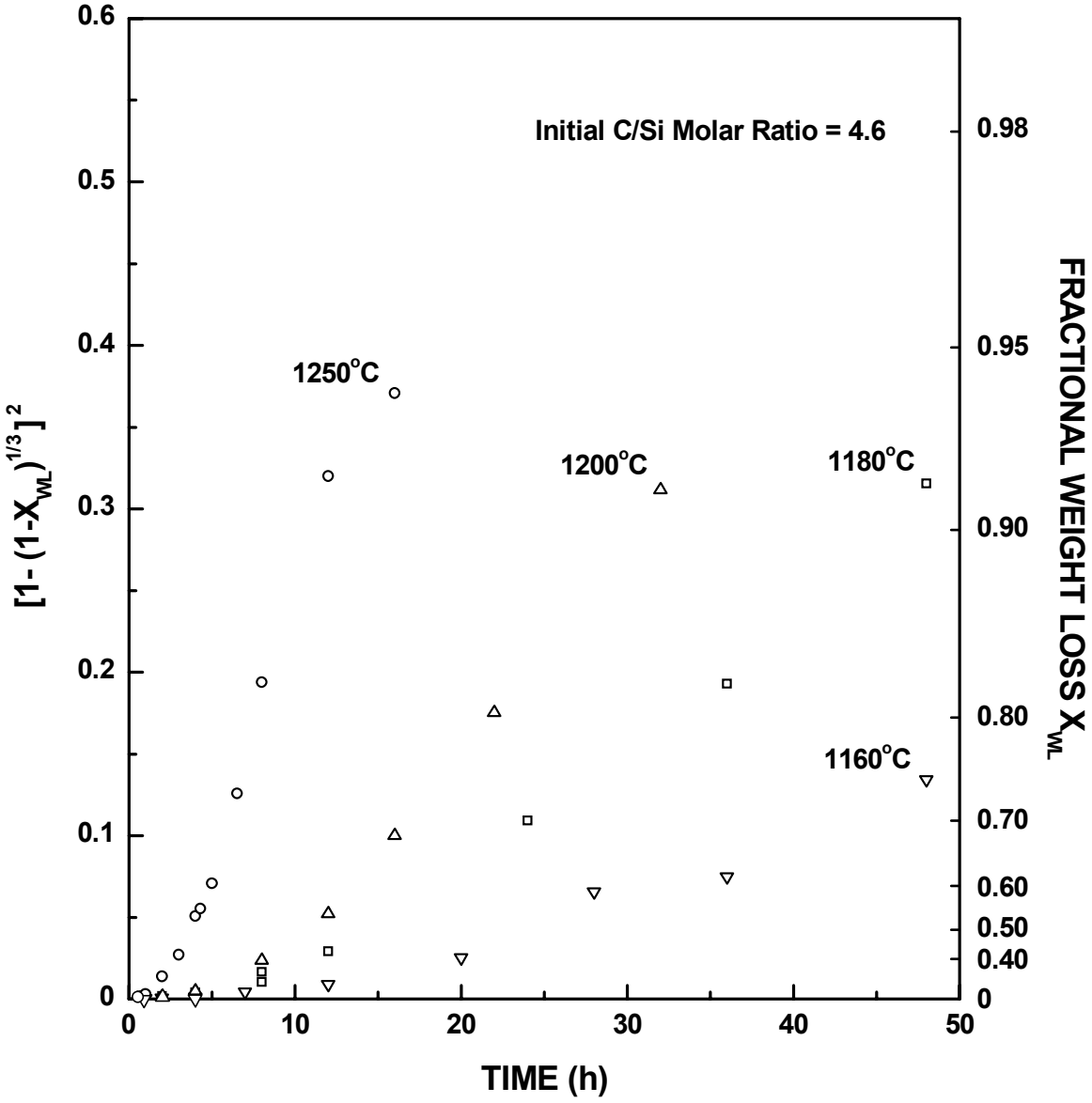

Figure D-2 Fitting of the SC8 CTR weight loss data to the Jander's equation

$$[1-(1-X)^{1/3}]^2 = kt$$

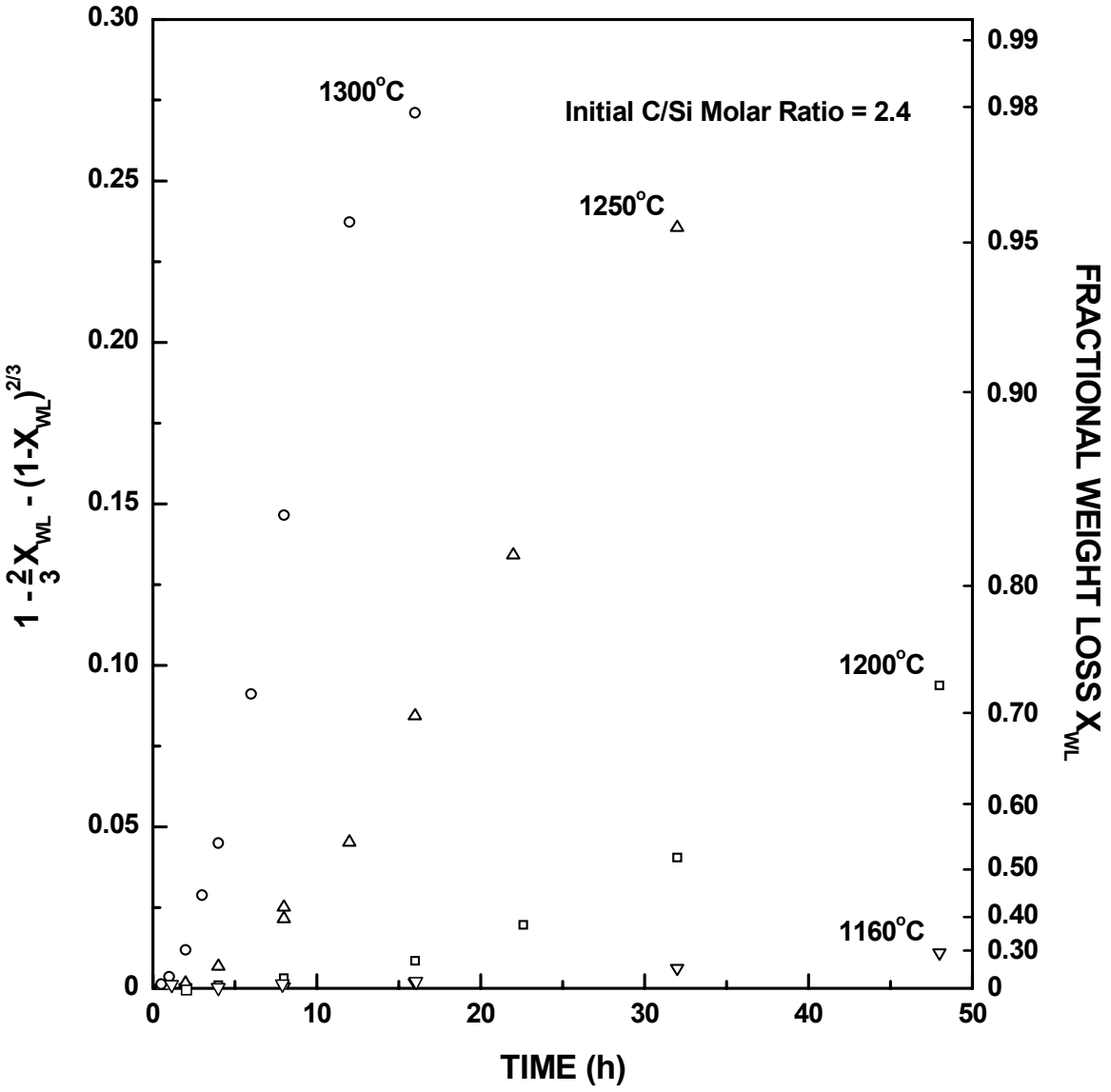

Figure D-3 Fitting of the SC35 CTR weight loss data to the Ginstling's equation:

$$1-\frac{2}{3}X-(1-X)^{2/3}=kt$$

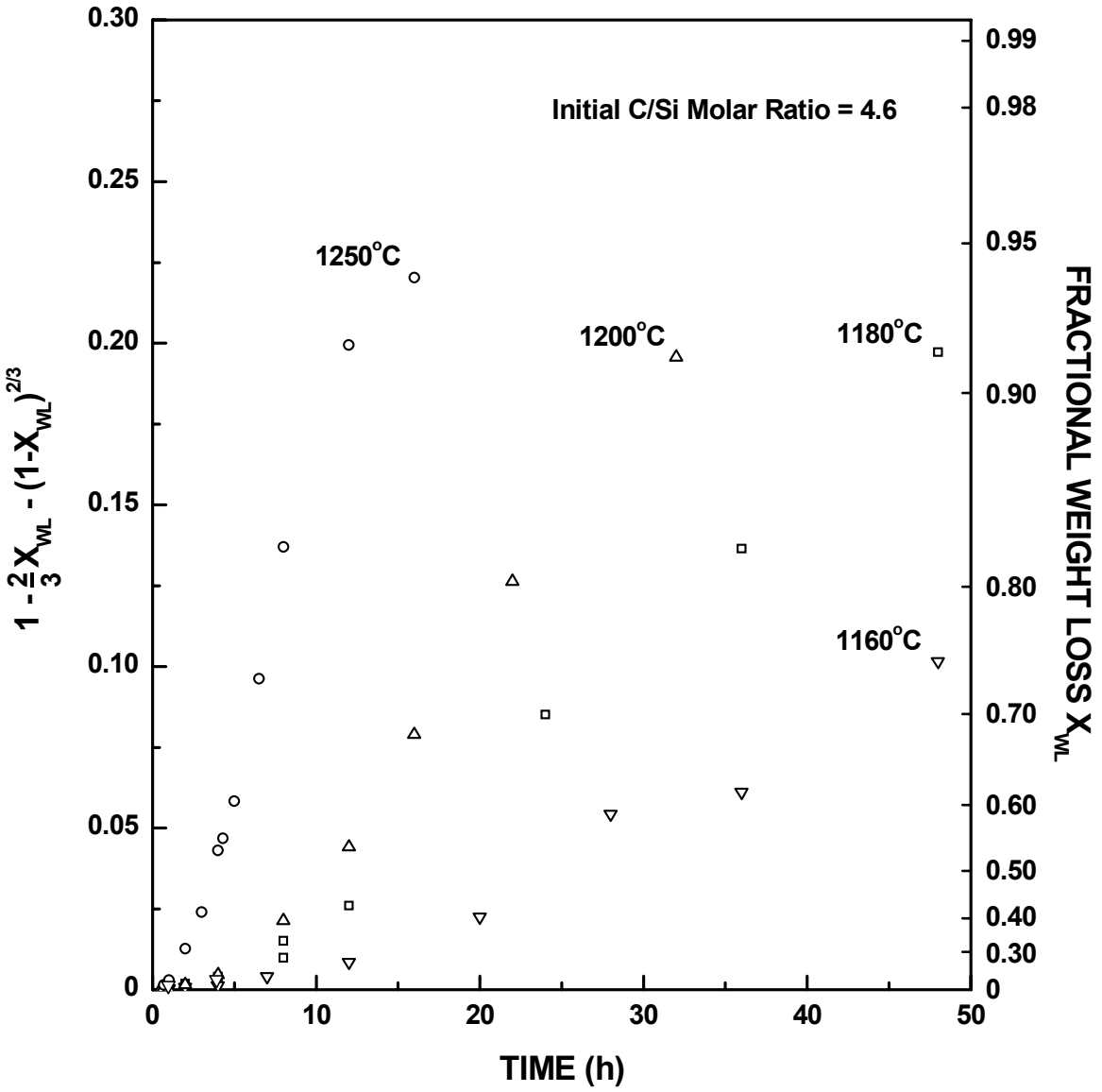

Figure D-4 Fitting of the SC8 CTR weight loss data to the Ginstling's equation:

$$1-\frac{2}{3}X-(1-X)^{2/3}=kt$$

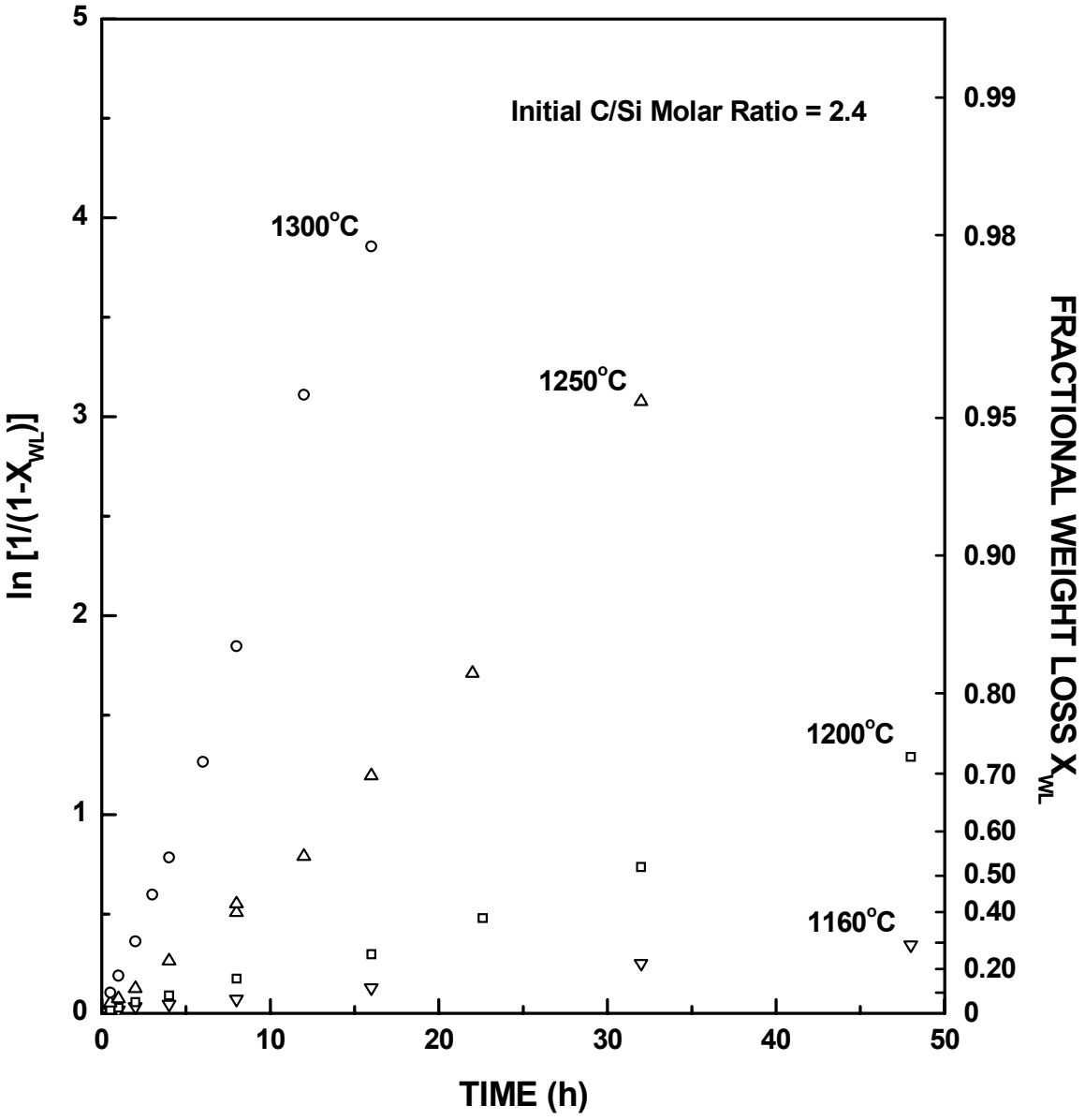

Figure D-5 Fitting of the SC35 CTR weight loss data to the First Order equation:

$$\ln\frac{1}{1-X} = kt$$

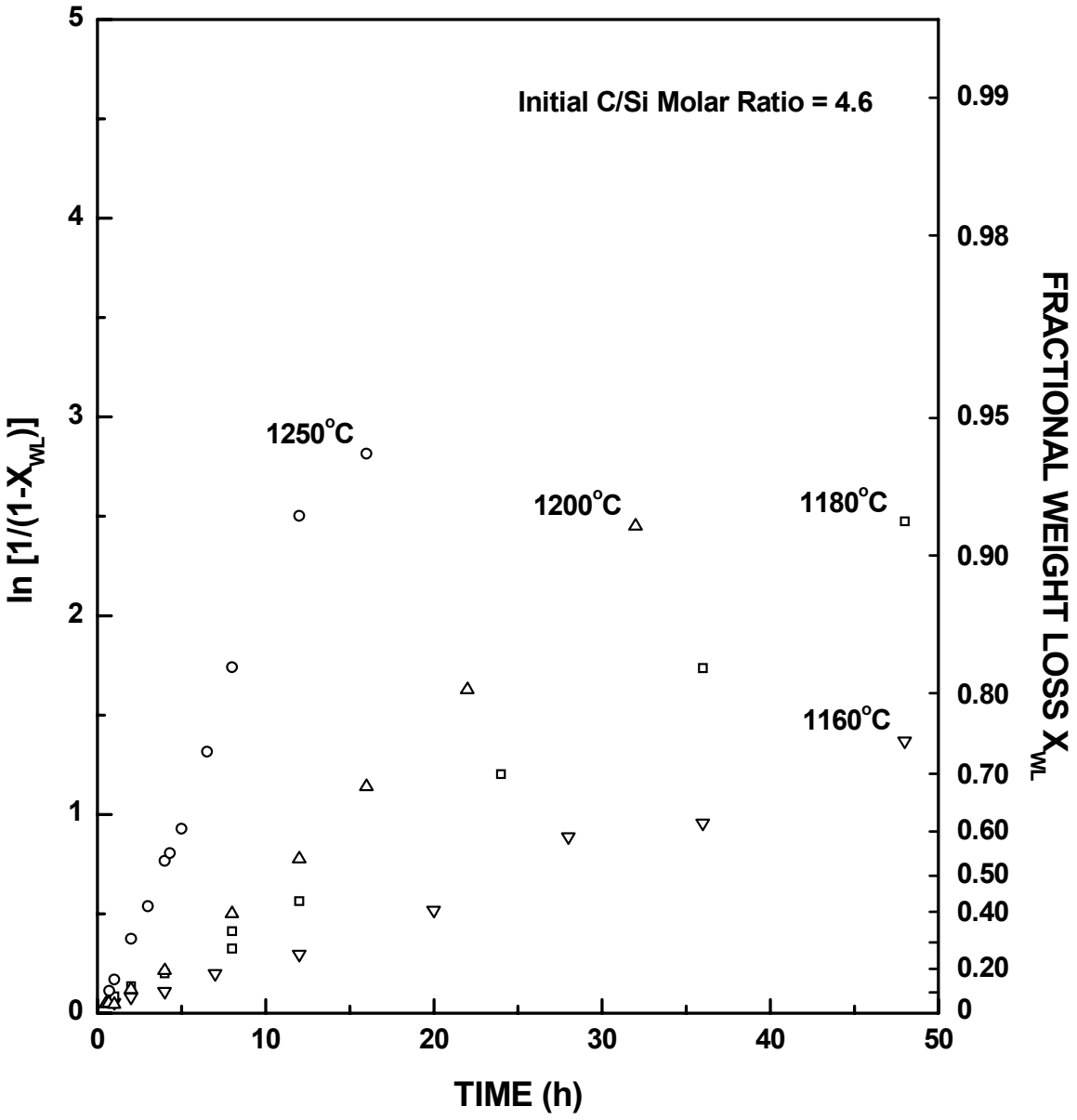

Figure D-6 Fitting of the SC8 CTR weight loss data to the First Order equation:

$$\ln\frac{1}{1-X} = kt$$

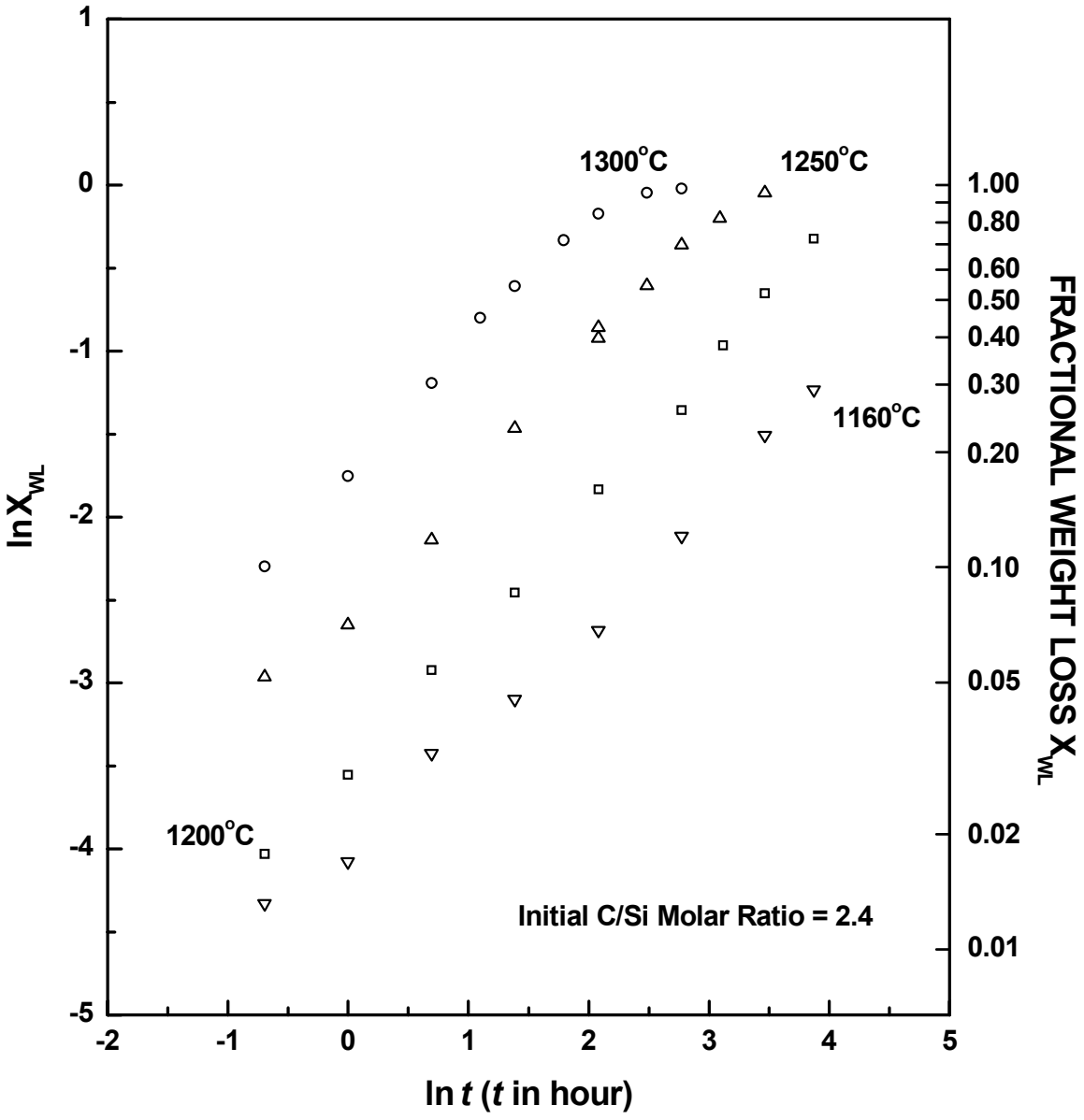

Figure D-7 Fitting of the SC35 CTR weight loss data to the Power Law equation: $X = (kt)^n$ or $\ln X = n \ln k + n \ln t$

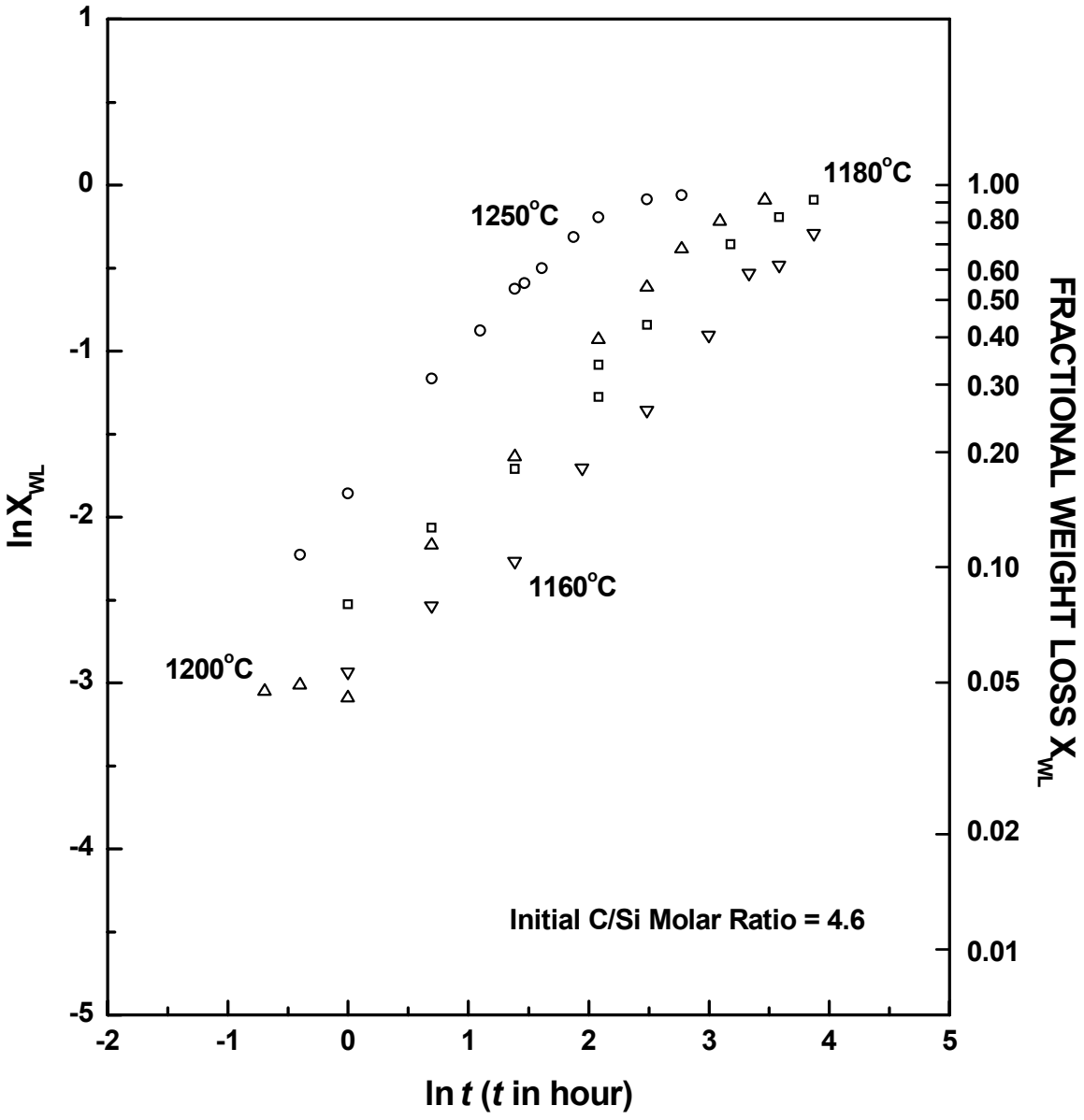

Figure D-8 Fitting of the SC8 CTR weight loss data to the Power Law equation:
$X = (kt)^n$ or $\ln X = n \ln k + n \ln t$

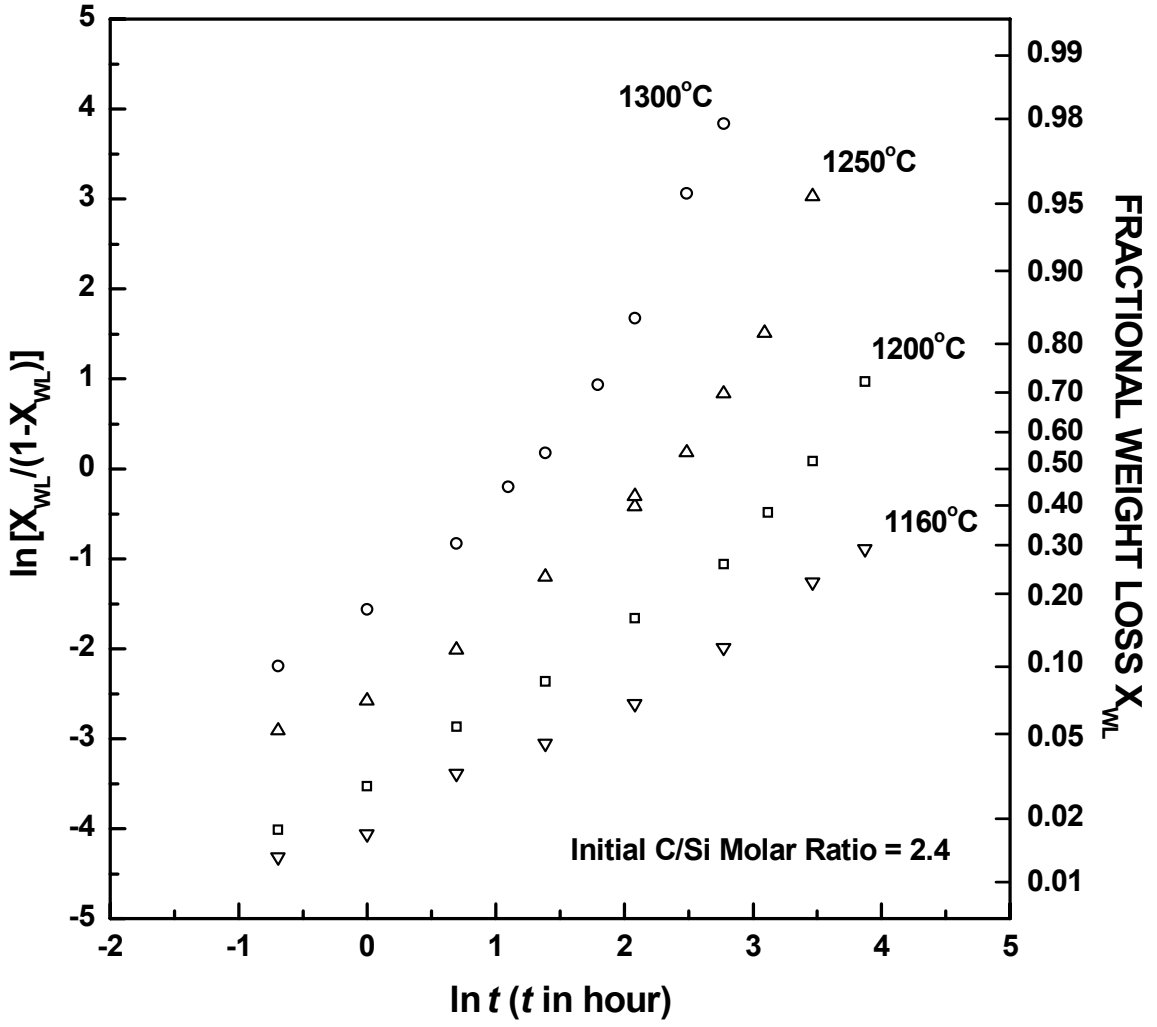

Figure D-9 Fitting of the SC35 CTR weight loss data to the Austin and Rickett equation:

$$\frac{X}{1-X} = (kt)^n \text{ or } \ln\frac{X}{1-X} = n\ln k + n\ln t$$

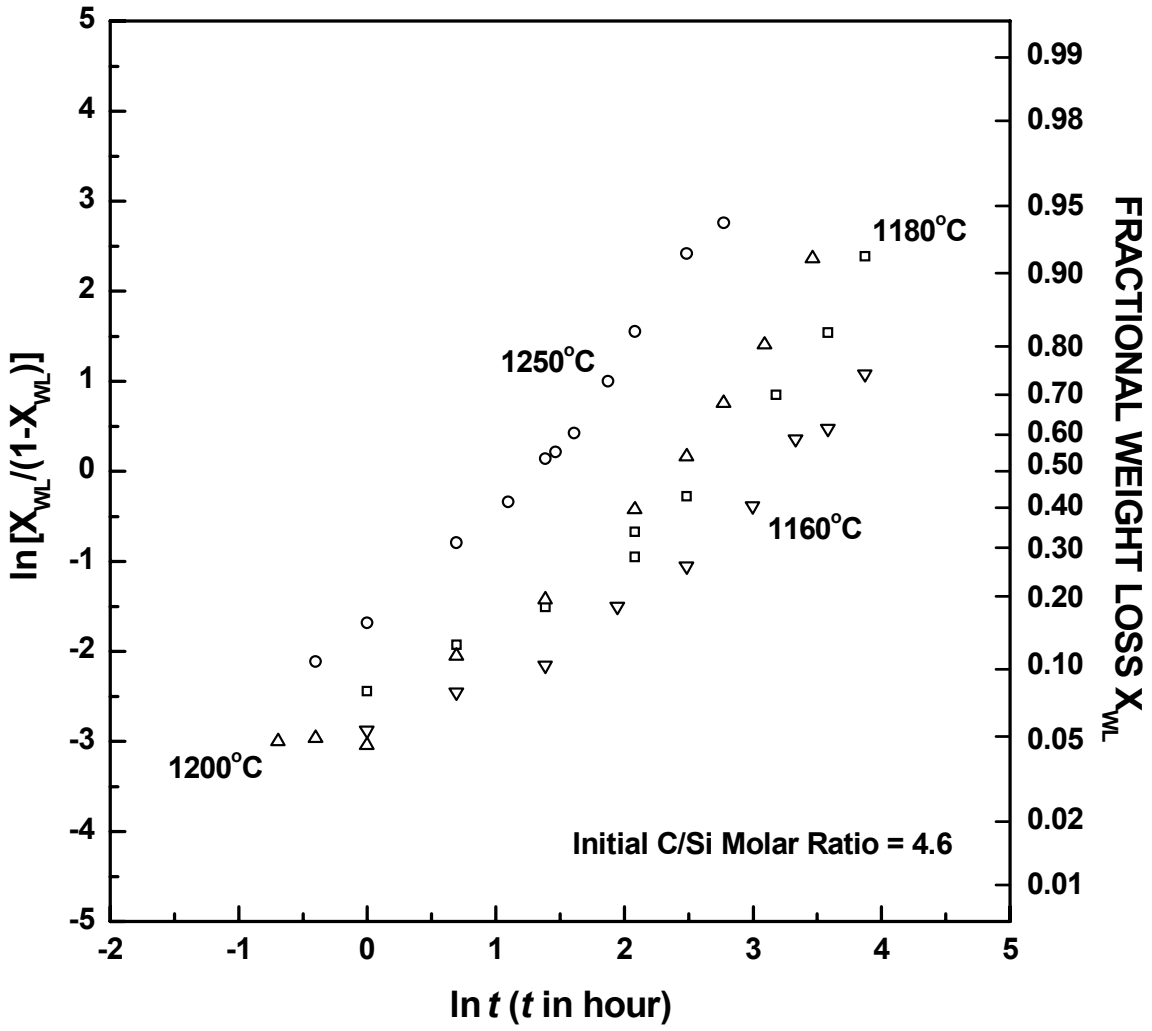

Figure D-10 Fitting of the SC8 CTR weight loss data to the Austin and Rickett equation:

$$\frac{X}{1-X} = (kt)^n \text{ or } \ln\frac{X}{1-X} = n\ln k + n\ln t$$

Table D-1 The reaction rate constants k_{FO} and the activation energy E for the carbothermal reduction reaction for SC35 samples.

Temperature (°C)	k_{FO} (h^{-1})	r_L	Fitting range for time t	Fitting range for X_{WL}
1160	$(7.01 \pm 0.14) \times 10^{-3}$	0.9988	0.5 - 48 h	0.0132-0.2909
1200	$(25.6 \pm 1.3) \times 10^{-3}$	0.9908	0.5 - 48 h	0.0178-0.7249
1250	$(91.6 \pm 5.2) \times 10^{-3}$	0.9871	0.5 - 32 h	0.0516-0.9539
1300	$(259 \pm 11) \times 10^{-3}$	0.9944	0.5 - 12 h	0.1005-0.9554
Reaction activation energy E (kJ/mol)		482 ± 23		

Table D-2 The reaction rate constants k_{FO} and the activation energy E for the carbothermal reduction reaction for SC8 samples.

Temperature (°C)	k_{FO} (h^{-1})	r_L	Fitting range for time t	Fitting range for X_{WL}
1160	$(28.1 \pm 1.1) \times 10^{-3}$	0.9949	1 - 48 h	0.0513-0.7458
1180	$(50.3 \pm 1.1) \times 10^{-3}$	0.9983	1 - 48 h	0.0800-0.9157
1200	$(77.8 \pm 1.7) \times 10^{-3}$	0.9986	1 - 32 h	0.0455-0.9138
1250	$(215 \pm 5) \times 10^{-3}$	0.9979	0.67 - 12 h	0.1078-0.9181
Reaction activation energy E (kJ/mol)		404 ± 18		

Note: The results in the above tables were obtained by fitting the weight loss kinetic data (after correction for moisture adsorption and blown-off powder, i.e., $X_{WL} = X_{WL\text{-}mb}$) to the First Order model. The linear correlation coefficient r_L and the range of fitting for the carbothermal reaction are also given in the tables.

APPENDIX E

DETERMINATION OF WHETHER THERE IS SiC IN PYROLYZED SAMPLES

In the quantitative XRD study, an assumption made was that there was no SiC formed in the pyrolyzed material. As a result, the fitted calibration curve was forced to pass through the origin. In Chapter IV, the author pointed out that this assumption was supported by the absence of any obvious SiC diffraction line in the XRD patterns and the electron diffraction patterns of the SC35 and/or SC8 pyrolyzed samples. In this section, another piece of evidence is provided to show that the amount of SiC in the pyrolyzed sample should be very small.

As described in Section 3.3.2, the "1100^{o}C/1495^{o}C" mixtures used for QXRD calibration curves include those which contain 1, 3 and 5 wt% of the fully converted (i.e., "1495^{o}C") powders and 99, 97 and 95 wt% of the pyrolyzed (i.e. "1100^{o}C") powders, respectively. The integrated intensities were obtained over the 2θ range for the two most intense SiC diffraction lines (i.e., over the ranges of ~33-38^{o} for the (111) line and ~58-62^{o} for the (220) line). By comparison, the integrated intensities for the pyrolyzed sample alone in the same 2θ ranges were also obtained. The integrated intensities values are shown in Table E-1. Each integral intensity value is the average from at least 5 scans. As described in Section 3.3.2, the XRD pattern was collected using a step scan mode with a step size of 0.01º and scan speed of 0.5 second/step.

Table E-1 shows that the integrated intensities for the pyrolyzed samples were either small positive or negative values. However, the values are so low that they can be considered to be zero within experimental error. Furthermore, Table E-1 shows that the

"1100°C /1495°C" mixture with as little as 1 wt% fully converted ("1495°C") sample has significantly larger (more positive) integrated intensities for both SiC lines in each sample (i.e., SC35 and SC8). This point is also illustrated clearly by the plots in Figure E-1. Therefore, it is reasonable to conclude that the amount of SiC in the pyrolyzed sample is very low, i.e., less than 1% by weight.

Table E-1 Integral intensities of SiC diffraction lines for the pyrolyzed material ("pyro") and some of the "1100°C/1495°C" mixtures for the SC8 and SC35 QXRD calibration curves.

Sample		Pyrolyzed	99% "1100°C" + 1% "1495°C"	97% "1100°C" + 3% "1495°C"	95% "1100°C" + 5% "1495°C"
SC35	$I_{(111)}$	3.12	7.70	15.12	22.32
	$I_{(220)}$	1.20	3.54	7.75	12.53
SC8	$I_{(111)}$	-1.87	1.38	7.08	11.23
	$I_{(220)}$	-1.45	-0.05	3.25	5.80

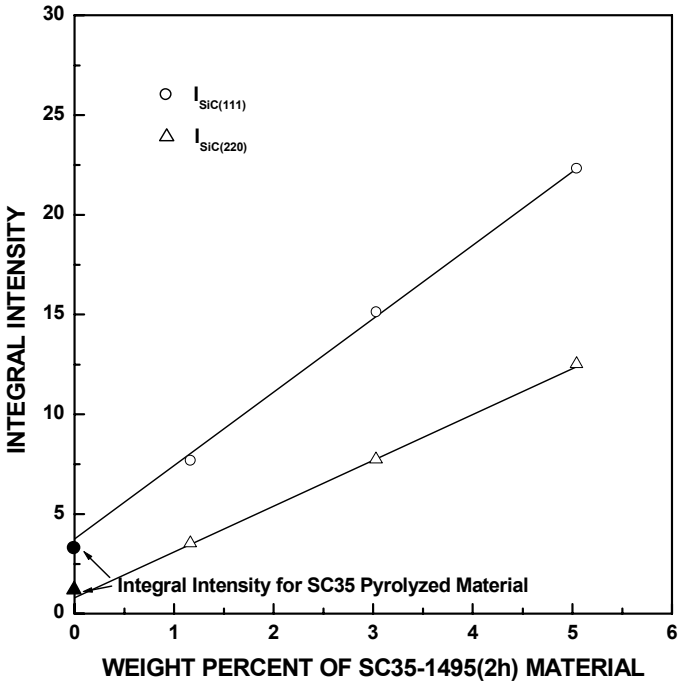

(a)

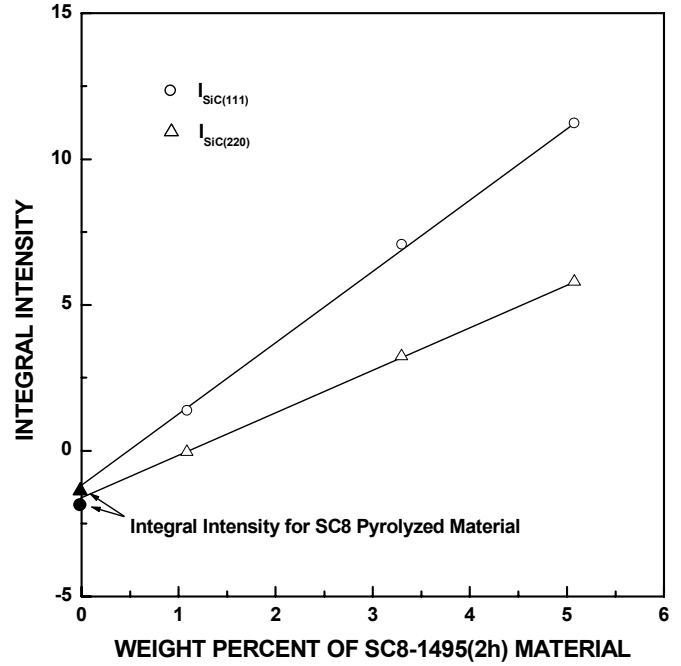

(b)

Figure E-1 Plots of the integral XRD intensity of SiC(111) and SiC(220) lines as a function of the weight percent of 1495°C CTR material in "1100°C/1495°C" mixtures for (a) SC35 samples and (b) SC8 samples. Also shown are the integral intensity values for the 1100°C-pyrolyzed materials.

APPENDIX F

SUMMARY OF GAS ADSORPTION ANALYSIS DATA

Table F-1 Summary of BET and Langmuir specific surface area data for the SC35, SC8, and SC42 pyrolyzed and CTR samples.

Sample ID	X_{WL}	SA_{BET} (m^2/g)	C	V_{m_BET} (cm^3/g)	r_{L_BET}	SA_{Lang} (m^2/g)	*b*	V_{m_Lang} (cm^3/g)	r_{L_Lang}
SC35-1100(2h) pyrolyzed	0	**0.7**	18.2	0.1	0.99213	1.1	0.11994	0.2	0.97553
SC35-1160(0.5h)	0.0132	**0.6**	50.4	0.1	0.99842	1.0	0.0589	0.2	0.99849
SC35-1160(1h)	0.0170	**0.9**	34.2	0.2	0.99920	1.3	0.0742	0.3	0.99747
SC35-1160(2h)	0.0326	3.5	-177.1	0.8	0.99876	**4.9**	0.0198	1.1	0.99970
SC35-1160(4h)	0.0451	**9.7**	354.6	2.2	0.99969	14.0	0.0314	3.2	0.99843
SC35-1160(8h)	0.0683	**13.8**	619.8	3.2	0.99968	19.9	0.0294	4.6	0.99845
SC35-1160(16h)	0.1203	**15.5**	222.9	3.6	0.99986	22.5	0.0334	5.2	0.99785
SC35-1160(32h)	0.2213	**24.9**	171.8	5.7	0.99993	36.1	0.0349	8.3	0.99736
SC35-1160(48h)	0.2909	**34.6**	172.6	7.9	0.99994	50.1	0.0350	11.5	0.99711
SC35-1200(0.5h)	0.0178	**2.5**	157.5	0.6	0.99954	3.7	0.0372	0.8	0.99870

Note: For the BET model, SA_{BET} is the BET specific surface area, ***C*** is the *C* constant, and r_{L_BET} is the linear correlation coefficient. For the Langmuir model, SA_{Lang} is the Langmuir specific surface area, ***b*** is the *b* constant, and r_{L_Lang} is the linear correlation coefficient. The specific surface area value (BET or Langmuir) in **bold** is the adopted specific surface area for that sample.

Table F-1 (continued)

Sample ID	X_{WL}	SA_{BET} (m^2/g)	C	V_{m_BET} (cm^3/g)	r_{L_BET}	SA_{Lang} (m^2/g)	*b*	V_{m_Lang} (cm^3/g)	r_{L_Lang}
SC35-1200(1h)	0.0286	7.0	-4010.2	0.2	1.59792	**10.0**	0.0272	2.3	0.99929
SC35-1200(2h)	0.0538	**11.2**	324.0	2.6	0.99970	16.2	0.0317	3.7	0.99841
SC35-1200(4h)	0.0859	**13.0**	227.6	3.0	0.99980	18.8	0.0335	4.3	0.99802
SC35-1200(8h)	0.1598	**19.1**	186.7	4.4	0.99990	27.7	0.0344	6.4	0.99758
SC35-1200(16h)	0.2577	**31.5**	149.2	7.2	0.99995	45.7	0.0362	10.5	0.99689
SC35-1200(22.6h)	0.3804	**48.1**	175.5	11.0	0.99994	69.4	0.0342	15.9	0.99707
SC35-1200(32h)	0.5208	**73.1**	153.4	16.8	0.99996	105.9	0.0359	24.3	0.99716
SC35-1200(48h)	0.7249	**130.9**	160.4	30.1	0.99996	189.8	0.0359	43.6	0.99699
SC35-1250(0.5h)	0.0516	**9.2**	329.8	2.1	0.99975	13.3	0.03170	3.1	0.99834
SC35-1250(1h)	0.0707	**10.2**	226.9	2.3	0.99982	14.8	0.03357	3.4	0.99801
SC35-1250(2h)	0.1179	**15.3**	214.7	3.5	0.99985	22.1	0.03367	5.1	0.99782
SC35-1250(4h)	0.2314	**25.7**	167.4	5.9	0.99993	37.2	0.03509	8.6	0.99735
SC35-1250(8h)	0.4108	**48.8**	161.1	11.2	0.99995	70.6	0.03514	16.2	0.99697
SC35-1250(12h)	0.5455	NA	NA	NA	NA	NA	NA	NA	NA
SC35-1250(16h)	0.6974	**116.9**	167.7	26.8	0.99996	169.7	0.03592	39.0	0.99708
SC35-1250(22h)	0.8191	**167.9**	169.2	38.6	0.99996	243.2	0.03538	55.9	0.99706

Table F-1 (continued)

Sample ID	X_{WL}	SA_{BET} (m^2/g)	C	V_{m_BET} (cm^3/g)	r_{L_BET}	SA_{Lang} (m^2/g)	*b*	V_{m_Lang} (cm^3/g)	r_{L_Lang}
SC35-1250(32h)	0.9539	**206.0**	180.3	47.3	0.99996	296.9	0.03386	68.2	0.99719
SC35-1300(0.5h)	0.1005	**12.0**	250.7	2.8	0.99978	17.3	0.03288	4.0	0.99813
SC35-1300(1h)	0.1733	**18.1**	147.5	4.1	0.99994	26.2	0.03656	6.0	0.99729
SC35-1300(2h)	0.3035	**35.0**	181.1	8.0	0.99992	50.6	0.03479	11.6	0.99726
SC35-1300(3h)	0.4497	NA	NA	NA	NA	NA	NA	NA	NA
SC35-1300(4h)	0.5438	**77.0**	171.9	17.7	0.99995	111.4	0.03492	25.6	0.99733
SC35-1300(6h)	0.7173	NA	NA	NA	NA	NA	NA	NA	NA
SC35-1300(8h)	0.8422	**172.3**	164.9	39.6	0.99996	249.8	0.03566	57.4	0.99694
SC35-1300(12h)	0.9554	**178.0**	185.5	40.9	0.99995	257.8	0.03484	59.2	0.99719
SC35-1300(16h)	0.9788	**76.0**	186.3	17.5	1.00000	109.7	0.03394	25.2	0.99700
SC8-1100(4h) pyrolyzed - Run1	0	**2.8**	242.4	0.6	0.99972	4.1	0.03286	0.9	0.99802
SC8-1100(4h) pyrolyzed - Run2	0	2.3	-86.2	0.5	0.99786	**3.3**	0.53550	0.8	0.99985
SC8-1120(1h)	0	2.4	-66.6	0.6	0.99714	**3.4**	0.00696	0.8	0.99993
SC8-1160(1h)	0.0531	4.9	-91.2	1.1	0.998323	**6.9**	0.01217	1.6	0.99990
SC8-1160(2h)	0.0792	18.2	-111.5	4.2	0.99852	**25.7**	0.01381	5.9	0.99983

Table F-1 (continued)

Sample ID	X_{WL}	SA_{BET} (m^2/g)	C	V_{m_BET} (cm^3/g)	r_{L_BET}	SA_{Lang} (m^2/g)	*b*	V_{m_Lang} (cm^3/g)	r_{L_Lang}
SC8-1160(4h)	0.1034	31.6	-129.8	7.2	0.998573	**44.4**	0.01568	10.2	0.99975
SC8-1160(7h)	0.1819	72.1	-197.8	16.6	0.998908	**102.1**	0.01963	23.5	0.99956
SC8-1160(12h)	0.2578	132.2	-380.0	30.4	0.999254	**188.1**	0.02296	43.2	0.99906
SC8-1160(20h)	0.4046	**247.4**	416.5	56.8	0.999737	355.5	0.02980	81.7	0.99812
SC8-1160(28h)	0.5881	**316.8**	166.5	72.8	0.999919	459.4	0.03545	105.5	0.99723
SC8-1160(36h)	0.6162	**351.4**	151.8	80.7	0.999949	508.2	0.03558	116.8	0.99680
SC8-1180(48h)	0.7458	**420.7**	133.9	96.6	0.999972	608.6	0.03653	139.8	0.99644
SC8-1180(1h)	0.0800	8.6	-120.0	2.0	0.99847	**12.2**	0.01570	2.8	0.99985
SC8-1180(2h)	0.1263	26.7	-129.0	6.1	0.99855	**37.6**	0.01575	8.6	0.99976
SC8-1180(4h)	0.1808	66.7	-170.0	15.3	0.99886	**94.4**	0.01855	21.7	0.99960
SC8-1180(8h)	0.3083	130.0	-614.6	29.9	0.99938	**185.4**	0.02450	42.6	0.99888
SC8-1180(12h)	0.4337	**216.2**	410.0	49.7	0.99973	311.0	0.03001	71.4	0.99811
SC8-1180(24h)	0.6999	**368.4**	143.6	84.6	0.99996	533.9	0.03640	122.6	0.99679
SC8-1180(36h)	0.8237	**473.7**	128.5	108.8	0.99998	685.4	0.03693	157.4	0.99630
SC8-1180(48h)	0.9188	**575.7**	124.5	132.3	0.99997	833.3	0.03738	191.4	0.99597
SC8-1200(0.5h)	0.0473	8.2	-146.8	1.9	0.99869	**11.6**	0.017809	2.7	0.99975

Table F-1 (continued)

Sample ID	X_{WL}	SA_{BET} (m^2/g)	C	V_{m_BET} (cm^3/g)	r_{L_BET}	SA_{Lang} (m^2/g)	*b*	V_{m_Lang} (cm^3/g)	r_{L_Lang}
SC8-1200(0.67h)	0.0606	12.5	-121.2	2.9	0.99852	**17.7**	0.015687	4.1	0.99981
SC8-1200(1h)	0.0455	24.2	-130.0	5.6	0.99857	**34.1**	0.015905	7.8	0.99976
SC8-1200(2h)	0.1200	51.6	-145.4	11.9	9.98772	**73.0**	0.017528	16.8	0.99968
SC8-1200(4h)	0.1997	106.7	-326.9	24.5	0.99920	**152.2**	0.023018	35.0	0.99919
SC8-1200(8h)	0.3943	199.1	**363.5**	45.7	0.99977	286.8	0.030772	65.9	0.99802
SC8-1200(12h)	0.5407	279.3	**184.2**	64.1	0.99991	404.7	0.034717	93.0	0.99736
SC8-1200(16h)	0.6802	385.0	**140.0**	88.4	0.99996	557.2	0.036359	128.0	0.99661
SC8-1200(22h)	0.8035	484.0	**128.8**	111.2	0.99997	700.7	0.037129	161.0	0.99614
SC8-1200(32h)	0.9138	603.1	**123.5**	138.5	0.99998	873.8	0.037576	200.7	0.99633
SC8-1250(0.67h)	0.1078	50.1	-237.1	11.5	0.99895	**69.6**	0.01756	16.0	0.99962
SC8-1250(1h)	0.1561	83.8	-427.5	19.2	0.99925	**117.0**	0.02019	26.9	0.99937
SC8-1250(2h)	0.3118	**153.0**	448.3	35.1	0.99972	215.3	0.02632	49.5	0.99861
SC8-1250(3h)	0.4163	**234.3**	175.1	53.8	0.99998	319.8	0.02720	73.5	0.99894
SC8-1250(4h)	0.5350	**278.4**	160.2	64.0	0.99995	393.3	0.03137	90.4	0.99764
SC8-1250(5h)	0.6051	**334.2**	147.7	76.8	0.99995	478.2	0.03369	109.9	0.99698
SC8-1250(6.5h)	0.7316	**446.8**	129.9	102.6	0.99997	640.4	0.03514	147.1	0.99661

Table F-1 (continued)

Sample ID	X_{WL}	SA_{BET} (m^2/g)	C	V_{m_BET} (cm^3/g)	r_{L_BET}	SA_{Lang} (m^2/g)	*b*	V_{m_Lang} (cm^3/g)	r_{L_Lang}
SC8-1250(8h)	0.8247	**547.1**	120.2	125.7	0.99997	740.5	0.02846	170.1	0.99808
SC8-1250(12h)	0.9181	**613.9**	124.5	141.0	0.99998	879.9	0.03550	202.1	0.99640
SC8-1250(16h)	0.9402	**662.0**	122.6	152.1	0.99998	949.0	0.03567	218.0	0.99636
SC42-600(2h)	0	260.4	-70.8	59.8	0.99797	**356.6**	0.00508	81.9	0.99998

Table F-2 Summary of BET and Langmuir specific surface area data for the glassy carbon obtained by heat treating phenolic resin at different temperatures in Ar. (The symbols in the first row have the same meaning as in Table F-1).

Heat Treatment Condition	**Run #**	SA_{BET} (m^2/g)	**C**	V_{m_BET} (cm^3/g)	r_{L_BET}	SA_{Lang} (m^2/g)	***b***	V_{m_Lang} (cm^3/g)	r_{L_Lang}
1100(2h)	1	**7.4**	1.8	1.7	0.70458	-31.6	-2.4	-7.3	-0.51953
1100(2h)	2	**0.2**	15.4	0.05	0.97894	0.4	0.1409	0.09	0.97208
1100(2h)	3	2.6	-164.7	0.6	0.99867	**3.6**	0.0161	0.8	0.99981
1300(2h)	1	1.8	-791.0	0.4	0.99891	**2.7**	0.0330	0.6	0.99866
1100(2h)-1475(2h)	1	**0.7**	8.0	0.2	0.98809	1.3	0.2661	0.3	0.97144
1100(2h)-1475(2h)	2	**0.7**	5.4	0.2	0.96098	1.7	0.4838	0.4	0.89749

Table F-3 Summary of micropore analysis results.

Sample ID	X_{WL}	V_{int}	k_{micro}	r_L	V_{micro} (cm^3/g)	$V_{BJH\text{-}Total}$ (cm^3/g)	V_{Pore} (cm^3/g)	$V_{micro\text{-}r}$ (%)	SA_{micro} (m^2/g)	$A_{BJH\text{-}Total}$ (m^2/g)	SA (m^2/g)	$SA_{micro\text{-}r}$ (%)
SC35-1100(2h) pyrolyzed	0	-0.123	0.063	0.9838	-0.0002	0.0016	0.0016	-11.6	-0.3	0.9	0.7	-50.1
SC35-1160(0.5h)	0.0132	-0.022	0.044	0.9903	0.0000	0.0012	0.0012	-2.9	0.0	0.6	0.6	-6.5
SC35-1160(1h)	0.0170	-0.084	0.070	0.9929	-0.0001	0.0015	0.0015	-8.6	-0.2	1.0	0.9	-25.5
SC35-1160(2h)	0.0326	0.474	0.127	0.9906	0.0007	0.0019	0.0028	25.9	1.5	1.3	4.9	30.7
SC35-1160(4h)	0.0451	0.556	0.507	0.9989	0.0009	0.0059	0.0073	11.8	1.9	6.9	9.7	19.3
SC35-1160(8h)	0.0683	0.932	0.694	0.9991	0.0014	0.0119	0.0138	10.5	3.1	10.2	13.8	22.4
SC35-1160(16h)	0.1203	0.689	0.849	0.9998	0.0011	0.0245	0.0255	4.2	2.4	13.8	15.5	15.5
SC35-1160(32h)	0.2213	0.829	1.416	0.9999	0.0013	0.0562	0.0571	2.2	3.0	23.8	24.9	12.1
SC35-1160(48h)	0.2909	1.162	1.963	1.0000	0.0018	0.0871	0.0882	2.0	4.2	33.0	34.6	12.2
SC35-1200(0.5h)	0.0178	0.075	0.145	0.9958	0.0001	0.0024	0.0025	4.6	0.3	2.1	2.5	11.0
SC35-1200(1h)	0.0286	0.591	0.325	0.9948	0.0009	0.0037	0.0051	17.9	1.9	3.9	10.0	19.4

Note: In the micropore analysis, $\boldsymbol{V_{int}}$ and $\boldsymbol{k_{micro}}$ are the y-intercept and the slope of the t-plot, respectively; $\boldsymbol{r_L}$ is the linear correlation coefficient for the fitting of the t-plot; $\boldsymbol{V_{micro}}$ is the micropore volume; $\boldsymbol{V_{BJH\text{-}Total}}$ is the maximum BJH cumulative specific pore volume; $\boldsymbol{V_{Pore}}$ is the total specific pore volume determined at a relative pressure of ~0.995; $\boldsymbol{V_{micro\text{-}r}}$ is the percentage of the micropore volume with respect to the total specific pore volume (i.e., $\boldsymbol{V_{micro\text{-}r}} = (\boldsymbol{V_{micro}} / \boldsymbol{V_{Pore}}) \times 100\%$); $\boldsymbol{SA_{micro}}$ is the micropore area; $\boldsymbol{A_{BJH\text{-}Total}}$ is the maximum BJH cumulative specific surface area; $\boldsymbol{SA}$ is the total specific surface area of the material (from the BET or Langmuir model); $\boldsymbol{SA_{micro\text{-}r}}$ is the percentage of the micropore area with respect to the total specific surface area (i.e., $\boldsymbol{SA_{micro\text{-}r}} = (\boldsymbol{SA_{micro}} / \boldsymbol{SA}) \times 100\%$).

Table F-3 (continued)

Sample ID	X_{WL}	V_{int}	k_{micro}	r_L	V_{micro} (cm^3/g)	$V_{BJH\text{-}Total}$ (cm^3/g)	V_{Pore} (cm^3/g)	$V_{micro\text{-}r}$ (%)	SA_{micro} (m^2/g)	$A_{BJH\text{-}Total}$ (m^2/g)	SA (m^2/g)	$SA_{micro\text{-}r}$ (%)
SC35-1200(2h)	0.0538	0.623	0.588	0.9989	0.0010	0.0079	0.0093	10.3	2.1	8.5	11.2	18.9
SC35-1200(4h)	0.0859	0.579	0.710	0.9994	0.0009	0.0150	0.0163	5.5	2.0	11.0	13.0	15.5
SC35-1200(8h)	0.1598	0.711	1.073	0.9998	0.0011	0.0362	0.0372	3.0	2.5	17.6	19.1	13.3
SC35-1200(16h)	0.2577	0.822	1.834	1.0000	0.0013	0.0768	0.0777	1.6	3.1	30.5	31.5	10.0
SC35-1200(22.6h)	0.3804	1.646	2.723	1.0000	0.0025	0.1272	0.1288	2.0	6.0	46.0	48.1	12.4
SC35-1200(32h)	0.5208	2.095	4.213	1.0000	0.0032	0.2162	0.2169	1.5	7.9	73.0	73.1	10.8
SC35-1200(48h)	0.7249	3.959	7.512	1.0000	0.0061	0.4007	0.4035	1.5	14.7	129.6	130.9	11.2
SC35-1250(0.5h)	0.0516	0.522	0.480	0.9993	0.0008	0.0069	0.0082	9.8	1.8	6.5	9.2	19.3
SC35-1250(1h)	0.0707	0.456	0.558	0.9995	0.0007	0.0117	0.0125	5.7	1.6	8.8	10.2	15.6
SC35-1250(2h)	0.1179	0.650	0.840	0.9996	0.0010	0.0248	0.0258	3.9	2.3	13.4	15.3	14.9
SC35-1250(4h)	0.2314	0.837	1.465	0.9999	0.0013	0.0584	0.0593	2.2	3.1	24.4	25.7	11.9
SC35-1250(8h)	0.4108	1.480	2.801	1.0000	0.0023	0.1341	0.1352	1.7	5.5	47.7	48.8	11.3
SC35-1250(12h)	0.5455	NA	NA	NA	NA	NA	NA	NA	NA	NA	NA	NA
SC35-1250(16h)	0.6974	3.789	6.657	1.0000	0.0059	0.3758	0.3772	1.6	13.9	117.6	116.9	11.9
SC35-1250(22h)	0.8191	5.511	9.548	1.0000	0.0085	0.5657	0.5678	1.5	20.2	169.5	167.9	12.0
SC35-1250(32h)	0.9539	7.436	11.582	1.0000	0.0115	0.8185	0.8159	1.4	26.9	212.5	206.0	13.0
SC35-1300(0.5h)	0.1005	0.579	0.645	0.9994	0.0009	0.0187	0.0197	4.6	2.0	10.3	12.0	16.7

Table F-3 (continued)

Sample ID	X_{WL}	V_{int}	k_{micro}	r_L	V_{micro} (cm^3/g)	$V_{BJH\text{-}Total}$ (cm^3/g)	V_{Pore} (cm^3/g)	$V_{micro\text{-}r}$ (%)	SA_{micro} (m^2/g)	$A_{BJH\text{-}Total}$ (m^2/g)	SA (m^2/g)	$SA_{micro\text{-}r}$ (%)
SC35-1300(1h)	0.1733	0.470	1.051	0.9999	0.0007	0.0375	0.0380	1.9	1.8	17.5	18.1	10.0
SC35-1300(2h)	0.3035	1.245	1.970	0.9999	0.0019	0.0891	0.0907	2.1	4.5	32.6	35.0	12.8
SC35-1300(3h)	0.4497	NA	NA	NA	NA	NA	NA	NA	NA	NA	NA	NA
SC35-1300(4h)	0.5438	2.655	4.350	1.0000	0.0041	0.2336	0.2359	1.7	9.7	74.4	77.0	12.6
SC35-1300(6h)	0.7173	NA	NA	NA	NA	NA	NA	NA	NA	NA	NA	NA
SC35-1300(8h)	0.8422	5.404	9.849	1.0000	0.0084	0.6104	0.6116	1.4	19.9	174.7	172.3	11.6
SC35-1300(12h)	0.9554	6.606	9.972	1.0000	0.0102	0.7490	0.7521	1.4	23.7	176.6	178.0	13.3
SC35-1300(16h)	0.9788	2.968	4.226	1.0000	0.0046	0.3204	0.3235	1.4	10.6	70.1	76.0	14.0
SC8-1100(4h) pyrolyzed - Run1	0	NA	NA	NA	NA	NA	NA	NA	NA	NA	2.8	NA
SC8-1100(4h) pyrolyzed - Run2	0	NA	NA	NA	NA	NA	NA	NA	NA	NA	3.3	NA
SC8-1120(1h)	0	0.035	0.599	0.9278	0.0009	0.0087	0.0096	9.7	1.9	0.6	3.4	56.0
SC8-1160(1h)	0.0531	0.120	0.248	0.9870	0.0015	0.0022	0.0117	12.8	3.1	0.7	6.9	44.5
SC8-1160(2h)	0.0792	NA	NA	NA	NA	NA	NA	NA	NA	NA	25.7	NA
SC8-1160(4h)	0.1034	0.981	1.808	0.9912	0.0079	0.0150	0.0266	29.9	16.4	9.1	44.4	36.9
SC8-1160(7h)	0.1819	2.528	4.470	0.9951	0.0158	0.0243	0.0473	33.4	33.0	26.7	102.1	32.3

Table F-3 (continued)

Sample ID	X_{WL}	V_{int}	k_{micro}	r_L	V_{micro} (cm^3/g)	$V_{BJH\text{-}Total}$ (cm^3/g)	V_{Pore} (cm^3/g)	$V_{micro\text{-}r}$ (%)	SA_{micro} (m^2/g)	$A_{BJH\text{-}Total}$ (m^2/g)	SA (m^2/g)	$SA_{micro\text{-}r}$ (%)
SC8-1160(12h)	0.2578	5.554	9.172	0.9974	0.0221	0.0506	0.0863	25.7	46.3	62.4	188.1	24.6
SC8-1160(20h)	0.4046	15.044	12.732	0.9994	0.0233	0.1267	0.1744	13.3	50.5	158.1	247.4	20.4
SC8-1160(28h)	0.5881	9.649	18.189	0.9999	0.0149	0.2033	0.2488	6.0	35.5	234.9	316.8	11.2
SC8-1160(36h)	0.6162	9.024	20.502	0.9999	0.0140	0.2396	0.2857	4.9	34.3	270.2	351.4	9.8
SC8-1160(48h)	0.7458	7.729	25.148	1.0000	0.0120	0.3220	0.3712	3.2	31.7	337.6	420.7	7.5
SC8-1180(1h)	0.0800	0.261	0.490	0.9880	0.0022	0.0109	0.0144	15.5	4.6	2.0	12.2	37.7
SC8-1180(2h)	0.1269	0.836	1.538	0.9902	0.0067	0.0143	0.0241	27.8	13.8	7.8	37.6	36.7
SC8-1180(4h)	0.1808	2.238	4.025	0.9949	0.0154	0.0241	0.0456	33.8	32.1	24.2	94.4	34.0
SC8-1180(8h)	0.3083	5.718	9.305	0.9981	0.0198	0.0556	0.0883	22.4	41.5	66.5	185.4	22.4
SC8-1180(12h)	0.4309	13.046	11.148	0.9993	0.0202	0.1122	0.1533	13.2	43.8	139.2	216.2	20.3
SC8-1180(24h)	0.6999	8.437	21.687	1.0000	0.0131	0.2806	0.3247	4.0	32.9	293.6	368.4	8.9
SC8-1180(36h)	0.8237	7.605	28.530	1.0000	0.0118	0.3769	0.4299	2.7	32.4	385.5	473.7	6.8
SC8-1180(48h)	0.9157	7.660	34.999	1.0000	0.0118	0.4833	0.5448	2.2	34.4	475.2	575.7	6.0
SC8-1200(0.5h)	0.0473	0.274	0.494	0.9925	0.0019	0.0106	0.0137	14.0	4.0	2.3	11.6	34.2
SC8-1200(0.67h)	0.0492	NA	NA	NA	NA	NA	NA	NA	NA	NA	17.7	NA
SC8-1200(1h)	0.0455	0.757	1.394	0.9913	0.0061	0.0146	0.0236	25.7	12.5	6.8	34.1	36.7
SC8-1200(2h)	0.1144	1.737	3.118	0.9935	0.0120	0.0187	0.0362	33.2	24.8	17.4	73.0	33.9

Table F-3 (continued)

Sample ID	X_{WL}	V_{int}	k_{micro}	r_L	V_{micro} (cm^3/g)	$V_{BJH\text{-}Total}$ (cm^3/g)	V_{Pore} (cm^3/g)	$V_{micro\text{-}r}$ (%)	SA_{micro} (m^2/g)	$A_{BJH\text{-}Total}$ (m^2/g)	SA (m^2/g)	$SA_{micro\text{-}r}$ (%)
SC8-1200(4h)	0.1944	4.411	7.353	0.9970	0.0184	0.0400	0.0693	26.6	38.4	49.3	152.2	25.3
SC8-1200(8h)	0.3951	11.499	10.362	0.9995	0.0178	0.0996	0.1433	12.4	38.8	128.2	199.1	19.5
SC8-1200(12h)	0.5407	9.838	15.770	0.9999	0.0152	0.1803	0.2224	6.8	35.3	202.8	279.3	12.7
SC8-1200(16h)	0.6802	7.961	22.842	1.0000	0.0123	0.2858	0.3321	3.7	31.6	305.3	385.0	8.2
SC8-1200(22h)	0.8035	7.591	29.195	1.0000	0.0117	0.3876	0.4417	2.7	32.4	393.9	484.0	6.7
SC8-1200(32h)	0.9138	7.389	36.795	1.0000	0.0114	0.5067	0.5721	2.0	33.9	496.3	603.1	5.6
SC8-1250(0.67h)	0.1078	6.872	3.050	0.9936	0.0106	0.0120	0.0324	32.8	22.4	17.6	69.6	32.2
SC8-1250(1h)	0.1561	1.788	5.493	0.9968	0.0151	0.0246	0.0537	28.1	32.0	36.9	117.0	27.4
SC8-1250(2h)	0.3118	3.346	7.555	0.9992	0.0165	0.0680	0.1107	14.9	36.1	92.8	153.0	23.6
SC8-1250(3h)	0.4163	NA	NA	NA	NA	NA	NA	NA	NA	NA	NA	NA
SC8-1250(4h)	0.5350	8.915	15.848	0.9999	0.0138	0.1837	0.2226	6.2	33.3	208.2	278.4	12.0
SC8-1250(5h)	0.5534	8.525	19.499	1.0000	0.0132	0.2383	0.2799	4.7	32.6	261.6	334.2	9.8
SC8-1250(6.5h)	0.6051	7.864	26.762	1.0000	0.0122	0.3425	0.3937	3.1	32.8	360.6	446.8	7.3
SC8-1250(8h)	0.7316	8.101	32.987	1.0000	0.0125	0.4381	0.4965	2.5	36.9	450.4	547.1	6.7
SC8-1250(12h)	0.8247	8.964	37.141	0.9999	0.0139	0.5257	0.5919	2.3	39.4	505.8	613.9	6.4
SC8-1250(16h)	0.9181	9.027	40.175	0.9999	0.0140	0.5924	0.6648	2.1	40.6	544.4	662.0	6.1

APPENDIX G

XRD PATTERNS FOR SC35 AND SC8 CTR SAMPLES

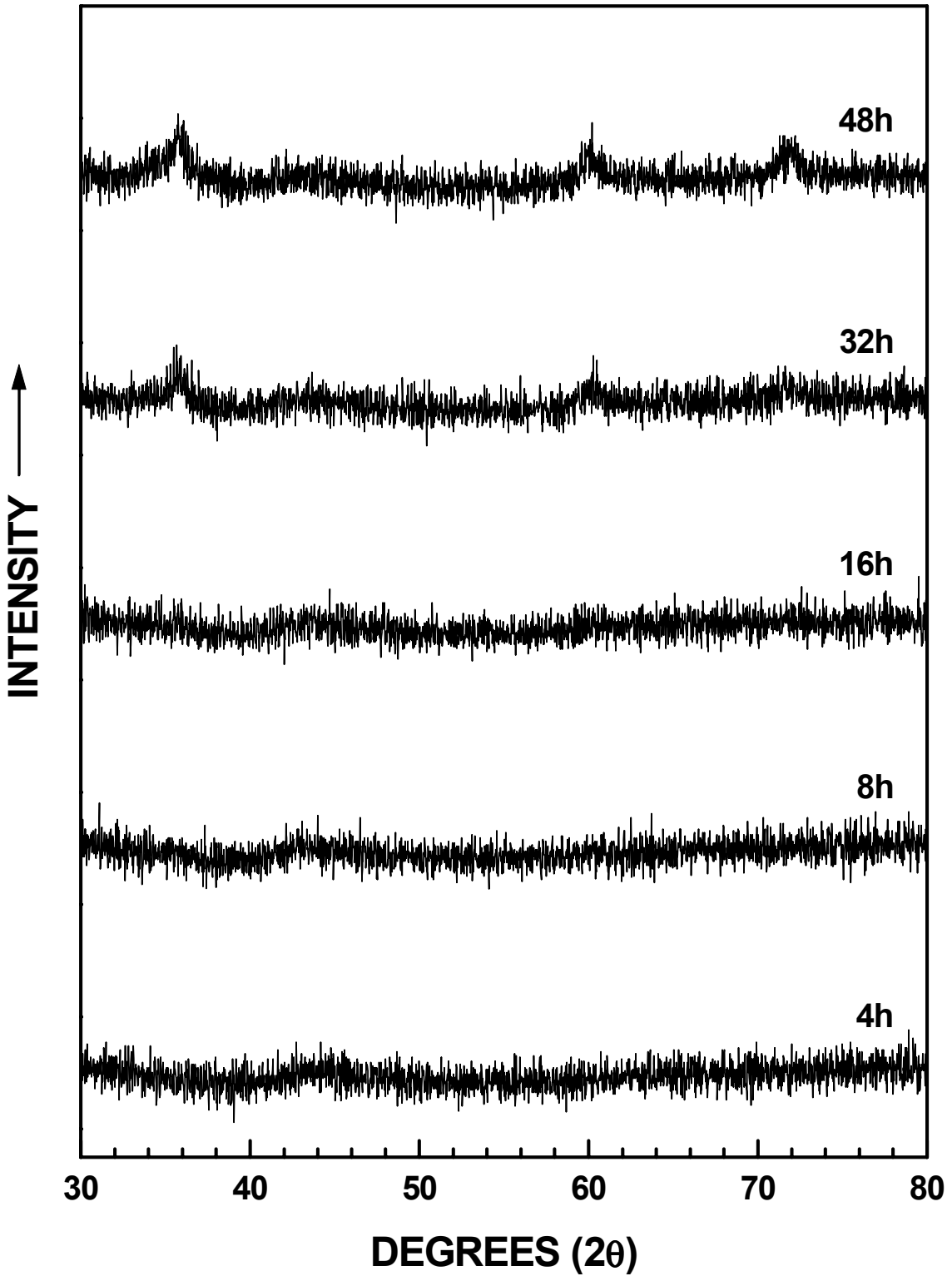

Figure G-1 XRD patterns of the SC35 samples heat treated at 1160^{o}C for different time.

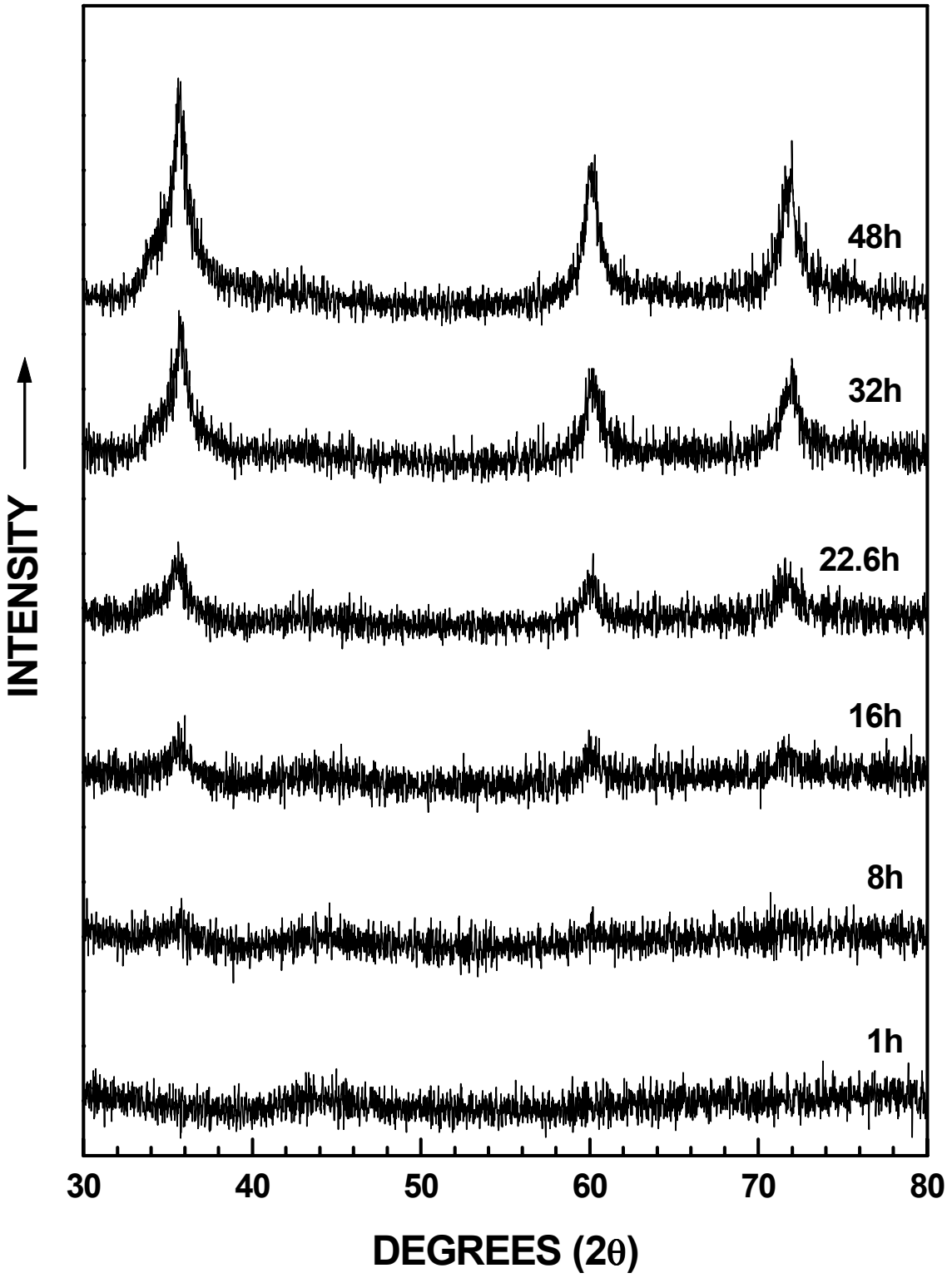

Figure G-2 XRD patterns of the SC35 samples heat treated at 1200^{o}C for different time.

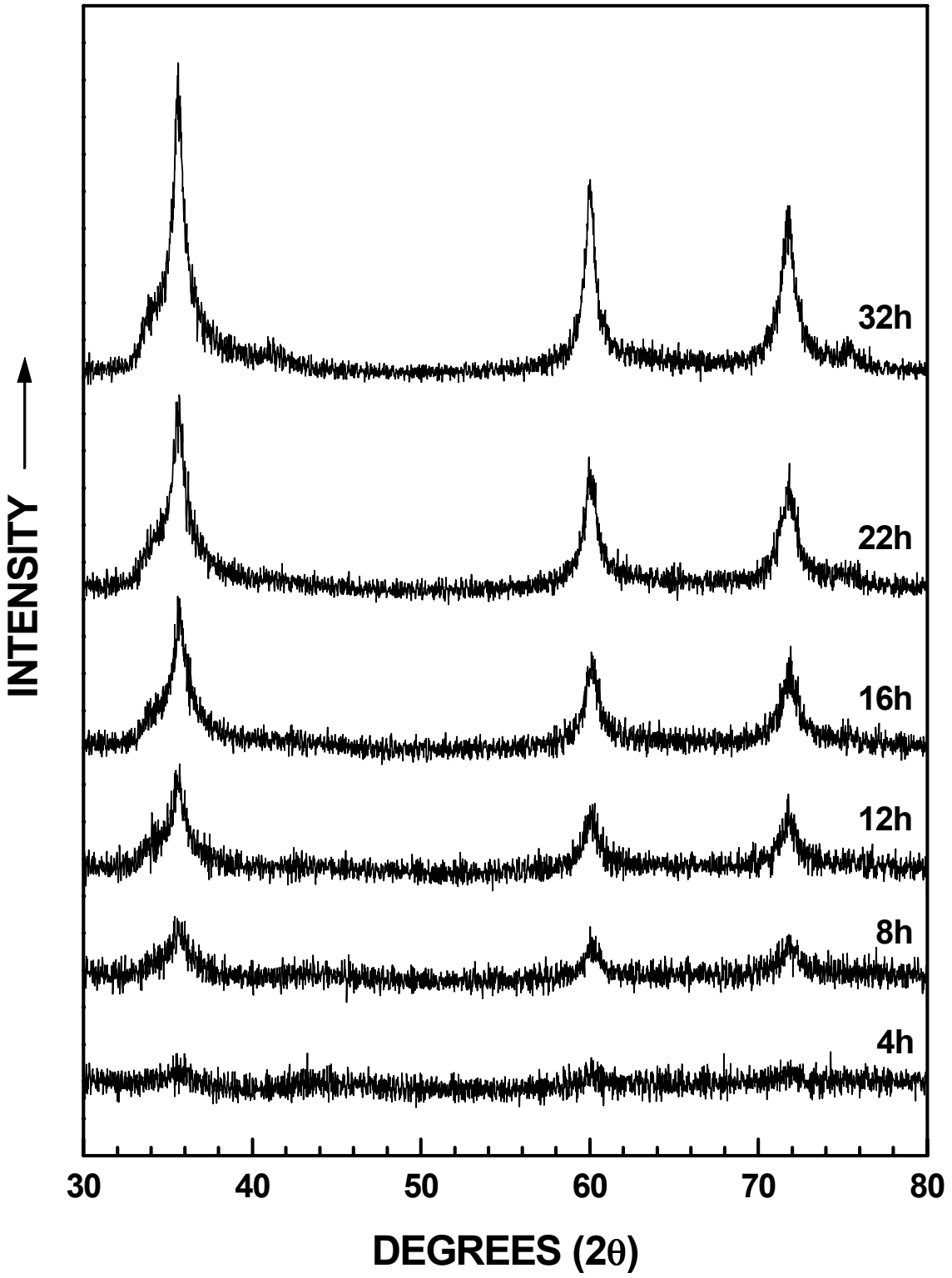

Figure G-3 XRD patterns of the SC35 samples heat treated at 1250^{o}C for different time.

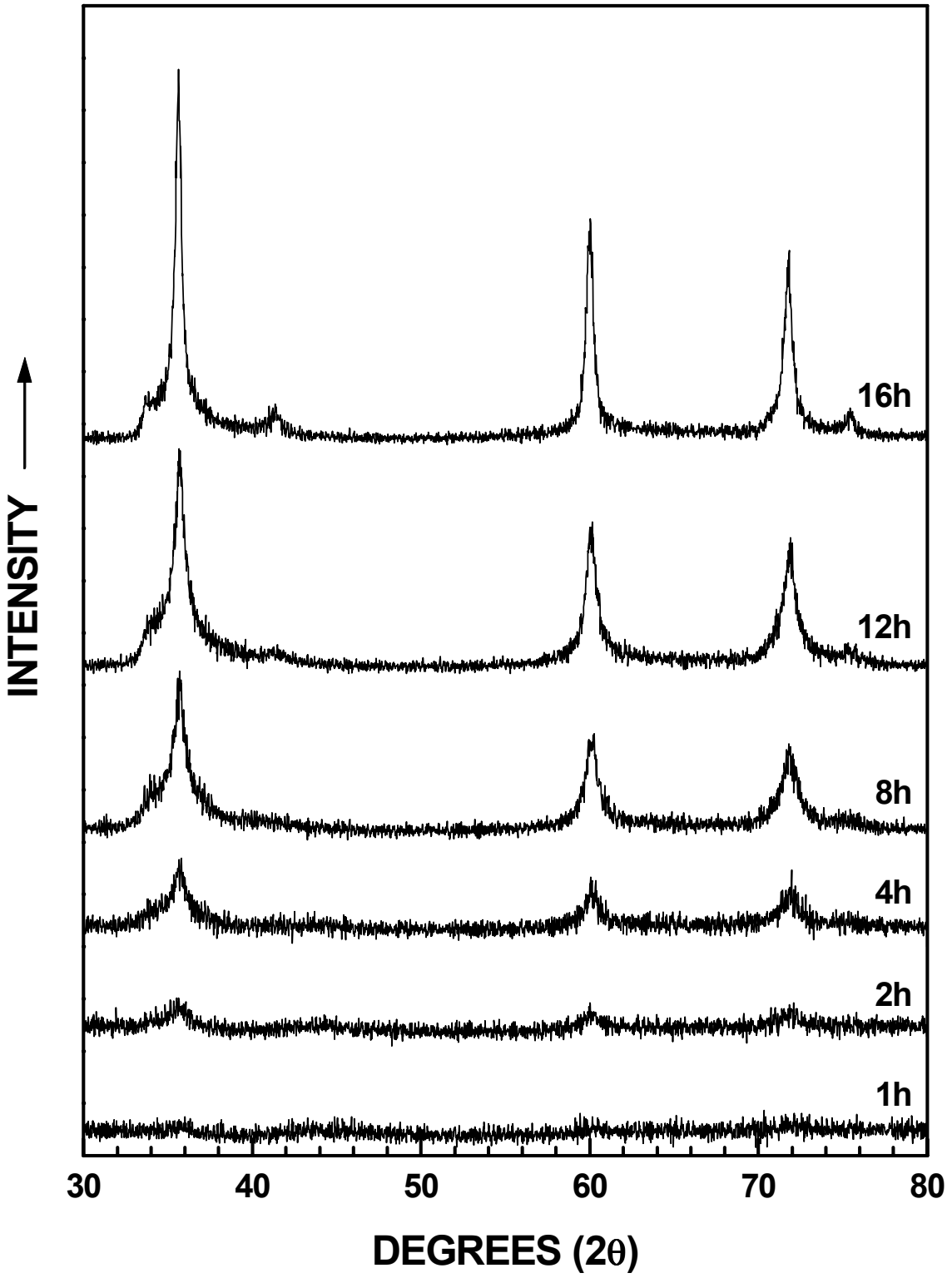

Figure G-4 XRD patterns of the SC35 samples heat treated at 1300^{o}C for different time.

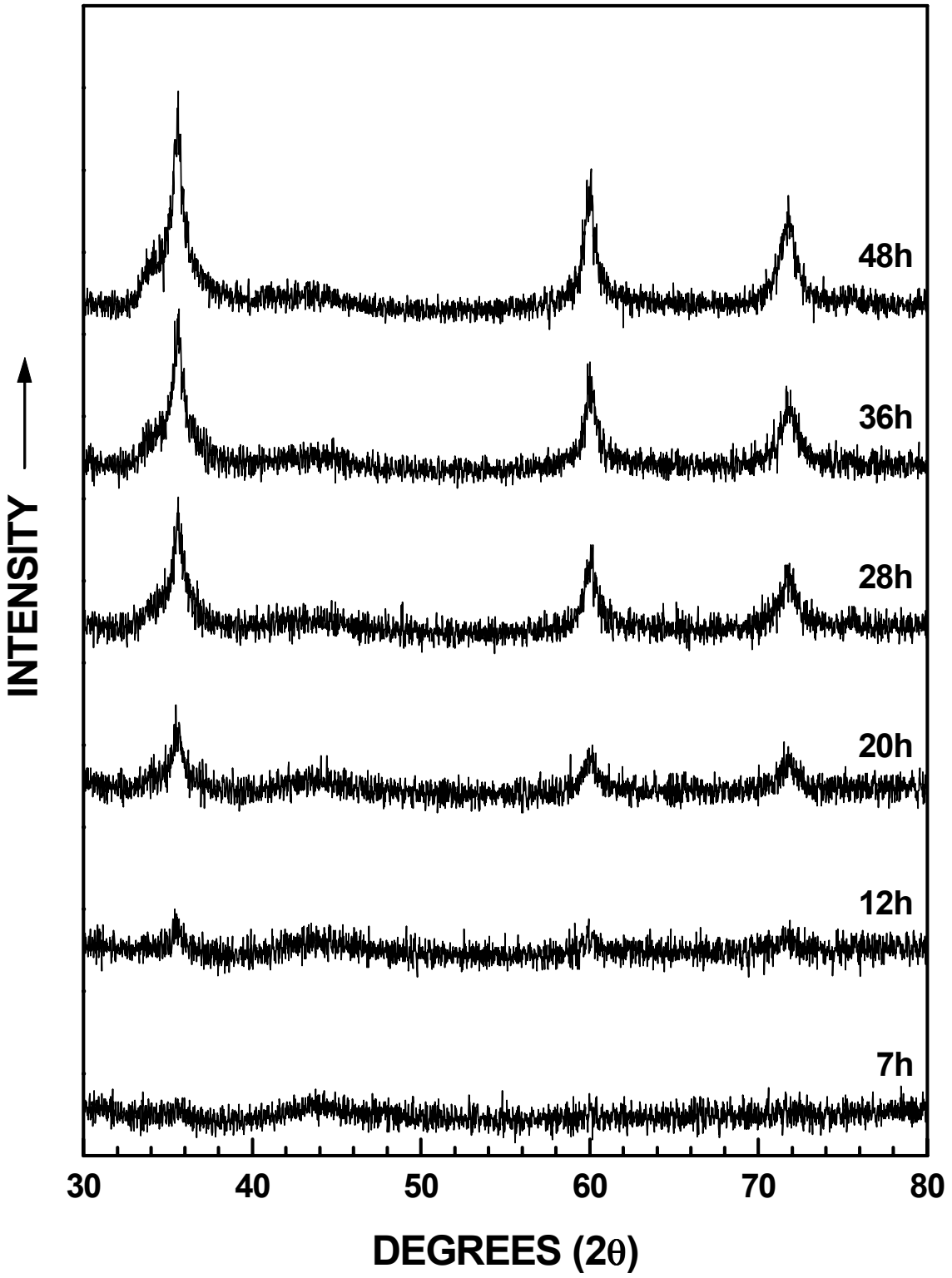

Figure G-5 XRD patterns of the SC8 samples heat treated at 1160^{o}C for different time.

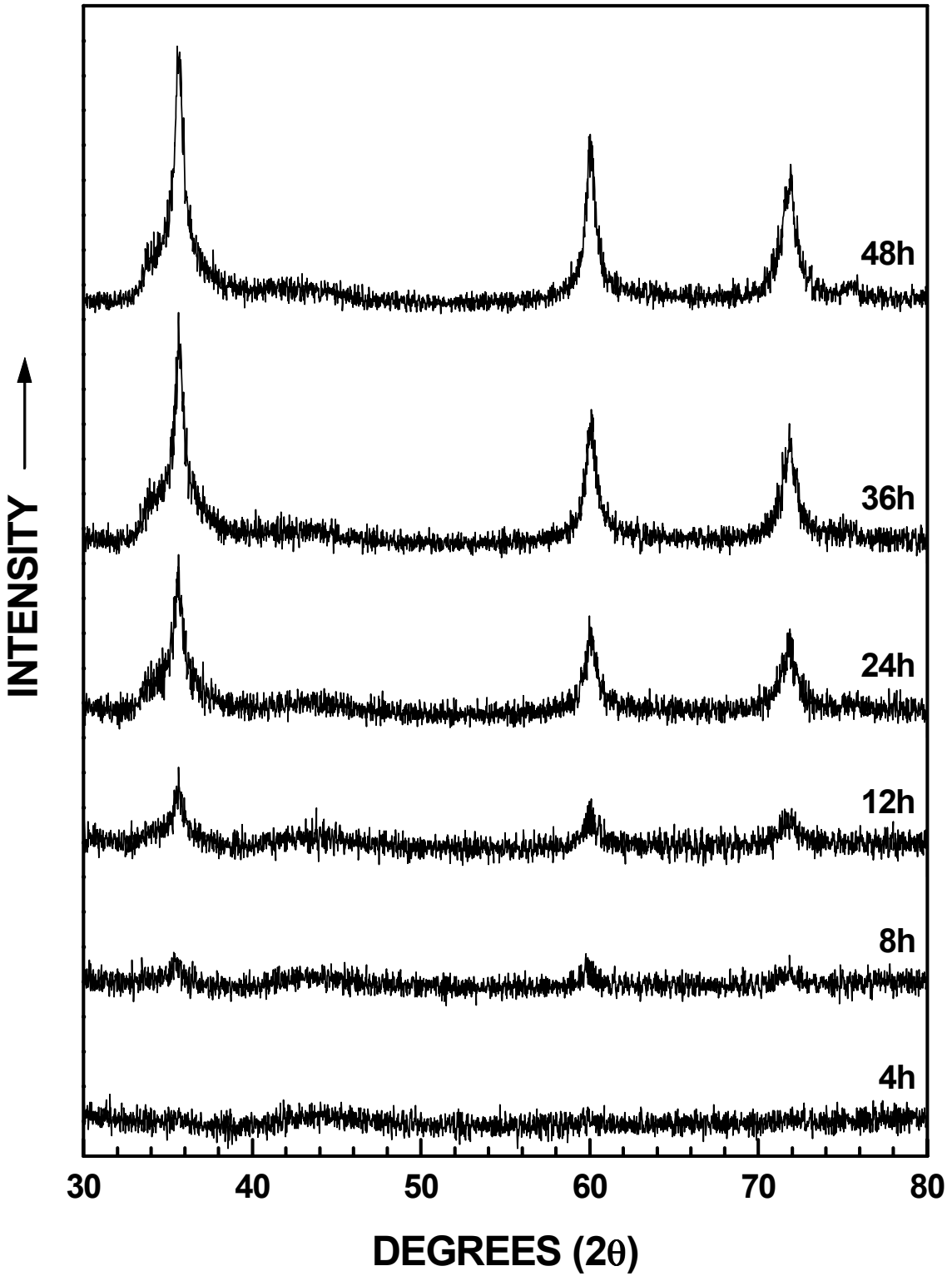

Figure G-6 XRD patterns of the SC8 samples heat treated at 1180^{o}C for different time.

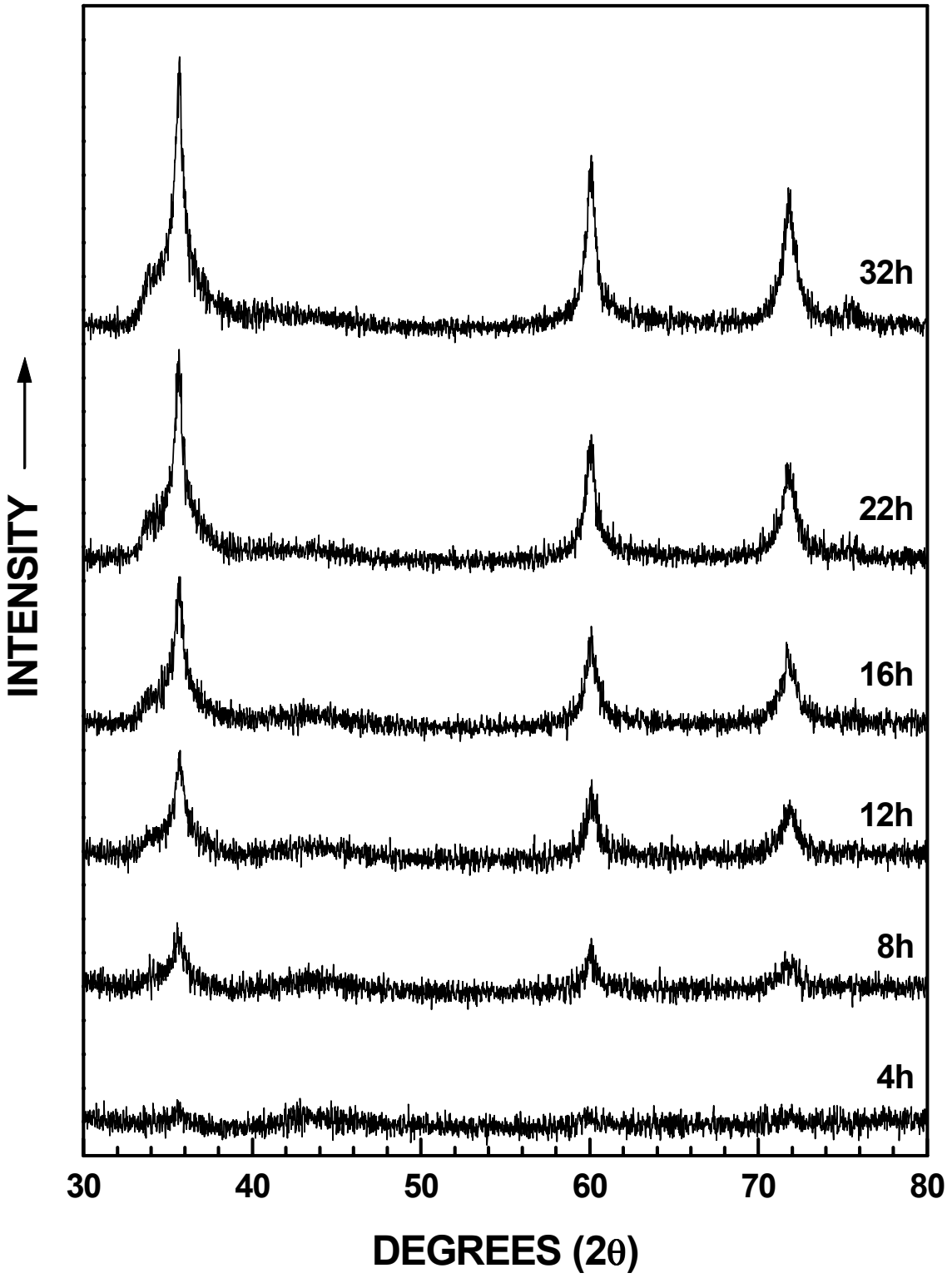

Figure G-7 XRD patterns of the SC8 samples heat treated at 1200^{o}C for different time.

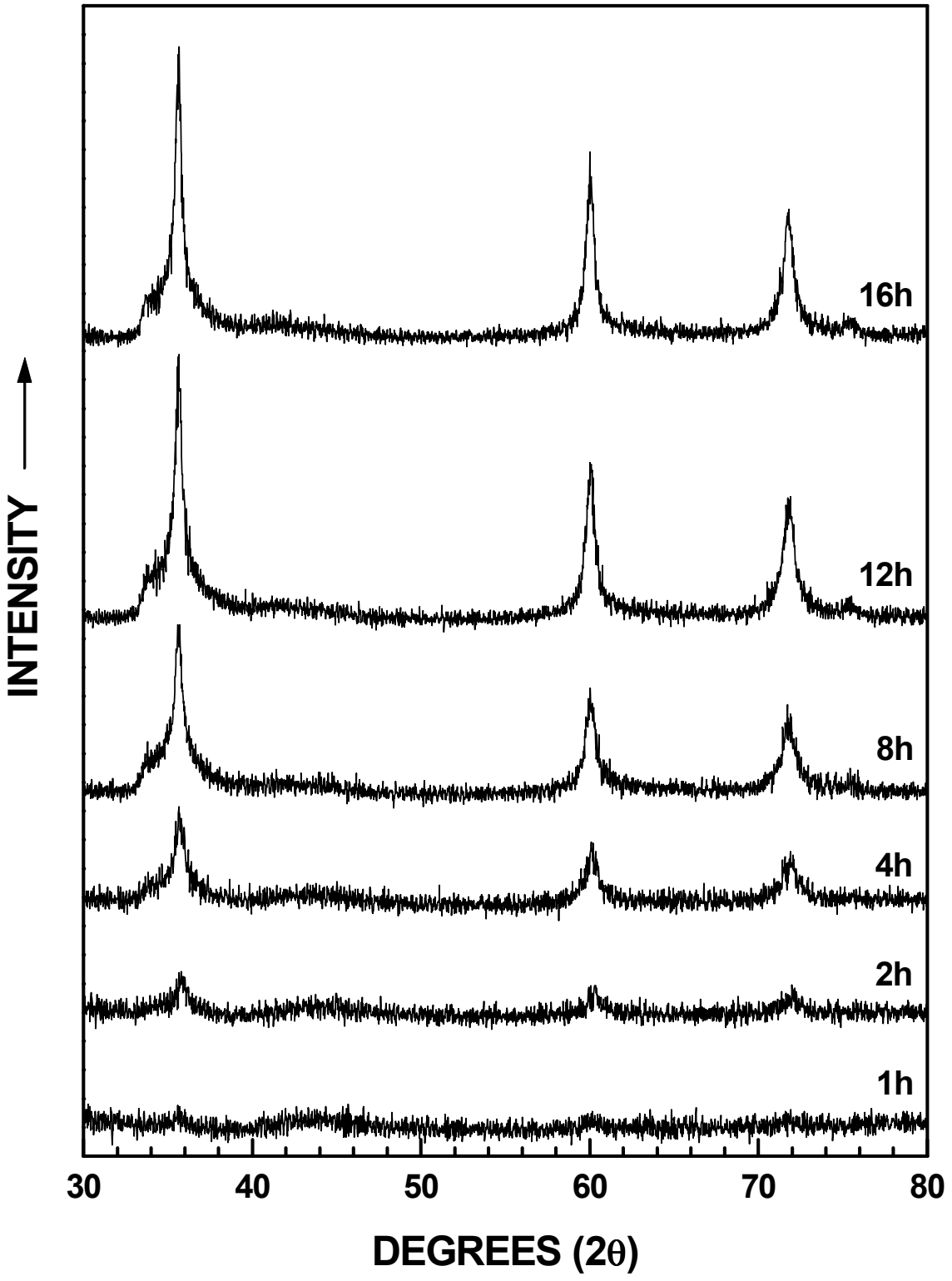

Figure G-8 XRD patterns of the SC8 samples heat treated at 1250^{o}C for different time.

APPENDIX H

SiC CRYSTALLITE SIZE FOR SC35 AND SC8 CTR PRODUCTS

Table H-1 Crystallite size data for the SC35 and SC8 CTR reaction products.

Sample	X_{WL}	D_{111} (nm)	D_{220} (nm)	D_{311} (nm)	D_{Avg} (nm)	Standard deviation (nm)
SC35-1160(48h)	0.2909	8.8	9.6	8.3	8.9	0.6
SC35-1200(16h)	0.2577	8.8	11.2	9.0	9.6	1.3
SC35-1200(22.5h)	0.3804	10.4	11.2	9.1	10.2	1.1
SC35-1200(32h)	0.5208	10.8	10.8	11.6	11.1	0.5
SC35-1200(48h)	0.7249	9.3	12.1	10.9	10.8	1.4
SC35-1250(8h)	0.4109	7.5	11.3	11.8	10.2	2.4
SC35-1250(12h)	0.5455	10.6	11.2	11.4	11.1	0.4
SC35-1250(16h)	0.6974	9.8	12.2	12.0	11.3	1.4
SC35-1250(22h)	0.8191	12.1	13.3	11.1	11.4	1.1
SC35-1250(32h)	0.9539	12.3	16.2	13.5	14.0	2.0
SC35-1300(2h)	0.3035	8.1	12.6	8.9	9.9	2.4
SC35-1300(3h)	0.4497	8.3	14.3	8.7	10.5	3.3
SC35-1300(4h)	0.5438	10.9	12.2	11.1	11.4	0.7
SC35-1300(6h)	0.7173	11.0	11.9	9.4	10.8	1.3
SC35-1300(8h)	0.8422	11.4	13.2	11.3	12.0	1.1
SC35-1300(12h)	0.9554	12.7	15.4	14.1	14.0	1.4
SC35-1300(16h)	0.9788	22.6	23.6	22.4	22.9	0.6
SC8-1160(12h)	0.2578	12.9	12.3	10.4	11.8	1.3
SC8-1160(20h)	0.4046	13.1	14.6	10.8	12.8	1.9

Note: D_{111}, D_{220}, D_{311} are crystallite size along the <111>, <220>, and <311> directions, respectively, of β-SiC. D_{Avg} is the average size over those three directions.

Table H-1 Continued

Sample	X_{WL}	D_{111} (nm)	D_{220} (nm)	D_{311} (nm)	D_{Avg} (nm)	Standard deviation (nm)
SC8-1160(28h)	0.5881	12.1	12.7	11.5	12.4	0.6
SC8-1160(36h)	0.6162	13.4	15.2	11.6	13.4	1.8
SC8-1160(48h)	0.7458	14.0	16.1	12.0	14.0	2.1
SC8-1180(8h)	0.3084	13.2	14.3	8.6	12.0	3.0
SC8-1180(12h)	0.4309	14.1	13.6	10.6	12.7	1.9
SC8-1180(24h)	0.6999	13.4	15.5	12.0	13.6	1.8
SC8-1180(36h)	0.8237	14.4	16.0	12.4	14.3	1.8
SC8-1180(48h)	0.9157	15.3	17.9	13.3	15.5	2.3
SC8-1200(8h)	0.3951	11.6	16.9	10.2	12.9	3.6
SC8-1200(12h)	0.5407	13.0	14.5	12.8	13.5	0.9
SC8-1200(16h)	0.6802	13.8	15.1	12.3	13.7	1.4
SC8-1200(22h)	0.8035	15.1	17.0	13.4	15.2	1.8
SC8-1200(32h)	0.9138	15.1	18.5	14.3	16.0	2.3
SC8-1250(2h)	0.3118	14.4	13.9	9.3	12.5	2.8
SC8-1250(3h)	0.4163	13.3	15.5	11.3	13.4	2.1
SC8-1250(4h)	0.5534	12.7	14.5	10.9	12.7	1.8
SC8-1250(5h)	0.6051	13.9	14.8	12.9	13.9	1.0
SC8-1250(6.5h)	0.7316	13.3	16.1	13.3	14.2	1.6
SC8-1250(8h)	0.8247	16.1	16.7	14.0	15.6	1.4
SC8-1250(12h)	0.9181	18.0	18.8	14.4	17.1	2.3
SC8-1250(16h)	0.9402	19.4	21.1	17.6	19.4	1.7

APPENDIX I

ADSORPTION ANALYSIS PLOTS FOR SC35 AND SC8 CTR PRODUCTS

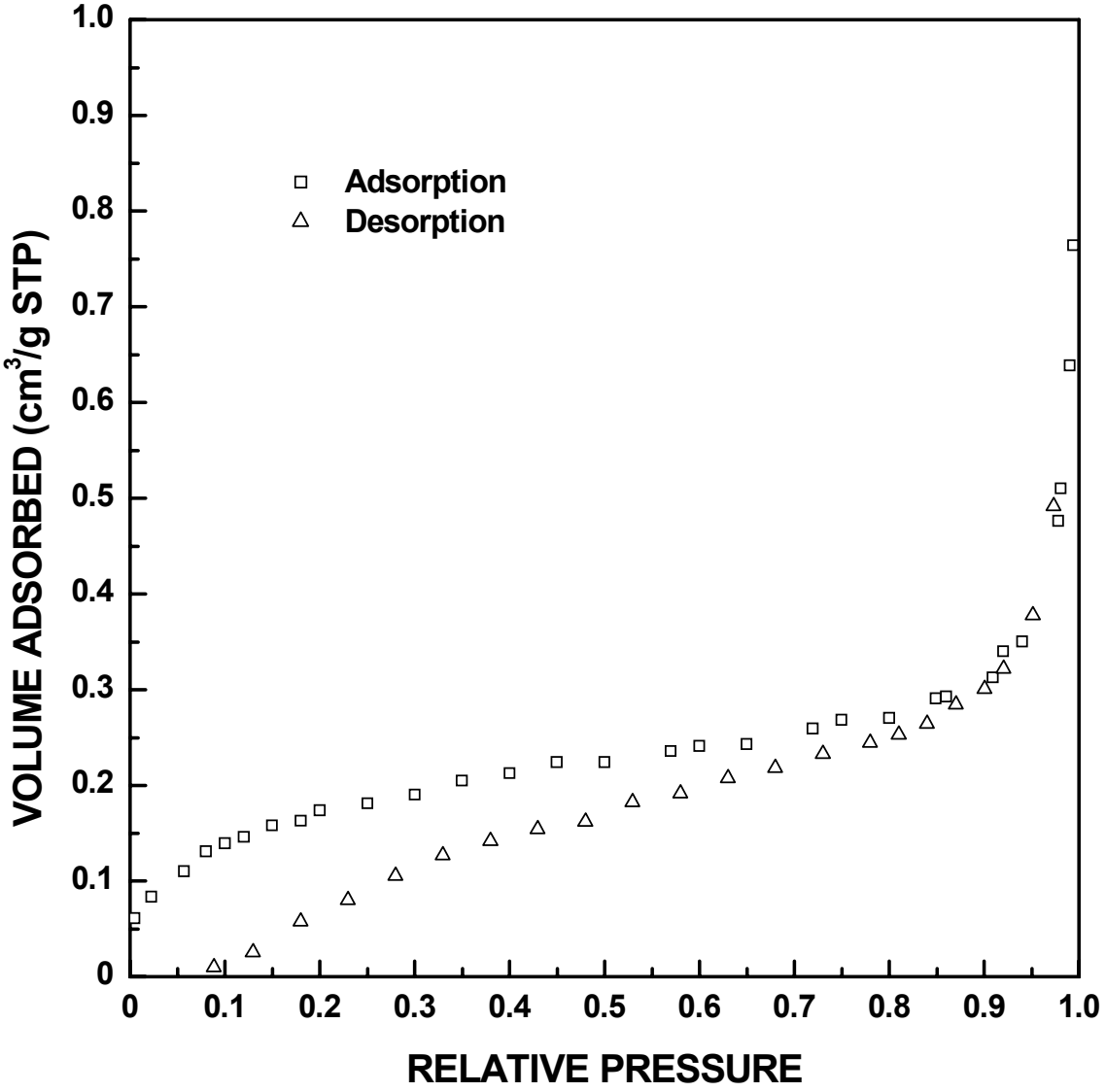

Figure I-1 Adsorption/desorption isotherm plots for SC35-1160(30min) sample (X_{WL} = 0.01).

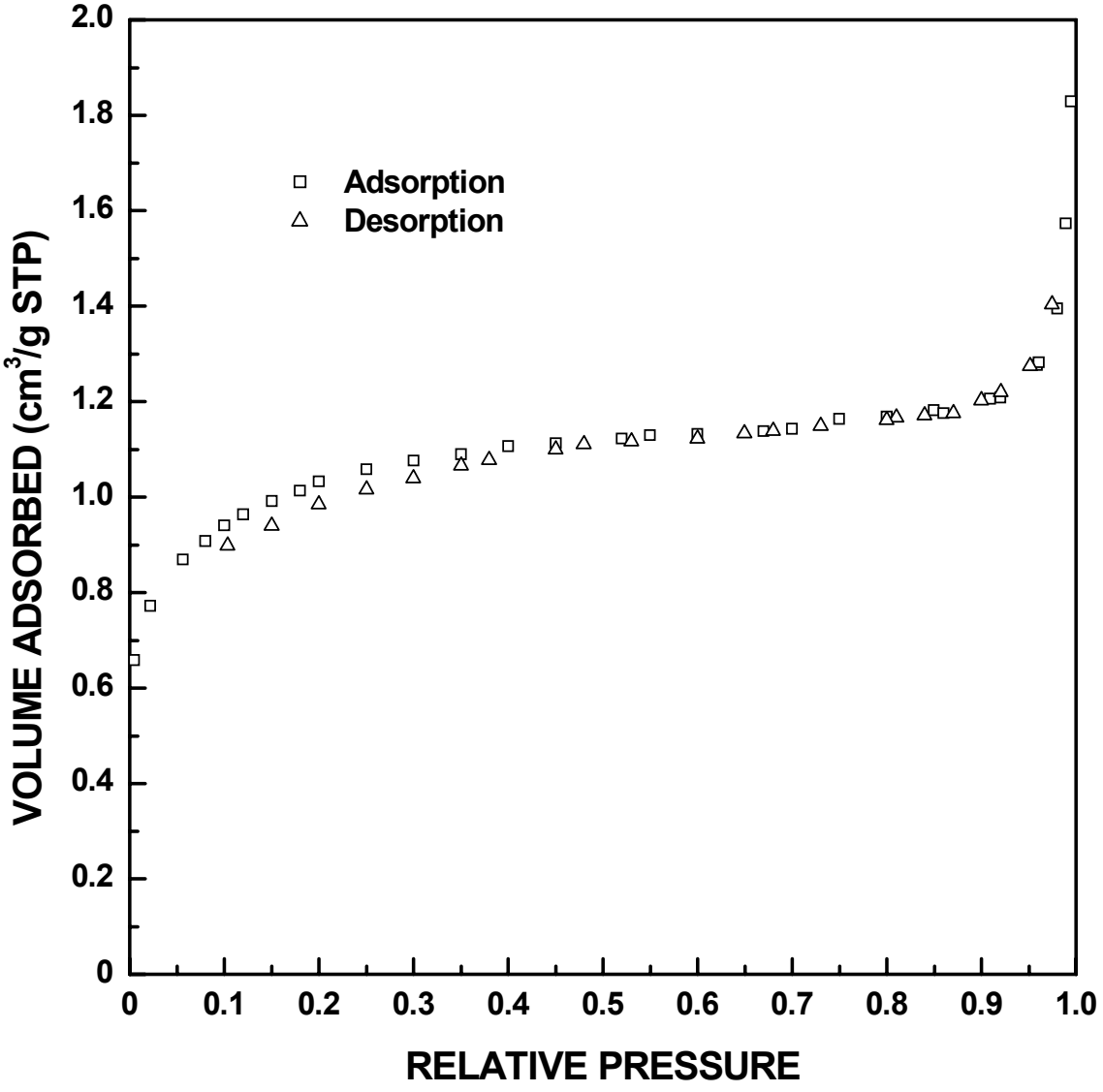

Figure I-2 Adsorption/desorption isotherm plots for SC35-1160(2h) sample (X_{WL} = 0.03).

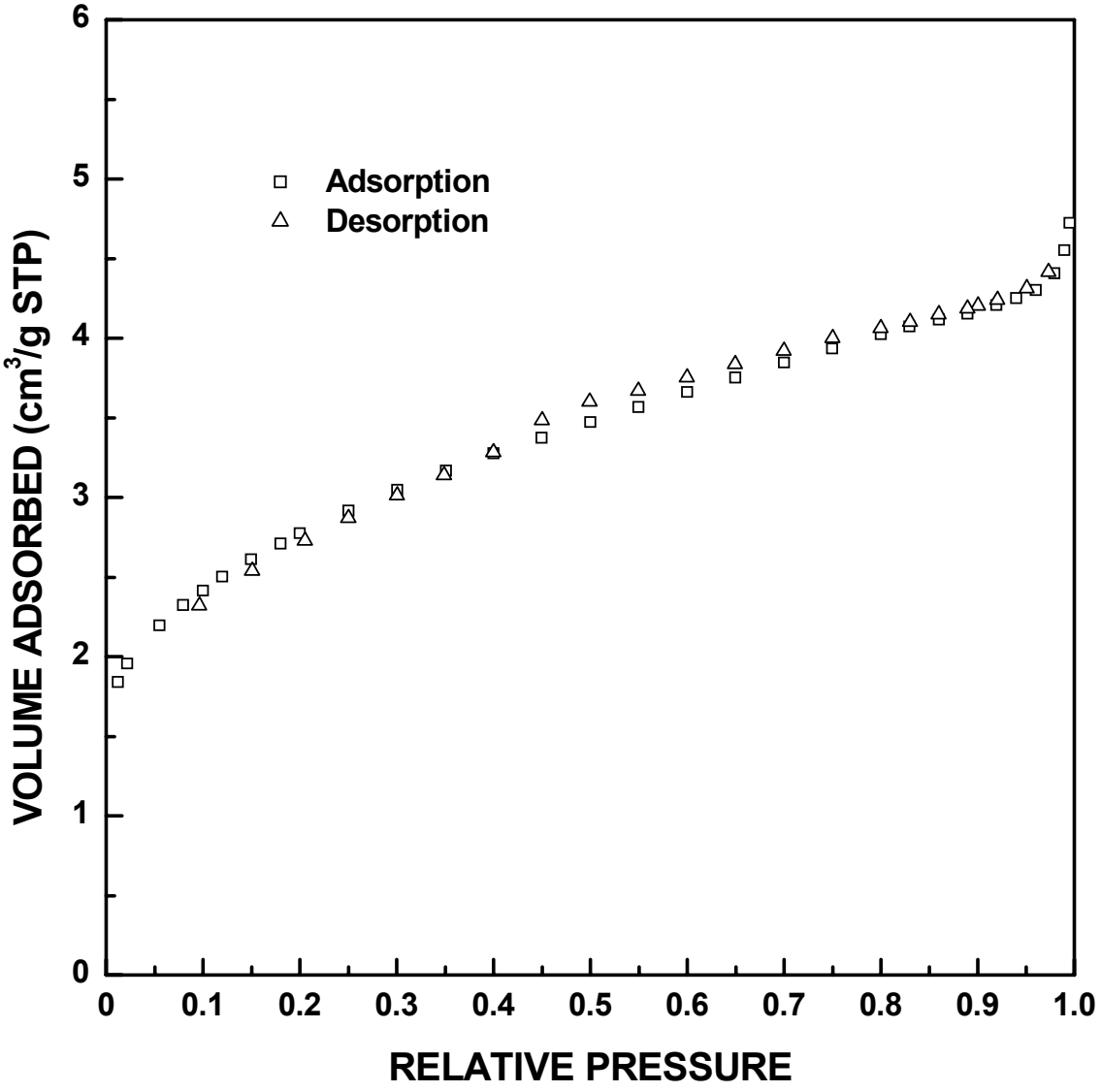

Figure I-3 Adsorption/desorption isotherm plots for SC35-1160(4h) sample (X_{WL} = 0.05).

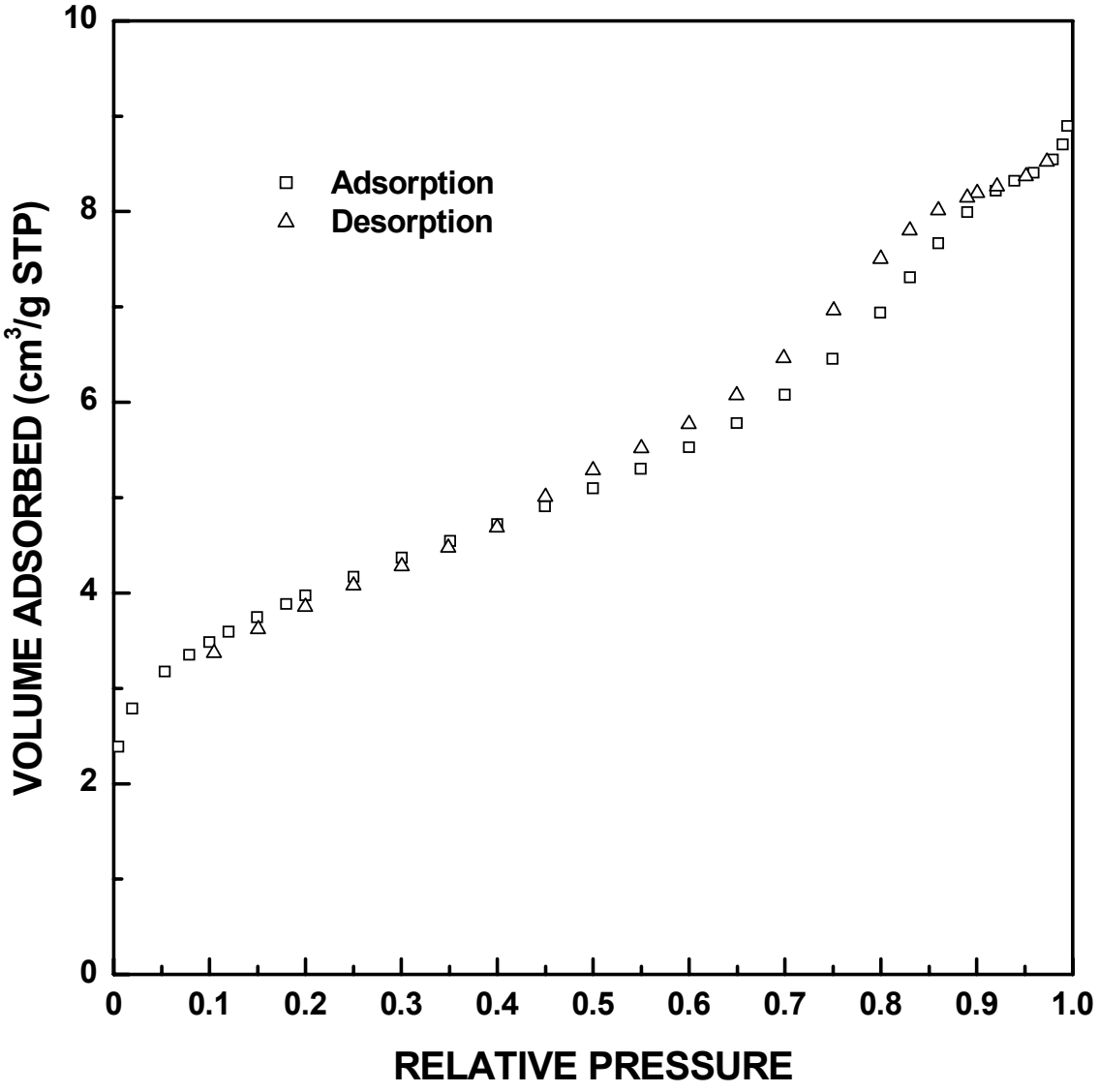

Figure I-4 Adsorption/desorption isotherm plots for SC35-1160(8h) sample (X_{WL} = 0.07).

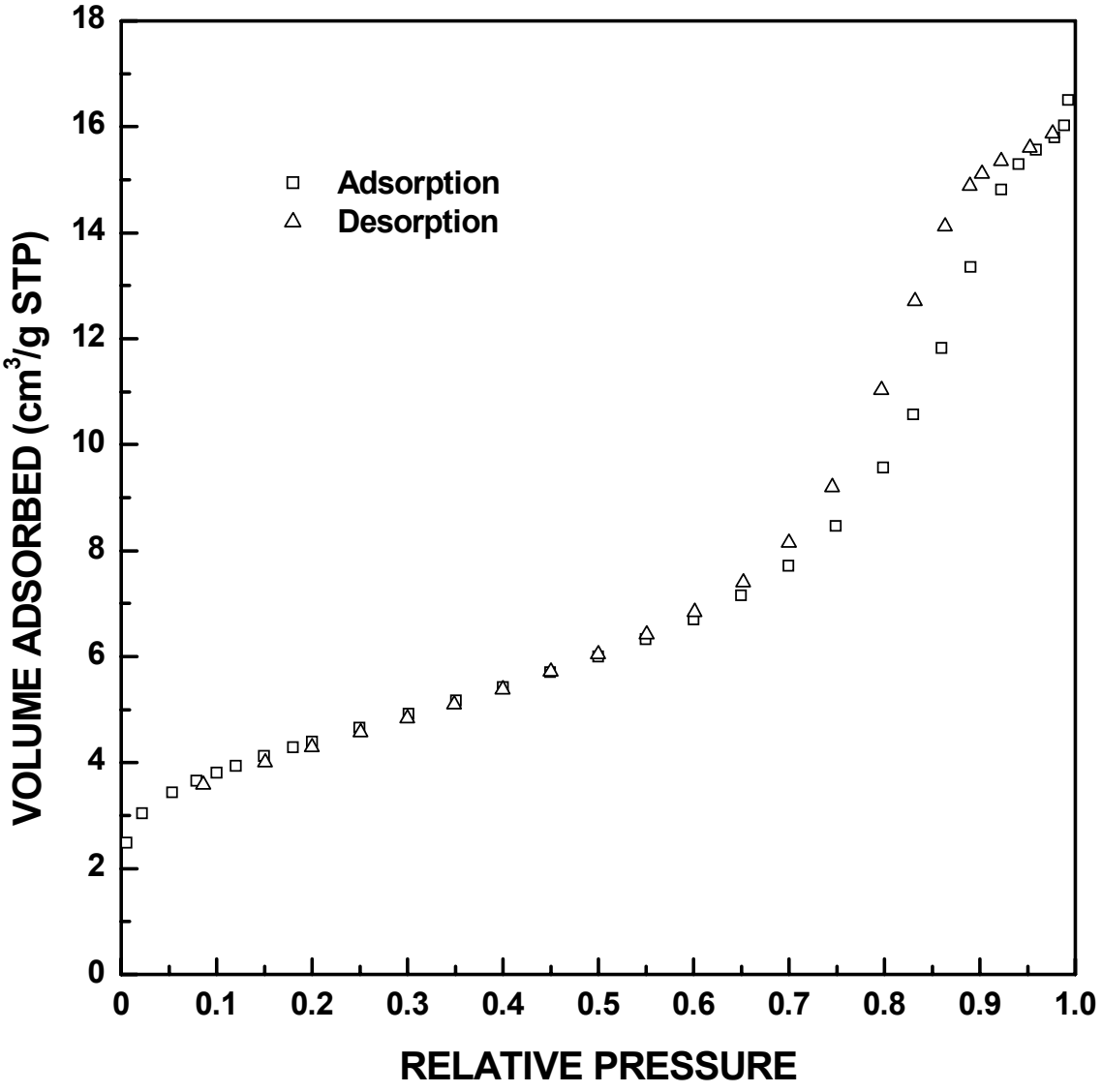

Figure I-5 Adsorption/desorption isotherm plots for SC35-1160(16h) sample (X_{WL} = 0.12).

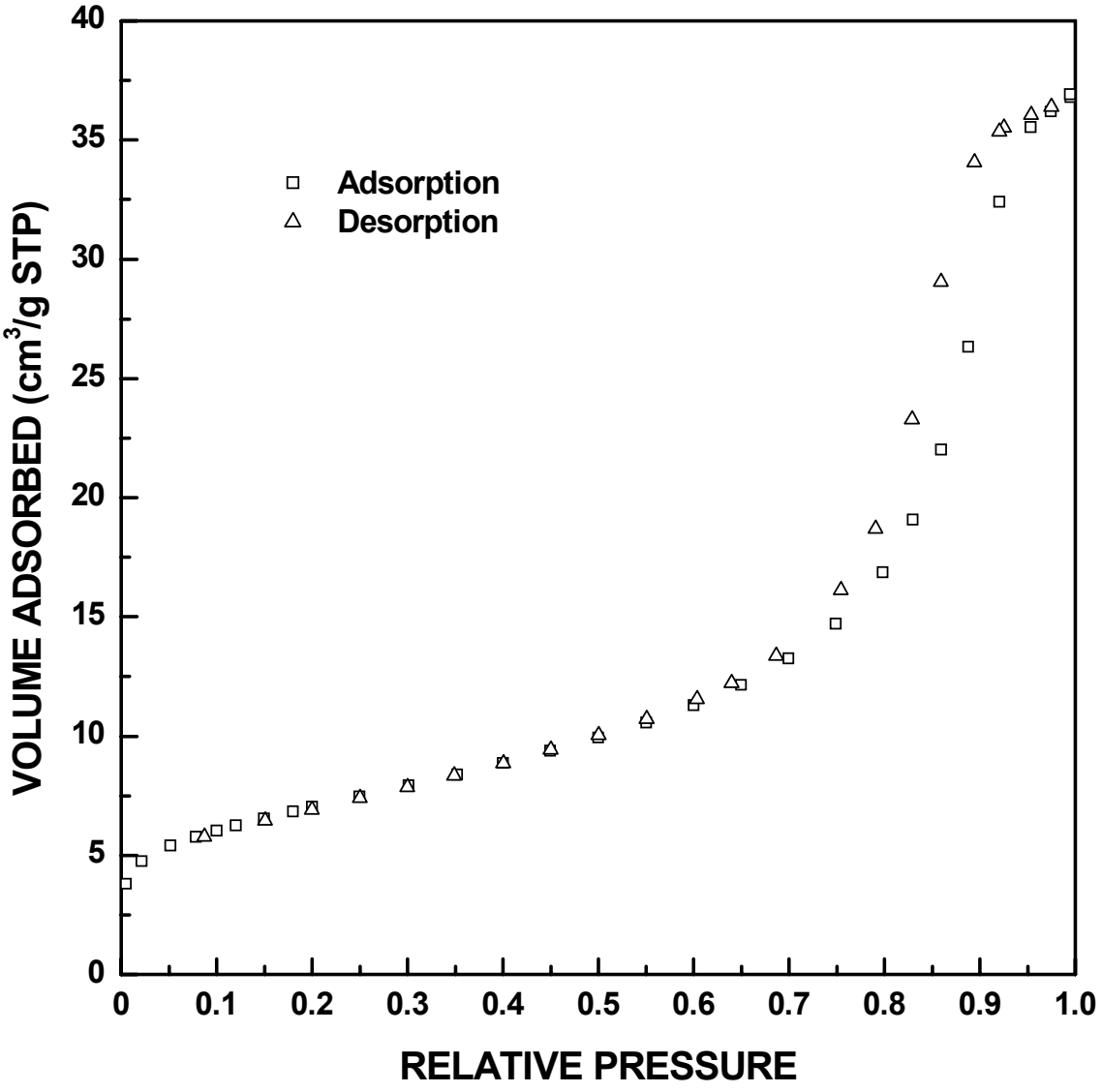

Figure I-6 Adsorption/desorption isotherm plots for SC35-1160(32h) sample (X_{WL} = 0.22).

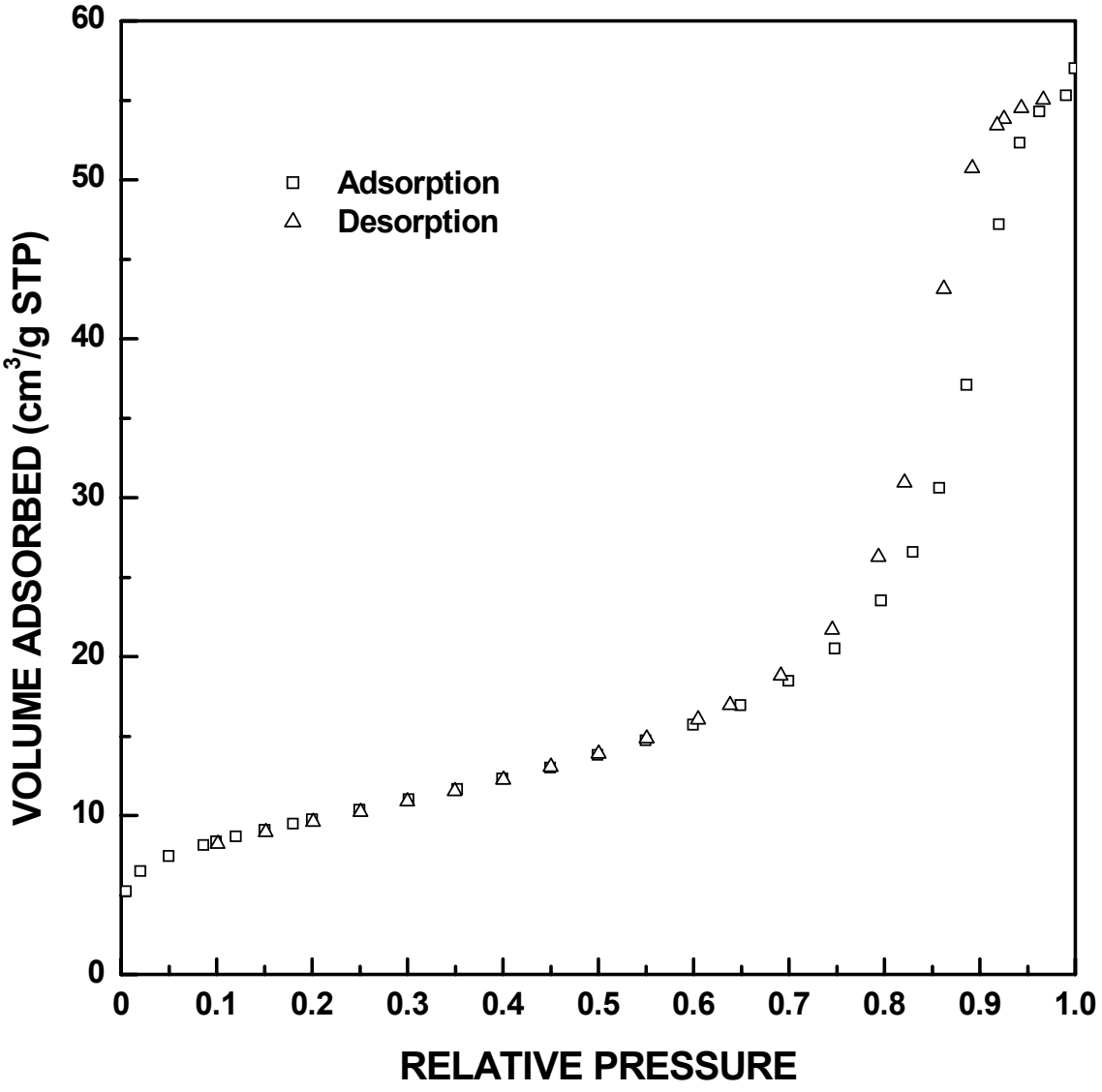

Figure I-7 Adsorption/desorption isotherm plots for SC35-1160(48h) sample (X_{WL} = 0.29).

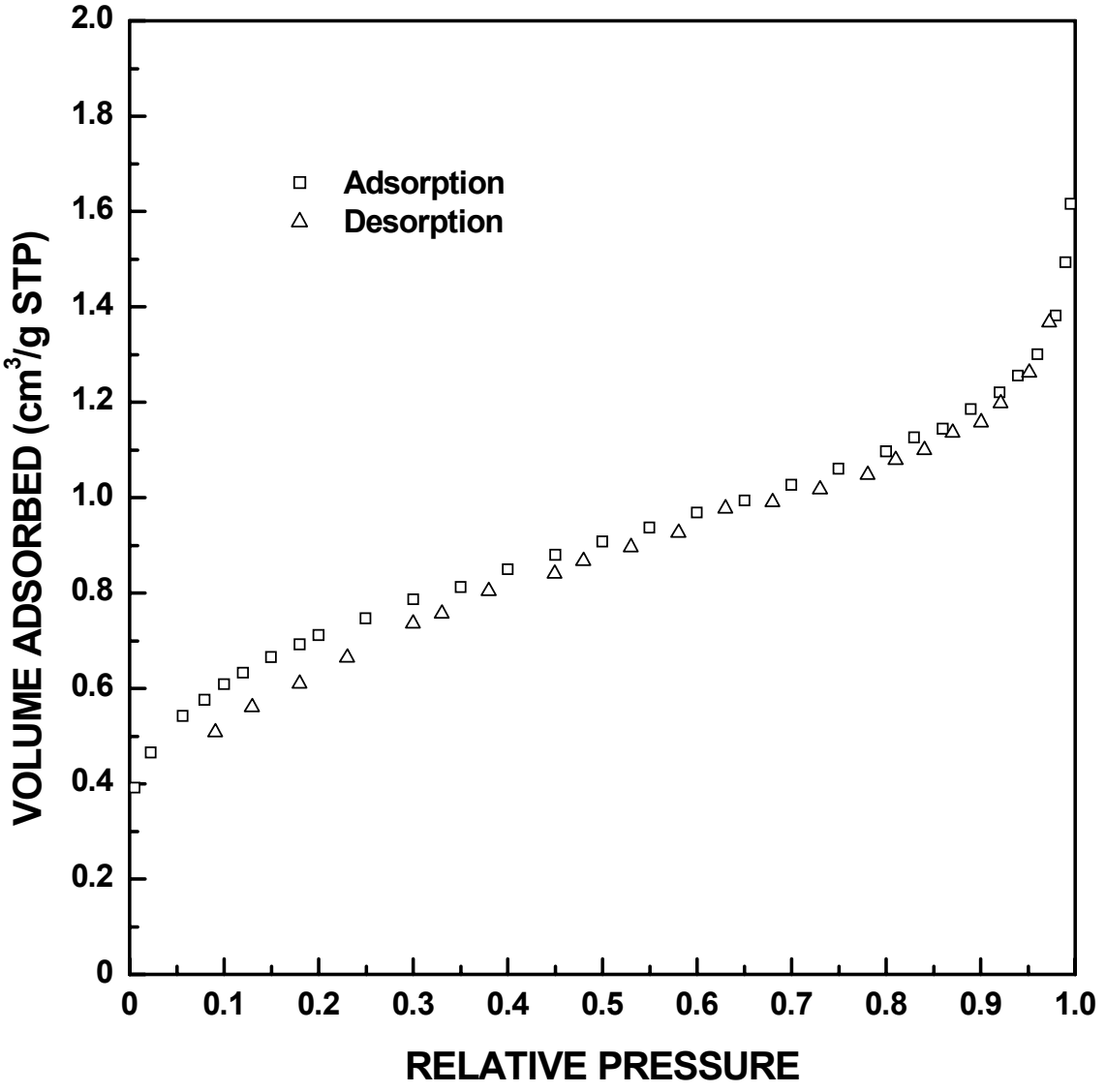

Figure I-8 Adsorption/desorption isotherm plots for SC35-1200(0.5h) sample (X_{WL} = 0.02).

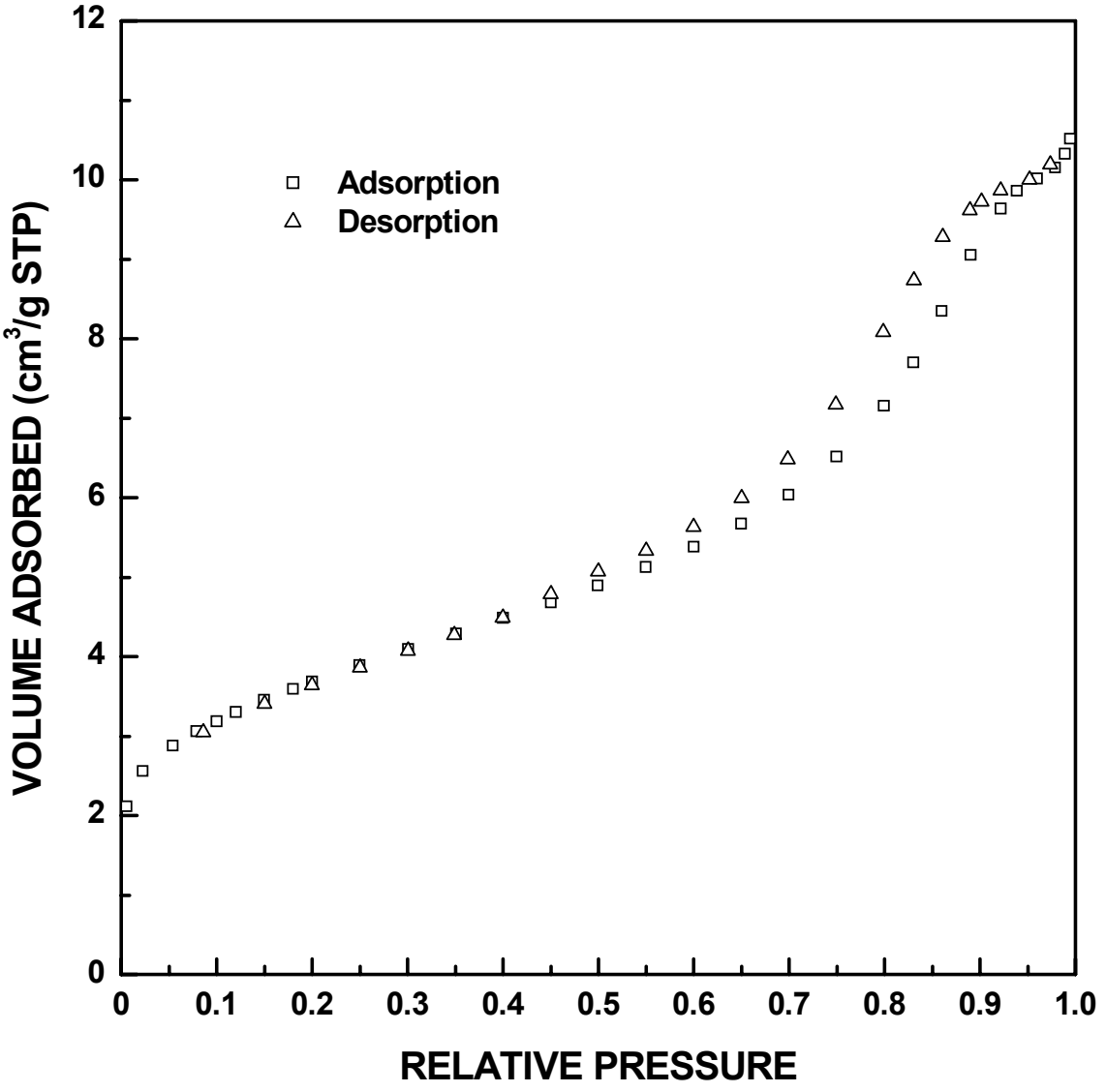

Figure I-9 Adsorption/desorption isotherm plots for SC35-1200(4h) sample (X_{WL} = 0.09).

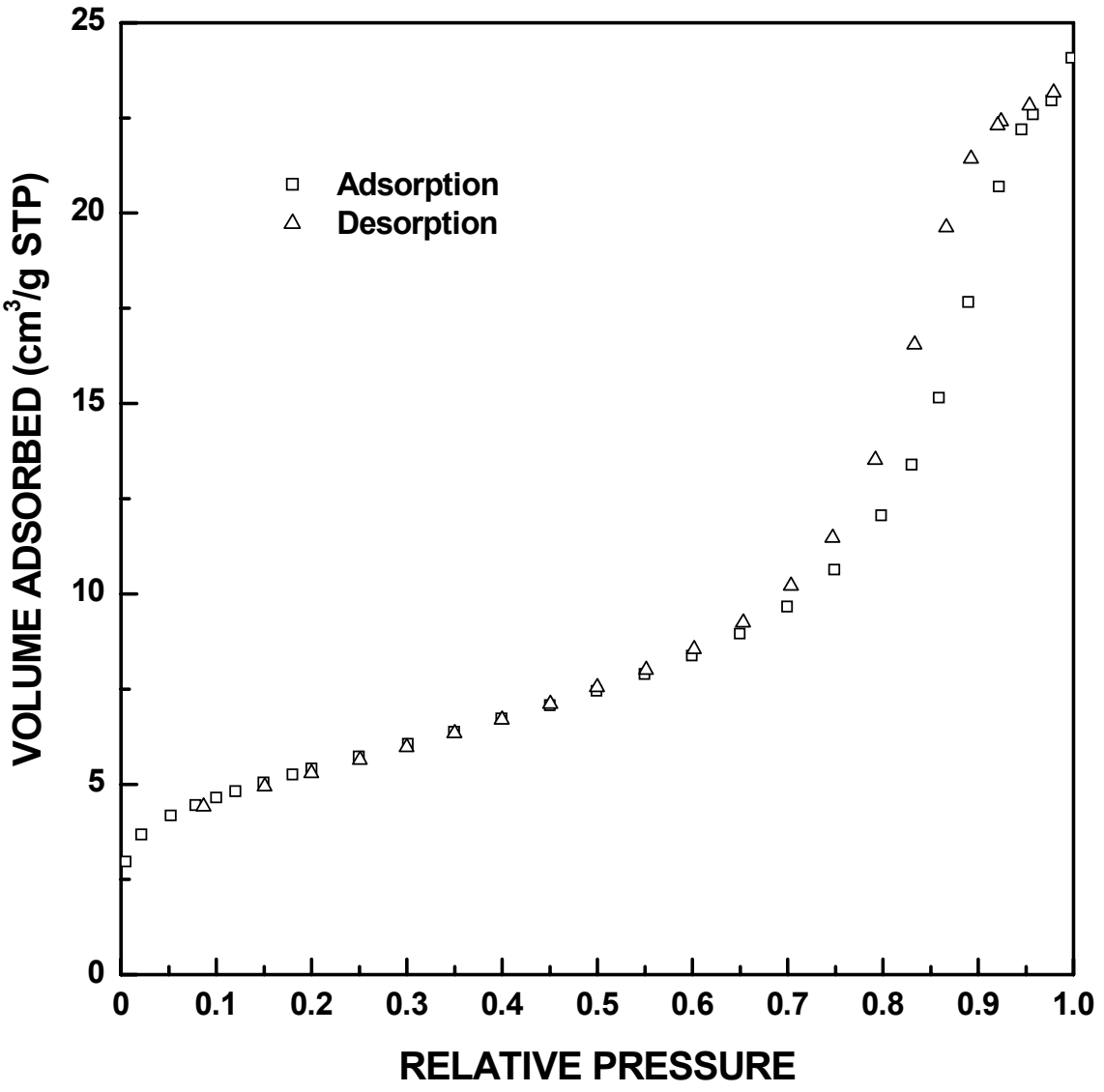

Figure I-10 Adsorption/desorption isotherm plots for SC35-1200(8h) sample (X_{WL} = 0.16).

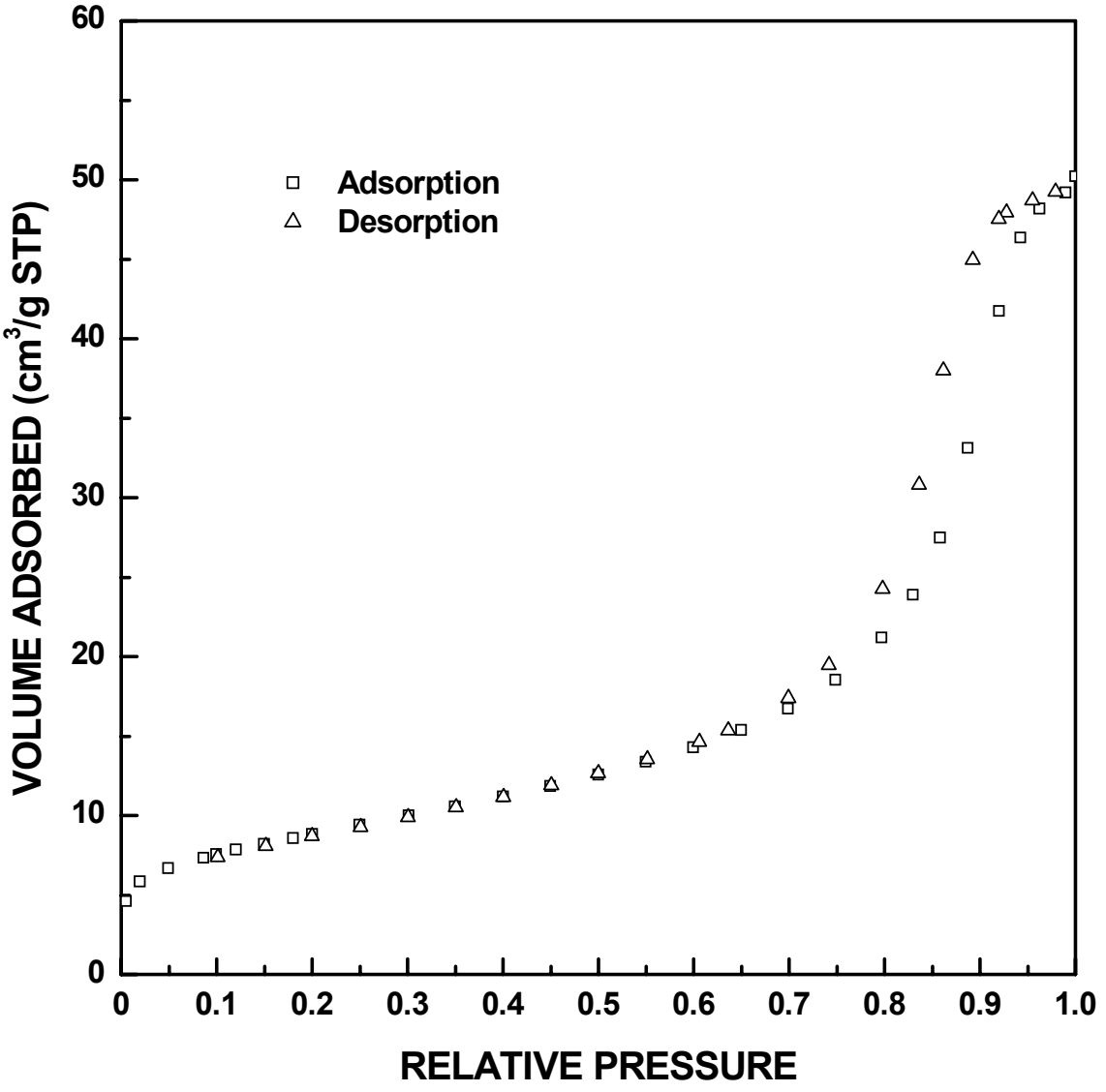

Figure I-11 Adsorption/desorption isotherm plots for SC35-1200(16h) sample (X_{WL} = 0.26).

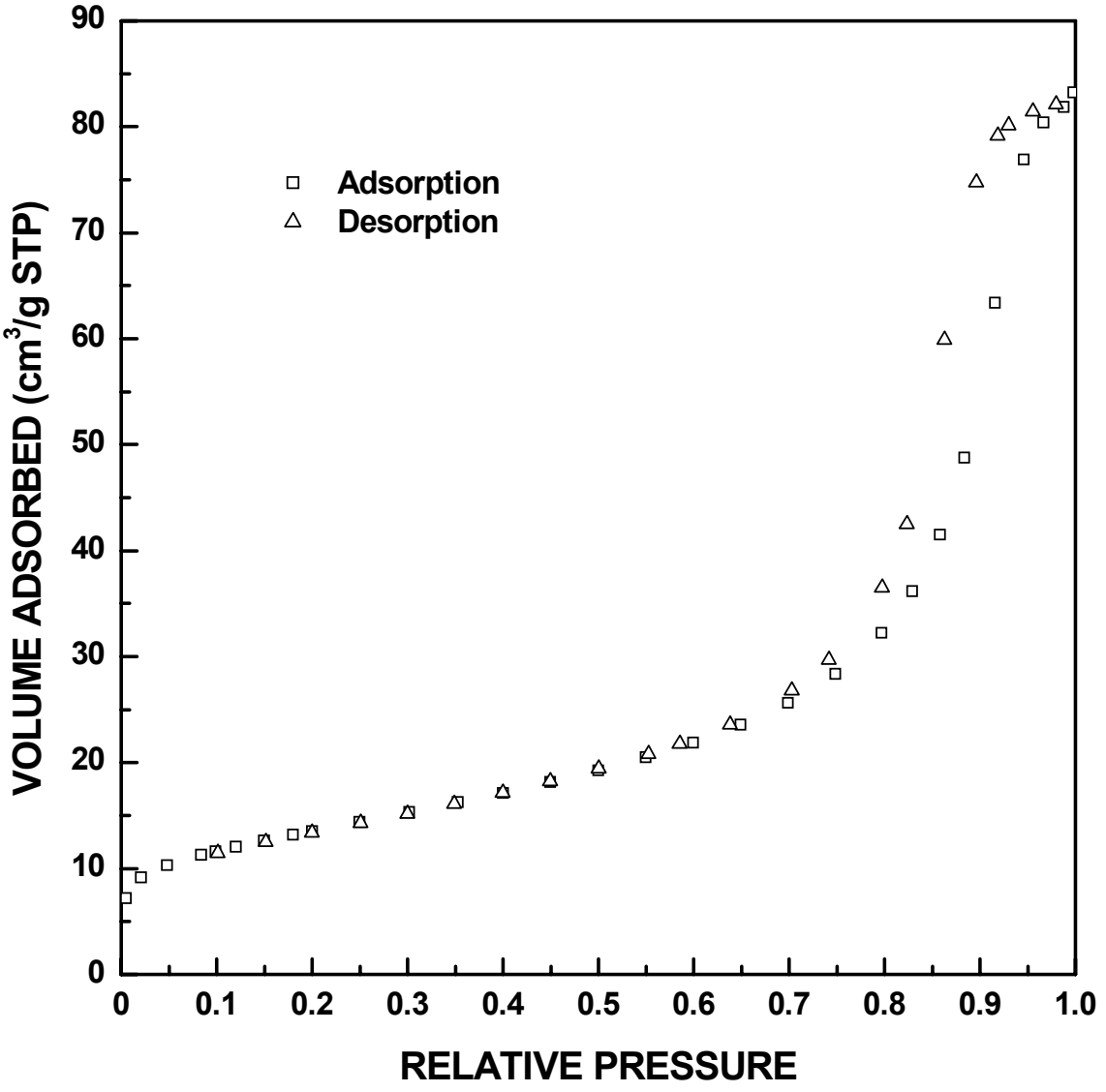

Figure I-12 Adsorption/desorption isotherm plots for SC35-1200(22.5h) sample (X_{WL} = 0.38).

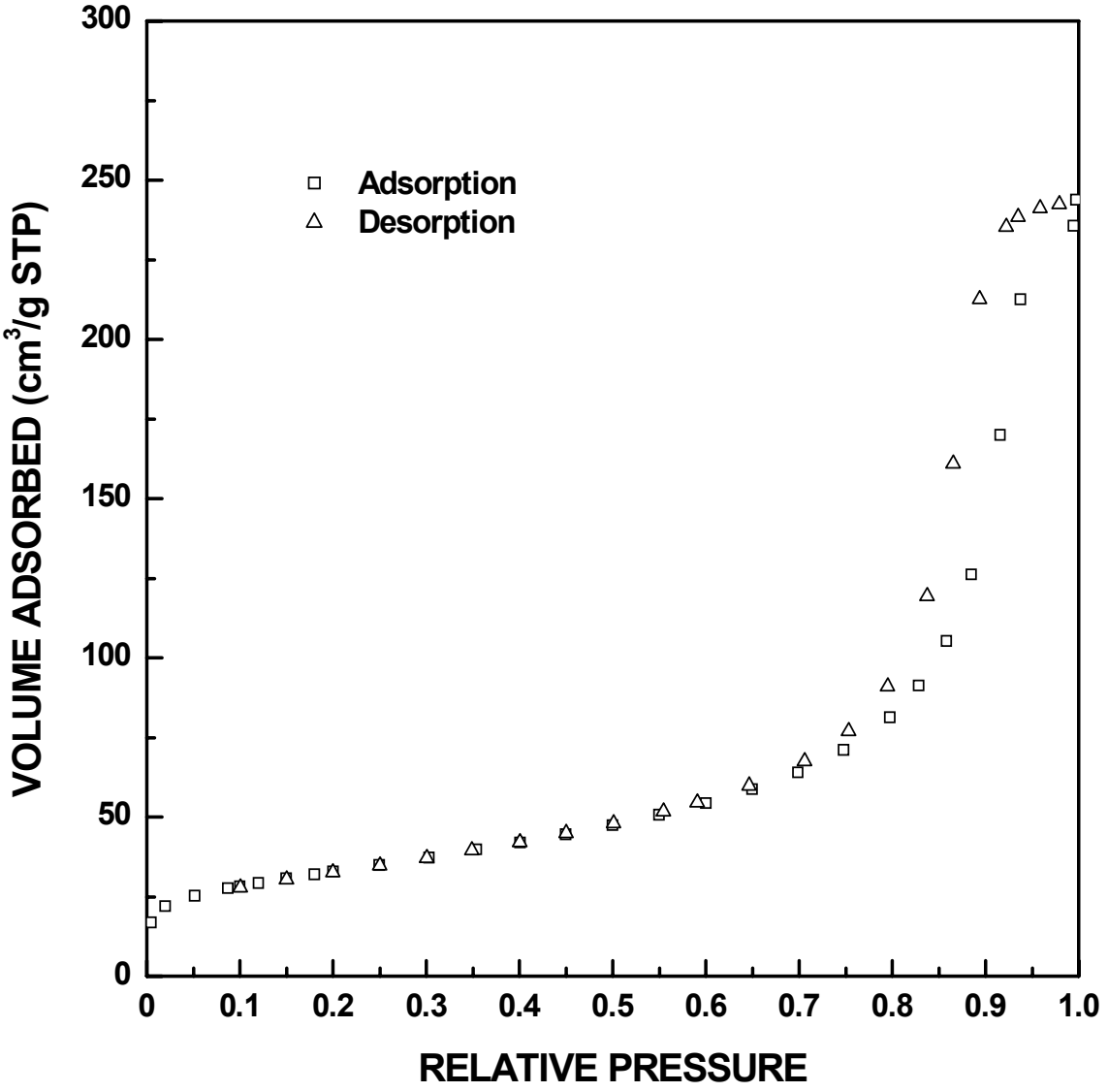

Figure I-13 Adsorption/desorption isotherm plots for SC35-1250(16h) sample (X_{WL} = 0.70).

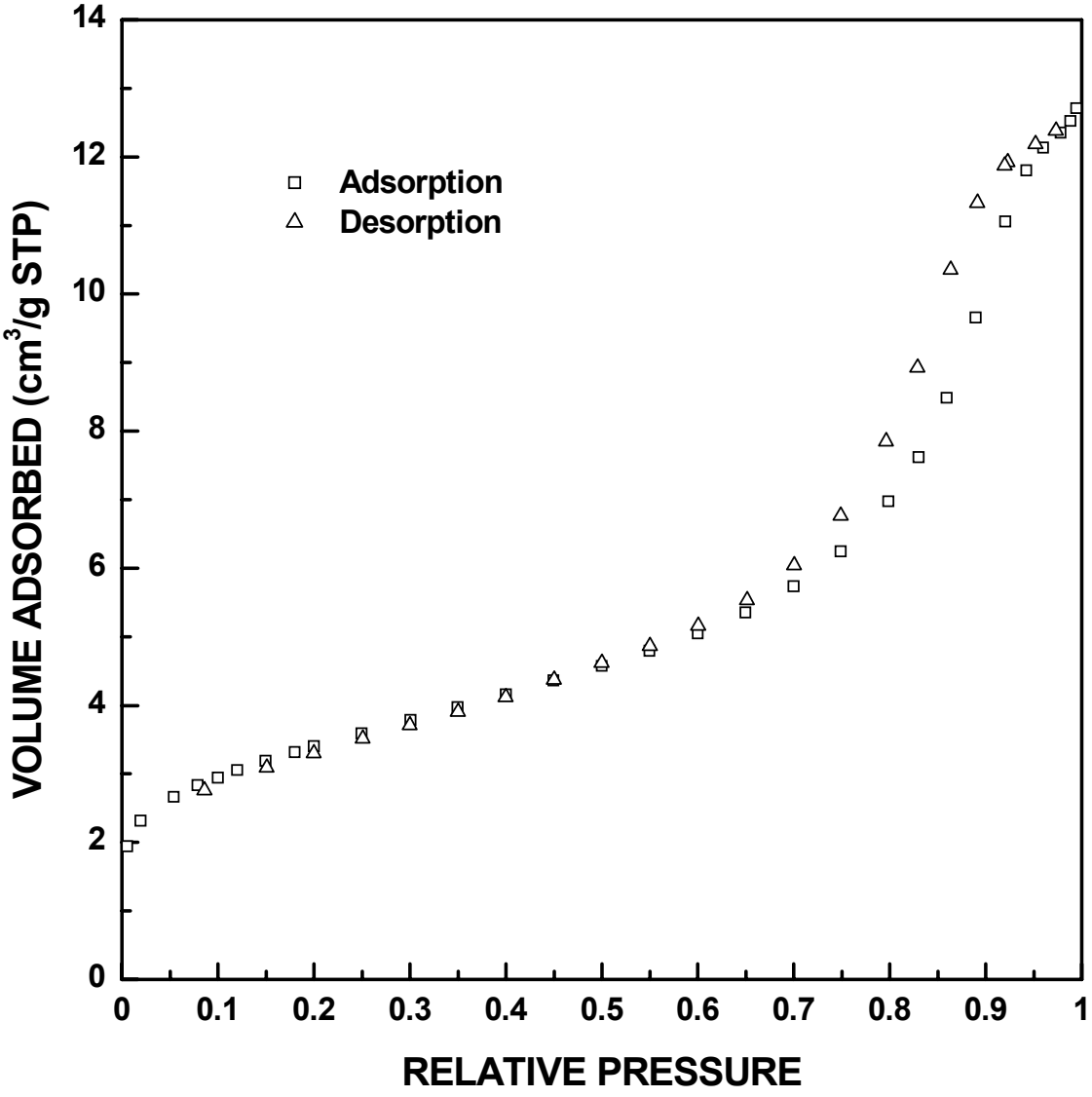

Figure I-14 Adsorption/desorption isotherm plots for SC35-1300(0.5h) sample (X_{WL} = 0.10).

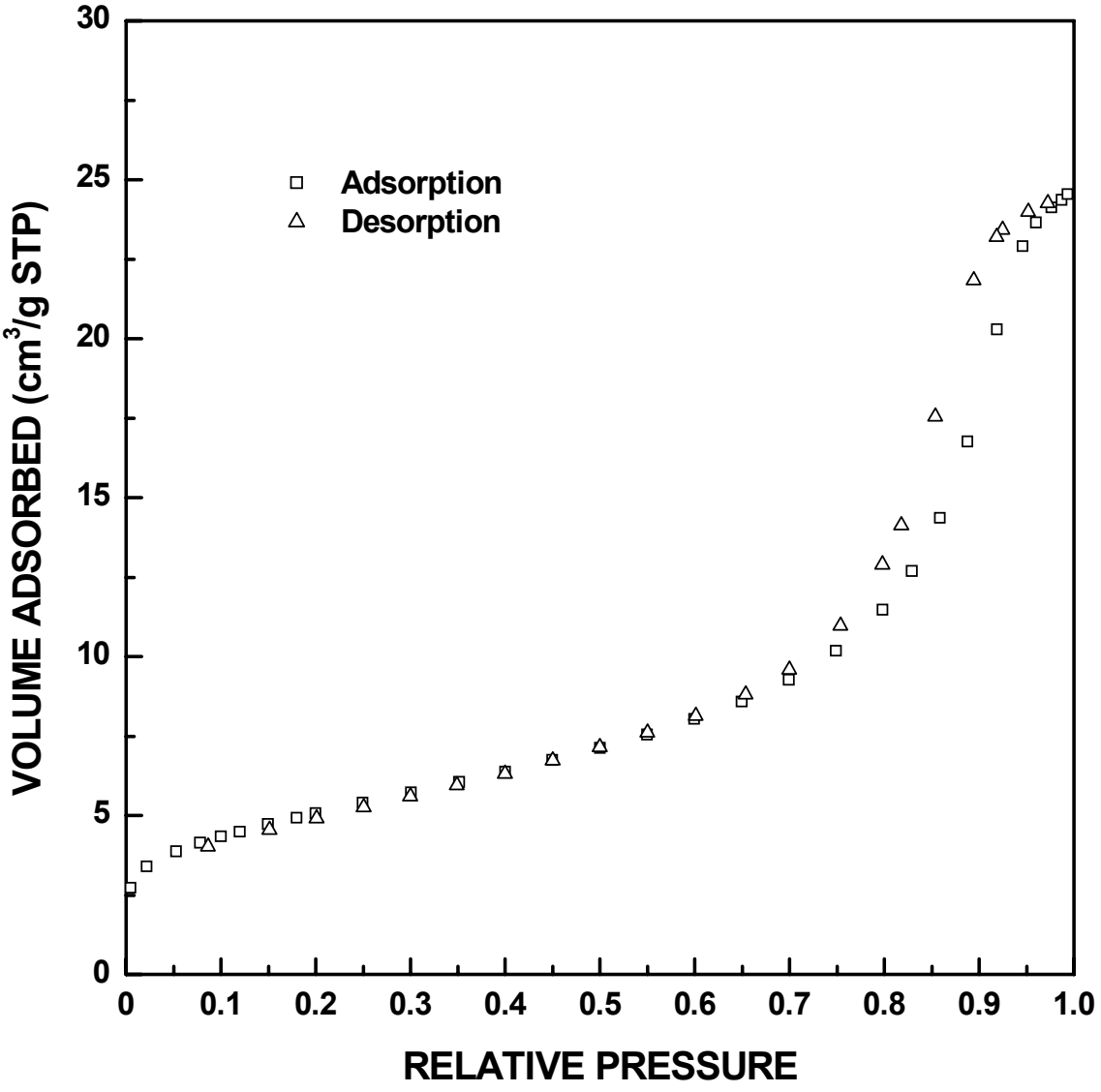

Figure I-15 Adsorption/desorption isotherm plots for SC35-1300(1h) sample (X_{WL} = 0.17).

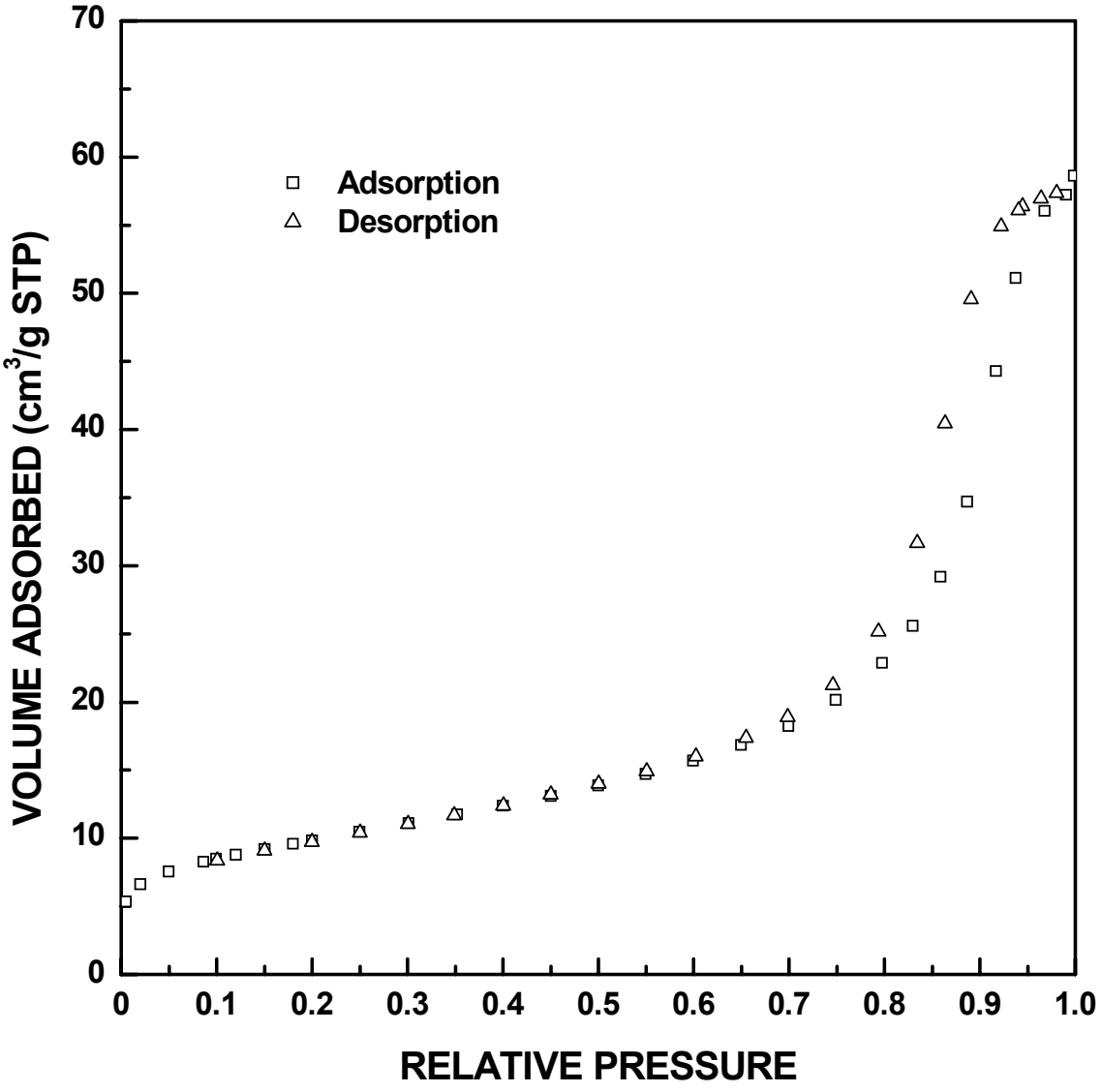

Figure I-16 Adsorption/desorption isotherm plots for SC35-1300(2h) sample (X_{WL} = 0.30).

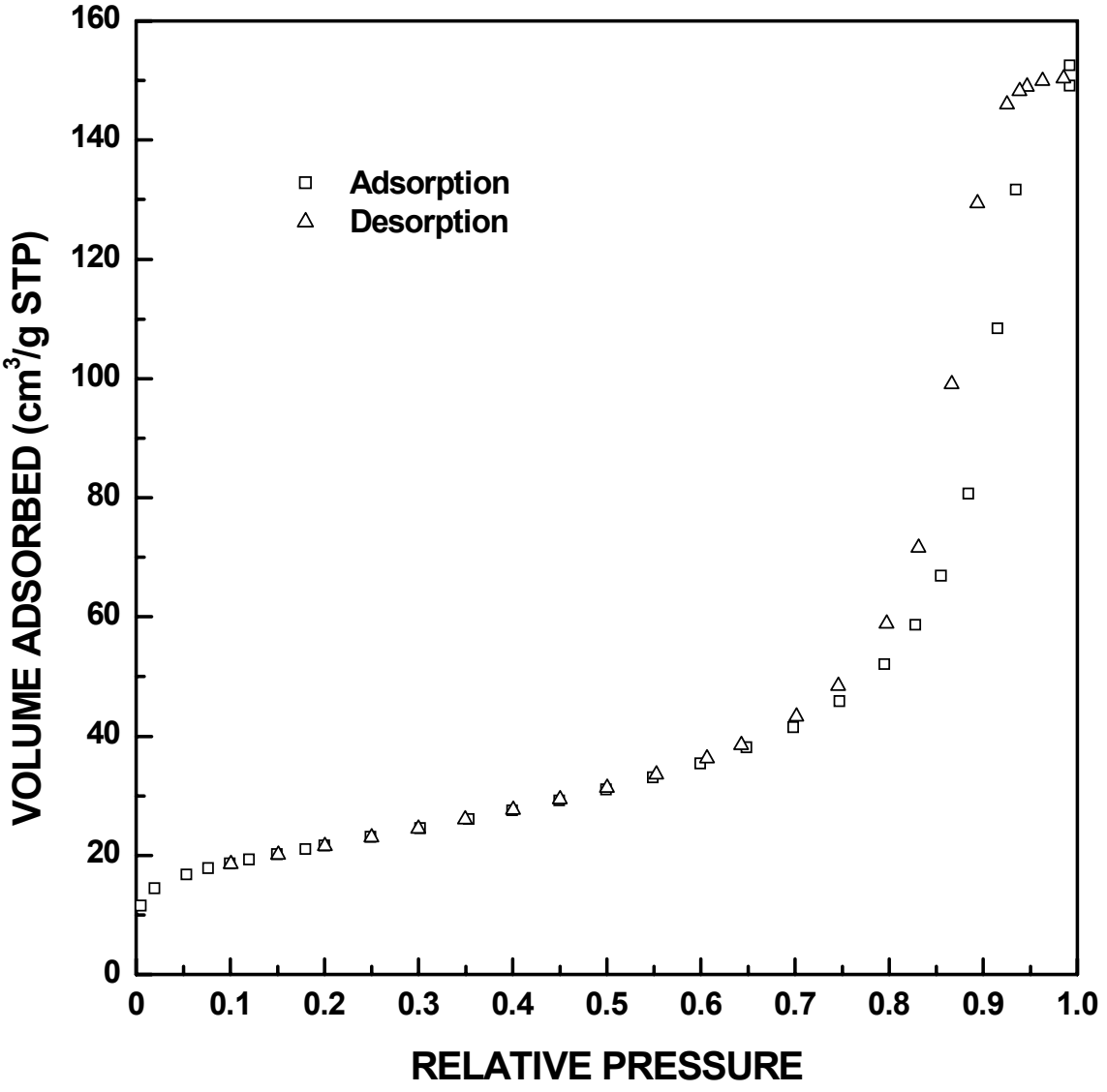

Figure I-17 Adsorption/desorption isotherm plots for SC35-1300(4h) sample (X_{WL} = 0.54).

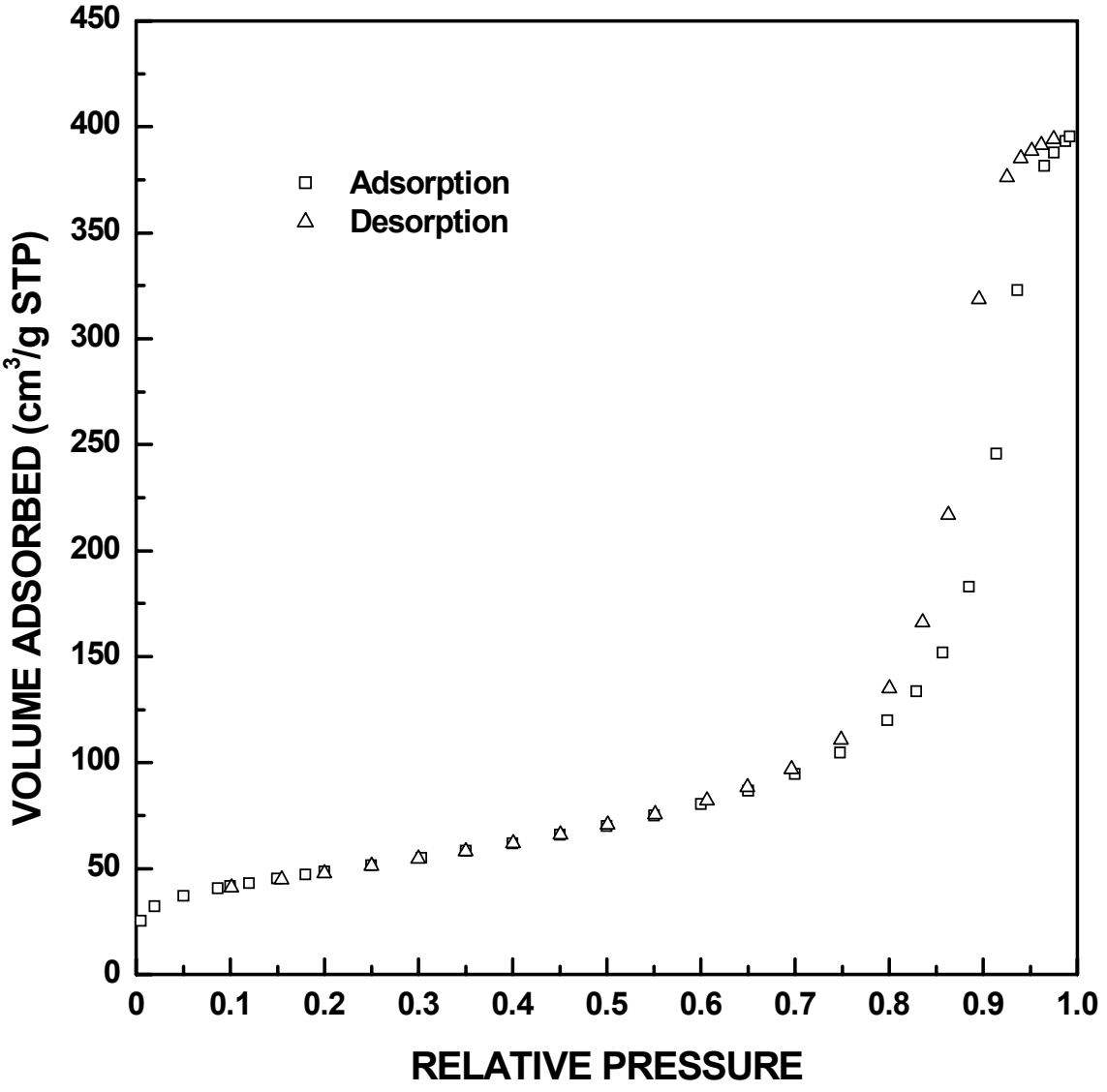

Figure I-18 Adsorption/desorption isotherm plots for SC35-1300(8h) sample (X_{WL} = 0.84).

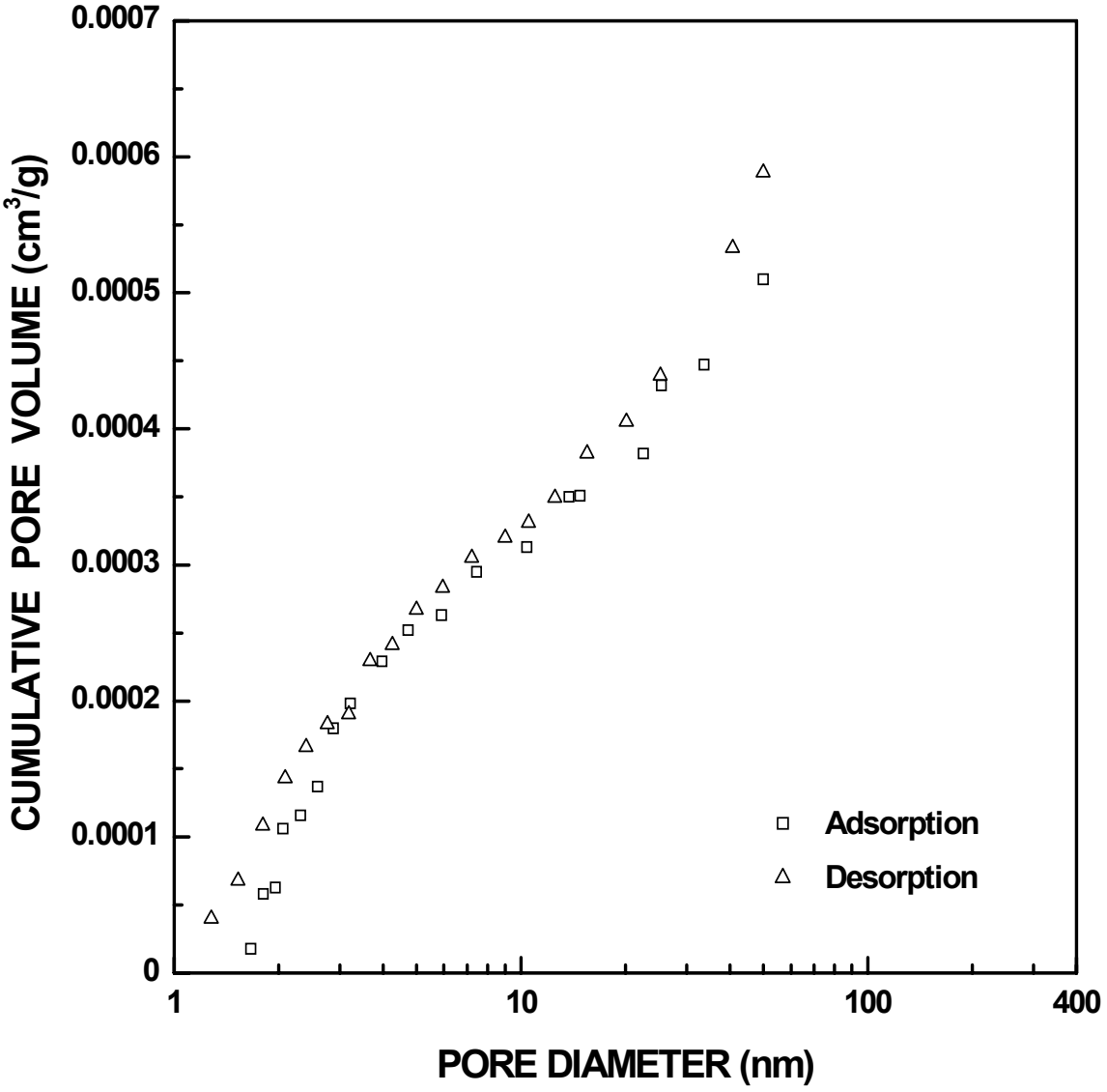

Figure I-19 Plots of cumulative specific pore volume vs. pore diameter for SC35-1160(30min) sample (X_{WL} = 0.01). The pore diameter was cut off at 50 nm.

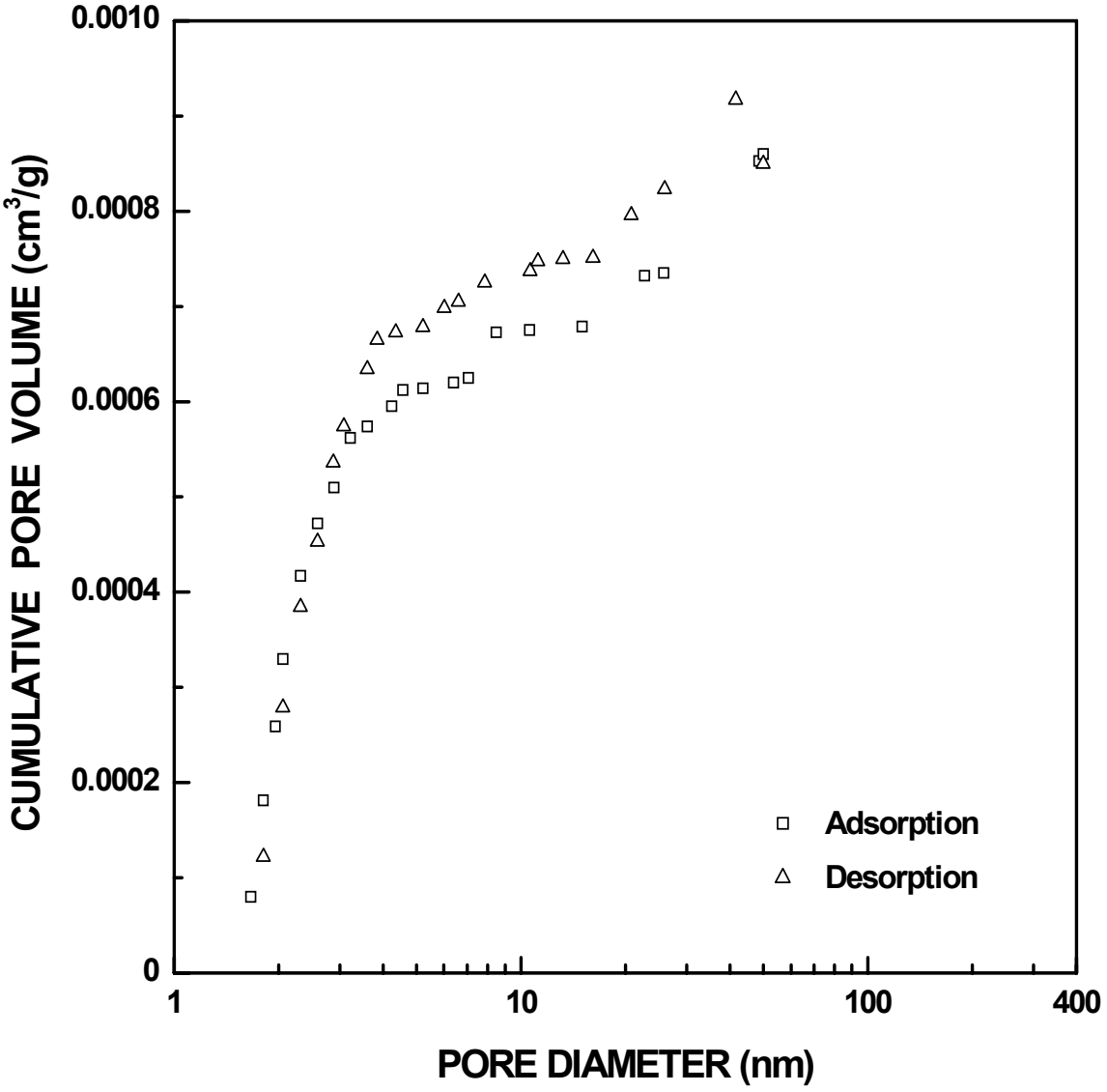

Figure I-20 Plots of cumulative specific pore volume vs. pore diameter for SC35-1160(2h) sample (X_{WL} = 0.03). The pore diameter was cut off at 50 nm.

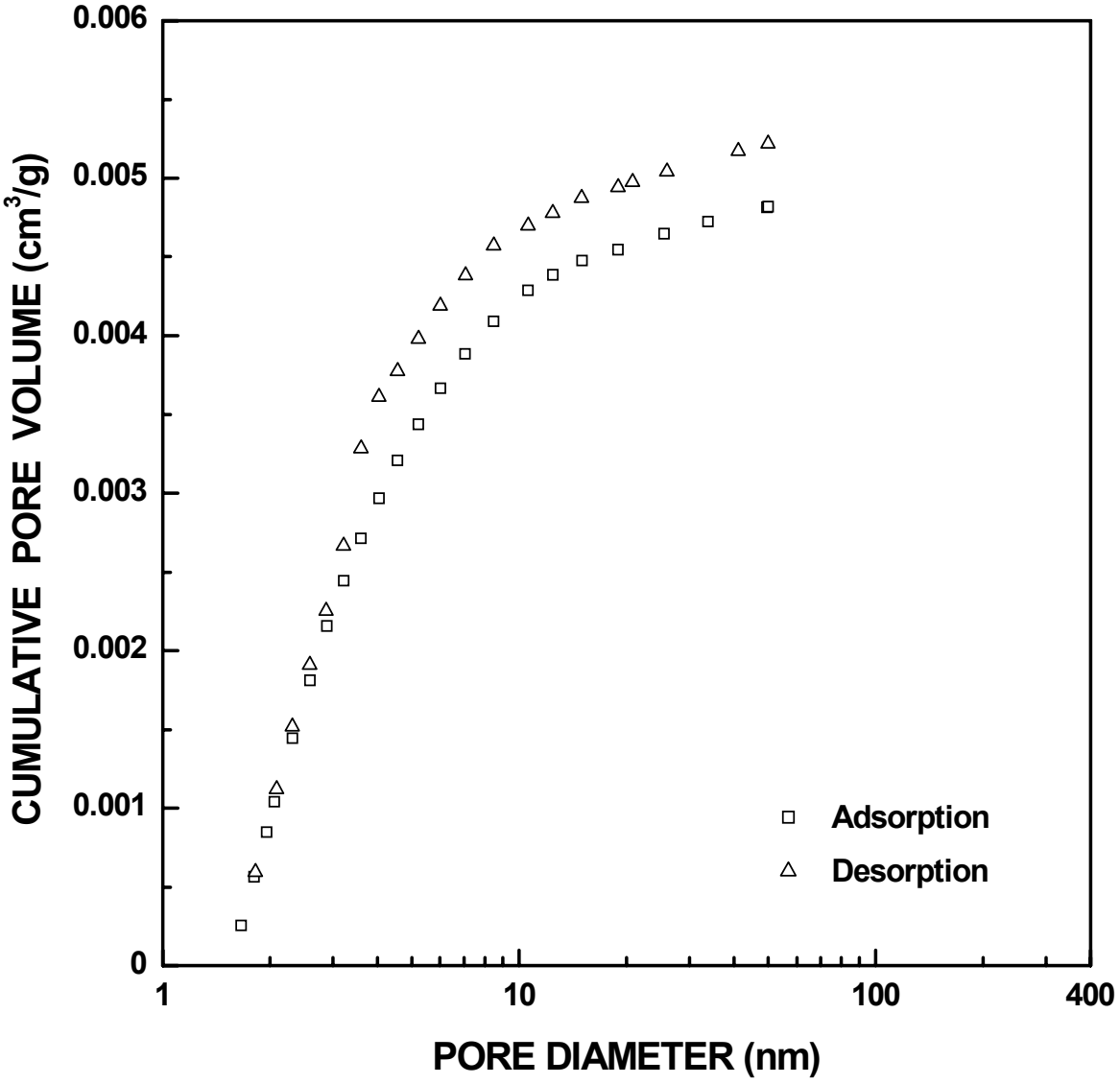

Figure I-21 Plots of cumulative specific pore volume vs. pore diameter for SC35-1160(4h) sample (X_{WL} = 0.05). The pore diameter was cut off at 50 nm.

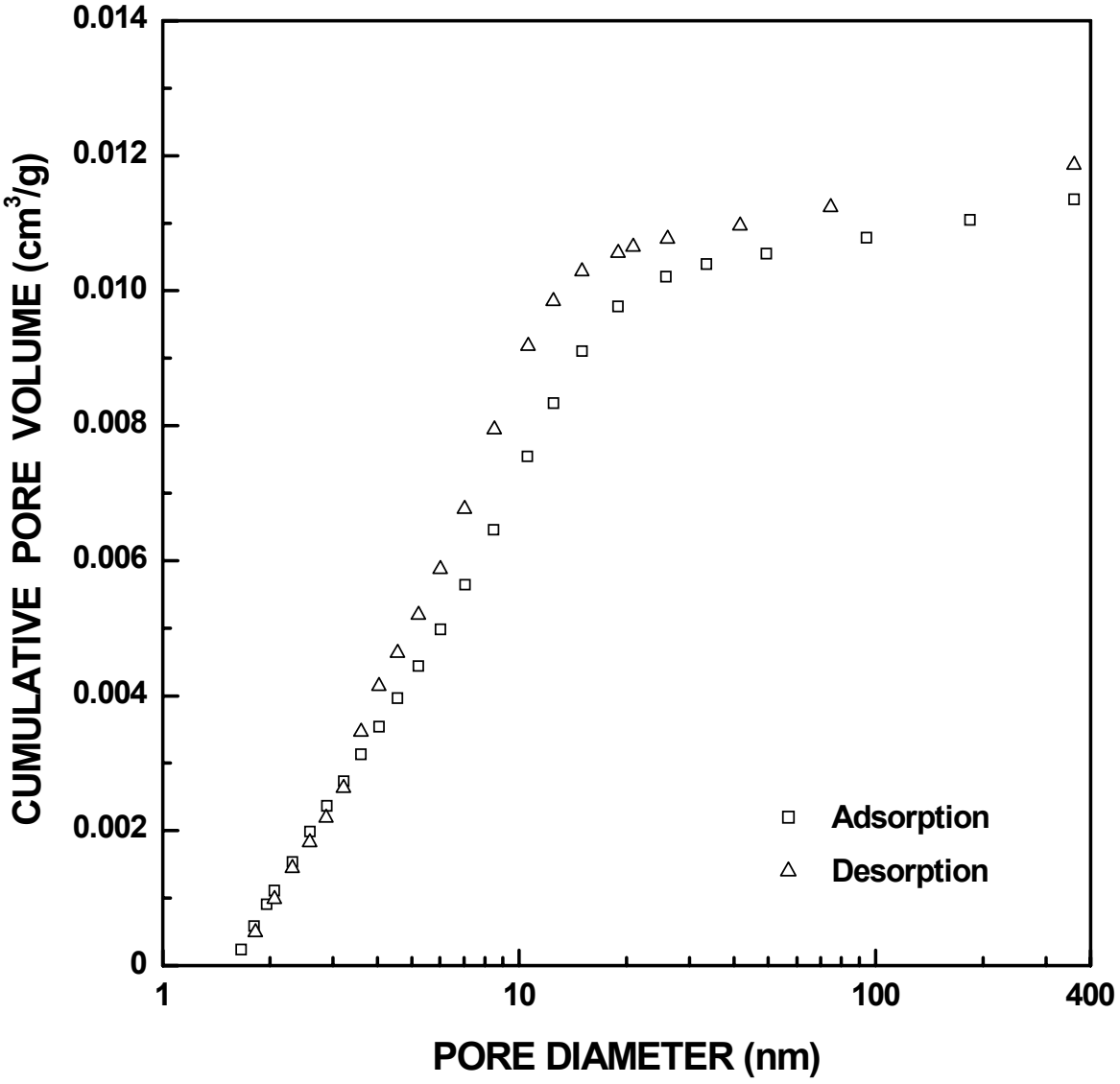

Figure I-22 Plots of cumulative specific pore volume vs. pore diameter for SC35-1160(8h) sample (X_{WL} = 0.07).

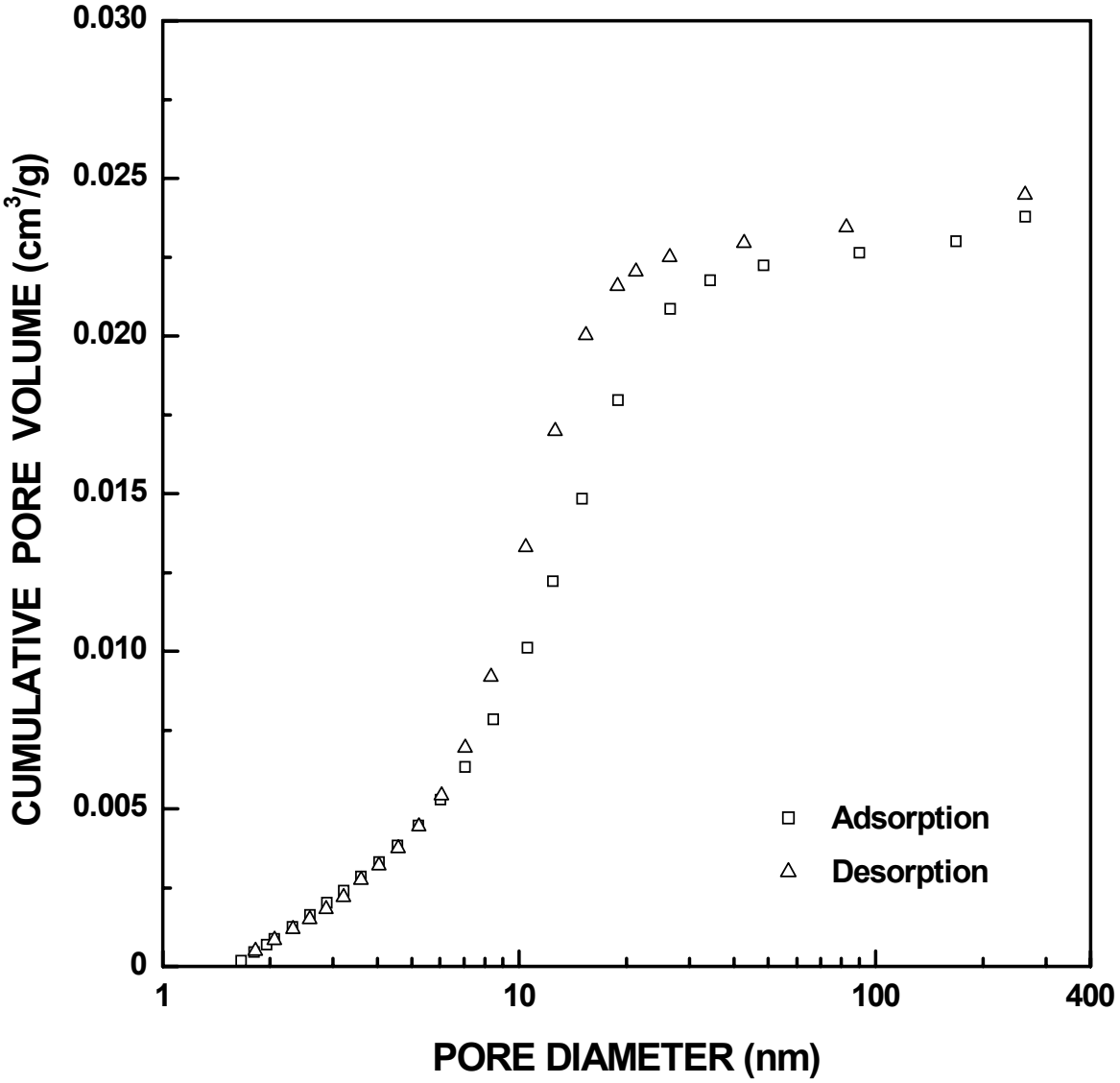

Figure I-23 Plots of cumulative specific pore volume vs. pore diameter for SC35-1160(16h) sample (X_{WL} = 0.12).

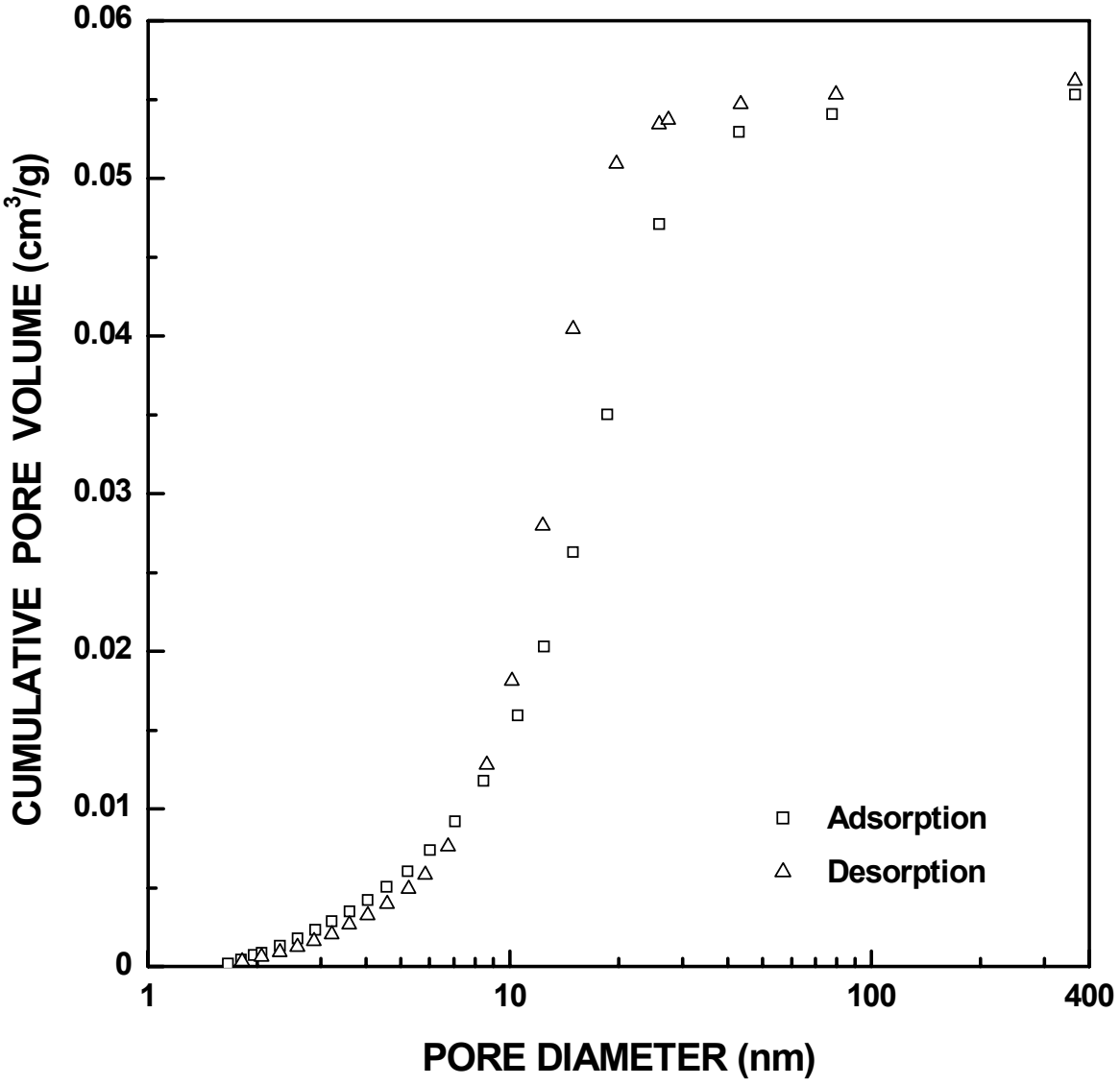

Figure I-24 Plots of cumulative specific pore volume vs. pore diameter for SC35-1160(32h) sample (X_{WL} = 0.22).

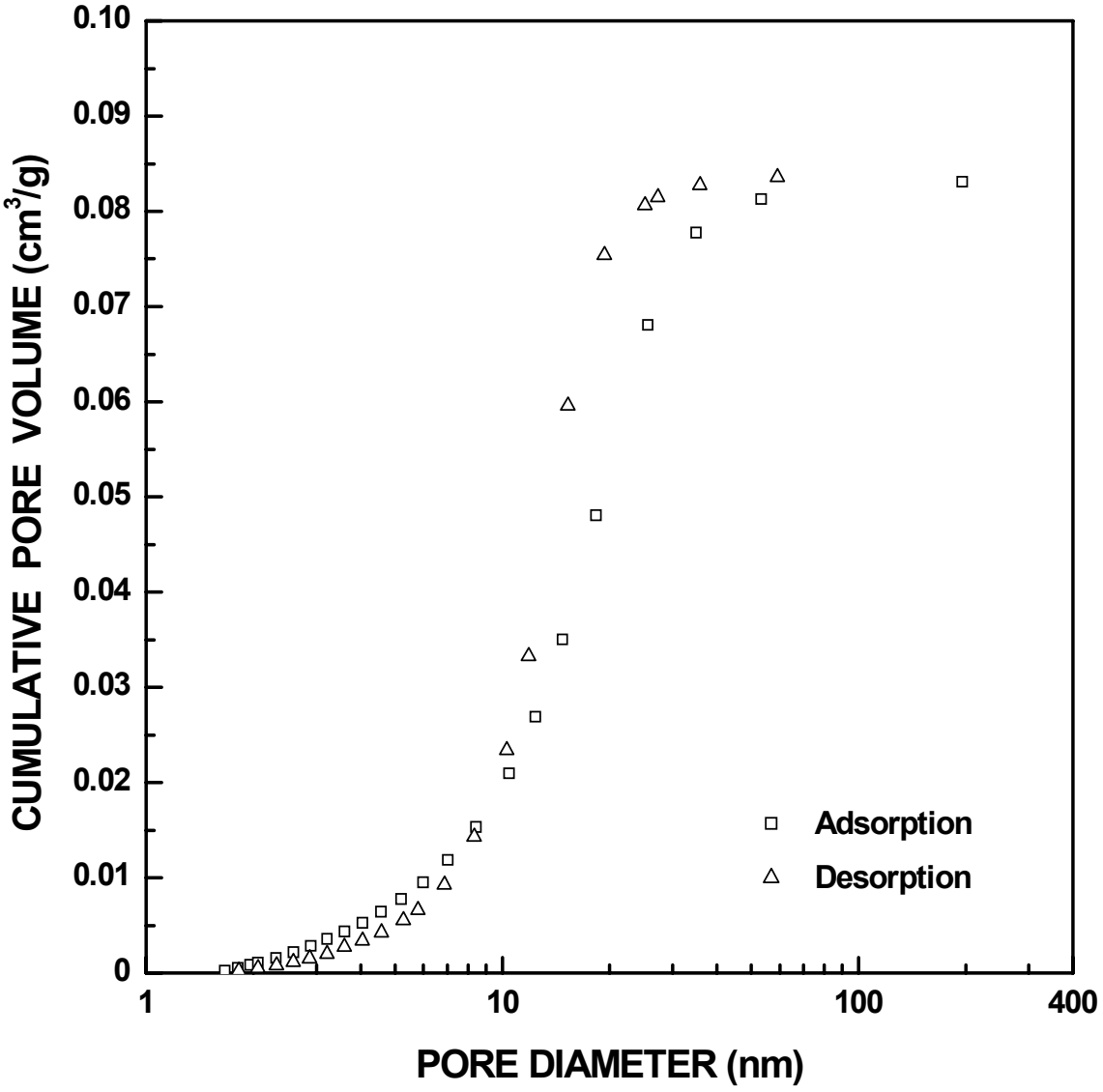

Figure I-25 Plots of cumulative specific pore volume vs. pore diameter for SC35-1160(48h) sample (X_{WL} = 0.29).

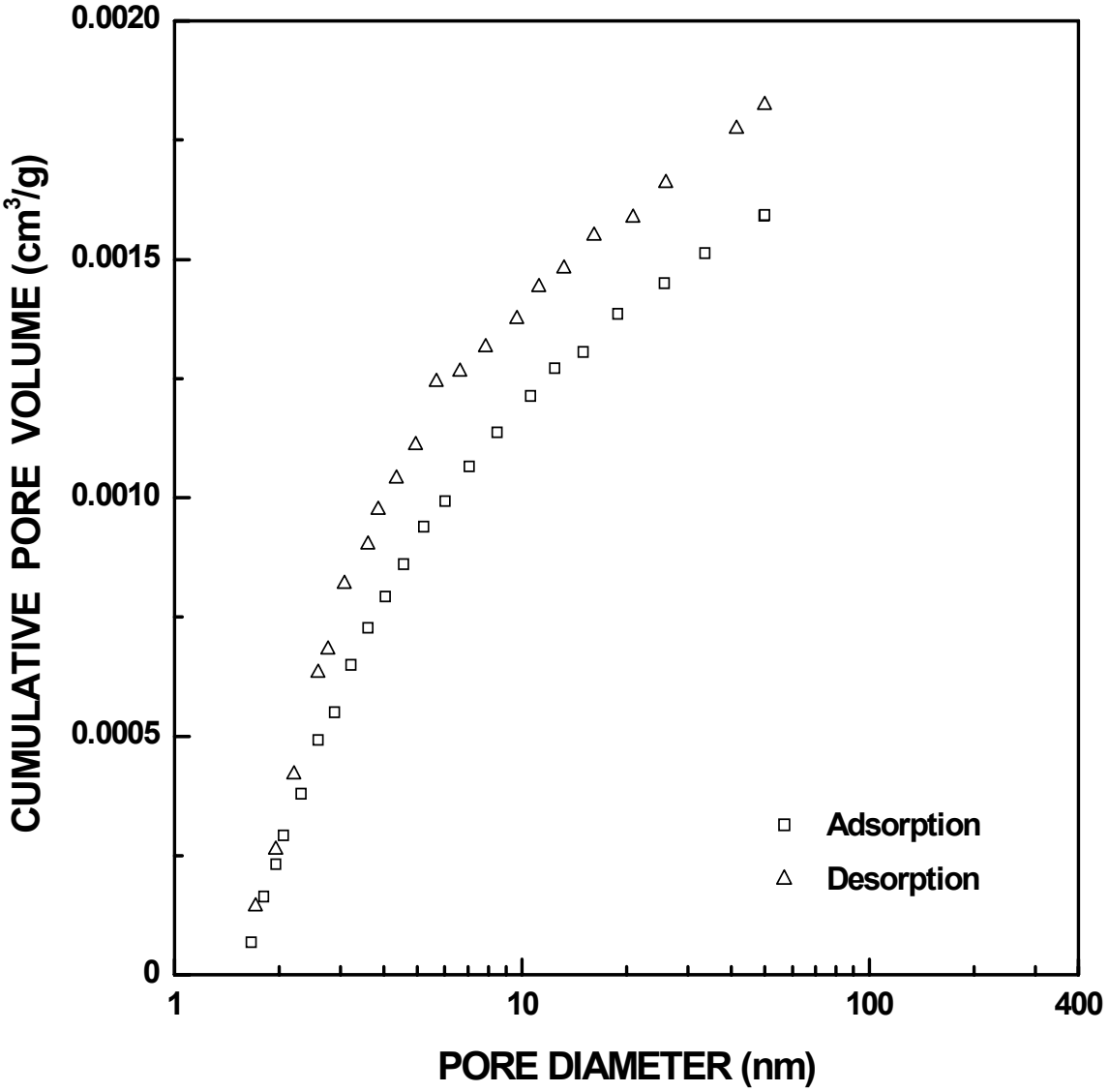

Figure I-26 Plots of cumulative specific pore volume vs. pore diameter for SC35-1200(30min) sample (X_{WL} = 0.02). The pore diameter was cut off at 50 nm.

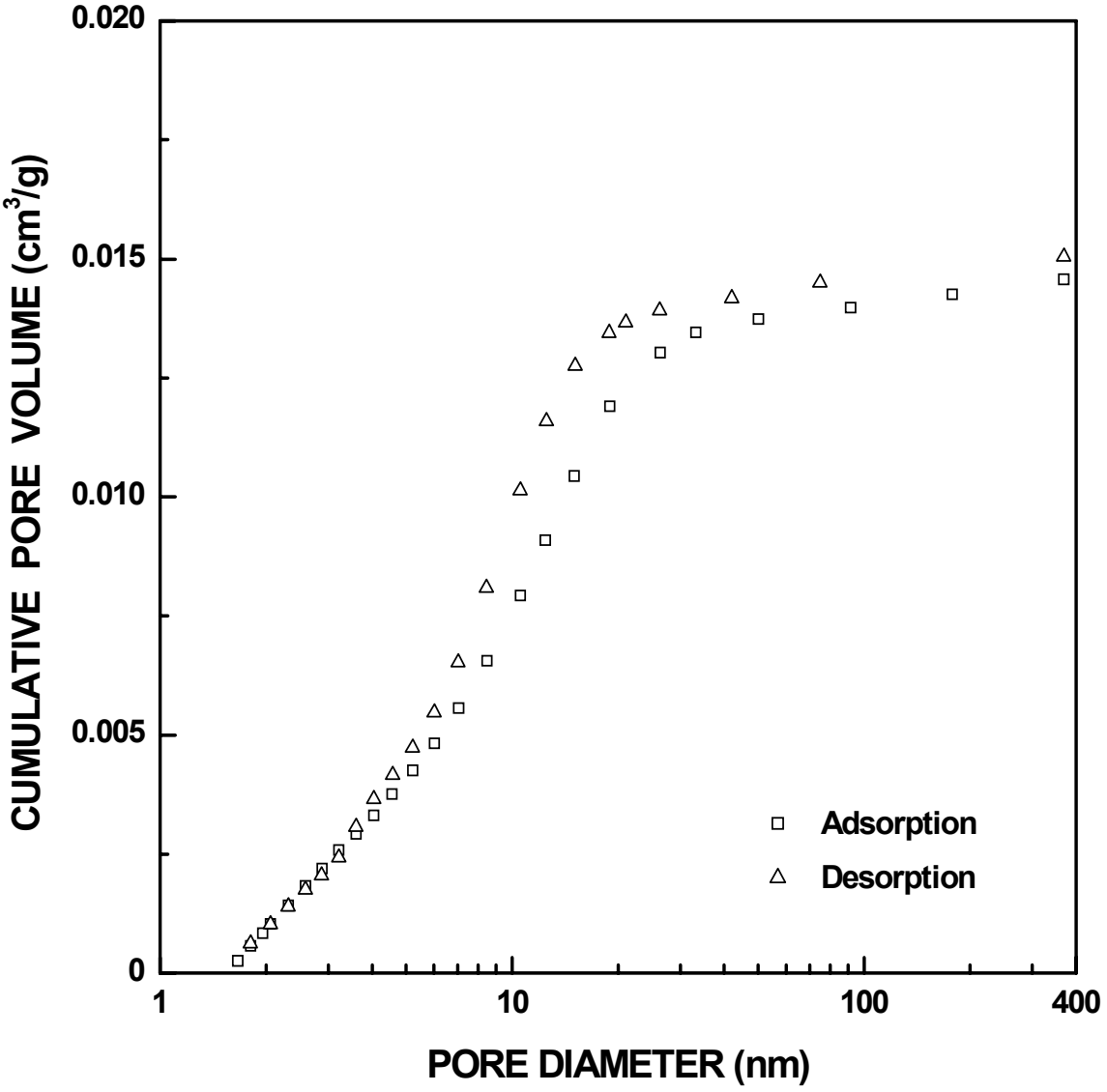

Figure I-27 Plots of cumulative specific pore volume vs. pore diameter for SC35-1200(4h) sample (X_{WL} = 0.09).

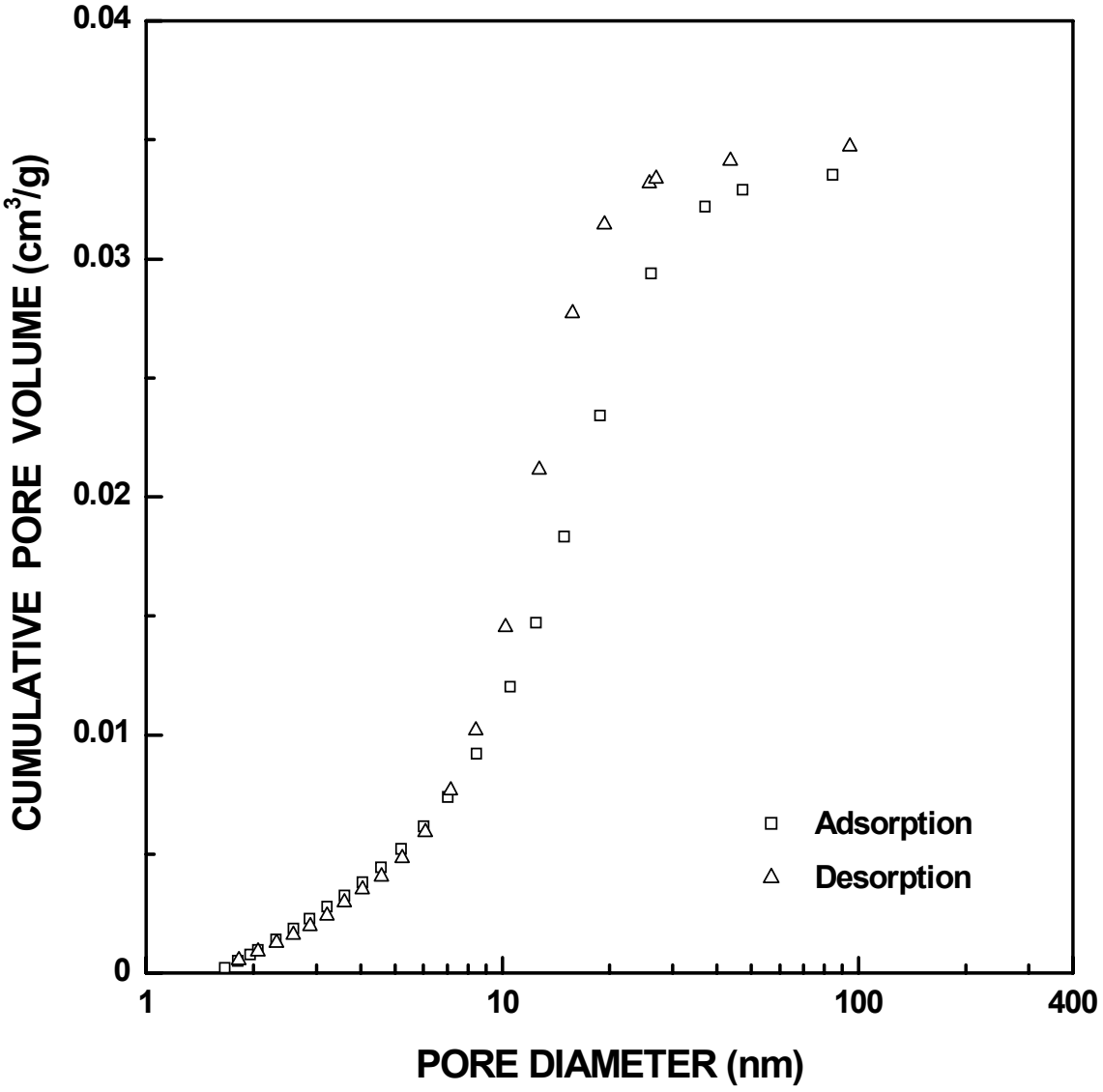

Figure I-28 Plots of cumulative specific pore volume vs. pore diameter for SC35-1200(8h) sample (X_{WL} = 0.16).

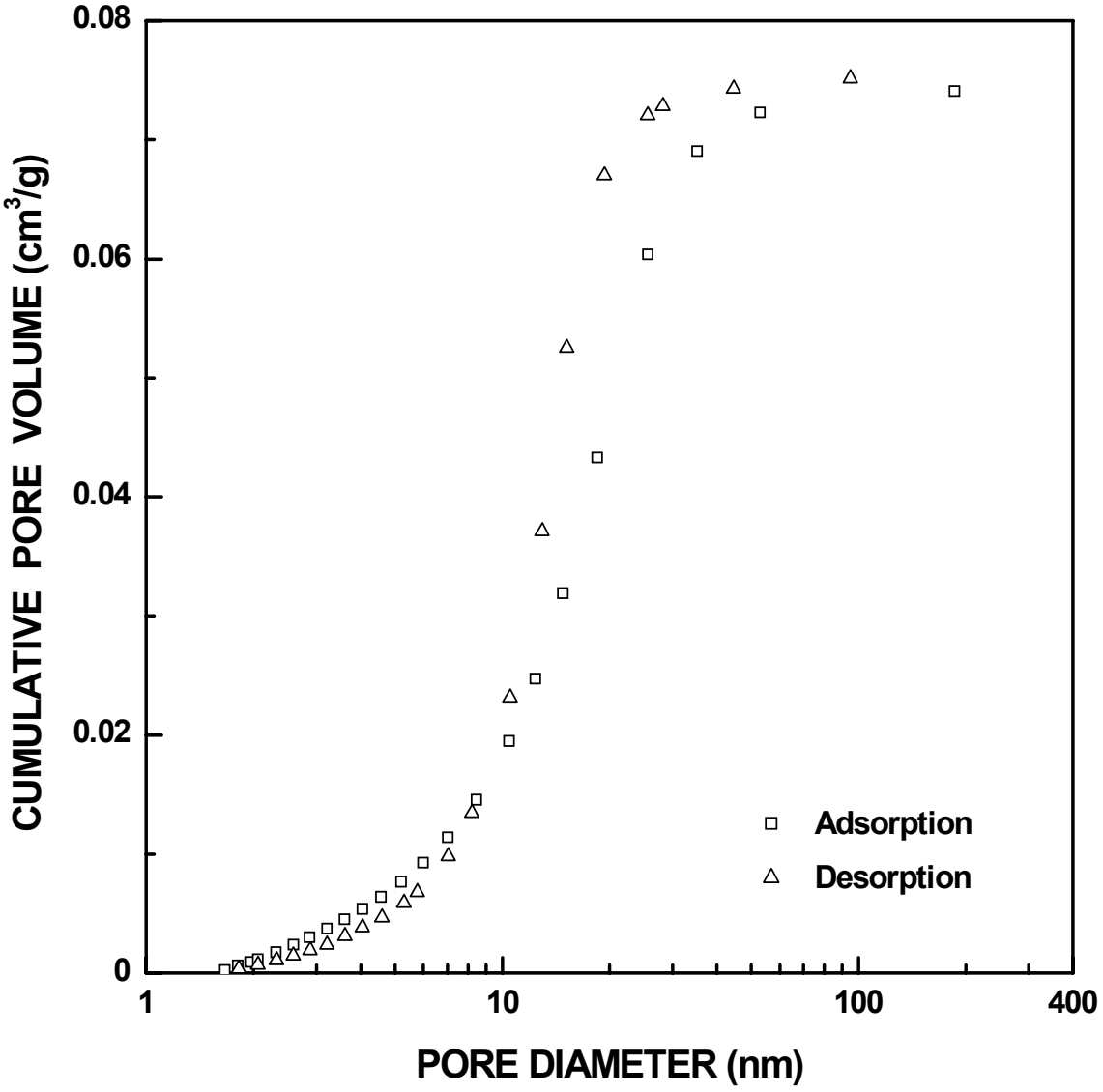

Figure I-29 Plots of cumulative specific pore volume vs. pore diameter for SC35-1200(16h) sample (X_{WL} = 0.26).

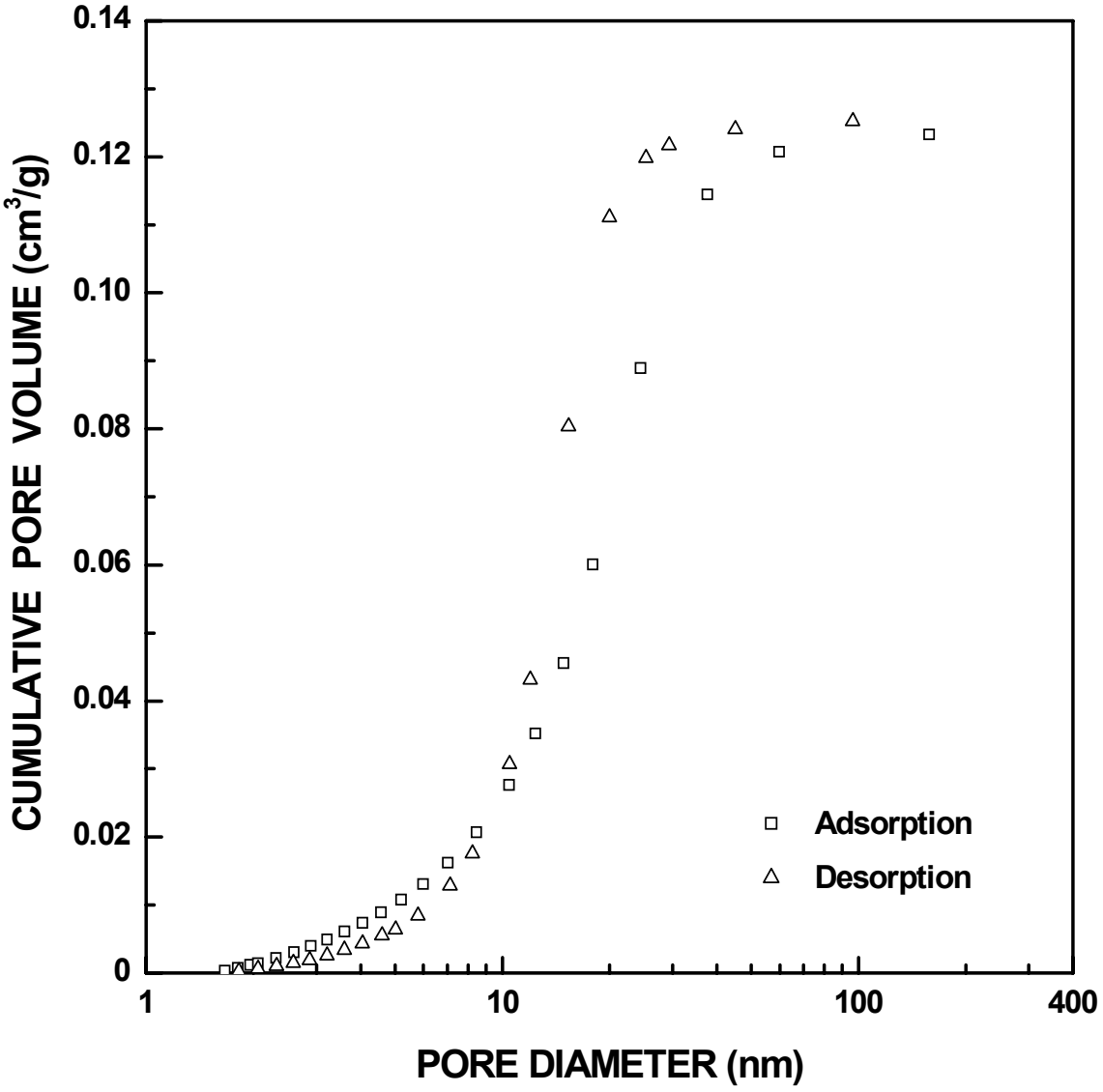

Figure I-30 Plots of cumulative specific pore volume vs. pore diameter for SC35-1200(22.5h) sample (X_{WL} = 0.38).

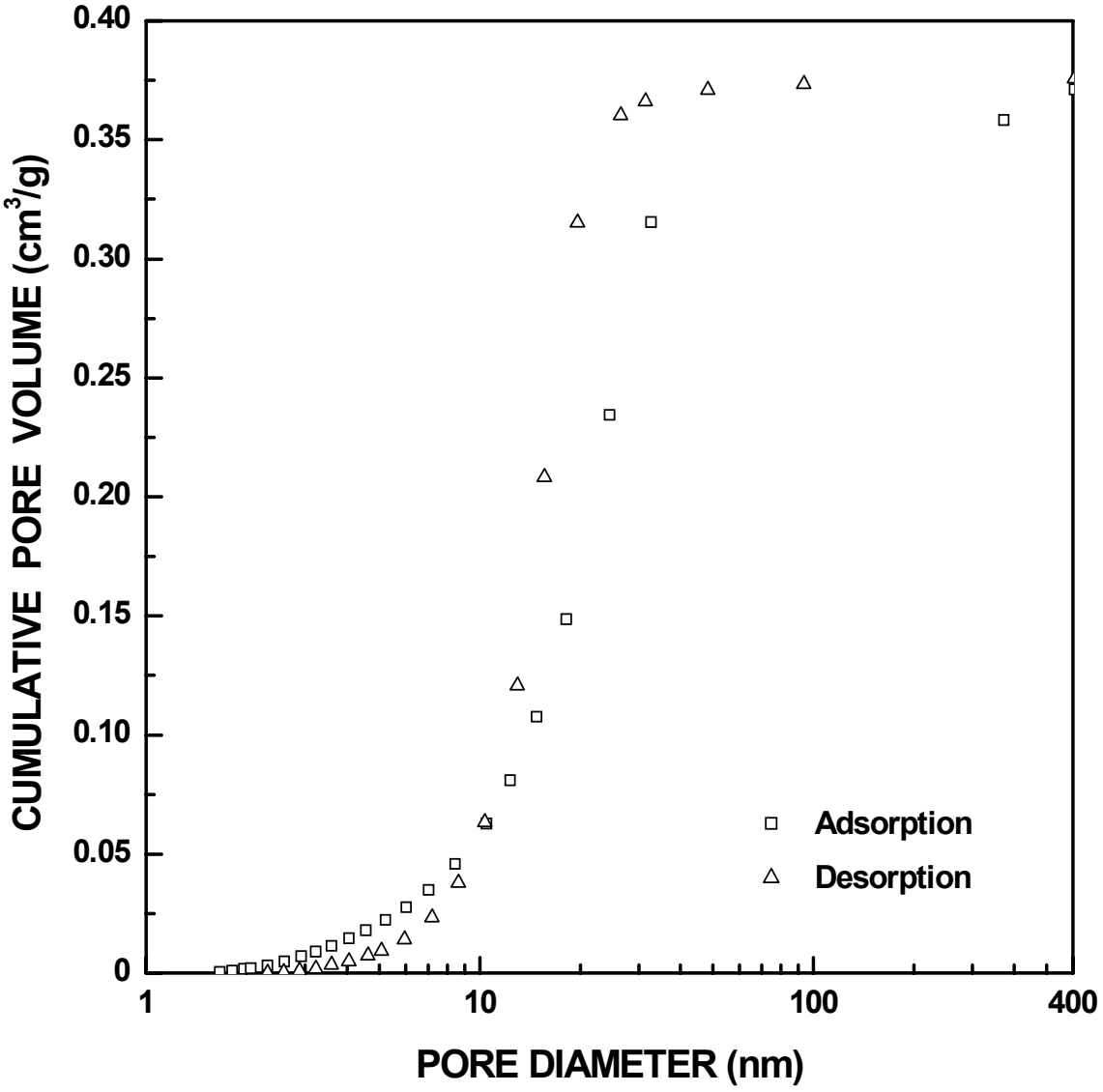

Figure I-31 Plots of cumulative specific pore volume vs. pore diameter for SC35-1250(16h) sample (X_{WL} = 0.70).

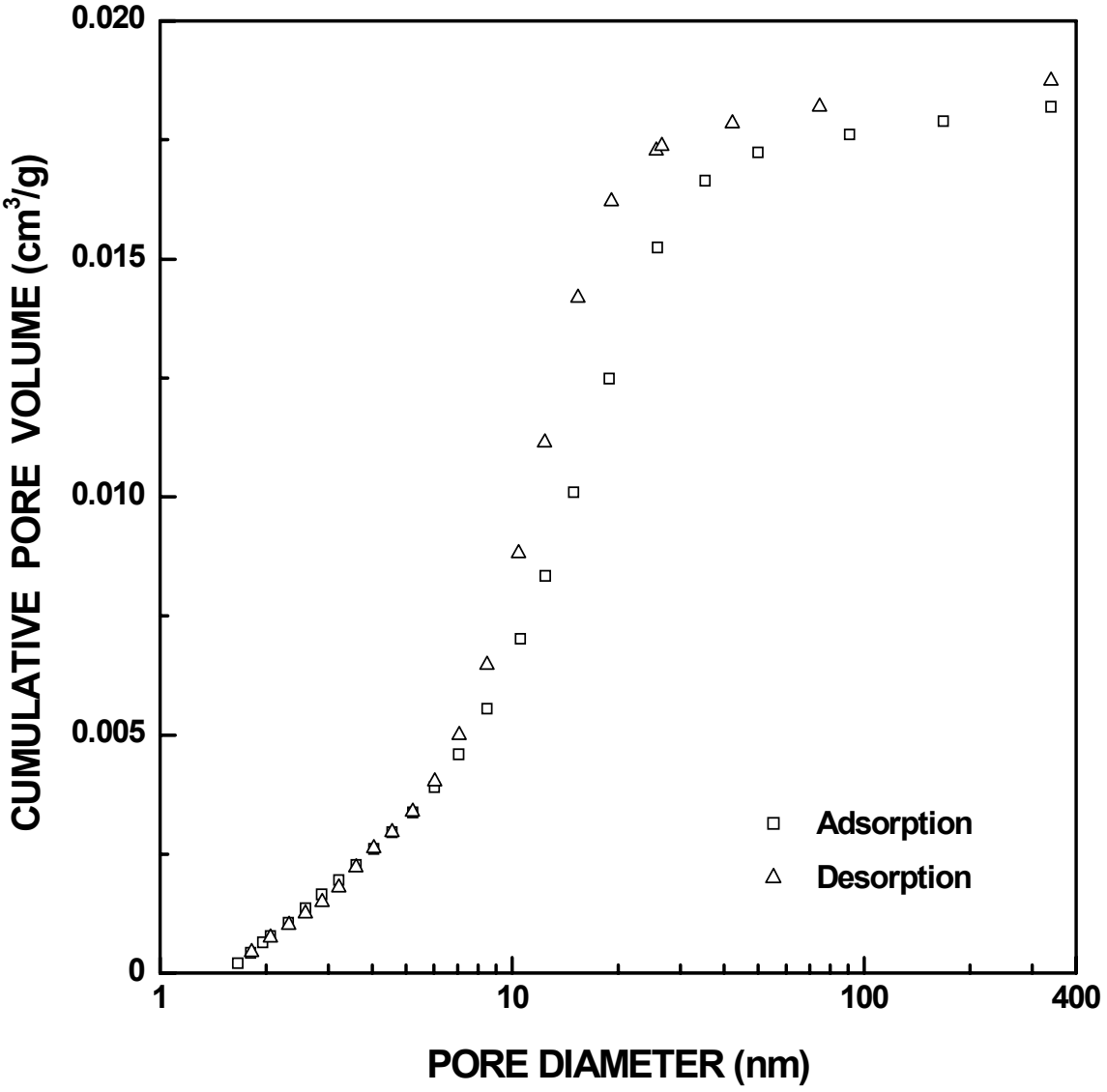

Figure I-32 Plots of cumulative specific pore volume vs. pore diameter for SC35-1300(30min) sample (X_{WL} = 0.10).

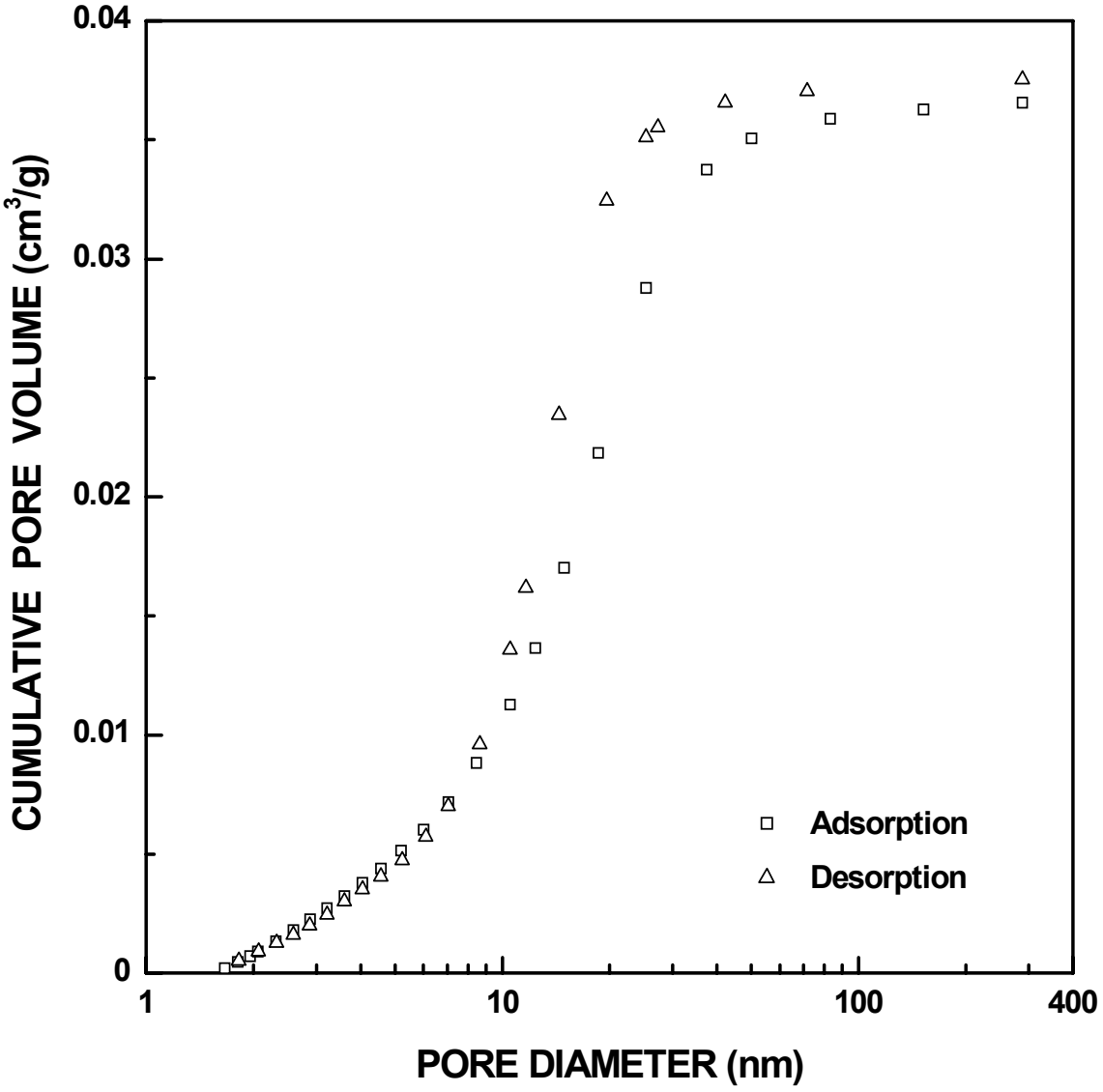

Figure I-33 Plots of cumulative specific pore volume vs. pore diameter for SC35-1300(1h) sample (X_{WL} = 0.17).

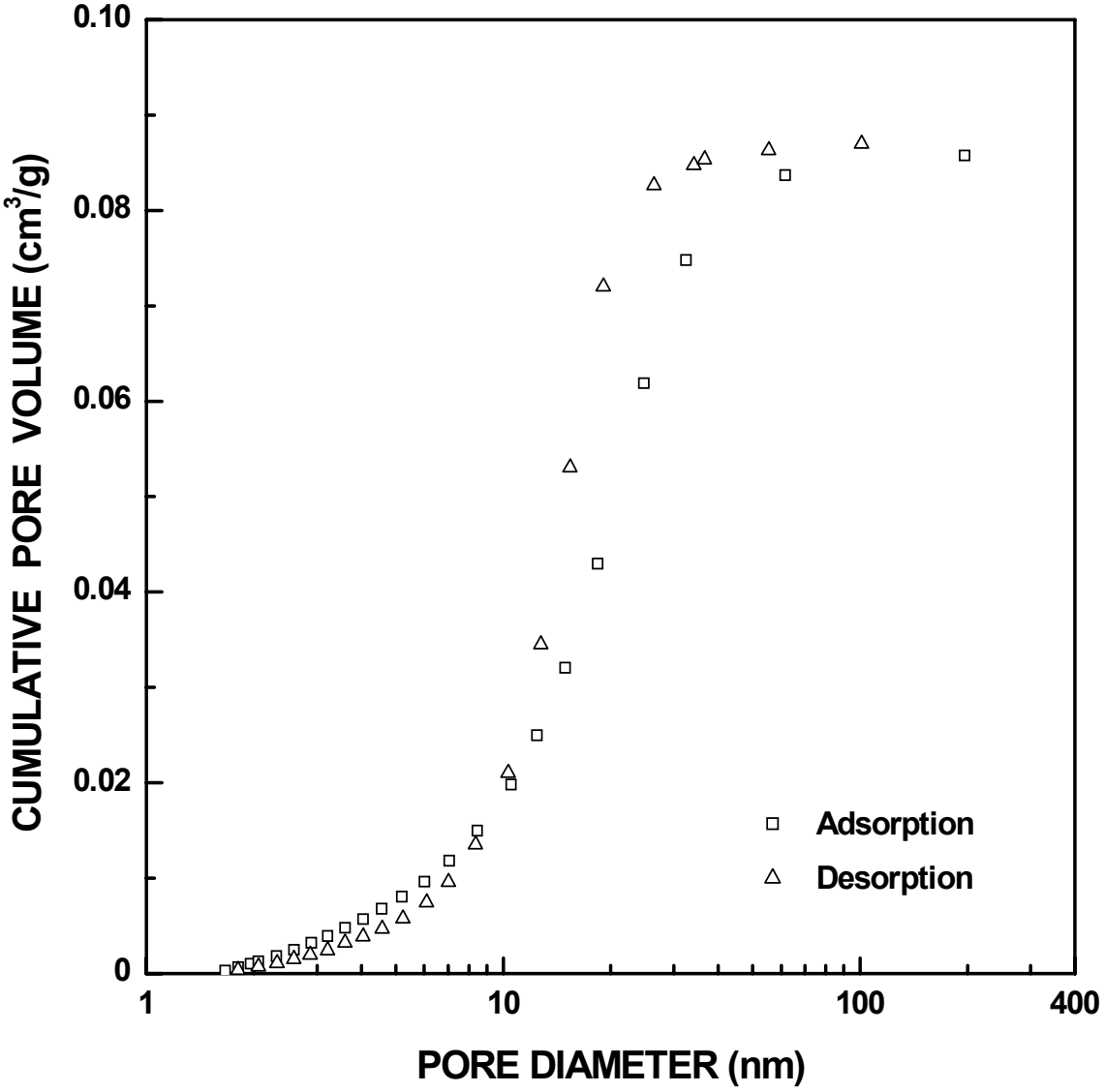

Figure I-34 Plots of cumulative specific pore volume vs. pore diameter for SC35-1300(2h) sample (X_{WL} = 0.30).

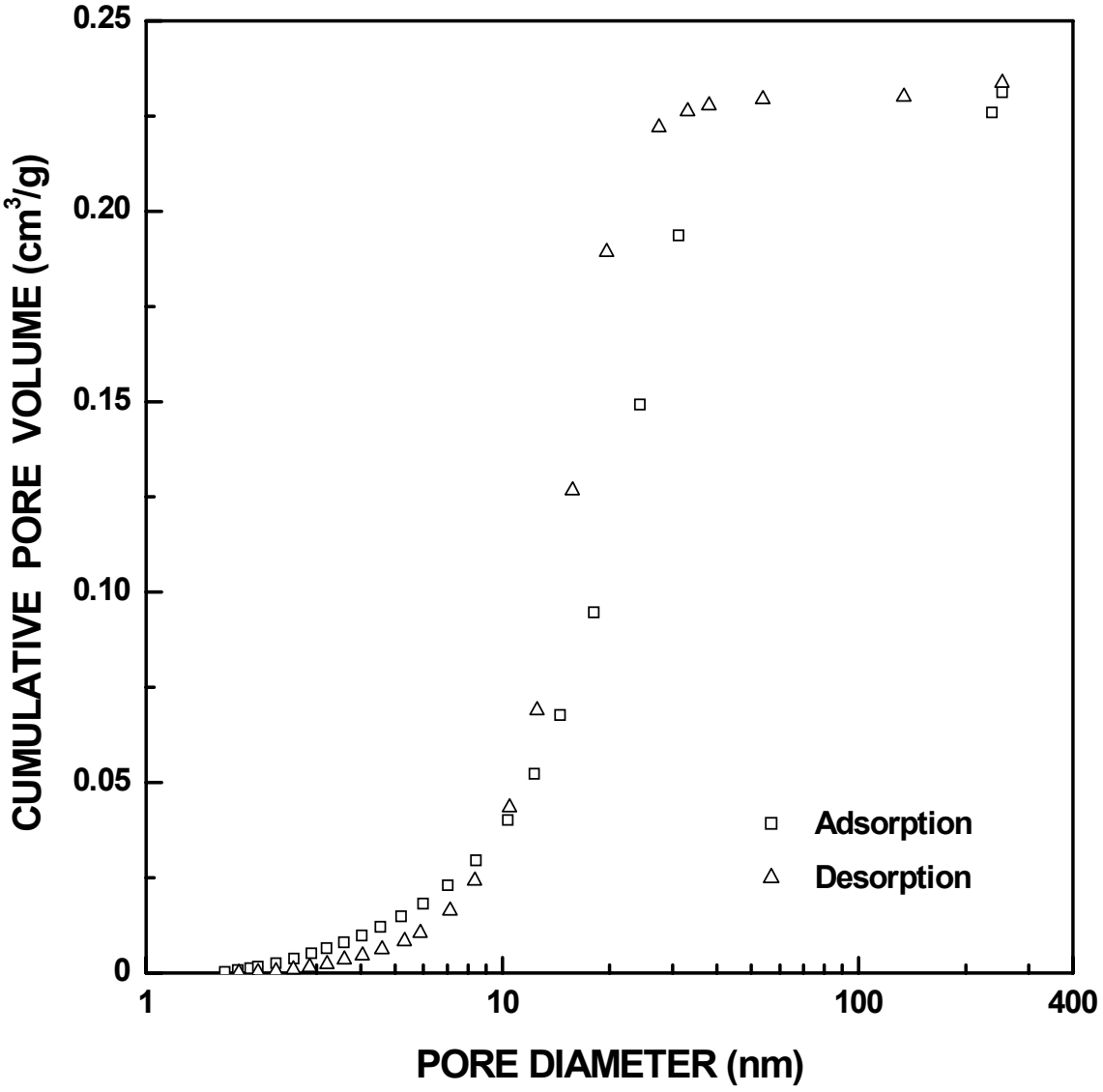

Figure I-35 Plots of cumulative specific pore volume vs. pore diameter for SC35-1300(4h) sample (X_{WL} = 0.54).

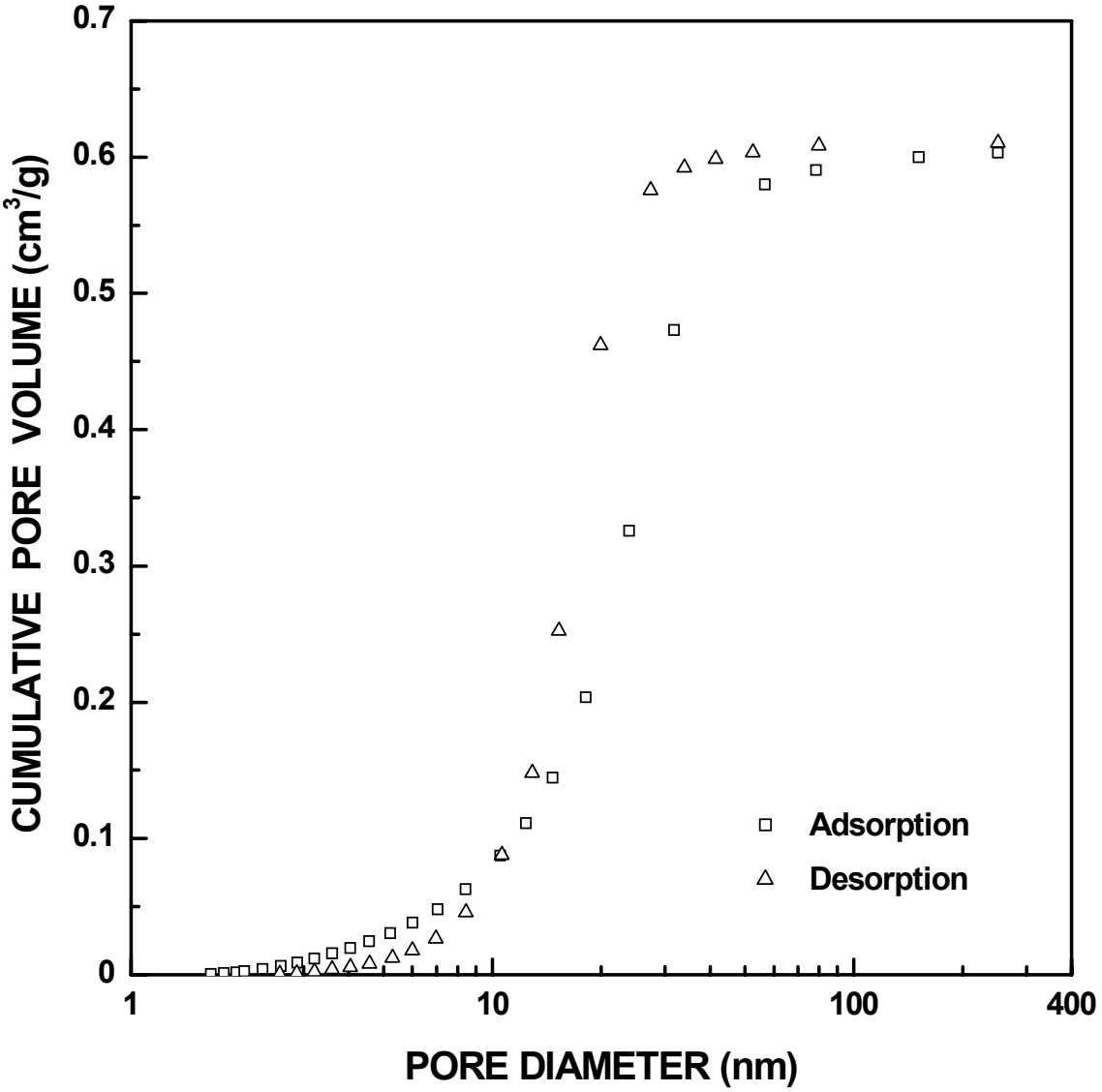

Figure I-36 Plots of cumulative specific pore volume vs. pore diameter for SC35-1300(8h) sample (X_{WL} = 0.84).

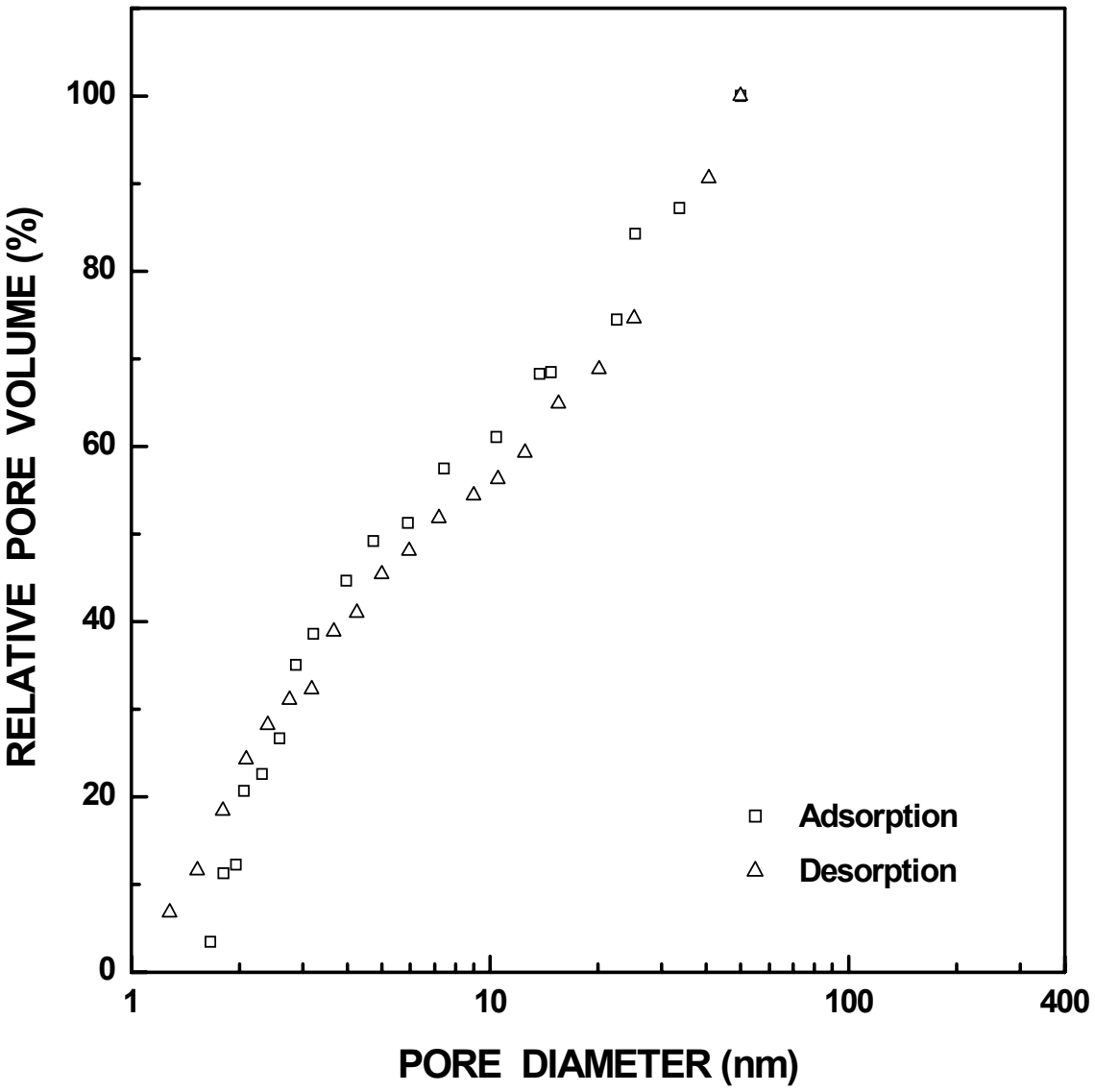

Figure I-37 Plots of relative ("normalized") pore volume vs. pore diameter for SC35-1160(30min) sample (X_{WL} = 0.01). The pore diameter was cut off at 50 nm.

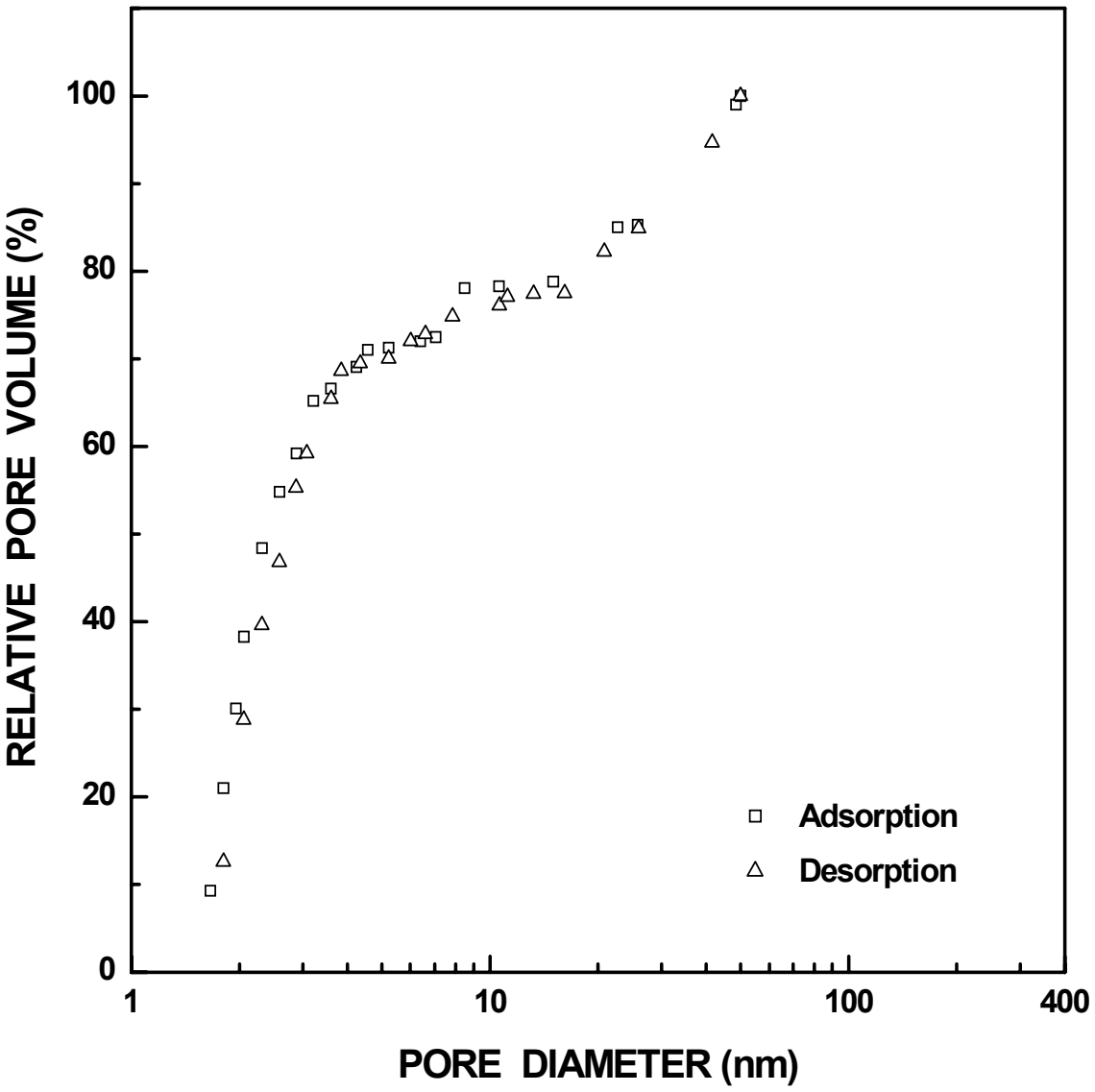

Figure I-38 Plots of relative ("normalized") pore volume vs. pore diameter for SC35-1160(2h) sample (X_{WL} = 0.03). The pore diameter was cut off at 50 nm.

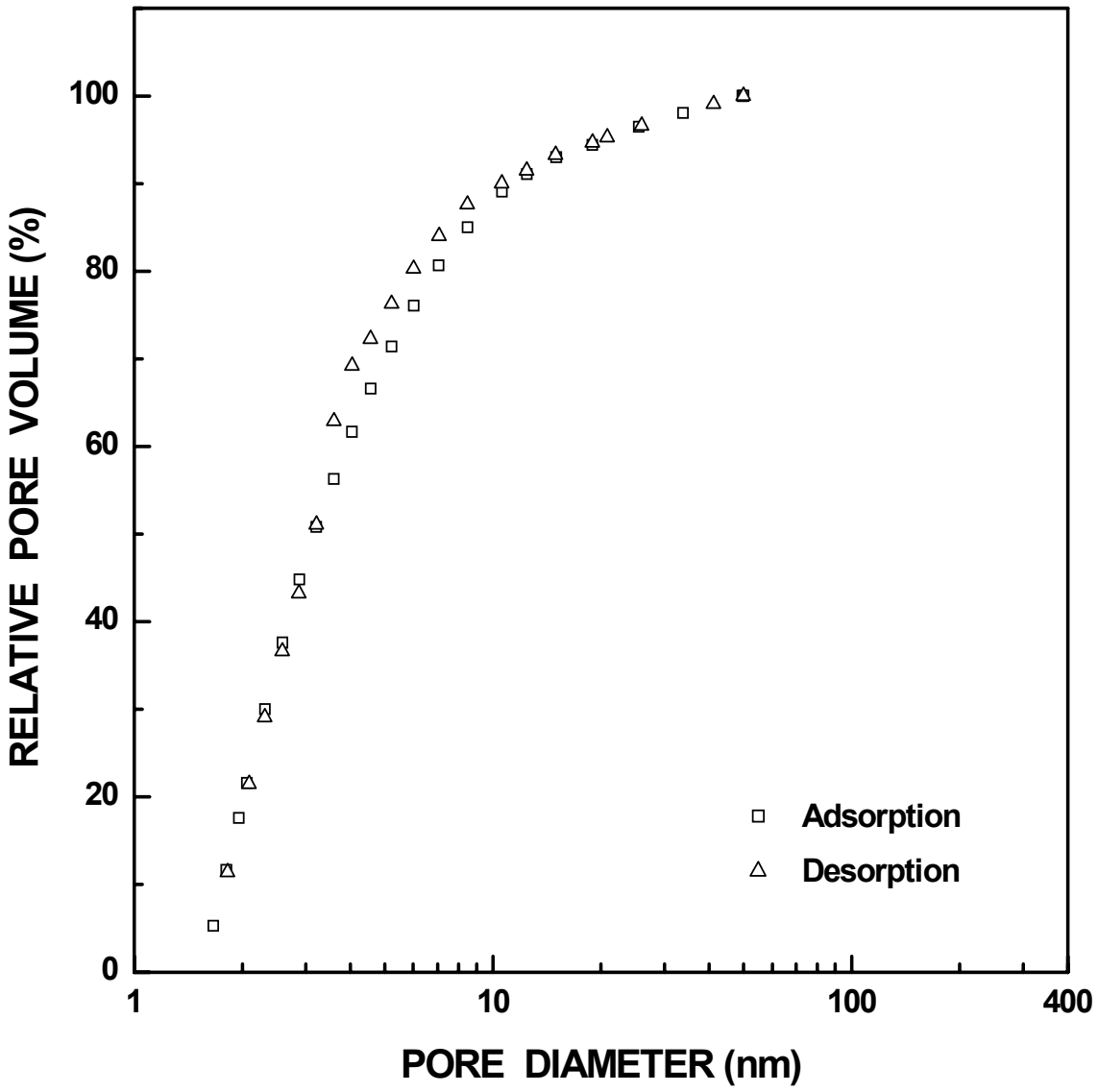

Figure I-39 Plots of relative ("normalized") pore volume vs. pore diameter for SC35-1160(4h) sample (X_{WL} = 0.05). The pore diameter was cut off at 50 nm.

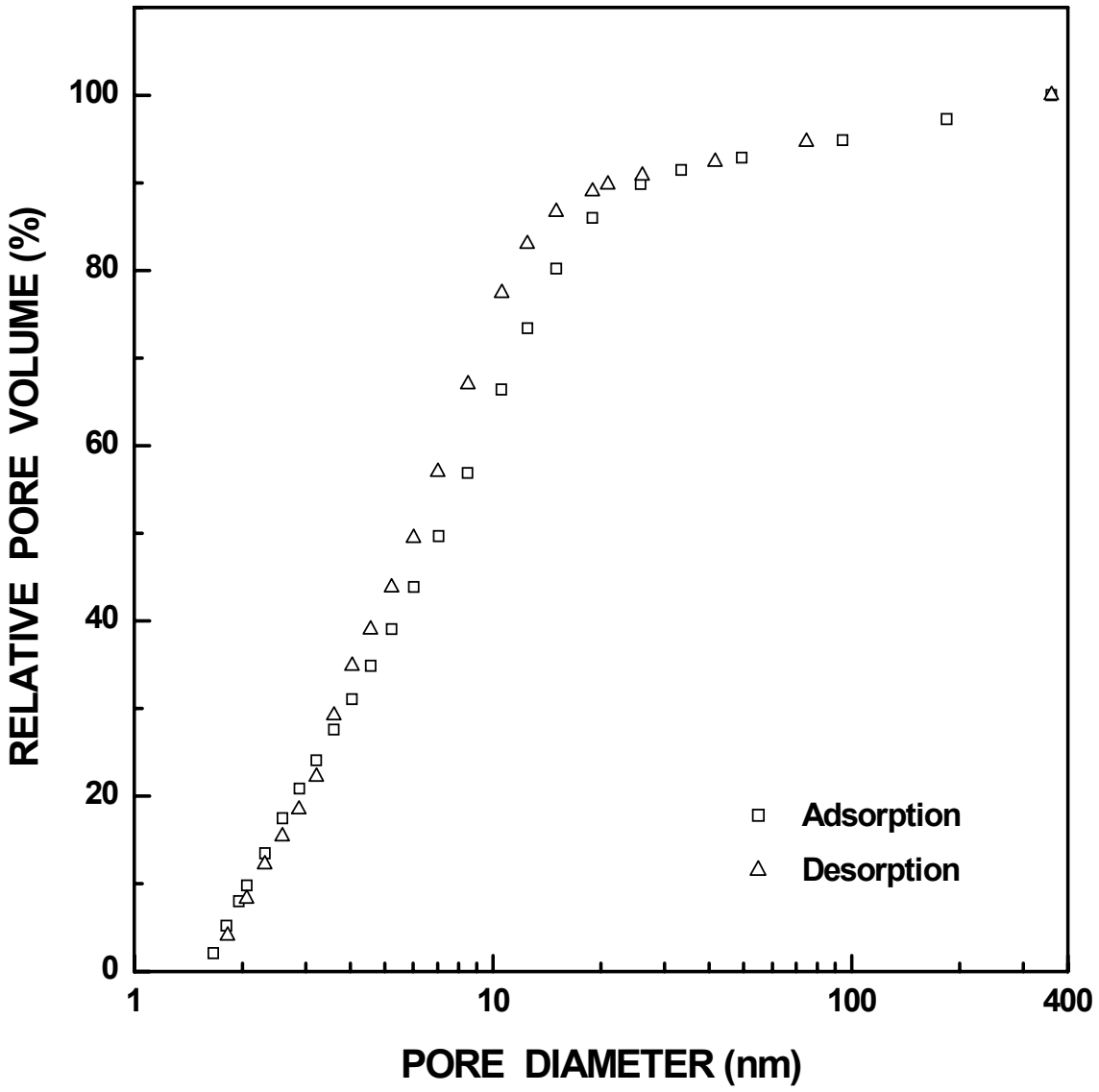

Figure I-40 Plots of relative ("normalized") pore volume vs. pore diameter for SC35-1160(8h) sample (X_{WL} = 0.07).

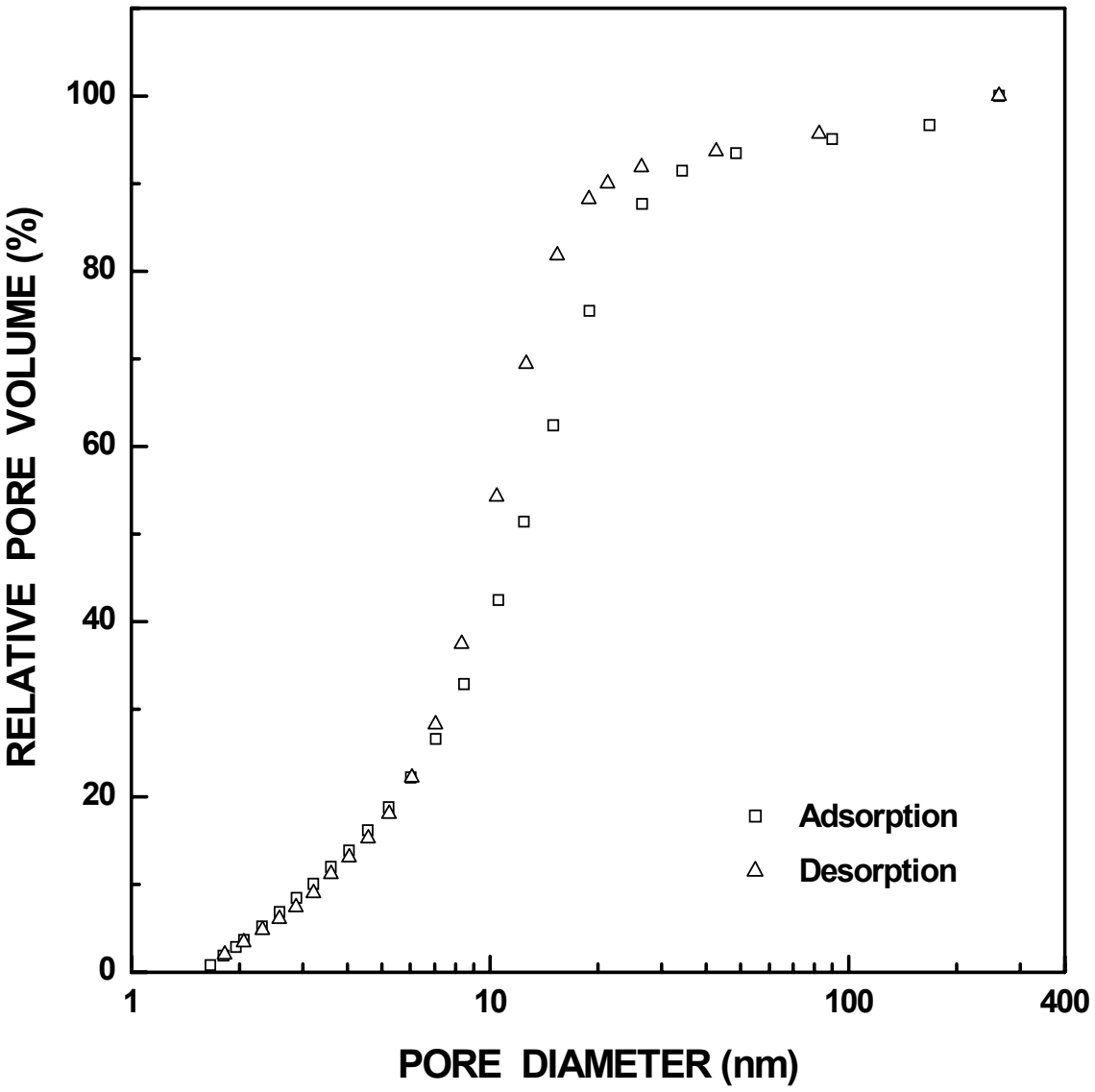

Figure I-41 Plots of relative ("normalized") pore volume vs. pore diameter for SC35-1160(16h) sample (X_{WL} = 0.12).

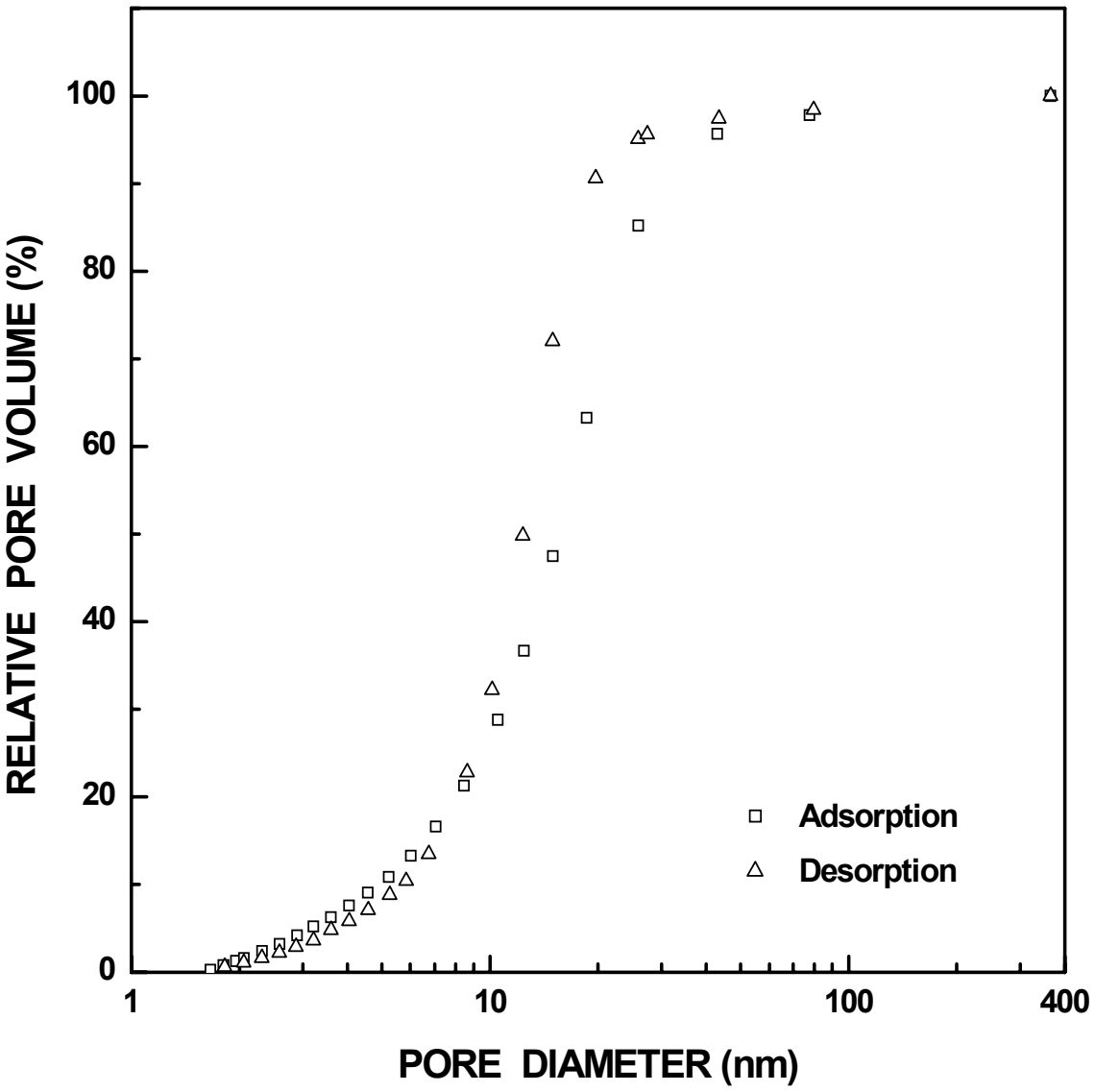

Figure I-42 Plots of relative ("normalized") pore volume vs. pore diameter for SC35-1160(32h) sample (X_{WL} = 0.22).

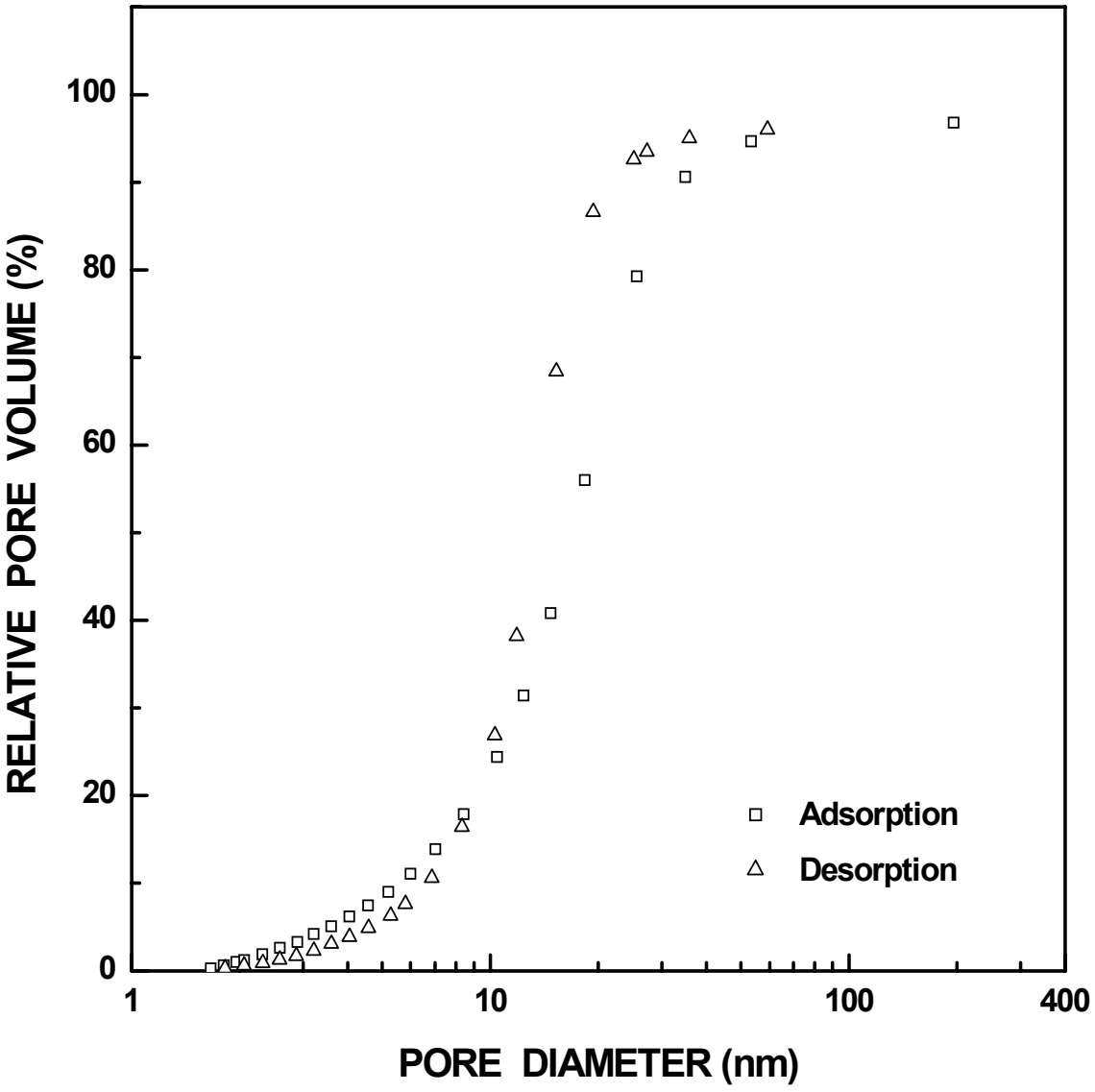

Figure I-43 Plots of relative ("normalized") pore volume vs. pore diameter for SC35-1160(48h) sample (X_{WL} = 0.29).

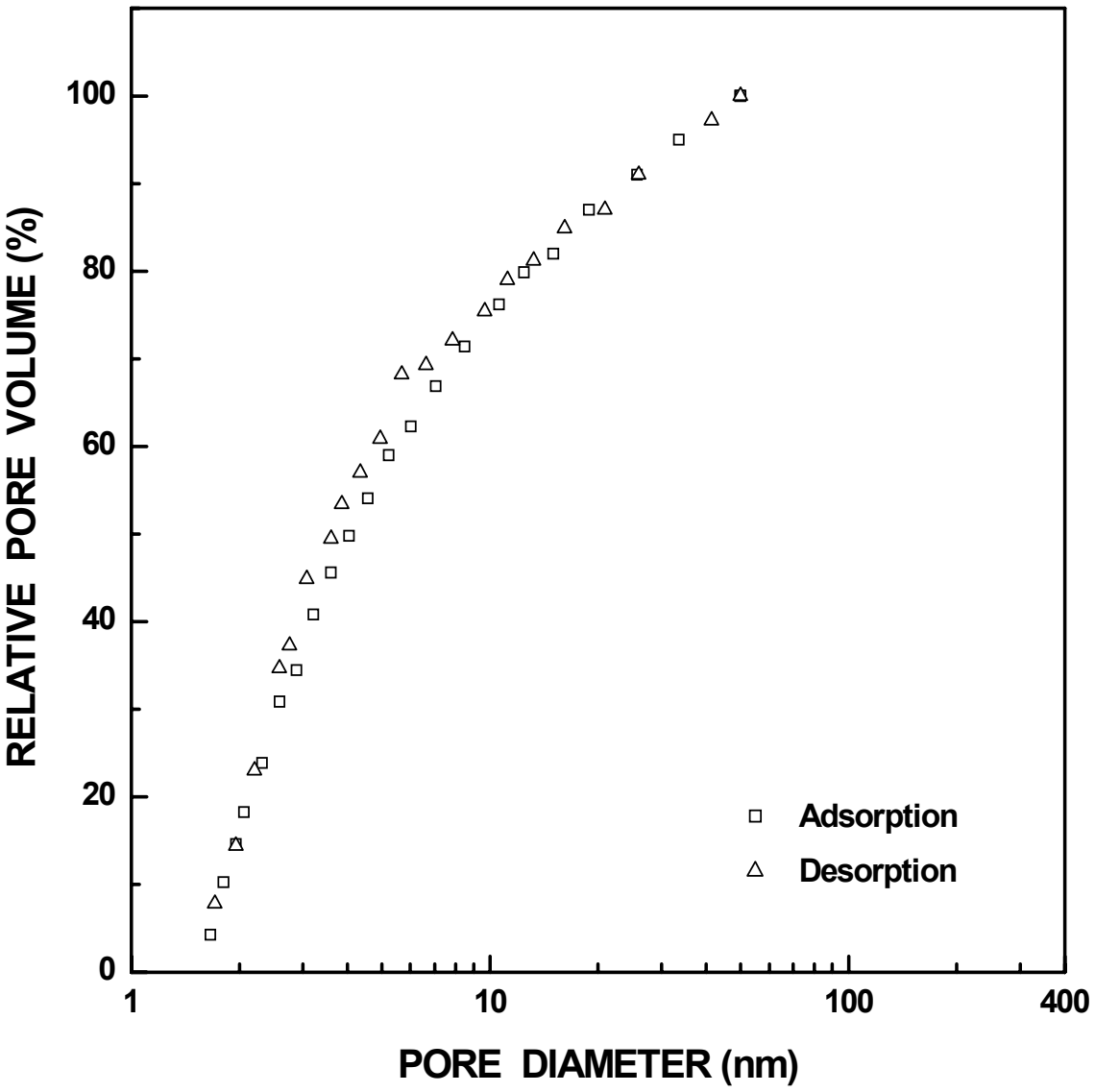

Figure I-44 Plots of relative ("normalized") pore volume vs. pore diameter for SC35-1200(30min) sample (X_{WL} = 0.02). The pore diameter was cut off at 50 nm.

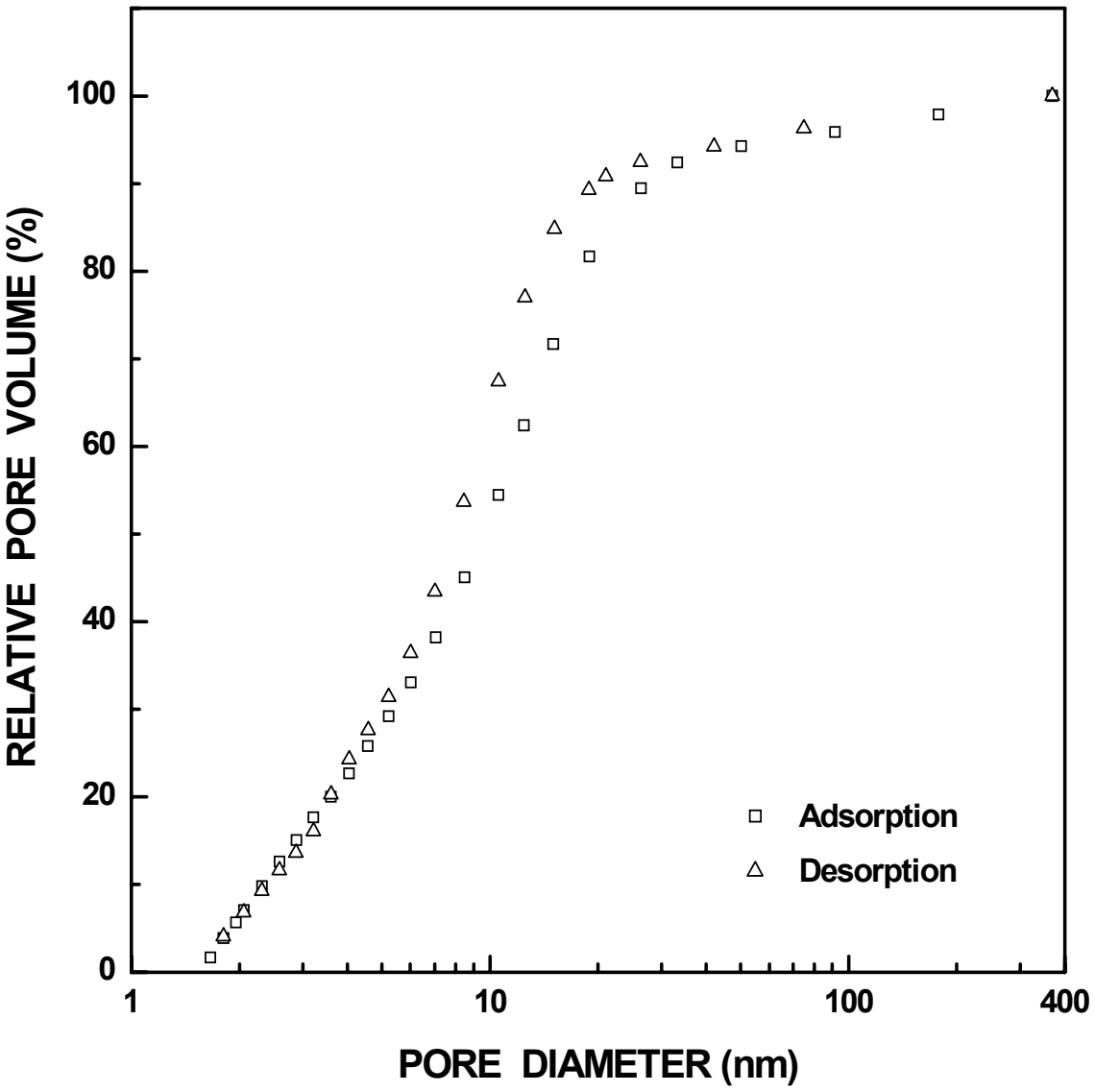

Figure I-45 Plots of relative ("normalized") pore volume vs. pore diameter for SC35-1200(4h) sample (X_{WL} = 0.09).

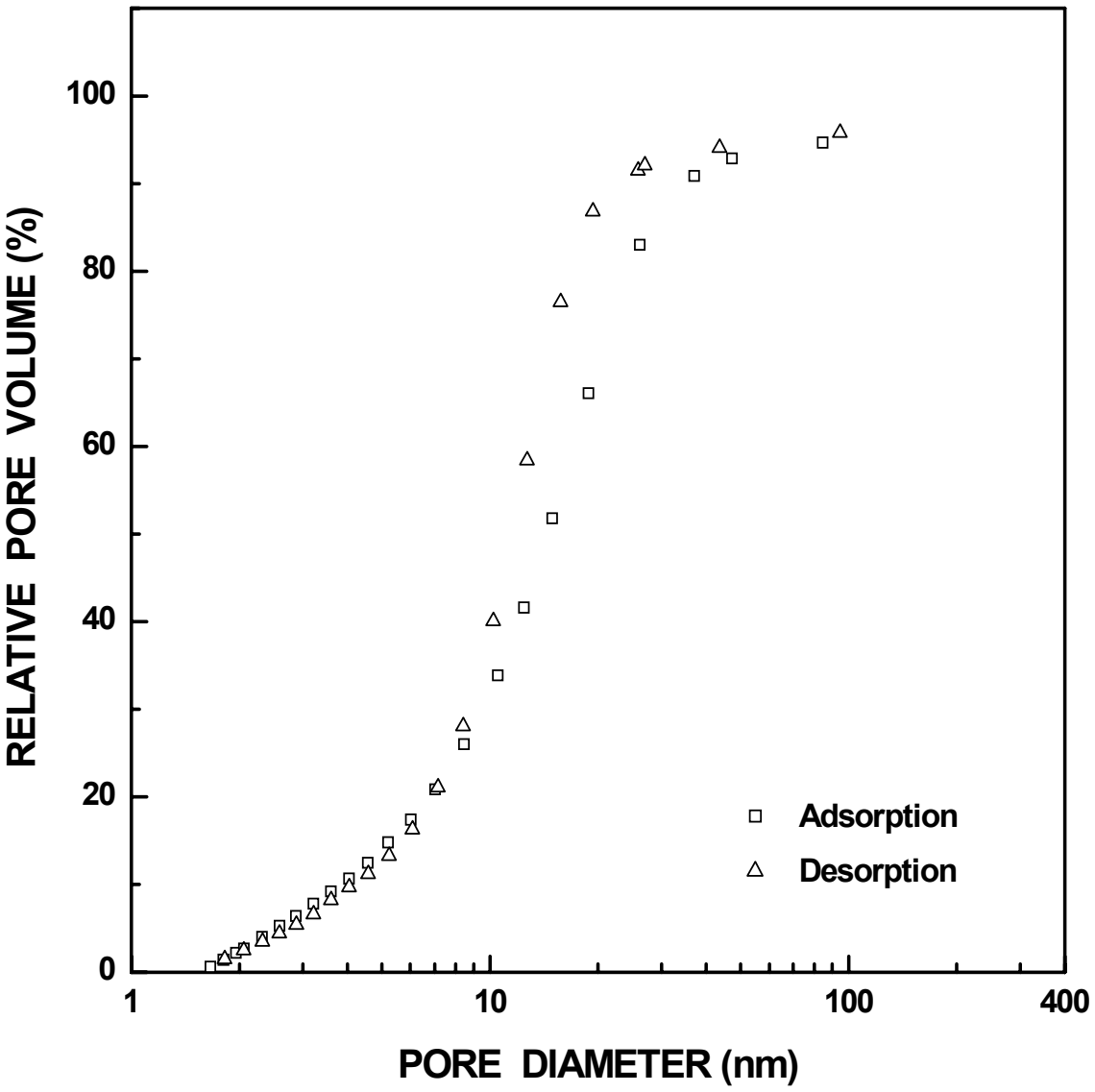

Figure I-46 Plots of relative ("normalized") pore volume vs. pore diameter for SC35-1200(8h) sample (X_{WL} = 0.16).

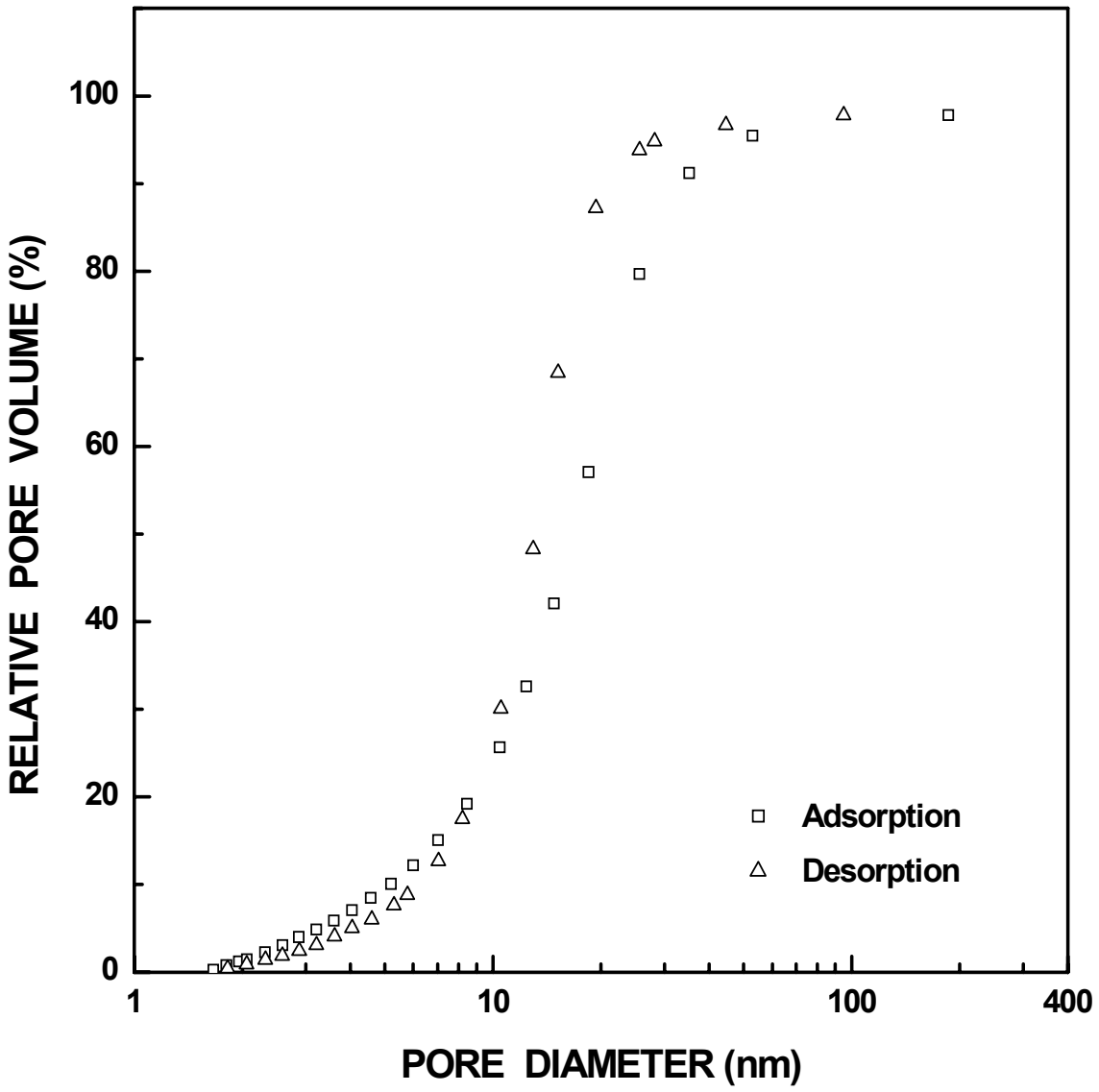

Figure I-47 Plots of relative ("normalized") pore volume vs. pore diameter for SC35-1200(16h) sample (X_{WL} = 0.26).

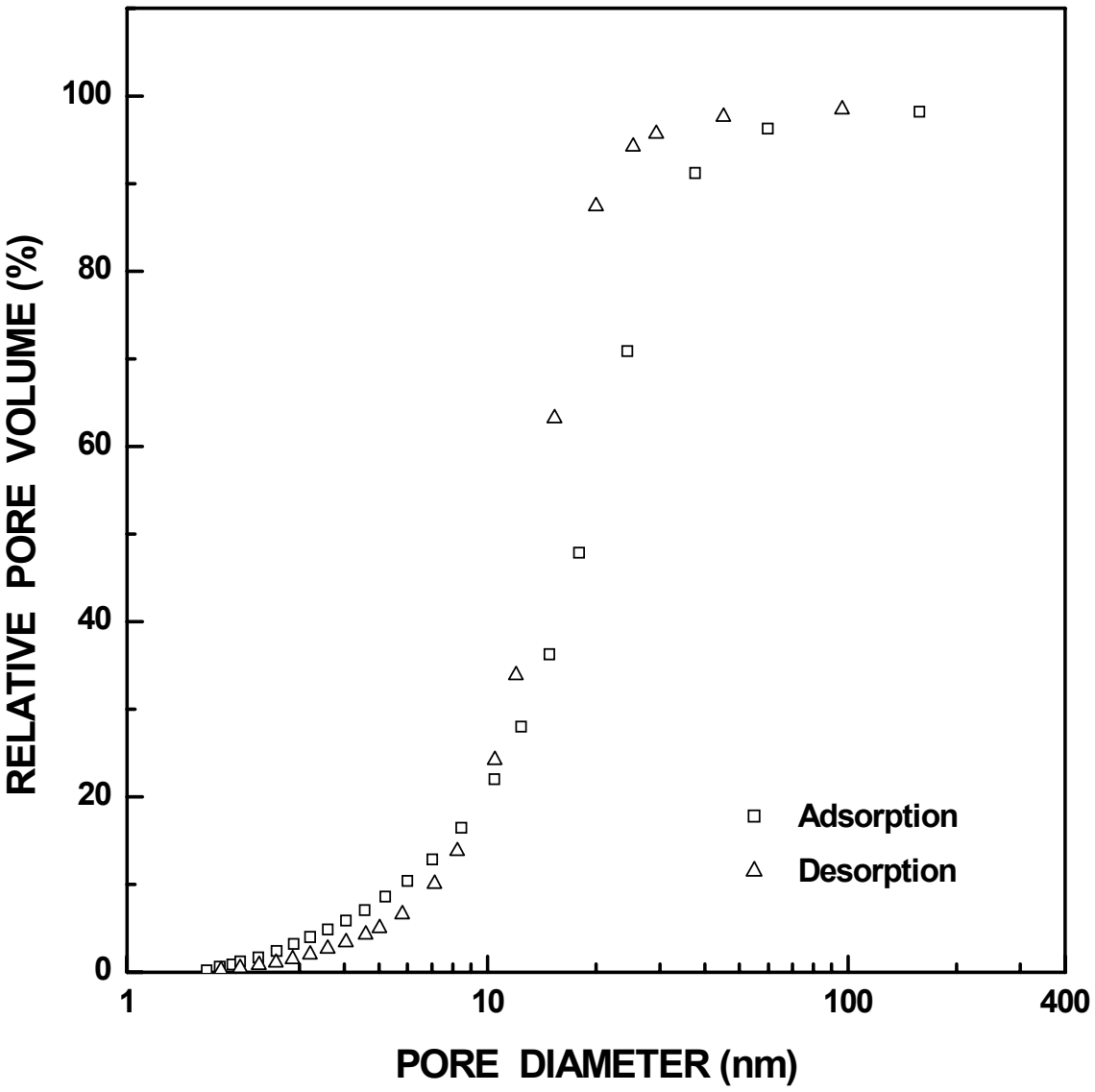

Figure I-48 Plots of relative ("normalized") pore volume vs. pore diameter for SC35-1200(22.5h) sample (X_{WL} = 0.38).

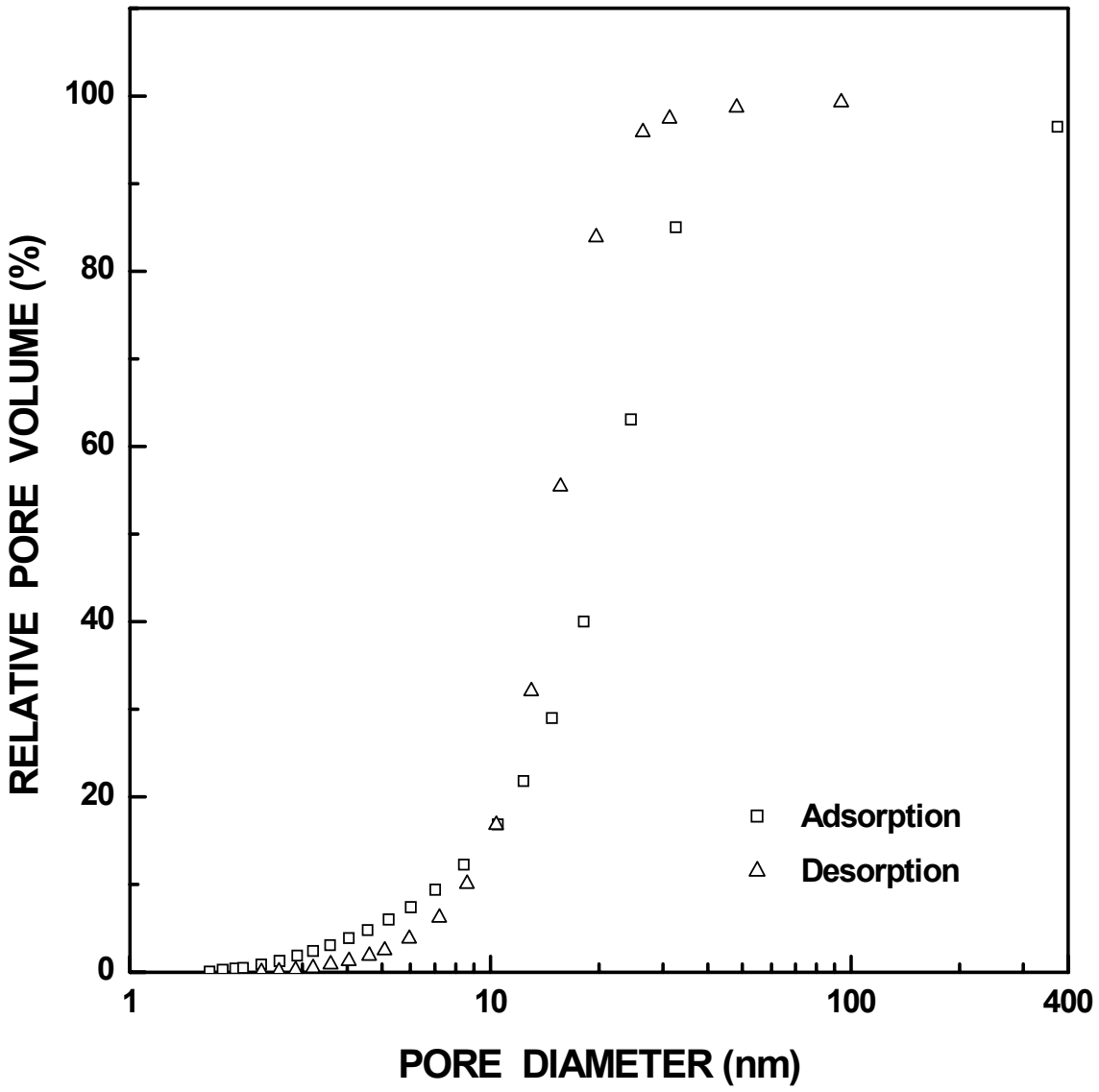

Figure I-49 Plots of relative ("normalized") pore volume vs. pore diameter for SC35-1250(16h) sample (X_{WL} = 0.70).

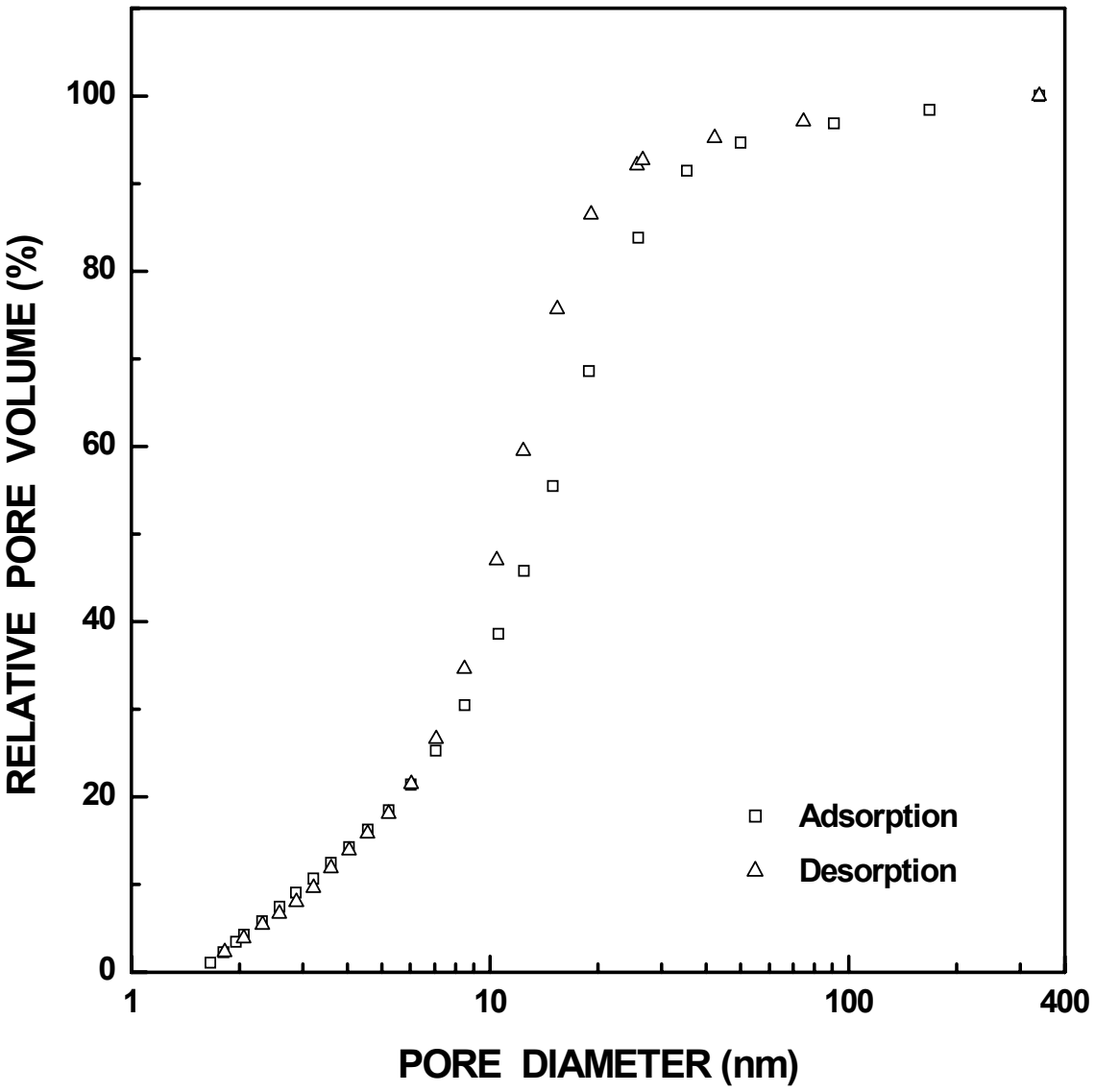

Figure I-50 Plots of relative ("normalized") pore volume vs. pore diameter for SC35-1300(30min) sample (X_{WL} = 0.10).

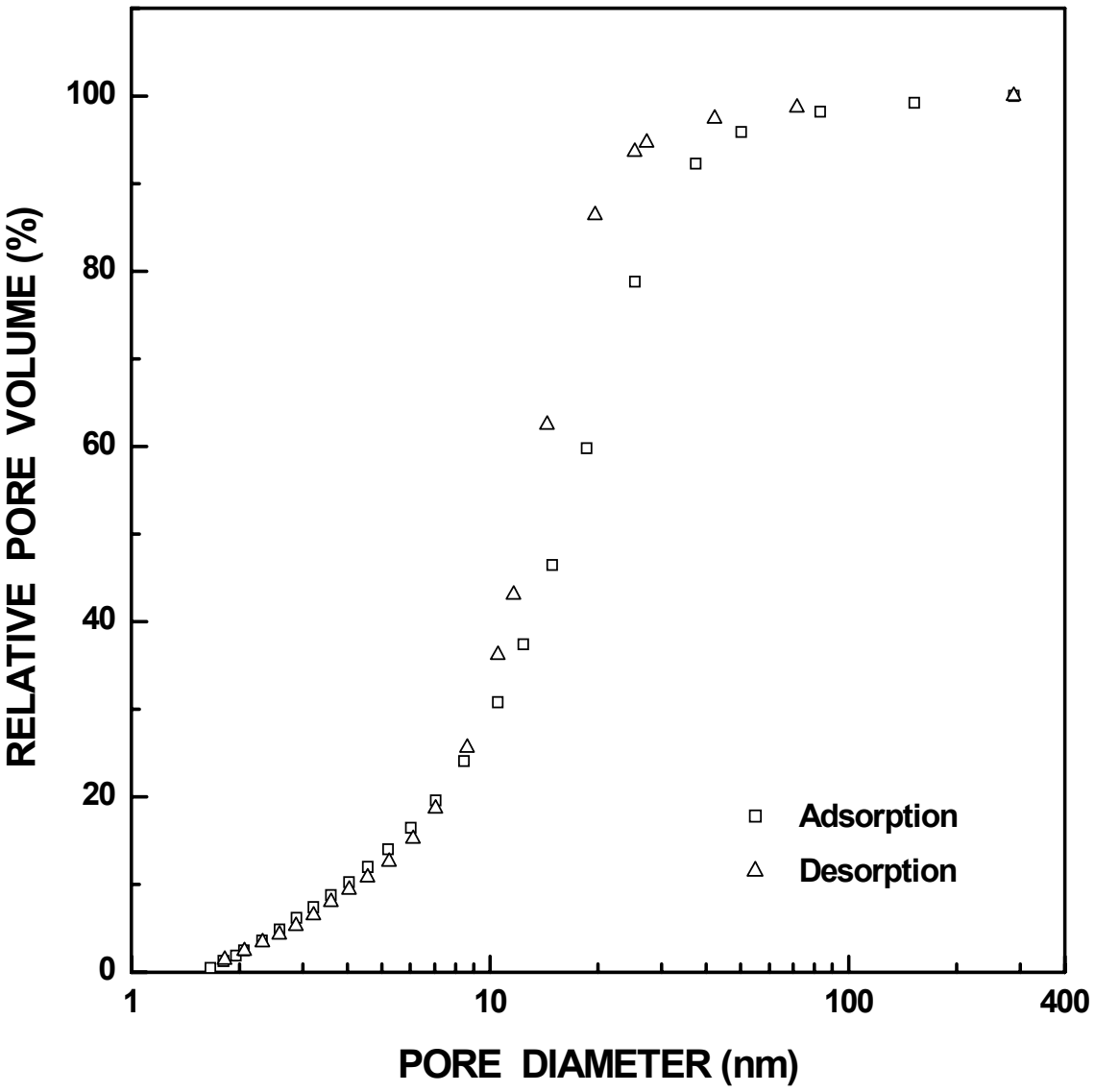

Figure I-51 Plots of relative ("normalized") pore volume vs. pore diameter for SC35-1300(1h) sample (X_{WL} = 0.17).

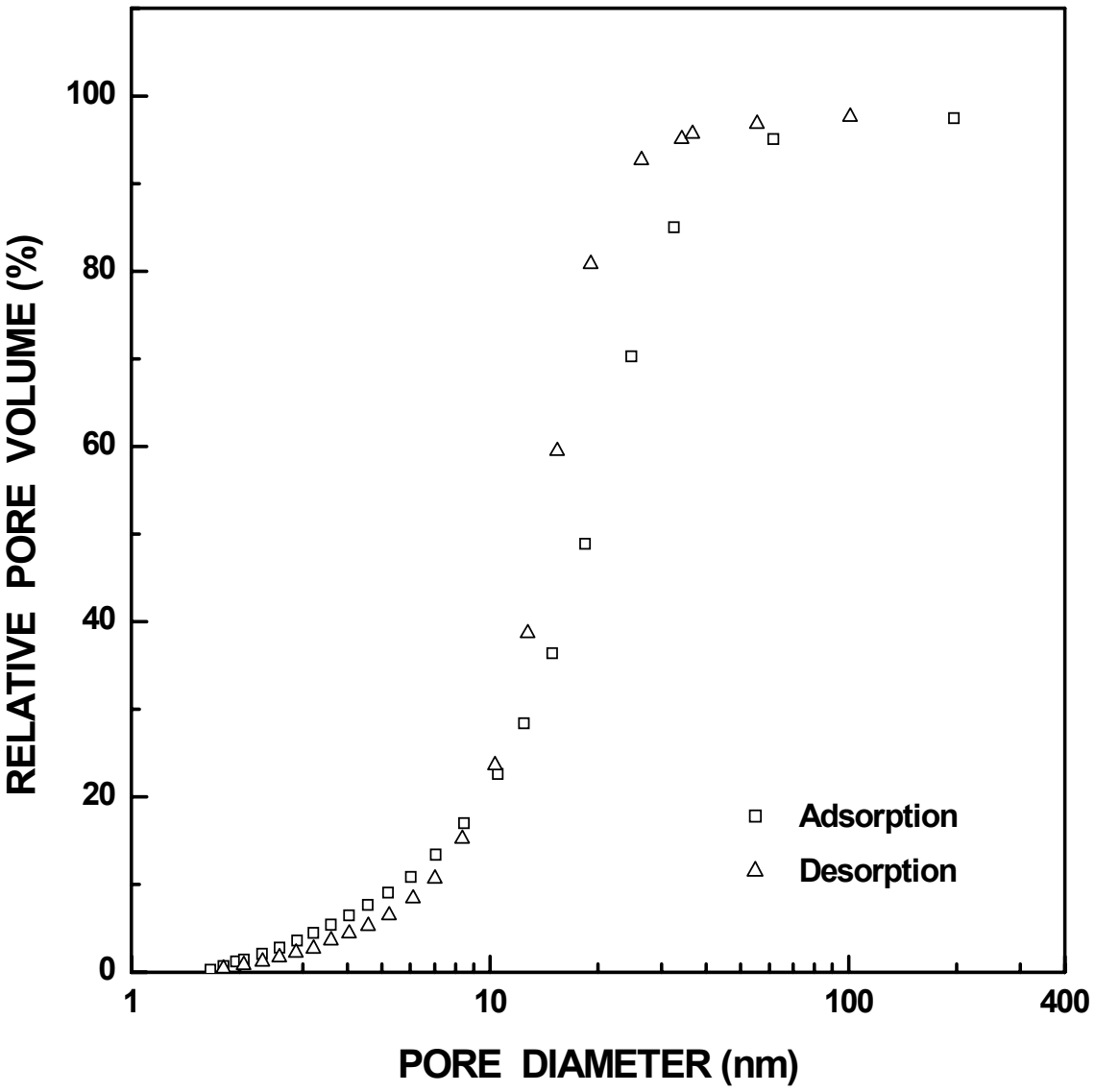

Figure I-52 Plots of relative ("normalized") pore volume vs. pore diameter for SC35-1300(2h) sample (X_{WL} = 0.30).

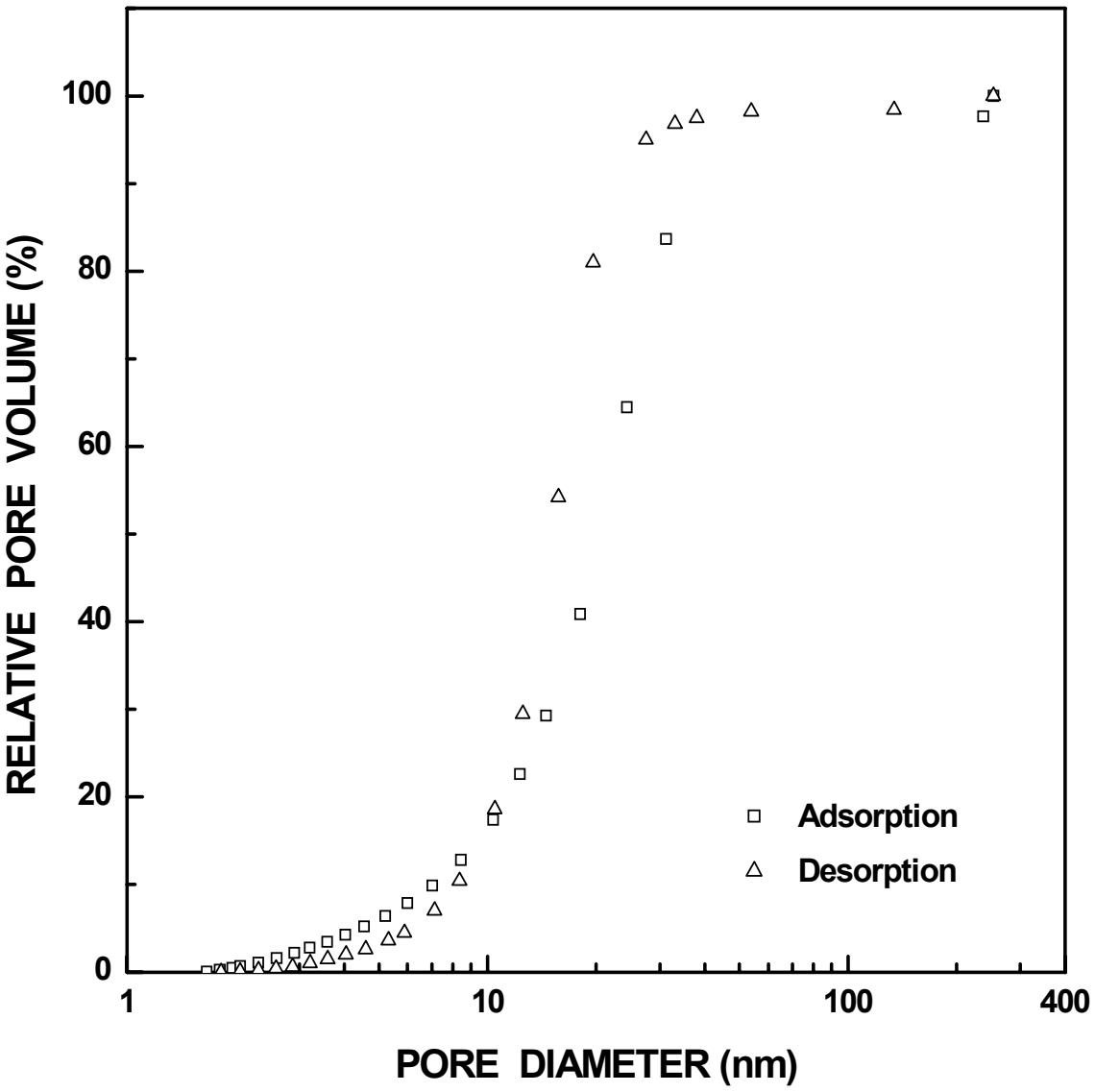

Figure I-53 Plots of relative ("normalized") pore volume vs. pore diameter for SC35-1300(4h) sample (X_{WL} = 0.54).

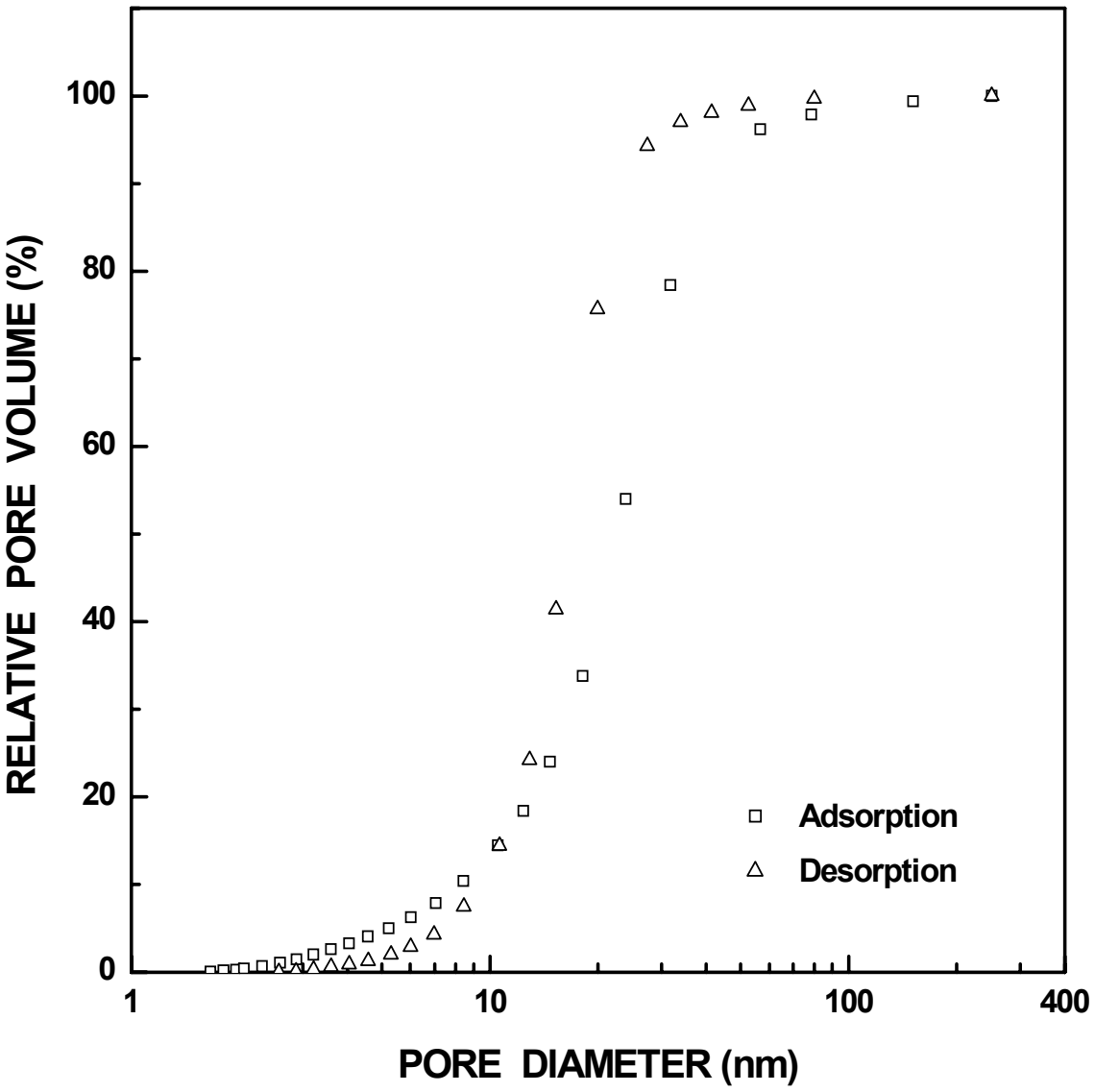

Figure I-54 Plots of relative ("normalized") pore volume vs. pore diameter for SC35-1300(8h) sample (X_{WL} = 0.84).

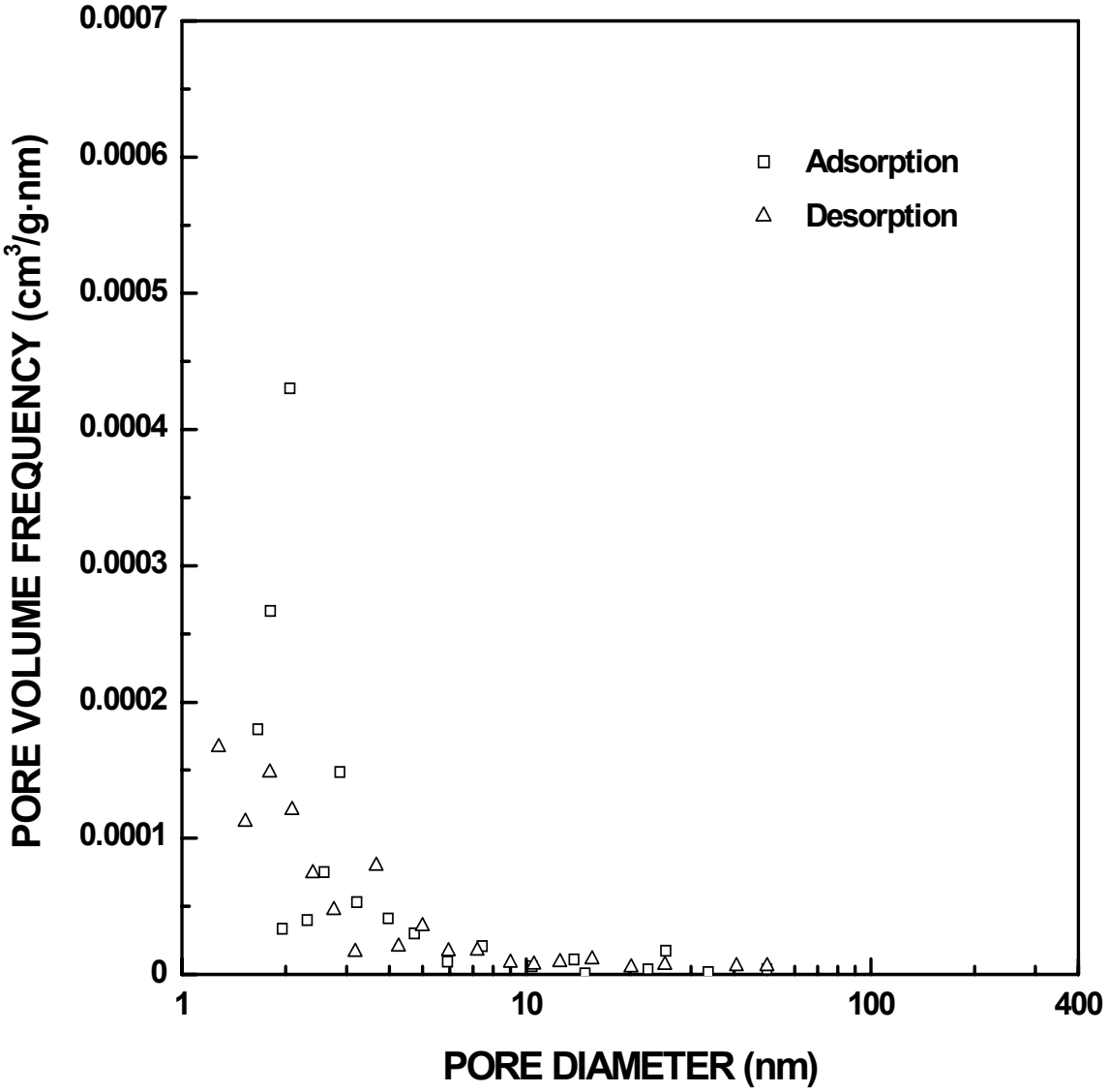

Figure I-55 Plots of specific pore volume frequency vs. pore diameter for SC35-1160(30min) sample (X_{WL} = 0.01). The pore diameter was cut off at 50 nm.

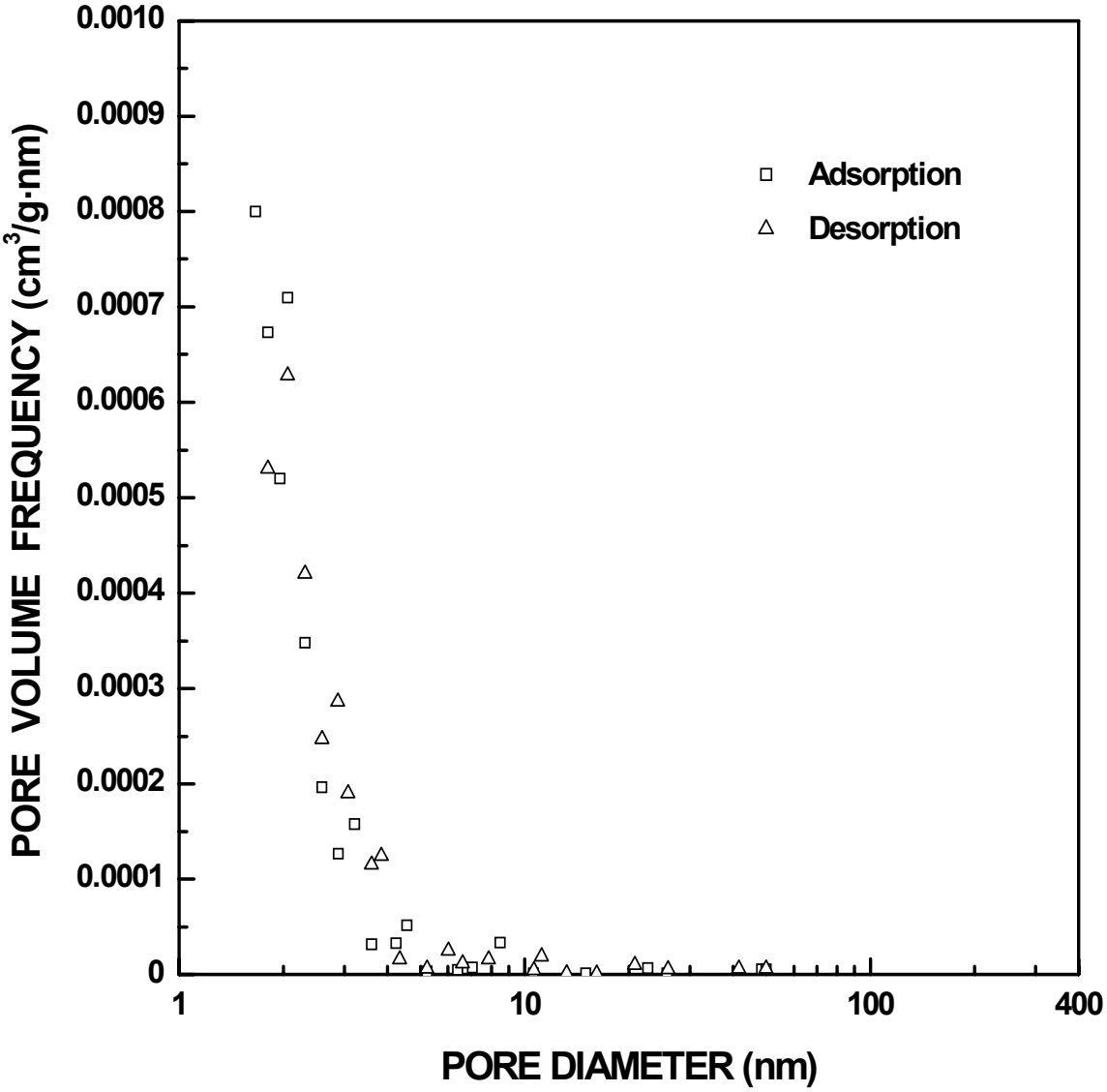

Figure I-56 Plots of specific pore volume frequency vs. pore diameter for SC35-1160(2h) sample (X_{WL} = 0.03). The pore diameter was cut off at 50 nm.

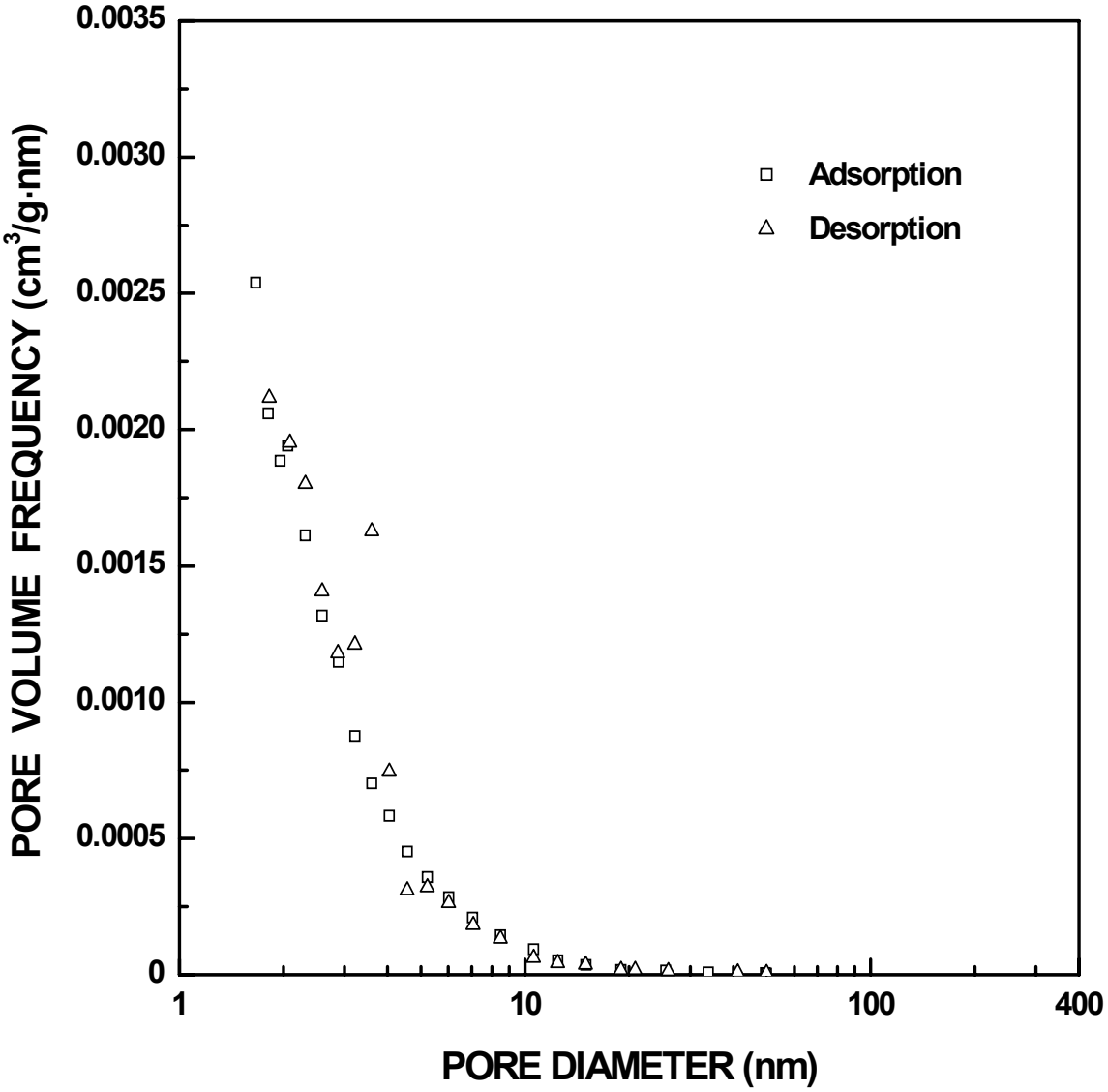

Figure I-57 Plots of specific pore volume frequency vs. pore diameter for SC35-1160(4h) sample (X_{WL} = 0.05). The pore diameter was cut off at 50 nm.

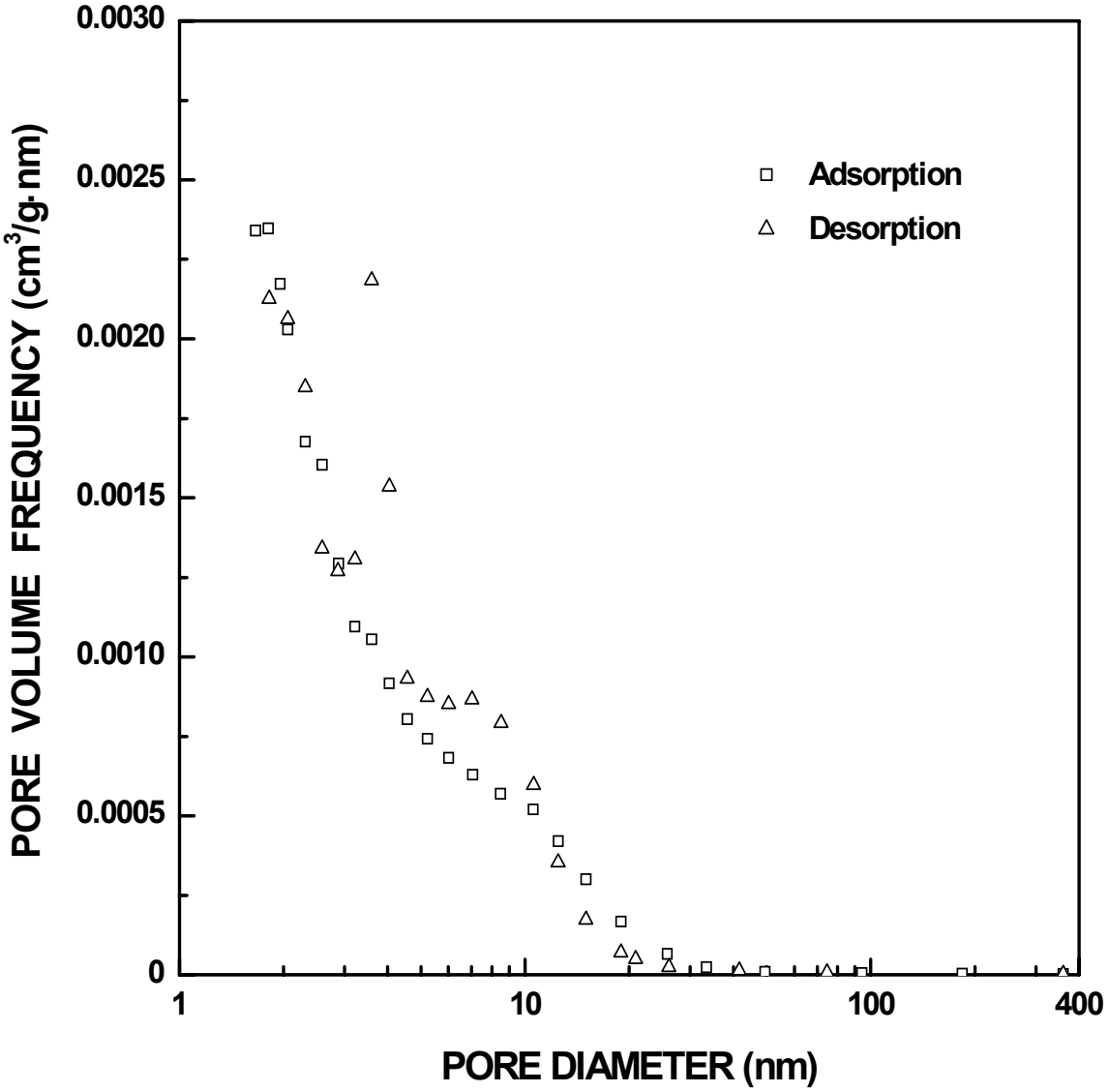

Figure I-58 Plots of specific pore volume frequency vs. pore diameter for SC35-1160(8h) sample (X_{WL} = 0.07).

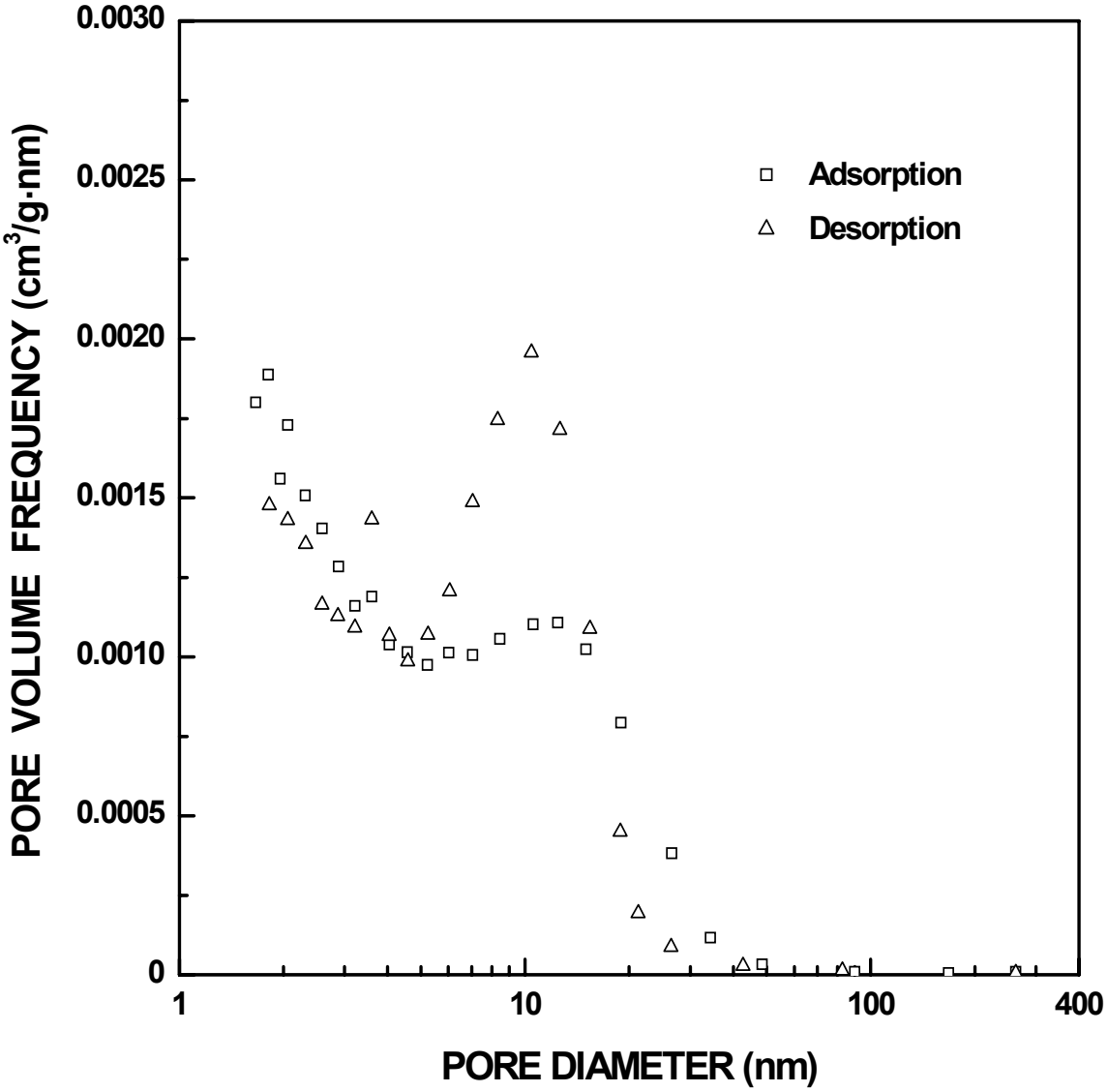

Figure I-59 Plots of specific pore volume frequency vs. pore diameter for SC35-1160(16h) sample (X_{WL} = 0.12).

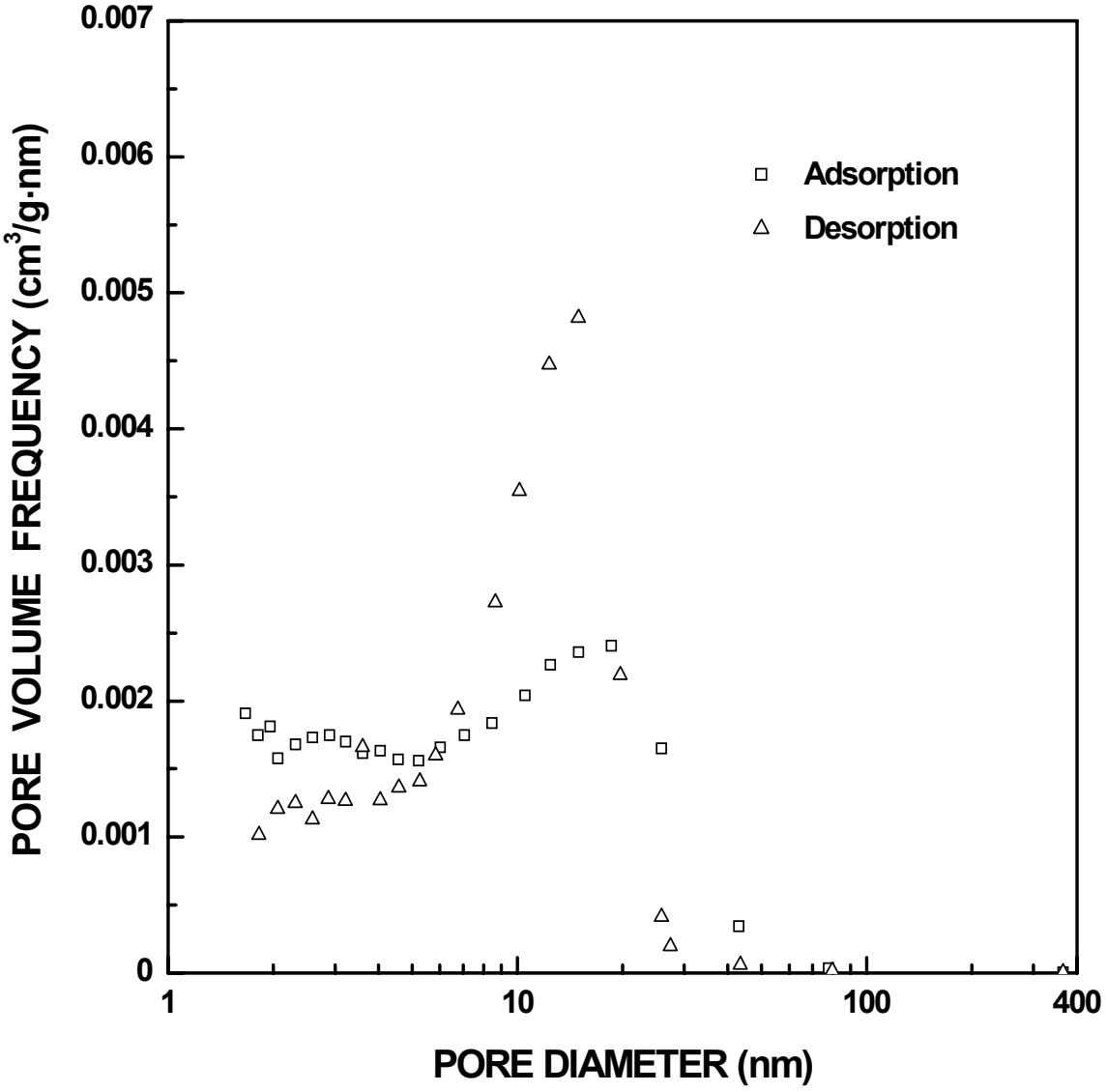

Figure I-60 Plots of specific pore volume frequency vs. pore diameter for SC35-1160(32h) sample (X_{WL} = 0.22).

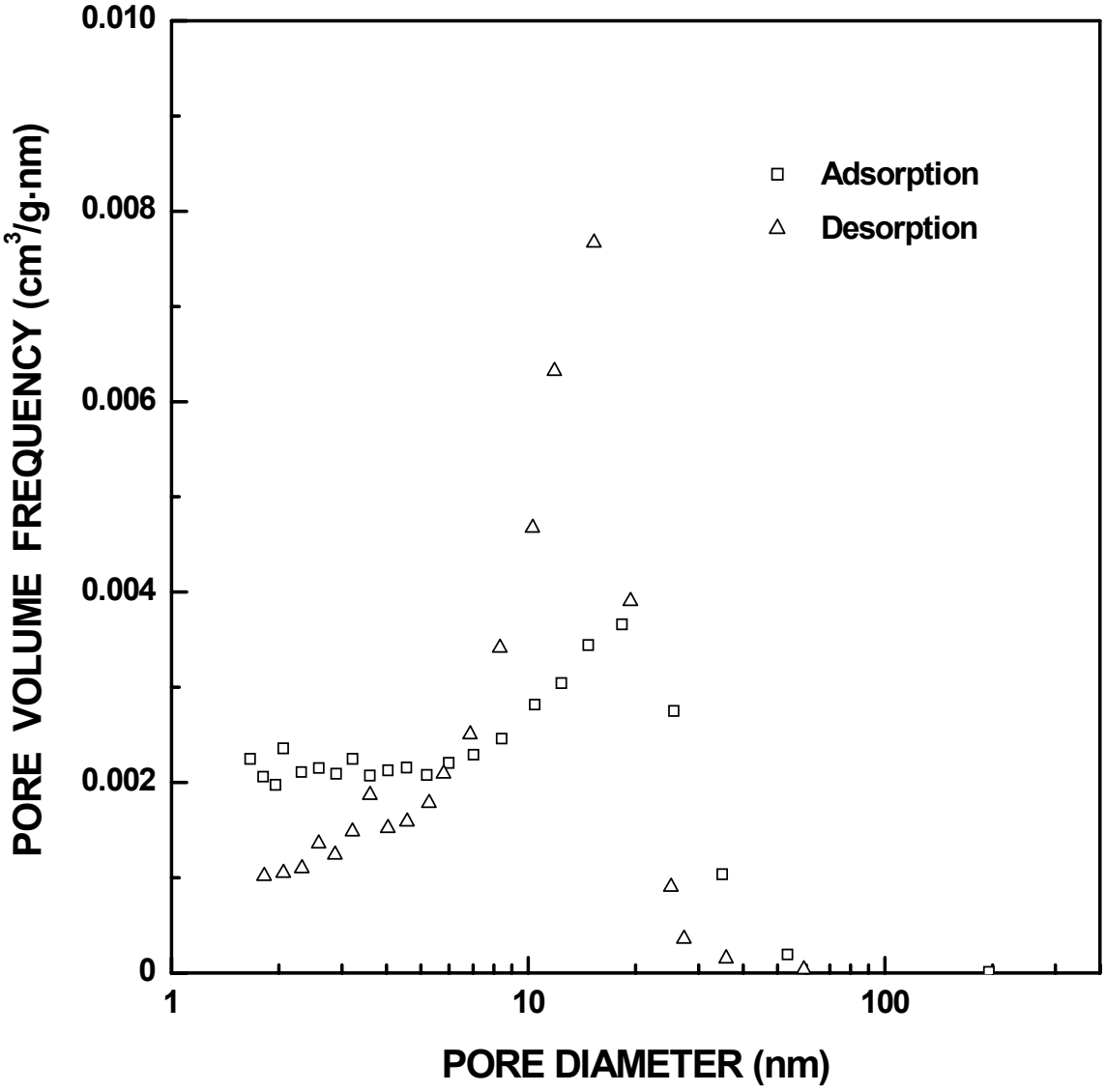

Figure I-61 Plots of specific pore volume frequency vs. pore diameter for SC35-1160(48h) sample (X_{WL} = 0.29).

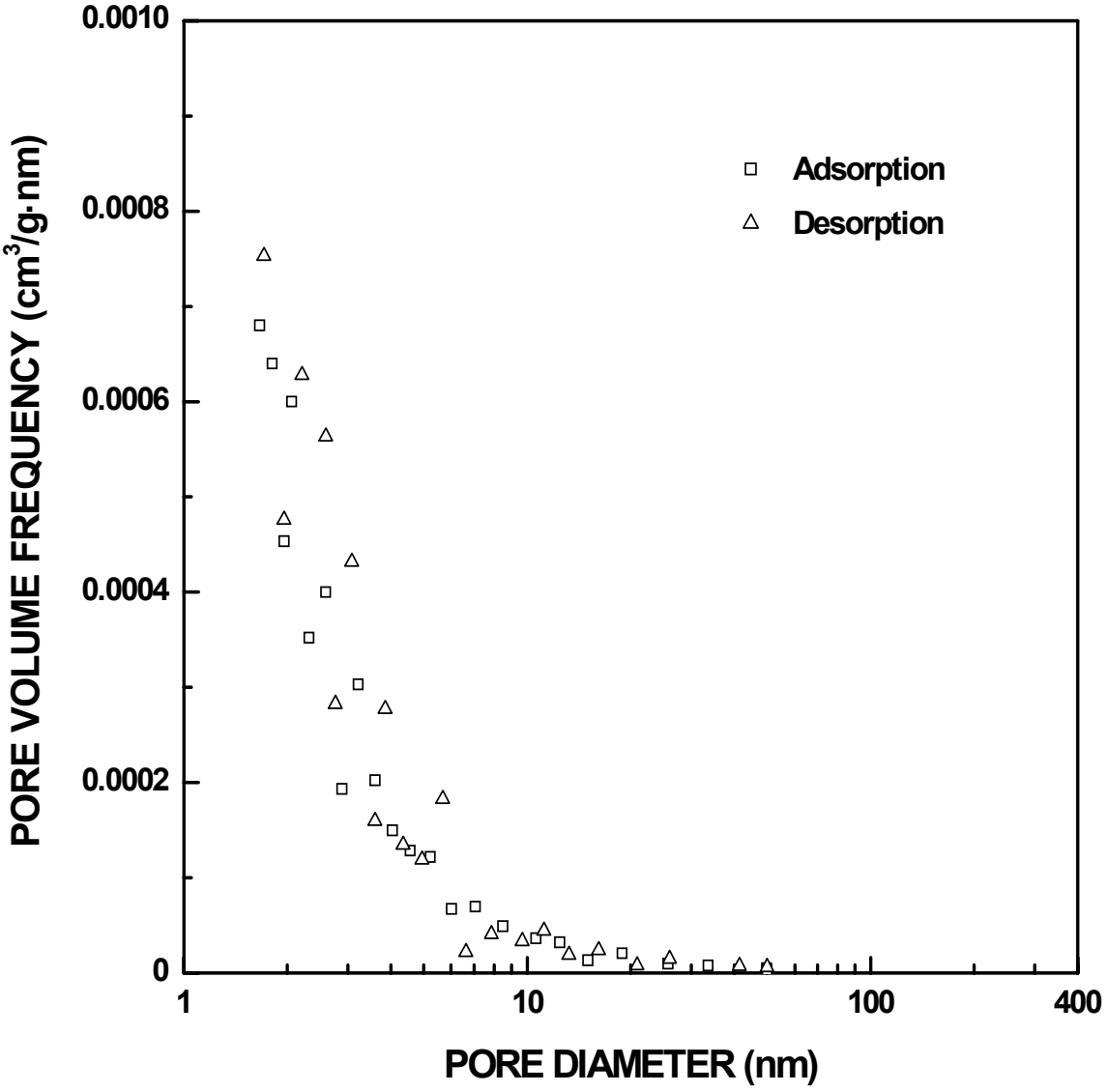

Figure I-62 Plots of specific pore volume frequency vs. pore diameter for SC35-1200(30min) sample (X_{WL} = 0.02).

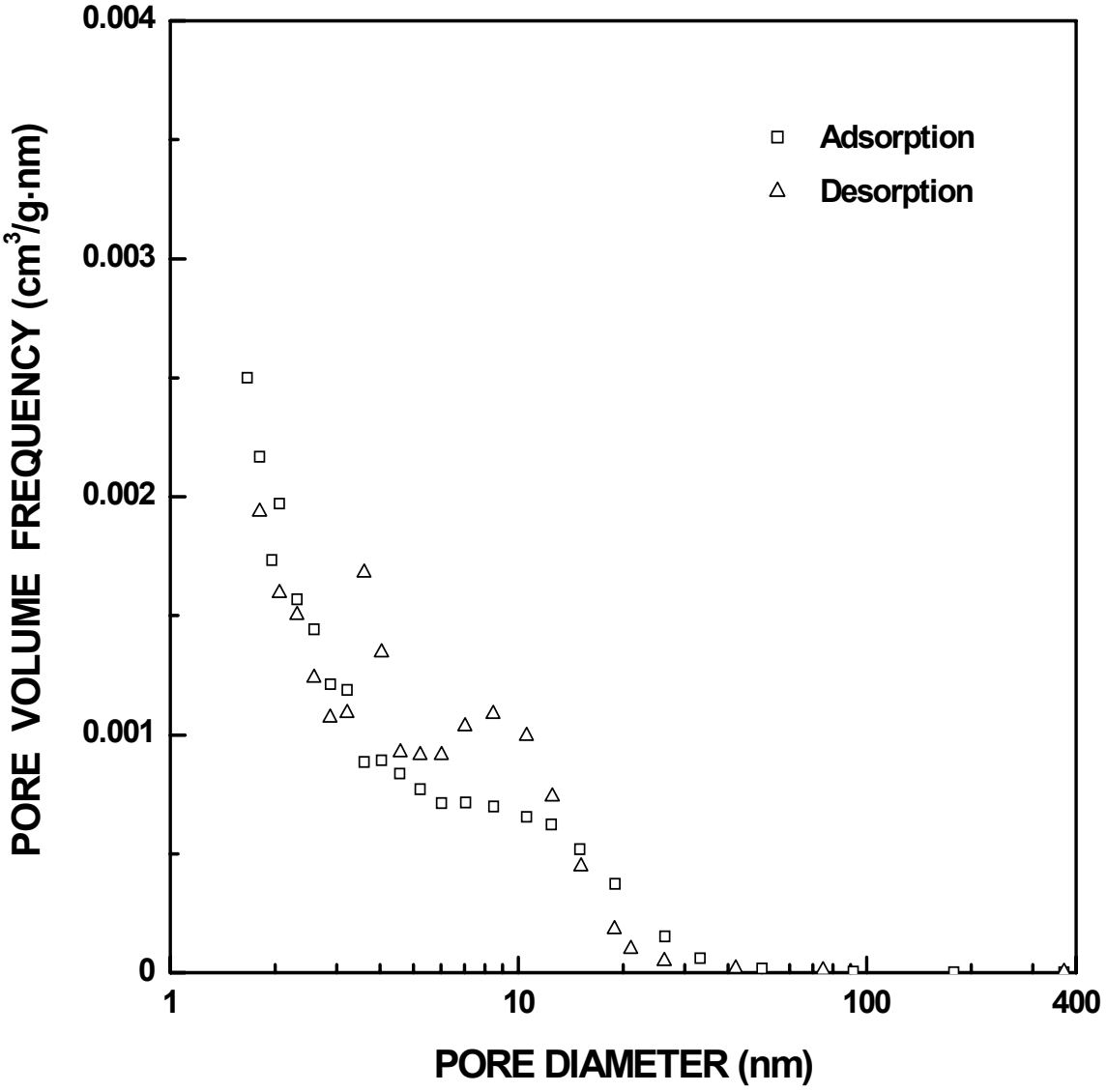

Figure I-63 Plots of specific pore volume frequency vs. pore diameter for SC35-1200(4h) sample (X_{WL} = 0.09).

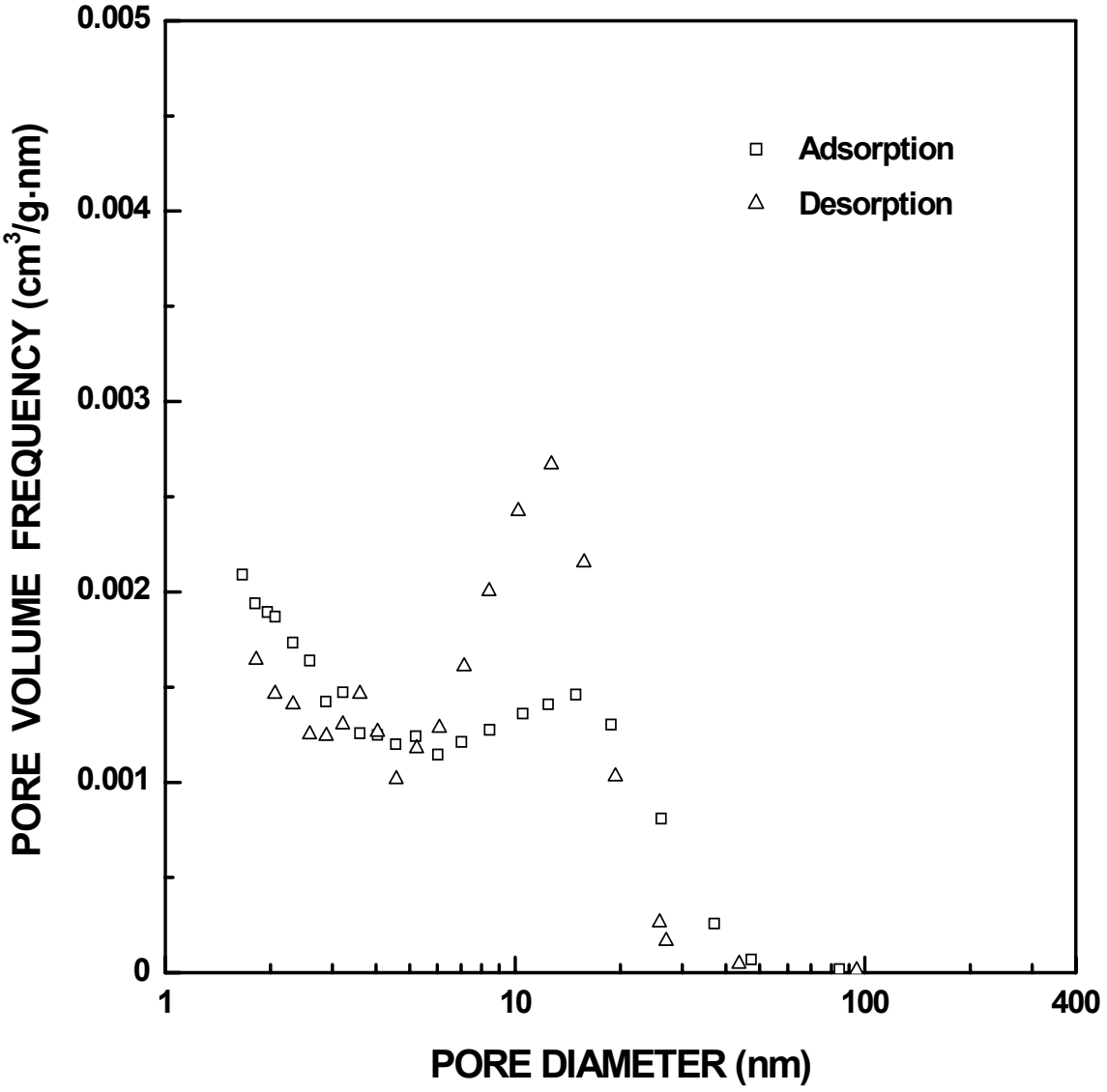

Figure I-64 Plots of specific pore volume frequency vs. pore diameter for SC35-1200(8h) sample (X_{WL} = 0.16).

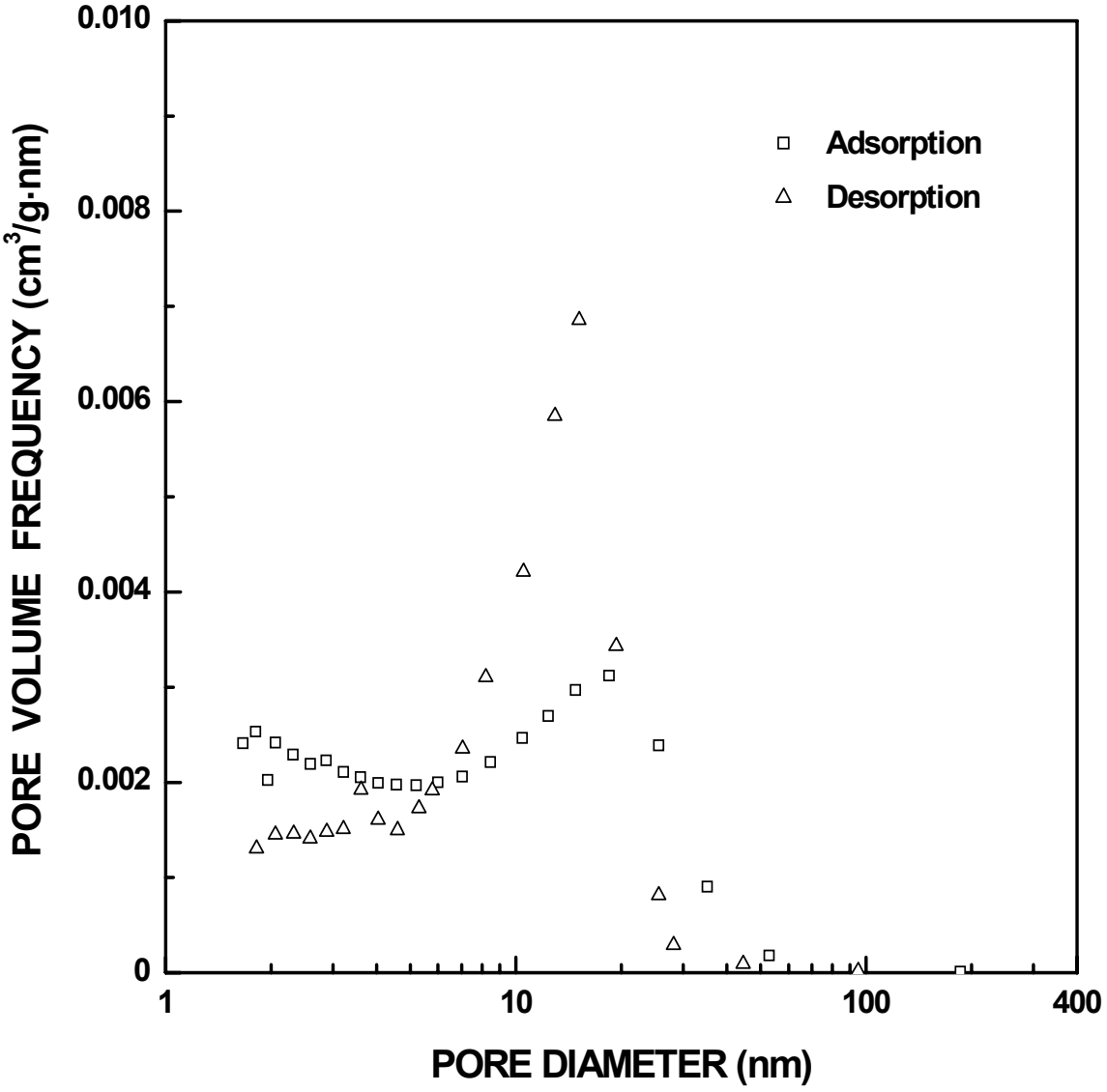

Figure I-65 Plots of specific pore volume frequency vs. pore diameter for SC35-1200(16h) sample (X_{WL} = 0.26).

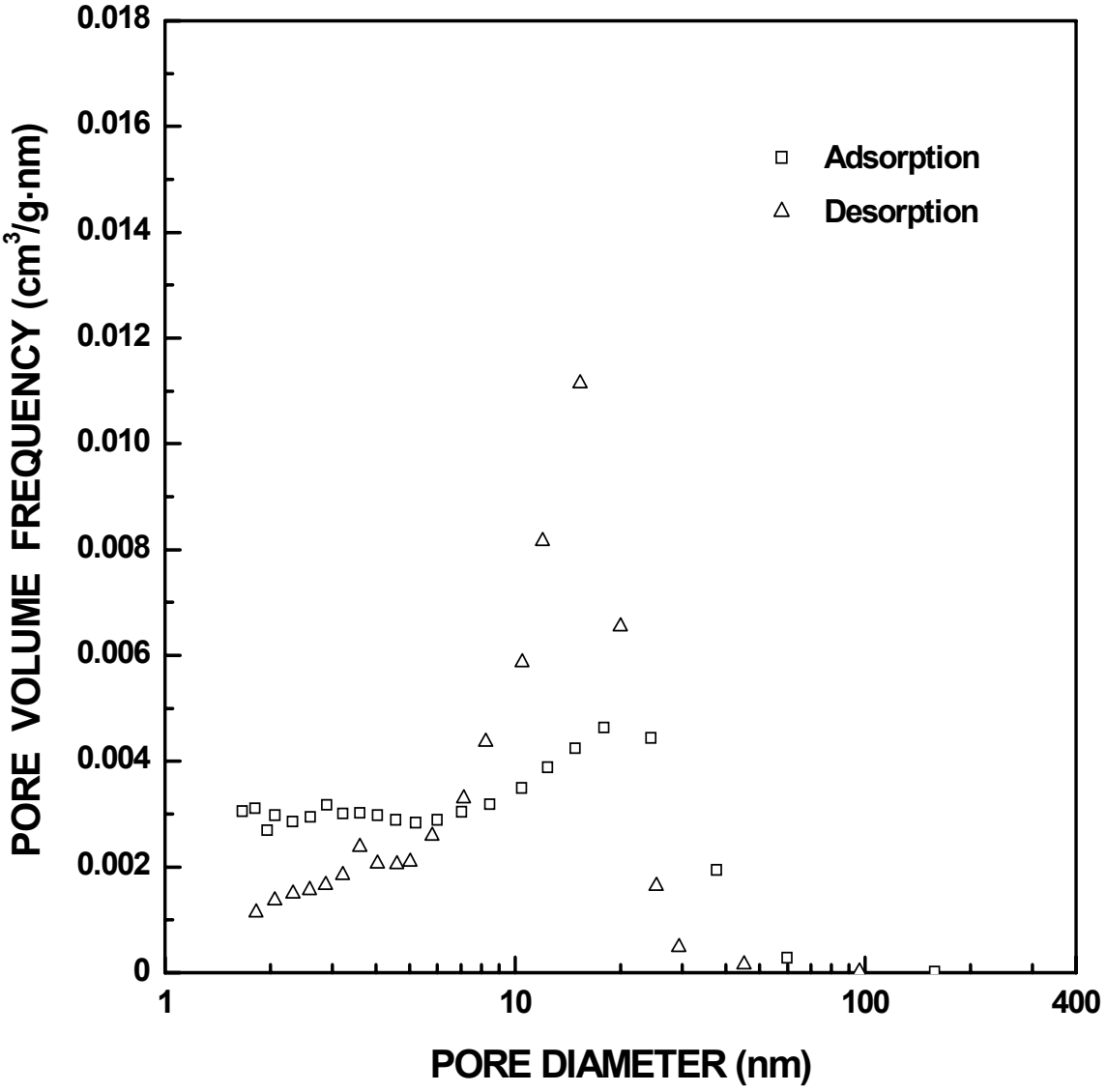

Figure I-66 Plots of specific pore volume frequency vs. pore diameter for SC35-1200(22.5h) sample (X_{WL} = 0.38).

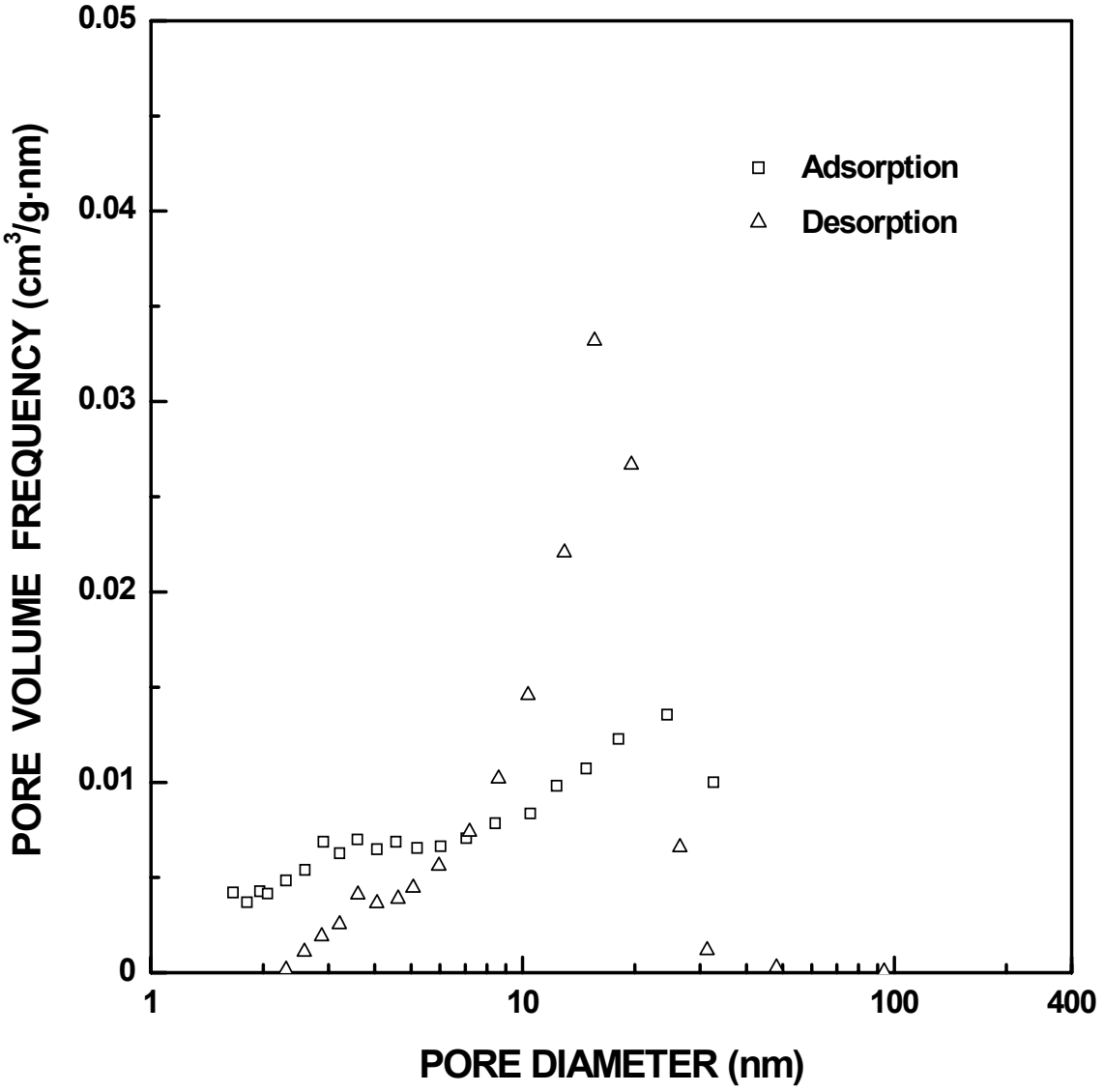

Figure I-67 Plots of specific pore volume frequency vs. pore diameter for SC35-1250(16h) sample (X_{WL} = 0.70).

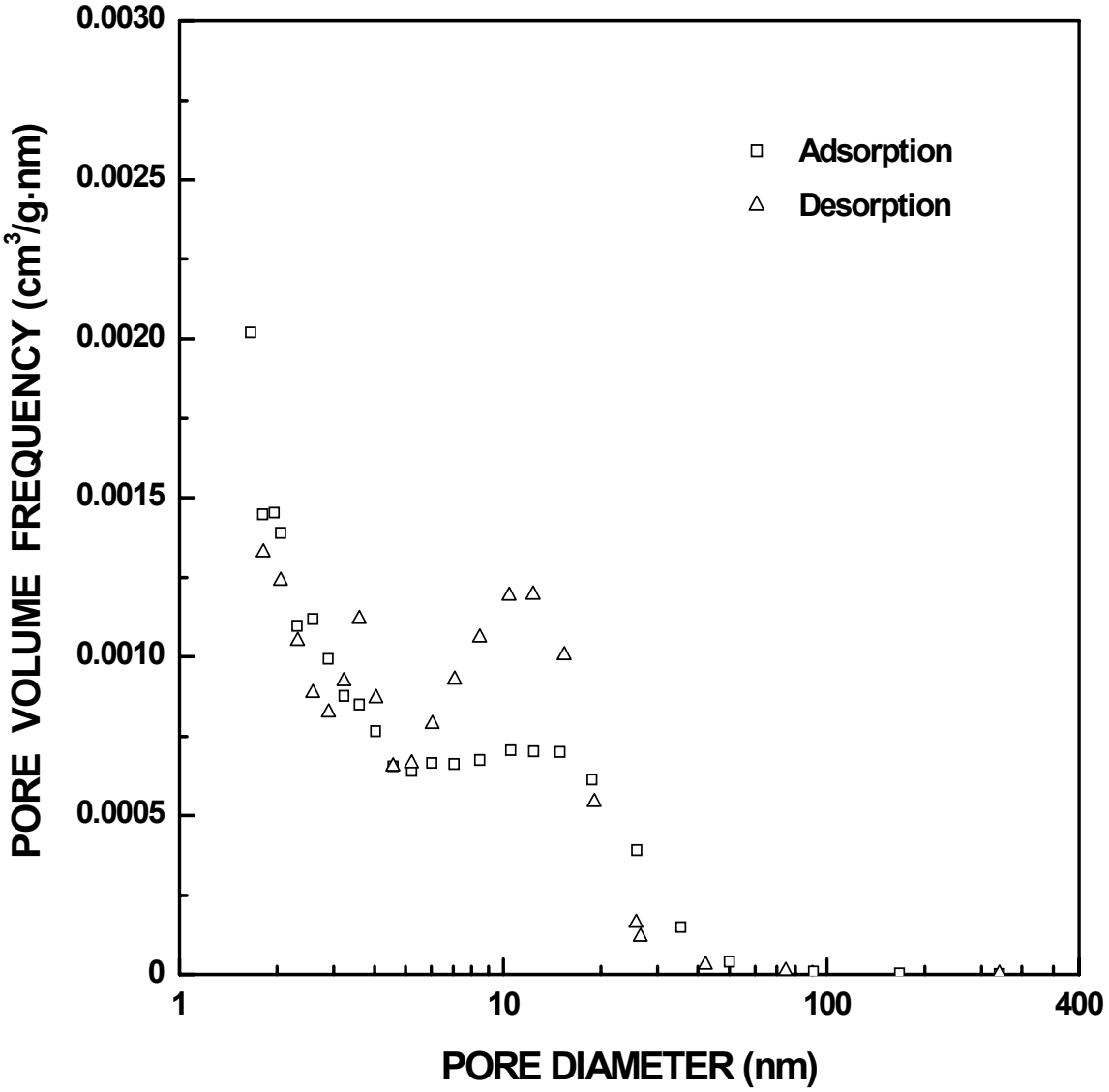

Figure I-68 Plots of specific pore volume frequency vs. pore diameter for SC35-1300(30min) sample (X_{WL} = 0.10).

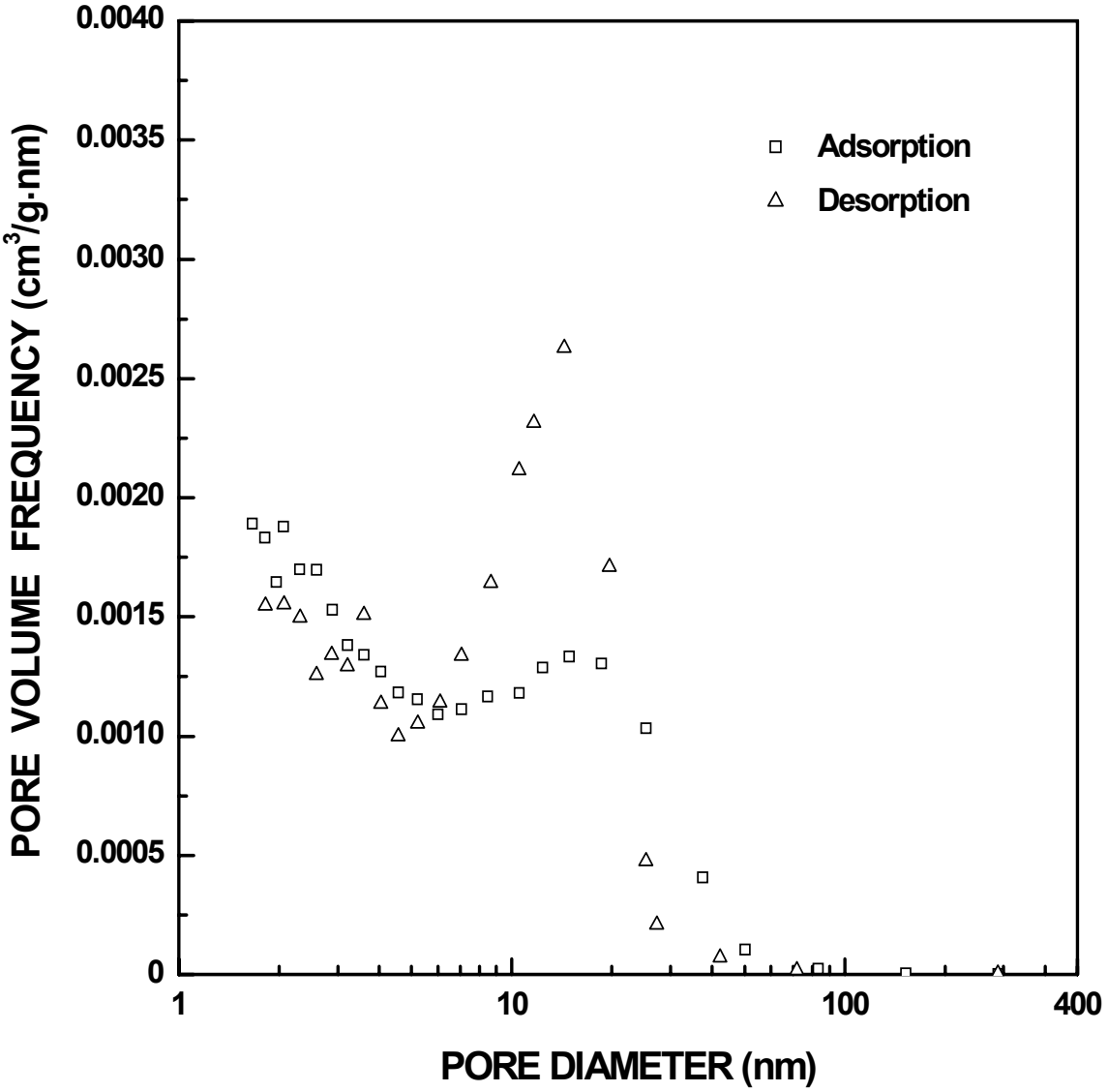

Figure I-69 Plots of specific pore volume frequency vs. pore diameter for SC35-1300(1h) sample (X_{WL} = 0.17).

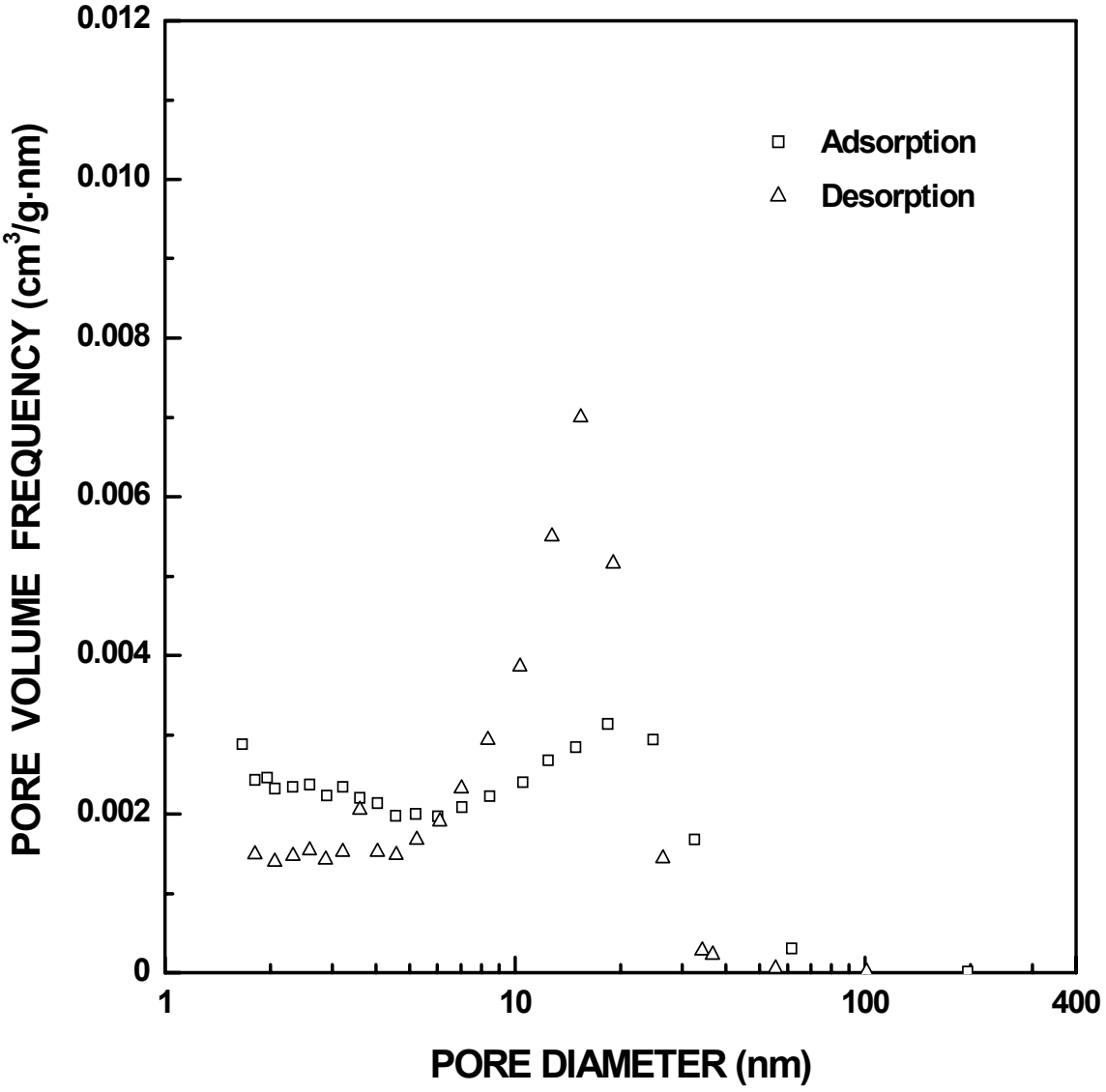

Figure I-70 Plots of specific pore volume frequency vs. pore diameter for SC35-1300(2h) sample (X_{WL} = 0.30).

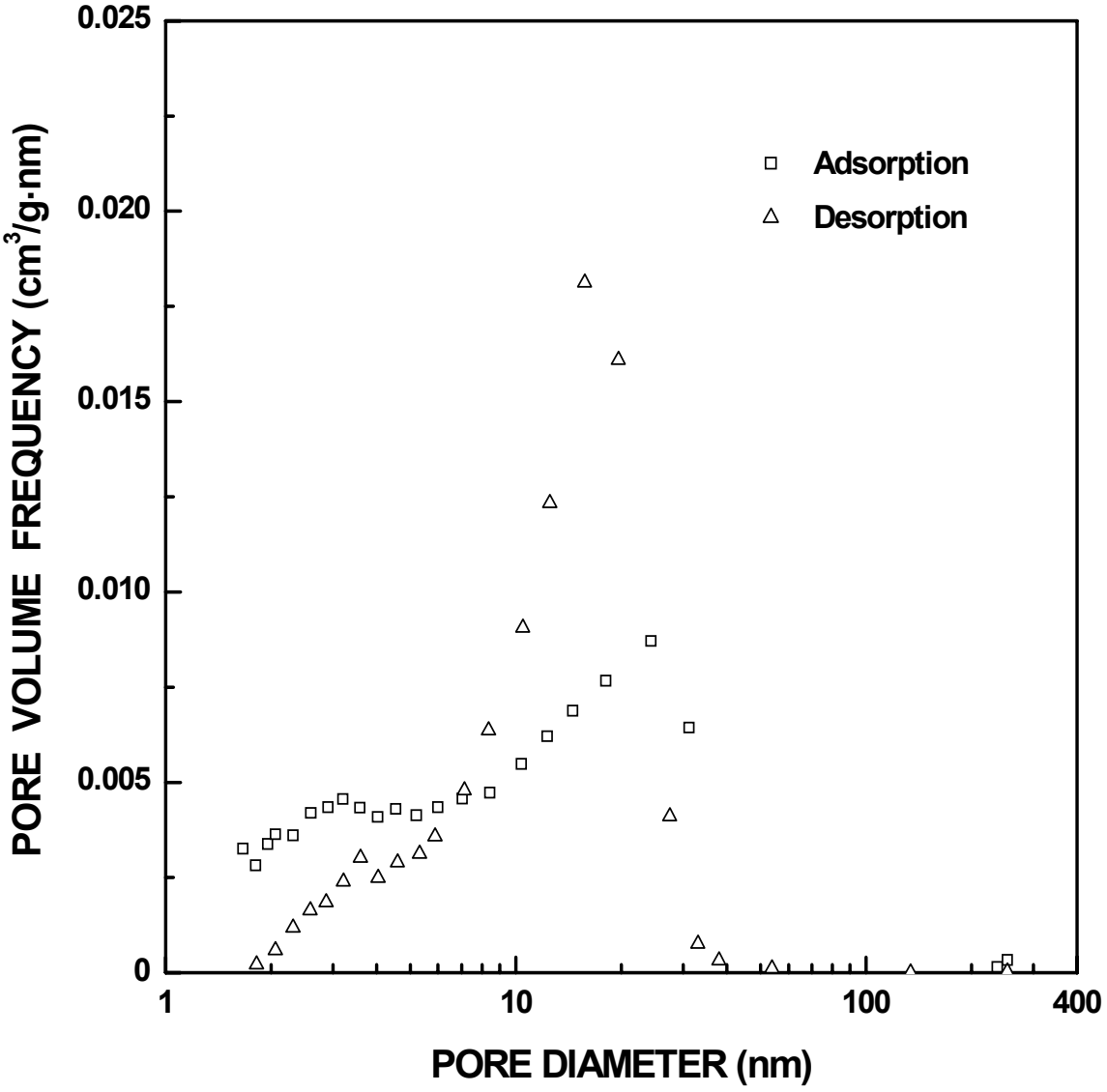

Figure I-71 Plots of specific pore volume frequency vs. pore diameter for SC35-1300(4h) sample (X_{WL} = 0.54).

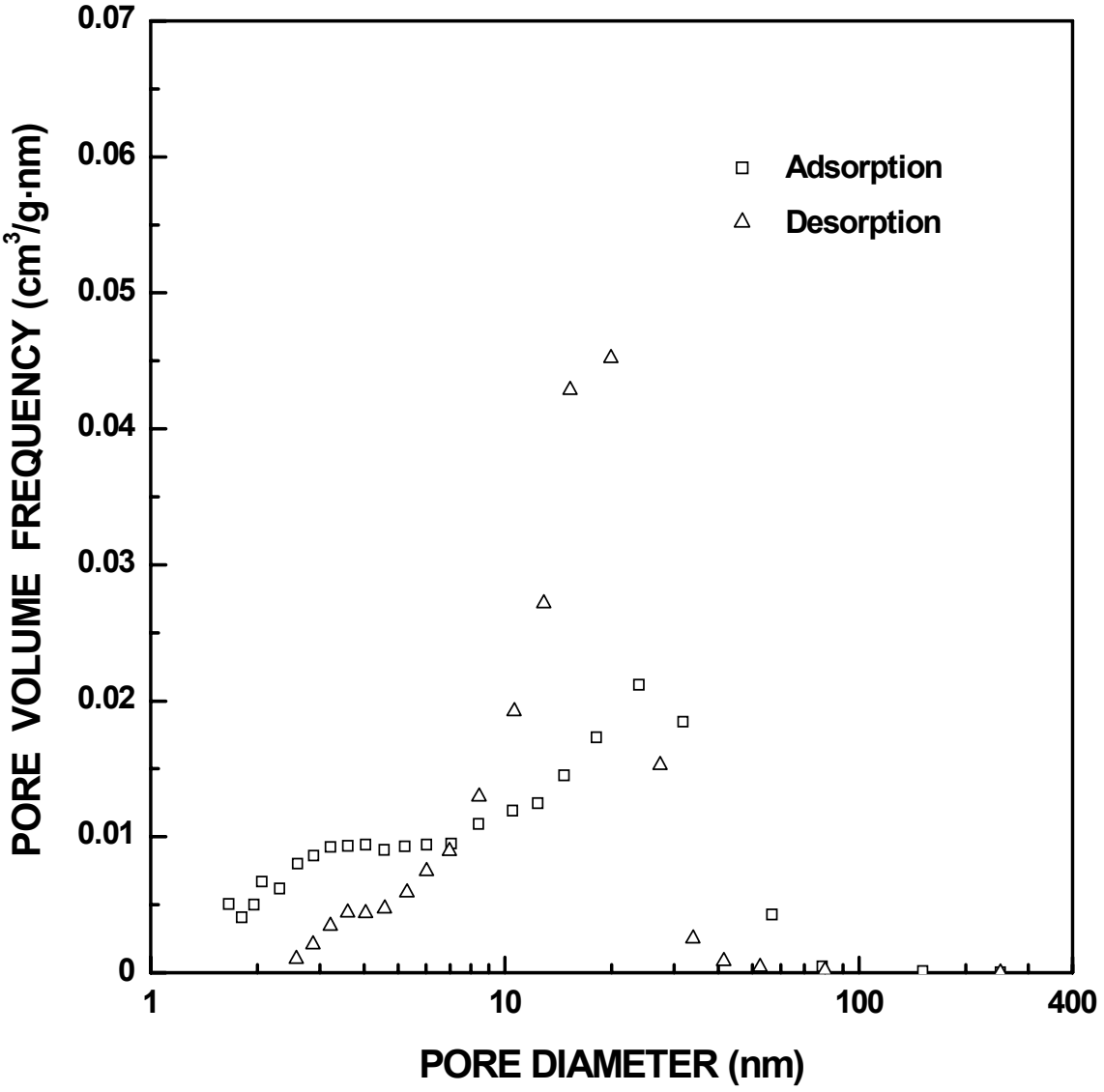

Figure I-72 Plots of specific pore volume frequency vs. pore diameter for SC35-1300(8h) sample (X_{WL} = 0.84).

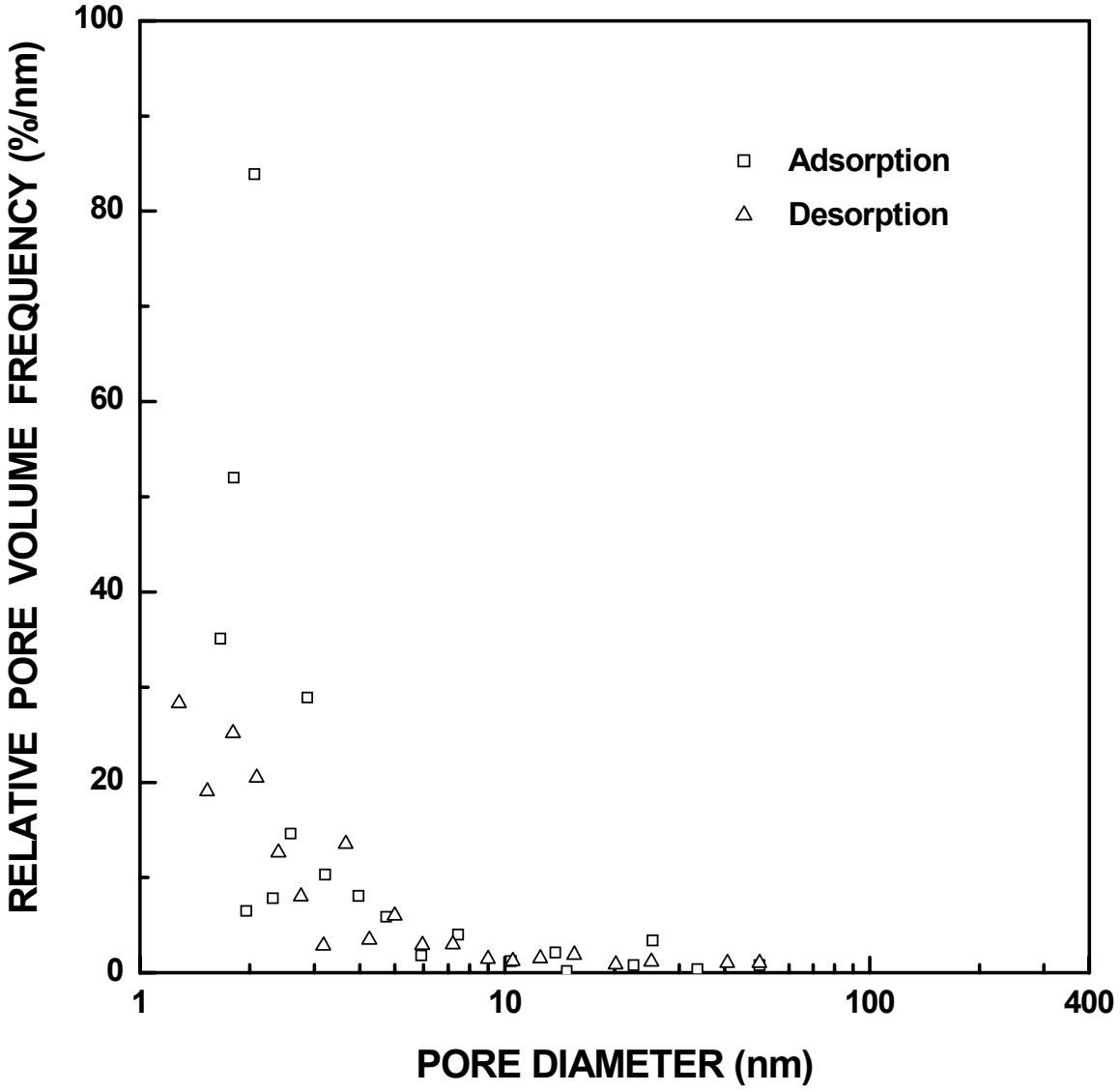

Figure I-73 Plots of relative ("normalized") pore volume frequency vs. pore diameter for SC35-1160(30min) sample (X_{WL} = 0.01). The pore diameter was cut off at 50 nm.

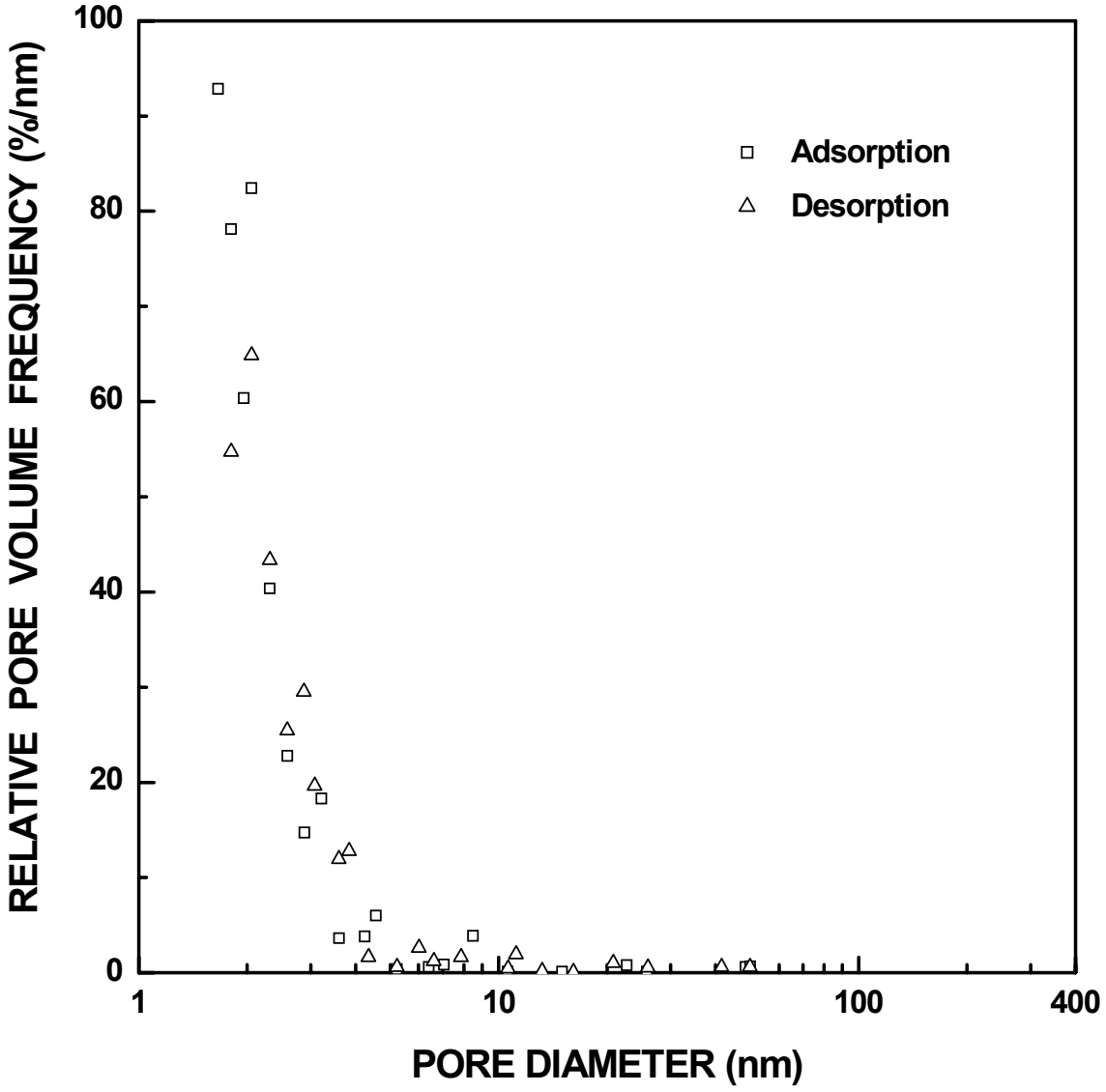

Figure I-74 Plots of relative ("normalized") pore volume frequency vs. pore diameter for SC35-1160(2h) sample (X_{WL} = 0.03). The pore diameter was cut off at 50 nm.

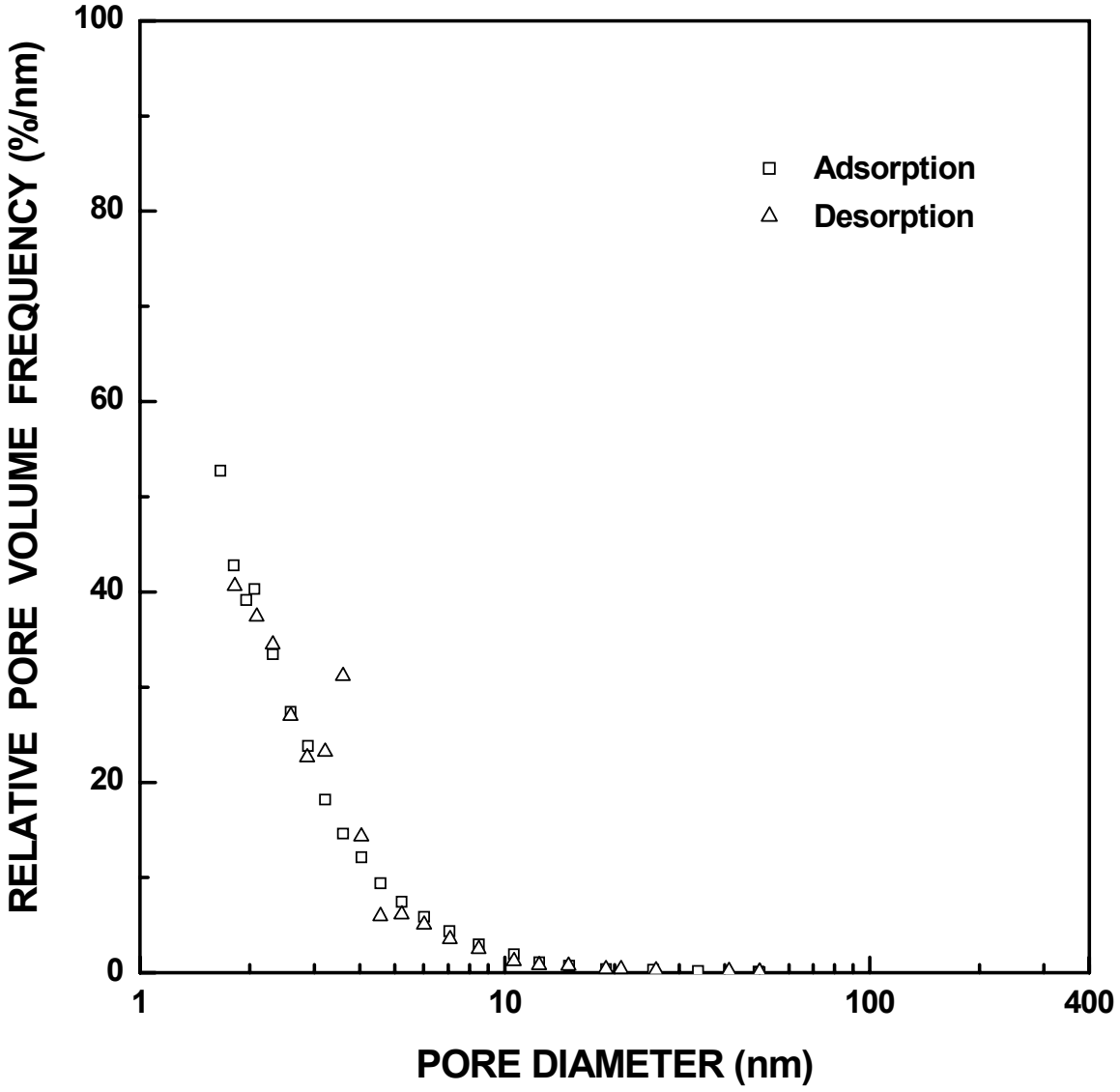

Figure I-75 Plots of relative ("normalized") pore volume frequency vs. pore diameter for SC35-1160(4h) sample (X_{WL} = 0.05). The pore diameter was cut off at 50 nm.

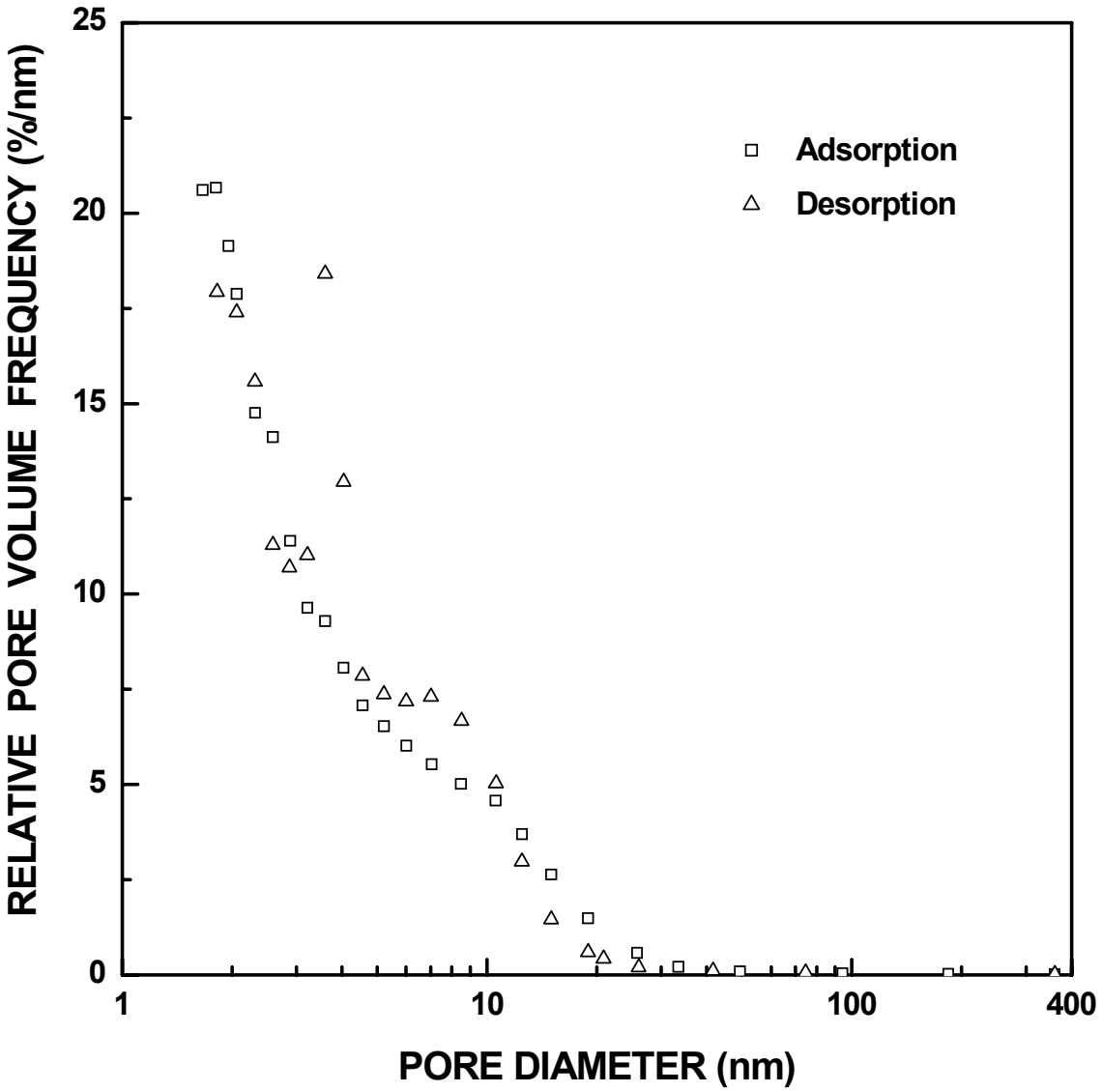

Figure I-76 Plots of relative ("normalized") pore volume frequency vs. pore diameter for SC35-1160(8h) sample (X_{WL} = 0.07).

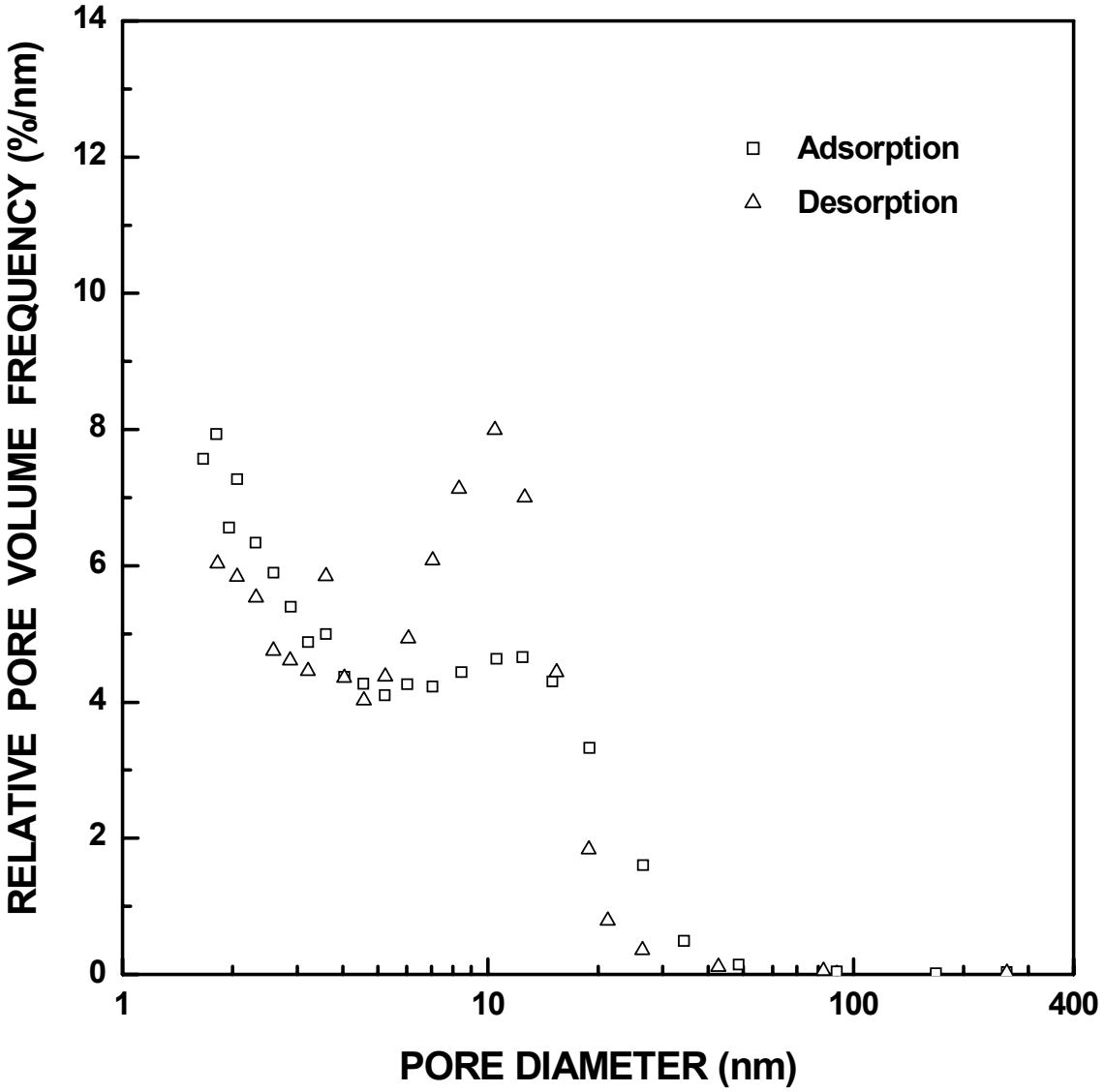

Figure I-77 Plots of relative ("normalized") pore volume frequency vs. pore diameter for SC35-1160(16h) sample (X_{WL} = 0.12).

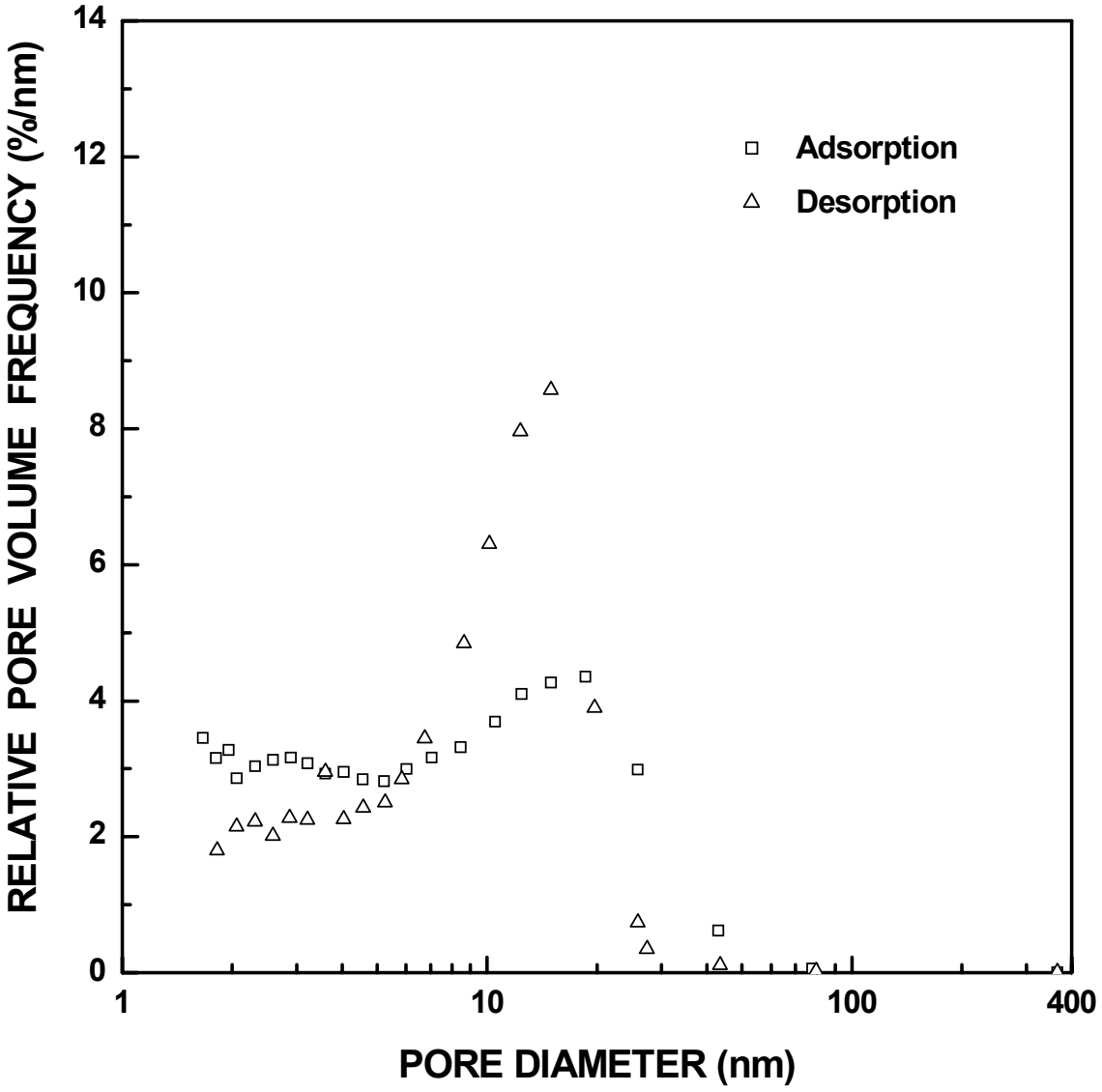

Figure I-78 Plots of relative ("normalized") pore volume frequency vs. pore diameter for SC35-1160(32h) sample (X_{WL} = 0.22).

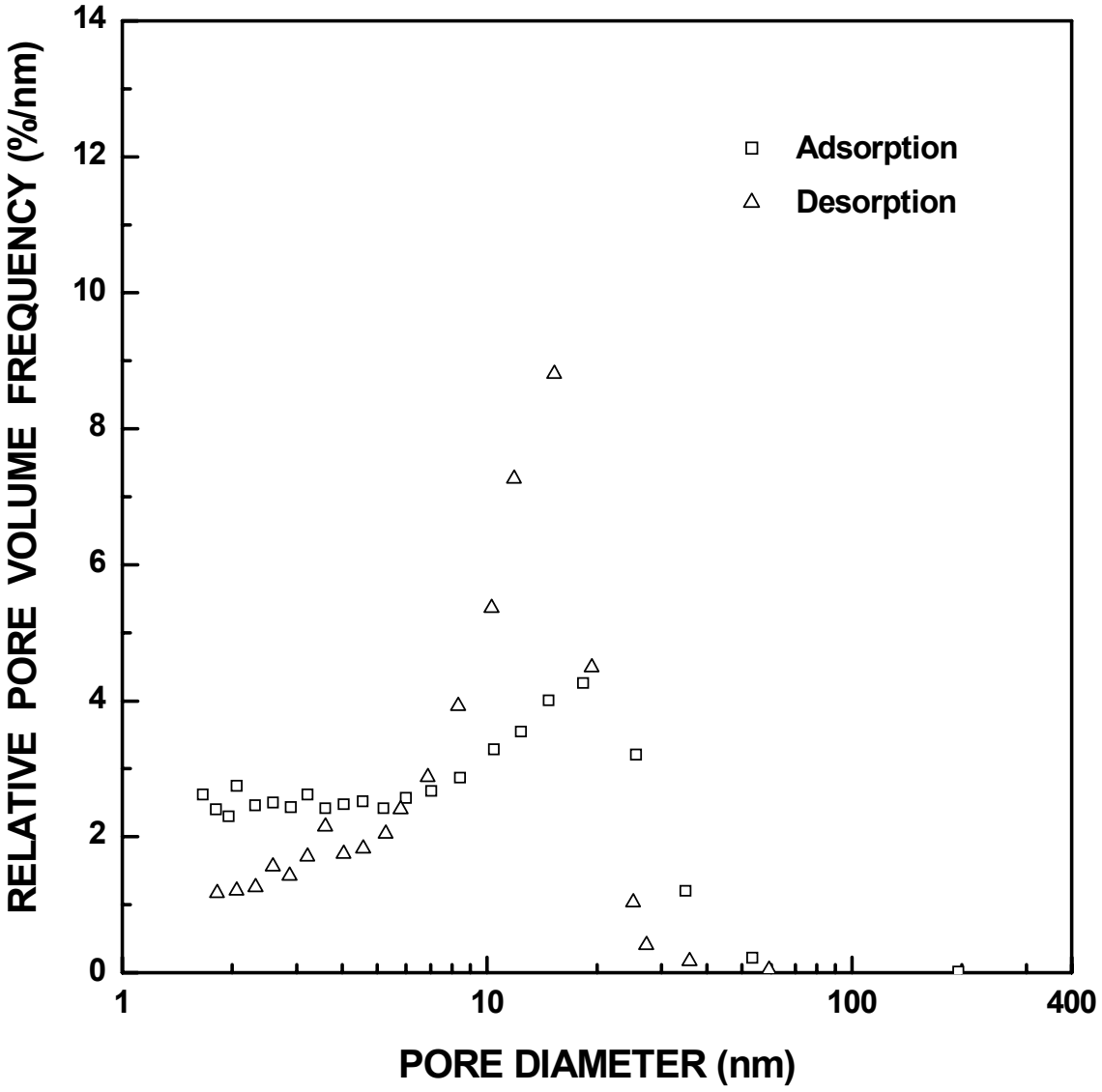

Figure I-79 Plots of relative ("normalized") pore volume frequency vs. pore diameter for SC35-1160(48h) sample (X_{WL} = 0.29).

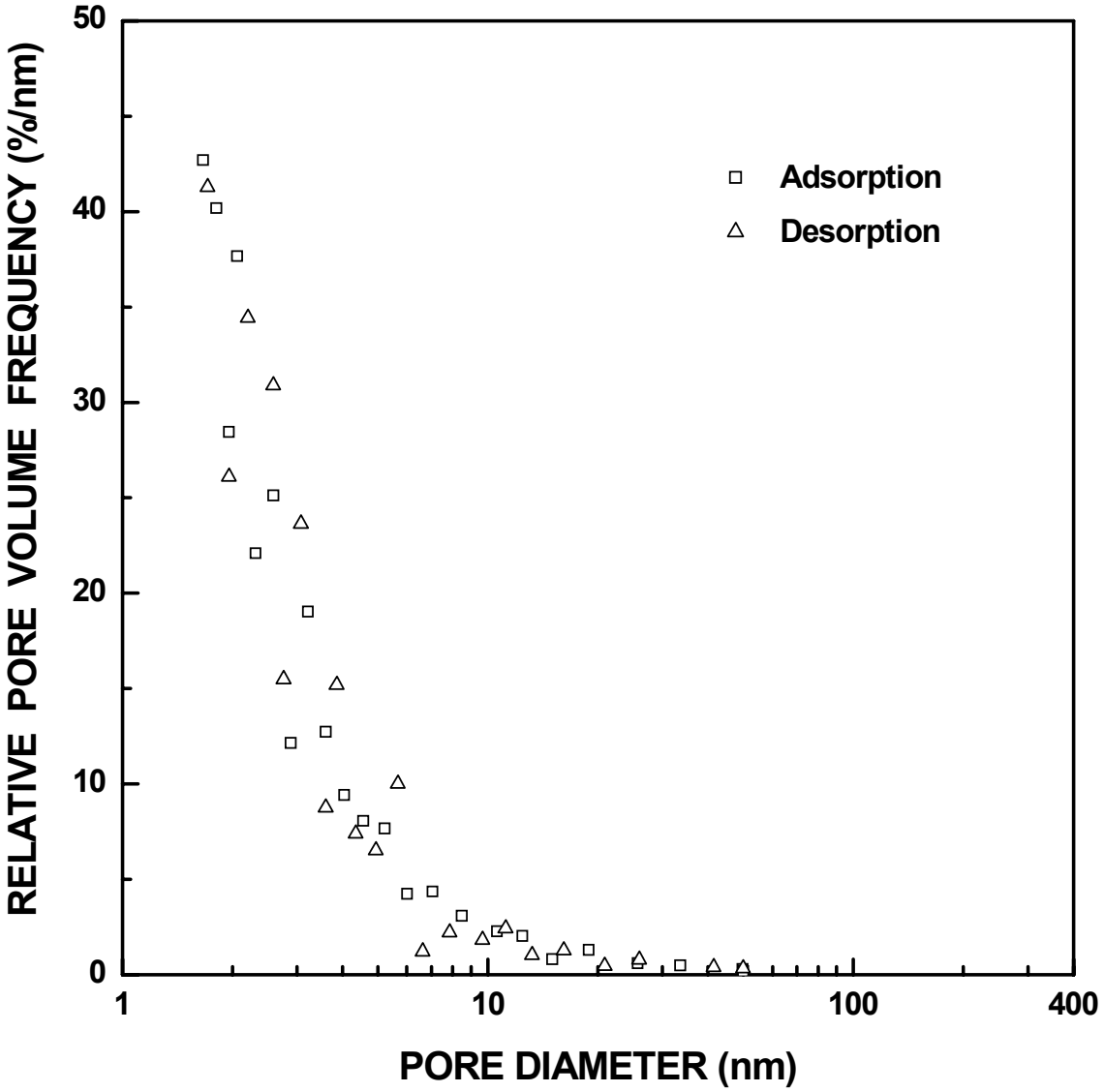

Figure I-80 Plots of relative ("normalized") pore volume frequency vs. pore diameter for SC35-1200(30min) ample (X_{WL} = 0.02). The pore diameter was cut off at 50 nm.

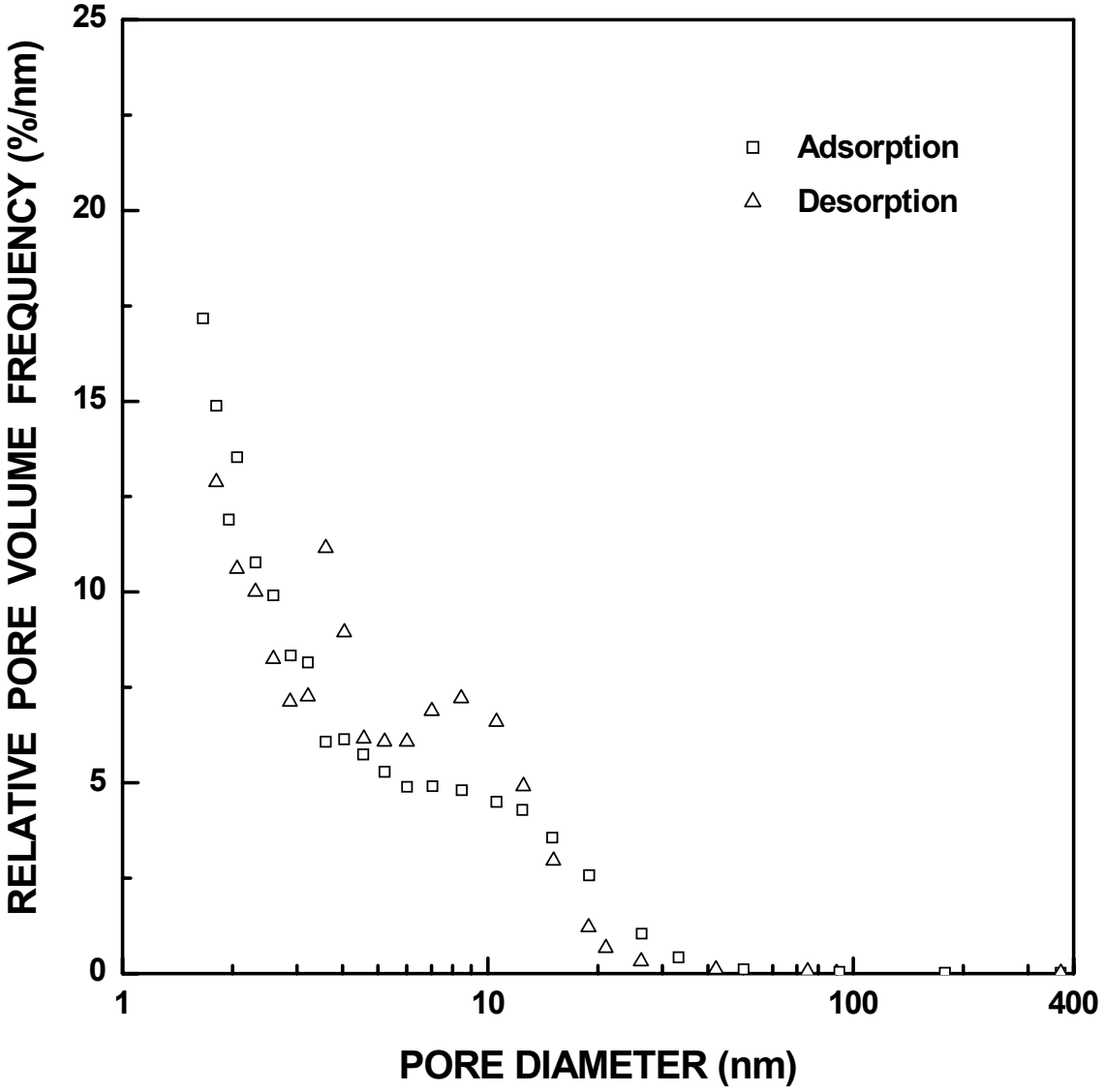

Figure I-81 Plots of relative ("normalized") pore volume frequency vs. pore diameter for SC35-1200(4h) ample (X_{WL} = 0.09).

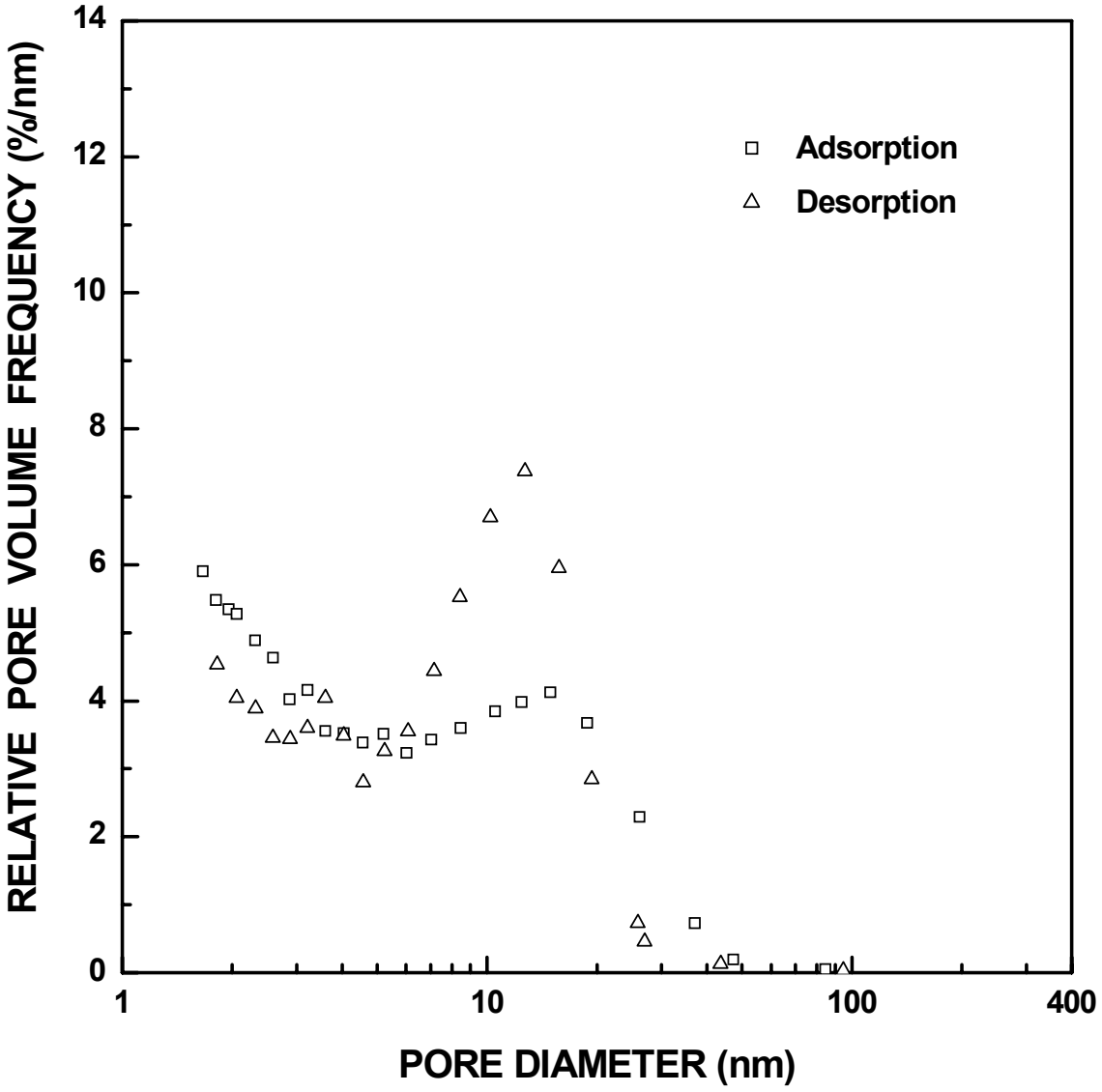

Figure I-82 Plots of relative ("normalized") pore volume frequency vs. pore diameter for SC35-1200(8h) sample (X_{WL} = 0.16).

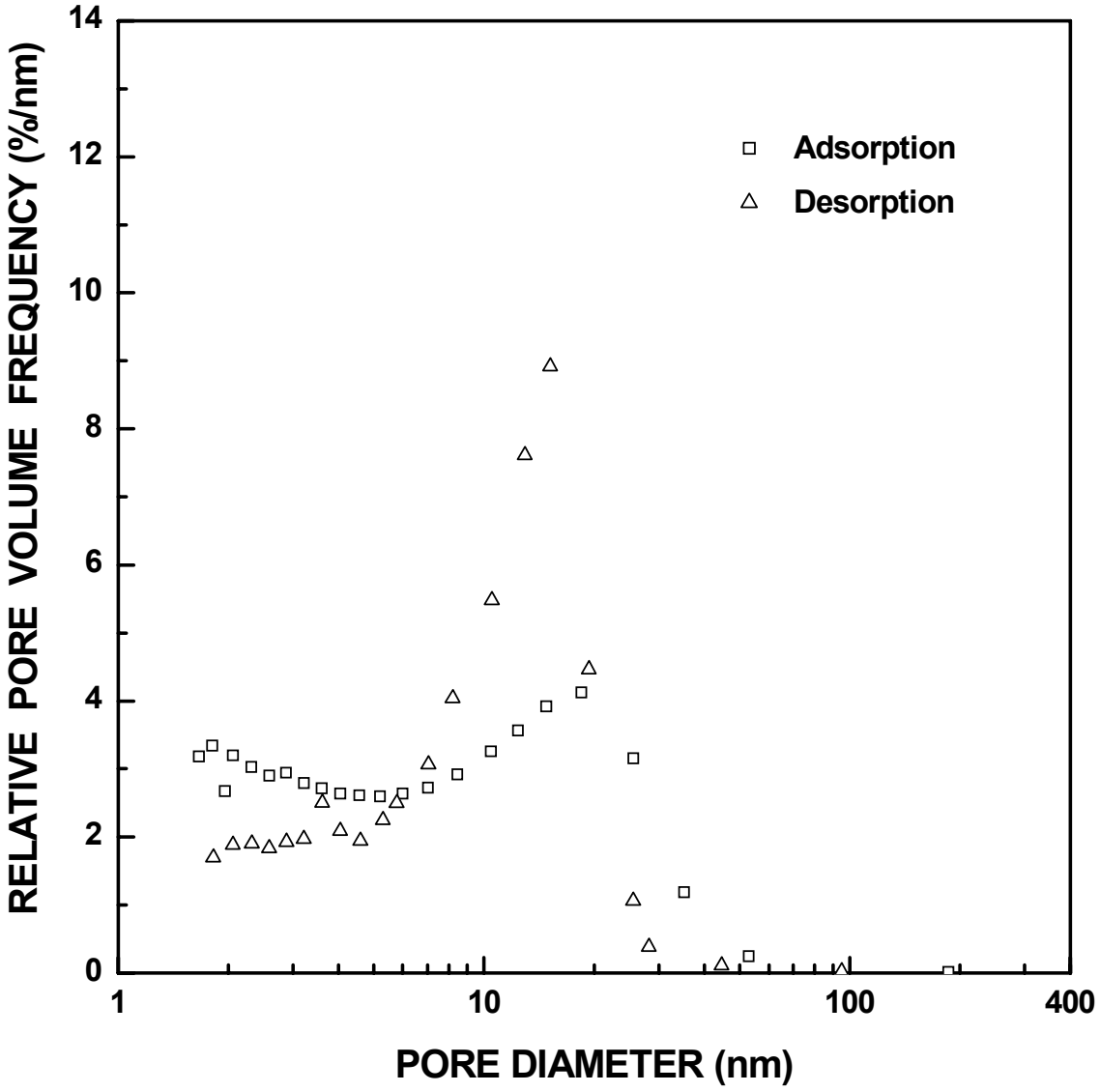

Figure I-83 Normalized pore volume frequency vs. pore diameter for SC35-1200(16h) sample (X_{WL} = 0.26).

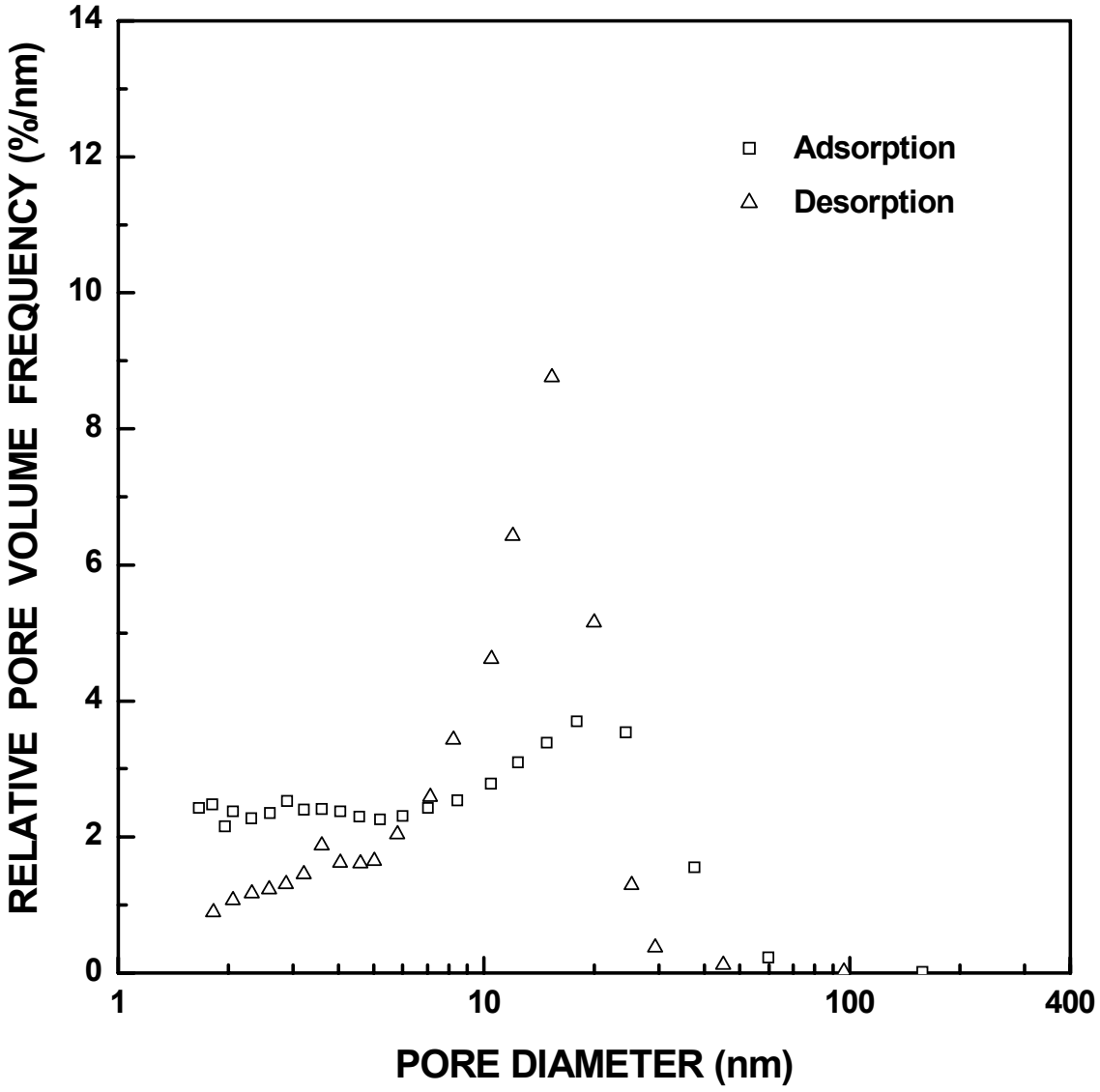

Figure I-84 Plots of relative ("normalized") pore volume frequency vs. pore diameter for SC35-1200(22.5h) sample (X_{WL} = 0.38).

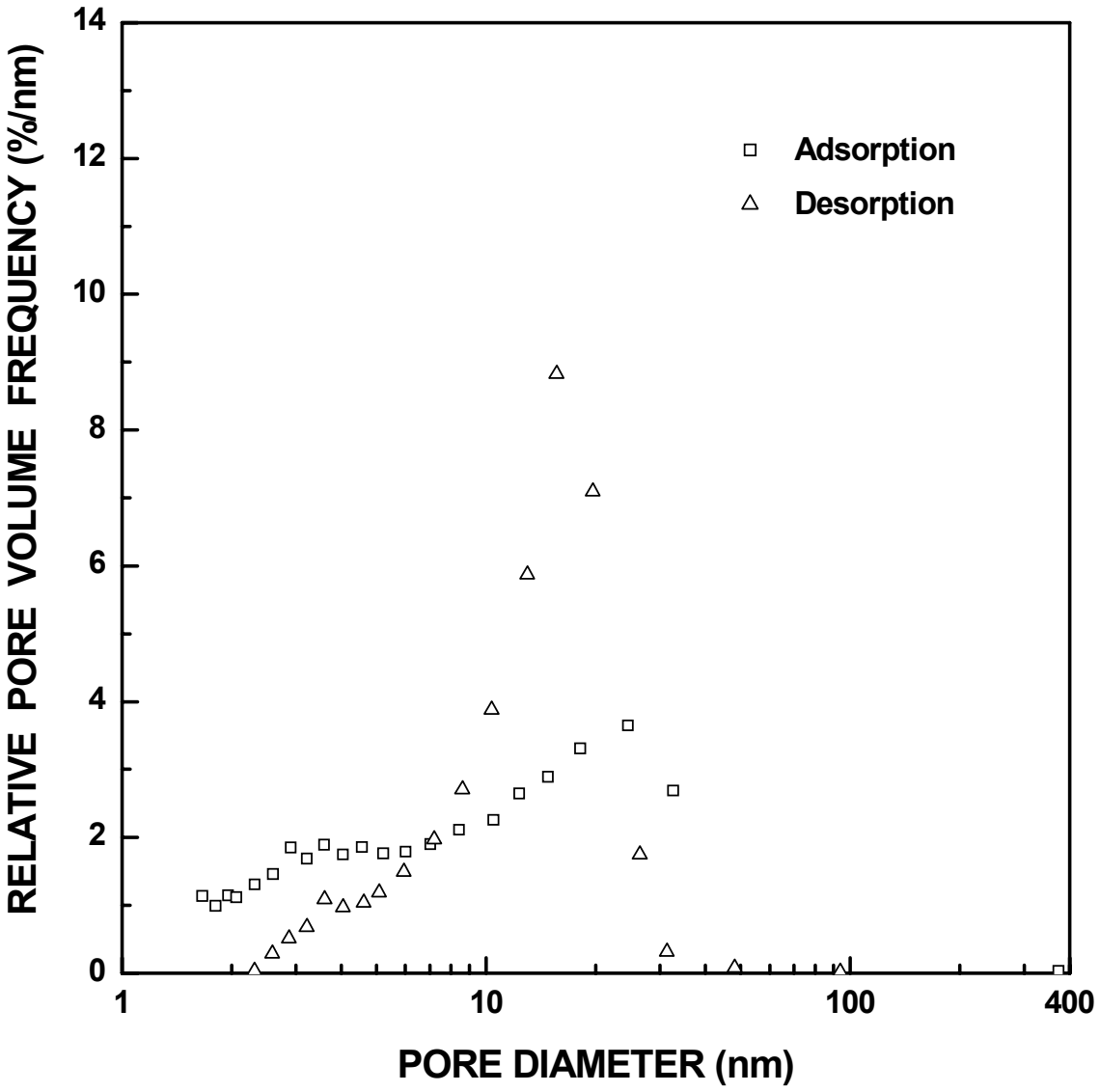

Figure I-85 Plots of relative ("normalized") pore volume frequency vs. pore diameter for SC35-1250(16h) sample (X_{WL} = 0.70).

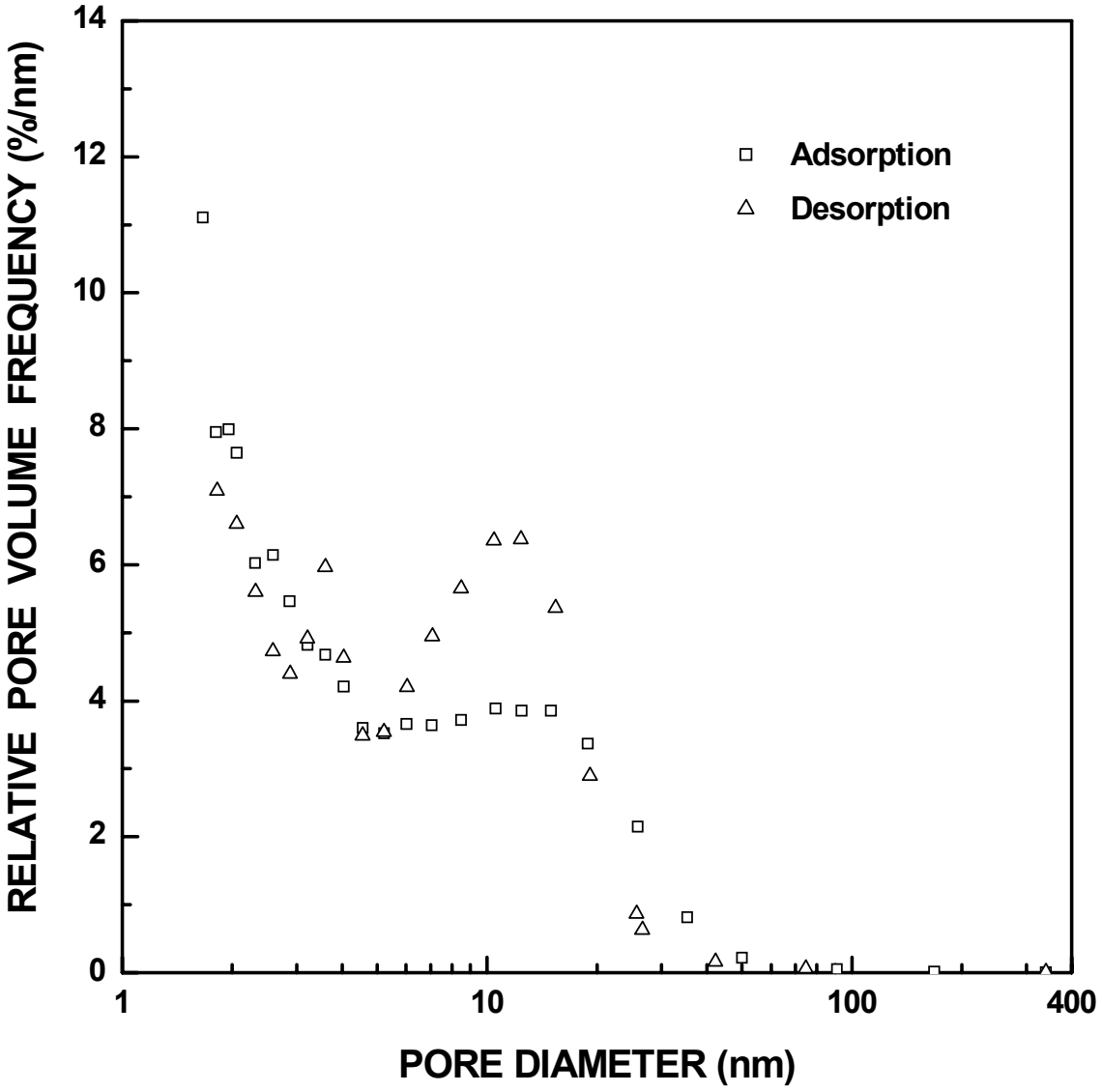

Figure I-86 Plots of relative ("normalized") pore volume frequency vs. pore diameter for SC35-1300(30min) sample (X_{WL} = 0.10).

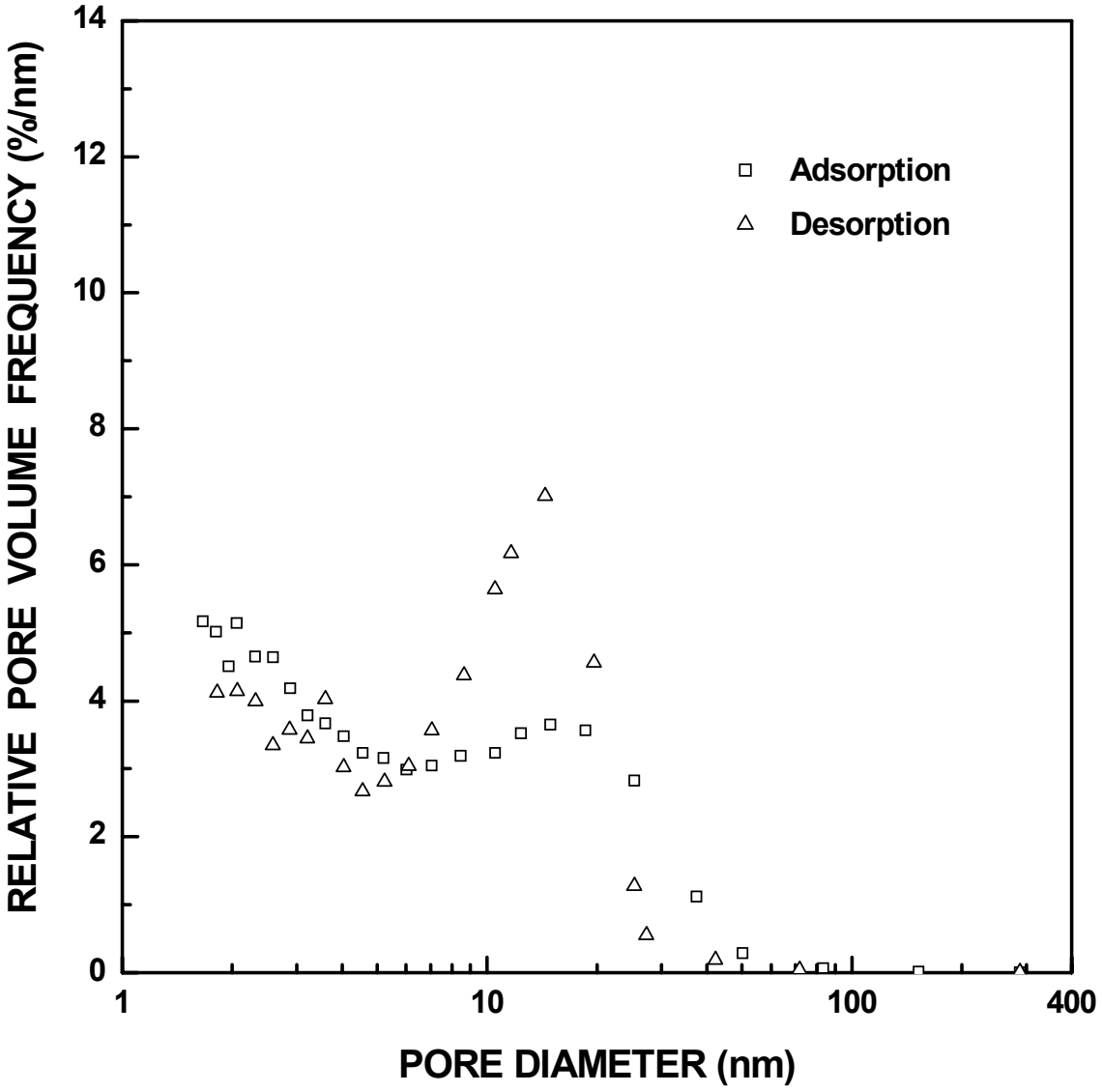

Figure I-87 Plots of relative ("normalized") pore volume frequency vs. pore diameter for SC35-1300(1h) sample (X_{WL} = 0.17).

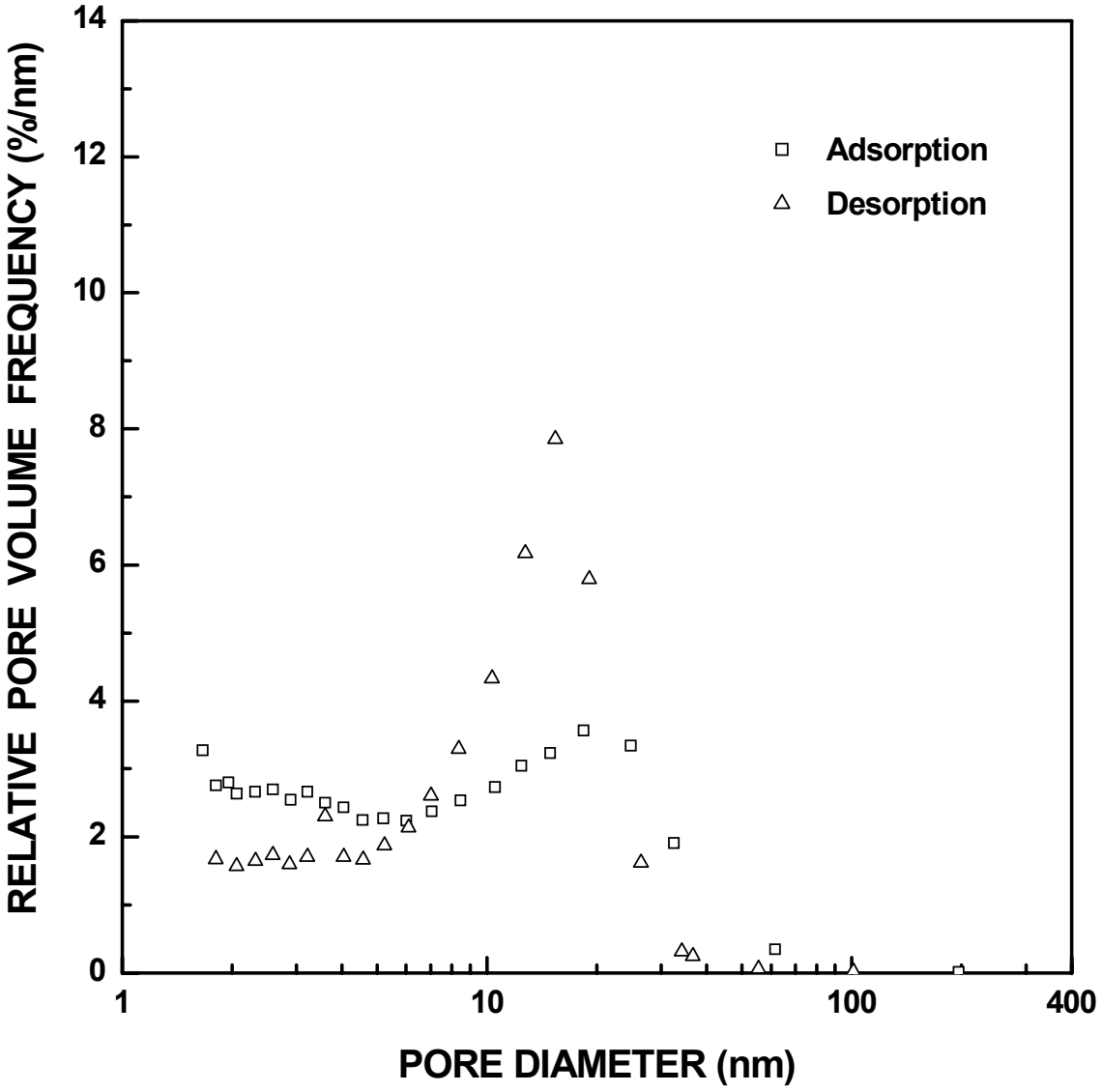

Figure I-88 Plots of relative ("normalized") pore volume frequency vs. pore diameter for SC35-1300(2h) sample (X_{WL} = 0.30).

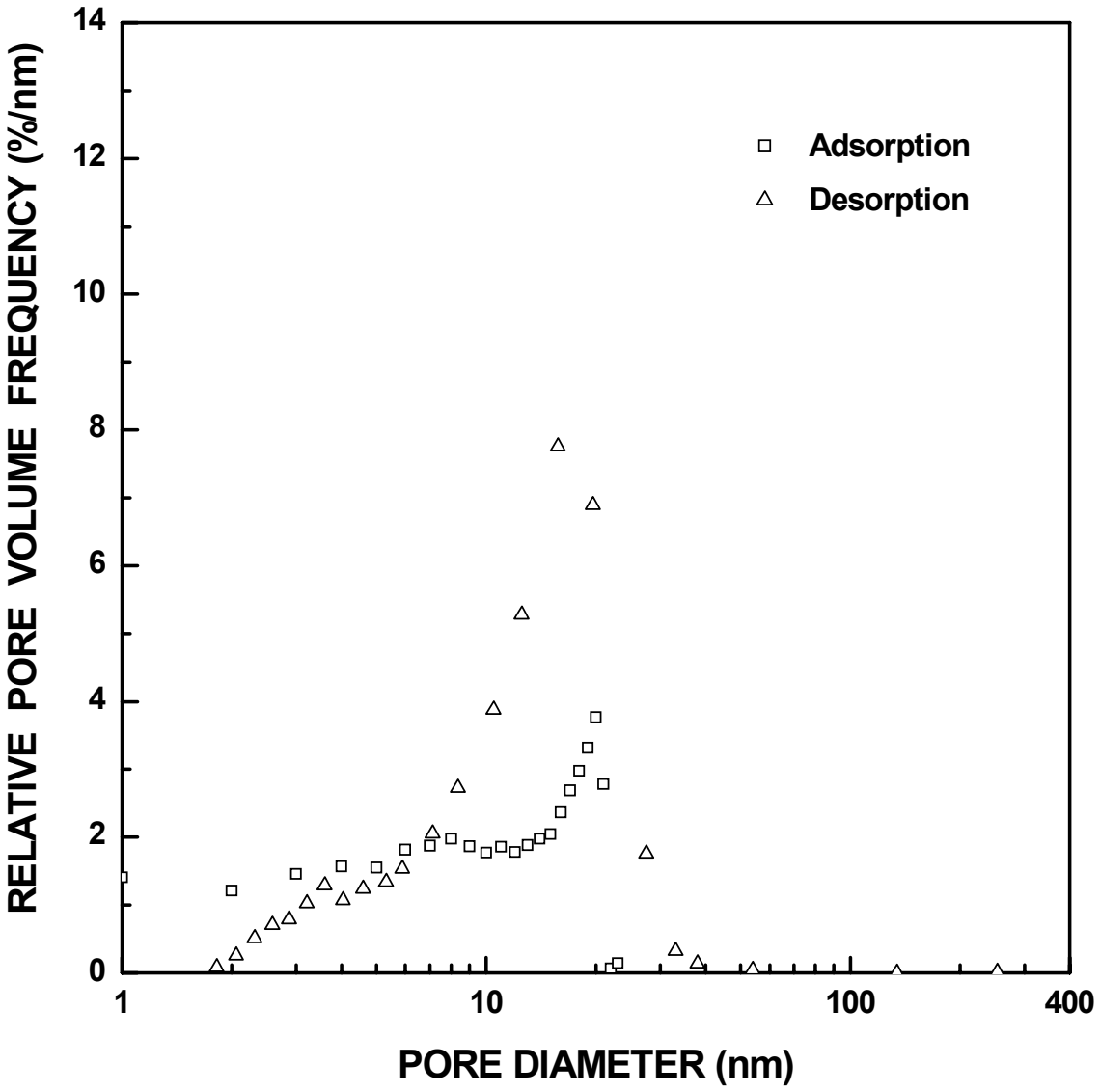

Figure I-89 Plots of relative ("normalized") pore volume frequency vs. pore diameter for SC35-1300(4h) sample (X_{WL} = 0.54).

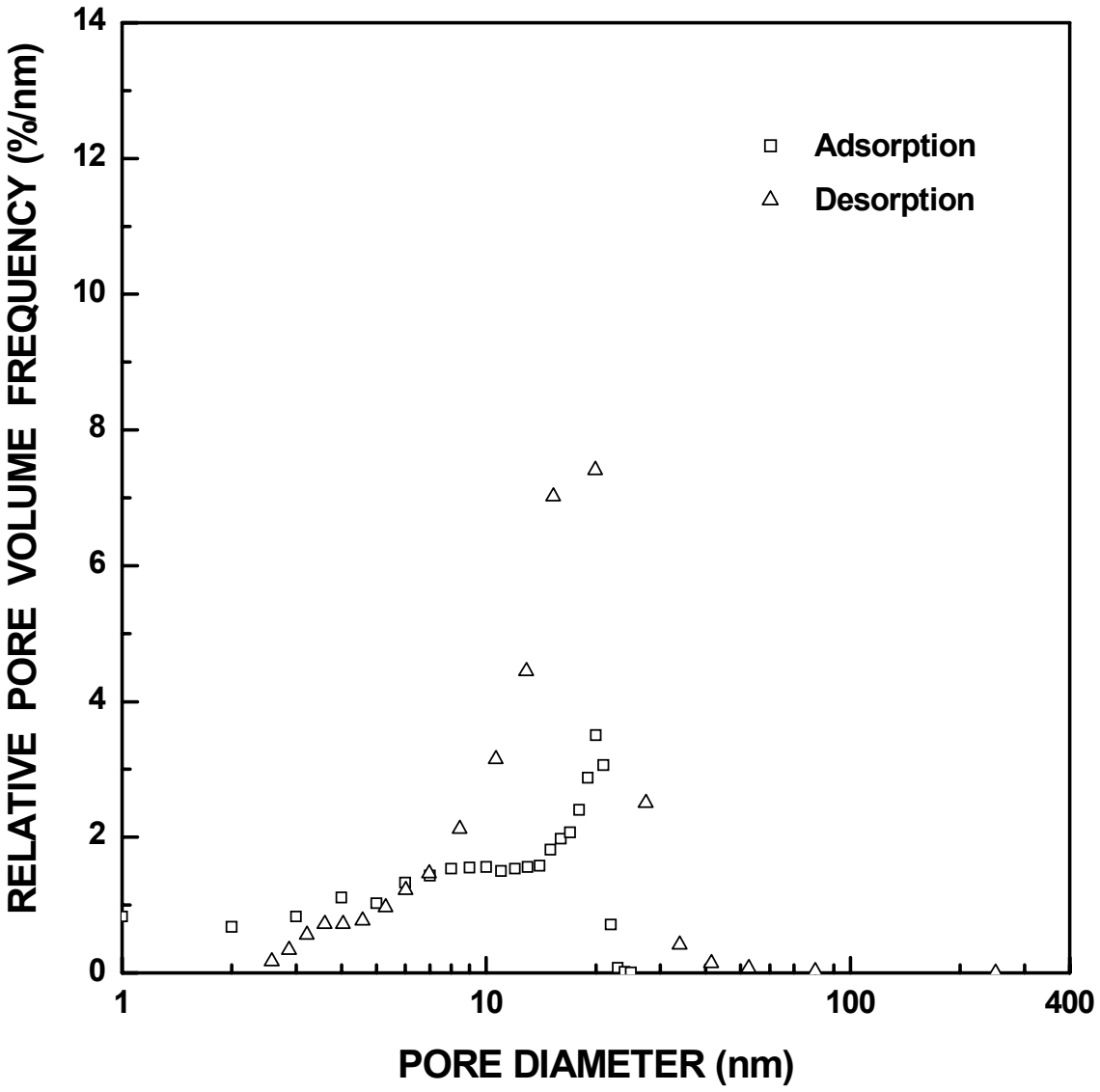

Figure I-90 Plots of relative ("normalized") pore volume frequency vs. pore diameter for SC35-1300(8h) sample (X_{WL} = 0.84).

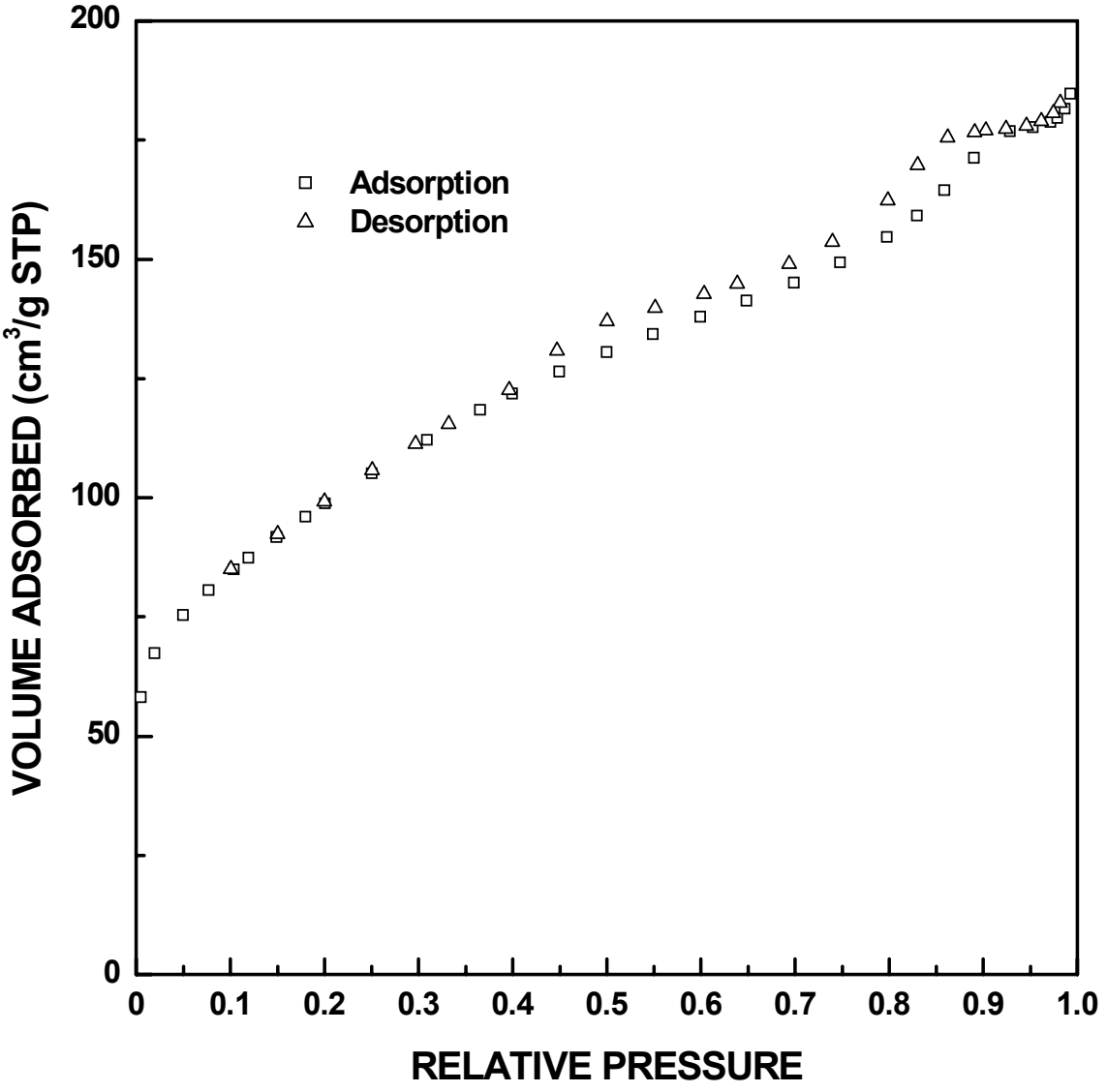

Figure I-91 Adsorption/desorption isotherm plots for SC8-1160(36h) sample (X_{WL} = 0.62).

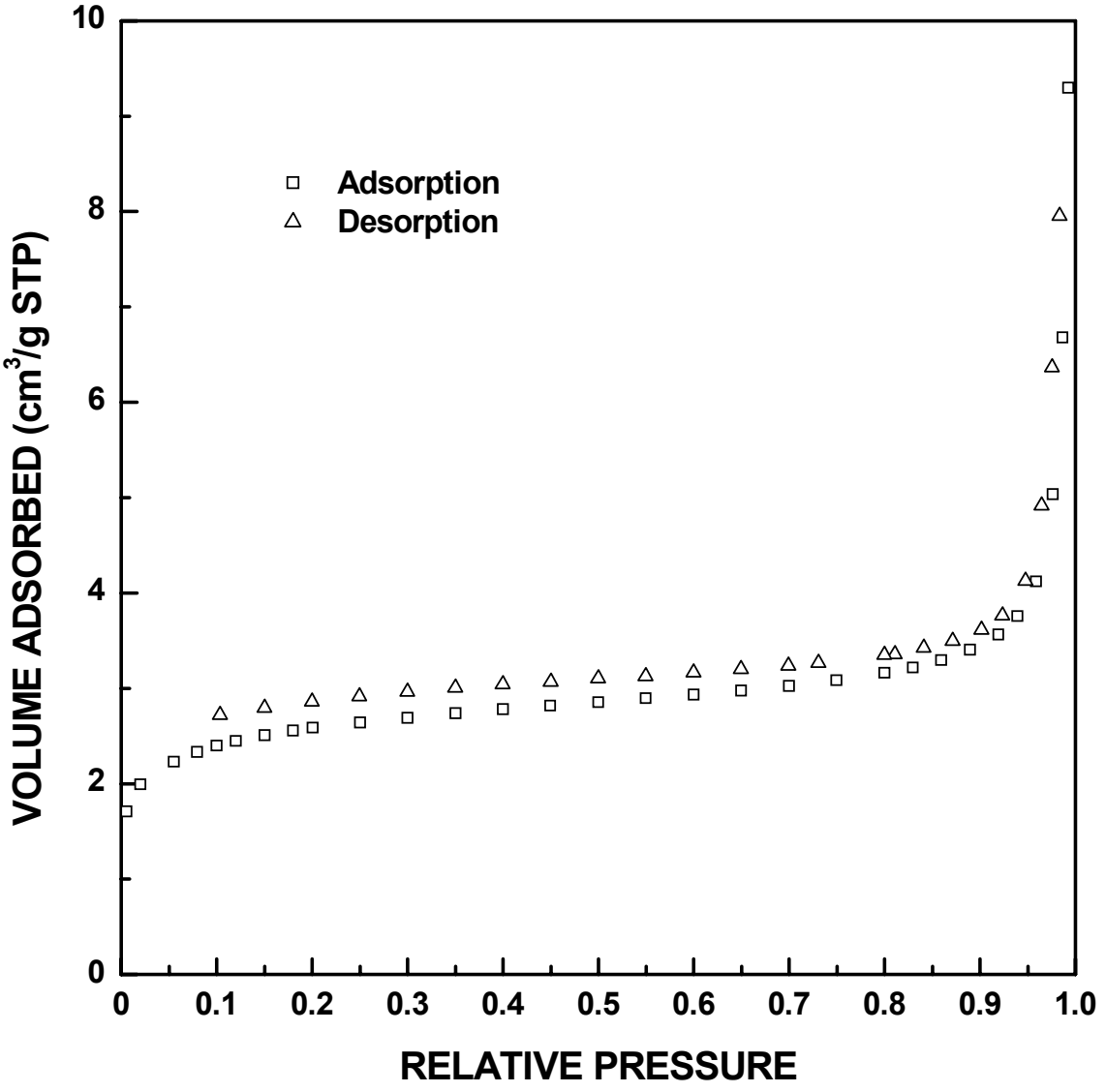

Figure I-92 Adsorption/desorption isotherm plots for SC8-1180(1h) sample (X_{WL} = 0.08).

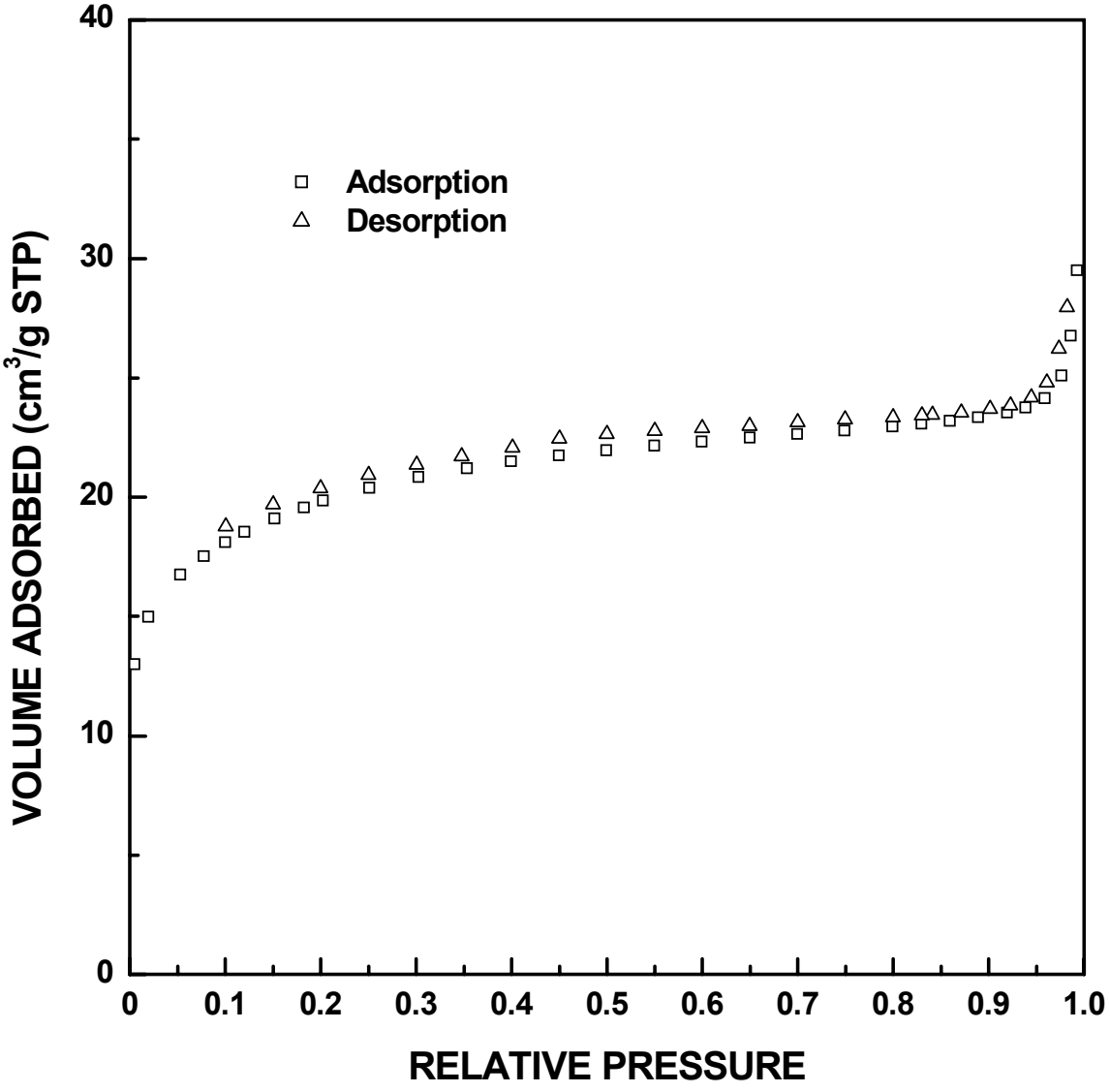

Figure I-93 Adsorption/desorption isotherm plots for SC8-1180(4h) sample (X_{WL} = 0.18).

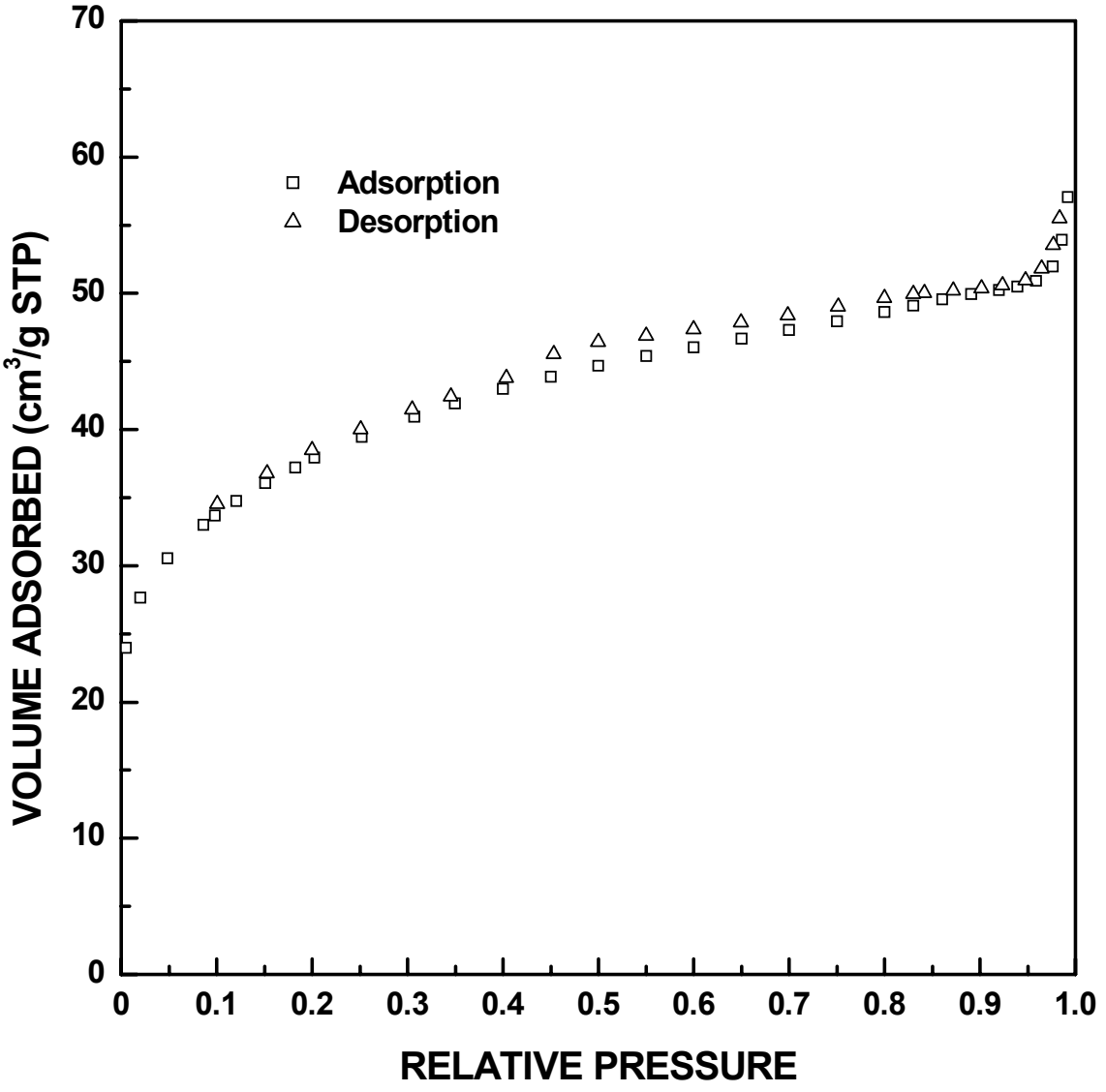

Figure I-94 Adsorption/desorption isotherm plots for SC8-1180(8h) sample (X_{WL} = 0.31).

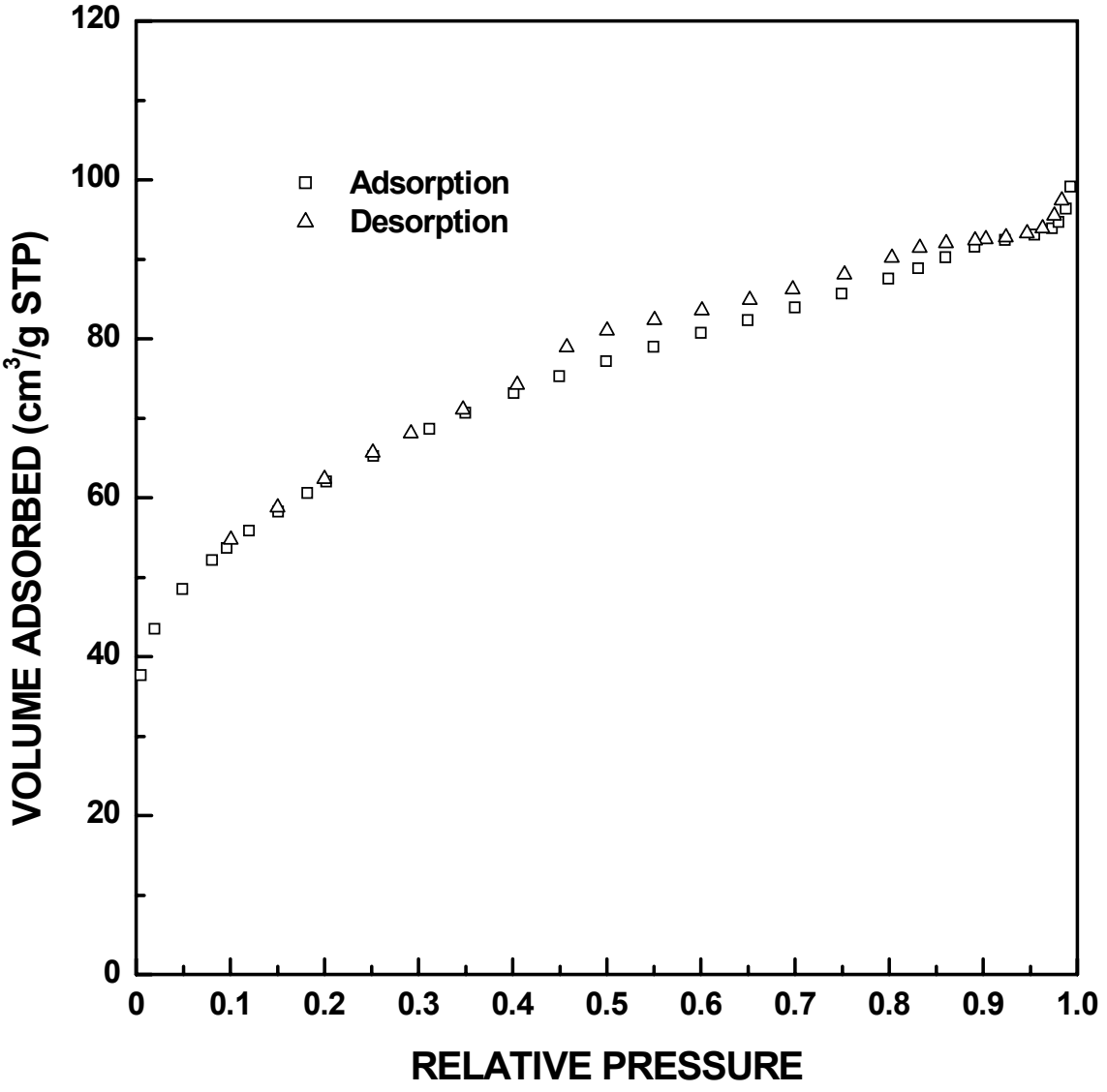

Figure I-95 Adsorption/desorption isotherm plots for SC8-1180(12h) sample (X_{WL} = 0.43).

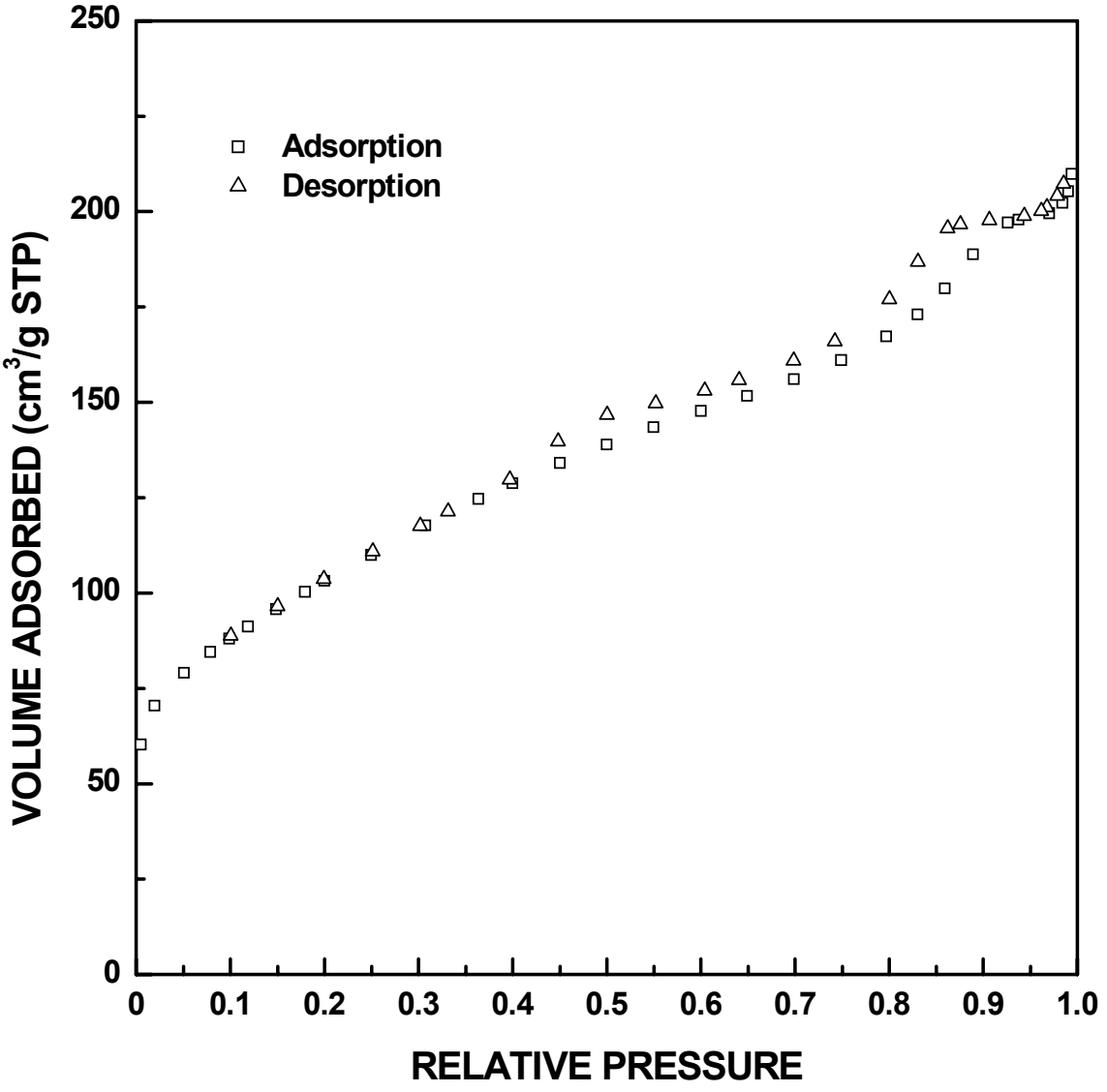

Figure I-96 Adsorption/desorption isotherm plots for SC8-1180(24h) sample (X_{WL} = 0.70).

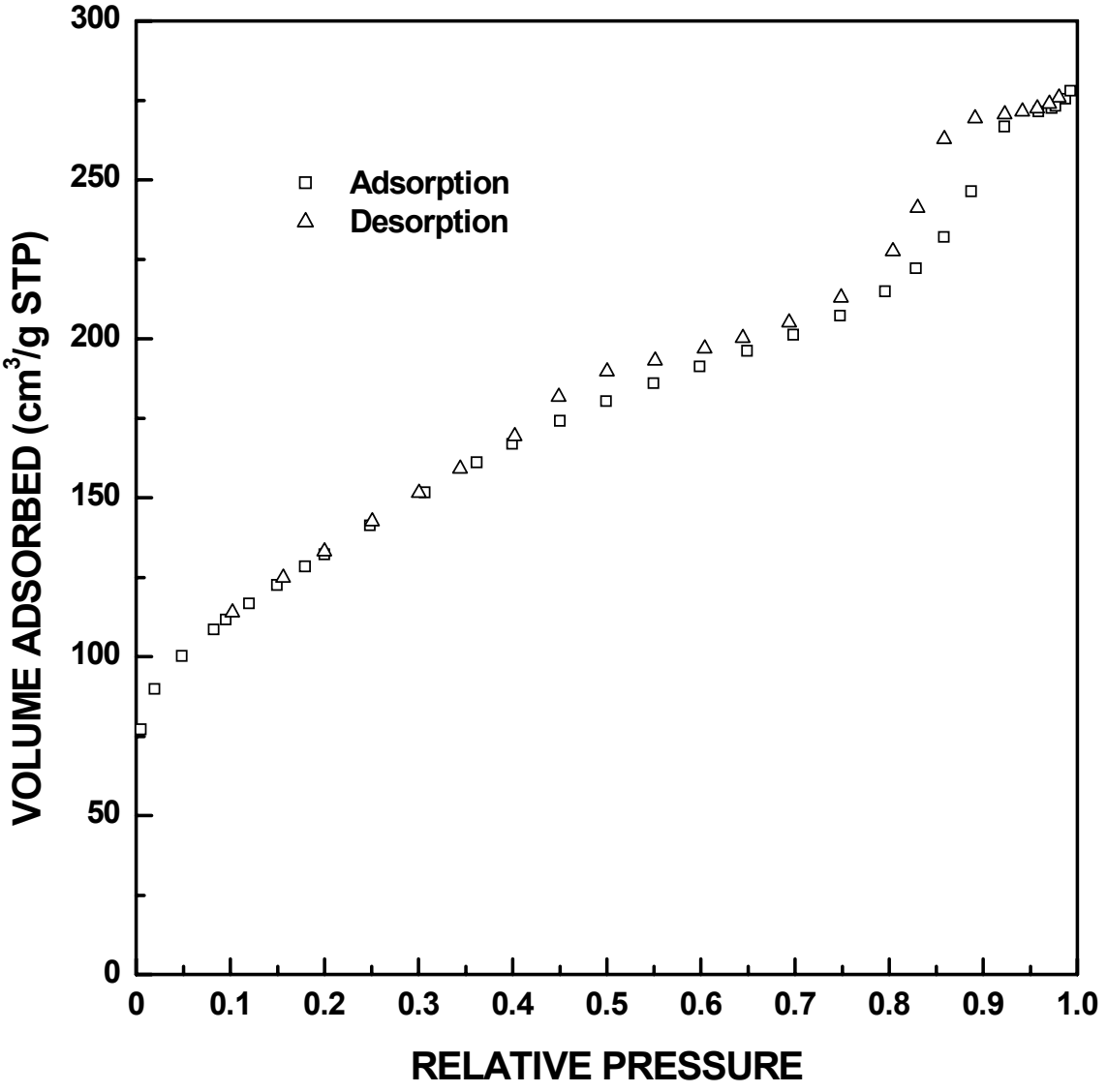

Figure I-97 Adsorption/desorption isotherm plots for SC8-1180(36h) sample (X_{WL} = 0.82).

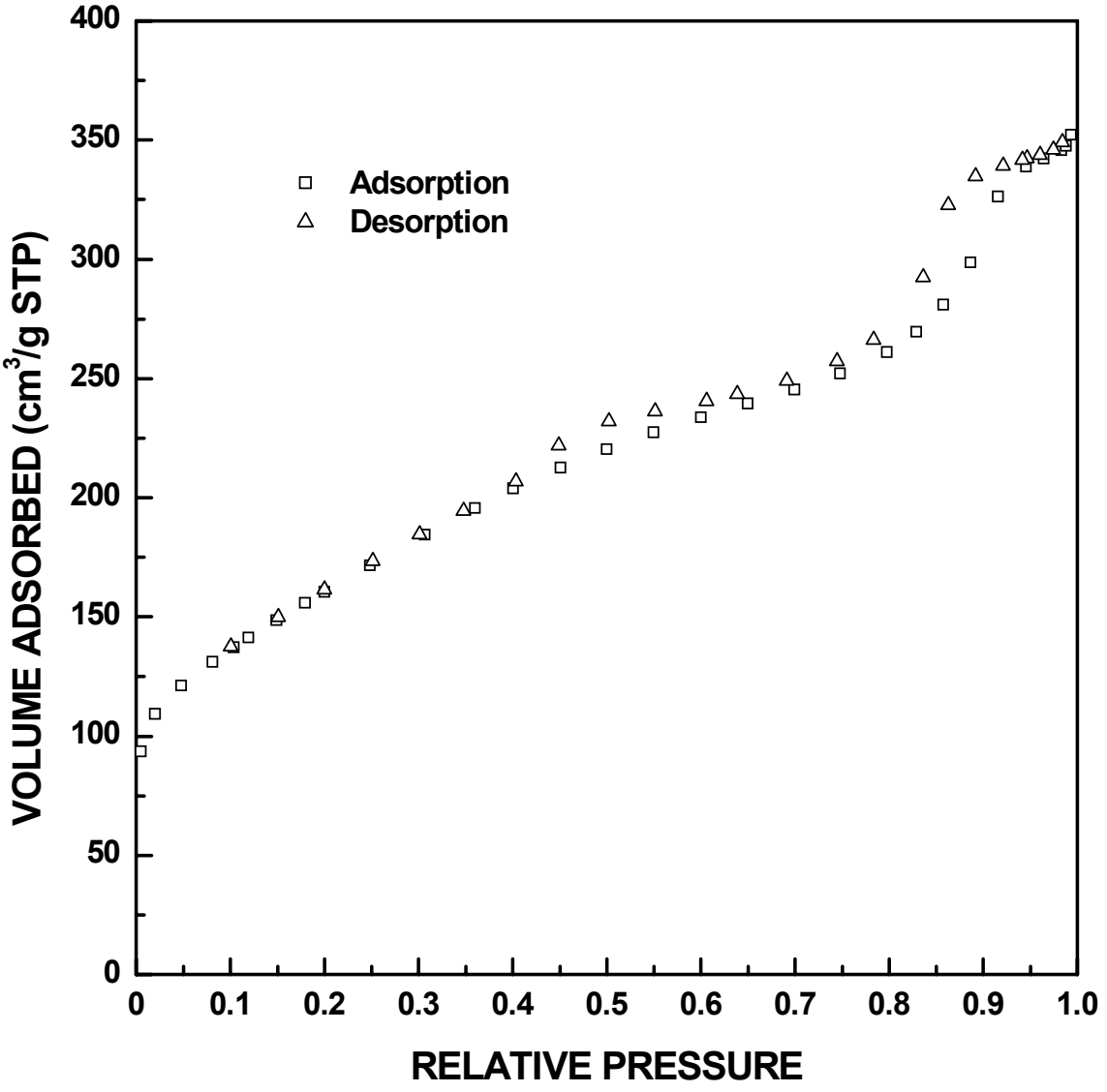

Figure I-98 Adsorption/desorption isotherm plots for SC8-1180(48h) sample (X_{WL} = 0.92).

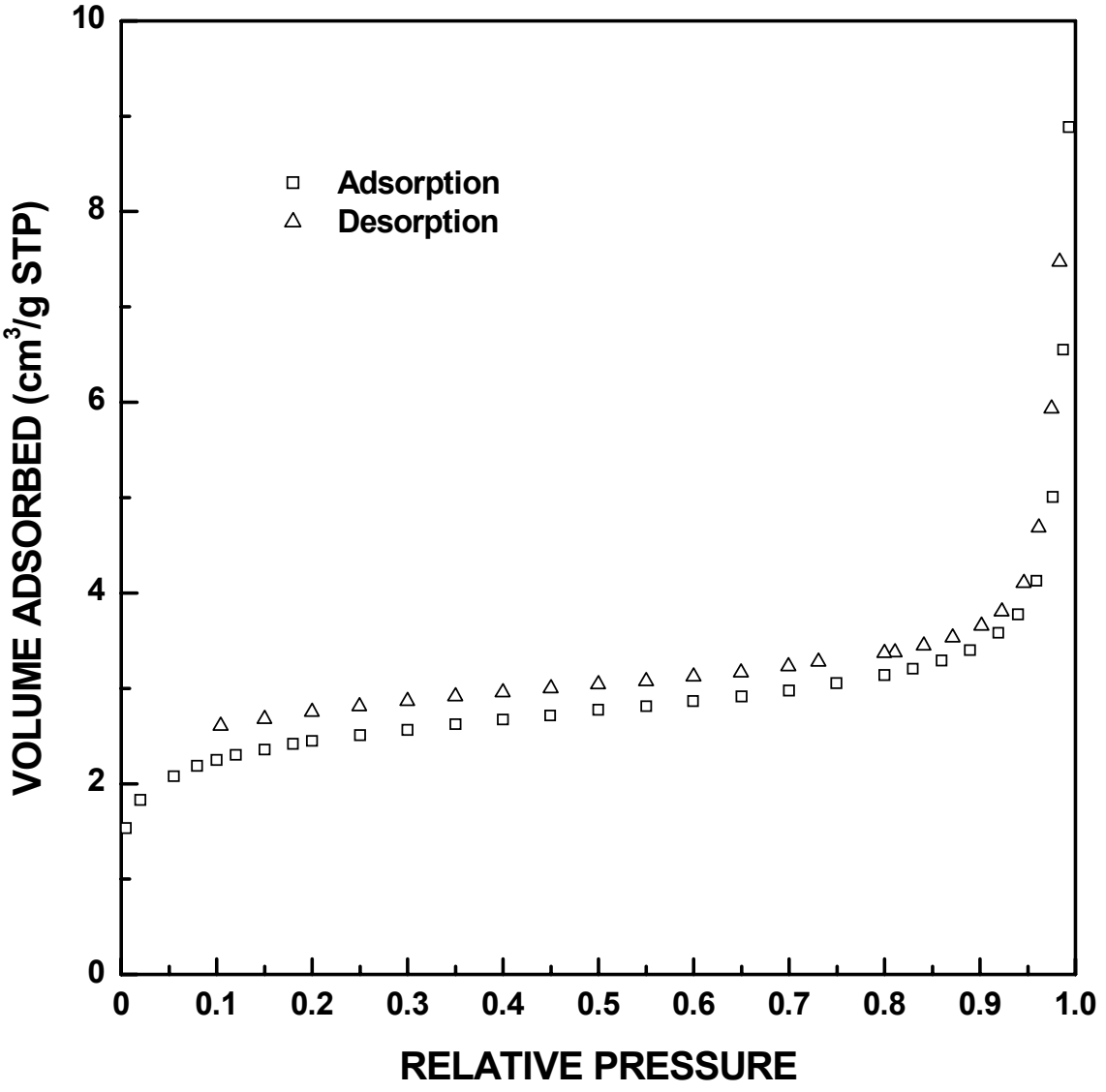

Figure I-99 Adsorption/desorption isotherm plots for SC8-1200(30min) sample (X_{WL} = 0.05).

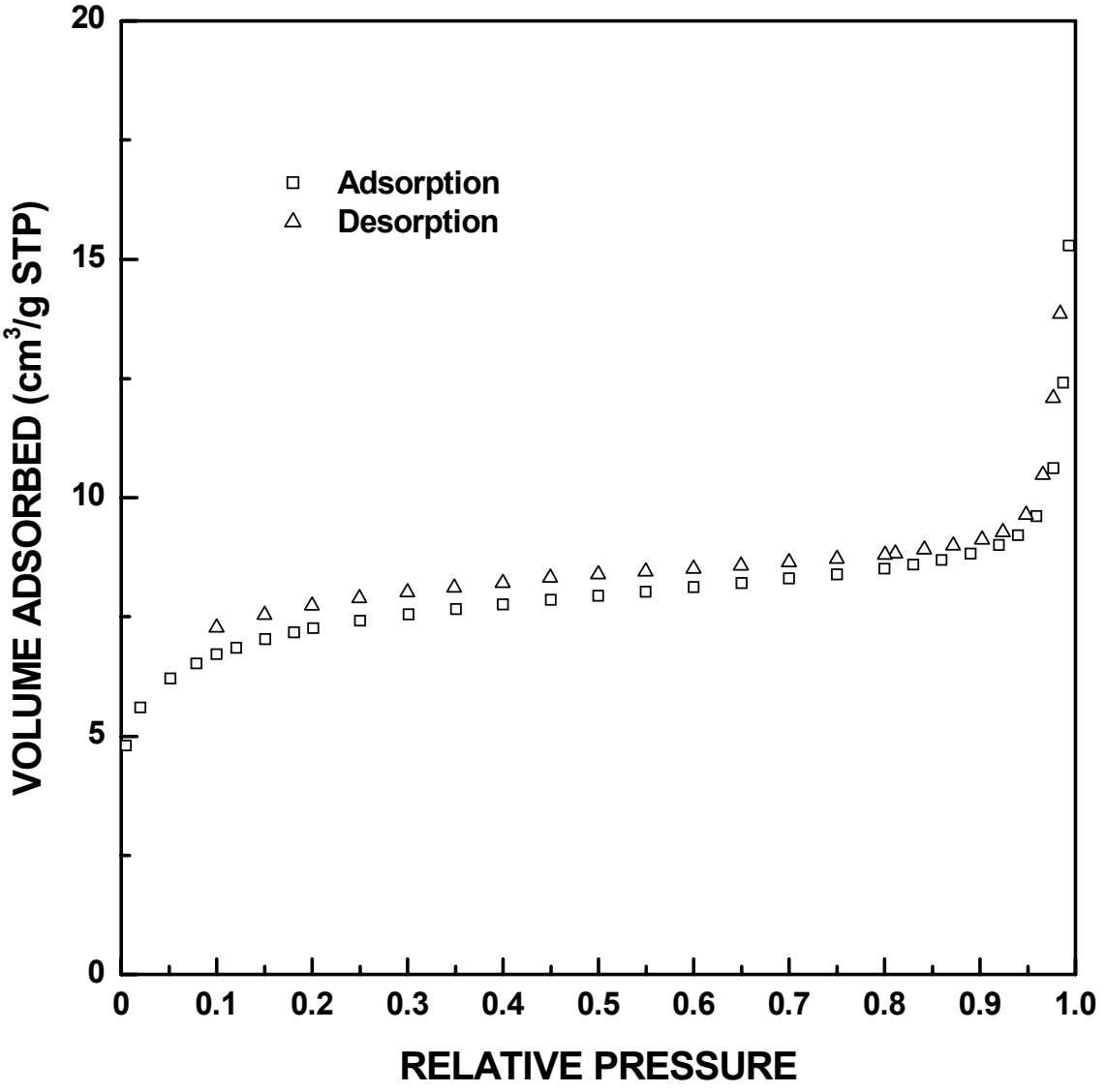

Figure I-100 Adsorption/desorption isotherm plots for SC8-1200(1h) sample (X_{WL} = 0.05).

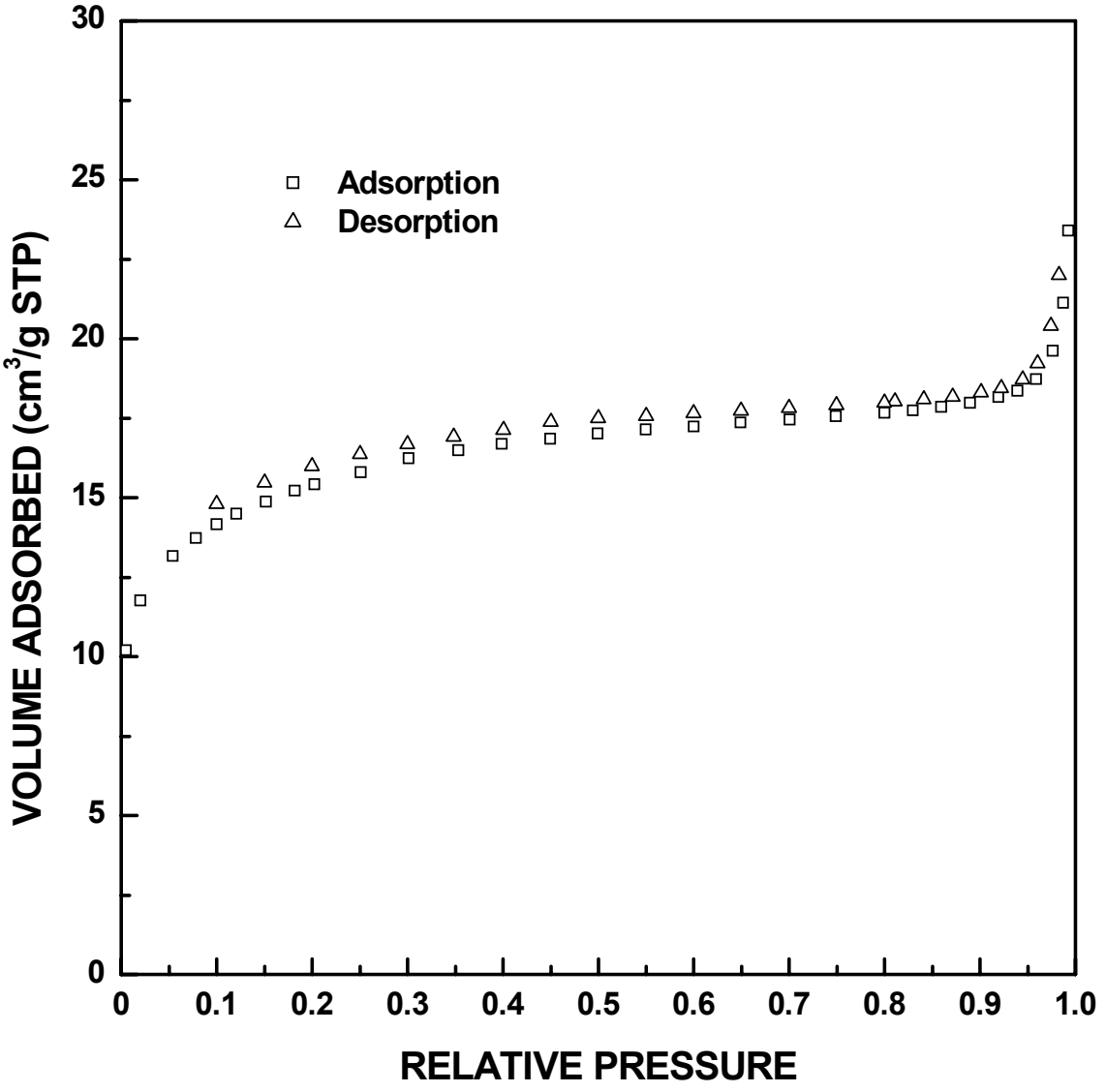

Figure I-101 Adsorption/desorption isotherm plots for SC8-1200(2h) sample (X_{WL} = 0.11).

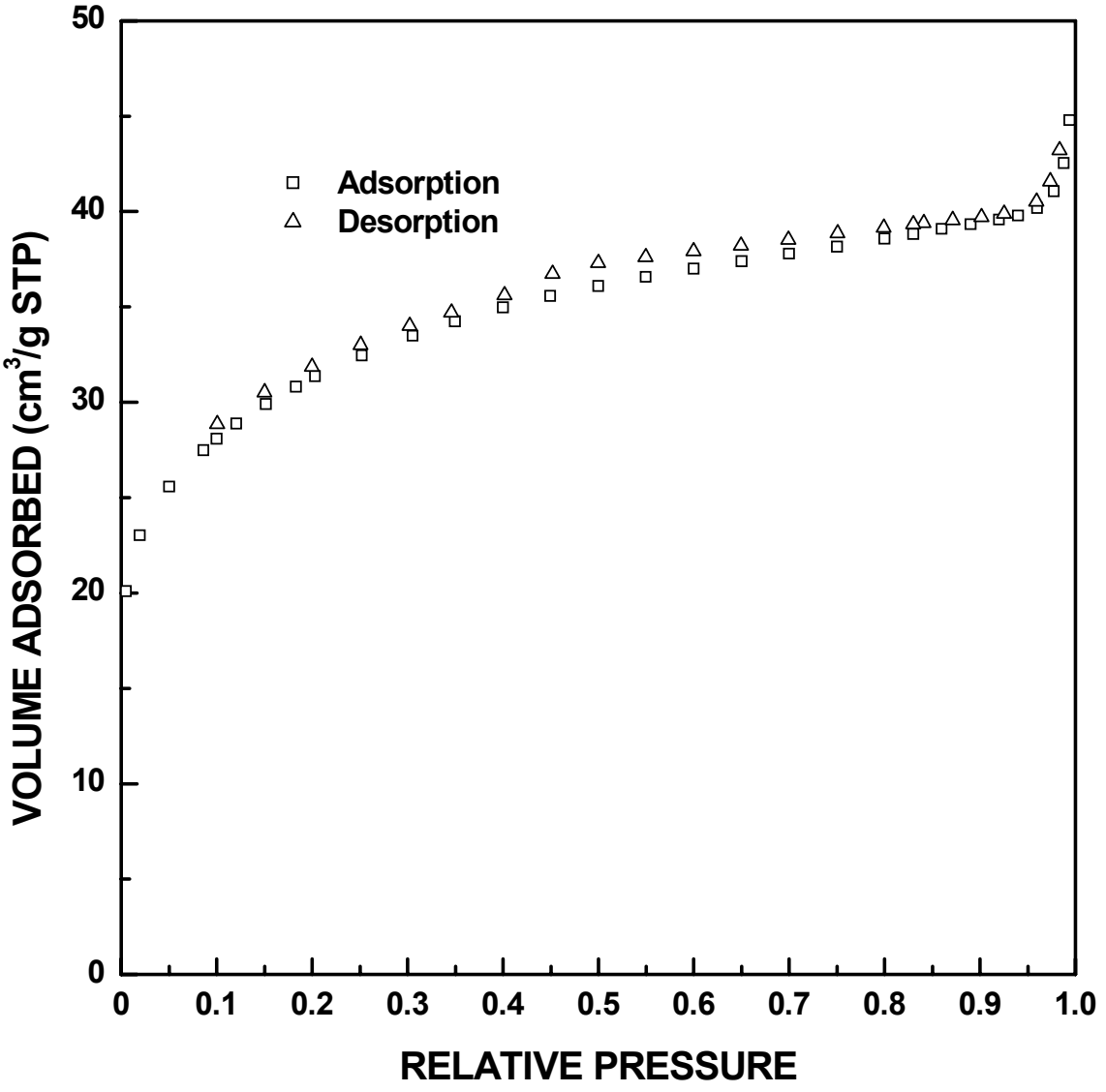

Figure I-102 Adsorption/desorption isotherm plots for SC8-1200(4h) sample (X_{WL} = 0.19).

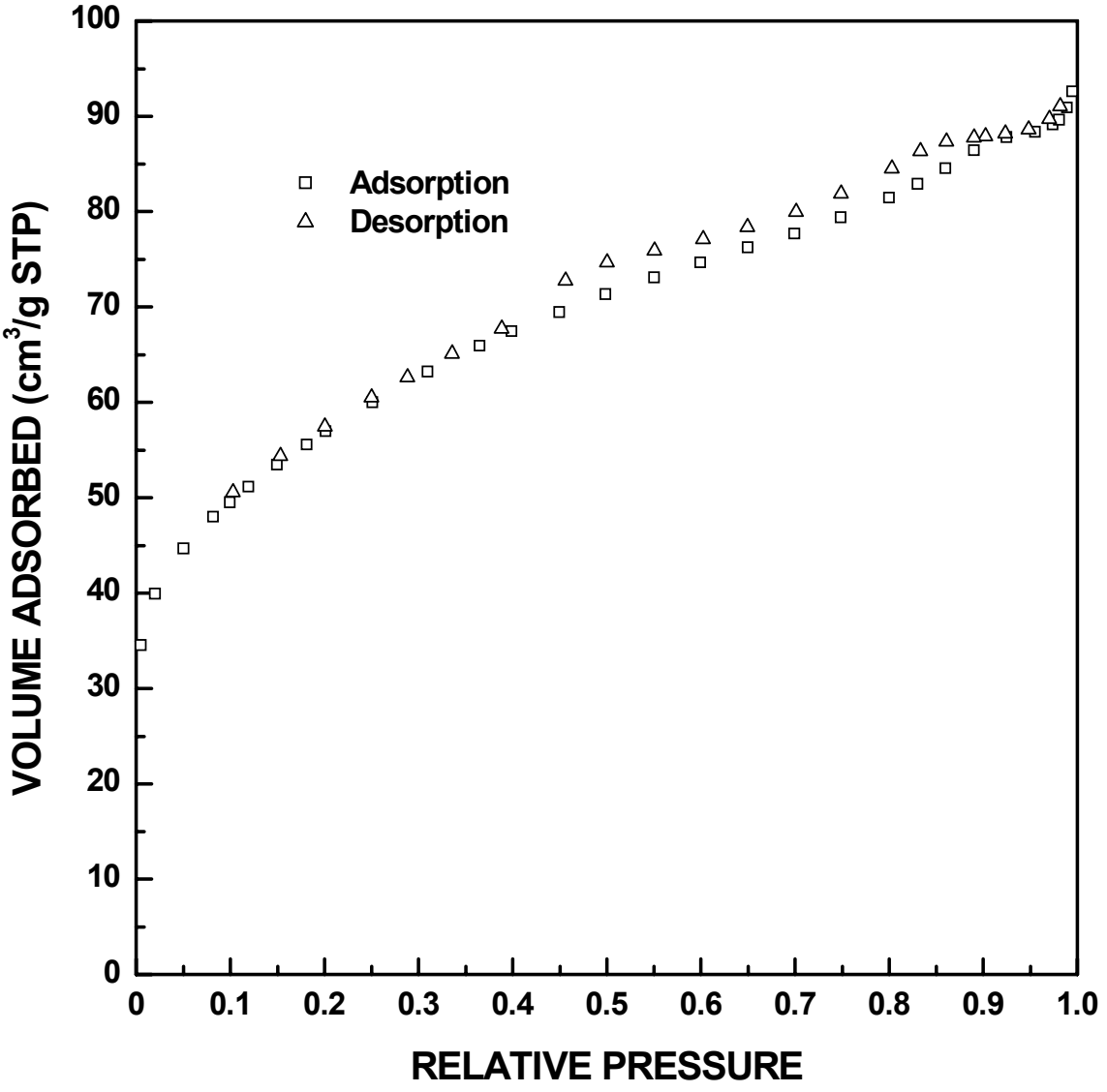

Figure I-103 Adsorption/desorption isotherm plots for SC8-1200(8h) sample (X_{WL} = 0.40).

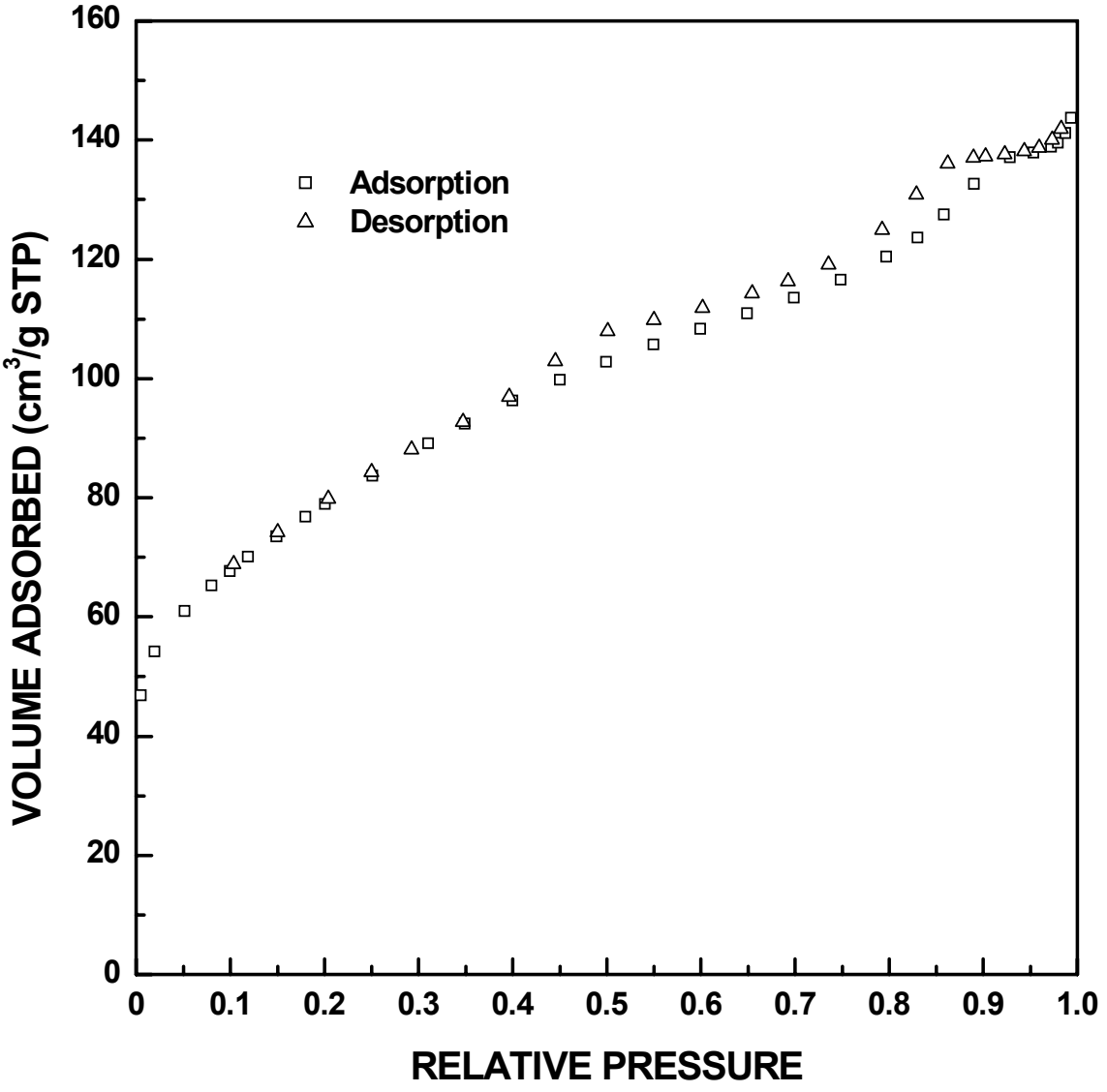

Figure I-104 Adsorption/desorption isotherm plots for SC8-1200(12h) sample (X_{WL} = 0.54).

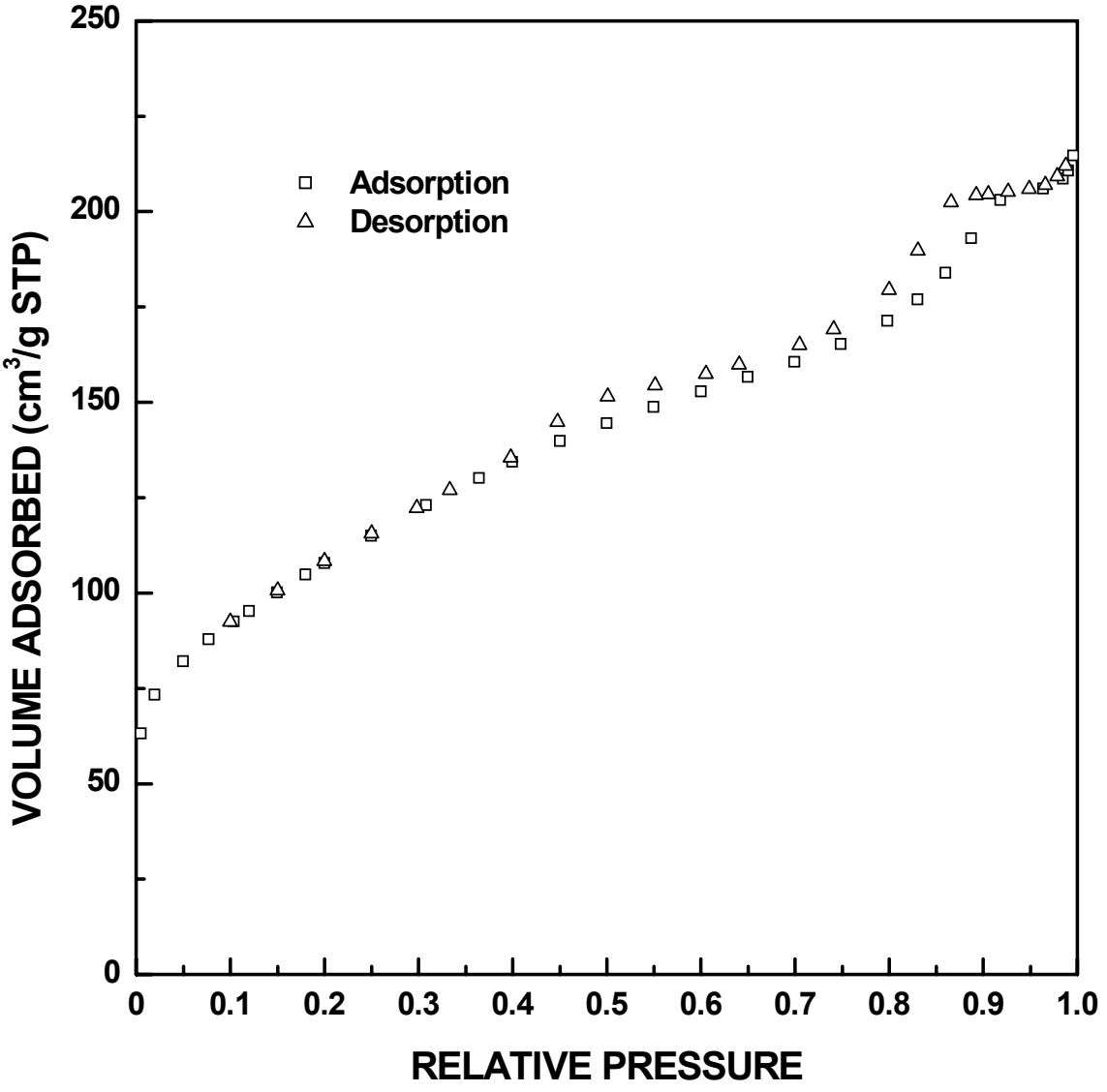

Figure I-105 Adsorption/desorption isotherm plots for SC8-1200(16h) sample (X_{WL} = 0.68).

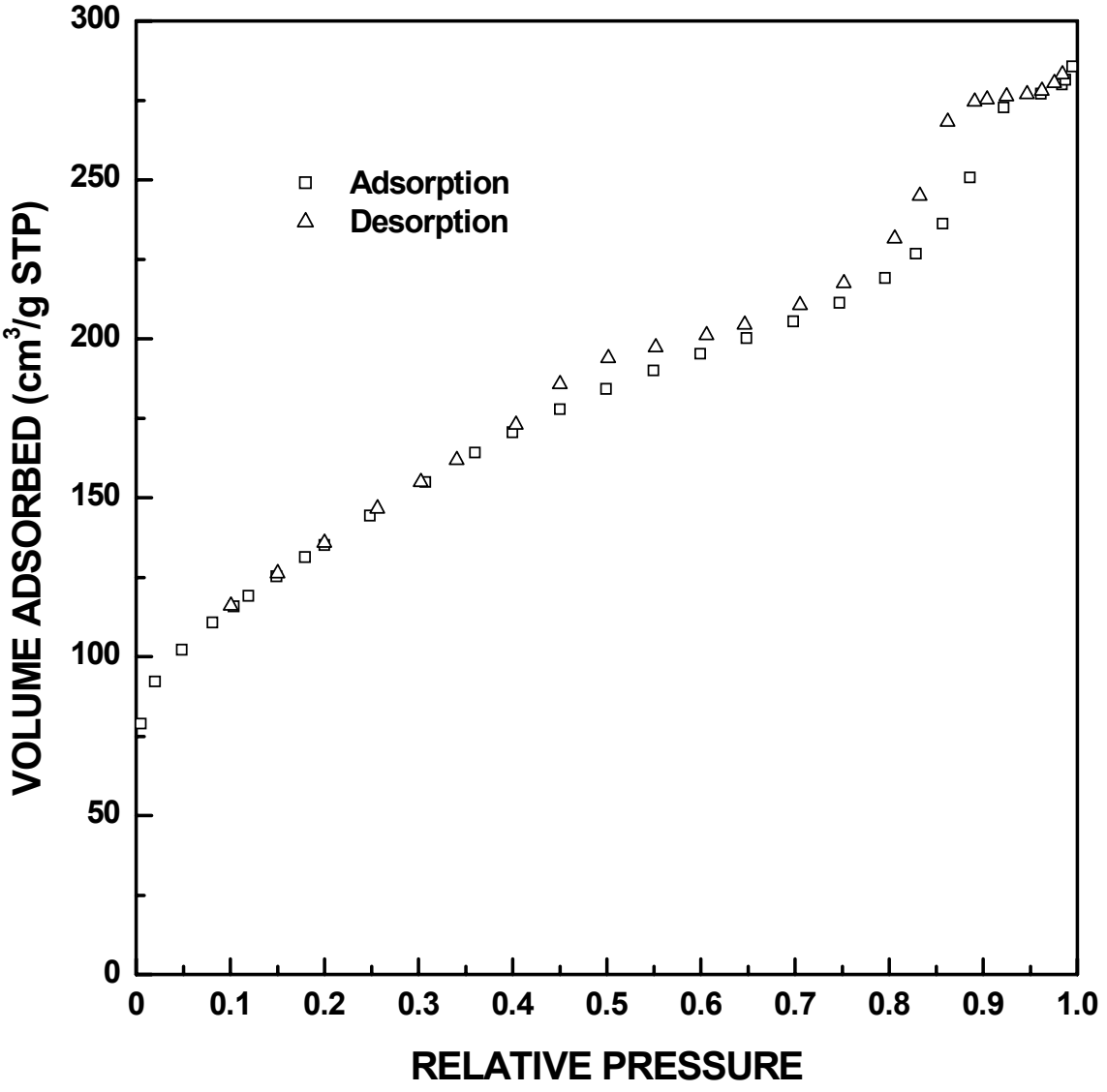

Figure I-106 Adsorption/desorption isotherm plots for SC8-1200(22h) sample (X_{WL} = 0.80).

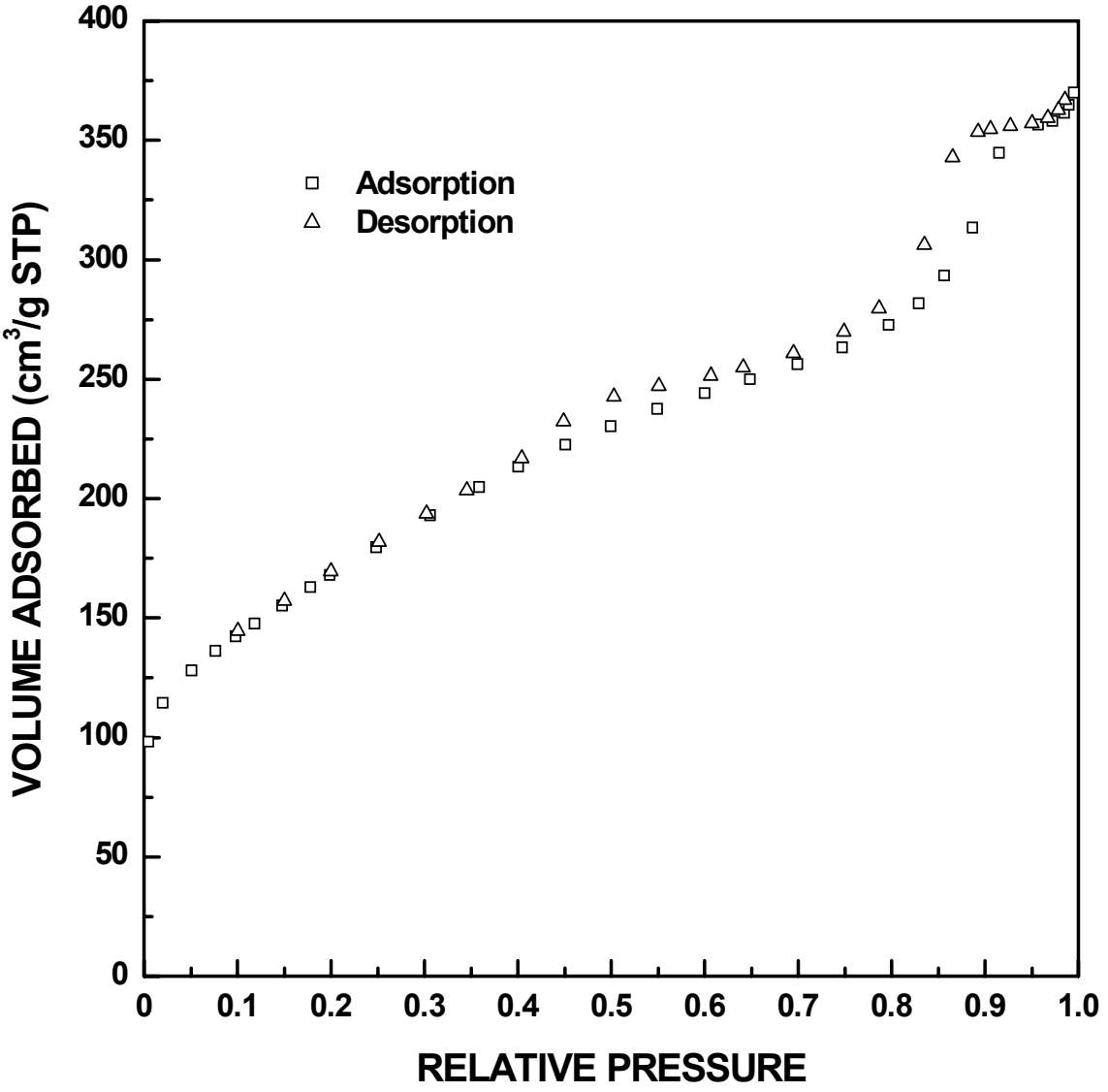

Figure I-107 Adsorption/desorption isotherm plots for SC8-1200(32h) sample (X_{WL} = 0.91).

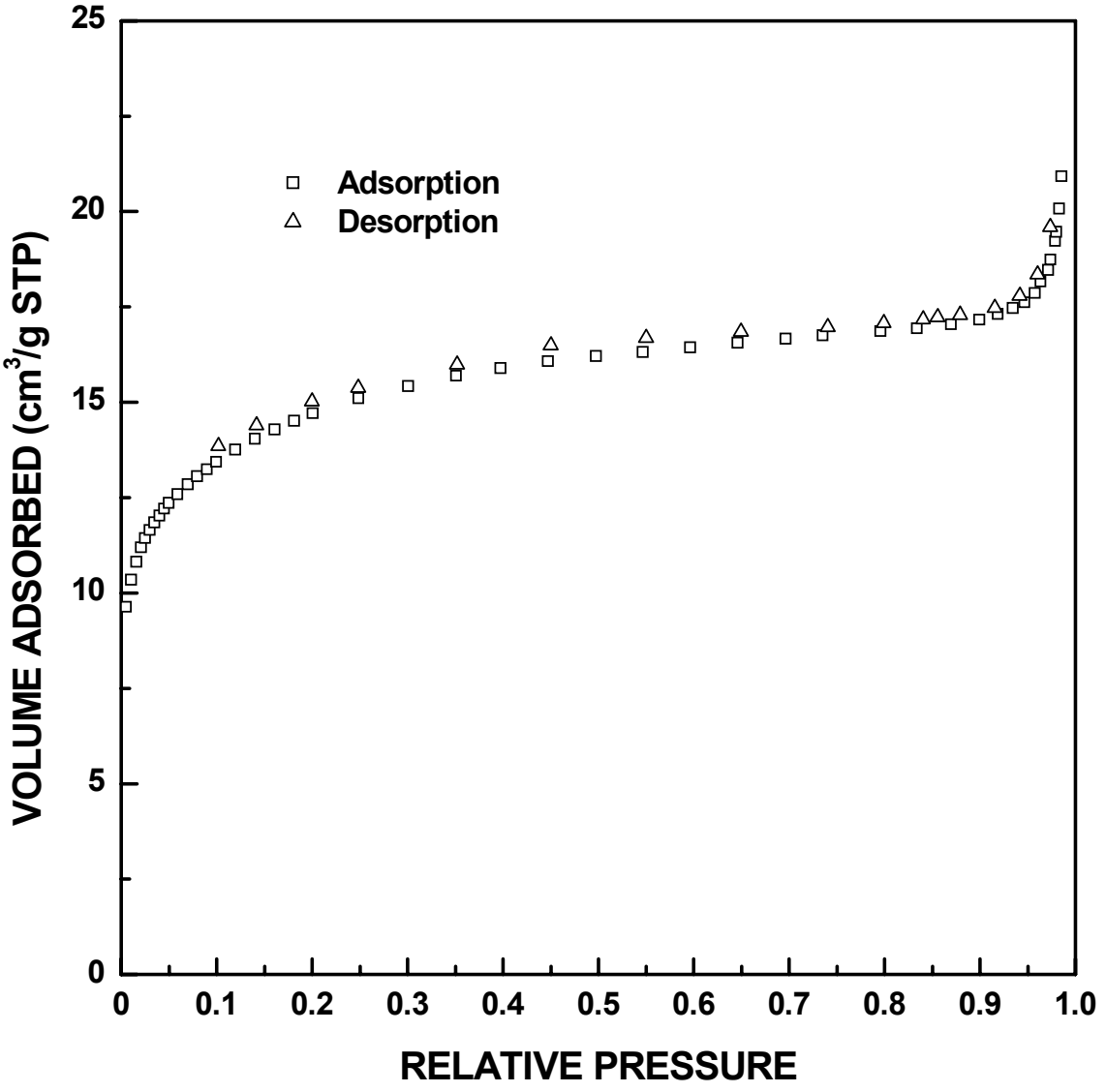

Figure I-108 Adsorption/desorption isotherm plots for SC8-1250(40min) sample (X_{WL} = 0.11).

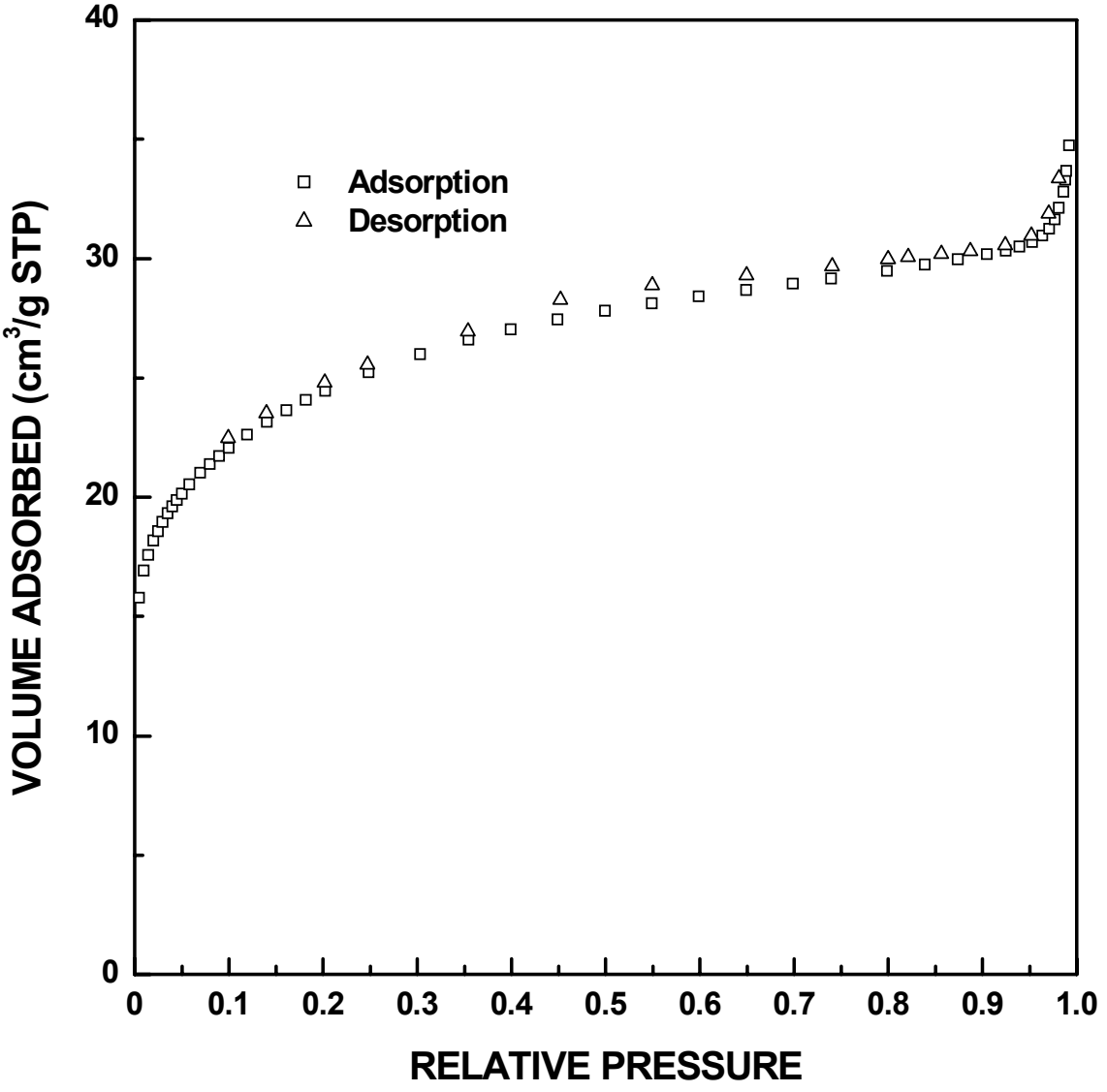

Figure I-109 Adsorption/desorption isotherm plots for SC8-1250(1h) sample (X_{WL} = 0.16).

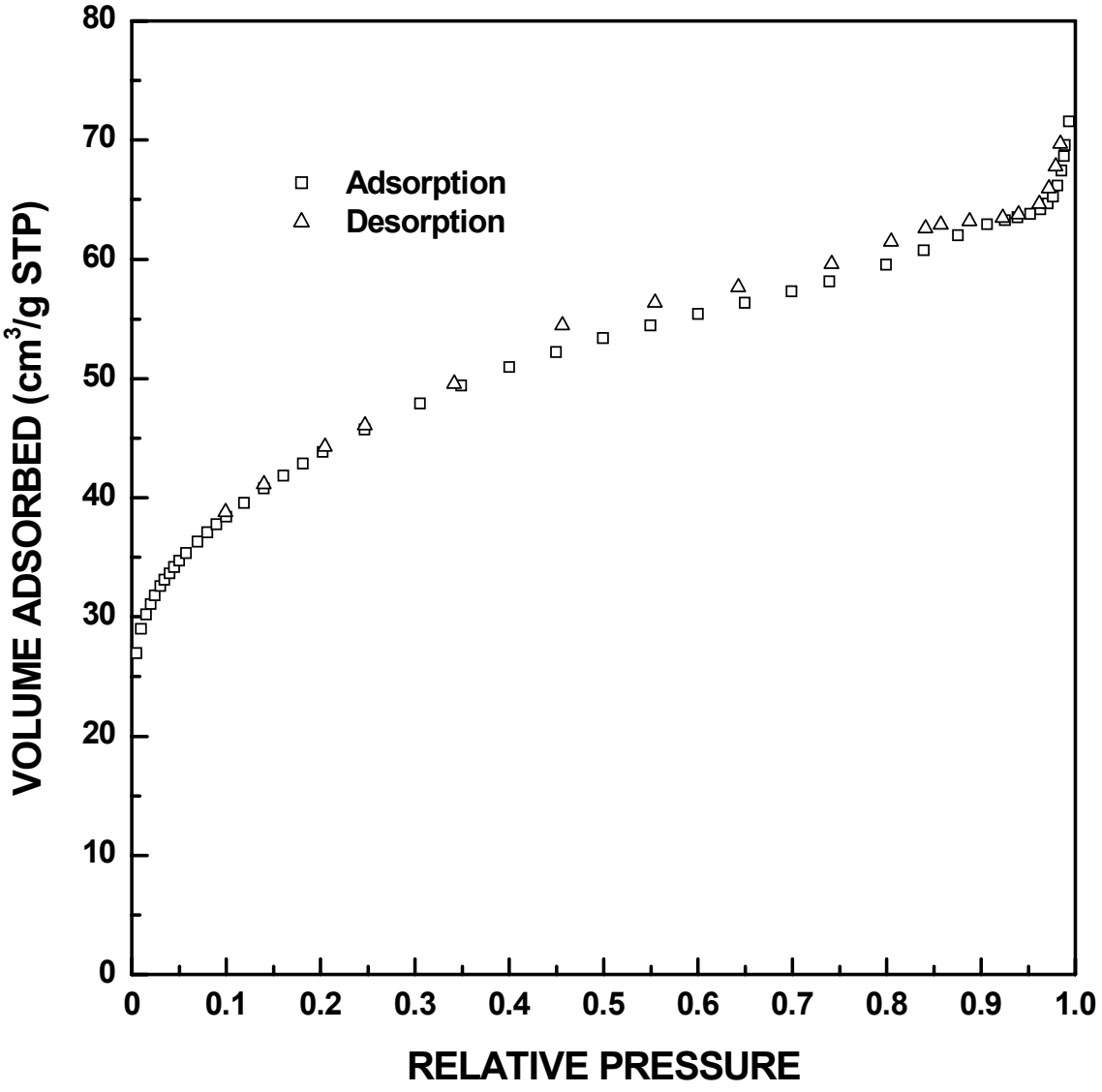

Figure I-110 Adsorption/desorption isotherm plots for SC8-1250(2h) sample (X_{WL} = 0.31).

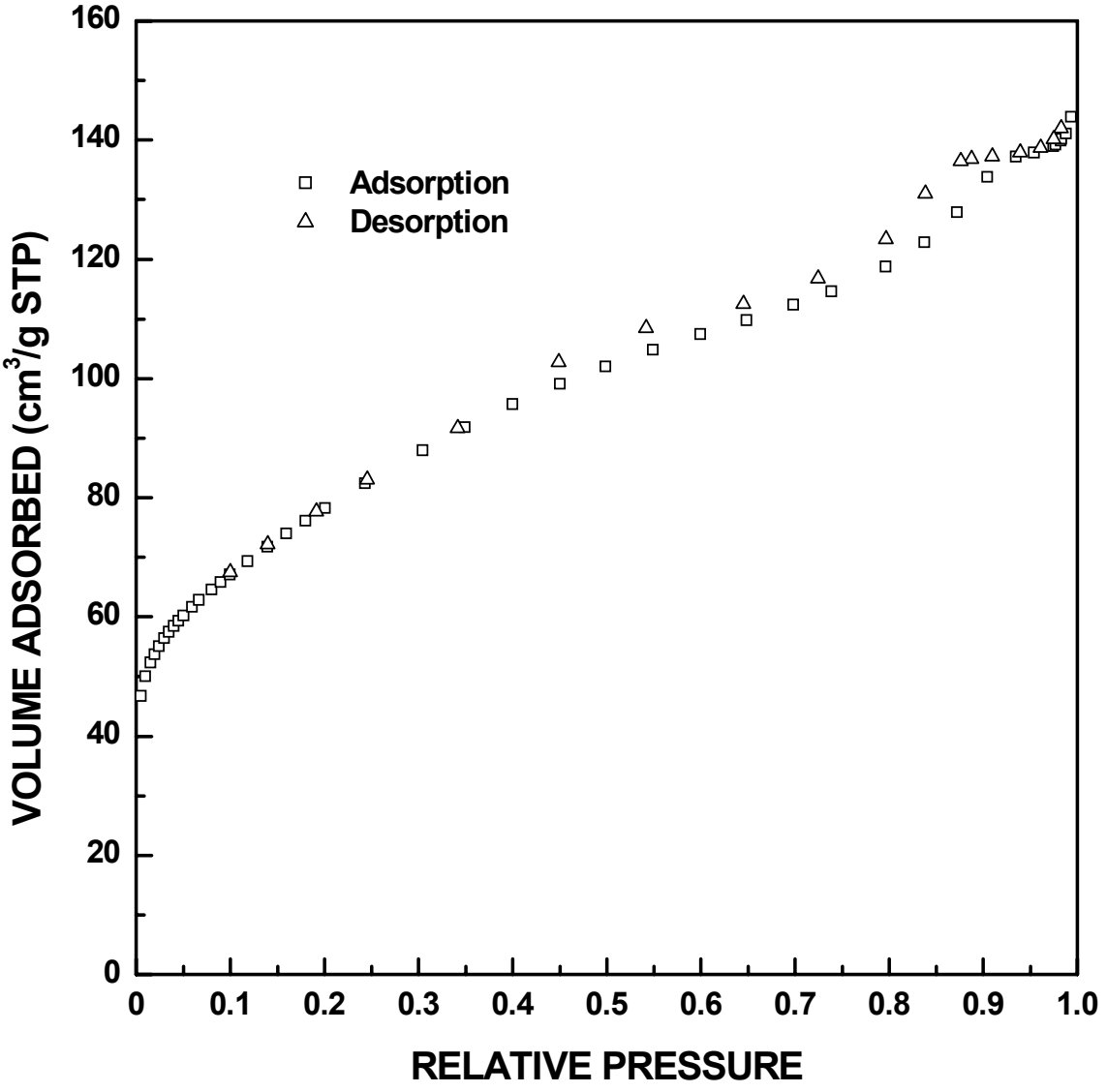

Figure I-111 Adsorption/desorption isotherm plots for SC8-1250(4h) sample (X_{WL} = 0.54).

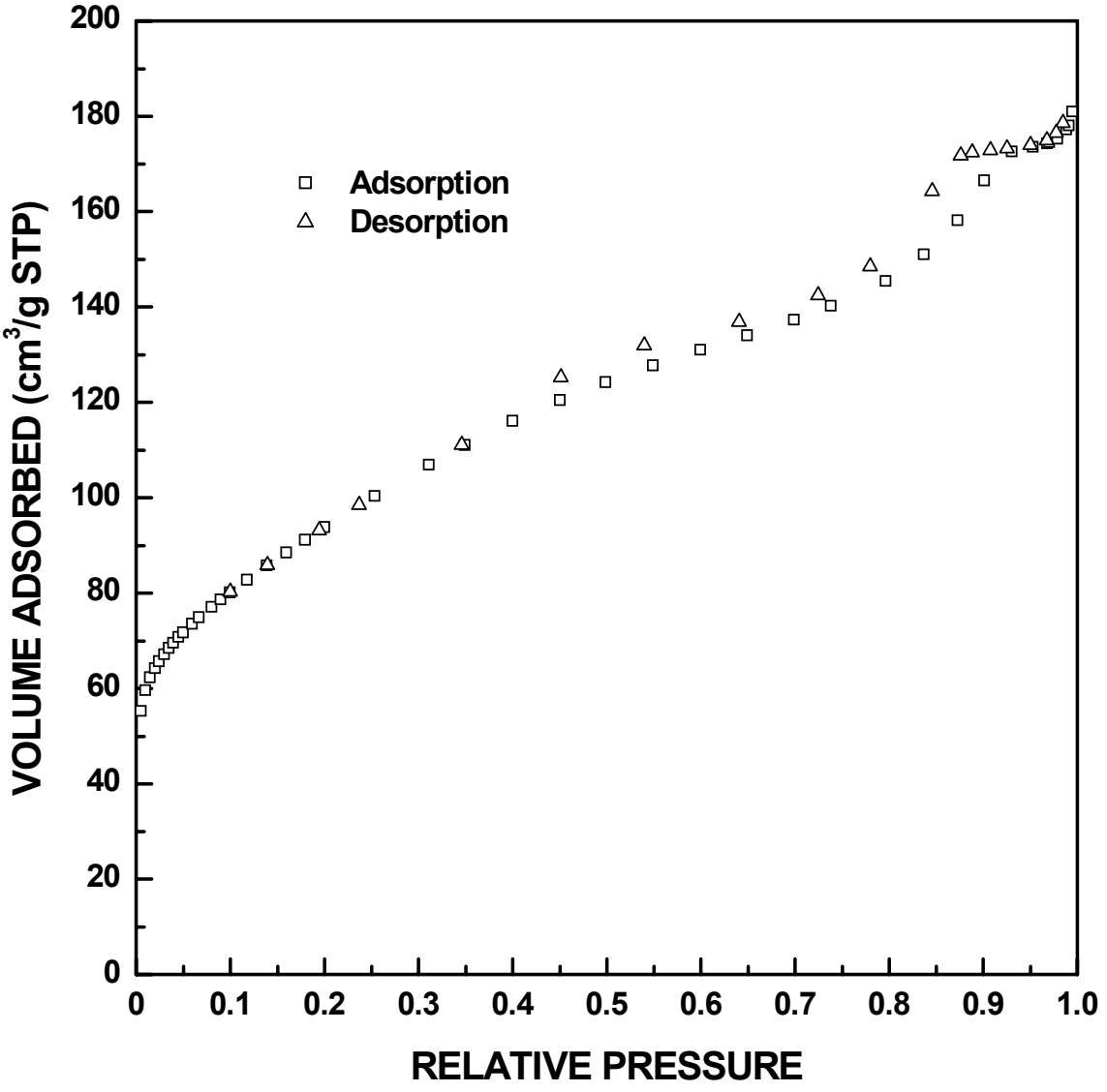

Figure I-112 Adsorption/desorption isotherm plots for SC8-1250(5h) sample (X_{WL} = 0.61).

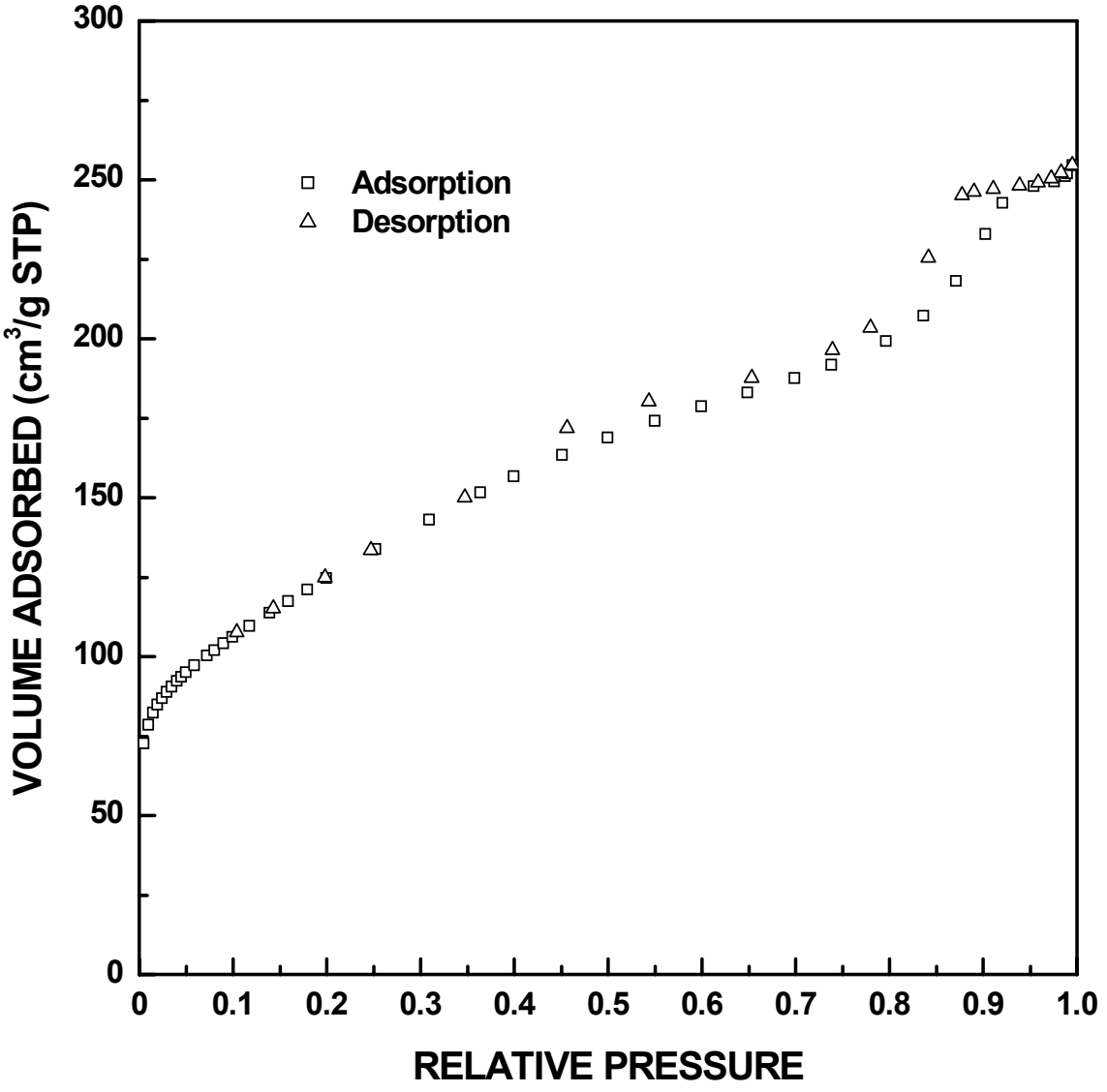

Figure I-113 Adsorption/desorption isotherm plots for SC8-1250(6.5h) sample (X_{WL} = 0.73).

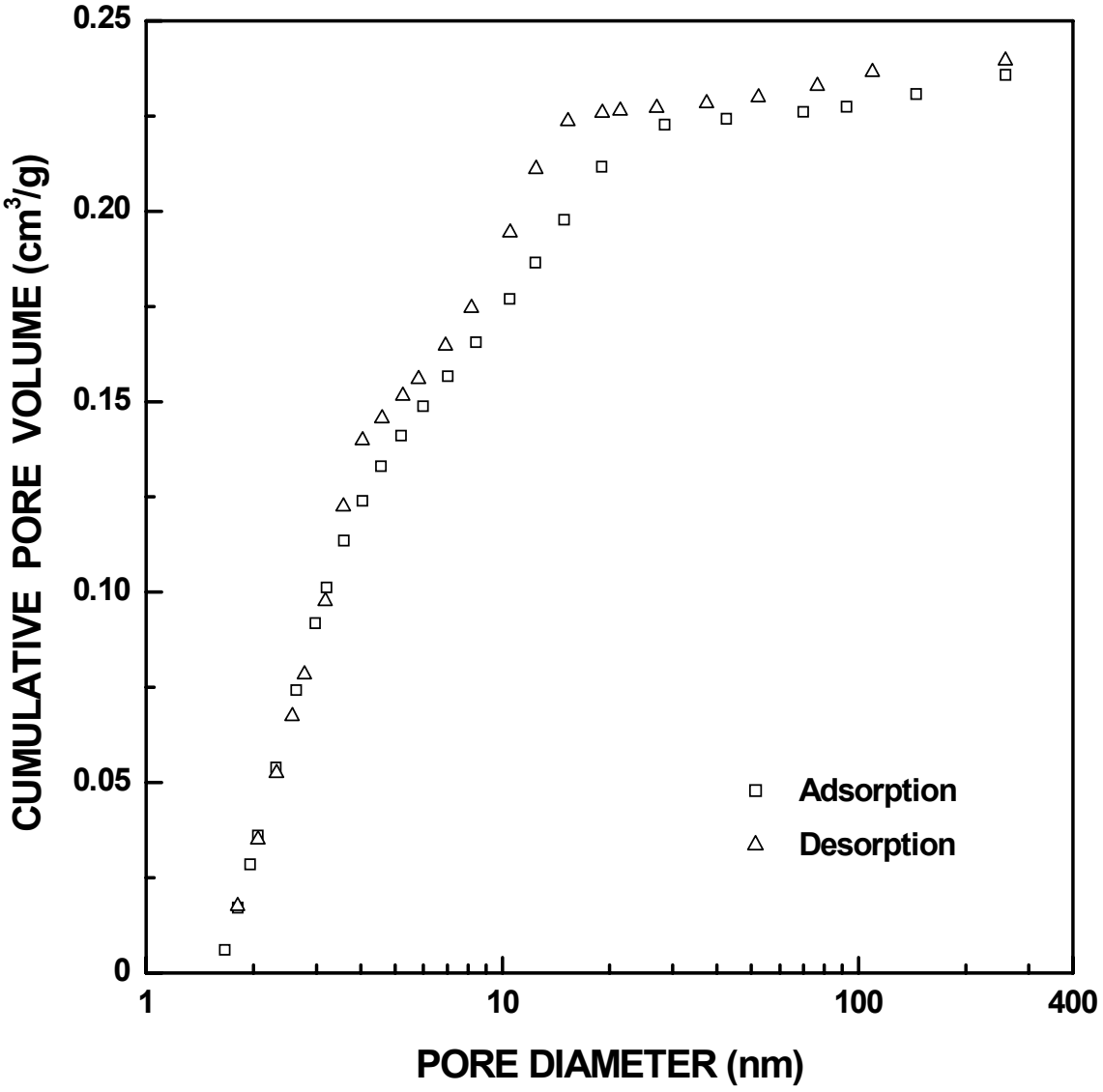

Figure I-114 Plots of cumulative specific pore volume vs. pore diameter for SC8-1160(36h) sample (X_{WL} = 0.62).

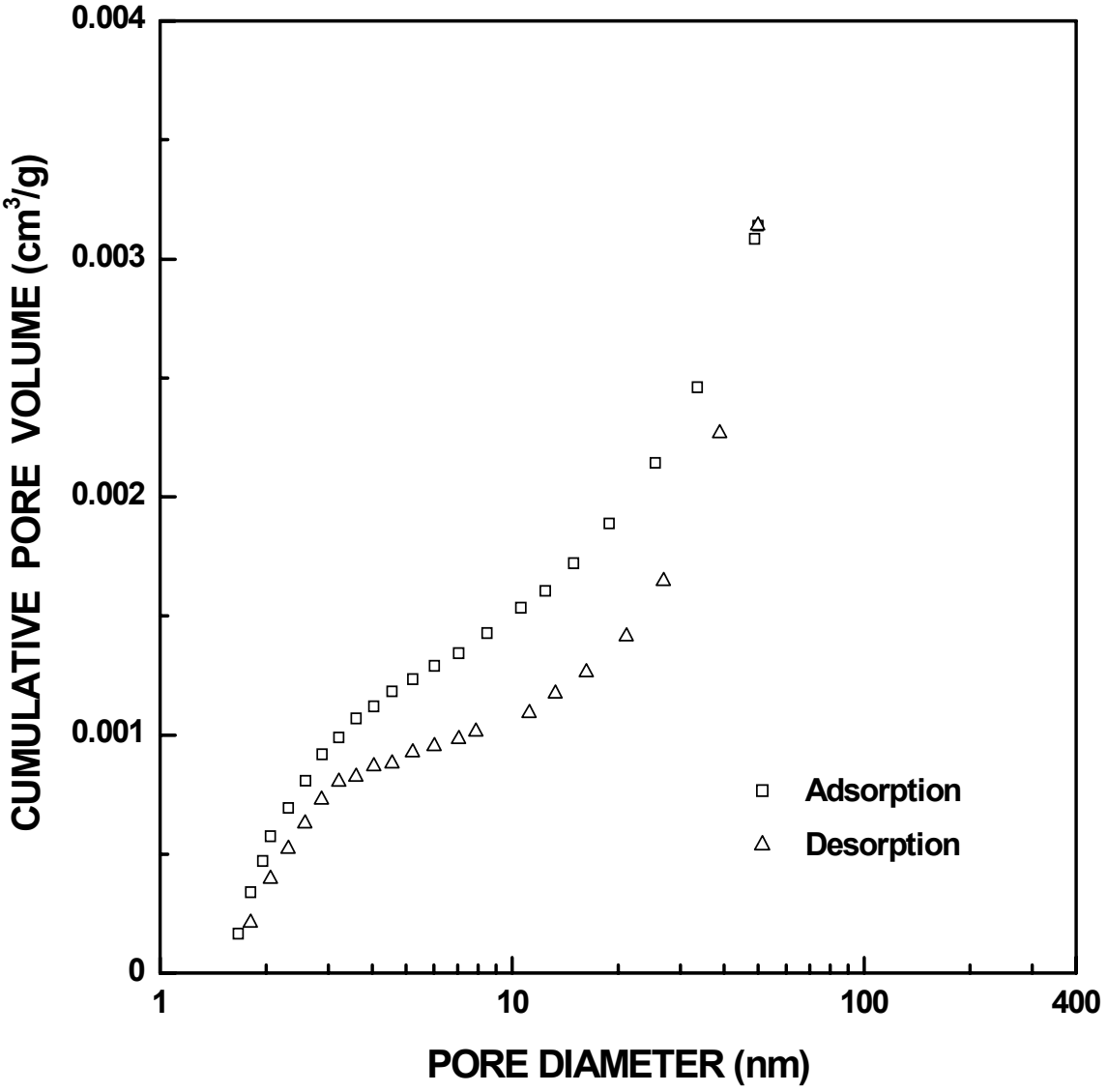

Figure I-115 Plots of cumulative specific pore volume vs. pore diameter for SC8-1180(1h) sample (X_{WL} = 0.08). The pore diameter was cut off at 50 nm.

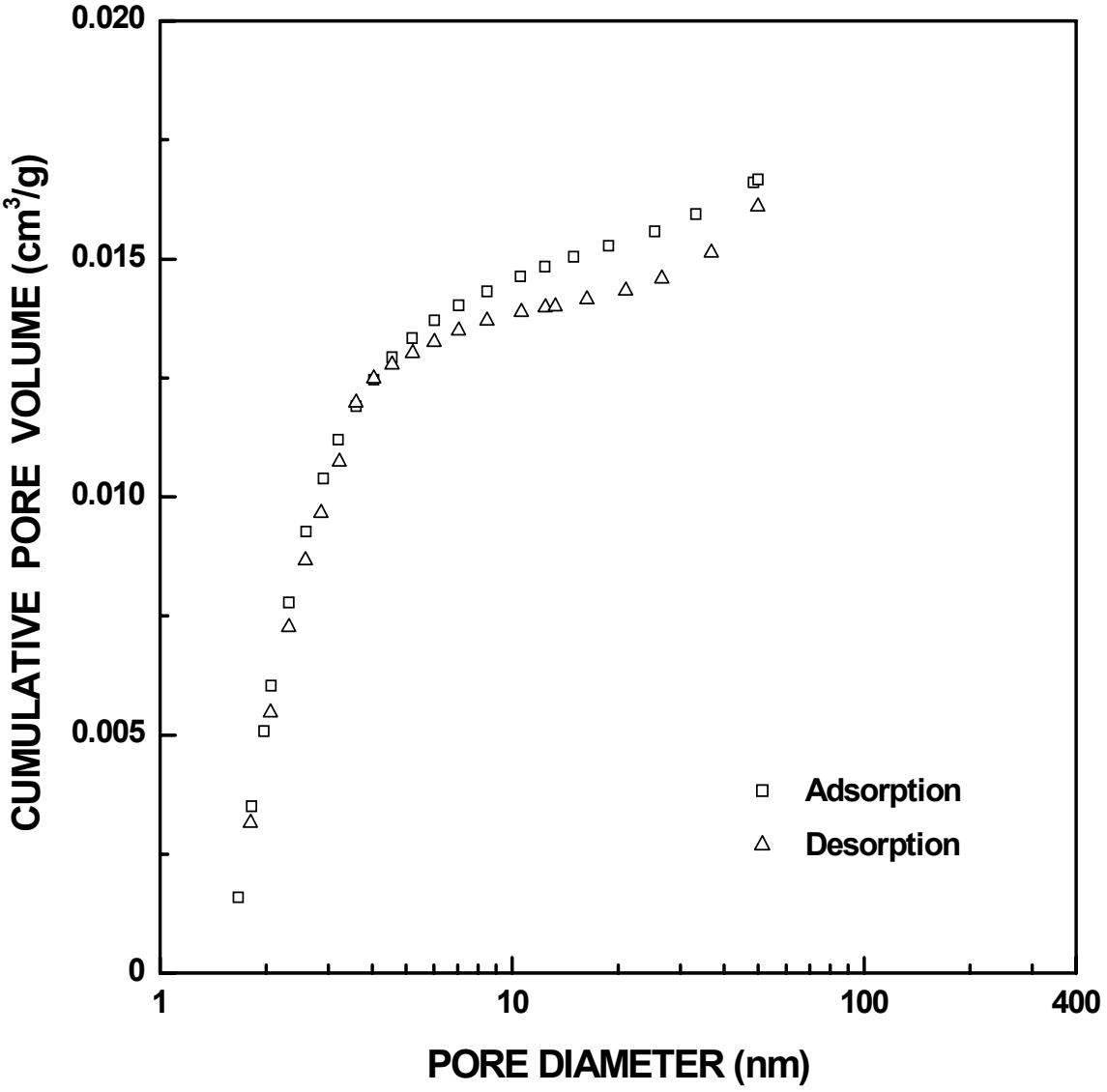

Figure I-116 Plots of cumulative specific pore volume vs. pore diameter for SC8-1180(4h) sample (X_{WL} = 0.18). The pore diameter was cut off at 50 nm.

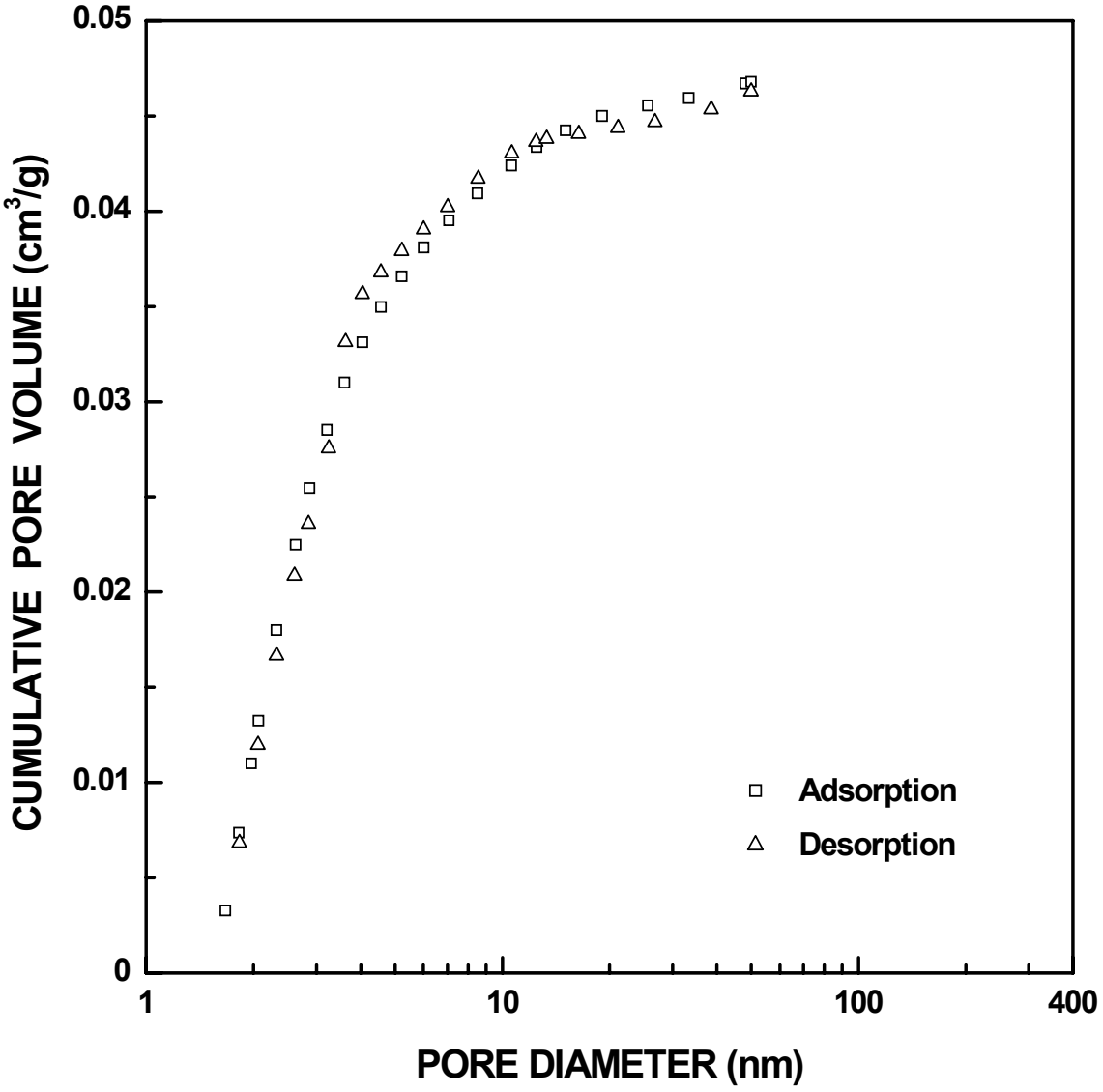

Figure I-117 Plots of cumulative specific pore volume vs. pore diameter for SC8-1180(8h) sample (X_{WL} = 0.31). The pore diameter was cut off at 50 nm.

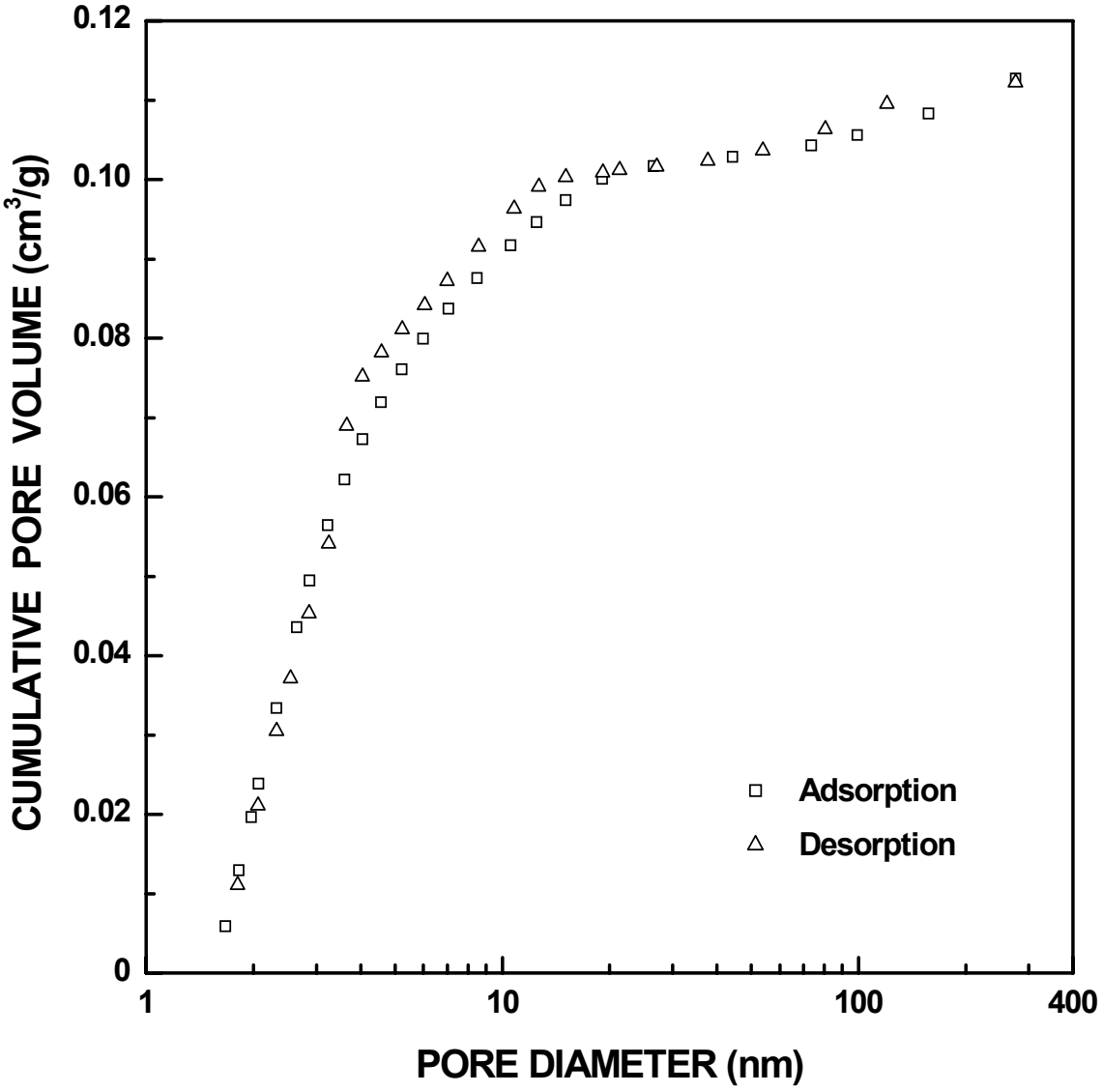

Figure I-118 Plots of cumulative specific pore volume vs. pore diameter for SC8-1180(12h) sample (X_{WL} = 0.43).

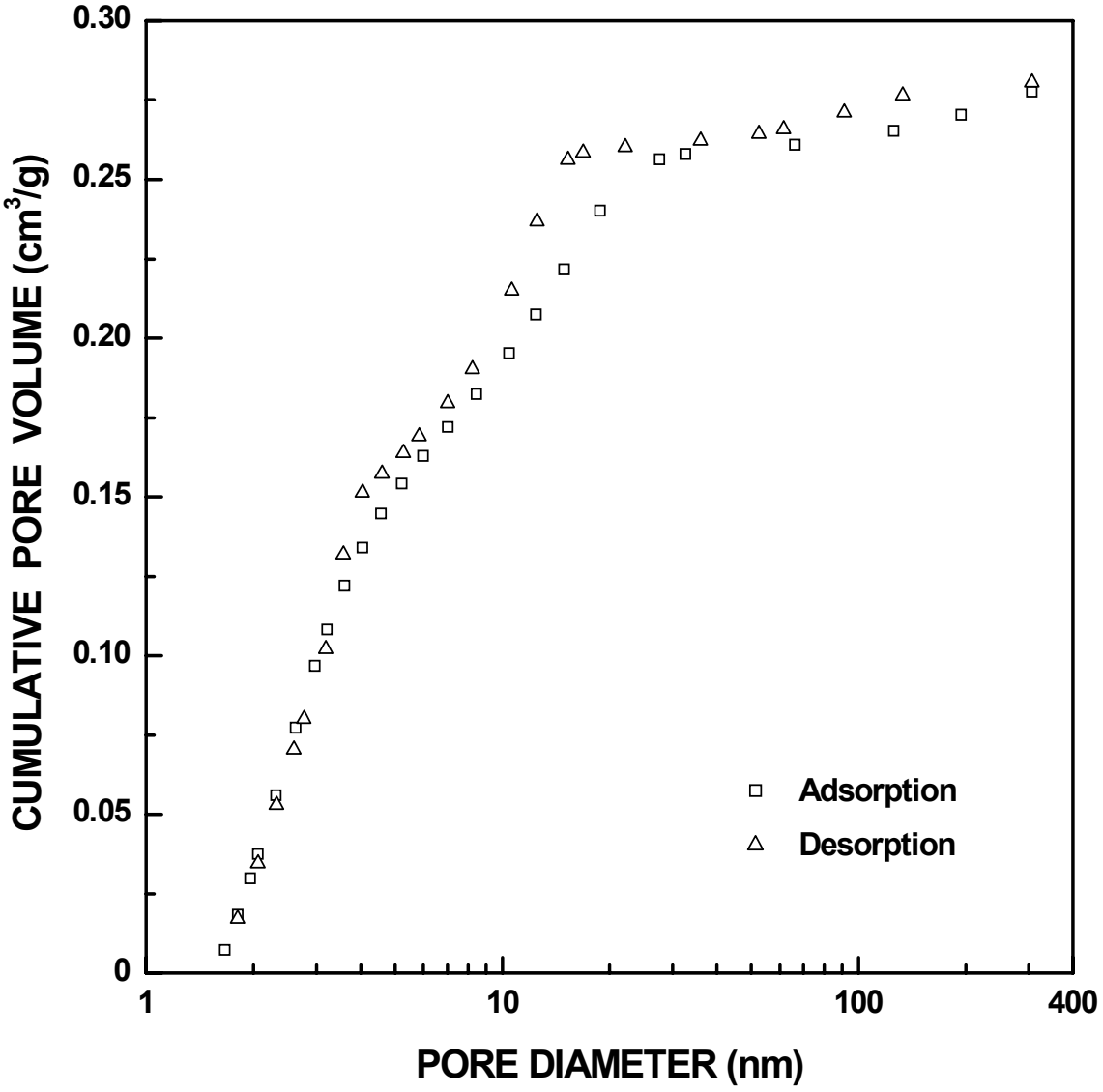

Figure I-119 Plots of cumulative specific pore volume vs. pore diameter for SC8-1180(24h) sample (X_{WL} = 0.70).

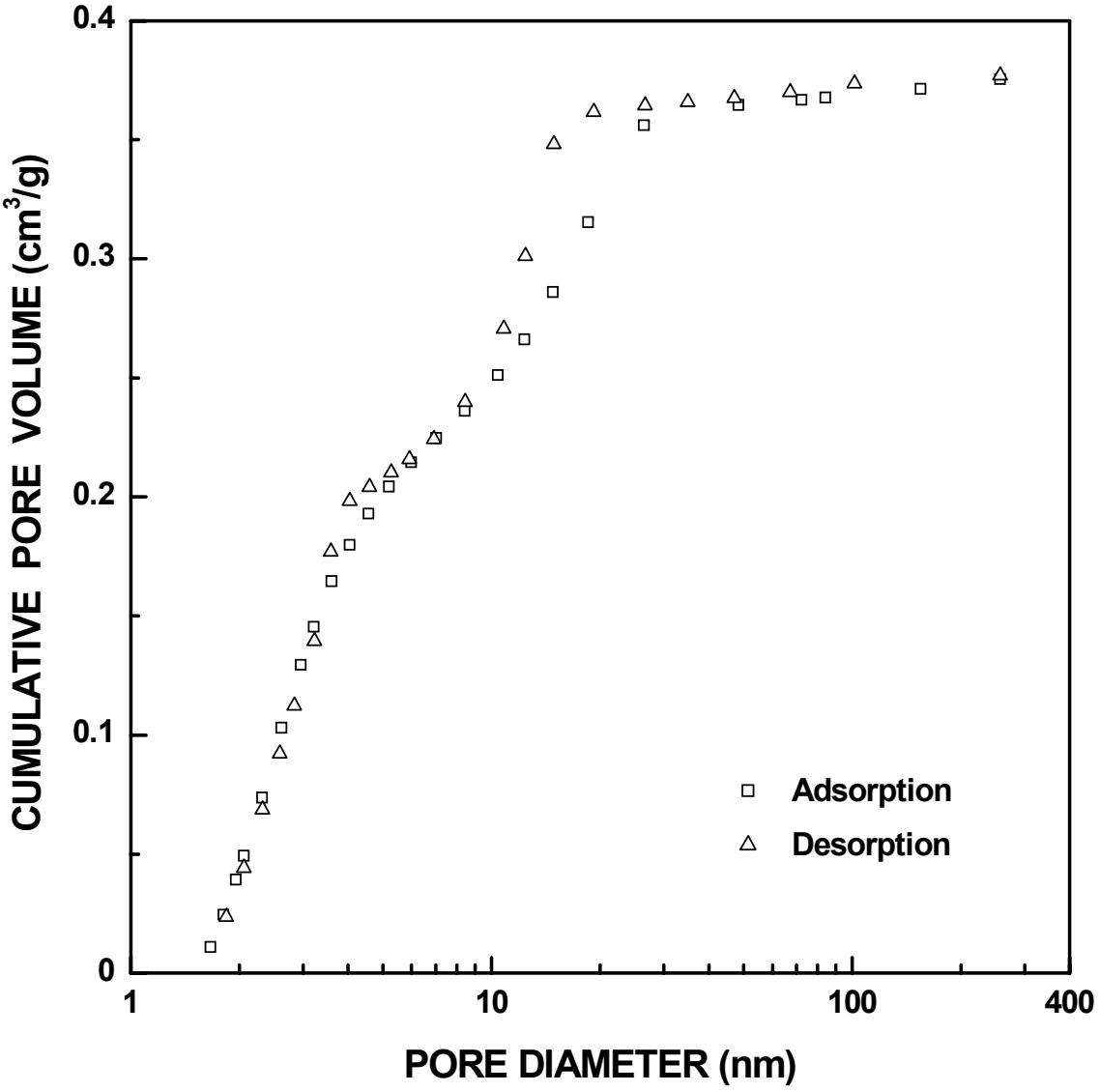

Figure I-120 Plots of cumulative specific pore volume vs. pore diameter for SC8-1180(36h) sample (X_{WL} = 0.82).

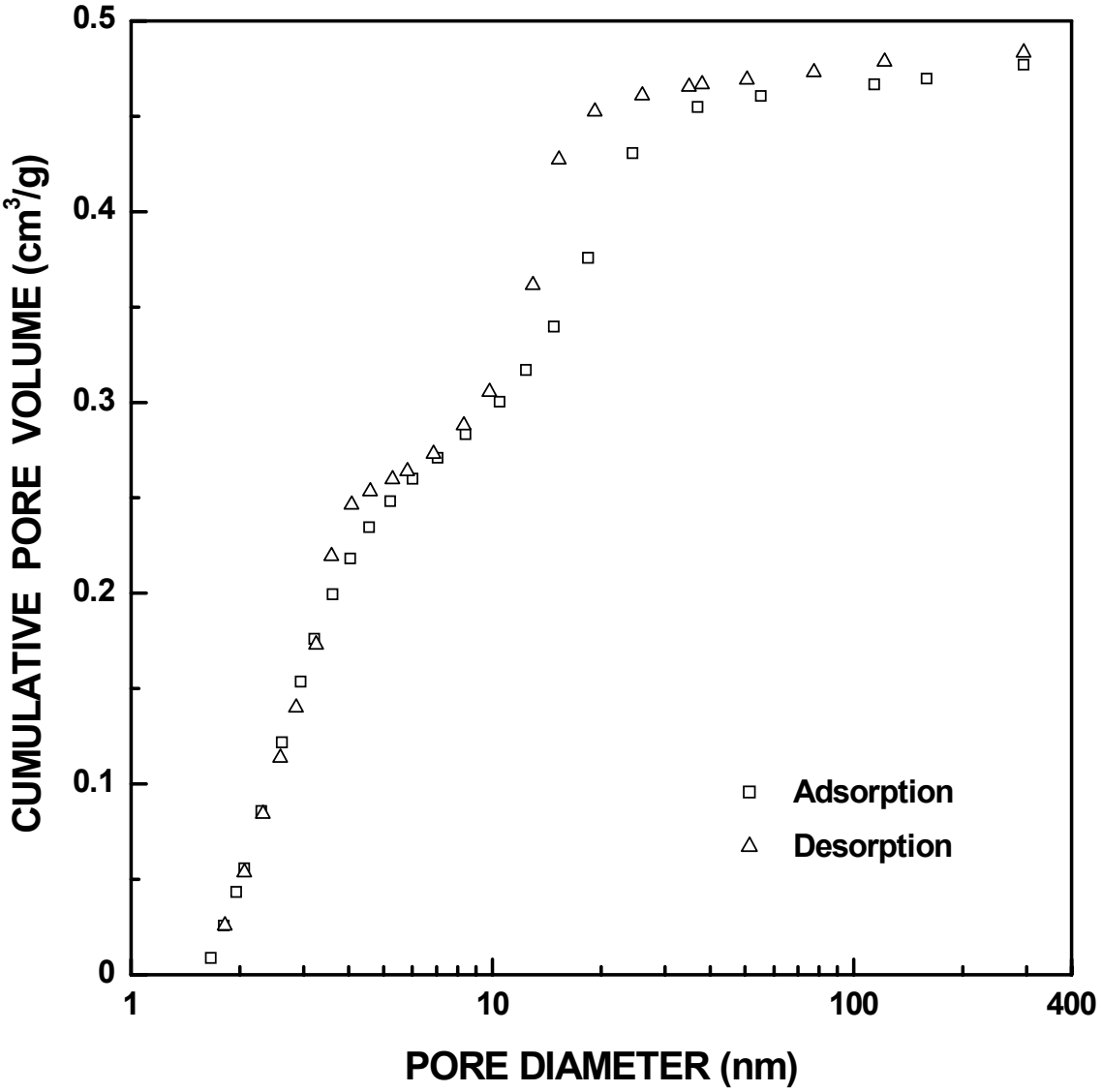

Figure I-121 Plots of cumulative specific pore volume vs. pore diameter for SC8-1180(48h) sample (X_{WL} = 0.92).

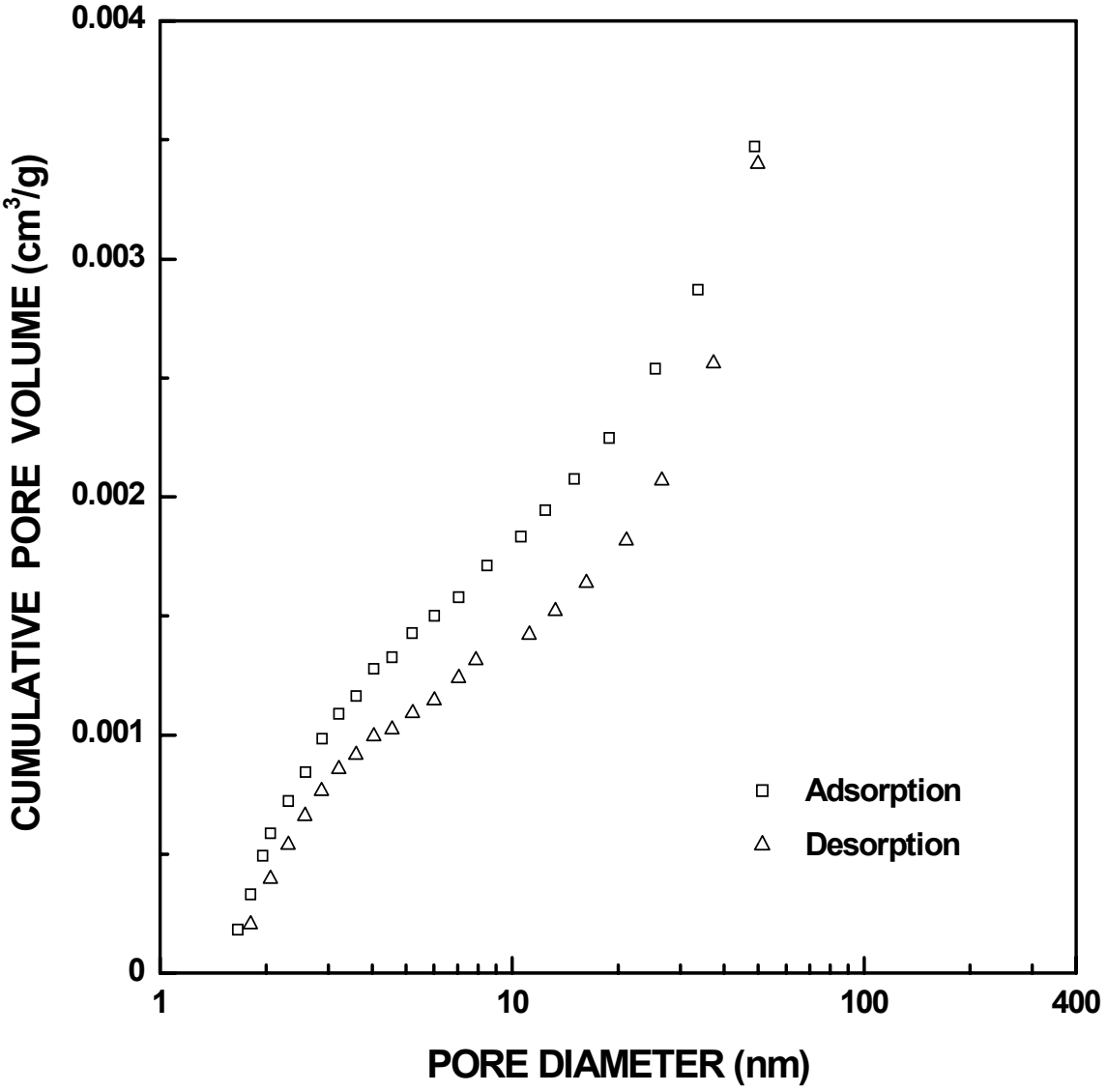

Figure I-122 Plots of cumulative specific pore volume vs. pore diameter for SC8-1200(30min) sample (X_{WL} = 0.05). The pore diameter was cut off at 50 nm.

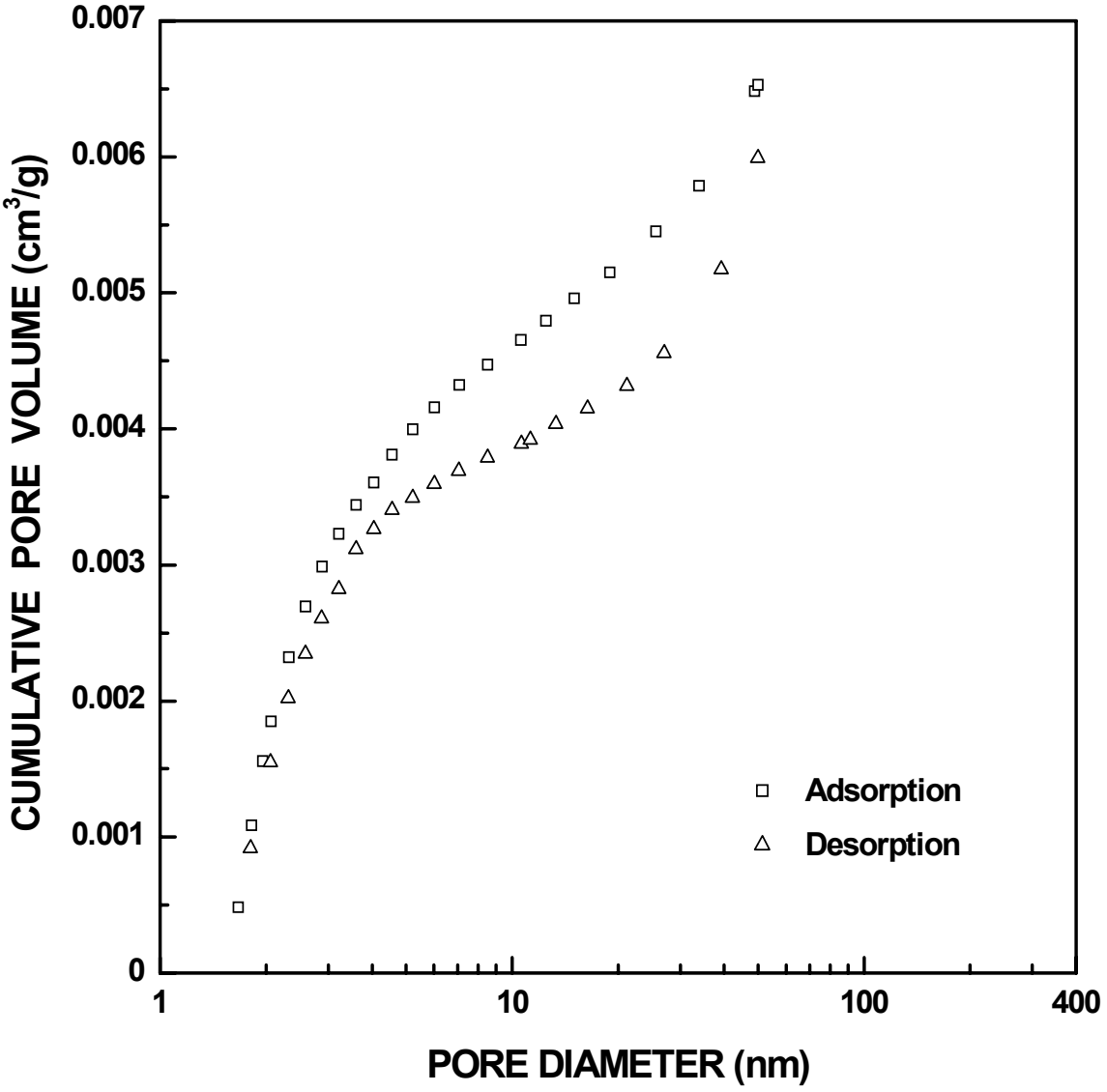

Figure I-123 Plots of cumulative specific pore volume vs. pore diameter for SC8-1200(1h) sample (X_{WL} = 0.05). The pore diameter was cut off at 50 nm.

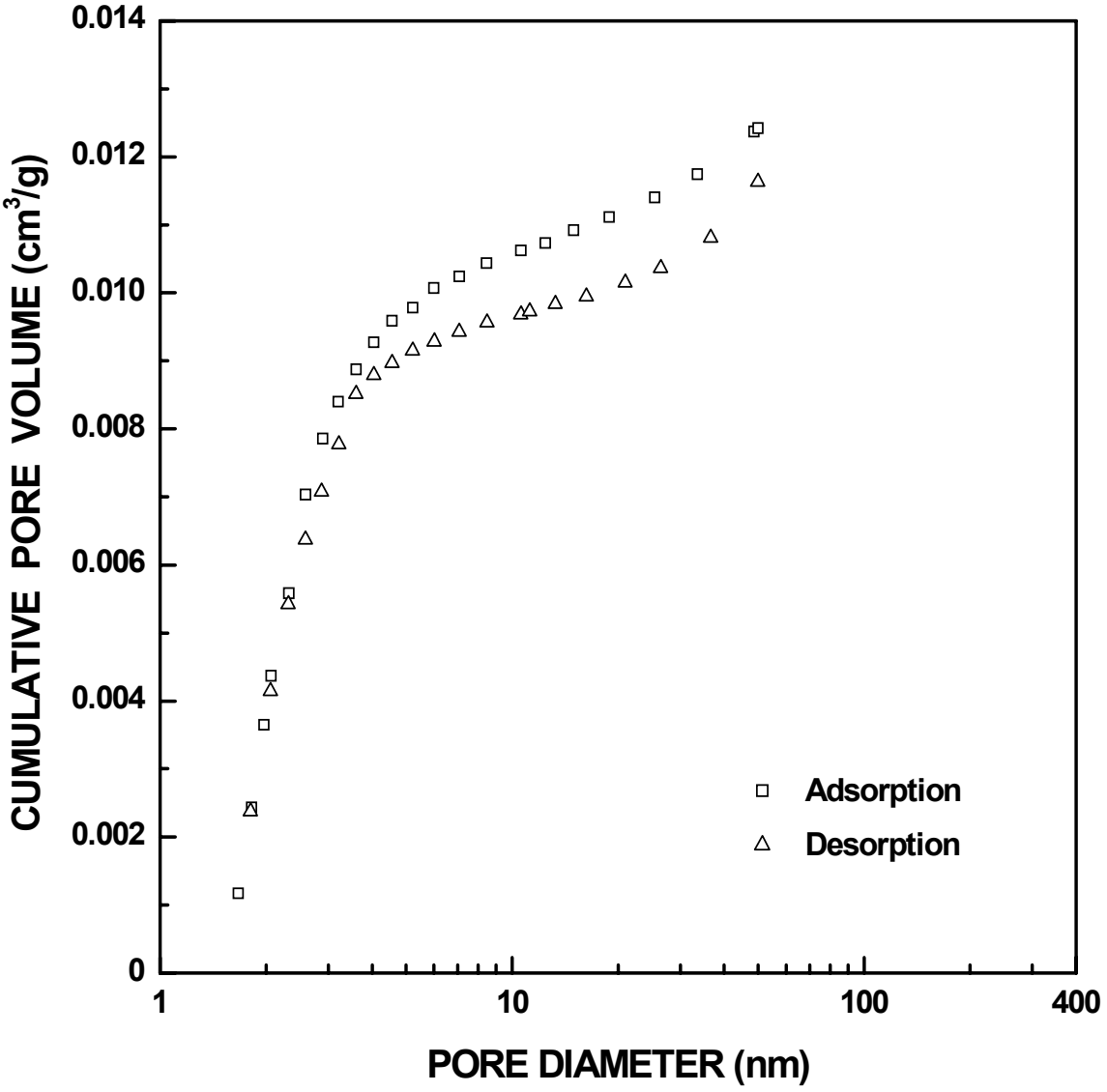

Figure I-124 Plots of cumulative specific pore volume vs. pore diameter for SC8-1200(2h) sample (X_{WL} = 0.11). The pore diameter was cut off at 50 nm.

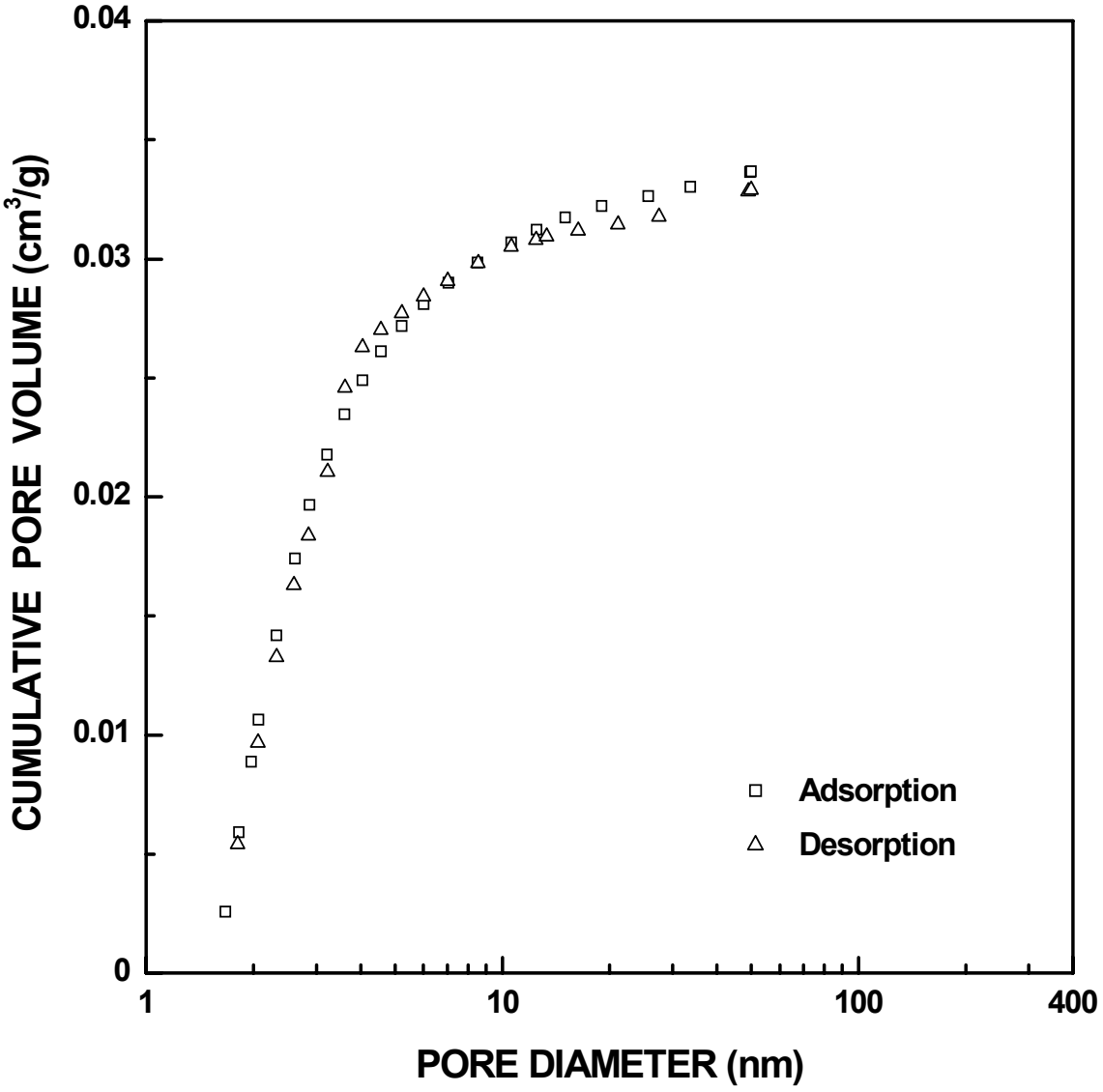

Figure I-125 Plots of cumulative specific pore volume vs. pore diameter for SC8-1200(4h) sample (X_{WL} = 0.19). The pore diameter was cut off at 50 nm.

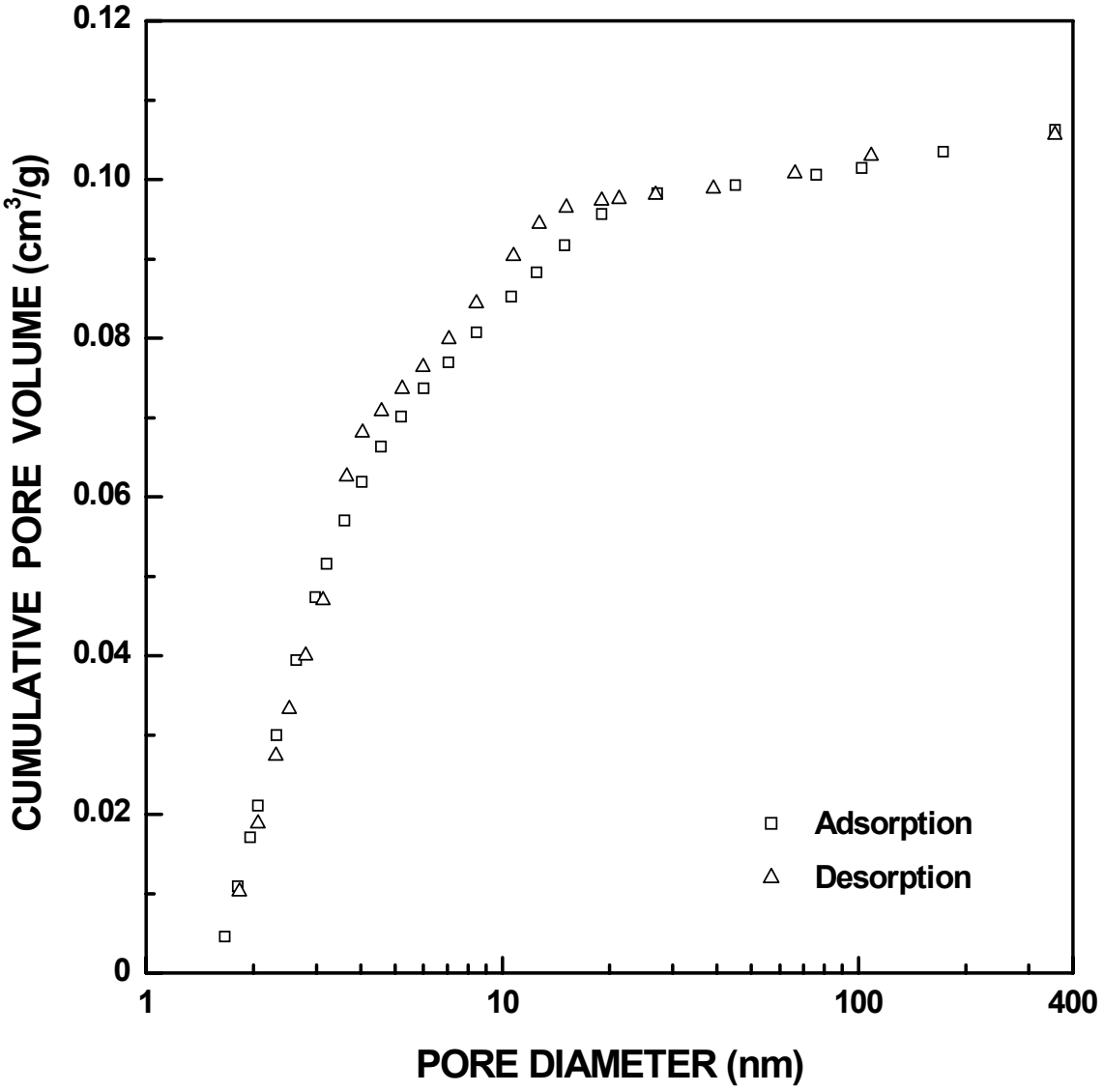

Figure I-126 Plots of cumulative specific pore volume vs. pore diameter for SC8-1200(8h) sample (X_{WL} = 0.40).

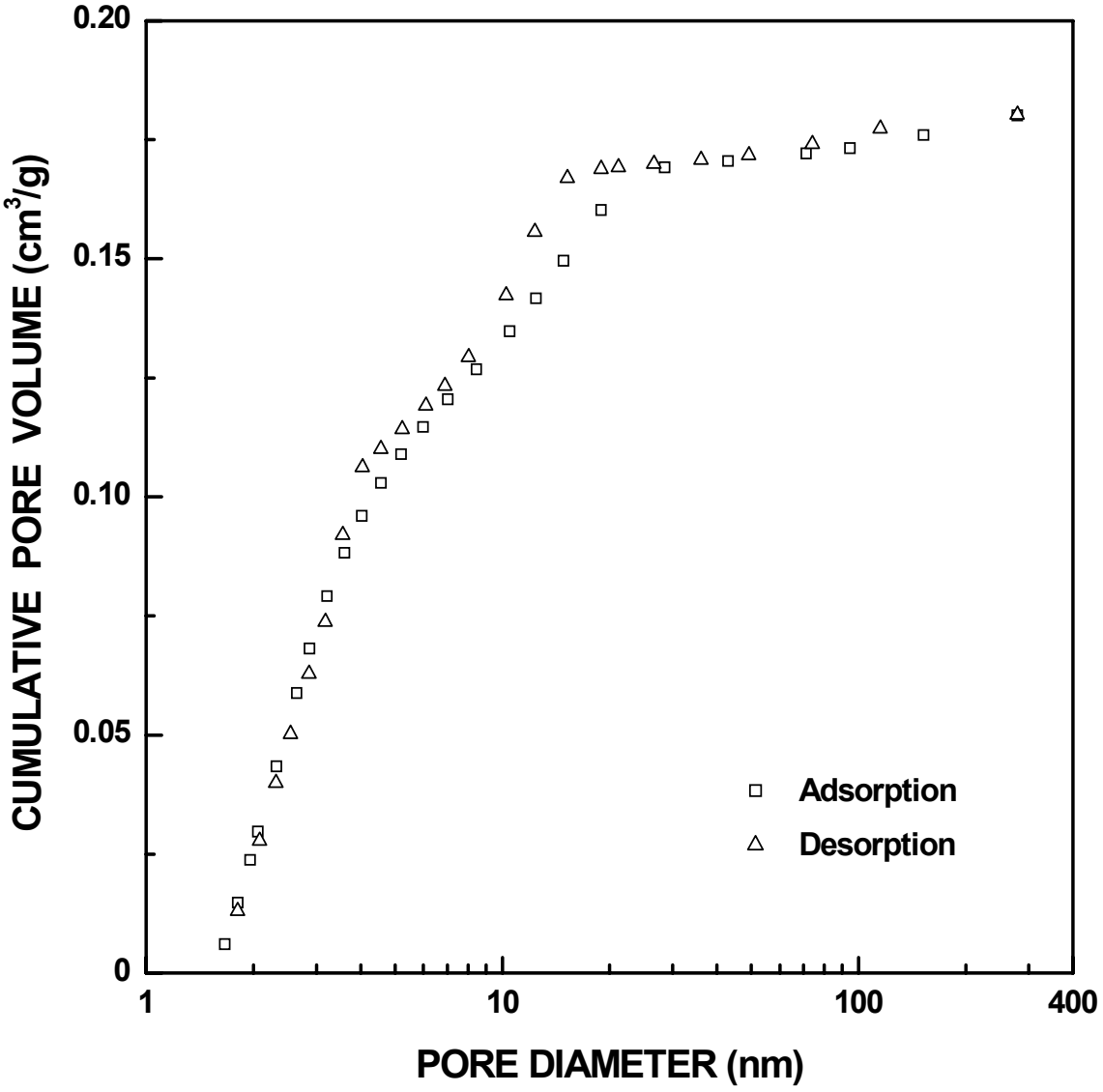

Figure I-127 Plots of cumulative specific pore volume vs. pore diameter for SC8-1200(12h) sample (X_{WL} = 0.54).

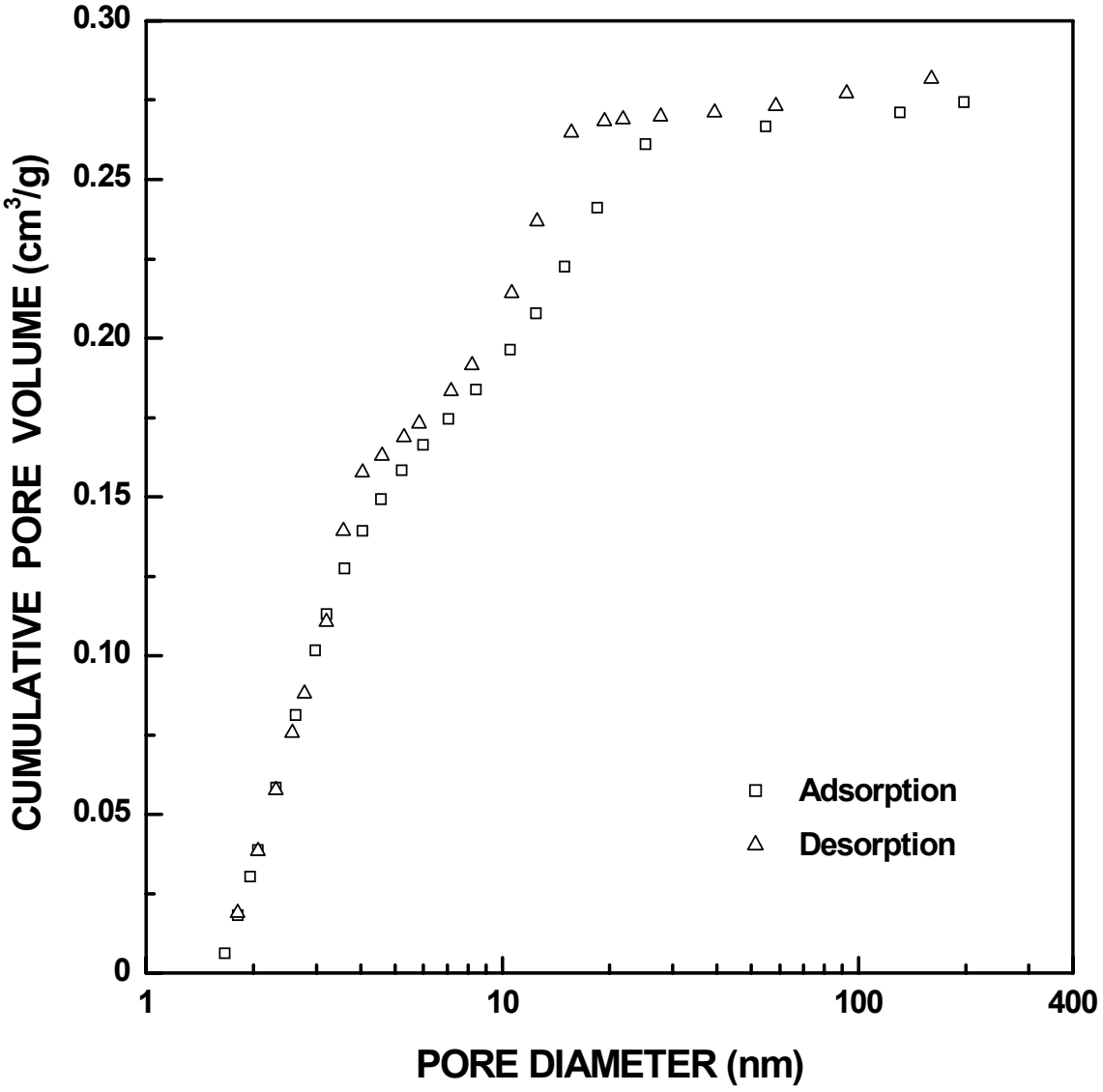

Figure I-128 Plots of cumulative specific pore volume vs. pore diameter for SC8-1200(16h) sample (X_{WL} = 0.68).

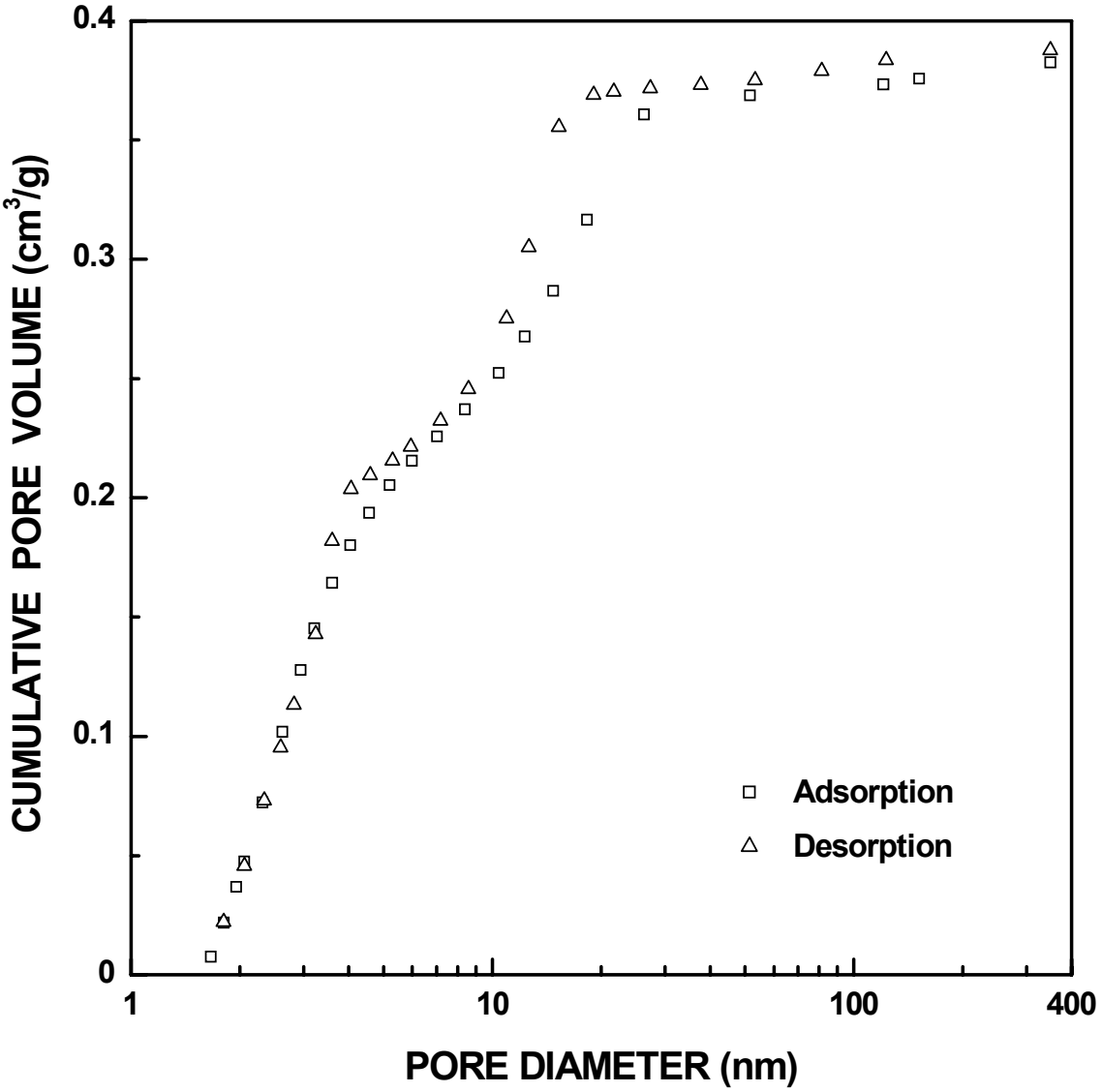

Figure I-129 Plots of cumulative specific pore volume vs. pore diameter for SC8-1200(22h) sample (X_{WL} = 0.80).

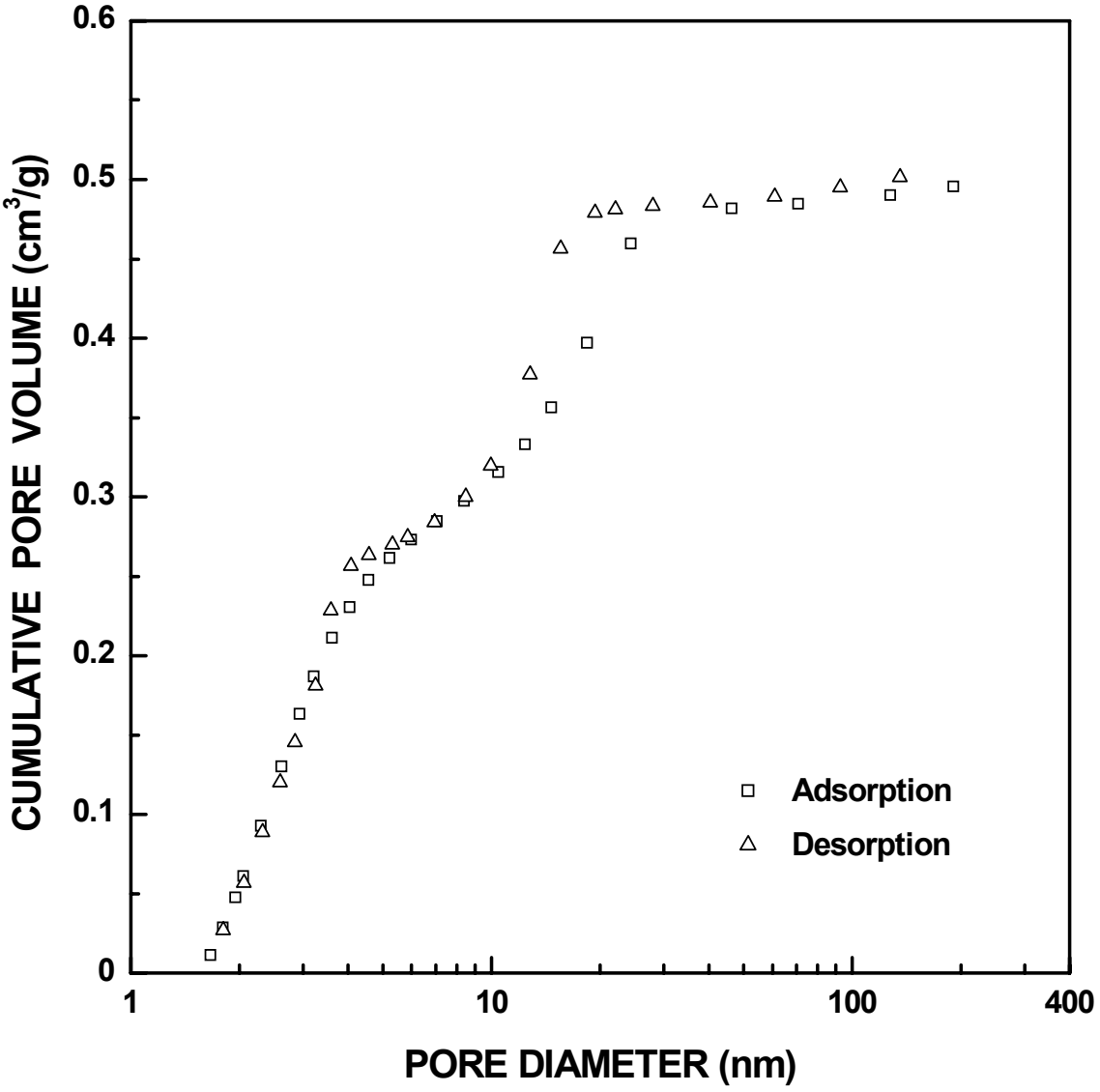

Figure I-130 Plots of cumulative specific pore volume vs. pore diameter for SC8-1200(32h) sample (X_{WL} = 0.91).

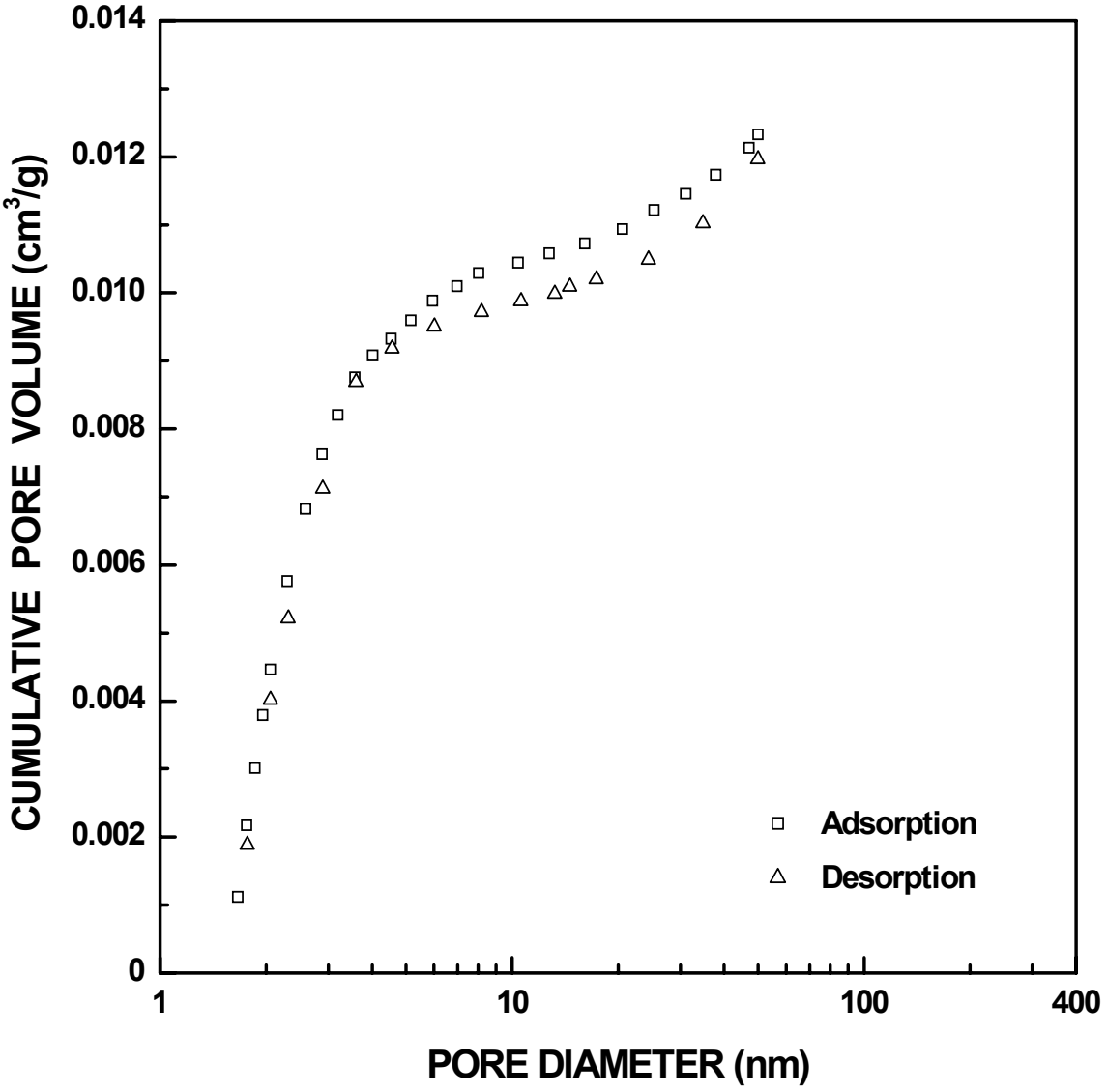

Figure I-131 Plots of cumulative specific pore volume vs. pore diameter for SC8-1250(40min) sample (X_{WL} = 0.11). The pore diameter was cut off at 50 nm.

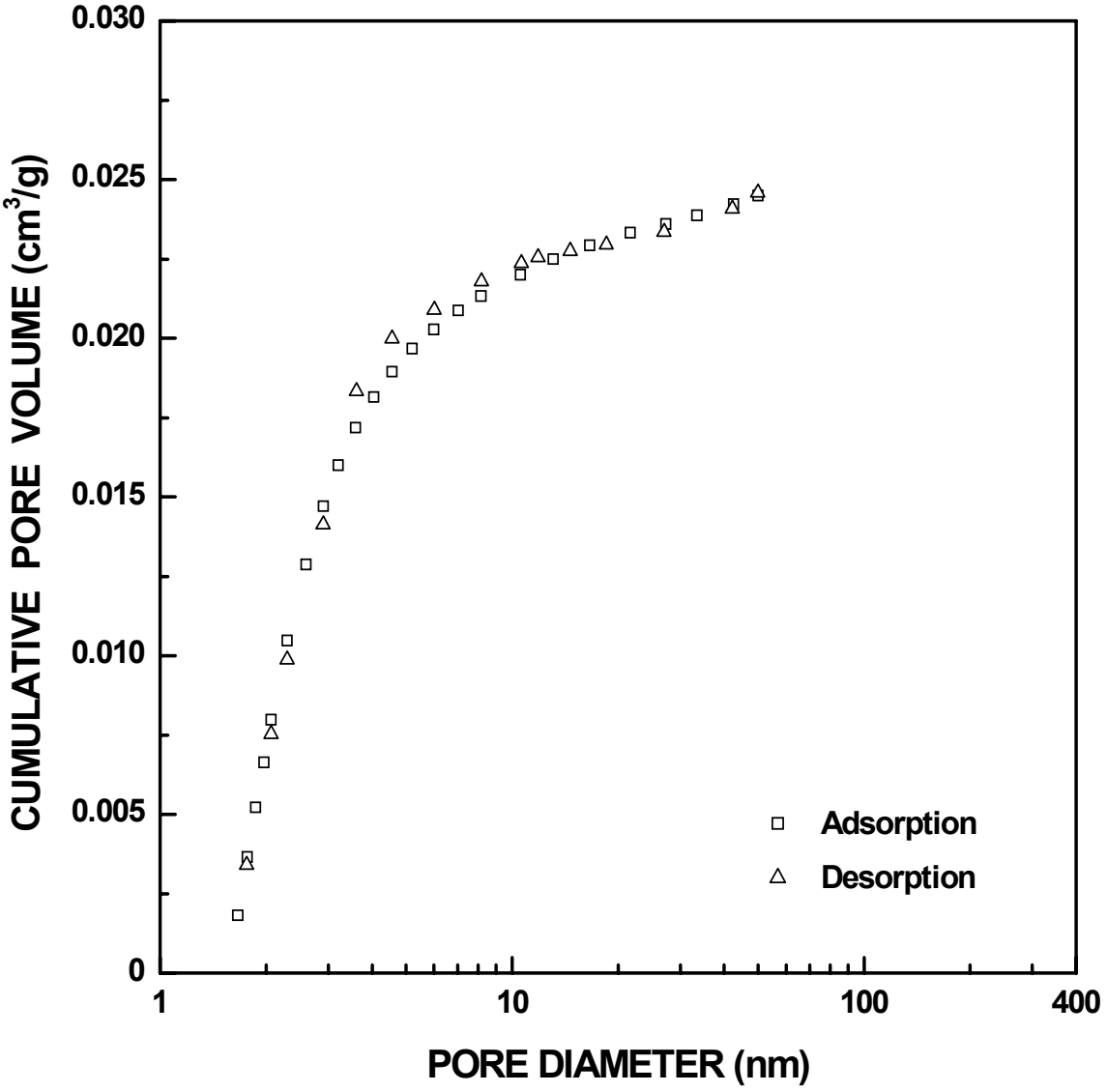

Figure I-132 Plots of cumulative specific pore volume vs. pore diameter for SC8-1250(1h) sample (X_{WL} = 0.16). The pore diameter was cut off at 50 nm.

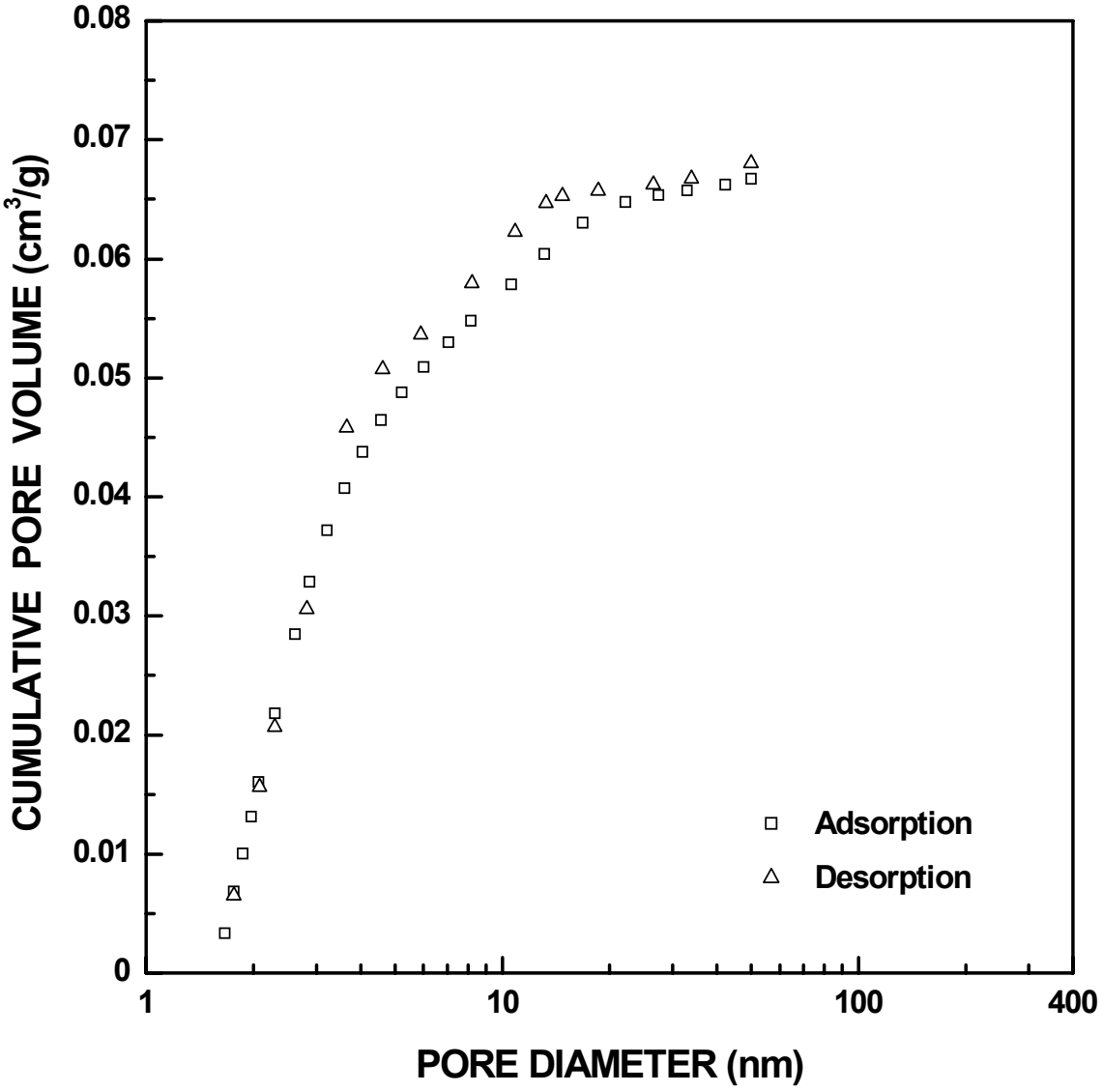

Figure I-133 Plots of cumulative specific pore volume vs. pore diameter for SC8-1250(2h) sample (X_{WL} = 0.31). The pore diameter was cut off at 50 nm.

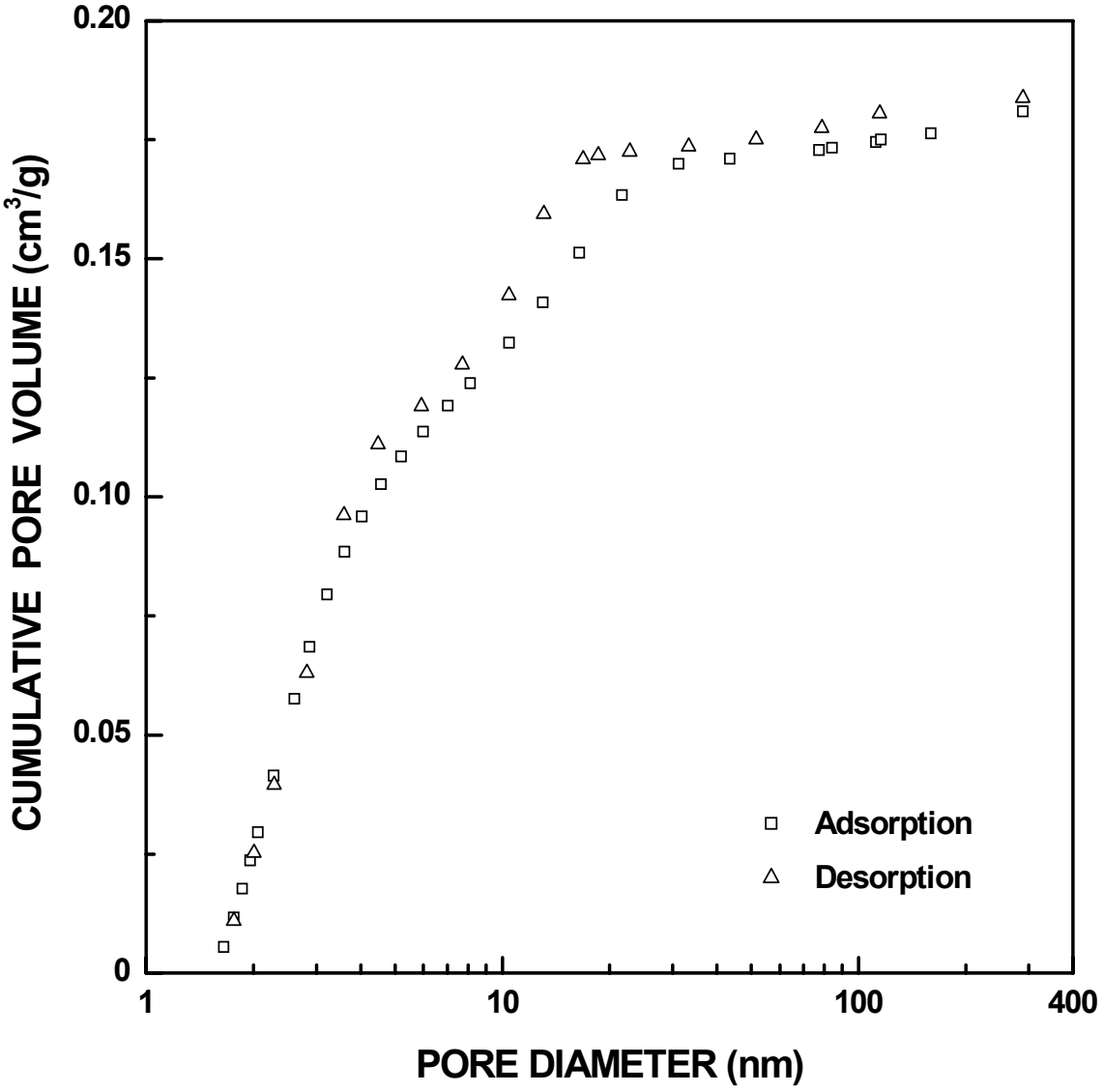

Figure I-134 Plots of cumulative specific pore volume vs. pore diameter for SC8-1250(4h) sample (X_{WL} = 0.54).

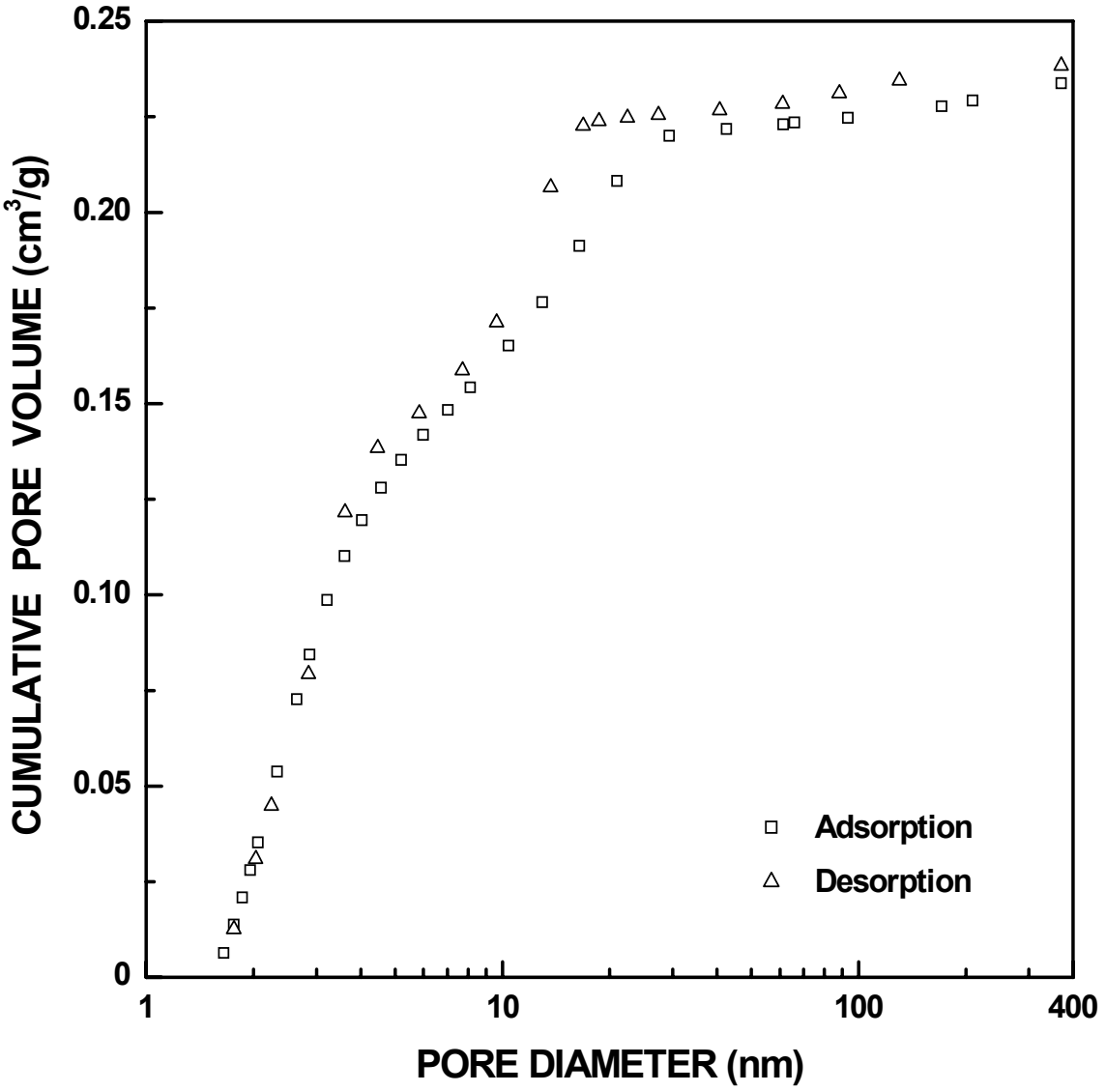

Figure I-135 Plots of cumulative specific pore volume vs. pore diameter for SC8-1250(5h) sample (X_{WL} = 0.61).

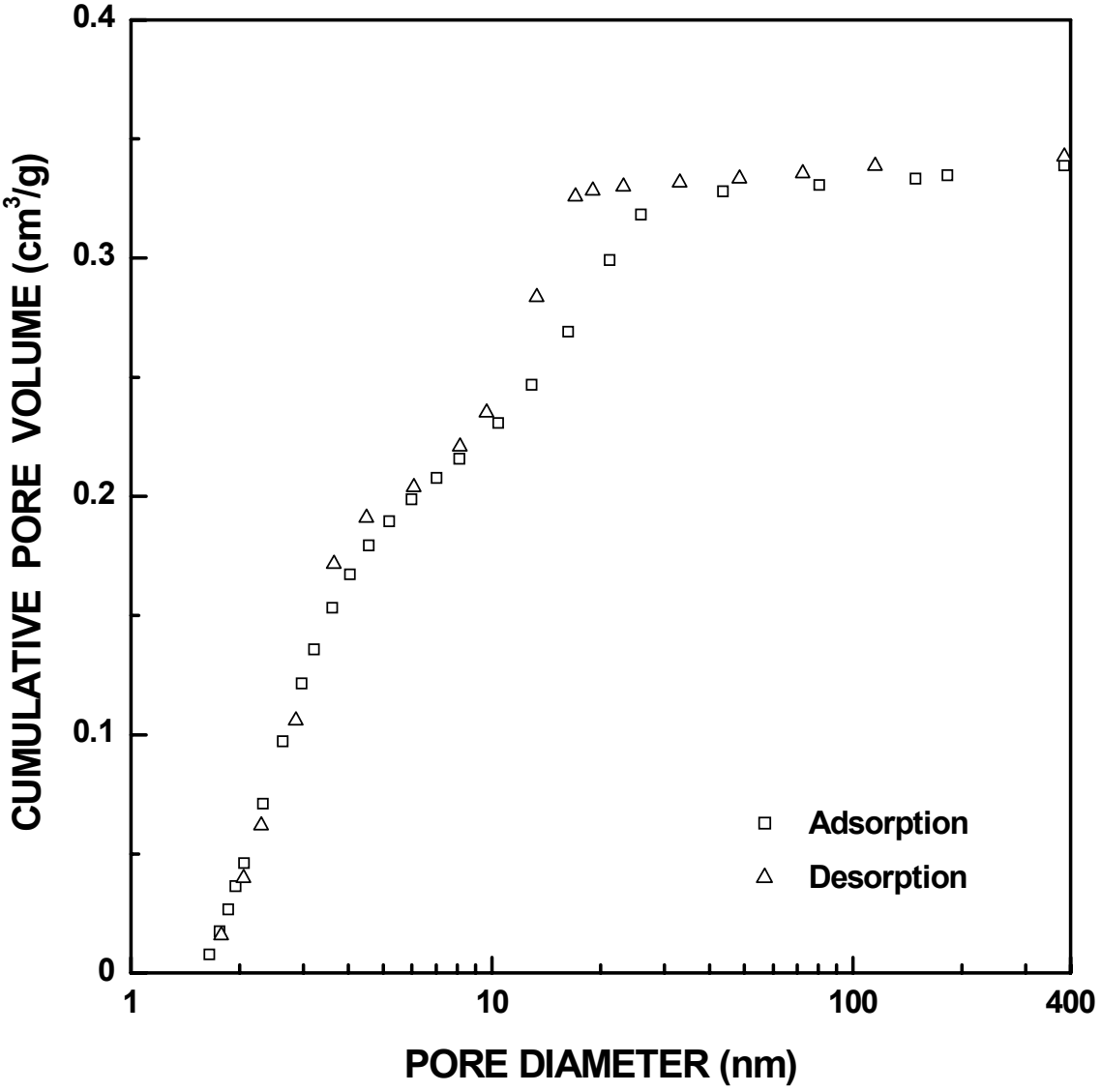

Figure I-136 Plots of cumulative specific pore volume vs. pore diameter for SC8-1250(6.5h) sample (X_{WL} = 0.73).

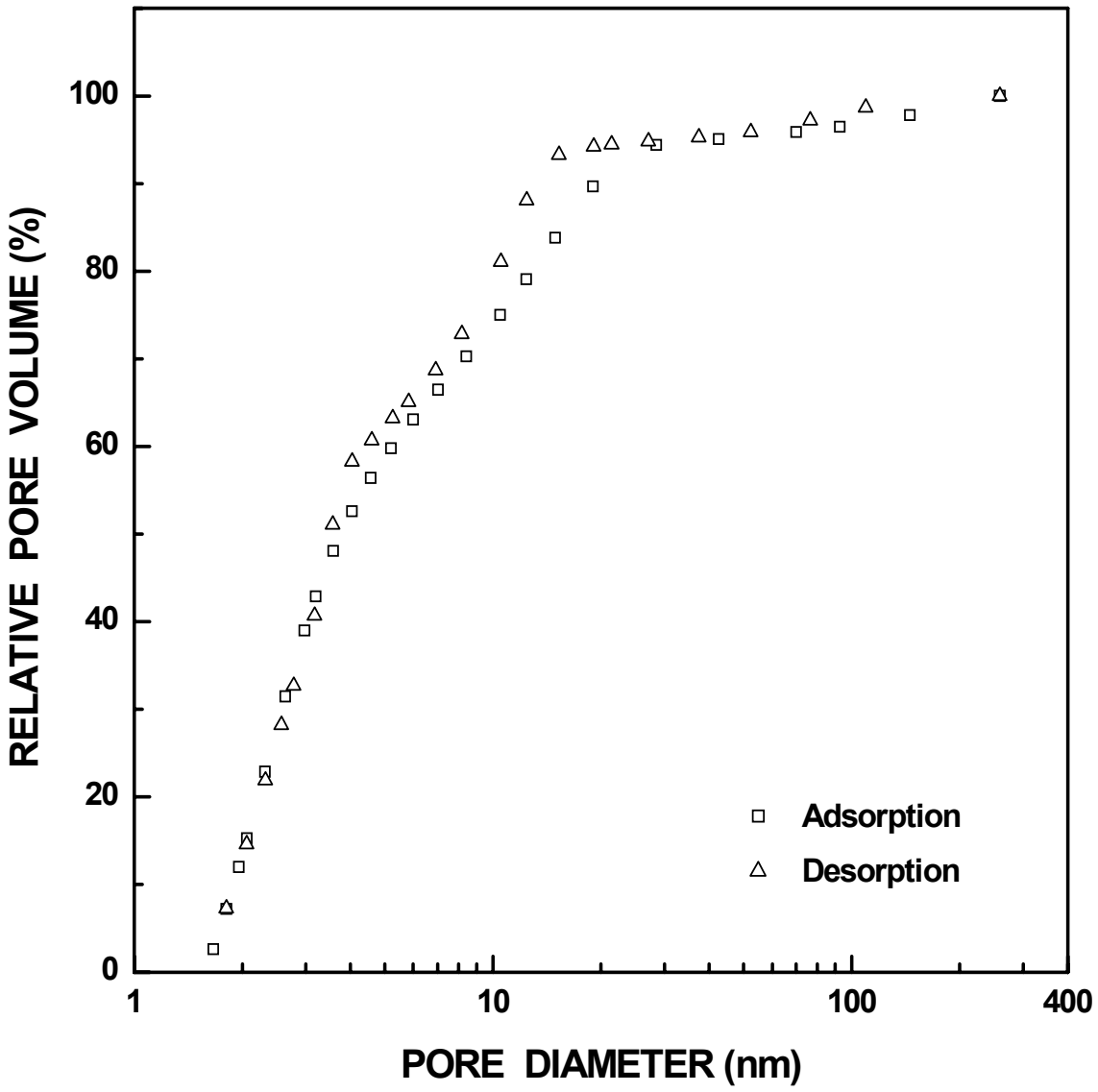

Figure I-137 Plots of relative ("normalized") pore volume vs. pore diameter for SC8-1160(36h) sample (X_{WL} = 0.62).

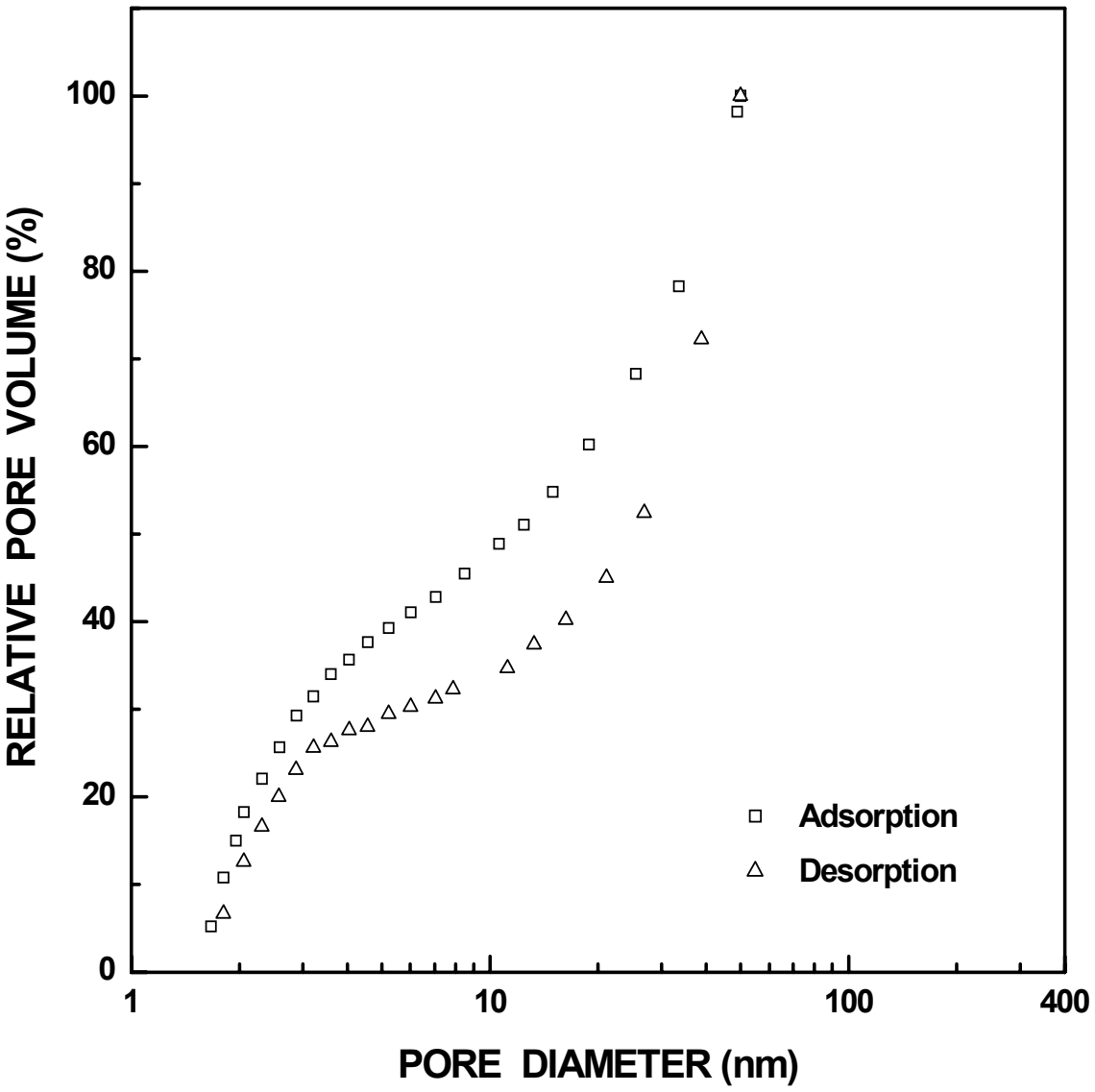

Figure I-138 Plots of relative ("normalized") pore volume vs. pore diameter for SC8-1180(1h) sample (X_{WL} = 0.08). The pore diameter was cut off at 50 nm.

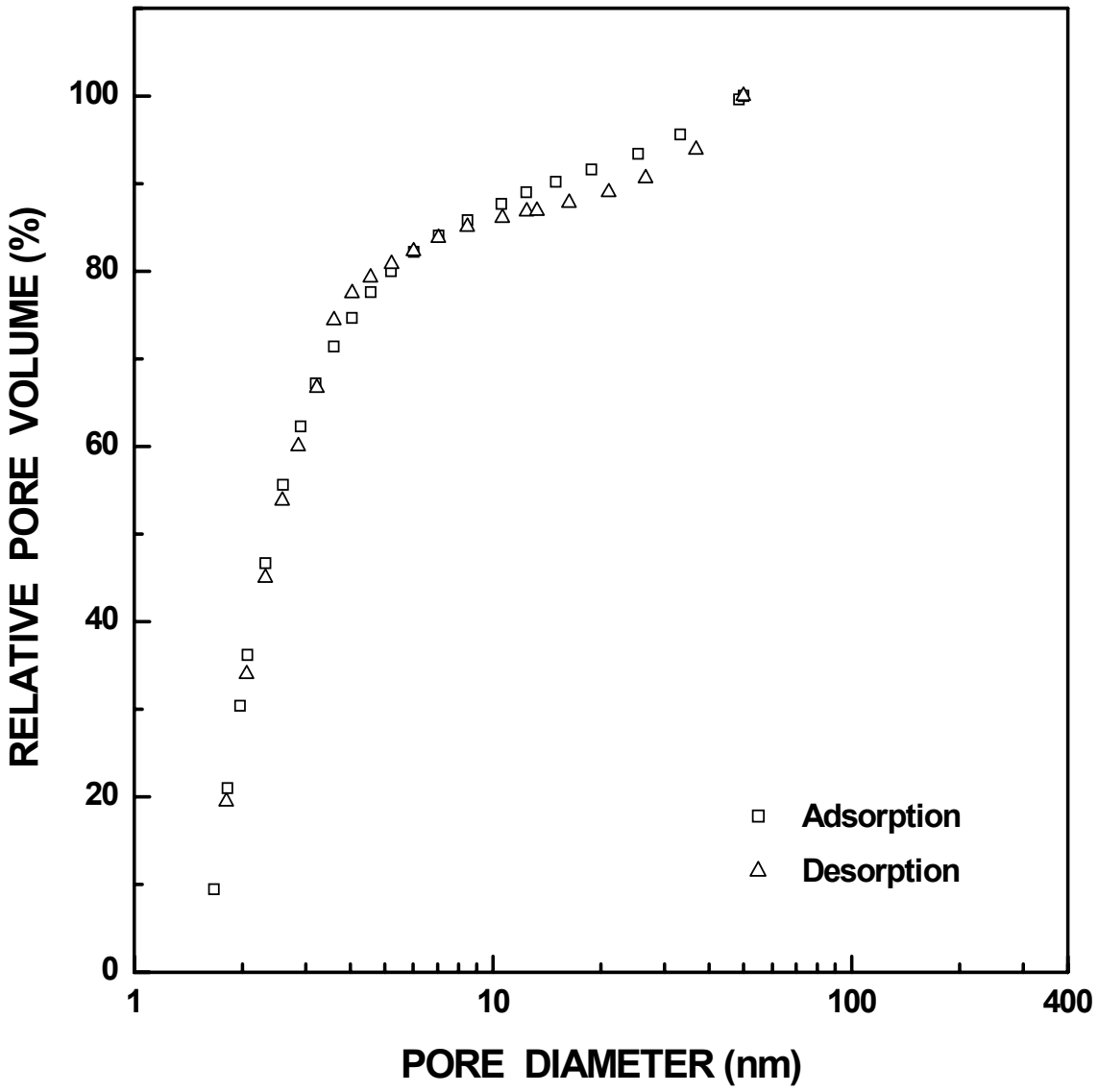

Figure I-139 Plots of relative ("normalized") pore volume vs. pore diameter for SC8-1180(4h) sample (X_{WL} = 0.18). The pore diameter was cut off at 50 nm.

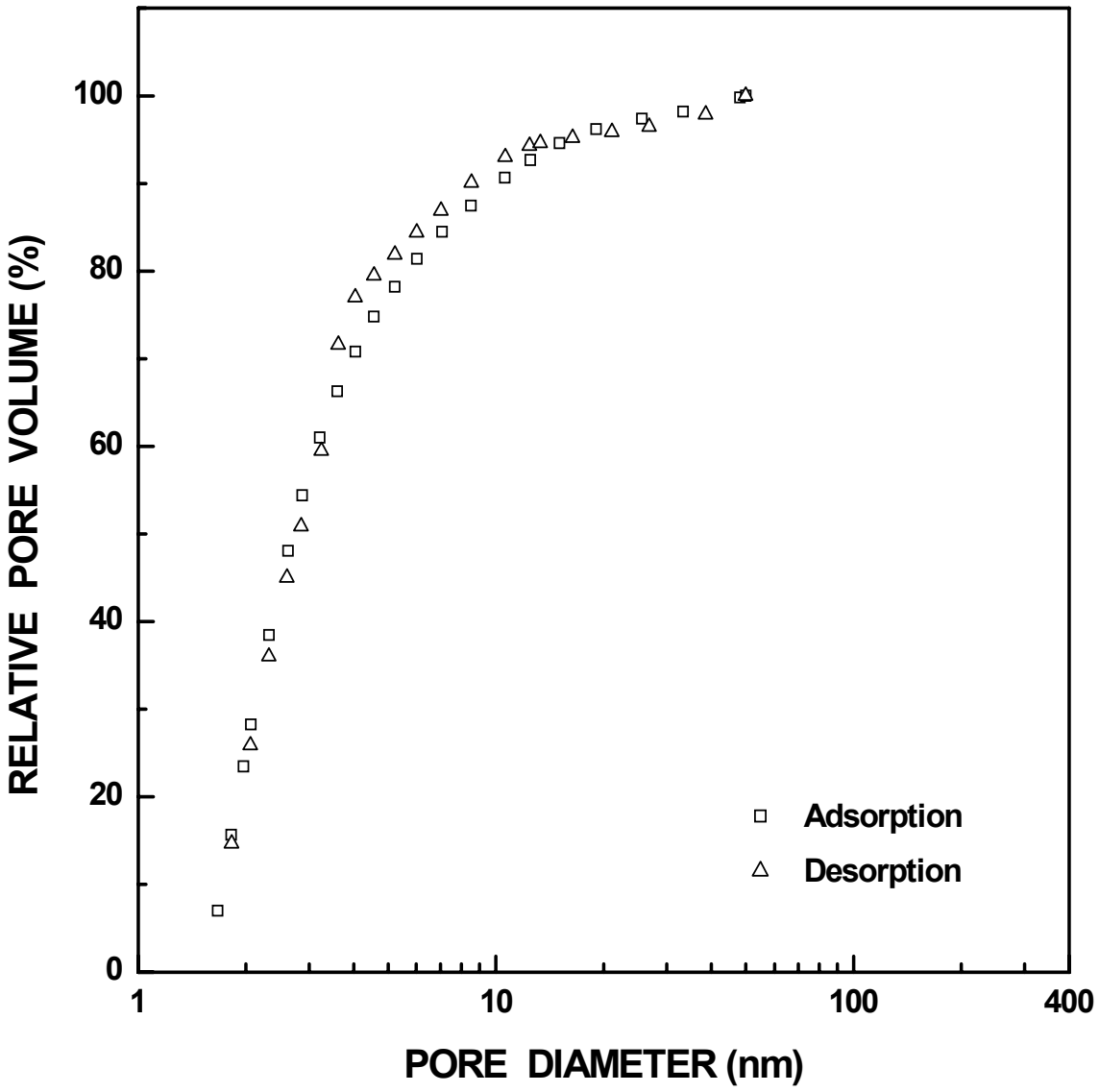

Figure I-140 Plots of relative ("normalized") pore volume vs. pore diameter for SC8-1180(8h) sample (X_{WL} = 0.31). The pore diameter was cut off at 50 nm.

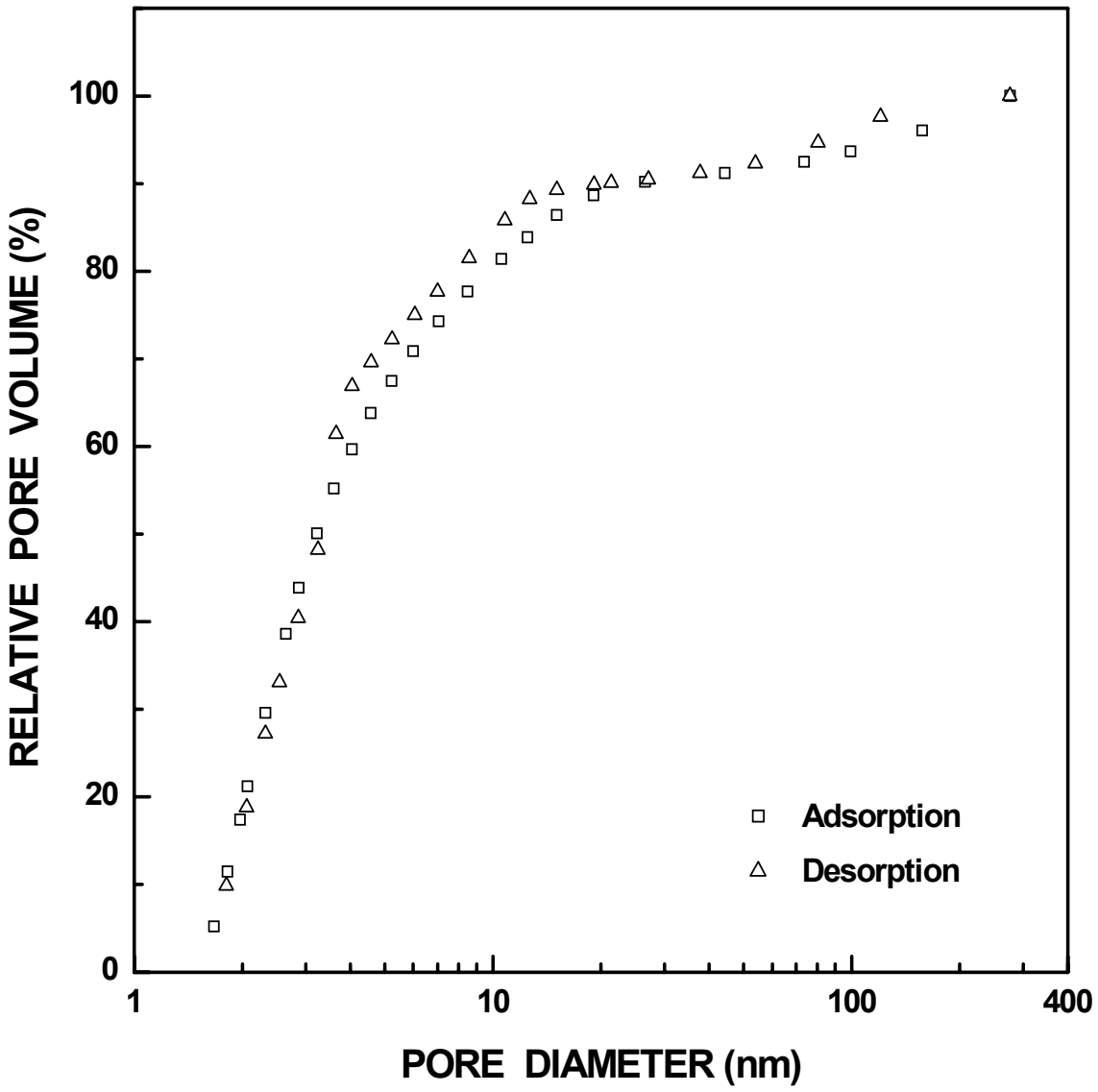

Figure I-141 Plots of relative ("normalized") pore volume vs. pore diameter for SC8-1180(12h) sample (X_{WL} = 0.43).

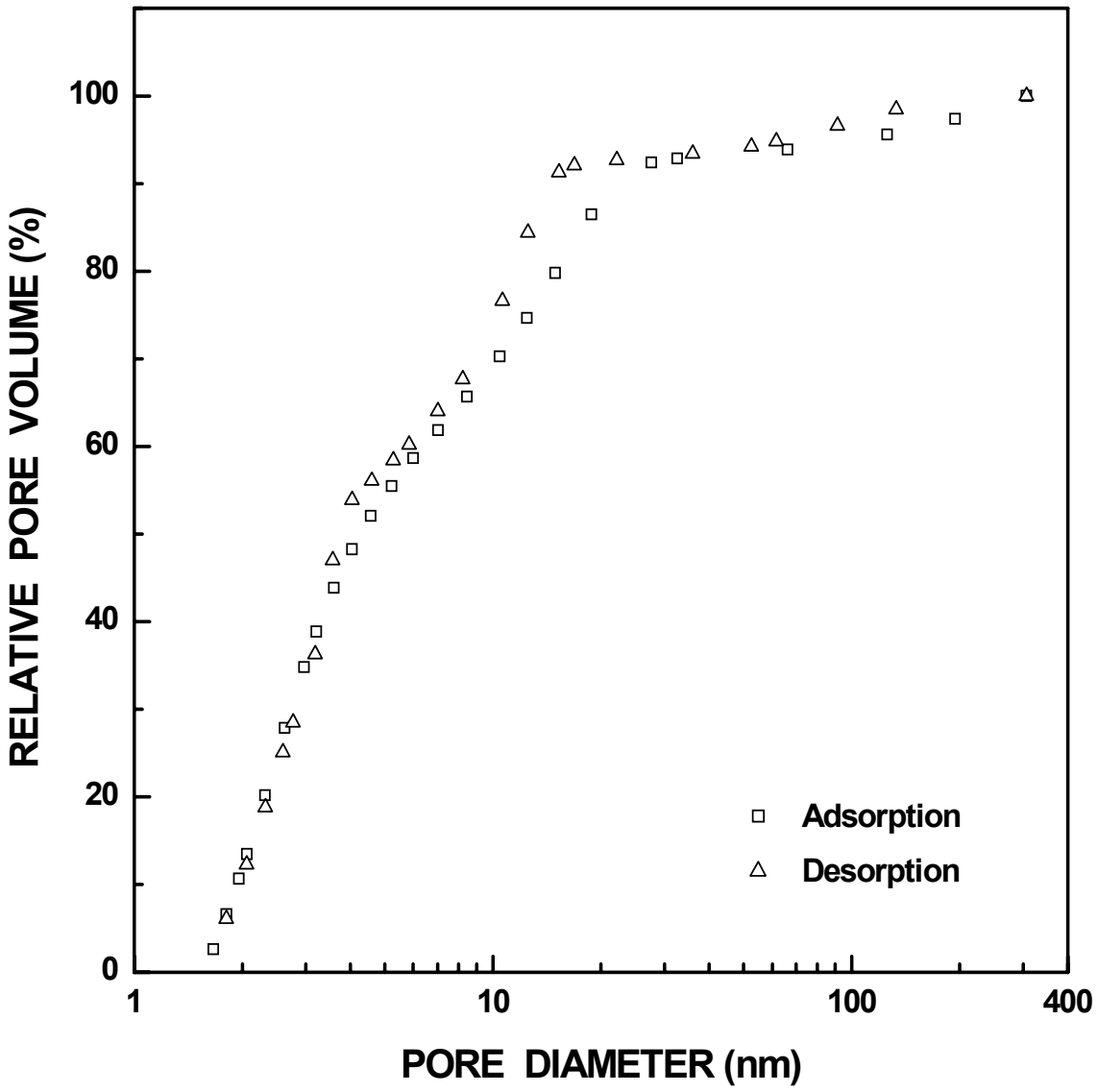

Figure I-142 Plots of relative ("normalized") pore volume vs. pore diameter for SC8-1180(24h) sample (X_{WL} = 0.70).

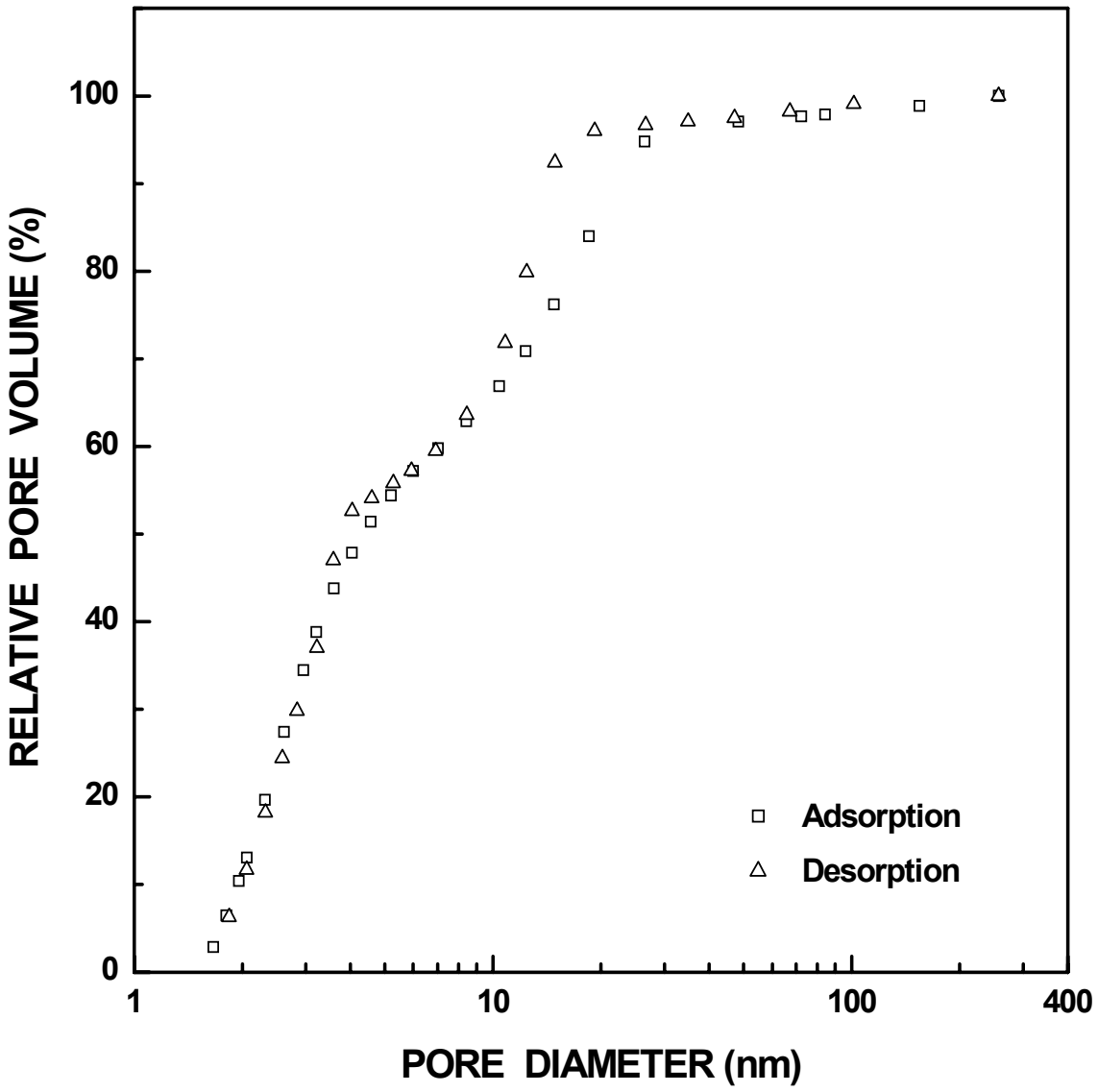

Figure I-143 Plots of relative ("normalized") pore volume vs. pore diameter for SC8-1180(36h) sample (X_{WL} = 0.82).

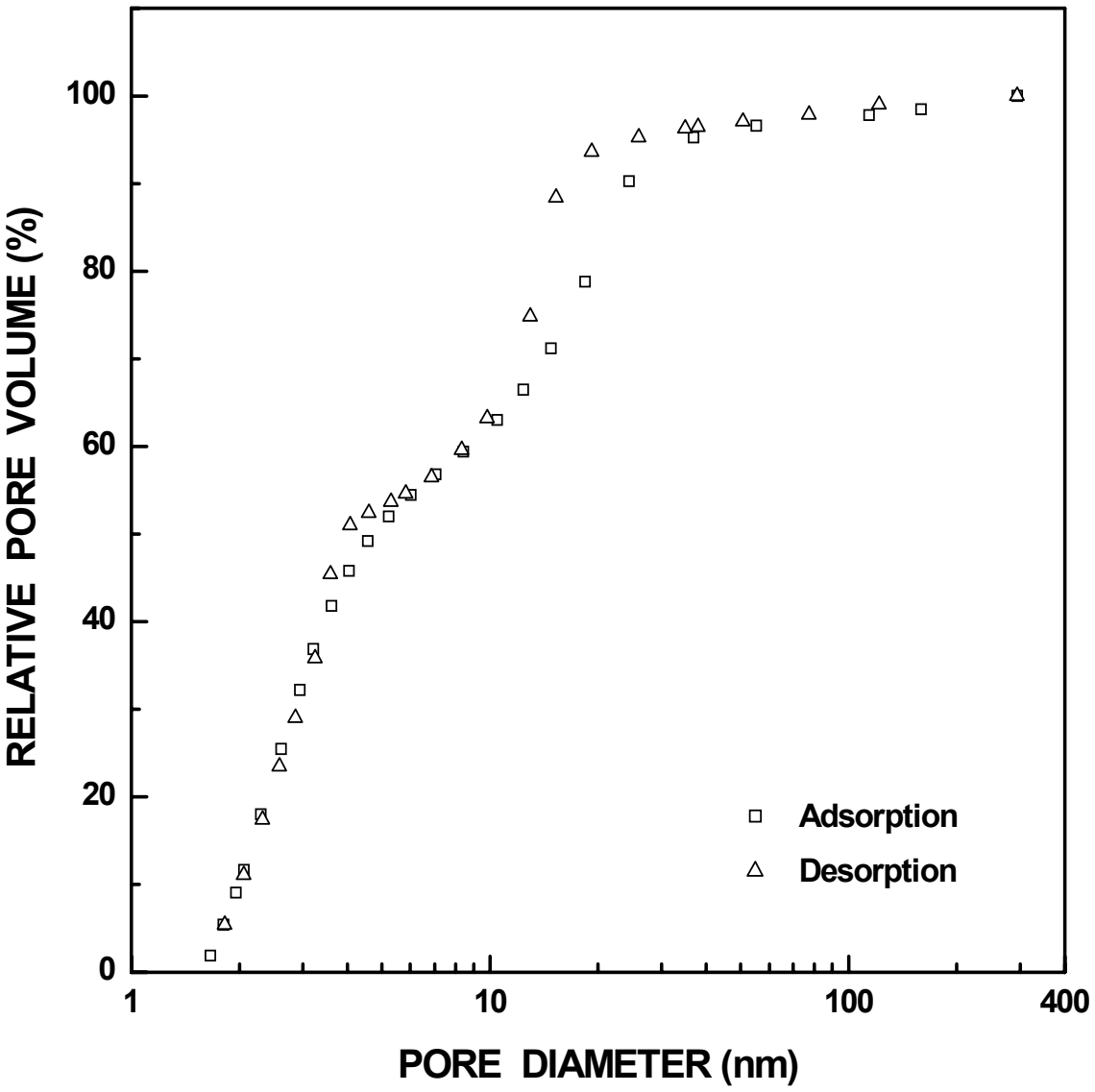

Figure I-144 Plots of relative ("normalized") pore volume vs. pore diameter for SC8-1180(48h) sample (X_{WL} = 0.92).

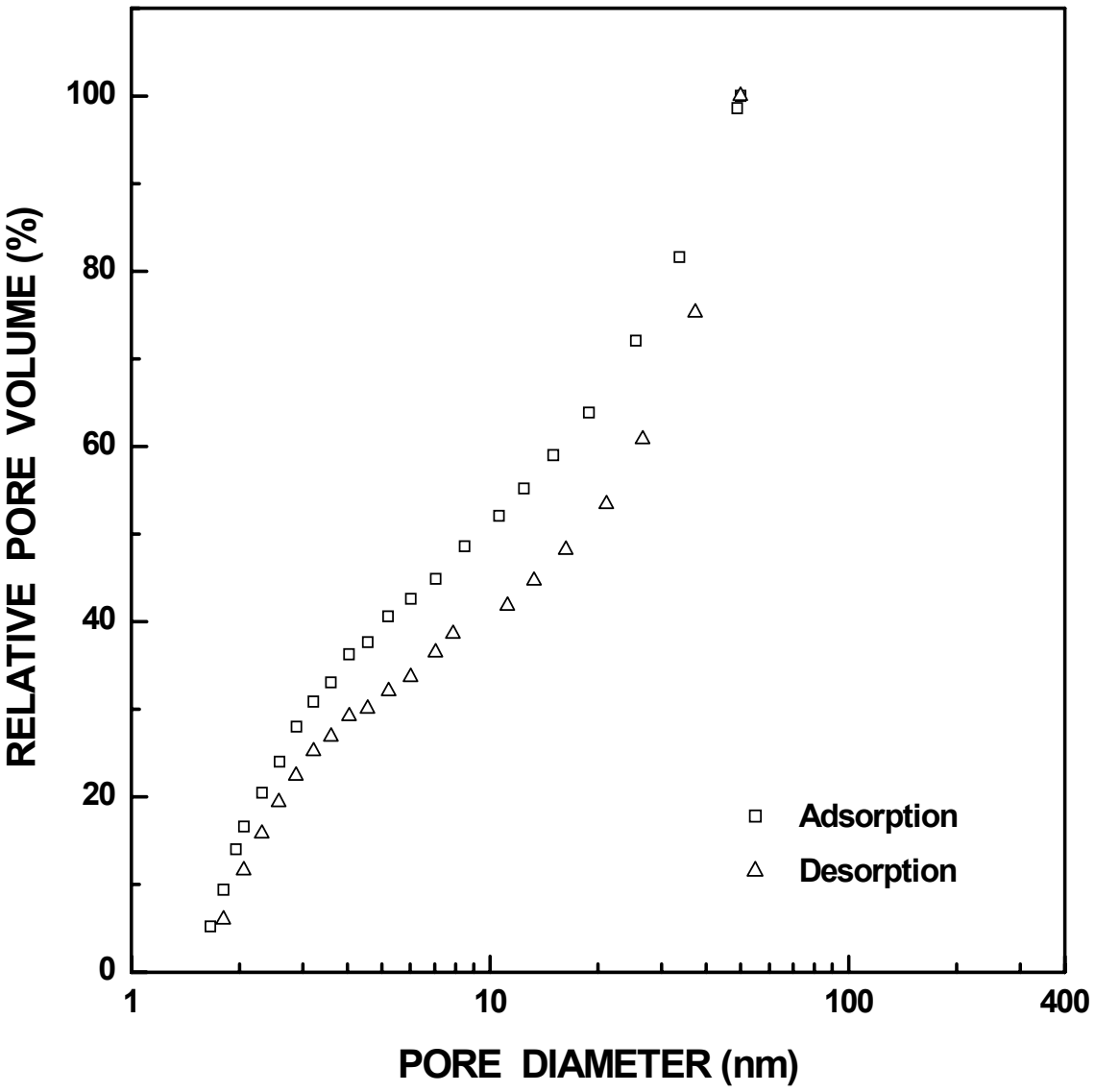

Figure I-145 Plots of relative ("normalized") pore volume vs. pore diameter for SC8-1200(0.5h) sample (X_{WL} = 0.05). The pore diameter was cut off at 50 nm.

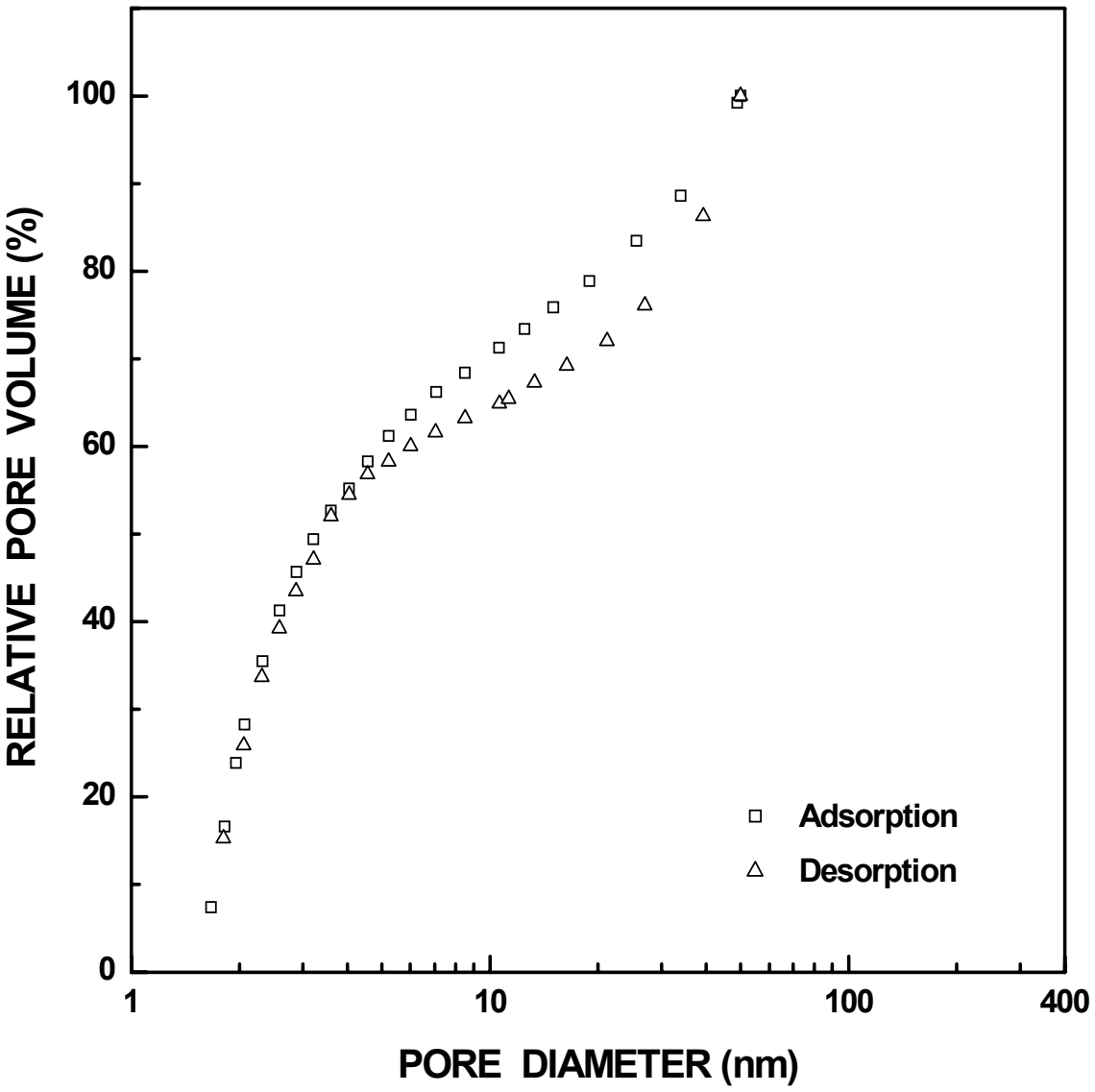

Figure I-146 Plots of relative ("normalized") pore volume vs. pore diameter for SC8-1200(1h) sample (X_{WL} = 0.05). The pore diameter was cut off at 50 nm.

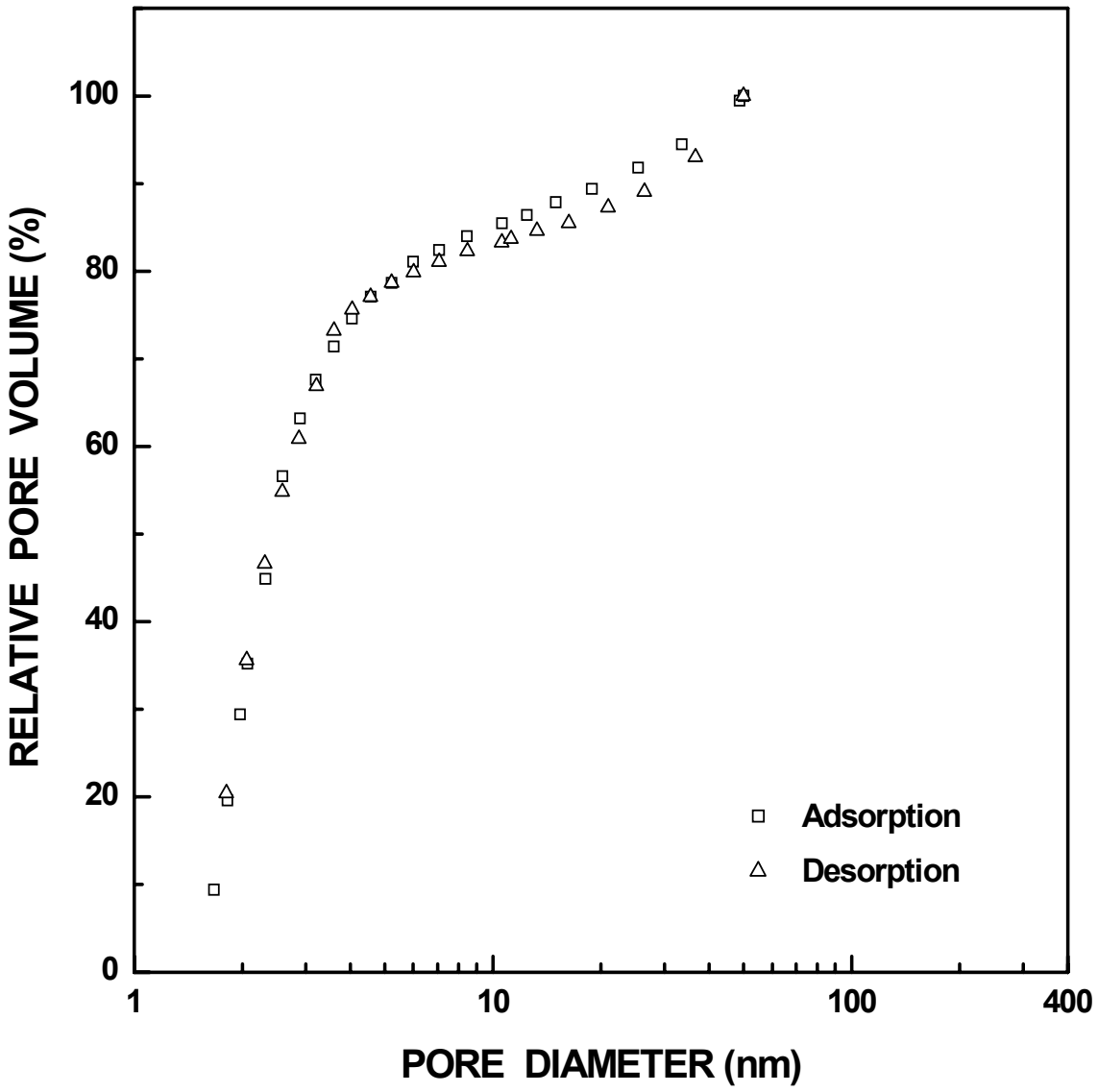

Figure I-147 Plots of relative ("normalized") pore volume vs. pore diameter for SC8-1200(2h) sample (X_{WL} = 0.11). The pore diameter was cut off at 50 nm.

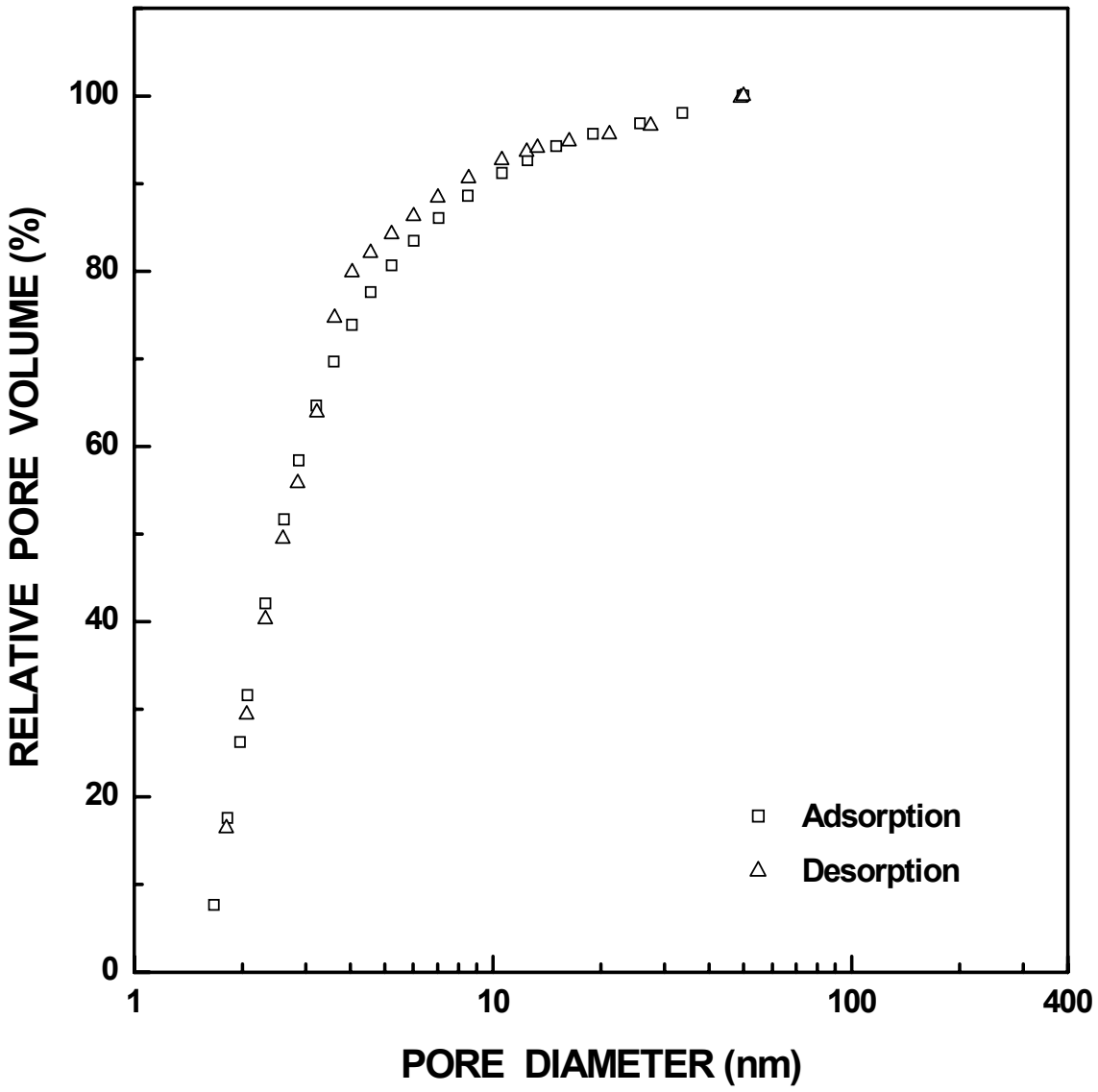

Figure I-148 Plots of relative ("normalized") pore volume vs. pore diameter for SC8-1200(4h) sample (X_{WL} = 0.19). The pore diameter was cut off at 50 nm.

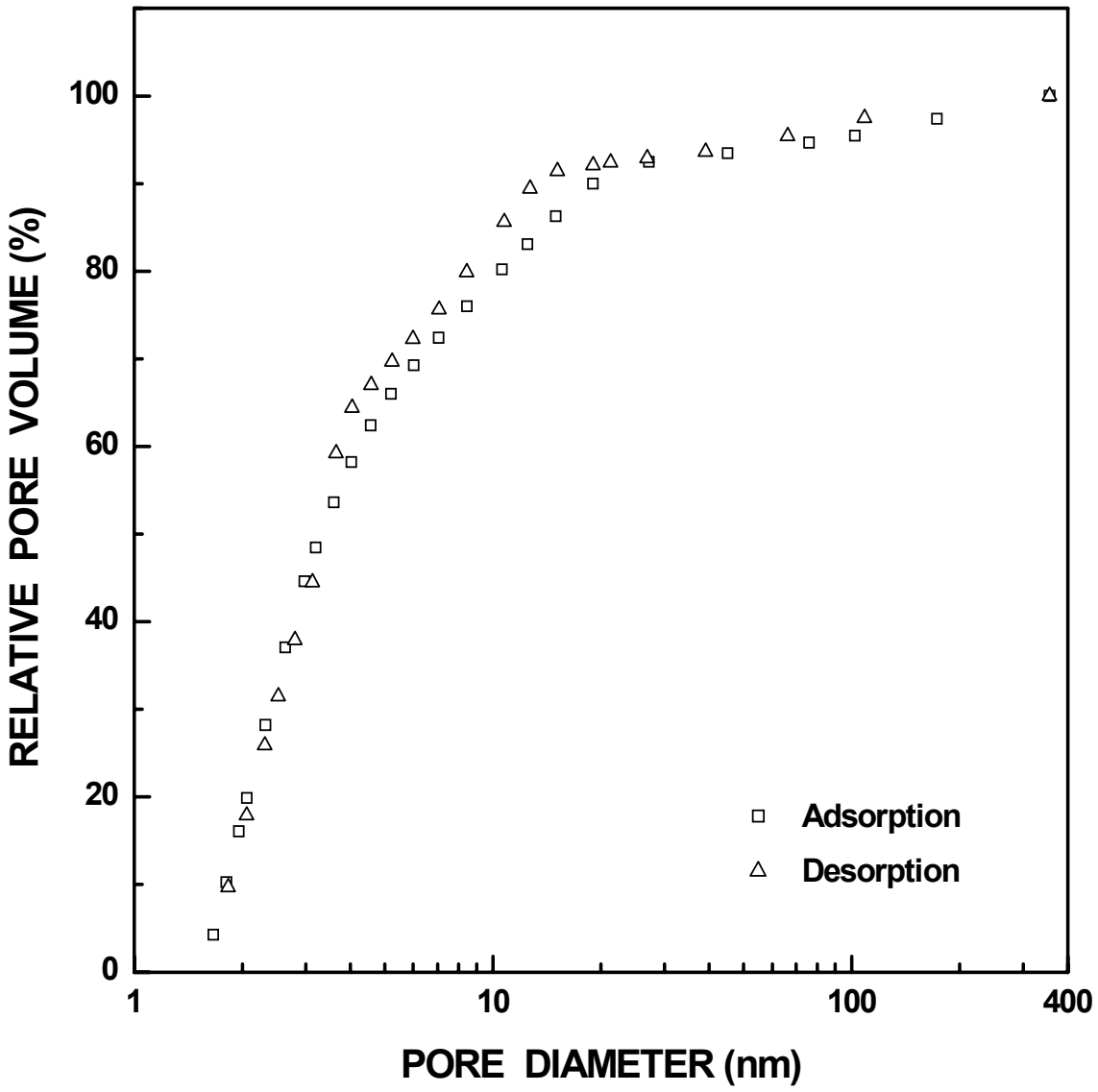

Figure I-149 Plots of relative ("normalized") pore volume vs. pore diameter for SC8-1200(8h) sample (X_{WL} = 0.40).

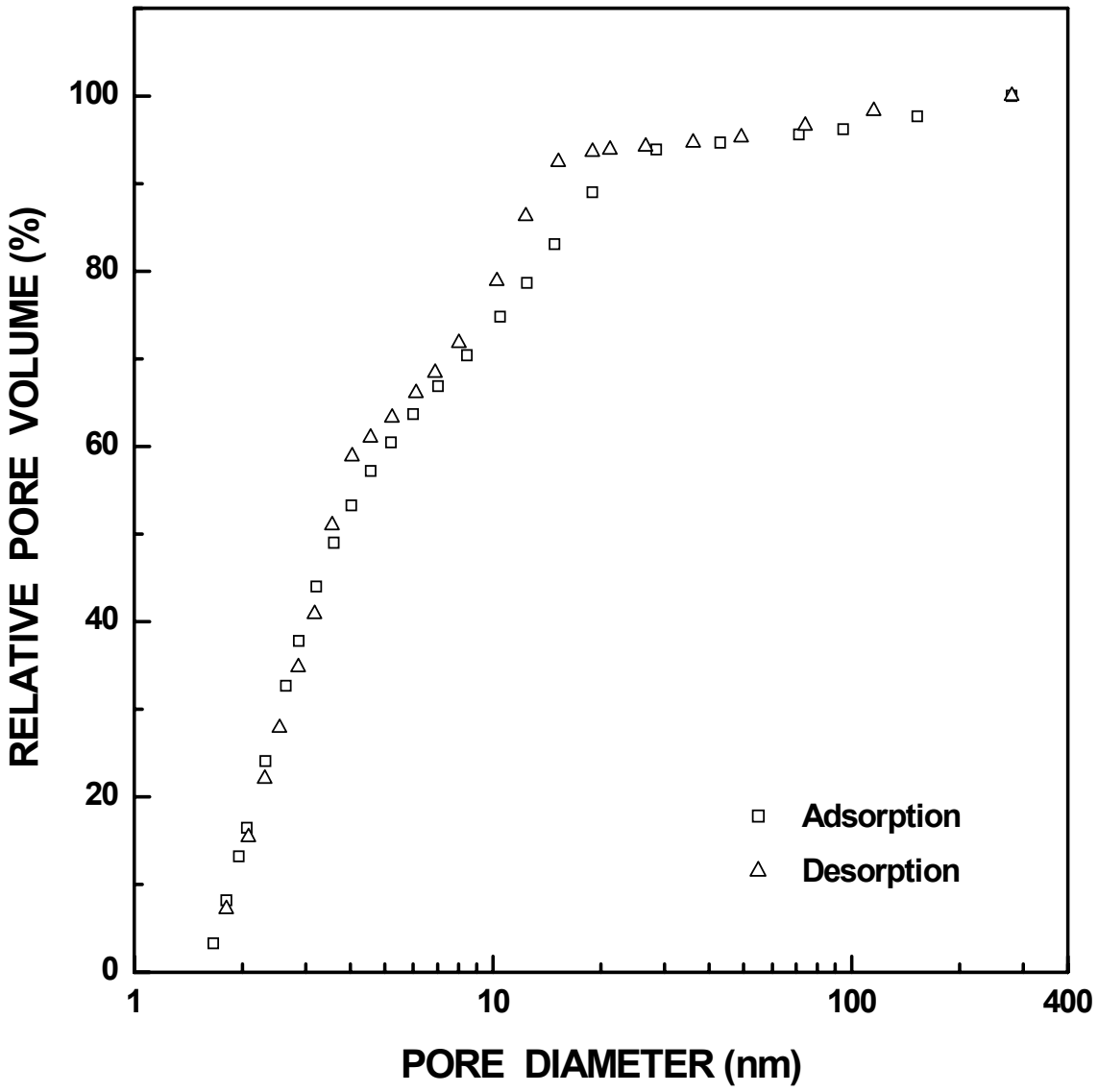

Figure I-150 Plots of relative ("normalized") pore volume vs. pore diameter for SC8-1200(12h) sample (X_{WL} = 0.54).

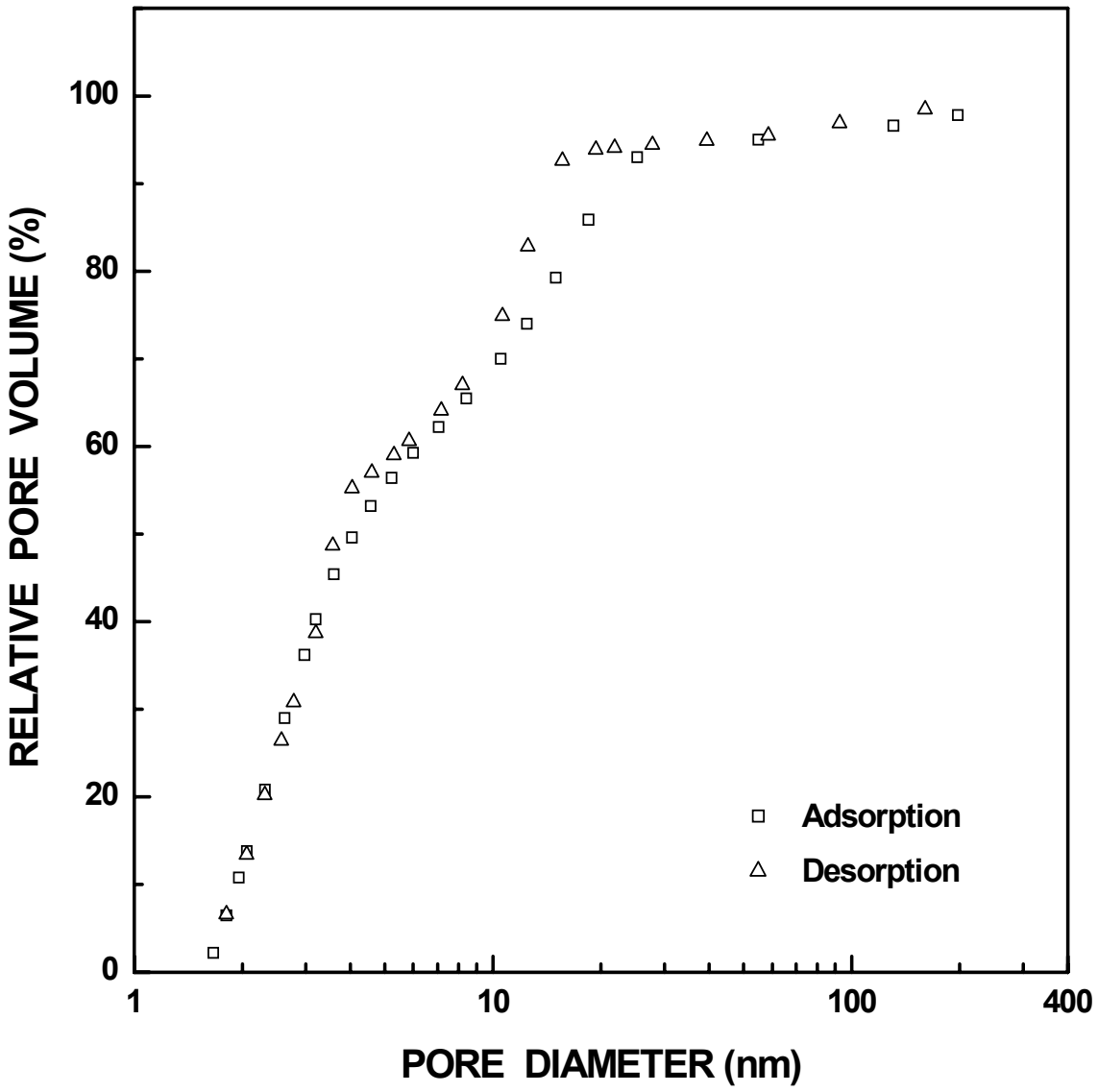

Figure I-151 Plots of relative ("normalized") pore volume vs. pore diameter for SC8-1200(16h) sample (X_{WL} = 0.68).

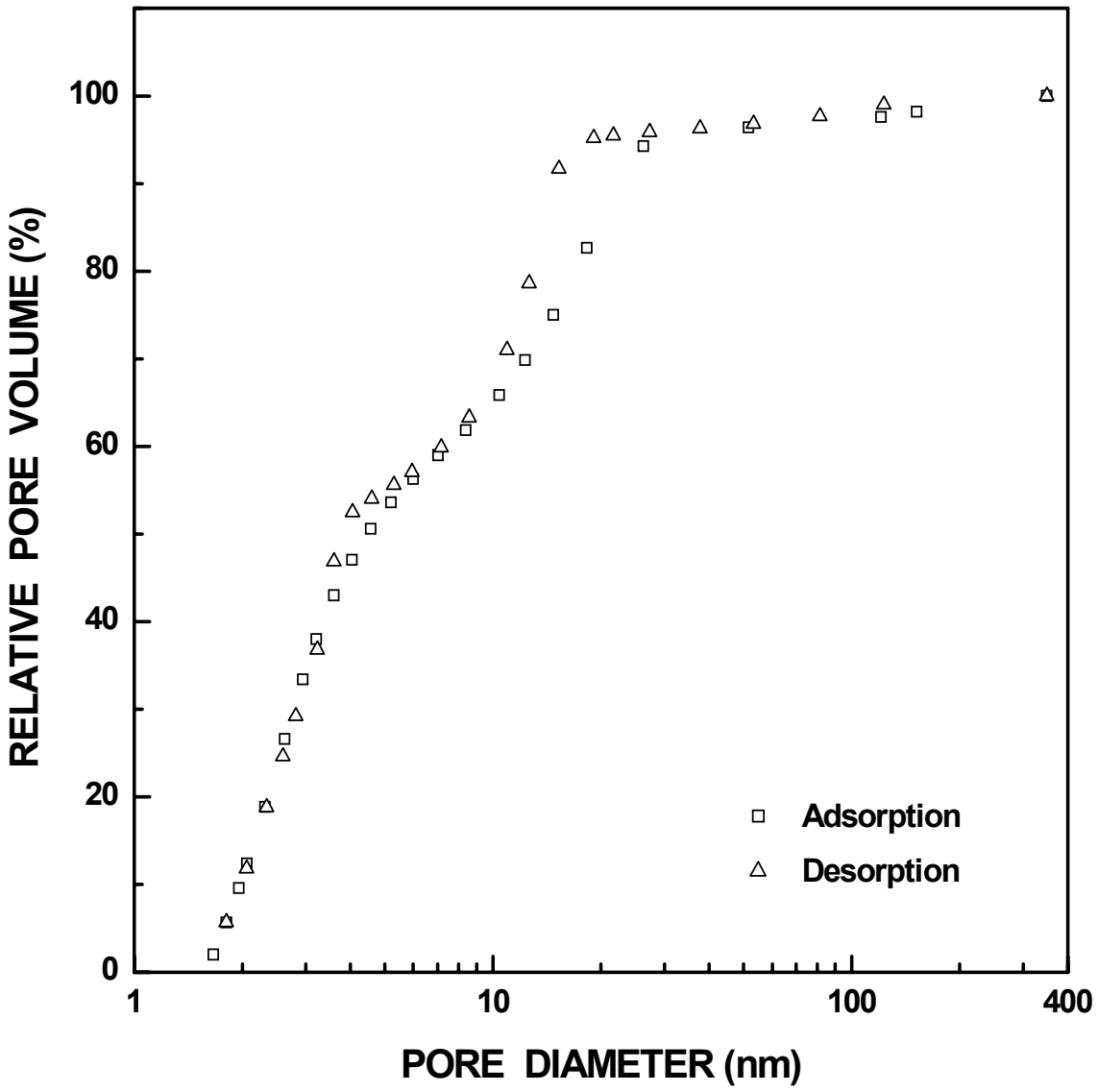

Figure I-152 Plots of relative ("normalized") pore volume vs. pore diameter for SC8-1200(22h) sample (X_{WL} = 0.80).

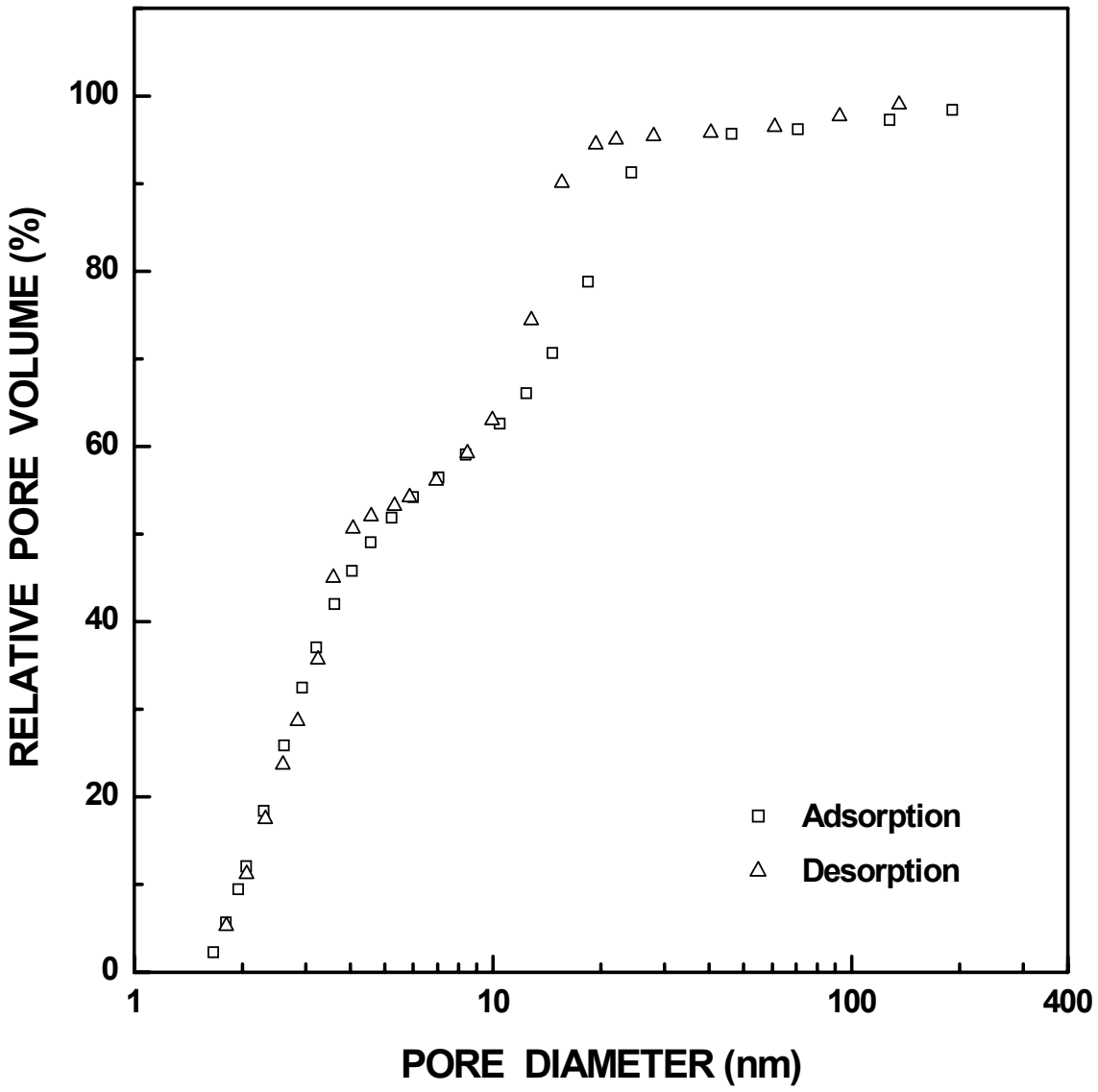

Figure I-153 Plots of relative ("normalized") pore volume vs. pore diameter for SC8-1200(32h) sample (X_{WL} = 0.91).

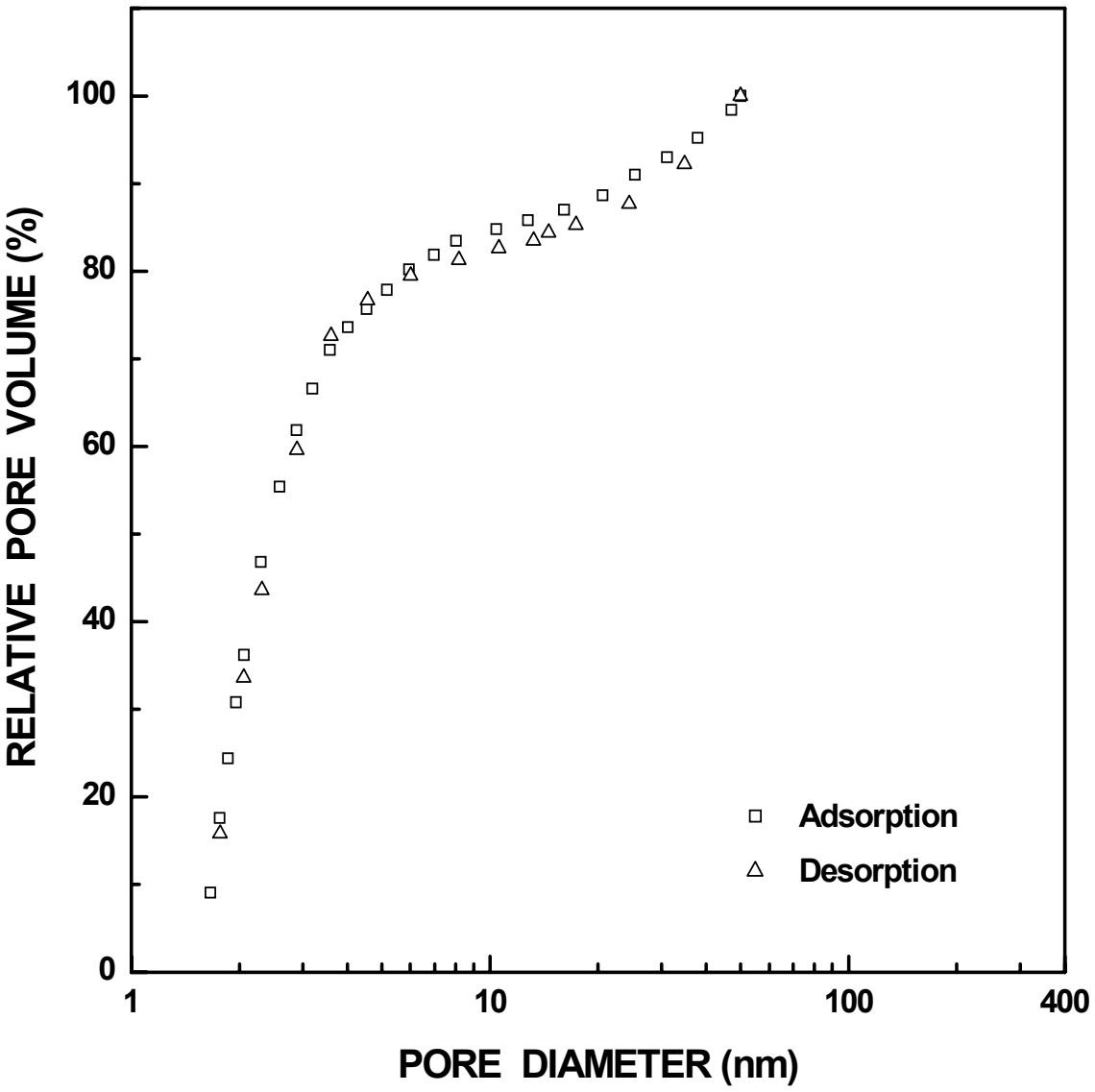

Figure I-154 Plots of relative ("normalized") pore volume vs. pore diameter for SC8-1250(40min) sample (X_{WL} = 0.11). The pore diameter was cut off at 50 nm.

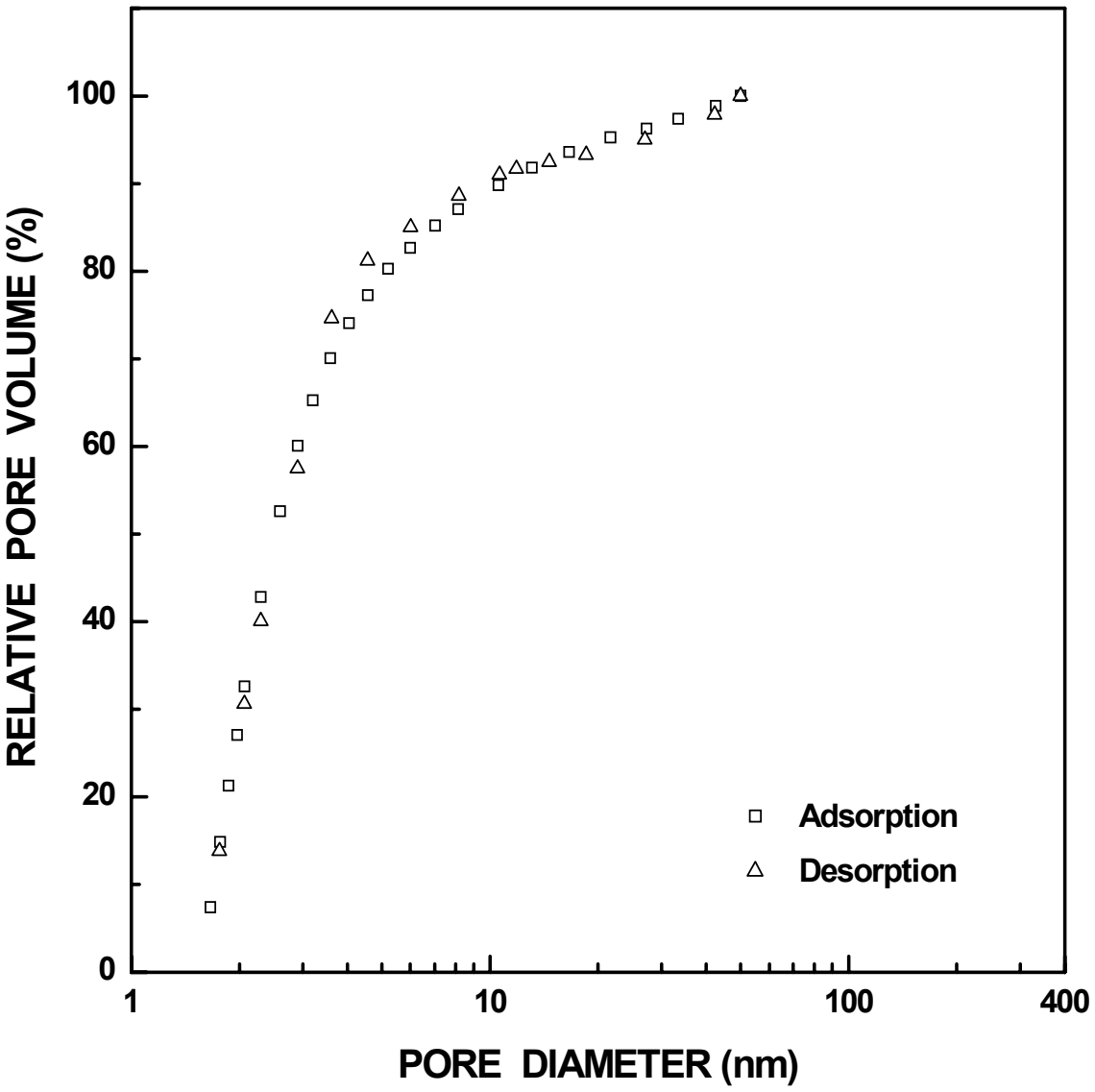

Figure I-155 Plots of relative ("normalized") pore volume vs. pore diameter for SC8-1250(1h) sample (X_{WL} = 0.16). The pore diameter was cut off at 50 nm.

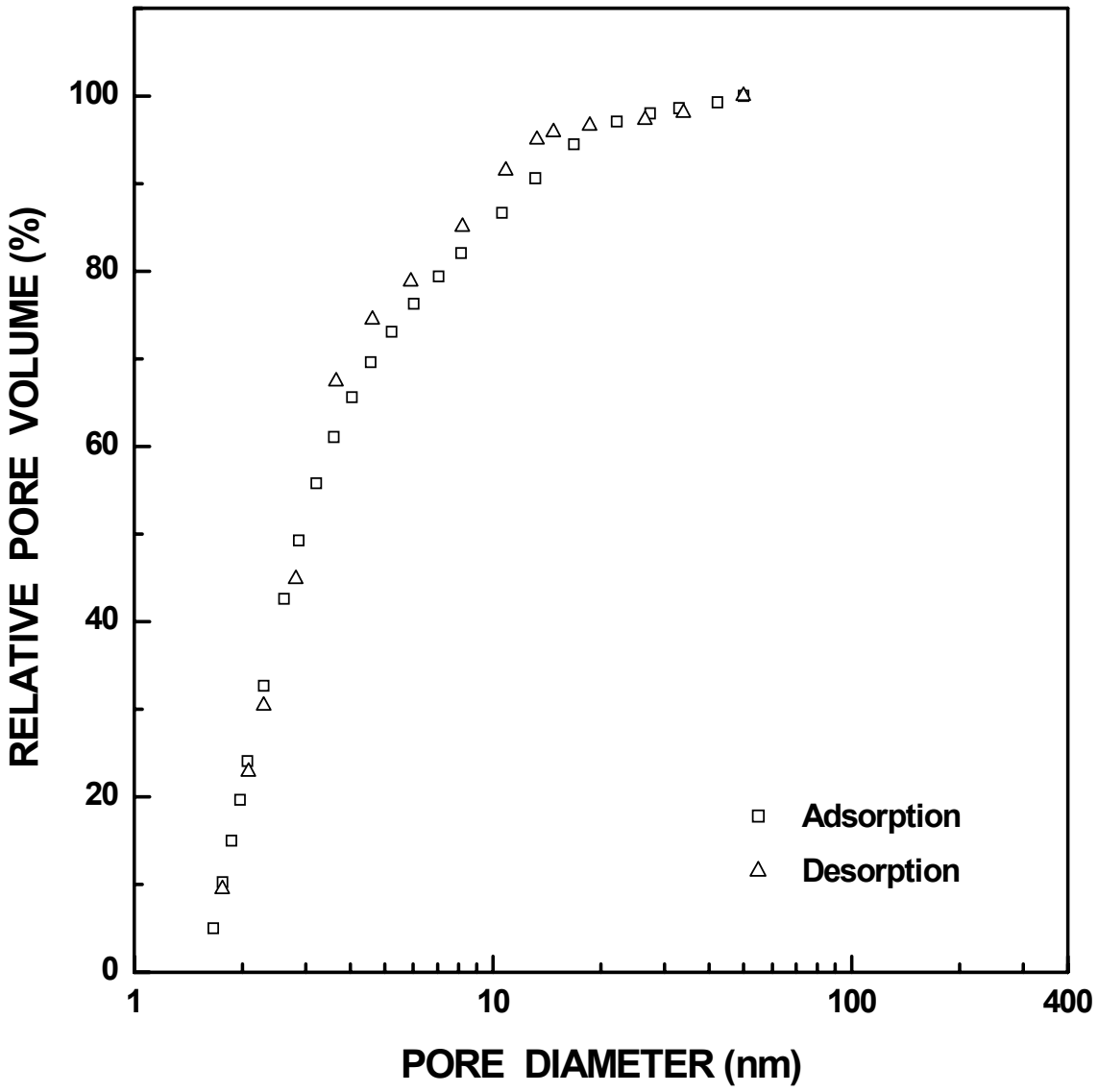

Figure I-156 Plots of relative ("normalized") pore volume vs. pore diameter for SC8-1250(2h) sample (X_{WL} = 0.31). The pore diameter was cut off at 50 nm.

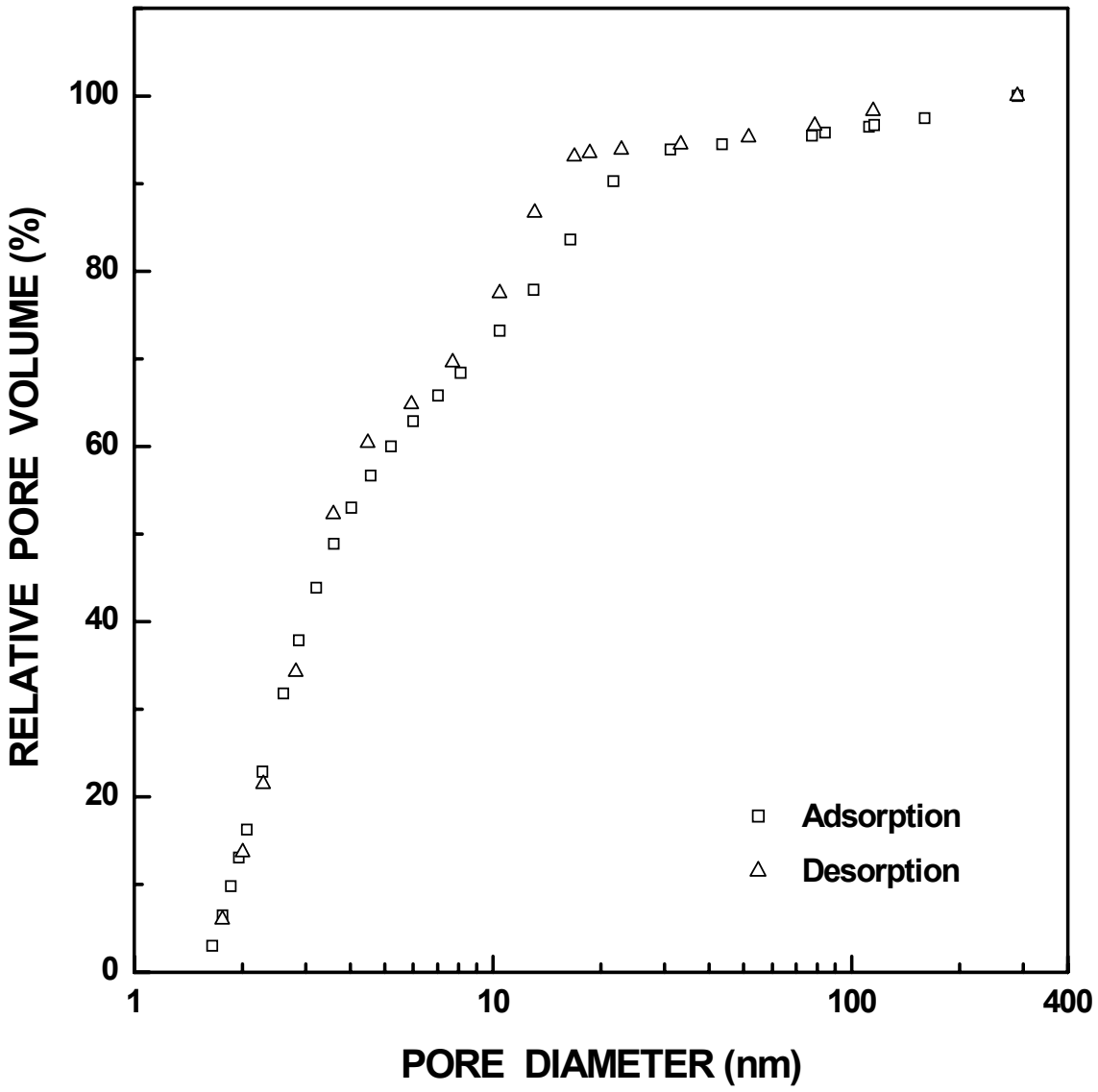

Figure I-157 Plots of relative ("normalized") pore volume vs. pore diameter for SC8-1250(4h) sample (X_{WL} = 0.54).

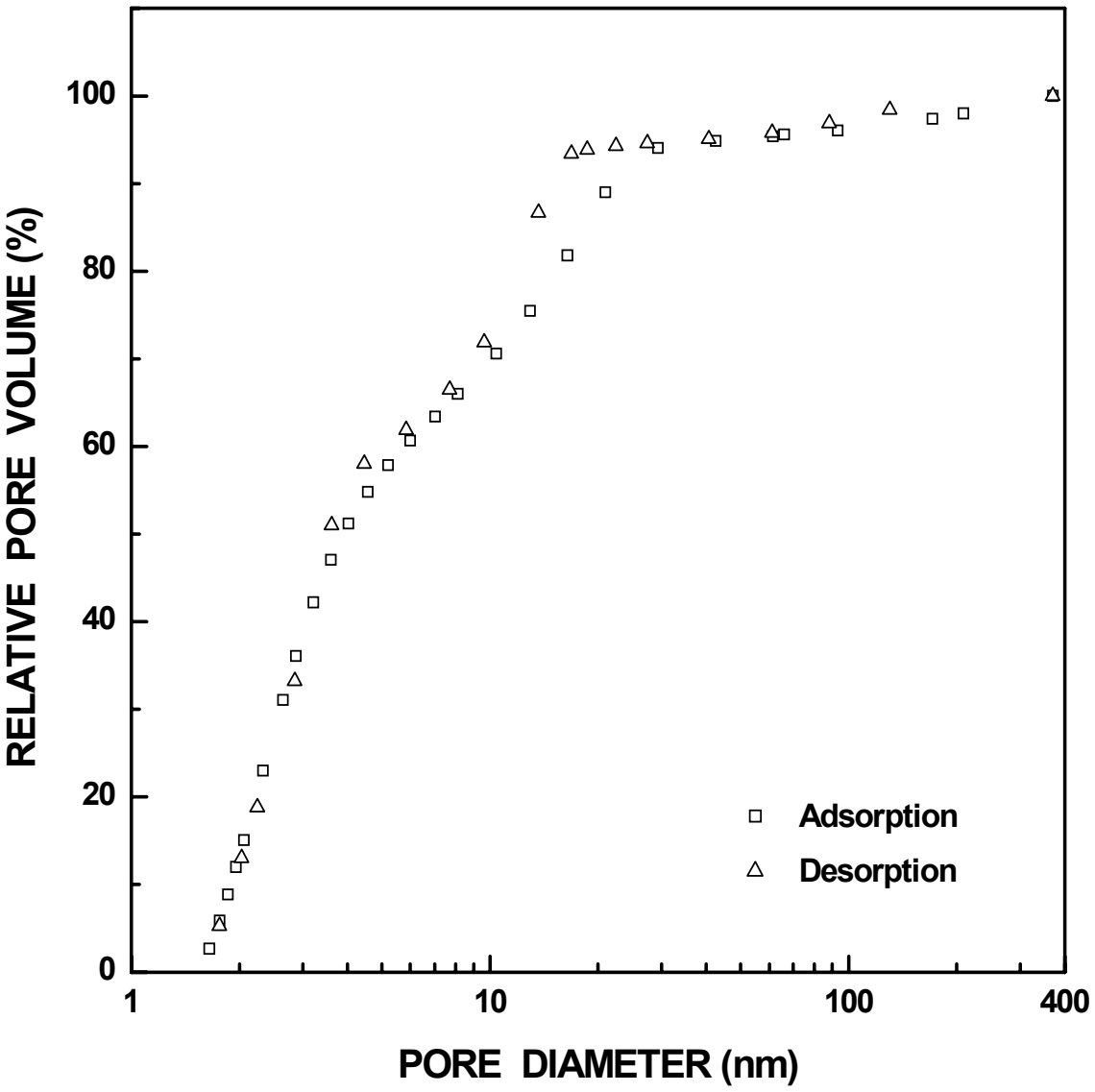

Figure I-158 Plots of relative ("normalized") pore volume vs. pore diameter for SC8-1250(5h) sample (X_{WL} = 0.61).

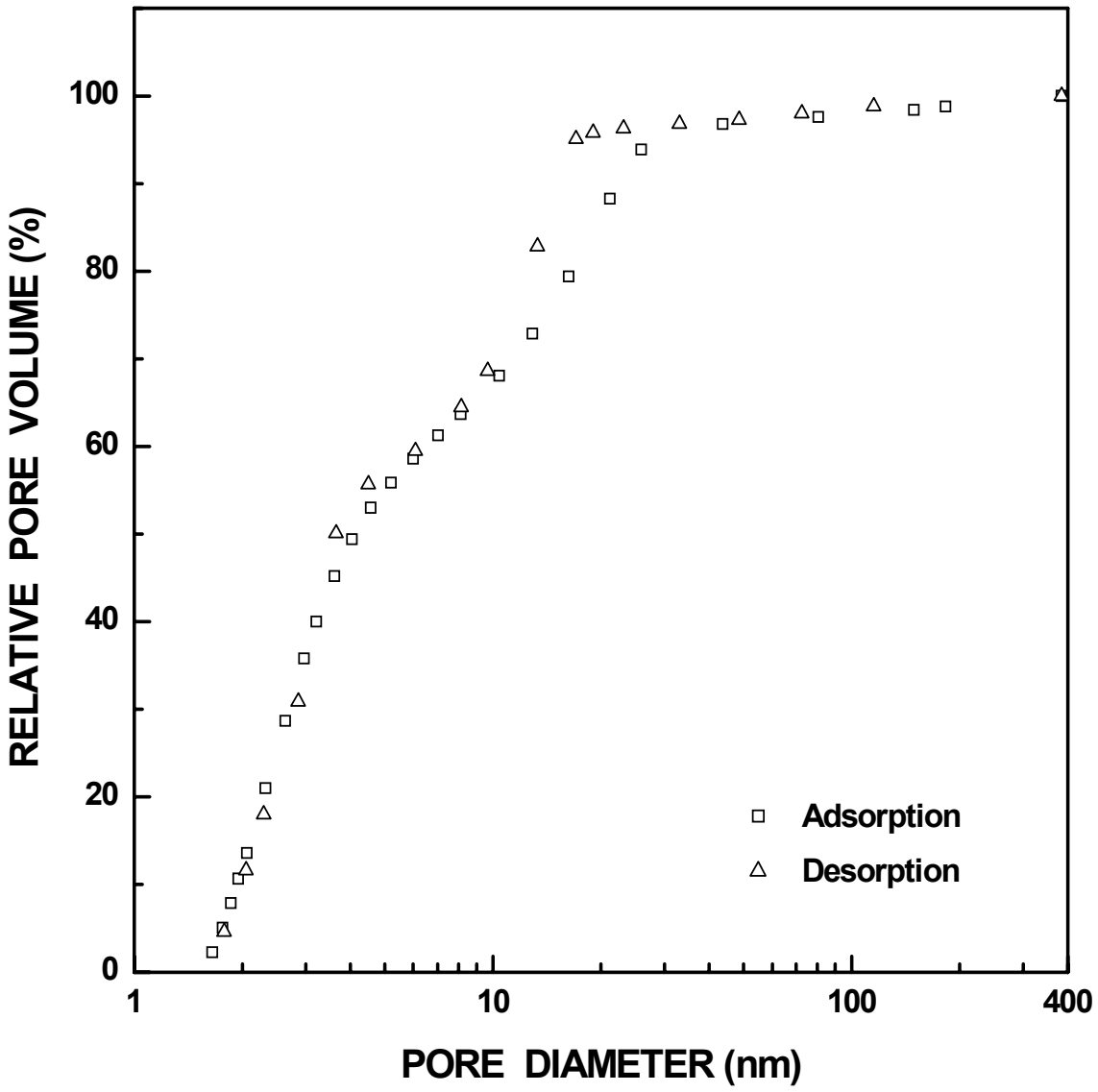

Figure I-159 Plots of relative ("normalized") pore volume vs. pore diameter for SC8-1250(6.5h) sample (X_{WL} = 0.73).

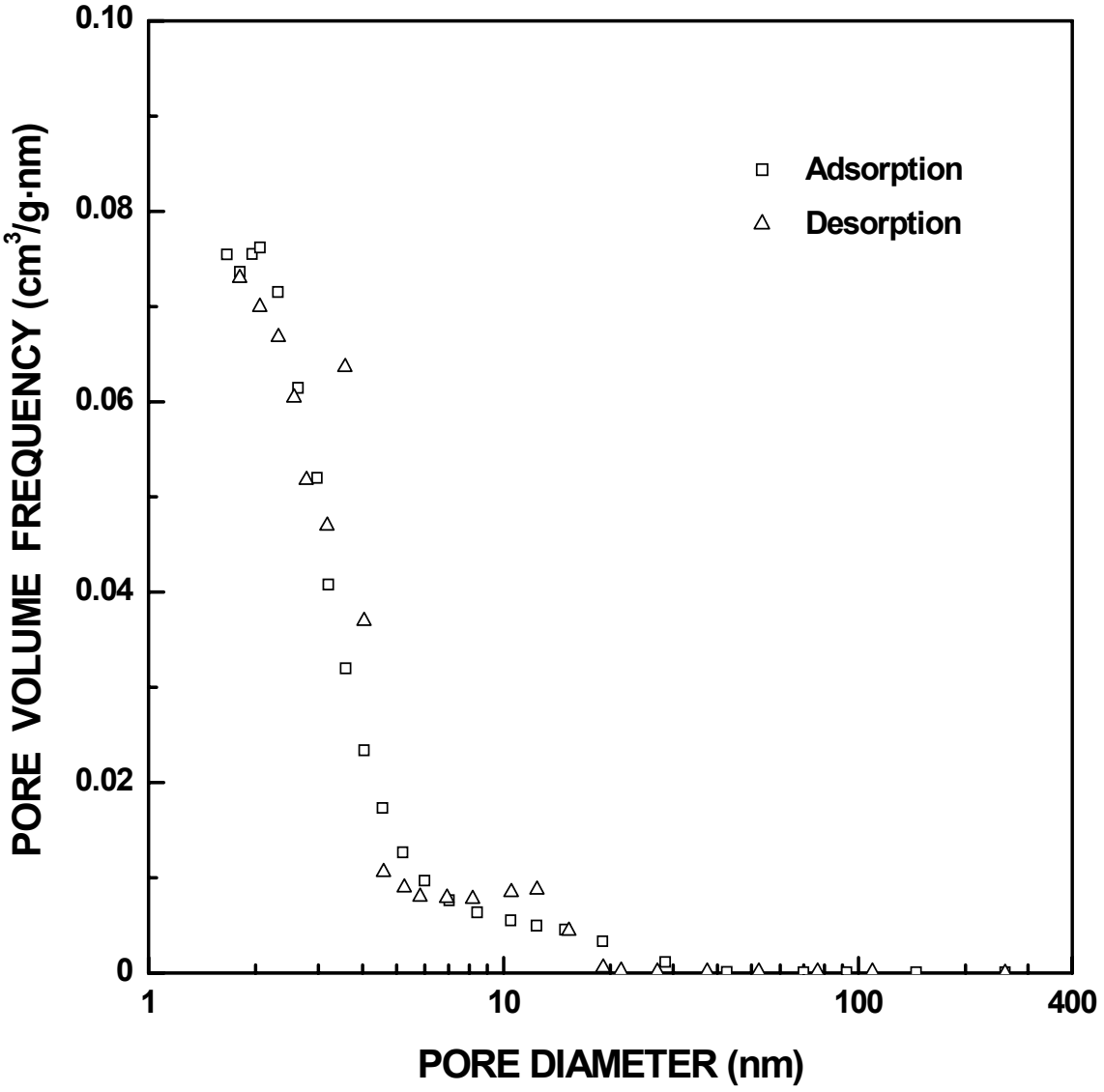

Figure I-160 Plots of specific pore volume frequency vs. pore diameter for SC8-1160(36h) sample (X_{WL} = 0.62).

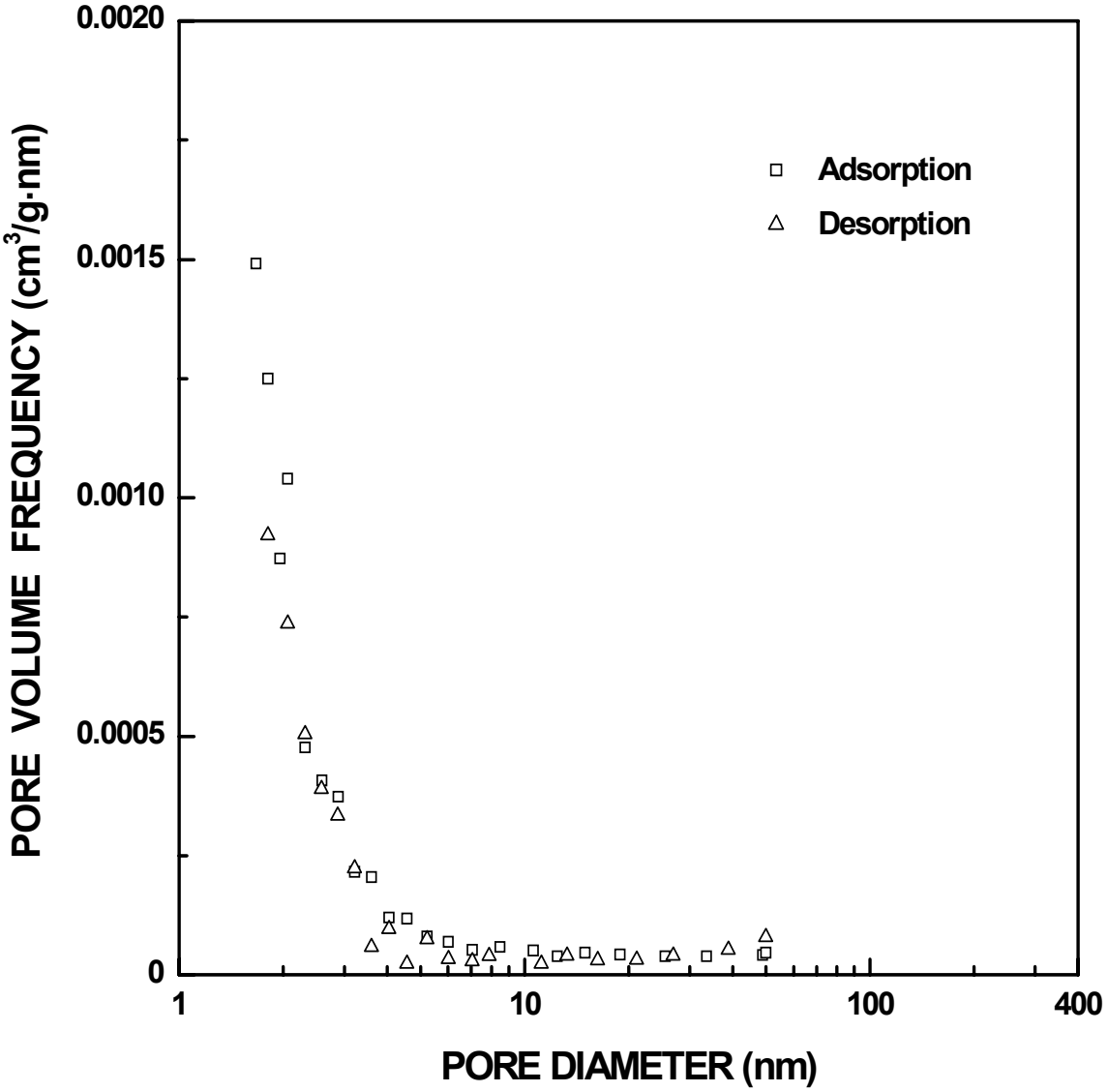

Figure I-161 Plots of specific pore volume frequency vs. pore diameter for SC8-1180(1h) sample (X_{WL} = 0.08). The pore diameter was cut off at 50 nm.

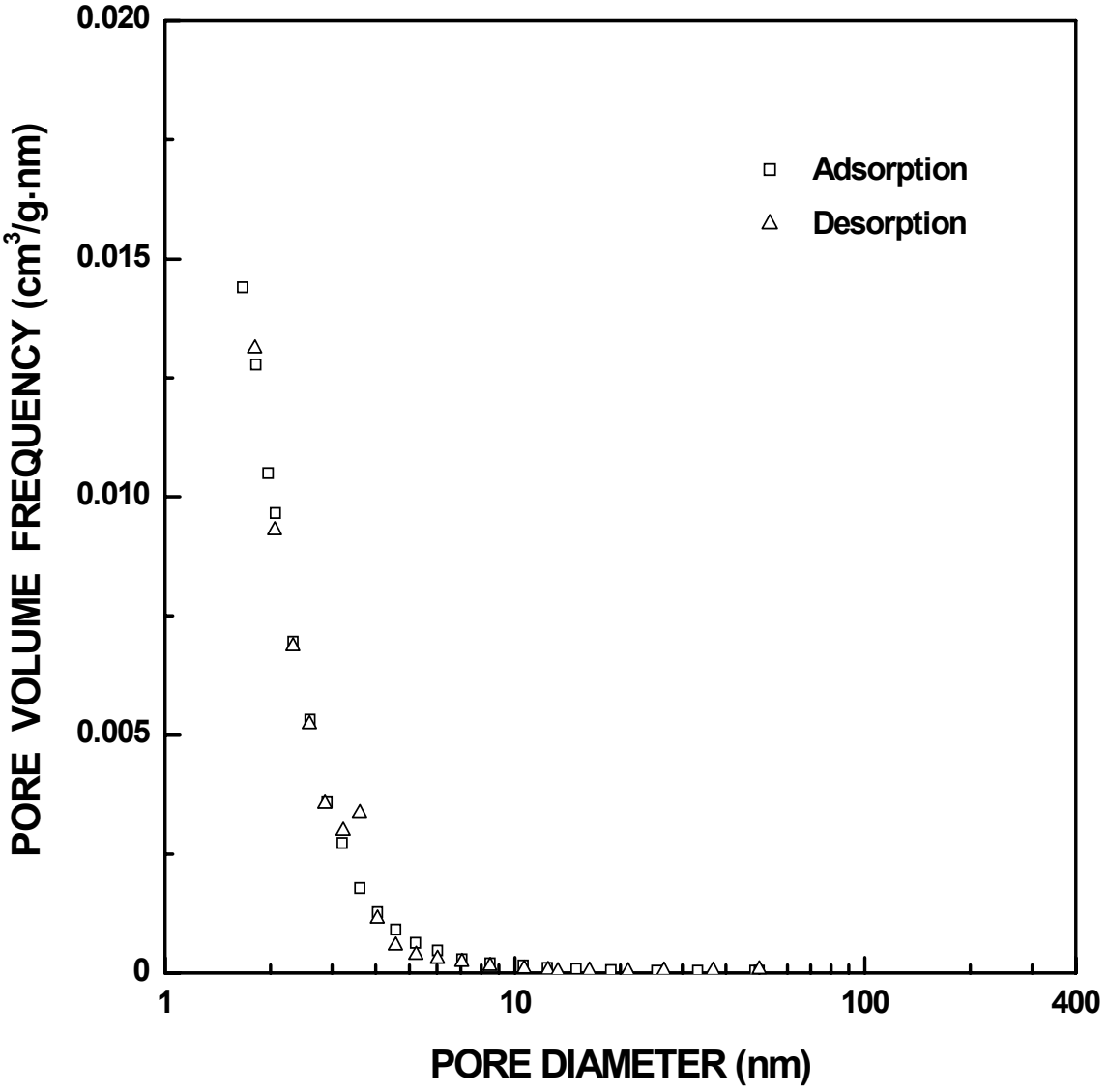

Figure I-162 Plots of specific pore volume frequency vs. pore diameter for SC8-1180(4h) sample (X_{WL} = 0.18). The pore diameter was cut off at 50 nm.

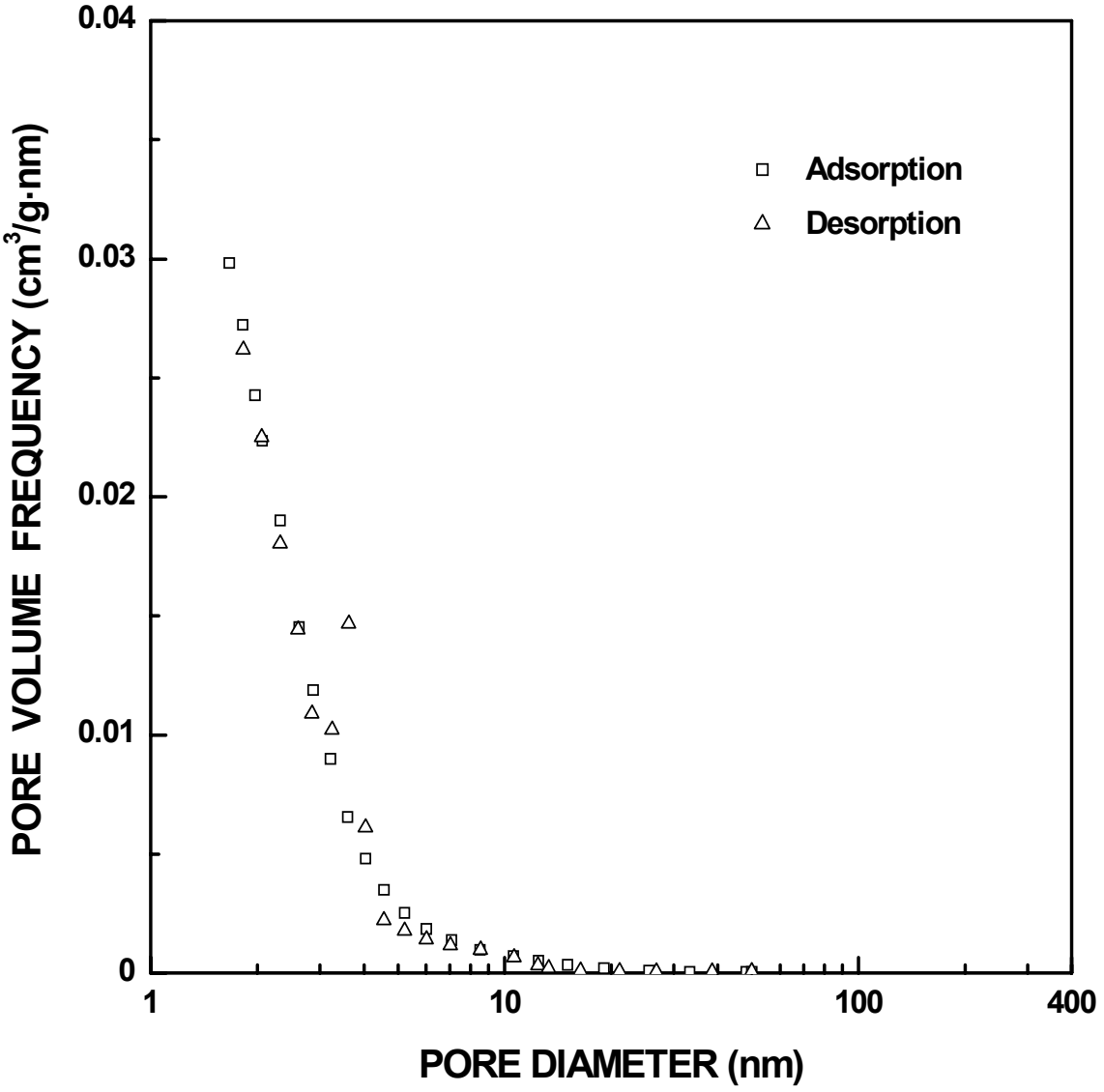

Figure I-163 Plots of specific pore volume frequency vs. pore diameter for SC8-1180(8h) sample (X_{WL} = 0.31). The pore diameter was cut off at 50 nm.

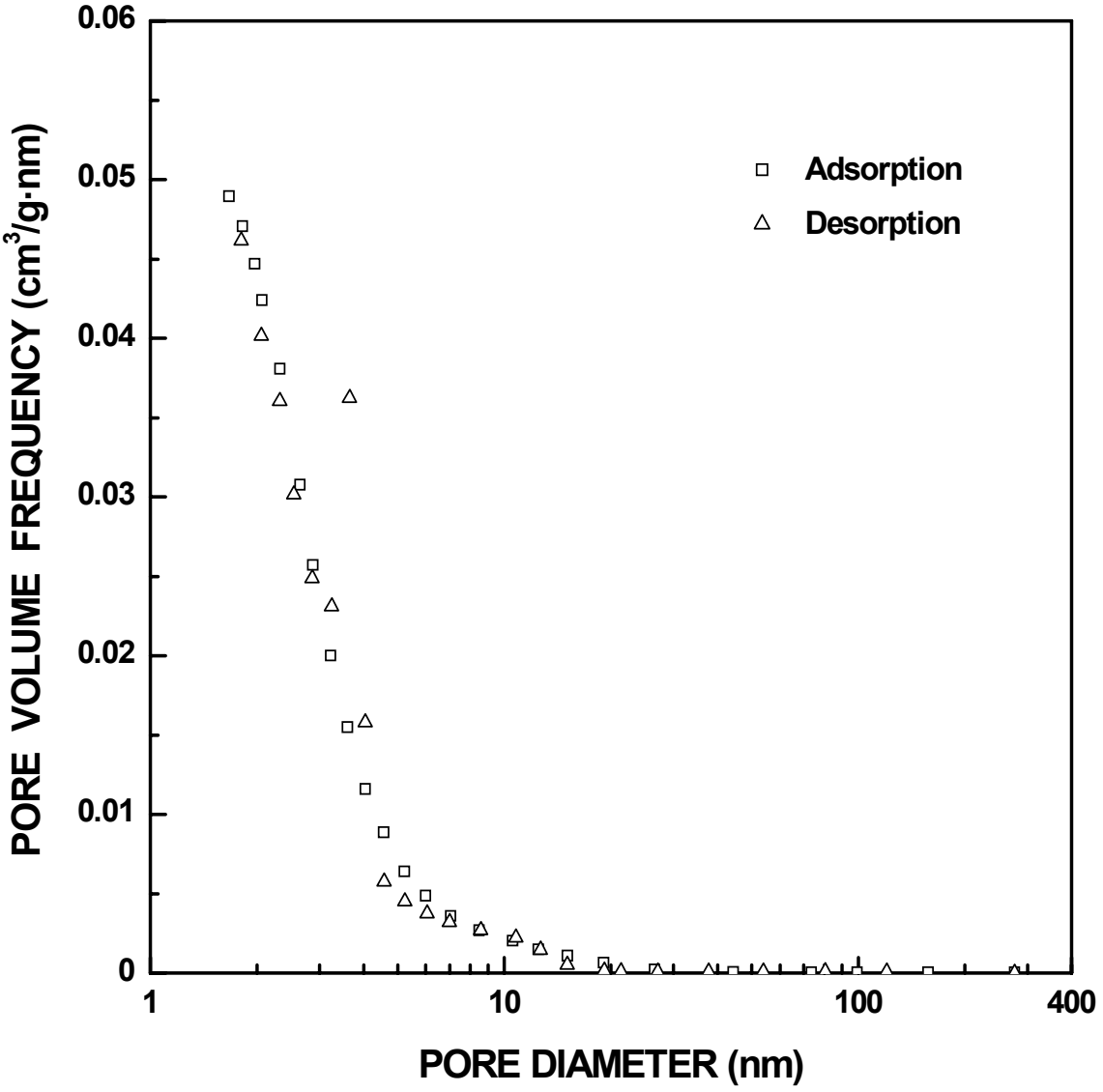

Figure I-164 Plots of specific pore volume frequency vs. pore diameter for SC8-1180(12h) sample (X_{WL} = 0.43).

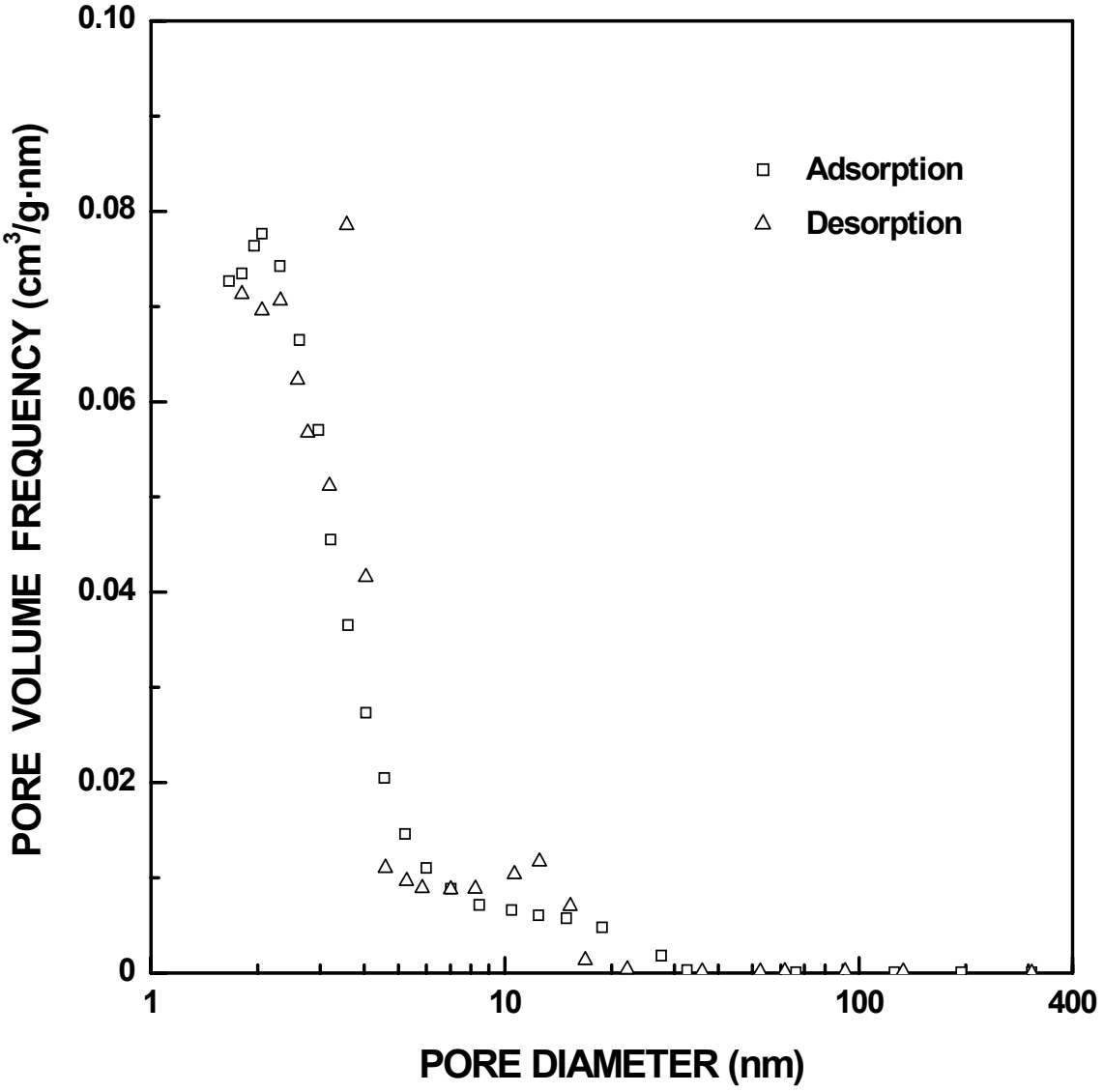

Figure I-165 Plots of specific pore volume frequency vs. pore diameter for SC8-1180(24h) sample (X_{WL} = 0.70).

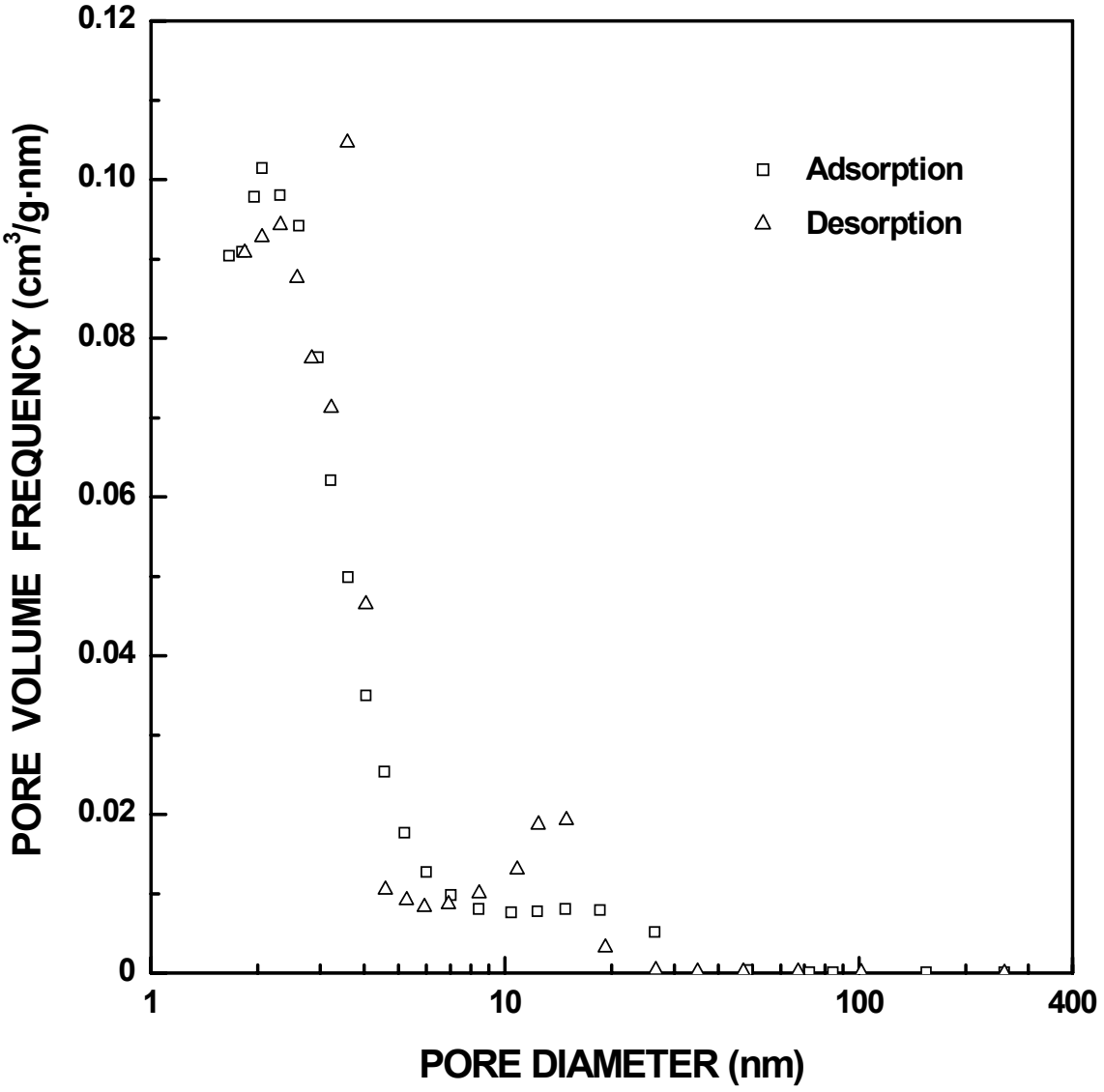

Figure I-166 Plots of specific pore volume frequency vs. pore diameter for SC8-1180(36h) sample (X_{WL} = 0.82).

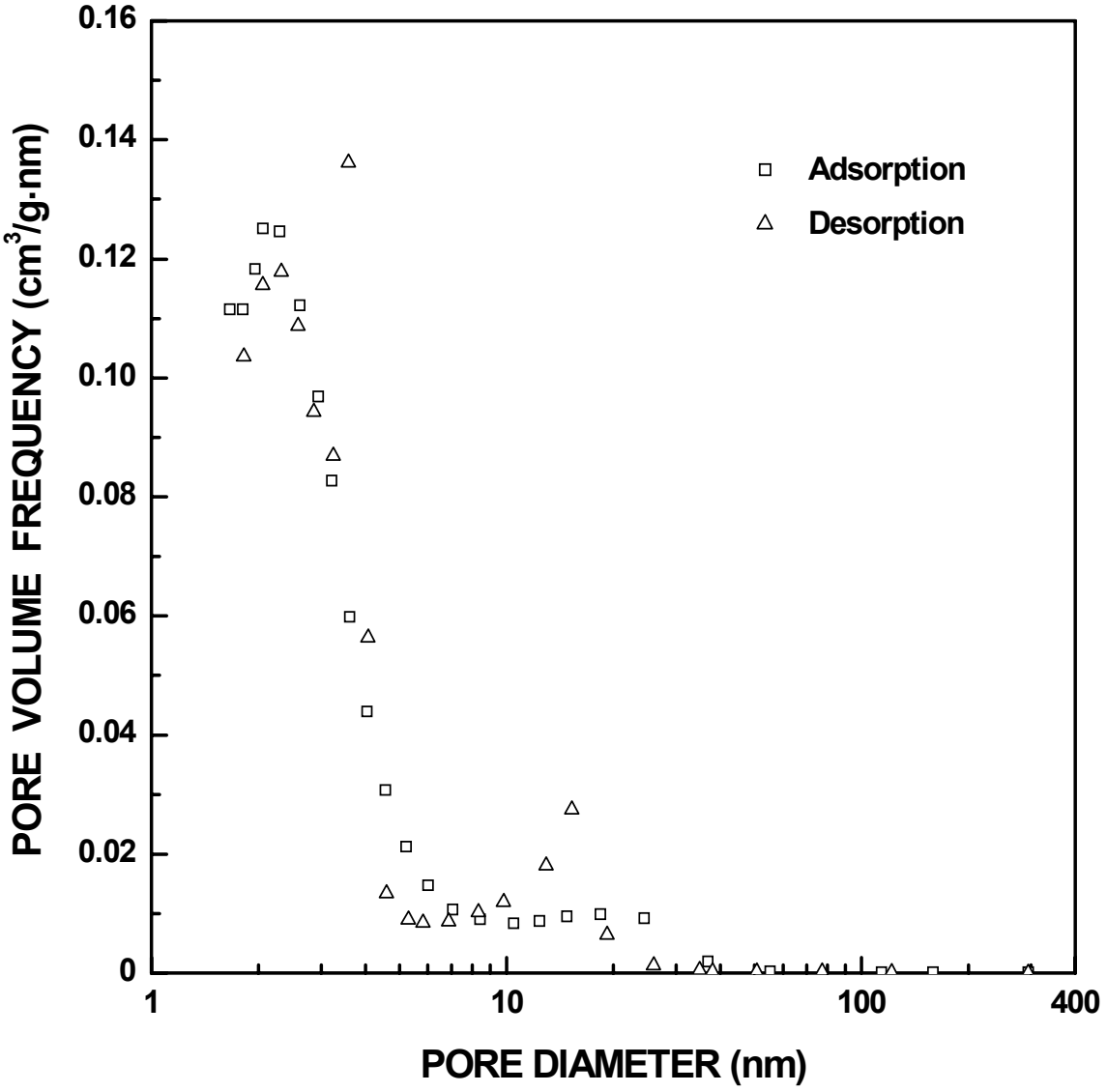

Figure I-167 Plots of specific pore volume frequency vs. pore diameter for SC8-1180(48h) sample (X_{WL} = 0.92).

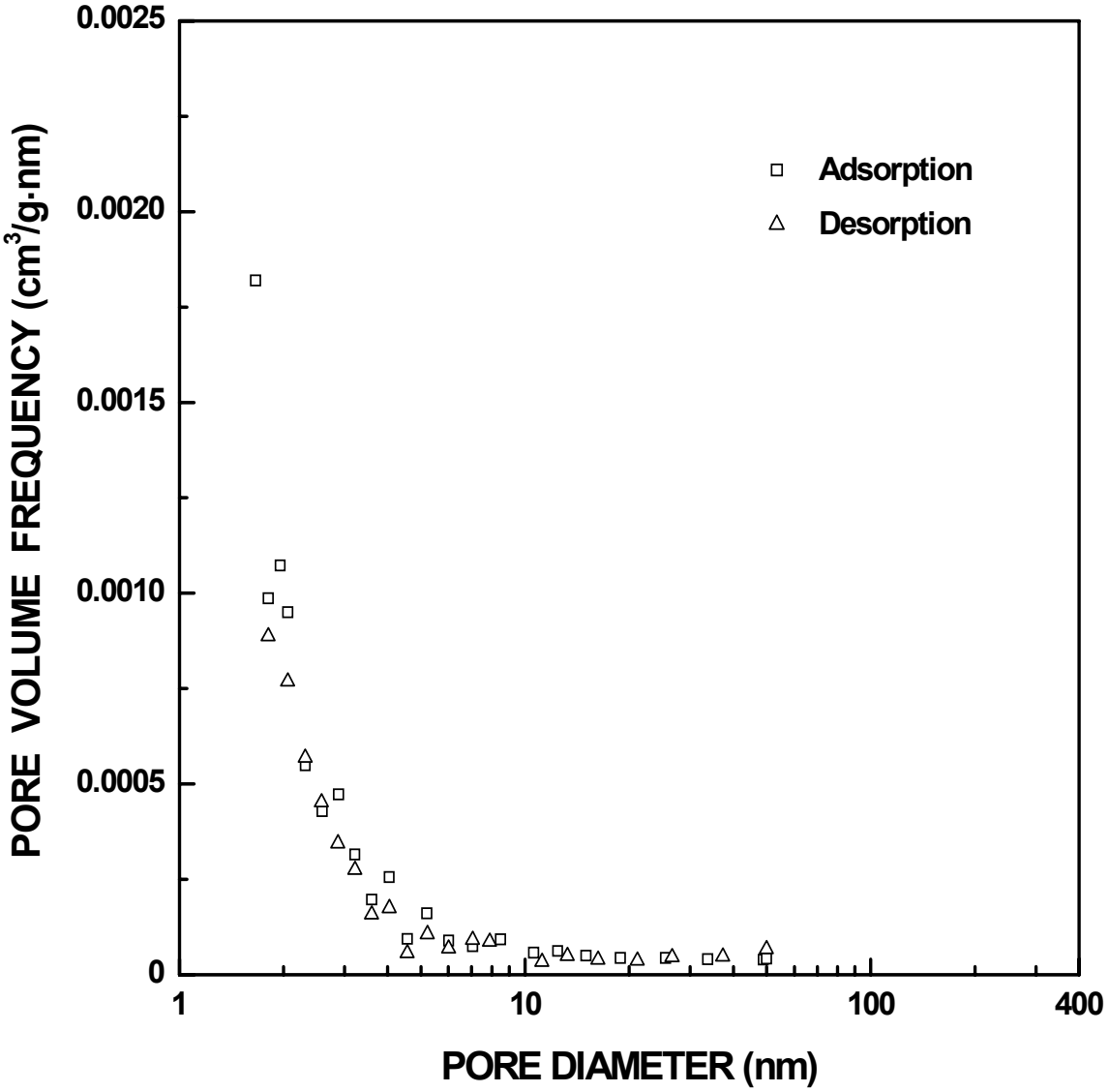

Figure I-168 Plots of specific pore volume frequency vs. pore diameter for SC8-1200(30min) sample (X_{WL} = 0.05). The pore diameter was cut off at 50 nm.

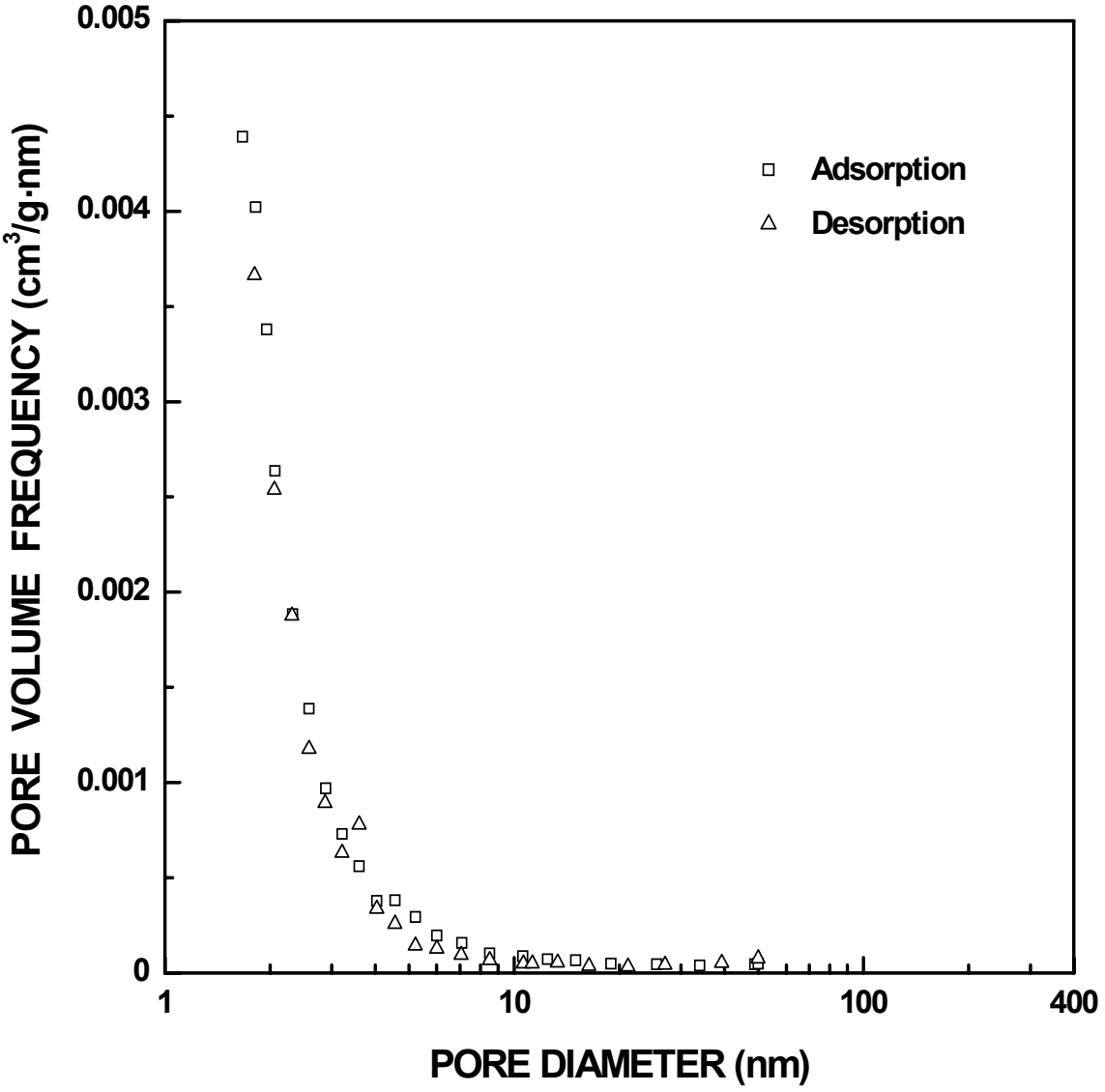

Figure I-169 Plots of specific pore volume frequency vs. pore diameter for SC8-1200(1h) sample (X_{WL} = 0.05). The pore diameter was cut off at 50 nm.

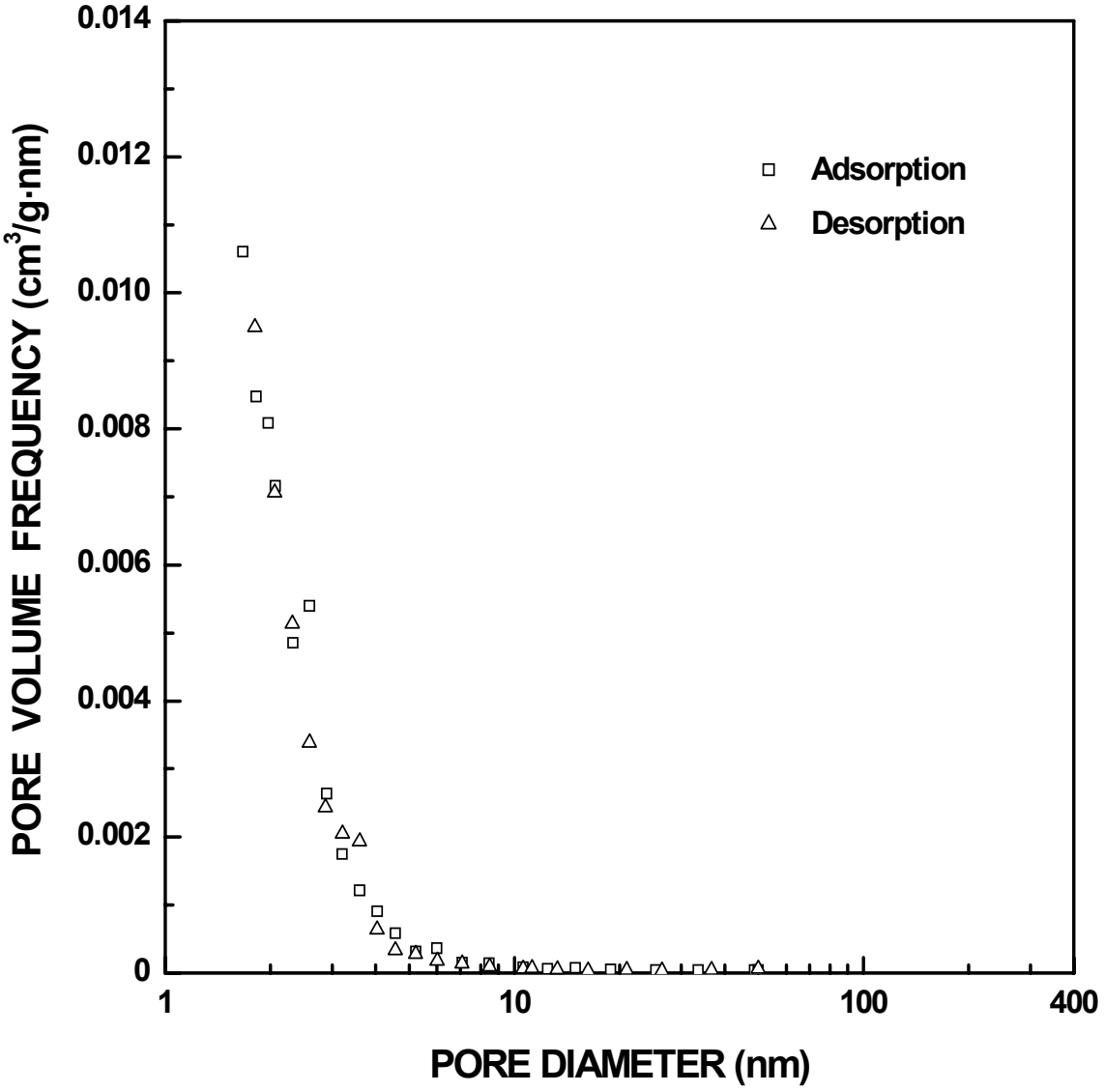

Figure I-170 Plots of specific pore volume frequency vs. pore diameter for SC8-1200(2h) sample (X_{WL} = 0.11). The pore diameter was cut off at 50 nm.

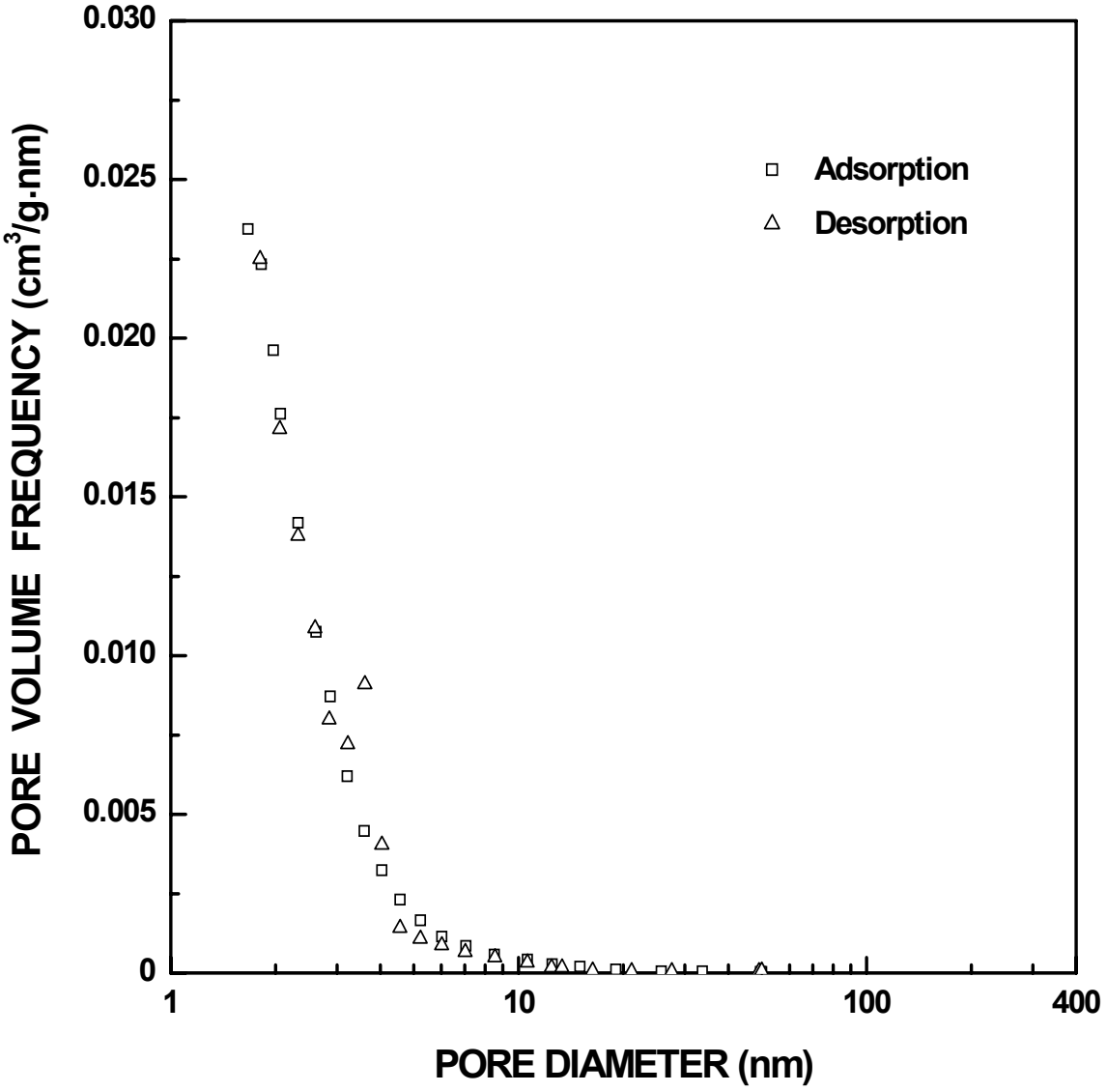

Figure I-171 Plots of specific pore volume frequency vs. pore diameter for SC8-1200(4h) sample (X_{WL} = 0.19). The pore diameter was cut off at 50 nm.

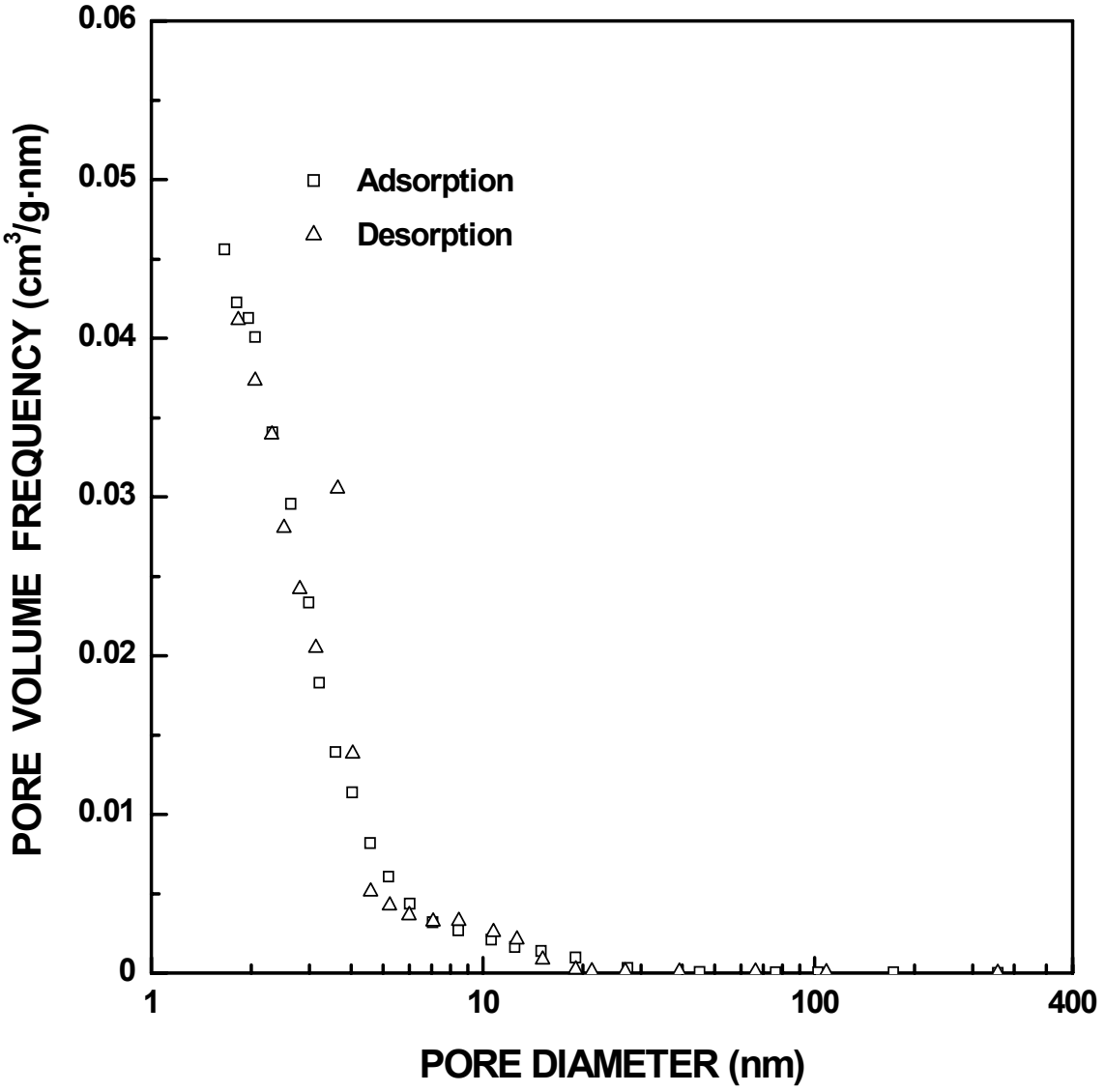

Figure I-172 Plots of specific pore volume frequency vs. pore diameter for SC8-1200(8h) sample (X_{WL} = 0.40).

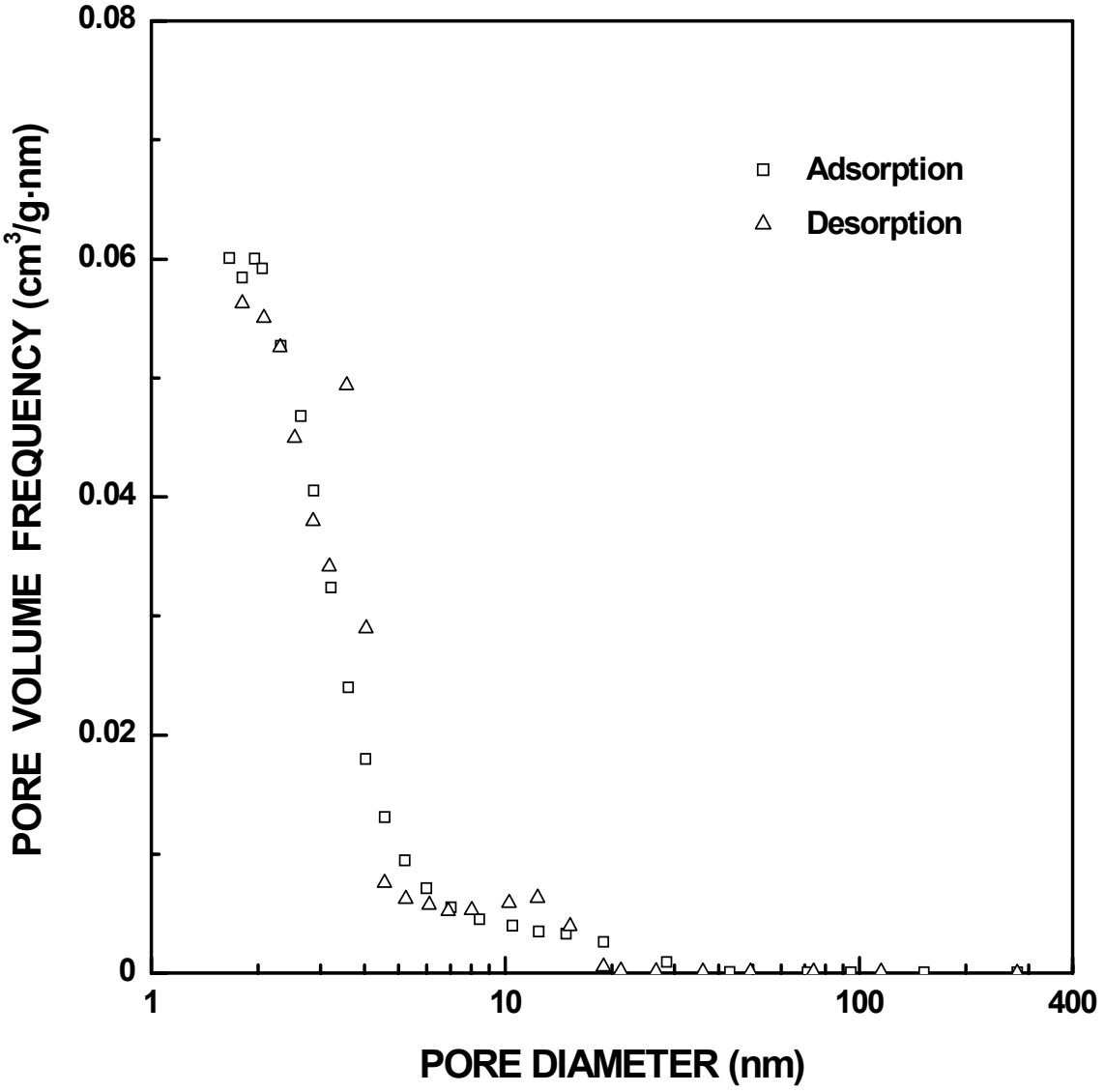

Figure I-173 Plots of specific pore volume frequency vs. pore diameter for SC8-1200(12h) sample (X_{WL} = 0.54).

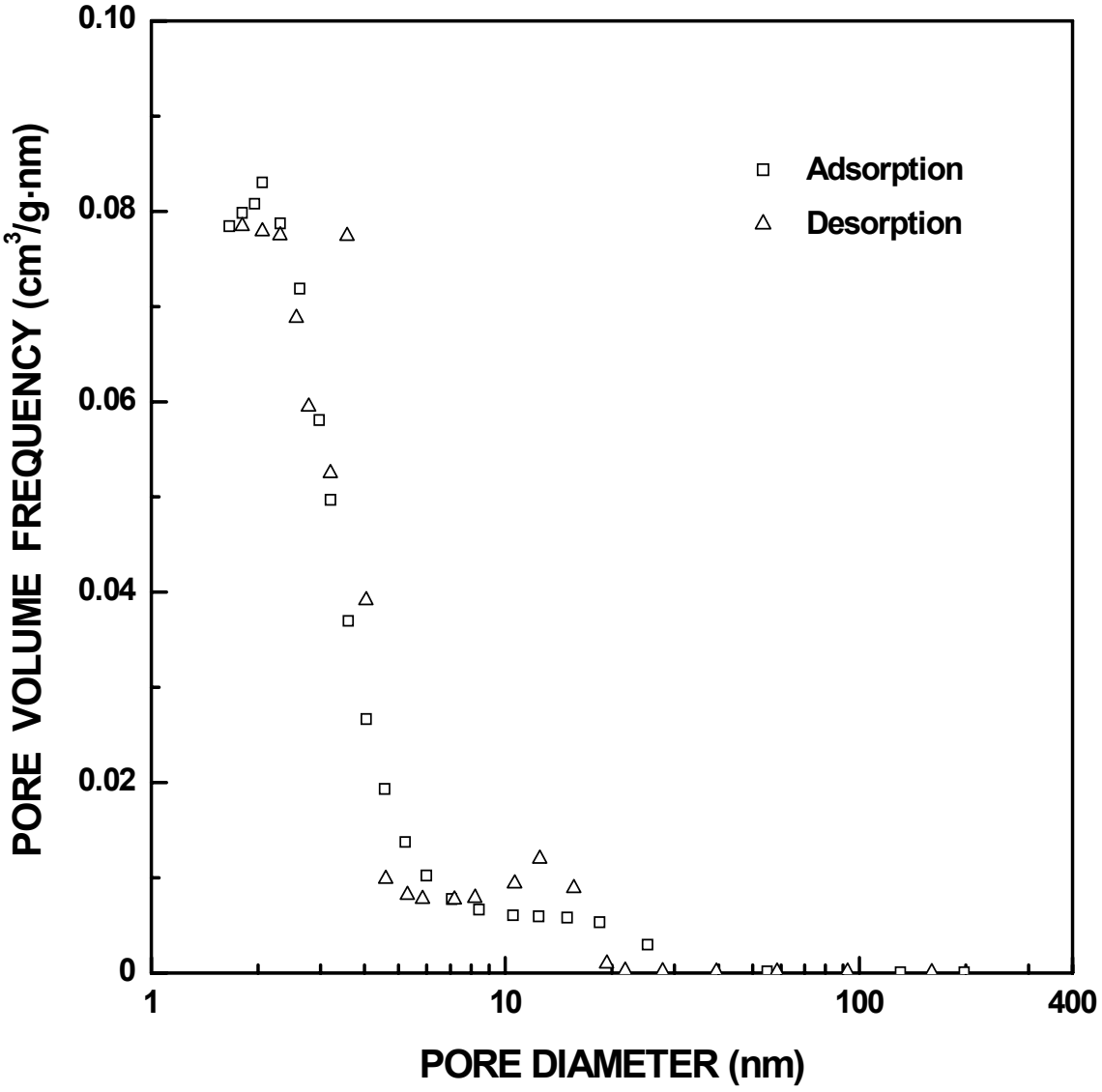

Figure I-174 Plots of specific pore volume frequency vs. pore diameter for SC8-1200(16h) sample (X_{WL} = 0.68).

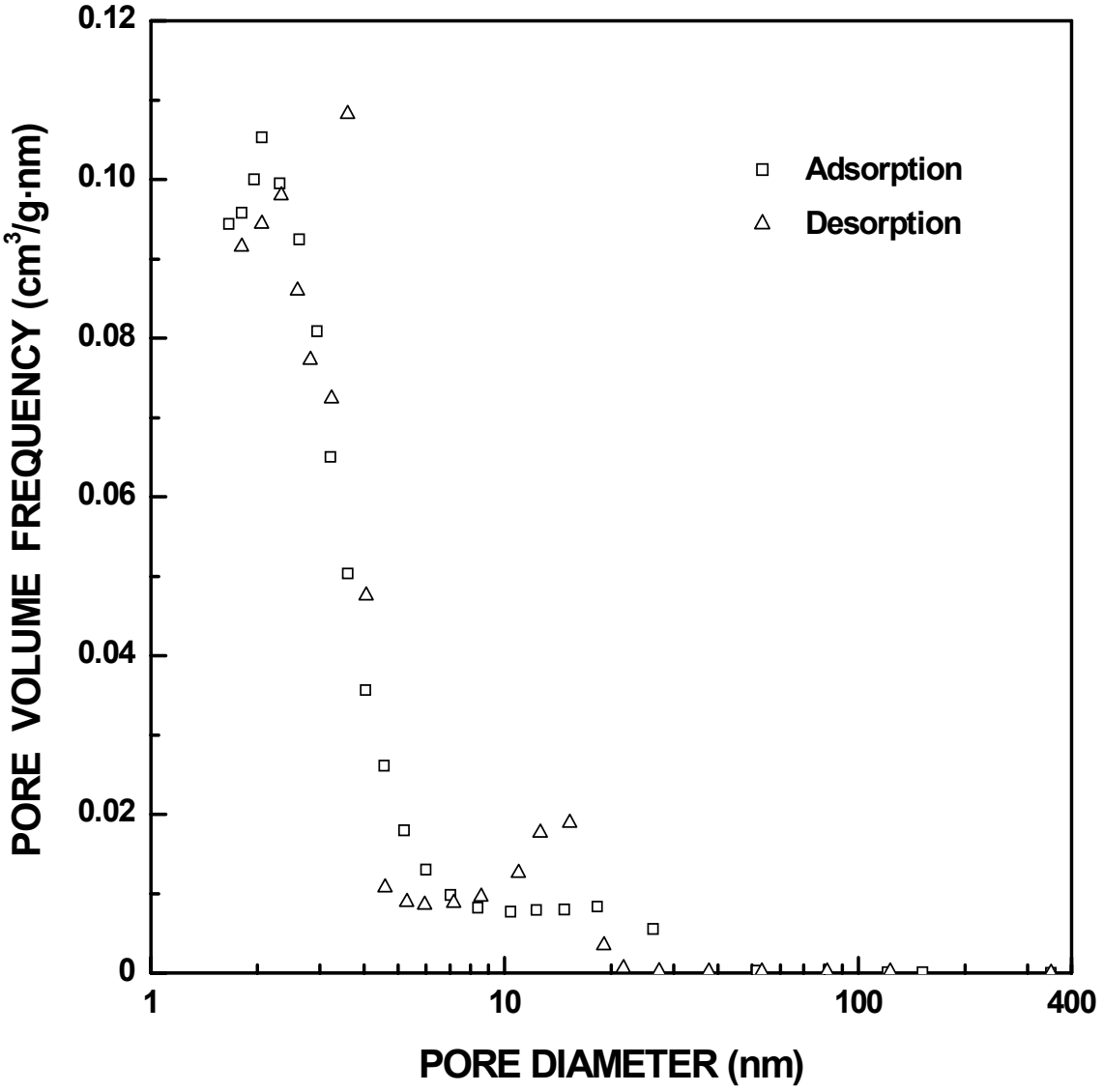

Figure I-175 Plots of specific pore volume frequency vs. pore diameter for SC8-1200(22h) sample (X_{WL} = 0.80).

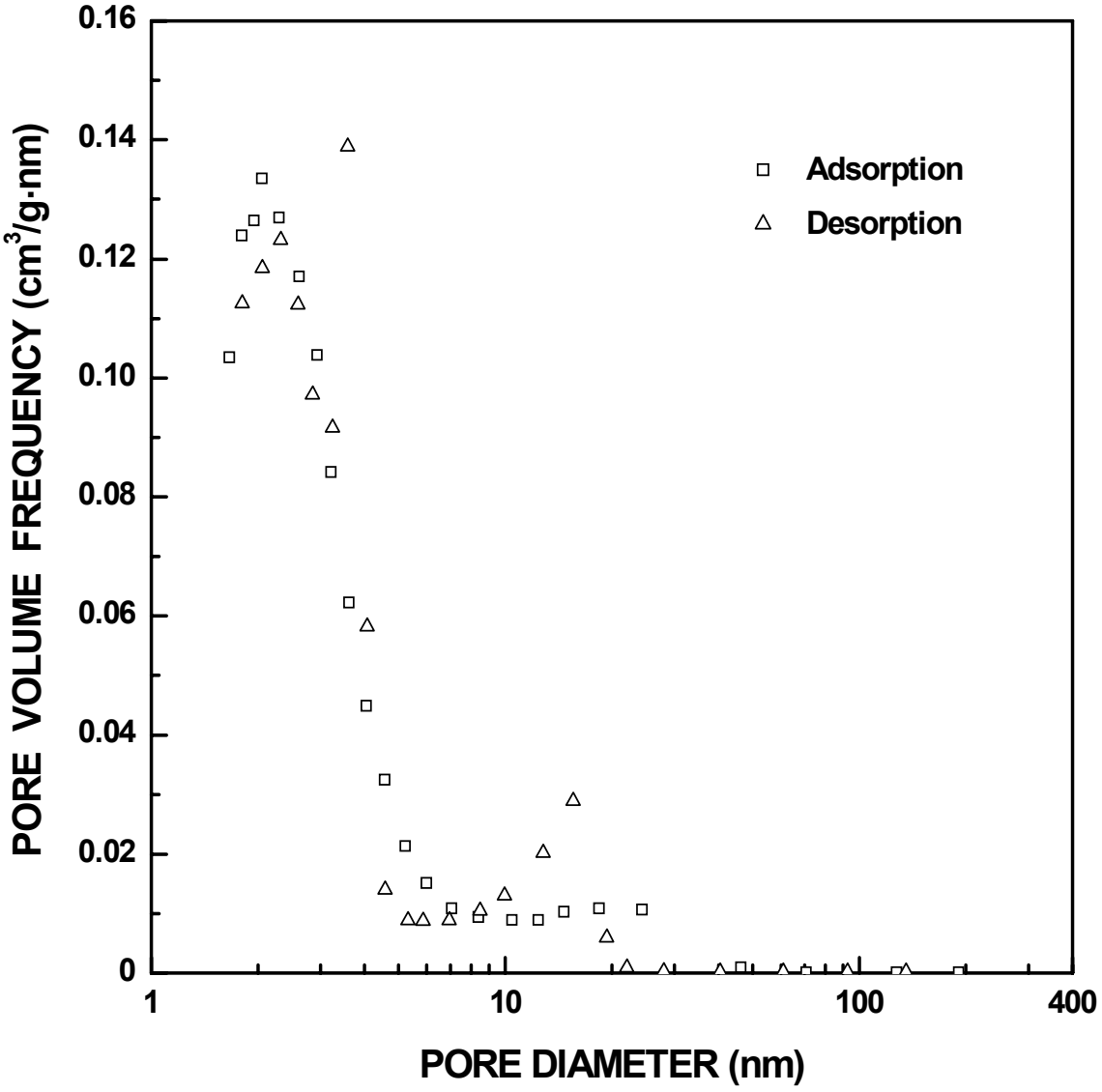

Figure I-176 Plots of specific pore volume frequency vs. pore diameter for SC8-1200(32h) sample (X_{WL} = 0.91).

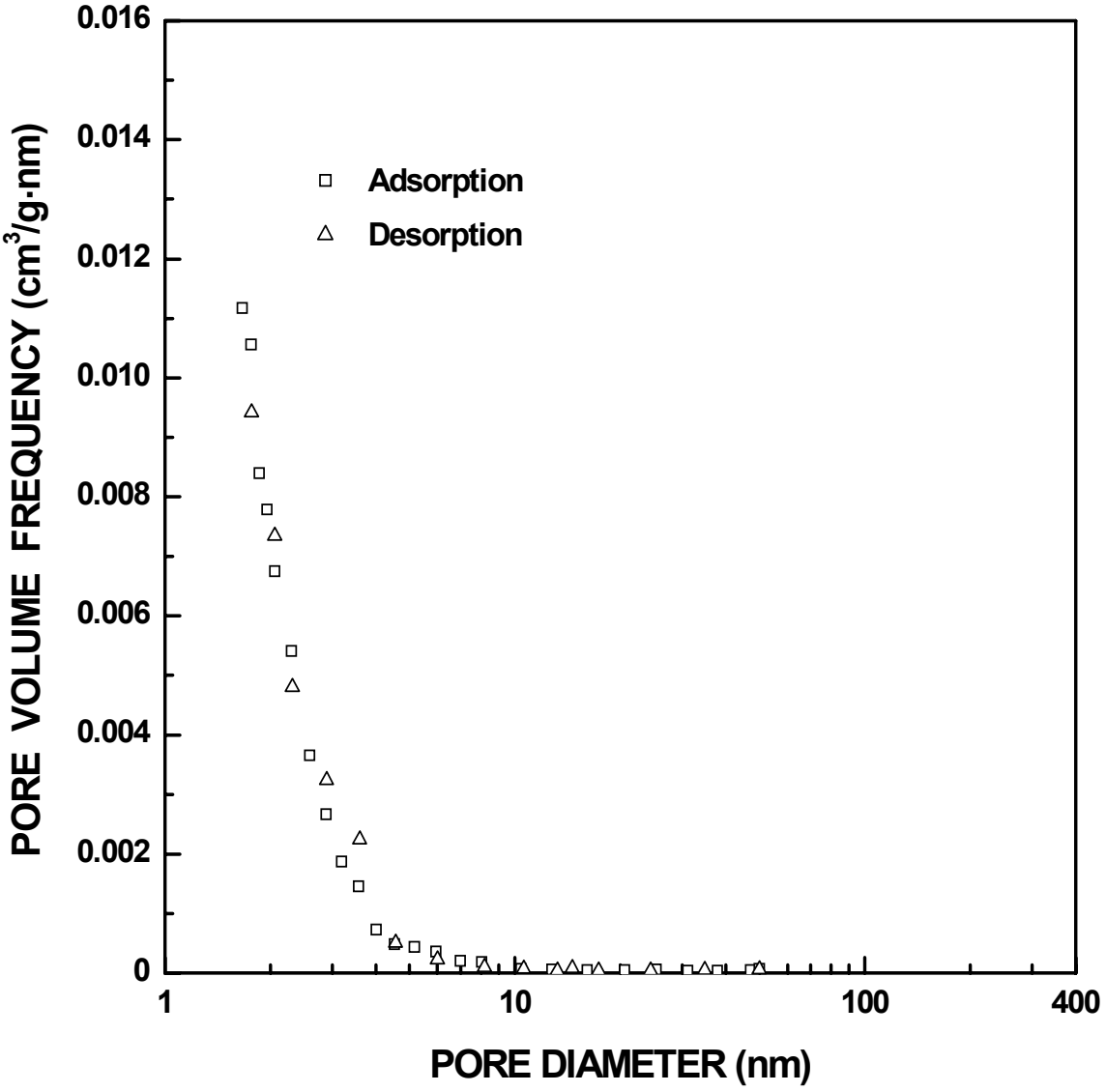

Figure I-177 Plots of specific pore volume frequency vs. pore diameter for SC8-1250(40min) sample (X_{WL} = 0.11). The pore diameter was cut off at 50 nm.

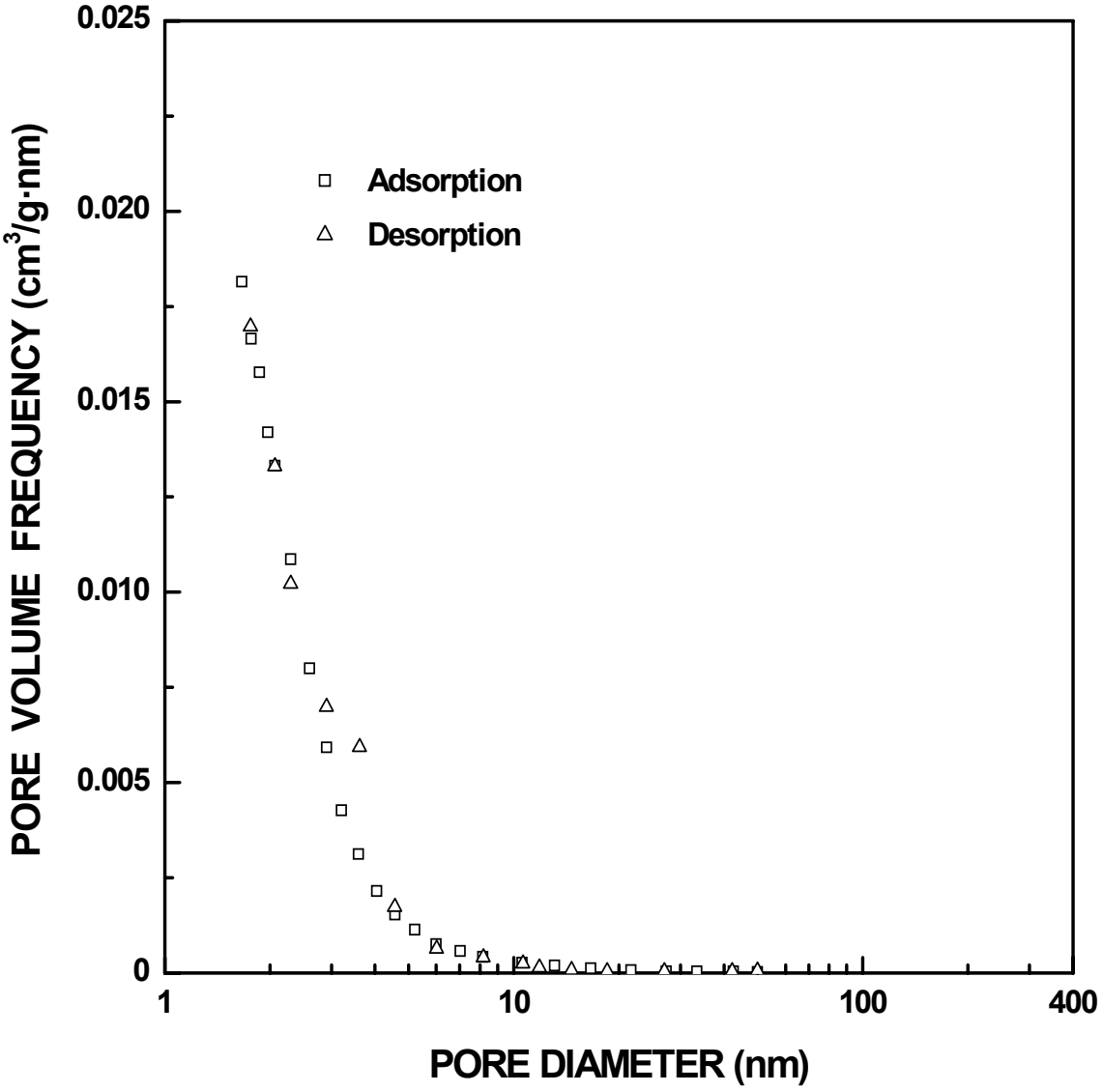

Figure I-178 Plots of specific pore volume frequency vs. pore diameter for SC8-1250(1h) sample (X_{WL} = 0.16). The pore diameter was cut off at 50 nm.

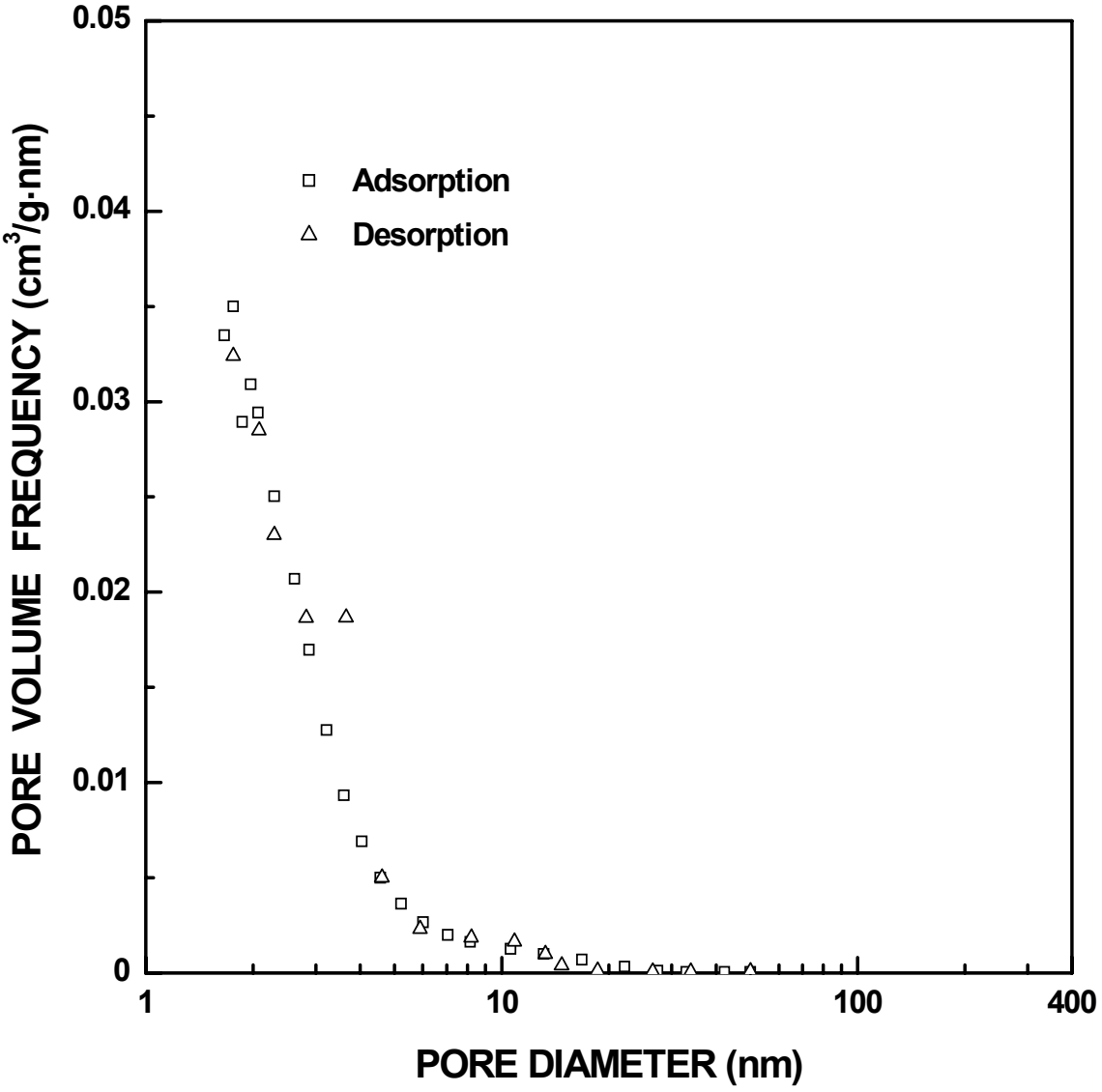

Figure I-179 Plots of specific pore volume frequency vs. pore diameter for SC8-1250(2h) sample (X_{WL} = 0.31). The pore diameter was cut off at 50 nm.

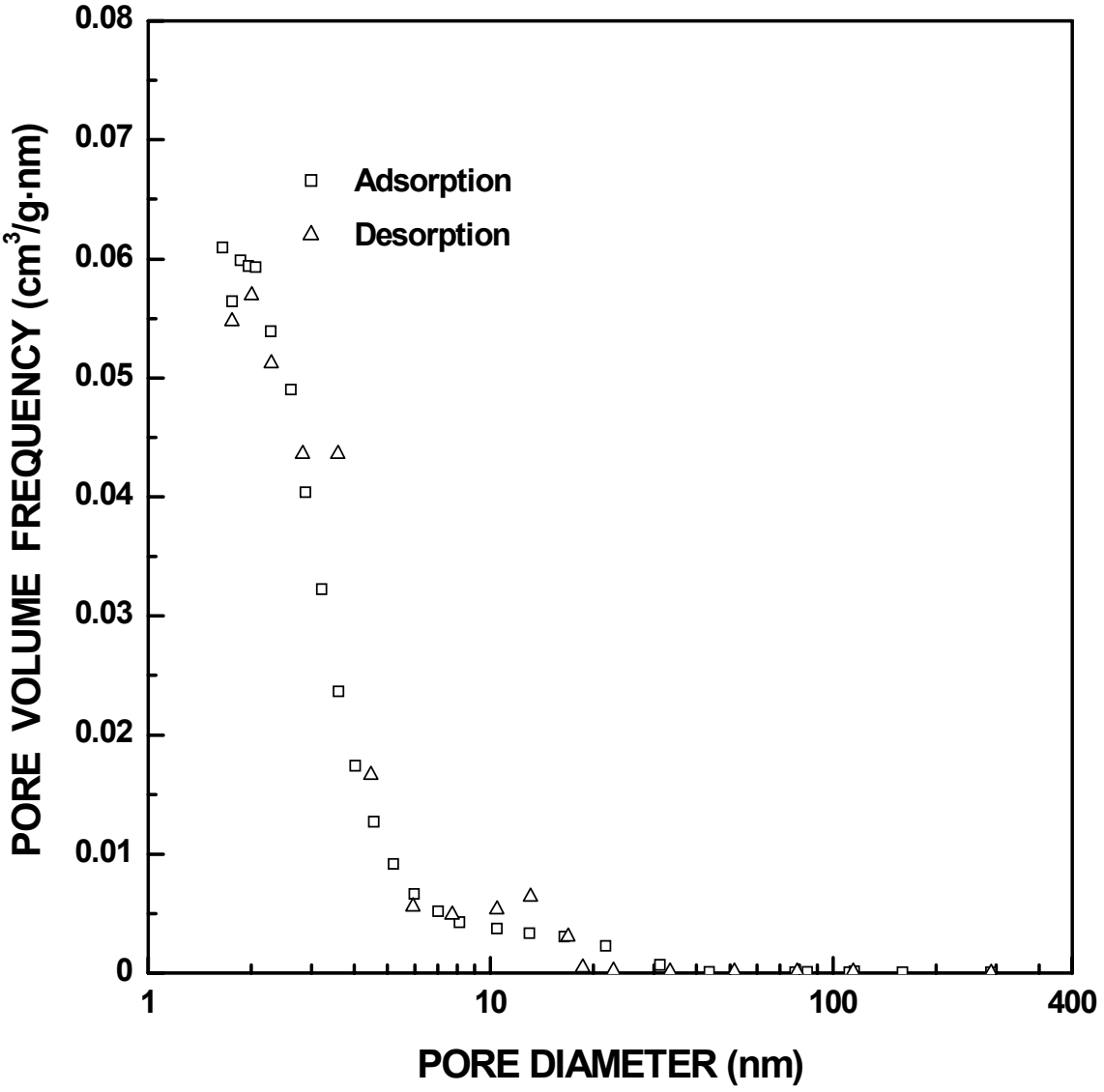

Figure I-180 Plots of specific pore volume frequency vs. pore diameter for SC8-1250(4h) sample (X_{WL} = 0.54).

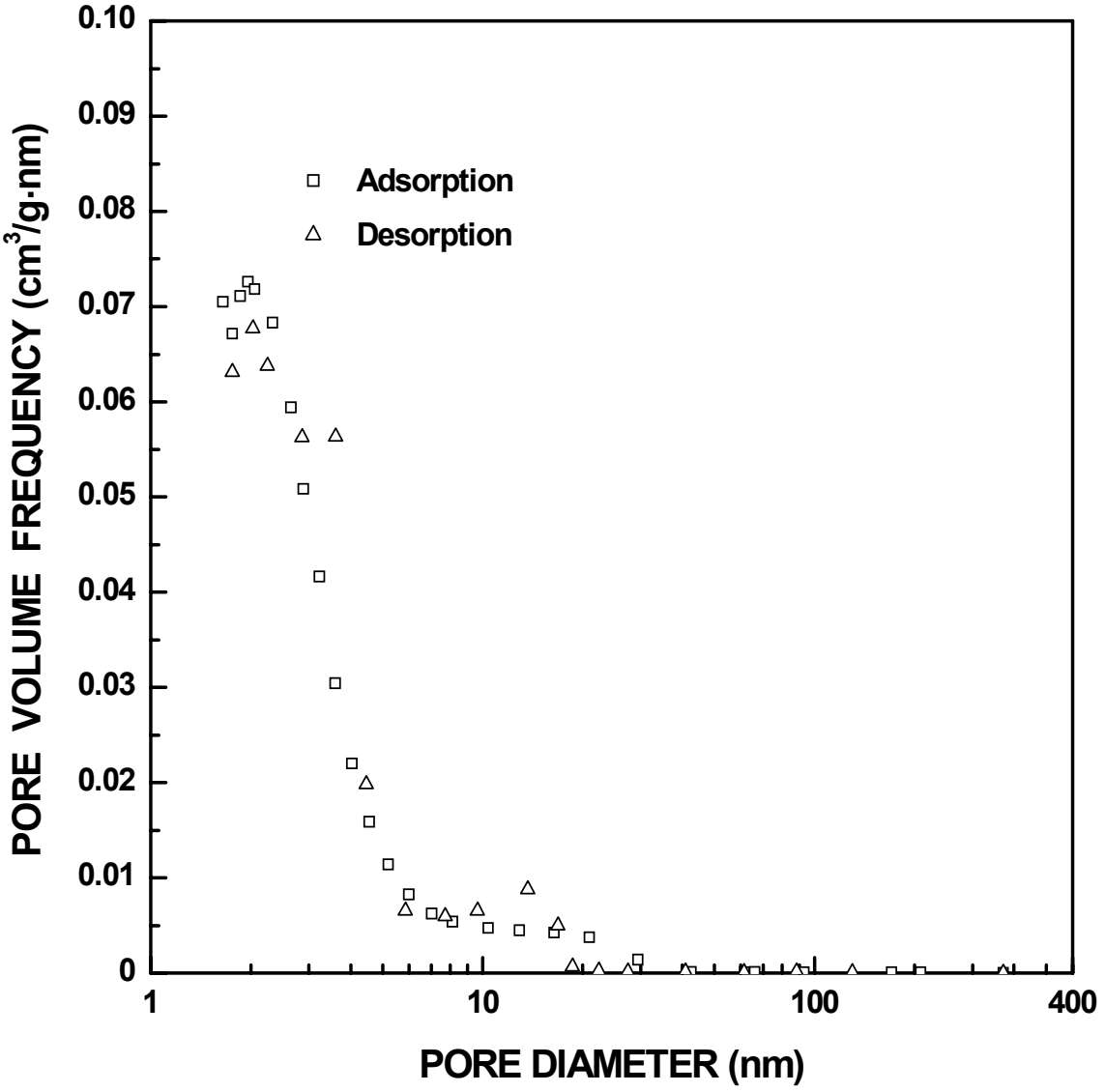

Figure I-181 Plots of specific pore volume frequency vs. pore diameter for SC8-1250(5h) sample (X_{WL} = 0.61).

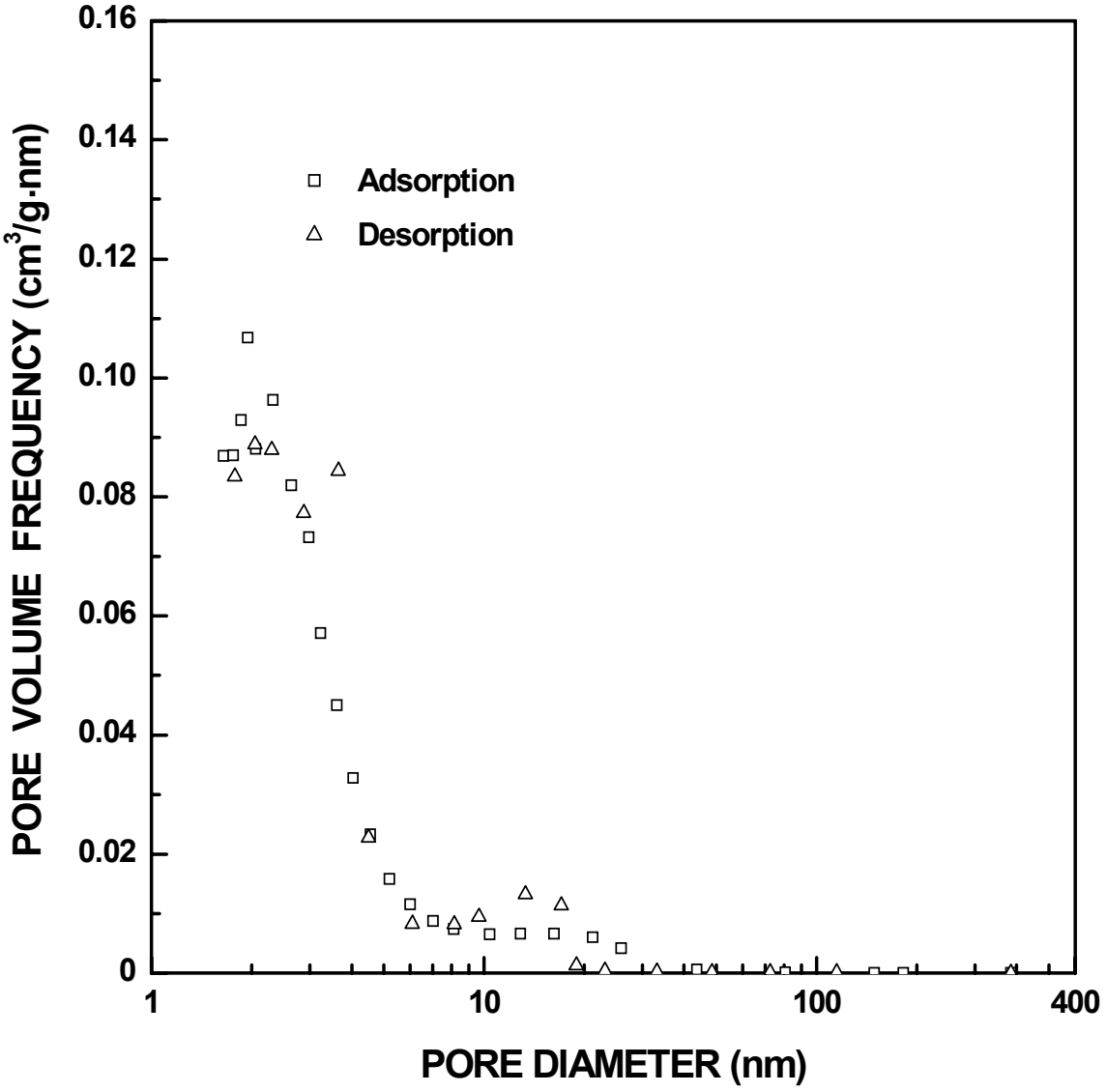

Figure I-182 Plots of specific pore volume frequency vs. pore diameter for SC8-1250(6.5h) sample (X_{WL} = 0.73).

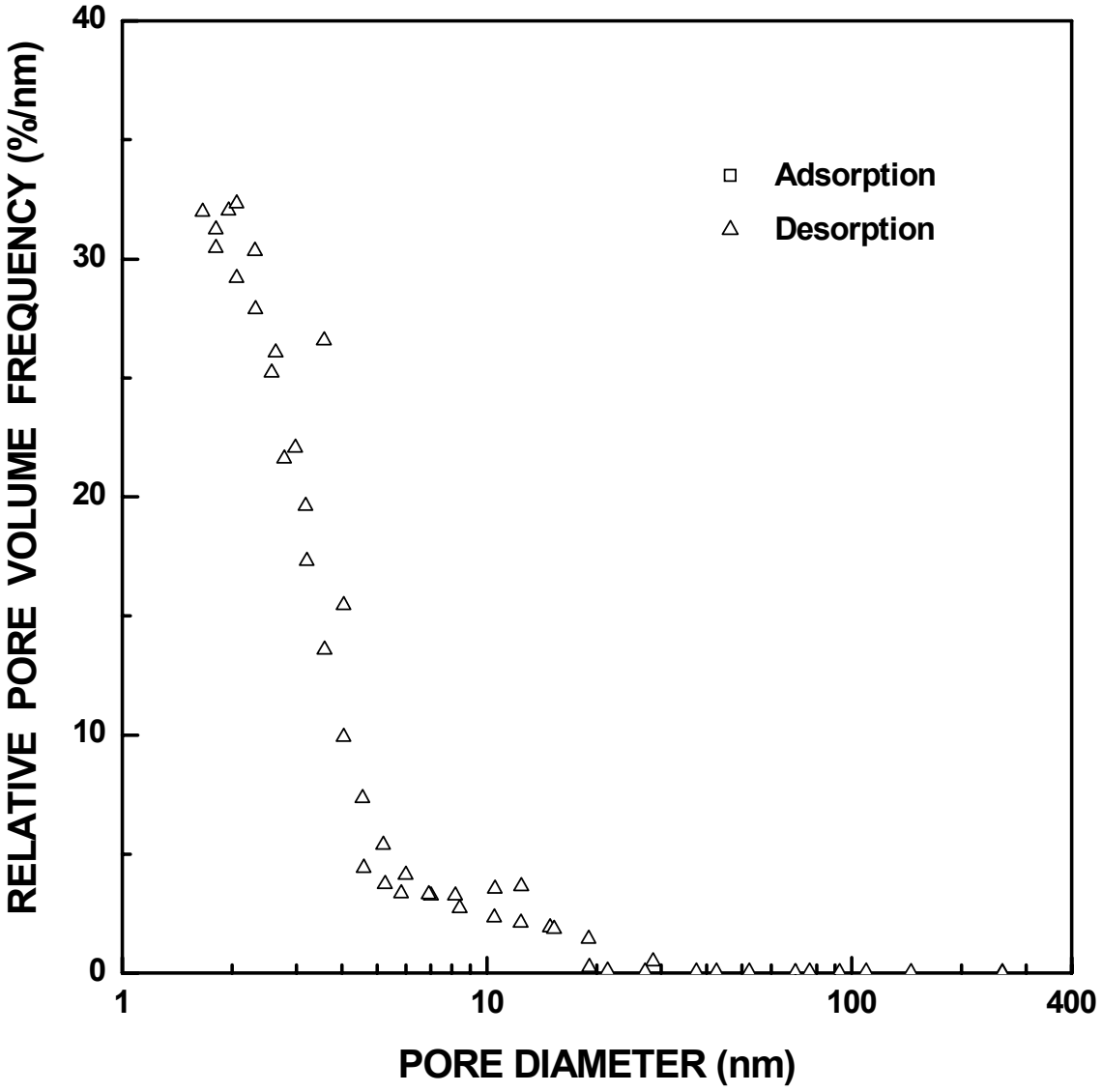

Figure I-183 Plots of relative ("normalized") pore volume frequency vs. pore diameter for SC8-1160(36h) sample (X_{WL} = 0.62).

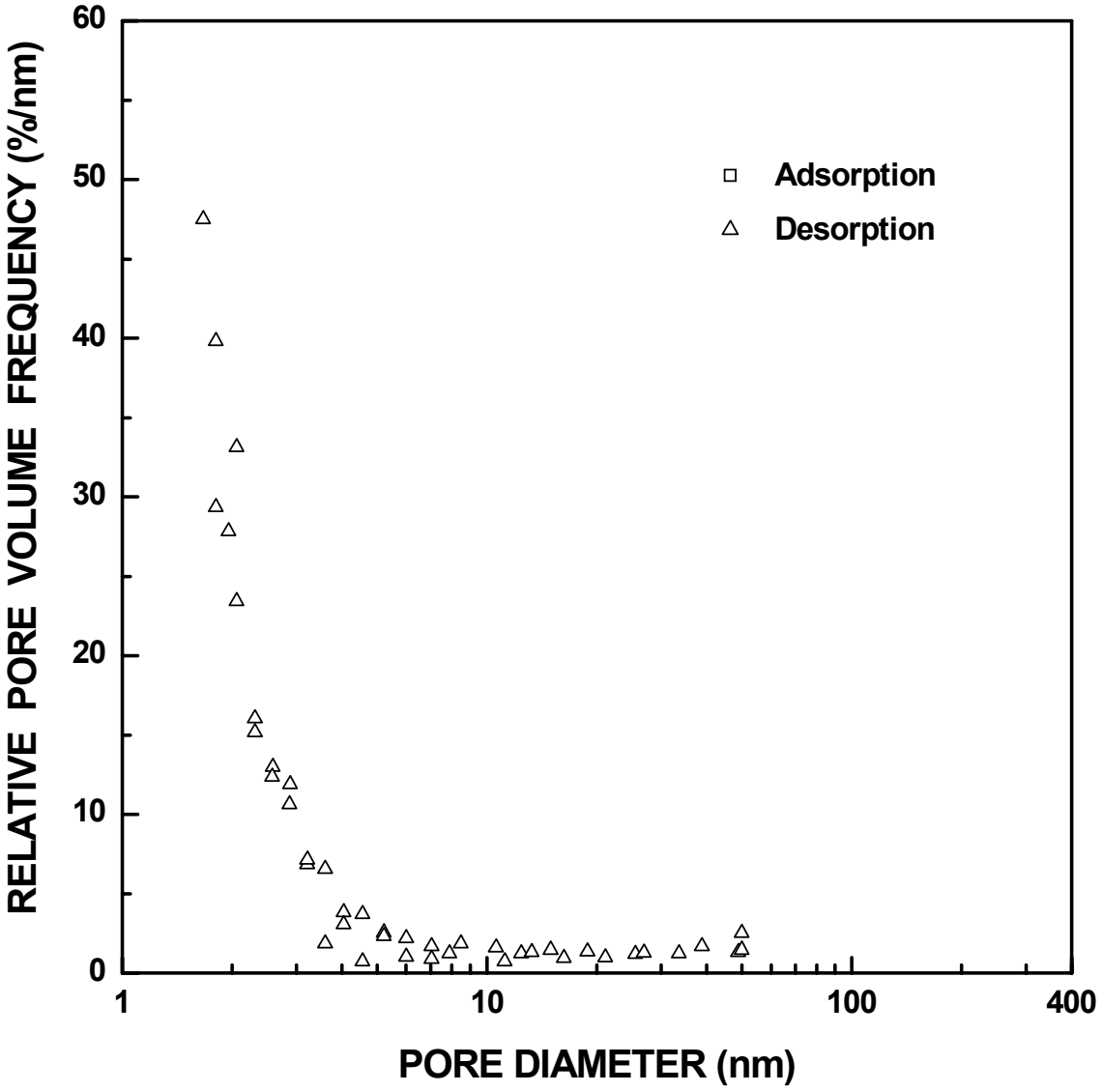

Figure I-184 Plots of relative ("normalized") pore volume frequency vs. pore diameter for SC8-1180(1h) sample (X_{WL} = 0.08). The pore diameter was cut off at 50 nm.

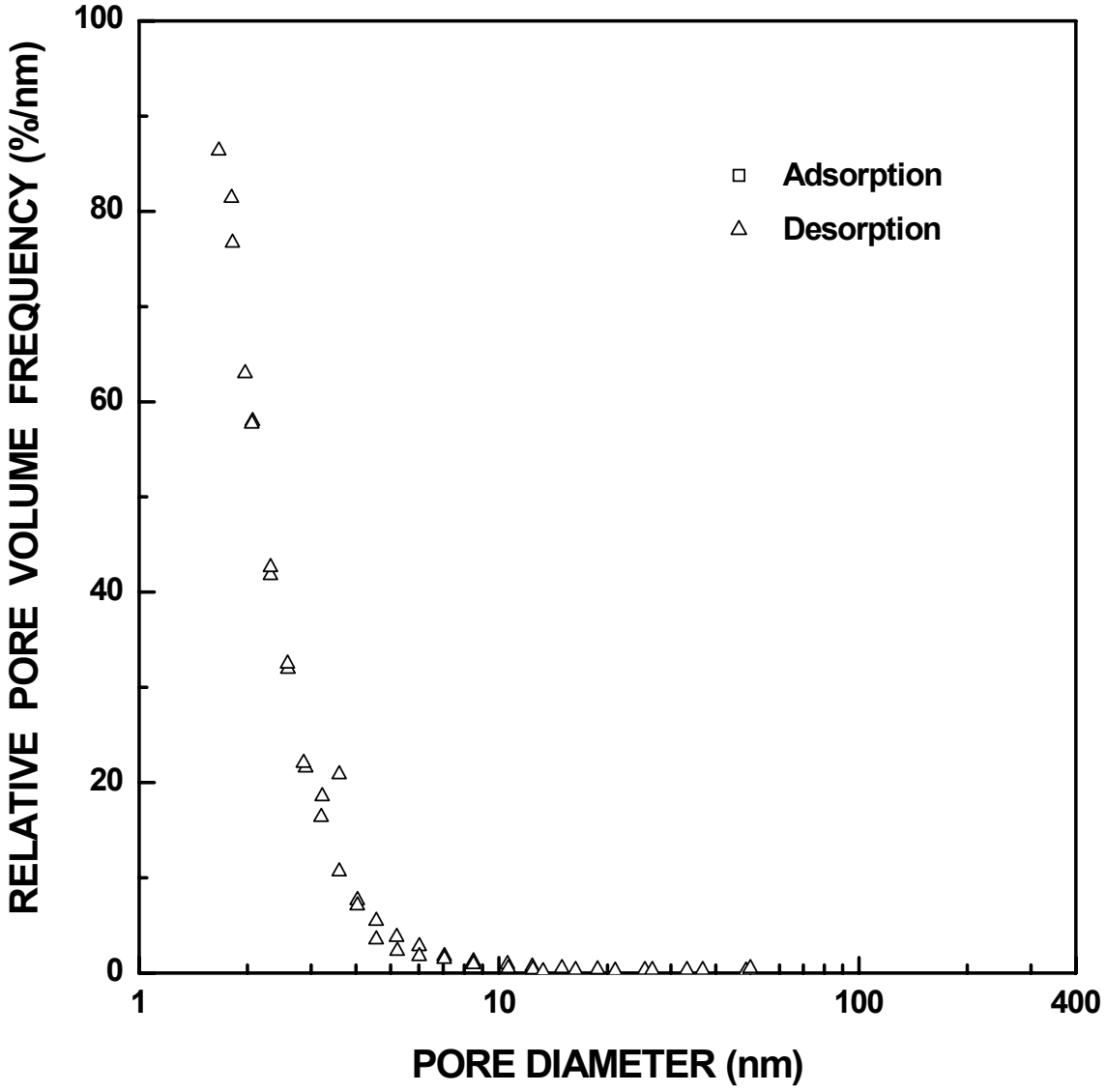

Figure I-185 Plots of relative ("normalized") pore volume frequency vs. pore diameter for SC8-1180(4h) sample (X_{WL} = 0.18). The pore diameter was cut off at 50 nm.

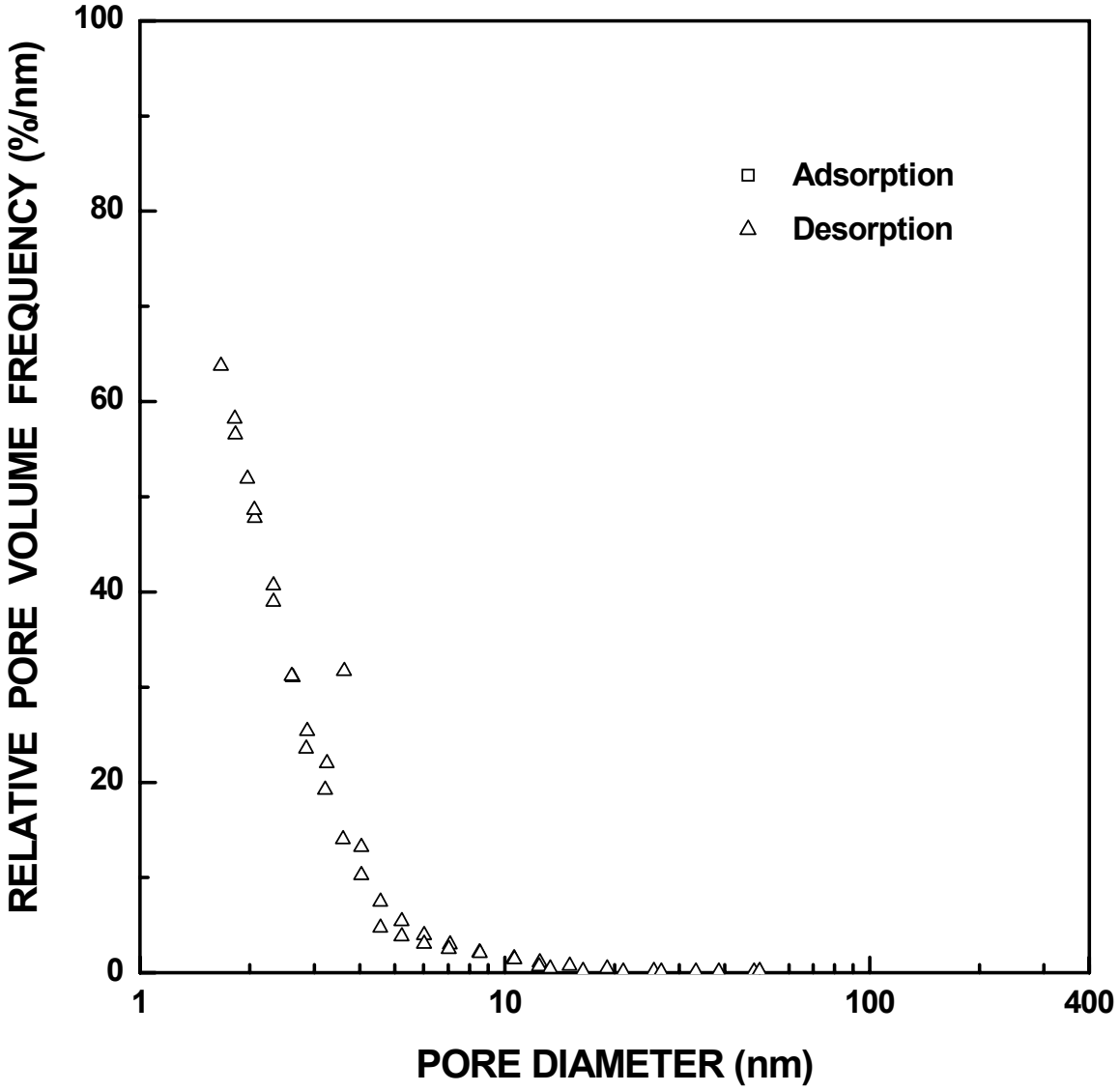

Figure I-186 Plots of relative ("normalized") pore volume frequency vs. pore diameter for SC8-1180(8h) sample (X_{WL} = 0.31). The pore diameter was cut off at 50 nm.

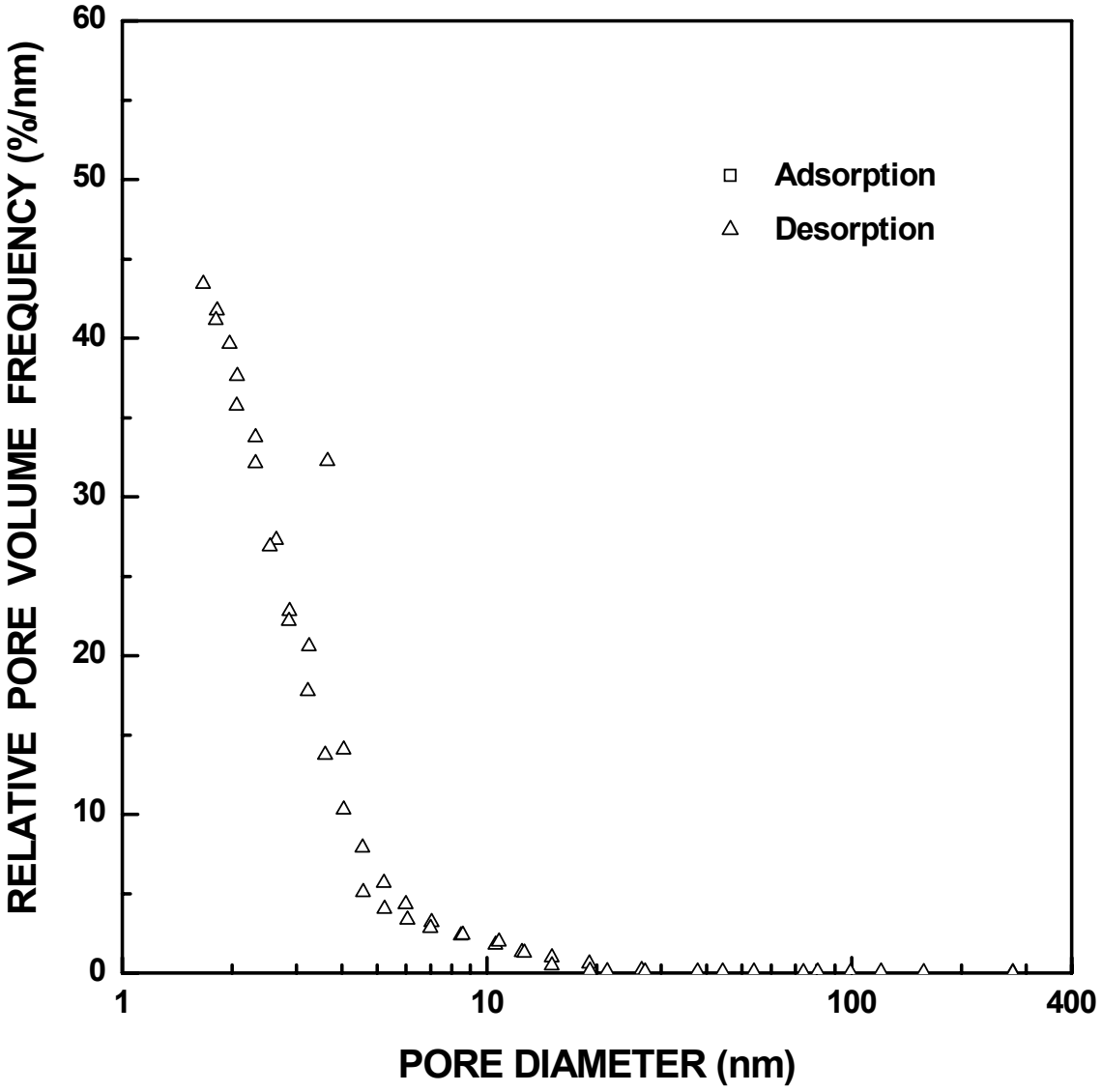

Figure I-187 Plots of relative ("normalized") pore volume frequency vs. pore diameter for SC8-1180(12h) sample (X_{WL} = 0.43).

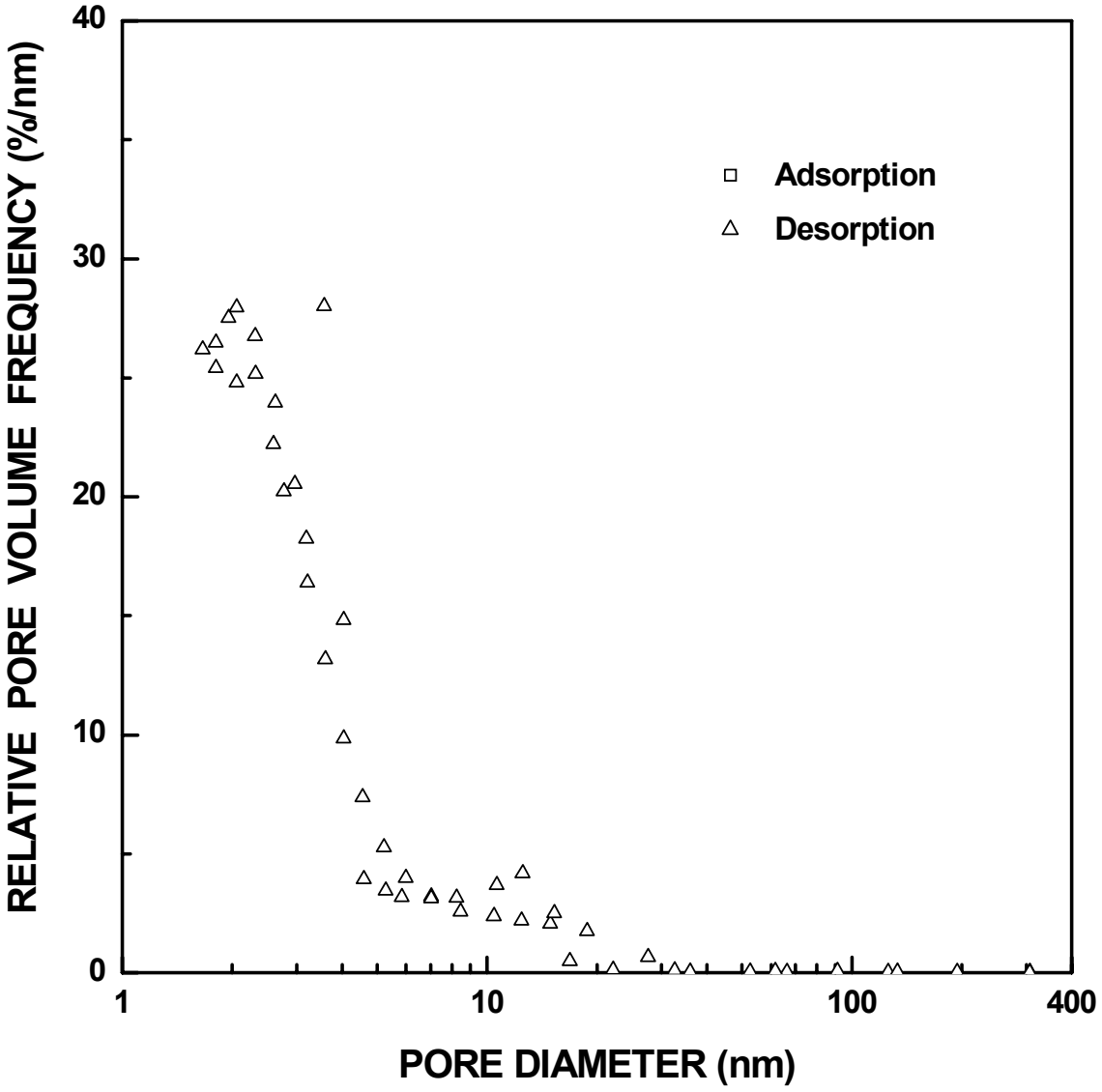

Figure I-188 Plots of relative ("normalized") pore volume frequency vs. pore diameter for SC8-1180(24h) sample (X_{WL} = 0.70).

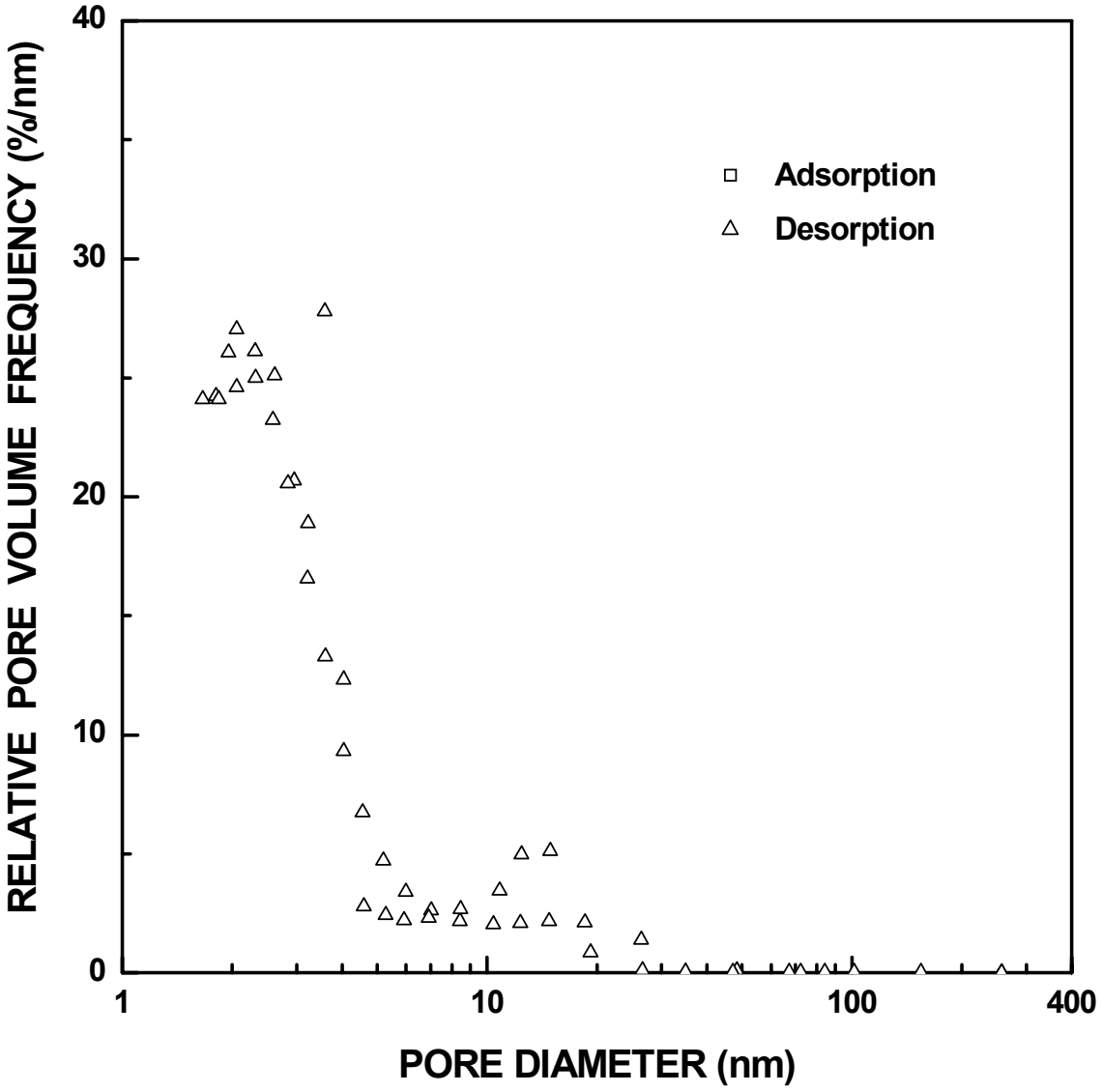

Figure I-189 Plots of relative ("normalized") pore volume frequency vs. pore diameter for SC8-1180(36h) sample (X_{WL} = 0.82).

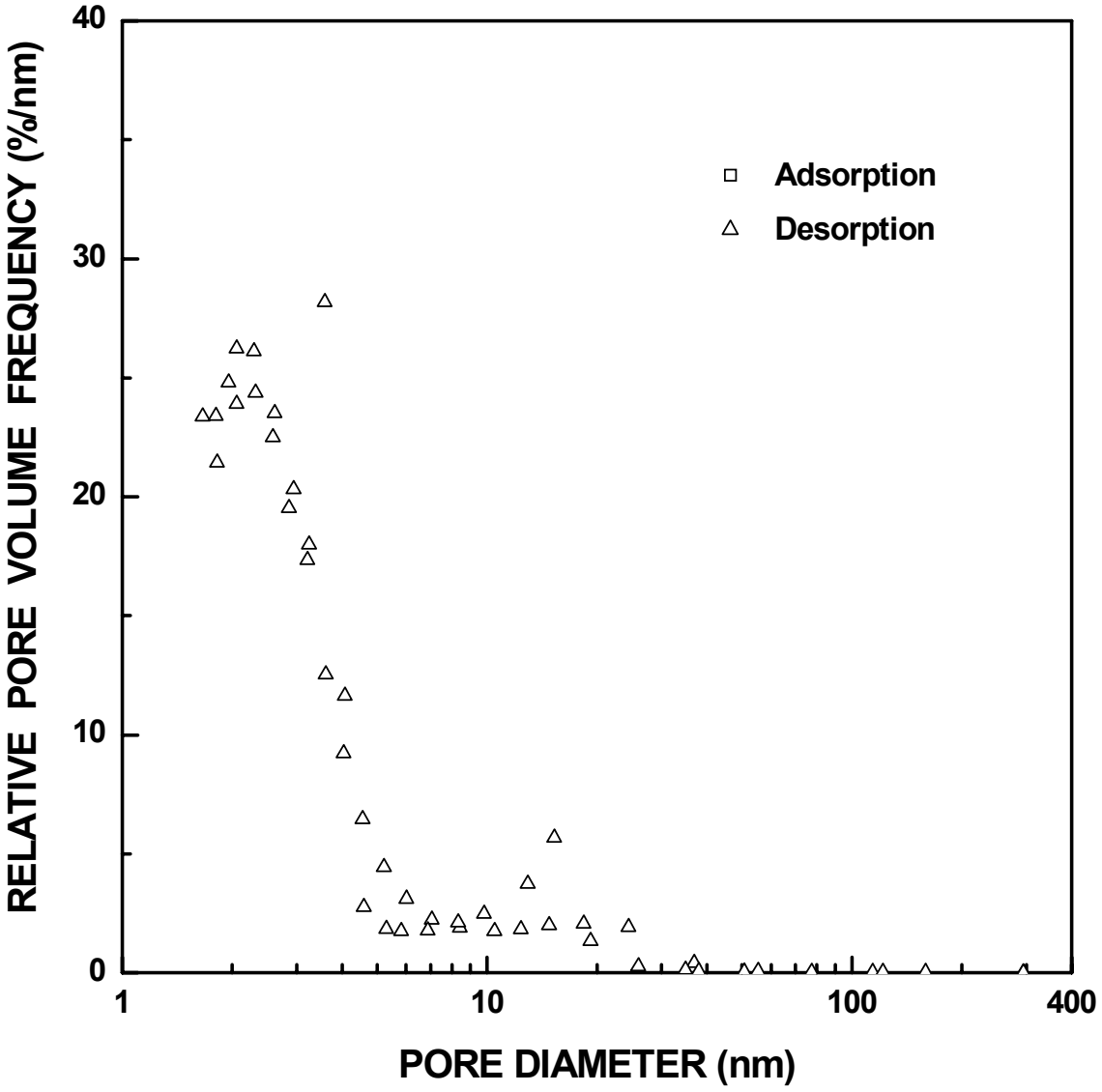

Figure I-190 Plots of relative ("normalized") pore volume frequency vs. pore diameter for SC8-1180(48h) sample (X_{WL} = 0.92).

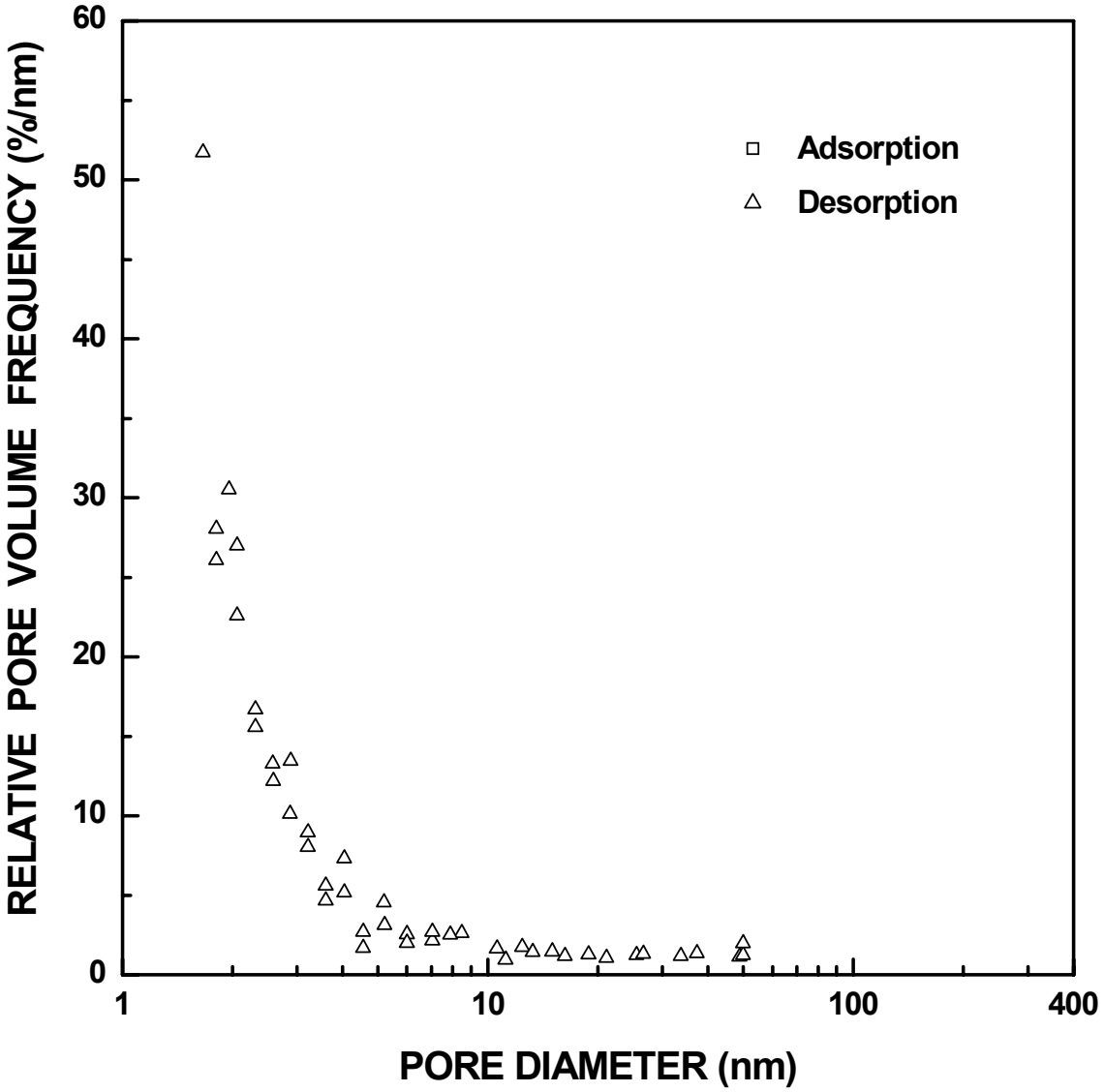

Figure I-191 Plots of relative ("normalized") pore volume frequency vs. pore diameter for SC8-1200(30min) sample (X_{WL} = 0.05). The pore diameter was cut off at 50 nm.

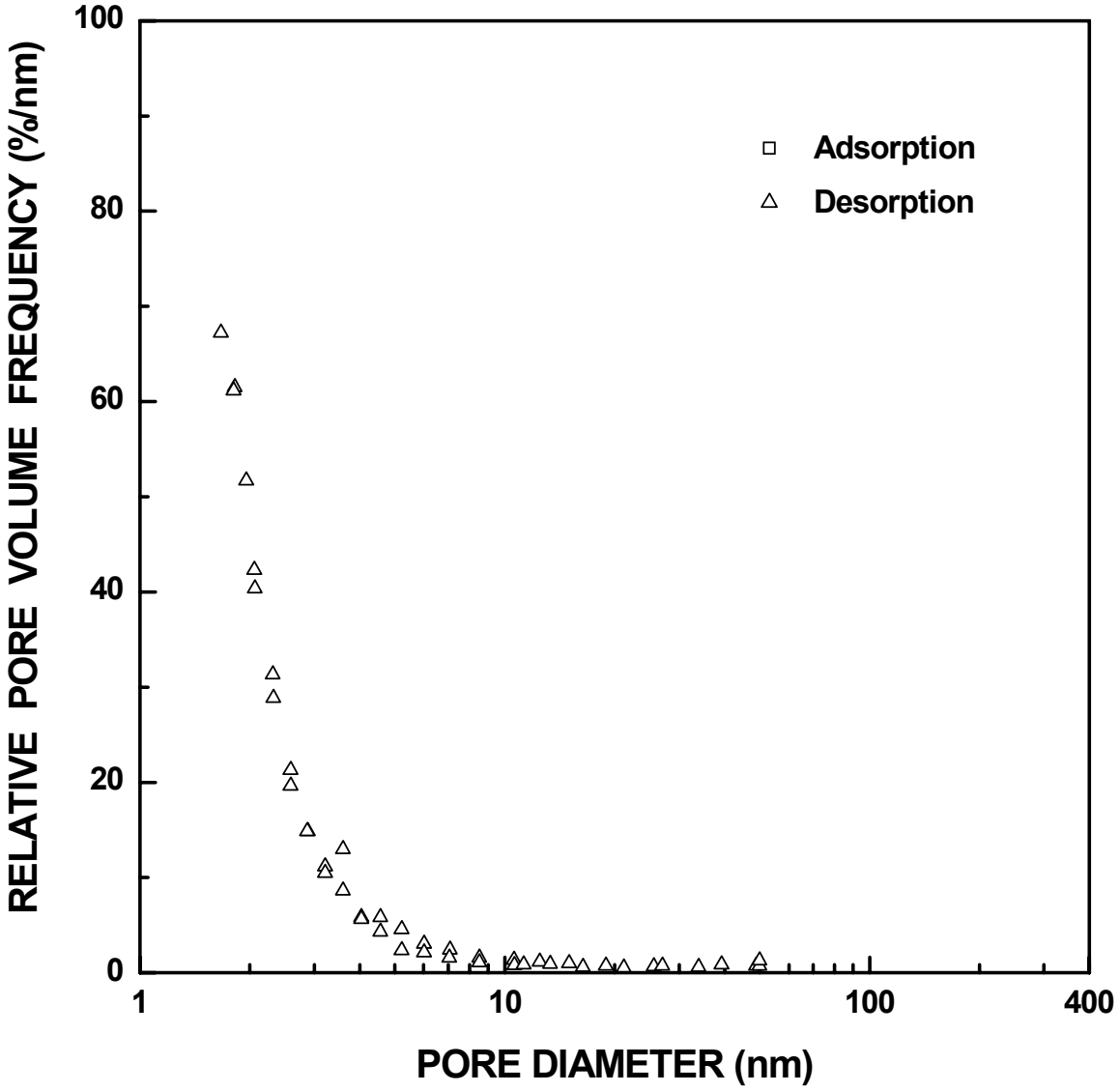

Figure I-192 Plots of relative ("normalized") pore volume frequency vs. pore diameter for SC8-1200(1h) sample (X_{WL} = 0.05). The pore diameter was cut off at 50 nm.

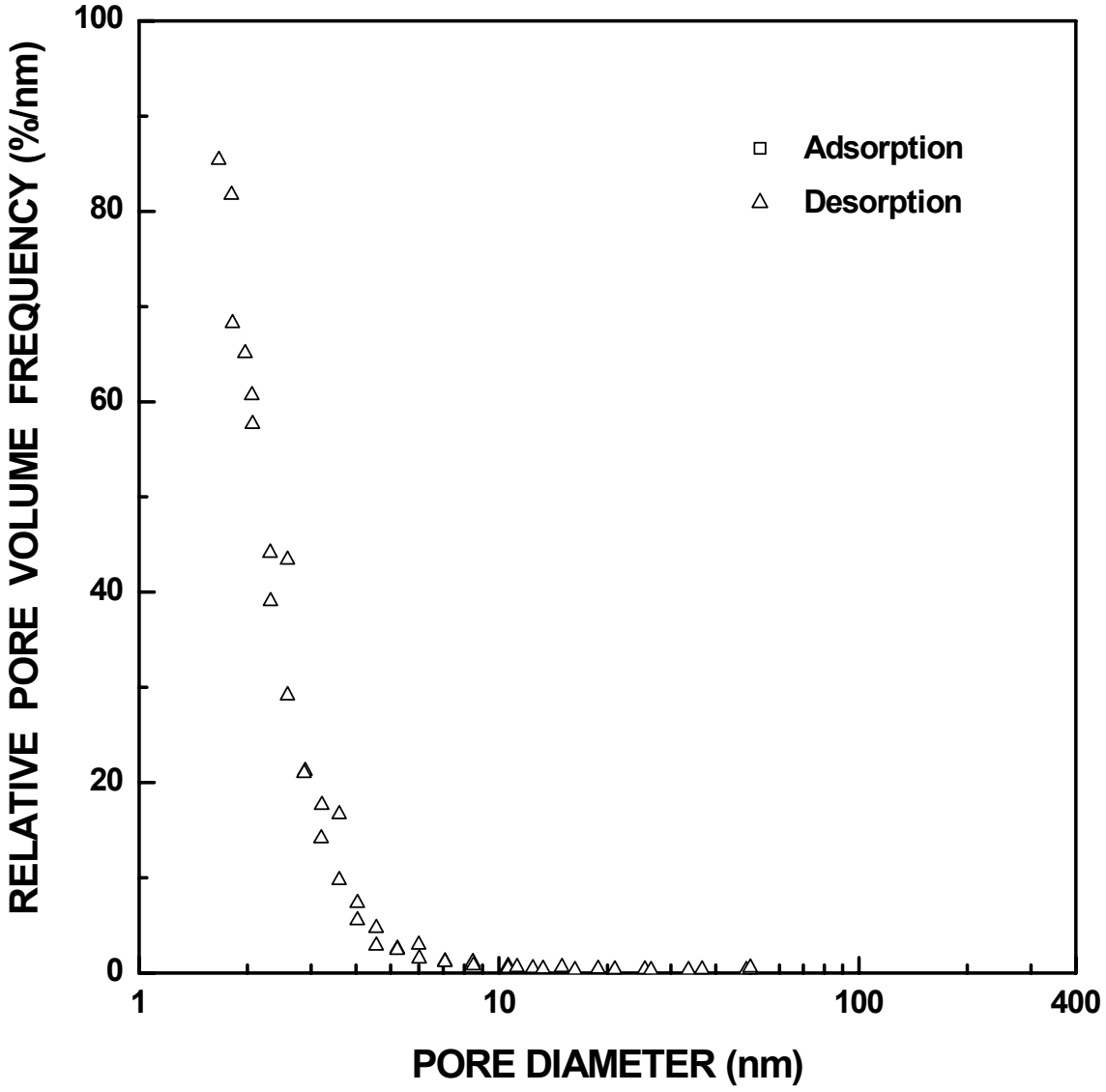

Figure I-193 Plots of relative ("normalized") pore volume frequency vs. pore diameter for SC8-1200(2h) sample (X_{WL} = 0.11). The pore diameter was cut off at 50 nm.

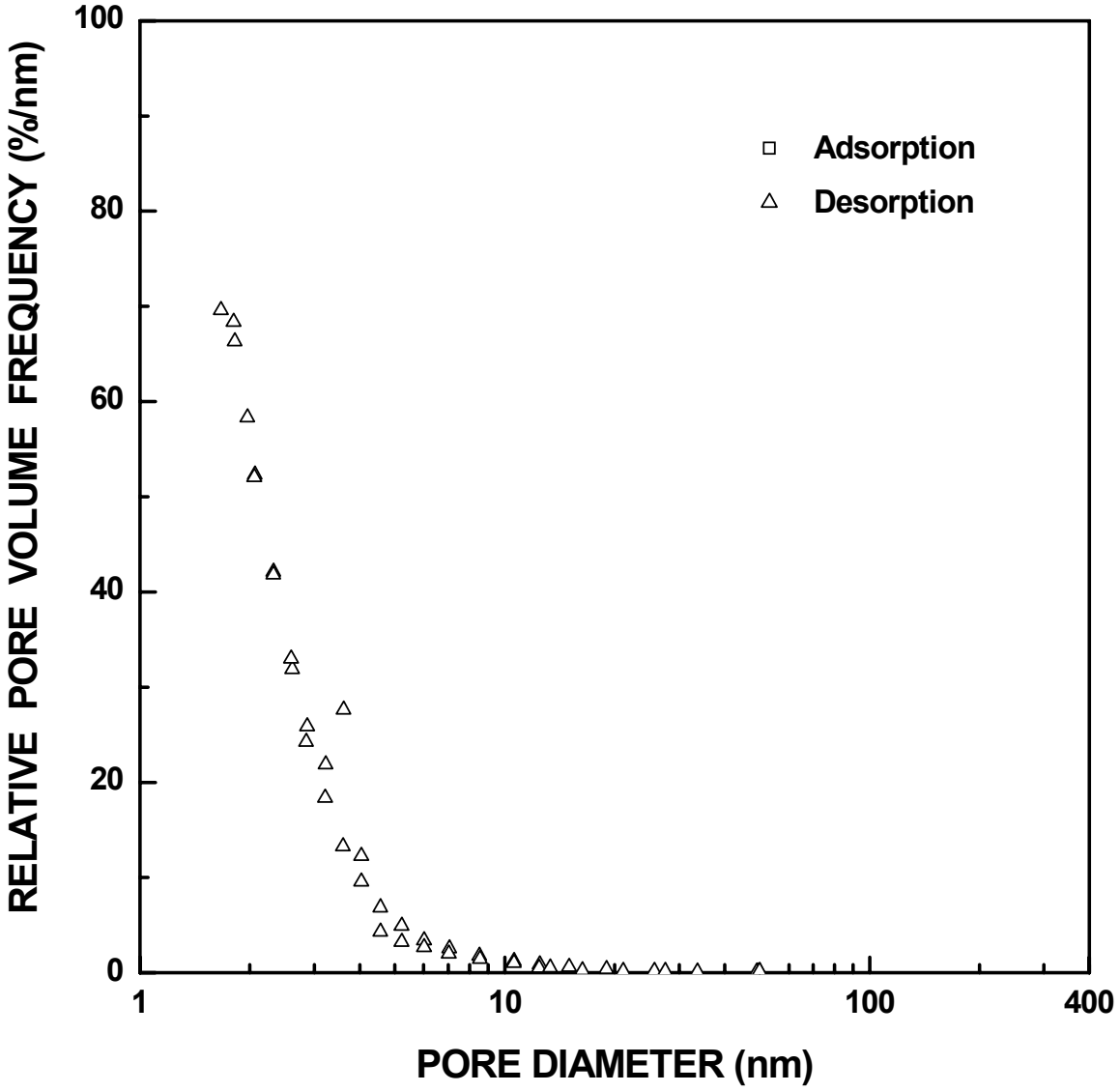

Figure I-194 Plots of relative ("normalized") pore volume frequency vs. pore diameter for SC8-1200(4h) sample (X_{WL} = 0.19). The pore diameter was cut off at 50 nm.

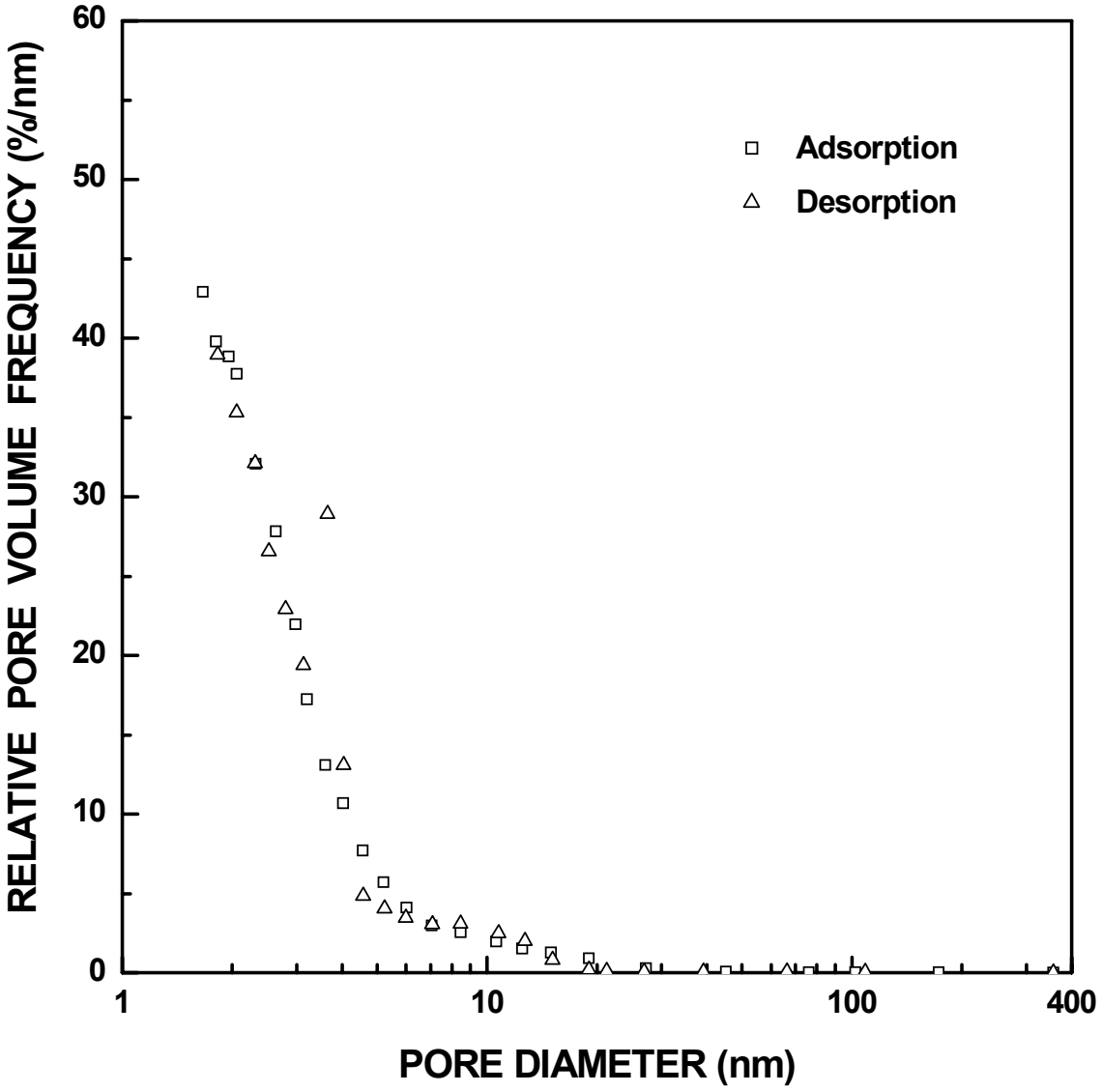

Figure I-195 Plots of relative ("normalized") pore volume frequency vs. pore diameter for SC8-1200(8h) sample (X_{WL} = 0.40).

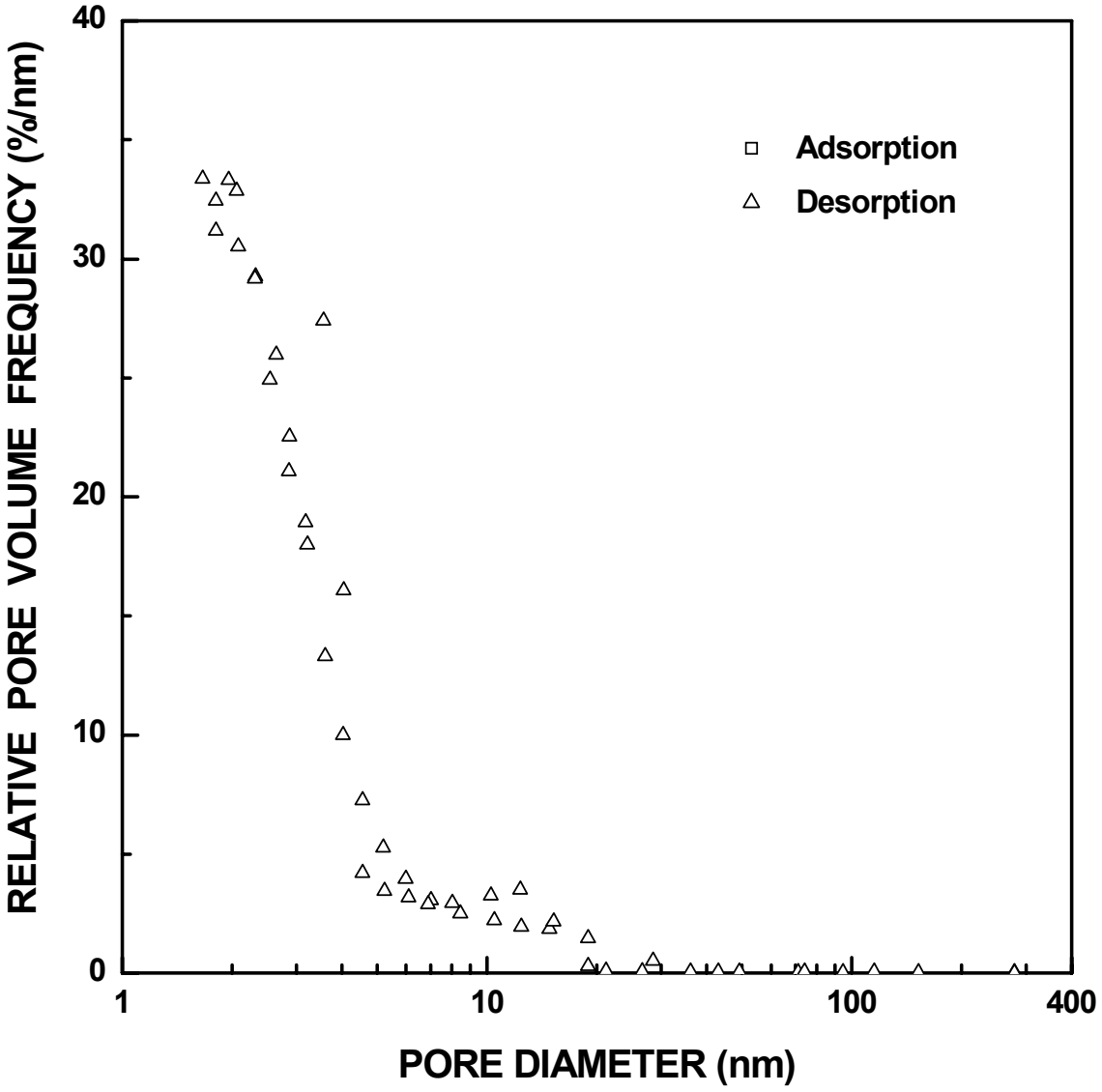

Figure I-196 Plots of relative ("normalized") pore volume frequency vs. pore diameter for SC8-1200(12h) sample (X_{WL} = 0.54).

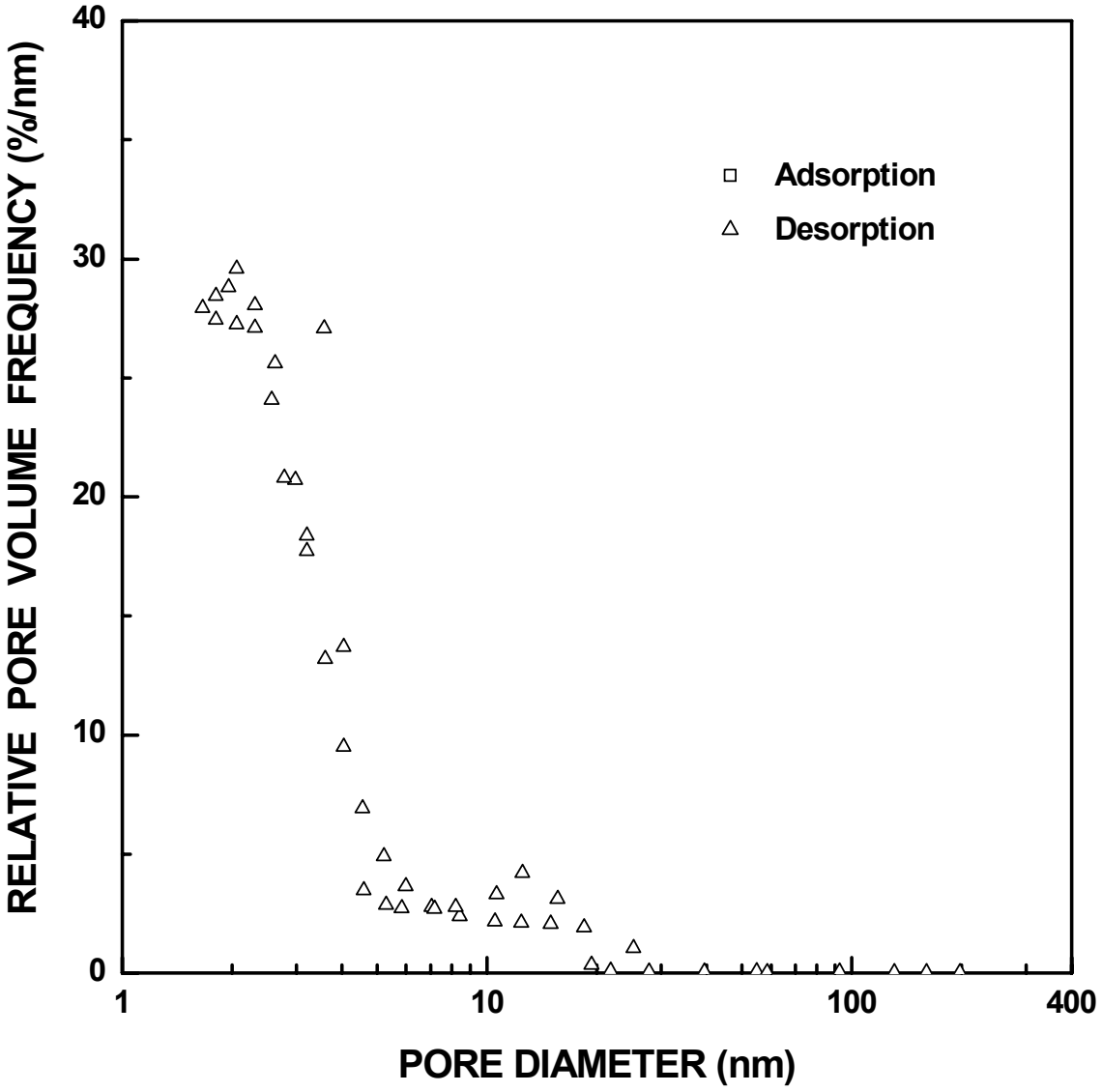

Figure I-197 Plots of relative ("normalized") pore volume frequency vs. pore diameter for SC8-1200(16h) sample (X_{WL} = 0.68).

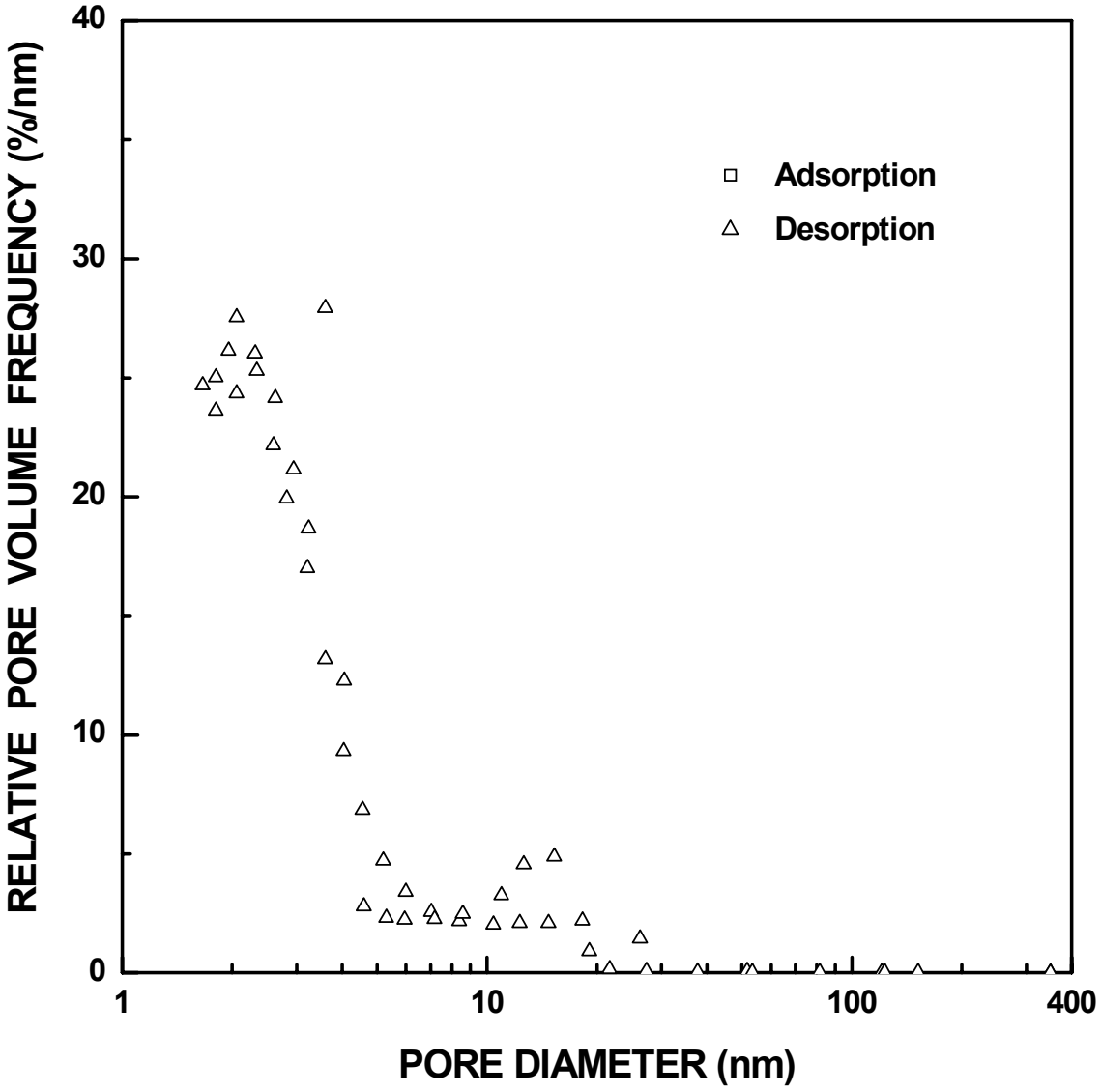

Figure I-198 Plots of relative ("normalized") pore volume frequency vs. pore diameter for SC8-1200(22h) sample (X_{WL} = 0.80).

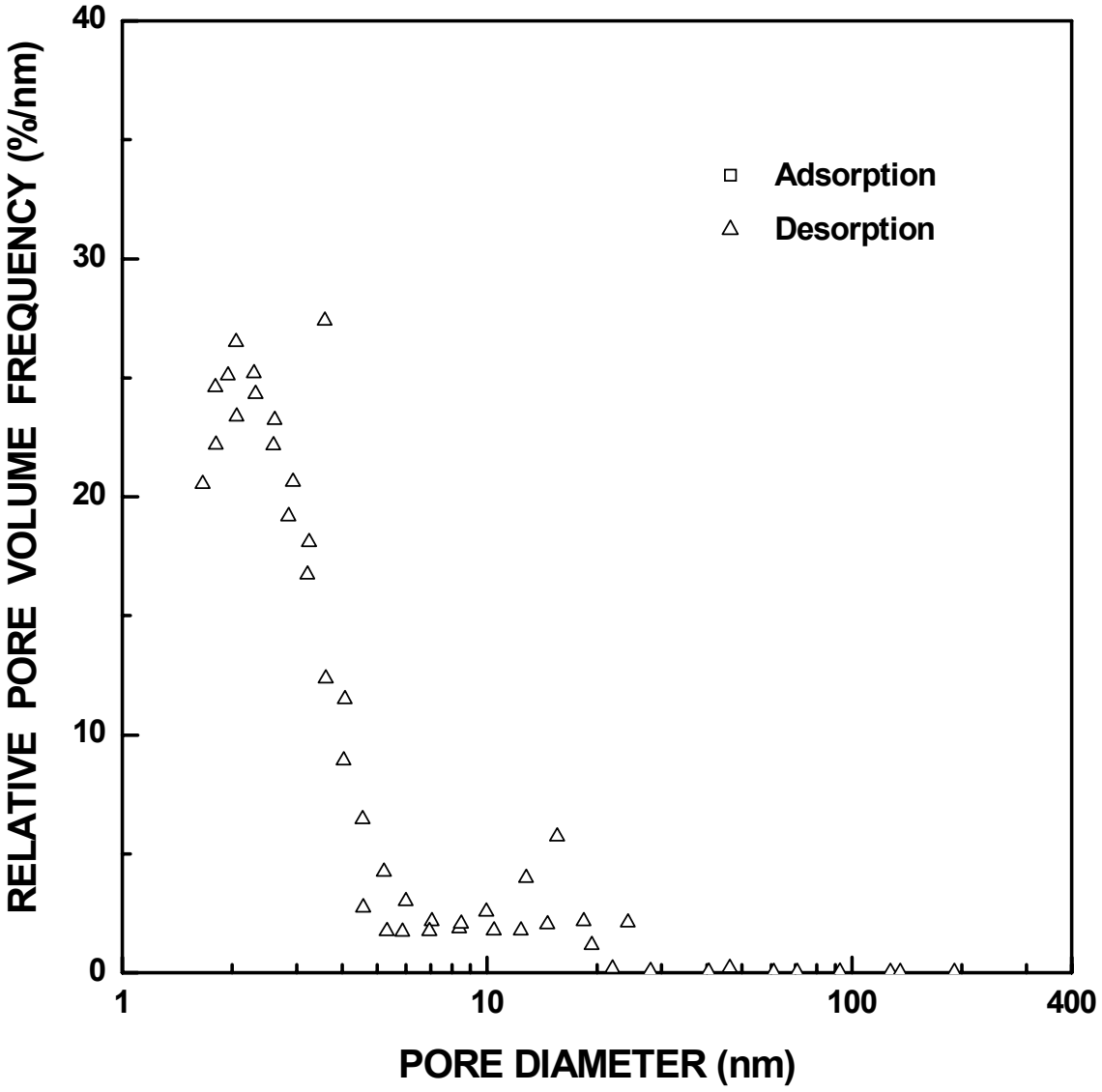

Figure I-199 Plots of relative ("normalized") pore volume frequency vs. pore diameter for SC8-1200(32h) sample (X_{WL} = 0.91).

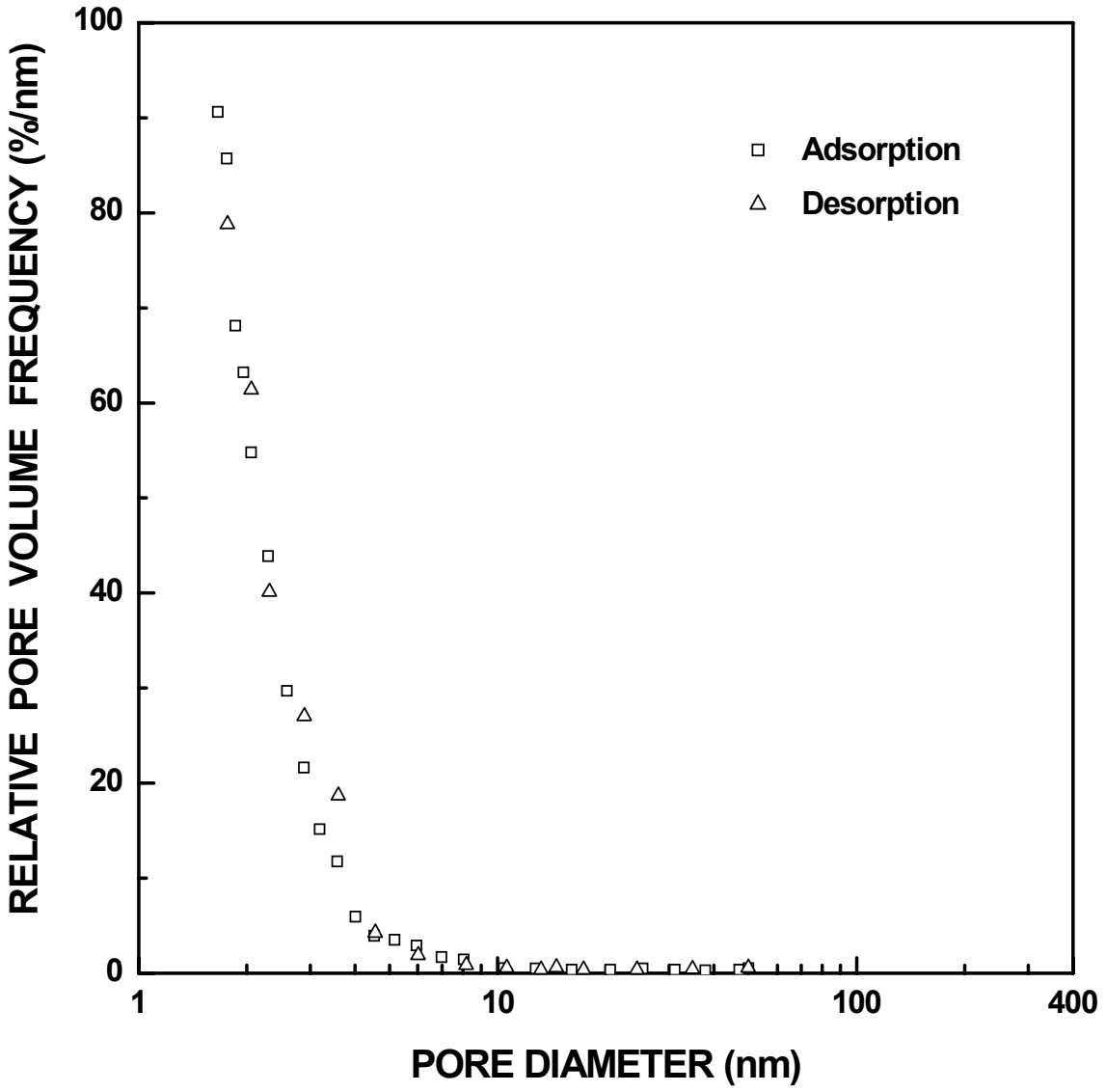

Figure I-200 Plots of relative ("normalized") pore volume frequency vs. pore diameter for SC8-1250(40min) sample (X_{WL} = 0.11). The pore diameter was cut off at 50 nm.

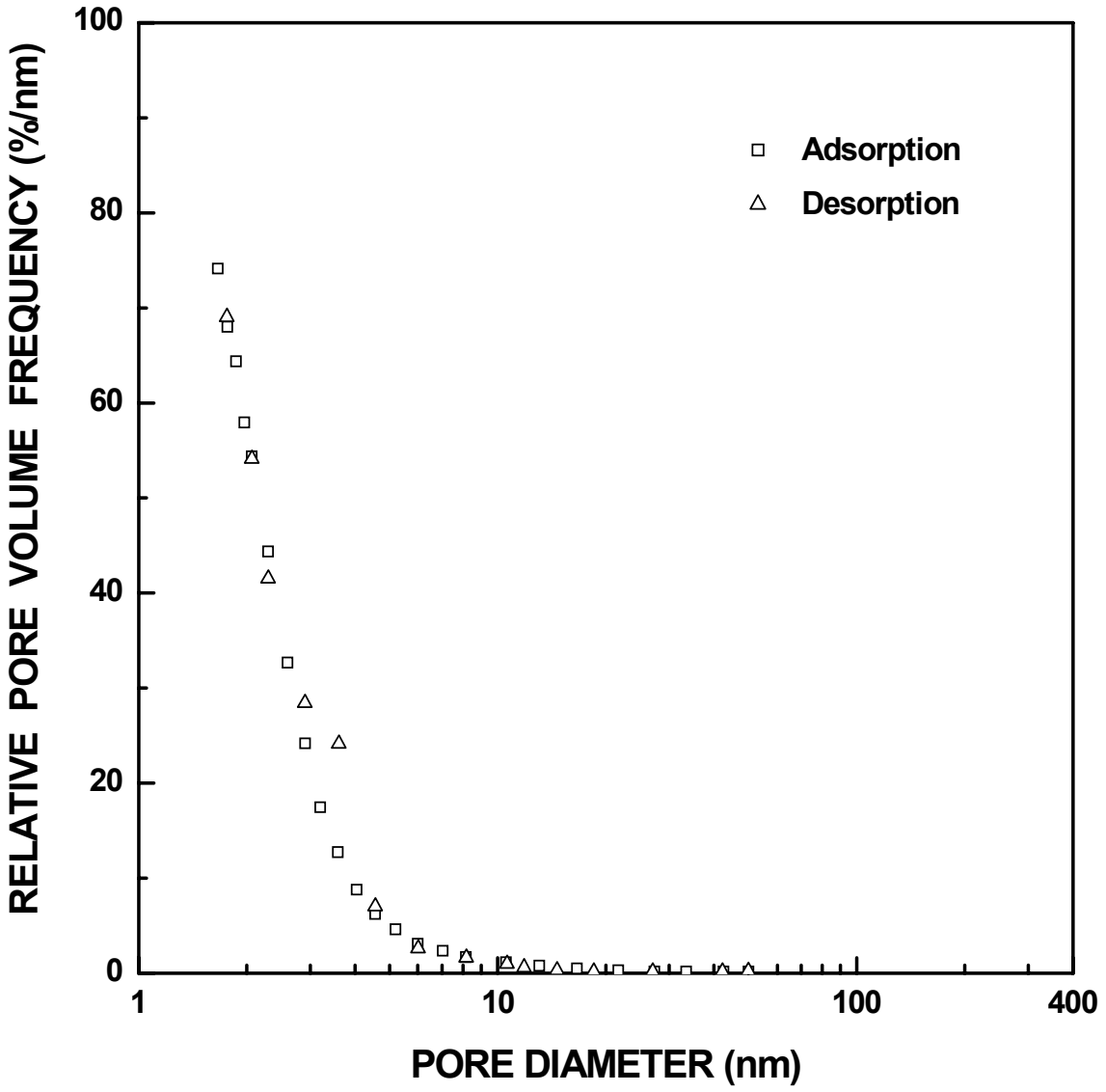

Figure I-201 Plots of relative ("normalized") pore volume frequency vs. pore diameter for SC8-1250(1h) sample (X_{WL} = 0.16). The pore diameter was cut off at 50 nm.

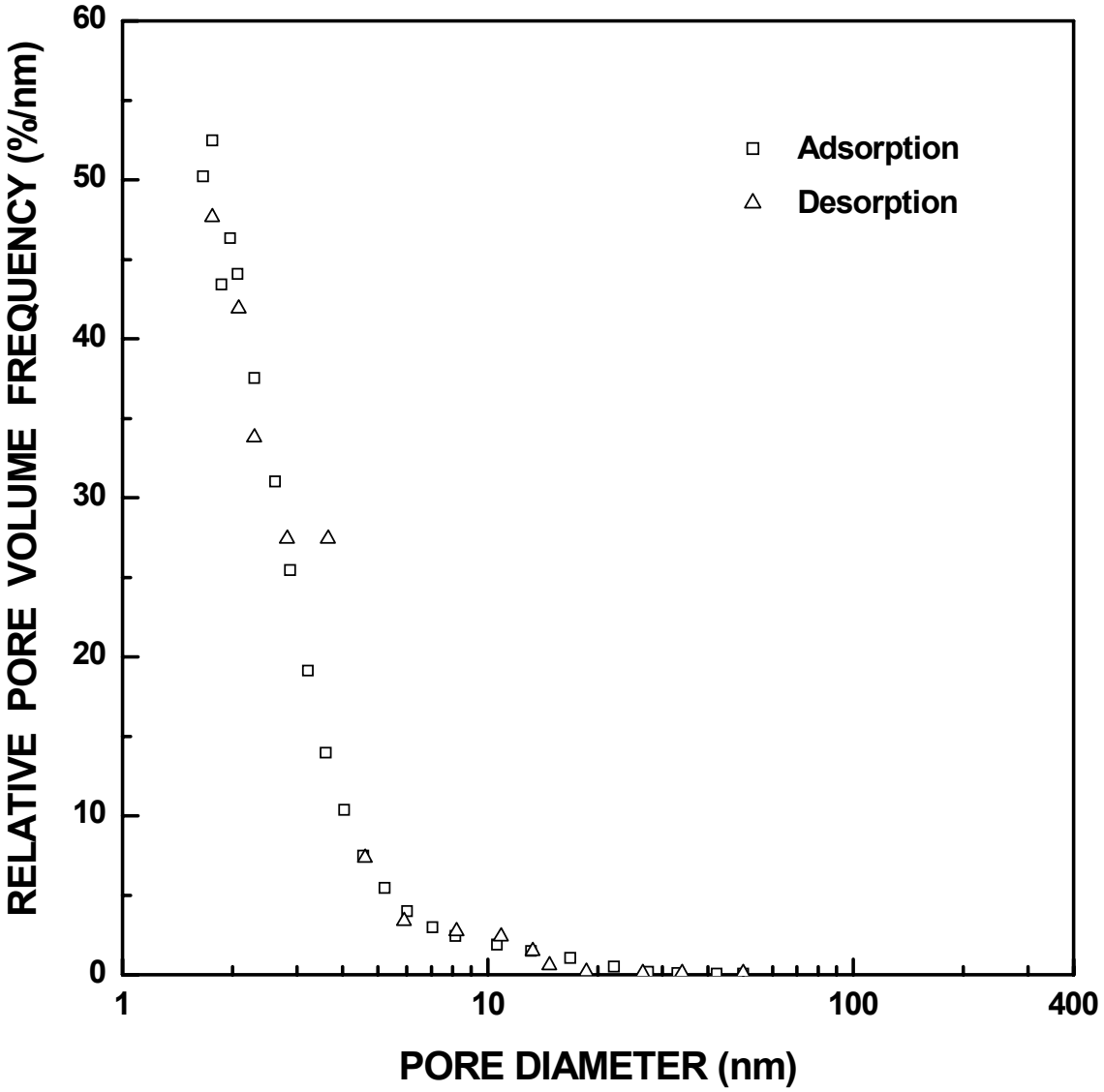

Figure I-202 Plots of relative ("normalized") pore volume frequency vs. pore diameter for SC8-1250(2h) sample (X_{WL} = 0.31). The pore diameter was cut off at 50 nm.

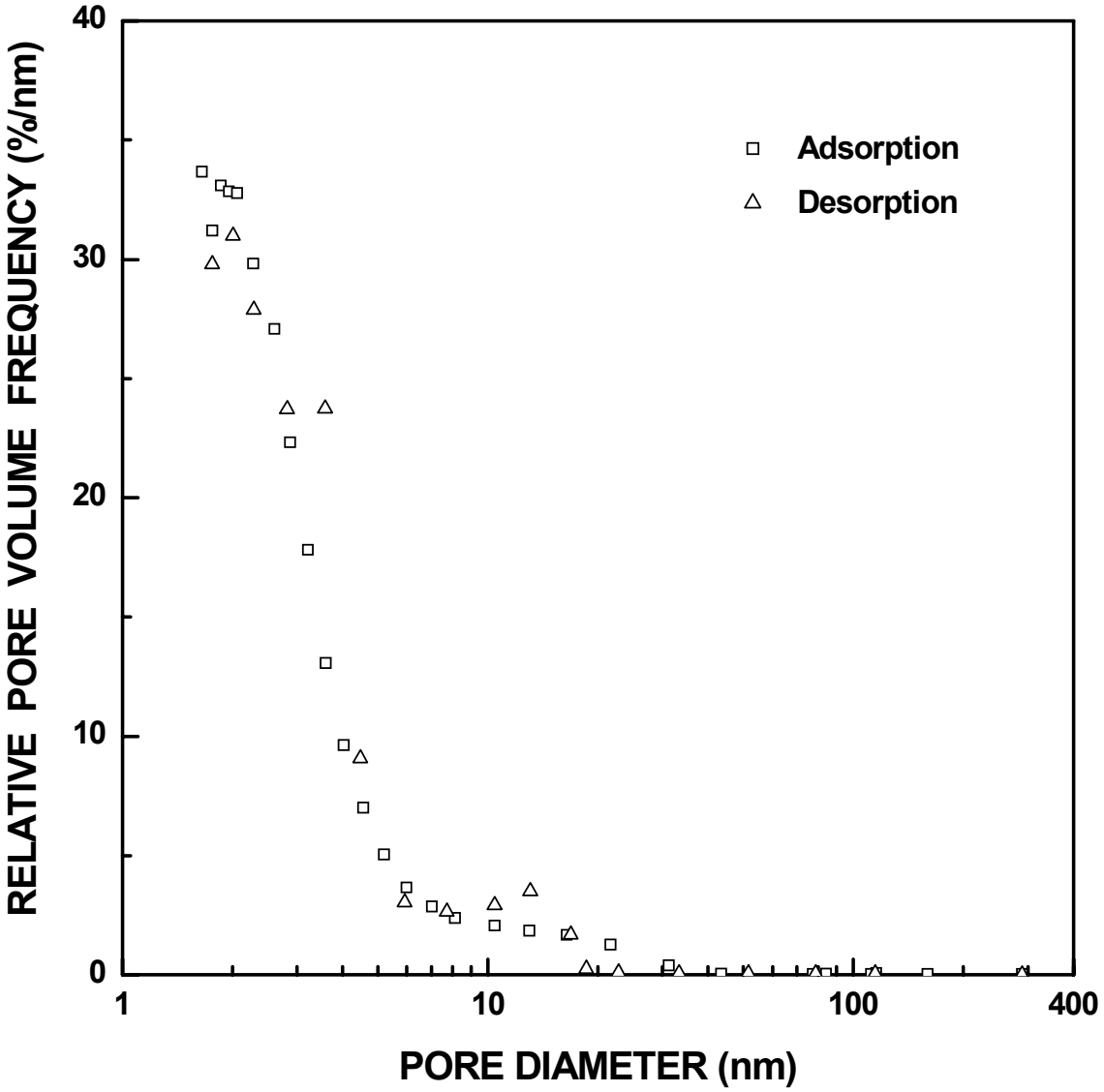

Figure I-203 Plots of relative ("normalized") pore volume frequency vs. pore diameter for SC8-1250(4h) sample (X_{WL} = 0.54).

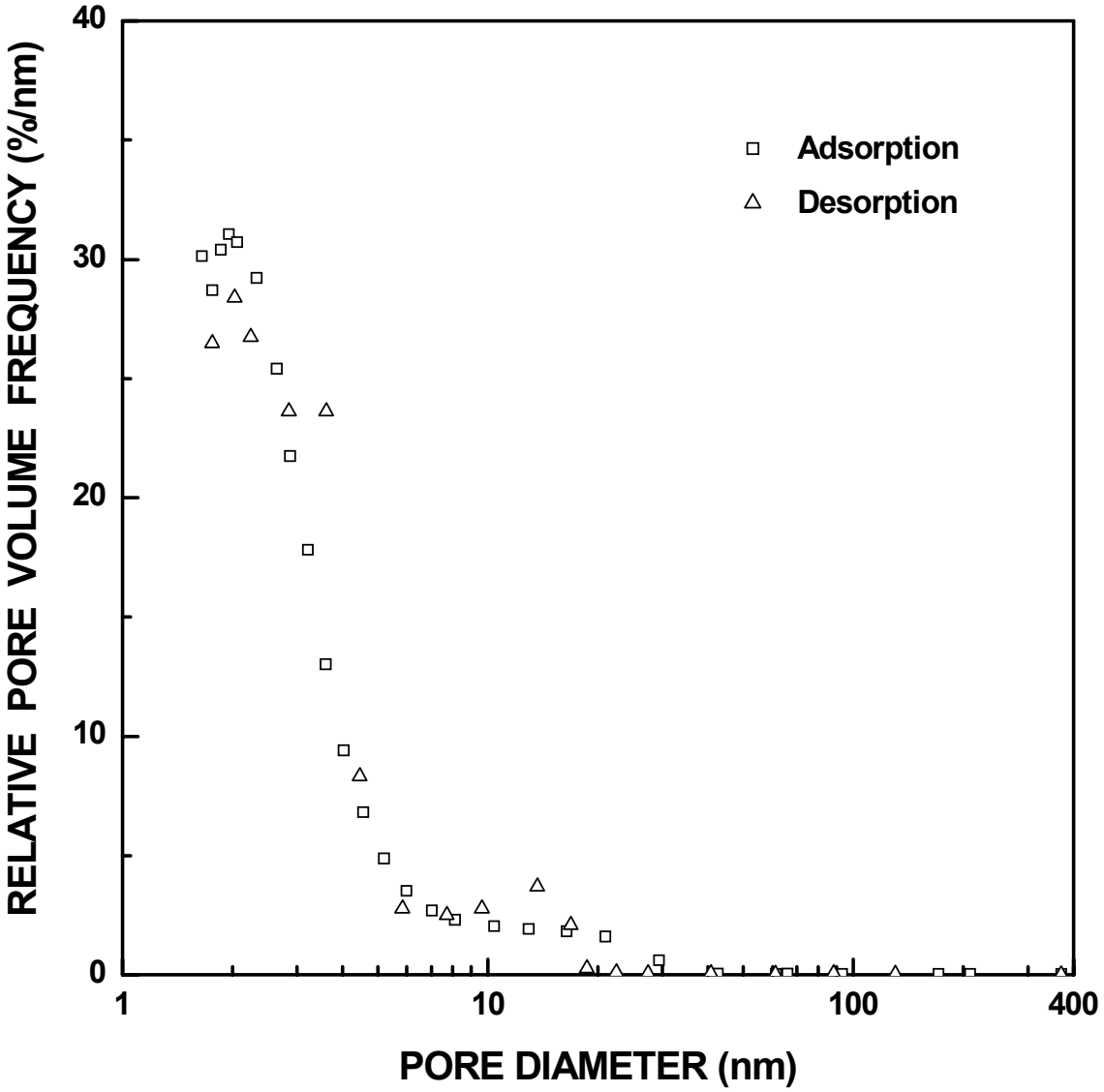

Figure I-204 Plots of relative ("normalized") pore volume frequency vs. pore diameter for SC8-1250(5h) sample (X_{WL} = 0.61).

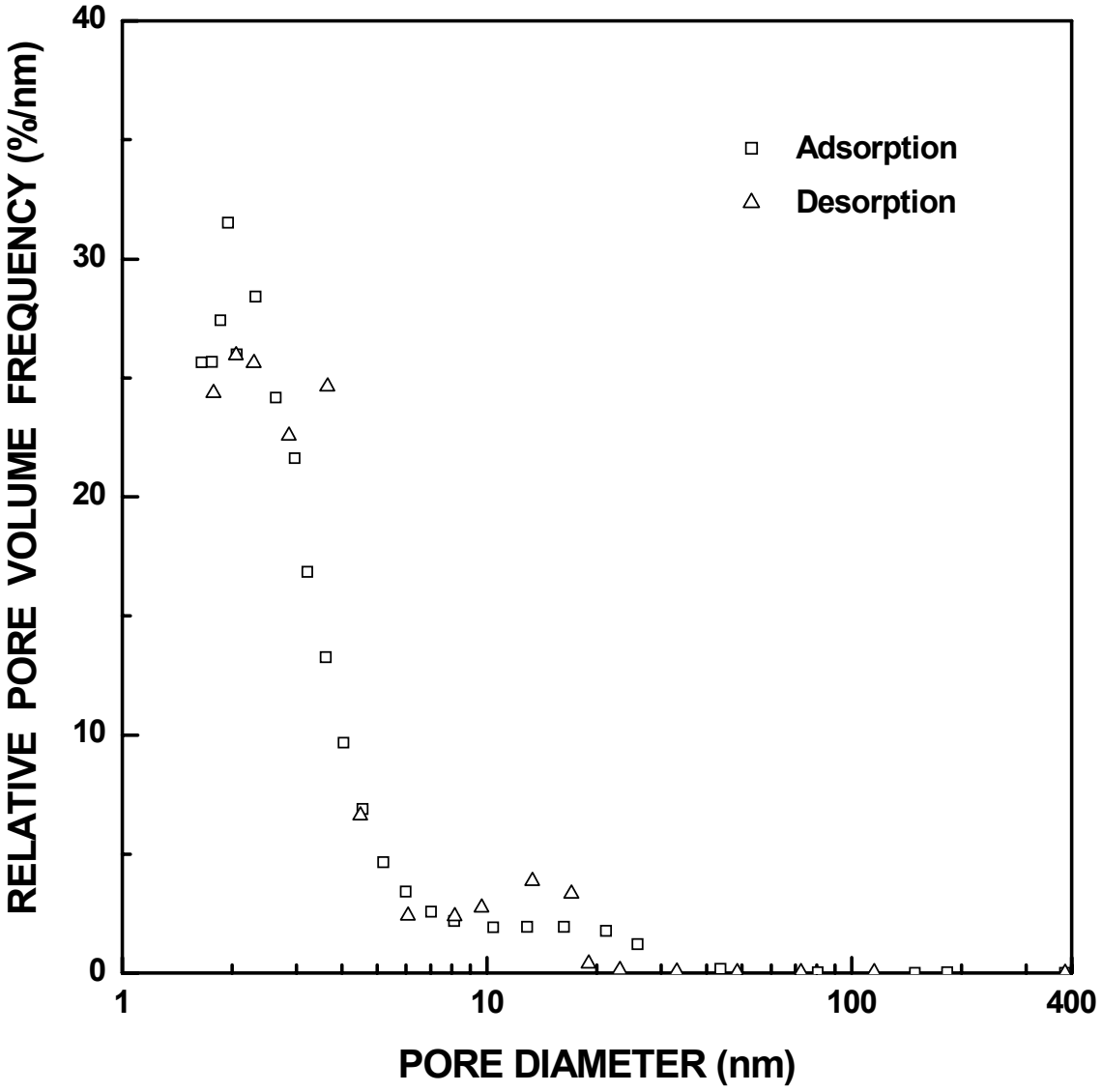

Figure I-205 Plots of relative ("normalized") pore volume frequency vs. pore diameter for SC8-1250(6.5h) sample (X_{WL} = 0.73).

REFERENCES

1. Alterolvitz et al., *Handbook of Optical Constants of Solids II*, edited by Palik, E. D., Academic Press, Orlando (1991), pp. 705-707.

2. Avery, R. G. and Ramsay, J. D. F., "The Sorption of Nitrogen in Porous Compacts of Silica and Zirconia Powders," *Journal of Colloid and Interface Science*, Vol. 42, No. 3, pp. 597-606 (1973).

3. Beecher, N. and Rosensweig, R.E., "Ablation Mechanisms in Plastics with Inorganic Reinforcement," *ARS Journal*, Vol. 31, pp. 532-539 (1961).

4. Benaissa, M., Werckmann, J., Ehert, G., Peschiera, E., Guille, J., and Ledoux, M. J., "Structural Studies of Active Carbon Used in the Growth of Silicon Carbide Catalyst Support," *Journal of Materials Science*, Vol. 29, pp. 4700-4707 (1994).

5. Blumenthal, J. L., Santy, M. J., and Burns, E. A., "Kinetic Studies of High-Temperature Carbon-Silica Reactions in Charred Silica-Reinforced Phenolic Resins," *AIAA journal*, Vol. 4, No. 6, pp. 1053-1057 (1966).

6. Borghesi, A. and Guizzetti, G., "Graphite (C)," in *Handbook of Optical Constants of Solids II*, edited by Palik, E. D., Academic Press, Orlando, pp. 449-460 (1991).

7. Bouillon, E., Langlais, F., and Pailler, R., et al., "Conversion Mechanisms of a Polycarbonsilane Precursor into a SiC-based Ceramic Material," *Journal of Materials Science*, Vol. 26, pp. 1333-1345 (1991).

8. Brinker, C. J. and Scherer, G. W., *Sol-Gel Science: The Physics and Chemistry of Sol-Gel Processing*, Academic Press, Boston (1990).

9. Čerovič, L., Milonjič, S. K., and Zec, S. P., "A Comparison of Sol-Gel Derived Silicon Carbide Powders from Saccharose and Activated Carbon," *Ceramics International*, Vol. 21, pp. 271-276 (1995).

10. Chen, C. Y., Lin, C. I., and Chen, S. H., "Kinetics of Synthesis of Silicon Carbide by Carbothermal Reduction of Silicon Dioxide," *British Ceramic Transactions*, Vol. 99, No. 2, pp. 57-62 (2000).

11. Chen, S. H. and Lin, C. I., "Effect of Contact Area on Synthesis of Silicon Carbide through Carbothermal Reduction of Silicon Dioxide," *Journal of Materials Science Letters*, Vol. 16, pp. 702-704 (1997).

12. Clegg, W. J., "Role of Carbon in the Sintering of Boron-Doped Silicon Carbide," *Journal of the American Ceramic Society*, Vol. 83, No. 5, pp. 1039-1043 (2000).

13. Crane, R. L. and Hollenberg, G. W, "Effect of carbon additions on the grain growth and strength of hot pressed silicon carbide," *Silicon Carbide – 1973, Proceedings of the Third International Conference on Silicon Carbide*, University of South Carolina Press, Columbia (1974).

14. Danka, G. and Siberglitt, R., "Comparison of Microwave Hybrid and Conventional Heating of Preceramic Polymers to Form Silicon Carbide and Silicon Oxycarbide Ceramics," *Journal of the American Ceramic Society*, Vol. 83, No. 7, pp. 1617-1625 (2000).

15. de Boer, J. H., Lippens, B. C., Linsen, B. G., Broekhoff, J. C. P., van den Heuvel, A., and Osinga, Th. J., "The *t*-Curve of Multimolecular N_2-Adsorption," *Journal of Colloid and Interface Science*, Vol. 21, pp. 405-414 (1966).

16. Do, D. D, *Adsorption Analysis: Equilibria and Kinetics*, Imperial College Press, London (1998).

17. Endo, M., Kim, Y. A., Hayashi, T., Nishimura, K., Matusita, T., Miyashita, K., and Dresselhaus, M. S., "Vapor-Grown Carbon Fibers (VGFs): Basic Properties and Their Battery Applications," *Carbon*, Vol. 39, pp. 1287-1297 (2001).

18. Fischbach, D. B. and Rorabaugh, M. E., "Glassy Carbon Graphitization: Density Change," *High Temperatures – High Pressures*, Vol. 9, pp. 199-205 (1977).

19. Francis, T. L. and Colbe, R. L., "Creep of polycrystalline silicon carbide," *Journal of the American Chemical Society*, Vol. 51, No. 2, pp. 115-116 (1968).

20. Furuta, T., Sanada, Y., and Honda, H., "Pore Structure of Phenol-Formaldehyde Resin Carbons," *Carbon*, Vol. 7, pp. 512-513 (1969).

21. Gregg, S. J. and Sing, K. S. W., *Adsorption, Surface Area and Porosity*, Academic Press, London (1982).

22. Greskovich, C. and Rosolowski, J. H., "Sintering of Covalent Solids," *Journal of the American Ceramic Society*, Vol. 59, No. 7-8, pp. 336-343 (1976).

23. Guichelaar, P. J., "Archeson Process," in *Carbide, Nitride and Boride Materials Synthesis and Processing*, edited by Weimer, A. W., Chapman & Hall, London pp. 115-128 (1997).

24. Haraguchi, K., Usami, Y., Yamamura, K., and Matsumoto, S., "Morphological Investigation of Hybrid Materials Composed of Phenolic Resin and Silica Prepared by in situ Polymerization," *Polymer*, Vol. 39, No. 25, pp. 6243-6250 (1998).

25. Haraguchi, K., Usami, Y., and Ono, Y., "The Preparation and Characterization of Hybrid Materials Composed of Phenolic Resin and Silica," *Journal of Materials Science*, Vol. 33, pp. 3337-3344 (1998).

26. Hasegawa, I., Nakamura, T., Motojima, S., and Kajiwara, M., "Silica Gel-Phenolic Resin Hybrid Fibres: New Precursors for Continuous β-Silicon Carbide Fibres," *Journal of Materials Chemistry*, Vol. 5, No. 1, pp. 193-194 (1995).

27. Henderson, J. B. and Tant, M. R., "A study of the kinetics of High-Temperature Carbon-Silica Reactions in an Ablative Polymer Composite", *Polymer Composites*, Vol. 4, No. 4, pp. 233-237 (1983).

28. Hojo, J., "Sintering Behavior of Ultrafine Silicon Carbide Powder," in *Silicon Carbide Ceramics 1, Fundamental and Solid Reaction*, edited by Somiya, S. and Inomata, Y., Elsevier Science, England, pp. 149-168 (1991).

29. Huang, D., Ikuhara, Y, Narisawa, M., and Okamura, K., "Characterization of β-Silicon Carbide Powders Synthesized by the Carbothermal Reduction of Silicon Carbide Precursors," *Journal of the American Ceramic Society*, Vol. 81, No. 12, pp. 3173-3176 (1998).

30. Huang, W. L., Cui, S. H., Liang, K. M., Yuan, Z. F., and Gu, S. R., "Evolution of Pore and Surface Characteristics of Silica Xerogels during Calcining," *Journal of Physics and Chemistry of Solids*, Vol. 63, pp. 645-650 (2002).

31. Hulbert, S. F., "Models for Solid-state Reactions in Powdered Compacts: A Review," *Journal of the British Ceramic Society*, Vol. 6, pp. 11 (1969).

32. Jenkins, R. and Snyder, R. L., *Introduction to X-ray Powder Diffractometry*, John Wiley & Sons, Inc., New York (1996).

33. Jung, Y. S., Kwon, O. J., and Oh, S. M., "Formation of Silica-Coated Carbon Powder and Conversion to Spherical β-Silicon Carbide by Carbothermal Reduction", *Journal of the American Ceramic Society*, Vol. 85, No. 8, pp. 2134-2136 (2002).

34. Jura, G. and Harkins, W. D., "An Adsorption Method for the Determination of the Area of a Solid without the Assumption of a Molecular Area, and the Area occupied by Nitrogen Molecules on the Surfaces of Solids," , *The Journal of Chemical Physics*, Vol. 11, No. 9, pp. 431-432 (1943).

35. Kawamura, K., Ozawa, S., and Endo, H. "Volume Expansion of Glass-Like Carbon Upon High Temperature Heat Treatment," *Carbon*, Vol. 41, No. 1, pp. 191-194 (2003).

36. Keller, N., Pham-Huu, C., Roy, S., Ledoux, M. J., Estournes C., and Guille, J., "Influence of the Preparation Conditions on the Synthesis of High Surface Area SiC for Use as a Heterogeneous Catalyst Support," *Journal of Materials Science*, Vol. 34, pp. 3189-3202 (1999).

37. Kevorkijan, V. M., Komac, M., and Kolar D., "Low-Temperature Synthesis of Sinterable SiC Powders by Carbothermal Reduction of Colloidal SiO_2," *Journal of Materials Science*, Vol. 27, No. 10, pp. 2705-2712 (1992).

38. Khalafalla, S. E. and Haas, L. A., "Kinetics of Carbothermal Reduction of Quartz Under Vacuum," *Journal of the American Ceramic Society*, Vol. 55, No. 8, pp. 414-417 (1972).

39. Kingery, W. D., Bowen, H. K., and Uhlmann, D. R., *Introduction to Ceramics*, J. Wiley & Sons Inc., New York (1976).

40. Klinger, N., Strauss, E. L., and Komarek, K. L., "Reactions Between Silica and Graphite," *Journal of the American Ceramic Society*, Vol. 49, No. 7, pp. 369-375 (1966).

41. Ko, T.-H., Kuo, W.-S., and Chang, Y.-H., "Microstructural Changes of Phenolic Resin During Pyrolysis," *Journal of Applied Polymer Science*, Vol. 81, No. 5, pp. 1084-1089 (2001).

42. Krishnarao, R. and Godkhindi, M. M., "Distribution o. in Rice Hulls and its Effect on the Formation of Silicon Carbide," *Ceramics International*, Vol. 18, pp. 243-249 (1992).

43. Krstic, V. D., "Production of Fine, High-Purity Beta Silicon Carbide Powders," *Journal of the American Ceramic Society*, Vol. 75, No. 1, pp. 170-174 (1992).

44. Laine, R. M. and Babonneau, F., "Preceramic Polymer Routes to Silicon Carbide," *Chemistry of Materials*, Vol. 5, pp. 260-279 (1993).

45. Lee, J. G. and Culter, I. B., "Formation of Silicon Carbide from Rice Hulls," *Ceramic Bulletin*, Vol. 54, No. 2, pp. 195-198 (1975).

46. Lee, J. G., Miller, P. D., and Cutler, I. B., "Carbothermal Reduction of Silica," in *Reactivity of Solids*, Edited by Wood, J., Linquist, O., Helgesson, C. and Vannerberg, N.-G., Plenum, New York, pp. 707-711(1977).

47. Li, J., Tian, J., and Dong, L., "Synthesis of SiC Precursors by a Two-step Sol-Gel Process and their Conversion to SiC Powders," *Journal of the European Ceramic Society*, Vol. 77, pp. 1853-1857 (2000).

48. Lorenz, C. D. and Ziff, R. M., "Precise Determination of the Bond Percolation Thresholds and Finite-Size Scaling Corrections for the SC, FCC, and BCC Lattices," *Physical Review E*, Vol. 57, No. 1, pp. 230-236 (1998).

49. Ma, C. C. M., Lin, J.-M., Chang, W.-C., and Ko, T.-H., "Carbon/Carbon Nanocomposites Derived from Phenolic Resin-Silica Hybrid Ceramers: Microstructure, Physical and Morphological Properties," *Carbon*, Vol. 40, pp. 977-984 (2002).

50. Mantell, C. L., *Carbon and Graphite Handbook*, Interscience Publishers, New York, (1968).

51. Martin, H. P., Ecke, R. and Müller, E., "Synthesis of Nanocrystalline Silicon Carbide Powder by Carbothermal Reduction," *Journal of the European Ceramic Society*, Vol. 18, pp. 1737-1742 (1998).

52. Meng, G. W., Cui, Z., Zhang, L. D., and Phillipp, F., "Growth and Characterization of Nanostructured β-SiC via Carbothermal Reduction of SiO_2 Xerogels Containing Carbon Nanoparticles," *Journal of Crystal Growth*, Vol. 209, pp. 801-806 (2000).

53. Miller, P. D., Lee, J. G, and Culter, I. B., "*Journal of the American Ceramic Society*, Vol. 62, No. 3-4, pp. 147-149 (1979).

54. Mizrah, T., Hoffmann, M., and Gauckler, L., "Pressureless Sintering of α-SiC," *Powder metallurgy international*, Vol. 16, No. 5, pp. 217 (1984).

55. Mizutani, T., "Compositional and Structural Modification of Amorphous SiO_2 by Low-Energy Ion and Neutral Beam Irradiation," *Journal of Non-Crystalline Solids*, Vol. 181, pp. 123-134 (1995).

56. Narisawa, M., Okabe, Y., Iguchi, M., Okamura, K., and Kurachi, Y., "Synthesis of Ultrafine SiC Powders from Carbon-Silica Hybridized Precursors with Carbothermic Reduction," *Journal of Sol-Gel Science and Technology*, Vol. 12, pp. 143-152 (1998).

57. Narisawa, M., Yamane, K., Okabe, Y., and Okamura, K., "Carbon-Silica Alloy Material as Silicon Carbide Precursor Prepared from Phenol Resin and Ethyl Silicate," *Journal of Materials Research*, Vol. 14, No. 12., pp. 4587-4593 (1999).

58. Narisawa, M., Okabe, Y., Okamura, K., and Kurachi, Y., "Synthesis of Nano Size Dispersed Silicon Carbide Particles by Firing Inorganic-Organic Hybrid Precursors," *Key Engineering Materials*, Vol. 159-160, pp. 101-106 (1999).

59. Ono, K. and Kurachi, Y., "Kinetic Studies on β-SiC Formation from Homogeneous Precursors," *Journal of Materials Science*, Vol. 26, pp. 388-392 (1991).

60. Patsalas, P. and Logothetidis, S., "Crystallization Effects and Diamond Formation in Amorphous Carbon Films Under Low Energy Ion Beam Irradiation," *Nuclear Instruments and Methods in Physics Research B*, Vol. 178, pp. 247-251 (2001).

61. Patsalas, P., Logothetidis, S., Douka, P., Gioti, M., Stergioudis G., Komninou, Ph., Nouet, G., and Karakostas, Th., "Polycrystalline Diamond Formation by Post-Growth Ion Bombardment of Sputter-Deposited Amorphous Carbon Films," *Carbon*, Vol. 37, pp. 865-869 (1999).

62. Patrick, L. and Choyke, W. J., "Optical Absorption in n-Type Cubic SiC," *Physical Review*, Vol. 186, No. 2, pp. 775-777 (1969).

63. Panigraphi, B. B., Roy, G. G., and Godkhindi M. M., "Kinetic Studies on Production of Silicon Carbide from Rice Husks," *British Ceramic Transactions*, Vol. 100, No. 1, pp. 29-34 (2001).

64. Parrill, T. M. and Chung, Y. W., "Surface-analysis of cubic silicon-carbide(001)," *Surface Science*, Vol. 243, No. 1-3, pp. 96-112 (1991).

65. Perrotta, A. J., Grubbs, D. K., Martin, E. S., Dando, N. R., McKinstry, H. A., and Huang, C.-Y., "Chemical Stabilization of β-Cristobalite," *Journal of the American Ceramic Society*, Vol. 72, No. 3, pp. 441-447 (1989).

66. Pham, H. T. M., Akkaya, T., de Boer, C., Visser, C. C. G., and Sarro, P. M., "Electrical and Optical Properties of PECVD SiC Thin Film for Surface Micromachined Devices," *Proceedings of SeSens 2002- Workshop on Semiconductor Sensors*, (2002).

67. Philipp, H. R., "Silicon Dioxide (SiO_2) (Glass)," in *Handbook of Optical Constants of Solids*, edited by Palik, E. D., Academic Press, Orlando, pp. 749-763 (1985).

68. Prochazka, S., "The Role of Boron and Carbon in the Sintering of Silicon Carbide," in *Special Ceramics*, Vol. 6, edited by Popper, P., The British Ceramic Research Association, U.K. (1975).

69. Raman, V., Bahl, O. P., and Dhawan, U., "Synthesis of Silicon Carbide Through the Sol-Gel Process from Different Precursors, " *Journal of Materials Science*, Vol. 30, pp. 2686-2693 (1995).

70. Sacks, M. D., "Effect of Composition and Heat Treatment Conditions on the Tensile Strength and Creep Resistance of SiC-Based Fibers," *Journal of the European Ceramic Society*, Vol. 19, pp.2305-2315 (1999).

71. Sacks, M. D. and Tseng, T.-Y., "Preparation of SiO_2 Glass from Model Powder Compacts: I, Formation and Characterization of Powders, Suspensions, and Green Compacts," *Journal of the American Ceramic Society*, Vol. 67, No. 8, pp. 526-532 (1984).

72. Sacks, M. D. and Tseng, T.-Y., "Preparation of SiO_2 Glass from Model Powder Compacts: II, Sintering," *Journal of the American Ceramic Society*, Vol. 67, No. 8, pp. 532-537 (1984).

73. Schwerdtfeger, K., "The Rate of Silica Reduction in Reducing Gases at 1500^{o}C," *Transactions of the Metallurgical Society of AIME*, Vol. 236, pp. 1152-1156 (1966).

74. Seo, W. S., Koumoto, K., and Arai, S., "Effects of Boron, Carbon, and Iron Content on the Stacking Fault Formation during Synthesis of β-SiC Particles in the System SiO2-C-H2", *Journal of the American Ceramic Society*, Vol. 81, No. 5, pp. 1255-1261 (1998).

75. Shimoo, T., "Effect of Carbonaceous Materials on Kinetics of Carbothermic Reduction of SiO_2," *Journal of the Japan Institute of Metals*, Vol. 54, No. 1, pp. 41-47 (1990).

76. Shimoo, T. and Mizutaki, F., "Effect of Particle Size of Carbon on the Reduction Rate of Powdered SiO_2-C Mixtuers," *Journal of the Japan Institute of Metals*, Vol. 53, No. 8, pp. 838-839 (1989).

77. Shimoo, T., Okamura, K., and Hayatsu, T., "Effect of Atmosphere on Pyrolysis of Nicalon," *Journal of Materials Science*, Vol. 31, pp. 4407-4413 (1996).

78. Sing, K. S. W., "Characterization of Adsorbents," in *Adsorption: Science and Technology*, edited by Rodrigues, A. E., LeVan, M. D. and Tondeur, D., Kluwer Academic Publishers, Netherlands, pp. 3-14 (1989).

79. Soraru, G. D., Babonneau, F., and Mackenzif, J. D., "Structural Evolutions from Polycarbosilane to SiC Ceramic," *Journal of Materials Science*, Vol. 25, pp. 3886-3893 (1990).

80. Takahashi, R., Sato, S., Sodesawa, T., Kawakita, M., and Ogura, K., "High Surface-Area Silica with Controlled Pore Size Prepared from Nanocomposite of Silica and Citric Acid," *Journal of Physical Chemistry B*, Vol. 104, pp. 12184-12191 (2000).

81. Tanaka, H. and Kurachi, Y., "Synthesis of β-SiC Powder from Organic Precursors and its sinterability," *Ceramics International*, Vol. 14, pp. 109-115 (1988).

82. Thomas, E. S., Thompson, J. G., Withers, R. L., Sterns, M., Xiao, Y., and Kirkpatrick, R. J., "Further Investigation of the Stabilization of β-Cristobalite," *Journal of the American Ceramic Society*, Vol. 77, No. 1, pp. 49-50 (1994).

83. Tibbetts, G. G., Doll, G. L., Gorkiewicz, D. W., Moleski, J. J., Perry, T. A., Dasch, C. J., and Balogh, M. J., "Physical Properties of Vapor-Grown Carbon Fibers," *Carbon*, Vol. 37, No. 7, pp. 1039-1047 (1993).

84. Underwood, E. E., *Quantitative Stereology*, Addison-Wesley Publishing Company, Reading, MA (1970).

85. Vaßen, R., Kaiser, A., Förster, J., Buchkremer, H. P., and Stover, D., "Densification of Ultrafine SiC Powders," *Journal of Materials Science*, Vol. 31, No. 14, 15, pp. 3623-3637 (1996).

86. van Dejen, F. K., and Metselaar, R., "The Chemistry of the Carbothermal Synthesis of β-SiC: Reaction Mechanism, Reaction Rate and Grain Growth," *Journal of the European Ceramic Society*, Vol. 7, pp. 177-184 (1991).

87. Viscomi, F. and Himmel, L., "Kinetic and Mechanistic Study on the Formation of Silicon Carbide from Silica Flour and Coke Breeze," *Journal of Metals*, No. 6, pp. 21-24 (1978).

88. Vodop'yanov, A. G., Baranov, S. V., and Kozhevnikov, G. N., "Reaction of Silicon Monoxide with Carbon at High Temperature," *Izvestiya Akademii Nauk SSSR, Metally* Vol. 3, pp. 28-31 (1983).

89. Wang, C.A., Sacks, M. D., Staab, G.A., and Cheng, Z., "Solution-based Processing of Nanocrystalline SiC," *Ceramic Engineering and Science Proceedings* Vol. 23, No. 4, pp. 701-709 (2002).

90. Wei, G. C., Kennedy, C. R., and Harris, L. A., "Synthesis of Sinterable SiC Powders by Carbothermic Reduction of Gel-Derived Precursors and Pyrolysis of Polycarbosilane," *Ceramic Bulletin*, Vol. 63, No. 8, pp. 1054-1061 (1984).

91. Weimer, A. W. "Thermochemistry and Kinetics," in *Carbide, Nitride and Boride Materials Synthesis and Processing*, edited by Weimer, A. W., Chapman & Hall, London, pp. 79-113 (1997).

92. Weimer, A. W., Nilsen, K. J., Cochran, G. A., and Roach, R. P., "Kinetics of Carbothermal Reduction Synthesis of Beta Silicon Carbide," *AIChE Journal*, Vol. 39, No. 3, pp. 493-502 (1993).

93. Withers, R. L., Thompson, J. G., and Welberry, T. R., "The Structure and Microstructure of α-Cristobalite and Its Relationship to β-Cristobalite," *Physics and Chemistry of Minerals*, Vol. 16, pp. 517-523 (1989).

94. Yajima, S., Hayashi, J., Omori, M., and Okamura, K. "Development of a Silicon Carbide Fibre with High Tensile Strength," *Nature*, Vol. 261, pp. 683-685 (1976).

95. Zallen, R., *The Physics of Amorphous Solids*, Wiley, New York (1983).